

# 食品暨化妝品安全研究中心

2020年09月01日~2021年08月31日

## 論文集(上)



**長庚科技大學**  
CHANG GUNG UNIVERSITY OF SCIENCE AND TECHNOLOGY



**CHANG GUNG UNIVERSITY OF SCIENCE AND TECHNOLOGY**

長庚科技大學  
食品暨化妝品安全研究中心

2020 年 09 月 01 日~ 2021 年 08 月 31 日

論文集

目 錄

(上冊)

序號	期刊論文	學校主要 負責教師	頁 碼
01	Mykhailenko, O., Petrikaitė, V., Korinek, M., El-Shazly, M., Chen, B. H., Yen, C. H., Hsieh, C. F., Bezruk, I., Dabrišiūtė, A., Ivanauskas, L., Georgiyants, V., & Hwang, T. L. (2021). Bio-guided bioactive profiling and HPLC-DAD fingerprinting of Ukrainian saffron ( <i>Crocus sativus</i> stigmas): Moving from correlation toward causation. <i>BMC Complementary Medicine and Therapies</i> , 21(1): 1-15. doi: 10.1186/s12906-021-03374-3	黃聰龍	1
02	Cheng, W. J., Chiang, C. C., Peng, M. T., Huang, Y. T., Huang, J. L., Chang, S. H., Yang, H. T., Chen, W. C., Kuo, J. J., & Hwang, T. L. (2021). Chronic obstructive pulmonary disease increases the risk of mortality among patients with colorectal cancer: A nationwide population-based retrospective cohort study. <i>International Journal of Environmental Research and Public Health</i> , 18(16): 8742. doi: 10.3390/ijerph18168742	黃聰龍	16



- |    |  |     |    |
|----|--|-----|----|
| 03 | Chao, J., Cheng, H. Y., Chang, M. L., Huang, S. S., Liao, J. W., Cheng, Y. C., Peng, W. H., & Pao, L. H. (2021). Gallic acid ameliorated impaired lipid homeostasis in a mouse model of high-fat diet-and streptozotocin-induced NAFLD and diabetes through improvement of $\beta$ -oxidation and ketogenesis. <i>Frontiers in Pharmacology</i> , 11: 606759. doi: 10.3389/fphar.2020.606759 | 鮑力恒 | 28 |
| 04 | Liu, Y. C., Kuo, R. L., & Shih, S. R. (2020). COVID-19: The first documented coronavirus pandemic in history. <i>Biomedical Journal</i> , 43(4): 328-333. doi: 10.1016/j.bj.2020.04.007  | 施信如 | 42 |
| 05 | Chen, P. J., Kuo, L. M., Wu, Y. H., Chang, Y. C., Lai, K. H., & Hwang, T. L. (2020). BAY 41-2272 attenuates CTGF expression via sGC/cGMP-independent pathway in TGF $\beta$ 1-activated hepatic stellate cells. <i>Biomedicines</i> , 8(9): 330. doi: 10.3390/biomedicines8090330  | 黃聰龍 | 48 |
| 06 | Elzoghby, A. O., Abdelmoneem, M. A., Hassanin, I. A., Abd Elwakil, M. M., Elnaggar, M. A., Mokhtar, S., Fang, J. Y., & Elkhodairy, K. A. (2020). Lactoferrin, a multi-functional glycoprotein: Active therapeutic, drug nanocarrier & targeting ligand. <i>Biomaterials</i> , 263: 120355. doi: 10.1016/j.biomaterials.2020.120355   | 方嘉佑 | 63 |

- 07 Li, S. L., Wu, H. C., Hwang, T. L., Lin, C. H., Yang, S. S., & Chang, H. S. (2020). Phytochemical investigation and anti-inflammatory activity of the leaves of *machilus japonica* var. *kusanoi*. *Molecules*, 25(18): 4149. doi: 10.3390/molecules25184149 黃聰龍 84
  
- 08 Yang, S. C., Tsai, Y. F., Pan, Y. L., & Hwang, T. L. (2020). Understanding the role of neutrophils in acute respiratory distress syndrome. *Biomedical Journal*, 44(4): 439-446. doi: 10.1016/j.bj.2020.09.001 黃聰龍 98
  
- 09 Hung, Y. C., Wang, P. W., Lin, T. Y., Yang, P. M., You, J. S., & Pan, T. L. (2020). Functional redox proteomics reveal that *Salvia miltiorrhiza* aqueous extract alleviates adriamycin-induced cardiomyopathy via inhibiting ROS-dependent apoptosis. *Oxidative Medicine and Cellular Longevity*, 2020: 5136934. doi: 10.1155/2020/5136934 潘台龍 106
  
- 10 Li, J. R., Tsai, S. J., Bai, Y. M., Hsu, J. W., Huang, K. L., Su, T. P., Li, C. T., Lin, W. C., Chen, T. J., Pan, T. L., & Chen, M. H. (2021). Cardiometabolic disease risk among siblings of patients with major depressive disorder. *Journal of Developmental Origins of Health and Disease*, 12(3): 530-535. doi: 10.1017/S2040174420000860 潘台龍 121

- 11 Lin, T. L., Lu, C. C., Lai, W. F., Wu, T. S.,  
Lu, J. J., Chen, Y. M., Tzeng, C. M., Liu, H.  
T., Wei, H., & Lai, H. C. (2021). Role of gut  
microbiota in identification of novel  
TCM-derived active metabolites. *Protein and  
Cell*, 12(5): 394-410. doi:  
10.1007/s13238-020-00784-w  
賴信志 127
  
- 12 Liu, Y. J., Lai, Y. J., Wang, R., Lo, Y. C., &  
Chiu, C. H. (2020). The effect of thermal  
processing on the saponin profiles of  
*momordica charantia* L. *Journal of Food  
Quality*, 2020: 8862020. doi:  
10.1155/2020/8862020  
邱群惠 144
  
- 13 Liu, Z. H., Huang, Y. C., Kuo, C. Y., Kuo, C.  
Y., Chin, C. Y., Yip, P. K., & Chen, J. P.  
(2020). Docosaheptaenoic acid-loaded  
polylactic acid core-shell nanofiber  
membranes for regenerative medicine after  
spinal cord injury: In vitro and in vivo study.  
*International Journal of Molecular Sciences*,  
21(19): 7031. doi: 10.3390/ijms21197031  
陳志平 151
  
- 14 Lu, Y. J., Lan, Y. H., Chuang, C. C., Lu, W.  
T., Chan, L. Y., Hsu, P. W., & Chen, J. P.  
(2020). Injectable thermo-sensitive chitosan  
hydrogel containing CPT-11-loaded  
EGFR-targeted graphene oxide and SLP2  
shRNA for localized drug/gene delivery in  
glioblastoma therapy. *International Journal of  
Molecular Sciences*, 21(19): 7111. doi:  
10.3390/ijms21197111  
陳志平 170

- 15 Liou, C. J., Wu, S. J., Shen, S. C., Chen, L. C., Chen, Y. L., & Huang, W. C. (2020). Phloretin ameliorates hepatic steatosis through regulation of lipogenesis and Sirt1/AMPK signaling in obese mice. *Cell & Bioscience*, 10(1): 1-14. doi: 10.1186/s13578-020-00477-1

黃文忠

198
- 16 Virly., Chiu, C. H., Tsai, T. Y., Yeh, Y. C., & Wang, R. (2020). Encapsulation of  $\beta$ -glucosidase within PVA fibers by CCD-RSM-guided coelectrospinning: A novel approach for specific mogroside sweetener production. *Journal of Agricultural and Food Chemistry*, 68(42): 11790-11801. doi: 10.1021/acs.jafc.0c02513

邱群惠

212
- 17 Ebada, S. S., Al-Jawabri, N. A., Youssef, F. S., El-Kashef, D. H., Knedel, T. O., Albohy, A., Korinek, M., Hwang, T. L., Chen, B. H., Lin, G. H., Lin, C. Y., Aldalaien, S. M., Disi, A. M., Janiak, C., & Proksch, P. (2020). Anti-inflammatory, antiallergic and COVID-19 protease inhibitory activities of phytochemicals from the Jordanian hawksbeard: Identification, structure–activity relationships, molecular modeling and impact on its folk medicinal uses. *RSC Advances*, 10(62): 38128-38141. doi: 10.1039/d0ra04876c

黃聰龍

224

- 18 Lan, M. Y., Hsu, Y. B., Lan, M. C., Chen, J. P., & Lu, Y. J. (2020). Polyethylene glycol-coated graphene oxide loaded with erlotinib as an effective therapeutic agent for treating nasopharyngeal cancer cells. *International Journal of Nanomedicine*, 15: 7569-7582. doi: 10.2147/IJN.S265437 陳志平 238
- 19 Mykhailenko, O., Korinek, M., Ivanauskas, L., Bezruk, I., Myhal, A., Petrikaitė, V., El-Shazly, M., Lin, G. H., Lin, C. Y., Yen, C. H., Chen, B. H., Georgiyants, V., & Hwang, T. L. (2020). Qualitative and quantitative analysis of Ukrainian *Iris* species: A fresh look on their antioxidant content and biological activities. *Molecules*, 25(19): 4588. doi: 10.3390/molecules25194588 黃聰龍 252
- 20 Chiang, C. C., Korinek, M., Cheng, W. J., & Hwang, T. L. (2020). Targeting neutrophils to treat acute respiratory distress syndrome in coronavirus disease. *Frontiers in Pharmacology*, 11: 572009. doi: 10.3389/fphar.2020.572009 黃聰龍 276
- 21 Wong, J., Chiang, Y. F., Shih, Y. H., Chiu, C. H., Chen, H. Y., Shieh, T. M., Wang, K. L., Huang, T. C., Hong, Y. H., & Hsia, S. M. (2020). *Salvia sclarea* L. essential oil extract and its antioxidative phytochemical sclareol inhibit oxytocin-induced uterine hypercontraction dysmenorrhea model by inhibiting the Ca<sup>2+</sup>–MLCK–MLC20 signaling cascade: An ex vivo and in vivo study. *Antioxidants*, 9(10): 991. doi: 10.3390/antiox9100991 邱群惠 290

- 22 Huang, W. C., Liou, C. J., Shen, S. C., Hu, S., Hsiao, C. Y., & Wu, S. J. (2020). Luteolin attenuates IL-1 $\beta$ -induced THP-1 adhesion to ARPE-19 cells via suppression of NF- $\kappa$ B and MAPK pathways. *Mediators of Inflammation*, 2020: 9421340. doi: 10.1155/2020/9421340  
黃文忠 306
  
- 23 Chen, M. H., Pan, T. L., Lin, W. C., Huang, K. L., Hsu, J. W., Li, C. T., Tsai, S. J., Su, T. P., Chen, T. J., & Bai, Y. M. (2021). Bidirectional association between migraine and depression among probands and unaffected siblings: A nationwide population-based study. *Journal of Affective Disorders*, 279: 687-691. doi: 10.1016/j.jad.2020.10.056  
潘台龍 321
  
- 24 Jose, G., Lu, Y. J., Hung, J. T., Yu, A. L., & Chen, J. P. (2020). Co-delivery of CPT-11 and panobinostat with anti-GD2 antibody conjugated immunoliposomes for targeted combination chemotherapy. *Cancers*, 12(11): 3211. doi: 10.3390/cancers12113211  
陳志平 326
  
- 25 Lu, C. S., Lin, C. W., Chang, Y. H., Chen, H. Y., Chung, W. C., Lai, W. Y., Ho, C. C., Wang, T. H., Chen, C. Y., Yeh, C. L., Wu, S., Wang, S. P., & Yang, P. C. (2020). Antimetabolite pemetrexed primes a favorable tumor microenvironment for immune checkpoint blockade therapy. *J Immunother Cancer*, 8(2): 1-16. doi: 10.1136/jitc-2020-001392  
王東弘 351  
陳琦媛



- 26 Liao, H. T., Lai, Y. T., Kuo, C. Y., & Chen, J. P. (2021). A bioactive multi-functional heparin-grafted aligned poly (lactide-co-glycolide)/curcumin nanofiber membrane to accelerate diabetic wound healing. *Materials Science and Engineering C*, 120: 111689. doi: 10.1016/j.msec.2020.111689 陳志平 367
  
- 27 Chang, Y. C., Chiang, C. C., Chang, Y. S., Chen, J. J., Wang, W. H., Fang, L. S., Chung, H. M., Hwang, T. L., & Sung, P. J. (2020). Novel caryophyllane-related sesquiterpenoids with anti-inflammatory activity from *Rumphella antipathes* (Linnaeus, 1758). *Marine Drugs*, 18(11): 554. doi: 10.3390/md18110554 黃聰龍 382
  
- 28 Peng, C. C., Huang, C. Y., Ahmed, A. F., Hwang, T. L., & Sheu, J. H. (2020). Anti-inflammatory cembranoids from a Formosa soft coral *Sarcophyton cherbonnieri*. *Marine Drugs*, 18(11): 573. doi: 10.3390/md18110573 黃聰龍 392
  
- 29 Teng, C. C., Tung, S. Y., Lee, K. C., Lee, K. F., Huang, W. S., Shen, C. H., Hsieh, M. C., Huang, C. Y., Sheen, J. M., & Kuo, H. C. (2021). Novel regulator role of CIL-102 in the epigenetic modification of TNFR1/TRAIL to induce cell apoptosis in human gastric cancer. *Food and Chemical Toxicology*, 147: 111856. doi: 10.1016/j.fct.2020.111856 郭星君 405

- 30 Chiang, C. C., Li, Y. R., Lai, K. H., Cheng, W. J., Lin, S. C., Wang, Y. H., Chen, P. J., Yang, S. H., Lin, C. C., & Hwang, T. L. (2020). Aqueous extract of kan-lu-hsiao-tu-tan ameliorates collagen-induced arthritis in mice by inhibiting oxidative stress and inflammatory responses. *Life*, 10(12): 313. doi: 10.3390/life10120313  
黃聰龍 417
  
- 31 Chen, G. C., Liu, C. H., & Wu, W. C. (2021). Electrochemical immunosensor for serum parathyroid hormone using voltammetric techniques and a portable simulator. *Analytica Chimica Acta*, 1143: 84-92. doi: 10.1016/j.aca.2020.11.045  
劉繼賢 434
  
- 32 Huang, W. C., Ting, N. C., Huang, Y. L., Chen, L. C., Lin, C. F., & Liou, C. J. (2020). *Helminthostachys zeylanica* water extract ameliorates airway hyperresponsiveness and eosinophil infiltration by reducing oxidative stress and Th2 cytokine production in a mouse asthma model. *Mediators of Inflammation*, 2020: 1702935. doi: 10.1155/2020/1702935  
黃文忠 443  
林傳福
  
- 33 Yang, S. C., Hsu, C. Y., Chou, W. L., Fang, J. Y., & Chuang, S. Y. (2020). Bioactive agent discovery from the natural compounds for the treatment of type 2 diabetes rat model. *Molecules*, 25(23): 5713. doi: 10.3390/molecules25235713  
許青雲 458  
方嘉佑

RESEARCH

Open Access



# Bio-guided bioactive profiling and HPLC-DAD fingerprinting of Ukrainian saffron (*Crocus sativus* stigmas): moving from correlation toward causation

Olha Mykhailenko<sup>1†</sup> , Vilma Petrikaitė<sup>2,3†</sup> , Michal Korinek<sup>4,5,6,7\*</sup> , Mohamed El-Shazly<sup>8,9</sup> , Bing-Hung Chen<sup>5,10</sup> , Chia-Hung Yen<sup>4</sup>, Chung-Fan Hsieh<sup>11</sup>, Ivan Bezruk<sup>1</sup> , Asta Dabrišiūtė<sup>2</sup>, Liudas Ivanauskas<sup>12</sup> , Victoriya Georgiyants<sup>1</sup> and Tsong-Long Hwang<sup>6,7,13,14\*</sup>

## Abstract

**Background:** Saffron or stigmas of *Crocus sativus* L. is one of the most valuable food products with interesting health-promoting properties. *C. sativus* has been widely used as a coloring and flavoring agent. Stigmas secondary metabolites showed potent cytotoxic effects in previous reports.

**Methods:** The present study investigated the chemical composition and the cytotoxic effect of Ukrainian saffron crude extracts and individual compounds against melanoma IGR39, triple-negative breast cancer MDA-MB-231, and glioblastoma U-87 cell lines in vitro using MTT assay. Several bioactivity in vitro assays were performed. The chemical profile of the water and hydroethanolic (70%, v/v) crude extracts of saffron stigmas was elucidated by HPLC-DAD analysis.

**Results:** Seven compounds were identified including crocin, picrocrocin, safranal, rutin, apigenin, caffeic acid, ferulic acid. Crocin, picrocrocin, safranal, rutin, and apigenin were the major active constituents of Ukrainian *C. sativus* stigmas. The hydroethanolic extract significantly reduced the viability of MDA-MB-231 and IGR39 cells and the effect was more potent in comparison with the water extract. However, the water extract was almost 5.6 times more active against the U-87 cell line (EC<sub>50</sub> of the water extract against U-87 was 0.15 ± 0.02 mg/mL, and EC<sub>50</sub> of the hydroethanolic extract was 0.83 ± 0.03 mg/mL). The pure compounds, apigenin, and caffeic acid also showed high cytotoxic activity against breast cancer, melanoma, and glioblastoma cell lines. The screening of the biological activities of stigmas water extract (up to 100 µg/mL) including anti-allergic, anti-virus, anti-neuraminidase, and anti-inflammatory effects revealed its inhibitory activity against neuraminidase enzyme by 41%.

\* Correspondence: [michalk@kmu.edu.tw](mailto:michalk@kmu.edu.tw); [htl@mail.cgu.edu.tw](mailto:htl@mail.cgu.edu.tw)

<sup>†</sup>Olha Mykhailenko and Vilma Petrikaitė contributed equally to this work.

<sup>4</sup>Graduate Institute of Natural Products, College of Pharmacy, Kaohsiung Medical University, Kaohsiung 80708, Taiwan

<sup>6</sup>Graduate Institute of Natural Products, College of Medicine, Chang Gung University, Taoyuan 33302, Taiwan

Full list of author information is available at the end of the article



© The Author(s). 2021 **Open Access** This article is licensed under a Creative Commons Attribution 4.0 International License, which permits use, sharing, adaptation, distribution and reproduction in any medium or format, as long as you give appropriate credit to the original author(s) and the source, provide a link to the Creative Commons licence, and indicate if changes were made. The images or other third party material in this article are included in the article's Creative Commons licence, unless indicated otherwise in a credit line to the material. If material is not included in the article's Creative Commons licence and your intended use is not permitted by statutory regulation or exceeds the permitted use, you will need to obtain permission directly from the copyright holder. To view a copy of this licence, visit <http://creativecommons.org/licenses/by/4.0/>. The Creative Commons Public Domain Dedication waiver (<http://creativecommons.org/publicdomain/zero/1.0/>) applies to the data made available in this article, unless otherwise stated in a credit line to the data.

**Conclusions:** The presented results revealed the qualitative and quantitative chemical composition and biological activity of *Crocus sativus* stigmas from Ukraine as a source of natural anticancer and neuraminidase inhibitory agents. The results of the extracts' bioactivity suggested future potential applications of saffron as a natural remedy against several cancers.

**Keywords:** *Crocus sativus*, Stigmas, Crude extract, HPLC, Cytotoxic activity

## Background

Saffron (*C. sativus* stigmas) is one of the most expensive spices that is cultivated in a few countries around the world [1]. The peculiarity of this spice along with its unique color and taste attracted the attention of scientists to investigate its nutritional and therapeutic properties [1, 2]. Saffron was used as a medicinal plant long before its use as a spice [3]. The healing properties of saffron against many human diseases were documented by ancient Mediterranean, Persian, and Arabian civilizations. Since the beginning of the twentieth century, a plethora of studies investigated the chemical and therapeutic properties of saffron using modern analytical, pharmacological, and clinical techniques to confirm its traditional use [2, 3].

The main producing countries of *C. sativus* are Iran, Morocco, and Spain. Italy, India, and France produce fewer quantities [2, 3]. The cultivation area of saffron is limited by environmental factors that affect its ontogenesis. Since 2015, Ukrainian farmers started the widespread cultivation of saffron for food-grade purposes [4]. Climatic conditions including temperature, humidity, light radiation, altitude, and soil conditions are different across Ukraine. These differences may affect the chemical composition and consequently the pharmacological properties of *C. sativus* harvested from different areas in Ukraine. Saffron is gaining popularity in Ukraine not only as a spice but as a medicinal raw material in folk medicine for eye diseases, diabetes, acute respiratory viral diseases, and cancers [5, 6]. According to the international standards (ISO/Technical Specification 3632), saffron stigmas from Ukraine are considered of high quality [4]. However, a complete chemical analysis of saffron cultivated in Ukraine has not yet been performed.

Cancer is one of the most devastating diseases that usually requires treatment with surgery and chemotherapy. These chemotherapeutics are known for dreadful effects on the quality of life and resistance triggering properties [7]. Therefore, there is a continuing need to search for alternative treatments from natural sources to decrease the dependence on chemical therapeutic agents and reduce chemotherapeutics' toxic side effects. Among various uses of saffron, it is also considered a potential antitumor natural remedy [3]. The literature contains encouraging data on the antitumor activity of various

saffron extracts and their components [8, 9], thus our attention was drawn to investigate the effects against some of the less-studied cancer cell lines.

The objective of this study was to compare the phytochemical content of the water and hydroethanolic (70%, v/v) crude extracts of *C. sativus* stigmas. The cytotoxic activity of the extracts and several individual compounds of saffron stigmas was evaluated against human melanoma IGR39, triple-negative breast cancer MDA-MB-231, and glioblastoma U-87 cell lines. Additionally, various bioactivities including antiallergic, anti-inflammatory, anti-viral, or anti-neuraminidase bioactivities of the water extract were assessed.

## Methods

### Reagents and chemicals

Acetonitrile and methanol were of HPLC grade and purchased from Roth GmbH (Karlsruhe, Germany). Reference compounds (crocin, safranal, apigenin, rutin, caffeic acid, ferulic acid, chlorogenic acid, gallic acid) were purchased from ChromaDex (Santa Ana, CA), Sigma-Aldrich (Saint Louis, MO), HWI Analytik GmbH, and Roth GmbH (Karlsruhe, Germany).

### Plant material

*Crocus sativus* L. (*Iridaceae* family) flowers were collected from the plantation in the village Lyubimivka (Kherson region, Ukraine) in November 2019 in accordance with the WHO Guidelines on Good Agricultural and Collection Practices (GACP) [10, 11]. The permission for harvest was obtained from the farmers according to the cooperation agreement. The raw material was collected and identified by Dr. Mykhailenko and the identification was verified by Dr. Gamulya (V.M. Karazin Kharkiv National University, Kharkiv, Ukraine). A specimen was deposited at the Herbarium of V.M. Karazin Kharkiv National University, Ukraine (CWN, voucher specimen No. CWN0056541). The flowers were collected manually, then the stigmas (saffron) were separated and dried for 2–3 h at 50 °C under forced air. Dried stigmas were stored in dark glass jars at 4 °C.

### Preparation of *C. sativus* stigmas extracts

**Water extract of *C. sativus* stigmas.** Saffron was ground in a mortar using a pestle. 5 g of stigmas powder was macerated with hot distilled water (500 ml, 80 °C) [12,

13], kept in a dark place for 24 h, then the extract was filtered. Maceration was repeated 2 more times with the residue under the same conditions. The resulting mixtures were combined, filtered, dried on a rotary evaporator at 80 °C.

*C. sativus* stigmas hydroethanolic (70%, v/v) extract was obtained with the same above method using ethanol/water 70/30 (v/v) (5 g, 500 mL) instead of water as the extracting solvent.

### Sample preparation for analysis

The dried extract (water and hydroethanolic, the weight of each sample was 0.01 g) was extracted with 10 mL of methanol using an ultrasonic bath at room temperature ( $20 \pm 2$  °C) for 30 min. The solution was filtered using a membrane filter (0.45 µm) before use. An aliquot of 10 µL was injected into the HPLC system for analysis. A standard solution was prepared by dissolving reference compounds including crocin, safranal, rutin, caffeic acid, chlorogenic acid, gallic acid, ferulic acid, and apigenin in methanol (1.0 mg/mL). These solutions were used for calibration. All samples were kept at 4 °C before use.

### HPLC conditions

Chromatographic separation of compounds was carried out using an ACE C<sub>18</sub> column (250 mm × 4.6 mm, 5.0 µm; Pennsylvania, USA). Elution was performed at a flow rate of 1 mL/min. The binary solvent system of the mobile phase consists of solvent A (0.1% acetic acid in water) and solvent B (acetonitrile). All solvents were filtered through a 0.23 µm membrane filter after ultrasonic degassing. A gradient elution was applied: 0 min – 95% A and 5% B, 7 min – 95% A and 5% B, 67 min – 0% A and 100% B, 69 min – 95% A and 5% B, 75 min – 95% A and 5% B. The column temperature was constant at 25 °C. The injection volume of the sample solution was 10 µL. The standard solutions including crocin, safranal, rutin, apigenin, caffeic acid, chlorogenic acid, gallic acid, and ferulic acid were used for the calibration of a standard curve using an external standard method. The picrocrocinn content in the extracts was recalculated as

safranal equivalent. Analysis was performed in duplicate. Validation of the HPLC method was performed according to certain parameters [14] including specificity, linearity, precision, the limit of detection (LOD), and limit of quantitation (LOQ) (Tables 1 and 2).

### Apparatus

Liquid chromatography separation was performed using the Shimadzu Nexera X2 LC-30 AD HPLC system (Shimadzu, Japan) formed of a quaternary pump, an on-line degasser, a column temperature controller, the SIL-30 AC autosampler (Shimadzu, Japan); the CTO-20 AC thermostat (Shimadzu, Japan), SPD-M20A diode array detector (DAD). Ultrasonic Cleaner Set as used for ultra-sonication (Wise Clean WUC-A06H, Witeg Labor-technik GmbH, Germany), pH-meter – Knick Electronic Battery-operated pH Meter 911 PH (Portamess, Germany), rotary evaporator (Heidolph 2 WB eco, Laborata400 efficient, Germany).

### Data analysis

All data processing was carried out using LabSolutions Analysis Data System (Shimadzu Corporation). Statistical analysis was performed by one-way analysis of variance (ANOVA) followed by Tukey's multiple comparison test with the software package Prism v.5.04 (GraphPad Software Inc., La Jolla, CA, USA). A *p*-value < 0.05 was considered significant.

### Cell culture

Human melanoma cancer cell line IGR39, human triple-negative breast cancer cell line MDA-MB-231, and human glioblastoma U-87 cell lines were obtained from the American Type Culture Collection (ATCC, Manassas, VA, USA). Cells were grown in DMEM Glutamax medium (Gibco, Carlsbad, CA, USA) containing 10% fetal bovine serum and 1% antibiotic mixture (10,000 U/mL penicillin and 10 mg/mL streptomycin; Gibco). All cells were incubated at 37 °C in a humidified atmosphere containing 5% CO<sub>2</sub>.

**Table 1** Calibration curves of the quantified reference standard compounds

Compound	Calibration curve <sup>a</sup>	Correlation coefficient $r^2$ ( $n = 6$ )	Linear range (µg/mL)	RSD, %	LOD <sup>b</sup> (ng/mL)	LOQ <sup>c</sup> (ng/mL)
1 Caffeic acid	$y = 57,646.8x - 3853.48$	0.9999218	0.72–91.92	1.56	20	60
2 Ferulic acid	$y = 54,955.4x - 638.345$	0.9999592	0.44–56.5	1.60	30	80
3 Rutin	$y = 16,072.5x + 1499.73$	0.9998787	0.16–20.24	1.07	96	290
4 Crocin	$y = 3789.03x + 220.836$	0.999588	1.15–147.2	1.28	100	300
5 Apigenin	$y = 50,138.3x + 5722.97$	0.9998899	0.2–25.76	0.53	25	80
6 Safranal	$y = 39,230.1x - 11,887.2$	0.999529	1.33–42.56	1.35	120	360
7 Gallic acid	$y = 32,880.6x - 612.983$	0.9999718	0.48–61.08	1.31	30	100
8 Chlorogenic acid	$y = 29,930.2x - 538.361$	0.9999502	0.36–46	1.29	20	70

Note: <sup>a</sup>concentration of compound (mg/mL); *y*, peak area; <sup>b</sup>LOD, limit of detection (*S/N* = 3); <sup>c</sup>LOQ, limit of quantification (*S/N* = 10)

**Table 2** Precision and repeatability of the quantified compounds

Compound		Concentrate (µg/mL)	Precision				Repeatability	
			Intra-Day (n = 3)		Inter-Day (n = 3)		Recovery (%)	RSD (%)
			RSD (%)	Accuracy (%)	RSD (%)	Accuracy (%)		
1	Caffeic acid	11.49	1.05	102.02	0.52	98.49	100.01	0.46
		45.96	1.08	98.78	0.67	99.73	99.39	0.99
		91.92	0.64	100.35	0.95	98.17	100.17	0.37
2	Ferulic acid	7.06	0.68	100.22	0.90	98.29	99.11	0.69
		28.25	0.93	98.20	0.29	99.31	99.60	0.57
		56.5	1.22	100.24	0.46	98.28	100.12	0.49
3	Rutin	2.53	1.26	100.35	0.62	100.15	100.18	0.55
		10.12	1.29	101.12	0.80	99.21	100.65	0.92
		20.24	0.76	99.56	1.14	100.94	99.78	0.31
4	Crocic acid	1.23	0.87	102.5	0.80	101.36	101.07	0.85
		18.4	1.25	99.19	0.91	100.37	98.99	1.06
		73.6	1.22	98.97	0.81	100.27	100.29	0.98
5	Apigenin	4	0.74	100.75	0.57	98.76	100.56	0.79
		16	0.89	100.89	0.29	98.62	98.96	0.71
		32	0.88	100.70	0.70	98.03	99.80	1.02
6	Safranal	1.33	0.57	101.53	0.67	101.07	100.27	0.65
		10.64	0.78	98.68	0.53	99.14	99.58	0.77
		42.56	1.02	100.47	0.86	100.12	99.14	1.04
7	Gallic acid	7.65	0.57	99.81	0.75	101.37	101.07	0.65
		30.35	0.78	99.56	0.24	102.14	99.69	0.56
		61.20	1.02	101.53	0.38	101.32	100.09	0.94
8	Chlorogenic acid	5.75	1.31	101.12	0.38	98.40	100.69	0.86
		23	0.42	99.08	0.73	99.43	99.58	1.05
		46	0.96	100.27	0.48	98.24	101.91	0.97

**Cell viability assay**

The cells were treated with saffron extracts and their viability was determined by the MTT assay (Sigma-Aldrich Co.) as described elsewhere [15]. The cells were exposed to various concentrations of the tested extracts (from 1 mg/mL to 31.25 µg/mL), and after measurement of formazan solution absorbance, EC<sub>50</sub> (half-maximal effective concentration of a drug/extract at which 50% of its maximum response is observed) values were calculated.

**Antiallergic activity in RBL-2H3 cells**

A methylthiazole tetrazolium (MTT) assay was used to measure the possible toxic effects of the samples on RBL-2H3 cells as previously described [16]. The maximally tolerated dose of DMSO was 0.5%, not affecting RBL-2H3 cell growth. Triton X-100 (0.5% solution) was used as the positive control causing the death of all cells in a well. The water stigmas extract was then subjected to an anti-allergic degranulation assay based on β-

hexosaminidase release in RBL-2H3 mast cells induced by calcium ionophore (A23187) or antigen (IgE plus DNP-BSA) according to the previous methodology [17, 18]. Briefly, RBL-2H3 cells seeded in the 96-wells plate ( $2 \times 10^4$  cells/well, A23187-induced assay) or 48-wells plate ( $3 \times 10^4$  cells/well, antigen-induced assay) at 37 °C in 5% CO<sub>2</sub> atmosphere for at least 5 h. then they were treated with samples or medium (untreated control) for 20 h. Cells were stimulated by the addition of calcium ionophore A23187 (1 µM) or cross-linking antigen DNP-BSA (100 ng/mL) to previously sensitized cells with anti-DNP IgE (0.1 µg/mL). After 1 h of incubation, the unstimulated cells were either lysed with 0.5% Triton X-100 solution for the total amount of β-hexosaminidase release or left untreated for the spontaneous release of β-hexosaminidase. Then aliquots of the wells' supernatants (50 µL) were incubated with an equal volume (50 µL) of 1 µM of p-NAG (p-nitrophenyl-N-acetyl-β-D-glucosaminide, in 0.1 M citrate buffer, pH 4.5) serving as the substrate for the released β-hexosaminidase. After 1



h of incubation at 37 °C, the reaction was quenched by the addition of 100  $\mu$ L of stop buffer (0.1 M  $\text{Na}_2/\text{NaHCO}_3$ , pH 10.0). Absorbance was measured at 405 nm on a microplate reader and the percentage inhibition of  $\beta$ -hexosaminidase release was calculated.

#### Anti-inflammatory activity in human neutrophils

Blood was taken from healthy human donors using a protocol approved by the Chang Gung Memorial Hospital review board. Neutrophils were isolated following the standard procedure [19]. The inhibition of superoxide anion generation (respiratory burst) was measured based on ferricytochrome *c* reduction as previously described [20]. Briefly, preheated neutrophils ( $6 \times 10^5$  cells·mL<sup>-1</sup>) and 0.5 mg/mL ferricytochrome *c* solution were treated with the tested compounds or DMSO (control) for 5 min, and activated with formyl-methionyl-leucyl-phenylalanine (fMLF, 100 nM)/cytochalasin B (CB, 1  $\mu$ g/mL) for 10 min. The absorbance was continuously monitored at 550 nm using Hitachi U-3010 spectrophotometer with constant stirring (Hitachi Inc., Tokyo, Japan). Calculations were based on the differences in absorbance with and without superoxide dismutase (SOD, 100 U/mL) divided by the extinction coefficient for the reduction of ferricytochrome *c* ( $\epsilon = 21.1/\text{mM}/10 \text{ mm}$ ). Elastase release (i.e., degranulation from azurophilic granules) was evaluated as described before [21]. Briefly, neutrophils were equilibrated with elastase substrate, MeO-Suc-Ala-Ala-Pro-Val-p-nitroanilide (100  $\mu$ M), at 37 °C for 2 min and then incubated with the sample for 5 min. Cells were activated by 100 nM fMLF and 0.5  $\mu$ g/mL CB, and changes in the absorbance at 405 nm corresponding to elastase release were continuously monitored. The results were expressed as the percent of the initial rate of elastase release in the fMLF/CB-activated drug-free control system.

#### Lipid droplet assay

Lipid droplet assay was performed according to a previous method using a BSA-conjugated oleic acid system in Huh7 cells as described previously [22]. Briefly, cells seeded in  $\mu$ Clear® 96-wells plates (Greiner Bio-ONE, Frickenhausen, Germany) were treated with oleic acid and the tested sample or DMSO for 18 h. Paraformaldehyde was used to fix the cells, which were stained with 2  $\mu$ g/mL Hoechst 33342 and 1  $\mu$ g/mL BODIPY® 493/503. High Content Imaging (HCS) instrument was used to take and analyze images of the nuclei and lipid droplets (ImageXpress Micro System, Molecular Devices, Sunnyvale, CA, USA). The diameter settings were 8–25  $\mu$ m for the nuclei and 0.5–2  $\mu$ m for the lipid droplets.

#### NRF2 activity

Nuclear transcription factor NRF2 activity was evaluated in HacaT normal cells and Huh7 cancer cells according to a previous methodology [23]. The cell line HaCaT/ARE (antioxidant response element) was developed using a HaCaT stable cell line carrying a fragment derived from pGL4.37[luc2P/ARE/Hygro] plasmid and the luciferase reporter gene luc2P. The reporter cells were cultured in Dulbecco's Modified Eagle's Medium (DMEM) (Gibco BRL, Grand Island, NY, USA) supplemented with penicillin (100 U/mL), streptomycin (100  $\mu$ g/mL), 10% heat-inactivated fetal bovine serum (HyClone, Logan, UT, USA), and 100  $\mu$ g/mL hygromycin at 37 °C in 5%  $\text{CO}_2$ . The cells were seeded ( $1 \times 10^4$  cells/well) in a 96-wells plate and treated with the sample for 18 h (single measurement). Resazurin (Cayman Chemical, Ann Arbor, MI, USA, final concentration of 0.1 mg/mL) was added and the cells were incubated for an additional 4 h at 37 °C. Fluorescence of the reduced resazurin in the supernatant of the cells (ex/em: 530 nm/590 nm) was detected using a Synergy HT Multi-Mode Reader (BioTek, Winooski, VT, USA) to determine cell viability. The cells were then harvested, and luciferase activity was measured according to the manufacturer's protocol (Promega Corporation, Madison, WI, USA). The luciferase activity was normalized to cell viability.

#### Protective against influenza and enterovirus

The anti-viral assay was performed by cytopathic effects of the extracts on the cells infected by influenza H1N1 [24], and enterovirus D68 [25]. Briefly, the 96-well tissue culture plates were seeded with MDCK cells ( $2 \times 10^4$  per well) or RD cells ( $2 \times 10^4$  cells /well) in E10 medium (DMEM containing 10% FBS, 100 U/mL penicillin (Gibco, USA), 100  $\mu$ g/mL streptomycin (Gibco, USA), 2 mM L-glutamine (L-glutamine) (Gibco, Brazil), 0.1 mM nonessential amino acid mixture (NEAA, Gibco, USA) and incubated under 5%  $\text{CO}_2$  for 16–24 h at 37 °C. Then, the culture medium was withdrawn and the wells were washed once with Dulbecco's phosphate-buffered saline (DPBS). The cells were infected with influenza virus (A/WSN/33) or enteroviruses at a nine-fold median tissue culture infective dose, with or without the addition of the samples. The treated cells were further incubated for 72 h at 37 °C. After 72 h, the medium was removed, and the cells were fixed with 4% paraformaldehyde for 1 h at room temperature. Then, 0.1% crystal violet was used to stain the cells for 20 min at room temperature. The cells density was measured by using a VICTOR3™ multilabel plate reader (PerkinElmer).

#### Neuraminidase activity assay

A baculovirus displayed neuraminidase NA9 on the surface (NA9-Bac) as a pseudotyped influenza virus was

used to evaluate the neuraminidase activity. An appropriate virus load of NA9-Bac was added into a 96-well plate and incubated with the extracts or compounds for 20 min at 37 °C. Then, each well was supplemented with 25 µL of diluted fluorescent MUNANA substrate. After incubation for 30 min at ambient temperature, 150 µL of stop solution was added. The fluorescence intensity was immediately detected using Synergy HT Multi-Mode Microplate Reader (BioTek). Zanamivir, a known neuraminidase inhibitor, was used as a positive control in this assay.

## Results and discussion

According to the reported data, the cytotoxic properties against different cancer cell lines were found for both the water and hydroethanolic extracts of *C. sativus* stigmas [1–3, 7, 9]. However, the research on the cytotoxic properties of *Crocus* spp. extracts against melanoma IGR39, triple-negative breast cancer MDA-MB-231, and glioblastoma U-87 cell lines is still lacking. Therefore, we studied the chemical composition and cytotoxic activity of Ukrainian saffron crude extracts against these cell lines, in addition to other bioactivities screening, to understand the potential applications of this medicinal plant.

### HPLC method validation

A validation study was conducted to demonstrate the applicability of the developed analytical method. The validation was done in terms of specificity, linearity, LOD, LOQ, precision, and recovery according to the International Conference on Harmonization guidelines [14]. The results are summarized in Tables 1 and 2. The regression equation for each reference standard compound, together with the LOD and LOQ values, are shown in Table 1. All the calibration curves showed acceptable linear regression ( $r^2 \geq 0.999$ ). The overall intra-day and interday precision RSDs were not more than 2.0%. The overall stability over 24 h and repeatability were not more than 2.0% for both parameters. The developed analytical method showed excellent precision with overall recovery in the range from 98 to 101% (RSD  $\leq 2.0\%$ ) for all compounds. Therefore, the method was precise, accurate, and sensitive enough for the simultaneous quantitative evaluation of all compounds in *C. sativus* extracts.

The specificity is the ability of a method to discriminate between the study analytes and other constituents in the sample. Specificity was demonstrated by the separation of the analytes from other interfering compounds. The determination of the main compounds in the tested solutions was done by comparing the retention times of the peaks and UV-spectrum with those of the standard

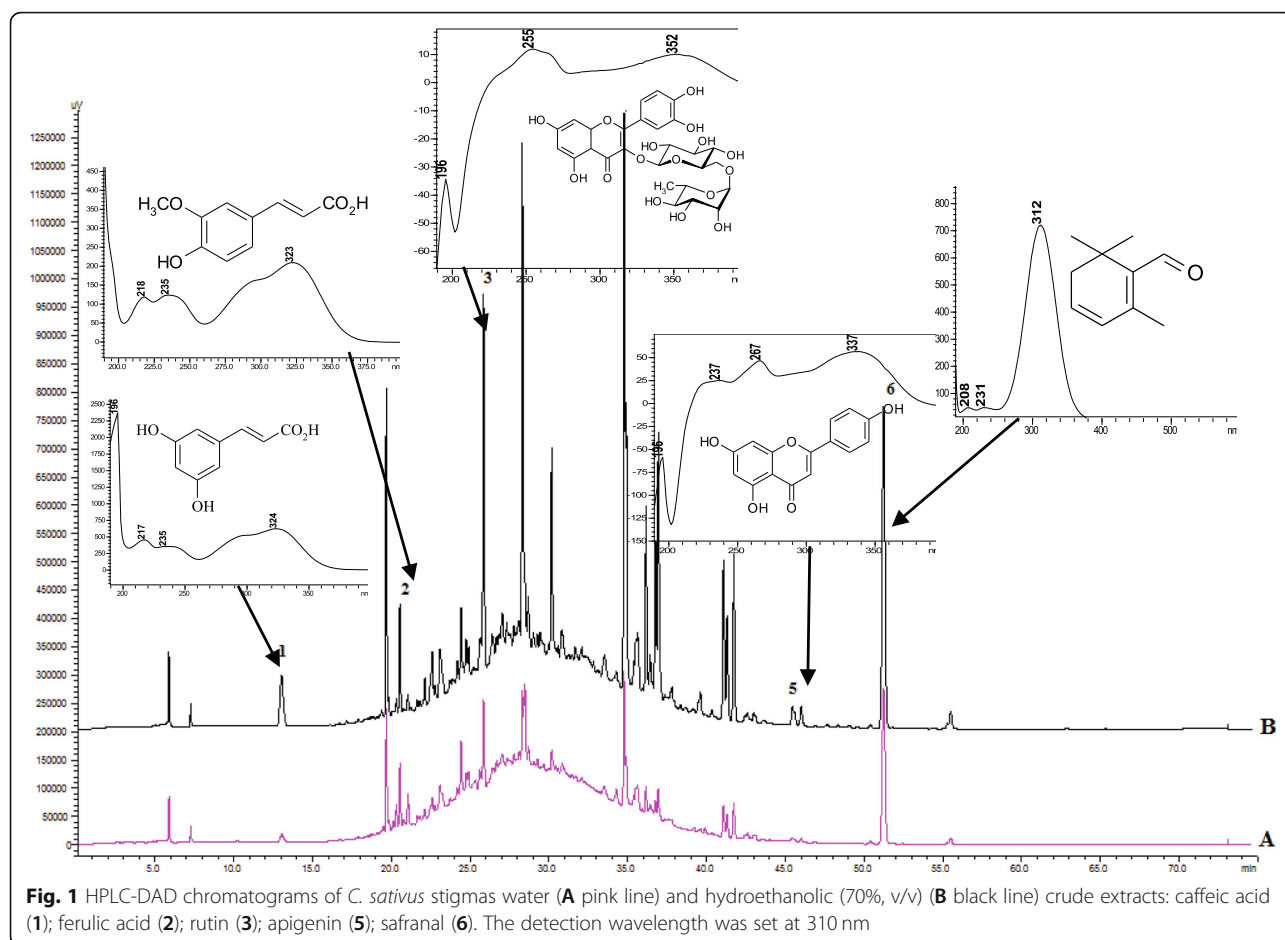
solution. The results showed that the conditions for the fingerprint analysis were repeatable and precise.

### Qualitative and quantitative analysis of the compounds

The extraction of the biologically active components from *C. sativus* stigmas was carried out under optimal conditions by maceration at room temperature in the dark to minimize the decomposition of the phenolic compounds and carotenoids [26]. To identify the composition of the active ingredients in the tested extracts, an HPLC-DAD method was used. The HPLC chromatograms of *Crocus* water and hydroethanolic (70%, v/v) crude extracts are shown in Figs. 1, 2 and 3. The determination of the compounds in the tested extracts was done by comparing the peak retention times and the UV spectra obtained from the chromatogram of the standard solution. The results of the components of the analysis of the crude extracts of Ukrainian *C. sativus* stigmas are presented in Table 3. Among the main and species-specific compounds in *C. sativus* stigmas extracts, the presence of crocin, safranal, and picrocrocin was analyzed. According to the published data, the quantitative content of crocin in the dried *C. sativus* stigmas from Italy, Greece, France, Spain varied depending on the growing conditions and processing methods. It ranged from 6 to 16% up to 30% [27].

In the current study, the content of crocin in Ukrainian saffron was 38 mg/g (3.8%) in the water and 163 mg/g (16.3%) in the hydroethanolic extract, respectively (Table 3). For comparison, the content of crocin (identified as *trans*-crocin bis( $\beta$ -D-gentiobiosyl) ester) in the methanol extracts of the Iranian and Azerbaijan saffron was 45.99 and 48.47 mg/g, respectively, and for the alcoholic extract from the Spanish saffron, the content was 11.95 mg/g [28]. Thus, the content of crocin in Ukrainian samples was at least 2–3 times higher. The high content of secondary metabolites in the Ukrainian saffron extracts might be due to concomitant factors including the location of the cultivation site, altitude, soil type, climate, quality of planting material, irrigation periods, and harvest time. Previously, we investigated the chemical composition of *C. sativus* stigmas from different regions of Ukraine and the results showed high content of crocin, picrocrocin, and safranal in the raw materials [4].

The content of picrocrocin was recalculated as a safranal equivalent and was detected in the hydroethanolic extract reaching the maximum limit described in the literature of 197 mg/g (19.7%). Picrocrocin was detected in a lower concentration in the water extract (62 mg/g). In previous studies, the content of picrocrocin was determined in the range of 7–16% in saffron samples [29]. The content of picrocrocin in saffron methanol extract from Azerbaijan was only 26.93 mg/g. This value was obtained using Waters HPLC system, a Spherisorb



ODS2 column (250 × 4.6 mm internal diameter) and the used mobile phase was a linear gradient of methanol in water from 10 to 100% containing 15% acetonitrile [28]. In the current analysis, we applied the Shimadzu system and ACE C<sub>18</sub> column (250 mm × 4.6 mm, 5.0 μm). The selected gradient system of mobile phases consisted of solvent A (0.1% acetic acid in water) and solvent B (acetonitrile). This system provided the best peak separation. The selection of 257, 330, and 440 nm as the detection wavelengths resulted in an acceptable response and allowed the detection of all three major compounds (crocin, picrocrocin, and safranal), phenolic acids, and flavonoids. The column temperature was maintained at 25 °C throughout the analysis. HPLC fingerprints for *C. sativus* stigmas extracts were developed.

In the studied crude extracts of Ukrainian saffron, the safranal content was 146.6 mg/g in the hydroethanolic and 10.81 mg/g in the stigmas water extract. In previous studies, the content of safranal in saffron raw materials from Spain was 6 mg/g [27, 30], and for the Iranian saffron, the values were 0.07–0.29 mg/g [31]. The analysis of ethanol, water, and methanol-water extracts of saffron stigmas from Saudi Arabia indicated the presence of

lower concentrations of crocin (10–16 mg/g) and safranal (5 mg/g) in comparison with our results [32].

In addition to the esters of crocetin, picrocrocin, and safranal, other biologically active compounds were identified in the Ukrainian saffron extracts. The current research presents the first data on the identification of flavonoid apigenin and rutin in *C. sativus* stigmas. It should be noted that the content of rutin and apigenin in the hydroethanolic *C. sativus* stigmas extract was significantly higher (14.8 mg/g and 8.38 mg/g, respectively) than in the water extract (3.07 mg/g and 0.96 mg/g).

According to the literature data, different phenolic acids such as caffeic, chlorogenic, and gallic were identified in the *C. sativus* stigmas [1]. Ferulic acid was only found in *C. cancellatus* subsp. *damascenus* stigmas [33]. However, in the crude extracts of Ukrainian saffron, chlorogenic and gallic acids were not identified. Ferulic and caffeic acids were found in the hydroethanolic extract of the Ukrainian stigmas extracts at 0.26 and 0.38 mg/g, respectively. In conclusion, the content of all detected constituents in the hydroethanolic extract was much higher than in the water extract.

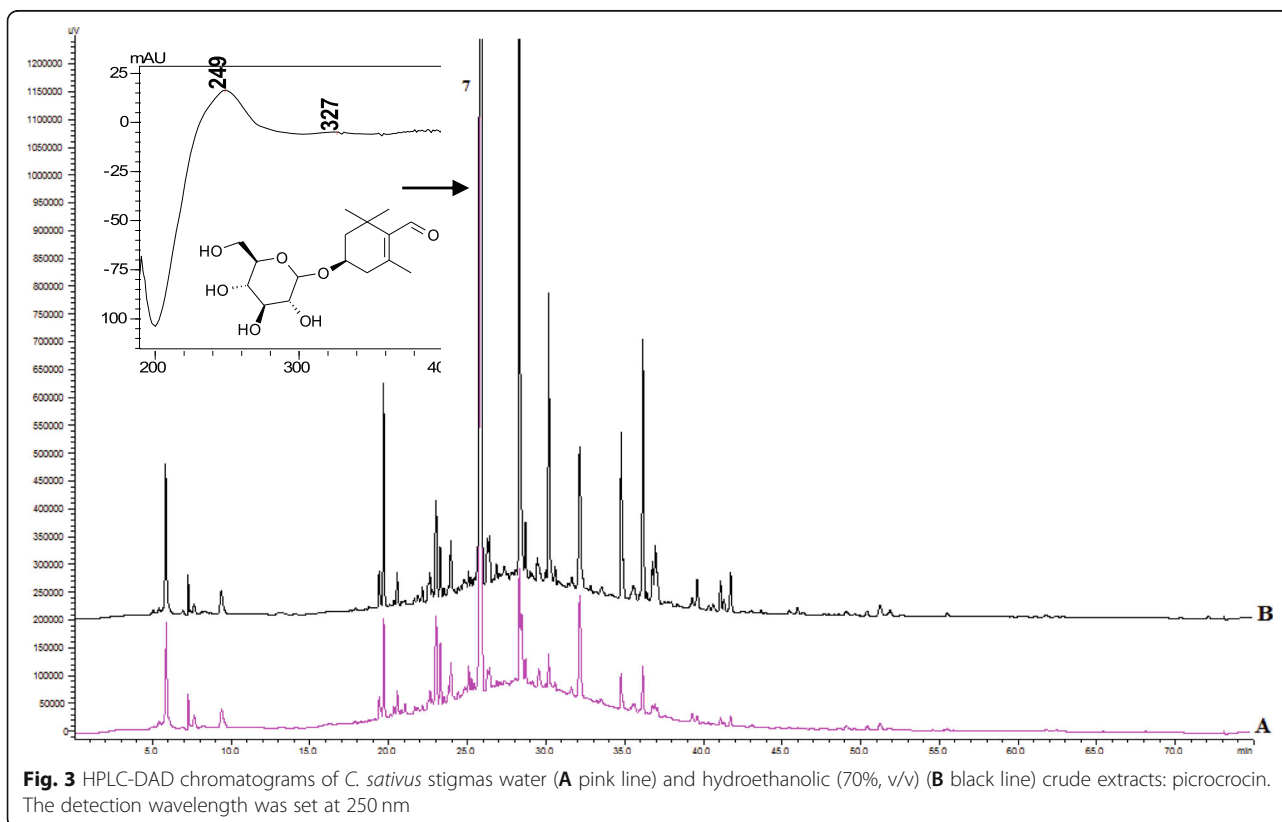
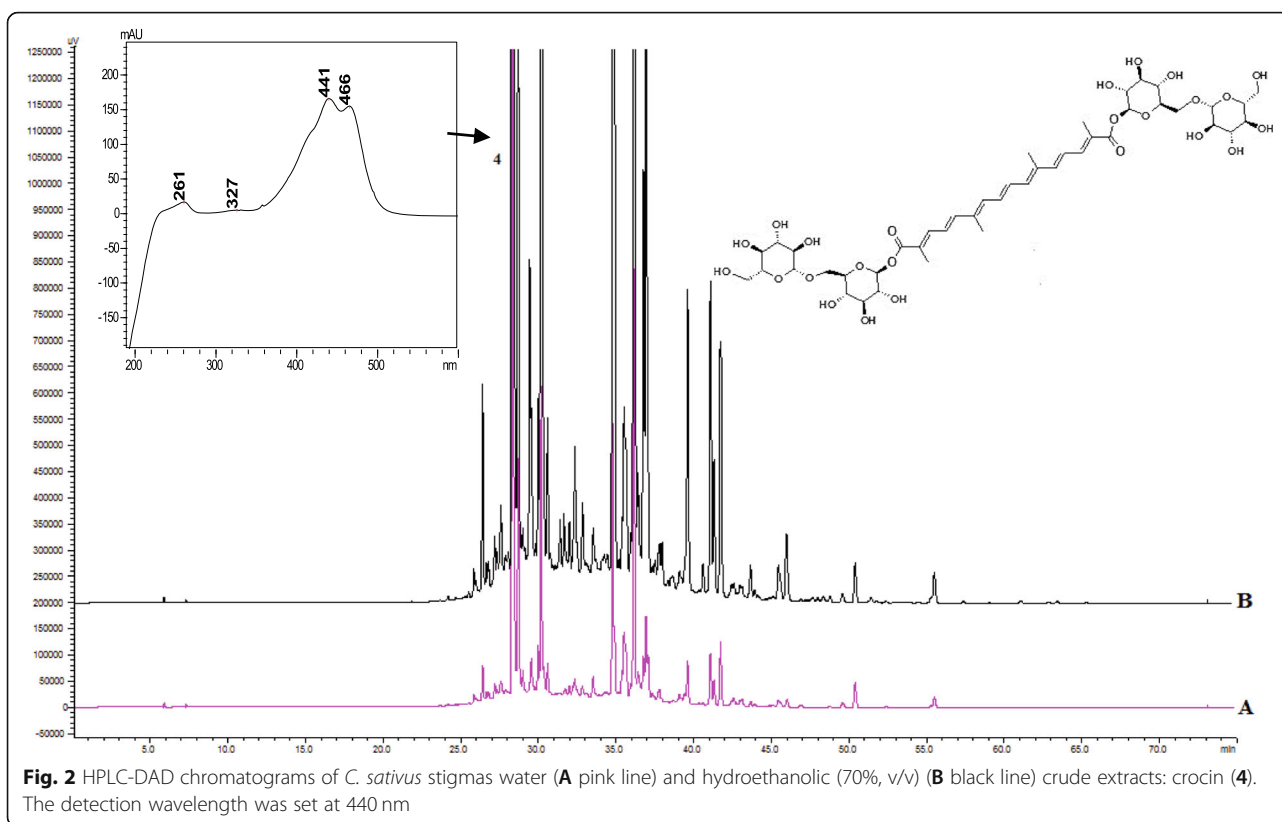


**Table 3** The content of biological active compounds (mg/g dry weight) in *Crocus sativus* stigmas water and hydroethanolic (70%, v/v) crude extracts

Compounds	RT, min	$\lambda$ , nm	UV, $\lambda_{max}$ , nm	Stigmas extract	
				Water	Hydroethanolic
Specific compounds					
Crocin	28.37	440	261, 440, 466	38.27 ± 0.03	163.02 ± 1.16
Picrocrocin	25.88	250	249, 327	62.25 ± 0.10	197.19 ± 5.60
Safranal	55.85	310	231, 312	10.81 ± 0.03	146.66 ± 3.07
Flavonoids					
Rutin	22.48	310	256, 352	3.07 ± 0.02	14.81 ± 0.41
Apigenin	47.90	250	237, 267, 337	0.96 ± 0.01	8.39 ± 0.15
Hydroxycinnamic acids					
Caffeic acid	14.18	310	217, 236, 342	0.11 ± 0.00	0.38 ± 0.01
Ferulic acid	21.64	310	218, 236, 323	0.13 ± 0.03	0.26 ± 0.00

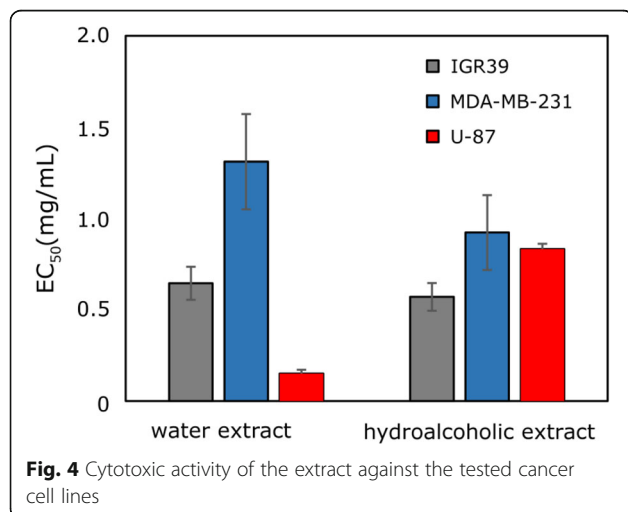
The quantitative analysis of the biologically active compounds in the crude extracts showed that crocin (identified as *trans*-crocin bis( $\beta$ -D-gentiobiosyl) ester), picrocrocin, and safranal were the major components of *C. sativus* stigmas extracts in agreement with the literature data [27–32]. Previous studies highlighted the importance of these compounds for the biological activities of saffron [2, 3, 8, 9]. In addition to these compounds, the presence of flavonoids with their antiproliferative and cytotoxic activities [34] encouraged us to evaluate the cytotoxic activity of Ukrainian saffron extracts.

#### Cytotoxic activity of saffron extracts

The in vitro cytotoxic activity of saffron extracts was investigated against human melanoma IGR39, triple-negative breast cancer MDA-MB-231, and glioblastoma U-87 cell lines (Fig. 4). Hydroethanolic (70%, v/v) crude extract of *C. sativus* stigmas significantly reduced the viability of breast cancer and melanoma cells in comparison with the water extract. However, the water

extract was about 5.6 times more active against the glioblastoma cell line ( $EC_{50}$  of the water extract against U-87 was  $0.15 \pm 0.02$  mg/mL, and  $EC_{50}$  of the hydroethanolic extract was  $0.83 \pm 0.03$  mg/mL). The higher activity of *Crocus* water extract against glioblastoma cell line might be due to the presence of hydrophilic biologically active compounds, such as amino acids, polysaccharides, carboxylic acids [3, 35]. In correlation with our results, several studies on plants such as *Inula helenium* [36], *Usnea longissimi* [37], and *Tragopogon porrifolius* [38] showed that water extracts exhibited higher activity against human U-87 glioblastoma compared with different ethanolic extracts. For instance, the published data [39] indicated that crocetin, a metabolite of major saffron component crocin, exhibited pronounced antitumor properties against U251, U87MG, U373, and U138 glioma cell lines. However, the saffron extract activity against the brain cancer cell line (U-87 cell line) was not reported before.

In other studies, saffron extracts showed antiproliferative activity against several types of cancer cell lines at higher concentrations. For example, *C. sativus* stigmas methanolic extract demonstrated antiproliferative activity against acute lymphoblastic leukemia cells (Jurkat cell line) ( $EC_{50} = 71 \pm 2.50$   $\mu$ g/mL) [40]. *C. sativus* stigmas aqueous extract showed a dose-dependent inhibitory effect on the growth of human transitional cell carcinoma (TCC 5637) and mouse fibroblast (L929) cell lines at concentrations ranging from 400  $\mu$ g/mL to 800  $\mu$ g/mL [41]. Also, the stigmas aqueous extract exhibited a potent dose-dependent antineoplastic effect on highly metastatic murine B16-F10 melanoma cell line (40.7 to 73.6%, at 250 to 1000  $\mu$ g/mL, 72 h treatment) [1]. In another study, the cytotoxic effect of saffron stigmas ethanolic extract was evaluated in HepG2 and HeLa cell lines ( $IC_{50}$  950 and 800  $\mu$ g/mL, respectively, 48 h) [42]. Saffron extract inhibited the





proliferation of HCT-116 cells by 54.5% at a concentration of 1 mg/mL [43]. According to Abd Razak et al. (2017) [44], saffron extract and its main components could affect carcinogenesis in different models in vitro and in vivo.

The saffron demonstrated also other activities related to protection against cancer including radical scavenging activity, anti-mutagenic and immunomodulatory effects [45, 46].

#### Cytotoxic activity of saffron individual compounds

To better understand how the activity could be related to the chemical composition, we evaluated the  $EC_{50}$  values for several major ingredients of saffron extracts (Fig. 5). According to the results of the current study, the most active substances against the tested breast cancer, melanoma, and glioblastoma cell lines were apigenin and caffeic acid with  $EC_{50}$  values ranging from 123.4 to 197.6  $\mu$ M. Other substances (crocin and rutin) did not show cell viability reducing activity even at the highest tested concentrations (up to 1 mM, data not shown). The lack of activity of crocin and rutin in our study may be also associated with the specificity towards the selected cell lines. Previous studies on human and animal cancer cell lines demonstrated the cytotoxic activity of saffron as well as its main constituents (crocins, crocetin, safranal, picrocrocin) against leukemia, carcinoma, sarcoma, stomach, liver, prostate, cervix, ovary, breast, skin, lung, and colorectal cancer cell models, often using high concentrations [2, 8, 47]. For instance, the antiproliferative effects of crocin against several cancer and non-cancer cell lines were reported, however, a very high concentration was needed to reach an  $EC_{50}$  value [48–50]. There is an evidence that high concentrations of crocin (0.625–10 mg/mL) significantly inhibited HL-60 cell proliferation [48], as well as dose-dependently induced apoptosis and cell cycle arrest at the G2/M phase in MDA-MB-231 cells (approx.  $IC_{50}$  5 mg/mL, 48 h) [49]. The authors, however, studied only the effect of an individual compound, crocin, but did not investigate the

cytotoxic activity of saffron stigmas whole extract. The cytotoxic bioactivity of crocin and its metabolite crocetin was compared in lung A549, cervical HeLa, ovarian SK-OV-3, colorectal HCT-116, liver HepG2 cell lines [50]. Crocetin ( $EC_{50}$  = 0.16–0.61 mmol/L), showed 5- to 18-folds higher cytotoxicity than crocin ( $EC_{50}$  = 2.0–5.5 mmol/L) [50] and crocetin further inhibited proliferation glycolytic cancer cell lines A549 and HeLa ( $IC_{50}$  0.11 mM for both cell lines) as well as lactate dehydrogenase (LDH) [51].

Several studies indicated that *C. sativus* extracts exhibited their cytotoxic effect due to the presence of not only crocin, picrocrocin, safranal, but also a plethora of phenolic compounds.

Apigenin is a common dietary flavonoid that showed the highest activity against melanoma IGR39 and breast cancer MDA-MB-231 cell lines ( $EC_{50}$  values were  $131.8 \pm 7.2$   $\mu$ M and  $123.4 \pm 19.0$   $\mu$ M, respectively) in our experiment (Fig. 5). The activity against the U-87 cell line was lower compared with caffeic acid. The results obtained were consistent with the previously described data [52, 53]. Apigenin reduced MDA-MB-231 cell viability at a similar concentration as in our experiments (12, 27, 42, and 49% inhibition at 25  $\mu$ M, 50  $\mu$ M, 75  $\mu$ M and 100  $\mu$ M, respectively) [54]. Apigenin also showed potent antiproliferative effect against human melanoma A375 cell line ( $EC_{50}$  was 33.02  $\mu$ M) [52]. This activity was higher compared to that against IGR39 cells in our experiments which could be explained by compound specificity against different cell lines. Previous literature showed the antitumor efficacy of apigenin against several types of cancer in vitro and in vivo [55]. For instance, apigenin showed antiproliferative properties against the glioblastoma U1242 and U87 cells [56], and human melanoma A375 and C8161 cells in a concentration- and time-dependent manner [57]. Regarding the molecular basis of its activity, apigenin inhibited cancer cell proliferation by triggering cell apoptosis, inducing autophagy, decreasing cancer cell motility, migration, and invasion [55], and regulating immune response [58]. Multiple signaling pathways were modulated by apigenin, including PI3K/AKT, MAPK/ERK, JAK/STAT, NF- $\kappa$ B, and Wnt/ $\beta$ -catenin [55].

In our experiment, caffeic acid showed a similar level of activity against the IGR39 and U-87 cell lines ( $EC_{50}$  values were  $150.5 \pm 11.4$   $\mu$ M and  $152.3 \pm 6.2$   $\mu$ M, respectively), and a slightly lower against the MDA-MB-231 cell line ( $EC_{50}$  was  $197.6 \pm 16.3$   $\mu$ M). According to the literature, caffeic acid reduced cell viability against the MCF-7 cell line ( $EC_{50}$  159  $\mu$ g/mL) [59] and against the HCT15 cell line (approx.  $EC_{50}$  800  $\mu$ M) in time and dose-dependent manner [60]. Caffeic acid previously demonstrated cytotoxic activity against SK-Mel-28 human melanoma [61] as well as hepatocellular carcinoma,

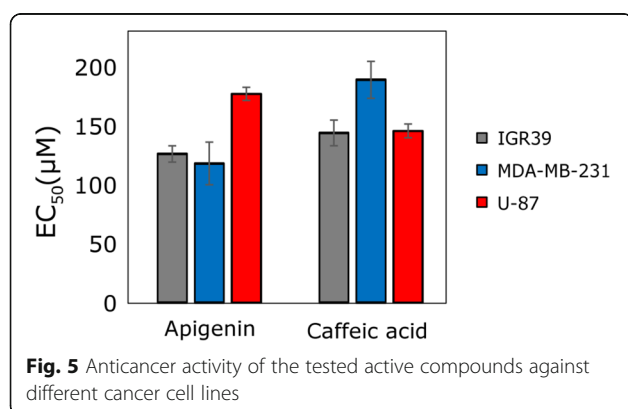




**Table 4** The bioactivity evaluation results of saffron water extract, including the NRF2, neuraminidase, lipid droplets, anti-inflammatory, antiallergic activity, anti-influenza and anti-enterovirus activity

Sample	Relative NRF2 activity <sup>a</sup> in HacaT cell <sup>b</sup> (% mean $\pm$ SD)	Relative NRF2 activity <sup>a</sup> in Huh7 cell <sup>b</sup> (% mean $\pm$ SD)	Neuraminidase inhibition activity <sup>c</sup> (% mean $\pm$ SD)	Lipid droplet inhibition activity <sup>d</sup> (% mean $\pm$ SD)	Superoxide anion generation, human neutrophils <sup>e</sup> (% mean $\pm$ SEM)	Elastase release, human neutrophils <sup>e</sup> (% mean $\pm$ SEM)	A23187-induced degranulation assay, RBL-2H3 cells <sup>f</sup> (% mean $\pm$ SD)	Antigen-induced degranulation assay, RBL-2H3 cells <sup>f</sup> (% mean $\pm$ SD)	Protective activity against influenza H1N1, MDCK cells <sup>g</sup>	Protective activity against enterovirus 68, RD cells <sup>g</sup>
Saffron stigmas (extr. H <sub>2</sub> O)	172.8	132.1	41.0 $\pm$ 5.8	108.7 $\pm$ 14.3	9.0 $\pm$ 1.9**	5.8 $\pm$ 1.3*	5.0 $\pm$ 4.6	20.3 $\pm$ 4.2	inactive	inactive
TBHQ <sup>h</sup>	684.3 $\pm$ 53.3	–	–	–	–	–	–	–	–	–
Luteolin <sup>i</sup>	–	23.8 $\pm$ 0.3	–	–	–	–	–	–	–	–
Zanamivir <sup>j</sup>	–	–	96.8 $\pm$ 0.2	–	–	–	–	–	–	–
TC <sup>k</sup>	–	–	–	9.1 $\pm$ 0.8	–	–	–	–	–	–

<sup>a</sup>Relative luciferase activity (NRF2) was calculated by normalizing luciferase activity to cell viability and presented as the fold to solvent control. Saffron stigmas 100  $\mu$ g/mL

<sup>b</sup>HacaT, a normal skin cell line. Huh7, a liver cancer cell line

<sup>c</sup>Neuraminidase inhibition assay. Saffron stigmas 100  $\mu$ g/mL

<sup>d</sup>Lipid droplet count: the average LD counts/cell of OA were used as a standard for 100% of fatty loading in the Huh7 cell line. Saffron stigmas 100  $\mu$ g/mL

<sup>e</sup>Results are presented as mean  $\pm$  SEM (n = 3) compared with the control (fMLF/CB). \*P < 0.05 and \*\*P < 0.01. Genistein served as the positive control and inhibited 99.7% of superoxide anion generation at 10  $\mu$ g/mL and 101.2 of elastase release at 30  $\mu$ g/mL [23]. Saffron stigmas 10  $\mu$ g/mL

<sup>f</sup>The cytotoxicity of the sample was evaluated by MTT assay (95.0  $\pm$  8.7%). Inhibition of  $\beta$ -hexosaminidase release was evaluated and the results are presented as mean  $\pm$  SD (n = 3) compared to the untreated control (DMSO). Dexamethasone (10 nM) was used as a positive control and inhibited 65.7 and 66.3% of A23187- and antigen-induced  $\beta$ -hexosaminidase release, respectively [23]. Saffron stigmas 100  $\mu$ g/mL

<sup>g</sup>The protective effects were evaluated based on the viability of cells infected by the virus. Saffron stigmas 50  $\mu$ g/mL. Inactive, no significant inhibition

<sup>h</sup>TBHQ, 2-(1,1-dimethylethyl)-1,4-benzenediol, was used as positive control for NRF2 activation. Drug concentration is 10  $\mu$ M

<sup>i</sup>Luteolin, was used as a negative control for NRF2 activation. The drug concentration is 50  $\mu$ M

<sup>j</sup>Zanamivir, was used as a positive control for neuraminidase inhibition. The drug concentration is 1  $\mu$ M

<sup>k</sup>TC, Triacsin C, is an inhibitor of long fatty acyl CoA synthetase and was used as a positive control for lipid droplet inhibition. The drug concentration is 1  $\mu$ M

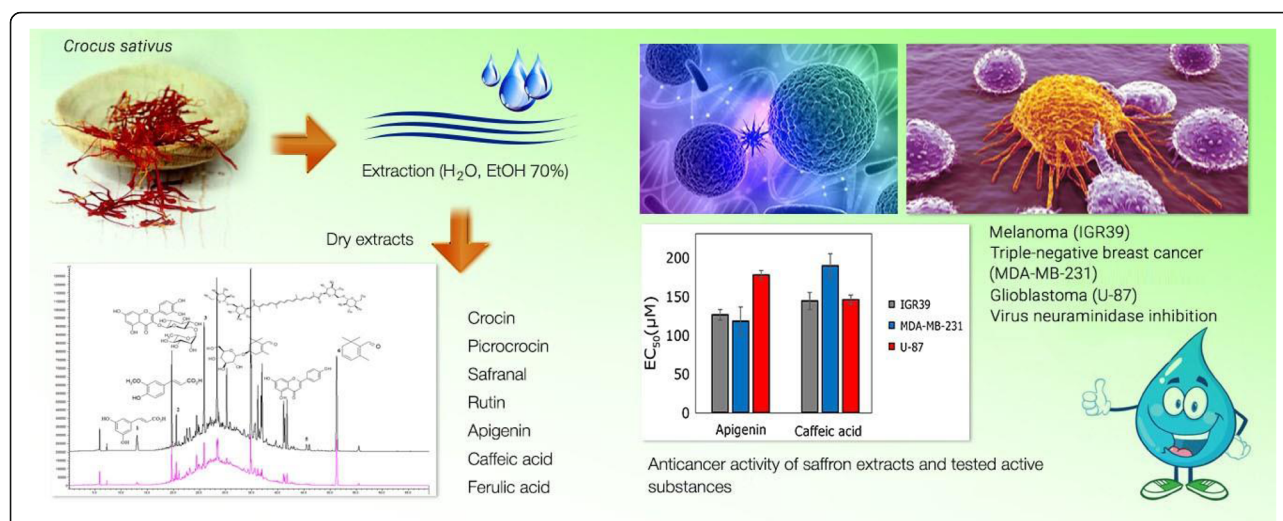


**Fig. 6** Overview of the study results on phytochemical analysis and antitumor and other bioactivities of Ukrainian saffron. Antitumor activity against melanoma, triple-negative breast cancer, and glioblastoma cell lines was evaluated in saffron extracts as well as individual compounds

preventing the exaggerated formation of ROS [62]. It promoted the death of tumor cells through DNA oxidation, as well as angiogenesis reduction of VEGF-induced vascularization and the suppression of MMP-2 and MMP-9 expression, acting as antioxidant and pro-oxidant at the same time [62].

Rutin is a flavonol that demonstrated several pharmacological activities, including antioxidant, cytoprotective, vasoprotective, anticarcinogenic, neuroprotective, and cardioprotective activities [63]. According to different studies, rutin could cause a significant reduction in tumor size justifying its antileukemic potential [64]. Rutin is also known to inhibit cancer cell growth by cell cycle arrest and/or apoptosis along with the inhibition of proliferation, angiogenesis, and/or metastasis in colorectal cell lines [63]. However, in our study rutin did not show a substantial cell growth inhibition towards IGR39, MDA-MB-231, or U-87 cells at concentration up to 1 mM (data not shown).

Previous literature data indicated that saffron extracts and their constituents, crocin, crocetin, and safranal, apigenin or caffeic acid exhibited a selective toxic effect against cancer cells while toxicity against normal cells was negligible in vitro [56, 62, 65, 66] or in vivo [67, 68]. The molecular mechanisms of saffron extract and its active components are not yet fully understood, and further studies are needed to justify the use of saffron extracts in cancer treatment.

#### Bioactivity screening and anti-neuraminidase activity

For the preliminary bioactivity analysis, the water extract of *C. sativus* stigmas was selected aiming to use the most eco-friendly solvent. There is a lack of studies on the anti-neuraminidase, anti-inflammatory, and antiviral

activity of the stigmas extracts. According to the results (Table 4), the water extract (100 μg/mL) inhibited neuraminidase enzymatic activity by 41.0% in comparison with the positive control, zanamivir (97.4% at 1 μM). Phenolic compounds including apigenin, rutin, and caffeic acid were detected in Ukrainian saffron. Previous studies indicated that plant extracts rich in phenolic content inhibited the enzymatic activity of viral neuraminidase [69]. Also, the amino acid composition of the plant extracts was shown to determine the activity against influenza A virus neuraminidase [70, 71]. In our previous investigation, we studied the composition of amino acids in the water extract of *C. sativus* stigmas and found high content of amino acids including tyrosine (326.6 μg/g), methionine (84 μg/g), and alanine (60 μg/g) [72]. The stigmas extract was inactive in the other bioactivity tests (Table 4), including the anti-allergic (degranulation assay, 100 μg/mL), anti-viral (influenza H1N1 and enterovirus D68, 50 μg/mL), anti-inflammatory (respiratory burst and degranulation, 10 μg/mL), NRF2 expression in normal and cancer cell line (100 μg/mL), and lipid droplets assay (100 μg/mL). Our results together with the literature data suggested that the high content of amino acids as well as the presence of phenolic compounds may correlate with the neuraminidase inhibitory effects of *C. sativus* stigmas water extract, while its higher concentration might be required for the other bioactivities.

#### Conclusion

The present study evaluated the cytotoxic activity of *Crocus sativus* stigmas from Ukraine and correlated results with its major constituents, as identified by HPLC analysis (Fig. 6). The water and hydroethanolic (70%, v/v

v) extracts exhibited a cytotoxic effect against melanoma IGR39, triple-negative breast cancer MDA-MB-231, and glioblastoma U-87 cell lines. The water extract of saffron stigmas possessed higher activity than the hydroethanolic extract against U-87 cell lines. This study also described the HPLC method for the qualitative analysis and quantitative determination of apocarotenoids, flavonoids, and phenol carboxylic acids in *C. sativus* stigmas extracts. Moreover, rutin, apigenin, and ferulic acid were identified in *C. sativus* stigmas for the first time. Apigenin and caffeic acid showed activity on the selected cancer lines. The results of the current study indicated the need for further research to determine the mechanisms responsible for the established anti-cancer activity.

#### Abbreviations

HPLC: High performance liquid chromatography; MTT assay: Assessing cell metabolic activity; EC<sub>50</sub>: Half maximal effective concentration; CB: cytochalasin B; DMEM: Dulbecco's modified Eagle's medium; DMSO: Dimethyl sulfoxide; DNP-BSA: Dinitrophenyl-conjugated bovine serum albumin; FBS: Fetal bovine serum; fMLF: formyl-methionyl-leucyl-phenylalanine; HPLC-DAD: High-performance liquid chromatography coupled with diode array detector; NRF2: Nuclear factor erythroid 2-related factor 2; RBL: Rat basophilic leukemia

#### Acknowledgments

The authors are thankful for the financial support provided by the Science Foundation of Lithuanian University of Health Sciences and Chang Gung University. The authors would like to thank the Center for Research Resources and Development, Kaohsiung Medical University for providing instrumentation support.

#### Authors' contributions

O.M., V.P., and M.K. conceived and designed the study; L.I., V.G., and T.-L.H. - Funding acquisition; O.M., M.K., I.B., V.P., A.D., C.-H.Y., C.-F.H., and B.-H.C. - Chemistry and pharmacology investigation; O.M., V.P., and L.I. O.M., V.P., and M.K. - Data analysis and interpretation; O.M., M.K., and M.E. - Writing - original draft; M.E., V.G., and T.H. - Writing - review & editing. V.G. and T.H. - Supervision. The authors read and approved the final manuscript.

#### Funding

This research was funded by the grants from the Ministry of Science and Technology (MOST 106-2320-B-255-003-MY3 and MOST 108-2320-B-255-003-MY3, MOST 109-2320-B-037-004-MY3, MOST 109-2327-B-255-001, MOST 109-2327-B-182-002 and MOST 109-2811-I-006-500), Chang Gung Memorial Hospital (CMRPF1G0241 ~ 3, CMRPF1J0051 ~ 3, and BMRP450), Chang Gung University (104-6576A3), Kaohsiung Medical University (KMU-DK109002-3), Taiwan. The funders had no role in the study design, data collection, and analysis, decision to publish, or preparation of the manuscript.

#### Availability of data and materials

All the materials will be available for research purposes upon request from the corresponding author.

#### Declarations

##### Consent for publication

Not applicable.

##### Ethics approval and consent to participate

The study was conducted according to the guidelines of the Declaration of Helsinki, and with the approval of the Institutional Review Board of Chang Gung Memorial Hospital (IRB No. 201802192A3). Written informed consent was obtained from all subjects involved in the study.

##### Competing interests

The authors have no conflicts of interest to declare.

#### Author details

<sup>1</sup>Department of Pharmaceutical Chemistry, National University of Pharmacy of Ministry of Health of Ukraine, 4-Valentinivska st, Kharkiv 61168, Ukraine. <sup>2</sup>Laboratory of Drug Targets Histopathology, Institute of Cardiology, Lithuanian University of Health Sciences, Sukilėlių pr. 13, LT-50162 Kaunas, Lithuania. <sup>3</sup>Institute of Biotechnology, Life Sciences Center, Vilnius University, Saulėtekio al. 7, LT-10257 Vilnius, Lithuania. <sup>4</sup>Graduate Institute of Natural Products, College of Pharmacy, Kaohsiung Medical University, Kaohsiung 80708, Taiwan. <sup>5</sup>Department of Biotechnology, College of Life Science, Kaohsiung Medical University, Kaohsiung 80708, Taiwan. <sup>6</sup>Graduate Institute of Natural Products, College of Medicine, Chang Gung University, Taoyuan 33302, Taiwan. <sup>7</sup>Research Center for Chinese Herbal Medicine, Research Center for Food and Cosmetic Safety, and Graduate Institute of Health Industry Technology, College of Human Ecology, Chang Gung University of Science and Technology, Taoyuan 33302, Taiwan. <sup>8</sup>Department of Pharmacognosy, Faculty of Pharmacy, Ain-Shams University, Organization of African Unity Street, Abassia, Cairo 11566, Egypt. <sup>9</sup>Department of Pharmaceutical Biology, Faculty of Pharmacy and Biotechnology, German University in Cairo, Cairo 11835, Egypt. <sup>10</sup>The Institute of Biomedical Sciences, National Sun Yat-sen University, Kaohsiung 80424, Taiwan. <sup>11</sup>Department of Biochemistry and Molecular Biology, College of Medicine, Chang Gung University, Taoyuan 33302, Taiwan. <sup>12</sup>Lithuanian University of Health Sciences, Department of Analytical and Toxicological Chemistry, A. Mickevičiaus g. 9, 44307 Kaunas, LT, Lithuania. <sup>13</sup>Department of Anesthesiology, Chang Gung Memorial Hospital, Taoyuan 33305, Taiwan. <sup>14</sup>Department of Chemical Engineering, Ming Chi University of Technology, New Taipei City 24301, Taiwan.

Received: 6 March 2021 Accepted: 29 June 2021

Published online: 21 July 2021

#### References

- Gismondi A, Serio M, Canuti L, Canini A. Biochemical, antioxidant and antineoplastic properties of Italian saffron (*Crocus sativus* L.). *Am J Plant Sci*. 2012;3(11):1573–80. <https://doi.org/10.4236/ajps.2012.311190>.
- Mykhailenko O, Kovalyov V, Goryacha O, Ivanauskas L, Georgiyants V. Biologically active compounds and pharmacological activities of species of the genus *Crocus*, A review. *Phytochem*. 2019;162:56–89. <https://doi.org/10.1016/j.phytochem.2019.02.004>.
- Mykhailenko O, Lesyk R, Finiuk N, Stoika R, Yushchenko T, Ocheretnyuk A, et al. *In vitro* anticancer activity screening of *Iridaceae* plants. *J Appl Pharm Sci*. 2020;10:59–63.
- Mykhailenko O, Desenko V, Ivanauskas L, Georgiyants V. Standard operating procedure of Ukrainian saffron cultivation according with good agricultural and collection practices to assure quality and traceability. *Ind Crop Prod*. 2020;151:112376–87. <https://doi.org/10.1016/j.indcrop.2020.112376>.
- Shatalova OM, Mykhailenko OO. The experimental study of anti-inflammatory activity of extracts from the plants of *Iridaceae* family. *Ukr Biopharm J*. 2019;1:39–43.
- Dwyer AV, Whitten DL, Hawrelak JA. Herbal medicines, other than St. John's wort, in the treatment of depression: a systematic review. *Altern Med Rev*. 2011;16(1):40–9.
- Lang-Schwarz C, Melcher B, Haumaier F, Schneider-Fuchs A, Lang-Schwarz K, Krugmann J, et al. Budding, tumor-infiltrating lymphocytes, gland formation, scoring leads to new prognostic groups in World Health Organization low-grade colorectal cancer with impact on survival. *Hum Pathol*. 2019;89:81–9. <https://doi.org/10.1016/j.humpath.2019.04.006>.
- Mzabri I, Addi M, Berrichi A. Traditional and modern uses of saffron (*Crocus sativus*). *Cosmetics*. 2019;6(4):63–74. <https://doi.org/10.3390/cosmetics6040063>.
- Samarghandian S, Borji A. Anticarcinogenic effect of saffron (*Crocus sativus* L.) and its ingredients. *Pharm Res*. 2014;6:99–107.
- WHO guidelines on good agricultural and collection practices (GACP) for Medicinal Plants. Switzerland: World Health Organization; 2003. p. 1–72. <http://apps.who.int/iris/bitstream/handle/10665/42783/9241546271.pdf?sequence=1>. Accessed 15 July 2021.
- Guideline on good agricultural and collection practice (GACP) for starting materials of herbal origin. European medicines for human use. London: EMA; 2006. p. 1–11. [https://www.ema.europa.eu/en/documents/scientific-guideline/guideline-good-agricultural-collection-practice-gacp-starting-materials-herbal-origin\\_en.pdf](https://www.ema.europa.eu/en/documents/scientific-guideline/guideline-good-agricultural-collection-practice-gacp-starting-materials-herbal-origin_en.pdf). Accessed 15 July 2021.

12. Atyane LH, Ben El Caid M, Serghini MA, Elmaimouni L. Influence of different extraction methods and the storage time on secondary metabolites of saffron. *Int J Eng Res Technol*. 2017;6:65–9.
13. Jafari SM, Tsimidou MZ, Rajabi H, Kyriakoudi. Saffron: Science, Technology and Health. 1st Ed. Chapter 16: A. Bioactive ingredients of saffron: extraction, analysis, applications. Sawston: In Woodhead Publishing Series in Food Science, Technology and Nutrition; 2020. p. 261–90. <https://doi.org/10.1016/B978-0-12-818638-1.00016-2>.
14. Q2 (R1) Validation of Analytical Procedures: Text and Methodology. CPMP/ICH/381/95, European Medicines Agency. 1995;1–15. [https://www.ema.europa.eu/en/documents/scientific-guideline/ich-q-2-r1-validation-analytical-procedures-text-methodology-step-5\\_en.pdf](https://www.ema.europa.eu/en/documents/scientific-guideline/ich-q-2-r1-validation-analytical-procedures-text-methodology-step-5_en.pdf). Accessed 15 July 2021.
15. Vilickiyte G, Raudone L, Petrikaite V. Phenolic fractions from *Vaccinium vitis-idaea* L. and assessment of their antioxidant and anticancer activities. *Antioxidants*. 2020;9(12):1261–81. <https://doi.org/10.3390/antiox9121261>.
16. Korinek M, Chen KM, Jiang YH, El-Shazly M, Stocker J, Chou CK, et al. Anti-allergic potential of *Typhonium blumei*: inhibition of degranulation via suppression of PI3K/PLC $\gamma$ 2 phosphorylation and calcium influx. *Phytomedicine*. 2016;23(14):1706–15. <https://doi.org/10.1016/j.phymed.2016.10.011>.
17. Chen BH, Wu PY, Chen KM, Fu TF, Wang HM, Chen CYJ. Antiallergic potential on RBL-2H3 cells of some phenolic constituents of *Zingiber officinale* (ginger). *Nat Prod*. 2009;72(5):950–3. <https://doi.org/10.1021/np800555y>.
18. Korinek M, Tsai YH, El-Shazly M, Lai KH, Backlund A, Wu SF, et al. Anti-allergic hydroxy fatty acids from *Typhonium blumei* explored through ChemGPS-NP. *Front Pharmacol*. 2017;8:356–36. <https://doi.org/10.3389/fphar.2017.00356>.
19. Boyum A. Isolation of mononuclear cells and granulocytes from human blood. Isolation of monuclear cells by one centrifugation, and of granulocytes by combining centrifugation and sedimentation at 1 g. *Scand J Clin Lab Invest Suppl*. 1968;97:77–89.
20. Korinek M, Hsieh PS, Chen YL, Hsieh PW, Chang SH, Wu YH, et al. Randialic acid B and tomentosolic acid block formyl peptide receptor 1 in human neutrophils and attenuate psoriasis-like inflammation *in vivo*. *Biochem Pharmacol*. 2021;190:114596. <https://doi.org/10.1016/j.bcp.2021.114596>.
21. Tsai YF, Chu TC, Chang WY, Wu YC, Chang FR, Yang SC, et al. 6-Hydroxy-5,7-dimethoxy-flavone suppresses the neutrophil respiratory burst via selective PDE4 inhibition to ameliorate acute lung injury. *Free Radic Biol Med*. 2017;106:379–92. <https://doi.org/10.1016/j.freeradbiomed.2017.03.002>.
22. Yen CH, Chang HS, Yang TH, Wang SF, Wu HC, Chen YC, et al. High-content screening of a Taiwanese indigenous plant extract library identifies *Syzygium simile* leaf extract as an inhibitor of fatty acid uptake. *Int J Mol Sci*. 2018;19(7):2130–45. <https://doi.org/10.3390/ijms19072130>.
23. Mykhailenko O, Korinek M, Ivanauskas L, Bezruk I, Myhal A, Petrikaitė V, et al. Qualitative and quantitative analysis of Ukrainian *Iris* species: a fresh look on their content and biological activities. *Molecules*. 2020;25(19):4588–612. <https://doi.org/10.3390/molecules25194588>.
24. Sethy B, Hsieh CF, Lin TJ, Hu PY, Chen YL, Lin CY, et al. Design, synthesis, and biological evaluation of itaconic acid derivatives as potential anti-influenza agents. *J Med Chem*. 2019;62(5):2390–403. <https://doi.org/10.1021/acs.jmedchem.8b01683>.
25. Hsieh CF, Jheng JR, Lin GH, Chen YL, Ho JY, Liu CJ, et al. Rosmarinic acid exhibits broad anti-enterovirus A71 activity by inhibiting the interaction between the five-fold axis of capsid VP1 and cognate sulfated receptors. *Emerg Microbes Infect*. 2020;9(1):1194–205. <https://doi.org/10.1080/22221751.2020.1767512>.
26. Sánchez-Vioque R, Santana-Méridas O, Polissio M, Vioque J, Astraka K, Alaiz M, et al. Polyphenol composition and *in vitro* antiproliferative effect of corn, tepal and leaf from *Crocus sativus* L. on human colon adenocarcinoma cells (Caco-2). *J Funct Foods*. 2016;24:18–25. <https://doi.org/10.1016/j.jff.2016.03.032>.
27. Ordoudi SA, Tsimidou MZ. Production practices and quality assessment of food crops. Dordrecht: Springer; 2004.
28. Caballero-Ortega H, Pereda-Miranda R, Riverón-Negrete L, Hernández JM, Medécigo-Ríos M, Castillo-Villanueva A, et al. Chemical composition of saffron (*Crocus sativus* L.) from four countries. *Acta Hort*. 2004;650:321–6.
29. del Campo CP, Carmona M, Maggi L, Kanakis CD, Anastasaki EG, Tarantilis PA, et al. Picrocrocins content and quality categories in different (345) worldwide samples of saffron (*Crocus sativus* L.). *J Agric Food Chem*. 2010;58(2):1305–12. <https://doi.org/10.1021/jf903336t>.
30. Valle García-Rodríguez M, López-Córcoles H, Alonso GL, Pappas CS, Polissio MG, Tarantilis PA. Comparative evaluation of an ISO 3632 method and an HPLC-DAD method for safranal quantity determination in saffron. *Food Chem*. 2017;221:838–43. <https://doi.org/10.1016/j.foodchem.2016.11.089>.
31. Hosseinzadeh H, Younesi HM. Antinociceptive and anti-inflammatory effects of *Crocus sativus* L. stigma and petals extracts in mice. *BMC Pharmacol*. 2002;2:1–8.
32. Alam P, Elkholy SF, Hosokawa M, Mahfouz SA, Sharaf-aidin MA. Simultaneous extraction and rapid HPLC based quantification of crocin and safranal in Saffron (*Crocus sativus* L.). *Int J Pharm*. 2016;8:224–7.
33. Loizzo MR, Marrelli M, Pugliese A, Conforti F, Nadjafi F, Menichini F, et al. *Crocus cancellatus* subsp. *damascenus* stigmas, chemical profile, and inhibition of  $\alpha$ -amylase,  $\alpha$ -glucosidase and lipase, key enzymes related to type 2 diabetes and obesity. *J Enzyme Inhib Med Chem*. 2016;31(2):212–8. <https://doi.org/10.3109/14756366.2015.1016510>.
34. Manthey JA, Guthrie N. Antiproliferative activities of citrus flavonoids against six human cancer cell lines. *J Agric Food Chem*. 2002;50(21):5837–43. <https://doi.org/10.1021/jf020121d>.
35. Del Campo CP, Garde-Cerdan T, Sanchez AM, Maggi L, Carmona M, Alonso GL. Determination of free amino acids and ammonium ion in saffron (*Crocus sativus* L.) from different geographical origins. *Food Chem*. 2009;114(4):1542–8. <https://doi.org/10.1016/j.foodchem.2008.11.034>.
36. Koc K, Ozdemir O, Ozdemir A, Dogru U, Turkez H. Antioxidant and anticancer activities of extract of *Inula helenium* (L.) in human U-87 MG glioblastoma cell line. *J Cancer Res Ther*. 2018;14(3):658–61. <https://doi.org/10.4103/0973-1482.187289>.
37. Emsen B, Ozdemir O, Engin T, Togar B, Cavusoglu S, Turkez H. Inhibition of growth of U87MG human glioblastoma cells by *Usnea longissima* ach. *An Acad Bras Cienc*. 2019;91(3):e20180994–1008. <https://doi.org/10.1590/0001-3765201920180994>.
38. Al-Rimawi F, Rishmawi S, Arikat SH, Khalid MF, Warad I, Salah Z. Anticancer activity, antioxidant activity, and phenolic and flavonoids content of wild *Tragopogon porrifolius* plant extracts. *Evid Based Complement Alternat Med*. 2016;2016:9612490–7.
39. Colapietro A, Mancini A, Vitale F, Martellucci S, Angelucci A, Llorens S, et al. Crocetin extracted from saffron shows antitumor effects in models of human glioblastoma. *Int J Mol Sci*. 2020;21(2):423–43. <https://doi.org/10.3390/ijms21020423>.
40. Makhlof H, Diab-Assaf M, Alghabsha M, Tannoury M, Chahine R, Saab AM. *In vitro* antiproliferative activity of saffron extracts against human acute lymphoblastic T-cell human leukemia. *Indian J Trad Knowl*. 2016;15:16–21.
41. Feizzadeh B, Afshari JT, Rakhshandeh H, Rahimi A, Brook A, Doosti H. Cytotoxic effect of saffron stigma aqueous extract on human transitional cell carcinoma and mouse fibroblast. *Urol J*. 2008;5(3):161–7.
42. Tavakkol-Afshari J, Brook A, Mousavi SH. Study of cytotoxic and apoptogenic properties of saffron extract in human cancer cell lines. *Food Chem Toxicol*. 2008;46(11):3443–7. <https://doi.org/10.1016/j.fct.2008.08.018>.
43. Aung HH, Wang CZ, Ni M, Fishbein A, Mehendale SR, Jie JT, et al. Crocin from *Crocus sativus* possesses significant anti-proliferation effects on human colorectal cancer cells. *Exp Oncol*. 2007;29(3):175–80.
44. Abd Razak S, Hamzah MSA, Yee FC, Abdul Kadir MR, Mat Nayan NH. A review on medicinal properties of saffron toward major diseases. *Int J Geogr Inf Syst*. 2017;23:98–116.
45. Bhandari PR. *Crocus sativus* L. (saffron) for cancer chemoprevention, a mini review. *J Tradit Complement Med*. 2015;5(2):81–7. <https://doi.org/10.1016/j.jtcme.2014.10.009>.
46. Baba SA, Malik AH, Wani ZA, Mohiuddin T, Shah Z, Abbas N, et al. Phytochemical analysis and antioxidant activity of different tissue types of *Crocus sativus* and oxidative stress alleviating potential of saffron extract in plants, bacteria, and yeast. *South African J Botany*. 2015;99:80–7. <https://doi.org/10.1016/j.sajb.2015.03.194>.
47. Chrysanthi DG, Dedes PG, Karamanos NK, Cordopatis P, Lamari FN. Crocetin inhibits invasiveness of MDA-MB-231 breast cancer cells via downregulation of matrix metalloproteinases. *Planta Med*. 2011;77(02):146–51. <https://doi.org/10.1055/s-0030-1250178>.
48. Sun Y, Xu HJ, Zhao YX, Wang LZ, Sun LR, Wang Z, et al. Crocin exhibits antitumor effects on human leukemia HL-60 cells *in vitro* and *in vivo*. *Evid Based Complement Alternat Med*. 2013;2013:690164–71.
49. Chen SS, Gu Y, Lu F, Qian DP, Dong TT, Ding ZH, et al. Antiangiogenic effect of crocin on breast cancer cell MDA-MB-231. *J Thorac Dis*. 2019;11(11):4464–73. <https://doi.org/10.21037/jtd.2019.11.18>.



50. Kim SH, Lee JM, Kim SC, Park CB, Lee PC. Proposed cytotoxic mechanisms of the saffron carotenoids crocin and crocetin on cancer cell lines. *Biochem Cell Biol.* 2014;92(2):105–11. <https://doi.org/10.1139/bcb-2013-0091>.
51. Granchi C, Fortunato S, Meini S, Rizzolio F, Caligiuri I, Tuccinardi T, et al. Characterization of the saffron derivative crocetin as an inhibitor of human lactate dehydrogenase 5 in the anticytolytic approach against cancer. *J Agric Food Chem.* 2017;65(28):5639–49. <https://doi.org/10.1021/acs.jafc.7b01668>.
52. Ghitu A, Schwiebs A, Radeke HH, Avram S, Zupko I, Bor A, et al. A comprehensive assessment of apigenin as an antiproliferative, proapoptotic, antiangiogenic and immunomodulatory phytochemical. *Nutrients.* 2019; 11:1–19.
53. Grigalius I, Petrikaite V. Relationship between antioxidant and anticancer activity of trihydroxyflavones. *Molecules.* 2017;22:1–12.
54. Chen D, Landis-Piowar KR, Chen MS, Dou QP. Inhibition of proteasome activity by the dietary flavonoid apigenin is associated with growth inhibition in cultured breast cancer cells and xenografts. *Breast Cancer Res.* 2007;9(6):R80–8. <https://doi.org/10.1186/bcr1797>.
55. Yan X, Qi M, Li P, Zhan Y, Shao H. Apigenin in cancer therapy, anti-cancer effects and mechanisms of action. *Cell Biosci.* 2017;7(1):50–66. <https://doi.org/10.1186/s13578-017-0179-x>.
56. Stump TA, Santee BN, Williams LP, Kunze RA, Heinze CE, Huseman ED, et al. The antiproliferative and apoptotic effects of apigenin on glioblastoma cells. *J Pharm Pharmacol.* 2017;69(7):907–16. <https://doi.org/10.1111/jphp.12718>.
57. Zhao G, Han X, Cheng W, Ni J, Zhang Y, Lin J, et al. Apigenin inhibits proliferation and invasion, and induces apoptosis and cell cycle arrest in human melanoma cells. *Oncol Rep.* 2017;37(4):2277–85. <https://doi.org/10.3892/or.2017.5450>.
58. Cardenas H, Arango D, Nicholas C, Duarte S, Nuovo GJ, He W, et al. Dietary apigenin exerts immune-regulatory activity in vivo by reducing NF- $\kappa$ B activity, halting leukocyte infiltration and restoring normal metabolic function. *Int J Mol Sci.* 2016;17(3):323–40. <https://doi.org/10.3390/ijms17030323>.
59. Rezaei-Seresht H, Cheshomi H, Falanji F, Movahedi F, Hashemian M, Mireskandari E. Cytotoxic activity of caffeic acid and gallic acid against MCF-7 human breast cancer cells, an *in silico* and *in vitro* study. *Avicenna J Phytomed.* 2019;9(6):574–86. <https://doi.org/10.22038/AJP.2019.13475>.
60. Jaganathan SK. Growth inhibition by caffeic acid, one of the phenolic constituents of honey, in HCT15 colon cancer cells. *Sci World J.* 2012;2012: 372345–53.
61. Pelinson LP, Assmann CE, Palma TV, da Cruz IBM, Pillat M, Mânica A, et al. Antiproliferative and apoptotic effects of caffeic acid on SK-Mel-28 human melanoma cancer cells. *Mol Biol Rep.* 2019;46(2):2085–92. <https://doi.org/10.1007/s11033-019-04658-1>.
62. Espindola KMM, Ferreira RG, Narvaez LEM, Silva Rosario ACR, da Silva AHM, Silva AGB, et al. Chemical and pharmacological aspects of caffeic acid and its activity in hepatocarcinoma. *Front Oncol.* 2019;9:541–51. <https://doi.org/10.3389/fonc.2019.00541>.
63. Ganeshpurkar A, Saluja AK. The pharmacological potential of rutin. *Saudi Pharm J.* 2017;25(2):149–64. <https://doi.org/10.1016/j.sjps.2016.04.025>.
64. Lin JP, Yang JS, Lin JJ, Lai KC, Lu HF, Ma CY, et al. Rutin inhibits human leukemia tumor growth in a murine xenograft model *in vivo*. *Environ Toxicol.* 2012;27(8):480–4. <https://doi.org/10.1002/tox.20662>.
65. Hoshyara R, Mollaei H. A comprehensive review on anticancer mechanisms of the main carotenoid of saffron, crocin. *J Pharm Pharmacol.* 2017;69(11): 1419–27. <https://doi.org/10.1111/jphp.12776>.
66. Moradzadeh M, Kalani MR, Avan A. The antileukemic effects of saffron (*Crocus sativus* L.) and its related molecular targets: a mini review. *J Cell Biochem.* 2019;120(4):4732–8. <https://doi.org/10.1002/jcb.27525>.
67. Milajerdi A, Djafarian K, Hosseini B. The toxicity of saffron (*Crocus sativus* L.) and its constituents against normal and cancer cells. *J Nutr Int Metab.* 2016; 3:23–32.
68. Hosseinzadeh H, Sadeghi Shakib S, Khadem Sameni A, Taghiabadi E. Acute and subacute toxicity of safranin, a constituent of saffron, in mice and rats. *Iran J Pharm Res.* 2013;12(1):93–9.
69. Liu J, Zu M, Chen K, Gao L, Min H, Zhuo W, et al. Screening of neuraminidase inhibitory activities of some medicinal plants traditionally used in Lingnan Chinese medicines. *BMC Complement Altern Med.* 2018; 18(1):102–13. <https://doi.org/10.1186/s12906-018-2173-1>.
70. Kobasa D, Wells K, Kawaoka Y. Amino acids responsible for the absolute sialidase activity of the influenza A virus neuraminidase: relationship to growth in the duck intestine. *J Virol.* 2001;75(23):11773–80. <https://doi.org/10.1128/JVI.75.23.11773-11780.2001>.
71. Kati WM, Montgomery D, Maring C, Stoll VS, Giranda V, Chen X, et al. Novel alpha- and beta-amino acid inhibitors of influenza virus neuraminidase. *Antimicrob Agents Chemother.* 2001;45(9):2563–70. <https://doi.org/10.1128/AAC.45.9.2563-2570.2001>.
72. Mykhailenko O, Ivanauskas L, Bezruk I, Lesyk R, Georgiyants V. Comparative investigation of amino acids content in the dry extracts of *Juno bucharica*, *Gladiolus hybrid zefir*, *Iris hungarica*, *Iris variegata* and *Crocus sativus* raw materials of Ukrainian flora. *Sci Pharm.* 2020;88(1):8–21. <https://doi.org/10.3390/scipharm88010008>.

## Publisher's Note

Springer Nature remains neutral with regard to jurisdictional claims in published maps and institutional affiliations.

**Ready to submit your research? Choose BMC and benefit from:**

- fast, convenient online submission
- thorough peer review by experienced researchers in your field
- rapid publication on acceptance
- support for research data, including large and complex data types
- gold Open Access which fosters wider collaboration and increased citations
- maximum visibility for your research: over 100M website views per year

**At BMC, research is always in progress.**

Learn more [biomedcentral.com/submissions](https://biomedcentral.com/submissions)





Article

# Chronic Obstructive Pulmonary Disease Increases the Risk of Mortality among Patients with Colorectal Cancer: A Nationwide Population-Based Retrospective Cohort Study

Wei-Jen Cheng <sup>1,2,3</sup> , Chih-Chao Chiang <sup>3,4</sup>, Meng-Ting Peng <sup>5</sup>, Yu-Tung Huang <sup>6</sup> , Jhen-Ling Huang <sup>6</sup> , Shang-Hung Chang <sup>6,7,8</sup>, Hsuan-Tzu Yang <sup>9</sup>, Wei-Chun Chen <sup>8,10</sup> , Jong-Jen Kuo <sup>1,2,3,11,\*</sup> and Tsong-Long Hwang <sup>12,13,14,15,\*</sup>



**Citation:** Cheng, W.-J.; Chiang, C.-C.; Peng, M.-T.; Huang, Y.-T.; Huang, J.-L.; Chang, S.-H.; Yang, H.-T.; Chen, W.-C.; Kuo, J.-J.; Hwang, T.-L. Chronic Obstructive Pulmonary Disease Increases the Risk of Mortality among Patients with Colorectal Cancer: A Nationwide Population-Based Retrospective Cohort Study. *Int. J. Environ. Res. Public Health* **2021**, *18*, 8742. <https://doi.org/10.3390/ijerph18168742>

Academic Editors: Lorraine Shack and Winson Cheung

Received: 2 August 2021

Accepted: 17 August 2021

Published: 19 August 2021

**Publisher's Note:** MDPI stays neutral with regard to jurisdictional claims in published maps and institutional affiliations.



**Copyright:** © 2021 by the authors. Licensee MDPI, Basel, Switzerland. This article is an open access article distributed under the terms and conditions of the Creative Commons Attribution (CC BY) license (<https://creativecommons.org/licenses/by/4.0/>).

- <sup>1</sup> Center for Traditional Chinese Medicine, Chang Gung Memorial Hospital, Taoyuan 333, Taiwan; misterarren@gmail.com
- <sup>2</sup> School of Traditional Chinese Medicine, College of Medicine, Chang Gung University, Taoyuan 333, Taiwan
- <sup>3</sup> Graduate Institute of Clinical Medical Sciences, College of Medicine, Chang Gung University, Taoyuan 333, Taiwan; moonlight0604@hotmail.com
- <sup>4</sup> Puxin Fengze Chinese Medicine Clinic, Taoyuan 326, Taiwan
- <sup>5</sup> Oncology and Hematology Division, Department of Internal Medicine, Linkou Medical Center, Chang Gung Memorial Hospital, Taoyuan 333, Taiwan; p.mengting@gmail.com
- <sup>6</sup> Center for Big Data Analytics and Statistics, Linkou Medical Center, Chang Gung Memorial Hospital, Taoyuan 333, Taiwan; anton.huang@gmail.com (Y.-T.H.); cratwoy0309@gmail.com (J.-L.H.); afen.chang@gmail.com (S.-H.C.)
- <sup>7</sup> Cardiovascular Division, Department of Internal Medicine, Linkou Medical Center, Chang Gung Memorial Hospital, Taoyuan 333, Taiwan
- <sup>8</sup> College of Medicine, Chang Gung University, Taoyuan 333, Taiwan; lionsmanic@gmail.com
- <sup>9</sup> Division of Thoracic and Cardiovascular Surgery, Department of Surgery, Linkou Medical Center, Chang Gung Memorial Hospital, Taoyuan, 333, Taiwan; b9205018@cgmh.org.tw
- <sup>10</sup> Gynecologic Oncology Service, Department of Obstetrics and Gynecology, Linkou Medical Center, Chang Gung Memorial Hospital, Taoyuan 333, Taiwan
- <sup>11</sup> Graduate Institute of Traditional Chinese Medicine, School of Traditional Chinese Medicine, College of Medicine, Chang Gung University, Taoyuan 333, Taiwan
- <sup>12</sup> Research Center for Chinese Herbal Medicine, Research Center for Food and Cosmetic Safety, Graduate Institute of Health Industry Technology, College of Human Ecology, Chang Gung University of Science and Technology, Taoyuan 333, Taiwan
- <sup>13</sup> Graduate Institute of Natural Products, College of Medicine, Chang Gung University, Taoyuan 333, Taiwan
- <sup>14</sup> Department of Anesthesiology, Chang Gung Memorial Hospital, Taoyuan 333, Taiwan
- <sup>15</sup> Department of Chemical Engineering, Ming-Chi University of Technology, New Taipei 243, Taiwan
- \* Correspondence: kjj308@gmail.com (J.-J.K.); htl@mail.cgu.edu.tw (T.-L.H.); Tel.: +886-3-211-8800 (ext. 5101) (J.-J.K.); +886-3-211-8800 (ext. 5523) (T.-L.H.)

**Abstract:** *Background:* Colorectal cancer (CRC) is the third leading cause of cancer-related deaths in Taiwan. Chronic obstructive pulmonary disease (COPD) is associated with CRC mortality in several population-based studies. However, this effect of COPD on CRC shows no difference in some studies and remains unclear in Taiwan's population. *Methods:* We conducted a retrospective cohort study using Taiwan's nationwide database. Patients newly diagnosed with CRC were identified from 2007 to 2012 via the Taiwan Cancer Registry dataset and linked to the National Health Insurance research database to obtain their medical records. Propensity score matching (PSM) was applied at a ratio of 1:2 in COPD and non-COPD patients with CRC. The 5-year overall survival (OS) was analyzed using the Cox regression method. *Results:* This study included 43,249 patients with CRC, reduced to 13,707 patients after PSM. OS was lower in the COPD group than in the non-COPD group. The adjusted hazard ratio (aHR) for COPD was 1.26 (95% confidence interval (CI), 1.19–1.33). Moreover, patients with CRC plus preexisting COPD showed a higher mortality risk in all stage CRC subgroup analysis. *Conclusions:* In this 5-year retrospective cohort study, patients with CRC and preexisting COPD had a higher mortality risk than those without preexisting COPD, suggesting these patients need more attention during treatment and follow-up.



**Keywords:** colorectal cancer; chronic obstructive pulmonary disease; overall survival; cancer registry; data linkage

## 1. Introduction

Colorectal cancer (CRC) is a common and fatal malignancy, estimated to reach 2.5 million cases worldwide by 2035 [1]. In Taiwan, the incidence of CRC has rapidly increased during the past decades (2460 cases in 1988, 6679 cases in 1998, 11,449 cases in 2008, and 16,525 cases in 2018, as analyzed by the Taiwan Cancer Registry (TwCR)) [2]. The clinical presentations of CRC include no symptoms (the majority in the early stage), symptoms caused by the local tumor (bloody stool, abdominal pain, bowel habit change, or iron-deficiency anemia) [3], and symptoms from metastatic cancer (liver, lung, bone, brain, etc.) [4]. Patients with symptomatic CRC usually have advanced conditions and poor prognoses at diagnosis [5]. Asymptomatic patients with CRC diagnosed by screening have a better risk against death, recurrence, survival, and disease-free interval than those not diagnosed by screening [6]. Since 2008, the Ministry of Health and Welfare (MOHW) of Taiwan has started screening for CRC in the Cancer Care Quality Accreditation Program [2]. However, CRC remained the third leading cause of cancer death, leading to 6436 deaths (12.8% of all cancer deaths, 27.3 deaths per 100,000 population) in 2019, according to the MOHW of Taiwan [7].

Chronic obstructive pulmonary disease (COPD) is a chronic lung disease caused by increased resistance of the small conducting airways leading to emphysematous destruction in the lung. The chronic inflammatory pulmonary response to toxic particles and gases, such as tobacco usage, contributes to airway pathological change in patients with COPD [8,9]. The processes contributing to the small airway obstruction include disruption of the epithelial barrier, accumulation of inflammatory mucous exudates, infiltration of inflammatory cells, and deposition of connective tissue in the small airways [10]. This chronic inflammatory lung disease is found to be a risk factor for CRC incidence in Taiwan [11]. Similarly, in Korea, patients with COPD tend to have CRC, compared to those without COPD, irrespective of smoking habits [12]. As disease prognosis, CRC patients with preexisting COPD also require more medically intensive care, have a higher reoperation rate, and exhibit a worse 30-day mortality rate postoperatively than those without COPD [13]. Moreover, patients with a previous COPD diagnosis have more postoperative complications and adverse outcomes [14,15]. In a longer follow-up of elderly patients of European database with CRC, COPD is a significant comorbidity that causes death [16].

COPD patients and their comorbid conditions are in relation to overall clinical outcomes [17]. A review of epidemiological data revealed that patients with COPD have various comorbidities [18], and cardiovascular diseases are the most frequent comorbidity associated with COPD [19]. Some comorbidities are also associated with tobacco usage or caused by COPD, including coronary heart disease, congestive heart failure, and lung cancer. Other comorbidities, such as systemic venous thromboembolism, diabetes, metabolic syndrome, might be associated with extrapulmonary chronic systemic inflammation in COPD patients [20,21]. Apart from that, several COPD comorbidities, such as cardiovascular diseases and metabolic syndrome, are usually observed in senile people. As a hypothesis suggests, this results from COPD comorbidities sharing the same signaling pathways of aging [22].

However, the CRC genetic and exposure to risk factors may vary in individuals or populations from different ethnical origins. For example, a recent South African cohort study showed contrary results that comorbidities including COPD did not affect the survival of patients with CRC [23]. In the Taiwan population, there has been no research on mortality in patients with CRC plus COPD. Therefore, we conducted a retrospective observational cohort study using the Taiwan National Health Insurance Research Database (NHIRD) to uncover the association between COPD and CRC.

## 2. Materials and Methods

### 2.1. Data Source

This study's data were obtained from the Health and Welfare Data Center (HWDC), including the NHIRD, TwCR data, and Causes of Death data, established by Taiwan's MOHW. The HWDC, an official unit for research, is a data repository site that centralizes the NHIRD and about 70 other health-related databases for data management and analysis. All datasets under HWDC were encrypted, de-identified, and linkable.

The NHIRD was established by Taiwan's National Health Insurance (NHI) Administration and has been used for various research and studies. Taiwan's NHI program was conducted in 1995, which insured 99% of the 23.5 million Taiwanese people. The NHIRD contains encrypted healthcare utilization data from NHI beneficiaries, including information on NHI registry data and inpatient and ambulatory care claims, such as diagnoses of disease, surgical procedure, spending, and detailed prescriptions [24]. The TwCR is a population-based cancer registry system established by the MOHW in 1979 [25]. The TwCR has record completeness of 98.4%, and it has been regarded as one of the world's highest-quality cancer registries [26]. Furthermore, since 2002, the TwCR has established a long-form database including cancer staging, detailed initial treatment, and recurrence information, which researchers have widely used for cancer recurrence studies [27]. In addition, the dataset provided demographic information and medical records of patients for further analysis, such as age, sex, date of birth, death, causes of death, cancer stage, recurrence condition, disease diagnosis, and inpatient and outpatient department prescriptions. The disease diagnosis for the current study was based on the *International Classification of Disease, Ninth Revision, Clinical Modification* (ICD-9-CM) from 2000 to 2015 or the ICD-10-CM from 2016, up to the end of the follow-up period.

### 2.2. Study Design and Population

This study used a retrospective cohort design. The latest data on the TwCR was from 2017, which was within the study duration. To investigate the 5-year overall survival (OS), we included patients newly diagnosed with CRC (ICD-9-CM code 153 and ICD-10-CM code C18) from 2007 to 2012. All medical records were reviewed since 2000 for clarification of COPD and other comorbidities. All patients from this cohort were followed up for five years. The exclusion criteria were invalid demographic data, missing cancer stage, and patients with CRC aged <20 years. COPD was identified as chronic bronchitis (ICD-9-CM code 491 and ICD-10-CM codes J41-J42), emphysema (ICD-9-CM code 492 and ICD-10-CM code J43), bronchiectasis (ICD-9-CM code 494 and ICD-10-CM code J47), and other types of chronic airway obstruction (ICD-9-CM code 496 and ICD-10-CM code J44). The diagnosis of COPD was made by pulmonologists with once hospitalization or twice visiting the outpatient department. Patients with CRC were classified into two groups according to the time of diagnosis of CRC and COPD. Any COPD diagnosed after CRC was excluded to avoid risk interference in this study. The study was conducted in accordance with the guidelines of the Declaration of Helsinki. The study protocol was reviewed by the Institutional Review Board of Chang Gung Memorial Hospital (IRB number 201900249B0) and approved on 4 March 2019. Any electronic information, patient identity, and organization were de-identified to protect patient privacy. Thus, the requirement for informed consent from patients was waived in this study.

### 2.3. Variables Definitions and Outcome Measurement

The major variables of our study cohort included age, sex, tumor-node-metastasis (TNM) cancer stage, and some clinical comorbidities. The pathological TNM stage from TwCR was classified into four categories based on the postoperative TNM classification. The clinical TNM stage was used if the pathological TNM stage was not available. In 2007–2009, the pathological TNM was recorded according to the sixth edition of the *Cancer Staging Manual* created by the American Joint Committee on Cancer (AJCC), whereas the seventh edition was used in 2010–2012. Disease comorbidities included diabetes

mellitus (ICD-9-CM code 250 and ICD-10-CM codes E08-E13), hypertension (ICD-9-CM codes 401–405 and ICD-10-CM codes I10-I16), hyperlipidemia (ICD-9-CM code 272 and ICD-10-CM code E78), prior myocardial infarction (ICD-9-CM codes 410–412 and ICD-10-CM codes I21-I25), congestive heart failure (ICD-9-CM code 428, ICD-10-CM code I50), chronic kidney disease (ICD-9-CM codes 585–586, ICD-10-CM code N18), and liver disease (ICD-9-CM code 570–573, ICD-10-CM code K70-K77). For disease survival analysis, we linked TwCR to the cause of death data, which provided the underlying cause for death as diagnosed by physicians, and we included deaths related to cancer as the outcome events. All other causes of death, such as suicide, homicide, traffic accident caused, or non-cancer-related medical conditions were identified as non-outcome events (censoring).

#### 2.4. Propensity Score Matching

We applied propensity score matching (PSM) to reduce the confounding effects of the two groups [28]. PSM with a ratio of 2:1 in the non-COPD and COPD groups with CRC was conducted based on the propensity scores of the probabilities accessed by age, sex, cancer stage, and comorbidities mentioned above. The matched group was used to examine the effects of COPD on the overall survival of patients with CRC.

#### 2.5. Statistical Analysis

Descriptive data were analyzed before and after PSM to compare COPD and non-COPD patients with CRC stratified by demographic data and comorbidities. Pearson's chi-square test and Student's *t*-test were used for categorical and continuous variables, respectively. We used the Cox-adjusted survival curves to demonstrate the cumulative probability of OS in the two groups. Hazard ratios (HRs) with 95% confidence intervals (CIs) were calculated using the Cox proportional hazards regression model. Multivariate analysis of the Cox model was adjusted for age, sex, cancer stage, and comorbidities. A two-tailed *p*-value < 0.05 indicated a statistically significant difference. Data processing and analysis were conducted using SAS statistical software version 9.4 (SAS Institute Inc., Cary, NC, USA).

### 3. Results

#### 3.1. Patient Characteristics

Between 2007 and 2012, 43,249 patients newly diagnosed with CRC were included in this study. A total of 103 and 2637 patients were excluded because of missing demographic data or missing cancer stage records, respectively. Overall, 19 patients aged <20 years were excluded from this study. According to the COPD records, patients were classified into two groups—before or after CRC was diagnosed. A total of 14,330 (33.13%) of 43,249 patients with CRC suffered from COPD during the follow-up period. Upon excluding COPD after CRC diagnosis, we found that 5736 patients had underlying COPD before being diagnosed with CRC. After PSM at a ratio of 1:2, there were 4569 and 9138 COPD and non-COPD patients, respectively (Figure 1). Before matching, there was a total of 17,052 (53.46%) male and 14,844 (46.54%) female CRC patients. The average age was 65.3 years. The demographic data showed that patients with COPD were older (68.13% were >70 years), and most were male. Hypertension (total 17,659 patients; 55.36%) and diabetes mellitus (total 9168 patients; 28.74%) were the most common comorbidities in patients with CRC. We also found that patients with CRC plus COPD had more major comorbidities, such as prior myocardial infarction (44.61% versus 19.62%, *p* < 0.001), congestive heart failure (19.93% versus 6.02%, *p* < 0.001), chronic kidney disease (9.82% versus 4.79%, *p* < 0.001), and liver diseases (36.65% versus 26.8%, *p* < 0.001), compared with those without COPD. The pathological cancer stage was evenly distributed in stages 1 to 4 in both COPD and non-COPD groups. The characteristics before and after PSM are presented in Table 1.

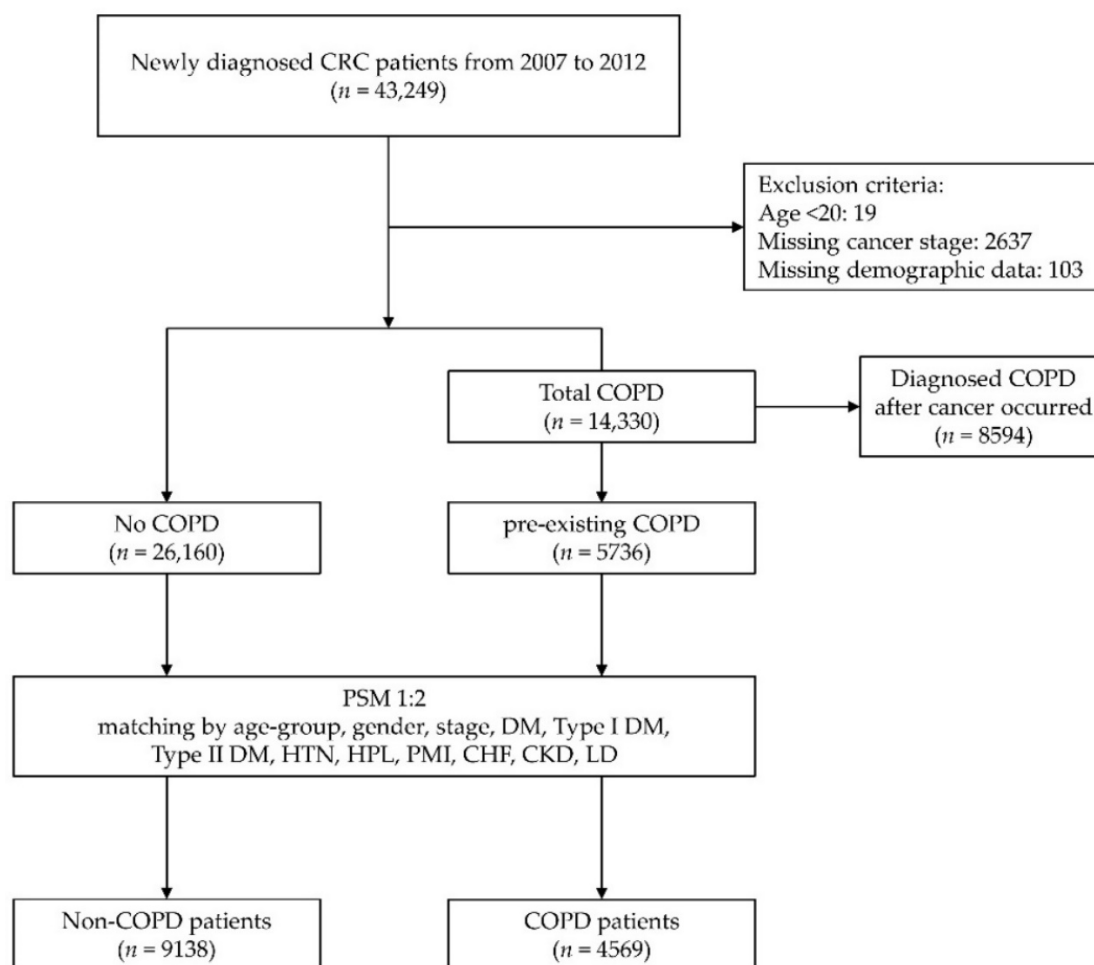


**Figure 1.** Flowchart of the patient enrollment process of this cohort study and variables used in propensity score matching. Abbreviations: CRC, colorectal cancer; COPD, chronic obstructive pulmonary disease; PSM, propensity score matching; DM, diabetes mellitus; HTN, hypertension; HPL, hyperlipidemia; PMI, prior myocardial infarction; CHF, congestive heart failure; CKD, chronic kidney disease; LD, liver disease.

**Table 1.** Clinical characteristics before and after PSM of study patients.

Variables	Before Matching			After Matching <sup>a</sup>		
	Non-COPD	COPD	<i>p</i> -Value *	Non-COPD	COPD	<i>p</i> -Value *
	(n = 26,160)	(n = 5736)		(n = 9138)	(n = 4569)	
<b>Sex</b>			<0.001			0.466
Female	12,506 (47.81)	2338 (40.76)		4102 (44.89)	2021 (44.23)	
Male	13,654 (52.19)	3398 (59.24)		5036 (55.11)	2548 (55.77)	
<b>Age, year (mean ± SD)</b>	63.47 ± 13.52	73.67 ± 11.04	<0.001	70.97 ± 10.72	71.93 ± 11.33	<0.001 <sup>b</sup>
<b>Age-group, year</b>			<0.001			0.950
20–29	174 (0.66)	1 (0.02)		2 (0.02)	1 (0.02)	
30–39	1021 (3.9)	23 (0.40)		48 (0.53)	23 (0.51)	
40–49	2570 (9.82)	120 (2.09)		224 (2.45)	120 (2.63)	
50–59	6602 (25.22)	537 (9.36)		1040 (11.38)	537 (11.75)	
60–69	6703 (25.6)	1147 (20)		2299 (25.16)	1124 (24.6)	
>70	9090 (34.72)	3908 (68.13)		5525 (60.46)	2764 (60.49)	

Table 1. Cont.

Variables	Before Matching			After Matching <sup>a</sup>		
	Non-COPD	COPD	<i>p</i> -Value *	Non-COPD	COPD	<i>p</i> -Value *
	( <i>n</i> = 26,160)	( <i>n</i> = 5736)		( <i>n</i> = 9138)	( <i>n</i> = 4569)	
<b>Cancer stage (pathology)</b>			<0.001			0.506
Stage I	6302 (24.09)	1330 (23.19)		2110 (23.09)	1093 (23.92)	
Stage II	6150 (23.51)	1301 (22.68)		2165 (23.69)	1037 (22.7)	
Stage III	6963 (26.62)	1472 (25.66)		2402 (26.29)	1194 (26.13)	
Stage IV	6745 (25.78)	1633 (28.47)		2461 (26.93)	1245 (27.25)	
<b>Comorbidity</b>						
DM	6900 (26.38)	2268 (39.54)	<0.001	3344 (36.59)	1671 (36.57)	0.980
Type I DM	266 (1.02)	97 (1.69)	<0.001	107 (1.17)	67 (1.47)	0.145
Type II DM	6702 (25.62)	2196 (38.28)	<0.001	3274 (35.83)	1619 (35.43)	0.650
Hypertension	13,233 (50.58)	4426 (77.16)	<0.001	6653 (72.81)	3286 (71.92)	0.273
Hyperlipidemia	8780 (33.56)	2648 (46.16)	<0.001	4066 (44.5)	2050 (44.87)	0.680
Prior myocardial infarction	5132 (19.62)	2559 (44.61)	<0.001	3026 (33.11)	1506 (32.96)	0.857
Congestive heart failure	1576 (6.02)	1143 (19.93)	<0.001	640 (7)	354 (7.75)	0.113
Chronic kidney disease	1252 (4.79)	563 (9.82)	<0.001	587 (6.42)	334 (7.31)	0.051
Liver diseases	7010 (26.8)	2102 (36.65)	<0.001	3002 (32.85)	1494 (32.7)	0.857

\* Pearson's chi-square test for categorical variables and Student's *t*-test for continuous variables. <sup>a</sup> PSM was conducted with a 2:1 ratio on 31,896 patients with CRC by sex, age group, cancer stage, and comorbidities. <sup>b</sup> Absolute mean difference = 0.09, with no significant difference. Abbreviations: PSM, propensity score matching; SD, standard deviation; DM, diabetes mellitus; CRC, colorectal cancer; COPD, chronic obstructive pulmonary disease.

### 3.2. Chronic Obstructive Pulmonary Disease Causes a Higher Mortality Rate in Patients with Colorectal Cancer

Since patients with COPD have more comorbidities and systemic disease, a European Eindhoven Cancer Registry study found that elderly patients with COPD have a worse OS [29]. Our data also revealed that patients with COPD were older and had more comorbidities than patients without COPD (Table 1). To reduce the effects of age and comorbidities between the study groups, we used PSM in a 2:1 ratio to reassign the study groups. After a 2:1 PSM, the variables of the investigated groups did not differ significantly, including gender, age group, cancer stage, and comorbidities (Table 1). Nevertheless, the overall age of the patients with COPD is higher than that of the patients without COPD ( $71.93 \pm 11.33$  versus  $70.97 \pm 10.72$  years old), with a significant *p*-value but a non-significant absolute standard mean difference (ASMD = 0.09).

Figure 2 illustrates the 5-year Cox-adjusted survival curves in the matched cohort. During the 5-year follow-up, patients with CRC and COPD had a significantly higher mortality risk than those in the non-COPD group (*p*-value < 0.001). Univariate and multivariate analysis for cancer-related mortality revealed an HR of 1.19 (95% CI 1.13–1.26) and 1.26 (95% CI 1.19–1.33), compared with the non-COPD group, respectively. Our work also indicates a lower mortality rate in young patients than in patients older than 70 (Table 2). Patients with stage IV CRC had a substantially higher mortality risk (HR, 17.25; 95% CI, 15.43–19.28) than patients with stage I CRC. Moreover, patients with comorbidities such as congestive heart failure (HR, 1.44; 95% CI, 1.30–1.59), chronic kidney disease (HR, 1.28; 95% CI, 1.15–1.42), and liver disease (HR, 1.08; 95% CI, 1.02–1.15) were associated with higher mortality risk. Notably, our work demonstrated that hyperlipidemia had a protective effect on cancer-related death in this cohort (HR, 0.82; 95% CI, 0.77–0.87). A PSM retrospective cohort study in Taiwan revealed a lower mortality risk for patients with gastric cancer among statin users [30]. For the subgroup analysis regarding the influence of COPD on OS in different CRC stages, the HR was 1.47 (95% CI 1.24–1.74) in stage I, 1.27 (95% CI 1.12–1.43) in stage II, 1.28 (95% CI 1.17–1.40) in stage III, and 1.25 (95% CI 1.17–1.33) in stage IV (Figure 3). These results showed that COPD increased the risk of patient mortality across all CRC stages.

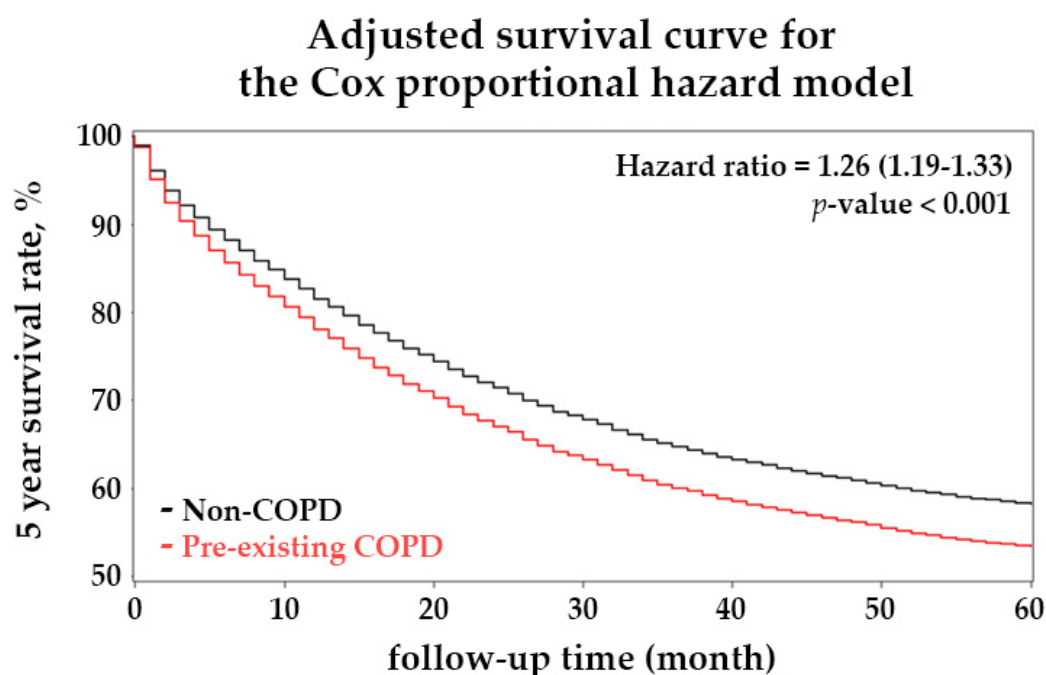


**Figure 2.** Five-year Cox-adjusted survival curves of patients with colorectal cancer (CRC) and with or without the preexisting chronic obstructive pulmonary disease (COPD) from this matched cohort study. Total 31,896 patients with CRC were matched by comorbidities using PSM with a 2:1 ratio, and the total number is reduced to 13,707 patients. Patients were followed up for 5 years after being diagnosed with CRC. The red line displays the Cox-adjusted survival curve of patients with CRC plus preexisting COPD, and the black line represents the control group.

**Table 2.** Cox regression model with adjusted and non-adjusted hazard ratios and 95% confidence intervals of 5-year overall survival among patients with colorectal cancer in this matched cohort. (Total  $n = 13,707$ ).

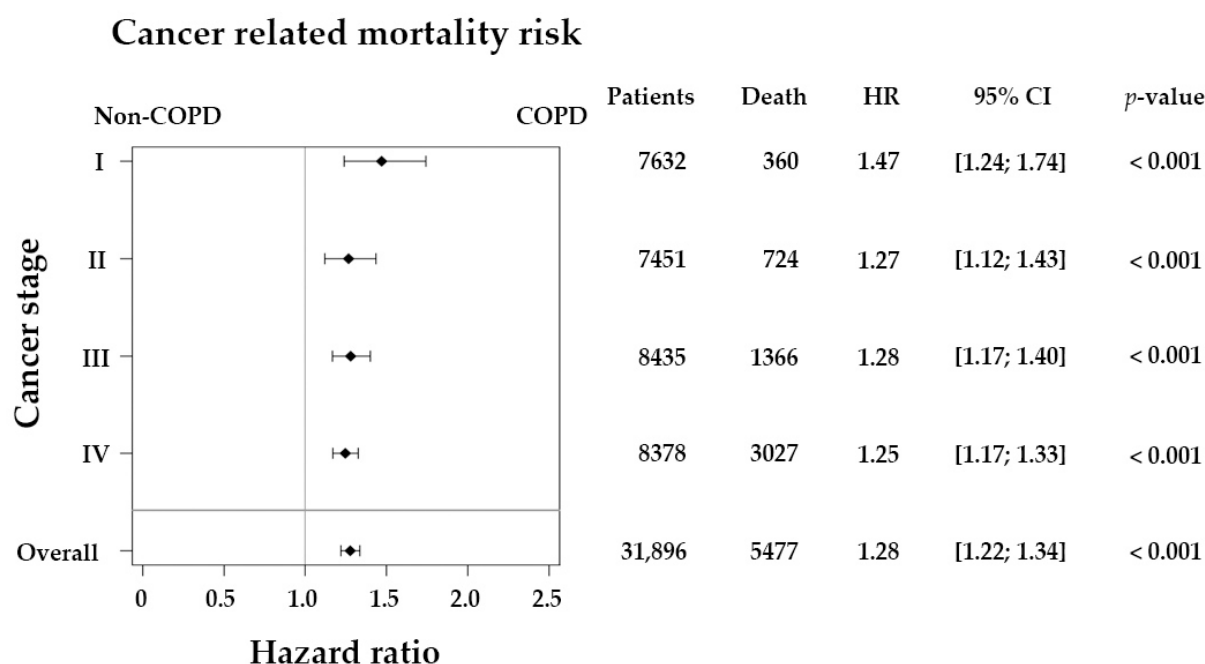
Variables	No. of Death	Univariate Analysis				Multivariate Analysis *			
		HR	95% CI		$p$ -Value	HR	95% CI		$p$ -Value
<b>COPD</b>									
No	3534	1 (reference)				1 (reference)			
Yes	1943	1.19	1.13	1.26	<0.001	1.26	1.19	1.33	<0.001
<b>Sex</b>									
Female	2469	1 (reference)				1 (reference)			
Male	3008	0.98	0.93	1.03	0.409	0.93	0.88	0.99	0.015
<b>Age-group, year</b>									
20–29	2	1.26	0.32	5.04	0.743	0.32	0.08	1.30	0.111
30–39	30	0.79	0.55	1.13	0.199	0.58	0.41	0.84	0.004
40–49	143	0.78	0.66	0.92	0.004	0.62	0.52	0.74	<0.001
50–59	449	0.48	0.44	0.53	<0.001	0.51	0.46	0.56	<0.001
60–69	1071	0.55	0.52	0.59	<0.001	0.60	0.56	0.64	<0.001
>70	3782	1 (reference)				1 (reference)			
<b>Cancer stage (pathology)</b>									
Stage I	360	1 (reference)				1 (reference)			
Stage II	724	2.21	1.95	2.51	<0.001	1.95	1.72	2.21	<0.001
Stage III	1366	4.02	3.58	4.52	<0.001	3.71	3.30	4.17	<0.001
Stage IV	3027	18.18	16.27	20.30	<0.001	17.25	15.43	19.28	<0.001
<b>Comorbidity</b>									
DM	2026	1.06	1.00	1.11	0.054	0.84	0.63	1.13	0.246
Type I DM	67	0.97	0.76	1.23	0.782	0.83	0.65	1.06	0.140
Type II DM	1979	1.06	1.00	1.12	0.039	1.33	1.00	1.78	0.053
Hypertension	3983	1.06	1.00	1.12	0.060	1.03	0.96	1.09	0.459
Hyperlipidemia	2214	0.78	0.74	0.82	<0.001	0.82	0.77	0.87	<0.001



Table 2. Cont.

Variables	No. of Death	Univariate Analysis				Multivariate Analysis *			
		HR	95% CI		p-Value	HR	95% CI		p-Value
Prior myocardial infarction	1743	0.95	0.89	1.00	0.057	0.97	0.91	1.03	0.283
Congestive heart failure	428	1.25	1.13	1.38	<0.001	1.44	1.30	1.59	<0.001
Chronic kidney disease	364	1.16	1.04	1.29	0.006	1.28	1.15	1.42	<0.001
Liver diseases	1712	0.90	0.85	0.95	<0.001	1.08	1.02	1.15	0.010

\* Multivariate analysis was adjusted for COPD, age group, sex, cancer stage, DM, Type I DM, Type II DM, HTN, HPL, PMI, CHF, CKD, and LD. Abbreviations: HR, hazard ratio; CI, confidence interval; COPD, chronic obstructive pulmonary disease; DM, diabetes mellitus.



**Figure 3.** Subgroup analysis of cancer-related mortality with Cox regression model adjusted for sex and age-group by cancer stage, without propensity score matching. Total 31,896 patients with colorectal cancer were followed up for 5 years. The forest plot displays adjusted hazard ratios (HRs) and 95% confidence intervals (CIs) between preexisting chronic obstructive pulmonary disease (COPD) patients and non-COPD groups with different cancer stages by multivariate analysis.

#### 4. Discussion

CRC accounts for approximately 10% of annually diagnosed malignancies and is the second and third most commonly diagnosed malignancy worldwide among females and males, respectively [1]. CRC caused approximately 881,000 deaths in 2018 and is the second leading cause of cancer-related deaths worldwide [31]. In Taiwan, CRC incidence has recently increased and is the third leading cause of cancer-related deaths [2,7]. Studies showed that chronic inflammatory lung disease, such as COPD, pneumoconiosis, and chronic rhinosinusitis, increased cancer incidence in Taiwan population-based cohort studies [11,32,33]. However, the relationship between COPD and CRC mortality has not yet been elucidated in Taiwan. In our study, patients with CRC and preexisting COPD had a higher mortality risk during the 5-year follow-up than those without preexisting COPD, according to our findings after PSM. Moreover, in all CRC stages, patients with preexisting COPD showed a higher mortality risk during the 5-year follow-up. Since COPD causes various health issues, we found that patients with CRC and preexisting COPD were older and had more comorbidities than those without preexisting COPD. Similarly, the elderly patients with CRC and COPD exhibited worse OS in a European Eindhoven Cancer Registry study [29]. Moreover, multiple comorbidities such as hypertension, diabetes mellitus, congestive heart failure, and chronic kidney disease are related to systemic inflammation,

which is a poor prognostic factor for CRC [34,35], contributing to tumor invasion, cancer cell proliferation, and distant metastasis [36]. Approximately 20–40% of patients with CRC preoperatively have increased systemic inflammation markers, such as neutrophil-to-lymphocyte ratio and modified Glasgow prognostic score based on C-reactive protein [36]. As a result, older age and multiple comorbidities may contribute to worse mortality during the 5-year follow-up of patients with CRC and preexisting COPD.

The treatment of CRC would be decided by a multidisciplinary team including a pathologist, a gastrointestinal physician, a surgeon, an oncologist, and a radiologist, based on disease severity and patient condition [37]. Curative surgery is the most optimal treatment option for patients with resectable CRC [1]. However, COPD causes more surgical complications, such as cor pulmonale, respiratory distress, and pulmonary infections. In a Spanish population-based study, COPD was associated with higher rates of in-hospital complications, intensive care unit admission, antibiotic administration, reoperation, and mortality [15]. Furthermore, according to a Danish population-based study, postoperative death within 30 day increases among patients with CRC and COPD [13], which may affect the surgical decision. Nevertheless, the European Eindhoven Cancer Registry study did not show differences in surgery or chemotherapy choice in primary treatment with the adjusted Cox regression model despite the high risk of adverse outcomes in patients with COPD [29]. A limitation of our study is that the initial cancer treatment is not enrolled in the survival analysis. Thus, we do not know whether or not COPD would affect the initial cancer treatment decision in this cohort study or even lead to a higher mortality rate.

Interestingly, our 5-year cohort study revealed that patients with CRC plus hyperlipidemia had a lower mortality risk with multivariate analysis. Statins, or hydroxymethylglutaryl coenzyme A reductase inhibitors, are one of the most used drugs for treating hyperlipidemia in the world. This finding implied that statin might have a protective effect on patients with CRC. A long-term retrospective cohort study in Taiwan also demonstrated that statin usage could lower the mortality rate among patients with gastric cancer [30]. Furthermore, a meta-analysis in 2021 showed that statin treatment has protective effects against CRCs [38]. In CRC, statins were found to activate bone morphogenetic protein-specific phosphatase and tensin homolog, as well as inhibit the phosphoinositide 3-kinase/protein kinase B/mechanistic target of the rapamycin signaling pathway [39]. Therefore, statin treatment might explain why hyperlipidemia played a protective role in the cohort. However, the actual medicinal utilization for the treatment of hyperlipidemia was not accounted for in the analysis of our study. Further study may be needed to ascertain our hypothesis.

Our study had several strengths. First, the NHI program in Taiwan insured 99% of the 23.5 million Taiwanese people, and 93% of hospitals provided the NHI service, meaning that the TwCR and NHIRD data used in this study covered the entire population in Taiwan. Thus, there was no selection bias in enrolling subjects. Moreover, the number of study subjects was large, and the rate of cases lost to follow-up in this cohort was very low because the NHI program sustained a high coverage rate since its founding in 1995.

Our study also had some limitations. We initially excluded 2740 (6.34%) patients with CRC in this study due to missing cancer stage or demographic data. However, this retrospective study did not evaluate some confounding factors, including body mass index, smoking history, socioeconomic state, lifestyle, dietary habits, actual medication usage for comorbidities, location of CRC, tumor size, or initial cancer treatment, because these data were incomplete or unavailable. Thus, we could not know whether these patients have any treatment after initial diagnosis, which may influence the analysis results. Moreover, the severity of COPD was not evaluated in our study, which may be distinguished by admissions with acute exacerbation or medication usage, also affecting the mortality risk in patients with COPD. Finally, our data did not analyze the influence of initial cancer treatment, tumor location, and therapeutic modalities on overall survival, even though the cancer treatments are based on the cancer stage of CRC. Further detailed research is needed to elucidate these results.



## 5. Conclusions

In conclusion, patients with CRC and preexisting COPD had a higher mortality risk than those without preexisting COPD during this 5-year retrospective cohort study, suggesting these patients need more attention during treatment and follow-up. However, further detailed studies considering some confounding factors such as COPD severity or cancer therapeutic modalities are needed to confirm these findings.

**Author Contributions:** Conceptualization: W.-J.C. and C.-C.C.; methodology: W.-J.C., M.-T.P. and Y.-T.H.; investigation: W.-J.C. and J.-L.H.; resources: S.-H.C. and H.-T.Y.; writing—original draft preparation: W.-J.C. and C.-C.C.; writing—review and editing: C.-C.C., M.-T.P., W.-C.C., J.-J.K. and T.-L.H.; supervision: J.-J.K. and T.-L.H. All authors have read and agreed to the published version of the manuscript.

**Funding:** This research was supported by grants from Chang Gung Memorial Hospital (CORPG5K0031, CMRPG3K0161, and CMRPG5K0151-1), Taiwan. The funders had no role in this research. The authors thank the statistical assistance and wish to acknowledge the support of the Maintenance Project of the Center for Big Data Analytics and Statistics (Grant CLRPG3D0048) at Chang Gung Memorial Hospital for study design and monitor, data analysis, and interpretation.

**Institutional Review Board Statement:** The study was conducted according to the guidelines of the Declaration of Helsinki and approved by the Institutional Review Board of Chang Gung Memorial Hospital (IRB number 201900249B0) on 2019/03/04.

**Informed Consent Statement:** Patient consent was waived by the Institutional Review Board of Chang Gung Memorial Hospital due to the study design.

**Data Availability Statement:** The data presented in this study are available on request from the corresponding author. The data are not publicly available due to the data utilization policy of HWDC.

**Acknowledgments:** We thank the Research Services Center for Health Information and Chang Gung University for administrative, technical, and funding support. This study is based, in part, on data from the National Health Insurance research database provided by the National Health Insurance Administration and managed by the Health and Welfare Data Science Center, Ministry of Health and Welfare. However, the interpretation and conclusions contained herein do not represent the position of Chang Gung Memorial Hospital, National Health Insurance Administration, and Ministry of Health and Welfare.

**Conflicts of Interest:** The authors declare no conflict of interest.

## References

1. Dekker, E.; Tanis, P.J.; Vleugels, J.L.A.; Kasi, P.M.; Wallace, M.B. Colorectal cancer. *Lancet* **2019**, *394*, 1467–1480. [\[CrossRef\]](#)
2. Lin, C.C.; Chen, T.H.; Wu, Y.C.; Fang, C.Y.; Wang, J.Y.; Chen, C.P.; Huang, K.W.; Jiang, J.K. Taiwan Society of Colon and Rectal Surgeons (TSCRS) Consensus for Cytoreduction Selection in Metastatic Colorectal Cancer. *Ann. Surg. Oncol.* **2021**, *28*, 1762–1776. [\[CrossRef\]](#) [\[PubMed\]](#)
3. Su, S.Y.; Huang, J.Y. Effect of nationwide screening program on colorectal cancer mortality in Taiwan: A controlled interrupted time series analysis. *Int. J. Colorectal Dis.* **2020**, *35*, 239–247. [\[CrossRef\]](#) [\[PubMed\]](#)
4. Siegel, R.L.; Miller, K.D.; Jemal, A. Cancer statistics, 2016. *CA Cancer J. Clin.* **2016**, *66*, 7–30. [\[CrossRef\]](#)
5. Moreno, C.C.; Mittal, P.K.; Sullivan, P.S.; Rutherford, R.; Staley, C.A.; Cardona, K.; Hawk, N.N.; Dixon, W.T.; Kitajima, H.D.; Kang, J.; et al. Colorectal Cancer Initial Diagnosis: Screening Colonoscopy, Diagnostic Colonoscopy, or Emergent Surgery, and Tumor Stage and Size at Initial Presentation. *Clin. Colorectal Cancer* **2016**, *15*, 67–73. [\[CrossRef\]](#) [\[PubMed\]](#)
6. Amri, R.; Bordeianou, L.G.; Sylla, P.; Berger, D.L. Impact of screening colonoscopy on outcomes in colon cancer surgery. *JAMA Surg.* **2013**, *148*, 747–754. [\[CrossRef\]](#) [\[PubMed\]](#)
7. Yang, C.Y. Deaths from colon cancer among farmers in Taiwan: A mortality odds ratio study. *J. Toxicol. Environ. Health A* **2019**, *82*, 1137–1142. [\[CrossRef\]](#)
8. Riesco, J.A.; Alcázar, B.; Trigueros, J.A.; Campuzano, A.; Pérez, J.; Lorenzo, J.L. Active smoking and COPD phenotype: Distribution and impact on prognostic factors. *Int. J. Chron. Obstruct. Pulmon. Dis.* **2017**, *12*, 1989–1999. [\[CrossRef\]](#)
9. Hogg, J.C.; Timens, W. The pathology of chronic obstructive pulmonary disease. *Annu. Rev. Pathol.* **2009**, *4*, 435–459. [\[CrossRef\]](#)
10. Hogg, J.C. Pathophysiology of airflow limitation in chronic obstructive pulmonary disease. *Lancet* **2004**, *364*, 709–721. [\[CrossRef\]](#)
11. Ho, C.H.; Chen, Y.C.; Wang, J.J.; Liao, K.M. Incidence and relative risk for developing cancer among patients with COPD: A nationwide cohort study in Taiwan. *BMJ Open* **2017**, *7*, e013195. [\[CrossRef\]](#)

12. Ahn, S.V.; Lee, E.; Park, B.; Jung, J.H.; Park, J.E.; Sheen, S.S.; Park, K.J.; Hwang, S.C.; Park, J.B.; Park, H.S.; et al. Cancer development in patients with COPD: A retrospective analysis of the National Health Insurance Service-National Sample Cohort in Korea. *BMC Pulm. Med.* **2020**, *20*, 170. [\[CrossRef\]](#) [\[PubMed\]](#)
13. Platon, A.M.; Erichsen, R.; Christiansen, C.F.; Andersen, L.K.; Sværke, C.; Montomoli, J.; Sørensen, H.T. The impact of chronic obstructive pulmonary disease on intensive care unit admission and 30-day mortality in patients undergoing colorectal cancer surgery: A Danish population-based cohort study. *BMJ Open Respir. Res.* **2014**, *1*, e000036. [\[CrossRef\]](#)
14. Flynn, D.E.; Mao, D.; Yerkovich, S.T.; Franz, R.; Iswariah, H.; Hughes, A.; Shaw, I.M.; Tam, D.P.L.; Chandrasegaram, M.D. The impact of comorbidities on post-operative complications following colorectal cancer surgery. *PLoS ONE* **2020**, *15*, e0243995. [\[CrossRef\]](#) [\[PubMed\]](#)
15. Baré, M.; Montón, C.; Mora, L.; Redondo, M.; Pont, M.; Escobar, A.; Sarasqueta, C.; de Larrea, N.F.; Briones, E.; Quintana, J.M. COPD is a clear risk factor for increased use of resources and adverse outcomes in patients undergoing intervention for colorectal cancer: A nationwide study in Spain. *Int. J. Chron. Obstruct. Pulmon. Dis.* **2017**, *12*, 1233–1241. [\[CrossRef\]](#)
16. Wang, R.; Han, L.; Dai, W.; Mo, S.; Xiang, W.; Li, Q.; Xu, Y.; Cai, G. Cause of death for elders with colorectal cancer: A real-world data analysis. *J. Gastrointest. Oncol.* **2020**, *11*, 269–276. [\[CrossRef\]](#) [\[PubMed\]](#)
17. Negewo, N.A.; Gibson, P.G.; McDonald, V.M. COPD and its comorbidities: Impact, measurement and mechanisms. *Respirology* **2015**, *20*, 1160–1171. [\[CrossRef\]](#) [\[PubMed\]](#)
18. Smith, M.C.; Wrobel, J.P. Epidemiology and clinical impact of major comorbidities in patients with COPD. *Int. J. Chron. Obstruct. Pulmon. Dis.* **2014**, *9*, 871–888. [\[CrossRef\]](#)
19. André, S.; Conde, B.; Frago, E.; Boléo-Tomé, J.P.; Areias, V.; Cardoso, J. COPD and Cardiovascular Disease. *Pulmonology* **2019**, *25*, 168–176. [\[CrossRef\]](#)
20. Cavaillès, A.; Brinchault-Rabin, G.; Dixmier, A.; Goupil, F.; Gut-Gobert, C.; Marchand-Adam, S.; Meurice, J.-C.; Morel, H.; Person-Tacnet, C.; Leroyer, C.; et al. Comorbidities of COPD. *Eur. Respir. Rev. Off. J. Eur. Respir. Soc.* **2013**, *22*, 454–475. [\[CrossRef\]](#)
21. Barnes, P.J.; Celli, B.R. Systemic manifestations and comorbidities of COPD. *Eur. Respir. J.* **2009**, *33*, 1165–1185. [\[CrossRef\]](#)
22. Barnes, P.J. Senescence in COPD and Its Comorbidities. *Annu. Rev. Physiol.* **2017**, *79*, 517–539. [\[CrossRef\]](#)
23. Bouter, C.; Bebington, B.; Maphosa, S.; Maher, H.; Gaylard, P.; Etheredge, H.R.; Fabian, J.; Prodehl, L.; Surridge, D.; Fourie, R.L.; et al. It's contrary—Comorbidity does not affect survival of South Africans with colorectal cancer: An analysis from the Colorectal Cancer in South Africa cohort. *S. Afr. Med. J.* **2020**, *110*, 382–388. [\[CrossRef\]](#) [\[PubMed\]](#)
24. Hsieh, C.-Y.; Su, C.-C.; Shao, S.-C.; Sung, S.-F.; Lin, S.-J.; Kao Yang, Y.-H.; Lai, E.C.-C. Taiwan's National Health Insurance Research Database: Past and future. *Clin. Epidemiol.* **2019**, *11*, 349–358. [\[CrossRef\]](#) [\[PubMed\]](#)
25. Chiang, C.-J.; Wang, Y.-W.; Lee, W.-C. Taiwan's Nationwide Cancer Registry System of 40 years: Past, present, and future. *J. Formos. Med. Assoc.* **2019**, *118*, 856–858. [\[CrossRef\]](#) [\[PubMed\]](#)
26. Allemani, C.; Matsuda, T.; Di Carlo, V.; Harewood, R.; Matz, M.; Nikšić, M.; Bonaventure, A.; Valkov, M.; Johnson, C.J.; Estève, J.; et al. Global surveillance of trends in cancer survival 2000–14 (CONCORD-3): Analysis of individual records for 37,513,025 patients diagnosed with one of 18 cancers from 322 population-based registries in 71 countries. *Lancet* **2018**, *391*, 1023–1075. [\[CrossRef\]](#)
27. Hsieh, M.-H.; Kung, P.-T.; Kuo, W.-Y.; Ke, T.-W.; Tsai, W.-C. Recurrence, death risk, and related factors in patients with stage 0 colorectal cancer: A nationwide population-based study. *Medicine* **2020**, *99*, e21688. [\[CrossRef\]](#) [\[PubMed\]](#)
28. Austin, P.C. An Introduction to Propensity Score Methods for Reducing the Effects of Confounding in Observational Studies. *Multivar. Behav. Res.* **2011**, *46*, 399–424. [\[CrossRef\]](#)
29. van de Schans, S.A.M.; Janssen-Heijnen, M.L.G.; Biesma, B.; Smeenk, F.W.J.M.; van de Poll-Franse, L.V.; Seynaeve, C.; Coebergh, J.W.W. COPD in cancer patients: Higher prevalence in the elderly, a different treatment strategy in case of primary tumours above the diaphragm, and a worse overall survival in the elderly patient. *Eur. J. Cancer* **2007**, *43*, 2194–2202. [\[CrossRef\]](#) [\[PubMed\]](#)
30. Yang, P.-R.; Tsai, Y.-Y.; Chen, K.-J.; Yang, Y.-H.; Shih, W.-T. Statin Use Improves Overall Survival of Patients with Gastric Cancer after Surgery and Adjuvant Chemotherapy in Taiwan: A Nationwide Matched Cohort Study. *Cancers* **2020**, *12*, 2055. [\[CrossRef\]](#) [\[PubMed\]](#)
31. Castejón, M.; Plaza, A.; Martínez-Romero, J.; Fernández-Marcos, P.J.; Cabo, R.; Díaz-Ruiz, A. Energy Restriction and Colorectal Cancer: A Call for Additional Research. *Nutrients* **2020**, *12*, 114. [\[CrossRef\]](#) [\[PubMed\]](#)
32. Hung, Y.P.; Teng, C.J.; Liu, C.J.; Hu, Y.W.; Hung, M.H.; Tzeng, C.H.; Liu, C.Y.; Yeh, C.M.; Chen, T.J.; Chiou, T.J. Cancer risk among patients with coal workers' pneumoconiosis in Taiwan: A nationwide population-based study. *Int. J. Cancer* **2014**, *134*, 2910–2916. [\[CrossRef\]](#) [\[PubMed\]](#)
33. Xia, C.X.; Kao, Y.W.; Qin, L.; Chen, M.C.; Shia, B.C.; Wu, S.Y. Cancer risk in chronic rhinosinusitis: A propensity score matched case-control cohort study. *Am. J. Transl. Res.* **2019**, *11*, 7146–7156.
34. McMillan, D.C. The systemic inflammation-based Glasgow Prognostic Score: A decade of experience in patients with cancer. *Cancer Treat. Rev.* **2013**, *39*, 534–540. [\[CrossRef\]](#)
35. Haram, A.; Boland, M.R.; Kelly, M.E.; Bolger, J.C.; Waldron, R.M.; Kerin, M.J. The prognostic value of neutrophil-to-lymphocyte ratio in colorectal cancer: A systematic review. *J. Surg. Oncol.* **2017**, *115*, 470–479. [\[CrossRef\]](#) [\[PubMed\]](#)
36. Tuomisto, A.E.; Mäkinen, M.J.; Väyrynen, J.P. Systemic inflammation in colorectal cancer: Underlying factors, effects, and prognostic significance. *World J. Gastroenterol.* **2019**, *25*, 4383–4404. [\[CrossRef\]](#) [\[PubMed\]](#)

- 
37. Brenner, H.; Kloor, M.; Pox, C.P. Colorectal cancer. *Lancet* **2014**, *383*, 1490–1502. [[CrossRef](#)]
  38. Li, L.; Cui, N.; Hao, T.; Zou, J.; Jiao, W.; Yi, K.; Yu, W. Statins use and the prognosis of colorectal cancer: A meta-analysis. *Clin. Res. Hepatol. Gastroenterol.* **2021**, *45*, 101588. [[CrossRef](#)] [[PubMed](#)]
  39. Ouahoud, S.; Jacobs, R.J.; Peppelenbosch, M.P.; Fühler, G.M.; Heijmans, J.; Diks, S.; Wildenberg, M.E.; Hawinkels, L.; Kodach, L.L.; Voorneveld, P.W.; et al. Kinome-wide analysis of the effect of statins in colorectal cancer. *Br. J. Cancer* **2021**, *124*, 1978–1987. [[CrossRef](#)]



# Gallic Acid Ameliorated Impaired Lipid Homeostasis in a Mouse Model of High-Fat Diet—and Streptozotocin-Induced NAFLD and Diabetes through Improvement of $\beta$ -oxidation and Ketogenesis

## OPEN ACCESS

### Edited by:

Stefano Fiorucci,  
University of Perugia, Italy

### Reviewed by:

Chung S. Yang,  
The State University of New Jersey,  
United States  
Lourdes M. Varela,  
Sevilla University, Spain

### \*Correspondence:

Li-Heng Pao  
paojh@mail.cgu.edu.tw  
Wen-Huang Peng  
whpeng@mail.cmu.edu.tw

### Specialty section:

This article was submitted to  
Gastrointestinal and Hepatic  
Pharmacology,  
a section of the journal  
Frontiers in Pharmacology

**Received:** 16 September 2020

**Accepted:** 24 December 2020

**Published:** 12 February 2021

### Citation:

Chao J, Cheng H-Y, Chang M-L,  
Huang S-S, Liao J-W, Cheng Y-C,  
Peng W-H and Pao L-H (2021) Gallic  
Acid Ameliorated Impaired Lipid  
Homeostasis in a Mouse Model of  
High-Fat Diet—and Streptozotocin-  
Induced NAFLD and Diabetes  
through Improvement of  $\beta$ -oxidation  
and Ketogenesis.  
Front. Pharmacol. 11:606759.  
doi: 10.3389/fphar.2020.606759

Jung Chao<sup>1</sup>, Hao-Yuan Cheng<sup>2</sup>, Ming-Ling Chang<sup>3</sup>, Shyh-Shyun Huang<sup>4</sup>, Jiunn-Wang Liao<sup>5</sup>,  
Yung-Chi Cheng<sup>6</sup>, Wen-Huang Peng<sup>7\*</sup> and Li-Heng Pao<sup>8,9\*</sup>

<sup>1</sup>Department of Chinese Pharmaceutical Sciences and Chinese Medicine Resources, China Medical University, Taichung, Taiwan, <sup>2</sup>Department of Nursing, Chung-Jen Junior College of Nursing, Health Sciences and Management, Chia-Yi, Taiwan, <sup>3</sup>Division of Hepatology, Department of Gastroenterology and Hepatology, Liver Research Center, Chang Gung Memorial Hospital, Linko, Taiwan, <sup>4</sup>School of Pharmacy, China Medical University, Taichung, Taiwan, <sup>5</sup>Graduate Institute of Veterinary Pathology, National Chung Hsing University, Taichung, Taiwan, <sup>6</sup>Department of Pharmacology, Yale University School of Medicine, New Haven, CT, United States, <sup>7</sup>Department of Chinese Pharmaceutical Sciences and Chinese Medicine Resources, China Medical University, Taichung, Taiwan, <sup>8</sup>Graduate Institute of Health Industry Technology, Research Center for Food and Cosmetic Safety, and Research Center for Chinese Herbal Medicine, College of Human Ecology, Chang Gung University of Science and Technology, Taoyuan, Taiwan, <sup>9</sup>Department of Gastroenterology and Hepatology, Chang Gung Memorial Hospital, Linko, Taiwan

Gallic acid (GA) is a simple polyphenol found in food and traditional Chinese medicine. Here, we determined the effects of GA administration in a combined mouse model of high-fat diet (HFD)-induced obesity and low-dose streptozotocin (STZ)-induced hyperglycemia, which mimics the concurrent non-alcoholic fatty liver disease (NAFLD) and type 2 diabetes pathological condition. By combining the results of physiological assessments, pathological examinations, metabolomic studies of blood, urine, liver, and muscle, and measurements of gene expression, we attempted to elucidate the efficacy of GA and the underlying mechanism of action of GA in hyperglycemic and dyslipidemic mice. HFD and STZ induced severe diabetes, NAFLD, and other metabolic disorders in mice. However, the results of liver histopathology and serum biochemical examinations indicated that daily GA treatment alleviated the high blood glucose levels in the mice and decelerated the progression of NAFLD. In addition, our results show that the hepatoprotective effect of GA in diabetic mice occurs in part through a partially preventing disordered metabolic pathway related to glucose, lipids, amino acids, purines, and pyrimidines. Specifically, the mechanism responsible for alleviation of lipid accumulation is related to the upregulation of  $\beta$ -oxidation and ketogenesis. These findings indicate that GA alleviates metabolic diseases through novel mechanisms.

**Keywords:** gallic acid, non-alcoholic fatty liver disease, metabolomics, diabetes,  $\beta$ -oxidation, ketogenesis

## INTRODUCTION

Diabetes is a multi-etiological chronic metabolic disorder that is primarily characterized by pathological and physiological changes induced by insulin resistance and impaired insulin secretion. Because of changes in lifestyle and improved living standards, the global incidence of diabetes has gradually increased from 153 million in 1980 to 347 million people in 2010 (Danaei et al., 2011). Moreover, the mortality rate associated with vascular complications induced by diabetes, including diabetic nephropathy, has also gradually increased. The World Health Organization estimated that by 2030, diabetes would become the seventh leading cause of death worldwide (Danaei et al., 2011). It is therefore imperative to develop safe and effective diabetic drugs as well as preventive and therapeutic strategies to combat diabetes-related secondary complications.

Naturally occurring phenolic acids are prevalent in human food products. Polyphenol compounds and polyphenol-rich diets facilitate prevention and treatment of diabetes (Dembinska-Kiec et al., 2008; Xiao et al., 2015). Among various types of naturally occurring polyphenols, GA is one of the simplest and exists in free forms, such as tannins, ellagitannin, theaflavin-3-gallate, and epigallocatechin gallate. GA is found in many dietary substances, including vegetables, fruits, red wine, and tea (Manach et al., 2005; Subramanian et al., 2015). Among them, tea is a particularly important source of GA. (Tomás-Barberán and Clifford, 2000). Many reports have been confirmed that catechin and gallic acid (GA) are the most important compounds among the other tea constituents (Liang et al., 2007; Wang et al., 2001; Mok et al., 2002; Lee et al., 2005; Yue et al., 2014). Previous research also pointed out that free-form GA also exists in tea (Kongpichitchoke et al., 2016). Different teas have different amounts of GA, ranging from 0.1% to 2% (Kongpichitchoke et al., 2016). It is worth noting that GA occurs in tea in free and esterified forms (Matthew et al., 1997). Esterified forms include galocatechin gallate (GCG), catechin gallate (CG), epicatechin gallate (ECG), epigallocatechin gallate (EGCG) (Quan et al., 2011).

GA has been reported to facilitate favorable biological activities, including radical scavenging, oxidation inhibition (Hsu and Yen, 2007), inflammation alleviation (Hsiang et al., 2013), obesity reduction (Hsu and Yen, 2007; Oi et al., 2012), and tumor suppression (Subramanian et al., 2015). Moreover, GA functions to alleviate metabolic diseases, including NAFLD (Chao et al., 2014) and diabetes, by upregulating the peroxisome proliferation-activated receptor (PPAR) in the liver, muscles, and adipose tissue, thereby reducing blood glucose (Gandhi et al., 2014), hepatic lipid peroxidation (Punithavathi et al., 2011b), diabetes induced myocardial dysfunction (Patel and Goyal, 2011), and diabetic nephropathy (Ahad et al., 2015) while enhancing pancreatic antioxidant activity (Punithavathi et al., 2011a). Additionally, studies have reported that GA inhibits the activities of glycogen phosphorylase (Kyriakis et al., 2015) and  $\alpha$ -glucosidase (Benalla et al., 2010). GA was also shown to protect pancreatic islet RINm5F  $\beta$ -cells from the proapoptotic effects of glucolipotoxicity (Sameermahmood et al., 2010). Hence, GA has been clearly shown to facilitate favorable

activities that alleviate diabetic symptoms. As GA intake, theoretically, facilitates systematic protection of the human body, a holistic approach should be taken to analyze its effects.

Naturally occurring products or functional foods exert moderate effects on the human body, in contrast to chemical drugs that serve as specific inhibitors of selective targets and thus exert considerable effects. Therefore, analyzing a naturally occurring product from a transcriptome or proteome perspective cannot comprehensively reflect its true functional mechanisms. Alternatively, a systems biology perspective allows for identification of metabolites in the terminal of biological systems, along with corresponding minor changes in their gene and protein expressions (Taylor et al., 2002). Consequently, analyzing the changes in the metabolites of an organism facilitates identification of subtle changes in the organism.

Previous studies primarily used conventional blood biochemical markers and examination of histopathological sections to investigate the mechanisms by which GA alleviates metabolic diseases (Hsu and Yen, 2007; Punithavathi et al., 2011b; Oi et al., 2012; Gandhi et al., 2014; Ahad et al., 2015), thus examining from a protein target perspective alone (Kyriakis et al., 2015; Benalla et al., 2010), which is largely unilateral in its understanding of related functional mechanisms. Therefore, the functions and mechanisms of GA in alleviating metabolic diseases merit re-examination. In this study, we hypothesized, when attempting to elucidate the preventive effects and mechanisms of GA on diabetes and non-alcoholic fatty liver disease, using these results is likely to provide strong evidence to support the preventive effects of daily consumption of this functional food on metabolic diseases. This study aimed to investigate the beneficial effects of GA on diabetes and non-alcoholic steatohepatitis (NASH) by metabolomics using an animal model. We used a high-fat diet (HFD) and streptozotocin (STZ) to induce diabetes in an animal model so as to evaluate the pharmacodynamics and mechanisms of GA in alleviating diabetes and NASH. The HFD-induced NAFLD model used showed signs similar to the NAFLD pathogenesis experienced by humans, incorporating obesity and other metabolic complications (Hebbard and George, 2011). A typical model, used in pharmacology, is to damage pancreatic  $\beta$ -cells through STZ to realize insufficient insulin secretion, thus inducing hyperglycemia and diabetes (Szkudelski, 2001). This study used a composite induction model that integrated the features of the aforementioned two models, conforming to the pathogenesis of type 2 diabetes in humans (Mu et al., 2006; Sawant et al., 2006). Moreover, previous studies have reported that this model can successfully induce NASH (Lo et al., 2011). Therefore, the present study also used the model to evaluate the effect of GA on NASH. A previous study used an NMR-based metabolomics strategy to examine the effect of GA on mice with NAFLD (Chao et al., 2014) by analyzing the changes in serum and urinary metabolites. This strategy enabled the identification of total metabolic changes in various tissues and organs but failed to reflect organ-oriented metabolic changes; hence, the specificity of related biomarkers needs to be further verified. Furthermore, high blood glucose and insulin resistance induced by HFD and STZ



can affect various organs and tissues in the human body, while the interactions between the organs can also augment disease progression. As such, here the changes in blood and urinary metabolites and the liver and muscular tissues metabolites were measured, the organs most likely to be affected by diabetes, to comprehensively investigate the functional mechanisms of GA in mice with diabetes and NASH. This study will therefore show results and proposed pathways that will help elucidate the multiple targets involved in the hepatoprotective activities of GA.

## MATERIALS AND METHODS

### Chemicals

GA (98%), heavy water ( $D_2O$ ; 99.9%), chloroform- $d$  containing tetramethylsilane (99.9%), STZ, 6-hydroxy-2,5,7,8-tetramethylchromane-2-carboxylic acid (Trolox), and potassium dihydrogen phosphate ( $KH_2PO_4$ ) were purchased from Sigma-Aldrich (St. Louis, MO, USA). Trimethylsilane propionic acid sodium salt (TSP) was obtained from Merck (Darmstadt, Germany). Sodium deuteroxide ( $NaOD$ ) was purchased from Cambridge Isotope Laboratories (Tewksbury, MA, USA). Test Diets 58Y1 (St. Louis, MO, USA) was used as the HFD, and LabDiet 5010 (Richmond, IN, USA) was used as the control diet.

### Animal Study and Sample Collection

In this study, the mice were raised according to the Guide for the Care and Use of Laboratory Animals published by the National Institutes of Health. The animal experimental protocol was approved by the Laboratory Animal Center Committee of Ghang Gung University of Science and Technology (IACUC-2014-009).

**Supplementary Figure S1** illustrates the experimental design flowchart. The animal experiment was designed and revised according to the 2010 Amendment Draft on Assessment Methods of Blood Glucose Function Regulated by Health Food (Ministry of Health and Welfare) and the model described in a previous study (Mu et al., 2006). Male 8 week old C57BL6/J mice (20–25 g) were purchased from BioLASCO, Taiwan. To decrease the variance of the model, each mouse was independently raised in a separate cage, with constant temperature and relative humidity of  $22 \pm 1^\circ C$  and  $55\% \pm 5\%$ , respectively. The light–dark cycle was 12 h (08:00 to 20:00).

**Supplementary Table S1** describes the diet composition and caloric ratio for each group. No limit was set for the amount of the regular diet and HFD given to the mice. The normal group was fed the regular diet, while the remaining groups were fed the HFD (Test Diets 58Y1). After night weeks, the mice were weighed (**Supplementary Figure S2**). An average weight  $>40$  g was set as the criterion for initiating the STZ injection. To prepare the injection reagent, STZ was dissolved in normal saline, and 0.1 M sodium citrate ( $pH = 4.5$ ) was used as the buffer solution. Each injection dose was 40 mg/kg. STZ was injected intraperitoneally once per day for two consecutive days in 9th week. Before the first injection, the mice were fasted for 16 h. After one week of STZ administration, the blood glucose levels of the mice were measured, and the mice were divided into three groups: normal group ( $n = 8$ ), diabetic group (HFD + STZ ( $n = 8$ ),

and treatment group (0.2% GA in HFD;  $n = 8$ ) according to the average blood glucose level. For the treatment, 0.2% GA was mixed with the HFD. The food intake and weights of the mice were measured weekly.

The amount of GA administered to the mice was determined based on the daily intake of tannic acid by humans (Sanyal et al., 1997). Tannic acid is a derivative of GA. The International Agency of Research on Cancer reported that its average human intake in the United States is approximately 1 g (Sanyal et al., 1997). Therefore, according to the average weight (60 kg) and daily tannic acid intake (1 g) of human adults published by the US Food and Drug Administration, the daily average GA intake is approximately 16.67 mg/kg, and states that multiplying the human equivalent dose by 12.3 yields the animal dose for mice (Food and Drug Administration, 2005); hence, the daily GA intake for mice is approximately 205.41 mg/kg. Accordingly, in the present study, the daily HFD intake for each mouse was approximately 3.0 g, the average weight of the mice was 40 g, and the diet for the treatment group contained 0.2% GA; thus, the average daily GA intake of each mouse was 150 mg/kg.

The mice were randomly selected on the 10th, 11th, 12th, and 15 th week for blood glucose testing to evaluate the effect of GA on blood glucose levels in mice. The oral glucose tolerance test (OGTT) was conducted on the 16 th week to assess the glucose metabolism of the mice. Mouse urine samples were collected on the 17 th week between 18:00 and 00:00 according to the circadian rhythm of the mice. The urine samples were centrifuged at 13,200 rpm to acquire the supernatant, and then stored in a  $-80^\circ C$  freezer. A urine sample was discarded if it was contaminated by mouse feces during sample collection.

The mice were fasted for 16 h before being euthanized by  $CO_2$  to ensure that liver glycogen was completely utilized. The blood samples of the euthanized mice were loaded into heparin-free or ethylenediaminetetraacetic acid-free tubes and incubated at  $23-25^\circ C$  for 30 min, followed by centrifugation (3000 rpm) at  $4^\circ C$  for 20 min. The supernatants recovered as the serum samples of the mice were used for conducting biochemical analysis. An organ weighing scale and the hematoxylin and eosin (H&E) staining method were used to assess the fat accumulation of the mice. Liver tissues were partially removed from the euthanized mice and immersed in the RNAlater® solution (Thermo Fisher Scientific Inc., Waltham, MA, USA). The tissue samples were stored at  $-20^\circ C$  to prevent RNA degradation and for later analysis *via* quantitative polymerase chain reaction (qPCR). The blood, urine, liver, and muscular tissue samples were used to conduct metabolomics analysis.

### Serum Biochemical Analysis, Serum Insulin and Biological Activity Tests

The following serum biochemical markers were assessed using a dry serum biochemical analyzer (Dry-Chem 4000i, Fujifilm, Saitama, Japan): aspartate (AST) and alanine transaminases (ALT), high-density lipoprotein (HDL), triglycerides (TG), and total cholesterol (TCHO).



## OGTT

The OGTT was used to determine the diabetes severity in the mice. A glucose solution (2 g/kg) was prepared one day prior to the test and settled overnight. The mice were fasted for 16 h before the test. First, the fasting glucose test was conducted (0 min); subsequently, the blood samples were collected at 30, 60, 90, and 120 min after orally feeding the mice to measure their blood glucose level, followed by statistical analysis.

## Histopathological Analysis

After the mice were euthanized, the liver lobes, thigh scale muscle, and organ fat were acquired and immersed in 10% formaldehyde to create paraffin sections (thickness = 4  $\mu$ m), followed by H&E staining. Accordingly, changes in the tissues were observed. The liver tissue sections were also dyed using Sirius red, a collagen fiber-specific dye, to determine liver fibrosis.

## NMR Metabolomics

The blood and urine samples frozen in the refrigerator were defrosted at room temperature (25°C), followed by centrifuging at 13,000 rpm for 15 min to remove insoluble substances. The blood samples were prepared by evenly mixing 100  $\mu$ L of serum with 500  $\mu$ L of phosphate buffer (0.57 g  $K_2HPO_4$  + 0.0981 g  $NaH_2PO_4$  + 0.81 NaCl in 100 ml  $D_2O$ , pH = 7.4). The urine samples were prepared by evenly mixing 100  $\mu$ L of urine with 500  $\mu$ L of phosphate buffer (0.38143 g  $K_2HPO_4$  + 0.06568 g  $NaH_2PO_4$  + 0.81 NaCl in 100 mL  $D_2O$ , pH = 7.4, 1 mM TSP). Next, 550  $\mu$ L of the blood or urine sample was loaded into a 5 mm NMR tube. The liver and muscle samples were processed according to the method described previously (An et al., 2013; Chao et al., 2014). Liver tissue and muscle tissue samples (~50 mg) were extracted with 0.4285 ml of pre-cooled methanol–water mixture (4/2.85, v/v) using a tissue homogenizer. After adding 0.4 ml chloroform to the methanol–water mixture, the solutions were separated into an upper methanol–water phase (with polar metabolites) and a lower chloroform phase (with lipophilic metabolites), which were collected separately following centrifugation (1,000  $\times$  g, 4°C, 10 min) and methanol–water or chloroform were then removed in vacuo. The polar extract was reconstituted using 600  $\mu$ L of phosphate buffer (0.38143 g  $K_2HPO_4$  + 0.06568 g  $NaH_2PO_4$  + 0.81 NaCl in 100 ml  $D_2O$ , pH = 7.4, 1 mM TSP). The lipophilic extract was reconstituted using 600  $\mu$ L of chloroform- $d$  containing TMS. Then, 550  $\mu$ L of each sample was transferred to a 5 mm NMR tube for NMR analysis.

The NMR instrument in the High Field Nuclear Magnetic Resonance Center of Academia Sinica was used. The experimental conditions were configured according to previous literature (Chao et al., 2014; Beckonert et al., 2007). The spectrum analysis was conducted according to the method described previously (Supplementary Table S2) (Beckonert et al., 2007; Chao et al., 2014).

The resulting  $^1H$ -NMR spectra were manually phased, baseline corrected, and calibrated to TSP or TMS at  $\delta$  = 0.00 ppm using Mestrenova software (version 8.0.2, Mestrelab research S.L.). The blood spectrum was not

subjected to normalization. In case of urine samples, the glucose signals (3.220–3.275, 3.300–3.560, 3.695–3.925, 4.600–4.700, and 5.160–5.280 ppm) and urea signal (5.600–6.000 ppm) were removed from the spectrum, and it was pretreated using total area normalization. The liver and muscular tissue spectra were normalized according to the tissue wet weight values.

For spectral resonance assignment purposes,  $^1H$ - $^1H$  correlation spectroscopy (COSY),  $^1H$ - $^1H$  total correlation spectroscopy (TOCSY),  $^1H$  J-resolved spectroscopy (JRES),  $^1H$ - $^{13}C$  heteronuclear single-quantum coherence (HSQC), and heteronuclear multiple bond correlation (HMBC) 2D NMR spectra were acquired on selected samples and processed as previously reported (An et al., 2013).

The resulting NMR datasets were imported into SIMCA-P version 13.0 (Umetrics, Umea, Sweden). All variables were scaled to Pareto (par) for multivariate statistical analyses and analyzed according to the previous study (Chao et al., 2014).

All results are presented as means  $\pm$  SE. The statistical analysis was performed using one-way analysis of variance (ANOVA), followed by Bonferroni's post hoc test. The criterion used for statistical significance was  $p < 0.05$ .

## Real-Time Fluorescence qPCR Analysis

The liver tissue samples were immersed in the RNeasy<sup>®</sup> solution (Thermo Fisher Scientific Inc.) and stored at  $-20^\circ C$ . An RNA extraction kit, RNeasy Plus Mini Kit (QIAGEN, Hilden, Germany), was used to extract the RNA from the mouse tissue. Next, a cDNA synthesis kit, QuantiTect Reverse Transcription Kit (QIAGEN), was used to conduct RNA reverse transcription. Applied Biosystems TaqMan analysis kit and TaqMan Universal MasterMix II were used to conduct qPCR analysis. The following genes were analyzed: PPAR alpha (PPAR $\alpha$ ) (assay ID Mm00440939\_m1), carnitine palmitoyltransferase 1 (CPT1, assay ID Mm01231183\_m1), medium-chain acyl-CoA dehydrogenase (MCAD, assay ID Mm01323360\_g1), sterol regulatory element-binding transcription factor 1 (SREBP-1, assay ID Mm00550338\_m1), fatty acid synthase (FAS assay ID Mm00662319\_m1), stearoyl-CoA desaturase-1 (SCD-1, assay ID Mm00772290\_m1), sterol regulatory element-binding transcription factor 2 (SREBP-2, assay ID Mm01306292\_m1), 3-hydroxy-3-methyl-glutaryl-CoA reductase (HMG-CoA reductase, assay ID Mm01282499\_m1), and 3-hydroxy-3-methyl-glutaryl-CoA synthase (HMG-CoA synthase, assay ID Mm01304569\_m1). Glyceraldehyde 3-phosphate dehydrogenase (GAPD; assay ID Mm99999915\_g1) was used as the reference gene to calculate the relative amounts of gene transcriptions. The TaqMan reagents were purchased from Applied Biosystems, Foster City, California, USA.

## Statistical Analyses

Numerical data are displayed as mean  $\pm$  standard deviation. One-way ANOVA was adopted, with the Tukey method used as the post hoc test.  $p < 0.05$  indicates statistical significance.

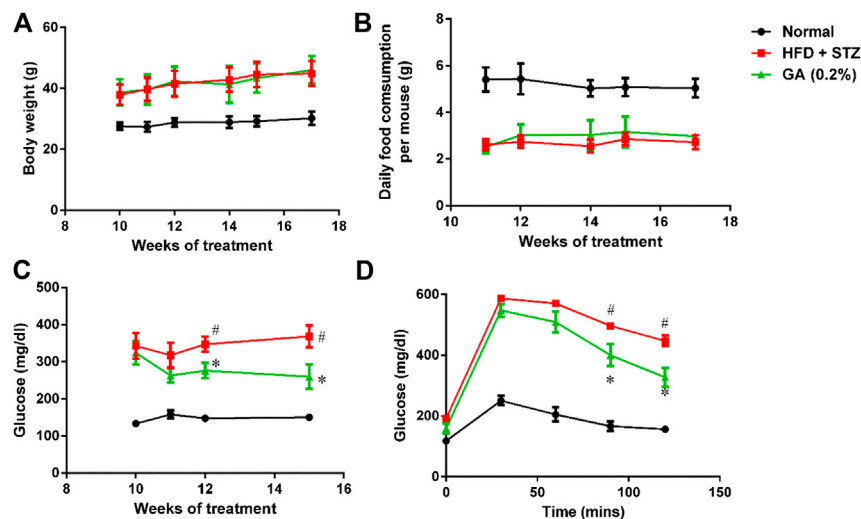


**FIGURE 1 |** Analysis of physiological and biochemical parameters **(A)** Mice body weights **(B)** Variations in food consumption per mouse **(C)** Random blood glucose (RBS) test **(D)** Oral glucose tolerance test (OGTT). Seven to eight mice from each group were subjected to the RBS test on the 10th, 11th, 12th, and 15th week. Six mice from each group were subjected to the OGTT on the 16th week. In the OGTT, fasting glucose was conducted at 0 min; subsequently, the mice were orally fed with glucose (2 g/kg), and the blood glucose contents were measured at 30, 60, 90, and 120 min. # significant difference between the diabetic (HFD + STZ) and control (normal) groups ( $p < 0.05$ ); \* significant difference between the treatment (GA 0.2%) and diabetic groups ( $p < 0.05$ ).

## RESULTS

### Pharmacodynamic Analysis of the Effect of GA on Mice With Diabetes Induced by HFD and STZ

#### Weight and Food Consumption Variations in the Normal, Diabetic, and Treatment Groups

The weights of the diabetic group (HFD + STZ) and treatment group (GA 0.2%) showed significant increase than that of the normal group (Figure 1A). The GA treatment did not alleviate the obesity of the mice fed with the HFD (Figure 1A) or affect the food consumption (Figure 1B).

#### Random Blood Glucose (RBS) Test and Oral Glucose Tolerance Test (OGTT)

The RBS level of the diabetic group was significantly higher than that of the normal group (Figure 1C). The OGTT also revealed that the diabetic group experienced post-challenge hyperglycemia (Figure 1D). Postprandial blood glucose is affected by several factors, including the function of pancreatic  $\beta$ -cells and the sensitivity of related tissues and organs (muscles, fat, and the liver) to insulin. Therefore, these results confirmed that diabetes was successfully induced in the mice. After GA treatment, the RBS level of the mice on the 15th week was significantly lower than that of the mice in the diabetic group (Figure 1C). Moreover, the OGTT showed that GA facilitated alleviation of the post-challenge hyperglycemia in diabetic mice (Figure 1D). Thus, the aforementioned results indicate that GA alleviates high blood glucose.

#### Organ Weight and Serum Biochemical Values

As shown in Figures 2A,B, the liver and kidney weights of the diabetic group were significantly higher than those of the normal

group. However, the liver weight of the treatment group was not significantly lower, while the kidney weight of the treatment group was significantly lower than the diabetic group.

The serum biochemical values revealed that compared with the normal group, the diabetic group demonstrated significantly higher AST and ALT levels (Figures 2C,I), indicating that the liver function of the diabetic group was severely impaired. Moreover, the diabetic group also exhibited severe lipid metabolic disorders (Figures 2E–G); the TG, TCHO, and HDL levels of the diabetic group were significantly higher than those of the normal group. The liver function indices of the treatment group demonstrated a decreasing trend, and the ALT level was significantly lower than that in the diabetic group. GA treatment also alleviated the high TG of the mice with induced diabetes; however, their TCHO and HDL levels were not affected by the treatment. The insulin secretion of the diabetic group was significantly lower than that of the normal group (Figure 2H), indicating that the pancreatic  $\beta$ -cells of the diabetic group were severely damaged. The insulin secretion of the treatment group was not significantly higher than that of the diabetic group.

#### Histological Analysis of Liver, Muscle, and Adipose Tissues

No abnormalities were observed in the liver sections of the normal group (Figure 3A and Table 1), while diffuse hepatic steatosis, identified by primarily macrovesicular steatosis, was observed in the diabetic group. However, microvesicular steatosis was also observed in several regions of the section (Figure 3A and Table 1); this agrees with a previous study (Hebbard and George, 2011). Furthermore, swollen liver cells, ballooning degeneration, and focal necrosis were also observed in the section of the diabetic group, indicating inflammation (Hebbard and George, 2011).

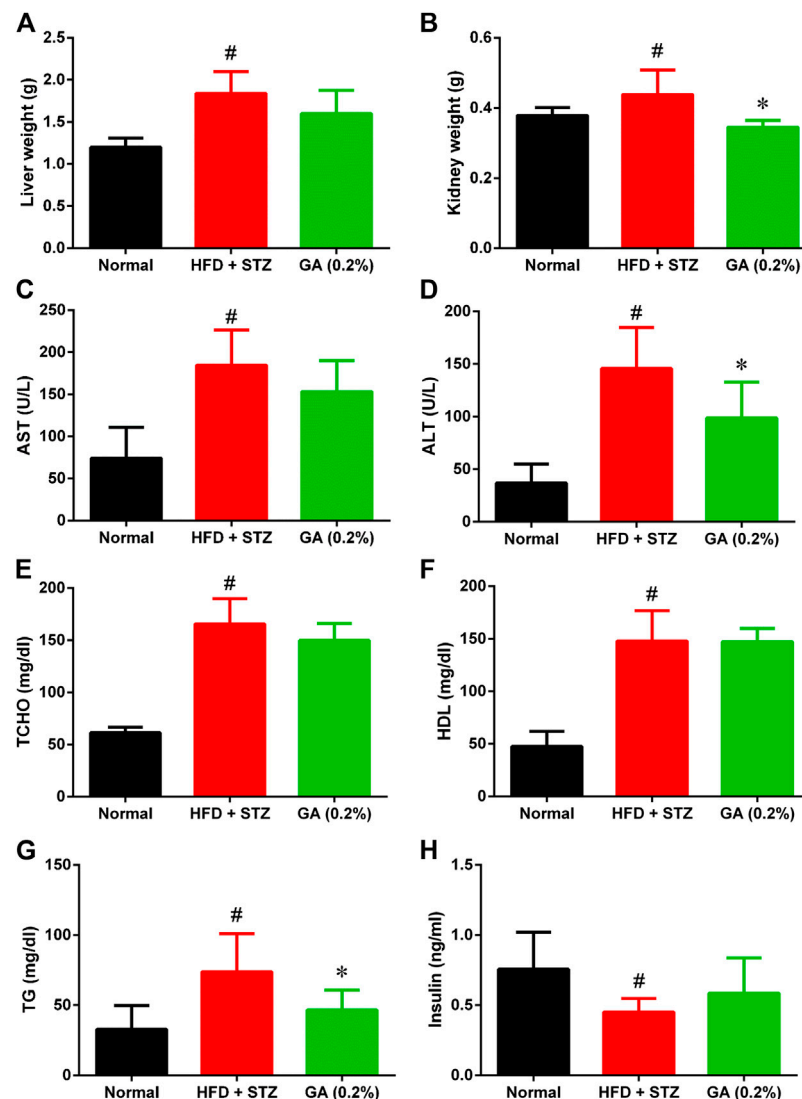


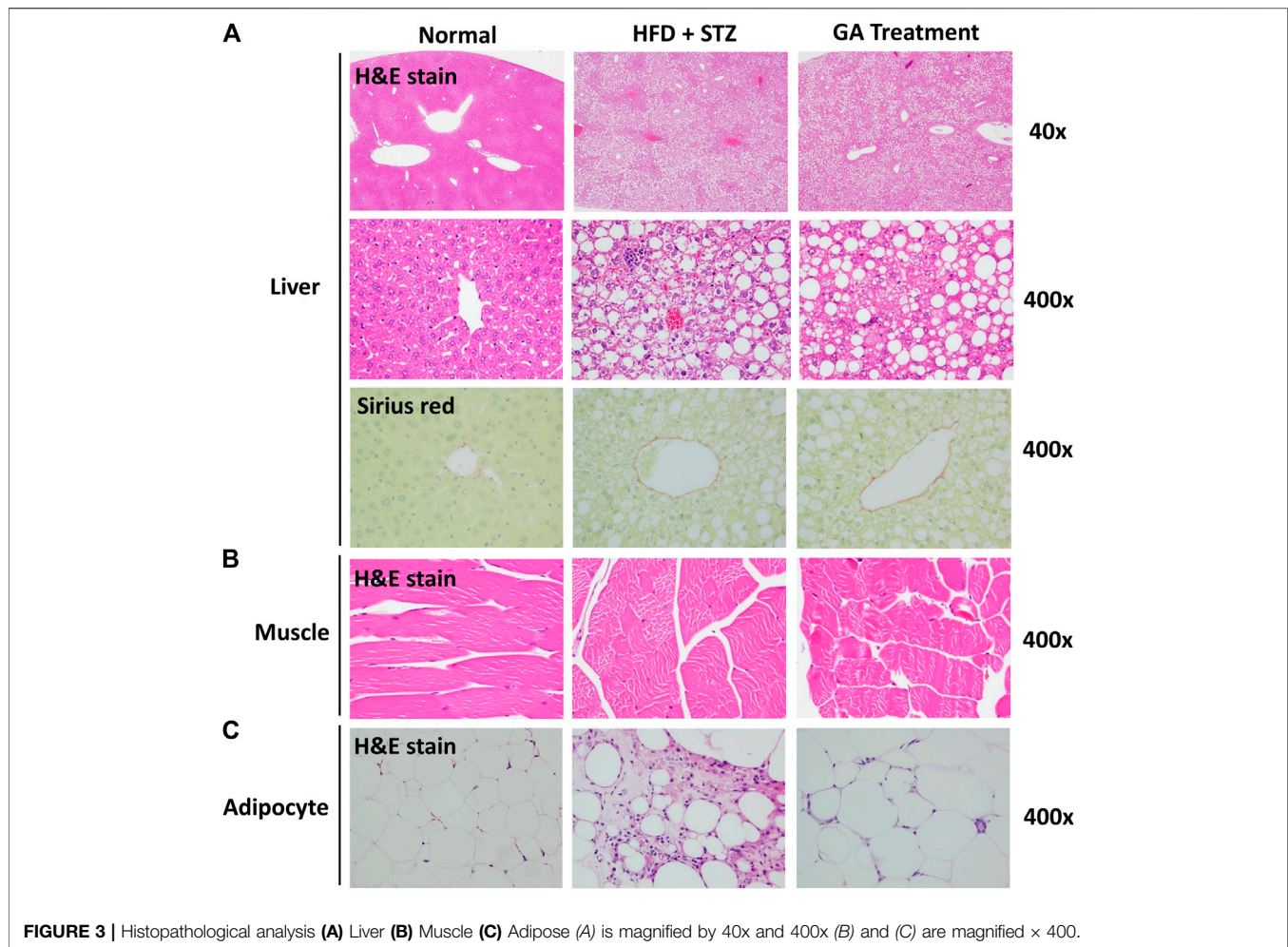
**FIGURE 2 |** Organ weight and serum biochemical values of mice (A) Liver weights (B) Kidney weights (C) Aspartate transaminase (AST) (D) Alanine transaminase (ALT) (E) Total cholesterol (TCHO) (F) High-density lipoprotein (HDL) (G) Triglycerides (TG) (H) Insulin. # indicates significant difference between the diabetes group (HFD + STZ) and control (normal) group ( $p < 0.05$ ); \* indicates significant difference between the treatment group (GA 0.2%) and diabetes group ( $p < 0.05$ ). Six to eight mice from each group were subjected to the AST and ALT test. Seven mice from the normal and diabetes groups were subjected to the insulin test, while five mice from the treatment group (GA 0.2%). Eight mice from each group were subjected to the remaining tests.

However, the Sirius red-dyed section of the diabetic group revealed no liver fibrosis (Figure 3A and Table 1).

Hepatocellular ballooning is an essential indicator distinguishing the symptoms of NAFLD and NASH (Hebbard and George, 2011). It is noteworthy that the GA treatment alleviated the ballooning degeneration of the mice (Figure 3A). The data confirmed that the liver disease animal model induced through HFD and STZ had already progressed to NASH. Therefore, the results indicate that GA can delay the progression of NAFLD. GA exerted a weak effect on macrovesicular steatosis, slightly decreasing the synthesis and accumulation of large liver vacuoles (Figure 3A and Table 1).

Thus, HFD and STZ can simultaneously induce NASH in a diabetes animal model, while GA can delay the progression of NASH.

Observation of the muscular tissue sections revealed no significant lesions in the normal or diabetic groups (Figure 3B). The adipose tissue sections showed that the adipose cells of the normal group were smaller than those of the other groups and exhibited no noticeable pathological changes (Figure 3C). In contrast, the diabetic group demonstrated hypertrophy in the adipose cells along with fat necrosis and steatitis. Compared with the normal group, the treatment group exhibited unclear cellular boundaries and enlarged adipose cells and lipid droplets



as well as macrophage infiltration; however, the extent of macrophage infiltrate was less than that in the diabetic group.

## Metabolomics Analysis on the Effect of GA on Mice With Diabetes Induced by HFD and STZ

### Metabolite Identification

An NMR-based metabolomics platform was used to analyze endogenous metabolites in the blood, urine, liver, and muscle tissue samples of the normal, diabetic, and treatment groups. The signals of the endogenous metabolites displayed on NMR spectra were categorized (Dumas et al., 2006; Xu et al., 2012; An et al., 2013; Shi et al., 2013), and Chenomx 7.6 software was used to verify them. The following metabolites were observed: serum (**Supplementary Table S3**), urine (**Supplementary Table S4**), water-soluble metabolites in the liver (**Supplementary Table S5**), lipid-soluble metabolites in the liver (**Supplementary Table S6**), and water-soluble metabolites in the muscles (**Supplementary Table S7**).

### Multivariate Analysis

To compare the metabolism of the diabetic group with that of the normal and treatment groups, a partial least squares discriminant

analysis (PLS-DA) with score plots was used to visualize the differences between the groups. As shown in the serum PLS-DA score plot, this metabolomics approach allows distinguishing between the effects induced by HFD and GA (**Figures 4A,I**). The score plots illustrate that from the T1 axis perspective, the diabetic group noticeably distinct from the normal group, indicating that the two groups exhibited dissimilar metabolic profiles, and that the diabetic group experienced severe metabolic disorders. However, the GA treatment did not markedly alleviate the disorders of water-soluble metabolites in the liver and urine (**Figures 4C,I**) but exerted a moderate effect on the disorders of lipid-soluble metabolites in the liver and water-soluble metabolites in the muscles (**Figures 4D,E**). It is noteworthy that the treatment group was distinct from the diabetic and normal groups, indicating that GA may exert an effect on multiple organs; however, it could only prevent some metabolic disorders. Therefore, the diabetic mice did not completely recover their health following GA treatment.

### Lipid Changes in Serum and Liver

To further describe the differences between the metabolisms of the mouse groups, dissimilar metabolites were categorized according to biological functions to conduct semi-quantitative analysis. The results revealed severe metabolic disorders in the mice with diabetes induced by HFD and STZ



**TABLE 1** | Pathological examination of liver.

	Liver	
	Microvesicular steatosis	Macrovesicular steatosis (ballooning degeneration)
Normal group	0.00	0.00
HFD + STZ group	5.00 ± 0.00	4.87 ± 0.33
GA treatment group	4.87 ± 0.33	4.37 ± 0.69

Lesion degree was graded from 1 to 5: 1 = minimal (<1%); 2 = slight (1–25%); 3 = moderate (26–50%); 4 = moderate/severe (51–75%); 5 = severe/high (76–100%). Values are presented as means ± SD (N = 8).

(Figure 5). Specifically, the cholesterol and total fatty acid contents showed significant increase (Figures 5A,B). Moreover, the ratio of monounsaturated fatty acids to polyunsaturated fatty acids of the diabetic group decreased significantly (Figure 3C), indicating that the HFD + STZ treatment increased oxidative stress in mice (An et al., 2013). Alternatively, GA treatment alleviated the serum

cholesterol metabolic disorder but not the accumulation of total fatty acids (Figures 5A,B). In addition, GA decreased oxidative stress in mice (Figure 5C).

Hepatic lipid analysis revealed that the liver lipid accumulation induced by HFD and STZ was primarily composed of TG, with a slight amount of cholesterol (Figure 5D). GA treatment decreased accumulation of hepatic lipids and alleviated hepatic steatosis, which concurred with the results of the histopathological sections (Figures 5E–H). The GA treatment partially prevented the accumulation of various lipids and alleviated the upregulated oxidative stress in the liver (Figure 5I).

### Changes in Serum Metabolites

As shown in Supplementary Table S8, HFD + STZ treatment induced changes in metabolic pathways in the mice, including glycolysis, the tricarboxylic acid (TCA) cycle, ketogenesis, amino acid metabolism, choline metabolism, and gut microbiota-related metabolism. The serum samples reflected the average total changes in the metabolites of various tissues and organs. The results indicated that the HFD + STZ treatment induced a

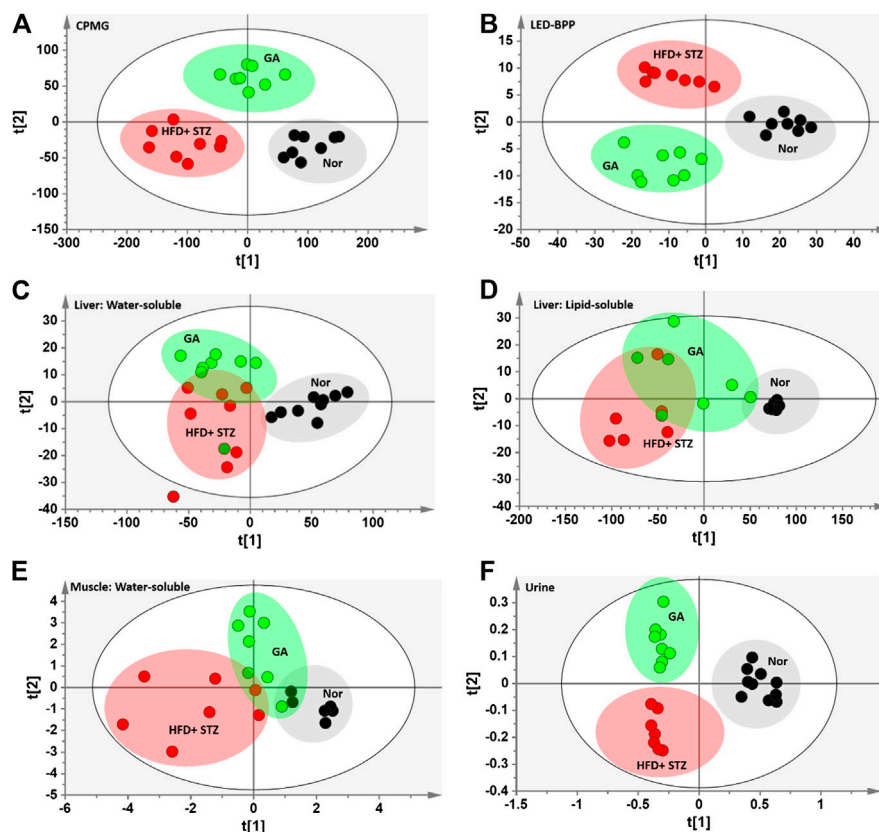


**FIGURE 4** | PLS-DA score plots (A) Carr-Purcell-Meiboom-Gill (CPMG) spectrum of serum samples for small molecule metabolites ( $R^2X = 0.736$ ,  $R^2Y = 0.875$ ,  $Q^2 = 0.845$ ) (B) Longitudinal eddy-current delay-bipolar pulse pair (LED-BPP) spectrum of serum samples for large-molecule metabolites ( $R^2X = 0.841$ ,  $R^2Y = 0.892$ ,  $Q^2 = 0.874$ ) (C) Nuclear Overhauser effect spectroscopy (NOESY) spectrum of liver samples for water-soluble metabolites ( $R^2X = 0.736$ ,  $R^2Y = 0.586$ ,  $Q^2 = 0.359$ ) (D) NOESY spectrum of liver samples for lipid-soluble metabolites ( $R^2X = 0.927$ ,  $R^2Y = 0.567$ ,  $Q^2 = 0.332$ ) (E) NOESY spectrum of muscle samples for water-soluble metabolites ( $R^2X = 0.433$ ,  $R^2Y = 0.618$ ,  $Q^2 = 0.435$ ) (F) NOESY spectrum of urine samples for metabolites ( $R^2X = 0.646$ ,  $R^2Y = 0.892$ ,  $Q^2 = 0.799$ ). Nor: normal group; HFD + STZ: diabetes group; GA: treatment group.

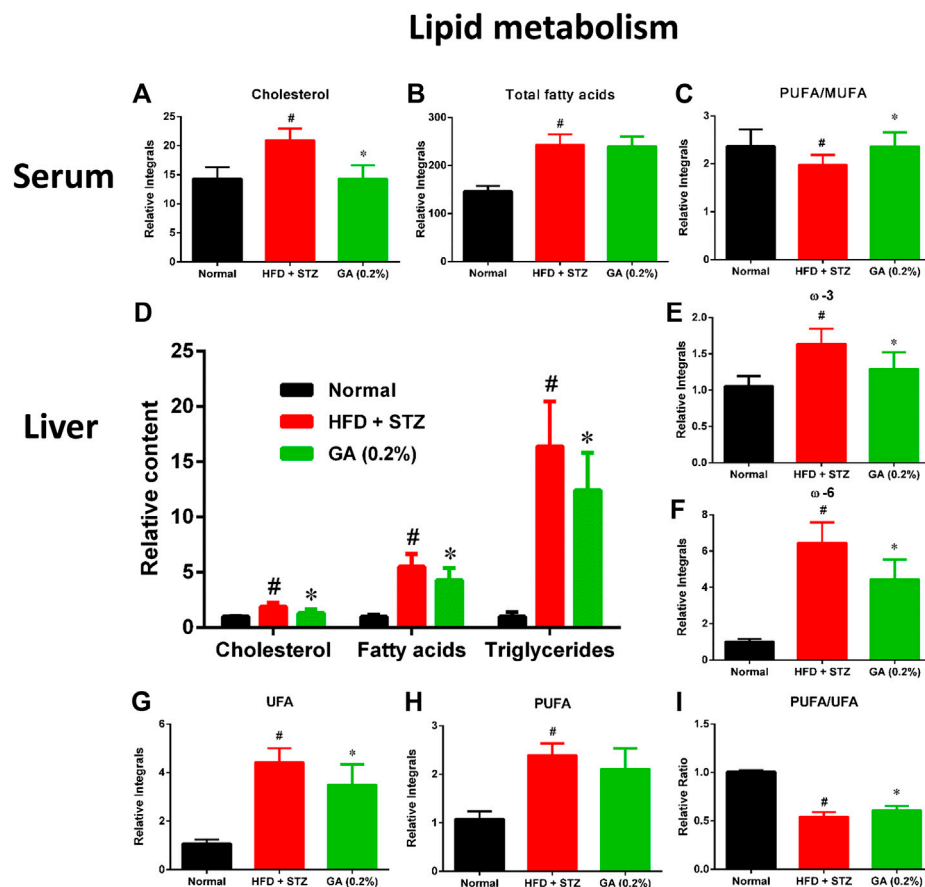


**FIGURE 5 |** Effect of GA on serum and hepatic lipid metabolism (A)–(C): serum lipids (D)–(I) hepatic lipids. # significant difference between the diabetic (HFD + STZ) and control (normal) groups ( $p < 0.05$ ); \* significant difference between the treatment (GA 0.2%) and diabetic groups ( $p < 0.05$ ).

systemic effect, while GA treatment partially prevented some metabolic disorders and upregulated ketogenesis in the blood (Figure 6).

### Changes in Urinary Metabolites

The HFD + STZ treatment induced changes in the urinary metabolites of various metabolic pathways, in particular metabolites involved in glycolysis, TCA cycle, creatine metabolism, amino acid metabolism, allantoin, and organic acids (Supplementary Table S9). The GA treatment prevented the downregulation of allantoin (Figure 7A) and the upregulation of urinary proteins and glucose in the mice induced with diabetes (Figure 7A). Hence, the GA treatment decreased the elevation of urinary protein and glucose levels.

### Changes in Hepatic Metabolites

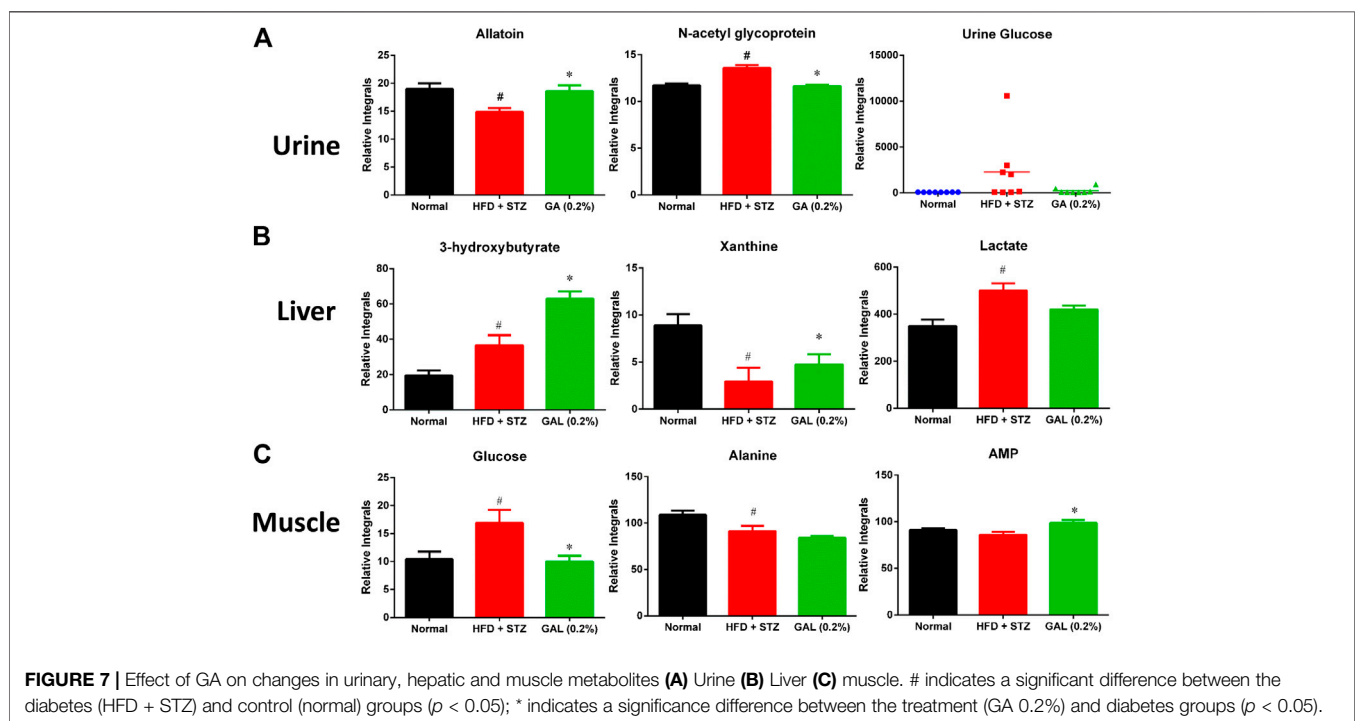
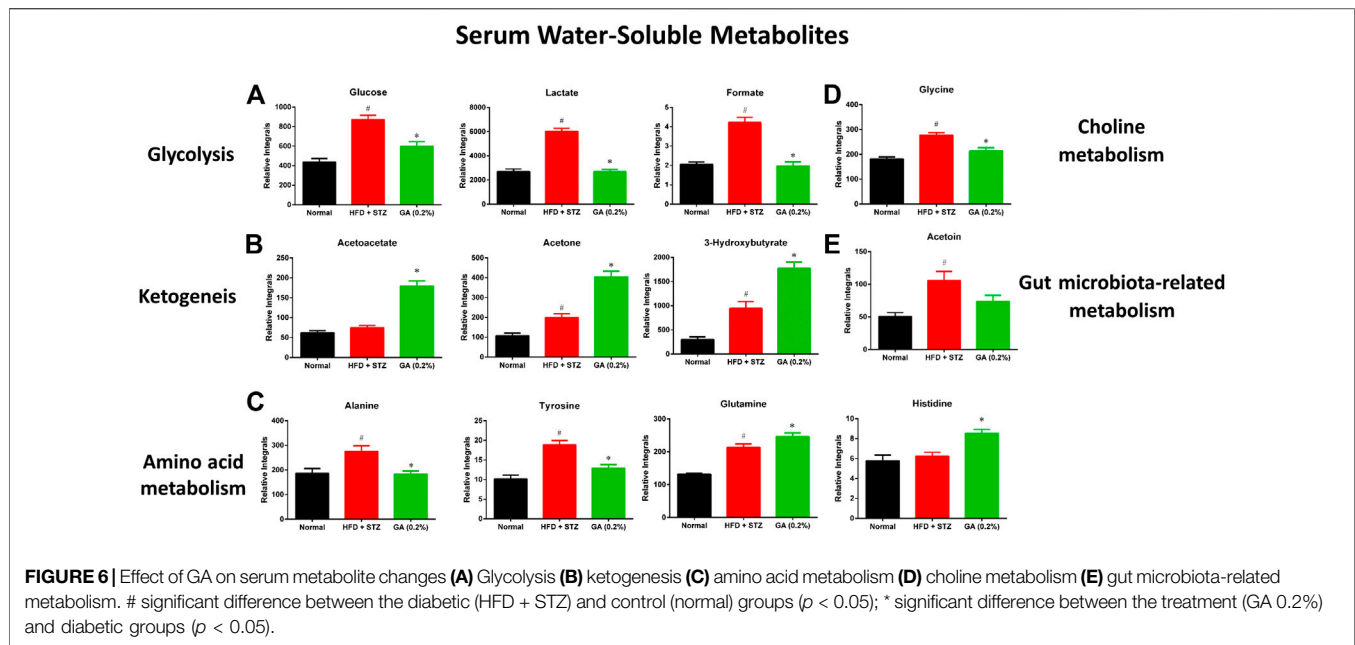
HFD + STZ treatment induced changes in the hepatic metabolism of the mice, including glycolysis and TCA cycles, ketogenesis, fatty acid metabolism, amino acid metabolism, purine metabolism, and choline metabolism (Supplementary Table S10); these changes showed similar

trend as those observed for the serum metabolites. Compared with the diabetic group, the GA treatment group demonstrated increased levels of ketogenesis. Furthermore, the GA treatment prevented the metabolic disorder of xanthine (Figure 7B) and decreased the elevation of lactate (Figure 7B) yet failed to alleviate the disordered energy metabolism. These results concur with those of a previous study (Chao et al., 2014).

### Changes in Muscle Metabolites

HFD + STZ treatment induced changes in only a few metabolites in the muscles of the mice (Supplementary Table S11), including the upregulation of glucose and inosine and downregulation of alanine. This indicates that HFD + STZ treatment exerted a small effect on the muscles of mice. The GA treatment decreased the glucose content in the muscular tissue of the mice as well as alleviated the downregulation of alanine; however, the extent of alleviation was not significant (Figure 7C). In addition, the GA treatment upregulated the adenosine monophosphate content in the muscular tissue of the mice with diabetes (Figure 7C).





## Gene Expression of Liver Lipid Metabolism

To investigate the differences between the gene expressions of liver lipid metabolites in the mouse groups, we analyzed the genes expressions of  $\beta$ -oxidation (Figure 8A), *de novo* lipogenesis (Figure 8B), and cholesterol synthesis (Figure 8C). The results revealed that the  $\beta$ -oxidation gene PPAR $\alpha$  of the diabetic group was significantly upregulated, while the CPT1 $\alpha$  and MCAD expressions were not

significantly different from those of the normal group. The GA treatment prevented and significantly decreased the upregulated PPAR $\alpha$  expression and increased the MCAD expression (Figure 8A). With respect to the *de novo* lipogenesis (Figure 8B), abundant gene expression of SCD-1 was observed in the diabetic group; this concurs with a previous study (Xie et al., 2010). The GA treatment downregulated the expression of SCD-1, but the extent of

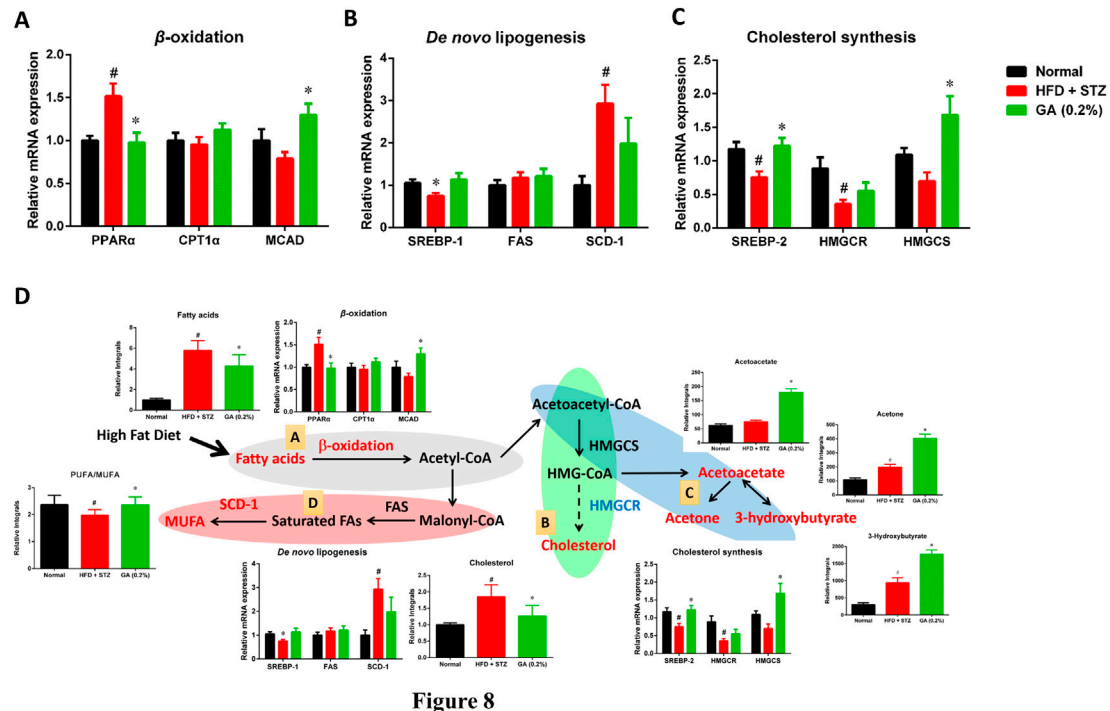


**FIGURE 8 |** Possible mechanisms used by GA in alleviating accumulation of hepatic lipids in diabetic and NASH mice, induced by HFD and STZ (A) Regulation of  $\beta$ -oxidation genes (B) regulation of *de novo* lipogenesis genes; (C) regulation of cholesterol synthesis genes; (D) possible mechanisms, A Lipolysis— $\beta$ -oxidation (gray); B cholesterol synthesis (green); C ketogenesis—*de novo* lipogenesis (red). Red indicates significant upregulation of metabolite or enzyme expression in diabetic mice, while blue indicates significant downregulation. Black indicates a metabolite or enzyme that is undetectable or exhibited non-significant changes. PPAR $\alpha$  (peroxisome proliferator-activated receptor alpha), CPT1 (carnitine palmitoyltransferase), MCAD (medium-chain acyl-CoA dehydrogenase), SREBP-1 (sterol regulatory element-binding transcription factor 1), FAS (fatty acid synthase), SCD-1 (stearoyl-CoA desaturase-1), SREBP-2 (sterol regulatory element-binding transcription factor 2), HMG-CoA reductase (3-hydroxy-3-methyl-glutaryl-CoA reductase), HMG-CoA synthase (3-hydroxy-3-methyl-glutaryl-CoA synthase). Metabolites: MUFA (monounsaturated fatty acid), HMG-CoA (3-hydroxy-3-methylglutaryl-coenzyme A). # significant difference between the diabetic (HFD + STZ) and control (normal) groups ( $p < 0.05$ ); \* significant difference between the treatment (GA 0.2%) and diabetic groups ( $p < 0.05$ ).

downregulation was not significant. For the cholesterol synthesis genes (Figure 8C), the expressions of SREBP-2 and HMGCR, in the liver of the mice with diabetes, were significantly downregulated. The GA treatment prevented the downregulation of SREBP-2 and upregulated the expression of HMGCS.

## DISCUSSION

### GA Alleviates High Blood Glucose in an Animal Model

From a pathophysiological perspective, insulin resistance (relative insufficient insulin), and impaired insulin secretion (insufficient insulin) are essential to diabetes occurrence.

However, it is very interesting that only few muscle metabolites exhibited metabolic disorders (Supplementary Table S11), indicating that the mechanism of HFD and STZ in inducing high blood glucose in the diabetes animal model primarily involved damage of pancreatic  $\beta$ -cells for STZ, while the effect on the insulin resistance of muscle tissues was less severe. Examining the high insulin secretion in the serum sample of the treatment group revealed that the

mechanism of GA to alleviate high blood glucose may be related to how GA relieves glucolipotoxicity and thus protects pancreatic  $\beta$ -cells from being damaged. Although the hyperglycemia caused by the model has less muscle involvement, it is still found that GA increased the content of adenosine monophosphate (AMP) in muscles, indicating that AMP-activated kinase (AMPK) may still be regulated in the process of lowering blood sugar (Doan et al., 2015). Whether GA decreases blood glucose by inducing AMP-activated kinase channels, requires further verification.

Previous studies have reported that GA can induce the expression of PPAR gamma (PPAR $\gamma$ ) in the liver, muscles, and fatty tissues (Gandhi et al., 2014). The activity of PPAR $\gamma$  is related to insulin sensitivity. Therefore, we postulated that the mechanism by which GA alleviates high blood glucose may also be associated with the upregulation of PPAR $\gamma$ .

### GA Alleviates NAFLD in an Animal Model

Previous studies have asserted that high blood glucose is an essential factor that progresses the disease condition of obese mice to NASH (Lo et al., 2011). Here, the histopathological sections demonstrated evident ballooning degeneration and focal necrosis in the mice liver cells, indicating that the disease condition had already progressed to

NASH (Hebbard and George, 2011). Noticeably, GA treatment alleviated this degeneration, implying that GA-mediated delay in the progression of NAFLD might be because of alleviation in the high blood glucose of the mice.

In addition, GA regulates the genes involved in the pathway and the changes in metabolites related to lipolysis ( $\beta$ -oxidation and ketogenesis), lipid synthesis (*de novo* lipogenesis), and cholesterol synthesis were examined. Accordingly, a hypothesis regarding the potential mechanisms of GA was proposed (Figure 8D).

- (1) Ketone bodies are by-products generated through  $\beta$ -oxidation (Laffel, 1999). Compared with the diabetic group (HFD + STZ), the treatment group exhibited noticeable upregulation of ketone bodies, in particular acetone, acetoacetate, and 3-hydroxybutyrate, indicating the increased  $\beta$ -oxidation of fatty acids in the treatment group. GA treatment upregulated the gene expression of medium-chain acyl-coenzyme A (CoA) dehydrogenase, verifying the inference that the increase in ketone bodies after GA treatment might be related to GA inducing  $\beta$ -oxidation in the liver (Figure 8D).
- (2) Increased  $\beta$ -oxidation increases the content of acetyl-CoA in the liver. Further analysis of the acetyl-CoA pathway revealed three plausible directions: *de novo* lipogenesis, cholesterol synthesis, or ketogenesis. Cholesterol synthesis first involves forming 3-hydroxy-3-methyl-glutaryl-CoA (HMG-CoA), followed by multiple steps for forming cholesterol. Moreover, HMG-CoA is an essential precursor of ketogenesis. Compared with the diabetic group, the treatment group demonstrated upregulated hydroxymethylglutaryl-CoA synthase expression (for catalyzing HMG-CoA synthesis), however, the expression of HMG-CoA reductase was not affected (for catalyzing cholesterol synthesis). In addition, the study results indicated that GA facilitates decreasing hepatic cholesterol and increasing ketone body formation. According to the aforementioned assertions, we inferred that GA treatment enables lipolysis, the products of which then undergo ketone metabolism instead of cholesterol synthesis (Figure 8D).
- (3) In case of the protein expression associated with *de novo* lipogenesis in the diabetic group, only that of SCD-1 was affected, while the rate-limiting FAS was not. SCD-1 converts saturated fatty acids to monounsaturated fatty acids (MUFAs). The substantial upregulation of SCD-1 might be related to the downregulation of polyunsaturated fatty acid (PUFA)/MUFA ratio in the blood and liver of the diabetic group. GA administration inhibited the expression of SCD-1 and prevented the downregulation of the PUFA/MUFA ratio (Figure 8D).

The long-term metabolic changes observed in this study do not know whether the up-regulation of  $\beta$ -oxidation and ketogenesis is the cause of the improvement of fatty liver or the result of the improvement of fatty liver. However, according to the results of experimental design, there are differences between the normal group, diabetic group (HFD + STZ) and GA treatment group.

Previous studies have indicated that genes related to fatty acid  $\beta$ -oxidation are up-regulated in HFD-induced obese mice. These genes are initially up-regulated (4 weeks) and then down-regulated (10 weeks) (Chan et al, 2008). In this study, HFD feeding lasted for 17 weeks. It is worth noting that in the GA group, the expression of MCAD increased significantly, which indicates that GA can upregulate genes related to  $\beta$ -oxidation. These results indicated that no compensatory adaptation occurred in response to HFD-induced short-term upregulation of genes related to fatty acid  $\beta$ -oxidation. The molecular mechanism of GA against  $\beta$ -oxidation needs to be further studied *in vitro*.

## HFD and STZ Induce Diabetes in an Animal Model and Cause Changes in Intestinal Microbiota Metabolism

Previous studies have indicated that the composition and quantity of intestinal microbiota in patients with obesity undergo substantial changes than in healthy people (Kumar et al., 2006); other studies have reported that the intestinal microbiota composition of mice with diabetes differs from nondiabetic mice, and that antibiotics can decrease the risk of diabetes (Brugman et al., 2006). These assertions indicate that changes in intestinal microbiota are crucial to the progression of metabolic diseases. This study confirmed the substantial upregulation of acetoin, which is related to pneumonia inducing *Klebsiella pneumoniae*, in the blood of the diabetic group. *K. pneumoniae* has been identified in the gastrointestinal tract and in patients with pyogenic liver abscesses (Fung et al., 2012), while urine metabolites related to intestinal microbiota metabolism, namely methylamine, hippurate, and trimethylamine, were downregulated. Hence, the intestinal microbiota in the diabetic mouse group may have undergone changes. Moreover, GA-rich fruits have reportedly facilitated the growth of probiotic bacteria in the intestine (Bialonska, et al., 2010). Here, we have confirmed that GA administration prevented the substantial upregulation of 2,3-butanediol, enabling serum acetoin to return to its regular level. However, GA was ineffective on urine metabolites, and its effect on balancing the growth of intestinal microbiota requires further verification.

## GA Alleviates Urine Protein and Urine Glucose in an Animal Model

The STZ-induced animal model used in this study is a typical diabetes and kidney disease model (Chow and Allen, 2015). This study verified that several mice in the diabetic group experienced severely high urine glucose. The kidney glucose absorption function of these mice may have been impaired; hence, loss of glucose through urination was detected, indicating that the kidneys of the mice may have also been damaged. The urine protein level of the diabetic group increased significantly, indicating that STZ-induced high blood glucose may have resulted in glomerular damage, thus generating additional urine protein, or that pathological change in the tubules may have prevented protein recycling. Urinary glucose was detected in only few mice in the treatment group,

and their urine protein levels returned to those like the control group. These results indicate that GA treatment can potentially alleviate STZ-induced diabetes and kidney disease.

## CONCLUSION

Herein, we administered HFD and STZ to induce metabolic disorders in diabetic mice. The relevant metabolic pathways were examined to elucidate the mechanisms of metabolic disorders that may cause HFD and STZ-induced diabetes and NAFLD (**Supplementary Figure S3**). The results revealed that HFD and STZ-induced severe metabolic disorders in the diabetic mice, including metabolic disorders related to glucose, lipids, amino acids, purines, and pyrimidines as well as changes in intestinal microbiota. However, GA treatment alleviated the high blood glucose of the mice and decelerated the progression of NAFLD. This study is the first, to the best of our knowledge, to report the association between alleviation of lipid accumulation by GA and upregulation of  $\beta$ -oxidation and ketogenesis. The results of this study may supplement those of pharmacodynamics studies and facilitate characterization of novel GA mechanisms in alleviating metabolic diseases.

## DATA AVAILABILITY STATEMENT

The original contributions presented in the study are included in the article/**Supplementary Material**, further inquiries can be directed to the corresponding authors.

## ETHICS STATEMENT

The animal study was reviewed and approved by the Laboratory Animal Center Committee of Ghang Gung University of Science and Technology (IACUC-2014-009).

## REFERENCES

- Ahad, A., Ahsan, H., Mujeib, M., and Siddiqui, W. A. (2015). Gallic acid ameliorates renal functions by inhibiting the activation of p38 MAPK in experimentally induced type 2 diabetic rats and cultured rat proximal tubular epithelial cells. *Chem. Biol. Interact.* 240, 292–303. doi:10.1016/j.cbi.2015.08.026
- An, Y., Xu, W., Li, H., Lei, H., Zhang, L., Hao, F., et al. (2013). High-fat diet induces dynamic metabolic alterations in multiple biological matrices of rats. *J. Proteome Res.* 12, 3755–3768. doi:10.1021/pr400398b
- Beckonert, O., Keun, H. C., Ebbs, T. M., Bundy, J., Holmes, E., Lindon, J. C., et al. (2007). Metabolic profiling, metabolomic and metabonomic procedures for NMR spectroscopy of urine, plasma, serum and tissue extracts. *Nat. Protoc.* 2, 2692–2703. doi:10.1038/nprot.2007.376
- Benalla, W., Bellahcen, S., and Bnouham, M. (2010). Antidiabetic medicinal plants as a source of alpha glucosidase inhibitors. *Curr. Diabetes Rev.* 6, 247–254. doi:10.2174/157339910791658826
- Bialonska, D., Ramnani, P., Kasimsetty, S. G., Muntha, K. R., Gibson, G. R., and Ferreira, D. (2010). The influence of pomegranate by-product and punicalagins on selected groups of human intestinal microbiota. *Int. J. Food Microbiol.* 140, 175–182. doi:10.1016/j.jfoodmicro.2010.03.038
- Brugman, S., Klatter, F. A., Visser, J. T., Wildeboer-Veloo, A. C., Harmsen, H. J., Rozing, J., et al. (2006). Antibiotic treatment partially protects against type 1 diabetes in the

## AUTHOR CONTRIBUTIONS

JC, H-YC, M-LC, S-SH, J-WL, W-HP, and L-HP conceived and designed the experiments; JC, J-WL, and L-HP performed the experiments and analyzed the data; H-YC, M-LC, S-SH, J-WL, W-HP, L-HP contributed reagents/materials/analysis tools.

## FUNDING

This research was funded by the Ministry of Science and Technology: MOST 107-2320-B-039 -030 -MY3 and MOST 109-2320-B-039-026. This research was also funded by the China Medical University (CMU106-N-24, CMU107-N-33, and CMU108-N-22) and a grant for the Chang Gung Medical Research Program (CMRPF1G0211 and CMRPF1G0212) from the Chang Gung Memorial Hospital. Further, this study was supported by the China Medical University under the Higher Education Sprout Project and Teaching Practice Research Program (1077170A), Ministry of Education, Taiwan.

## ACKNOWLEDGMENTS

The authors would like to thank Editage for editorial assistance. The NMR spectra were obtained at the core facility for metabolomics analysis supported by National Core Facility Program for Biotechnology, Taiwan.

## SUPPLEMENTARY MATERIAL

The Supplementary Material for this article can be found online at: <https://www.frontiersin.org/articles/10.3389/fphar.2020.606759/full#supplementary-material>.

- bio-breeding diabetes-prone rat. Is the gut flora involved in the development of type 1 diabetes? *Diabetologia*. 49, 2105–2108. doi:10.1007/s00125-006-0334-0
- Chan, M. Y., Zhao, Y., and Heng, C. K. (2008). Sequential responses to high-fat and high-calorie feeding in an obese mouse model. *Obesity* 16, 972–978. doi:10.1038/oby.2008.32
- Chao, J., Huo, T. I., Cheng, H. Y., Tsai, J. C., Liao, J. W., Lee, M. S., et al. (2014). Gallic acid ameliorated impaired glucose and lipid homeostasis in high fat diet-induced NAFLD mice. *PLoS One* 9, e96969. doi:10.1371/journal.pone.0096969
- Chow, B. S., and Allen, T. J. (2015). Mouse models for studying diabetic nephropathy. *Curr. Protoc. Mouse Biol.* 5, 85–94. doi:10.1002/9780470942390.mo140192
- Danaei, G., Finucane, M. M., Lu, Y., Singh, G. M., Cowan, M. J., Paciorek, C. J., et al. 2011. National, regional, and global trends in fasting plasma glucose and diabetes prevalence since 1980: systematic analysis of health examination surveys and epidemiological studies with 370 country-years and 2.7 million participants. *Lancet* 378, 31–40. doi:10.1016/S0140-6736(11)60679-X
- Dembinska-Kiec, A., Mykkänen, O., Kiec-Wilk, B., and Mykkänen, H. (2008). Antioxidant phytochemicals against type 2 diabetes. *Br. J. Nutr.* 99 E Suppl 1, ES109–17. doi:10.1017/S000711450896579X
- Doan, K. V., Ko, C. M., Kinyua, A. W., Yang, D. J., Choi, Y. H., Oh, I. Y., et al. (2015). Gallic acid regulates body weight and glucose homeostasis through AMPK activation. *Endocrinology* 156, 157–168. doi:10.1210/en.2014-1354



- Dumas, M. E., Barton, R. H., Toye, A., Cloarec, O., Blancher, C., Rothwell, A., et al. (2006). Metabolic profiling reveals a contribution of gut microbiota to fatty liver phenotype in insulin-resistant mice. *Proc. Natl. Acad. Sci. U.S.A.* 103, 12511–12516. doi:10.1073/pnas.0601056103
- Food and Drug Administration (2015). Guidance for Industry: estimating the maximum safe starting dose in initial clinical trials for therapeutics in adult healthy volunteers. Available at: <http://www.fda.gov/cder/Guidance/5541fnl.pdf/>. (Accessed July 14, 2015).
- Fung, C. P., Lin, Y. T., Lin, J. C., Chen, T. L., Yeh, K. M., Chang, F. Y., et al. (2012). *Klebsiella pneumoniae* in gastrointestinal tract and pyogenic liver abscess. *Emerg. Infect. Dis.* 18, 1322–1325. doi:10.3201/eid1808.111053
- Gandhi, G. R., Jothi, G., Antony, P. J., Balakrishna, K., Paulraj, M. G., Ignacimuthu, S., et al. (2014). Gallic acid attenuates high-fat diet fed-streptozotocin-induced insulin resistance via partial agonism of PPAR $\gamma$  in experimental type 2 diabetic rats and enhances glucose uptake through translocation and activation of GLUT4 in PI3K/p-Akt signaling pathway. *Eur. J. Pharmacol.* 745, 201–216. doi:10.1016/j.ejphar.2014.10.044
- Hebbard, L., and George, J. (2011). Animal models of nonalcoholic fatty liver disease. *Nat. Rev. Gastroenterol. Hepatol.* 8, 35–44. doi:10.1038/nrgastro.2010.191
- Hsiang, C. Y., Hseu, Y. C., Chang, Y. C., Kumar, K. J., Ho, T. Y., and Yang, H. L. (2013). Toona sinensis and its major bioactive compound gallic acid inhibit LPS-induced inflammation in nuclear factor- $\kappa$ B transgenic mice as evaluated by *in vivo* bioluminescence imaging. *Food Chem.* 136, 426–434. doi:10.1016/j.foodchem.2012.08.009
- Hsu, C. L., and Yen, G. C. (2007). Effect of gallic acid on high fat diet-induced dyslipidaemia, hepatosteatosis and oxidative stress in rats. *Br. J. Nutr.* 98, 727–735. doi:10.1017/S000711450774686X
- Kongpichitchoke, T., Chiu, M. T., Huang, T. C., and Hsu, J. L. (2016). Gallic acid content in Taiwanese teas at different degrees of fermentation and its antioxidant activity by inhibiting PKC $\delta$  activation: *in vitro* and *in silico* studies. *Molecules* 21, 1346. doi:10.3390/molecules21101346
- Kumar, P. S., Leys, E. J., Bryk, J. M., Martinez, F. J., Moeschberger, M. L., and Griffen, A. L. (2006). Changes in periodontal health status are associated with bacterial community shifts as assessed by quantitative 16S cloning and sequencing. *J. Clin. Microbiol.* 44, 3665–3673. doi:10.1128/JCM.00317-06
- Kyriakis, E., Stravodimos, G. A., Kantsadi, A. L., Chatzileontiadou, D. S., Skamnaki, V. T., and Leonidas, D. D. (2015). Natural flavonoids as antidiabetic agents. The binding of gallic and ellagic acids to glycogen phosphorylase *b*. *FEBS Lett.* 589, 1787–1794. doi:10.1016/j.febslet.2015.05.013
- Laffel, L. (1999). Ketone bodies: a review of physiology, pathophysiology and application of monitoring to diabetes. *Diabetes Metab. Res. Rev.* 15, 412–426. doi:10.1002/(SICI)1520-7560(199911/12)15:6<412::AID-DMRR72>3.0.CO;2-E
- Lee, Y. H., Song, K. W., Ko, Y. O., Kim, S. M., and Chung, D. S. (2005). Studies on methods of rising seeding in native tea tree (*Camellia sinensis* L.). *J. Korean Tea Soc.* 11, 85–92.
- Liang, H., Liang, Y., Dong, J., Lu, J., Xu, H., and Wang, H. (2007). Decaffeination of fresh green tea leaf (*Camellia sinensis*) by hot water treatment. *Food Chem.* 101, 1468–1473. doi:10.1016/j.foodchem.2006.03.054
- Lo, L., McLennan, S. V., Williams, P. F., Bonner, J., Chowdhury, S., McCaughan, G. W., et al. (2011). Diabetes is a progression factor for hepatic fibrosis in a high fat fed mouse obesity model of non-alcoholic steatohepatitis. *J. Hepatol.* 55, 435–444. doi:10.1016/j.jhep.2010.10.039
- Manach, C., Williamson, G., Morand, C., Scalbert, A., and Rémésy, C. (2005). Bioavailability and bioefficacy of polyphenols in humans. I. Review of 97 bioavailability studies. *Am. J. Clin. Nutr.* 81, 230S–242S. doi:10.1093/ajcn/81.1.230S
- Matthew, E. H., and Douglas, A. B. (1997). Tea chemistry. *Crit. Rev. Plant Sci.* 16 (5), 415–480.
- Mok, C. K. (2002). Suppression of browning of green tea by extraction with organic acids. *Food Eng. Prog.* 6, 215–221.
- Mu, J., Woods, J., Zhou, Y. P., Roy, R. S., Li, Z., Zycband, E., et al. (2006). Chronic inhibition of dipeptidyl peptidase-4 with a sitagliptin analog preserves pancreatic beta-cell mass and function in a rodent model of type 2 diabetes. *Diabetes* 55, 1695–1704. doi:10.2337/db05-1602
- Oi, Y., Hou, I. C., Fujita, H., and Yazawa, K. (2012). Antiobesity effects of Chinese black tea (Pu-erh tea) extract and gallic acid. *Phytother. Res.* 26, 475–481. doi:10.1002/ptr.3602
- Patel, S. S., and Goyal, R. K. (2011). Cardioprotective effects of gallic acid in diabetes-induced myocardial dysfunction in rats. *Pharmacogn. Res.* 3, 239–245. doi:10.4103/0974-8490.89743
- Punithavathi, V. R., Prince, P. S., Kumar, R., and Selvakumari, J. (2011). Antihyperglycaemic, antilipid peroxidative and antioxidant effects of gallic acid on streptozotocin induced diabetic Wistar rats. *Eur. J. Pharmacol.* 650, 465–471. doi:10.1016/j.ejphar.2010.08.059
- Punithavathi, V. R., Stanely Mainzen Prince, P., Kumar, M. R., and Selvakumari, C. J. (2011). Protective effects of gallic acid on hepatic lipid peroxide metabolism, glycoprotein components and lipids in streptozotocin-induced type II diabetic Wistar rats. *J. Biochem. Mol. Toxicol.* 25, 68–76. doi:10.1002/jbt.20360
- Quan, V. V., Costas, E. S., Minh, H. N., John, B. G., and Paul, D. R. (2011). Isolation of green tea catechins and their utilization in the food industry. *Food Rev. Int.* 27 (3), 227–247. doi:10.1080/87559129.2011.563397
- Sameermahmood, Z., Raji, L., Saravanan, T., Vaidya, A., Mohan, V., and Balasubramanyam, M. (2010). *Phytother. Res.* 24 Suppl 1, S83–S94. doi:10.1002/ptr.2926
- Sanyal, R., Darroudi, F., Parzefall, W., Nagao, M., and Knasmüller, S. (1997). Inhibition of the genotoxic effects of heterocyclic amines in human derived hepatoma cells by dietary bioantimutagens. *Mutagenesis* 12, 297–303. doi:10.1093/mutage/12.4.297
- Sawant, S. P., Dnyanmote, A. V., Mitra, M. S., Chilakapati, J., Warbritton, A., Latendresse, J. R., et al. (2006). Protective effect of type 2 diabetes on acetaminophen-induced hepatotoxicity in male Swiss-Webster mice. *J. Pharmacol. Exp. Therapeut.* 316, 507–519. doi:10.1124/jpet.105.094326
- Shi, X., Xiao, C., Wang, Y., and Tang, H. (2013). Gallic acid intake induces alterations to systems metabolism in rats. *J. Proteome Res.* 12, 991–1006. doi:10.1021/pr301041k
- Subramanian, A. P., John, A. A., Vellayappan, M. V., Balaji, A., Jaganathan, S. K., Supriyanto, E., et al. (2015). Gallic acid: prospects and molecular mechanisms of its anticancer activity. *RSC Adv.* 5, 35608–35621. doi:10.1039/C5RA02727F
- Szkudelski, T. (2001). The mechanism of alloxan and streptozotocin action in B cells of the rat pancreas. *Physiol. Res.* 50, 537–546. doi:10.1007/s00125-007-0886-7
- Taylor, J., King, R. D., Altmann, T., and Fiehn, O. (2002). Application of metabolomics to plant genotype discrimination using statistics and machine learning. *Bioinformatics* 18 Suppl 2, S241–S248. doi:10.1093/bioinformatics/18.suppl\_2.s241
- Tomás-Barberán, F. A., and Clifford, M. N. (2000). Dietary hydroxybenzoic acid derivatives—nature, occurrence and dietary burden. *J. Sci. Food Agric.* 80, 1024–1032. doi:10.1002/(SICI)1097-0010(20000515)80:7<1024::AID-JSFA567>3.0.CO;2-S
- Wang, H., and Helliwell, K. (2001). Determination of flavonols in green tea and black tea leaves and green tea infusions by high performance liquid chromatography. *Food Res. Int.* 34, 223–227. doi:10.1016/S0963-9969(00)00156-3
- Xiao, J., Ni, X., Kai, G., and Chen, X. (2015). Advance in dietary polyphenols as aldose reductases inhibitors: structure-activity relationship aspect. *Crit. Rev. Food Sci. Nutr.* 55, 16–31. doi:10.1080/10408398.2011.584252
- Xie, Z., Li, H., Wang, K., Lin, J., Wang, Q., Zhao, G., et al. (2010). Analysis of transcriptome and metabolome profiles alterations in fatty liver induced by high-fat diet in rat. *Metab. Clin. Exp.* 59, 554–560. doi:10.1016/j.metabol.2009.08.022
- Xu, W., Wu, J., An, Y., Xiao, C., Hao, F., Liu, H., et al. (2012). Streptozotocin-induced dynamic metabonomic changes in rat biofluids. *J. Proteome Res.* 11, 3423–3435. doi:10.1021/pr300280t
- Yue, Y., Chu, G. X., Liu, X. S., Tang, X., Wang, W., Liu, G. J., et al. (2014). TMDb: a literature-curated database for small molecular compounds found from tea. *BMC Plant Biol.* 14, 243–250. doi:10.1186/s12870-014-0243-1

**Conflict of Interest:** The authors declare that the research was conducted in the absence of any commercial or financial relationships that could be construed as a potential conflict of interest.

Copyright © 2021 Chao, Cheng, Chang, Huang, Liao, Cheng, Peng and Pao. This is an open-access article distributed under the terms of the Creative Commons Attribution License (CC BY). The use, distribution or reproduction in other forums is permitted, provided the original author(s) and the copyright owner(s) are credited and that the original publication in this journal is cited, in accordance with accepted academic practice. No use, distribution or reproduction is permitted which does not comply with these terms.

Available online at [www.sciencedirect.com](http://www.sciencedirect.com)

ScienceDirect

Biomedical Journal

journal homepage: [www.elsevier.com/locate/bj](http://www.elsevier.com/locate/bj)

## Review Article

# COVID-19: The first documented coronavirus pandemic in history

Yen-Chin Liu <sup>a,1</sup>, Rei-Lin Kuo <sup>a,b,c,d,1</sup>, Shin-Ru Shih <sup>a,b,c,e,f,\*</sup><sup>a</sup> The Research Center for Emerging Viral Infection, Chang Gung University, Taoyuan, Taiwan<sup>b</sup> Graduate Institute of Biomedical Sciences, College of Medicine, Chang Gung University, Taoyuan, Taiwan<sup>c</sup> Department of Medical Biotechnology and Laboratory Science, Chang Gung University, Taoyuan, Taiwan<sup>d</sup> Division of Allergy, Asthma, and Rheumatology, Department of Pediatrics, Chang Gung Memorial Hospital at Linkou, Taoyuan, Taiwan<sup>e</sup> Clinical Virology Laboratory, Chang Gung Memorial Hospital at Linkou, Taoyuan, Taiwan<sup>f</sup> Research Center for Chinese Herbal Medicine, Research Center for Food and Cosmetic Safety, Graduate Institute of Health Industry Technology, College of Human Ecology, Chang Gung University of Science and Technology, Taoyuan, Taiwan

Prof. Shin-Ru Shih

## ARTICLE INFO

## Article history:

Received 27 April 2020

Accepted 29 April 2020

Available online 5 May 2020

## Keywords:

COVID-19

SARS-COV-2

Coronavirus

Pandemic

## ABSTRACT

The novel human coronavirus disease COVID-19 has become the fifth documented pandemic since the 1918 flu pandemic. COVID-19 was first reported in Wuhan, China, and subsequently spread worldwide. The coronavirus was officially named severe acute respiratory syndrome coronavirus 2 (SARS-CoV-2) by the International Committee on Taxonomy of Viruses based on phylogenetic analysis. SARS-CoV-2 is believed to be a spillover of an animal coronavirus and later adapted the ability of human-to-human transmission. Because the virus is highly contagious, it rapidly spreads and continuously evolves in the human population. In this review article, we discuss the basic properties, potential origin, and evolution of the novel human coronavirus. These factors may be critical for studies of pathogenicity, antiviral designs, and vaccine development against the virus.

Currently, people all over the world have been affected by coronavirus disease 2019 (COVID-19), which is the fifth pandemic after the 1918 flu pandemic. As of now, we can trace the first report and subsequent outbreak from a cluster of novel human pneumonia cases in Wuhan City, China, since late December 2019. The earliest date of symptom onset was 1 December 2019. The symptomatology of these patients,

including fever, malaise, dry cough, and dyspnea, was diagnosed as viral pneumonia [1,2]. Initially, the disease was called Wuhan pneumonia by the press because of the area and pneumonia symptoms. Whole-genome sequencing results showed that the causative agent is a novel coronavirus. Therefore, this virus is the seventh member of the coronavirus family to infect humans [3]. The World Health Organization

\* Corresponding author. Research Center for Emerging Viral Infections, Chang Gung University, 259 Wenhua 1st Rd, Gueishan, Tao-Yuan 333, Taiwan.

E-mail address: [srshih@mail.cgu.edu.tw](mailto:srshih@mail.cgu.edu.tw) (S.-R. Shih).

Peer review under responsibility of Chang Gung University.

<sup>1</sup> These authors contributed equally to this article.

<https://doi.org/10.1016/j.bj.2020.04.007>

2319-4170/© 2020 Chang Gung University. Publishing services by Elsevier B.V. This is an open access article under the CC BY-NC-ND license (<http://creativecommons.org/licenses/by-nc-nd/4.0/>).



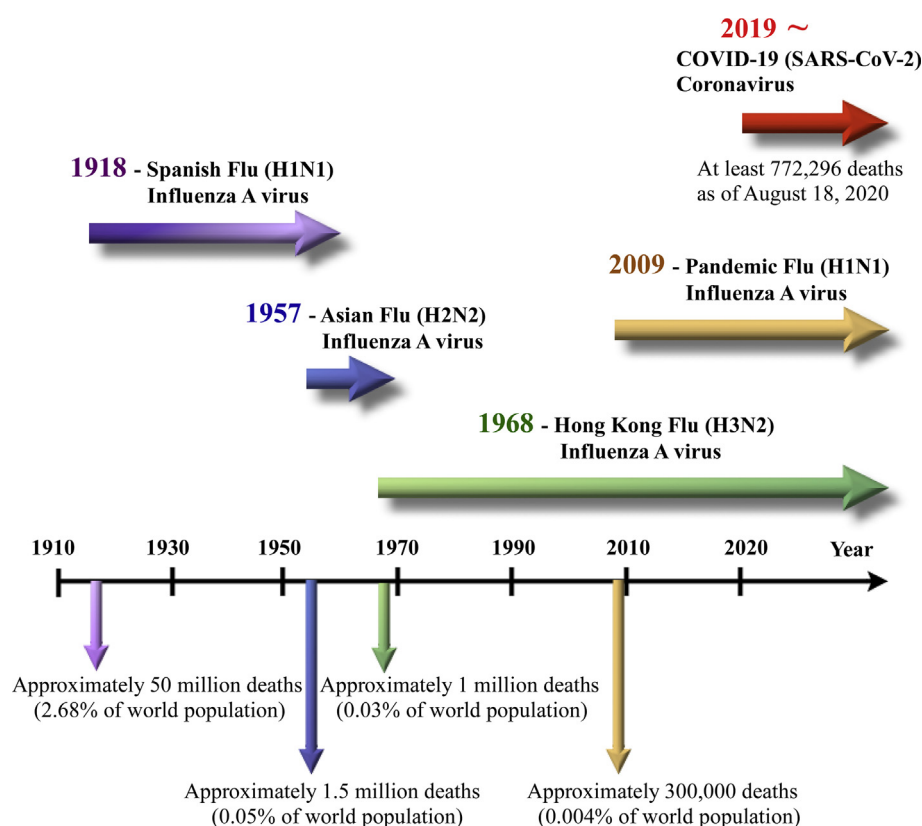


Fig. 1 A timeline of five pandemics since 1918 and the globally circulating viruses afterward.

(WHO) temporarily termed the new virus 2019 novel coronavirus (2019-nCoV) on 12 January 2020 and then officially named this infectious disease coronavirus disease 2019 (COVID-19) on 12 February 2020. Later, the International Committee on Taxonomy of Viruses (ICTV) officially designated the virus as SARS-CoV-2 based on phylogeny, taxonomy and established practice [4]. Subsequently, human-to-human transmission of COVID-19 occurring within Hong Kong has been shown in clinical data [5]. Since COVID-19 initially emerged in China, the virus has evolved for four months and rapidly spread to other countries worldwide as a global threat. On 11 March 2020, the WHO finally made the assessment that COVID-19 can be characterized as a pandemic, following 1918 Spanish flu (H1N1), 1957 Asian flu (H2N2), 1968 Hong Kong flu (H3N2), and 2009 Pandemic flu (H1N1), which caused an

estimated 50 million, 1.5 million, 1 million, and 300,000 human deaths, respectively [6–9] [Fig. 1].

### Virology – morphology, gene structure and replication

SARS-CoV-2 is an enveloped and spherical particle approximately 120 nm in diameter containing a positive-sense single-stranded RNA genome. It belongs to the subfamily Coronavirinae, family Coronaviridae, and order Nidovirales. The RNA genome of SARS-CoV-2 contains a 5' methyl-guanosine cap, poly (A)-tail, and 29,903 nucleotides according to WH-Human 1 coronavirus (WHCV) [3,10]. It is classified as a beta-coronavirus ( $\beta$ CoV) [lineage B] and is the seventh

Table 1 Classification of human coronaviruses.

Strain	Discovery	Genera-Lineage	Cellular Receptor	Natural Host	Intermediate Host	Respiratory Symptom
HCoV-229E	1966	$\alpha$	Aminopeptidase N (CD13)	Bats	Camelids	Mild
HCoV-OC43	1967	$\beta$ -A	9-O-Acetylated sialic acid (SA)	Rodents	Cattle	Mild
SARS-CoV	2003	$\beta$ -B	ACE2	Bats	Masked palm civets	Severe acute
HCoV-NL63	2004	$\alpha$	ACE2	Bats	Unknown	Mild
HCoV-HKU1	2005	$\beta$ -A	9-O-Acetylated sialic acid (SA)	Rodents	Unknown	Mild
MERS-CoV	2012	$\beta$ -C	DPP4	Bats	Dromedary camels	Severe acute
SARS-CoV-2	2019	$\beta$ -B	ACE2	Bats	Pangolin?	Severe acute

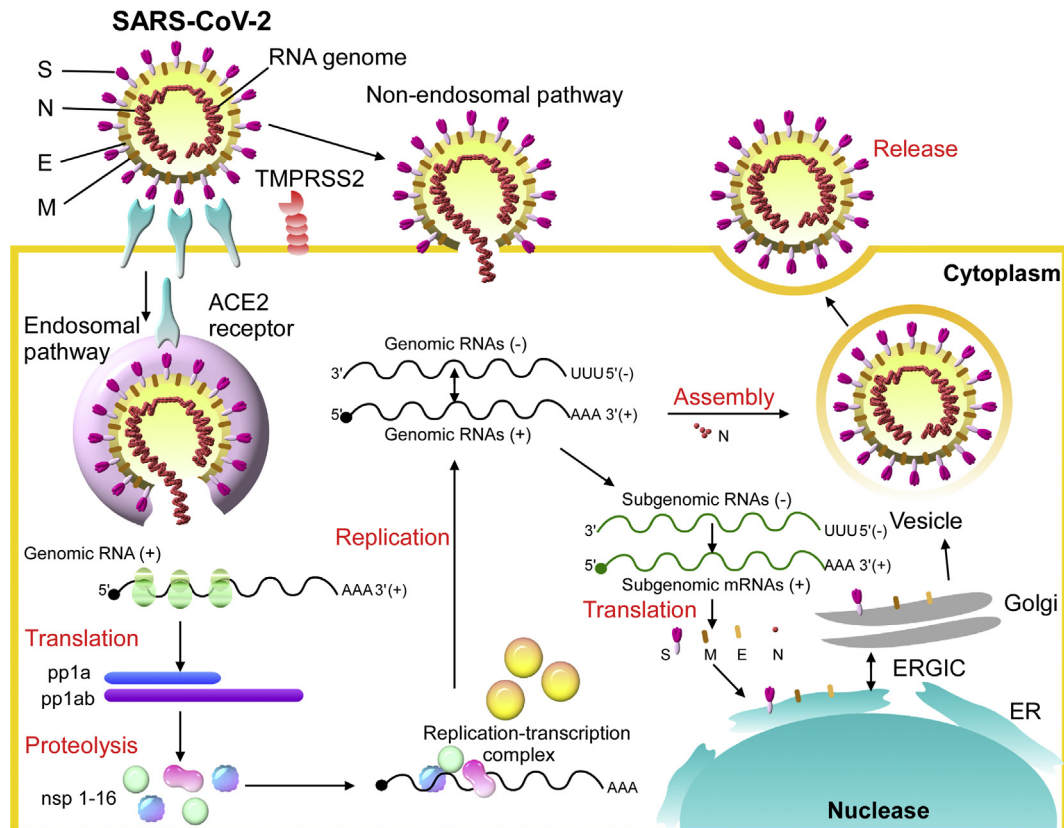


Fig. 2 The putative life cycle of SARS-CoV-2.

coronavirus to infect humans, following 2  $\alpha$ CoV (HCoV-229E and HKU-NL63) and 4  $\beta$ CoV (HCoV-OC43 [lineage A], HCoV-HKU1 [lineage A], severe acute respiratory syndrome SARS-CoV [lineage B] and Middle East respiratory syndrome MERS-CoV [lineage C]) [11–14]. It has been shown that bats and rodents are the gene sources of most  $\alpha$ CoVs and  $\beta$ CoVs, however, avian species are the gene sources of most  $\delta$ CoVs and  $\gamma$ CoVs by evolutionary analyses. The human coronavirus (HCoV) strains HCoV-NL63, HCoV-229E, HCoV-HKU1, and HCoV-OC43 usually cause mild, self-limiting upper respiratory tract infections, such as the common cold [15,16]. However, SARS-CoV, MERS-CoV, and SARS-CoV-2 can cause severe acute respiratory syndrome and result in life-threatening disease [17–19] [Table 1].

SARS-CoV-2 transcribes nine subgenomic RNAs, and its genome comprises a 5' untranslated region including a 5' leader sequence; an open reading frame (ORF) 1a/ab encoding nonstructural proteins (nsp) for replication; four structural proteins including spike (S), envelope (E), membrane (M) and nucleocapsid (N); several accessory proteins such as ORF 3a, 6, 7a/b, and 8; and a 3' untranslated region. The replicase polyprotein pp1a/ab encodes and is proteolytically cleaved into 16 putative nsps, including nsp3 (papain-like protease), nsp5 (3C-like protease), nsp12 (RNA-dependent RNA polymerase [RdRp]), nsp13 (helicase), and other nsps [10,13,20]. The spike glycoprotein of SARS-CoV-2 binds to angiotensin-converting enzyme 2 (ACE2) in human and Chinese horseshoe bats,

civet for cell entry, that is also dependent on S protein priming by the serine protease TMPRSS2. A similar panel of mammalian cell lines can be infected with SARS-CoV-2-S and SARS-CoV-S [21–24]. The spike protein could be cleaved by host proteases into the S1 and S2 subunits, which are responsible for receptor recognition and membrane fusion, respectively. S1 also can be divided into an N-terminal domain (NTD) and a C-terminal domain (CTD). The S1 CTD of SARS-CoV-2, but not the NTD, showed strong affinity for human ACE2 (hACE2). The receptor-binding domain (RBD) within SARS-CoV-2 CTD is the key region that interacts with the hACE2 receptor with higher affinity than the RBD of SARS-CoV by 10- to 20-fold with kinetic quantification [23,25]. The putative life cycle of SARS-CoV-2 in host cells begins from spike protein and hACE2 receptor binding. The conformational change in the S protein after receptor binding facilitates viral envelope fusion with the cell membrane through the endosomal pathway. The viral RNA genome is then released into the cytoplasm and translated into viral replicase polyproteins pp1a and 1 ab, which can be cleaved into small products by virus-encoded proteinases. The polymerase transcribes a series of subgenomic mRNAs by discontinuous transcription. The subgenomic mRNAs are finally translated into viral structural proteins. The S, E and M proteins enter the endoplasmic reticulum (ER) and Golgi apparatus, and the N protein is combined with the positive-stranded genomic RNA to form a nucleoprotein complex. The structural proteins and nucleoprotein complex

are assembled with the viral envelope at the ER–Golgi intermediate compartment. The newly assembled viral particles are then released from the infected cell [Fig. 2].

## Ecology - the potential origin of the virus

All human coronaviruses have animal origins, namely, natural hosts. Bats may be the natural hosts of HCoV-229E, SARS-CoV, HCoV-NL63, and MERS-CoV. Furthermore, HCoV-OC43 and HKU1 probably originated from rodents [26–28]. Bats are undoubtedly important and the major natural reservoirs of alpha-coronaviruses and beta-coronaviruses [29]. Domestic animals can suffer from disease as intermediate hosts that cause virus transmission from natural hosts to humans; for example, SARS-CoV and MERS-CoV crossed the species barriers into masked palm civets and camels, respectively [30,31] [Table 1]. SARS-CoV-2 sequenced at the early stage of the COVID-19 outbreak only shares 79.6% sequence identity with SARS-CoV through early full-length genomic comparisons. However, it is highly identical (96.2%) at the whole-genome level to Bat-CoV RaTG13, which was previously detected in *Rhinolophus affinis* from Yunnan Province, over 1500 km from Wuhan [21]. Bats are likely reservoir hosts for SARS-CoV-2; however, whether Bat-CoV RaTG13 directly jumped to humans or transmits to intermediate hosts to facilitate animal-to-human transmission remains inconclusive. No intermediate host sample was obtained by scientists in an initial cluster of infections of the Huanan Seafood and Wildlife Market in Wuhan, where the sale of wild animals may be the source of zoonotic infection. Furthermore, the earliest three patients with symptom onset had no known history of exposure to the Huanan market [1]. Therefore, there may be multiple sources of COVID-19 in the beginning. According to previous studies by metagenomic sequencing for the samples from Malayan pangolins (*Manis javanica*) in Guangxi and Guangdong, China, it has been suggested that pangolins might be the intermediate hosts between bats and humans because of the similarity of the pangolin coronavirus to SARS-CoV-2 [32,33]. However, the additional phylogenetic analyses effectively trace COVID-19 infection sources. In addition to the zoonotic origins of SARS-CoV-2 by natural evolution, there are still some disputes about the origin of the virus because its spike protein seems to perfectly interact with the human receptor in contributing to human-to-human transmission after evolution in a short period. Nevertheless, more direct evidence is required to clarify the arguments.

## Evolution of SARS-COV-2 during the past few months

Replication of RNA viruses could generate mutations due to the low proofreading ability of their RdRP. The genome variations generated by viral RdRP could be beneficial for an emerging virus to adapt to new hosts. However, previous studies have shown that the mutation rates could vary in RNA viruses [34]. The synonymous substitution rate for

coronaviruses might be approximately  $1 \times 10^{-3}$ /synonymous site/year, which is lower than some other RNA viruses. The mutation rate during coronavirus replication could be partially controlled by the viral exoribonuclease nsp14 [35,36]. Nevertheless, SARS-CoV-2 has been continuously evolving to different groups worldwide during the pandemic.

According to the information of nCoV-19 (SARS-CoV-2) sequences submitted to the GISAID database in January 2020, the virus was first collected in late December 2019 from Wuhan, China. However, those viral sequences varied from the latest submitted sequence collected in early April 2020 from North America. Since the viral sequences continuously change, the construction of a phylogenetic network is crucial to investigate the adaption of the virus in different human populations and environments. Although the virus keeps evolving within humans who could also be susceptible to other human coronaviruses, recombination between SARS-CoV-2 and old human coronaviruses, such as HCoV-229E, OC43, NL63, and HKU1, has not been found. Nevertheless, a recent study claimed that three genetic types of the virus have been circulating globally [37]. The study demonstrated that the genotypes could also correlate to the geographic locations, while the sample size and analysis methods in the study are still being argued in the research field [38]. Therefore, it is still unclear whether the evolution of SARS-CoV-2 could be affected by replication environments, such as genetic and immunological restrictions in different human populations. With evolutionary pressure, the selection of SARS-CoV-2 mutations will be ongoing. The investigation of the geographic patterns of SARS-CoV-2 variations will provide information on vaccine development for different populations.

## Conclusions

Human coronaviruses usually cause mild upper respiratory diseases. However, in the past two decades, two coronaviruses transmitted from animals, SARS-CoV and MERS-CoV, have caused severe pneumonia and death in humans. In addition, since late December 2019, the COVID-19 pandemic has spread globally and consequently resulted in at least 772,296 deaths worldwide as of August 18, 2020 [39]. Due to the high sequence homology with a coronavirus isolated from bats, SARS-CoV-2 is considered a zoonotic origin coronavirus. Undoubtedly, SARS-CoV-2 has become the fifth human coronavirus, and it is possible that this virus will continuously circulate in the human population in the future. Because specific antiviral treatments and vaccines are still under development, testing, quarantine, and social distancing are encouraged to prevent virus spread. Nonetheless, since the virus keeps mutating and evolving during the pandemic, studies on viral pathogenicity, treatments and prophylactic vaccines should closely consider the genetic characteristics of the virus.

## Conflict of interest statement

The authors declare no conflicts of interest.

## Acknowledgements

This work was financially supported by the Research Center for Emerging Viral Infections from The Featured Areas Research Center Program within the framework of the Higher Education Sprout Project by the Ministry of Education in Taiwan and the Ministry of Science and Technology, Taiwan (MOST 108-3017-F-182-001).

## REFERENCES

- [1] Huang C, Wang Y, Li X, Ren L, Zhao J, Hu Y, et al. Clinical features of patients infected with 2019 novel coronavirus in Wuhan, China. *Lancet* 2020;395:497–506.
- [2] Zhu N, Zhang D, Wang W, Li X, Yang B, Song J, et al. A novel coronavirus from patients with pneumonia in China, 2019. *N Engl J Med* 2020;382:727–33.
- [3] Wu F, Zhao S, Yu B, Chen YM, Wang W, Song ZG, et al. A new coronavirus associated with human respiratory disease in China. *Nature* 2020;579:265–9.
- [4] Coronaviridae Study Group of the International Committee on Taxonomy of V. The species Severe acute respiratory syndrome-related coronavirus: classifying 2019-nCoV and naming it SARS-CoV-2. *Nat Microbiol* 2020;5:536–44.
- [5] Chan JF, Yuan S, Kok KH, To KK, Chu H, Yang J, et al. A familial cluster of pneumonia associated with the 2019 novel coronavirus indicating person-to-person transmission: a study of a family cluster. *Lancet* 2020;395:514–23.
- [6] Johnson NP, Mueller J. Updating the accounts: global mortality of the 1918–1920 “Spanish” influenza pandemic. *Bull Hist Med* 2002;76:105–15.
- [7] Kain T, Fowler R. Preparing intensive care for the next pandemic influenza. *Crit Care* 2019;23:337.
- [8] Simonsen L, Clarke MJ, Schonberger LB, Arden NH, Cox NJ, Fukuda K. Pandemic versus epidemic influenza mortality: a pattern of changing age distribution. *J Infect Dis* 1998;178:53–60.
- [9] Viboud C, Simonsen L, Fuentes R, Flores J, Miller MA, Chowell G. Global mortality impact of the 1957–1959 influenza pandemic. *J Infect Dis* 2016;213:738–45.
- [10] Chan JF, Kok KH, Zhu Z, Chu H, To KK, Yuan S, et al. Genomic characterization of the 2019 novel human-pathogenic coronavirus isolated from a patient with atypical pneumonia after visiting Wuhan. *Emerg Microb Infect* 2020;9:221–36.
- [11] Chan JF, To KK, Tse H, Jin DY, Yuen KY. Interspecies transmission and emergence of novel viruses: lessons from bats and birds. *Trends Microbiol* 2013;21:544–55.
- [12] Chan JF, Lau SK, To KK, Cheng VC, Woo PC, Yuen KY. Middle East respiratory syndrome coronavirus: another zoonotic betacoronavirus causing SARS-like disease. *Clin Microbiol Rev* 2015;28:465–522.
- [13] Wu A, Peng Y, Huang B, Ding X, Wang X, Niu P, et al. Genome composition and divergence of the novel coronavirus (2019-nCoV) originating in China. *Cell Host Microbe* 2020;27:325–8.
- [14] Chen Y, Liu Q, Guo D. Emerging coronaviruses: genome structure, replication, and pathogenesis. *J Med Virol* 2020;92:418–23.
- [15] Yin Y, Wunderink RG. MERS, SARS and other coronaviruses as causes of pneumonia. *Respirology* 2018;23:130–7.
- [16] Jevsnič M, Ursic T, Zigon N, Lusa L, Krivec U, Petrovec M. Coronavirus infections in hospitalized pediatric patients with acute respiratory tract disease. *BMC Infect Dis* 2012;12:365.
- [17] Rota PA, Oberste MS, Monroe SS, Nix WA, Campagnoli R, Icenogle JP, et al. Characterization of a novel coronavirus associated with severe acute respiratory syndrome. *Science* 2003;300:1394–9.
- [18] Reusken CB, Haagmans BL, Muller MA, Gutierrez C, Godeke GJ, Meyer B, et al. Middle East respiratory syndrome coronavirus neutralising serum antibodies in dromedary camels: a comparative serological study. *Lancet Infect Dis* 2013;13:859–66.
- [19] Zaki AM, van Boheemen S, Bestebroer TM, Osterhaus AD, Fouchier RA. Isolation of a novel coronavirus from a man with pneumonia in Saudi Arabia. *N Engl J Med* 2012;367:1814–20.
- [20] Gao Y, Yan L, Huang Y, Liu F, Zhao Y, Cao L, et al. Structure of the RNA-dependent RNA polymerase from COVID-19 virus. *Science* 2020. in press.
- [21] Zhou P, Yang XL, Wang XG, Hu B, Zhang L, Zhang W, et al. A pneumonia outbreak associated with a new coronavirus of probable bat origin. *Nature* 2020;579:270–3.
- [22] Hoffmann M, Kleine-Weber H, Schroeder S, Kruger N, Herler T, Erichsen S, et al. SARS-CoV-2 cell entry depends on ACE2 and TMPRSS2 and is blocked by a clinically proven protease inhibitor. *Cell* 2020;181:271–280.e8.
- [23] Wang Q, Zhang Y, Wu L, Niu S, Song C, Zhang Z, et al. Structural and functional basis of SARS-CoV-2 entry by using human ACE2. *Cell* 2020. in press.
- [24] Walls AC, Park YJ, Tortorici MA, Wall A, McGuire AT, Veesler D. Structure, function, and antigenicity of the SARS-CoV-2 spike glycoprotein. *Cell* 2020;181:281–92.e6.
- [25] Wrapp D, Wang N, Corbett KS, Goldsmith JA, Hsieh CL, Abiona O, et al. Cryo-EM structure of the 2019-nCoV spike in the prefusion conformation. *Science* 2020;367:1260–3.
- [26] Su S, Wong G, Shi W, Liu J, Lai ACK, Zhou J, et al. Epidemiology, genetic recombination, and pathogenesis of coronaviruses. *Trends Microbiol* 2016;24:490–502.
- [27] Forni D, Cagliani R, Clerici M, Sironi M. Molecular evolution of human coronavirus genomes. *Trends Microbiol* 2017;25:35–48.
- [28] Tao Y, Shi M, Chommanard C, Queen K, Zhang J, Markotter W, et al. Surveillance of bat coronaviruses in Kenya identifies relatives of human coronaviruses NL63 and 229E and their recombination history. *J Virol* 2017;91:e01953-16.
- [29] Woo PC, Lau SK, Lam CS, Lau CC, Tsang AK, Lau JH, et al. Discovery of seven novel Mammalian and avian coronaviruses in the genus deltacoronavirus supports bat coronaviruses as the gene source of alphacoronavirus and betacoronavirus and avian coronaviruses as the gene source of gammacoronavirus and deltacoronavirus. *J Virol* 2012;86:3995–4008.
- [30] Guan Y, Zheng BJ, He YQ, Liu XL, Zhuang ZX, Cheung CL, et al. Isolation and characterization of viruses related to the SARS coronavirus from animals in southern China. *Science* 2003;302:276–8.
- [31] Haagmans BL, Al Dhahiry SH, Reusken CB, Raj VS, Galiano M, Myers R, et al. Middle East respiratory syndrome coronavirus in dromedary camels: an outbreak investigation. *Lancet Infect Dis* 2014;14:140–5.
- [32] Lam TT, Shum MH, Zhu HC, Tong YG, Ni XB, Liao YS, et al. Identifying SARS-CoV-2 related coronaviruses in Malayan pangolins. *Nature* 2020. in press.
- [33] Zhang T, Wu Q, Zhang Z. Probable pangolin origin of SARS-CoV-2 associated with the COVID-19 outbreak. *Curr Biol* 2020;30:1578.
- [34] Hanada K, Suzuki Y, Gojobori T. A large variation in the rates of synonymous substitution for RNA viruses and its relationship to a diversity of viral infection and transmission modes. *Mol Biol Evol* 2004;21:1074–80.

- 
- [35] Denison MR, Graham RL, Donaldson EF, Eckerle LD, Baric RS. Coronaviruses: an RNA proofreading machine regulates replication fidelity and diversity. *RNA Biol* 2011;8:270–9.
- [36] Eckerle LD, Lu X, Sperry SM, Choi L, Denison MR. High fidelity of murine hepatitis virus replication is decreased in nsp14 exoribonuclease mutants. *J Virol* 2007;81:12135–44.
- [37] Forster P, Forster L, Renfrew C, Forster M. Phylogenetic network analysis of SARS-CoV-2 genomes. *Proc Natl Acad Sci USA* 2020;117:9241–3.
- [38] Mavian C, Pond SK, Marini S, Magalis BR, Vandamme AM, Dellicour S, et al. Sampling bias and incorrect rooting make phylogenetic network tracing of SARS-COV-2 infections unreliable. *Proc Natl Acad Sci USA* 2020. in press.
- [39] JHU. COVID-19 dashboard by the center for systems science and engineering (CSSE) at Johns Hopkins University (JHU). 2020. <https://coronavirus.jhu.edu/map.html>. [Accessed 11 May 2020].





## Article

# BAY 41-2272 Attenuates CTGF Expression via sGC/cGMP-Independent Pathway in TGF $\beta$ 1-Activated Hepatic Stellate Cells

Po-Jen Chen <sup>1,†</sup> , Liang-Mou Kuo <sup>2,†</sup>, Yi-Hsiu Wu <sup>3</sup>, Yu-Chia Chang <sup>4</sup> , Kuei-Hung Lai <sup>4,5</sup> and Tsong-Long Hwang <sup>3,4,6,7,8,\*</sup>

<sup>1</sup> Department of Cosmetic Science, Providence University, Taichung 433719, Taiwan; litlep@hotmail.com

<sup>2</sup> Department of General Surgery, Chang Gung Memorial Hospital at Chiayi, Chiayi 613016, Taiwan; kuo33410@yahoo.com.tw

<sup>3</sup> Graduate Institute of Natural Products, College of Medicine, Chang Gung University, Taoyuan 333323, Taiwan; modemt看@gmail.com

<sup>4</sup> Research Center for Chinese Herbal Medicine, Graduate Institute of Health Industry Technology, College of Human Ecology, Chang Gung University of Science and Technology, Taoyuan 333323, Taiwan; yychang03@mail.cgu.edu.tw (Y.-C.C.); mos19880822@gmail.com (K.-H.L.)

<sup>5</sup> Graduate Institute of Pharmacognosy, College of Pharmacy, Taipei Medical University, Taipei 110301, Taiwan

<sup>6</sup> Research Center for Food and Cosmetic Safety, College of Human Ecology, Chang Gung University of Science and Technology, Taoyuan 333323, Taiwan

<sup>7</sup> Department of Anaesthesiology, Chang Gung Memorial Hospital, Taoyuan 333423, Taiwan

<sup>8</sup> Department of Chemical Engineering, Ming Chi University of Technology, New Taipei City 243303, Taiwan

\* Correspondence: htl@mail.cgu.edu.tw; Tel.: +886-3-211-8800 (ext. 5523)

† These authors contributed equally to this work.

Received: 3 August 2020; Accepted: 3 September 2020; Published: 4 September 2020



**Abstract:** Activation of hepatic stellate cells (HSCs) is a critical pathogenic feature of liver fibrosis and cirrhosis. BAY 41-2272 is a canonical non-nitric oxide (NO)-based soluble guanylyl cyclase (sGC) stimulator that triggers cyclic guanosine monophosphate (cGMP) signaling for attenuation of fibrotic disorders; however, the impact of BAY 41-2272 on HSC activation remains ill-defined. Transforming growth factor (TGF) $\beta$  and its downstream connective tissue growth factor (CTGF) or cellular communication network factor 2, CCN2) are critical fibrogenic cytokines for accelerating HSC activation. Here, we identified that BAY 41-2272 significantly inhibited the TGF $\beta$ 1-induced mRNA and protein expression of CTGF in mouse primary HSCs. Indeed, BAY 41-2272 increased the sGC activity and cGMP levels that were potentiated by two NO donors and inhibited by a specific sGC inhibitor, ODQ. Surprisingly, the inhibitory effects of BAY 41-2272 on CTGF expression were independent of the sGC/cGMP pathway in TGF $\beta$ 1-activated primary HSCs. BAY 41-2272 selectively restricted the TGF $\beta$ 1-induced phosphorylation of Akt but not canonical Smad2/3 in primary HSCs. Together, we illustrate a unique framework of BAY 41-2272 for inhibiting TGF $\beta$ 1-induced CTGF upregulation and HSC activation via a noncanonical Akt-dependent but sGC/cGMP-independent pathway.

**Keywords:** Akt; BAY 41-2272; CTGF; hepatic stellate cell; sGC

## 1. Introduction

The overwhelming activation and proliferation of hepatic stellate cells (HSCs) is an important factor in hepatic fibrosis, an advanced pathogenic condition in liver cirrhosis, portal hypertension, and hepatocellular carcinoma. During acute or chronic injuries, star-like shaped HSCs shift from quiescent non-proliferative status to active state with contractile, proliferative, and fibrogenic properties,



leading to pro-inflammatory growth factor generation and extracellular matrix (ECM) protein production to initiate matrix deposition in the liver [1–3]. Targeting activated HSCs has been proposed as a potential strategy to remedy liver diseases, returning activated HSCs to a quiescent status or repressing proliferation of activated HSCs. Therefore, identification of anti-fibrotic agents and their underlying molecular mechanisms of action is desirable for removing factors causing HSC activation [4–7].

The nitric oxide (NO)/soluble guanylate cyclase (sGC)/cyclic guanosine monophosphate (cGMP) pathway tightly controls important physiological functions in several human body organs; therefore, it has been considered as a worthwhile therapeutic target for many diseases including cardiopulmonary, neuronal, and fibrotic disorders [8–11]. sGC is a heterodimeric enzyme catalyzing the conversion of GTP to cGMP. The activation of native reduced sGC is canonically triggered by NO that in turn binds to the heme moiety of sGC to produce cGMP. There are various small molecules, sGC stimulators and sGC activators, that induce the activity of heme-dependent reduced sGC and heme-independent oxidized sGC, respectively [12,13]. Emerging evidence suggests that both sGC stimulators and activators affect tissue fibrosis inhibition via elevating intracellular levels of cGMP [11,14,15]; hence, pharmacological induction of sGC may be a promising approach to impede HSC activation.

Transforming growth factor (TGF) $\beta$  is a pivotal fibrogenic cytokine to stimulate HSC activation. The TGF $\beta$  levels are typically low in quiescent HSCs but are upregulated and released from deposits in the ECM after liver injury. TGF $\beta$ s activate HSCs for adaptation of fibroblast shape, contractility, proliferation, and migratory phenotype [16–18]. Targeting the local TGF $\beta$  activity or inhibiting TGF $\beta$  signaling is ideal for affecting HSC activation, which is the focus of this research strategy. The TGF $\beta$ -induced activation of HSCs during liver fibrosis takes place via canonical Smad-dependent or noncanonical Smad-independent signaling such as the Akt pathway [18,19]. It has been documented that TGF $\beta$  induced the connective-tissue growth factor (CTGF or cellular communication network factor 2, CCN2) expression via Smad and Stat3 signaling pathways in HSCs [20]. The pro-fibrotic CTGF is also upregulated and promotes the pathogenic process of liver fibrosis including cell proliferation, contractility, migration, and ECM production in activated HSCs [21–23]. The TGF $\beta$ –CTGF axis serves as a promising pathogenic pathway to affect HSC activation; however, its regulatory signaling is still elusive.

BAY 41-2272 is a regular non-nitric oxide (NO)-based sGC stimulator and is used to ameliorate the fibrosis in the lung, systemic sclerosis, peritoneal stripping, pulmonary hypertension, cardiomyocyte hypertrophy, and chronic renal disease [24–29]. To date, no studies have addressed the impact of BAY 41-2272 on HSC activation in detail. We investigated the possible capacity of BAY 41-2272 to affect sGC/cGMP in TGF $\beta$ 1-activated mouse-primary HSCs. In the present study, BAY 41-2272 significantly attenuated the TGF $\beta$ 1-induced CTGF expression and cell proliferation in primary HSCs. Unexpectedly, the inhibitory effects of BAY 41-2272 on CTGF upregulation were independent on the sGC/cGMP pathway. BAY 41-2272 alternatively inhibited the noncanonical Akt instead of canonical Smad2/3 pathway in TGF $\beta$ 1-primed HSCs. Our findings provide a mechanistic basis for BAY 41-2272 activity as a potential agent for Akt-dependent inhibition of TGF $\beta$ 1-instigated CTGF induction and HSC activation that is distinct from the canonical sGC/cGMP and Smad signaling.

## 2. Experimental Section

### 2.1. Reagents

BAY 41-2272 was purchased from Calbiochem (La Jolla, CA, USA). BAY 58-2667 was obtained from BioVision (Mountain, PA, USA). Recombinant human TGF $\beta$ 1 was from R&D Systems (Minneapolis, MN, USA). TRIzol reagents were from Thermo Fisher Scientific (Waltham, MA, USA). iScript cDNA synthesis kit and power SYBR green PCR master mix were purchased from Bio-Rad (Hercules, CA, USA). WST-1 Assay Kit was obtained from Roche Applied Sciences (Mannheim, Germany). Antibodies against phospho-Akt (S473), phospho-Akt (T308), Akt, phospho-Smad2, phospho-Smad3, and Smad2/3 were

purchased from Cell Signaling Technology (Beverly, MA, USA). Antibodies against GAPDH and CTGF were obtained from Santa Cruz Biotechnology (Santa Cruz, CA, USA). Other chemicals were purchased from Sigma (St. Louis, MO, USA).

## 2.2. Isolation of Mouse Primary HSCs

The study was approved by and followed the guidelines of the Institutional Animal Care and Use Committee of Chang Gung University, Taiwan (IACUC approval No.: CGU15-085 and date: 11 November 2015). We purchased 8- to 10-week-old C57BL/6 male mice from BioLASCO (Taiwan). Five mice were kept in a cage under a 12–12-h light–dark cycle and were provided with water and food. HSCs were isolated from livers of 8- to 10-week-old C57BL/6 male mice using a modified, previously described procedure [30,31]. Briefly, mice were euthanized by CO<sub>2</sub> and perfused with normal saline via the inferior vena cava followed by injection with 0.1% (*w/v*) collagenase IV in HBSS. Livers were taken out and agitated in 0.1% (*w/v*) collagenase IV at 37 °C for 10 min. Cells were filtered through a nylon mesh and purified via Percoll gradient centrifugation. The isolated HSCs were cultured in Roswell Park Memorial Institute (RPMI) 1640 media supplemented with 10% fetal bovine serum and 10% horse serum at 37 °C in a humidified incubator with 5% CO<sub>2</sub>. The purity of HSCs was above 95%, as confirmed by their astrocytes, intracellular lipid droplets, and vitamin A autofluorescence [32]. HSCs were cultured for 7 days and then spread out as the next generation. The fifth to seventh generation of HSCs were seeded overnight for the following experiments.

## 2.3. Cell Viability

HSCs were cultured and starved in RPMI 1640 media for 24 h. Cells were treated with indicated compounds and then activated with TGFβ1 (5 ng/mL) for 0, 24, or 48 h. Cells were subsequently incubated with the WST-1 reagent at 37 °C for 2 h. The cell viability was monitored spectrophotometrically at 450 nm (Thermo Fisher Scientific; Waltham, MA, USA).

## 2.4. Western Blotting

Cell pellets were suspended in lysis buffer (50 mM 4-(2-hydroxyethyl)-1-piperazineethanesulfonic acid (HEPES), 100 mM NaCl, 1 mM ethylenediaminetetraacetic acid (EDTA), 2 mM Na<sub>3</sub>VO<sub>4</sub>, 5% 2-mercaptoethanol, and 1% Triton-X-100) and then centrifuged at 14,000× *g* for 20 min at 4 °C. Total protein concentration were determined by using a BCA Protein Assay Kit (Pierce, Rockford, IL, USA). We mixed 30 µg cell lysates with sample buffer (62.5 mM Tris-HCl (pH 6.8), 4% SDS, 5% β-mercaptoethanol, 2.5 mM Na<sub>3</sub>VO<sub>4</sub>, 0.0125% bromophenol blue, 10 mM di-N-pentyl phthalate, and 8.75% glycerol) at 100 °C for 5 min, separated by 10% or 12% sodium dodecyl sulfate polyacrylamide gel electrophoresis (SDS-PAGE), electrophoresed onto a nitrocellulose membrane, and assayed by immunoblotting with specific primary antibodies against phospho-Akt S473 (catalog no. 4060, Cell Signaling), phospho-Akt T308 (catalog no. 2965, Cell Signaling), Akt (catalog no. 4691, Cell Signaling), phospho-Smad2 (catalog no. 3108, Cell Signaling), phospho-Smad3 (catalog no. 9520, Cell Signaling), Smad2/3 (catalog no. 5678, Cell Signaling), GAPDH (catalog no. sc-32233, Santa Cruz Biotechnology), and CTGF (catalog no. sc-25440, Santa Cruz Biotechnology) at 4 °C for 16 h and horseradish peroxidase-conjugated secondary antibodies at room temperature for 1 h. The protein levels were determined using an enhanced chemiluminescence system and a densitometer (UVP, Upland, CA, USA).

## 2.5. Immunofluorescence Staining

Cells placed on cover slides were fixed with 4% formaldehyde for 10 min and then incubated with 5% goat serum for 60 min. Protein levels were determined using primary antibodies against CTGF (catalog no. sc-25440, Santa Cruz Biotechnology) in 5% bovine serum albumin (BSA) at room temperature for 1 h and fluorescein isothiocyanate (FITC)-conjugated secondary antibody for another 1 h. Nuclei were counterstained with Hoechst (1 µg/mL). Images were obtained by fluorescent microscopy (OLYMPUS IX 81; Olympus, Tokyo, Japan).

## 2.6. RNA Isolation and Quantitative Real-Time PCR

Total RNA was extracted from HSCs using TRIzol reagent and 1 µg RNA was used as a template for cDNA synthesis by iScript cDNA Synthesis Kit according to the manufacturer's protocol. mRNA levels were determined using Power SYBR Green PCR Master Mix and quantitative PCR with CFX Connect Real-Time PCR Detection System (Bio-Rad, Hercules, CA, USA). Primers for mouse *CTGF* (5'-GGAATTGTGACCTGAGTGACT-3' and 5'-TGAGCCAGCCATTCTTAATAAAG-3') and mouse *GAPDH* (5'-AAGGAGTAAGAAACCCTGGAC-3' and 5'-GATGGAAATTGTGAGGGAGATG-3') were used. The real-time PCR was conducted at 95 °C for 10 min, followed by 40 cycles of denaturation at 95 °C for 15 s, and annealing/extension at 60 °C for 1 min. PCR conditions were optimized to achieve a single peak by melting curve analysis on the CFX Connect system.

## 2.7. Determination of Intracellular cGMP Levels

HSCs were preincubated with ODQ (1 µM) and/or indicated phosphodiesterase (PDE) inhibitors for 15 min and then treated with BAY 41-2272 (0.3–10 µM), BAY 63-2521 (0.3–10 µM), or BAY 58-2667 (0.3–10 µM) in the presences or absence of S-nitroso-N-acetyl penicillamine (SNAP; 0.1 µM) or sodium nitroprusside (SNP; 0.1 µM) for another 15 min at 37 °C. The intracellular cGMP levels were detected using the commercial enzyme immunoassay (EIA) system (catalog no. RPN226, GE Healthcare, Little Chalfont, Buckinghamshire, UK) according to the manufacturer's protocol.

## 2.8. sGC Activity Assay

HSCs were suspended and sonicated in sGC lysis buffer (25 mM Tris-HCl (pH 7.5), 250 mM sucrose, 2 mM EDTA, 5 mM MgCl<sub>2</sub>, 100 µM phenylmethylsulfonyl fluoride (PMSF), 10 µg/mL leupeptin, and 10 µM pepstatin A). After centrifugation at 250× *g* for 5 min at 4 °C, the supernatant was centrifuged at 16,000× *g* for 15 min at 4 °C. The cytosolic fraction was mixed with the indicated test agents in sGC reaction buffer (25 mM Tris-HCl (pH 7.5), 15 mM MgCl<sub>2</sub>, 2 mM 3-isobutyl 1-methylxanthine, 15 mM creatine phosphate, 6 units creatine phosphokinase, 2 mM GTP) for 20 min at 30 °C and then stopped by heating at 100 °C for 3 min. cGMP levels were measured to determine the sGC activity using a commercial EIA system (catalog no. RPN226, GE Healthcare, Little Chalfont, Buckinghamshire, UK).

## 2.9. Statistical Analysis

Data were expressed as the mean ± standard error of mean (SD). Statistical comparisons were made between two groups using Student's *t*-test. *p* < 0.05 was considered statistically significant.

# 3. Results

## 3.1. BAY 41-2272 sGC Stimulator Inhibited TGFβ1-Induced CTGF Expression and Cell Proliferation in Primary HSCs

To evaluate the biological significance of sGC/cGMP signaling in primary HSCs, we first evaluated the effect of a typical sGC stimulator BAY 41-2272 on TGFβ1-induced CTGF expression that is a critical pro-fibrotic cytokine for HSC activation. BAY 41-2272 dose-dependently (1–10 µM) inhibited the CTGF expression in primary TGFβ1-activated HSCs, as determined by Western blot and immunofluorescent staining (Figure 1A,B). The TGFβ1-induced proliferation of primary HSCs was also significantly restricted by BAY 41-2272 (10 µM; Figure 1C), suggesting that the compound may serve as an agent to ameliorate HSC activation.

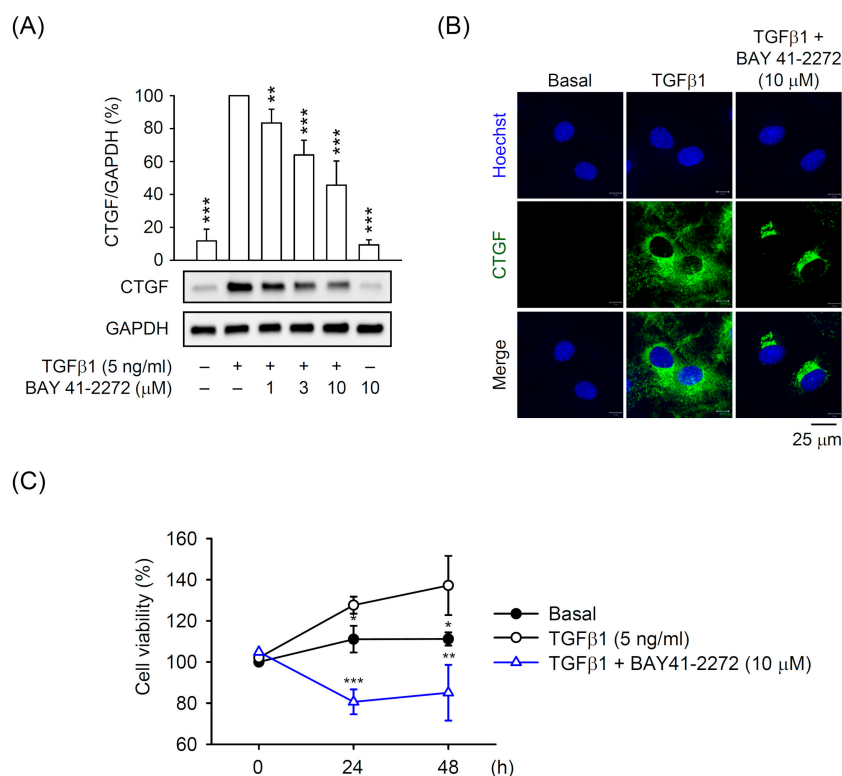


**Figure 1.** BAY 41-2272 repressed the transforming growth factor (TGF)β1-induced connective tissue growth factor (CTGF) expression in hepatic stellate cells (HSCs). HSCs were preincubated with BAY 41-2272 (1–10 μM) for 30 min before activation by TGFβ1 (5 ng/mL) for another (A,B) 6 h or (C) 24–48 h. Expression of CTGF and GAPDH was determined by (A) Western blot and (B) immunofluorescent staining using the corresponding antibodies. (C) Cell viability was measured using the WST-1 Assay Kit and monitored spectrophotometrically at 450 nm. All data are expressed as mean ± SD (*n* = 3). \* *p* < 0.05, \*\* *p* < 0.01, \*\*\* *p* < 0.001 compared with the TGFβ1 alone.

BAY 41-2272 is a non-NO-based sGC stimulator; two distinctly different NO donors, SNP and SNAP, were used to synergistically enhance sGC/cGMP signaling. A selectively heme-site inhibitor of sGC, ODQ, was also used to examine the molecular actions of BAY 41-2272 in primary HSCs. BAY 41-2272 (3 or 10 μM) increased the intracellular cGMP levels in primary HSCs, and both SNP (0.1 μM) and SNAP (0.1 μM) synergistically enhanced the BAY 41-2272 (10 μM)-increased cGMP levels. ODQ blocked all BAY 41-2272 (10 μM)-induced cGMP production in primary HSCs (Figure 2A). Similarly, BAY 41-2272 (10 μM) induced the sGC activity in vitro that was further activated by SNP (0.1 μM) or SNAP (0.1 μM) and blocked by ODQ (1 μM) (Figure 2B), suggesting that BAY 41-2272 can trigger sGC/cGMP signaling in primary HSCs.

### 3.2. The BAY 41-2272-Inhibited CTGF Expression and Cell Proliferation Was not via sGC/cGMP Pathway in TGFβ1-Activated Primary HSCs

To examine whether the inhibitory effects of BAY 41-2272 on HSC activation is through the activated sGC/cGMP signaling, we checked the CTGF expression in TGFβ1-activated primary HSCs in the presence or absence of inhibitors, ODQ (sGC inhibitor), and KT5823 (cGMP-dependent protein kinase (PKG) inhibitor). Surprisingly, the BAY 41-2272-repressed mRNA and protein expressions of CTGF were not affected by ODQ (1 μM) or KT5823 (3 μM) in TGFβ1-activated HSCs (Figure 3). Moreover, the NO donors SNAP (0.1 μM) and SNP (0.1 μM) did not alter the inhibitory effects of BAY 41-2272 on the TGFβ1-induced mRNA and protein expression of CTGF in primary HSCs (Figure 4A–C). The BAY 41-2272-repressed cell proliferation was not changed in the presence of SNAP or SNP in

TGF $\beta$ 1-activated primary HSCs (Figure 4D), suggesting that the effects of BAY 41-2272 against HSC activation may be independent on its canonical sGC/cGMP signaling.

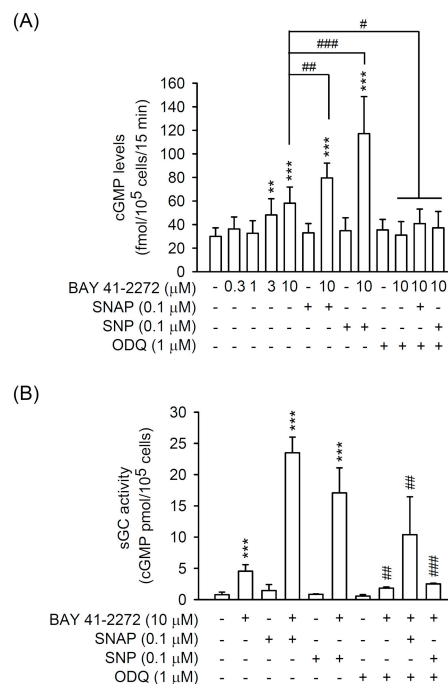


**Figure 2.** BAY 41-2272 increased the soluble guanylyl cyclase (sGC) activity and cyclic guanosine monophosphate (cGMP) formation in HSCs. **(A)** HSCs were preincubated with or without ODQ (1  $\mu$ M) sGC inhibitor for 15 min and then treated with BAY 41-2272 (0.3–10  $\mu$ M) in the presence or absence of S-nitroso-N-acetyl penicillamine (SNAP) (0.1  $\mu$ M) or sodium nitroprusside (SNP) (0.1  $\mu$ M) NO donors for another 15 min. **(B)** The cytosolic fractions from HSCs were mixed with or without ODQ (1  $\mu$ M), BAY 41-2272 (10  $\mu$ M), SNAP (0.1  $\mu$ M), and/or SNP (0.1  $\mu$ M) at 30 °C for 20 min. The cGMP levels were assayed using enzyme immunoassay (EIA) kits. All data are expressed as mean  $\pm$  SD ( $n$  = 4). \*\*  $p$  < 0.01, \*\*\*  $p$  < 0.001 compared with the basal; #  $p$  < 0.05, ##  $p$  < 0.01, ###  $p$  < 0.001 compared with (A) BAY 41-2272 (10  $\mu$ M) alone and (B) the corresponding BAY 41-2272 with or without SNAP or SNP.

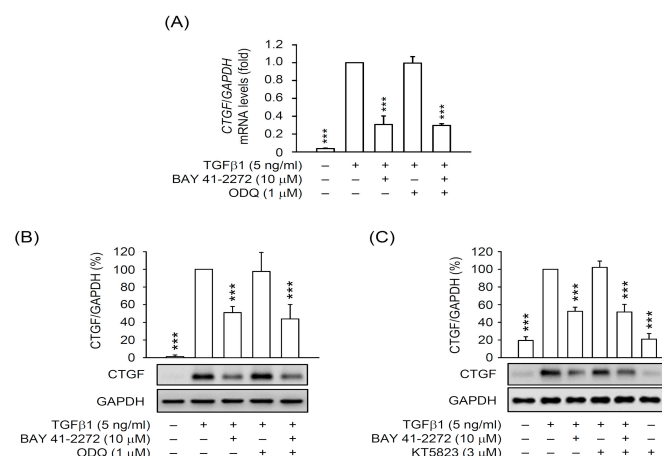


**Figure 3.** The inhibitory effect of BAY 41-2272 on CTGF expression was independent of the sGC pathway in TGF $\beta$ 1-activated HSCs. HSCs were pretreated with or without ODQ (1  $\mu$ M) or KT5823 (cGMP-dependent protein kinase (PKG) inhibitor) (3  $\mu$ M) PKG inhibitors for 15 min. HSCs were sequentially incubated with BAY 41-2272 (10  $\mu$ M) for 30 min before activation by TGF $\beta$ 1 (5 ng/mL) for another 6 h. **(A)** mRNA levels of CTGF or GAPDH were determined by quantitative RT-PCR. **(B,C)** Expressed CTGF and GAPDH proteins were determined by Western blot using the corresponding antibodies. All data are expressed as mean  $\pm$  SD ( $n$  = 3). \*\*\*  $p$  < 0.001 compared with the TGF $\beta$ 1 alone.



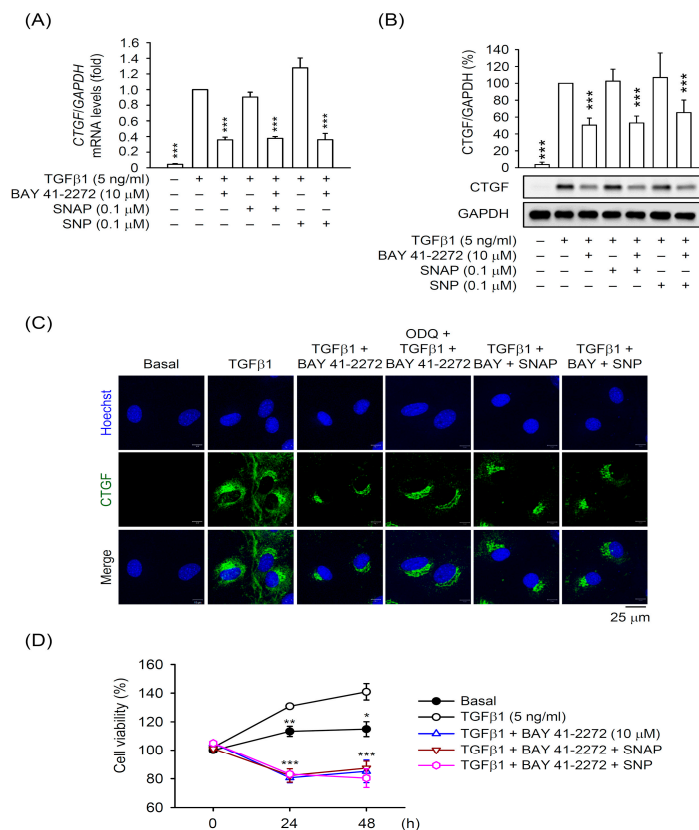


**Figure 4.** NO donors did not affect the inhibition of TGFβ1-activated HSCs by BAY 41-2272. HSCs were preincubated with BAY 41-2272 (10 μM) in the presence or absence of SNAP (0.1 μM) or SNP (0.1 μM) for 30 min before activation by TGFβ1 (5 ng/mL) for another (A–C) 6 h or (D) 24–48 h. (A) mRNA levels of CTGF and GAPDH were determined by quantitative RT-PCR. (B,C) Expressed CTGF and GAPDH proteins were measured by (B) Western blot and (C) immunofluorescent staining using the corresponding antibodies. (D) Cell viability was measured using the WST-1 assay and monitored spectrophotometrically at 450 nm. All data are expressed as mean ± SD (*n* = 3). \* *p* < 0.05, \*\* *p* < 0.01, \*\*\* *p* < 0.001 compared with the TGFβ1 alone.

### 3.3. PDE9 Modulated the BAY 41-2272-Mediated sGC/cGMP Signaling But not CTGF Inhibition in Primary HSCs

cGMP-dependent phosphodiesterases (PDEs; PDE1, 2, 3, 5, 6, 9, 10, and 11) are responsible for the conversion from active cGMP to inactive 5'GMP [33]. To further understand the effect of the sGC/cGMP pathway on HSC activation, we used PDE inhibitors to examine the cGMP production and CTGF expression in primary HSCs. First, the non-specific PDE inhibitor 3-isobutyl-1-methylxanthine (IBMX) apparently increased the BAY 41-2272-induced intracellular cGMP levels in the presence or absence of SNAP or SNP. The cGMP levels were also inhibited by ODQ (Figure 5A). We also screened the isozyme-specific inhibitors of PDEs (vinpocetine for PDE1, erythro-9-(2-hydroxy-3-nonyl)adenine (EHNA) for PDE2, zaprinast and tadalafil for PDE5, BAY 73-6691 for PDE9) to check the BAY 41-2272-induced cGMP production in HSCs. The PDE9 inhibitor BAY 73-6691 showed the strongest effect on increasing the BAY 41-2272-induced cGMP levels (Figure 5B), suggesting that PDE9 is important for the sGC/cGMP pathway in HSCs. However, the PDE9 inhibitor did not change the inhibitory effect of BAY 41-2272 on CTGF expression in TGFβ1-activated HSCs (Figure 5C). This demonstrates further that the inhibitory effect of BAY 41-2272 on CTGF expression is via the sGC/cGMP-independent pathway.



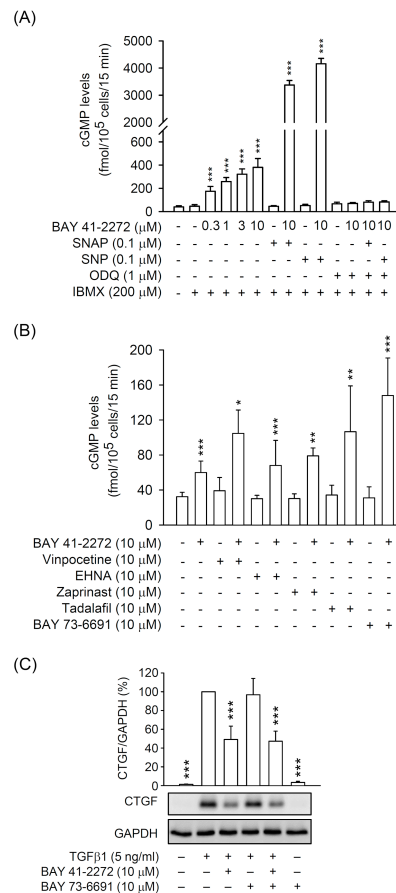


**Figure 5.** Phosphodiesterase (PDE) inhibitors increase the BAY 41-2272-mediated cGMP formation but not CTGF expression in HSCs. **(A,B)** HSCs were preincubated with or without **(A)** IBMX (200  $\mu$ M) and/or ODQ (1  $\mu$ M) or **(B)** specific PDE inhibitors for 15 min and then treated with BAY 41-2272 (0.3–10  $\mu$ M) in the presence or absence of SNAP (0.1  $\mu$ M) or SNP (0.1  $\mu$ M) for another 15 min. The cGMP levels were assayed using EIA kits. **(C)** HSCs were pretreated with or without BAY 73-6691 (10  $\mu$ M) PDE9 inhibitor for 15 min. HSCs were sequentially incubated with BAY 41-2272 (10  $\mu$ M) for 30 min before activation by TGF $\beta$ 1 (5 ng/mL) for another 6 h. Expressed CTGF and GAPDH were measured by Western blot using the corresponding antibodies. All data are expressed as mean  $\pm$  SD ( $n = 4$ ). \*  $p < 0.05$ , \*\*  $p < 0.01$ , \*\*\*  $p < 0.001$  compared with the basal **(A,B)** or TGF $\beta$ 1 alone **(C)**.

### 3.4. The TGF $\beta$ 1-Induced CTGF Expression is Independent of cGMP Formation in Primary HSCs

The sGC stimulator BAY 41-2272 has the potential of inhibiting HSC activation by prohibiting CTGF in TGF $\beta$ 1-activated primary HSCs; however, this is separate from its ability to elicit sGC activity and cGMP formation. To further characterize the correlation between sGC/cGMP signaling and pro-fibrotic CTGF expression, we used another heme-dependent sGC stimulator, BAY 63-2521, and a heme-independent sGC activator, BAY 58-2667, to analyze the cGMP formation and TGF $\beta$ 1-induced CTGF expression in primary HSCs. BAY 63-2521 (10  $\mu$ M) alone increased the intracellular cGMP generation in HSCs that was further increased by synergetic incubation with NO donors SNP (0.1  $\mu$ M) or SNAP (0.1  $\mu$ M). Moreover, the PDE inhibitor IBMX increased the BAY 63-2521-induced cGMP levels in HSCs with or without SNAP or SNP. All the increased cGMP levels were inhibited by ODQ (1  $\mu$ M) (Figure 6A). On the other hand, BAY 58-2667 had no effect on cGMP formation in HSCs, even in the presence of SNAP, SNP, IBMX, and/or ODQ (Figure 6B,C). These results indicate that heme-independent sGC is the major type of sGC in HSCs and may have unique functions in these cells.

BAY 63-2521 and BAY 58-2667 did not affect CTGF expression in TGF $\beta$ 1-activated HSCs (Figure 7A,B). An analog of cGMP, 8-Br-cGMP (bromo-cGMP), also did not alter the TGF $\beta$ 1-induced CTGF expression in HSCs (Figure 7C), suggesting that cGMP signaling may not be involved in

CTGF production in TGF $\beta$ 1-activated HSCs. Together, the activated sGC/cGMP signaling exhibits no advantage for blocking HSC activation via preventing CTGF expression.

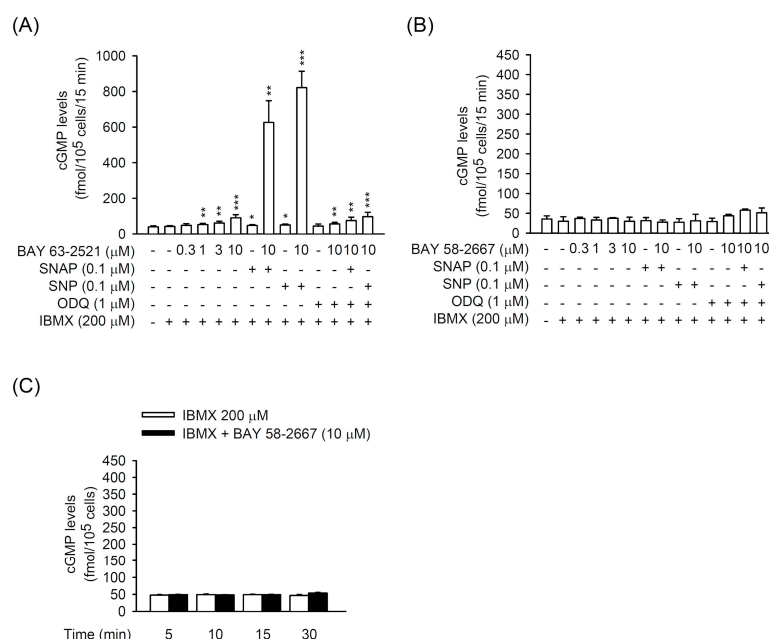


**Figure 6.** Effects of BAY 63-2521 and BAY 58-2667 on cGMP formation in HSCs. HSCs were preincubated with or without IBMX (200  $\mu$ M) and/or ODQ (1  $\mu$ M) for 15 min and then treated with (A) BAY 63-2521 (0.3–10  $\mu$ M) or (B,C) BAY 58-2667 (0.3–10  $\mu$ M) in the presence or absence of SNAP (0.1  $\mu$ M) or SNP (0.1  $\mu$ M) for another (A,B) 15 min or (C) various time intervals (5–30 min). The cGMP levels were assayed using EIA kits. All data are expressed as mean  $\pm$  SD ( $n = 4$ ). \*  $p < 0.05$ , \*\*  $p < 0.01$ , \*\*\*  $p < 0.001$  compared with the basal.

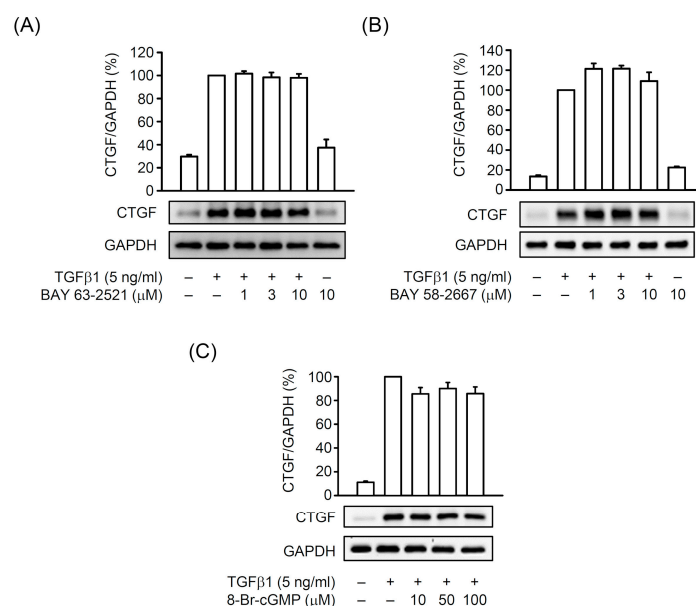


**Figure 7.** Effects of BAY 63-2521, BAY 58-2667, and 8-Br-cGMP on TGF $\beta$ 1-induced CTGF expression in HSCs. HSCs were preincubated with (A) BAY 63-2521 (1–10  $\mu$ M), (B) BAY 58-2667 (1–10  $\mu$ M), or (C) 8-Br-cGMP (10–100  $\mu$ M) for 30 min before activation by TGF $\beta$ 1 (5 ng/mL) for another 6 h. Expressed CTGF and GAPDH were determined by Western blot using the corresponding antibodies. All data are expressed as mean  $\pm$  SD ( $n = 3$ ).

### 3.5. BAY 41-2272 Selectively Inhibited the TGFβ1-Induced Akt Activation in Primary HSCs

The TGFβ-activated Smad and non-Smad pathways have been well-documented as the predominant fibrotic signaling in HSCs during liver fibrosis [16,17]. We checked the effect of BAY 41-2272 on Smad2/3 and Akt phosphorylation in TGFβ1-activated HSCs to investigate its downstream signaling. TGFβ1 (5 ng/mL) significantly triggered the phosphorylation of Smad2, Smad3, and Akt within 20 min, and BAY 41-2272 (10 μM) selectively reduced the TGFβ1-activated Akt but not Smad2/3 in primary HSCs (Figure 8A,B). The sGC inhibitor ODQ (1 μM) did not affect BAY 41-2272-inhibited Akt activation in TGFβ1-activated HSCs (Figure 8C), suggesting that the inhibitory effect of BAY 41-2272 may be mediated through Akt instead of the sGC/cGMP and Smad pathway in HSCs. Inhibition of phosphoinositide 3-kinase (PI3K) signaling in HSCs attenuates liver fibrosis [34,35]. Similarly, LY294002 PI3K inhibitor dose-dependently (1–10 μM) attenuated the Akt phosphorylation, CTGF expression, and cell viability in TGFβ1-activated primary HSCs (Figure 8D,E). During HSC activation, BAY 41-2272-based restriction of TGFβ1-induced CTGF expression may be selectively modulated through Akt-dependent but sGC/cGMP- and Smad-independent pathway.

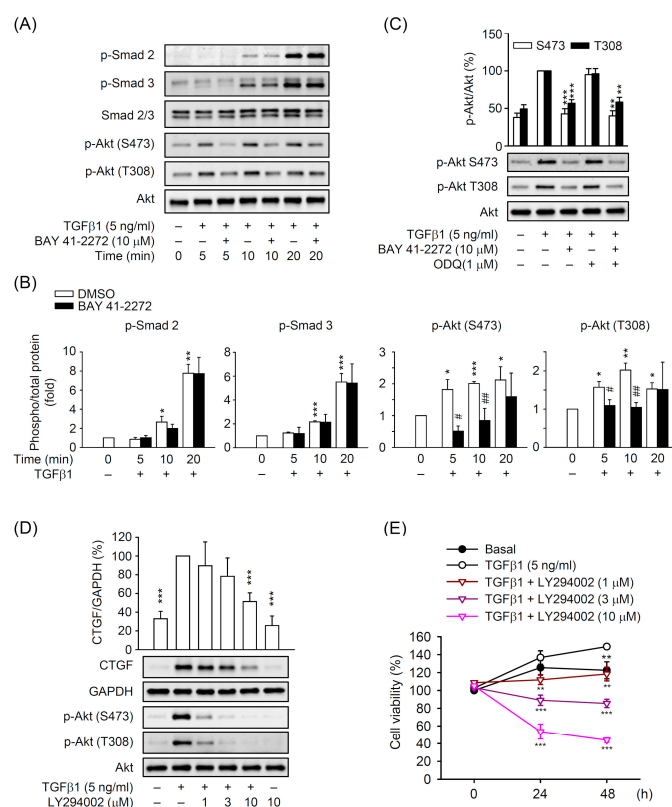


**Figure 8.** The BAY 41-2272-inhibited CTGF expression was dependent on Akt signaling in TGFβ1-activated HSCs. HSCs were pretreated with or without ODQ (1 μM) for 15 min. HSCs were sequentially incubated with (A–C) BAY 41-2272 (10 μM) or (D,E) LY294002 (1–10 μM) Akt signaling inhibitor for 30 min before activation by TGFβ1 (5 ng/mL) for another (A,B) 5–20 min, (C,D) 10 min, or (E) 24–48 h. (A–D) Protein levels were determined by Western blot using antibodies against p-Smad2, p-Smad3, Smad2/3, p-Akt (S473 or T308), Akt, CTGF, or GAPDH. (E) Cell viability was measured using the WST-1 assay and monitored spectrophotometrically at 450 nm. All data are expressed as mean ± SD (n = 3). \* p < 0.05, \*\* p < 0.01, \*\*\* p < 0.001 compared with the basal (B) or TGFβ1 alone (C–E). # p < 0.05, ## p < 0.01 compared with the corresponding DMSO group.

## 4. Discussion

The fibrogenic cytokines TGFβ and CTGF trigger HSC activation as a pathogenic factor during liver fibrosis. Emerging evidence shows that stopping TGFβ–CTGF upregulation and sGC modulators

are effective ways to control HSC activation [11,16,20,23]; however, the full understanding of their correlation is still elusive. BAY 41-2272 is a well-described sGC stimulator that is used to ameliorate fibrotic lesion [24–29], but its application in HSC remains undefined. In the present study, we manifested the pharmacological effects and mechanisms of BAY 41-2272 and sGC/cGMP signaling in TGF $\beta$ -activated primary mouse HSCs. BAY 41-2272 remarkably restricted the TGF $\beta$ 1-induced CTGF upregulation and cell proliferation in mouse primary HSCs, along with increased cGMP levels and sGC activity. However, the inhibitory effects of BAY 41-2272 on TGF $\beta$ 1-induced HSC activation and induction of sGC/cGMP signaling are astonishingly unconnected. BAY 41-2272 restricted the Akt activation instead of canonical Smad2/3 pathway in TGF $\beta$ 1-activated HSCs, providing a plausible cellular basis for the mechanistic actions of BAY 41-2272 and Akt for HSC activation.

A growing body of evidence indicates that reversing to quiescent status or preventing proliferation is an effective way to treat activated HSCs [4,36,37]. TGF $\beta$  has been well-established for inducing HSCs into an activated status and becoming, in turn, myofibroblast-like cells with proliferative, contractile, and fibrogenic properties [16–18]. TGF $\beta$  signaling upregulates another fibrogenic factor, CTGF, which contributes to HSC activation [20,38,39]; inhibition of CTGF is an option for attenuating HSC activation [40–42]. In this study, we used isolated primary HSCs to address the possibility of targeting TGF $\beta$ 1-induced CTGF expression. Both RNA and protein levels of CTGF are upregulated in TGF $\beta$ 1-activated HSCs and hence the inhibitory effects of BAY 41-2272 on CTGF upregulation and HSC proliferation should be relevant to its anti-fibrotic effect on HSC activation (Figures 1 and 3). Therefore, targeting CTGF upregulation may be an effective way of attenuating TGF $\beta$ -induced HSC activation.

The NO/sGC/cGMP pathway maintains various physiological homeostasis, and induction of sGC/cGMP signaling has been proposed to inhibit fibrogenesis [11,43]. However, the role of NO in regulating HSCs remains controversial. For example, the nitrovasodilator-mediated contraction and proliferation of HSCs are both NO/cGMP-dependent and -independent [14,44,45]. Lipopolysaccharide (LPS) triggers HSCs to release NO, but this is not related to HSC-induced hepatocyte proliferation [46,47]. Moreover, release of NO inhibits HSC activation [48]. Therefore, NO signaling may show diverse functions during HSC activation. SNP and SNAP act as NO donors via enzymatic oxidation and chemical reaction, respectively [49]. Both SNP and SNAP synergistically potentiated the BAY 41-2272-induced sGC activities and cGMP levels in HSCs (Figure 2); however, SNP and SNAP did not affect the BAY 41-2272-inhibited CTGF upregulation and proliferation of HSCs (Figure 4). We suggest that NO production may not participate in TGF $\beta$ 1-induced HSC activation, although it augments sGC/cGMP signaling.

sGCs are expressed in HSCs and not in hepatocytes [50] and are divided into reduced and oxidized forms that possess heme-dependent and heme-independent properties, respectively [11,13]. Many sGC modulators have been developed: (1) sGC stimulators to sensitize the reduced and heme-containing sGC to NO, and (2) sGC activators to activate oxidized and heme-free sGC [51–53] to generate cGMP. Exposure of 8-Br-cGMP cGMP analog leads to an inhibition of TGF $\beta$ -induced fibrogenesis in renal, cardiac, and dermal fibroblasts [26,54,55], suggesting that the sGC/cGMP pathway may be preferential signaling for TGF $\beta$ -induced HSC activation. Here, the BAY 41-2272 sGC stimulator showed potent inducible and inhibitory effects on cGMP levels and TGF $\beta$ 1-increased CTGF expression in HSCs (Figures 1 and 2). However, only increased cGMP levels and sGC activity but not decreased CTGF expression was reversed by the ODQ sGC inhibitor in BAY 41-2272-treated HSCs (Figures 2 and 3). Importantly, the elevation of cGMP signaling by KT5823 (PKG inhibitor), BAY 73-6691 (PDE9 inhibitor), and 8-Br-cGMP (cGMP analog) failed to alter the TGF $\beta$ 1-induced CTGF expression in HSCs (Figure 3C, Figure 5C, and Figure 7C). Together, our results may support the existence of a unique framework making TGF $\beta$ -based HSC activation independent of sGC/cGMP signaling.

Emerging evidence has indicated the potential application of sGC modulators for treating a fibrotic lesion in the liver, skin, lung, and kidneys [11,15]. Riociguat (BAY 63-2521) is an sGC stimulator used for treating pulmonary hypertension that has attenuated cholestatic fibrogenesis and cirrhotic portal hypertension in rats [56,57]. IW-1973 and praliciguat sGC stimulators prevented hepatic fibrosis

in models of non-alcoholic steatohepatitis [51,58]. Oral administration of BAY 60-2770 sGC activator prevented the carbon tetrachloride-induced hepatic fibrous collagen formation in rats [59]. Noticeably, BAY 41-2272 can quell fibrogenesis in various fibrotic disorders [24–29]; however, its effects on liver fibrosis is limited. In the present study, we evaluated the effects of BAY 41-2272 and BAY 63-2521 sGC stimulators, and BAY 58-2667 sGC activator on TGF $\beta$ 1-mediated HSC activation. Only BAY 41-2272 inhibited the TGF $\beta$ 1-induced CTGF expression in primary HSCs (Figure 1). BAY 63-2521 that synergistically increased cGMP levels with NO donors and BAY 58-2667 failed to alter the CTGF upregulation in TGF $\beta$ 1-activated HSCs (Figures 6 and 7). We propose that BAY 41-2272 may be distinct from other sGC modulators and exhibits two diverse pathways in HSCs: (1) canonical NO/sGC/cGMP-dependent signaling for undefined functions, and (2) sGC-independent repression of TGF $\beta$ 1-triggered HSC activation.

In general, TGF $\beta$  binding with the TGF $\beta$  receptor leads to phosphorylation of the receptor-activated Smad2 and Smad3. Additionally, non-canonical Smad-independent signaling pathways such as PI3K/Akt are activated by TGF $\beta$  and provide a broad TGF $\beta$ -induced intracellular crosstalk [18,19]. Targeting PI3K/Akt signaling also restrains the progression of HSC activation, including cell proliferation and CTGF expression [34,35,60–62], supporting the biological significance of the PI3K/Akt pathway for TGF $\beta$ -dependent HSC activation. In this study, BAY 41-2272 reduced the TGF $\beta$ 1-induced phosphorylation of Akt but not canonical Smad2/3. Pharmacological inhibition of PI3K/Akt also apparently blocked the TGF $\beta$ 1-induced CTGF expression and proliferation of HSCs (Figure 8). Because the effect of BAY 41-2272 on Akt phosphorylation was transient, we cannot exclude the possibility that the inhibitory effects of BAY 41-2272 in HSCs are mediated by other targets. This is the first time that BAY 41-2272 was explored to treat TGF $\beta$ -mediated HSC activation via targeting the PI3K/Akt that plays an important role in this process.

## 5. Conclusions

We illustrate that the BAY 41-2272 sGC stimulator attenuates the TGF $\beta$ 1-induced CTGF expression and cell proliferation through the Akt signaling and not the sGC/cGMP pathway in mouse primary HSCs. Our results provide a novel insight into the TGF $\beta$ 1- and BAY 41-2272-based regulatory networks and molecular profiles for HSC activation.

**Author Contributions:** P.-J.C., L.-M.K., Y.-H.W., Y.-C.C., and K.-H.L. designed and performed the experiments and analyzed the data. P.-J.C. and T.-L.H. wrote and completed the manuscript. T.-L.H. supervised the entire study. All authors have read and agreed to the published version of the manuscript.

**Funding:** This research was funded by the Chang Gung Medical Research Foundation (BMRP450, CMRPG6J0141-3, CMRPF1G0241-3, and CMRPF1J0051-3), and the Ministry of Science and Technology (MOST 109-2320-B-126-003-MY3, MOST 106-2320-B-255-003-MY3, MOST 108-2320-B-255-003-MY3, MOST 108-2320-B-126-001, and MOST 107-2320-B-182A-004-MY2), Taiwan.

**Conflicts of Interest:** The authors declare no conflict of interest. The funders had no role in the design of the study; in the collection, analyses, or interpretation of data; in the writing of the manuscript, or in the decision to publish the results.

## References

1. Tsuchida, T.; Friedman, S.L. Mechanisms of hepatic stellate cell activation. *Nat. Rev. Gastroenterol. Hepatol.* **2017**, *14*, 397–411. [[CrossRef](#)] [[PubMed](#)]
2. Cai, X.; Wang, J.; Wang, J.; Zhou, Q.; Yang, B.; He, Q.; Weng, Q. Intercellular crosstalk of hepatic stellate cells in liver fibrosis: New insights into therapy. *Pharmacol. Res.* **2020**, *155*, 104720. [[CrossRef](#)] [[PubMed](#)]
3. Khomich, O.; Ivanov, A.V.; Bartosch, B. Metabolic Hallmarks of Hepatic Stellate Cells in Liver Fibrosis. *Cells* **2019**, *9*, 24. [[CrossRef](#)] [[PubMed](#)]
4. Huang, Y.; Deng, X.; Liang, J. Modulation of hepatic stellate cells and reversibility of hepatic fibrosis. *Exp. Cell Res.* **2017**, *352*, 420–426. [[CrossRef](#)]
5. Higashi, T.; Friedman, S.L.; Hoshida, Y. Hepatic stellate cells as key target in liver fibrosis. *Adv. Drug Deliv. Rev.* **2017**, *121*, 27–42. [[CrossRef](#)]

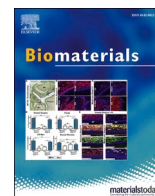


6. Kuo, L.M.; Chen, P.J.; Sung, P.J.; Chang, Y.C.; Ho, C.T.; Wu, Y.H.; Hwang, T.L. The Bioactive Extract of *Pinnigorgia* sp. Induces Apoptosis of Hepatic Stellate Cells via ROS-ERK/JNK-Caspase-3 Signaling. *Mar. Drugs* **2018**, *16*, 19. [\[CrossRef\]](#)
7. Schuppan, D.; Ashfaq-Khan, M.; Yang, A.T.; Kim, Y.O. Liver fibrosis: Direct antifibrotic agents and targeted therapies. *Matrix Biol.* **2018**, *68–69*, 435–451. [\[CrossRef\]](#)
8. Evgenov, O.V.; Pacher, P.; Schmidt, P.M.; Hasko, G.; Schmidt, H.H.; Stasch, J.P. NO-independent stimulators and activators of soluble guanylate cyclase: Discovery and therapeutic potential. *Nature reviews. Drug Discov.* **2006**, *5*, 755–768. [\[CrossRef\]](#)
9. Wobst, J.; Kessler, T.; Dang, T.A.; Erdmann, J.; Schunkert, H. Role of sGC-dependent NO signalling and myocardial infarction risk. *J. Mol. Med.* **2015**, *93*, 383–394. [\[CrossRef\]](#)
10. Hollas, M.A.; Ben Aissa, M.; Lee, S.H.; Gordon-Blake, J.M.; Thatcher, G.R.J. Pharmacological manipulation of cGMP and NO/cGMP in CNS drug discovery. *Nitric Oxide* **2019**, *82*, 59–74. [\[CrossRef\]](#)
11. Hu, L.; Wang, Z.; Yi, R.; Yi, H.; Xiao, S.; Chen, Z.; Hu, G.; Li, Q. Soluble Guanylate Cyclase: A New Therapeutic Target for Fibrotic Diseases. *Curr. Med. Chem.* **2017**, *24*, 3203–3215. [\[CrossRef\]](#) [\[PubMed\]](#)
12. Priviero, F.B.; Webb, R.C. Heme-dependent and independent soluble guanylate cyclase activators and vasodilation. *J. Cardiovasc. Pharmacol.* **2010**, *56*, 229–233. [\[CrossRef\]](#) [\[PubMed\]](#)
13. Xiao, S.; Li, Q.; Hu, L.; Yu, Z.; Yang, J.; Chang, Q.; Chen, Z.; Hu, G. Soluble Guanylate Cyclase Stimulators and Activators: Where are We and Where to Go? *Mini Rev. Med. Chem.* **2019**, *19*, 1544–1557. [\[CrossRef\]](#) [\[PubMed\]](#)
14. Perri, R.E.; Langer, D.A.; Chatterjee, S.; Gibbons, S.J.; Gadgil, J.; Cao, S.; Farrugia, G.; Shah, V.H. Defects in cGMP-PKG pathway contribute to impaired NO-dependent responses in hepatic stellate cells upon activation. *Am. J. Physiol. Gastrointest. Liver Physiol.* **2006**, *290*, G535–G542. [\[CrossRef\]](#)
15. Sandner, P.; Stasch, J.P. Anti-fibrotic effects of soluble guanylate cyclase stimulators and activators: A review of the preclinical evidence. *Respir. Med.* **2017**, *122* (Suppl. S1), S1–S9. [\[CrossRef\]](#)
16. Dewidar, B.; Meyer, C.; Dooley, S.; Meindl-Beinker, A.N. TGF-beta in Hepatic Stellate Cell Activation and Liver Fibrogenesis-Updated 2019. *Cells* **2019**, *8*, 1419. [\[CrossRef\]](#)
17. Fabregat, I.; Caballero-Diaz, D. Transforming Growth Factor-beta-Induced Cell Plasticity in Liver Fibrosis and Hepatocarcinogenesis. *Front. Oncol.* **2018**, *8*, 357. [\[CrossRef\]](#)
18. Fabregat, I.; Moreno-Caceres, J.; Sanchez, A.; Dooley, S.; Dewidar, B.; Giannelli, G.; Ten Dijke, P.; Consortium, I.-L. TGF-beta signalling and liver disease. *FEBS J.* **2016**, *283*, 2219–2232. [\[CrossRef\]](#)
19. Carthy, J.M. TGFbeta signaling and the control of myofibroblast differentiation: Implications for chronic inflammatory disorders. *J. Cell. Physiol.* **2018**, *233*, 98–106. [\[CrossRef\]](#)
20. Liu, Y.; Liu, H.; Meyer, C.; Li, J.; Nadalin, S.; Konigsrainer, A.; Weng, H.; Dooley, S.; ten Dijke, P. Transforming growth factor-beta (TGF-beta)-mediated connective tissue growth factor (CTGF) expression in hepatic stellate cells requires Stat3 signaling activation. *J. Biol. Chem.* **2013**, *288*, 30708–30719. [\[CrossRef\]](#)
21. Colak, Y.; Senates, E.; Coskunpinar, E.; Oltulu, Y.M.; Zemheri, E.; Ozturk, O.; Doganay, L.; Mesci, B.; Yilmaz, Y.; Enc, F.Y.; et al. Concentrations of connective tissue growth factor in patients with nonalcoholic fatty liver disease: Association with liver fibrosis. *Dis. Markers* **2012**, *33*, 77–83. [\[CrossRef\]](#)
22. Ramazani, Y.; Knops, N.; Elmonem, M.A.; Nguyen, T.Q.; Arcolino, F.O.; van den Heuvel, L.; Levchenko, E.; Kuypers, D.; Goldschmeding, R. Connective tissue growth factor (CTGF) from basics to clinics. *Matrix Biol.* **2018**, *68–69*, 44–66. [\[CrossRef\]](#)
23. Huang, G.; Brigstock, D.R. Regulation of hepatic stellate cells by connective tissue growth factor. *Front. Biosci.* **2012**, *17*, 2495–2507.
24. Wang, Y.; Kramer, S.; Loof, T.; Martini, S.; Kron, S.; Kawachi, H.; Shimizu, F.; Neumayer, H.H.; Peters, H. Enhancing cGMP in experimental progressive renal fibrosis: Soluble guanylate cyclase stimulation vs. phosphodiesterase inhibition. *Am. J. Physiol. Ren. Physiol.* **2006**, *290*, F167–F176. [\[CrossRef\]](#) [\[PubMed\]](#)
25. Masuyama, H.; Tsuruda, T.; Sekita, Y.; Hatakeyama, K.; Imamura, T.; Kato, J.; Asada, Y.; Stasch, J.P.; Kitamura, K. Pressure-independent effects of pharmacological stimulation of soluble guanylate cyclase on fibrosis in pressure-overloaded rat heart. *Hypertens. Res.* **2009**, *32*, 597–603. [\[CrossRef\]](#) [\[PubMed\]](#)
26. Beyer, C.; Zenzmaier, C.; Palumbo-Zerr, K.; Mancuso, R.; Distler, A.; Dees, C.; Zerr, P.; Huang, J.; Maier, C.; Pachowsky, M.L.; et al. Stimulation of the soluble guanylate cyclase (sGC) inhibits fibrosis by blocking non-canonical TGFbeta signalling. *Ann. Rheum. Dis.* **2015**, *74*, 1408–1416. [\[CrossRef\]](#)
27. Kadoya, H.; Satoh, M.; Nagasu, H.; Sasaki, T.; Kashiwara, N. Deficiency of endothelial nitric oxide signaling pathway exacerbates peritoneal fibrosis in mice. *Clin. Exp. Nephrol.* **2015**, *19*, 567–575. [\[CrossRef\]](#)

28. Matei, A.E.; Beyer, C.; Gyorfi, A.H.; Soare, A.; Chen, C.W.; Dees, C.; Bergmann, C.; Ramming, A.; Friebe, A.; Hofmann, F.; et al. Protein kinases G are essential downstream mediators of the antifibrotic effects of sGC stimulators. *Ann. Rheum. Dis.* **2018**, *77*, 459. [[CrossRef](#)]
29. Lambers, C.; Boehm, P.M.; Karabacak, Y.; Samaha, E.; Benazzo, A.; Jaksch, P.; Roth, M. Combined Activation of Guanylate Cyclase and Cyclic AMP in Lung Fibroblasts as a Novel Therapeutic Concept for Lung Fibrosis. *Biomed Res. Int.* **2019**, 2019. [[CrossRef](#)]
30. Chen, C.H.; Kuo, L.M.; Chang, Y.; Wu, W.; Goldbach, C.; Ross, M.A.; Stolz, D.B.; Chen, L.; Fung, J.J.; Lu, L.; et al. In Vivo immune modulatory activity of hepatic stellate cells in mice. *Hepatology* **2006**, *44*, 1171–1181. [[CrossRef](#)]
31. Yu, M.C.; Chen, C.H.; Liang, X.; Wang, L.; Gandhi, C.R.; Fung, J.J.; Lu, L.; Qian, S. Inhibition of T-cell responses by hepatic stellate cells via B7-H1-mediated T-cell apoptosis in mice. *Hepatology* **2004**, *40*, 1312–1321. [[CrossRef](#)] [[PubMed](#)]
32. Liu, C.; Gaca, M.D.; Swenson, E.S.; Vellucci, V.F.; Reiss, M.; Wells, R.G. Smads 2 and 3 are differentially activated by transforming growth factor-beta (TGF-beta) in quiescent and activated hepatic stellate cells. Constitutive nuclear localization of Smads in activated cells is TGF-beta-independent. *J. Biol. Chem.* **2003**, *278*, 11721–11728. [[CrossRef](#)] [[PubMed](#)]
33. Lugnier, C.; Meyer, A.; Talha, S.; Geny, B. Cyclic nucleotide phosphodiesterases: New targets in the metabolic syndrome? *Pharmacol. Ther.* **2020**, *208*, 107475. [[CrossRef](#)] [[PubMed](#)]
34. Son, G.; Hines, I.N.; Lindquist, J.; Schrum, L.W.; Rippe, R.A. Inhibition of phosphatidylinositol 3-kinase signaling in hepatic stellate cells blocks the progression of hepatic fibrosis. *Hepatology* **2009**, *50*, 1512–1523. [[CrossRef](#)] [[PubMed](#)]
35. Son, M.K.; Ryu, Y.L.; Jung, K.H.; Lee, H.; Lee, H.S.; Yan, H.H.; Park, H.J.; Ryu, J.K.; Suh, J.K.; Hong, S.; et al. HS-173, a novel PI3K inhibitor, attenuates the activation of hepatic stellate cells in liver fibrosis. *Sci. Rep.* **2013**, *3*, 3470. [[CrossRef](#)] [[PubMed](#)]
36. Jia, Y.; Wang, F.; Guo, Q.; Li, M.; Wang, L.; Zhang, Z.; Jiang, S.; Jin, H.; Chen, A.; Tan, S.; et al. Curcumin induces RIPK1/RIPK3 complex-dependent necroptosis via JNK1/2-ROS signaling in hepatic stellate cells. *Redox Biol.* **2018**, *19*, 375–387. [[CrossRef](#)] [[PubMed](#)]
37. Zhang, C.Y.; Yuan, W.G.; He, P.; Lei, J.H.; Wang, C.X. Liver fibrosis and hepatic stellate cells: Etiology, pathological hallmarks and therapeutic targets. *World J. Gastroenterol.* **2016**, *22*, 10512–10522. [[CrossRef](#)]
38. Gao, R.; Brigstock, D.R. Connective tissue growth factor (CCN2) induces adhesion of rat activated hepatic stellate cells by binding of its C-terminal domain to integrin alpha(v)beta(3) and heparan sulfate proteoglycan. *J. Biol. Chem.* **2004**, *279*, 8848–8855. [[CrossRef](#)]
39. Chen, L.; Charrier, A.L.; Leask, A.; French, S.W.; Brigstock, D.R. Ethanol-stimulated differentiated functions of human or mouse hepatic stellate cells are mediated by connective tissue growth factor. *J. Hepatol.* **2011**, *55*, 399–406. [[CrossRef](#)]
40. Seo, H.Y.; Lee, S.H.; Lee, J.H.; Kang, Y.N.; Hwang, J.S.; Park, K.G.; Kim, M.K.; Jang, B.K. Src Inhibition Attenuates Liver Fibrosis by Preventing Hepatic Stellate Cell Activation and Decreasing Connective Tissue Growth Factor. *Cells* **2020**, *9*, 558. [[CrossRef](#)]
41. Chen, A.; Zheng, S. Curcumin inhibits connective tissue growth factor gene expression in activated hepatic stellate cells in vitro by blocking NF-kappaB and ERK signalling. *Br. J. Pharmacol.* **2008**, *153*, 557–567. [[CrossRef](#)] [[PubMed](#)]
42. Hao, C.; Xie, Y.; Peng, M.; Ma, L.; Zhou, Y.; Zhang, Y.; Kang, W.; Wang, J.; Bai, X.; Wang, P.; et al. Inhibition of connective tissue growth factor suppresses hepatic stellate cell activation In Vitro and prevents liver fibrosis In Vivo. *Clin. Exp. Med.* **2014**, *14*, 141–150. [[CrossRef](#)] [[PubMed](#)]
43. Sandner, P.; Berger, P.; Zenzmaier, C. The Potential of sGC Modulators for the Treatment of Age-Related Fibrosis: A Mini-Review. *Gerontology* **2017**, *63*, 216–227. [[CrossRef](#)] [[PubMed](#)]
44. Kawada, N.; Kuroki, T.; Uoya, M.; Inoue, M.; Kobayashi, K. Smooth muscle alpha-actin expression in rat hepatic stellate cell is regulated by nitric oxide and cGMP production. *Biochem. Biophys. Res. Commun.* **1996**, *229*, 238–242. [[CrossRef](#)] [[PubMed](#)]
45. Failli, P.; De, F.R.; Caligiuri, A.; Gentilini, A.; Romanelli, R.G.; Marra, F.; Batignani, G.; Guerra, C.T.; Laffi, G.; Gentilini, P.; et al. Nitrovasodilators inhibit platelet-derived growth factor-induced proliferation and migration of activated human hepatic stellate cells. *Gastroenterology* **2000**, *119*, 479–492. [[CrossRef](#)]

46. Thirunavukkarasu, C.; Watkins, S.C.; Gandhi, C.R. Mechanisms of endotoxin-induced NO, IL-6, and TNF-alpha production in activated rat hepatic stellate cells: Role of p38 MAPK. *Hepatology* **2006**, *44*, 389–398. [\[CrossRef\]](#)
47. Uemura, T.; Gandhi, C.R. Inhibition of DNA synthesis in cultured hepatocytes by endotoxin-conditioned medium of activated stellate cells is transforming growth factor-beta and nitric oxide-independent. *Br. J. Pharmacol.* **2001**, *133*, 1125–1133. [\[CrossRef\]](#)
48. Urtasun, R.; Cubero, F.J.; Vera, M.; Nieto, N. Reactive nitrogen species switch on early extracellular matrix remodeling via induction of MMP1 and TNFalpha. *Gastroenterology* **2009**, *136*, 1410–1422. [\[CrossRef\]](#)
49. Wang, P.G.; Xian, M.; Tang, X.; Wu, X.; Wen, Z.; Cai, T.; Janczuk, A.J. Nitric oxide donors: Chemical activities and biological applications. *Chem. Rev.* **2002**, *102*, 1091–1134. [\[CrossRef\]](#)
50. Hall, K.C.; Bernier, S.G.; Jacobson, S.; Liu, G.; Zhang, P.Y.; Sarno, R.; Catanzano, V.; Currie, M.G.; Masferrer, J.L. sGC stimulator pralicigat suppresses stellate cell fibrotic transformation and inhibits fibrosis and inflammation in models of NASH. *Proc. Natl. Acad. Sci. USA* **2019**, *116*, 11057–11062. [\[CrossRef\]](#)
51. Hwang, T.L.; Tang, M.C.; Kuo, L.M.; Chang, W.D.; Chung, P.J.; Chang, Y.W.; Fang, Y.C. YC-1 potentiates cAMP-induced CREB activation and nitric oxide production in alveolar macrophages. *Toxicol. Appl. Pharmacol.* **2012**, *260*, 193–200. [\[CrossRef\]](#) [\[PubMed\]](#)
52. Breitenstein, S.; Roessig, L.; Sandner, P.; Lewis, K.S. Novel sGC Stimulators and sGC Activators for the Treatment of Heart Failure. *Handb. Exp. Pharmacol.* **2017**, *243*, 225–247. [\[CrossRef\]](#) [\[PubMed\]](#)
53. Sandner, P.; Zimmer, D.P.; Milne, G.T.; Follmann, M.; Hobbs, A.; Stasch, J.P. Soluble Guanylate Cyclase Stimulators and Activators. *Handb. Exp. Pharmacol.* **2019**. [\[CrossRef\]](#)
54. Abdelaziz, N.; Colombo, F.; Mercier, I.; Calderone, A. Nitric oxide attenuates the expression of transforming growth factor-beta(3) mRNA in rat cardiac fibroblasts via destabilization. *Hypertension* **2001**, *38*, 261–266. [\[CrossRef\]](#) [\[PubMed\]](#)
55. Hewitson, T.D.; Martic, M.; Darby, I.A.; Kelynack, K.J.; Bisucci, T.; Tait, M.G.; Becker, G.J. Intracellular cyclic nucleotide analogues inhibit in vitro mitogenesis and activation of fibroblasts derived from obstructed rat kidneys. *Nephron. Exp. Nephrol.* **2004**, *96*, e59–e66. [\[CrossRef\]](#)
56. Frey, R.; Becker, C.; Saleh, S.; Unger, S.; van der Mey, D.; Muck, W. Clinical Pharmacokinetic and Pharmacodynamic Profile of Riociguat. *Clin. Pharmacokinet.* **2018**, *57*, 647–661. [\[CrossRef\]](#)
57. Schwabl, P.; Brusilovskaya, K.; Supper, P.; Bauer, D.; Konigshofer, P.; Riedl, F.; Hayden, H.; Fuchs, C.D.; Stift, J.; Oberhuber, G.; et al. The soluble guanylate cyclase stimulator riociguat reduces fibrogenesis and portal pressure in cirrhotic rats. *Sci. Rep.* **2018**, *8*, 9372. [\[CrossRef\]](#)
58. Flores-Costa, R.; Alcaraz-Quiles, J.; Titos, E.; Lopez-Vicario, C.; Casulleras, M.; Duran-Guell, M.; Rius, B.; Diaz, A.; Hall, K.; Shea, C.; et al. The soluble guanylate cyclase stimulator IW-1973 prevents inflammation and fibrosis in experimental non-alcoholic steatohepatitis. *Br. J. Pharmacol.* **2018**, *175*, 953–967. [\[CrossRef\]](#)
59. Knorr, A.; Hirth-Dietrich, C.; Alonso-Alija, C.; Harter, M.; Hahn, M.; Keim, Y.; Wunder, F.; Stasch, J.P. Nitric oxide-independent activation of soluble guanylate cyclase by BAY 60-2770 in experimental liver fibrosis. *Arzneimittel-Forschung* **2008**, *58*, 71–80. [\[CrossRef\]](#)
60. Lei, Y.; Wang, Q.L.; Shen, L.; Tao, Y.Y.; Liu, C.H. MicroRNA-101 suppresses liver fibrosis by downregulating PI3K/Akt/mTOR signaling pathway. *Clin. Res. Hepatol. Gastroenterol.* **2019**, *43*, 575–584. [\[CrossRef\]](#)
61. Lao, Y.; Li, Y.; Zhang, P.; Shao, Q.; Lin, W.; Qiu, B.; Lv, Y.; Tang, L.; Su, S.; Zhang, H.; et al. Targeting Endothelial Erk1/2-Akt Axis as a Regeneration Strategy to Bypass Fibrosis during Chronic Liver Injury in Mice. *Mol. Ther.* **2018**, *26*, 2779–2797. [\[CrossRef\]](#) [\[PubMed\]](#)
62. Lv, J.; Bai, R.; Wang, L.; Gao, J.; Zhang, H. Artesunate may inhibit liver fibrosis via the FAK/Akt/beta-catenin pathway in LX-2 cells. *BMC Pharmacol. Toxicol.* **2018**, *19*, 64. [\[CrossRef\]](#) [\[PubMed\]](#)





## Review

# Lactoferrin, a multi-functional glycoprotein: Active therapeutic, drug nanocarrier & targeting ligand

Ahmed O. Elzoghby<sup>a,b,c,d,\*</sup>, Mona A. Abdelmoneem<sup>c,e,1</sup>, Islam A. Hassanin<sup>c,f,1</sup>,  
 Mahmoud M. Abd Elwakil<sup>c,g</sup>, Manar A. Elnaggar<sup>c,h</sup>, Sarah Mokhtar<sup>c,d</sup>, Jia-You Fang<sup>i,j,k</sup>,  
 Kadria A. Elkhodairy<sup>c,d</sup>

<sup>a</sup> Center for Engineered Therapeutics, Division of Engineering in Medicine, Department of Medicine, Brigham and Women's Hospital, Harvard Medical School, Boston, MA, 02115, USA

<sup>b</sup> Harvard-MIT Division of Health Sciences & Technology (HST), Cambridge, MA, 02139, USA

<sup>c</sup> Cancer Nanotechnology Research Laboratory (CNRL), Faculty of Pharmacy, Alexandria University, Alexandria, 21521, Egypt

<sup>d</sup> Department of Industrial Pharmacy, Faculty of Pharmacy, Alexandria University, Alexandria, 21521, Egypt

<sup>e</sup> Department of Pharmaceutics, Faculty of Pharmacy, Damanhur University, Damanhur, 22516, Egypt

<sup>f</sup> Department of Biotechnology, Institute of Graduate Studies and Research, Alexandria University, Alexandria, 21526, Egypt

<sup>g</sup> Laboratory of Innovative Nanomedicine, Faculty of Pharmaceutical Sciences, Hokkaido University, Kita-12, Nishi-6, Kita-ku, Sapporo, 060-0812, Japan

<sup>h</sup> Nanotechnology Program, School of Sciences & Engineering, The American University in Cairo (AUC), New Cairo, 11835, Egypt

<sup>i</sup> Pharmaceutics Laboratory, Graduate Institute of Natural Products, Chang Gung University, Taoyuan, 333, Taiwan

<sup>j</sup> Research Center for Industry of Human Ecology, Research Center for Chinese Herbal Medicine, Chang Gung University of Science and Technology, Kweishan, Taoyuan, 333, Taiwan

<sup>k</sup> Department of Anesthesiology, Chang Gung Memorial Hospital, Kweishan, Taoyuan, 333, Taiwan

## ARTICLE INFO

## Keywords:

Lactoferrin  
 Nanoparticles  
 Drug delivery  
 Cancer therapy  
 Tumor targeting  
 Anti-viral drugs  
 Immunomodulatory functions  
 Bone engineering

## ABSTRACT

Recent progress in protein-based nanomedicine, inspired by the success of Abraxane® albumin-paclitaxel nanoparticles, have resulted in novel therapeutics used for treatment of challenging diseases like cancer and viral infections. However, absence of specific drug targeting, poor pharmacokinetics, premature drug release, and off-target toxicity are still formidable challenges in the clinic. Therefore, alternative protein-based nanomedicines were developed to overcome those challenges. In this regard, lactoferrin (Lf), a glycoprotein of transferrin family, offers a promising biodegradable well tolerated material that could be exploited both as an active therapeutic and drug nanocarrier. This review highlights the major pharmacological actions of Lf including anti-cancer, antiviral, and immunomodulatory actions. Delivery technologies of Lf to improve its pries and enhance its efficacy were also reviewed. Moreover, different nano-engineering strategies used for fabrication of drug-loaded Lf nanocarriers were discussed. In addition, the use of Lf for functionalization of drug nanocarriers with emphasis on tumor-targeted drug delivery was illustrated. Besides its wide application in oncology nano-therapeutics, we discussed the recent advances of Lf-based nanocarriers as efficient platforms for delivery of anti-parkinsonian, anti-Alzheimer, anti-viral drugs, immunomodulatory and bone engineering applications.

## 1. Introduction

Though discovered in 1939 in bovine milk, lactoferrin (Lf) was reported to be an iron-containing protein [1]. Then after, its structure and chemical properties were detailed in a study published in 1960 [2]. Subsequently, Lf was found to be related to the superfamily of

iron-binding glycoproteins, namely transferrins [3]. Beyond this point, Lf emerged as a focus in many research disciplines, aiming to discover its multitude functions. In this regard, we carried out a search on PubMed library to assess the progress in Lf research, in particular, Lf-based nanoparticles in cancer therapy. Our search results showed an increasing pattern of research on Lf role in cancer therapy, since

\* Corresponding author. Center for Engineered Therapeutics, Division of Engineering in Medicine, Department of Medicine, Brigham and Women's Hospital, Harvard Medical School, Boston, MA, 02115, USA.

E-mail address: [aelzoghby@bwh.harvard.edu](mailto:aelzoghby@bwh.harvard.edu) (A.O. Elzoghby).

<sup>1</sup> Those authors have equal contribution.

<https://doi.org/10.1016/j.biomaterials.2020.120355>

Received 30 April 2020; Received in revised form 18 August 2020; Accepted 31 August 2020

Available online 9 September 2020

0142-9612/© 2020 Elsevier Ltd. All rights reserved.



emerged as early as 1992 (Fig. 1). Furthermore, the rising progress to the field of nanomedicine by 2005 dragged the researchers' attention towards Lf and its potential application as a drug nanocarrier, and more specifically, the implications of Lf nanoparticles in cancer therapy [4]. Notably, Lf research patterns reached its maximum interest in 2018, with about 21 published articles discussing various roles of Lf in cancer therapy, and 32 research papers about Lf nanoparticles of which 11 articles focusing on cancer therapeutics.

Since Lf is a natural protein present in the milk, the chances of eliciting any adverse immune reaction would be minimal [5]. Primarily, the particles fabricated based on Lf protein prepared by mild methods that do not involve any chemical reactions. Studies of our laboratory and other research groups on Lf NPs have shown excellent safety properties even after systemically administered at high doses concentrations with the liver and hematological biochemical parameters are retained [6].

## 2. Structural and biological properties

Lf is a red to salmon-pink whey protein with a large molecular size of ~80 kDa. It is found in milk and in a smaller percentage in bile and tears [7]. It has an isoelectric point (pI) of 8.0–8.5, hence it is positively charged at physiological pH 7.4 [8].

### 2.1. Molecular structure

In 1984, the molecular structure and amino acid sequence of human Lf were discovered. Lf is made of two globular lobes of ~700 amino acids stabilized by disulfide bonds. The two globular lobes are linked by a flexible alpha helix, and they are called amino and carboxy terminal regions or simply N-lobe and C-lobe [9]. Lf undergoes denaturation at two different temperatures for the two lobes; ~60 °C and ~90 °C [7]. Regarding its amino acid composition, cysteine provides thiol groups for the 16 and 17 intramolecular disulfide bonds stabilizing the lobes in human & bovine Lf, respectively with no free sulfhydryl groups. Asparagine provides potential glycosylation sites on N and C-lobes. Histidine, two tyrosine molecules and aspartic acid are essential for iron binding. Arginine is essential for carbonate binding. In addition, the carbohydrate content showed a residue of terminal sialic acid [9,10].

### 2.2. Iron binding

Lf binds to a wide variety of ions and substances including cations (e.g. Iron, & copper), anions (e.g. carbonate & bicarbonate) and substances (e.g. lipopolysaccharides, heparin, glycosaminoglycans and DNA). Structurally, Lf is two times more capable to bind to and transfer iron

than transferrin [7,9]. Lf has three isoforms, Lf- $\alpha$ , Lf- $\beta$  and Lf- $\gamma$ , which have different iron binding ability and ribonuclease activity. Lf- $\alpha$  can bind to iron but has no ribonuclease efficacy unlike Lf- $\beta$  and Lf- $\gamma$  which have ribonuclease action and cannot bind to iron [9]. When Lf binds to a ferric ion, it binds to a carbonate ion synergistically. Lf binds to the ferric ions by a strong bond that can resist pH as low as 4 while binds to other metals with much less affinity [8,9].

### 2.3. Tertiary structure & glycosylation

Lf can bind to iron in a reversible manner resulting in different 3D conformations; apo-Lf (iron-free), monoferric Lf and holo-Lf which is saturated with two ferric ions. Apo-Lf has an open conformation and is susceptible to proteolysis while holo-Lf has a closed conformation and is more resistant to proteolysis [9,11]. Human milk Lf is linked to poly-N-acetyl-lactosaminic glycans in each lobe while bovine Lf contains  $\alpha$ -1,3-linked galactose moieties in the terminal non-reducing location. These glycans increase the stability of Lf against proteases and acidic pH [9,12].

### 2.4. Receptors

Initially, Lf interacts with sulfated proteoglycans at the cell surface and then binds specifically with membrane receptors to stimulate ERK1/2 and PI3K/Akt pathways in the cells. Lf membrane internalization receptors include low density lipoprotein related proteins (LRP1/CD91, LRP2/Megalin), transferrin binding receptors (TFR1, TFR2), as well as ferritin and ferroportin required for iron transfer. The expression of receptors is commonly higher at the surface of cancer cells due to their high metabolic rate [13,14]. In addition, Lf can enter the cells via charge-based interaction where its positive charge enables its interaction with negatively charged cell surface glycosaminoglycans [15]. Meng et al. developed Lf-conjugated N-trimethylated chitosan NPs that have displayed significantly higher cellular uptake into 16HBE and SH-SY5Y cells compared with the negatively charged PLGA NPs [16]. The cationic NPs were easily attracted to cells because of the electrostatic interactions between the negatively charged cell membranes and positively charged NPs. An additional Lf receptor is intelectin 1 (Omentin-1), which is a lectin expressed in intestinal epithelia responsible for Lf uptake [17]. Moreover, the intestinal cells also express iron absorption receptors such as divalent metal ion receptor (DMT1) receptors that enhance intestinal uptake of Fe-Lf [18]. Furthermore, Lf binds to Toll-like receptor 4 (TLR4) that is responsible for Lf-mediated induction of NF- $\kappa$ B pathway and C-X-C-motif cytokine receptor 4 (CXCR4) that facilitates Lf-mediated stimulation of Akt signaling [19,20].

### 2.5. Absorption & oral bioavailability

After oral dose of bLf, the absolute oral bioavailability was nearly 1% because of its protein nature [21,22]. In addition to its hydrolysis by pepsin, ionization of the amino acids responsible for holding Lf structure is changed by the stomach low pH leading to changes in its secondary and tertiary structure [21,23]. Next, Lf is further completely broken down by the small intestine proteases (trypsin, chymotrypsin, amino and carboxyl peptidase). Other studies found that Lf was partially degraded by trypsin into fragments of different sizes, where the larger fragments (>~30 kDa) showed resistance to proteolysis [21,23]. In contrast, Lf was found to survive enzymes in the small intestine of adult rats [21]. Moreover, holo-Lf can survive pepsin digestion in the stomach if the acidity is not enough [24]. Intact Lf molecule reached peripheral blood from the intestine 10–20 min after intragastric intubation and localized in different tissues [22]. After bLf resists the intestinal enzymatic degradation, it binds to LPR receptors on M cells in payer's patches and absorbed into blood and tissues in an immunoreactive form. Takeuchi et al. showed that intraduodenally administered bLf enters the

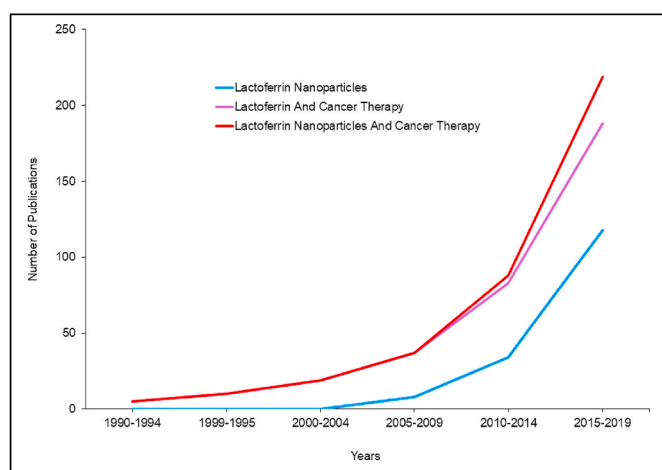


Fig. 1. The research progress timeline of Lf nanoparticles in cancer therapy field.



body through the intestinal lymphatic pathway and reaches the whole body through the thoracic lymph fluid [21]. Overall, gastric-mediated degradation of Lf is controversial. A clinical study conducted by Troost et al. found that Lf is systematically absorbed through the gastrointestinal tract (more than 60%), in its intact form, after ~ 30 min. The pH range (4.0–7.0) that allowed the absorption of Lf was higher than the pH needed for digestion with pepsin (1.5–2.0) [25]. However, another clinical trial demonstrated contradictory results [26]. The mechanism of Lf degradation, as well as its degradation products, are still poorly understood.

## 2.6. Half-life and metabolism

Lf has a short half-life in the body estimated to be about 10 min after i.v. administration [21]. According to Peen et al., recombinant human Lf has a half-life of about 12.6 min and completely removed after 7 h of injection [27]. Once it is transferred by the lymphatic pathway across the intestinal wall, it is rapidly internalized by the liver and excreted into the gall bladder [21]. In the liver, Lf is rapidly cleared from circulation by the action of LRP-mediated internalization by hepatocytes [28]. Intact and fragments of Lf of maternal origin were found in breast-fed infants' urine, so kidneys must be responsible for part of the excretion of Lf [9,27]. Another way to clear Lf from the circulation and interstitial space is by the phagocytes where Lf is engulfed by receptor-mediated endocytosis. The iron carried by the Lf is then carried by ferritin [9, 27]. With this very short half-life, there is a thought that the Lf carried inside lymphocytes survive for longer time and carry out its function in the body [21].

## 3. Pharmacological activities of lactoferrin

Lf possesses a wide array of different functions including anticancer activity, anti-inflammatory, a potential role in bone health preservation and cognitive function improvement in patients with Alzheimer's disease (Fig. 2).

### 3.1. Iron homeostasis

Being an iron-binding glycoprotein, Lf was hypothesized to possess a key role in intestinal absorption of iron across the brush border membrane of human enterocytes owing to the presence of specific receptors for Lf [29]. A recent meta-analysis study concluded that daily oral

administration of bLf showed similar efficacy to ferrous sulfate with lower gastrointestinal complications in pregnant women with iron deficiency [30]. On the contrary, using a genetic mouse model of Lf deficiency (LFKO), the ablation of Lf resulted in a mild iron overload [31]. These studies anticipate that the role of Lf in iron absorption is controversial, and that Lf might function by scavenging free iron in the gut, controlling microbial pathogenesis and prevent free-radical induced cellular damage [32,33].

### 3.2. Antimicrobial activity

#### 3.2.1. Anti-bacterial activity

Lf exerts its antimicrobial action towards a wide array of microbes such as bacteria, fungi, viruses and parasites by two different mechanisms [34,35]. (a) A bacteriostatic activity mediated by sequestering free iron essential for bacterial growth and proliferation; (b) A bactericidal function, Lf may interact directly, through its highly cationic N-terminus, with the negatively charged lipopolysaccharide of gram-negative bacteria causing cell membrane damage [36]. In addition, supplementation with Lf may decrease the risk of necrotizing enterocolitis by altering the intestinal microbiota in premature infants [37]. A randomized study on *H. Pylori* positive patients reported that bLf in combination with a 7-day triple therapy was effective with higher eradication rates than other regimens [38].

A specific bactericidal activity was reported for Lf and Lf chimera (synthetic Lf peptides). The Lf bacterial killing mechanism was attributed to membrane disruption followed by intracellular internalization [39,40]. Then, Lf or Lf chimera would result in alteration of gene expression. For instance, PspA, an antigen which protects pneumococci against host complement system, was down-regulated by treatment with Lf chimera. Whereas, treatment with Lf resulted in decreased expression of luxS gene, and therefore, inhibiting biofilm synthesis [39]. The bactericidal activity of Lf-chimera, could be extended towards their ability to cause perturbation for bacterial cells, leading to programmed cell death type II. Moreover, membrane perturbation of *V. Cholera* was due to binding of Lf and Lf-peptides to specific sites on *V. Cholera* membrane [40].

#### 3.2.2. Antiviral activity

Lf showed antiviral efficacy against HIV, HCV, HBV, Influenza viruses, HPV, and poliovirus, by direct binding to the surface of the virus [41], iron scavenging or by competition for binding to host cells [42,43].

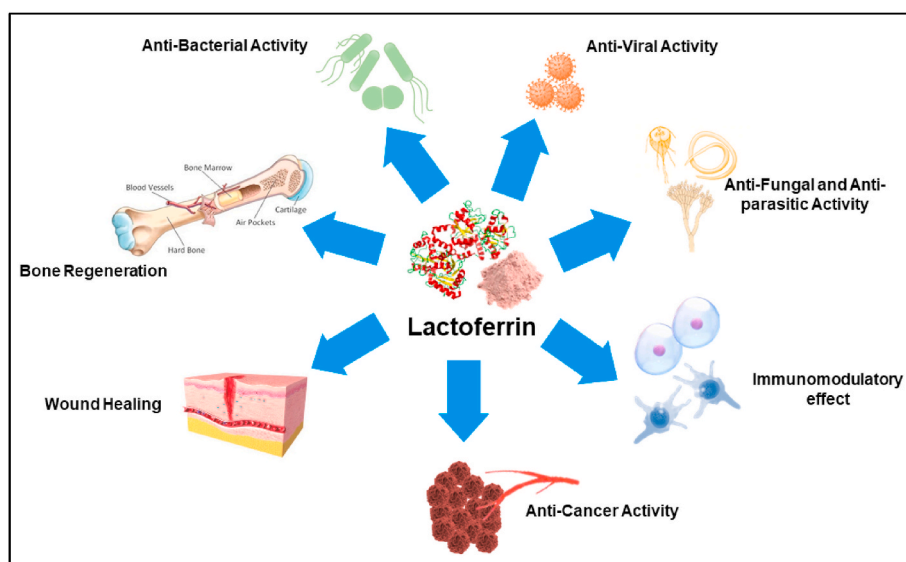


Fig. 2. A schematic diagram illustrating different pharmacological actions of Lf.

This is mediated by its ability to activate NK cells and enhance aggregation and adhesion of neutrophils. According to Lang et al., Lf blocks the binding of Severe Acute Respiratory Syndrome Coronavirus (SARS-CoV) to the host cell [44]. Thus, Lf could prevent the infection of SARS-CoV by inhibiting the early attachment of viral spike protein to the heparan sulfate proteoglycans (HSPGs) at the host cell surface (Fig. 3). The over-expression of the anti-apoptotic protein Bcl-2 has showed an activity against the viral nucleoprotein, preventing the translocation of the viral components from the nucleus to the cytoplasm [45]. Similarly, it was demonstrated that Lf can inhibit caspase-3 activity, preventing influenza virus-induced apoptosis and hence, it results in sequestration of viral nucleoproteins into the nucleus, preventing virus assembly and propagation in MDCK cells [46]. Additionally, Lf binds to viral III and IIIa polypeptides of Adenovirus causing infection neutralization [47]. An anti-HCV activity was demonstrated by a decrease in the RNA titer with Lf monotherapy; suggesting the effective use of Lf as an adjuvant therapy for Ribavirin and Interferon in HCV treatment [48].

### 3.2.3. Antiparasitic and antifungal activity

Lf may exert its antiparasitic action through iron scavenging and depletion [49,50]. Additionally, an amoebicidal activity was explained by binding of apo-Lf to the lipid membrane of the parasite causing its disruption and damage [51]. The spectrum of Lf activity was further extended to *plasmodium* spp. Lf inhibits the sporozoite invasion by competition on heparan sulfate proteoglycans (HSPG) found on hepatocytes [52] and also inhibits the growth of *P. falciparum* by generation of oxygen free radicals and damaging the membrane of the parasite [53]. In addition, an antifungal activity of Lf was demonstrated against *Candida* spp. by competing with the pathogen for the iron [54]. Recently, Lf was shown to act synergistically with lactoperoxidase; for the prevention of oral candidiasis [55].

### 3.3. Anticarcinogenic activity

Lf was reported to exhibit anti-cancer efficacy via different mechanisms [56–58]. Table 1 summarizes some of the most promising anti-carcinogenic mechanisms of Lf.

Some studies showed that bLf functions as a specific inhibitor of the activity of the plasma membrane V-ATPase, and reducing the acidity of tumor microenvironment, thus suppressing tumor growth and metastasis. This was supported by preferential cytotoxicity bLf against the highly metastatic cancer cells PC-3, Mg-63, Hs 578T and MDA-MB-231, characterized by higher levels of V-ATPase compared to the non-cancer cells [73,74]. The selectivity of bLf compared to other conventional V-ATPase inhibitors is also mediated by suppression of the lysosomal V-ATPase [75]. Moreover, the anticancer apoptotic activity of Lf was shown to be indirectly related to the inhibition of inhibitors of apoptosis

**Table 1**

Anti-carcinogenic activity of Lf against various tumor types.

Cancer Type	Protein	Outcome	Ref.
Breast	hLf	Arrest cancer cells in the G0/G1 phase, induction apoptosis and modulation of Bcl-2 and Bax expressions.	[59]
	bLf	Suppression of V-H + ATPase and reducing the acidity of tumor microenvironment.	[60]
Cervix	hLf	Increased expression of Fas & reduced ratio of Bcl-2/Bax.	[61]
	hLf	Upregulation of NK cells, increased infiltration of CD4 <sup>+</sup> & CD8 <sup>+</sup> peripheral T lymphocytes, elevated serum IFN- $\gamma$ , IL-2 and TNF- $\alpha$ in tumor-bearing mice.	[62]
Prostate	bLf	Inhibits the plasma membrane V-ATPase, reducing the tumoral acidity and suppressing tumor progression and metastasis in PC-3 cells.	[63]
Colon	hLf, bLf and CbLf	Increased expression of TGF- $\beta$ 1, stimulated IL-18 secretion in Caco-2 cells.	[64]
	bLf	Enhanced infiltration of CD4 <sup>+</sup> & CD8 <sup>+</sup> cells, increased production of IL-18.	[65]
NPC	hLf	Downregulation of PDPK1 via the MAPK/c-Jun pathway and suppression of K18-facilitated AKT stimulation.	[66]
Leukemia	hLf	LF-induced apoptosis of Jurkat T cells by interactions with the E2F1 or Bcl-2 target genes.	[67]
Lung	hLf	Antiproliferative effects attributed to the elevated levels of hypophosphorylated Rb in H1299 cells.	[68]
	bLf	Decreased levels of TNF- $\alpha$ , IL-4, IL-6, and IL-10 cytokines, limiting inflammation and restricting tumor proliferation.	[69]
OSCC	bLf	Selective suppression of growth through mTOR/S6K & JAK/STAT3 signaling pathways and triggering of apoptosis in OSCC.	[70]
Head & Neck	Recombinant hLf	LF induced growth inhibitory effects via p27/cyclin E-dependent signaling pathway by regulating Akt phosphorylation.	[71]
GBM	hLf	Suppression of the proliferation of NMD and FN primary cells as well as U87MG cells by reducing the expression of cyclin D1 and D4.	[72]

**hLf:** Human Lactoferrin; **bLf:** Bovine Lactoferrin; **NPC:** Nasopharyngeal Carcinoma; **OSCC:** Oral Squamous Cell Carcinoma; **GBM:** Glioblastoma; **TMZ:** Temozolomide.

(IAP), for instance, Survivin. Survivin is expressed in various cancer cells and inhibits the effect of caspase leading to cancer evade apoptosis. Lf causes down-regulation of Survivin gene expression. The anti-survivin

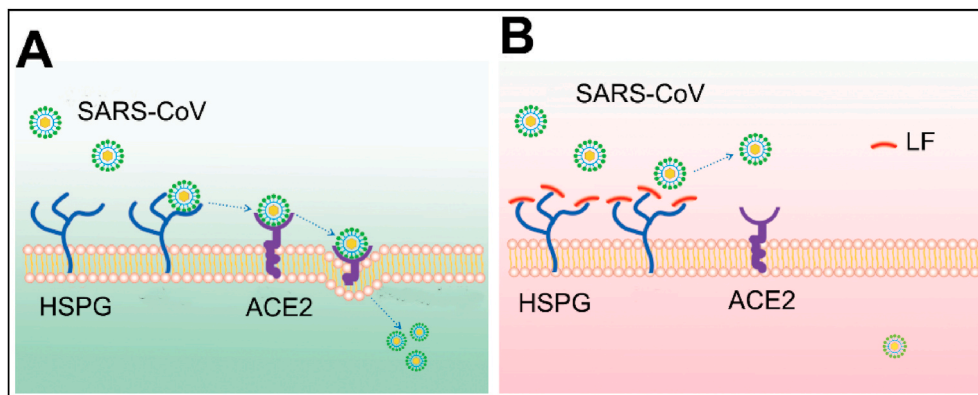


**Fig. 3.** Antiviral activity of Lf towards SARS-CoV. (A) SARS-CoV utilizes Heparan Sulfate Proteoglycans (HSPG) to roll on host cells and subsequently identify potential specific entry receptors. (B) Upregulation of Lf and allocations to HSPGs to prevent initial contact between virus particles and subsequent infection [44].

activity was reported by nano-formulated bLf against colon CSCs and tumors (Fig. 4). More importantly, Lf up-regulates inhibitors of IAP, HTRA2 and SMAC, which activates the cleavage of caspases, mainly caspases 8, 9, and 3. Therefore, induction of apoptosis in cancer cells via Lf was attributed, mainly, to inhibition of IAPs [76].

Lf also rapidly internalizes into cancer cells and increases the sensitivity of resistant tumors to the action of chemotherapeutics such as doxorubicin (DOX) thus overcoming chemo-resistance [77]. In addition, Lf nanocarriers could increase the expression of cytokines TNF- $\alpha$ , and IFN- $\gamma$  with anticancer activity. Interestingly, the iron saturation of Lf could be linked to its anticancer efficacy so that the iron saturated holo-Lf exhibited higher anti-tumor efficacy than apo-Lf or native Lf while the mechanism is still unclear [78].

### 3.4. Wound healing

The ability of Lf to promote wound healing is well reported through different mechanisms [79]. Talactoferrin (TLf), a recombinant human Lf, helps production of pro-inflammatory cytokines IL-6, IL-8, TNF- $\alpha$  and MIP-1 $\alpha$ . It also increases the expression of hyaluronan required for forming granulation tissue, upregulates platelet derived growth factor and promotes keratinocyte proliferation and migration essential for wound re-epithelization, in addition to cellular protection from apoptosis [80]. TLf was found to be safe and effective in Phase II clinical trials in patients with diabetic ulcers [81].

## 4. Delivery of lactoferrin as active therapeutic

### 4.1. Microparticles

Chitosan microparticles (mean size 4.9  $\mu\text{m}$ ) were developed via emulsification-solvent evaporation for controlled release of Lf (Table 2) [82]. The microparticles demonstrated high Lf loading (16.7%, w/w) together with gradual controlled release of Lf over a period of 24 h. However, the microparticles may be disintegrated in the gastric acidic conditions due to solubility of chitosan in acidic pH so it was not suitable for oral delivery. Therefore, Lf was encapsulated into calcium alginate microparticles prepared by electrostatic complexation then coated with chitosan. The microparticles maintained their integrity in the GIT at

both pH 1.2 and 6.8 which would be useful for the intestinal delivery of Lf [83,84].

### 4.2. Nanoparticles

To increase its oral absorption, cationic Fe-bLf was electrostatically adsorbed onto calcium phosphate nanocrystals (NCs) and then coated with a thin layer of chitosan. The chitosan-coated NCs were further encapsulated in alginate gel to provide protection against GIT degradation [18]. In the acidic stomach environment, alginate exists in unionized state forming a matrix around the inner core to protect the entrapped Fe-bLf. Reaching the alkaline intestinal pH, the ionized sodium alginate is formed releasing the Lf content. The mucoadhesive nature of Fe-bLf NCs, mediated by the interaction between the positively charged of both iron and chitosan with the negative charged of the mucus, enabled increased internalization in the intestinal tissue layer of the nanocarriers. Moreover, LPR and DMT1 receptors on intestinal cells help the absorption process of the nanocarriers (Fig. 5) [14]. The alginate/chitosan-coated Lf NCs displayed promising activity against different types of solid tumors [14,85] and osteoarthritis [86].

### 4.3. Liposomes

Incorporation of bLf into liposomes was found to improve its anti-inflammatory action following its oral or intra-articular administration by improving its resistance to gastric digestion and hence increasing its intestinal absorption [87]. Moreover, liposomal Lf showed higher cytotoxicity against cancer cells by increasing its intracellular accumulation and protecting from lysosomal or proteasomal degradation [88, 89].

### 4.4. PEGylation

PEGylated Lf can be synthesized by direct conjugation between and the free amino moieties of bLf and the branched PEG N-hydroxy-succinimide (NHS) esters. Alternatively, bLf could be coupled to two p-nitrophenyl esters of linear 5 and 30 kDa PEG [90]. Compared to PEG-NHS, slower reaction rates but remarkably higher degradation stabilities could be achieved using PEG-p-nitrophenyl active esters.

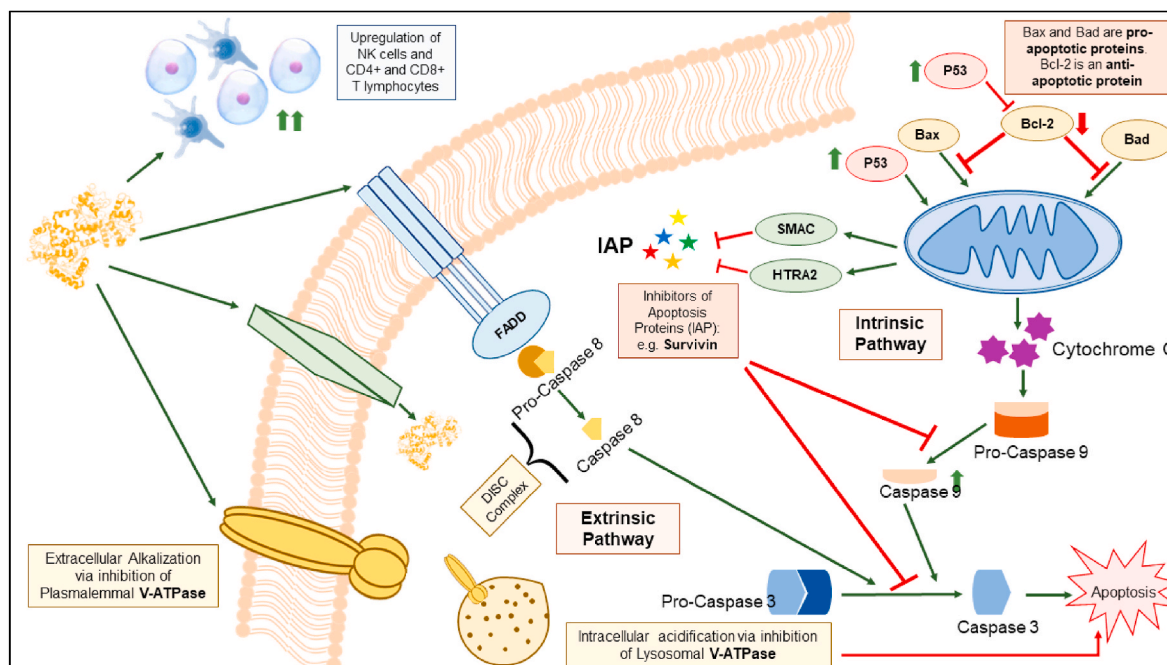


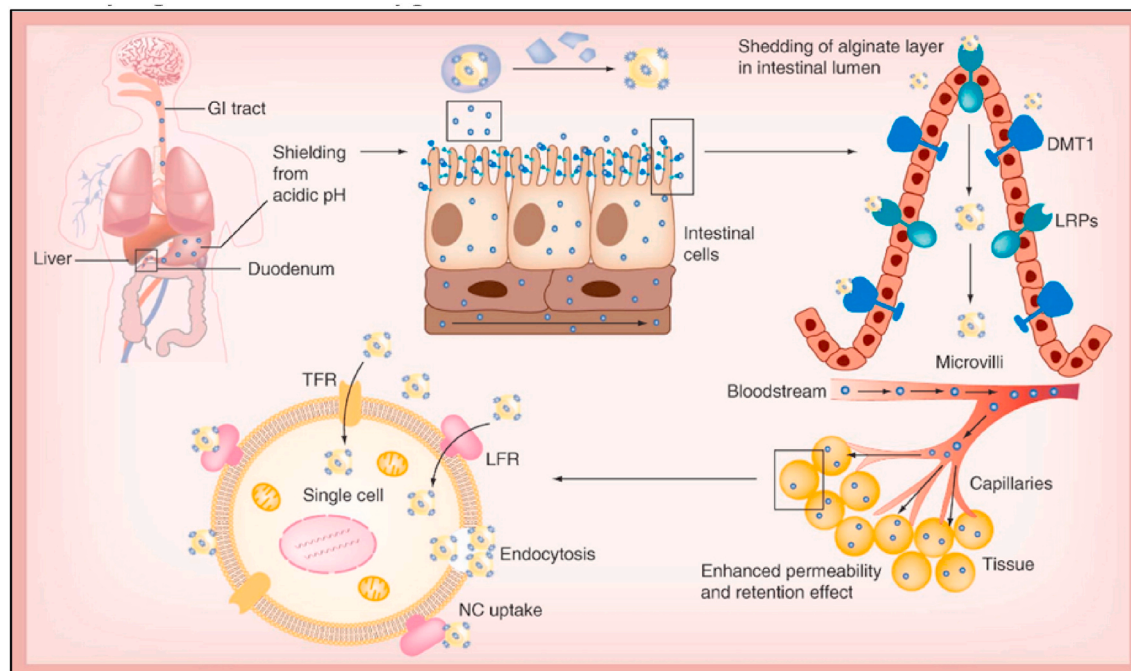
Fig. 4. Schematic representation of the major anti-cancer mechanisms of Lf.

**Table 2**

Representative examples of drug delivery systems developed as Lf carriers.

Drug delivery system	Preparation technique	Indication	Outcome	Ref.
Chitosan/alginate/calcium complex microparticles	Emulsification–evaporation	Anti-inflammatory effect	The MPs exhibited more powerful inhibition of edema and faster recovery than Lf solution.	[84]
Bioadhesive tablets	Direct compression	Anti-inflammatory	Tablet has reduced Swelling of the oral ulcer, due to the immune regulatory function of b-Lf.	[94]
AEC-CCo-CP-bLf-NCs	Nanoprecipitn./ionic gelation	Antiparasitic <i>Toxoplasma gondii</i>	Two-fold increased bioavailability of bLf, significantly decreased parasitic load and increased survival of mice up to 25 days.	[95]
AEC-CCo-CP-bLf-NCs	Nanoprecipitn./ionic gelation	Treatment of Osteoarthritis	Significantly reduced joint inflammation and decreased expression of catabolic genes.	[86]
AEC-CCo-CP-bLf-NCs	Nanoprecipitn./ionic gelation	Colon cancer therapy	None of the treated mice developed tumors or exhibited any toxic effects.	[85]
20k-PEG-bLf	Carbodiimide coupling	–	5.4-fold prolonged serum half-life and 2-fold increased proteolytic half-life over unmodified Lf.	[91]
40 k-PEG-bLf	Carbodiimide coupling	–	8.7-fold longer plasma half-life and 6-fold increased proteolytic half-life than unmodified Lf.	[92]
Multi-lamellar liposomes	Thin-film hydration	Anti-inflammatory effects	Liposomal bLf pretreatment significantly suppressed any GPT or GOT increase in serum induced by CCl <sub>4</sub> .	[87]
Liposomes	Thin-film hydration	Anti-tumoral effects	Entrapment of Apo bLf into liposomes increased its anticancer effect on melanoma cells.	[88]
Multi-lamellar liposomes	Thin-film hydration	Hepatoprotective effects	Liposo. Lf exhibited powerful anti-inflammatory action against CCl <sub>4</sub> -induced liver injury.	[89]

Alginate chitosan calcium phosphate bLf nanocapsules: AEC-CCo-CP-bLf-NCs.

**Fig. 5.** Proposed mechanisms of absorption of Fe-bLf loaded polymeric NPs in cancer therapy. Maximal Uptake was achieved through iron receptors; DMT1 in addition to LRP receptors. Through EPR mediated effect, the NPs reached cancer tissue and subsequently internalized through pinocytosis utilizing Tf and Lf receptors [14].

PEGylation of Lf improved its oral bioavailability so that the proteolytic half-life of 20k and 40 kDa-PEG-bLf has been increased by 2-fold and 6-fold, respectively compared to unmodified Lf [91,92]. Intragastric injection of 20k-PEG-bLf at a dose of 30 mg/kg into rat stomach increased its intestinal absorbed amount by 10-fold and prolonged plasma half-life by 5.4-fold relative to unmodified Lf. PEGylated bLf enhanced its hepatoprotective effect against CCl<sub>4</sub>-induced liver injury by increasing the SOD activities and ROS scavenging in mitochondria, leading to the reduced activity of AST and ALT [93]. The 40k-PEG-bLf displayed enhanced hepatoprotection and improved pharmacokinetics in comparison with both unmodified bLf and 20 k-PEG-bLf conjugates.

## 5. Preparation techniques of lactoferrin nanocarriers

### 5.1. Sol-in-oil emulsion

In this technique, the drug is simply mixed with the protein aqueous solution in the presence of oil phase. When the oil phase was added to the soluble mixtures of drug and protein, the drug was adsorbed to protein molecules forming emulsified aggregates. The complex aggregates were disaggregated by sonication and then cooled resulting in their precipitation with formation of solidified drug-protein particles. Finally, the formed particles are cleaned off oil. Different drugs e.g. temozolamide [96], fluorouracil (5-FU) [97], Oxaliplatin [98] and siRNA [6] have been successfully loaded into Lf by this method



**Table 3**

Representative examples of Lf-based nanocarriers for drug delivery applications.

Method of preparation	Drug	Indication	Outcomes	Ref.
Lf NPs Sol-oil chemistry	DOX	HCC	Minimized the cardiotoxicity of DOX and enhanced its efficacy and bioavailability.	[122]
Lf NPs Sol-oil chemistry	5-FU	Melanoma	Higher intracellular uptake, prolonged retention and 2.7-fold improved cytotoxicity against B16F10 melanoma cells.	[97]
Lf NPs Sol-oil chemistry	EFV	HIV Therapy	> two-fold increased anti-HIV-1 activity in comparison with free drug.	[123]
Lf NPs Sol-oil chemistry	TMZ	Glioma treatment	Significant reduction of tumor volume and improved median survival time.	[96]
Lf NPs Sol-oil chemistry	Carboplatin	Retinoblastoma	Higher anti-proliferative activity against retinoblastoma cells than soluble carboplatin.	[124]
Lf NPs Desolvation	CUR	In vitro optimization	The NPs exhibited a particle size of 214.7 nm with encapsulation efficiency of 53.7%.	[99]
Mann-Lf NPs Thermal treatment	Shikonin	Colorectal cancer	The NPs elicited immunogenic cell death and repolarizing TAMs to M1 macrophages.	[102]
TPGS-TAT Lf NPs Thermal treatment	Simvastatin	Glioma	The NPs repolarized TAMs to M1 phenotype & increased ROS-induced mitochondrial apoptosis.	[101]
Lf NPs Nab technology	Fenretinide	HCC	Enhanced oral bioavailability & anti-cancer effect of GA, thus decreasing its toxicity.	[104]
Lf NPs Nab technology	Gambogic acid	HCC	Enhanced oral bioavailability & anti-cancer effect of GA, thus decreasing its toxicity.	[104]
Lf NPs Nab technology	Oleanolic acid	Improved bioavailability	Increased dissolution and enhanced oral absorption of OA.	[105]
Lf-Drug conjugate Carbodiimide coupling	CUR	Colorectal cancer	Lower IC <sub>50</sub> of NPs (0.5 µg/ml) against HCT116 cells than free curcumin (3.3 µg/ml) after 48 h.	[112]
Lf-Drug conjugate Carbodiimide coupling	DOX	Prostate cancer	Orally Fe-bLf-DOX inhibited tumor growth, prolonged survival, reduced DOX toxicity.	[77]
Lf-Drug conjugate Free-radical graft copolymerization	EGCG	Antioxidant	Higher antioxidant activity of Lf-polyphenol conjugates than control Lf in both ABTS scavenging and reducing power assays.	[116]
Lf-Drug conjugate coated MSNPs	CA			
	Gallic acid	Breast cancer	The Lf-MSNPs showed higher cytotoxic effect against MCF-7 breast cancer cells.	[114]
Lf-shell oily core nanocapsules	PMT & Ellagic acid	Breast cancer		
	Sorafenib & Quercetin	HCC	The LA/Lf-NCs exhibited better uptake into HepG2 cells with 2-fold decrease of IC <sub>50</sub> compared to free drugs.	[121]
Lf/ChS electrostatic nanocomplex	DOX & Ellagic acid	NSCLC	Higher cytotoxic effect and uptake into A549 cancer cells triggered by Tf & CD44 receptors.	[110]
Lf-zein amphiphilic micelles	Rapamycin & Wogonin	Breast cancer	Enhanced synergistic cytotoxicity & suppression of MCF-7 cells & EAT tumor growth.	[118]
	Dasatinib & Fe <sub>3</sub> O <sub>4</sub> NPs		1.35-fold higher cytotoxicity against MDA-MB-231 via external magnetic field.	[119]

Doxorubicin: DOX; 5-Fluorouracil: 5-FU; Efavirenz: EFV; Temozolomide: TMZ; Curcumin: CUR; Epigallocatechin gallate: EGCG; Pemetrexed: PMT; Chlorogenic acid: CA; Ehrlich Ascites Tumor: EAT.

(Table 3). The Lf NPs prepared using this method offered several advantages including small particle size 60–90 nm and high drug loading (50% loading). moreover, the NPs displayed pH-responsive drug release with higher release at endosomal pH (pH 5 and 6) which can be advantageous for tumor targeted drug delivery. This behavior can be attributed to the conformational change or shrinkage of Lf in that acidic milieu. Since this technique does not need any harsh chemical treatments such as using stabilizing or cross-linking agents, we anticipate that Lf molecules may revert back to their native conformation and regain their receptor binding epitopes [6]. However, some limitations of this technique can arise from the difficulty of oil removal and the effect of sonication on the structural integrity of protein molecules.

## 5.2. Desolvation

Lf nanoparticles could be prepared by desolvation technique by addition of a miscible organic solvent of the drug to the aqueous protein solution at adjusted pH. When the solution turns turbid, revealing particle formation, a crosslinking agent e.g. glutaraldehyde solution was added to harden the particles. Curcumin-loaded Lf NPs prepared by desolvation exhibited a particle size of 214.7 nm with encapsulation efficiency of 53.7% [99]. The nanoparticles were optimized by varying different factors e.g. protein concentration, solvent ratio, temperature, sonication strength, flow rate, cross-linking agent and pH. Smaller particles were formed by heating the protein at 35–60 °C. At high temperature, protein unfolding increased the exposure of the SH groups resulting in increased intra-crosslinking of protein macromolecules thus producing smaller nanoparticles [100]. Generally, desolvation is

advantageous to other preparation techniques of protein NPs by its simplicity with no need for harsh conditions including high shearing or heating, that might influence the structural stability of proteins.

## 5.3. Thermal denaturation

Lf NPs can be prepared by controlled thermal denaturation at 61 and 93 °C corresponding to its two lobes. The hydrophobic domains usually become exposed upon protein unfolding resulting in its aggregation via hydrophobic interaction. The protein nanoparticles prepared by thermal denaturation exhibited high pH stability that can be attributed to the strong hydrophobic bonding formed between protein macromolecules following their unfolding. Moreover, the outer glycan components of Lf extending into the external aqueous medium can enhance the stability of the protein nanoparticles by increasing the steric repulsion.

Simvastatin and fenretinide were co-encapsulated into TPGS-TAT-modified Lf NPs (177 nm) prepared by heat denaturation-driven protein self-assembly process [101]. An aqueous Lf solution was stirred on the oil bath at 80 °C for 10 min followed by dropwise addition of organic solution of both drug and cell-penetrating peptide TPGS-TAT (developed by TAT was conjugated to D-α-tocopheryl polyethylene glycol succinate). In a consequent study, the same thermal denaturation procedure was used for preparation of mannosylated Lf NPs (150 nm) for code-livery of shikonin and JQ1 [102]. Loading of the antioxidant polyphenol cichoric acid to Lf by heating to 95 °C at pH 7 resulted in formation of NPs with a diameter of about 67 nm with higher antioxidant capacity than free cichoric acid [103]. This technique can be considered as a green one that does not require toxic cross-linkers or organic solvents.



#### 5.4. Albumin-bound nanoparticle (Nab) technology

Being glycoprotein rich in cysteine with 14 disulfide bonds, Lf has a great tendency to form nanoparticles (NPs) via albumin-bound technology (Nab). Homogenization of protein solution induces the formation of a protein layer coating the drug particles where the S–S bonds were broken and new bonds were formed due to the local heat generated because of the high shearing. Gambogic acid and oleanolic acid (OA) were loaded into Lf nanoparticles with size about 100–200 nm by Nab technology [104,105]. The solution of OA, in mixture of methylene dichloride and ethanol (7:3), was cooled to 25 °C and then slowly added to the aqueous Lf solution. The two solutions were mixed and homogenized at 50 MPa for three cycles followed by evaporated at 45 °C under reduced pressure then freeze-dried without adding any cryoprotectant. In addition, the hydrophilic structure of LF make the particles readily redispersed in aqueous solution.

#### 5.5. Electrostatic nanocomplexes

Polyelectrolyte complexes (PEC) were formed based on electrostatic interactions between positively charged Lf, with higher isoelectric point ( $pI \approx 8.5$ ) than most of other proteins ( $pI \approx 5$ ) and negatively charged polysaccharides in aqueous solutions. Aqueous solutions of Lf and polysaccharide can be mixed at ambient temperature to form electrostatic nanocomplexes followed by heating up to 92 °C above the thermal denaturation temperature of Lf to promote protein aggregation and particulate formation [106]. For example, Lf/N-succinyl chitosan/galactomannan nanocomplexes were formed by their simple mixing at 1:2:3 and 1:3:2 ratios prior to thermal treatment [107]. Alternatively, Lf NPs with a diameter of 200–400 nm were first formed by thermal denaturation followed by electrostatic complexation with negatively charged polysaccharides e.g. alginate, carrageenan, or pectin [108]. Reversal of the particle surface charge from positive to a negative value indicated successful coating by a layer of the polysaccharide. Yan et al. has used heat-denatured Lf/pectin PEC NPs as a carrier for curcumin [109]. Curcumin was released in a pH-dependent manner showing higher release at acidic pH. This pattern can be explained by the weakened Lf/pectin electrostatic attraction at acidic pH due to protonation of pectin carboxylic groups. The encapsulated curcumin showed higher antioxidant capacities through DPPH radical scavenging ability.

Lf can also form electrostatic nanocomplexes with anionic polysaccharides without need for further heating. In our laboratory, novel nanocomplexes were developed based on the electrostatic complexation between positively charged Lf and negatively charged chondroitin sulfate [110]. The hydrophobic phytochemistry ellagic acid, converted into water soluble nanosuspension, was co-encapsulated together with water soluble cytotoxic drug DOX into the hydrophilic Lf-ChS nanoparticles. As the pH of Lf solution decreases far below its isoelectric point, Lf macromolecules become strongly positively charged resulting in formation of a strong and stable nanocomplex at pH 3.5 with smaller size 138.2 nm. Similarly, Lf-hyaluronic acid-EGCG ternary nanocomplexes were formed via hydrophobic and electrostatic interactions as well as hydrogen bonding [111].

#### 5.6. Lactoferrin-drug nanoconjugates

The structure of Lf makes it capable to chemically conjugate with various hydrophobic moieties or drugs. Utilizing the hydrophilic property of Lf in enhancing the water solubility of the hydrophobic drugs where the conjugated structures drive the self-assembly forming nanomicelles in aqueous media. Chaharband et al. has prepared Lf-curcumin conjugate where the carboxylic moiety of Lf was activated via carbodiimide reagent and then coupled to the hydroxyl group of curcumin forming an ester bond [112]. The conjugate of curcumin to Lf macromolecule was self-assembled into nanostructures with a size of 165 nm. By increasing the Cur-Lf molar ratio from 10 to 40, the

conjugation ratio was also increased from 0.85 to 4.52, respectively. Similarly, Lf-deferasirox conjugate was prepared via ester bond carbodiimide coupling and self-assembled into nanoparticles with a size of 100–500 nm [113]. In another investigation, DOX-Lf conjugate were prepared also via carbodiimide coupling reaction forming amide bond through activating the carboxylic moiety of Lf and attaching it to the amino group of DOX [77].

In our laboratory, the chemotherapeutic drug pemetrexed was chemically coupled to Lf via carbodiimide coupling. The Lf-drug conjugate was anchored onto the surface of aminated mesoporous silica nanoparticles entrapping the herbal drug ellagic acid [114]. The synergistic combination showed enhanced internalization and cytotoxicity against MCF-7 breast cancer cells as revealed by lower combination index value ( $CI = 0.885$ ) in comparison with soluble drugs.

In addition to carbodiimide coupling, Lf conjugates with the polyphenolic drugs epigallocatechin gallate (EGCG), chlorogenic acid (CA) and gallic acid (GA) were successfully elaborated by free-radical graft copolymerization in aqueous media using ascorbic acid/ $H_2O_2$  redox pair system [115,116]. Moreover, Maillard reaction was used for covalent bond formation between carbohydrate (glucose or polydextrose) and Lf-CA conjugate resulting in higher thermal stability [117].

#### 5.7. Amphiphilic micelles

Nanosized micelles can be developed by the aqueous self-assembly of amphiphilic co-polymers. In our laboratory, an amphiphilic co-polymer was synthesized by chemical carbodiimide coupling of the hydrophobic corn protein zein to the hydrophilic Lf protein [118,119]. Upon dispersion in aqueous solution, the chemical conjugate was self-assembled into nano-micelles (276.6 nm) with a low CMC value. This property protected the micelles from dis-assembly after dilution as a result of injection into systemic circulation. Two lipophilic drugs; rapamycin and wogonin were efficiently entrapped into the hydrophobic core of zein-Lf micelles whereas the hydrophilic Lf shell enabled prolonged circulation. The protein amino groups of Lf allowed further crosslinking of the micelles using glutaraldehyde leading to lower particle diameter and higher colloidal stability. In comparison to the commonly used synthetic amphiphilic co-polymers (e.g. PLA-PEG), zein-Lf co-polymer is considered GRAS (Generally recognized as safe) material composed of natural protein components with much less cost and toxicity [120].

#### 5.8. Lactoferrin shell-oily core nanocapsules

Polymeric oily-core nanocapsules are commonly used for solubilization and controlled delivery of hydrophobic drugs. The NCs are composed of a polymeric shell enveloping an oily core for drug encapsulation. The hydrophobic synthetic polymers (e.g. PLGA or PCL) are among the most commonly used shell forming materials for that type of NCs. However, besides their high cost, numerous toxicity issues have been raised related to their acidic degradation products or immunological reactions. In our laboratory, an oily core composed of Capryol PGMC was used for solubilization of the hydrophobic drugs sorafenib and quercetin [121]. SFB was pre-complexed with phospholipid to maximize its incorporation in the oily phase. A surrounding shell of cationic Lf was electrostatically attached onto the negatively charged oily core to form liver tumor-targeted NCs exploiting the Lf interaction with its receptors upregulated by liver cancer cells. To further enhance tumor targeting, lactobionic or glycyrrhetic acid was chemically anchored to the Lf shell where they bind with ASGP or GA receptors on HCC cells, respectively [121].

#### 5.9. Lactoferrin-inorganic nanocomposites

Inspired by the emerging role of inorganic materials in therapy and diagnosis, hybrid nanocomposites were fabricated by chemical coupling

of Lf to various types of inorganic nanoparticles (Table 4). As an extraordinary theranostic agent, tiny gadolinium oxide ( $Gd_2O_3$ ) NPs (13.4 nm) were synthesized and stabilized with coating layers of poly (acrylic acid) and reduced albumin. Carbodiimide reaction was then used to develop nanocomposites by chemical coupling of Lf and RGD dimer to the surface of the NPs to enhance BBB permeation and tumor internalization, respectively [125]. Similarly, cisplatin was loaded into hybrid  $Fe_3O_4/Gd_2O_3$  NPs modified with Lf and RGD dimer to enhance ferroptosis of brain tumor [126]. Cisplatin induced generation of  $H_2O_2$  while  $Fe^{2+}$  and  $Fe^{3+}$  released from the NPs resulted in ROS generation. As a result, synergistic inhibition of cancer growth was achieved.

For combined cancer therapy, Lf-inorganic NPs can be combined with chemotherapy to elicit synergistic anticancer effect. Porous magnetic NPs showed excellent capacity of absorbing magnetic and optical wavelengths resulting in heat generation to kill cancer cells. Therefore, mesoporous  $Fe_3O_4/SiO_2$  NPs (PMNSs) and maghemite NPs (MMNPs) were synthesized by hydrothermal method then chemically modified with Lf for tumor targeting and then physically loaded with DOX [127, 128]. The combination of chemo- and photothermal/magnetic therapy showed enhanced antitumor efficacy. Lf was also used to chemically modify the surface of graphene oxide/ $Fe_3O_4$  NPs ( $GO@Fe_3O_4$  NPs) to increase their accumulation into glioma cells [129]. The resultant nanocomposites showed acid-responsive release of DOX with enhanced killing of glioma C6 cells. In another investigation, ultrasmall graphene nanosponge-supported lipid bilayers (40 nm) were co-loaded with docetaxel (DTX) and gasified perfluorohexane (PFH). This nanoplateform acted as a photothermal agent for combined gasification/chemo-thermotherapy of cancer by releasing both drug and heat under exposure to near-infrared laser irradiation [130]. The surface of nanosponge was further modified with Lf via chemical conjugation to the lipid bilayer. Lf increased the lateral bilayer fluidity and enhanced its penetration into tumor spheroids mediated by transcytosis.

Lf-silver nanocomplexes have been reported for their efficient

antibacterial activity [131]. For example, Lf was used to modify the surface of silver nanoparticles (AgNPs) resulting in a synergistic anti-biofilm efficacy against *S. aureus* and *P. aeruginosa* [132]. Moreover, the adsorbed Lf layer was found to decrease the cytotoxicity of silver NPs [133]. Quantum dots, as potent fluorescent imaging agents, were chemically coupled to Lf via a tumor cleavable bond to prevent systemic toxicity of its Cd component [134]. The cationic Lf-QD conjugate was used to electrostatically decorate drug-loaded nanocapsules to enhance their tumor accumulation. The QD-induced fluorescence enabled tracing the biodistribution of nanocarriers and their internalization into breast cancer cells. Silica nanoparticles were also coupled to Lf to enhance their brain delivery. The Lf-modified silica NPs (25 nm) exhibited the highest transport across the cerebral endothelial cells via Lf receptor-mediated transcytosis [135]. In addition, Lf was successfully used to modify the surface of ellagic acid-loaded mesoporous silica NPs (MSNPs) to enhance their accumulation into breast tumor tissue. The carbodiimide-activated carboxylic group of Lf was coupled to the amino groups of APTES-modified MSNPs [136]. On the other hand, few studies reported the use of Lf protein to stabilize the highly luminescent gold nanoclusters [137,138]. Those Lf-gold nanocomposites might have future applications in tissue imaging and cancer theranostics.

## 6. Design of Lf-targeted nanocarriers

By virtue of its receptors overexpressed by cancer cells and some other tissues such as brain, Lf was increasingly exploited to modify the surface of drug nanocarriers. Two main strategies have been investigated for the design of Lf surface-modified nanocarriers; covalent conjugation and electrostatic complexation. Chemical conjugation was utilized using various coupling reactions such as carbodiimide and maleimide thiol coupling methods. High yield and conjugation efficiency was obtained when carbodiimide and maleimide thiol coupling were used for conjugating Lf to SLNs [139] and PEGylated liposomes [140] with conjugation efficiency of 71.02% and 74%, respectively. In addition, Lf was coupled to the surface of poly(propylene imine) dendrimer using N-c-maleimidobutyl-oxysuccinimide ester (GMBS) as a linker. This heterobifunctional cross-linking agents inhibit the polymerization that can be obtained using homo-bifunctional cross-linking reagents e.g. dimethyl suberimidate [141].

## 7. Pharmaceutical applications

### 7.1. Brain delivery

Many challenges including the tight junctions between brain endothelial cells, their low pinocytic activity, presence of efflux pump systems and inactivating enzymes hamper efficient delivery of drugs and genes to the brain across the blood brain barrier (BBB) [142]. Lf receptors including LRP1 and LRP2 (megalin) are well expressed in glioma cells, brain microvessels and neurons (Fig. 6) [143]. In addition, Lf bears positive charge in physiologic pH, which facilitates its uptake into negatively charged brain capillary endothelial cells (BCECs). Therefore, Lf-modified nanocarriers are internalized by receptor- and adsorptive-mediated endocytosis into BCECs and glioma cells. In comparison with Tf, Lf-conjugated dendrimers for gene delivery showed 2.2-fold increased uptake and 2.3-fold increased brain gene expression in BCECs with lesser accumulation in liver, spleen and kidney [144]. In contrast to Tf, the lower plasma concentration of endogenous Lf, its positive charge as well as unidirectional transport of Lf across the BCEC monolayer might result in higher brain accumulation of Lf-conjugated vector [145,146]. Chan and coworkers have recently investigated the vasculature of U87-MG glioblastoma xenograft model [147]. The authors found that 97% of the NPs could enter the tumors through an active *trans*-endothelial process rather than the commonly known passive extravasation transport mechanism through the inter-endothelial gaps. This suggested mechanism may account for the entry of

**Table 4**  
Lf-inorganic nanocomposites for drug delivery & tissue imaging applications.

Inorganic NPs	Drug	Major outcomes	Ref.
$Gd_2O_3$ NPs	–	Ultra-BBB permeable MRI theranostics which enhanced the effect of radiotherapy in orthotopic glioblastoma models.	[125]
$Fe_3O_4/Gd_2O_3$ NPs	CDDP	Enhanced ferroptosis of cancer cells.	[126]
Mesoporous $Fe_3O_4/SiO_2$ NPs Mesoporous maghemite NPs	DOX	Combined DOX/magnetic/PTT therapy significantly inhibited growth and metastasis of breast cancer to lung while reduced cardiotoxicity.	[127, 128]
$GO@Fe_3O_4$ Nanocomposites	DOX	Increased cytotoxic efficacy to glioma cells.	[129]
Graphene nanosponge-supported lipid bilayer	DTX PFH	LF conjugation increased the tumor accumulation and penetration of NPs by increasing its bilayer fluidity.	[130]
Silver nanoparticles (AgNPs)	–	Enhanced antibacterial and antibiofilm properties and reduced toxicity.	[132, 133]
CdTe QDs	CXB HNK	The theranostic LF-QD nanocapsules enabled fluorescence imaging of breast cancer cells after their uptake with enhanced cytotoxicity.	[134]
Mesoporous Silica NPs	PMT ELA	The NPs exhibited high internalization and synergistic killing of breast cancer cells.	[135, 136]
Gold quantum clusters	–	LF hybridization successfully stabilized the gold nanoclusters in wide pH range.	[137, 138]

Cisplatin: CDDP; Doxorubicin: DOX; Docetaxel: DTX; Perfluorohexane: PFH; Celecoxib: CXB; Honokiol: HNK; Pemetrexed: PMT; Ellagic acid: ELA.

Lf-modified nanocarriers to brain through the brain capillary endothelial cells. The NPs may bind to endothelial cells followed by their transport into the tumor through vesicles and transcellular channels. Therefore, this mechanism can further strengthen the concept of Lf-mediated transcytosis, and its role in enhancing penetration into deep tumor tissues. Lf-targeted huperezine A-loaded nanoemulsion has shown higher accumulation in hCMEC/D3 brain cells via transcytosis compared with untargeted nanoemulsion [16]. Furthermore, Kumari et al. has confirmed that Lf NPs accumulated in brain tissue and delivered high temozolamide concentrations to tumor through transcytosis across BBB reaching the brain tumor site [96].

### 7.1.1. Brain tumors

Lf-conjugated PEG-PCL polymersomes (POS), with around 40 Lf molecules per POS, were co-loaded with DOX and Tetradrine (Tet) (Table 5). Although particles had 220 nm diameter which increases the mononuclear phagocytic system (MPS) clearance, the full PEGylation protected it and increased their circulation time [148]. Notably, Lf modification increased the concentration of POS more in right hemisphere compared to the un-modified ones, while Tet, as MDR inhibitor, enhanced their cellular uptake by decreasing cellular resistance thus resulting in the smallest tumor volume and longest survival time. In another investigation, Lf-modified procationic liposomes (PCLs) loaded with DOX, showed longest survival time on Wistar male rats inoculated with C6 glioma cells compared with control group. Lf-conjugation increases cellular uptake into glioma C6 cells; while PCLs uptake occur via adsorption-mediated endocytosis solely, Lf-PCLs uptake occur via receptor- and adsorption-mediated endocytosis [149]. To further enhance the penetration of Lf-modified nanocarriers, tLyP-1, a tumor-homing peptide, was co-administered with Lf-modified paclitaxel (PTX)-loaded polyethylene glycol-poly(lactic acid) (PEG-PLA) NPs. tLyP-1 enhanced the tissue penetration of NPs via the neuropilin-1-dependent (NRP-1) internalization pathway, especially because NRP-1 receptors are specifically expressed on endothelial cells of tumor blood vessels [150]. While Lf modification improved cellular uptake of the NPs relative to unmodified NPs.

In addition to drug delivery, the cationic nature of Lf enabled both high binding capacity of **nucleic acids** as well as endosomolytic activity mediated by proton sponge effect that contributed in escape of Lf NPs from endolysosomal compartment into the cytoplasm where siRNA can bind with RNA-induced silencing (RISC) complex. As an efficient combination therapy for glioblastoma multiforme (GBM) was enabled by

development of Aurora Kinase B (AKB) siRNA-loaded Lf NPs, to enhance BBB crossing, co-administered with TMZ treatment [6]. AKB was found to be overexpressed in malignant glioma where it induces degradation of the tumor suppressor gene p53 thus triggering tumor growth. As a result, the combined TMZ treatment and AKB silencing has significantly improved the survival of treated mice from 14 to 33 days.

Lf could be also used to enhance brain accumulation of nanoparticles through **intranasal route** based on the high expression of LfR on the nasal epithelial cells and olfactory linings. Both Lf and hyaluronate were coupled to the surface of acid-responsive lenalidomide-conjugated FePt alloy nanoparticles. While hyaluronic acid enhanced brain tumor targeting by its CD44 binding ability, Lf facilitated the olfactory uptake through enhanced mucosal and nasal penetration, which led to brain accumulation of the nanoconjugates. Also, LfR are overexpressed on the surface of glioma cells, thus increasing their specific uptake by cancer cells. In addition to this direct intranasal transport, Lf-modified nanoconjugates absorbed into blood circulation will most likely target brain delivery since LfR are overexpressed on the surface of brain endothelium [151]. The acidic microenvironment of lysosome resulted in cleavage of the pH sensitive hydrazone bond between drug and NPs to trigger the drug release. The NPs efficiently generated reactive oxygen species (ROS) due to release of Fe and Pt which increased its cytotoxicity against U87MG cells.

### 7.1.2. Parkinson disease (PD)

The Lf receptors are found to be upregulated by neurons involved in the pathophysiology of Parkinson and Alzheimer's diseases [152,153]. Both diseases are characterized by iron overload in specific areas in the brain. Since Lf plays an important role in iron metabolism, its therapeutic effect in Parkinson Disease (PD) and Alzheimer has been studied as metal chelator [154]. In case of PD, Lf is overexpressed in activated microglia where it plays an important neuroprotective role. This was evident for both apo- (iron-free) and holo- (iron-saturated) Lf. The suggested Lf neuroprotective mechanisms could be mediated through the increase of the mitochondrial transmembrane potential, indicating better mitochondrial activity [155]. Another hypothesis for the neuroprotective activity of Lf is iron-dependent, where Lf suppressed transferrin receptors and divalent metal transporter, leading to enhanced iron internalization [156]. Further, Lf is associated with upregulation of brain-derived neurotrophic factor (BDNF), in addition to activation of the pathway of regulated protein kinases-mitogen activated protein kinase (ERK/MAPK). Interestingly, Lf protects dopaminergic neurons in

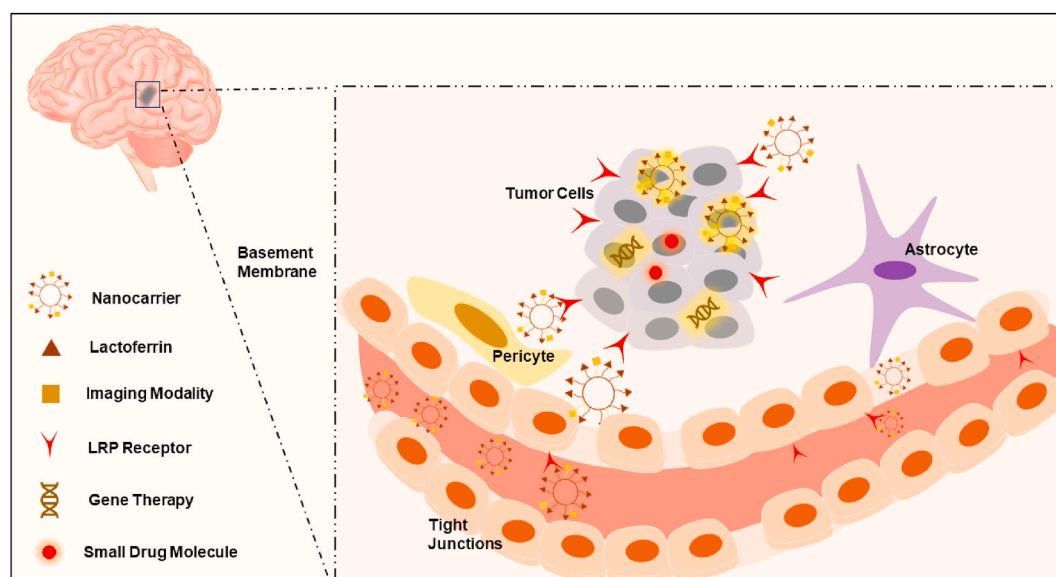


Fig. 6. Schematic illustration of the brain targeting mechanism of Lf.

**Table 5**

Representative examples of Lf-modified nanocarriers for brain targeted drug delivery.

Delivery system	Cargo	Lf surface modification	Model of study	Disease	Outcomes	Ref.
Lf-PEG-PAMAM dendrimer	hGDNF	Maleimide thiol coupling	Rotenone induced PD rats	Parkinson's disease	4-fold higher enhanced expression of reporter genes in the brain.	[161]
Lf-PDNCs SPIO NPs	CUR	Carbodiimide coupling	RG2 cells bearing rats	Orthotopic brain tumor	30% prolonged animal survival. Self-responsive fluorescence & MRI.	[170]
Lf/FA-PLGA NPs	ETP	Carbodiimide coupling	HBMECs & U87MG cells	Glioblastoma	two-fold increased permeability coefficient across the BBB.	[171]
Lf-SLNs	DTX	Carbodiimide coupling	U-87 MG cells & mice	Glioblastoma	enhanced cytotoxicity of DTX with lower IC50 values.	[139]
Lf-TMX -SLNs	CRM	Carbodiimide coupling	U87MG cells and	Glioblastoma multiforme	10 times increase in BBB permeability coefficient.	[172]
Lf-PEG-BSA NPs	DOX	Electrostatic complexation	BCECs, C6 glioma cells & SD rats	Glioma	Strongest cytotoxicity and highest uptake both in BCECs and C6 cells.	[173]
Lf-MPNA nanogels	Fe <sub>3</sub> O <sub>4</sub> NPs	Carbodiimide coupling	C6 cells, NIH/3T3 cells & rats	Glioma diagnosis	Novel specific MRI contrast agent for glioma diagnosis in vivo.	[174]
Lf-modified liposomes	Senktide	Maleimide thiol coupling	Male SD rats & HBMECs	Schizophrenia	Significant increase of dialysate dopamine in nucleus accumbens shell.	[175]
LF-PAMAM dendrimer	hGDNF	Maleimide thiol coupling	BCECs, Male 6-OHDA rat model	Parkinson's disease	Enhanced locomotor activity, lowered dopaminergic neuronal loss and increased monoamine levels.	[176]
Lf-PEG-PLGA & PEG-PLGA NPs	Urocortin	Maleimide thiol coupling	bEnd.3 cells, 6-OHDA rat	Parkinson's disease	The uptake was 2.5-fold higher and caused a transient inflammation in liver, kidney, and spleen.	[177]
Lf-PEG-PCL & PEG-PCL NPs	NAP peptide	Maleimide thiol coupling	16HBE140-cells, Male ICR mice	Alzheimer disease	The intranasal administration lead to around 1.5-fold increase of uptake to the brain.	[178]
Lf-PEG-PLA & PEG-PLA NPs	PTX	Maleimide thiol coupling	BCECs & C6 cells	Glioblastoma	Enhanced cancer targeting, vascular extravasation & deeper penetration.	[150]
Lf-PEG-PCL & PEG-PCL Polymersomes	DOX & TET	carbodiimide coupling	C6 Cells, & SD rats	Glioma	2.3-fold stronger cell inhibition with the lowest IC <sub>50</sub> . Addition of LF reduced spleen accumulation.	[148]
Lf-PEG-PLGA & PEG-PLGA Polymersomes	S14G-humanin	Maleimide thiol coupling	Male Kunming mice	Brain diseases	Better brain uptake Vs Tf or BSA & lower leakage during circulation due to lower proton permeability.	[168, 169]
Lf-CHETA/PC procationic liposomes	Coumarin-6	Electrostatic complexation	Co-culture of BCECs & astrocytes	Brain diseases	Lf lip. showed receptor & absorption mediated endocytosis, with enhanced activity & lower cytotoxicity.	[179]

Polyamidoamine: PAMAM; Sprague Dawley: SD; Polydiacetylene: PDNCs; Curcumin: CUR; Poly (lactide-co-glycolide): PLGA; Etoposide: ETP; Human brain-microvascular endothelial cells: HBMECs; Solid lipid NPs: SLNs; Docetaxel: DTX; Tamoxifen: TMX; Carmustine: CRM; Doxorubicin: DOX; 6-hydroxydopamine: 6-OHDA; Polycaprolactone: PCL; Human bronchial epithelial cells: 16HBE140-cells; Brain capillary endothelial cells: BCECs; Phosphatidylcholine: PC; Tetrandrine: TET; Paclitaxel: PTX.

the nigrostriatal area by decreasing levels of  $\alpha$ -synuclein through upregulation of hypoxia-inducible factor 1 $\alpha$  [157].

In addition to its intrinsic activity, Lf and borneol were used together to modify the surface of dopamine-loaded nanoparticles (Lf-BNPs) for enhanced permeability and striatum-specificity for treatment of PD [158]. The NPs could alleviate the 6-hydroxydopamine-induced striatum lesion in rats by effective delivery of dopamine after intranasal administration. Similarly, dopaminergic SK-N-SH cells were protected against rotenone-induced neurotoxicity in dopaminergic neurons using Lf nanoparticles encapsulating curcumin prepared by sol/oil chemistry [159].

The use of genes such as glial cell line-derived neurotrophic factor (GDNF) encoding gene showed a great promise in PD therapy due to the stimulatory effect of GDNF on dopaminergic neurons [160]. In order to achieve successful brain delivery, hGDNF was encapsulated in Lf-functionalized PAMAM nanoparticles. Lf-modified NPs showed the highest GDNF expression compared to saline and Tf-modified nanoparticles. Compared to viral vectors, higher expression of hGDNF was achieved by continuous administration of Lf-modified NPs in chronic rotenone-induced model. This extended administration enhanced locomotor activity, decreased loss of dopaminergic neurons in addition to improved levels of monoamine neurotransmitters in PD rats [161].

### 7.1.3. Alzheimer

Increased iron in Alzheimer disease is associated with oxidative stress, reactive oxygen species and nitric oxide synthase production. Lf has an anti-oxidative effect as it acts as iron chelator in the brain to restore iron hemostasis. It also has anti-inflammatory activity, leading to decreased levels of TNF- $\alpha$  and IL-6 [162]. These results were further confirmed in a three-month clinical trial, with decreased serum amyloid

$\beta$ , p-tau, and MAPK1 [163]. Wang et al. found that the intranasal administration of Lf led to a reduction in  $\beta$ -amyloid deposition through activation of  $\alpha$ -secretase which increased the metabolism of amyloid precursor protein. This led to amelioration in cognitive function and learning ability in treated animals [164]. Recently, Bartolome et al. found that salivary Lf could be a promising biomarker for non-invasive early detection of Alzheimer's disease, as it was shown to have specifically lower salivary levels [165].

Lf-polyamidoamine dendrimeric nanoparticles (PAMAM-Lf) were designed for the efficient delivery of rivastigmine (RIV) to Alzheimer's model. Administration of Lf-PAMAM NPs in Alzheimer's animal model enhanced the brain bio-availability of RIV and increased AChE activity resulting in higher Ach level and improved memory deficit than unmodified dendrimers [166]. Application of the hydrophilic peptide, neuron growth factor (NGF), for management of Alzheimer's disease is a feasible strategy. However, delivering therapeutic peptides to the brain faces many challenges such as degradation in serum and failure to bypass BBB. To deliver NGF across BBB, Lf-decorated liposomes were developed. The NGF Permeability across HBMECs/HAS monolayer showed higher penetration for Lf/NGF liposomes compared to non-targeted liposomes and free NGF [167]. In another hand, the viability of A $\beta$ -insulted SK-N-MC cells was increased upon incubation with Lf/NGF-liposomes. Similarly, encapsulation of another neuro-protective peptide, S14G-humanin, into Lf-modified polymersomes inhibited the overexpression of caspase-3 and Bax and enhanced cholinesterase activity. As a result, they efficiently protected the hippocampus of rats against learning and memory deficits triggered by using amyloid- $\beta$ 25-35 [168,169].



## 7.2. Colon cancer targeting

Lf was proposed as a safe alternative with powerful antitumor activity specifically against colon cancer. First, the anti-inflammatory effect of Lf on colon cancer was widely reported in literature. In Lf knockout mice, NF- $\kappa$ B was upregulated resulting in an aggravated inflammatory response as evidenced by the increased levels of the nuclear p65 protein expression, p65<sup>+</sup> cell numbers, and IKK $\alpha$ / $\beta$ . Furthermore, the pro-inflammatory cytokines (IL-1 $\beta$ , IL-6, TNF- $\alpha$ ) were found to be upregulated, which can cause AKT and mTOR deregulation and subsequent tumor progression [180]. Lf may also induce apoptosis in colon cancer cells by several pathways including induction of caspase 3/7, activation of p53 tumor suppressor gene, and enhancing expression of the pro-apoptotic genes; TP5313, PMAIP-1, and SFN thereby promoting subsequent cell death in HT-29 cells [57].

Ingestion of Lf was correlated with an elevation in the activity of NK cells, and increases in CD16<sup>+</sup>/CD56<sup>+</sup> subset of NK cells in the blood, which was consistent with regression of colorectal polyps. bLf was concluded not to induce activation/inhibition of immune system but rather increase the responsiveness of the immune system [181,182]. In addition to its anti-inflammatory and immunomodulatory effects, bLf was shown to have antioxidant effect by increasing the transcription of antioxidant related genes: *GCLC* and *GCLM*, involved in glutathione synthesis and scavenging of reactive oxygen species (ROS) [57]. Selenium-saturated bovine Lf (Se-bLf) showed a promising anti-oxidative property in HT-29 cells treated with 250  $\mu$ M of H<sub>2</sub>O<sub>2</sub>, by increasing the activity of the enzymes glutathione peroxidase, glutathione s-transferase and glutathione reductase showing a protective effect against cancer development [183].

Nano-formulations of bLf were found to confer a promising efficacy against colon cancer; owing to its both colon targeting and antitumor effects. Lf can target cells colon cancer cells and may internalize itself utilizing these receptors regulated by intestinal epithelial cells [57]. Liposomal bovine Lf was able to inhibit the expression of TNF- $\alpha$  mRNA expression in colorectal RKO and RCN-9 cells resulting in a lower inflammation, as demonstrated by reduced numbers of neutrophils associated with suppression of colorectal polyps [184]. In a study by Kanwar et al., alginate coated, chitosan conjugated, calcium phosphate, Fe saturated bLf nanocapsules (AEC-CCo-CP-Fe-bLf NCs) with a size of 396.1 nm were effective against triple positive cancer stem like Caco-2 cells [14]. These nanocarriers were able to localize at the tumor site by EPR effect and then internalize utilizing LRP1, transferrin and Lf receptors in addition to iron receptors: DMT1, ferroprotein, and ferritin receptors, which were believed to play a major role in the absorption of Fe-bLf NCs [185]. These NCs showed enhanced efficacy compared to Fe-bLf NCs; due to better efficient delivery of Lf by the coating polymers, chitosan and alginate. Additionally, treatment of Caco-2 bearing mice with the NPs has downregulated anti-apoptotic factors including Survivin and Bcl-2, while upregulated pro-apoptotic Bax, Fas, caspase-3 and caspase-9 [14]. Consequently, modification of the surface of AEC-CCo-CP-Fe-bLf nanocapsules with LNA (EpCAM and nucleolin)-aptamer enhanced tumor targeting via binding to the cell surface receptors; EpCAM and nucleolin and hence translocate into the nucleus [186]. The uptake of the targeted NCs into Caco-2 cells was enhanced by 2.84 folds through receptor mediated internalization. The mice treated with both non-targeted and targeted NCs showed a significant decrease in the tumor volume by 6.8 and 2.91 folds, respectively.

The nanocapsules were then modified by addition of zinc ferrite to a solution of apo-Lf in the presence of sodium bicarbonate to produce zinc ferrite saturated bovine Lf (Zn-Fe-bLf) which was then encapsulated in a similar way into alginate-coated chitosan nanogel. The antitumor activity of the Zn-Fe-bLf NCs 24 nm was enhanced as demonstrated by dramatic reduction in tumor volume in human xenograft colonic adenocarcinoma to 0.10 mm<sup>3</sup> compared to the vehicle NCs (52.28 mm<sup>3</sup>) and control group (93.51 mm<sup>3</sup>). Application of magnetic field and

photothermal laser after treatment with Zn-Fe-bLf NCs resulted in further tumor reduction. Moreover, the presence of Zn may improve CT scanning signal intensity of the NCs compared to Fe-bLf revealing efficient multimodule nanotheranostic properties [185].

Lf NPs could also be used as a carrier for chemotherapeutic drugs such as oxaliplatin and 5-Fluorouracil to enhance their targetability to colon cancer. The NPs exhibited enhanced cytotoxicity against COLO-205 cells as shown by lower IC<sub>50</sub> (1.08 and 0.98  $\mu$ g/ml for Lf-5FU and Lf-oxalo NPs, respectively) compared to free drug (IC<sub>50</sub> of = 2.27 and 2.22  $\mu$ g/ml for free 5FU and free oxaliplatin, respectively). The nano-formulations showed a 7-fold decrease in AFC (structural deformity which turns into colon adenocarcinoma) compared to a 3-fold decrease by the free drugs in azoxymethane induced AFC in Wistar rats [98].

## 7.3. Liver cancer targeting

Lf binds specifically to LRP and asialoglycoprotein receptors (ASGPR) that facilitate its internalization into hepatocellular carcinoma (HCC). Therefore, modification of PEGylated liposomes with Lf improved their uptake into ASGPR-positive cells including HepG2, BEL7402, and SMMC7721 but not in ASGPR-negative cells [187]. DOX-loaded Lf-PEG-liposomes exhibited higher anticancer efficacy in HepG2 bearing mice relative to free drug.

For combined HCC therapy, we have prepared Lf-coated oily core nanocapsules for synergistic delivery of sorafenib and quercetin [121]. The dual targeted lactobionic acid/Lf-NCs exhibited enhanced uptake into HepG2 cells and higher anti-tumor effect in HCC mice model compared to free drugs. For oral targeted HCC therapy, Lf-coated gliadin NPs co-encapsulating celecoxib and diosmin showed a synergistic anticancer action due to their common inhibitory effects on COX-2, NF- $\kappa$ B and TNF- $\alpha$  [188,189]. The high stability of Lf-GLNPs is probably due to surface coating of GL-NPs by Lf providing both hydrophilic surface and charge-based stabilization. In addition, the glycan chains of Lf may add steric stabilization mechanism. The Lf-coated NPs exhibited enhanced internalization and improved anti-tumor efficacy against HepG2 cells at 48 h and HCC-bearing mice. Lf-targeted gliadin NPs demonstrated a remarkable inhibition of NF- $\kappa$ B and TNF- $\alpha$  expression compared with the positive control.

## 7.4. Breast cancer targeting

After oral administration, the small size FebLf NCs (80 nm) induced apoptosis of claudin-low, triple-negative MDA-MB-231 breast cancer cells through mitochondrial depolarization, downregulation of the apoptosis inhibitory proteins; survivin, and livin as well as PI3K followed by activation of caspase-3 [18]. By virtue of their superparamagnetic properties, FebLf NCs can be considered as suitable cancer nanotheranostic agent for MRI contrast imaging and magnetic guided cancer therapy. In another investigation, Lf-coated DOX-loaded porous magnetite nanospheres (PMNSs) were developed for synergistic chemo-magnetic field photothermal therapy of breast cancer [190]. The injected Lf-DOX-PMNSs significantly into 4T1 bearing mice suppressed the proliferation of 4T1 cells and tumor weight by activating both the extrinsic pathway of apoptosis via upregulation of the TNF- $\alpha$  mRNA and enhancing the intrinsic Bax mRNA expression. The Lf coating layer not only enhanced the drug targeting to tumor site but also prolonged its circulation by forming protein corona that can evade clearance by RES and showed acid responsive drug release at tumor microenvironment.

In addition to its intrinsic anticancer effect, Lf was exploited as a hydrophilic shell of amphiphilic micelles co-encapsulating two water insoluble drugs rapamycin and wogonin within its hydrophobic core composed of the plant protein zein [118]. In addition to its active tumor targeting properties, the brush-like hydrophilic Lf corona increased the micellar stability, inhibited their opsonization and prolonged their systemic circulation leading to maximized accumulation at tumor site by the EPR effect. In a consequent study, oleic acid-coated Fe<sub>3</sub>O<sub>4</sub> NPs were



encapsulated together with dasatinib in the micellar hydrophobic zein core [119]. Attributed to their superparamagnetic characteristics, the micelles showed enhanced cytotoxicity against MDA-MB-231 cells upon application of external magnetic field. In another approach, Lf was electrostatically anchored onto the surface of zein nanospheres co-loaded were the hydrophobic aromatase inhibitor exemestane and the herbal flavonoid luteolin [191]. Lf-modified NPs enhanced their targeting to breast cancer cells resulting in improved cytotoxic effect against MCF-7 and 4T1 breast cancer cells with 2.5-fold higher selectivity index SI to cancer cells rather than normal cells compared to the free drugs.

Another interesting application of holo-Lf is its ability to relief of hypoxia in TME of solid tumors. Hypoxia is known to reduce the efficacy of radiotherapy by weakening the radiation-induced cell DNA damage. The presence of Fe in the structure of holo-Lf can induce decomposition of  $H_2O_2$  to oxygen thus alleviating the hypoxic TME. Through its oxygen generation capacity, Lf-PEGylated DOX-loaded liposomes showed synergistic anticancer effect and increased survival rate of mice when combined with 4 Gy X-ray radiation in breast cancer bearing mice which could be confirmed by photoacoustic imaging [78]. Lf NPs were also used to enhance the efficacy of breast cancer photodynamic therapy by encapsulation of photosensitizer (PS) Chlorine e6 (Ce6). The NPs inhibited the aggregation of the hydrophobic Ce6 in aqueous media thus improving its efficacy to generate ROS [192]. Under light irradiation, the NPs triggered a remarkable cell death in SK-OV-3 and MDA-MD 231 cells 4 folds higher than that of free Ce6.

### 7.5. Lung cancer targeting

Lf receptors were found to be upregulated on the bronchial epithelial cells therefore, Lf-modified lipid nanocarriers were used for the targeted delivery of PTX to lung cancer therapy [193]. Lf-targeted lipid NPs showed enhanced cytotoxicity against BEAS-2B human bronchial epithelial cells, relative to non-targeted NPs and free PTX. After intravenous administration into rats, the Lf-NPs showed higher amounts of drug accumulated in lung tissue relative to non-targeted NPs.

Beside the use of Lf-targeted nanocarriers for systemic therapy of lung cancer, the inhalable Lf-targeted nanocomposites have emerged as a promising alternative to avoid the systemic toxicity and enhance deep

lung deposition [194]. For this purpose, different Lf-targeted NPs were prepared for synergistic lung cancer treatment and then transformed into inhalable nanocomposites via spray-drying with suitable pulmonary inert carriers. Examples of those nanocarriers include; (i) HA/Lf layer-by-layer coated lipid nanoparticles co-encapsulating rapamycin--phospholipid complex and berberine-sodium lauryl sulfate hydrophobic ion pair [195], (ii) Lf-chondroitin electrostatic nanocomplex co-loaded with DOX hydrochloride and ellagic acid nanocrystal soluble form [110], and (iii) Lf/chondroitin layer-by-layer functionalized monoolein liquid crystalline NPs co-entrapping pemetrexed and resveratrol (Fig. 7) [196]. All those nanocarriers exhibited favorable physicochemical properties such as small size, improved drug release pattern, improved uptake and enhanced cytotoxic effect against A549 lung cancer cells. for deep lung deposition, those nanocarriers were mixed with drying aids such as mannitol, maltodextrin, leucine or their combinations prior to spray-drying to form inhalable nanocomposites. The inhalable powder demonstrated favorable aerosolization efficiency (MMAD of 2.68–3.28  $\mu m$  and FPF of 55.5–89.58% %) revealing efficient particle deposition into deep lung tissues. After reaching lung tissues, the carriers dissolved releasing the nanoparticles followed by internalization into lung cancer cells by virtue of their Lf, HA, or chondroitin-based receptor mediated endocytosis. In lung cancer bearing mice, all the prepared inhalable nanocomposites displayed powerful anti-cancer efficacy by reducing the lung weight, decreasing the number and diameters of lung adenomatous foci, downregulating the level of proliferative and angiogenic markers and increasing the apoptotic markers compared to intravenously administered nanocarriers.

### 7.6. Prostate cancer targeting

Lf demonstrated direct cytotoxic action against highly metastatic PC-3 prostate cancer cells via inhibition of V-ATPase and subsequent reduction of the ability of those cells to acidify the TME. Moreover, Lf induced phenotypic changes of DU-145 and LNCaP reducing their invasive properties. Lf also downregulated the expression of steroid hormone receptors (e.g. estrogen receptor  $ER\alpha$  and, progesterone receptor PR) and increased the expression of oncosuppressive miRNAs (e.g. miR-133a and miR-200b) in DU-145 cells [197].

As a targeting ligand for prostate cancer cells, Lf modification of

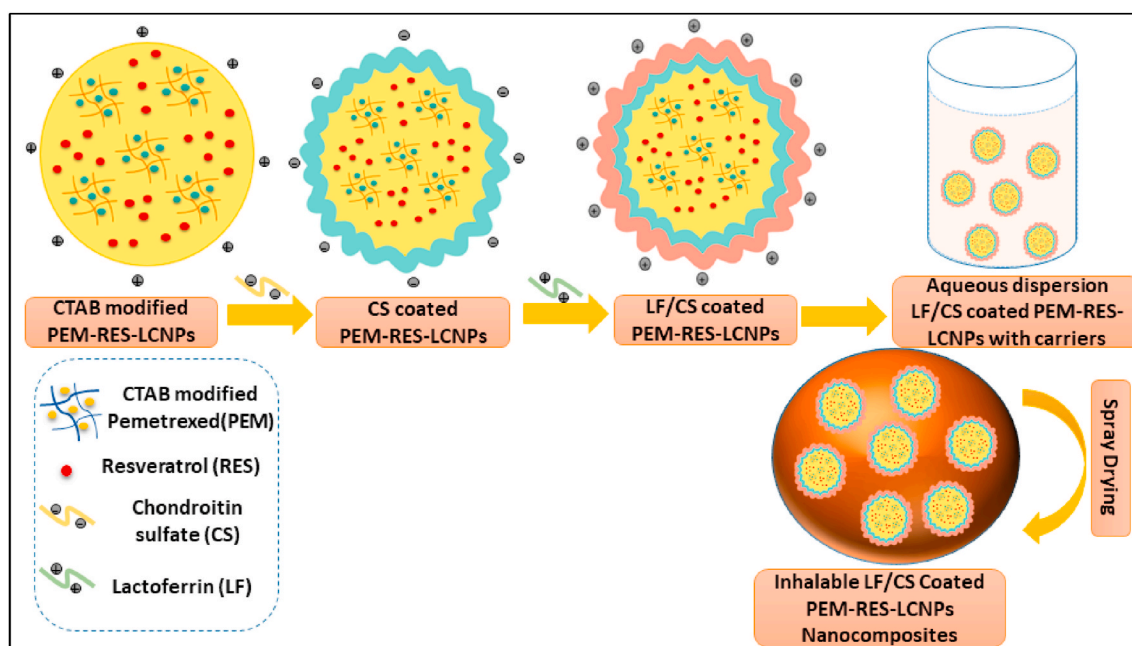


Fig. 7. Schematic diagram illustrating the formation of inhalable PEM/RES-loaded liquid crystalline monoolein NPs for lung cancer targeting [196].

diaminobutyric polypropylenimine dendriplexes enhanced the delivery and transfection of the encapsulated plasmid DNA encoding TNF $\alpha$ , TRAIL or IL-12 to prostate cancer cells after intravenous administration [198]. The Lf-targeted dendriplexes resulted in much stronger suppression of PC-3 and DU145 tumors in comparison with Tf-modified dendriplexes. Conjugates of DOX to iron saturated Lf (Fe-bLf-DOX) showed higher cytotoxicity against DU145 prostate cancer cells and lower toxicity against non-cancerous RWPE-1 cells compared to iron free Apo-bLf-DOX and free DOX [77]. Besides it increases uptake into cancer cells via interaction with additional receptors, the iron acts as an essential effector of DOX induced cytotoxicity. As a result, Fe-bLf-DOX exhibited superior efficacy in decreasing Bcl-2 expression levels associated with elevated PTEN expression. After internalization into the endo-lysosome, DOX was released upon cleavage of the covalent amide bond between drug and the bLf protein by the hydrolytic enzymes and the acidic environment thus resulting in increased nuclear accumulation of DOX. Therefore, the Lf-DOX conjugate could be considered as DOX prodrug while including a functional carrier bLf with cytotoxic nature thus causing decrease in the LC<sub>50</sub> of DOX by more than 4 folds. Another interesting property of Lf conjugate is inhibiting the efficacy of membrane efflux pumps in efflux DOX out of cells resulting in higher retention of drug in the prostate cancer cells [77]. Thus, bLf-DOX conjugate induced both down-regulation of P-gp as well as the bypass of P-gp [77].

### 7.7. Cancer theranostics

Modification of the surface of curcumin-loaded magnetic polydiacetylene nanocarriers (PDNCs) with Lf significantly improved their brain accumulation by enhancing BBB penetration resulting in powerful suppression of orthotopic brain tumor and increasing the animal survival by about 30%. At the same time, the NPs ability to exhibit both self-responsive fluorescence and MRI contrast imaging upon cellular internalization enabled cell trafficking and imaging-assisted cancer therapy. Thus, the Lf-targeted magnetic PDNCs can be promising theranostic application for targeting gliomas [170].

Another promising imaging probe for cancer, highly fluorescent CdTe quantum dots (QDs) were conjugated to Lf-targeted nanocapsules. The oily core of nanocapsules co-solubilizing celecoxib and honokiol was electrostatically coated with anionic chondroitin sulfate layer followed by a cationic Lf-QDs conjugate corona [199]. The covalent bond formed between Lf and QDs prohibited the systemic release of Cd into circulation and guarantee the site-specific release of QDs only at tumor sites. The QDs luminescence was quenched *in vitro* upon conjugation with Lf (OFF state) due to electron/energy transfer mechanism. Upon intracellular uptake into MCF-7 cells, luminescence was restored (ON state) due to detachment of surface-bound ligands from QDs in cytosolic environment confirm and monitor intracellular uptake of our nanoparticles that was confirmed using confocal microscopy. *In vivo*, tumor tissues of Lf-QDs-CS-NCs treated mice group showed the highest fluorescence intensity compared with liver and kidney that proved their effective localization in the tumor tissue.

Recently, Lf and RGD dimer dual-modified extremely small (13.4 nm) gadolinium oxide nanoparticles were prepared as highly efficient theranostics of GBM. The NPs successfully crossed the BBB due to its small diameter and Lf binding to its receptors then enter brain tumor cells by RGD2-integrin  $\alpha v \beta 3$  interaction, and thus can be used for MRI-guided radiosensitization of brain tumors [125]. The NPs exhibited high contrast MRI as indicated by extraordinary relaxivities thus showing much better signal enhancement for T1-weighted MRI of tumors than commercial Gd-chelates.

### 7.8. Nuclear targeting

One of the most interesting properties of Lf is its ability to reach the nucleus. On this regard, Lf has great potential for macromolecular delivery to cytoplasm and nucleus such as nucleic acids (siRNA, mRNA,

shRNA and DNA) and gene editing machinery (Cas9 and sgRNA). Furthermore, by virtue of its cationic charge, Lf can bind to RNA and DNA and activates transcription. It was reported early in 1992 that Lf can easily traffic to the nucleus of K562 cells in temperature-dependent manner [200]. In 5637 bladder carcinoma, U87MG, MCF7, NIH3T3 and HeLa cells, a pentapeptide enriched in basic amino acids (Gly-Arg-Arg-Arg-Arg), derived from the N-terminal portion of human Lf was internalized within 10 min into the nucleus and mainly nucleoli [201]. Nuclear localization of Lf was also observed in human THP-1 monocytic and bovine rectal epithelial cells [202,203].

In addition, a cell penetrating peptide derived from lactoferricin termed as L5a CPP (RRWQW) was shown to efficiently deliver DNA into the nucleus of human A549 lung cancer cells without induction of cytotoxic effect [204]. Compared to Tf, Lf was shown to be apically internalized into Caco-2 intestinal epithelial cells and then localized to the nuclei while Tf was internalized from the basolateral side and localized in the cytoplasm [205]. Nuclear trafficking of Lf was shown to be mediated by non-endocytic mechanism in some studies, which offers an easy way to escape from endosomes and late lysosomes for functional delivery of nucleic acids to cytoplasm and nucleus. More sophisticated investigations are required to fully understand the nuclear targeting mechanism of Lf and its nanoparticulate form in different cell lines to make the best use of Lf for wide therapeutic applications.

### 7.9. Immunomodulatory applications

Being a key component in the mammalian innate immune system, Lf plays an essential role in the host defense against pathogens and inflammation where its deficiency may precipitate infection recurrence [206]. The cationic nature of Lf contributes to its ability to bind to surface molecules found on immune cells, triggering signaling cascades leading to immune cells activation and maturation [207]. Bovine Lf exerts its immunostimulatory effect through its immunogenic forms which are formed by enzymatic digestion in the GIT [208]. Oral Lf is thought to send signals through receptors on the epithelium of the intestine and immune cells as macrophages and lymphocytes [22]. Moreover, the absorbed Lf can prime the immune system where an enhanced cytokine release was demonstrated including cytokines related to early (TNF- $\alpha$ , IL-6, IL-10) and adaptive (IL-12p40, IFN- $\gamma$ , IL-4) immunity. Overall, two possible explanations may account for the immunomodulatory effects of Lf: a) Immune cells express Lf receptors. Therefore, a receptor-mediated interaction between Lf and immune cells or indirect uptake of Lf by immune cells, results in the priming of immune system, b) Secondly, Lf may help educate the immune cells present in the GIT microenvironment. The immune cells will be transported via the lymphatic system to lymph nodes or spleen [209].

A study by Mulder et al. showed that oral supplementation of bLf in humans provided immunomodulatory effect through T-cell activation and anti-oxidant effect [210]. Moreover, Lf was shown to contribute to inflammatory response by granulocyte accumulation and activation, inducing phagocytosis and augmentation of natural killer cells activity (Fig. 8) [211,212]. Being an innate immunity component, the immuno-modulatory activity of Fe-bLf dramatically augmented the anti-tumor efficacy of Fe-bLf-DOX in prostate cancer bearing mice [77]. This was demonstrated as reduced serum levels of the tumor promoting cytokines IL-5, IL-6 and IL-17 and elevated levels of IFN $\gamma$  and TNF $\alpha$  as well as GM-CSF, CCL17 and CCL4 responsible for triggering intra-tumoral infiltration of cytotoxic T cells and macrophages.

Lf nanocarriers were also used for remodeling of the immunosuppressive tumor microenvironment. The surface of Lf nanoparticles was modified with TPGS-coupled TAT cell penetrating peptide to enhance the BBB penetration of simvastatin and fenretinide drug combination. Interaction of Lf with LRP-1 receptors expressed by brain capillary endothelial cells (BCEC) and U87 glioma cells enhanced BBB permeation while TAT peptide increased the intracranial tumor penetration by 1.5 folds higher than that of un-modified Lf nanoparticles [101].

Simvastatin was reported to remodel TME and functional plasticity of TAMs whereas fenretinide induces ROS production and also can reverse the pro-tumoral M2-macrophages to the anti-tumoral M1 TAMs and reduce angiogenesis. The nanoparticles showed powerful synergistic cytotoxic effect against glioma cells in vitro and inhibited the tumor growth in vivo. Mechanistically, the dual drug loaded NPs succeeded to remodel since they effectively repolarized M2-TAM to M1-TAM as demonstrated by downregulating CD206 (TAM2 biomarker) and increasing the expression of iNOS and STAT1 (TAM1 biomarkers). The nanoparticles also improved the infiltration of cytotoxic NK cells into the tumor as revealed by overexpression of the NK cell marker Nkp44. Moreover, it increased ROS production which in turn induced mitochondrial apoptosis.

Another example of application of Lf NPs in TME immune-reprogramming includes the use of mannoseylated Lf nanoparticles for combined delivery of shikonin and JQ1 for both metabolic and of TME [102]. The nanoparticles targeted mannose and LRP-1 receptors over-expressed by TAMs and cancer cells, respectively. The dual drug loaded nanoparticles could remodel the TME via different pathways. First, the NPs elicited antitumor immunity mediated by SHK ability to induce immunogenic cell death. As a result, the nanoparticles enhanced maturation of dendritic cells and hence increased the amount of tumor infiltrating CD8<sup>+</sup> T cells [102]. Moreover, the SHK-loaded NPs suppressed cancer glucose metabolism through inhibition of pyruvate kinase M2 resulting in reduced lactate production and hence repolarizing M2-TAMs. On the other hand, JQ1 can decrease PD-L1 expression on cancer cells and downregulate Foxp3 and CTLA-4 in the tumor-infiltrating regulatory T cells (Tregs) so the NPs dramatically reduced the percentage of the intratumor infiltrating Tregs.

#### 7.10. Antiviral drug delivery

The anti-HIV drug Indinavir (IDV) suffers from poor entry into brain due to efflux by the P-glycoprotein expressed in BBB. Chemical coupling of Lf to the surface of indinavir-loaded nanoemulsion (Lf-IDV-NEs) has enhanced its BBB penetration and increased its residence time in brain [213]. As a result, after administration into rat model, Lf-coupled nanoemulsion remarkably increased the brain concentration of IDV compared to free drug. Encapsulation of the antiretroviral drug

Zidovudine (AZT) into Lf NPs for oral delivery resulted in improved pharmacokinetics (4 fold increase in AUC and 2-fold increase in Tmax and  $t_{1/2}$ ), higher efficacy and 2-fold lower organs related toxicities compared to free drug while keeping the antiviral activity unaltered [214].

Lf nanoparticles co-encapsulating the anti-HIV-1 drug Efavirenz and the anti-microbial drug curcumin (ECNPs) were used as a vaginal microbicide for multipurpose prevention technologies (MPT) [215]. After topical application in rats, the NPs could deliver higher drug amounts in vaginal lavage while showed significantly lower drug absorption in vaginal tissue and plasma relative to its free form. An anti-retroviral drug combination (zidovudine, efavirenz and lamivudine) was encapsulated into Lf NPs to improve their absorption and hence increase their anti-HIV efficacy [216]. The NPs showed pH-dependent drug release behavior with very low initial burst effect while most of the entrapped drugs were released at pH 5 with minimal toxicity to the erythrocytes and less tissue-related inflammation.

#### 7.11. Bone engineering

Lf exhibits favorable modulatory effects on bone cells and enhances bone growth thus it can be used as a bone growth factor for bone regeneration and bone engineering. Addition of Recombinant human Lf (rhLf) to the culture media of NHOst human osteoblast cells resulted in increased level of alkaline phosphatase (ALP), a marker for osteogenic activity, and enhanced ERK1/2 activation, which is a part of proliferative signaling. Treatment of piglet with rhLf has increased the serum calcium and bone mineral density compared to control piglets [217].

Treatment of MC3T3 osteoblast precursor cells with rhLf for 24 h resulted in increase in the anti-apoptotic Wnt5a together with an increase in Akt phosphorylation, while down-regulated caspase 3, which is a marker of cell apoptosis. Therefore, tyramine-coupled rhLf was enzymatically cross-linked using horseradish peroxidase and hydrogen peroxide into injectable hydrogel for encapsulation of MC3T3 cells. A remarkable increased expression of ERK (a proliferation marker) and RunX2 (a differentiation marker) was observed in the encapsulated MC3T3 cells. The cells maintained their differentiation ability as revealed by expression of collagen I protein, and osteocalcin after 21 days post culture in mineralization media [218,219]. A number of

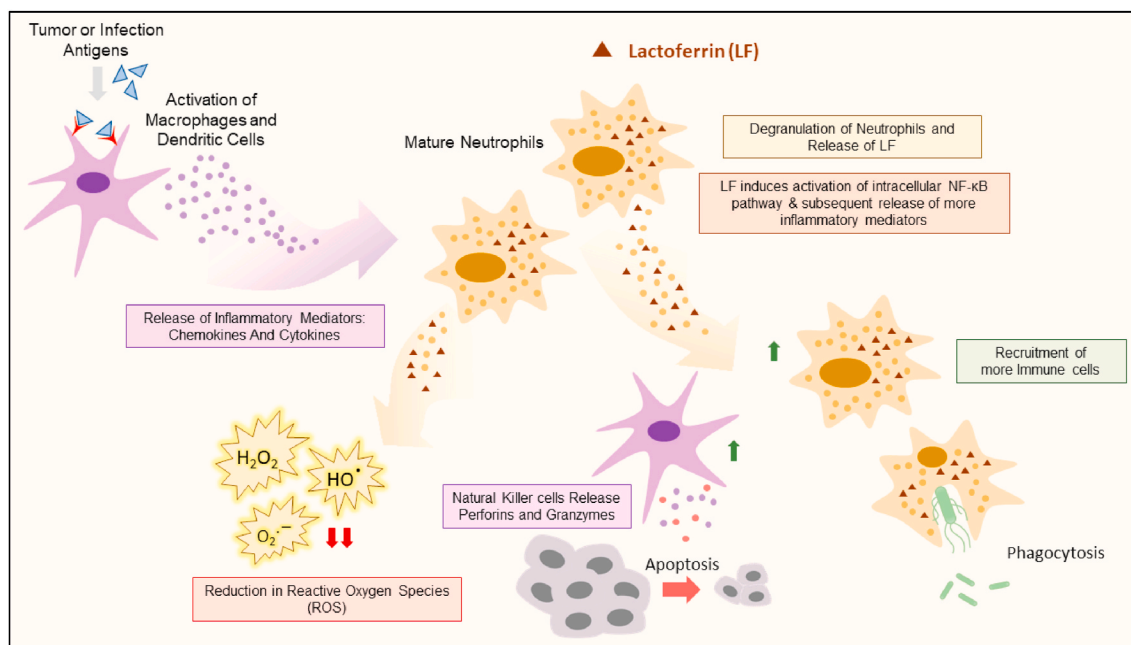


**Fig. 8.** Immuno-modulatory mechanisms of Lf. Lf triggers differentiation, maturation and activation of immune cells through NF-κB pathway, leading to enhanced activity of immune cells; NK and PMN cells.

studies suggested that Lf-induced osteogenic activity and proliferation of osteoblasts may be mediated by binding with TGF- $\beta$  receptors and stimulating TGF- $\beta$  canonical pathways, or by activation of MAPK pathways [220].

Due to its antiapoptotic effect on osteoblasts and suppression of osteoclastogenesis, Lf can be considered as anabolic factor for anti-osteoporotic therapy [221]. Different studies found that hydroxyapatite nanocrystals (HA) and Lf had a synergistic effect on bone homeostasis. To increase its bioavailability and prolong its action, Lf was electrostatically adsorbed onto HA nanocrystals forming a single protein layer well exposed to cells. Lf/HA combination resulted in several beneficial effects [222]. This includes enhancing the expression of RUNX2 mRNA, Osterix and IBSP, common markers of osteoblast differentiation confirming a synergistic effect on osteogenic differentiation and formation of bone matrix. Moreover, Lf reduced the apoptotic effect of HA on osteoblasts, suppressed the stimulatory effect of HA on osteoclasts and stimulated osteoblasts to produce osteoprotegerin (OPG) that reduce the activity of osteoclasts [86].

## 8. Challenges and limitations

Despite the promising role of Lf as a drug nanocarrier and tumor-targeting ligand with anti-cancer and immunomodulatory functions, some challenges have to be overcome prior to clinical translation. First, the cationic nature of Lf can cause toxicity and adverse inflammatory response [223]. Positively charged NPs are known to suffer from higher non-specific uptake and rapid clearance from blood by macrophages of liver, spleen and lung compared to anionic and neutral particles [224]. Mitochondrial damage and cell necrosis were observed after injection of cationic liposomes or chitosan NPs mostly mediated by inhibition of the cation-binding site of Na<sup>+</sup>/K<sup>+</sup>-ATPase [225]. Moreover, high expression levels of the inflammatory cytokines e.g. IL6, CXCL2 and CCL2 were detected in lung, spleen and liver of rats after administration of cationic micelles and liposomes [223]. We anticipate that the effect of positive charge of Lf macromolecules can be alleviated via its electrostatic complexation with polyanionic polysaccharides to form nanocomplexes with negative or low positive charge according to the complexation ratio. Another approach might involve the formation of multi-stage nanocarriers via encapsulation of the cationic Lf NPs within negatively charged or PEGylated phospholipid bilayers. This approach avoids the toxicity of the released cationic Lf NPs into circulation while makes use of their positive charge in enhancing their uptake into cancer cells via charge-mediated transcytosis. The positive charge of Lf can also be beneficial for endosomal escape particularly for gene delivery.

Second, the short half-life of Lf after systemic administration due to the action of proteolytic enzymes and its oral susceptibility after oral intake may lead to inadequate delivery. Many effective strategies have been successfully implemented to prolong its half-life and increase its oral stability including PEGylation, encapsulation or chemical cross-linking [90,226]. Finally, although the reported safety and biocompatibility of Lf, the use of bovine Lf might induce possible immunogenicity with undesired reactions. Antibodies against bovine Lf have been detected in the serum of mice treated with Lf-coated nanocapsules [134]. Therefore, the use of recombinant Lf can overcome this limitation (discussed below).

## 9. Clinical trials & future perspectives

Bovine Lf (bLf), is commercially available and well tolerated form of Lf with similar biological functions to human Lf but with lower cost. Based on the results of several toxicological studies on bovine milk derived Lf (cMDLf), including an acute, a 4 week, a 13-week, and two chronic oral toxicity studies in rats, as well as hypersensitivity, allergenicity and mutagenicity studies, it can be concluded that cMDLf does not produce adverse effects, not mutagenic and unlikely to be a clinically relevant allergen or the primary causative agent of any immunologically

driven hypersensitivity consumption. bLf is recognized by the US Food and Drug Administration and the European Food Safety Authority as GRAS (generally recognized as safe) component for numerous indications [227–229]. Table S1 lists some of the Lf-based products available in the pharmaceutical market. Many studies and clinical trials have demonstrated the safety and tolerability of orally administered rhLf in treatment of non-small cell lung cancer and renal cell carcinoma [5,75]. We have summarized the most important outcomes of the clinical trials based on Lf products for various applications (Table S2).

Talactoferrin (TLf) is a recombinant human Lf which is intended for oral administration. Production of recombinant human Lf may proceed using different expression systems, including fungi, animals, plants and viruses. Nevertheless, recombinant human Lf, produced by *Aspergillus awamori*, has been directed toward therapeutic uses [230,231]. More prominently, TLf has shown to modulate the immunity in various pathological conditions. For instance, TLf was demonstrated to induce INF- $\gamma$  dependent activation of NK cells and CD8<sup>+</sup> cells in the gut associated lymphoid tissue (GALT), Peyer's patches as well as systemically. In addition, the subsequent effect was further extended towards inhibition of neu<sup>+</sup> tumors [232]. Moreover, TLf showed a comparable antitumor effect to human Lf and bovine Lf in colon and liver cancer cells, through induction of apoptosis, chemokine C-C motif ligand 20 (CCL20) secretion and TGF- $\beta$ 1 expression [233]. Furthermore, it was shown that topically, TLf enhanced the release of key inflammatory mediators, such as IL-8, IL-6, TNF- $\alpha$  and macrophage inflammatory protein-1 alpha, which are responsible for tissue repair, and subsequently wound healing [81].

In addition to recombinant human Lf, a lot of research is directed to Lf-derived peptides. The peptides Lf (1–11), Lactoferricin (17–41) and Lactoferrampin (268–284), are the three major peptides derived from Lf showing pharmacological actions: antibacterial, antiviral, antiparasitic, antifungal and anticarcinogenic activities. It worth noting that Lactoferricin B, corresponding to residues 17–41 of bLf, was reported to exert more potent antimicrobial activity than Lf [234]. Table S3 elucidates biological functions of Lf peptides. Being chemically modified, LTX-315 is a 9-mer cationic peptide derived from bovine Lf and possess an anti-tumor activity, especially against solid tumors [235,236]. The mechanism of oncolytic property resides in the activation of local anti-tumor immunity, alone or combined with chemotherapeutic agents. In this regard, LTX-315 was shown to promote the infiltration of CD4<sup>+</sup> and CD8<sup>+</sup> cells to the tumor sites, in addition to a reduction in myeloid derived-suppressor cells (MDSC) and CD4<sup>+</sup> regulatory T cells. The modulation of the tumor micro-environment exhibited by LTX-315 paved the way to a more pronounced anti-tumor activity when combined with DOX [236]. Furthermore, it was demonstrated that mitochondrial permeabilization through Bcl-2 family protein dependent pathway, was an additional anti-tumor mechanism of LTX-315 [237].

## Declaration of competing interest

The authors declare that they have no known competing financial interests or personal relationships that could have appeared to influence the work reported in this paper.

## Appendix A. Supplementary data

Supplementary data to this article can be found online at <https://doi.org/10.1016/j.biomaterials.2020.120355>.

## References

- [1] M.S. Sorensen, The Proteins in Whey, *Whey. Compte rendu des Travaux du Laboratoire de Carlsberg Ser. Chim.* 23 (1939) 55–99.
- [2] M.L. Groves, The isolation of a red protein from Milk2, *J. Am. Chem. Soc.* 82 (13) (1960) 3345–3350.
- [3] E.N. Baker, P.F. Lindley, New perspectives on the structure and function of transferrins, *J. Inorg. Biochem.* 47 (1) (1992) 147–160.



- [4] D. Astruc, Introduction to Nanomedicine, *Molecules* 21 (1) (2015). E4-E4.
- [5] A. Aboda, W. Taha, I. Attia, A. Gad, M. Mahmoud Mostafa, M. Abdelfattah Abdelwaddod, M. Mohsen, R. Kaur Kanwar, J.R. Kanwar, Chapter 8 - iron bond bovine lactoferrin for the treatment of cancers and anemia associated with cancer cachexia, in: M.R. Singh, D. Singh, J.R. Kanwar, N.S. Chauhan (Eds.), *Advances and Avenues in the Development of Novel Carriers for Bioactives and Biological Agents*, Academic Press, 2020, pp. 243–254.
- [6] S. Kumari, D. Bhattacharya, N. Rangaraj, S. Chakravarty, A.K. Kondapi, N.M. Rao, Aurora kinase B siRNA-loaded lactoferrin nanoparticles potentiate the efficacy of temozolomide in treating glioblastoma, *Nanomedicine* 13 (20) (2018) 2579–2596.
- [7] N.A. McCarthy, A.L. Kelly, J.A. O'Mahony, M.A. Fenelon, Sensitivity of emulsions stabilised by bovine  $\beta$ -casein and lactoferrin to heat and CaCl<sub>2</sub>, *Food Hydrocolloids* 35 (2014) 420–428.
- [8] S.A. González-Chávez, S. Arévalo-Gallegos, Q. Rascón-Cruz, Lactoferrin: structure, function and applications, *Int. J. Antimicrob. Agents* 33 (4) (2009) 301.e1–301.e8.
- [9] L. Adlerova, A. Bartoskova, M. Faldyna, Lactoferrin: a review, *Vet. Med.* 53 (9) (2008) 457–468.
- [10] F.J. Castellino, W.W. Fish, K.G. Mann, Structural studies on bovine lactoferrin, *J. Biol. Chem.* 245 (17) (1970) 4269–4275.
- [11] B.F. Anderson, H.M. Baker, G.E. Norris, D.W. Rice, E.N. Baker, Structure of human lactoferrin: crystallographic structure analysis and refinement at 2.8 Å resolution, *J. Mol. Biol.* 209 (4) (1989) 711–734.
- [12] B. Lönnedal, S. Iyer, Lactoferrin: molecular structure and biological function, *Annu. Rev. Nutr.* 15 (1) (1995) 93–110.
- [13] I. Gupta, R. Sehgal, R.K. Kanwar, V. Punj, J.R. Kanwar, Nanocapsules loaded with iron-saturated bovine lactoferrin have antimicrobial therapeutic potential and maintain calcium, zinc and iron metabolism, *Nanomedicine* 10 (8) (2015) 1289–1314.
- [14] J.R. Kanwar, G. Mahidhara, K. Roy, S. Sasidharan, S. Krishnakumar, N. Prasad, R. Sehgal, R.K. Kanwar, Fe-bLf nanoformulation targets survivin to kill colon cancer stem cells and maintains absorption of iron, calcium and zinc, *Nanomedicine* 10 (1) (2015) 35–55.
- [15] J. Kanwar, K. Roy, Y. Patel, S. Zhou, M. Rawat Singh, D. Singh, M. Nasir, R. Sehgal, A. Sehgal, R. Singh, S. Garg, R. Kanwar, Multifunctional iron bound lactoferrin and nanomedical approaches to enhance its bioactive functions, *Molecules* 20 (2015) 9703–9731.
- [16] Q. Meng, A. Wang, H. Hua, Y. Jiang, Y. Wang, H. Mu, Z. Wu, K. Sun, Intranasal delivery of Huperzine A to the brain using lactoferrin-conjugated N-trimethylated chitosan surface-modified PLGA nanoparticles for treatment of Alzheimer's disease, *Int. J. Nanomed.* 13 (2018) 705–718.
- [17] Y. Akiyama, K. Oshima, T. Kuhara, K. Shin, F. Abe, K. Iwatsuki, D. Nadano, T. Matsuda, A lactoferrin-receptor, intelectin 1, affects uptake, sub-cellular localization and release of immunochemically detectable lactoferrin by intestinal epithelial Caco-2 cells, *J. Biochem.* 154 (5) (2013) 437–448.
- [18] J.R. Kanwar, S.K. Kamalapuram, S. Krishnakumar, R.K. Kanwar, Multimodal iron oxide (Fe<sub>3</sub>O<sub>4</sub>)-saturated lactoferrin nanocapsules as nanotheranostics for real-time imaging and breast cancer therapy of claudin-low, triple-negative (ER(-)/PR(-)/HER2(-)), *Nanomedicine* 11 (3) (2016) 249–268.
- [19] Y. Takayama, R. Aoki, R. Uchida, A. Tajima, A. Aoki-Yoshida, Role of CXCR chemokine receptor type 4 as a lactoferrin receptor, *Biochemistry and cell biology = Biochimie et biologie cellulaire* 95 (1) (2017) 57–63.
- [20] K. Ando, K. Hasegawa, K. Shindo, T. Furusawa, T. Fujino, K. Kikugawa, H. Nakano, O. Takeuchi, S. Akira, T. Akiyama, J. Gohda, J. Inoue, M. Hayakawa, Human lactoferrin activates NF- $\kappa$ B through the Toll-like receptor 4 pathway while it interferes with the lipopolysaccharide-stimulated TLR4 signaling, *FEBS J.* 277 (9) (2010) 2051–2066.
- [21] T. Takeuchi, T. Jyonotsuka, N. Kamemori, G. Kawano, H. Shimizu, K. Ando, E. Harada, Enteric-formulated lactoferrin was more effectively transported into blood circulation from gastrointestinal tract in adult rats, *Exp. Physiol.* 91 (6) (2006) 1033–1040.
- [22] R. Fischer, H. Debbabi, A. Blais, M. Dubarry, M. Rautureau, P.N. Boyaka, D. Tome, Uptake of ingested bovine lactoferrin and its accumulation in adult mouse tissues, *Int. Immunopharm.* 7 (10) (2007) 1387–1393.
- [23] X. Yao, Development of a Novel Drug Delivery System to Enhance the Oral Bioavailability of Lactoferrin, University of Auckland, 2015.
- [24] B. Lönnedal, Lactoferrin Receptors in Intestinal Brush Border Membranes, *Lactoferrin*, Springer, 1994, pp. 171–175.
- [25] F.J. Troost, J. Steijns, W.H. Saris, R.J. Brummer, Gastric digestion of bovine lactoferrin in vivo in adults, *J. Nutr.* 131 (8) (2001) 2101–2104.
- [26] F.J. Troost, W.H. Saris, R.J. Brummer, Orally ingested human lactoferrin is digested and secreted in the upper gastrointestinal tract in vivo in women with ileostomies, *J. Nutr.* 132 (9) (2002) 2597–2600.
- [27] P.F. Levay, M. Viljoen, Lactoferrin: a general review, *Haematologica* 80 (3) (1995) 252–267.
- [28] J.R. Kanwar, R.M. Samarasinghe, R. Sehgal, R.K. Kanwar, Nano-lactoferrin in diagnostic, imaging and targeted delivery for cancer and infectious diseases, *J. Canc. Sci. Ther.* 4 (3) (2012) 31–42.
- [29] P.F. Levay, M. Viljoen, Lactoferrin: a general review, *Haematologica* 80 (3) (1995) 252–267.
- [30] H. Abu Hashim, O. Foda, E. Ghayaty, Lactoferrin or ferrous salts for iron deficiency anemia in pregnancy: a meta-analysis of randomized trials, *Eur. J. Obstet. Gynecol. Reprod. Biol.* 219 (2017) 45–52.
- [31] P.P. Ward, M. Mendoza-Meneses, G.A. Cunningham, O.M. Conneely, Iron status in mice carrying a targeted disruption of lactoferrin, *Mol. Cell Biol.* 23 (1) (2003) 178–185.
- [32] L. Sanchez, M. Calvo, J.H. Brock, Biological role of lactoferrin, *Arch. Dis. Child.* 67 (5) (1992) 657–661.
- [33] D.A. Baldwin, E.R. Jenny, P. Aisen, The effect of human serum transferrin and milk lactoferrin on hydroxyl radical formation from superoxide and hydrogen peroxide, *J. Biol. Chem.* 259 (21) (1984) 13391–13394.
- [34] P. Valenti, G. Antonini, Lactoferrin: an important host defence against microbial and viral attack, *Cell. Mol. Life Sci.* : CMLS 62 (22) (2005) 2576–2587.
- [35] E.N. Baker, H.M. Baker, A structural framework for understanding the multifunctional character of lactoferrin, *Biochimie* 91 (1) (2009) 3–10.
- [36] R.T. Ellison 3rd, T.J. Giehl, F.M. LaForce, Damage of the outer membrane of enteric gram-negative bacteria by lactoferrin and transferrin, *Infect. Immun.* 56 (11) (1988) 2774–2781.
- [37] K. Vongbavit, M.A. Underwood, Prevention of necrotizing enterocolitis through manipulation of the intestinal microbiota of the premature infant, *Clin. Therapeut.* 38 (4) (2016) 716–732.
- [38] F. Di Mario, G. Aragona, N. Dal Bo, G.M. Cavestro, L. Cavallaro, V. Iori, G. Comparato, G. Leandro, A. Pilotto, A. Franze, Use of bovine lactoferrin for *Helicobacter pylori* eradication, Digestive and liver disease, official journal of the Italian Society of Gastroenterology and the Italian Association for the Study of the Liver 35 (10) (2003) 706–710.
- [39] N. León-Sicaïros, U.A. Angulo-Zamudio, J.E. Vidal, C.A. López-Torres, J. G. Bolscher, K. Nazmi, R. Reyes-Cortes, M. Reyes-López, M. de la Garza, A. Canizalez-Román, Bactericidal effect of bovine lactoferrin and synthetic peptide lactoferrin chimera in *Streptococcus pneumoniae* and the decrease in luxS gene expression by lactoferrin, *Biometals* : an international journal on the role of metal ions in biology, biochemistry, and medicine 27 (5) (2014) 969–980.
- [40] E. Acosta-Smith, K. Viveros-Jiménez, A. Canizalez-Román, M. Reyes-Lopez, J.G. M. Bolscher, K. Nazmi, H. Flores-Villaseñor, G. Alapizco-Castro, M. de la Garza, J. J. Martínez-García, J. Velazquez-Roman, N. Leon-Sicaïros, Bovine lactoferrin and lactoferrin-derived peptides inhibit the growth of *Vibrio cholerae* and other *Vibrio* species, *Front. Microbiol.* 8 (2017) 2633.
- [41] P.P. Ward, E. Paz, O.M. Conneely, Multifunctional roles of lactoferrin: a critical overview, *Cell. Mol. Life Sci.* : CMLS 62 (22) (2005) 2540–2548.
- [42] J.R. Kanwar, R.M. Samarasinghe, R. Sehgal, Nano-lactoferrin in diagnostic, imaging and targeted delivery for cancer and infectious diseases, *J. Canc. Sci. Ther.* 4 (3) (2012) 031–042, 04(03).
- [43] R.K. Kanwar, N. Singh, S. Gurudev, J.R. Kanwar, Targeting hepatitis B virus and human papillomavirus induced carcinogenesis: novel patented therapeutics, *Recent Pat. Anti-Infect. Drug Discov.* 6 (2) (2011) 158–174.
- [44] J. Lang, N. Yang, J. Deng, K. Liu, P. Yang, G. Zhang, C. Jiang, Inhibition of SARS pseudovirus cell entry by lactoferrin binding to heparan sulfate proteoglycans, *PLoS One* 6 (8) (2011) e23710-e23710.
- [45] W.J. Wurzer, O. Planz, C. Ehrhardt, M. Giner, T. Silberzahn, S. Pleschka, S. Ludwig, Caspase 3 activation is essential for efficient influenza virus propagation, *EMBO J.* 22 (11) (2003) 2717–2728.
- [46] A. Pietrantoni, E. Dofrelli, A. Tinari, M.G. Ammendolia, S. Puzelli, C. Fabiani, I. Donatelli, F. Superti, Bovine lactoferrin inhibits influenza A virus induced programmed cell death in vitro, *Biometals* : an international journal on the role of metal ions in biology, biochemistry, and medicine 23 (3) (2010) 465–475.
- [47] A. Pietrantoni, A.M. Di Biase, A. Tinari, M. Marchetti, P. Valenti, L. Seganti, F. Superti, Bovine lactoferrin inhibits adenovirus infection by interacting with viral structural polypeptides, *Antimicrob. Agents Chemother.* 47 (8) (2003) 2688–2691.
- [48] M. Kaito, M. Iwasa, N. Fujita, Y. Kobayashi, Y. Kojima, J. Ikoma, I. Imoto, Y. Adachi, H. Hamano, K. Yamauchi, Effect of lactoferrin in patients with chronic hepatitis C: combination therapy with interferon and ribavirin, *J. Gastroenterol. Hepatol.* 22 (11) (2007) 1894–1897.
- [49] O. Cirioni, A. Giacometti, F. Barchiesi, G. Scalise, Inhibition of growth of *Pneumocystis carinii* by lactoferrins alone and in combination with pyrimethamine, clarithromycin and minocycline, *J. Antimicrob. Chemother.* 46 (4) (2000) 577–582.
- [50] N. Leon-Sicaïros, M. Reyes-Lopez, A. Canizalez-Roman, R.M. Bermudez-Cruz, J. Serrano-Luna, R. Arroyo, M. de la Garza, Human hololactoferrin: endocytosis and use as an iron source by the parasite *Entamoeba histolytica*, *Microbiology* 151 (Pt 12) (2005) 3859–3871.
- [51] N. Leon-Sicaïros, F. Lopez-Soto, M. Reyes-Lopez, D. Godínez-Vargas, C. Ordaz-Pichardo, M. de la Garza, Amoebicidal activity of milk, apo-lactoferrin, sIgA and lysozyme, *Clin. Med. Res.* 4 (2) (2006) 106–113.
- [52] P. Sinnis, T.E. Willnow, M.R. Briones, J. Herz, V. Nussenzweig, Remnant lipoproteins inhibit malaria sporozoite invasion of hepatocytes, *J. Exp. Med.* 184 (3) (1996) 945–954.
- [53] G. Fritsch, G. Sawatzki, J. Treumer, A. Jung, D.T. Spira, *Plasmodium falciparum*: inhibition in vitro with lactoferrin, desferrierrithiocin, and desferrirocine, *Exp. Parasitol.* 63 (1) (1987) 1–9.
- [54] C.H. Kirkpatrick, I. Green, R.R. Rich, A.L. Schade, Inhibition of growth of *Candida albicans* by iron-unsaturated lactoferrin: relation to host-defense mechanisms in chronic mucocutaneous candidiasis, *J. Infect. Dis.* 124 (6) (1971) 539–544.
- [55] M. Nakano, M. Suzuki, H. Wakabayashi, K. Hayama, K. Yamauchi, F. Abe, S. Abe, Synergistic Anti-candida Activities of Lactoferrin and the Lactoperoxidase System, 2019.
- [56] C. Luzi, F. Brisdeli, R. Iorio, A. Bozzi, V. Carnicelli, A. Di Giulio, A.R. Lizzi, Apoptotic effects of bovine apo-lactoferrin on HeLa tumor cells, *Cell Biochem. Funct.* 35 (1) (2017) 33–41.



- [57] R. Jiang, B. Lonnerdal, Bovine lactoferrin and lactoferricin exert antitumor activities on human colorectal cancer cells (HT-29) by activating various signaling pathways, *Biochem. Cell. Biol.* 95 (1) (2017) 99–109.
- [58] Y. Zhang, A. Nicolau, C.F. Lima, L.R. Rodrigues, Bovine lactoferrin induces cell cycle arrest and inhibits mTOR signaling in breast cancer cells, *Nutr. Canc.* 66 (8) (2014) 1371–1385.
- [59] J. Wang, Q. Li, K. Li, Y. Ou, Z. Han, D. Gao, J. Li, Effects of adenovirus vectors mediated human lactoferrin cDNA on mice bearing EMT6 breast carcinoma, *Pharmazie* 66 (9) (2011) 704–709.
- [60] C.S. Pereira, J.P. Guedes, M. Gonçalves, L. Loureiro, L. Castro, H. Gerós, L. R. Rodrigues, M. Corte-Real, Lactoferrin selectively triggers apoptosis in highly metastatic breast cancer cells through inhibition of plasmalemmal V-H+ATPase, *Oncotarget* 7 (38) (2016) 62144–62158.
- [61] W.Y. Li, Q.W. Li, Z.S. Han, Z.L. Jiang, H. Yang, J. Li, X.B. Zhang, Growth suppression effects of recombinant adenovirus expressing human lactoferrin on cervical cancer in vitro and in vivo, *Cancer Biother. Radiopharm.* 26 (4) (2011) 477–483.
- [62] H. Shi, W. Li, Inhibitory effects of human lactoferrin on U14 cervical carcinoma through upregulation of the immune response, *Oncology letters* 7 (3) (2014) 820–826.
- [63] J.P. Guedes, C.S. Pereira, L.R. Rodrigues, M. Corte-Real, Bovine milk lactoferrin selectively kills highly metastatic prostate cancer PC-3 and osteosarcoma MG-63 cells in vitro, *Frontiers in oncology* 8 (2018), 200–200.
- [64] B. Lonnerdal, R. Jiang, X. Du, Bovine lactoferrin can be taken up by the human intestinal lactoferrin receptor and exert bioactivities, *J. Pediatr. Gastroenterol. Nutr.* 53 (6) (2011) 606–614.
- [65] T. Kuhara, M. Iigo, T. Itoh, Y. Ushida, K. Sekine, N. Terada, H. Okamura, H. Tsuda, Orally administered lactoferrin exerts an antitumour effect and enhances production of IL-18 in the intestinal epithelium, *Nutr. Canc.* 38 (2) (2000) 192–199.
- [66] M. Deng, W. Zhang, H. Tang, Q. Ye, Q. Liao, Y. Zhou, M. Wu, W. Xiong, Y. Zheng, X. Guo, Z. Qin, W. He, M. Zhou, J. Xiang, X. Li, J. Ma, G. Li, Lactotransferrin acts as a tumor suppressor in nasopharyngeal carcinoma by repressing AKT through multiple mechanisms, *Oncogene* 32 (36) (2013) 4273–4283.
- [67] S.H. Lee, H.M. Hwang, C.W. Pyo, D.H. Hahm, S.Y. Choi, E2F1-directed activation of Bcl-2 is correlated with lactoferrin-induced apoptosis in Jurkat leukemia T lymphocytes, *Biomaterials: an international journal on the role of metal ions in biology, biochemistry, and medicine* 23 (3) (2010) 507–514.
- [68] H.J. Son, S.H. Lee, S.Y. Choi, Human lactoferrin controls the level of retinoblastoma protein and its activity, *Biochemistry and cell biology = Biochimie et biologie cellulaire* 84 (3) (2006) 345–350.
- [69] Y.T. Tung, H.L. Chen, C.C. Yen, P.Y. Lee, H.C. Tsai, M.F. Lin, C.M. Chen, Bovine lactoferrin inhibits lung cancer growth through suppression of both inflammation and expression of vascular endothelial growth factor, *J. Dairy Sci.* 96 (4) (2013) 2095–2106.
- [70] C. Chea, M. Miyauchi, T. Inubushi, N. Febriyanti Ayuningtyas, A. Subarnbhesaj, P.T. Nguyen, M. Shrestha, S. Haing, K. Ohta, T. Takata, Molecular mechanism of inhibitory effects of bovine lactoferrin on the growth of oral squamous cell carcinoma, *PloS One* 13 (1) (2018), e0191683.
- [71] Y. Xiao, C.L. Monitto, K.M. Minhas, D. Sidransky, Lactoferrin down-regulates G1 cyclin-dependent kinases during growth arrest of head and neck cancer cells, *Clin. Canc. Res. : an official journal of the American Association for Cancer Research* 10 (24) (2004) 8683–8686.
- [72] A. Arcella, M.A. Oliva, S. Staffieri, S. Aalberti, G. Grillea, M. Madonna, M. Bartolo, L. Pavone, F. Giangaspero, G. Cantore, A. Frati, In vitro and in vivo effect of human lactoferrin on glioblastoma growth, *J. Neurosurg.* 123 (4) (2015) 1026–1035.
- [73] C.S. Pereira, J.P. Guedes, M. Goncalves, L. Loureiro, L. Castro, H. Geros, L. R. Rodrigues, M. Corte-Real, Lactoferrin selectively triggers apoptosis in highly metastatic breast cancer cells through inhibition of plasmalemmal V-H+ATPase, *Oncotarget* 7 (38) (2016) 62144–62158.
- [74] L. Stransky, K. Cotter, M. Forgas, The function of V-ATPases in cancer, *Physiol. Rev.* 96 (3) (2016) 1071–1091.
- [75] J.P. Guedes, C.S. Pereira, L.R. Rodrigues, M. Corte-Real, Bovine milk lactoferrin selectively kills highly metastatic prostate cancer PC-3 and osteosarcoma MG-63 cells in vitro, *Frontiers in oncology* 8 (2018) 200.
- [76] J.A. Gibbons, J.R. Kanwar, R.K. Kanwar, Iron-free and iron-saturated bovine lactoferrin inhibit survivin expression and differentially modulate apoptosis in breast cancer, *BMC Canc.* 15 (2015) 425.
- [77] J.S. Shankaranarayanan, J.R. Kanwar, A.J. Al-Juhaishi, R.K. Kanwar, Doxorubicin conjugated to immunomodulatory anticancer lactoferrin displays improved cytotoxicity overcoming prostate cancer chemo resistance and inhibits tumour development in TRAMP mice, *Sci. Rep.* 6 (2016) 32062.
- [78] Z. Zhang, J. Yang, Q. Min, C. Ling, D. Maiti, J. Xu, L. Qin, K. Yang, Holo-lactoferrin modified liposome for relieving tumor hypoxia and enhancing radiochemotherapy of cancer, *Small* 15 (6) (2019), e1803703.
- [79] Y. Takayama, R. Aoki, Roles of lactoferrin on skin wound healing, *Biochemistry and cell biology = Biochimie et biologie cellulaire* 90 (3) (2012) 497–503.
- [80] L. Tang, J.J. Wu, Q. Ma, T. Cui, F.M. Andreopoulos, J. Gil, J. Valdes, S.C. Davis, J. Li, Human lactoferrin stimulates skin keratinocyte function and wound re-epithelialization, *Br. J. Dermatol.* 163 (1) (2010) 38–47.
- [81] J. Engelmayer, P. Blezinger, A. Varadhachary, Talactoferrin stimulates wound healing with modulation of inflammation, *J. Surg. Res.* 149 (2) (2008) 278–286.
- [82] H. Onishi, Y. Machida, K. Koyama, Preparation and in vitro characteristics of lactoferrin-loaded chitosan microparticles, *Drug Dev. Ind. Pharm.* 33 (6) (2007) 641–647.
- [83] K. Koyama, H. Onishi, O. Sakata, Y. Machida, Preparation and in vitro evaluation of chitosan-coated alginate/calcium complex microparticles loaded with fluorescein-labeled lactoferrin, *Yakugaku Zasshi* 129 (12) (2009) 1507–1514.
- [84] H. Onishi, K. Koyama, O. Sakata, Y. Machida, Preparation of chitosan/alginate/calcium complex microparticles loaded with lactoferrin and their efficacy on carrageenan-induced edema in rats, *Drug Dev. Ind. Pharm.* 36 (8) (2010) 879–884.
- [85] J.R. Kanwar, G. Mahidhara, R.K. Kanwar, Novel alginate-enclosed chitosan-calcium phosphate-loaded iron-saturated bovine lactoferrin nanocarriers for oral delivery in colon cancer therapy, *Nanomedicine* 7 (10) (2012) 1521–1550.
- [86] R.M. Samarasinghe, R.K. Kanwar, J.R. Kanwar, The effect of oral administration of iron saturated-bovine lactoferrin encapsulated chitosan-nanocarriers on osteoarthritis, *Biomaterials* 35 (26) (2014) 7522–7534.
- [87] A. Ishikado, H. Imanaka, T. Takeuchi, E. Harada, T. Makino, Liposomalization of lactoferrin enhanced its anti-inflammatory effects via oral administration, *Biol. Pharm. Bull.* 28 (9) (2005) 1717–1721.
- [88] A. Roseanu, P.E. Florian, M. Moisei, L.E. Sima, R.W. Evans, M. Trif, Liposomalization of lactoferrin enhanced its anti-tumoral effects on melanoma cells, *Biomaterials* 23 (3) (2010) 485–492.
- [89] J. Ma, R. Guan, H. Shen, F. Lu, C. Xiao, M. Liu, T. Kang, Comparison of anticancer activity between lactoferrin nanoliposome and lactoferrin in Caco-2 cells in vitro, *Food Chem. Toxicol.* 59 (2013) 72–77.
- [90] K. Kato, N. Tamaki, Y. Saito, T. Fujimoto, A. Sato, Amino group PEGylation of bovine lactoferrin by linear polyethylene glycol-p-nitrophenyl active esters, *Biol. Pharmaceut. Bull.* 33 (7) (2010) 1253–1255.
- [91] Y. Nojima, Y. Suzuki, K. Iguchi, T. Shiga, A. Iwata, T. Fujimoto, K. Yoshida, H. Shimizu, T. Takeuchi, A. Sato, Development of poly(ethylene glycol) conjugated lactoferrin for oral administration, *Bioconjugate Chem.* 19 (11) (2008) 2253–2259.
- [92] Y. Nojima, Y. Suzuki, K. Yoshida, F. Abe, T. Shiga, T. Takeuchi, A. Sugiyama, H. Shimizu, A. Sato, Lactoferrin conjugated with 40-kDa branched poly(ethylene glycol) has an improved circulating half-life, *Pharm. Res. (N. Y.)* 26 (9) (2009) 2125–2132.
- [93] A. Sugiyama, A. Sato, T. Takeuchi, PEGylated lactoferrin enhanced its hepatoprotective effects on acute liver injury induced by carbon tetrachloride in rats, *Food Chem. Toxicol.* 47 (7) (2009) 1453–1458.
- [94] Y. Takahashi, C. Takeda, I. Seto, G. Kawano, Y. Machida, Formulation and evaluation of lactoferrin bioadhesive tablets, *Int. J. Pharm.* 343 (1–2) (2007) 220–227.
- [95] N. Anand, R. Sehgal, R.K. Kanwar, M.L. Dubey, R.K. Vasishta, J.R. Kanwar, Oral administration of encapsulated bovine lactoferrin protein nanocapsules against intracellular parasite *Toxoplasma gondii*, *Int. J. Nanomed.* 10 (2015) 6355–6369.
- [96] S. Kumari, S.M. Ahsan, J.M. Kumar, A.K. Kondapi, N.M. Rao, Overcoming blood brain barrier with a dual purpose Temozolomide loaded Lactoferrin nanoparticles for combating glioma (SERP-17-12433), *Sci. Rep.* 7 (1) (2017) 6602.
- [97] S. Kumari, A.K. Kondapi, Lactoferrin mediated targeted delivery of 5-fluorouracil for enhanced therapeutic efficacy, *Int. J. Biol. Macromol.* 95 (2017) 232–237.
- [98] F. Ahmed, S. Kumari, A.K. Kondapi, Evaluation of antiproliferative activity, safety and biodistribution of oxaliplatin and 5-fluorouracil loaded lactoferrin nanoparticles for the management of colon adenocarcinoma: an in vitro and an in vivo study, *Pharm. Res. (N. Y.)* 35 (9) (2018) 178.
- [99] A.P. Pandey, M.P. More, K.P. Karande, R.V. Chitalkar, P.O. Patil, P.K. Deshmukh, Optimization of desolvation process for fabrication of lactoferrin nanoparticles using quality by design approach, *Artificial cells, nanomedicine, and biotechnology* 45 (6) (2017) 1–14.
- [100] A.C. Altling, R.J. Hamer, C.G. de Kruif, R.W. Visschers, Cold-set globular protein gels: interactions, structure and rheology as a function of protein concentration, *J. Agric. Food Chem.* 51 (10) (2003) 3150–3156.
- [101] X. Mo, Z. Zheng, Y. He, H. Zhong, X. Kang, M. Shi, T. Liu, Z. Jiao, Y. Huang, Antiglioma via regulating oxidative stress and remodeling tumor-associated macrophage using lactoferrin-mediated biomimetic codelivery of simvastatin/fenretinide, *J. Contr. Release* 287 (2018) 12–23.
- [102] H. Wang, Y. Tang, Y. Fang, M. Zhang, H. Wang, Z. He, B. Wang, Q. Xu, Y. Huang, Reprogramming tumor immune microenvironment (TIME) and metabolism via biomimetic targeting codelivery of shikonin/JQ1, *Nano Lett.* 19 (5) (2019) 2935–2944.
- [103] J. Li, C. Zhao, L. Wei, X. Li, F. Liu, M. Zhang, X. Liu, Y. Wang, Preservation of cichoric acid antioxidant properties loaded in heat treated lactoferrin nanoparticles, *Molecules* 23 (10) (2018).
- [104] Z.H. Zhang, X.P. Wang, W.Y. Ayman, W.L. Munyendo, H.X. Lv, J.P. Zhou, Studies on lactoferrin nanoparticles of gambogic acid for oral delivery, *Drug Deliv.* 20 (2) (2013) 86–93.
- [105] X. Xia, H. Liu, H. Lv, J. Zhang, J. Zhou, Z. Zhao, Preparation, characterization, and in vitro/vivo studies of oleanolic acid-loaded lactoferrin nanoparticles, *Drug Des. Dev. Ther.* 11 (2017) 1417–1427.
- [106] C. Bengoechea, O.G. Jones, A. Guerrero, D.J. McClements, Formation and characterization of lactoferrin/pectin electrostatic complexes: impact of composition, pH and thermal treatment, *Food Hydrocolloids* 25 (5) (2011) 1227–1232.
- [107] A.V. Il'in, D.V. Kurek, A.A. Zubareva, M. M, N.M. Mestechkina, V.P. Varlamov, Preparation and Characterization of Biopolymer Nanoparticles Based on Lactoferrin-Polysaccharide Complexes, *Reactive and Functional Polymers*, vol. 102, 2016, pp. 33–38.
- [108] I. Peinado, U. Lesmes, A. Andres, J.D. McClements, Fabrication and morphological characterization of biopolymer particles formed by electrostatic

- complexation of heat treated lactoferrin and anionic polysaccharides, *Langmuir* 26 (12) (2010) 9827–9834.
- [109] J.K. Yan, W.Y. Qiu, Y.Y. Wang, J.Y. Wu, Biocompatible polyelectrolyte complex nanoparticles from lactoferrin and pectin as potential vehicles for antioxidative curcumin, *J. Agric. Food Chem.* 65 (28) (2017) 5720–5730.
- [110] M.M. Abd Elwakil, M.T. Mabrouk, M.W. Helmy, E.A. Abdelfattah, S.K. Khiste, K.A. Elkhodairy, A.O. Elzoghby, Inhalable lactoferrin-chondroitin nanocomposites for combined delivery of doxorubicin and ellagic acid to lung carcinoma, *Nanomedicine* 13 (16) (2018) 2015–2035.
- [111] R. Liu, X. Yan, Z. Liu, D.J. McClements, F. Liu, X. Liu, Fabrication and characterization of functional protein-polysaccharide-polyphenol complexes assembled from lactoferrin, hyaluronic acid and (-)-epigallocatechin gallate, *Food Funct* 10 (2) (2019) 1098–1108.
- [112] F. Chaharband, G. Kamalinia, F. Atyabi, S.A. Mortazavi, Z.H. Mirzaie, R. Dinarvand, Formulation and in vitro evaluation of curcumin-lactoferrin conjugated nanostructures for cancerous cells, *Artificial cells, nanomedicine, and biotechnology* 46 (3) (2018) 626–636.
- [113] G. Kamalinia, F. Khodaghali, F. Atyabi, M. Amini, F. Shaerzadeh, M. Sharifzadeh, R. Dinarvand, Enhanced brain delivery of deferasirox-lactoferrin conjugates for iron chelation therapy in neurodegenerative disorders: in vitro and in vivo studies, *Mol. Pharm.* 10 (12) (2013) 4418–4431.
- [114] O.M. Ali, A.A. Bekhit, S.N. Khattab, M.W. Helmy, Y.S. Abdel-Ghany, M. Teleb, A.O. Elzoghby, Synthesis of lactoferrin mesoporous silica nanoparticles for pemetrexed/ellagic acid synergistic breast cancer therapy, *Colloids Surf. B Biointerfaces* 188 (2020) 110824.
- [115] F. Liu, D. Wang, C. Sun, D.J. McClements, Y. Gao, Utilization of interfacial engineering to improve physicochemical stability of beta-carotene emulsions: multilayer coatings formed using protein and protein-polyphenol conjugates, *Food Chem.* 205 (2016) 129–139.
- [116] F. Liu, C. Sun, W. Yang, F. Yuan, Y. Gao, Structural characterization and functional evaluation of lactoferrin–polyphenol conjugates formed by free-radical graft copolymerization, *RSC Adv.* 5 (20) (2015) 15641–15651.
- [117] F. Liu, C. Sun, D. Wang, F. Yuan, Y. Gao, Glycosylation improves the functional characteristics of chlorogenic acid–lactoferrin conjugate, *RSC Adv.* 5 (95) (2015) 78215–78228.
- [118] S.A. Sabra, A.O. Elzoghby, S.A. Sheweita, M. Haroun, M.W. Helmy, M.A. Eldemellawy, Y. Xia, D. Goodale, A.L. Allan, S. Rohani, Self-assembled amphiphilic zein-lactoferrin micelles for tumor targeted co-delivery of rapamycin and wogonin to breast cancer, *Eur. J. Pharm. Biopharm. : official journal of Arbeitsgemeinschaft für Pharmazeutische Verfahrenstechnik e.V* 128 (2018) 156–169.
- [119] S.A. Sabra, S.A. Sheweita, M. Haroun, D. Ragab, M.A. Eldemellawy, Y. Xia, D. Goodale, A.L. Allan, A.O. Elzoghby, S. Rohani, Magnetically guided self-assembled protein micelles for enhanced delivery of dasatinib to human triple-negative breast cancer cells, *J. Pharmaceut. Sci.* 108 (5) (2019) 1713–1725.
- [120] M.S. Alqahtani, M.S. Islam, S. Podaralla, R.S. Kaushik, J. Reineke, T. Woyengo, O. Perumal, Food protein based core-shell nanocarriers for oral drug delivery: effect of shell composition on in vitro and in vivo functional performance of zein nanocarriers, *Mol. Pharm.* 14 (3) (2017) 757–769.
- [121] M.A. Abdelmoneem, M.A. Elnaggar, R.S. Hammady, S.M. Kamel, M.W. Helmy, M.A. Abdulkader, A. Zaky, J.Y. Fang, K.A. Elkhodairy, A.O. Elzoghby, Dual-targeted lactoferrin shell-oily core nanocapsules for synergistic targeted/herbal therapy of hepatocellular carcinoma, *ACS Appl. Mater. Interfaces* 11 (30) (2019) 26731–26744.
- [122] K. Golla, B. Cherukuvada, F. Ahmed, A.K. Kondapi, Efficacy, safety and anticancer activity of protein nanoparticle-based delivery of doxorubicin through intravenous administration in rats, *PLoS One* 7 (12) (2012), e51960.
- [123] P. Kumar, Y.S. Lakshmi, A.K. Kondapi, An oral formulation of efavirenz-loaded lactoferrin nanoparticles with improved biodistribution and pharmacokinetic profile, *HIV Med.* 18 (7) (2017) 452–462.
- [124] F. Ahmed, M.J. Ali, A.K. Kondapi, Carboplatin loaded protein nanoparticles exhibit improved anti-proliferative activity in retinoblastoma cells, *Int. J. Biol. Macromol.* 70 (2014) 572–582.
- [125] Z. Shen, T. Liu, Z. Yang, Z. Zhou, W. Tang, W. Fan, Y. Liu, J. Mu, L. Li, V. I. Bregadze, S.K. Mandal, A.A. Druzina, Z. Wei, X. Qiu, A. Wu, X. Chen, Small-sized gadolinium oxide based nanoparticles for high-efficiency theranostics of orthotopic glioblastoma, *Biomaterials* 235 (2020) 119783.
- [126] Z. Shen, T. Liu, Y. Li, J. Lau, Z. Yang, W. Fan, Z. Zhou, C. Shi, C. Ke, V.I. Bregadze, S.K. Mandal, Y. Liu, Z. Li, T. Xue, G. Zhu, J. Munasinghe, G. Niu, A. Wu, X. Chen, Fenton-reaction-acceleratable magnetic nanoparticles for ferroptosis therapy of orthotopic brain tumors, *ACS Nano* 12 (11) (2018) 11355–11365.
- [127] M. Sharifi, A. Hasan, N.M.Q. Nanakali, A. Salih, F.A. Qadir, H.A. Muhammad, M. S. Shekha, F.M. Aziz, K.M. Amen, F. Najafi, H. Yousefi-Manesh, M. Falahati, Combined chemo-magnetic field-photothermal breast cancer therapy based on porous magnetite nanospheres, *Sci. Rep.* 10 (1) (2020) 5925.
- [128] M. Sharifi, S. Jafari, A. Hasan, B.A. Paray, G. Gong, Y. Zheng, M.J.A.B.S. Falahati, Engineering, Antimetastatic Activity of Lactoferrin-Coated Mesoporous Maghemite Nanoparticles in Breast Cancer Enabled by Combination Therapy, 2020.
- [129] M.M. Song, H.L. Xu, J.X. Liang, H.H. Xiang, R. Liu, Y.X. Shen, Lactoferrin modified graphene oxide iron oxide nanocomposite for glioma-targeted drug delivery, *Materials science & engineering, C, Materials for biological applications* 77 (2017) 904–911.
- [130] Y.L. Su, K.T. Chen, Y.C. Sheu, S.Y. Sung, R.S. Hsu, C.S. Chiang, S.H. Hu, The penetrated delivery of drug and energy to tumors by lipo-graphene nanosponges for photolytic therapy, *ACS Nano* 10 (10) (2016) 9420–9433.
- [131] P. Pomastowski, M. Sprynskyy, P. Žuvela, K. Rafińska, M. Milanowski, J.J. Liu, M. Yi, B. Buszewski, Silver-lactoferrin nanocomplexes as a potent antimicrobial agent, *J. Am. Chem. Soc.* 138 (25) (2016) 7899–7909.
- [132] S.S.I. Abdalla, H. Katas, J.Y. Chan, P. Ganasan, F. Azmi, M.F.M. Busra, Antimicrobial activity of multifaceted lactoferrin or graphene oxide functionalized silver nanocomposites biosynthesized using mushroom waste and chitosan 10 (9) (2020) 4969–4983.
- [133] P.S. Nayak, S.M. Borah, H. Gogoi, S. Asthana, R. Bhatnagar, A.N. Jha, S. Jha, Lactoferrin adsorption onto silver nanoparticle interface: implications of corona on protein conformation, nanoparticle cytotoxicity and the formulation adjuvanticity, *Chem. Eng. J.* 361 (2019) 470–484.
- [134] A.S. AbdelHamid, D.G. Zayed, M.W. Helmy, S.M. Ebrahim, M. Bahey-El-Din, E.A. Zein-El-Dein, S.A. El-Gizawy, A.O.J.N. Elzoghby, Lactoferrin-tagged quantum dots-based theranostic nanocapsules for combined COX-2 inhibitor/herbal therapy of breast cancer 13 (20) (2018) 2637–2656.
- [135] Y. Song, D. Du, L. Li, J. Xu, P. Dutta, Y. Lin, Vitro study of receptor-mediated silica nanoparticles delivery across blood–brain barrier, *ACS Appl. Mater. Interfaces* 9 (24) (2017) 20410–20416.
- [136] O.M. Ali, A.A. Bekhit, S.N. Khattab, M.W. Helmy, Y.S. Abdel-Ghany, M. Teleb, A.O.J.C. Elzoghby, S.B. Biointerfaces, Synthesis of Lactoferrin Mesoporous Silica Nanoparticles for Pemetrexed/ellagic Acid Synergistic Breast Cancer Therapy, vol. 188, 2020, p. 110824.
- [137] P.L. Xavier, K. Chaudhari, P.K. Verma, S.K. Pal, T. Pradeep, Luminescent quantum clusters of gold in transferrin family protein, lactoferrin exhibiting FRET, *Nanoscale* 2 (12) (2010) 2769–2776.
- [138] K. Chaudhari, P.L. Xavier, T. Pradeep, Understanding the evolution of luminescent gold quantum clusters in protein templates, *ACS Nano* 5 (11) (2011) 8816–8827.
- [139] I. Singh, R. Swami, D. Pooja, M.K. Jeengar, W. Khan, R. Sistla, Lactoferrin bioconjugated solid lipid nanoparticles: a new drug delivery system for potential brain targeting, *J. Drug Target.* 24 (3) (2016) 212–223.
- [140] F.Y. Huang, W.J. Chen, W.Y. Lee, S.T. Lo, T.W. Lee, J.M. Lo, In vitro and in vivo evaluation of lactoferrin-conjugated liposomes as a novel carrier to improve the brain delivery, *Int. J. Mol. Sci.* 14 (2) (2013) 2862–2874.
- [141] L.Y. Lim, P.Y. Koh, S. Somani, M. Al Robaian, R. Karim, Y.L. Yean, J. Mitchell, R. J. Tate, R. Edrada-Ebel, D.R. Blatchford, M. Mullin, C. Dufes, Tumor regression following intravenous administration of lactoferrin- and lactoferricin-bearing dendriplexes, *Nanomedicine* 11 (6) (2015) 1445–1454.
- [142] A.V. Kabanov, E.V. Batrakova, New technologies for drug delivery across the blood brain barrier, *Curr. Pharmaceut. Des.* 10 (12) (2004) 1355–1363.
- [143] Y.A. Suzuki, V. Lopez, B. Lonnerdal, Mammalian lactoferrin receptors: structure and function, *Cell. Mol. Life Sci.* 62 (22) (2005) 2560–2575.
- [144] R. Huang, W. Ke, Y. Liu, C. Jiang, Y. Pei, The use of lactoferrin as a ligand for targeting the polyamidoamine-based gene delivery system to the brain, *Biomaterials* 29 (2) (2008) 238–246.
- [145] C. Fillebeen, L. Descamps, M.P. Dehouck, L. Fenart, M. Benaissa, G. Spik, R. Cecchelli, A. Pierce, Receptor-mediated transcytosis of lactoferrin through the blood-brain barrier, *J. Biol. Chem.* 274 (11) (1999) 7011–7017.
- [146] A.O. Elzoghby, M.M. Abd-Elwakil, K. Abd-Elalsam, M.T. Elsayed, Y. Hashem, O. Mohamed, Natural polymeric nanoparticles for brain-targeting: implications on drug and gene delivery, *Curr. Pharmaceut. Des.* 22 (22) (2016) 3305–3323.
- [147] S. Sindhwani, A.M. Syed, J. Ngai, B.R. Kingston, L. Maiorino, J. Rothschild, P. MacMillan, Y. Zhang, N.U. Rajesh, T. Hoang, J.L.Y. Wu, S. Wilhelm, A. Zilman, S. Gadde, A. Sulaiman, B. Ouyang, Z. Lin, L. Wang, M. Egeblad, W.C.W. Chan, The entry of nanoparticles into solid tumours, *Nat. Mater.* 19 (5) (2020) 566–575.
- [148] Z. Pang, L. Feng, R. Hua, J. Chen, H. Gao, S. Pan, X. Jiang, P. Zhang, Lactoferrin-conjugated biodegradable polymersome holding doxorubicin and tetrandrine for chemotherapy of glioma rats, *Mol. Pharm.* 7 (6) (2010) 1995–2005.
- [149] H. Chen, Y. Qin, Q. Zhang, W. Jiang, L. Tang, J. Liu, Q. He, Lactoferrin modified doxorubicin-loaded procatonic liposomes for the treatment of gliomas, *Eur. J. Pharmaceut. Sci.* 44 (1–2) (2011) 164–173.
- [150] D. Miao, M. Jiang, Z. Liu, G. Gu, Q. Hu, T. Kang, Q. Song, L. Yao, W. Li, X. Gao, M. Sun, J. Chen, Co-administration of dual-targeting nanoparticles with penetration enhancement peptide for anti-glioblastoma therapy, *Mol. Pharm.* 11 (1) (2014) 90–101.
- [151] A. Pandey, K. Singh, S. Patel, R. Singh, K. Patel, K. Sawant, Hyaluronic acid tethered pH-responsive alloy-drug nanoconjugates for multimodal therapy of glioblastoma: an intranasal route approach, *Mater. Sci. Eng. C Mater. Biol. Appl.* 98 (2019) 419–436.
- [152] C. Bi, A. Wang, Y. Chu, S. Liu, H. Mu, W. Liu, Z. Wu, K. Sun, Y. Li, Intranasal delivery of rosiglitone to the brain with lactoferrin-modified PEG-PLGA nanoparticles for Parkinson's disease treatment, *Int. J. Nanomed.* 11 (2016) 6547–6559.
- [153] X. Yan, L. Xu, C. Bi, D. Duan, L. Chu, X. Yu, Z. Wu, A. Wang, K. Sun, Lactoferrin-modified rotigotine nanoparticles for enhanced nose-to-brain delivery: LESA-MS/MS-based drug biodistribution, pharmacodynamics, and neuroprotective effects, *Int. J. Nanomed.* 13 (2018) 273–281.
- [154] P. Martorell, S. Llopis, N. Gonzalez, D. Ramón, G. Serrano, A. Torrens, J. M. Serrano, M. Navarro, S. Genovés, A nutritional supplement containing lactoferrin stimulates the immune system, extends lifespan, and reduces amyloid  $\beta$  peptide toxicity in *Caenorhabditis elegans*, *Food science & nutrition* 5 (2) (2017) 255–265.
- [155] J. Wang, M. Bi, H. Liu, N. Song, J. Xie, The protective effect of lactoferrin on ventral mesencephalon neurons against MPP+ is not connected with its iron binding ability, *Sci. Rep.* 5 (2015) 10729.

- [156] H. Liu, H. Wu, N. Zhu, Z. Xu, Y. Wang, Y. Qu, J. Wang, Lactoferrin protects against iron dysregulation, oxidative stress, and apoptosis in 1-methyl-4-phenyl-1,2,3,6-tetrahydropyridine (MPTP)-induced Parkinson's disease in mice, *J. Neurochem.* 152 (3) (2020) 397–415.
- [157] S.F. Xu, Y.H. Zhang, S. Wang, Z.Q. Pang, Y.G. Fan, J.Y. Li, Z.Y. Wang, C. Guo, Lactoferrin ameliorates dopaminergic neurodegeneration and motor deficits in MPTP-treated mice, *Redox biology* 21 (2019) 101090.
- [158] S. Tang, A. Wang, X. Yan, L. Chu, X. Yang, Y. Song, K. Sun, X. Yu, R. Liu, Z. Wu, P. Xue, Brain-targeted intranasal delivery of dopamine with borneol and lactoferrin co-modified nanoparticles for treating Parkinson's disease, *Drug Deliv.* 26 (1) (2019) 700–707.
- [159] V.S. Bollimpelli, P. Kumar, S. Kumari, A.K. Kondapi, Neuroprotective effect of curcumin-loaded lactoferrin nano particles against rotenone induced neurotoxicity, *Neurochem. Int.* 95 (2016) 37–45.
- [160] J.H. Kordower, M.E. Emborg, J. Bloch, S.Y. Ma, Y. Chu, L. Leventhal, J. McBride, E.-Y. Chen, S. Palfi, B.Z. Rothberg, Neurodegeneration prevented by lentiviral vector delivery of GDNF in primate models of Parkinson's disease, *Science* 290 (5492) (2000) 767–773.
- [161] R. Huang, W. Ke, Y. Liu, D. Wu, L. Feng, C. Jiang, Y. Pei, Gene therapy using lactoferrin-modified nanoparticles in a rotenone-induced chronic Parkinson model, *J. Neurol. Sci.* 290 (1–2) (2010) 123–130.
- [162] M.S. Lepanto, L. Rosa, R. Paesano, P. Valenti, A. Cutone, Lactoferrin in aseptic and septic inflammation, *Molecules* 24 (7) (2019).
- [163] W.A. Mohamed, R.M. Salama, M.F. Schaal, A pilot study on the effect of lactoferrin on Alzheimer's disease pathological sequelae: impact of the p-Akt/PTEN pathway, *Biomedicine & pharmacotherapy = Biomedecine & pharmacotherapie* 111 (2019) 714–723.
- [164] C. Guo, Z.H. Yang, S. Zhang, R. Chai, H. Xue, Y.H. Zhang, J.Y. Li, Z.Y. Wang, Intranasal lactoferrin enhances  $\alpha$ -secretase-dependent amyloid precursor protein processing via the ERK1/2-CREB and HIF-1 $\alpha$  pathways in an Alzheimer's disease mouse model, *Neuropsychopharmacology : official publication of the American College of Neuropsychopharmacology* 42 (13) (2017) 2504–2515.
- [165] M. González-Sánchez, F. Bartolome, D. Antequera, V. Puertas-Martín, P. González, A. Gómez-Grande, S. Llamas-Velasco, A. Herrero-San Martín, D. Pérez-Martínez, A. Villarejo-Galende, M. Atienza, M. Palomar-Bonet, J. L. Cantero, G. Perry, G. Orive, B. Ibañez, H. Bueno, V. Fuster, E. Carro, Decreased salivary lactoferrin levels are specific to Alzheimer's disease, *EBioMedicine* 57 (2020) 102834.
- [166] A. Gothwal, H. Singh, S.K. Jain, A. Dutta, A. Borah, U. Gupta, Behavioral and biochemical implications of dendritic rivastigmine in memory-deficit and Alzheimer's induced rodents, *ACS Chem. Neurosci.* 10 (8) (2019) 3789–3795.
- [167] Y.C. Kuo, C.T. Wang, Protection of SK-N-MC cells against beta-amyloid peptide-induced degeneration using neuron growth factor-loaded liposomes with surface lactoferrin, *Biomaterials* 35 (22) (2014) 5954–5964.
- [168] Y. Yu, Z. Pang, W. Lu, Q. Yin, H. Gao, X. Jiang, Self-assembled polymersomes conjugated with lactoferrin as novel drug carrier for brain delivery, *Pharm. Res. (N. Y.)* 29 (1) (2012) 83–96.
- [169] Y. Yu, X. Jiang, S. Gong, L. Feng, Y. Zhong, Z. Pang, The proton permeability of self-assembled polymersomes and their neuroprotection by enhancing a neuroprotective peptide across the blood-brain barrier after modification with lactoferrin, *Nanoscale* 6 (6) (2014) 3250–3258.
- [170] J.H. Fang, T.L. Chiu, W.C. Huang, Y.H. Lai, S.H. Hu, Y.Y. Chen, S.Y. Chen, Dual-targeting lactoferrin-conjugated polymerized magnetic polydiacetylene-assembled nanocarriers with self-responsive fluorescence/magnetic resonance imaging for in vivo brain tumor therapy, *Adv Healthc Mater* 5 (6) (2016) 688–695.
- [171] Y.C. Kuo, Y.C. Chen, Targeting delivery of etoposide to inhibit the growth of human glioblastoma multiforme using lactoferrin- and folic acid-grafted poly (lactide-co-glycolide) nanoparticles, *Int. J. Pharm.* 479 (1) (2015) 138–149.
- [172] Y.C. Kuo, S.J. Cheng, Brain targeted delivery of curmestine using solid lipid nanoparticles modified with tamoxifen and lactoferrin for antitumor proliferation, *Int. J. Pharm.* 499 (1–2) (2016) 10–19.
- [173] Z. Su, L. Xing, Y. Chen, Y. Xu, F. Yang, C. Zhang, Q. Ping, Y. Xiao, Lactoferrin-modified poly(ethylene glycol)-grafted BSA nanoparticles as a dual-targeting carrier for treating brain gliomas, *Mol. Pharm.* 11 (6) (2014) 1823–1834.
- [174] L. Jiang, Q. Zhou, K. Mu, H. Xie, Y. Zhu, W. Zhu, Y. Zhao, H. Xu, X. Yang, pH/temperature sensitive magnetic nanogels conjugated with Cy5.5-labeled lactoferrin for MR and fluorescence imaging of glioma in rats, *Biomaterials* 34 (30) (2013) 7418–7428.
- [175] M.A. De Luca, F. Lai, F. Corrias, P. Caboni, Z. Bimpisidis, E. Maccioni, A.M. Fadda, G. Di Chiara, Lactoferrin- and antitransferrin-modified liposomes for brain targeting of the NK3 receptor agonist senktide: preparation and in vivo evaluation, *Int. J. Pharm.* 479 (1) (2015) 129–137.
- [176] R. Huang, L. Han, J. Li, F. Ren, W. Ke, C. Jiang, Y. Pei, Neuroprotection in a 6-hydroxydopamine-lesioned Parkinson model using lactoferrin-modified nanoparticles, *J. Gene Med.* 11 (9) (2009) 754–763.
- [177] K. Hu, Y. Shi, W. Jiang, J. Han, S. Huang, X. Jiang, Lactoferrin conjugated PEG-PLGA nanoparticles for brain delivery: preparation, characterization and efficacy in Parkinson's disease, *Int. J. Pharm.* 415 (1–2) (2011) 273–283.
- [178] Z. Liu, M. Jiang, T. Kang, D. Miao, G. Gu, Q. Song, L. Yao, Q. Hu, Y. Tu, Z. Pang, H. Chen, X. Jiang, X. Gao, J. Chen, Lactoferrin-modified PEG-co-PCL nanoparticles for enhanced brain delivery of NAP peptide following intranasal administration, *Biomaterials* 34 (15) (2013) 3870–3881.
- [179] H. Chen, L. Tang, Y. Qin, Y. Yin, J. Tang, W. Tang, X. Sun, Z. Zhang, J. Liu, Q. He, Lactoferrin-modified procationic liposomes as a novel drug carrier for brain delivery, *Eur. J. Pharmaceut. Sci.* 40 (2) (2010) 94–102.
- [180] Q. Ye, Y. Zheng, S. Fan, Z. Qin, N. Li, A. Tang, F. Ai, X. Zhang, Y. Bian, W. Dang, J. Huang, M. Zhou, Y. Zhou, W. Xiong, Q. Yan, J. Ma, G. Li, Lactoferrin deficiency promotes colitis-associated colorectal dysplasia in mice, *PLoS One* 9 (7) (2014), e103298.
- [181] M. Iigo, D.B. Alexander, J. Xu, M. Futakuchi, M. Suzui, T. Kozu, T. Akasu, D. Saito, T. Kakizoe, K. Yamauchi, F. Abe, M. Takase, K. Sekine, H. Tsuda, Inhibition of intestinal polyp growth by oral ingestion of bovine lactoferrin and immune cells in the large intestine, *Biometals : an international journal on the role of metal ions in biology, biochemistry, and medicine* 27 (5) (2014) 1017–1029.
- [182] T. Kozu, G. Iinuma, Y. Ohashi, Y. Saito, T. Akasu, D. Saito, D.B. Alexander, M. Iigo, T. Kakizoe, H. Tsuda, Effect of orally administered bovine lactoferrin on the growth of adenomatous colorectal polyps in a randomized, placebo-controlled clinical trial, *Canc. Prev. Res.* 2 (11) (2009) 975–983. Philadelphia, Pa.
- [183] H. Burrow, R.K. Kanwar, G. Mahidhara, J.R. Kanwar, Effect of selenium-saturated bovine lactoferrin (Se-bLF) on antioxidant enzyme activities in human gut epithelial cells under oxidative stress, *Anti Canc. Agents Med. Chem.* 11 (8) (2011) 762–771.
- [184] Y. Sugihara, X. Zuo, T. Takata, S. Jin, M. Miyauti, A. Isikado, H. Imanaka, M. Tatsuka, G. Qi, F. Shimamoto, Inhibition of DMH-DSS-induced colorectal cancer by liposomal bovine lactoferrin in rats, *Oncology letters* 14 (5) (2017) 5688–5694.
- [185] S.K. Kamalapuram, R.K. Kanwar, K. Roy, R. Chaudhary, R. Sehgal, J.R. Kanwar, Theranostic multimodal potential of zinc-doped ferrite-saturated metal-binding protein-loaded novel nanocapsules in cancers, *Int. J. Nanomed.* 11 (2016) 1349–1366.
- [186] K. Roy, R.K. Kanwar, J.R. Kanwar, LNA aptamer based multi-modal, Fe<sub>3</sub>O<sub>4</sub>-saturated lactoferrin (Fe<sub>3</sub>O<sub>4</sub>-bLF) nanocarriers for triple positive (EpCAM, CD133, CD44) colon tumor targeting and NIR, MRI and CT imaging, *Biomaterials* 71 (2015) 84–99.
- [187] M. Wei, X. Guo, L. Tu, Q. Zou, Q. Li, C. Tang, B. Chen, Y. Xu, C. Wu, Lactoferrin-modified PEGylated liposomes loaded with doxorubicin for targeting delivery to hepatocellular carcinoma, *Int. J. Nanomed.* 10 (2015) 5123–5137.
- [188] M.A. Abdelmoneem, M. Mahmoud, A. Zaky, M.W. Helmy, M. Sallam, J.Y. Fang, K. A. Elkhodairy, A.O. Elzoghby, Decorating protein nanospheres with lactoferrin enhances oral COX-2 inhibitor/herbal therapy of hepatocellular carcinoma, *Nanomedicine* 13 (19) (2018) 2377–2395.
- [189] M.A. Abdelmoneem, M. Mahmoud, A. Zaky, M.W. Helmy, M. Sallam, J.Y. Fang, K. A. Elkhodairy, A.O. Elzoghby, Dual-targeted casein micelles as green nanomedicine for synergistic phytotherapy of hepatocellular carcinoma, *J. Contr. Release* 287 (2018) 78–93.
- [190] M. Sharifi, A. Hasan, N.M.Q. Nanakali, A. Salihi, F.A. Qadir, H.A. Muhammad, M. S. Shekha, F.M. Aziz, K.M. Amen, F. Najafi, H. Yousefi-Manesh, M. Falahati, Combined chemo-magnetic field-photothermal breast cancer therapy based on porous magnetite nanospheres, *Sci. Rep.* 10 (1) (2020) 5925.
- [191] S.A. El-Lakany, N.A. Elgindy, M.W. Helmy, M.M. Abu-Serie, A.O. Elzoghby, Lactoferrin-decorated vs PEGylated zein nanospheres for combined aromatase inhibitor and herbal therapy of breast cancer, *Exp. Opin. Drug Deliv.* 15 (9) (2018) 835–850.
- [192] M.G. Adimoolam, V. A., M.R. Nalam, M.V. Sunkara, Chlorin e6 loaded lactoferrin nanoparticles for enhanced photodynamic therapy, *J. Mater. Chem. B* 5 (46) (2017) 9189–9196.
- [193] V. Pandey, K.R. Gajbhiye, V. Soni, Lactoferrin-appended solid lipid nanoparticles of paclitaxel for effective management of bronchogenic carcinoma, *Drug Deliv.* 22 (2) (2015) 199–205.
- [194] H.M. Abdelaziz, M. Gaber, M.M. Abd-Elwakil, M.T. Mabrouk, M.M. Elgohary, N. M. Kamel, D.M. Kabary, M.S. Freag, M.W. Samaha, S.M. Mortada, K. A. Elkhodairy, J.Y. Fang, A.O. Elzoghby, Inhalable particulate drug delivery systems for lung cancer therapy: nanoparticles, microparticles, nanocomposites and nanoaggregates, *J. Contr. Release* 269 (2018) 374–392.
- [195] D.M. Kabary, M.W. Helmy, E.A. Abdelfattah, J.Y. Fang, K.A. Elkhodairy, A. O. Elzoghby, Inhalable multi-compartmental phospholipid enveloped lipid core nanocomposites for localized mTOR inhibitor/herbal combined therapy of lung carcinoma, *Eur. J. Pharm. Biopharm.* 130 (2018) 152–164.
- [196] H.M. Abdelaziz, A.O. Elzoghby, M.W. Helmy, E.-Z.A. Abdelfattah, J.-Y. Fang, M. W. Samaha, M.S. Freag, Inhalable lactoferrin/chondroitin-functionalized monolein nanocomposites for localized lung cancer targeting, *ACS Biomater. Sci. Eng.* 6 (2) (2020) 1030–1042.
- [197] T.V. Zadvyorniy, N.Y. Lukianova, T.V. Borikun, V.F. Chekhun, Effects of exogenous lactoferrin on phenotypic profile and invasiveness of human prostate cancer cells (DU145 and LNCaP) in vitro, *Exp. Oncol.* 40 (3) (2018) 184–189.
- [198] N. Altawajry, S. Somani, J.A. Parkinson, R.J. Tate, P. Keating, M. Warzecha, G. R. Mackenzie, H.Y. Leung, C. Dukes, Regression of prostate tumors after intravenous administration of lactoferrin-bearing polypropylenimine dendriplexes encoding TNF- $\alpha$ , TRAIL, and interleukin-12, *Drug Deliv.* 25 (1) (2018) 679–689.
- [199] A.S. Abdelhamid, D.G. Zayed, M.W. Helmy, S.M. Ebrahim, M. Bahey-El-Din, E. A. Zein-El-Dein, S.A. El-Gizawy, A.O. Elzoghby, Lactoferrin-tagged quantum dots-based theranostic nanocapsules for combined COX-2 inhibitor/herbal therapy of breast cancer, *Nanomedicine* 13 (20) (2018) 2637–2656.
- [200] C. Garré, G. Bianchi-Scarrà, M. Sirtio, M. Musso, R. Ravazzolo, Lactoferrin binding sites and nuclear localization in K562(S) cells, *J. Cell. Physiol.* 153 (3) (1992) 477–482.
- [201] S. Penco, S. Scarfi, M. Giovine, G. Damonte, E. Millo, B. Villaggio, M. Passalacqua, M. Pozzolini, C. Garré, U. Benatti, Identification of an import signal for, and the nuclear localization of, human lactoferrin, *Biotechnol. Appl. Biochem.* 34 (3) (2001) 151–159.



- [202] L. Håversen, B.G. Ohlsson, M. Hahn-Zoric, L.A. Hanson, I. Mattsby-Baltzer, Lactoferrin down-regulates the LPS-induced cytokine production in monocytic cells via NF-kappa B, *Cell. Immunol.* 220 (2) (2002) 83–95.
- [203] J. Rybaczuk, D. Khalek, E. Kieckens, A.G. Skirtach, E. Cox, D. Vanrompay, Lactoferrin translocates to the nucleus of bovine rectal epithelial cells in the presence of *Escherichia coli* O157:H7, *Vet. Res.* 50 (1) (2019) 75.
- [204] B.R. Liu, Y.W. Huang, R.S. Aronstam, H.J. Lee, Identification of a short cell-penetrating peptide from bovine lactoferrin for intracellular delivery of DNA in human A549 cells, *PLoS One* 11 (3) (2016), e0150439.
- [205] K. Ashida, H. Sasaki, Y.A. Suzuki, B. Lönnnerdal, Cellular internalization of lactoferrin in intestinal epithelial cells, *Biomaterials: an international journal on the role of metal ions in biology, biochemistry, and medicine* 17 (3) (2004) 311–315.
- [206] P. Puddu, P. Valenti, S. Gessani, Immunomodulatory effects of lactoferrin on antigen presenting cells, *Biochimie* 91 (1) (2009) 11–18.
- [207] D. Legrand, E. Ellass, M. Carpentier, J. Mazurier, Lactoferrin: a modulator of immune and inflammatory responses, *Cell. Mol. Life Sci.* : CMLS 62 (22) (2005) 2549–2559.
- [208] H. Debbabi, M. Dabarry, M. Rautureau, D. Tomé, Bovine lactoferrin induces both mucosal and systemic immune response in mice, *J. Dairy Res.* 65 (2) (1998) 283–293.
- [209] S.S. Comstock, E.A. Reznikov, N. Contractor, S.M. Donovan, Dietary bovine lactoferrin alters mucosal and systemic immune cell responses in neonatal piglets, *J. Nutr.* 144 (4) (2014) 525–532.
- [210] A.M. Mulder, P.A. Connellan, C.J. Oliver, C.A. Morris, L.M. Stevenson, Bovine lactoferrin supplementation supports immune and antioxidant status in healthy human males, *Nutr. Res. (N.Y.)* 28 (9) (2008) 583–589.
- [211] I. Kurose, T. Yamada, R. Wolf, D.N. Granger, P-selectin-dependent leukocyte recruitment and intestinal mucosal injury induced by lactoferrin, *J. Leukoc. Biol.* 55 (6) (1994) 771–777.
- [212] A. Szuster-Ciesielska, T. Kaminska, M. Kandefer-Szerszen, Phagocytosis-enhancing effect of lactoferrin on bovine peripheral blood monocytes in vitro and in vivo, *Arch. Vet. Pol.* 35 (1–2) (1995) 63–71.
- [213] Z. Karami, M.R. Saghati, Z. Jazani, S. Rezaee, K. Rostamizadeh, M. Hamidi, Neuropharmacokinetic evaluation of lactoferrin-treated indinavir-loaded nanoemulsions: remarkable brain delivery enhancement, *Drug Dev. Ind. Pharm.* 45 (5) (2019) 736–744.
- [214] P. Kumar, Y.S. Lakshmi, B. C. K. Golla, A.K. Kondapi, Improved safety, bioavailability and pharmacokinetics of zidovudine through lactoferrin nanoparticles during oral administration in rats, *PLoS One* 10 (10) (2015), e0140399.
- [215] Y.S. Lakshmi, P. Kumar, G. Kishore, C. Bhaskar, A.K. Kondapi, Triple combination MPT vaginal microbicide using curcumin and efavirenz loaded lactoferrin nanoparticles, *Sci. Rep.* 6 (2016) 25479.
- [216] P. Kumar, Y.S. Lakshmi, A.K. Kondapi, Triple drug combination of zidovudine, efavirenz and lamivudine loaded lactoferrin nanoparticles: an effective nano first-line regimen for HIV therapy, *Pharm. Res. (N. Y.)* 34 (2) (2017) 257–268.
- [217] Q. Li, J. Zhao, W. Hu, J. Wang, T. Yu, Y. Dai, N. Li, Effects of recombinant human lactoferrin on osteoblast growth and bone status in piglets, *Anim. Biotechnol.* 29 (2) (2018) 90–99.
- [218] A.A. Amini, L.S. Nair, Recombinant human lactoferrin as a biomaterial for bone tissue engineering: mechanism of antiapoptotic and osteogenic activity, *Advanced healthcare materials* 3 (6) (2014) 897–905.
- [219] A.A. Amini, H.M. Kan, Z. Cui, P. Maye, L.S. Nair, Enzymatically cross-linked bovine lactoferrin as injectable hydrogel for cell delivery, *Tissue Eng.* 20 (21–22) (2014) 2830–2839.
- [220] Y. Li, W. Zhang, F. Ren, H. Guo, Activation of TGF-beta canonical and noncanonical signaling in bovine lactoferrin-induced osteogenic activity of C3H10T1/2 mesenchymal stem cells, *Int. J. Mol. Sci.* 20 (12) (2019).
- [221] M. Montesi, S. Panseri, M. Iafisco, A. Adamiano, A. Tampieri, Effect of hydroxyapatite nanocrystals functionalized with lactoferrin in osteogenic differentiation of mesenchymal stem cells, *J. Biomed. Mater. Res.* 103 (1) (2015) 224–234.
- [222] M. Montesi, S. Panseri, M. Iafisco, A. Adamiano, A. Tampieri, Coupling hydroxyapatite nanocrystals with lactoferrin as a promising strategy to fine regulate bone homeostasis, *PLoS One* 10 (7) (2015), e0132633.
- [223] K.B. Knudsen, H. Northved, P.E. Kumar, A. Permin, T. Gjetting, T.L. Andresen, S. Larsen, K.M. Wegener, J. Lykkesfeldt, K. Jantzen, S. Loft, P. Møller, M. Roursgaard, In vivo toxicity of cationic micelles and liposomes, *Nanomed. Nanotechnol. Biol. Med.* 11 (2) (2015) 467–477.
- [224] E. Blanco, H. Shen, M. Ferrari, Principles of nanoparticle design for overcoming biological barriers to drug delivery, *Nat. Biotechnol.* 33 (9) (2015) 941–951.
- [225] X. Wei, B. Shao, Z. He, T. Ye, M. Luo, Y. Sang, X. Liang, W. Wang, S. Luo, S. Yang, S. Zhang, C. Gong, M. Gou, H. Deng, Y. Zhao, H. Yang, S. Deng, C. Zhao, L. Yang, Z. Qian, J. Li, X. Sun, J. Han, C. Jiang, M. Wu, Z. Zhang, Cationic nanocarriers induce cell necrosis through impairment of Na<sup>+</sup>/K<sup>+</sup>-ATPase and cause subsequent inflammatory response, *Cell Res.* 25 (2) (2015) 237–253.
- [226] T. Takeuchi, T. Jyonotsuka, N. Kamemori, G. Kawano, H. Shimizu, K. Ando, E. Harada, Enteric-formulated lactoferrin was more effectively transported into blood circulation from gastrointestinal tract in adult rats, *Exp. Physiol.* 91 (6) (2006) 1033–1040.
- [227] P. Manzoni, M. Rinaldi, S. Cattani, L. Pagni, M.G. Romeo, H. Messner, I. Stolfi, L. Decembrino, N. Laforgia, F. Vagnarelli, L. Memo, L. Bordignon, O.S. Saia, M. Maule, E. Gallo, M. Mostert, C. Magnani, M. Quercia, L. Bollani, R. Pedicino, L. Renzullo, P. Betta, F. Mosca, F. Ferrari, R. Magaldi, M. Stronati, D. Farina, S. For the Italian task force for the, t.I.S.o.N. Prevention of neonatal fungal infections, bovine lactoferrin supplementation for prevention of late-onset sepsis in very low-birth-weight neonates: a randomized trial, *J. Am. Med. Assoc.* 302 (13) (2009) 1421–1428.
- [228] P. Manzoni, I. Stolfi, H. Messner, S. Cattani, N. Laforgia, M.G. Romeo, L. Bollani, M. Rinaldi, E. Gallo, M. Quercia, M. Maule, M. Mostert, L. Decembrino, R. Magaldi, F. Mosca, F. Vagnarelli, L. Memo, P.M. Betta, M. Stronati, D. Farina, Bovine lactoferrin prevents invasive fungal infections in very low birth weight infants: a randomized controlled trial, *Pediatrics* 129 (1) (2012) 116.
- [229] M. A. Agency Response Letter GRAS Notice No. GRN 000611 | FDA, WWW Document, <https://www.fda.gov/food/gras-notice-inventory/agency-response-letter-gras-notice-no-grn-000611>, 2016. (Accessed 28 September 2019).
- [230] H.D. Solomons, Talactoferrin, *Germs* 2 (3) (2012) 121.
- [231] C. Conesa, M. Calvo, L. Sánchez, Recombinant human lactoferrin: a valuable protein for pharmaceutical products and functional foods, *Biotechnol. Adv.* 28 (6) (2010) 831–838.
- [232] M. Spadaro, C. Curcio, A. Varadhachary, F. Cavallo, J. Engelmayr, P. Blezinger, F. Pericle, G. Forni, Requirement for IFN-gamma, CD8+ T lymphocytes, and NKT cells in talactoferrin-induced inhibition of neu+ tumors, *Canc. Res.* 67 (13) (2007) 6425–6432.
- [233] R. Jiang, X. Du, B. Lonnerdal, Comparison of bioactivities of talactoferrin and lactoferrins from human and bovine milk, *J. Pediatr. Gastroenterol. Nutr.* 59 (5) (2014) 642–652.
- [234] W. Bellamy, M. Takase, H. Wakabayashi, K. Kawase, M. Tomita, Antibacterial spectrum of lactoferricin B, a potent bactericidal peptide derived from the N-terminal region of bovine lactoferrin, *J. Appl. Bacteriol.* 73 (6) (1992) 472–479.
- [235] H.W. Liao, C. Garriss, C. Pfirsche, S. Rickelt, S. Arlauckas, M. Siwicki, R. H. Kohler, R. Weissleder, V. Sundvold-Gjerstad, B. Sveinbjornsson, O. Rekdal, M. J. Pittet, LTX-315 sequentially promotes lymphocyte-independent and lymphocyte-dependent antitumor effects, *Cell Stress* 3 (11) (2019) 348–360.
- [236] K.A. Camilio, M.Y. Wang, B. Mauseth, S. Waagene, G. Kvalheim, O. Rekdal, B. Sveinbjornsson, G.M. Maelandsmo, Combining the oncolytic peptide LTX-315 with doxorubicin demonstrates therapeutic potential in a triple-negative breast cancer model, *Breast Cancer Res.* 21 (1) (2019) 9.
- [237] H. Zhou, S. Forveille, A. Sauvat, V. Sica, V. Izzo, S. Durand, K. Müller, P. Liu, L. Zitvogel, Ø. Rekdal, O. Kepp, G. Kroemer, The oncolytic peptide LTX-315 kills cancer cells through Bax/Bak-regulated mitochondrial membrane permeabilization, *Oncotarget* 6 (29) (2015) 26599–26614.

## Article

# Phytochemical Investigation and Anti-Inflammatory Activity of the Leaves of *Machilus japonica* var. *kusanoi*

Shiou-Ling Li <sup>1,2</sup>, Ho-Cheng Wu <sup>2</sup>, Tsong-Long Hwang <sup>3,4,5</sup> , Chu-Hung Lin <sup>6</sup>,  
Shuen-Shin Yang <sup>1</sup> and Hsun-Shuo Chang <sup>1,2,7,8,\*</sup> 

<sup>1</sup> School of Pharmacy, College of Pharmacy, Kaohsiung Medical University, Kaohsiung 807, Taiwan; shioulingli1211@gmail.com (S.-L.L.); cindy828204@gmail.com (S.-S.Y.)

<sup>2</sup> Graduate Institute of Natural Products, College of Pharmacy, Kaohsiung Medical University, Kaohsiung 807, Taiwan; duncanwu762001@gmail.com

<sup>3</sup> Graduate Institute of Natural Products, College of Medicine, Chang Gung University, Taoyuan 333, Taiwan; htl@mail.cgu.edu.tw

<sup>4</sup> Research Center for Industry of Human Ecology, Research Center for Chinese Herbal Medicine, and Graduate Institute of Health Industry Technology, College of Human Ecology, Chang Gung University of Science and Technology, Taoyuan 333, Taiwan

<sup>5</sup> Department of Anesthesiology, Chang Gung Memorial Hospital, Taoyuan 333, Taiwan

<sup>6</sup> Botanical Drug Technology Division, Biomedical Technology and Device Research Laboratories, Industrial Technology Research Institute, Hsinchu 300, Taiwan; chuhung.lin@gmail.com

<sup>7</sup> Drug Development and Value Creation Research Center, Kaohsiung Medical University, Kaohsiung 807, Taiwan

<sup>8</sup> Department of Medical Research, Kaohsiung Medical University Hospital, Kaohsiung 807, Taiwan

\* Correspondence: hschang@kmu.edu.tw; Tel.: +886-7-312-1101 (ext. 2664)

Academic Editors: Lars P. Christensen and Derek J. McPhee

Received: 17 August 2020; Accepted: 5 September 2020; Published: 10 September 2020



**Abstract:** In a series of anti-inflammatory screenings of lauraceous plants, the methanolic extract of the leaves of *Machilus japonica* var. *kusanoi* (Hayata) J.C. Liao showed potent inhibition on both superoxide anion generation and elastase release in human neutrophils. Bioassay-guided fractionation of the leaves of *M. japonica* var. *kusanoi* led to the isolation of twenty compounds, including six new butanolides, machinolides A–F (**1**–**6**), and fourteen known compounds (**7**–**20**). Their structures were characterized by 1D and 2D NMR, UV, IR, CD, and MS data. The absolute configuration of the new compounds were unambiguously confirmed by single-crystal X-ray diffraction analyses (**1**, **2**, and **3**) and Mosher's method (**4**, **5**, and **6**). In addition, lignans, (+)-eudesmin (**11**), (+)-methylpiperitol (**12**), (+)-pinoselinol (**13**), and (+)-galbelgin (**16**) exhibited inhibitory effects on *N*-formyl-methionyl-leucyl-phenylalanine/cytochalasin B (fMLP/CB)-induced superoxide anion generation in human neutrophils with IC<sub>50</sub> values of 8.71 ± 0.74 μM, 2.23 ± 0.92 μM, 6.81 ± 1.07 μM, and 7.15 ± 2.26 μM, respectively. The results revealed the anti-inflammatory potentials of Formosan *Machilus japonica* var. *kusanoi*.

**Keywords:** *Machilus japonica* var. *kusanoi*; lauraceae; butanolide; lignan; anti-inflammatory activity

## 1. Introduction

Neutrophils play an important role in the human body against infections [1]. In response to immune stimulation, activated neutrophils generate a series of cytotoxic substances, such as the superoxide anion (O<sub>2</sub><sup>•−</sup>), a precursor of other ROS, granule proteases, and bioactive lipids. The superoxide anion is known to cause damage to cells and tissues, stimulate macrophages, and trigger a cascade of inflammatory pathways [2]. Neutrophil elastase is one of the serine proteases stored in large amounts in neutrophil granules and is involved in the nonoxidative pathway of the intracellular



and extracellular immune response [3]. Neutrophil elastase is stimulated by neutrophils and causes the destruction of tissue in chronic inflammatory disease [2]. Besides, the persistent overexpression of neutrophils is involved in various conditions, such as rheumatoid arthritis, asthma, psoriasis, and ischemic heart disease.

Lauraceous plants are a dominant family in South and East Asia, consisting of aromatic trees and shrubs. They stand out, resulting in its economic benefits and diverse bioactivities. A previous investigation showed that some lauraceous plants exhibit bioactivities, such as cytotoxicity, anti-tuberculosis, anti-inflammatory, and antiplatelet activities [4]. Recently, we completed the anti-inflammatory screening of 174 methanolic extracts from 60 Taiwanese lauraceous plants. Among the screening results, the methanolic extract of the leaves of *Machilus japonica* var. *kusanoi* showed potent anti-inflammatory activity on both superoxide anion generation and elastase release in human neutrophils.

The *Machilus* genus comprises about 100 species with accepted names, mainly distributed in East Asia [5]. Previous studies of *Machilus* species identified various classes of chemical constituents, such as lignans, flavonoids, and terpenoids [4]. *M. japonica* var. *kusanoi* is a large evergreen tree endemic to Taiwan and is distributed in broad-leaved forests from lowlands up to 1400 m throughout the island [5]. Few investigations of *M. japonica* var. *kusanoi* have been published before. Only ten compounds were isolated from this plant [6–8], and only antimicrobial along with anti- $\alpha$ -glucosidase activity of this plant have been found previously [8,9]. Based on anti-inflammatory screening results and the rare investigation of the leaves from *M. japonica* var. *kusanoi*, the aims of this study are the isolation of components from the leaves of *M. japonica* var. *kusanoi* and the evaluation of their anti-inflammatory effects.

## 2. Results

After anti-inflammatory assay-guided fractionation of the leaves of *M. japonica* var. *kusanoi*, we successfully isolated six new butanolides (1–6) (Figure 1) and 14 known compounds (7–20) (Supplementary Materials, Figure S1). The phytochemical spectra of compounds 1 to 6 are available in the Supplementary Materials, Figures S2–S57. In particular, Mosher's method and X-ray crystallographic analysis were applied to determine the absolute configuration of the new compounds. Moreover, anti-inflammatory effects of isolates on neutrophil pro-inflammatory responses were evaluated by the suppression of *N*-formyl-methionyl-leucyl-phenylalanine/cytochalasin B (fMLP/CB)-induced superoxide anion ( $O_2^{\bullet-}$ ) generation and elastase release. The structure identification of the new compounds and anti-inflammatory activity results are illustrated below.

Compound 1 was obtained as colorless needles. Its molecular formula was determined as  $C_{15}H_{28}O_4$  from high-resolution electrospray ionization mass spectroscopy (HRESIMS) data ( $m/z$  295.18923 [ $M + Na$ ] $^+$  (calcd. for 295.18853)), implying two degrees of unsaturation. The infrared spectroscopy (IR) spectrum showed typical absorptions of  $C=O$  ( $1736\text{ cm}^{-1}$ ) for  $\gamma$ -lactone and hydroxy groups ( $3433\text{ cm}^{-1}$ ). The  $^1H$ -NMR spectrum of 1 displayed signals of three oxymethines at  $\delta_H$  3.59 (1H, m, H-11), 4.45 (1H, qd,  $J = 6.6, 3.2\text{ Hz}$ , H-4), and 4.31 (1H, dd,  $J = 4.8, 3.2\text{ Hz}$ , H-3), two methyl groups including one doublet methyl group at  $\delta_H$  1.43 (3H, d,  $J = 6.6\text{ Hz}$ , H-5) and one triplet methyl group at  $\delta_H$  0.91 (3H, t,  $J = 7.0\text{ Hz}$ , H-15), and alkyl side chains at  $\delta_H$  1.66 (1H, m, H-6b),  $\delta_H$  1.82 (1H, m, H-6a), and  $\delta_H$  1.26–1.47 (14H, m, H-7–H-10, H-12–H-14) (Table 1). The  $\gamma$ -lactone was confirmed by IR spectrum, the  $^1H$ - $^1H$  correlation spectroscopy (COSY) correlations between H-2/H-3/H-4/H-5 and the heteronuclear multiple bond correlation (HMBC) between H-2/C-1 ( $\delta$  177.5), C-3 ( $\delta$  71.2), H-3/C-1, and H-4/C-3 (Figure 2). The doublet methyl group (C-5) was connected to C-4, based on the COSY correlations between H-5/H-4, and HMBC correlations between H-5/C-3, C-4 ( $\delta$  78.8) (Figure 2). The HMBC showed correlations H-6/C-2 ( $\delta$  47.6), C-3, C-7 ( $\delta$  27.5), and C-8 ( $\delta$  29.4), which supported that the alkyl chain was located at C-2 (Figure 2). The key correlations in the nuclear Overhauser enhancement spectroscopy (NOESY) spectrum (H-2 showed correlation with H-3, H-4, and no correlation with H-5; H-3 showed correlation with H-4 and no correlation with H-5)

confirmed that H-2, H-3, and H-4 were in the same phase (Figure 3). However, a remaining hydroxy group ( $\delta_C$  71.9) was located at a position of the alkyl chain which cannot be determined by NMR spectrum. Finally, the location of the remaining hydroxy group and the absolute configuration of **1** was further confirmed by single-crystal X-ray diffraction (Figure 4). The results proved that the stereochemistry of **1** should be shown as 2*R*,3*S*,4*S*,11*R*-form in the Oak Ridge thermal ellipsoid plot program (ORTEP) diagram. Thus, compound **1** was elucidated and named machinolide A.

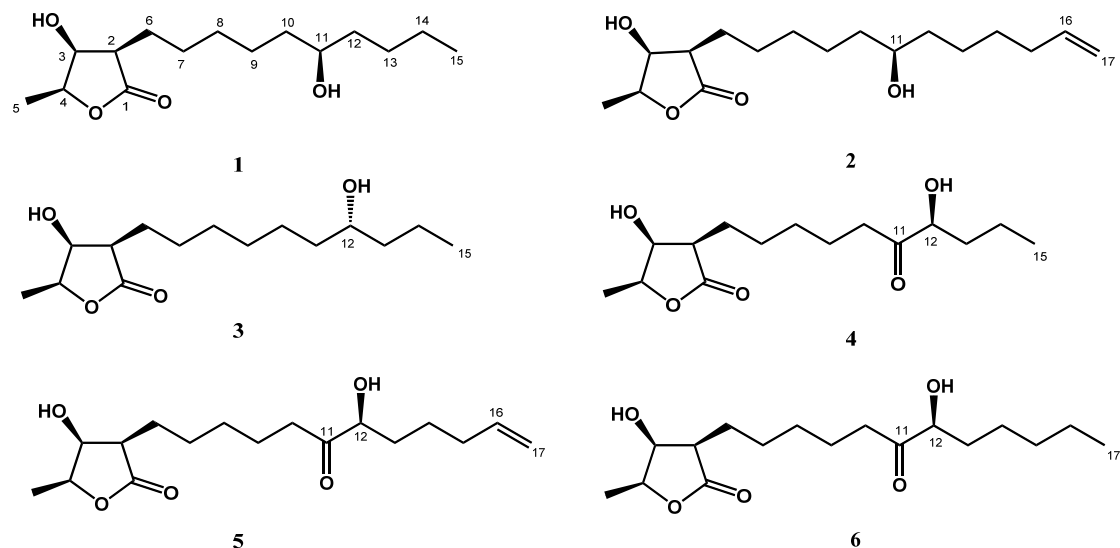


Figure 1. Structures of new compounds 1–6.

Table 1.  $^1\text{H}$  and  $^{13}\text{C}$ -NMR data of machinolides A–C (1–3).

Position	1 <sup>a</sup>		2 <sup>b</sup>		3 <sup>b</sup>	
	$\delta_{\text{H}}$ (m, <i>J</i> in Hz)	$\delta_{\text{C}}$	$\delta_{\text{H}}$ (m, <i>J</i> in Hz)	$\delta_{\text{C}}$	$\delta_{\text{H}}$ (m, <i>J</i> in Hz)	$\delta_{\text{C}}$
1		177.5		177.4		177.4
2	2.57, dt (9.8, 4.8)	47.6	2.57, dt (10.2, 4.6)	47.6	2.57, dt (8.7, 4.8)	47.6
3	4.31, dd (4.8, 3.2)	71.2	4.31, dd (4.6, 3.2)	71.3	4.31, dd (4.8, 3.2)	71.3
4	4.45, qd, (6.6, 3.2)	78.8	4.45, qd (6.6, 3.2)	78.7	4.45, qd (6.6, 3.2)	78.7
5	1.43, d (6.6)	13.7	1.44, d (6.6)	13.7	1.44, d (6.6)	13.7
6	1.82, m	23.1	1.84, m	23.2	1.84, m	23.3
	1.66, m		1.67, m		1.65, m	
7	1.26~1.47, m	27.5	1.32~1.51, m	27.6	1.30~1.49, m	27.5
8	1.26~1.47, m	29.4	1.32~1.51, m	29.4	1.30~1.49, m	29.3 <sup>c</sup>
9	1.26~1.47, m	25.1	1.32~1.51, m	25.1 <sup>c</sup>	1.30~1.49, m	29.4 <sup>c</sup>
10	1.26~1.47, m	37.16 <sup>c</sup>	1.32~1.51, m	37.2 <sup>d</sup>	1.30~1.49, m	25.5
11	3.59, m	71.9	3.59, m	71.9	1.30~1.49, m	37.4
12	1.26~1.47, m	37.19 <sup>c</sup>	1.32~1.51, m	37.4 <sup>d</sup>	3.60, m	71.8
13	1.26~1.47, m	27.8	1.32~1.51, m	25.2 <sup>c</sup>	1.30~1.49, m	39.7
14	1.26~1.47, m	22.7	1.37, m	28.9	1.30~1.49, m	18.8
15	0.91, t (7.0)	14.0	2.07, m	33.7	0.93, t (7.2)	14.1
16			5.81, ddt (17.1, 10.2, 6.6)	138.9		
			5.00, ddt (17.1, 3.3, 1.5)			
17			4.94, ddt (10.2, 3.3, 1.5)	114.4		

<sup>a</sup>  $^1\text{H}$  (400 MHz,  $\text{CDCl}_3$ ) and  $^{13}\text{C}$ -NMR (100 MHz,  $\text{CDCl}_3$ ). <sup>b</sup>  $^1\text{H}$  (600 MHz,  $\text{CDCl}_3$ ) and  $^{13}\text{C}$ -NMR (150 MHz,  $\text{CDCl}_3$ ).

<sup>c,d</sup> the data in the same column are interchangeable.

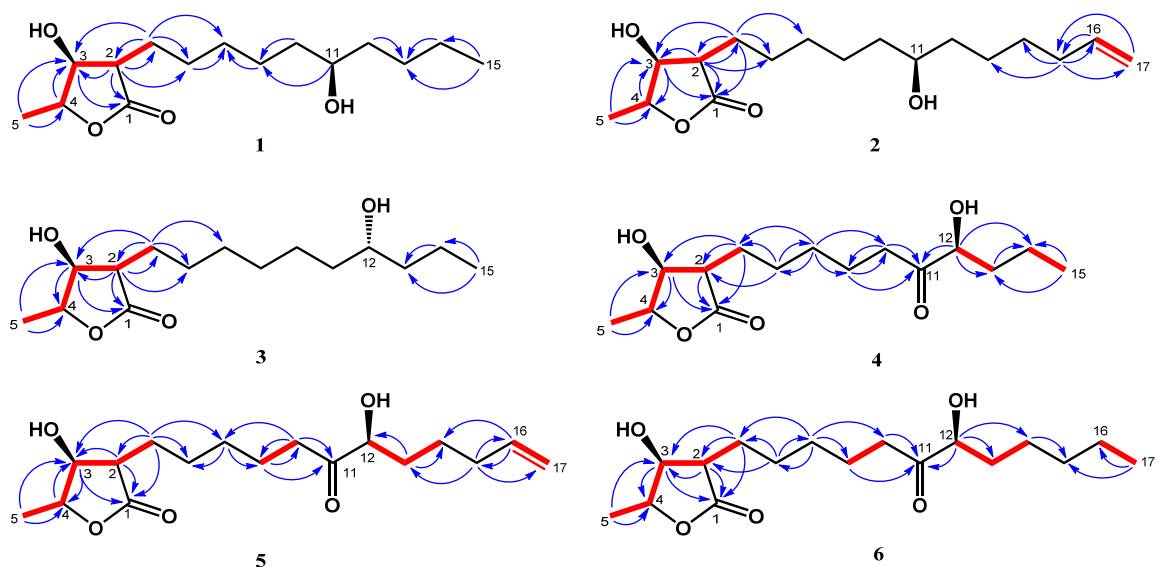


Figure 2. Key  $^1\text{H}$ - $^1\text{H}$  COSY (—) and HMBC (H→C) correlations of machinolides A–F (1–6).

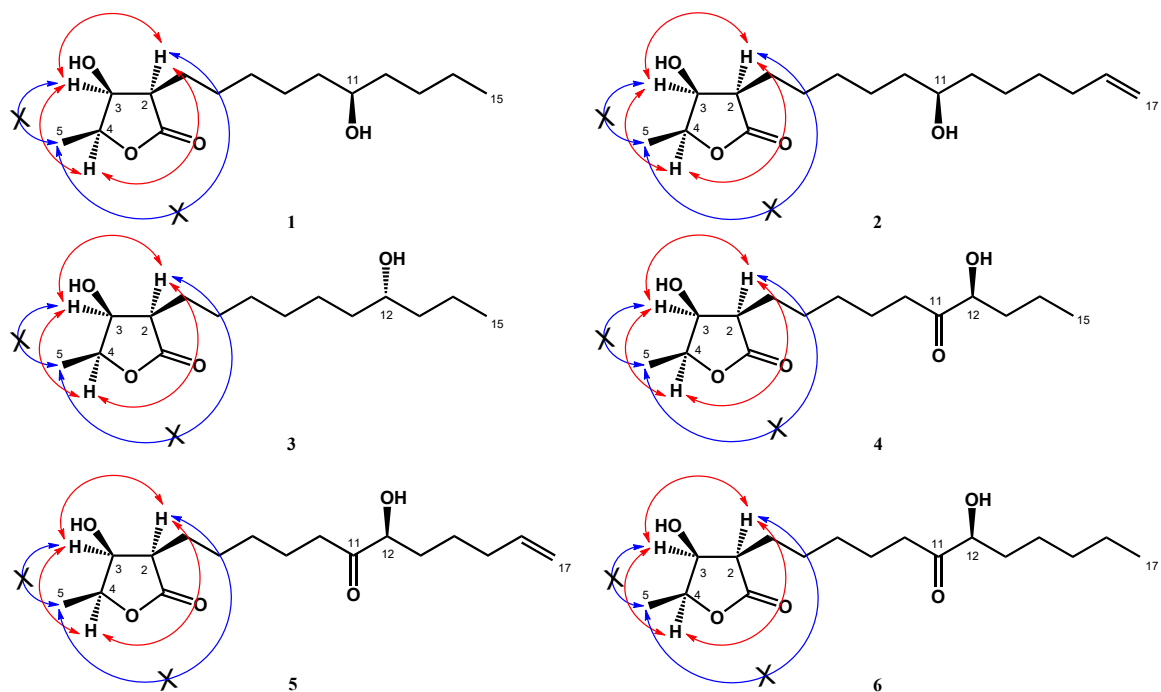


Figure 3. NOESY (H↔H) correlations of machinolides A–F (1–6).

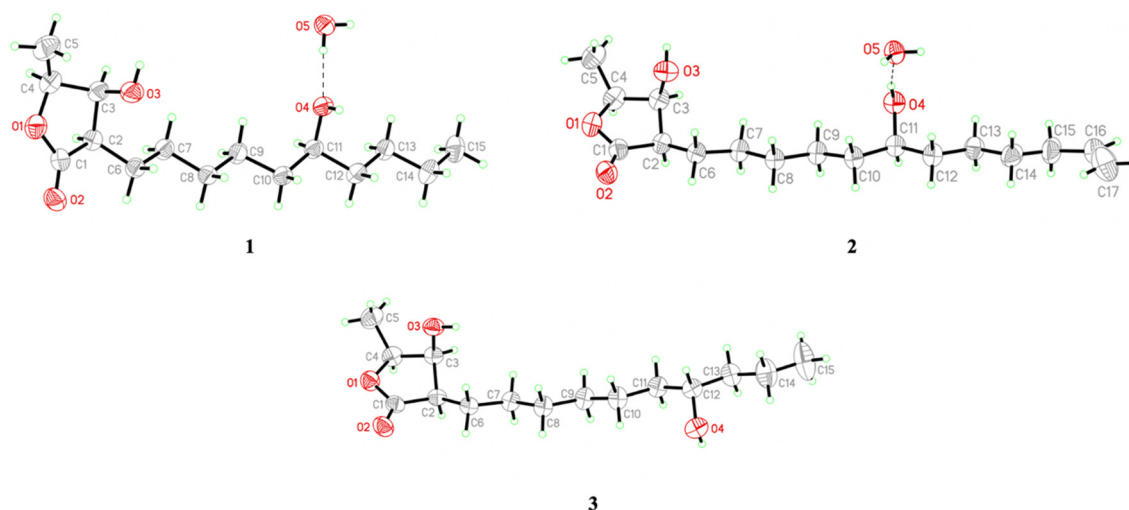


Figure 4. Perspective drawing of X-ray structures of machinolides A–C (1–3).

Compound **2** was isolated as colorless needles. Its molecular formula was established as  $C_{17}H_{30}O_4$  by HREIMS data ( $m/z$  321.20370  $[M + Na]^+$  (calcd. for 321.20363)). The  $^1H$ -NMR spectrum of **2** was similar to that of **1**, except for the presence of a terminal double bond at  $\delta_H$  5.81 (1H, ddt,  $J = 17.1, 10.2, 6.6$  Hz, H-16), 4.94 (1H, ddt,  $J = 10.2, 3.3, 1.5$  Hz, H-17b), and 5.00 (1H, ddt,  $J = 17.1, 3.3, 1.5$  Hz, H-17a) in **2** (Table 1). Comparison of  $^{13}C$ -NMR spectrum of **2** and **1** also supported the presence of a terminal double bond [ $\delta_C$  138.9 (C-16), 114.4 (C-17)] in **2**. The HMBC correlations between H-15/C-16, C-17 and H-16, H-17/C-15 ( $\delta$  33.7) were further confirmed that the terminal double bond was located at C-16 and C-17 (Figure 2). The NOESY correlations of **2** were similar to those of **1**, indicating that H-2, H-3 and H-4 were in the same phase in **2** (Figure 3). The absolute configuration of **2** was confirmed by single-crystal X-ray diffraction and assigned as 2*R*,3*S*,4*S*,11*S*-form (Figure 4). According to the above data, the structure of **2** was determined and named machinolide B.

Compound **3** was yielded as colorless needles and assigned the molecular formula  $C_{15}H_{28}O_4$  through analysis of its HRESIMS data ( $m/z$  273.20656  $[M + H]^+$  (calcd. for 273.20658)). All the spectra of **3** were similar to those of **1**. However, electron ionization mass spectra (EIMS) showed the different fragments between **3** ( $m/z$  215 (56), 186 (37)) and **1** ( $m/z$  229 (39), 200 (24)), which suggests that the position of the hydroxy group in the alkyl chain was different. The hydroxy group of **3** was located at C-12 and the absolute configuration of **3** was assigned as 2*R*,3*S*,4*S*,12*R*-form, which were both determined by single-crystal X-ray diffraction (Figure 4). Therefore, compound **3** was named machinolide C, and its structure was further confirmed by COSY and HMBC experiments (Figure 2).

Compound **4** was obtained as a colorless oil. The ESIMS analysis of **4** showed the  $[M+H]^+$  ion at  $m/z$  287, in agreement with the molecular formula of  $C_{15}H_{26}O_5$ , as confirmed by HRESIMS. Compound **4** had similar IR and  $^1H$ -NMR spectra to those of **3**, except for the presence of a ketone group at C-11 ( $\delta$  212.6) in the  $^{13}C$ -NMR spectrum (Table 2). The HMBC correlation between H-9, H-10, H-12/C-11, and H-12/C-11, C-13, C-14 supported the position of the ketone group and hydroxy group at C-11 and C-12, respectively (Figure 2). The planar structure of **4** was decided. The CD spectrum of **4** showed a negative cotton effect at 219.5 nm, which was similar to malleastrumolide A [10]. Thus, the absolute configuration of C-2 was determined as *R*-form. The NOESY correlations between H-2/H-3, H-2/H-4, and H-3/H-4 confirmed that H-2, H-3, and H-4 were in the same phase (Figure 3). Hence, the absolute configuration of **4** was determined as 2*R*,3*S*,4*S*-form. Based on the  $^{13}C$ -NMR-based empirical rules, the chemical shifts of C-3 and C-4 in **4** were similar to those of 2*R*,3*S*,4*S*-form compounds in the literature [11]. According to these two pieces of evidence, the absolute configuration of C-2, C-3, and C-4 in **4** was established to be 2*R*,3*S*,4*S*-form. The absolute configuration of C-12 was determined by Mosher's method [12]. Based on the  $\Delta\delta$  values of the (*S*)-MTPA and

(*R*)-MTPA esters in chloroform-*d*<sub>1</sub>, the absolute configuration of C-12 was established as *S*-form (Figure 5). Accordingly, the absolute configuration of **4** was defined as 2*R*,3*S*,4*S*,12*S*. The structure of **4** was confirmed and named machinolide D.

**Table 2.** <sup>1</sup>H and <sup>13</sup>C-NMR data of machinolides D–F (**4**–**6**).

Position	<b>4</b> <sup>a</sup>		<b>5</b> <sup>b</sup>		<b>6</b> <sup>b</sup>	
	δ <sub>H</sub> (m, <i>J</i> in Hz)	δ <sub>C</sub>	δ <sub>H</sub> (m, <i>J</i> in Hz)	δ <sub>C</sub>	δ <sub>H</sub> (m, <i>J</i> in Hz)	δ <sub>C</sub>
<b>1</b>		177.4		177.3		177.7
<b>2</b>	2.55, dt (9.9, 5.0)	47.5	2.56, dt (9.8, 4.5)	47.5	2.54, dt (10.0, 5.0)	47.5
<b>3</b>	4.31, dd (5.0, 3.0)	71.3	4.30, br t (4.5)	71.3	4.30, dd (5.0, 3.1)	71.1
<b>4</b>	4.45, qd (6.5, 3.0)	78.8	4.54, qd (6.4, 2.9)	78.7	4.44, qd (6.0, 3.1)	79.0
<b>5</b>	1.44, d (6.5)	13.7	1.44, d (6.4)	13.7	1.42, d (6.0)	13.7
<b>6</b>	1.80, m	23.1	1.84, m	23.1	1.79, m	23.1
	1.67, m		1.67, m		1.64, m	
<b>7</b>	1.35~1.55, m	27.4	1.33~1.58, m	27.4	1.24~1.52, m	27.3
<b>8</b>	1.35~1.55, m	29.0	1.33~1.58, m	29.0	1.24~1.52, m	29.0
<b>9</b>	1.67, m	23.2	1.67, m	23.2	1.64, m	23.2
<b>10</b>	2.40~2.54, m	37.7	2.46, m	37.7	2.46, m	37.7
<b>11</b>		212.6		212.4		212.7
<b>12</b>	4.17, dd (7.5, 3.9)	76.3	4.17, dd (7.2, 3.6)	76.3	4.15, dd (7.4, 3.8)	76.5
<b>13</b>	1.35~1.55, m	35.9	1.84, m	33.1	1.79, m	33.7
			1.33~1.58, m		1.24~1.52, m	
<b>14</b>	1.35~1.55, m	18.2	1.33~1.58, m	24.0	1.24~1.52, m	24.5
<b>15</b>	0.95, t (6.9)	13.9	2.09, m	33.3	1.24~1.52, m	31.6
<b>16</b>			5.78, ddt (17.2, 10.4, 6.8)	138.1	1.24~1.52, m	22.5
			5.03, m			
<b>17</b>			4.98, m	115.1	0.88, t (6.8)	14.0

<sup>a</sup> <sup>1</sup>H (600 MHz, CDCl<sub>3</sub>) and <sup>13</sup>C-NMR (150 MHz, CDCl<sub>3</sub>). <sup>b</sup> <sup>1</sup>H (400 MHz, CDCl<sub>3</sub>) and <sup>13</sup>C-NMR (100 MHz, CDCl<sub>3</sub>).

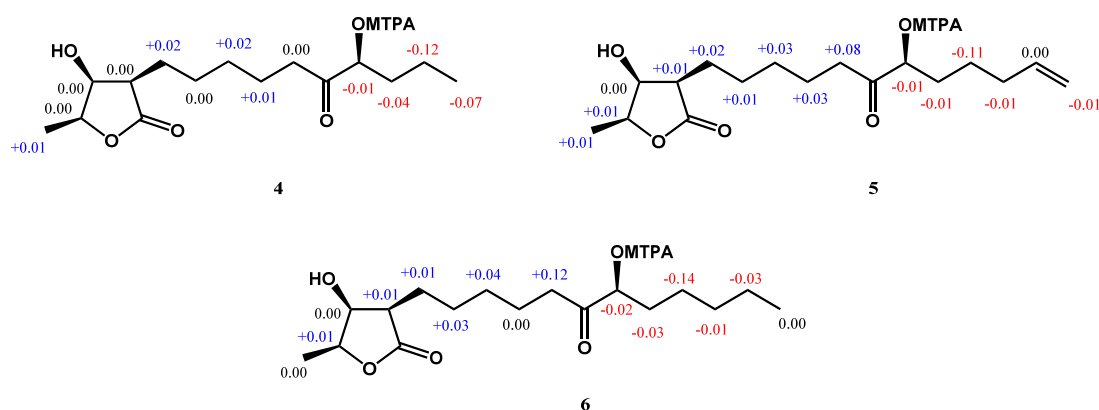


**Figure 5.** Results with the modified Mosher's method ( $\Delta\delta_{S-R}$ ) of machinolides D–F (**4**–**6**).

Compound **5** was isolated as a colorless oil. The ESIMS ( $m/z$  313 [ $M + H$ ]<sup>+</sup>) and HRESIMS ( $m/z$  335.18295 [ $M + Na$ ]<sup>+</sup> (calcd. for 335.18290)) data were used to establish the molecular formula of compound **5** as C<sub>17</sub>H<sub>28</sub>O<sub>5</sub>. The <sup>1</sup>H-NMR spectrum of **5** was similar to that of **4**, except for the presence of a terminal double bond at δ<sub>H</sub> 5.78 (1H, ddt, *J* = 17.2, 10.4, 6.8 Hz, H-16), 4.98 (1H, m, H-17b), and 5.03 (1H, m, H-17a) in **4** (Table 2). The HMBC correlation between H-15/C-16, C-17, H-16/C-15, and the COSY correlation between H-16/H-17 supports the presence of a terminal double bond (Figure 2). The CD spectrum (a negative cotton effect at 217.5 nm) and NOESY correlation (Figure 3) of **5** were also similar to **4**. Moreover, in accordance with the <sup>13</sup>C-NMR-based empirical rules [11], the chemical shifts of C-3 and C-4 in **5** were similar to those of 2*R*,3*S*,4*S*-form compounds in the previous data [11], showing that the absolute configuration of **6** was 2*R*,3*S*,4*S*-form. The absolute configuration of C-12



in **5** was established as *S*-form by Mosher's method (Figure 5). On the basis of the above results, the structure and absolute configuration of **5** were determined and named machinolide E.

Compound **6** was purified as a colorless oil. Its molecular formula of  $C_{17}H_{30}O_5$ , two protons more than **5**, was determined by EIMS ( $m/z$  315  $[M + H]^+$ ) and HRESIMS  $m/z$  337.19849  $[M + Na]^+$  (calcd. for 337.19855). The difference between **6** and **5** is that the terminal double bond in **5** is replaced by the ethyl group in **6**. The HMBC correlations between H-17/C-15, C-16, and the COSY correlation between H-16/H-17 (Figure 2) also supported the presence of the ethyl group. The absolute configuration of **6** was elucidated as *2R,3S,4S,12S*-form by the CD spectrum, NOESY correlation, and Mosher's method. As determined by the above observations, the structure of **6** was elucidated as a new compound and named machinolide F.

By comparison of the experiments and reported spectroscopic data ( $[\alpha]_D$ , UV, IR, NMR, and MS), known compounds were identified as one apocarotenoid: blumenol A (**7**) [13], one benzenoid: amisbenzoic acid (**8**) [14], one chlorophyll: pheophytin a (**9**) [15], one coumarin: isofraxidin (**10**) [16], six lignans: (+)-eudesmin (**11**) [17], (+)-methylpiperitol (**12**) [18], (+)-pinosresinol (**13**) [19], (+)-syringaresinol (**14**) [20], (2*S,5S*)-diveratryl-(3*R,4S*)-dimethyltetrahydrofuran (**15**) [21], and (+)-galbelgin (**16**) [22], three sesquiterpenoids:  $\beta$ -eudesmol (**17**) [23], caryophyllene oxide (**18**), and clovane-2 $\alpha,9\beta$ -diol (**19**) [24], and one steroid:  $\beta$ -sitosterol (**20**) [25].

In this study, eight isolates present in sufficient amounts (**1**, **2**, **3**, **6**, **11–13**, and **16**) were evaluated for an inhibitory effect on fMLP/CB-induced superoxide anion ( $O_2^{\bullet-}$ ) generation and elastase release (Table 3). (+)-Eudesmin (**11**), (+)-methylpiperitol (**12**), (+)-pinosresinol (**13**), and (+)-galbelgin (**16**) displayed inhibitory activity on superoxide anions in fMLP/CB-stimulated human neutrophils with  $IC_{50}$  values of  $8.71 \pm 0.74 \mu M$ ,  $2.23 \pm 0.92 \mu M$ ,  $6.81 \pm 1.07 \mu M$ , and  $7.15 \pm 2.26 \mu M$ , respectively. LY294002 (Sigma-Aldrich), a potent phosphatidylinositol 3-kinase (PI3K) inhibitor, was used as a positive control to inhibit  $O_2^{\bullet-}$  generation and elastase release, with  $IC_{50}$  values of  $2.17 \pm 0.53$ , and  $6.38 \pm 1.72 \mu M$ , respectively.

**Table 3.** Effect of compounds on superoxide anion generation and elastase release in fMLP/CB-stimulated human neutrophils.

Compound	Superoxide Anion	Elastase Release
	$IC_{50}$ ( $\mu M$ ) <sup>a</sup>	$IC_{50}$ ( $\mu M$ ) <sup>a</sup>
machinolide A ( <b>1</b> )	>10	>10
machinolide B ( <b>2</b> )	>10	>10
machinolide C ( <b>3</b> )	>10	>10
machinolide F ( <b>6</b> )	>10	>10
(+)-eudesmin ( <b>11</b> )	$8.71 \pm 0.74$	>10
(+)-methylpiperitol ( <b>12</b> )	$2.23 \pm 0.92$	>10
(+)-pinosresinol ( <b>13</b> )	$6.81 \pm 1.07$	>10
(+)-galbelgin ( <b>16</b> )	$7.15 \pm 2.26$	>10
LY294002 <sup>b</sup>	$2.17 \pm 0.53$	$6.38 \pm 1.72$

<sup>a</sup> Concentration necessary for 50% inhibition ( $IC_{50}$ ). <sup>b</sup> Positive control.

### 3. Discussion

Inflammation is triggered by infection or tissue injury. In our series of anti-inflammatory screenings of lauraceous plants, the leaves of *M. japonica* var. *kusanoi* stand out as a research candidate. Focusing on the anti-inflammatory activity results in this paper, the lignans, (+)-eudesmin (**11**), (+)-methylpiperitol (**12**), (+)-pinosresinol (**13**), and (+)-galbelgin (**16**) exhibited inhibitory activities on superoxide anion generation. (+)-Methylpiperitol (**12**) showed better anti-inflammatory activity than (+)-eudesmin (**11**), suggesting the methylenedioxy group may enhance the anti-inflammatory activity. (+)-Methylpiperitol (**12**) exhibited similar anti-inflammatory activity as (+)-pinosresinol (**13**), indicating the replacement of the methoxy group may not influence anti-inflammatory activity. The results suggested that the

furofuran-type lignan containing a methylenedioxy group showed the best anti-inflammatory activity in this study. More importantly, this is the first report on the anti-inflammatory activity of *M. japonica* var. *kusanoi*.

Butanolides ( $\gamma$ -butyrolactones) are four-carbon heterocyclic lactone ring structures reported from some specific families (Myristicaceae [26], Meliaceae [10], Actinomycetes [27–31]), especially in Lauraceae plants (*Machilus* sp. [32–34], *Lindera* sp. [35,36], *Litsea* sp. [37], *Cinnamomum* sp. [38–40], *Persea* sp. [41]). The characteristic butanolides in Lauraceae plants contain an alkyl side chain group at C-2, a hydroxy group at C-3, and one methyl group at C-4, with or without a double bond between C-2/C-3 and C-2/C-6. In this report, six new compounds, machinolides A–F (1–6), were butanolide compounds without a double bond between C-2/C-3 or C-2/C-6. This type of butanolide has not been isolated from *Machilus* before, which might improve our understanding of secondary metabolites from *Machilus* species. The chemical results can contribute to the chemotaxonomy of *Machilus* species.

Although the potency of the lignans exhibiting anti-inflammatory activity in this study was similar to bioactive lignans described in the literature [42], it is worth noting that most of the lignans with anti-inflammatory activity in this study have not been reported previously. Besides, there are no anti-inflammatory medicines act via inhibiting superoxide anion and neutrophil elastase. The research shows some lead compounds and will help develop novel anti-inflammatory drugs.

#### 4. Materials and Methods

##### 4.1. General Experiment Procedures

Optical rotations were measured on a Jasco P-2000 polarimeter (Jasco, Kyoto, Japan), and IR spectra (ATR) were acquired with a Jasco FT/IR-4600 spectrometer. We recorded 1D ( $^1\text{H}$ ,  $^{13}\text{C}$ , DEPT) and 2D (COSY, NOESY, HSQC, HMBC) NMR spectra on a Varian Germini-2000 spectrometer (Varian, Inc. Vacuum Technologies, Lexington, MA, USA) operated at 200 ( $^1\text{H}$ ) and 50 MHz ( $^{13}\text{C}$ ), a Varian Unityplus-400 spectrometer (Varian, Inc. Vacuum Technologies, Lexington, MA, USA) operated at 400 ( $^1\text{H}$ ) and 100 MHz ( $^{13}\text{C}$ ), a Varian Mercuryplus-400 spectrometer (Varian, Inc. Vacuum Technologies, Lexington, MA, USA) operated at 400 ( $^1\text{H}$ ) and 100 MHz ( $^{13}\text{C}$ ), and a Varian VNMRs-600 spectrometer (Varian, Inc. Vacuum Technologies, Lexington, MA, USA) operated at 600 ( $^1\text{H}$ ) and 150 MHz ( $^{13}\text{C}$ ). Low-resolution mass spectra were obtained with POLARIS Q Thermo Finnigan (Thermo Fisher Scientific, Chicago, IL, USA), Waters ZQ 4000 (Waters, Milford, MA, USA), and VG Quattro GC/MS/MS/DS (Waters, Milford, MA, USA) mass spectrometers. EIMS were taken on a JEOL JMS-700 mass spectrometer (JEOL, Tokyo, Japan). HRESIMS were recorded on a Bruker APEX II mass spectrometer (Bruker, Karlsruhe, Germany) and VARIAN 901-MS (Varian, CA, USA). Silica gel (70–230 and 230–400 mesh; Silicycle, QC, Canada) was used for column chromatography (CC), and silica gel 60 F254 (Merck, Darmstadt, Germany) and RP-18 F254S (Merck, Darmstadt, Germany) were used for thin layer chromatography (TLC) and preparative TLC, respectively, visualized with a  $\text{Ce}_2(\text{SO}_4)_3$  aqueous solution. Further purification was performed by medium-performance liquid chromatography (MPLC; ceramic pump: VSP-3050; EYELA, Kyoto, Japan).

##### 4.2. Plant Material

The leaves of *Machilus japonica* var. *kusanoi* (Hayata) J.C. Liao were collected in March 2018 in Mudan Township, Pingtung County, Taiwan, and identified by I.-S.C. A voucher specimen (Chen 5480) was deposited with the herbarium of the College of Pharmacy, Kaohsiung Medical University, Kaohsiung, Taiwan.

##### 4.3. Extraction and Isolation

Dried leaves (5.8 kg) of *M. japonica* var. *kusanoi* were extracted at room temperature with methanol (MeOH) (30 L) three times to yield a MeOH extract (730 g). The MeOH extract was suspended in water and partitioned with ethyl acetate (EtOAc) to give a water layer (265.4 g), EtOAc layer (390 g),

and precipitate (72 g). The EtOAc layer (390 g) was taken and 100 g were subjected to column chromatography (silica gel; *n*-hexane/EtOAc 100/0 to 0/100 EtOAc, then washed with 100% acetone and 100% methanol) to yield six fractions (Fr. 1–6). Fr. 3 (15.1 g) was subjected to open column (silica gel; *n*-hexane/acetone 6/1 to 2/1, column size: 3 × 70 cm) to yield 13 fractions (Fr.3-1–3-13). Fr. 3-9 was subjected to MPLC (RP-18; water/methanol 1:1; column size: 1.5 × 30 cm) to give seven fractions (Fr. 3-9-1–3-9-7). Fr. 3-9-1 was subjected to MPLC (silica gel; *n*-hexane/CH<sub>2</sub>Cl<sub>2</sub>/EtOAc 2/2/1 to 1/1/1; column size: 1 × 30 cm) to afford 14 fractions (Fr. 3-9-1-1–3-9-1-14) and compound 7 (30.5 mg). Fr. 3-9-1-11 was subjected to MPLC (silica gel; *n*-hexane/CH<sub>2</sub>Cl<sub>2</sub>/methanol 15/20/1; column size: 1 × 30 cm) to produce compound 6 (14.0 mg). Fr. 3-9-2 was subjected to MPLC (silica gel; *n*-hexane/CH<sub>2</sub>Cl<sub>2</sub>/EtOAc 2/2/1; column size: 1 × 30 cm) to obtain 10 fractions (Fr. 3-9-2-1–3-9-2-10). Fr. 3-9-2-9 was subjected to MPLC (silica gel; *n*-hexane/CH<sub>2</sub>Cl<sub>2</sub>/EtOAc 2/1/1; column size: 1 × 30 cm) to afford compound 11 (10.7 mg). Fr. 3-9-3 was subjected to MPLC (silica gel; *n*-hexane/acetone 2/1; column size: 1 × 30 cm) to furnish compound 19 (1.0 mg). Fr. 3-10 was separated with Sephadex LH-20 (column size: 3 × 70 cm) and eluted with methanol to provide seven fractions (3-10-1–3-10-7). Fr. 3-10-2 was subjected to MPLC (silica gel; H<sub>2</sub>O/methanol 1/1 to 2/3; column size: 1.5 × 30 cm) to gain 14 fractions (Fr. 3-10-2-1–3-10-2-14). Fr. 3-10-2-4 was subjected to MPLC (silica gel; CH<sub>2</sub>Cl<sub>2</sub>/EtOAc 3/1; column size: 1 × 30 cm) to obtain compound 4 (5.3 mg). Fr. 3-10-2-7 was subjected to MPLC (silica gel; CH<sub>2</sub>Cl<sub>2</sub>/EtOAc 3/1; column size: 1 × 30 cm) to produce compound 5 (0.9 mg). Fr. 3-10-2-13 was subjected to MPLC (silica gel; CH<sub>2</sub>Cl<sub>2</sub>/EtOAc 4/1; column size: 1 × 30 cm) to yield compound 2 (2.3 mg). Fr. 3-10-2-15 was subjected to MPLC (silica gel; CH<sub>2</sub>Cl<sub>2</sub>/acetone 15/1; column size: 1 × 30 cm) to afford five fractions (Fr. 3-10-2-15-1–3-10-2-15-5). Fr. 3-10-2-15-3 was subjected to MPLC (silica gel; CH<sub>2</sub>Cl<sub>2</sub>/EtOAc 3/1; column size: 1 × 30 cm) to give compounds 3 (2.8 mg) and 1 (5.9 mg). Fr. 3-10-4 was subjected to MPLC (silica gel; H<sub>2</sub>O/methanol 2/3; column size: 1 × 30 cm) to produce 11 fractions (Fr. 3-10-4-1–3-10-4-11). Fr. 3-10-4-2 was subjected to MPLC (silica gel; *n*-hexane/CH<sub>2</sub>Cl<sub>2</sub>/EtOAc 2/2/1; column size: 1 × 30 cm) to furnish compound 8 (0.5 mg). Fr. 3-10-5 was subjected to MPLC (RP-18; water/methanol 2/1 to 1/1; column size: 1 × 30 cm) to give compound 10 (0.3 mg). Fr. 3-7 was subjected to MPLC (silica gel; *n*-hexane/EtOAc 3/1 to 3/2; column size: 1.5 × 30 cm) to give five fractions (Fr. 3-7-1–3-7-5). Fr. 3-7-3 was subjected to MPLC (RP-18; water/methanol 1/1 to 1/3; column size: 1.5 × 30 cm) to provide nine fractions (Fr. 3-7-3-1–3-7-3-9). Fr. 3-7-3-5 was subjected to MPLC (silica gel; *n*-hexane/CH<sub>2</sub>Cl<sub>2</sub>/EtOAc 4/2/1; column size: 1 × 30 cm) to afford 10 fractions (Fr. 3-7-3-5-1–3-7-3-5-10). Fr. 3-7-3-5-4 was subjected to MPLC (silica gel; *n*-hexane/CH<sub>2</sub>Cl<sub>2</sub>/EtOAc 1/3/0.3; column size: 1 × 30 cm) to give compound 12 (4.6 mg). Fr. 3-7-3-7 was subjected to MPLC (silica gel; *n*-hexane/CH<sub>2</sub>Cl<sub>2</sub>/EtOAc 4/2/1; column size: 1 × 30 cm) to produce nine fractions (Fr. 3-7-3-7-1–3-7-3-7-9). Fr. 3-7-3-7-2 was subjected to MPLC (silica gel; *n*-hexane/CH<sub>2</sub>Cl<sub>2</sub>/EtOAc 6/2/1; column size: 1 × 30 cm) to obtain compounds 15 (0.2 mg) and 16 (2.5 mg). Fr. 3-7-3-7-6 was subjected to MPLC (RP-18; water/methanol 1/3; column size: 1 × 30 cm) to give compound 17 (2.9 mg). Fr. 3-11 was separated with Sephadex LH-20 (column size: 3 × 70 cm) and eluted with methanol to provide 11 fractions (3-11-1–3-11-11). Fr. 3-11-7 was subjected to MPLC (RP-18; water/acetone 3/2; column size: 1 × 30 cm) to give compound 13 (0.5 mg). Fr. 2 was subjected to column chromatography (silica gel; *n*-hexane/CH<sub>2</sub>Cl<sub>2</sub>/acetone 17/1/1 to 10/1/1) to yield ten fractions (Fr. 2-1–2-10). Fr. 2-4 was subjected to MPLC (silica gel; *n*-hexane/acetone 40/1 to 20/1; column size: 2 × 30 cm) to yield nine fractions (Fr. 2-4-1–2-4-9). Fr. 2-4-3 was subjected to MPLC (RP-18; water/acetone 1/5; column size: 1.5 × 30 cm) to produce nine fractions (Fr. 2-4-3-1–2-4-3-9). Fr. 2-4-3-3 was subjected to MPLC (silica gel; *n*-hexane/acetone 40/0.5; column size: 1 × 30 cm) to afford eight fractions (Fr. 2-4-3-3-1–2-4-3-3-8). Fr. 2-4-3-3-3 was subjected to HPLC to obtain two fractions (Fr. 2-4-3-3-3-1–2-4-3-3-3-2). Fr. 2-4-3-3-3-2 was further separated with prep. RP-18 TLC (water/acetonitrile = 1/10) to give compound 18 (1.9 mg). Fr. 2-7 was subjected to column chromatography (silica gel; *n*-hexane/CH<sub>2</sub>Cl<sub>2</sub>/acetone 20/4/1 to 12/4/1) to produce eight fractions (Fr. 2-7-1–2-7-8). Fr. 2-7-2 was subjected to MPLC (silica gel; *n*-hexane/CH<sub>2</sub>Cl<sub>2</sub>/acetone 12/4/1; column size: 2 × 30 cm) to give compound 20 (1.6 g). Fr. 2-8 was subjected to column chromatography (silica gel; *n*-hexane/CH<sub>2</sub>Cl<sub>2</sub>/acetone 16/16/1 to 8/16/1) to afford 14 fractions (Fr. 2-8-1–2-8-14). Fr. 2-8-7 was subjected to MPLC (silica gel; *n*-hexane/acetone 6/1; column

size:  $1.5 \times 30$  cm) to produce seven fractions (Fr. 2-8-7-1–2-8-7-7). Fr. 2-8-7-5 was subjected to MPLC (silica gel; *n*-hexane/ $\text{CH}_2\text{Cl}_2$ /acetone 16/16/1; column size:  $1 \times 30$  cm) to produce compound **9** (15.2 mg). Fr. 4 was subjected to column chromatography (silica gel; *n*-hexane/acetone 5/1 to 3/1) to yield six fractions (Fr. 4-1–4-6). Fr. 4-5 was separated with Sephadex LH-20 (column size:  $3 \times 70$  cm) and eluted with methanol to provide six fractions (4-5-1–4-5-6). Fr. 4-5-4 was subjected to MPLC (RP-18; water/methanol 1/1; column size:  $1.5 \times 30$  cm) to produce six fractions (Fr. 4-5-4-1–4-5-4-6). Fr. 4-5-4-1 was subjected to MPLC (RP-18; water/methanol 1/1; column size:  $1 \times 30$  cm) to afford four fractions (Fr. 4-5-4-1-1–4-5-4-1-4). Fr. 4-5-4-1-1 was subjected to MPLC (silica gel; *n*-hexane/ $\text{CH}_2\text{Cl}_2$ /acetone 2/2/1; column size:  $1 \times 30$  cm) to give compound **14** (1.6 mg). (Supplementary Materials, Figure S58)

#### 4.3.1. Machinolide A (**1**)

Colorless needles;  $[\alpha]_{\text{D}}^{25} -29.6$  (*c* 0.30, MeOH); IR  $\nu_{\text{max}}$  (ATR): 3433 (OH), 1736 ( $\gamma$ -lactone)  $\text{cm}^{-1}$ ;  $^1\text{H-NMR}$  and  $^{13}\text{C-NMR}$  (Table 1); ESIMS  $m/z$  273  $[\text{M} + \text{H}]^+$ ; EIMS  $m/z$  (rel. int.): 254 ( $[\text{M} - \text{H}_2\text{O}]^+$ , 3), 215 (56), 186 (37), 129 (99), 57 (100); HRESIMS  $m/z$  295.18923  $[\text{M} + \text{Na}]^+$  (calcd. for  $\text{C}_{15}\text{H}_{28}\text{NaO}_4$ , 295.18853).

#### 4.3.2. Machinolide B (**2**)

Colorless needles;  $[\alpha]_{\text{D}}^{25} -42.1$  (*c* 0.092, MeOH); IR  $\nu_{\text{max}}$  (ATR): 3436 (OH), 1737 ( $\gamma$ -lactone)  $\text{cm}^{-1}$ ;  $^1\text{H-NMR}$  and  $^{13}\text{C-NMR}$  (Table 1); ESIMS  $m/z$  299  $[\text{M} + \text{H}]^+$ ; HRESIMS  $m/z$  321.20370  $[\text{M} + \text{Na}]^+$  (calcd. for  $\text{C}_{17}\text{H}_{30}\text{NaO}_4$ , 321.20363).

#### 4.3.3. Machinolide C (**3**)

Colorless needles;  $[\alpha]_{\text{D}}^{25} -42.0$  (*c* 0.14, MeOH); IR  $\nu_{\text{max}}$  (ATR): 3321 (OH), 1743 ( $\gamma$ -lactone)  $\text{cm}^{-1}$ ;  $^1\text{H-NMR}$  and  $^{13}\text{C-NMR}$  (Table 2); ESIMS  $m/z$  273  $[\text{M} + \text{H}]^+$ ; EIMS  $m/z$  (rel. int.): 254 ( $[\text{M} - \text{H}_2\text{O}]^+$ , 3), 229 (39), 200 (24), 129 (80), 57 (100); HRESIMS  $m/z$  273.20656  $[\text{M} + \text{H}]^+$  (calcd. for  $\text{C}_{15}\text{H}_{29}\text{O}_4$ , 273.20658).

#### 4.3.4. Machinolide D (**4**)

Colorless oil;  $[\alpha]_{\text{D}}^{27} -42.5$  (*c* 0.25, MeOH); IR  $\nu_{\text{max}}$  (ATR): 3437 (OH), 1752 ( $\gamma$ -lactone), 1708 ( $\text{C}=\text{O}$ )  $\text{cm}^{-1}$ ; CD  $\lambda_{\text{ext}}$  (MeOH) ( $\Delta\epsilon$ ): 280 (+15.43), 219.5 (−54.44) nm;  $^1\text{H-NMR}$  and  $^{13}\text{C-NMR}$  (Table 3); ESIMS  $m/z$  287  $[\text{M} + \text{H}]^+$ ; HRESIMS  $m/z$  309.16726  $[\text{M} + \text{Na}]^+$  (calcd. for  $\text{C}_{15}\text{H}_{26}\text{NaO}_5$ , 309.16725).

#### 4.3.5. Machinolide E (**5**)

Colorless oil;  $[\alpha]_{\text{D}}^{26} -35.4$  (*c* 0.145, MeOH); IR  $\nu_{\text{max}}$  (ATR): 3445 (OH), 1748 ( $\gamma$ -lactone), 1713 ( $\text{C}=\text{O}$ )  $\text{cm}^{-1}$ ; CD  $\lambda_{\text{ext}}$  (MeOH) ( $\Delta\epsilon$ ): 280.5 (+17.23), 217.5 (−52.40) nm;  $^1\text{H-NMR}$  and  $^{13}\text{C-NMR}$  (Table 3); ESIMS  $m/z$  313  $[\text{M} + \text{H}]^+$ ; HRESIMS  $m/z$  335.18295  $[\text{M} + \text{Na}]^+$  (calcd. for  $\text{C}_{17}\text{H}_{28}\text{NaO}_5$ , 335.18290).

#### 4.3.6. Machinolide F (**6**)

Colorless oil;  $[\alpha]_{\text{D}}^{20} -39.4$  (*c* 0.85, MeOH); IR  $\nu_{\text{max}}$  (ATR): 3440 (OH), 1751 ( $\gamma$ -lactone), 1705 ( $\text{C}=\text{O}$ )  $\text{cm}^{-1}$ ; CD  $\lambda_{\text{ext}}$  (MeOH) ( $\Delta\epsilon$ ): 280.5 (+17.34), 217.5 (−52.74) nm;  $^1\text{H-NMR}$  and  $^{13}\text{C-NMR}$  (Table 3); ESIMS  $m/z$  315  $[\text{M} + \text{H}]^+$ ; HRESIMS  $m/z$  337.19849  $[\text{M} + \text{Na}]^+$  (calcd. for  $\text{C}_{17}\text{H}_{30}\text{NaO}_5$ , 337.19855).

#### 4.4. X-Ray Crystallographic Data for Machinolide A (**1**), Machinolide B (**2**), and Machinolide C (**3**)

The absolute configurations of **1**, **2**, and **3** were determined from data collected on a Bruker D8 VENTURE single-crystal XRD equipped with Oxford Cryostream 800<sup>+</sup>. Crystallographic data for **1**:  $\text{C}_{15}\text{H}_{30}\text{O}_5$ ,  $M = 290.39$ , size  $0.220 \times 0.097 \times 0.057$   $\text{mm}^3$ , orthorhombic, space group  $P2_12_12_1$ ,  $a = 4.72807(10)$  Å,  $b = 12.9141(3)$  Å,  $c = 27.8178(6)$  Å,  $\alpha = \beta = \gamma = 90^\circ$ ,  $V = 1698.53(6)$  Å<sup>3</sup>,  $T = 200(2)$  K,  $Z = 4$ ,  $d_{\text{calcd}} = 1.136$   $\text{Mg/m}^3$ ,  $\lambda(\text{Cu K}\alpha) = 1.54178$  Å,  $F(000) = 640$ , reflections collected/independent

reflections 9080/3467 [R(int) = 0.0307], final *R* indices  $R_1 = 0.0331$ ,  $wR_2 = 0.0928$ , GOF on  $F^2 = 1.046$ , absolute structure parameter =  $-0.02(7)$ .

Crystallographic data for **2**:  $C_{17}H_{32}O_5$ ,  $M = 316.42$ , size  $0.397 \times 0.052 \times 0.036$  mm<sup>3</sup>, orthorhombic, space group  $P2_12_12_1$ ,  $a = 4.76120(10)$  Å,  $b = 12.8614(4)$  Å,  $c = 30.6325(9)$  Å,  $\alpha = \beta = \gamma = 90^\circ$ ,  $V = 1875.80(9)$  Å<sup>3</sup>,  $Z = 4$ ,  $d_{\text{calcd}} = 1.120$  Mg/m<sup>3</sup>,  $\lambda(\text{Cu K}\alpha) = 1.54178$  Å,  $F(000) = 696$ , reflections collected/independent reflections 10397/3812 [R(int) = 0.0366], final *R* indices  $R_1 = 0.0568$ ,  $wR_2 = 0.1537$ , GOF on  $F^2 = 1.036$ , absolute structure parameter =  $-0.01(14)$ .

Crystallographic data for **3**:  $C_{15}H_{28}O_4$ ,  $M = 272.37$ , size  $0.392 \times 0.089 \times 0.014$  mm<sup>3</sup>, orthorhombic, space group  $P2_12_12_1$ ,  $a = 4.75710(10)$  Å,  $b = 9.7931(2)$  Å,  $c = 35.3857(8)$  Å,  $\alpha = \beta = \gamma = 90^\circ$ ,  $V = 1648.50(6)$  Å<sup>3</sup>,  $T = 200(2)$  K,  $Z = 4$ ,  $d_{\text{calcd}} = 1.097$  Mg/m<sup>3</sup>,  $\lambda(\text{Cu K}\alpha) = 1.54178$  Å,  $F(000) = 600$ , reflections collected/independent reflections 15562/3377 [R(int) = 0.0525], final *R* indices  $R_1 = 0.0431$ ,  $wR_2 = 0.1152$ , GOF on  $F^2 = 1.037$ , absolute structure parameter =  $0.02(10)$ .

#### 4.5. Preparation of (S)-MTPA and (R)-MTPA Esters of **4a**, **4b**, **5a**, **5b**, **6a**, and **6b** from **4**, **5**, and **6**

Compound **4** (1.0 mg, 3.5 µmol) and pyridine-*d*<sub>5</sub> (10.9 µL, 135.4 µmol) was transferred to a vial. The contents of the vial were dissolved in chloroform-*d*<sub>1</sub> (1090 µL, **4** = 3.5 mM). *R*-(-)-MPTA-Cl (10.9 µL, 58.3 µmol) was added to the vial, the vial was capped and the contents were stirred at room temperature (2–4 h). The (S)-MTPA ester (**4a**) was purified by prep. TLC plate (*n*-hexane/EtOAc = 1/1), and its <sup>1</sup>H-NMR spectra were obtained. The (R)-MTPA ester (**4b**) was prepared with (S)-MTPA chloride in the same manner. The same method was used to prepare the (S)- and (R)-MTPA esters of **5a**, **5b**, **6a**, and **6b** (Supplementary Materials, Figures S59–S64).

#### 4.6. Superoxide Anion and Elastase Release Assays

The ability of the test compounds to modulate superoxide anion generation and elastase release by neutrophils was evaluated according to the studies published by co-author Professor Tsong-Long Hwang [2,43]. The superoxide generation assay was based on the reduction of ferricytochrome *c* by superoxide dismutase (SOD). Elastase substrate (methoxysuccinyl-Ala-Ala-Pro-Val-p-nitroanilide, 100 µM; Merck) was used to detect elastase release. Elastase level was detected at OD405 nm using a spectrophotometer. PI3K inhibitor LY29002 served as a positive control for the neutrophil assays. All assays were repeated at least three times. Results are presented as mean ± standard error of the mean (SEM). The Student's *t*-test was used to compare the test compound with a DMSO (0.1%) control. A probability of less than 0.05 was considered significant.

### 5. Conclusions

Six new butanolides, machinolides A–F (**1**–**6**), together with 14 known compounds, were obtained from the leaves of *M. japonica* var. *kusanoi*. The absolute configurations of these new compounds were assigned by their CD spectrum, single-crystal X-ray diffraction analyses, and Mosher's method. Hence, absolute configurations of all new compounds were determined as 2*R*,3*S*,4*S*-form in a furan ring, and the chiral center in the side chain group was *R*-form in **1** and **3**, and *S*-form in **2**, **4**, **5**, and **6**. Besides, butanolides and lignans were major skeletons in this study. Bioactivity results indicated that lignans could reduce superoxide anion generation in fMLP/CB-stimulated human neutrophils, and the anti-inflammatory activities of those compounds were as potent as compounds in the literature [42]. Furthermore, the structure-activity relationship (SAR) discussion of anti-inflammatory activity compounds indicated that furofuran lignan with methylenedioxy was the most active structure. To our knowledge, this is the first report on anti-inflammatory activity from the leaves of *M. japonica* var. *kusanoi* and the results are helpful to patients with inflammation-related disease.

**Supplementary Materials:** Figure S1: Structures of known compounds **7**–**20**, Figures S2–S57: The phytochemical spectra of compounds **1**–**6**. Figure S58: Extraction and isolation of the leaves from *M. japonica* var. *kusanoi*, Figures S59–S64: The phytochemical spectra of compounds **4a**, **4b**, **5a**, **5b**, **6a**, and **6b**. Table S1: Inhibitory effects



of crude extracts from the leaves of *M. japonica* var. *kusanoi* on superoxide anion generation and elastase release in fMLP/CB-induced human neutrophils.

**Author Contributions:** Conceptualization, H.-S.C.; Methodology, H.-S.C., C.-H.L., and T.-L.H.; Formal Analysis, H.-S.C. and T.-L.H.; Investigation, S.-L.L.; Resources, H.-S.C.; Data Curation, H.-S.C., S.-S.Y., and T.-L.H.; Writing—Original Draft Preparation, S.-L.L. and H.-C.W.; Writing—Review and Editing, H.-S.C. and T.-L.H.; Visualization, H.-S.C.; Supervision, H.-S.C.; Project Administration, H.-S.C.; Funding Acquisition, H.-S.C. All authors have read and agreed to the published version of the manuscript.

**Funding:** This study was supported by the Ministry of Science and Technology, R.O.C. (MOST 109-2628-B-037-015), and a Kaohsiung Medical University grant (KMU-TC108A03-8 and KMU-TC108A03-9).

**Acknowledgments:** We thank the Center for Research Resources and Development of Kaohsiung Medical University for providing a nuclear magnetic resonance (NMR) spectrometer, and also senior technician Chyi-Jia Wang for measuring the 2D NMR data.

**Conflicts of Interest:** The authors declare no conflict of interest.

## References

- Chiang, C.-C.; Cheng, W.-J.; Korinek, M.; Lin, C.-Y.; Hwang, T.-L. Neutrophils in Psoriasis. *Front. Immunol.* **2019**, *10*, 2376. [\[CrossRef\]](#)
- Hwang, T.-L.; Su, Y.-C.; Chang, H.-L.; Leu, Y.-L.; Chung, P.-J.; Kuo, L.-M.; Chang, Y.-J. Suppression of superoxide anion and elastase release by C18 unsaturated fatty acids in human neutrophils. *J. Lipid Res.* **2009**, *50*, 1395–1408. [\[CrossRef\]](#) [\[PubMed\]](#)
- Korkmaz, B.; Horwitz, M.; Jenne, D.E.; Gauthier, F. Neutrophil Elastase, Proteinase 3, and Cathepsin G as Therapeutic Targets in Human Diseases. *Pharmacol. Rev.* **2010**, *62*, 726–759. [\[CrossRef\]](#) [\[PubMed\]](#)
- Chang, H.-S.; Chen, I.-S. Chemical constituents and bioactivity of Formosan lauraceous plants. *J. Food Drug Anal.* **2016**, *24*, 247–263. [\[CrossRef\]](#) [\[PubMed\]](#)
- Liao, J.C. *Lauraceae in Flora of Taiwan*, 2nd ed.; Editorial Committee of the Flora of Taiwan: Taipei, Taiwan, 1996; Volume 2, pp. 1433–1499.
- Masao, T.; Yang, T.H.; Teh, L.S. Studies on the alkaloids of Formosan Lauraceous plants. I. Alkaloids of *Machilus kusanoi* Hayata. (1). The isolation of L-(-)-N-norarmepavine. *Yakugaku Zasshi* **1963**, *83*, 15–18. [\[CrossRef\]](#)
- Teh, L.S. Studies on the alkaloids of Formosan Lauraceous plants. II. Alkaloids of *Machilus Kusanoi* Hayata. (2). The isolation of dl-coclaurine. *Yakugaku Zasshi* **1963**, *83*, 19–21. [\[CrossRef\]](#)
- Lee, S.-S.; Lin, Y.-S.; Chen, C.-K. Three Adducts of Butenolide and Apigenin Glycoside from the Leaves of *Machilus japonica*. *J. Nat. Prod.* **2009**, *72*, 1249–1252. [\[CrossRef\]](#)
- Ho, C.-L.; Hsu, K.-P.; Tseng, Y.-H.; Wang, E.I.-C.; Liao, P.-C.; Chou, J.-C.; Lin, C.-N.; Su, Y.-C. Composition and antimicrobial activities of the leaf essential oil of *Machilus kusanoi* from Taiwan. *Nat. Prod. Commun.* **2011**, *6*. [\[CrossRef\]](#)
- Du, Y.; Abedi, A.K.; Valenciano, A.L.; Fernáandez-Murga, M.L.; Cassera, M.B.; Rasamison, V.E.; Applequist, W.L.; Miller, J.S.; Kingston, D.G.I. Isolation of the New Antiplasmodial Butanolide, Malleastrumolide A, from *Malleastrum* sp. (Meliaceae) from Madagascar. *Chem. Biodivers.* **2017**, *14*, e1700331. [\[CrossRef\]](#)
- Lorenzo, M.; Brito, I.; Cueto, M.; D’Croz, L.; Darias, J. <sup>13</sup>C NMR-Based Empirical Rules to Determine the Configuration of Fatty Acid Butanolides. Novel  $\gamma$ -Dilactones from *Pterogorgia* spp. *Org. Lett.* **2006**, *8*, 5001–5004. [\[CrossRef\]](#)
- Hoye, T.R.; Jeffrey, C.S.; Shao, F. Mosher ester analysis for the determination of absolute configuration of stereogenic (chiral) carbinol carbons. *Nat. Protoc.* **2007**, *2*, 2451–2458. [\[CrossRef\]](#)
- Pardede, A.; Adfa, M.; Kusnanda, A.J.; Ninomiya, M.; Koketsu, M. Flavonoid rutinoides from *Cinnamomum parthenoxylon* leaves and their hepatoprotective and antioxidant activity. *Med. Chem. Res.* **2017**, *26*, 2074–2079. [\[CrossRef\]](#)
- Chang, C.-W.; Chang, H.-S.; Cheng, M.-J.; Peng, C.-F.; Chen, I.-S. Identification of Five New Minor Constituents from the Whole Plant of *Amisotolype hispida*. *Helvetica Chim. Acta* **2015**, *98*, 347–358. [\[CrossRef\]](#)
- Liu, C.-M.; Kao, C.-L.; Wu, H.-M.; Li, W.-J.; Huang, C.-T.; Li, H.-T.; Chen, C.-Y. Antioxidant and Anticancer Aporphine Alkaloids from the Leaves of *Nelumbo nucifera* Gaertn. cv. *Rosa-plena*. *Molecules* **2014**, *19*, 17829–17838. [\[CrossRef\]](#)

16. Wu, M.-D.; Cheng, M.-J.; Lin, R.-J.; Chan, H.-Y.; Hsieh, S.-Y.; Chang, H.-S.; Lin, C.-L.; Chen, J.-J. Chemical Constituents of the Fungus *Biscogniauxia cylindrospora*. *Chem. Nat. Compd.* **2019**, *55*, 924–926. [\[CrossRef\]](#)
17. Zhang, W.; Wang, Y.; Geng, Z.; Guo, S.; Cao, J.; Zhang, Z.; Pang, X.; Chen, Z.; Du, S.S.; Deng, Z. Antifeedant Activities of Lignans from Stem Bark of *Zanthoxylum armatum* DC. against *Tribolium castaneum*. *Molecules* **2018**, *23*, 617. [\[CrossRef\]](#)
18. Holzbach, J.C.; Lopes, L.M.X. Aristolactams and Alkamides of *Aristolochia gigantea*. *Molecules* **2010**, *15*, 9462–9472. [\[CrossRef\]](#)
19. Lee, S.Y.; Woo, K.W.; Kim, C.S.; Lee, D.U.; Lee, K.R. New Lignans from the Aerial Parts of *Rudbeckia laciniata*. *Helvetica Chim. Acta* **2013**, *96*, 320–325. [\[CrossRef\]](#)
20. Sribuham, T.; Sriphana, U.; Thongsri, Y.; Yenjai, C. Chemical constituents from the stems of *Alyxia schlechteri*. *Phytochem. Lett.* **2015**, *11*, 80–84. [\[CrossRef\]](#)
21. Park, C.H.; Kim, K.H.; Lee, I.K.; Lee, S.Y.; Choi, S.U.; Lee, J.H.; Lee, K.R. Phenolic constituents of *Acorus gramineus*. *Arch. Pharmacol. Res.* **2011**, *34*, 1289–1296. [\[CrossRef\]](#)
22. Rye, C.E.; Barker, D. Asymmetric Synthesis of (+)-Galbelgin, (–)-Kadangustin J, (–)-Cyclogalgravin and (–)-Pycnanthulignenes A and B, Three Structurally Distinct Lignan Classes, Using a Common Chiral Precursor. *J. Org. Chem.* **2011**, *76*, 6636–6648. [\[CrossRef\]](#) [\[PubMed\]](#)
23. You, C.-X.; Yang, K.; Wang, C.-F.; Zhang, W.; Wang, Y.; Han, J.; Fan, L.; Du, S.S.; Geng, Z.; Deng, Z. Cytotoxic Compounds Isolated from *Murraya tetramera* Huang. *Molecules* **2014**, *19*, 13225–13234. [\[CrossRef\]](#) [\[PubMed\]](#)
24. Collado, I.G.; Hanson, J.R.; Macías-Sánchez, A.J.; Mobbs, D. The Biotransformation of Some Clovanes by *Botrytis cinerea*. *J. Nat. Prod.* **1998**, *61*, 1348–1351. [\[CrossRef\]](#) [\[PubMed\]](#)
25. Ashour, A.; Amer, M.; Marzouk, A.M.; Shimizu, K.; Kondo, R.; El-Sharkawy, S. Corncobs as a Potential Source of Functional Chemicals. *Molecules* **2013**, *18*, 13823–13830. [\[CrossRef\]](#)
26. Lopes, N.P.; Silva, D.H.S.; Kato, M.J.; Yoshida, M. Butanolides as a common feature of *Iryanthera lancifolia* and *Virola surinamensis*. *Phytochemistry* **1998**, *49*, 1405–1410. [\[CrossRef\]](#)
27. Franco, C.M.M.; Borde, U.P.; Vijayakumar, E.K.S.; Chatterjee, S.; Blumbach, J.; Ganguli, B.N. Butalactin, a new butanolide antibiotic. Taxonomy, fermentation, isolation and biological activity. *J. Antibiot.* **1991**, *44*, 225–231. [\[CrossRef\]](#)
28. Nihira, T.; Shimizu, Y.; Kim, H.S.; Yamada, Y. Structure-activity relationships of virginiae butanolide C, an inducer of virginiamycin production in *Streptomyces virginiae*. *J. Antibiot.* **1988**, *41*, 1828–1837. [\[CrossRef\]](#)
29. Kim, H.S.; Tada, H.; Nihira, T.; Yamada, Y. Purification and characterization of virginiae butanolide C-binding protein, a possible pleiotropic signal-transducer in *Streptomyces virginiae*. *J. Antibiot.* **1990**, *43*, 692–706. [\[CrossRef\]](#)
30. Hoshino, S.; Wakimoto, T.; Onaka, H.; Abe, I. Chojalactones A–C, Cytotoxic Butanolides Isolated from *Streptomyces* sp. Cultivated with Mycolic Acid Containing Bacterium. *Org. Lett.* **2015**, *17*, 1501–1504. [\[CrossRef\]](#)
31. Li, F.; Chen, D.; Lu, S.; Yang, G.; Zhang, X.; Chen, Z.; Fan, S.; Wu, S.-H.; He, J. Anti-Influenza A Viral Butanolide from *Streptomyces* sp. Smu03 Inhabiting the Intestine of *Elephas maximus*. *Viruses* **2018**, *10*, 356. [\[CrossRef\]](#)
32. Cheng, M.-J.; Tsai, I.-L.; Lee, S.-J.; Jayaprakasam, B.; Chen, I.-S. Steryl epoxide, secobutanolide and butanolides from the stem wood of *Machilus zuihoensis*. *Phytochemical* **2005**, *66*, 1180–1185. [\[CrossRef\]](#) [\[PubMed\]](#)
33. Liu, M.-T.; Lin, S.; Gan, M.; Liu, B.; Zi, J.; Song, W.-X.; Zhang, Y.-L.; Fan, X.-N.; Liu, Y.; Tan, W.; et al. Butanolide derivatives from the bark of *Machilus yaoshansis*. *J. Asian Nat. Prod. Res.* **2012**, *14*, 713–720. [\[CrossRef\]](#)
34. Kim, W.; Lyu, H.-N.; Kwon, H.-S.; Kim, Y.S.; Lee, K.-H.; Kim, -Y.; Chakraborty, G.; Choi, K.Y.; Yoon, H.S.; Kim, K.-T. Obtusilactone B from *Machilus Thunbergii* Targets Barrier-to-Autointegration Factor to Treat Cancer. *Mol. Pharmacol.* **2012**, *83*, 367–376. [\[CrossRef\]](#) [\[PubMed\]](#)
35. Yang, C.-P.; Huang, G.-J.; Huang, H.-C.; Chen, Y.-C.; Chang, C.-I.; Wang, S.-Y.; Chen, I.-S.; Tseng, Y.-H.; Chien, S.-C.; Kuo, Y.-H. A New Butanolide Compound from the Aerial Part of *Lindera akoensis* with Anti-inflammatory Activity. *Molecules* **2012**, *17*, 6585–6592. [\[CrossRef\]](#) [\[PubMed\]](#)
36. Tsai, I.-L.; Hung, C.-H.; Duh, C.-Y.; Chen, I.-S. Cytotoxic Butanolides and Secobutanolides from the Stem Wood of Formosan *Lindera communis*. *Planta Medica* **2002**, *68*, 142–145. [\[CrossRef\]](#)
37. Cheng, M.-J.; Wang, T.-A.; Lee, S.-J.; Chen, I.-S. A new butanolide and a new secobutanolide from *Litsea lili* var. *nunkao-tahangensis*. *Nat. Prod. Res.* **2010**, *24*, 647–656. [\[CrossRef\]](#)

38. Shen, K.-H.; Lin, E.-S.; Kuo, P.-L.; Chen, C.-Y.; Hsu, Y.-L. Isolinderanolide B, a Butanolide Extracted From the Stems of *Cinnamomum subavenium*, Inhibits Proliferation of T24 Human Bladder Cancer Cells by Blocking Cell Cycle Progression and Inducing Apoptosis. *Integr. Cancer Ther.* **2011**, *10*, 350–358. [\[CrossRef\]](#)
39. Yang, S.-Y.; Wang, H.-M.; Wu, T.-W.; Chen, Y.-J.; Shieh, J.-J.; Lin, J.-H.; Ho, T.-F.; Luo, R.-J.; Chen, C.-Y.; Chang, C.-C. Subamolide B Isolated from Medicinal Plant *Cinnamomum subavenium* Induces Cytotoxicity in Human Cutaneous Squamous Cell Carcinoma Cells through Mitochondrial and CHOP-Dependent Cell Death Pathways. *Evid. Based Complement Alternat. Med.* **2013**, *2013*, 1–13. [\[CrossRef\]](#)
40. Chen, C.-Y.; Hsu, Y.-L.; Chen, Y.-Y.; Hung, J.-Y.; Huang, M.-S.; Kuo, P.-L. Isokotomolide A, a new butanolide extracted from the leaves of *Cinnamomum kotoense*, arrests cell cycle progression and induces apoptosis through the induction of p53/p21 and the initiation of mitochondrial system in human non-small cell lung cancer A549 cells. *Eur. J. Pharmacol.* **2007**, *574*, 94–102. [\[CrossRef\]](#)
41. Le Dang, Q.; Kwon, H.R.; Choi, Y.H.; Choi, G.J.; Jang, K.S.; Park, M.S.; Lim, C.H.; Ngoc, L.H.; Kim, J.-C. Nematicidal activity against *Bursaphelenchus xylophilus* of isoobtusilactone A isolated from *Persea americana*. *Nematology* **2010**, *12*, 247–253. [\[CrossRef\]](#)
42. Kuo, P.; Hung, H.-Y.; Nian, C.-W.; Hwang, T.-L.; Cheng, J.-C.; Kuo, D.-H.; Lee, E.-J.; Tai, S.-H.; Wu, T.-S. Chemical Constituents and Anti-inflammatory Principles from the Fruits of *Forsythia suspensa*. *J. Nat. Prod.* **2017**, *80*, 1055–1064. [\[CrossRef\]](#) [\[PubMed\]](#)
43. Hwang, T.-L.; Li, G.-L.; Lan, Y.-H.; Chia, Y.-C.; Hsieh, P.-W.; Wu, Y.-H.; Wu, Y.-C. Potent inhibition of superoxide anion production in activated human neutrophils by isopedicin, a bioactive component of the Chinese medicinal herb *Fissistigma oldhamii*. *Free. Radic. Boil. Med.* **2009**, *46*, 520–528. [\[CrossRef\]](#) [\[PubMed\]](#)

**Sample Availability:** Samples of all compounds are available from the authors.



© 2020 by the authors. Licensee MDPI, Basel, Switzerland. This article is an open access article distributed under the terms and conditions of the Creative Commons Attribution (CC BY) license (<http://creativecommons.org/licenses/by/4.0/>).

Available online at [www.sciencedirect.com](http://www.sciencedirect.com)

ScienceDirect

Biomedical Journal

journal homepage: [www.elsevier.com/locate/bj](http://www.elsevier.com/locate/bj)

## Review Article

# Understanding the role of neutrophils in acute respiratory distress syndrome

Shun-Chin Yang<sup>a,b</sup>, Yung-Fong Tsai<sup>c,d</sup>, Yen-Lin Pan<sup>e</sup>,  
Tsong-Long Hwang<sup>b,c,f,g,\*</sup>

<sup>a</sup> Department of Anesthesiology, Taipei Veterans General Hospital and National Yang-Ming University, Taipei, Taiwan

<sup>b</sup> Graduate Institute of Natural Products, College of Medicine, Chang Gung University, Taoyuan, Taiwan

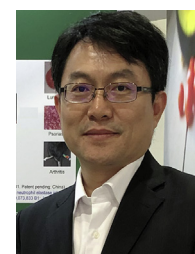
<sup>c</sup> Department of Anesthesiology, Chang Gung Memorial Hospital at Linkou, Taoyuan, Taiwan

<sup>d</sup> Graduate Institute of Clinical Medical Sciences, College of Medicine, Chang Gung University, Taoyuan, Taiwan

<sup>e</sup> Department of Pharmacy, Cheng Hsin General Hospital, Taipei, Taiwan

<sup>f</sup> Research Center for Chinese Herbal Medicine, Research Center for Food and Cosmetic Safety, and Graduate Institute of Health Industry Technology, College of Human Ecology, Chang Gung University of Science and Technology, Taoyuan, Taiwan

<sup>g</sup> Department of Chemical Engineering, Ming Chi University of Technology, New Taipei City, Taiwan



Prof. Tsong-Long Hwang

## ARTICLE INFO

## Article history:

Received 23 July 2020

Accepted 8 September 2020

Available online 10 September 2020

## Keywords:

ARDS

Neutrophil

Inflammation

## ABSTRACT

Acute respiratory distress syndrome (ARDS) is difficult to treat and is associated with a high mortality rate. The most severe form of coronavirus disease 2019 (COVID-19) also leads to life-threatening ARDS. Neutrophil counts are positively correlated with disease severity in ARDS. Neutrophil activation not only plays a significant role in immune defense against infections, but also causes tissue damage and leads to inflammatory diseases. Activated neutrophils rapidly migrate to inflamed lung tissue, releasing toxic granular contents and generating neutrophil extracellular traps. In the last few decades, it has become apparent that neutrophils occupy a central role in ARDS pathology. In this review, we summarize the neutrophil inflammatory responses and their relationships to ARDS. According to the current literature, understanding the function of neutrophils may be helpful in the treatment of ARDS.

Acute respiratory distress syndrome (ARDS) is a life-threatening respiratory condition with an increasing incidence rate, ranging from 20 to 40%, and a mortality rate of approximately 40% [1,2]. On account of the outbreak of

coronavirus disease 2019 (COVID-19), 29–42% COVID-19 patients developed ARDS and 15–52% of COVID-19 ARDS cases resulted in fatality [3,4]. Initially, the American-European Consensus Conference for ARDS defined acute lung injury

\* Corresponding author. Graduate Institute of Natural Products, College of Medicine, Chang Gung University, 259, Wenhua 1st Rd., Gueishan, Taoyuan 333, Taiwan.

E-mail address: [htl@mail.cgu.edu.tw](mailto:htl@mail.cgu.edu.tw) (T.-L. Hwang).

Peer review under responsibility of Chang Gung University.

<https://doi.org/10.1016/j.bj.2020.09.001>

2319-4170/© 2020 Chang Gung University. Publishing services provided by Elsevier B.V. This is an open access article under the CC BY-NC-ND license (<http://creativecommons.org/licenses/by-nc-nd/4.0/>).

(ALI) and ARDS as separate conditions. ALI was regarded as a less severe presentation of ARDS [5]. The Berlin definition of ARDS was updated, classified into mild, moderate, and severe grades based on the pulmonary oxygenation level. Due to its similarity to mild ARDS, ALI was removed from the Berlin definition [6]. The clinical symptoms and signs of ARDS are characterized by hypoxemia, marked diffuse bilateral pulmonary infiltrates, and extensive pulmonary edema. Studies of histological events of ARDS demonstrated that pulmonary edema is induced by increased vascular permeability, followed by protein-rich fluid in the alveolar space and accumulation of activated immune cells. The diffuse alveolar damage and accumulated immune cells lead to compromised gas exchange and respiratory failure [7,8]. Neutrophil infiltration in inflamed lung is a hallmark of ARDS [9]. Activated neutrophils trigger oxidative stress, release proteases, and form neutrophil extracellular traps (NETs), resulting in lung damage. However, neutrophils also play a role in the repair of inflamed lung tissues. Neutrophils are involved in the proliferation of type II pneumocytes during the repair phase after inflammatory lung injury [10]. It has been reported that neutropenia does not result in improved recovery in ARDS patients [11,12]. Although numerous studies have explored the pathogenesis of ARDS, there is still a lack of consensus regarding ARDS progression and effective pharmacotherapeutic treatment. Understanding the functional implications of neutrophils will allow exploration of applicable therapeutic strategies to reduce neutrophil-induced inflammatory lung injury. This review will focus on the roles of neutrophils and related immune products associated with ARDS.

## Overview of lung inflammatory injury

The pathogenesis of ARDS is complex and classified as direct or indirect. Most commonly, direct injury results from infectious damage to lung tissue. The causes of lung injury by infectious stimuli are not fully known. Pneumococcus and influenza A virus originally infect bronchial epithelium, induce upper airway and alveolar damage, recruit neutrophils and macrophages, and amplify cytokine and chemokine production [13,14]. Severe acute respiratory syndrome coronavirus 2 (SARS-CoV-2) infects pulmonary tissues, resulting in accumulation of massive amounts of immune cells and leads to an inflammatory cytokine storm. In COVID-19 ARDS patients, cytokine storm is a common characteristic. Patients with COVID-19 ARDS have elevated plasma levels of inflammatory cytokines, including interleukin (IL)-1 $\beta$ , IL-6, IL-8, granulocyte colony-stimulating factor, interferon gamma, and tumor necrosis factor alpha (TNF- $\alpha$ ). An excess of inflammatory cytokines further causes immune cell infiltration into inflamed lungs to induce alveolar damage and diminish lung function [3,15,16]. Another cause of direct lung injury is mechanical tissue damage, such as pulmonary contusion and inhalation of injurious materials. Pulmonary contusions primarily contribute to ARDS in traumatic patients by priming the innate immune response and enhancing the activity of toll-like receptor 4 resulting in excess production of pro-inflammatory mediators [17,18]. Additionally, indirect

pulmonary injuries can be explained by the “2-hit hypothesis” which states that an inflammatory response related to extra-pulmonary area stimulus (first hit) is followed by systemic inflammatory response (second hit) that can induce lung injury. Common triggers of indirect lung injury induced by systemic inflammatory response include sepsis, shock, acute pancreatitis, bone fracture, and massive blood transfusion [19,20]. It has been shown that severe systemic inflammatory response resulting from sepsis produces numerous circulating inflammatory mediators. These mediators reach the bronchial and alveolar tissues and activate resident macrophages that attract inflammatory cells. Excess recruitment of immune cells not only occludes lung microcirculation but also releases cytotoxic products to damage surrounding tissues [21,22]. Moreover, the pathogenesis of transfusion-related acute lung injury (TRALI) occurs through antibody-dependent mechanisms. The first hit contributes to the underlying inflammatory condition of the patient. The second hit is related to antibodies in the transfused blood product [23]. Neutrophils are thought to mediate the development of TRALI. The antibodies from transfused blood components bind to the pulmonary endothelium followed by accumulation and activation of neutrophils. Activated neutrophils undergo respiratory burst and release ROS, release proteolytic enzymes by degranulation, and form NETs, which further contribute to lung inflammation [24].

## Role of neutrophils in ARDS

Our research, along with other studies, has provided insights into the pathogenic role of neutrophils in various inflammatory states, including sepsis and ARDS [25,26]. Neutrophils are the first immune cells recruited to the site of inflammation following stimulation by chemotactic factors released from damaged pulmonary tissues. Both exogenous and endogenous inflammatory stimuli can be recognized by specific receptors of human neutrophils. This further promotes the recruitment and activation of circulating neutrophils. These activated neutrophils produce several cytotoxic products, including ROS, granular enzymes, NETs, and various pro-inflammatory cytokines [27]. Moreover, these immune products trigger several chemotactic signals to induce positive feedback, further enhancing inflammation. The overwhelming activation of neutrophils contributes to surrounding tissue damage and even lung dysfunction [Fig. 1] [28]. In COVID-19 ARDS patients, higher counts of neutrophil are observed and represent a predictor of poor outcome [29]. Therefore, strategies to diminish neutrophils in lung tissue, including decreasing neutrophil recruitment and impairing neutrophil immune functions, have been predicted to attenuate lung injury.

## Neutrophil recruitment in ARDS

Neutrophil migration from the circulatory system into inflamed lung tissue can be initiated by both infectious and sterile inflammatory stimuli. Neutrophils attach to the vascular endothelium, and then migrate following a



chemokine gradient [30]. These chemoattractive signals are recognized by local immune cells, which produce inflammatory mediators that further boost neutrophil recruitment. In ARDS, endothelial cells activate and capture circulating neutrophils [31,32]. Neutrophils are sequestered through selectin-mediated binding, triggering “inside-out” activation of integrins, such as CD11a/CD18, which binds to intercellular adhesion molecules (ICAMs) from the endothelium [33].

Neutrophil rolling is a form of migration along the endothelial wall and is facilitated by specialized structure like membrane extensions and uropods. The rolling neutrophils become flattened and polarized to generate the forward-moving force, and then slowly crawl along the endothelial cells [34]. This slow rolling, or crawling, delays the neutrophils’ passage through the inflammatory tissue. This phenomenon augments neutrophil recruitment through chemokine signaling. Crawling neutrophils can either pass between the endothelial cells or through them to exit the vessel lumen. Finally, the migrating neutrophils detach from the vessel wall and move into the inflamed respiratory tissues [35–37].

Once activated, pulmonary neutrophils exhibit various immune responses, including increased nicotinamide adenine dinucleotide phosphate (NADPH) oxidase activity and release of proteolytic enzymes [38,39]. Overwhelming NADPH oxidase activity and proteolytic enzyme release are associated with surrounding respiratory tissue damage. Therefore, strategies to reduce neutrophil migration may be useful in the alleviation of pulmonary tissue damage [40,41]. Consistently, several chemical compounds were shown to diminish neutrophil migration in animal models. Decreasing neutrophil recruitment decreases production of cytotoxic

mediators [42,43], whereas increased neutrophils in pulmonary tissue demonstrably contributes to the pathogenesis of ARDS. Notably, studies of human and animals with neutropenia and ARDS showed poor recovery [11,12]. Evidences that neutrophils promoted both pulmonary inflammation and repair explain these findings. Neutrophils participate in the remodeling of damaged lung tissue through release of MMP-9 and the Wnt/ $\beta$ -catenin pathway [44,45]. The role of neutrophil recruitment in ARDS is complex and still needs to be explored.

### ARDS and neutrophil oxidative stress

In response to infectious and sterile stimuli, neutrophils contribute to the progression of ARDS through the assembly and activation of the ROS-producing NADPH oxidase complex (NOX2) [46,47]. NOX2, located on the membrane, reduces oxygen into superoxide anion and releases it outside the cell. Superoxide anion is highly reactive and spontaneously dismutates into a more stable hydrogen peroxide ( $H_2O_2$ ).  $H_2O_2$  can pass through cell membrane and distribute to either extracellular or intracellular areas. The enzyme myeloperoxidase uses  $H_2O_2$  to produce a series of more reactive products, including hydroxyl radicals and hypochlorous acid [48,49]. ROS are harmful to pulmonary tissues, indicating that reducing ROS production is beneficial to mitigate lung inflammatory injury [50,51]. SARS-CoV-2 infections cause redox imbalance and induce ROS accumulation. Oxidative stress produced from downregulation of superoxide dismutase 3 expression in lung tissues is observed in elderly patients with

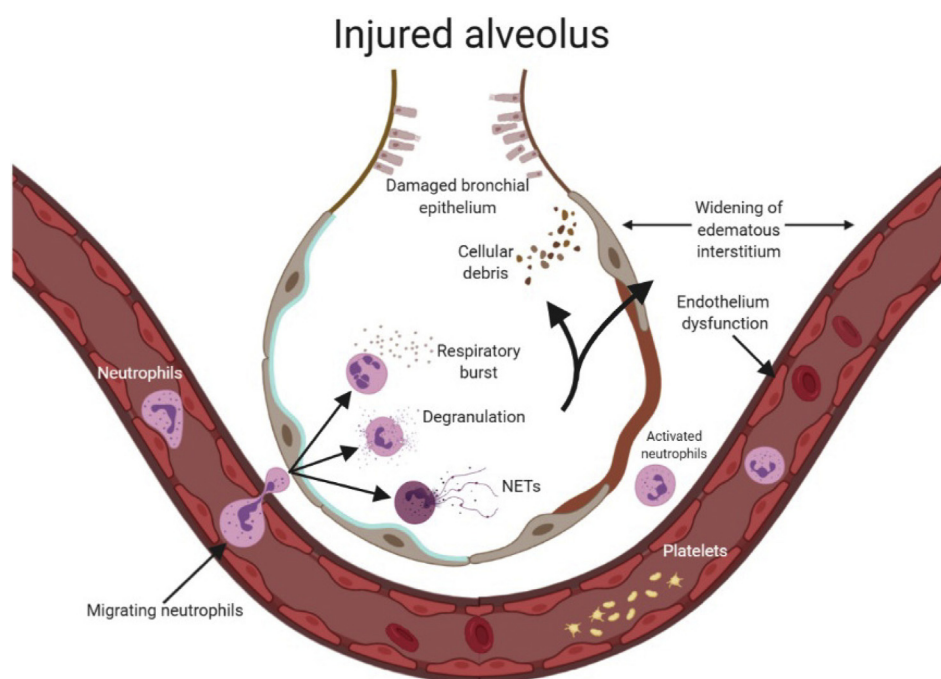


Fig. 1 Schematic diagram of neutrophil-mediated lung injury. Neutrophils migrate to inflamed lung tissue. This is followed by respiratory burst, degranulation, and NET formation in an injured alveolus. These immune responses lead to bronchial epithelial damage, cell debris production from dying cells attracting more immune cells, and endothelium dysfunction causing widening of edematous interstitium, further impairing oxygenation.

COVID-19, and the oxidative damage is closely related to poor outcome in elderly COVID-19 patients [52,53].

Several mechanisms of ROS are known. First, ROS directly damages the DNA of target cells. Previous research has shown that ROS produced from activated neutrophils induces oxidative DNA damage in respiratory epithelial cells [54,55]. Moreover, hyperoxia with 95% oxygen induces either neutrophil influx or oxidative DNA damage in neonate lung epithelial cells [56]. Second, ROS triggers peroxidation of lipid membranes, thus contributing to target cell lysis. The products of lipid peroxidation are also used as a measure of the level of tissue injury. In animal lung injury models, the level of lipid peroxidation was related to the severity of pulmonary tissue injury [57,58]. Third, ROS induces intracellular protein phosphorylation and transcription factor activation to promote the release of pro-inflammatory mediators. For instance, mitogen-activated protein (MAP) kinases can be activated by ROS to mediate cell death in response to stress, suggesting that the phosphorylation of MAP kinases have a major role in promotion of lung inflammatory injury [59,60]. Moreover, ROS triggers the activation of NF- $\kappa$ B, an important transcription factor that controls pro-inflammatory mediator release, to augment lung inflammatory injuries [61,62]. Research on the anti-oxidant  $\alpha$ -tocopherol showed that ROS production and related expression of NF- $\kappa$ B in activated neutrophils was decreased, and lung inflammatory injury was ameliorated in the presence of  $\alpha$ -tocopherol [63]. Similarity, another study showed that paraquat, an oxidant inducer, triggered ROS generation and release of inflammatory mediators, such as TNF- $\alpha$ , and IL-1 $\beta$ . The mechanisms of paraquat to heighten lung inflammation included activation of Jun N-terminal kinase (JNK) MAP kinase and NF- $\kappa$ B [64]. ROS damages the pulmonary endothelium, which is the barrier between the blood and vessels. Intracellular calcium signals are activated by ROS to increase endothelium permeability during pulmonary inflammatory process [65,66]. Cooperatively, neutrophil oxidative stress induces pulmonary endothelial and epithelial barrier dysfunctions. Barrier dysfunction increases neutrophil infiltration into lung tissues, and then these accumulated pulmonary neutrophils secrete several cytotoxic agents followed by worsening of pulmonary tissue damage, further enhancing the progression of ARDS [67].

#### **ARDS and neutrophil degranulation**

Neutrophil granules contain both pro- and anti-inflammatory substances that can be released to kill pathogens or for remodeling tissues. This process is called degranulation [68,69]. Neutrophils release membrane-bound vesicles, which contain various types of cytoplasmic granules associated with the progression of ARDS. The primary granules (also known as azurophilic granules) contain myeloperoxidase and many proteolytic proteins, including neutrophil elastase and cathepsin G. These granular proteins play major roles in microbicidal responses [70]. The secondary granules contain proteins that degrade the extracellular matrix. The tertiary granules contain few antimicrobials but store several metalloproteases [71,72]. During the inflammatory process, signals from receptors on the plasma membrane are transduced to the cytoplasm, which trigger the delivery of granule-

associated proteins to the cell surface and secretion of their contents out of the cells. The regulation mechanisms are numerous, including calcium signaling, src family kinases, MAP kinases, and GTPase-related signaling [73,74].

Neutrophilic infiltration into respiratory inflammatory tissues is a means of defending the host against pathogens, however, overwhelming extracellular release of neutrophil granular enzymes have been implicated in triggering collateral pulmonary tissue damage in ARDS [75,76]. Neutrophil elastase is a primary granular proteolytic enzyme and impacts lung inflammatory injury. Elastase can degrade pulmonary extracellular matrix proteins and cleave epithelial-cadherin to break respiratory cell-cell adhesion. Moreover, elastase has been shown to damage pulmonary vascular endothelial glycocalyx during the pulmonary inflammatory process [77–79]. Myeloperoxidase, the other primary granular enzyme, catalyzes H<sub>2</sub>O<sub>2</sub> to produce toxic ROS, which has been demonstrated to be a local mediator of alveolar damage [80]. The family of matrix metalloproteinases (MMPs) are released from the secondary and tertiary granules. Previous research showed that the expression of MMPs was correlated with the progression of ARDS. The enhanced expression of MMPs was related to inflammation-induced endothelial injury and impaired oxygenation in ARDS [81,82]. Another study revealed that MMP inhibitors suppressed MMP expression in plasma and lung tissue, decreased inflammatory mediator release, and attenuated lung inflammatory injury [83,84].

#### **ARDS and NET formation**

NETs are extracellular fibrous net-like structures, which have neutrophil granular proteins, such as myeloperoxidase or neutrophil elastase, coated on the backbone structures of DNA [85,86]. The mechanisms that induce NET formation have been explored, but signaling pathways involved are not completely understood. Raf/MEK/Erk signaling is activated to induce ROS production in the process of NET formation. Upon activation, the granular enzymes, myeloperoxidase and elastase, are released into the nucleus to induce nuclear disintegration. These granular enzymes coupled with PAD4 trigger chromatin decondensation and release. This mixture of granular enzymes and chromatin is expelled, followed by cell membrane rupture [87–89].

NETs are thought to be part of an innate immune mechanism for pathogen clearance; however, there are increasing concerns about the potential of NETs to initiate and propagate inflammatory damages in host tissues. Interestingly, both sterile and infective inflammations promote NET formation. During sterile inflammation, the components of NETs were found in lung and plasma of TRALI patients and mice. Treatment with DNase 1 decreased NET formation and lung injury [90,91]. Moreover, NET formation was observed in ventilator-induced lung injury. Previous human and animal studies showed that NET formation in the alveolar space was higher in bronchoalveolar lavage fluid from subjects with ventilator-induced ARDS. However, decreasing NET formation was not related to the shortening of mechanical ventilation [92–94]. During infective inflammation, NETs captured respiratory syncytial virus or influenza virus particles in patients and mice with respiratory infection. Nevertheless, cumulative

NET formation not only obstructed small airways, but also damaged alveolar–capillary to induce lung inflammatory injury [95–97]. The characteristics of lung tissue in ARDS demonstrated intensive neutrophil infiltration of lung tissue and NETs entwined with alveoli were exhibited in infected mice. The progression of inflammation further induced alveolar damage and pulmonary edema. Treatment with DNase I degraded NETs and reduced inflammatory cytokines, indicating that decreasing NET formation ameliorated lung injury and improved survival [98–100].

The severity and mortality of COVID-19 ARDS are correlated to higher neutrophil counts and NET level [29,101]. NETs play a significant role in producing a cytokine storm [102,103]. Furthermore, NETs have the ability to trigger immuno-thrombosis. The pulmonary capillary from patients with COVID-19 ARDS is filled with microthrombus and NETs. Microthrombi and fibrin deposition in lungs results in reduced oxygenation and further induces ARDS in COVID-19 patients [104–106].

## Conclusion

Although neutrophil immune responses are involved in ARDS, many questions remain unanswered. Neutrophils produce pro-inflammatory mediators and also augment inflammatory damage, implying that targeting neutrophils is a potential therapeutic for ARDS and COVID-19. However, on the basis of evidence supporting the fact that neutropenia does not attenuate ARDS, perhaps neutrophils play different roles in various phases of acute inflammation. The eventual goal is to determine when and how neutrophil activation is beneficial so as to tilt the balance toward benefit rather than harm.

## Conflicts of interest

The authors declare no competing financial interests.

## Acknowledgements

This research was supported by the grants from the Ministry of Science Technology (MOST 107-2320-B-075-001-MY3, MOST 108-2320-B-255-003-MY3, MOST 109-2327-B-182-002, and MOST 109-2327-B-255-001). The funders had no role in the study design, data collection and analysis, decision to publish, or preparation of the manuscript.

## REFERENCES

- [1] Pham T, Rubenfeld GD. Fifty years of research in ARDS. The epidemiology of acute respiratory distress syndrome. A 50th birthday review. *Am J Respir Crit Care Med* 2017;195:860–70.
- [2] Sigurdsson MI, Sigvaldason K, Gunnarsson TS, Moller A, Sigurdsson GH. Acute respiratory distress syndrome: nationwide changes in incidence, treatment and mortality over 23 years. *Acta Anaesthesiol Scand* 2013;57:37–45.
- [3] Huang C, Wang Y, Li X, Ren L, Zhao J, Hu Y, et al. Clinical features of patients infected with 2019 novel coronavirus in Wuhan, China. *Lancet* 2020;395:497–506.
- [4] Wu C, Chen X, Cai Y, Xia J, Zhou X, Xu S, et al. Risk factors associated with acute respiratory distress syndrome and death in patients with coronavirus disease 2019 pneumonia in Wuhan, China. *JAMA Intern Med* 2020;180:1–11.
- [5] Bernard GR, Artigas A, Brigham KL, Carlet J, Falke K, Hudson L, et al. The American-European Consensus Conference on ARDS. Definitions, mechanisms, relevant outcomes, and clinical trial coordination. *Am J Respir Crit Care Med* 1994;149:818–24.
- [6] Force ADT, Ranieri VM, Rubenfeld GD, Thompson BT, Ferguson ND, Caldwell E, et al. Acute respiratory distress syndrome: the Berlin Definition. *J Am Med Assoc* 2012;307:2526–33.
- [7] Papazian L, Calfee CS, Chiumello D, Luyt CE, Meyer NJ, Sekiguchi H, et al. Diagnostic workup for ARDS patients. *Intensive Care Med* 2016;42:674–85.
- [8] Bourenne J, Carvelli J, Papazian L. Evolving definition of acute respiratory distress syndrome. *J Thorac Dis* 2019;11:S390–3.
- [9] Zemans RL, Matthay MA. What drives neutrophils to the alveoli in ARDS? *Thorax* 2017;72:1–3.
- [10] Paris AJ, Liu Y, Mei J, Dai N, Guo L, Spruce LA, et al. Neutrophils promote alveolar epithelial regeneration by enhancing type II pneumocyte proliferation in a model of acid-induced acute lung injury. *Am J Physiol Lung Cell Mol Physiol* 2016;311:L1062–75.
- [11] Yacoub AT, Mojica L, Jones L, Knab A, Alrabaa S, Greene J. The role of corticosteroids in adult respiratory distress syndrome caused by viridans group streptococci bacteremia in neutropenic patients. *Mediterr J Hematol Infect Dis* 2014;6:e2014055.
- [12] Mokart D, van Craenenbroeck T, Lambert J, Textoris J, Brun JP, Sannini A, et al. Prognosis of acute respiratory distress syndrome in neutropenic cancer patients. *Eur Respir J* 2012;40:169–76.
- [13] Gotts JE, Bernard O, Chun L, Croze RH, Ross JT, Nessler N, et al. Clinically relevant model of pneumococcal pneumonia, ARDS, and nonpulmonary organ dysfunction in mice. *Am J Physiol Lung Cell Mol Physiol* 2019;317:L717–36.
- [14] Shah RD, Wunderink RG. Viral pneumonia and acute respiratory distress syndrome. *Clin Chest Med* 2017;38:113–25.
- [15] Yelleswaram S, Smith P, Burn T, Covington M, Juvekar A, Li Y, et al. Inhibition of cytokine signaling by ruxolitinib and implications for COVID-19 treatment. *Clin Immunol* 2020;218:108517.
- [16] McElvaney OJ, McEvoy N, McElvaney OF, Carroll TP, Murphy MP, Dunlea DM, et al. Characterization of the inflammatory response to severe COVID-19 illness. *Am J Respir Crit Care Med* 2020;202:812–21.
- [17] Hoth JJ, Martin RS, Yoza BK, Wells JD, Meredith JW, McCall CE. Pulmonary contusion primes systemic innate immunity responses. *J Trauma* 2009;67:14–21.
- [18] Daurat A, Millet I, Roustan JP, Maury C, Taourel P, Jaber S, et al. Thoracic Trauma Severity score on admission allows to determine the risk of delayed ARDS in trauma patients with pulmonary contusion. *Injury* 2016;47:147–53.
- [19] Eworuke E, Major JM, Gilbert McClain LI. National incidence rates for acute respiratory distress syndrome (ARDS) and ARDS cause-specific factors in the United States (2006–2014). *J Crit Care* 2018;47:192–7.
- [20] Hoegl S, Burns N, Angulo M, Francis D, Osborne CM, Mills TW, et al. Capturing the multifactorial nature of ARDS - "Two-hit" approach to model murine acute lung injury. *Phys Rep* 2018;6:e13648.



- [21] Deitch EA. Gut-origin sepsis: evolution of a concept. *Surgeon* 2012;10:350–6.
- [22] Whitney JE, Zhang B, Koterba N, Chen F, Bush J, Graham K, et al. Systemic endothelial activation is associated with early acute respiratory distress syndrome in children with extrapulmonary sepsis. *Crit Care Med* 2020;48:344–52.
- [23] Roubinian N. TACO and TRALI: biology, risk factors, and prevention strategies. *Hematology Am Soc Hematol Educ Program* 2018;2018:585–94.
- [24] Jongerius I, Porcelijn L, van Beek AE, Semple JW, van der Schoot CE, Vlaar APJ, et al. The role of complement in transfusion-related acute lung injury. *Transfus Med Rev* 2019;33:236–42.
- [25] Polverino E, Rosales-Mayor E, Dale GE, Dembowski K, Torres A. The role of neutrophil elastase inhibitors in lung diseases. *Chest* 2017;152:249–62.
- [26] Yang SC, Chang SH, Hsieh PW, Huang YT, Ho CM, Tsai YF, et al. Dipeptide HCH6-1 inhibits neutrophil activation and protects against acute lung injury by blocking FPR1. *Free Radic Biol Med* 2017;106:254–69.
- [27] Yang SC, Chen PJ, Chang SH, Weng YT, Chang FR, Chang KY, et al. Luteolin attenuates neutrophilic oxidative stress and inflammatory arthritis by inhibiting Raf1 activity. *Biochem Pharmacol* 2018;154:384–96.
- [28] Aulakh GK. Neutrophils in the lung: "the first responders". *Cell Tissue Res* 2018;371:577–88.
- [29] Liu Y, Du X, Chen J, Jin Y, Peng L, Wang HHX, et al. Neutrophil-to-lymphocyte ratio as an independent risk factor for mortality in hospitalized patients with COVID-19. *J Infect* 2020;81:e6–12.
- [30] Williams AE, Jose RJ, Mercer PF, Brealey D, Parekh D, Thickett DR, et al. Evidence for chemokine synergy during neutrophil migration in ARDS. *Thorax* 2017;72:66–73.
- [31] Zindel J, Kubes P. DAMPs, PAMPs, and LAMPs in immunity and sterile inflammation. *Annu Rev Pathol* 2020;15:493–518.
- [32] Vassallo A, Wood AJ, Subburayalu J, Summers C, Chilvers ER. The counter-intuitive role of the neutrophil in the acute respiratory distress syndrome. *Br Med Bull* 2019;131:43–55.
- [33] Lam FW, Da Q, Guillory B, Cruz MA. Recombinant human vimentin binds to P-selectin and blocks neutrophil capture and rolling on platelets and endothelium. *J Immunol* 2018;200:1718–26.
- [34] Hind LE, Vincent WJ, Huttenlocher A. Leading from the back: the role of the uropod in neutrophil polarization and migration. *Dev Cell* 2016;38:161–9.
- [35] Proebstl D, Voisin MB, Woodfin A, Whiteford J, D'Acquisto F, Jones GE, et al. Pericytes support neutrophil subendothelial cell crawling and breaching of venular walls in vivo. *J Exp Med* 2012;209:1219–34.
- [36] Matsumoto M, Hirata T. Moesin regulates neutrophil rolling velocity in vivo. *Cell Immunol* 2016;304–305:59–62.
- [37] Maas SL, Soehnlein O, Viola JR. Organ-specific mechanisms of transendothelial neutrophil migration in the lung, liver, kidney, and aorta. *Front Immunol* 2018;9:2739.
- [38] Zhao C, Itagaki K, Gupta A, Odom S, Sandler N, Hauser CJ. Mitochondrial damage-associated molecular patterns released by abdominal trauma suppress pulmonary immune responses. *J Trauma Acute Care Surg* 2014;76:1222–7.
- [39] Endo D, Fujimoto K, Hirose R, Yamanaka H, Homme M, Ishibashi KI, et al. Genetic phagocyte NADPH oxidase deficiency enhances nonviable *Candida albicans*-induced inflammation in mouse lungs. *Inflammation* 2017;40:123–35.
- [40] Qin X, Zhu G, Huang L, Zhang W, Huang Y, Xi X. LL-37 and its analog FF/CAP18 attenuate neutrophil migration in sepsis-induced acute lung injury. *J Cell Biochem* 2019;120:4863–71.
- [41] Faller S, Hausler F, Goefl A, von Itter MA, Gyllenram V, Hoetzel A, et al. Hydrogen sulfide limits neutrophil transmigration, inflammation, and oxidative burst in lipopolysaccharide-induced acute lung injury. *Sci Rep* 2018;8:14676.
- [42] Chen CY, Tsai YF, Huang WJ, Chang SH, Hwang TL. Propofol inhibits endogenous formyl peptide-induced neutrophil activation and alleviates lung injury. *Free Radic Biol Med* 2018;129:372–82.
- [43] Baudiss K, de Paula Vieira R, Cicko S, Ayata K, Hossfeld M, Ehrat N, et al. C1P attenuates lipopolysaccharide-induced acute lung injury by preventing NF-kappaB activation in neutrophils. *J Immunol* 2016;196:2319–26.
- [44] Blazquez-Prieto J, Lopez-Alonso I, Amado-Rodriguez L, Huidobro C, Gonzalez-Lopez A, Kuebler WM, et al. Impaired lung repair during neutropenia can be reverted by matrix metalloproteinase-9. *Thorax* 2018;73:321–30.
- [45] Zemans RL, Briones N, Campbell M, McClendon J, Young SK, Suzuki T, et al. Neutrophil transmigration triggers repair of the lung epithelium via beta-catenin signaling. *Proc Natl Acad Sci USA* 2011;108:15990–5.
- [46] Nguyen GT, Green ER, Mecas J. Neutrophils to the ROScues: mechanisms of NADPH oxidase activation and bacterial resistance. *Front Cell Infect Microbiol* 2017;7:373.
- [47] Teixeira G, Szyndralewicz C, Molango S, Carnesecchi S, Heitz F, Wiesel P, et al. Therapeutic potential of NADPH oxidase 1/4 inhibitors. *Br J Pharmacol* 2017;174:1647–69.
- [48] Winterbourn CC, Kettle AJ, Hampton MB. Reactive oxygen species and neutrophil function. *Annu Rev Biochem* 2016;85:765–92.
- [49] Pak O, Sydykov A, Kosanovic D, Schermuly RT, Dietrich A, Schroder K, et al. Lung ischaemia-reperfusion injury: the role of reactive oxygen species. *Adv Exp Med Biol* 2017;967:195–225.
- [50] Wagner J, Strosing KM, Spassov SG, Lin Z, Engelstaedter H, Tacke S, et al. Sevoflurane posttreatment prevents oxidative and inflammatory injury in ventilator-induced lung injury. *PloS One* 2018;13:e0192896.
- [51] Nadeem A, Siddiqui N, Al-Harbi NO, Attia SM, AlSharari SD, Ahmad SF. Acute lung injury leads to depression-like symptoms through upregulation of neutrophilic and neuronal NADPH oxidase signaling in a murine model. *Int Immunopharm* 2017;47:218–26.
- [52] Abouhashem AS, Singh K, Azzazy HME, Sen CK. Is low alveolar type II cell SOD3 in the lungs of elderly linked to the observed severity of COVID-19? *Antioxid Redox Signal* 2020;33:59–65.
- [53] Silvagno F, Vernone A, Pescarmona GP. The role of glutathione in protecting against the severe inflammatory response triggered by COVID-19. *Antioxidants* 2020;9:624.
- [54] Gould NS, White CW, Day BJ. A role for mitochondrial oxidative stress in sulfur mustard analog 2-chloroethyl ethyl sulfide-induced lung cell injury and antioxidant protection. *J Pharmacol Exp Ther* 2009;328:732–9.
- [55] Park JS, Park YJ, Kim HR, Chung KH. Polyhexamethylene guanidine phosphate-induced ROS-mediated DNA damage caused cell cycle arrest and apoptosis in lung epithelial cells. *J Toxicol Sci* 2019;44:415–24.
- [56] Auten RL, Whorton MH, Nicholas Mason S. Blocking neutrophil influx reduces DNA damage in hyperoxia-exposed newborn rat lung. *Am J Respir Cell Mol Biol* 2002;26:391–7.
- [57] Binder CJ, Papac-Milicevic N, Witztum JL. Innate sensing of oxidation-specific epitopes in health and disease. *Nat Rev Immunol* 2016;16:485–97.
- [58] Fukuhara K, Nakashima T, Abe M, Masuda T, Hamada H, Iwamoto H, et al. Suplatast tosylate protects the lung against

- hyperoxic lung injury by scavenging hydroxyl radicals. *Free Radic Biol Med* 2017;106:1–9.
- [59] Usatyuk PV, Vepa S, Watkins T, He D, Parinandi NL, Natarajan V. Redox regulation of reactive oxygen species-induced p38 MAP kinase activation and barrier dysfunction in lung microvascular endothelial cells. *Antioxid Redox Signal* 2003;5:723–30.
  - [60] Dias-Freitas F, Metelo-Coimbra C, Roncon-Albuquerque Jr R. Molecular mechanisms underlying hyperoxia acute lung injury. *Respir Med* 2016;119:23–8.
  - [61] Jiang K, Guo S, Yang C, Yang J, Chen Y, Shaikat A, et al. Barbaloin protects against lipopolysaccharide (LPS)-induced acute lung injury by inhibiting the ROS-mediated PI3K/AKT/NF-kappaB pathway. *Int Immunopharm* 2018;64:140–50.
  - [62] Wang J, Huang J, Wang L, Chen C, Yang D, Jin M, et al. Urban particulate matter triggers lung inflammation via the ROS-MAPK-NF-kappaB signaling pathway. *J Thorac Dis* 2017;9:4398–412.
  - [63] Rocksén D, Ekstrand-Hammarström B, Johansson L, Bucht A. Vitamin E reduces transendothelial migration of neutrophils and prevents lung injury in endotoxin-induced airway inflammation. *Am J Respir Cell Mol Biol* 2003;28:199–207.
  - [64] Shen H, Wu N, Wang Y, Han X, Zheng Q, Cai X, et al. JNK inhibitor SP600125 attenuates paraquat-induced acute lung injury: an in vivo and in vitro study. *Inflammation* 2017;40:1319–30.
  - [65] Di A, Mehta D, Malik AB. ROS-activated calcium signaling mechanisms regulating endothelial barrier function. *Cell Calcium* 2016;60:163–71.
  - [66] Liu XY, Xu HX, Li JK, Zhang D, Ma XH, Huang LN, et al. Neferine protects endothelial glycocalyx via mitochondrial ROS in lipopolysaccharide-induced acute respiratory distress syndrome. *Front Physiol* 2018;9:102.
  - [67] Kellner M, Noonepalle S, Lu Q, Srivastava A, Zemskov E, Black SM. ROS signaling in the pathogenesis of acute lung injury (ALI) and acute respiratory distress syndrome (ARDS). *Adv Exp Med Biol* 2017;967:105–37.
  - [68] Lacy P. Mechanisms of degranulation in neutrophils. *Allergy Asthma Clin Immunol* 2006;2:98–108.
  - [69] Mollinedo F. Neutrophil degranulation, plasticity, and cancer metastasis. *Trends Immunol* 2019;40:228–42.
  - [70] Bedouhene S, Dang PM, Hurtado-Nedelec M, El-Benna J. Neutrophil degranulation of azurophil and specific granules. *Methods Mol Biol* 2020;2087:215–22.
  - [71] Soehnlein O. Multiple roles for neutrophils in atherosclerosis. *Circ Res* 2012;110:875–88.
  - [72] Pham CT. Neutrophil serine proteases: specific regulators of inflammation. *Nat Rev Immunol* 2006;6:541–50.
  - [73] Miranda-Ribera A, Lecchi C, Bronzo V, Scaccabarozzi L, Sartorelli P, Franciosi F, et al. Down-regulatory effect of alpha 1-acid glycoprotein on bovine neutrophil degranulation. *Comp Immunol Microbiol Infect Dis* 2010;33:291–306.
  - [74] Armstrong CL, Miralda I, Neff AC, Tian S, Vashishta A, Perez L, et al. Filifactor alocis promotes neutrophil degranulation and chemotactic activity. *Infect Immun* 2016;84:3423–33.
  - [75] Rebetz J, Semple JW, Kapur R. The pathogenic involvement of neutrophils in acute respiratory distress syndrome and transfusion-related acute lung injury. *Transfus Med Hemother* 2018;45:290–8.
  - [76] Moraes TJ, Zurawska JH, Downey GP. Neutrophil granule contents in the pathogenesis of lung injury. *Curr Opin Hematol* 2006;13:21–7.
  - [77] Mebratu YA, Tesfagzi Y. IL-17 plays a role in respiratory syncytial virus-induced lung inflammation and emphysema in elastase and LPS-injured mice. *Am J Respir Cell Mol Biol* 2018;58:717–26.
  - [78] Suzuki K, Okada H, Takemura G, Takada C, Kuroda A, Yano H, et al. Neutrophil elastase damages the pulmonary endothelial glycocalyx in lipopolysaccharide-induced experimental endotoxemia. *Am J Pathol* 2019;189:1526–35.
  - [79] Boxio R, Wartelle J, Nawrocki-Raby B, Lagrange B, Malleret L, Hirche T, et al. Neutrophil elastase cleaves epithelial cadherin in acutely injured lung epithelium. *Respir Res* 2016;17:129.
  - [80] Aratani Y. Myeloperoxidase: its role for host defense, inflammation, and neutrophil function. *Arch Biochem Biophys* 2018;640:47–52.
  - [81] Fligiel SE, Standiford T, Fligiel HM, Tashkin D, Strieter RM, Warner RL, et al. Matrix metalloproteinases and matrix metalloproteinase inhibitors in acute lung injury. *Hum Pathol* 2006;37:422–30.
  - [82] Zinter MS, Delucchi KL, Kong MY, Orwoll BE, Spicer AS, Lim MJ, et al. Early plasma matrix metalloproteinase profiles. A novel pathway in pediatric acute respiratory distress syndrome. *Am J Respir Crit Care Med* 2019;199:181–9.
  - [83] Wang CT, Zhang L, Wu HW, Wei L, Xu B, Li DM. Doxycycline attenuates acute lung injury following cardiopulmonary bypass: involvement of matrix metalloproteinases. *Int J Clin Exp Pathol* 2014;7:7460–8.
  - [84] Albaiceta GM, Gutierrez-Fernandez A, Garcia-Prieto E, Puente XS, Parra D, Astudillo A, et al. Absence or inhibition of matrix metalloproteinase-8 decreases ventilator-induced lung injury. *Am J Respir Cell Mol Biol* 2010;43:555–63.
  - [85] Van Avondt K, Hartl D. Mechanisms and disease relevance of neutrophil extracellular trap formation. *Eur J Clin Invest* 2018;48:e12919.
  - [86] Brinkmann V, Reichard U, Goosmann C, Fauler B, Uhlemann Y, Weiss DS, et al. Neutrophil extracellular traps kill bacteria. *Science* 2004;303:1532–5.
  - [87] Hakkim A, Fuchs TA, Martinez NE, Hess S, Prinz H, Zychlinsky A, et al. Activation of the Raf-MEK-ERK pathway is required for neutrophil extracellular trap formation. *Nat Chem Biol* 2011;7:75–7.
  - [88] Papayannopoulos V. Neutrophil extracellular traps in immunity and disease. *Nat Rev Immunol* 2018;18:134–47.
  - [89] Burgener SS, Schroder K. Neutrophil extracellular traps in host defense. *Cold Spring Harb Perspect Biol* 2020;12:a037028.
  - [90] Caudrillier A, Kessenbrock K, Gilliss BM, Nguyen JX, Marques MB, Monestier M, et al. Platelets induce neutrophil extracellular traps in transfusion-related acute lung injury. *J Clin Invest* 2012;122:2661–71.
  - [91] Thomas GM, Carbo C, Curtis BR, Martinod K, Mazo IB, Schatzberg D, et al. Extracellular DNA traps are associated with the pathogenesis of TRALI in humans and mice. *Blood* 2012;119:6335–43.
  - [92] Bendib I, de Chaisemartin L, Granger V, Schlemmer F, Maitre B, Hue S, et al. Neutrophil extracellular traps are elevated in patients with pneumonia-related acute respiratory distress syndrome. *Anesthesiology* 2019;130:581–91.
  - [93] Yildiz C, Palaniyar N, Otulakowski G, Khan MA, Post M, Kuebler WM, et al. Mechanical ventilation induces neutrophil extracellular trap formation. *Anesthesiology* 2015;122:864–75.
  - [94] Mikacenic C, Moore R, Dmyterko V, West TE, Altemeier WA, Liles WC, et al. Neutrophil extracellular traps (NETs) are increased in the alveolar spaces of patients with ventilator-associated pneumonia. *Crit Care* 2018;22:358.
  - [95] Cortjens B, de Boer OJ, de Jong R, Antonis AF, Sabogal Pineros YS, Lutter R, et al. Neutrophil extracellular traps cause airway obstruction during respiratory syncytial virus disease. *J Pathol* 2016;238:401–11.



- [96] Juliana A, Zonneveld R, Plotz FB, van Meurs M, Wilschut J. Neutrophil-endothelial interactions in respiratory syncytial virus bronchiolitis: an understudied aspect with a potential for prediction of severity of disease. *J Clin Virol* 2020;123:104258.
- [97] Ashar HK, Mueller NC, Rudd JM, Snider TA, Achanta M, Prasanthi M, et al. The role of extracellular histones in influenza virus pathogenesis. *Am J Pathol* 2018;188:135–48.
- [98] Liu S, Su X, Pan P, Zhang L, Hu Y, Tan H, et al. Neutrophil extracellular traps are indirectly triggered by lipopolysaccharide and contribute to acute lung injury. *Sci Rep* 2016;6:37252.
- [99] Gan TT, Yang YL, Hu F, Chen XC, Zhou JW, Li Y, et al. TLR3 regulated poly I:C-induced neutrophil extracellular traps and acute lung injury partly through p38 MAP kinase. *Front Microbiol* 2018;9:3174.
- [100] Lefrancais E, Mallavia B, Zhuo HJ, Calfee CS, Looney MR. Maladaptive role of neutrophil extracellular traps in pathogen-induced lung injury. *JCI Insight* 2018;3:e98178.
- [101] Terpos E, Ntanas-Stathopoulos I, Elalamy I, Kastiris E, Sergeantanis TN, Politou M, et al. Hematological findings and complications of COVID-19. *Am J Hematol* 2020;95:834–47.
- [102] Barnes BJ, Adrover JM, Baxter-Stoltzfus A, Borczuk A, Cools-Lartigue J, Crawford JM, et al. Targeting potential drivers of COVID-19: neutrophil extracellular traps. *J Exp Med* 2020;217:e20200652.
- [103] Zuo Y, Yalavarthi S, Shi H, Gockman K, Zuo M, Madison JA, et al. Neutrophil extracellular traps in COVID-19. *JCI Insight* 2020;5:e138999.
- [104] Whyte CS, Morrow GB, Mitchell JL, Chowdary P, Mutch NJ. Fibrinolytic abnormalities in acute respiratory distress syndrome (ARDS) and versatility of thrombolytic drugs to treat COVID-19. *J Thromb Haemost* 2020;18:1548–55.
- [105] Zhang H, Zhou P, Wei Y, Yue H, Wang Y, Hu M, et al. Histopathologic changes and SARS-CoV-2 immunostaining in the lung of a patient with COVID-19. *Ann Intern Med* 2020;172:629–32.
- [106] Middleton EA, He XY, Denorme F, Campbell RA, Ng D, Salvatore SP, et al. Neutrophil extracellular traps (NETs) contribute to immunothrombosis in COVID-19 acute respiratory distress syndrome. *Blood* 2020;136:1169–79.

## Research Article

# Functional Redox Proteomics Reveal That *Salvia miltiorrhiza* Aqueous Extract Alleviates Adriamycin-Induced Cardiomyopathy via Inhibiting ROS-Dependent Apoptosis

Yu-Chiang Hung,<sup>1</sup> Pei-Wen Wang<sup>2</sup>,<sup>3</sup> Tung-Yi Lin,<sup>3</sup> Pei-Ming Yang,<sup>4,5</sup> Jyh-Sheng You,<sup>6</sup> and Tai-Long Pan<sup>6,7,8</sup>

<sup>1</sup>Department of Chinese Medicine, College of Medicine, Kaohsiung Chang Gung Memorial Hospital and Chang Gung University, Kaohsiung, Taiwan

<sup>2</sup>Department of Medical Research, China Medical University Hospital, China Medical University, Taichung, Taiwan

<sup>3</sup>Department of Traditional Chinese Medicine, Chang Gung Memorial Hospital, Keelung, Taiwan

<sup>4</sup>TMU Research Center of Cancer Translational Medicine, Taipei Medical University, Taipei, Taiwan

<sup>5</sup>Graduate Institute of Cancer Biology and Drug Discovery, College of Medical Science and Technology, Taipei Medical University, Taipei, Taiwan

<sup>6</sup>School of Traditional Chinese Medicine, Chang Gung University, Taoyuan, Taiwan

<sup>7</sup>Liver Research Center, Chang Gung Memorial Hospital, Taoyuan, Taiwan

<sup>8</sup>Research Center for Chinese Herbal Medicine and Research Center for Food and Cosmetic Safety, College of Human Ecology, Chang Gung University of Science and Technology, Taoyuan, Taiwan

Correspondence should be addressed to Pei-Wen Wang; [pwwang5105@hotmail.com](mailto:pwwang5105@hotmail.com) and Tai-Long Pan; [pan@mail.cgu.edu.tw](mailto:pan@mail.cgu.edu.tw)

Received 8 July 2020; Revised 14 August 2020; Accepted 19 August 2020; Published 10 September 2020

Academic Editor: Peeter Karihtala

Copyright © 2020 Yu-Chiang Hung et al. This is an open access article distributed under the Creative Commons Attribution License, which permits unrestricted use, distribution, and reproduction in any medium, provided the original work is properly cited.

The anticancer agent adriamycin (ADR) has long been recognized to induce a dose-limiting cardiotoxicity, while *Salvia miltiorrhiza* (SM) is a Chinese herb widely used for the treatment of cardiovascular disorders and its aqueous extract (SMAE) has shown anticancer as well as antioxidant effects. In the current study, we aimed at investigating the synergistic effect and potent molecular mechanisms of SMAE with a focus on the cardioprotective benefit observed under ADR adoption. Histopathological analysis indicated that SMAE could substantially alleviate cardiomyopathy and cell apoptosis caused by ADR. Meanwhile, the two-dimensional electrophoresis (2-DE) oxyblots demonstrated that SMAE treatment could effectively reduce carbonylation of specific proteins associated with oxidative stress response and various metabolic pathways in the presence of ADR. SMAE application also showed protective efficacy against ADR-mediated H9c2 cell death in a dose-dependent manner without causing any cytotoxicity and significantly attenuated the reactive oxygen species production. Particularly, the simultaneous administration of ADR and SMAE could remarkably suppress the growth of breast cancer cells. We also noticed that there was a marked upregulation of detoxifying enzyme system in the presence of SMAE, and its exposure also contributed to an increase in Nrf2 and HO-1 content as well. SMAE also amended the ERK/p53/Bcl-xL/caspase-3 signaling pathways and the mitochondrial dysfunction, which eventually attribute to apoptotic cathepsin B/AIF cascades. Correspondingly, both the ERK1/2 inhibitor (U0126) and pan-caspase inhibitor (Z-VAD-FMK) could at least partially abolish the ADR-associated cytotoxicity in H9c2 cells. Collectively, these results support that ROS apoptosis-inducing molecule release is closely involved in ADR-induced cardiotoxicity while SMAE could prevent or mitigate the causative cardiomyopathy through controlling multiple targets without compromising the efficacy of chemotherapy.

## 1. Introduction

The anthracycline antibiotic adriamycin (ADR), also known as doxorubicin, is the commonly used chemotherapeutic agent for the treatment of various cancers. However, the severe cardiotoxicity of ADR greatly restricts its clinical utilization [1, 2]. Although ADR-related injury appears to be multifactorial and complicated, oxidative stress and mitochondrial dysfunction have been proposed to majorly account for the pathogenesis of ADR-induced cardiomyopathy [3–6]. Moreover, cardiomyocytes apoptosis can be a pivotal event by which ADR causes deterioration of cardiac system but the detailed molecular mechanisms still remain unclear. Several chemical agents have been used to prevent the ADR-induced cardiotoxicity; nevertheless, treatment with these drugs is known to have certain disadvantages. Dexrazoxane (DXR), for example, is the only FDA-approved drug for treating ADR-associated cardiomyopathy; however, it might increase the risk of infection, myelosuppression, and second primary malignancies [7, 8]. Therefore, the development of alternative cardioprotectants with low toxicity is urgently needed for cancer survivors.

A great amount of effort has been made towards perfecting the clinical applications of herbal medicine that are frequently used in combination to improve the therapeutic efficacy [9]. Of note, *Salvia miltiorrhiza* (SM) has been prescribed for treating cardiovascular disorders since a long time [10]. The water-soluble components extracted from SM including salvianolic acids A, B, and C have garnered much interest as a multitargeted therapy owing to their antioxidant effects on free radicals. Additionally, *Salvia miltiorrhiza* aqueous extract (SMAE) has been utilized widely for the treatment of coronary heart disease, atherosclerosis, and ischemic cardiovascular diseases [11, 12]. Our previous research has also revealed that SMAE provides a protective effect against adriamycin- (ADR-) induced cardiomyopathy and hepatic damage [13]. However, the molecular pathways associated with the SMAE-mediated advantageous effect in managing the cardiotoxicity resulting from ADR treatment have not been thoroughly investigated. Herein, we used animal and cellular models to verify whether ADR-induced cardiomyopathy could be relieved by SMAE and also evaluate the synergistic effect on cancer cells.

ROS generation caused by ADR administration would disturb the normal redox balance and produce huge oxidative stress, which subsequently stimulates the carbonylation of specific groups of proteins involved in physiological dysfunction and induces cardiomyocyte apoptosis [14–16]. The most largely studied oxidative stress-caused by a modification of proteins is the formation of carbonyl groups which can react with 2,4-dinitrophenylhydrazine (DNP) and are discovered by redox proteomics [17, 18]. The appearance of carbonylated proteins has been considered as a hallmark of ROS-induced change of protein which might be helpful to predict novel targets for the diagnosis and prognosis of diseases. Furthermore, the functional “signature network” analyzed with MetaCore™ pathway generates global cellular mechanisms underlying different protein levels and imitates

signaling pathways based on the integration of molecular and clinical information [19].

The present study has shed light on the cellular mechanisms involved with SMAE, exhibiting its protective effect and inhibition of ADR-induced cardiomyopathy. Additionally, our findings should offer an opportunity to execute novel therapeutic strategies and sensitive markers for the clinical usage of ADR.

## 2. Materials and Methods

**2.1. Materials.** Specific antibodies to GAPDH, SOD, catalase, p53, Nrf2, and HO-1 were purchased from Santa Cruz (Santa Cruz, CA, USA). Monoclonal antibodies to  $\beta$ -actin were obtained from Millipore (Burlingame, CA, USA). Polyclonal antibodies to caspase-3, -9, PARP, Bax, Bcl-xL, phospho-p53, ERK, and phospho-ERK were purchased from Cell Signaling (Beverly, MA, USA). U0126 and Z-VAD-FMK were obtained from Enzo Life Science (New York, NY, USA).

**2.2. Prepare the Extract of *Salvia miltiorrhiza*.** The air-dried roots of cultivated *Salvia miltiorrhiza* Bunge (Labiateae) were purchased from a Traditional Chinese Medicine dispensary in Taiwan and authenticated by the experts in pharmacognosy. The preparation of *Salvia miltiorrhiza* aqueous extract (SMAE) was as reported by the method of Liu [20]. Briefly, the hot-water extract was prepared by boiling the dried roots with distilled water for 5 hr. The concentration used in each experiment was calculated upon the dry weight of the SMAE extract (mg/mL), which was resuspended in freshly prepared double distilled and deionized water as purified by the Milli-Q filtration system (Millipore).

**2.3. ADR-Induced Heart Failure on Animal Model.** Male Wistar rats, body weight 250–300 g, were maintained on a normal rat chow diet. The rats were randomly divided into three groups: CTL, ADR, and ADR plus SMAE. Five rats that received ready-to-use ADR (Adriablastina RD 10 mg-INS-040731, Pfizer Inc.) were administered by intraperitoneal injection in six equal doses (each containing 3 mg/kg ADR) over a period of 2 weeks, with a total cumulative dose of 18 mg/kg ADR, and five CTL rats were injected with an identical volume of normal saline. Five rats were administered with 100 mg/kg/day of SMAE via oral delivery with ADR injections. At the end of the 5-week posttreatment period, the heart was removed and separately stored for histomorphologic examination and protein expression analysis [13]. Thereby, we utilized the short-term model to evaluate cardiotoxicity, while a previous study had shown that 10 mg/kg ADR application would result in 80% mortality [21], which was consistent with our findings. The rats were treated according to the Ethical Guidelines of the Animal Center, and the experimental protocol was reviewed and approved by the Institutional Animal Care and Use Committee of Chang Gung University (CGU08-61).

**2.4. Histology and Immunohistochemistry.** The heart tissue fixed by 5% neutral buffered formalin was immersed in paraffin and then sliced into 5  $\mu$ m sections. The sample slices were stained with Masson's trichrome (MT) for a histological

assessment. Immunohistochemistry with caspase 3 was applied to specimens as previously described [22]. The histological changes were observed by using optical microscopy (Olympus BX51, Japan) in nonconsecutive, randomly chosen 400 $\times$  histological fields. The digital photomicrographs were then processed with DP-72.

**2.5. TUNEL Assay.** Apoptosis was assessed by terminal deoxynucleotidyl transferase-mediated dUTP biotin nick end labeling (TUNEL) using ApopTag<sup>®</sup> Plus Peroxidase in situ Apoptosis Detection Kit (Millipore) according to the manufacturer's instructions. The slides were counterstained with hematoxylin and mounted. The numbers of stained and unstained cells were then counted from randomly chosen fields per slide within a high-power field ( $\times 400$  magnification) under an Olympus BX50 microscope [22].

**2.6. Two-Dimensional Polyacrylamide Gel Electrophoresis (2-D PAGE).** The procedure has been reported previously [23]. Proteins (150  $\mu$ g for 2-DE oxyblot or 250  $\mu$ g for silver stain) were solubilized in the rehydrated buffer and applied onto 13 or 18 cm Immobiline DryStrip 3-10NL on the IPGphor IEF System (GE Healthcare). The running conditions of the IEF (isoelectric focusing) follow 30 V, 12 h; 100 V, 1 h; 250 V, 1 h; 500 V, 0.5 h; 1,000 V, 0.5 h; 4,000 V, 0.5 h; and 8,000 V, up to 80 kVh.

**2.7. Derivatization of Protein Carbonyls and DNP Immunostaining.** IPG strips were incubated in 2 N HCl with 10 mM DNPH at 25°C for 15 min after IEF; strips were then washed with 2 M Tris-Base/30% glycerol for 15 min [24]. The IPG strips were used for molecular weight-dependent separation of proteins by SDS-PAGE and transferred the protein blotting to a membrane which was incubated overnight at 4°C with the anti-DNP antibody in TBST containing 5% milk. The blots were washed and incubated goat anti-rabbit IgG HRP conjugate for 2 hrs. Enhanced chemiluminescence (PerkinElmer, CA, USA) was used for detection.

**2.8. In-Gel Enzymatic Digestion and Mass Spectrometry.** Spots of interest were excised and in-gel digested with trypsin according to previously described procedures [25]. Monoisotopic peptide masses were assigned and used for database searches with the MASCOT search engine (<http://www.matrixscience.com>) (Matrix Science, London). Search parameters were set as follows: a maximum allowed peptide mass error of 50 ppm and consideration of one incomplete cleavage per peptide.

**2.9. Biological Network Analysis Using MetaCore<sup>™</sup>.** Apply MetaCore<sup>™</sup> software (vers. 5.2 build 17389, GeneGo, St. Joseph, MI, USA) to reveal associated ontological classes and relevant pathways, which were represented among the proteins identified by the 2-DE and peptide mass fingerprint [25].

**2.10. Cell Culture and MTT Assay.** Rat cardiomyoblast-derived H9c2 cell was purchased from the Food Industry Research and Development Institute. The H9c2 and MCF-7 cells were maintained in DMEM medium containing 10%

fetal bovine serum (FBS) at 37°C in a humidified atmosphere of 5% CO<sub>2</sub>. Cell viability was determined by MTT. A total of  $1 \times 10^4$  cells were seeded in 24-well plates for 24 hours (h) and made quiescent by incubating in medium containing 0.2% FBS overnight. After treating with various concentrations (0, 0.3125, 0.625, 1.25, 2.5, 5, and 10 mg/mL) of SMAE for 48 h, isopropanol solution mixed with tetrazolium salt was added to the wells and incubated for additional 4 h at 37°C [26]. The optical density of the dissolved material was measured spectrophotometrically at 570 nm, and assays were performed in triplicate.

**2.11. Image Analysis for Generation of Intracellular ROS under SMAE Application.**  $2 \times 10^3$  H9c2 cells were seeded in a slide chamber, grown to 60% confluence, and cultured in serum-free DMEM medium overnight. Cells were then incubated with 2.5 mg/mL of SMAE for 6 h. Carboxy-H<sub>2</sub>DCFDA (4  $\mu$ M, dissolved in PBS) was added to the wells and incubated for 30 min at 37°C. To terminate the reaction, the cells were washed with PBS twice. Next, 500  $\mu$ L culture medium was added to each well and incubated for 20 min at 37°C. The cells were observed and photographed using a fluorescent microscope (Olympus BX51) under the DP72 Photo-Image system. Image-Pro<sup>®</sup> plus 4.5 (Media Cybernetics, Bethesda, MD) image analysis software was used to quantify image signals [27].

**2.12. Western Blot Analysis.** Samples proteins were isolated by cell lysis buffer (Cell Signaling, MA, USA) and measured using the Bradford Protein Assay Kit (AMRESCO, OH, USA). Total proteins were separated with 10% SDS-polyacrylamide gel electrophoresis and transferred to PVDF membrane (PALL). Next, the blots were incubated with specific primary antibody overnight at 4°C after blocking and further incubated with a peroxidase-labeled anti-mice or -rabbit IgG for 2 h; blots were then washed and incubated goat anti-rabbit and anti-mouse IgG (Chemicon) HRP conjugate for 2 hrs. Enhanced chemiluminescence (PerkinElmer, USA) was used for signal detection. The level of expression of  $\beta$ -actin was used as a gel loading control [27].

**2.13. Statistical Analysis.** All values were presented as the mean  $\pm$  SD. Statistical analysis of the mean values was carried out with the ANOVA test using SPSS software (SPSS Inc., Chicago, IL, USA). Differences were considered as being significant at  $p < 0.05$ .

### 3. Results

**3.1. Effects of SMAE on the Pathological Characteristics, Caspase-3 Level, and Apoptosis in ADR-Exposed Cardiomyocyte of Rats.** Drug-caused cardiotoxicity has become a critical issue linked to the therapeutic efficiency. Given that the protective effects of SMAE were evaluated by the extent of collagen accumulation and death of cardiomyocyte *in vivo*. As shown in Figure 1(a), ADR-applied hearts showed moderate damage characterized with collagen accumulation as detected by the use of Masson's trichrome staining, while the morphology of control tissue remained normal. Conversely, the rats which were simultaneously subjected to



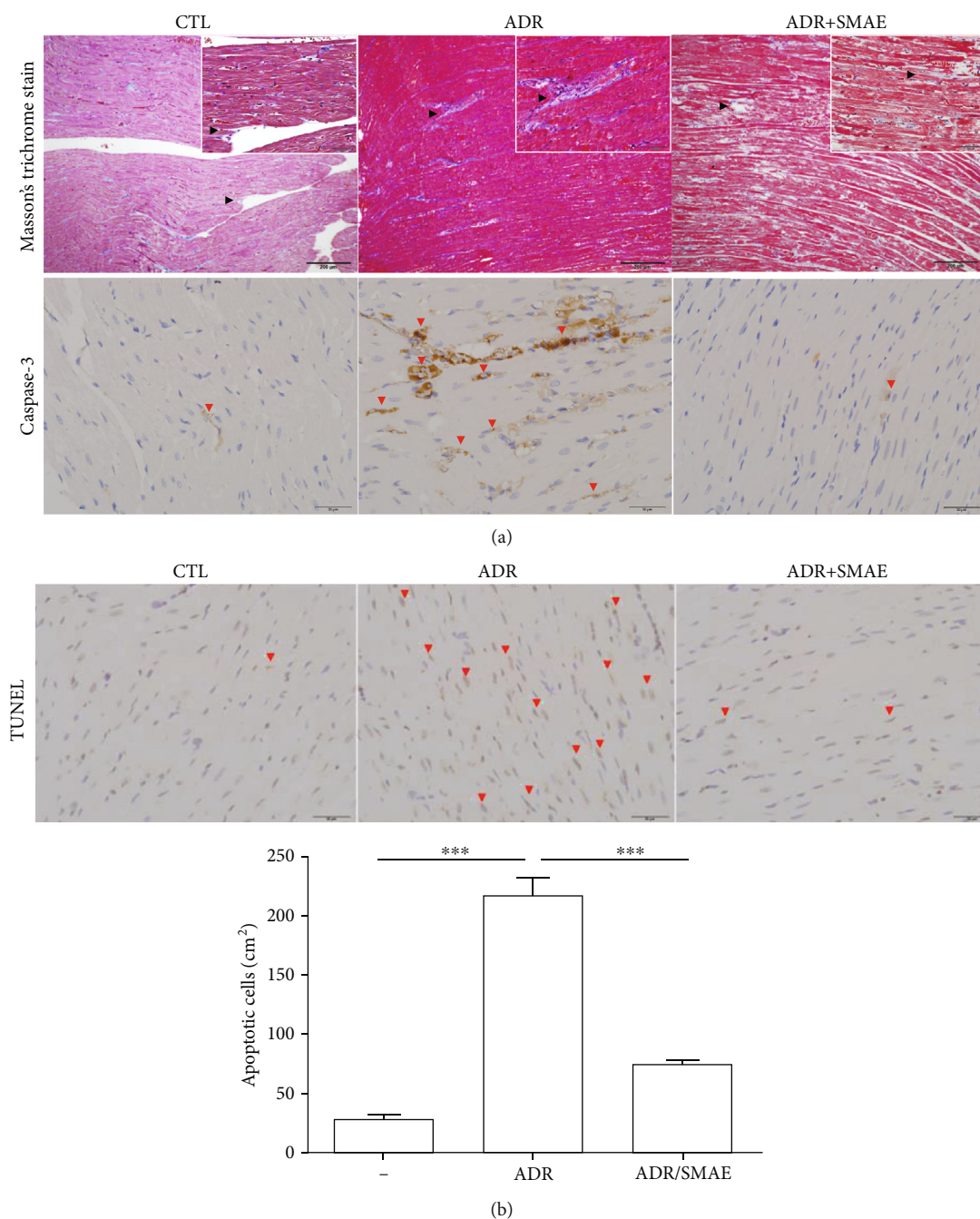


FIGURE 1: (a) Upper panels: histologic examination of heart tissue by Masson's trichrome staining and immunohistochemical analysis for control group, ADR-treated group, and ADR+SMAE group. The positive signals showing blue color demonstrated an accumulation of collagen and were zoomed in by white squares (indicated by black arrows; original magnification:  $\times 200$ ). Lower panels: the regions with differently expressed caspase-3 were indicated by red arrows. Original magnification:  $\times 400$ . (b) Terminal deoxynucleotidyl transferase dUTP nick end labeling (TUNEL) experiment was performed with immunohistochemical examination of rat heart, and the red arrows indicated TUNEL-positive signals. The quantification of the TUNEL-positive cardiomyocytes per cm<sup>2</sup> in various treatments was shown by bar chart. Data are mean  $\pm$  SD (\*\* $p < 0.001$ ).

SMAE and ADR treatment presented normal heart histological characteristics, and no sign of cardiac fibrogenesis was detected. Furthermore, cardiomyocytes apoptosis as a consequence of ADR exposure was also evaluated, which was characterized by the presence of altered heart foci. The immunohistochemistry examination showed that they

stained positively for caspase-3. In contrast, caspase-3 signal was rarely identified in samples treated with SMAE. Meanwhile, the terminal deoxynucleotidyl transferase-mediated dUTP biotin nick end labeling (TUNEL) results showed significantly increased cell death in the ADR-applied samples compared with the control; reversely, a minor apoptotic



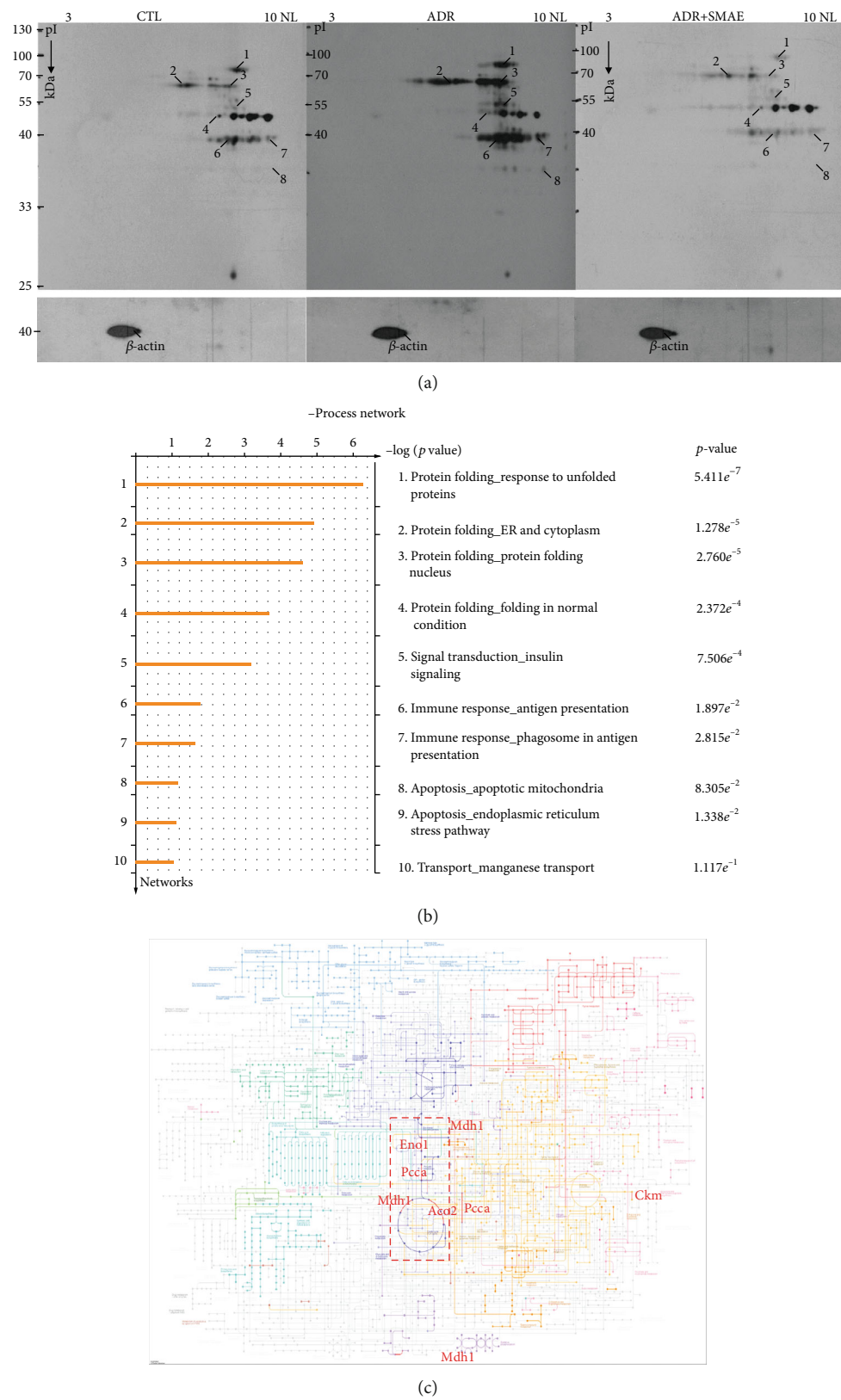


FIGURE 2: (a) Images of the 2-DE oxyblot. Analysis of protein oxidation levels in DNP-derivatized cellular proteins among the control group, ADR-treated group, and ADR+SMAE group. A significant reduction in the carbonylation levels of proteins are identified in the ADR+SMAE-applied group compared to the ADR group. (b) Top-ranked pathways from the GeneGo MetaCore™ pathway analysis. Pathways were ranked according to *p* values, and bars represent the inverse log of the *p* value. (c) The KEGG analysis indicated that several metabolisms processed in mitochondria were affected under the ADR treatments.

TABLE 1: List of identified oxidation of proteins in rat heart tissue.

Spot no.	Protein name	Accession number	Mw/pI	Score (coverage) <sup>1</sup>	Match fragment	Location	Function
1	ACON	Q9ER34	86.121/7.87	175 (37%)	23	Mitochondrion	Catalyzes the isomerization of citrate to isocitrate via cis-aconitate.
2	GRP75	P48721	74.097/5.97	189 (49%)	24	Mitochondrion	May play a role in the control of cell proliferation and cellular aging.
3	PCCA	P14882	82.198/7.59	113 (32%)	16	Mitochondrion matrix	This is one of the 2 subunits of the biotin-dependent propionyl-CoA carboxylase (PCC), a mitochondrial enzyme involved in the catabolism of odd chain fatty acids, branched-chain amino acids isoleucine, threonine, methionine, and valine and other metabolites.
4	ENOA	P04764	47.440/6.16	171 (54%)	18	Cytoplasm or cell membrane.	Multifunctional enzyme that, as well as its role in glycolysis, plays a part in various processes such as growth control, hypoxia tolerance and allergic responses.
5	ALDH2	P11884	56.966/6.63	125 (36%)	14	Mitochondrion matrix	An aldehyde + H <sub>2</sub> O + NAD <sup>+</sup> = a carboxylate + H <sup>+</sup> + NADH
6	KCRM	P00564	43.246/6.58	78 (26%)	9	Cytoplasm.	Creatine kinase isoenzymes play a central role in energy transduction in tissues with large, fluctuating energy demands, such as skeletal muscle, heart, brain, and spermatozoa.
7	ODPA	P26284	43.883/8.49	56 (20%)	8	Mitochondrion matrix	The pyruvate dehydrogenase complex catalyzes the overall conversion of pyruvate to acetyl-CoA and CO <sub>2</sub> , and thereby links the glycolytic pathway to the tricarboxylic cycle.
8	MDHM	P04636	36.117/8.93	84 (42%)	12	Mitochondrion matrix	(S)-malate + NAD <sup>+</sup> = H <sup>+</sup> + NADH + oxaloacetate

<sup>1</sup>SwissProt 2020\_02 (562253 sequences; 202348262 residues).

signal was detected in the ADR/SMAE-treated group (Figure 1(b)), implying a strong protection of SMAE against ADR-induced cardiocytotoxicity.

**3.2. Detection of the Protein Carbonylation with 2-DE Oxyblot and Functional Network Analysis.** Oxidative modification of proteins resulting from ADR application has been implicated as one of the leading causes of cardiac cell death. Meanwhile, carbonylation of proteins due to oxidative modification has been reported to impair their normal function in various metabolic processes. In our present study, changes in oxidized proteins among different groups were delineated by 2-DE oxyblots. The extent of protein oxidation was dramatically upregulated in the ADR group with respect to the control sample. Interestingly, there was a remarkably decreasing tendency for the protein carbonylation in the ADR/SMAE group, indicating that SMAE could effectively scavenge ROS induced by ADR (Figure 2(a)). The protein spots with significant and meaningful changes were indicated by Arabic numerals and were subjected to a PMF analysis after using MALDI-TOF mass spectrometry. Table 1 summarizes the detailed results obtained after using the MASCOT database searching. The individual carbonylated proteins separated by 2-DE analysis were normalized according to the intensity of the proteins. The eight targeted proteins which were uncovered by 2-DE oxyblot analysis were further dissected

with the MetaCore™ software to elucidate the intracellular events and the mechanisms associated with ADR-related heart injury. The biological networks were built based on the uploaded proteins, and the biological process was appointed to each network as shown in Figure 2(b). The specific interaction pathways showed that differentially expressed proteins under the influence of ADR and SMAE administration were majorly involved in the following cellular pathways: protein folding response to unfolded proteins ( $p = 5.411 \times 10^{-7}$ ), protein folding in ER and cytoplasm ( $p = 1.278 \times 10^{-5}$ ), and apoptosis in mitochondria ( $p = 8.305 \times 10^{-2}$ ). The  $p$  value demonstrates the significance of the assigned GO process on the basis of assembly size as compared with the subnetworks derived from the input protein list. According to the KEGG pathway analysis, glyoxylate and dicarboxylate metabolism, TCA cycle, pyruvate metabolism, and carbon metabolism were largely impaired due to ROS-mediated cell apoptosis and protein degradation (Figure 2(c)).

**3.3. Evaluation of Protective Effect of SMAE against the Cytotoxicity Observed in ADR-Applied H9c2 Cells.** To verify the drug safety and pharmaceutical effects of SMAE in vitro, cell viability was investigated by MTT assays. At first, H9c2 cells were treated with 0~10 mg/mL SMAE for 48 h, and cell viability was not affected under 2.5 mg/mL

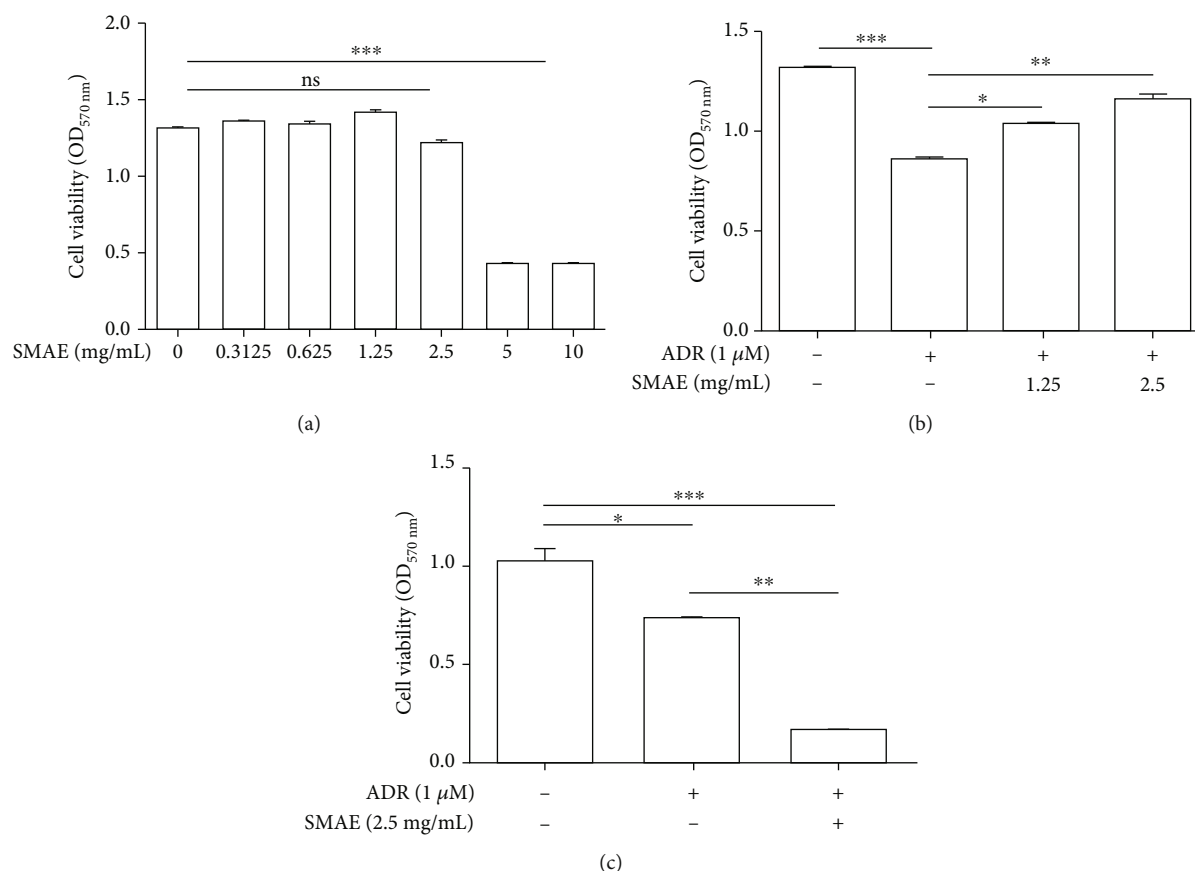


FIGURE 3: (a) Safety of SMAE extract upon H9c2 cell viability was measured by the MTT assays. H9c2 cells were treated with various concentrations of SMAE ( $x$ -axis). Data are mean  $\pm$  SD of three independent experiments, carried out in triplicate (ns means no significance, \*\*\* $p$  < 0.001). (b) Viability of H9c2 cell was determined with or without 1 micro M ADR under exposure to 1.25 and 2.5 mg/mL SMAE, respectively. The quantified results were indicated by the bar chart. Results represent the mean  $\pm$  SD of three independent experiments (\* $p$  < 0.05, \*\* $p$  < 0.01, \*\*\* $p$  < 0.001). (c) Synergistic effect of ADR and SMAE upon breast cancer cell (MCF-7) was determined with or without 1 micro M ADR under exposure to 2.5 mg/mL SMAE. The quantified results were indicated by the bar chart. Results represent the mean  $\pm$  SD of three independent experiments (\* $p$  < 0.05, \*\* $p$  < 0.01, \*\*\* $p$  < 0.001).

(Figure 3(a)). Next, SMAE application could effectively attenuate the cell death caused by the ADR exposure in a dose-dependent fashion (Figure 3(b)). The above response analysis highlighted that the optimal concentration of SMAE should be 2.5 mg/mL, while SMAE could effectively abolish the ADR-mediated cytotoxicity without causing any damage to cardiomyocytes.

**3.4. Detection of Synergistic Cytotoxic Activities of ADR and SMAE in Breast Cancer Cells.** The synergistic cytotoxic activities of ADR and SMAE were tested on the breast cancer cell line (MCF-7). The results demonstrated that SMAE could enhance the inhibitory effects of ADR, which was used to treat breast cancer. The findings suggested that the simultaneous administration of SMAE followed by chemotherapeutic agent treatment was better than the individual drug intervention (Figure 3(c)).

**3.5. The Effect of SMAE on Cellular ROS Production and on Antioxidant Enzymes.** Since ADR application creates an excessive amount of ROS, oxidative modification of biological molecules such as DNA and protein in the cytosol might

induce consecutive apoptosis. Dichlorofluorescein (DCF) fluorescent intensity (Figure 4(a)) showed that ADR treatment promoted intracellular ROS production within 6 hours compared with the control group while treatment with 2.5 mg/mL SMAE could largely reduce the oxidative stress. We also assessed the content of oxidative stress markers, including catalase and superoxide dismutase (SOD) in the H9c2 cells. Again, treatment conducted with SMAE could significantly promote the catalase and SOD content compared with the control group as well as with the ADR-exposed subjects, thus protecting the liver against ROS damage (Figure 4(b)). To further elucidate the molecular mechanism related to the regulation of the antioxidant enzymes, Nrf2 and HO-1 which act as the predominant contributors for the activation of the antioxidant system were determined by western blot analysis. In line with this result, ADR exposure remarkably suppressed Nrf2 and HO-1 expression as compared to the control, while SMAE treatment synchronously stimulated the levels of Nrf2 and HO-1 in a dose-dependent manner (Figure 4(c)).  $\beta$ -Actin was used as a loading control. These findings suggest that SMAE could effectively repeal ADR-mediated ROS generation.

**3.6. SMAE Modulates the Molecular Pathways of Apoptosis Induced by ADR.** To further address the signaling events underlying the apoptotic response of H9c2 cells after exposure to ADR with or without SMAE application, we investigated the MAPK cascades which might trigger downstream signaling such as p53 pathway associated with apoptosis induction. The peaks of phosphorylated ERK1/2 and p53 protein induction were detected at 24 hours following 1  $\mu$ M of ADR treatment compared to the control, while exposure to SMAE dramatically inhibited ERK1/2 and p53 phosphorylation which was stimulated by ADR. Total ERK1/2 and p53 content showed no significant changes over time (Figure 5(a)). In parallel with the result mentioned above, the ERK1/2 inhibitor (10  $\mu$ M U0126) moderately suppressed ERK1/2 and p53 phosphorylation, which was stimulated by ADR while administration of SMAE with U0126 significantly arrested the levels of ERK1/2 and p53 phosphorylation, which reflects that SMAE could restore the ADR-caused apoptosis via ERKs/p53 signaling transduction pathway (Figure 5(b)). The increased expression of p53 is associated with Bcl-2 family genes, which elicit the cytochrome c release, activation of caspase-9 and caspase-3, and eventually cell apoptosis. Furthermore, we demonstrated that the pretreatment of SMAE with or without U0126 significantly induced the Bcl-xL/Bax ratio, which was negatively accompanied by cytochrome c release into the cytoplasm and coordinately inhibited the cell apoptosis (Figure 5(c)). In line with our findings, we measured the signaling marker proteins, caspase-3, and PARP by western blot analysis. Active forms of caspase-3 and cleaved PARP (89 kDa) were increased under the treatment of ADR, whereas the application of SMAE with or without U0126 almost completely blocked the activation of these apoptotic proteins as shown in Figure 5(d). As expected, we demonstrated that SMAE combined with or without the pan-caspase inhibitors (z-VAD-FMK) could also effectively attenuate ADR-induced apoptosis associated with a cleavage of PARP (Figure 5(e)). These results showed that the antiapoptotic effect of SMAE may be involved in modulating p53 signaling and Bcl-xL through ERK-dependent pathways. According to the abovementioned findings, a pan-caspase inhibitor could not entirely arrest ADR-induced cell death, which was manifested by cleavage of PARP. It raised the possibility that SMAE could attenuate the cardiomyotoxicity through another pathway such as the cathepsin B/apoptosis-inducing factor- (AIF-) dependent event. Western blotting results showed that ADR treatment stimulated the level of cathepsin B but significantly suppressed AIF while SMAE strongly inhibiting the expression of cathepsin B, and a corresponding increase in the levels of AIF was observed (Figure 5(f)).

## 4. Discussion

Adriamycin (ADR) is a well-established and highly effective antineoplastic agent used to treat several cancers such as breast cancer and leukemia. The clinical application of ADR has been hindered as it has caused various cardiac disorders characterized by a broad spectrum of symptoms [16, 28]. It has been reported that approximately 10% of patients

exposed to ADR or its derivatives will develop cardiac complications after the cessation of chemotherapy. In this regard, the herbal medicine which has been widely used for heart protection or treatment of cancers may serve as a promising cardioprotective strategy against ADR-elicited cardiomyopathy [9, 29, 30]. Here, we have revealed the protective function and underlying molecular mechanisms of SMAE against ADR-induced cardiotoxicity *in vivo* and *in vitro*.

The *in vivo* results represented that ADR exposure initiates cardiomyopathy and stimulates specific genes involved in the apoptotic process such as the caspase-3 signaling pathway, which was verified by the reduction of cell growth under ADR treatment. SMAE exposure could ameliorate heart fibrogenesis and restore the cell survival via eliminating the expression of caspase-3 without causing any cytotoxicity to cardiomyocytes. Most importantly, SMAE utilization does not affect the efficacy of anticancer drugs but strongly suppresses the viability of cancer cells to exhibit a synergistic effect.

Growing evidence shows that ROS plays a critical role in ADR-mediated cardiocytotoxicity and the accumulation of ROS in mitochondria will finally result in cell apoptosis and will have an impact on cellular metabolism [31]. Hence, the inhibition or removal of ROS may be utilized for alleviating the heart injury caused by the ADR treatment. Particularly, SMAE comprises of several bioactive components including salvianolic acids (A and B), caffeic acid, 3,4-dihydroxyphenyl lactic acid (danshensu), and tanshinone and is confirmed to have antioxidant, anti-inflammatory, and anticancer effects [13, 32, 33]. The results have demonstrated that SMAE administration significantly restricted the production of carbonylated protein and oxidative stress induced by ADR application as shown in 2-DE oxyblot and DCF analysis. It has also been demonstrated that SMAE could induce Nrf2, which activates the Nrf2 –ARE pathway to stimulate the expression of multiple antioxidant enzymes such as HO-1. Accordingly, SMAE can prevent oxidative damage by elevating the levels of SOD and catalase in the ADR-exposed H9c2 cells. Taken together, these results imply that SMAE at least partially attenuated ADR-induced cardiomyopathy via regulating the protein carbonylation as well as the antioxidant system to relieve the ROS-mediated apoptosis.

The most striking feature observed in 2-DE oxyblot analysis is that lots of mitochondrial proteins showed significant and meaningful changes in redox state under different treatments modality. It is well-established that biomolecule oxidation is closely linked to a series of pathological events; the accumulation of redox-dependent posttranslational modification of certain key proteins would lead to ER stress and subsequent activation of the mitochondrial apoptotic pathway. The heart is one of the highest ATP-consuming organs and most of ATP is generated by the mitochondria through primarily oxidative phosphorylation [34–38]. Furthermore, network analysis has suggested that ADR-caused heart damage is majorly caused by impaired protein folding due to oxidative stress and mitochondrial dysfunction. Intertwined with this, the specific proteins including ACON, GRP75, PCCA, ENOA, KCRM, ODP, and MDHC which are mostly associated with critical metabolic processes in

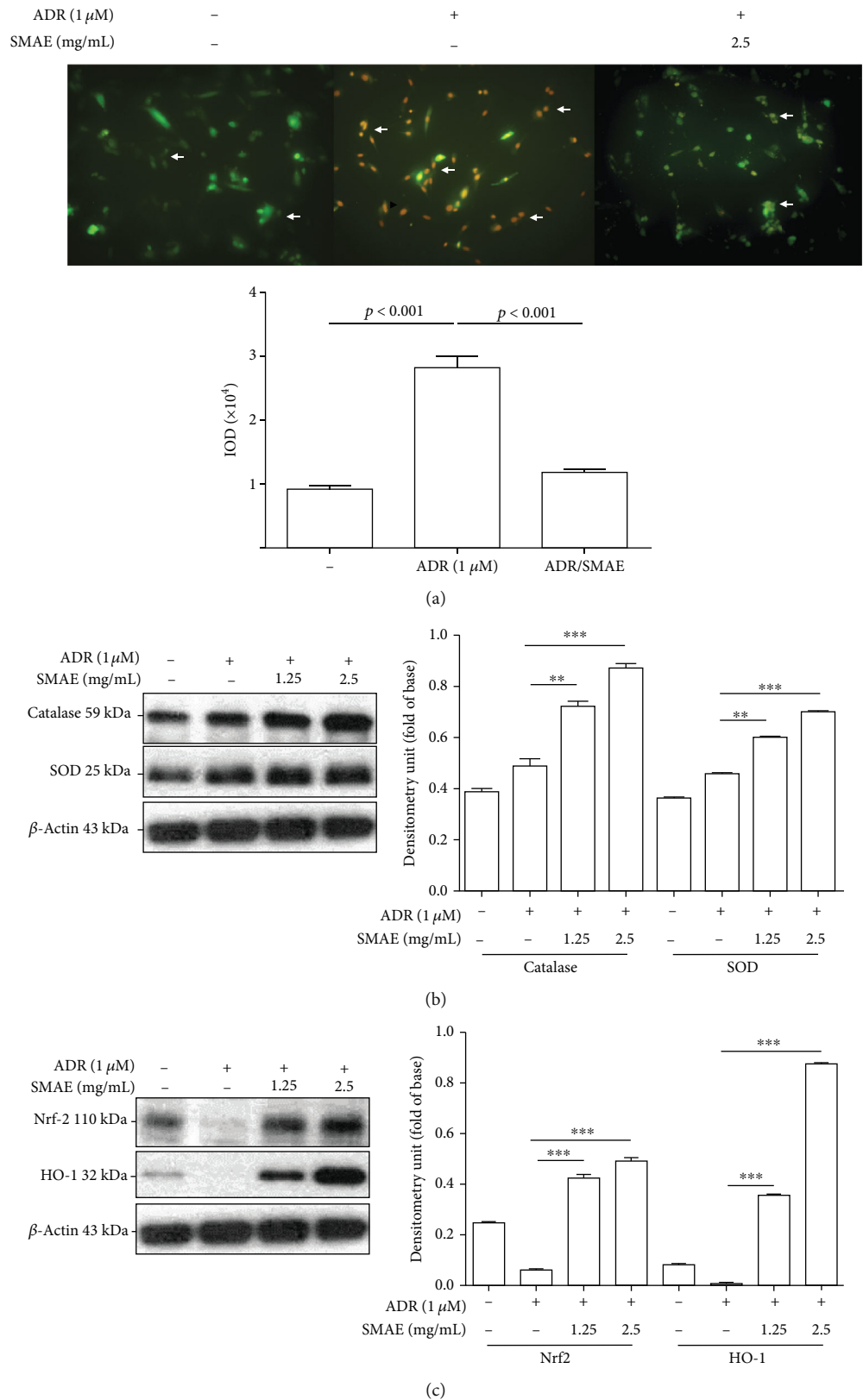


FIGURE 4: (a) H9c2 cells were incubated with or without 1 micro M ADR and 2.5 mg/mL SMAE. The DCF fluorescence signal was observed under a fluorescence microscope and demonstrated by arrows. (b) Validation of changes in protein expression after different treatments. Protein levels of catalase and SOD were determined by a Western blot analysis. (c) The expression of Nrf2 and HO-1 was evaluated with Western blot analysis.  $\beta$ -Actin was used as an internal control. The quantified results were indicated by the bar chart and represent the mean  $\pm$  SD of three independent experiments. (\*\* $p < 0.01$ , \*\*\* $p < 0.001$ ).



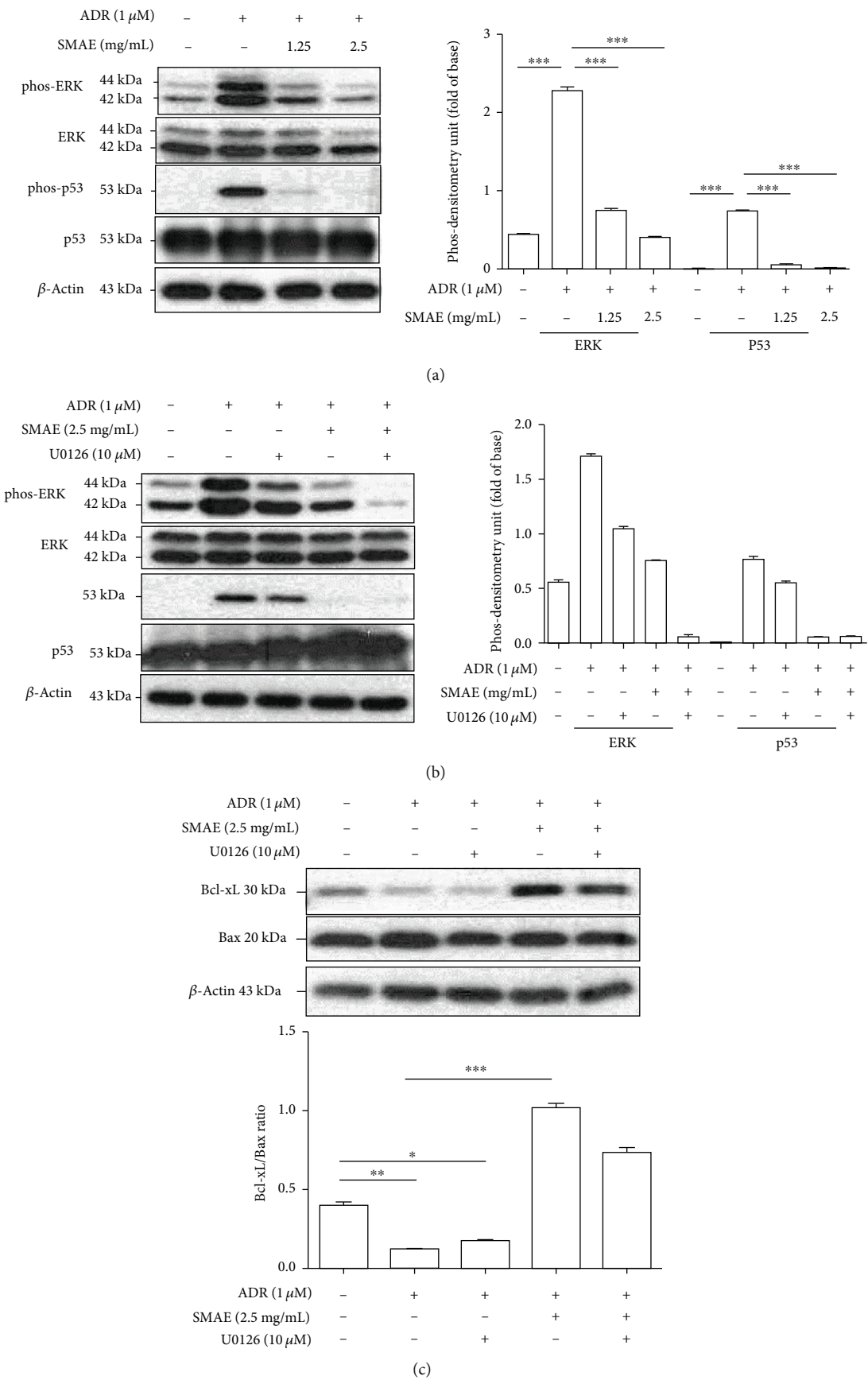


FIGURE 5: Continued.

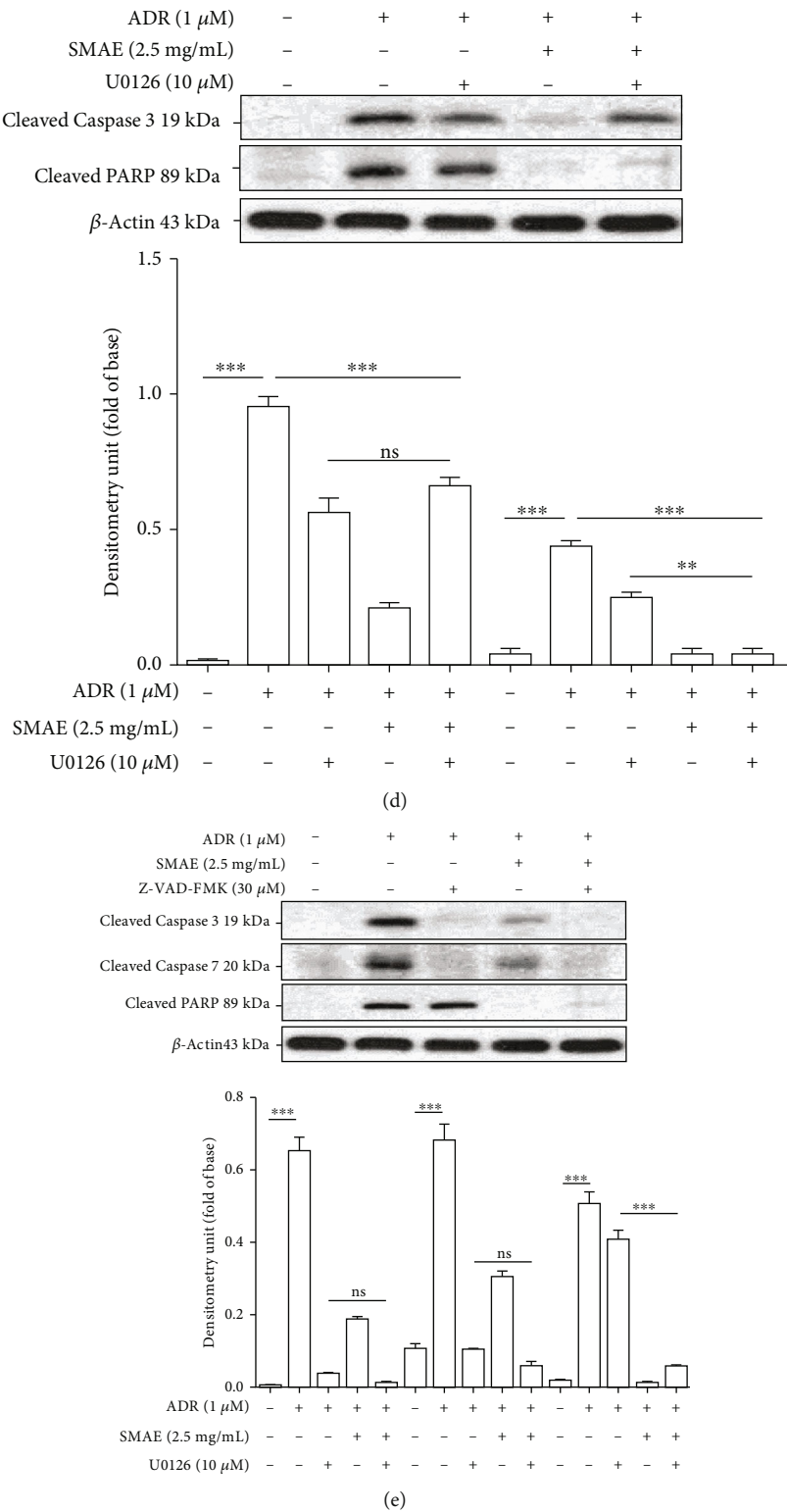


FIGURE 5: Continued.

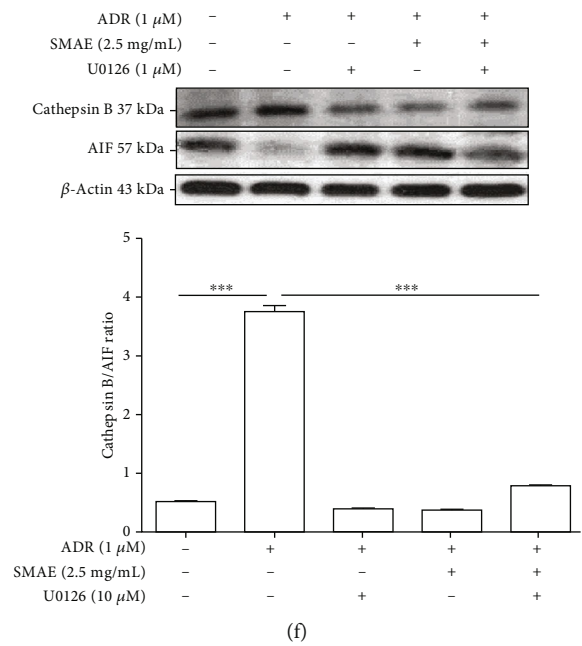


FIGURE 5: (a) Western blot analysis for phosphorylation and total protein levels of ERK1/2 and p53 with different treatments. The phosphorylation levels of ERK1/2 and p53 were normalized by total protein levels. Results represent the mean  $\pm$  SD of three independent experiments ( $***p < 0.001$ ). GAPDH was applied as the loading control. (b) Cells were preincubated with or without U0126 for 0.5 h and then treated with or without ADR and SMAE for 24 h. The phosphorylation levels of ERK1/2 and p53 were normalized by total protein levels.  $\beta$ -Actin was used as an internal control. Results represent the mean  $\pm$  SD of three independent experiments. (c) The protein levels of Bcl-xL and Bax with or without treatments of U0126, ADR, and SMAE were determined by western blotting assays. Density ratio of Bcl-xL over Bax was measured by densitometer, and  $\beta$ -actin was used as an internal control. The quantified results were indicated by the bar chart. (d) Cleavage of caspase-3 and PARP with or without treatments of U0126, ADR, and SMAE was determined by western blotting assays.  $\beta$ -actin was used as an internal control. The quantified results were indicated by the bar chart. (e) Cleavage of caspase-3 and PARP with or without treatments of Z-VAD-FMK (30  $\mu$ M), ADR, and SMAE was determined by western blotting assays.  $\beta$ -Actin was used as an internal control. The quantified results were indicated by the bar chart. (f) SMAE efficacy on protection against ADR induced cathepsin B/AIF-mediated apoptosis. The quantified results were indicated by the bar chart. Results represent the mean  $\pm$  SD of three independent experiments ( $***p < 0.001$ ).

mitochondria are highly oxidatively modified under ADR application, leading to cardiomyopathy, whereas SMAE treatment could remarkably abolish the oxidative stress via promoting the antioxidant capacity and therefore maintaining the normal physiological function of cardiomyocytes. These findings clearly explain that the heart is the most vulnerable organ which is greatly impacted by ADR application. Of these proteins, aconitase (ACON) that is considered as a biomarker for oxidative stress and serves as an intramitochondrial sensor of redox status participates in the tricarboxylic acid (TCA) cycle [39]. Previous reports have indicated that the decrease in ACON activity is related to specific disorders [40]. In our study, ACON was seen to be highly carbonylated after ADR treatment and caused functional impairment, whereas oxidative modification was reversed under the SAME administration, suggesting its involvement and protective role in the management of ADR-induced toxicity occurring in cardiac mitochondria. Similarly, the PCCA protein is responsible for the formation of carboxybiotin upon the hydrolysis of ATP in the TCA cycle [41]. Enzyme function was impacted by oxidative modification caused by ADR while SMAE exposure attenuated the degree of carbonylation of PCCA to retain normal characteristics. Pyruvate dehydrogenase complex (ODPA) irre-

versibly decarboxylates pyruvate to acetyl coenzyme A, thereby linking glycolysis to the TCA cycle and defining a critical step in cellular bioenergetics [42]. It was noticed that ADR elicited ROS, which resulted in protein damage via carbonylation, which ultimately caused an obstacle for energy production in mitochondria. In accordance with the network analysis result, it was evident that the ADR application would interfere with particular metabolic pathways which are crucial to maintain heart functions including glyoxylate metabolism, TCA cycle, and pyruvate metabolic process. Moreover, the most oxidizable proteins are largely linked to these metabolisms. The glucose-regulated protein 75 (GRP75), belongs to the family of chaperone protein, is particularly sensitive to oxidative stress, and reduces the toxicity by oxidation itself [43]. Current evidences have indicated that the oxidation of specific chaperons could induce the apoptosis in cells to offer a checkpoint after oxidative injury. Herein, much less carbonylated GRP75 presents the possible roles of SMAE treatment in the preventive effect against ROS-mediated damage to the cardiomyocytes. In summary, increases in the production of ROS due to ADR application are significantly greater than those that can be neutralized by intracellular antioxidant defenses and result in the generation of huge oxidative stress, finally leading to apoptosis of

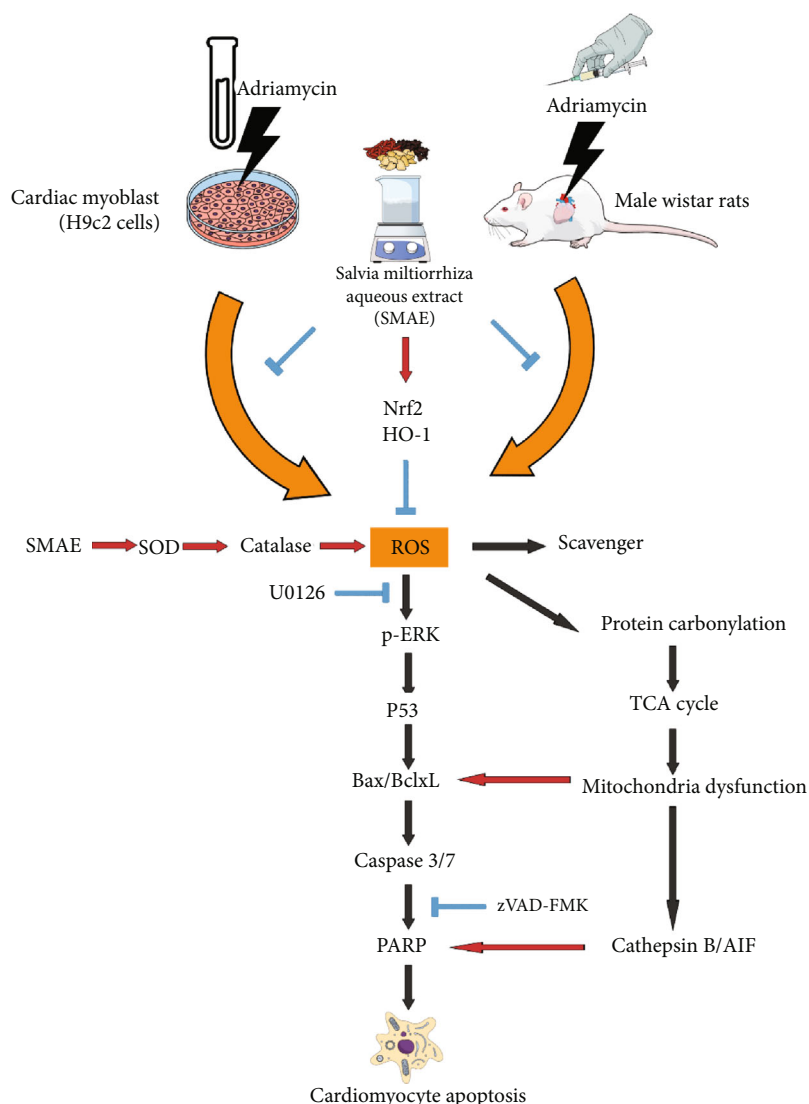


FIGURE 6: Schematic diagram of ADR-mediated cardiomyopathy through suppression of antioxidant enzymes and inducing oxidative modification of specific proteins involved in mitochondria metabolism. SMAE application could protect the heart cells against ADR damage via enhancement of antioxidant system as well as inhibition of ERK/p53- and cathepsin B/AIF-mediated apoptotic cascades.

cardiomyocytes. Of the various oxidative injuries, protein carbonylation has been considered as a potential mechanism involved in mitochondrial dysfunction, metabolic defects, and the exact contribution of carbonylation-induced dysfunction of these proteins to overall heart deficit.

Moreover, the ERK signaling pathways are proposed to be involved in NF- $\kappa$ B transactivation during oxidative stress in myoblasts [44]. As indicated in the previous investigation, ERK phosphorylation may contribute to the initiation of p53-dependent mechanisms, which stimulate the levels of the proapoptotic Bax protein and inhibit bcl-2 expression [45]. In the current study, ERK activation followed by p53 phosphorylation, cleavage of caspase3/7, and PARP were also performed in the western blotting data. Particularly, individual administration of U0126 or Z-VAD-FMK could not entirely block the cleavage of PARP; nevertheless, pretreatment with SMAE as well as U0126 totally attenuated ADR-induced ERK1/2 phosphorylation, Bcl-xL/Bax ratio, and sub-

sequent activation of PARP. Similarly, cotreatment of SMAE and inhibitor Z-VAD-FMK performed the powerful ability to absolutely suppress the caspase protein activation and PARP cleavage, an irreversible step toward apoptosis. These findings suggest that SMAE could protect against the ADR-caused cardiomyocyte apoptosis via multiple mechanisms except the ERK/p53/PARP signaling pathway. Consistently, SMAE treatment could also prevent ADR-caused cell death via cathepsin B-initiated partial extrinsic apoptotic cascade accompanied by the nuclear translocation of AIF, which emphasizes the important roles of mitochondria in ADR-induced cardiotoxicity as well as the protective function of SMAE.

Overall, it is clearly seen that the SMAE administration provides protection against ADR-induced cardiotoxicity via activating antioxidant enzymes and Nrf2/HO-1 signaling cascades. The apoptosis mediated by protein carbonylation and subsequent mitochondria dysfunction is diminished by

SMAE application, while SMAE also inhibits ERK/p53 signaling pathway, which in turn downregulates the Bcl-xL/Bax protein ratio leading to cytochrome c release followed by caspase protein activation and PARP cleavage. In addition to the caspase-dependent pathway, the SMAE application could regulate the cathepsin B/AIF cascade and relieve the ADR-caused cell death (Figure 6). Our study offers an insight into the molecular mechanisms of ADR-related apoptosis taking place in cardiomyocytes and presents the potent clinical implication of herbal medicine which can be used for treating cancers along with the ADR administration, which is associated with the serious side effect of cardiotoxicity.

## Data Availability

(1) The Western blotting and gel image data used to support the findings of this study have been deposited in the database of Chinese medicine laboratory in Chang Gung University. (2) The Western blotting and gel image data used to support the findings of this study are included within the article. (3) The Western blotting and gel image data used to support the findings of this study are available from the corresponding author upon request.

## Conflicts of Interest

The authors declare no conflicts of interest.

## Authors' Contributions

Yu-Chiang Hung and Pei-Wen Wang designed the protocol and prepared the manuscript; Tung-Yi Lin, Jyh-Sheng You, and Tai-Long Pan helped in conducting the experiment; Pei-Ming Yang helped in performing the statistical analysis; Tai-Long Pan was in charge of the whole experiment and proofreading of the manuscript.

## Acknowledgments

This work was supported by a grant from the Ministry of Science and Technology for Yu-Chiang Hung (MOST108-2320-B-182-022), for Pei-Wen Wang (MOST109-2320-B-039-040), and for Tai-Long Pan (MOST108-2320-B-182-024-MY3) and Chang Gung Memorial Hospital (CMRPD1J0191, BMRP445), Taiwan.

## References

- [1] C. Carvalho, R. Santos, S. Cardoso et al., "Doxorubicin: the good, the bad and the ugly effect," *Current Medicinal Chemistry*, vol. 16, no. 25, pp. 3267–3285, 2009.
- [2] B. Kalyanaraman, "Teaching the basics of the mechanism of doxorubicin-induced cardiotoxicity: have we been barking up the wrong tree?," *Redox Biology*, vol. 29, p. 101394, 2020.
- [3] Y. Octavia, C. G. Tocchetti, K. L. Gabrielson, S. Janssens, H. J. Crijns, and A. L. Moens, "Doxorubicin-induced cardiomyopathy: from molecular mechanisms to therapeutic strategies," *Journal of Molecular and Cellular Cardiology*, vol. 52, no. 6, pp. 1213–1225, 2012.
- [4] D. Cappetta, A. De Angelis, L. Sapio et al., "Oxidative stress and cellular response to doxorubicin: a common factor in the complex milieu of anthracycline cardiotoxicity," *Oxidative Medicine and Cellular Longevity*, vol. 2017, Article ID 1521020, 13 pages, 2017.
- [5] K. Renu, V. G. Abilash, P. B. Tirupathi Pichiah, and S. Arunachalam, "Molecular mechanism of doxorubicin-induced cardiomyopathy – An update," *European Journal of Pharmacology*, vol. 818, pp. 241–253, 2018.
- [6] V. Schwach, R. H. Slaats, and R. Passier, "Human pluripotent stem cell-derived cardiomyocytes for assessment of anticancer drug-induced cardiotoxicity," *Front Cardiovasc Med.*, vol. 7, p. 50, 2020.
- [7] S. M. Swain and P. Vici, "The current and future role of dexrazoxane as a cardioprotectant in anthracycline treatment: expert panel review," *Journal of Cancer Research and Clinical Oncology*, vol. 130, no. 1, pp. 1–7, 2004.
- [8] P. Reichardt, M. D. Tabone, J. Mora, B. Morland, and R. L. Jones, "Risk-benefit of dexrazoxane for preventing anthracycline-related cardiotoxicity: re-evaluating the European labeling," *Future Oncology*, vol. 14, no. 25, pp. 2663–2676, 2018.
- [9] Z. Wang, F. Qi, Y. Cui et al., "An update on Chinese herbal medicines as adjuvant treatment of anticancer therapeutics," *Bioscience Trends*, vol. 12, no. 3, pp. 220–239, 2018.
- [10] M. Y. Tsai, W. L. Hu, C. C. Lin et al., "Prescription pattern of Chinese herbal products for heart failure in Taiwan: a population-based study," *International Journal of Cardiology*, vol. 228, pp. 90–96, 2017.
- [11] Z. M. Li, S. W. Xu, and P. Q. Liu, "Salvia miltiorrhiza Burge (Danshen): a golden herbal medicine in cardiovascular therapeutics," *Acta Pharmacologica Sinica*, vol. 39, no. 5, pp. 802–824, 2018.
- [12] J. Ren, L. Fu, S. H. Nile, J. Zhang, and G. Kai, "Salvia miltiorrhiza in treating cardiovascular diseases: a review on its pharmacological and clinical applications," *Frontiers in Pharmacology*, vol. 10, p. 753, 2019.
- [13] J. S. You, T. L. Pan, and Y. S. Lee, "Protective effects of Danshen (Salvia Miltiorrhiza) on adriamycin-induced cardiac and hepatic toxicity in rats," *Phytotherapy Research*, vol. 21, no. 12, pp. 1146–1152, 2007.
- [14] M. Stërba, O. Popelová, A. Vávrová et al., "Oxidative stress, redox signaling, and metal chelation in anthracycline cardiotoxicity and pharmacological cardioprotection," *Antioxidants & Redox Signaling*, vol. 18, no. 8, pp. 899–929, 2013.
- [15] M. Songbo, H. Lang, C. Xinyong, X. Bin, Z. Ping, and S. Liang, "Oxidative stress injury in doxorubicin-induced cardiotoxicity," *Toxicology Letters*, vol. 307, pp. 41–48, 2019.
- [16] N. Wenningmann, M. Knapp, A. Ande, T. R. Vaidya, and S. Ait-Oudhia, "Insights into doxorubicin-induced cardiotoxicity: molecular mechanisms, preventive strategies, and early monitoring," *Molecular Pharmacology*, vol. 96, no. 2, pp. 219–232, 2019.
- [17] C. Lennicke, J. Rahn, N. Heimer, R. Lichtenfels, L. A. Wessjohann, and B. Seliger, "Redox proteomics: methods for the identification and enrichment of redox-modified proteins and their applications," *Proteomics*, vol. 16, no. 2, pp. 197–213, 2016.
- [18] G. Colombo, M. L. Garavaglia, E. Astori et al., "Protein carbonylation in human bronchial epithelial cells exposed to cigarette smoke extract," *Cell Biology and Toxicology*, vol. 35, no. 4, pp. 345–360, 2019.



- [19] P. W. Wang, Y. C. Cheng, Y. C. Hung et al., "Red raspberry extract protects the skin against UVB-induced damage with antioxidative and anti-inflammatory properties," *Oxidative Medicine and Cellular Longevity*, vol. 2019, Article ID 9529676, 14 pages, 2019.
- [20] K. Liu, J. W. Zhang, X. G. Liu et al., "Correlation between macroscopic characteristics and tissue-specific chemical profiling of the root of *Salvia miltiorrhiza*," *Phytomedicine*, vol. 51, pp. 104–111, 2018.
- [21] T. Nakahara, T. Tanimoto, A. D. Petrov, K. Ishikawa, H. W. Strauss, and J. Narula, "Rat model of cardiotoxic drug-induced cardiomyopathy," *Methods in Molecular Biology*, vol. 1816, pp. 221–232, 2018.
- [22] T. L. Pan, T. H. Wu, P. W. Wang et al., "Functional proteomics reveals the protective effects of saffron ethanolic extract on hepatic ischemia-reperfusion injury," *Proteomics*, vol. 13, no. 15, pp. 2297–2311, 2013.
- [23] J. Y. Fang, P. W. Wang, C. H. Huang, M. H. Chen, Y. R. Wu, and T. L. Pan, "Skin aging caused by intrinsic or extrinsic processes characterized with functional proteomics," *Proteomics*, vol. 16, no. 20, pp. 2718–2731, 2016.
- [24] P. W. Wang, T. Y. Lin, Y. C. Hung et al., "Characterization of fibrinogen as a key modulator in patients with Wilson's diseases with functional proteomic tools," *International Journal of Molecular Sciences*, vol. 20, no. 18, p. 4528, 2019.
- [25] T. L. Pan, P. W. Wang, C. C. Huang, C. T. Yeh, T. H. Hu, and J. S. Yu, "Network analysis and proteomic identification of vimentin as a key regulator associated with invasion and metastasis in human hepatocellular carcinoma cells," *Journal of Proteomics*, vol. 75, no. 15, pp. 4676–4692, 2012.
- [26] T. L. Pan, P. W. Wang, Y. L. Leu, T. H. Wu, and T. S. Wu, "Inhibitory effects of *Scutellaria baicalensis* extract on hepatic stellate cells through inducing G2/M cell cycle arrest and activating ERK-dependent apoptosis via Bax and caspase pathway," *Journal of Ethnopharmacology*, vol. 139, no. 3, pp. 829–837, 2012.
- [27] P. W. Wang, Y. C. Hung, T. Y. Lin et al., "Comparison of the biological impact of UVA and UVB upon the skin with functional proteomics and immunohistochemistry," *Antioxidants*, vol. 8, no. 12, p. 569, 2019.
- [28] J. V. McGowan, R. Chung, A. Maulik, I. Piotrowska, J. M. Walker, and D. M. Yellon, "Anthracycline chemotherapy and cardiotoxicity," *Cardiovascular Drugs and Therapy*, vol. 31, no. 1, pp. 63–75, 2017.
- [29] A. Hosseini and A. Sahebkar, "Reversal of doxorubicin-induced cardiotoxicity by using phytotherapy: a review," *J Pharmacopuncture*, vol. 20, no. 4, pp. 243–256, 2017.
- [30] C. H. Huang, H. P. Chang, S. Y. Su et al., "Traditional Chinese medicine is associated with a decreased risk of heart failure in breast cancer patients receiving doxorubicin treatment," *Journal of Ethnopharmacology*, vol. 229, pp. 15–21, 2019.
- [31] J. M. Berthiaume and K. B. Wallace, "Adriamycin-induced oxidative mitochondrial cardiotoxicity," *Cell Biology and Toxicology*, vol. 23, no. 1, pp. 15–25, 2007.
- [32] L. Wang, X. Zhang, J. Y.-W. Chan et al., "A novel danshensu derivative prevents cardiac dysfunction and improves the chemotherapeutic efficacy of doxorubicin in breast cancer cells," *Journal of Cellular Biochemistry*, vol. 117, no. 1, pp. 94–105, 2016.
- [33] Y. S. Lin, Y. C. Shen, C. Y. Wu et al., "Danshen improves survival of patients with breast cancer and dihydroisotanshinone I induces ferroptosis and apoptosis of breast cancer cells," *Frontiers in Pharmacology*, vol. 10, p. 1226, 2019.
- [34] F. S. Carvalho, A. Burgeiro, R. Garcia, A. J. Moreno, R. A. Carvalho, and P. J. Oliveira, "Doxorubicin-induced cardiotoxicity: from bioenergetic failure and cell death to cardiomyopathy," *Medicinal Research Reviews*, vol. 34, no. 1, pp. 106–135, 2014.
- [35] Z. V. Varga, P. Ferdinandy, L. Liaudet, and P. Pacher, "Drug-induced mitochondrial dysfunction and cardiotoxicity," *American Journal of Physiology. Heart and Circulatory Physiology*, vol. 309, no. 9, pp. H1453–H1467, 2015.
- [36] A. T. Akhmedov, V. Rybin, and J. Marín-García, "Mitochondrial oxidative metabolism and uncoupling proteins in the failing heart," *Heart Failure Reviews*, vol. 20, no. 2, pp. 227–249, 2015.
- [37] F. L. Sheeran and S. Pepe, "Mitochondrial bioenergetics and dysfunction in failing heart," *Advances in Experimental Medicine and Biology*, vol. 982, pp. 65–80, 2017.
- [38] S. Ichihara, Y. Suzuki, J. Chang et al., "Involvement of oxidative modification of proteins related to ATP synthesis in the left ventricles of hamsters with cardiomyopathy," *Scientific Reports*, vol. 7, no. 1, p. 9243, 2017.
- [39] O. V. Lushchak, M. Piroddi, F. Galli, and V. I. Lushchak, "Aconitase post-translational modification as a key in linkage between Krebs cycle, iron homeostasis, redox signaling, and metabolism of reactive oxygen species," *Redox Report*, vol. 19, no. 1, pp. 8–15, 2013.
- [40] J. Talib and M. J. Davies, "Exposure of aconitase to smoking-related oxidants results in iron loss and increased iron response protein-1 activity: potential mechanisms for iron accumulation in human arterial cells," *Journal of Biological Inorganic Chemistry*, vol. 21, no. 3, pp. 305–317, 2016.
- [41] P. Wongkittichote, N. Ah Mew, and K. A. Chapman, "Propionyl-CoA carboxylase - a review," *Molecular Genetics and Metabolism*, vol. 122, no. 4, pp. 145–152, 2017.
- [42] W. Sun, Q. Liu, J. Leng, Y. Zheng, and J. Li, "The role of pyruvate dehydrogenase complex in cardiovascular diseases," *Life Sciences*, vol. 121, pp. 97–103, 2015.
- [43] Y. C. Hung, P. W. Wang, T. L. Pan, G. Bazylak, and Y. L. Leu, "Proteomic screening of antioxidant effects exhibited by radix *Salvia miltiorrhiza* aqueous extract in cultured rat aortic smooth muscle cells under homocysteine treatment," *Journal of Ethnopharmacology*, vol. 124, no. 3, pp. 463–474, 2009.
- [44] G. Abdelhamid and A. O. S. El-Kadi, "Buthionine sulfoximine, an inhibitor of glutathione biosynthesis, induces expression of soluble epoxide hydrolase and markers of cellular hypertrophy in a rat cardiomyoblast cell line: roles of the NF- $\kappa$ B and MAPK signaling pathways," *Free Radical Biology & Medicine*, vol. 82, pp. 1–12, 2015.
- [45] J. Liu, W. Mao, B. Ding, and C. S. Liang, "ERKs/p 53 signal transduction pathway is involved in doxorubicin-induced apoptosis in H9c2 cells and cardiomyocytes," *American Journal of Physiology. Heart and Circulatory Physiology*, vol. 295, no. 5, pp. H1956–H1965, 2008.

## Original Article

**Cite this article:** Li J-R, Tsai S-J, Bai Y-M, Hsu J-W, Huang K-L, Su T-P, Li C-T, Lin W-C, Chen T-J, Pan T-L, and Chen M-H. Cardiometabolic disease risk among siblings of patients with major depressive disorder. *Journal of Developmental Origins of Health and Disease* doi: [10.1017/S2040174420000860](https://doi.org/10.1017/S2040174420000860)

Received: 20 April 2020

Revised: 4 July 2020


Accepted: 18 August 2020

### Keywords:

Unaffected siblings; major depressive disorder; metabolic disorder; cerebrocardiovascular diseases

**Address for correspondence:** Mu-Hong Chen, MD, PhD, Department of Psychiatry, No. 201, Shih-Pai Road, Sec. 2, 11217, Taipei, Taiwan. Tel.: 886-2-28344012; Fax: 886-2-28344012. Email: [kremer7119@gmail.com](mailto:kremer7119@gmail.com)  
Tai-Long Pan, PhD, School of Traditional Chinese Medicine, Chang Gung University, Taoyuan, Taiwan. Tel.: 886-2-28344012; Fax: 886-2-28344012. Email: [pan@mail.cgu.edu.tw](mailto:pan@mail.cgu.edu.tw)

# Cardiometabolic disease risk among siblings of patients with major depressive disorder

Jia-Ru Li<sup>1</sup>, Shih-Jen Tsai<sup>1,2</sup>, Ya-Mei Bai<sup>1,2</sup>, Ju-Wei Hsu<sup>1,2</sup>, Kai-Lin Huang<sup>1,2</sup>, Tung-Ping Su<sup>1,2,3</sup>, Cheng-Ta Li<sup>1,2</sup>, Wei-Chen Lin<sup>1,2</sup>, Tzeng-Ji Chen<sup>4,5</sup>, Tai-Long Pan<sup>6,7,8</sup> and Mu-Hong Chen<sup>1,2</sup> 

<sup>1</sup>Department of Psychiatry, Taipei Veterans General Hospital, Taipei, Taiwan; <sup>2</sup>Department of Psychiatry, College of Medicine, National Yang-Ming University, Taipei, Taiwan; <sup>3</sup>Department of Psychiatry, Cheng Hsin General Hospital, Taipei, Taiwan; <sup>4</sup>Department of Family Medicine, Taipei Veterans General Hospital, Taipei, Taiwan; <sup>5</sup>Institute of Hospital and Health Care Administration, National Yang-Ming University, Taipei, Taiwan; <sup>6</sup>School of Traditional Chinese Medicine, Chang Gung University, Taoyuan, Taiwan; <sup>7</sup>Research Center for Industry of Human Ecology, Chang Gung University of Science and Technology, Taoyuan, Taiwan and <sup>8</sup>Liver Research Center, Division of Hepatology, Department of Gastroenterology and Hepatology, Chang Gung Memorial Hospital, Taoyuan, Taiwan

## Abstract

Studies have suggested an association between metabolic and cerebrocardiovascular diseases and major depressive disorder (MDD). However, the risk of metabolic and cerebrocardiovascular diseases in the unaffected siblings of patients with MDD remains uncertain. Using the Taiwan National Health Insurance Research Database, 22,438 unaffected siblings of patients with MDD and 89,752 age-/sex-matched controls were selected and followed up from 1996 to the end of 2011. Individuals who developed metabolic and cerebrocardiovascular diseases during the follow-up period were identified. Compared with the controls, the unaffected siblings of patients with MDD had a higher prevalence of metabolic diseases, such as hypertension (5.0% vs. 4.5%,  $p = 0.007$ ), dyslipidemia (5.6% vs. 4.8%,  $p < 0.001$ ), and obesity (1.7% vs. 1.5%,  $p = 0.028$ ), and cerebrocardiovascular diseases, such as ischemic stroke (0.6% vs. 0.4%,  $p < 0.005$ ) and ischemic heart disease (2.1% vs. 1.7%,  $p < 0.001$ ). Logistic regression analyses revealed that the unaffected siblings of patients with MDD were more likely to develop hypertension, dyslipidemia, ischemic stroke, and ischemic heart diseases during the follow-up period than the controls. Our study revealed a familial coaggregation between MDD and metabolic and cerebrocardiovascular diseases. Additional studies are required to investigate the shared pathophysiology of MDD and metabolic and cerebrocardiovascular diseases.

Depression, which is characterized by sadness, loss of interest, anhedonia, lack of appetite, feelings of guilt, low self-esteem or self-worth, sleep disturbance, feelings of tiredness, and poor concentration, is one of the commonest mental disorders worldwide and is estimated to affect over 300 million people globally.<sup>1</sup> Moreover, it affects the individual's well-being and ability to perform socially defined roles and tasks.<sup>2</sup> The global point prevalence rate was 4.7% (4.4%–5.0%), and the pooled annual incidence was 3.0% (2.4%–3.8%).<sup>3</sup> Although the pathophysiology of major depressive disorder (MDD) remains unclear, a number of factors, including biogenic amine deficiency, neurogenesis, genetic, environmental, immunologic, and endocrine factors, were suggested to be associated with MDD development.<sup>4</sup>

In addition, depression has been associated with shortened life expectancy and impaired quality of life.<sup>5,6</sup> Mortality risk over relatively short periods could be attributed to unnatural causes of death, including suicide and unintentional injuries.<sup>7,8</sup> By contrast, mortality risk over longer periods may be due to chronic physical conditions associated with depression, such as cerebrocardiovascular diseases and metabolic disorders.<sup>7,8</sup> Indeed, evidence confirmed the elevated risks of cerebrocardiovascular and metabolic diseases among patients with MDD.<sup>9–11</sup> Similarly, other psychiatric disorders, including schizophrenia or bipolar disorder, were also found to have higher risks of metabolic and cerebrocardiovascular diseases.<sup>12–14</sup>

Researchers further assessed whether individuals, especially the first-degree relatives (i.e., siblings), at increased familial risk of psychiatry disorders, may have elevated rates of cerebrocardiovascular or metabolic diseases.<sup>15–21</sup> Toma *et al.* revealed that cardiovascular risk score based on the sum of the presence of diabetes, hypertension, obesity, dyslipidemia, stroke, angina, and myocardial infarction was highest among adolescents with bipolar disorder having familial bipolar disorder, intermediate among adolescents with bipolar disorder having no familial bipolar disorder and lowest in healthy comparisons without bipolar disorder and familial bipolar disorder.<sup>17</sup> Sobczak *et al.* found the healthy first-degree relatives of patients with bipolar disorder were prone to having increased level of omega-6 polyunsaturated fatty acids and lower level of

high-density lipoprotein cholesterol.<sup>18</sup> Mannie *et al.* demonstrated that the individuals with a family history of depressive disorder had elevated systolic blood pressure and diminished insulin sensitivity compared with those without family history.<sup>20</sup> The major limitations of the aforementioned studies included small sample size, cross-sectional study design, and only inclusion of young subjects that may limit the generalizability.

In the current study, using the Taiwan National Health Insurance Research Database (NHIRD), with a large sample size and longitudinal study design, we investigated the risks of metabolic diseases, namely type 2 diabetes mellitus, hypertension, and dyslipidemia, and the risks of cerebrocardiovascular diseases, namely stroke and ischemic heart disease, among the unaffected siblings of patients with MDD. We hypothesized that the unaffected siblings of patients with MDD have an increased risk of subsequent metabolic and cerebrocardiovascular diseases during the follow-up period compared with the controls.

## Methods

### Data source

Taiwan National Health Research Institute audits and releases the Taiwan NHIRD for scientific and study purposes. Individual medical records included in the NHIRD are anonymous to protect patient privacy. Comprehensive information on insured individuals is included in the database, including demographic data, dates of clinical visits, disease diagnoses, and medical interventions. In this study, using each resident's unique personal identification number, all of the information was linked. Subsequently, following the method of Kuo *et al.* and Cheng *et al.*, family kinships in the NHIRD were used for genealogy reconstruction.<sup>22,23</sup> The diagnostic codes used were based on the International Classification of Diseases, 9th Revision, Clinical Modification (ICD-9-CM). The NHIRD has been used extensively in many epidemiologic studies in Taiwan.<sup>23–26</sup>

### Inclusion criteria for the unaffected siblings of patients with MDD and the control group

Individuals who were born before 1990 and had the siblings with MDD (ICD-9-CM codes: 296.2x, 296.3x) but had no personal diagnosis of severe mental disorders (ICD-9-CM codes: 295, 296, 297) at any time were enrolled as the study group. The age-, sex-, income-, level-of-urbanization-and birth-time-matched (1:4) control group was randomly identified after eliminating the study cases, those who had been given a diagnosis of severe mental disorders at any time, and those with any sibling with severe mental disorders. The study and control groups were included and followed from 1996 to the end of 2011. The occurrence of metabolic (type 2 diabetes, hypertension, dyslipidemia, obesity) and cerebrocardiovascular (stroke, ischemic heart diseases) diseases was identified during the follow-up period. Metabolic and cerebrocardiovascular diseases were diagnosed by board-certified physicians. Level of urbanization (level 1 to level 5; level 1: most urbanized region; level 5: least urbanized region) was also assessed for our study.<sup>27</sup> This study was approved by the Institutional Review Board of Taipei Veterans General Hospital.

### Statistical analysis

For between-group comparisons, the F test was used for continuous variables and Pearson's  $\chi^2$  test for nominal variables, where

appropriate. After adjusting for demographic data (age, sex, income, and level of urbanization), logistic regression models were used to investigate the odds ratios (OR) of subsequent metabolic diseases (type 2 diabetes, hypertension, dyslipidemia, obesity) between study and control cohorts. Logistic regression models with the additional adjustment of metabolic diseases were performed to assess the likelihoods of subsequent cerebrocardiovascular diseases (stroke, ischemic heart disease) between study and control groups. In addition, logistic regression analyses stratified by sex were also examined to clarify the role of sex in the risks of subsequent metabolic and cerebrocardiovascular diseases. A 2-tailed  $p$ -value of less than 0.05 was considered statistically significant. All data processing and statistical analyses were performed with Statistical Package for Social Science (SPSS) version 19 software (SPSS Inc.) and Statistical Analysis Software (SAS) version 9.1 (SAS Institute, Cary, NC).

## Results

The demographic characteristics and prevalence of metabolic and cerebrocardiovascular diseases of the study sample were listed in Table 1. In all, 22,438 unaffected siblings of patients with MDD and 89,752 controls were enrolled in our study, with an average age of  $32.81 \pm 8.22$  years. The unaffected siblings of patients with MDD had the higher prevalence of metabolic diseases, such as hypertension (5.0% vs. 4.5%,  $p = 0.007$ ), dyslipidemia (5.6% vs. 4.8%,  $p < 0.001$ ), obesity (1.7% vs. 1.5%,  $p = 0.028$ ), and cerebrocardiovascular diseases, such as ischemic heart disease (2.1% vs. 1.7%,  $p < 0.001$ ), any stroke (1.3% vs. 1.1%,  $p = 0.006$ ), and ischemic stroke (0.6% vs. 0.4%,  $p = 0.005$ ) compared with the controls (Table 1).

Logistic regression analyses with an adjustment of demographic data (age, sex, level of urbanization, and income) found that the unaffected siblings of patients with MDD were more likely to have hypertension (OR: 1.12, 95% CI: 1.04–1.21), dyslipidemia (OR: 1.21, 95% CI: 1.13–1.29), and obesity (OR: 1.14, 95% CI: 1.01–1.27) later in life compared with the controls (Table 2). Further analyses with additional adjustment of metabolic diseases found that the unaffected siblings of patients with MDD had increased risks of developing any stroke (OR: 1.18, 95% CI: 1.03–1.35), ischemic stroke (OR: 1.30, 95% CI: 1.06–1.60), and ischemic heart disease (OR: 1.21, 95% CI: 1.08–1.36) during the follow-up period compared with the control group (Table 3). Subanalyses stratified by sex reported that brothers of patients with MDD had the elevated risks of developing hypertension (OR: 1.16, 95% CI: 1.06–1.26), dyslipidemia (OR: 1.22, 95% CI: 1.12–1.33), ischemic stroke (OR: 1.33, 95% CI: 1.03–1.71), and ischemic heart disease (OR: 1.20, 95% CI: 1.04–1.40) compared with the controls; sisters of patients with MDD were prone to developing dyslipidemia (OR: 1.18, 95% CI: 1.05–1.32), type 2 diabetes (OR: 1.20, 95% CI: 1.04–1.38), obesity (OR: 1.16, 95% CI: 1.00–1.34), and ischemic heart disease (OR: 1.23, 95% CI: 1.02–1.48) (Tables 2 and 3).

## Discussion

Our findings supported the study hypothesis that the unaffected siblings of patients with MDD exhibit a higher prevalence of subsequent metabolic and cerebrovascular diseases, especially dyslipidemia, ischemic stroke, and ischemic heart disease compared with the controls. In addition, the unaffected sisters of patients with MDD were more likely to develop type 2 diabetes later in life compared with the controls.

**Table 1.** Demographic data and prevalence of the metabolic and cerebrocardiovascular disorders among the siblings of patients with major depression and controls

	Siblings of patients with major depression (n = 22,438)	Controls (n = 89,752)	p-Value
Age (years, SD)	32.81 (8.22)	32.81 (8.22)	0.992
Sex (n, %)			1.000
Male	11,223 (50.0)	44,892 (50.0)	
Female	11,215 (50.0)	44,860 (50.0)	
Prevalence of metabolic disorders			
Hypertension (n, %)	1112 (5.0)	4047 (4.5)	<b>0.007</b>
Age at diagnosis (years, SD)	38.22 (11.91)	38.54 (11.98)	0.420
Dyslipidemia (n, %)	1260 (5.6)	4299 (4.8)	<b>&lt;0.001</b>
Age at diagnosis (years, SD)	36.29 (11.63)	36.10 (11.91)	0.609
Type 2 diabetes (n, %)	596 (2.7)	2253 (2.5)	0.217
Age at diagnosis (years, SD)	36.02 (12.83)	36.68 (12.57)	0.253
Obesity (n, %)	389 (1.7)	1371 (1.5)	<b>0.028</b>
Age at diagnosis (years, SD)	27.63 (9.41)	27.04 (8.78)	0.247
Prevalence of cerebrocardiovascular disorders			
Any stroke (n, %)	289 (1.3)	963 (1.1)	<b>0.006</b>
Age at diagnosis (years, SD)	35.47 (14.61)	35.82 (15.67)	0.740
Ischemic stroke (n, %)	133 (0.6)	400 (0.4)	<b>0.005</b>
Age at diagnosis (years, SD)	43.20 (14.21)	42.84 (14.32)	0.804
Hemorrhagic stroke (n, %)	82 (0.4)	349 (0.4)	0.669
Age at diagnosis (years, SD)	27.70 (12.73)	29.02 (14.63)	0.451
Ischemic heart disease (n, %)	467 (2.1)	1506 (1.7)	<b>&lt;0.001</b>
Age at diagnosis (years, SD)	38.55 (13.47)	40.10 (13.43)	<b>0.028</b>
Level of urbanization (n, %)			1.000
1 (most urbanized)	6373 (28.4)	25,492 (28.4)	
2	7897 (35.2)	31,588 (35.2)	
3	3072 (13.7)	12,288 (13.7)	
4	2142 (9.5)	8568 (9.5)	
5 (most rural)	2954 (13.2)	11,816 (13.2)	
Income-related insured amount (n, %)			1.000
≤15,840 NTD/month	6527 (29.1)	26,108 (29.1)	
15,841–25,000NTD/month	7583 (33.8)	30,332 (33.8)	
≥25,001NTD/month	8328 (37.1)	33,312 (37.1)	

NTD: new Taiwan dollar; SD: standard deviation.

**Table 2.** Logistic regression analyses of the metabolic disorders among the siblings of patients with major depression and controls<sup>a</sup>

	Hypertension (OR, 95% CI)	Dyslipidemia (OR, 95% CI)	Type 2 diabetes (OR, 95% CI)	Obesity (OR, 95% CI)
Siblings of patients with major depression	<b>1.12 (1.04–1.21)</b>	<b>1.21 (1.13–1.29)</b>	1.06 (0.97–1.17)	<b>1.14 (1.01–1.27)</b>
Brothers of patients with major depression	<b>1.16 (1.06–1.26)</b>	<b>1.22 (1.12–1.33)</b>	0.97 (0.86–1.11)	1.10 (0.91–1.33)
Sisters of patients with major depression	1.03 (0.90–1.19)	<b>1.18 (1.05–1.32)</b>	<b>1.20 (1.04–1.38)</b>	<b>1.16 (1.00–1.34)</b>

OR: Odds ratio; CI: Confidence interval. **Bold** type means the statistical significance.<sup>a</sup>Adjusted for demographic data.



**Table 3.** Logistic regression analyses of the cerebrocardiovascular disorders among the siblings of patients with major depression and controls<sup>a</sup>

	Any stroke (OR, 95% CI)	Ischemic stroke (OR, 95% CI)	Hemorrhagic stroke (OR, 95% CI)	Ischemic heart disease (OR, 95% CI)
Siblings of patients with major depression	<b>1.18 (1.03–1.35)</b>	<b>1.30 (1.06–1.60)</b>	0.93 (0.73–1.19)	<b>1.21 (1.08–1.36)</b>
Brothers of patients with major depression	1.18 (0.99–1.41)	<b>1.33 (1.03–1.71)</b>	0.99 (0.73–1.34)	<b>1.20 (1.04–1.40)</b>
Sisters of patients with major depression	1.17 (0.94–1.45)	1.25 (0.88–1.78)	0.84 (0.56–1.26)	<b>1.23 (1.02–1.48)</b>

OR: Odds ratio; CI: Confidence interval. **Bold** type means the statistical significance.<sup>a</sup>Adjusted for demographic data and metabolic diseases.

Studies have found an association between the family history of severe mental disorders and cardiometabolic diseases. Huang *et al.* reported an increased risk of type 2 diabetes among the unaffected siblings of patients with schizophrenia.<sup>21</sup> Mannie *et al.* assessed the cardiometabolic conditions between healthy controls and young people who had no personal history of depression but had a family history of depressive illness and demonstrated that those with a family history of depression had elevated systolic blood pressure and arterial stiffness and diminished insulin sensitivity compared with the controls.<sup>20</sup> They suggested that young people who had a family history of depression were more likely to have an altered cardiovascular risk profile in young adulthood even if depressive symptoms were absent, which may be due to the common risk factors between MDD and cardiometabolic diseases.

Our findings of the increased likelihoods of metabolic and cerebrocardiovascular diseases in the unaffected siblings of patients with MDD were in agreement with those of Mannie *et al.*<sup>20</sup> The genetic liability, common environmental factors, and epigenetic interactions may contribute to the familial coaggregation of MDD and metabolic and cerebrocardiovascular diseases.<sup>28–31</sup> The hypothesis of a genetic overlap between depression and metabolic and cerebrocardiovascular diseases has been supported by studies describing coshared genetics and possible risk gene pathway.<sup>32,33</sup> For instance, the 12q chromosome has been linked to depression, hypertension, dyslipidemia, obesity, stroke, and ischemic heart disease.<sup>34–37</sup> Amare *et al.* reviewed 24 cardiovascular and metabolic disease genes implicated in depression, bipolar disorder, or both and found that BDNF, CREB1, GNAS, and POMC played crucial roles in the pathophysiology of both cardiometabolic diseases and mood disorders.<sup>33</sup> Thus, at least one or a few genes or gene variants across these loci may explain the pleiotropic or comorbid linkage of the aforementioned phenotypes.

The pathophysiology underlying the association between depression vulnerability and cardiometabolic diseases is unknown. Lower central serotonergic responsivity, a biomarker of depression vulnerability, has been suggested to be associated with cardiometabolic risks and carotid artery atherosclerosis.<sup>38,39</sup> Muldoon *et al.* revealed that lower central serotonergic responsivity was associated with obesity, dyslipidemia, higher systolic and diastolic blood pressure, greater insulin resistance, and less physical activity.<sup>38</sup> Muldoon *et al.* further reported that a 1 standard deviation lower prolactin response was associated with the greater intima-media thickness of carotid artery and found that the metabolic syndrome mediated, but did not fully account for, the association between lower central serotonergic responsivity and greater intima-media thickness.<sup>39</sup> Beyond the serotonergic hypothesis of depression vulnerability and cardiometabolic risks, the dysregulated hypothalamic–pituitary–adrenal (HPA) axis may play a crucial role in this relationship.<sup>40</sup> Mannie *et al.* compared 49 young people who had not been depressed themselves but who had a family history of

MDD with a group of 55 participants who had no personal and family history of depression and demonstrated that at-risk young people had a higher level of waking salivary cortisol than the comparison subjects on both workdays and nonworkdays.<sup>40</sup> Previous studies have suggested that an alteration of HPA axis, such as cortisol hypersecretion, was significantly related to the risks of metabolic and cardiovascular diseases.<sup>41–43</sup>

The role of sex in the risk of metabolic and cerebrocardiovascular diseases between study and control groups was another interesting finding in our study. Block *et al.* suggested that younger female patients with MDD were more likely to have metabolic diseases than those without MDD, and they further found that age may attenuate this association.<sup>44</sup> Gil *et al.* found a significant relationship of depressive symptoms with elevated glucose levels in women and with obesity in men.<sup>45</sup> Furthermore, depressive symptoms were considered to be associated with metabolic diseases among Japanese urban men.<sup>46</sup> Alemany *et al.* hypothesized that metabolic disease is a maturity-onset disease, and levels of androgens and estrogens could account for differences between the sexes and delayed manifestation of metabolic syndrome by counterbalancing the pathogenetic force of glucocorticoids toward metabolic syndrome.<sup>47</sup> The fluctuations of sex hormones that flag reproductive events in women may affect metabolic and neurochemical pathways that are linked to both MDD and metabolic and cerebrocardiovascular diseases.<sup>48</sup> Additional studies are required to investigate the effect of sex on metabolic and cerebrocardiovascular diseases between patients with MDD and their relatives.

This study had several limitations. First, the prevalence of cerebrocardiovascular disease and MDD may be underestimated because only those who sought medical help and consultation were enrolled. However, the diagnoses of metabolic and cerebrocardiovascular diseases were made by board-certified physicians. Therefore, the diagnostic validity was improved. In addition, the other clinical scenario of undetected or untreated depression and other psychiatric disorders in unaffected relatives may be also possible. Not only risks of metabolic and cerebrocardiovascular diseases but also risks of mental disorders should be closely monitored among unaffected relatives, such as siblings in current study. Second, the prevalence of metabolic and cerebrocardiovascular diseases rise with age. In current study, the lifetime prevalence of metabolic and cerebrocardiovascular diseases may be underestimated owing to the not-long-enough (15 years) follow-up duration. Future studies with a longer follow-up duration (>15 years) would be required to validate our findings. Third, some factors, such as environmental factors, personal lifestyle, education, occupation, and engagement in physical activity, were not available in the Taiwan NHIRD. Therefore, we could not examine the influence of these factors.

In conclusion, the unaffected siblings of patients with MDD had a slightly higher risk of subsequent hypertension, dyslipidemia, obesity, ischemic stroke, and ischemic heart disease later in life



compared with the controls. The unaffected sisters of patients with MDD were more likely to develop type 2 diabetes later in life compared with the controls. Our study revealed a familial coaggregation between MDD and metabolic and cerebrocardiovascular diseases in a large sample. Our findings suggest that clinicians should pay more attention to the cardiometabolic health of the unaffected siblings of patients with MDD. Screening those siblings of patients with MDD to evaluate the risk of metabolic and cerebrocardiovascular diseases, even those siblings without MDD per se, may be a valuable strategy of risk stratification in public health. Additional studies are required to investigate the shared pathophysiology between MDD and cardiometabolic diseases.

**Acknowledgements.** We thank Mr I-Fan Hu for his friendship and support.

We thank Dr JRL, Prof TLP, and Dr MHC, who designed the study, wrote the protocol and manuscripts, Dr JWH, Dr YMB, Dr TPS, Dr CTL, Dr SJT, Dr KLH, and Dr WCL, who assisted with the preparation and proof-reading of the manuscript, and Dr YMB, Dr MHC, and Dr TJC, who provided the advices on statistical analysis.

**Financial support.** The study was supported by grant from Taipei Veterans General Hospital (V103E10-001, V104E10-002, V105E10-001-MY2-1, V105A-049, V106B-020, V107B-010, V107C-181) and Ministry of Science and Technology, Taiwan (107-2314-B-075-063-MY3, 108-2314-B-075-037). The funding source had no role in any process of our study.

**Conflict of interest.** None.

**Ethical standards.** None.

## References

- Aleksandrova LR, Phillips AG, Wang YT. Antidepressant effects of ketamine and the roles of AMPA glutamate receptors and other mechanisms beyond NMDA receptor antagonism. *J Psychiatry Neurosci*. 2017; 42, 222–229.
- Buist-Bouwman MA, De Graaf R, Vollebergh WA, Alonso J, Bruffaerts R, Ormel J. Functional disability of mental disorders and comparison with physical disorders: a study among the general population of six European countries. *Acta Psychiatr Scand*. 2006; 113, 492–500.
- Ferrari AJ, Somerville AJ, Baxter AJ, et al. Global variation in the prevalence and incidence of major depressive disorder: a systematic review of the epidemiological literature. *Psychol Med*. 2013; 43, 471–481.
- Jesulola E, Micalos P, Baguley IJ. Understanding the pathophysiology of depression: from monoamines to the neurogenesis hypothesis model – are we there yet? *Behav Brain Res*. 2018; 341, 79–90.
- Cuijpers P, Vogelzangs N, Twisk J, Kleiboeer A, Li J, Penninx BW. Comprehensive meta-analysis of excess mortality in depression in the general community versus patients with specific illnesses. *Am J Psychiatry*. 2014; 171, 453–462.
- O'Neil A, Stevenson CE, Williams ED, Mortimer D, Oldenburg B, Sanderson K. The health-related quality of life burden of co-morbid cardiovascular disease and major depressive disorder in Australia: findings from a population-based, cross-sectional study. *Qual Life Res*. 2013; 22, 37–44.
- Cuijpers P, Smit F. Excess mortality in depression: a meta-analysis of community studies. *J Affect Disord*. 2002; 72, 227–236.
- Gilman SE, Sucha E, Kingsbury M, Horton NJ, Murphy JM, Colman I. Depression and mortality in a longitudinal study: 1952–2011. *Cmaj*. 2017; 189, e1304–e1310.
- Miettola J, Niskanen LK, Viinamäki H, Kumpusalo E. Metabolic syndrome is associated with self-perceived depression. *Scand J Prim Health Care*. 2008; 26, 203–210.
- O'Connor C M, Gurbel PA, Serebruany VL. Depression and ischemic heart disease. *Am Heart J*. 2000; 140, 63–69.
- Dong JY, Zhang YH, Tong J, Qin LQ. Depression and risk of stroke: a meta-analysis of prospective studies. *Stroke*. 2012; 43, 32–37.
- Chen MH, Pan TL, Hsu JW, et al. Risk of type 2 diabetes in adolescents and young adults with attention-deficit/hyperactivity disorder: a nationwide longitudinal study. *J Clin Psychiatry*. 2018; 79.
- Mitchell AJ, Vancampfort D, Sweers K, van Winkel R, Yu W, De Hert M. Prevalence of metabolic syndrome and metabolic abnormalities in schizophrenia and related disorders – a systematic review and meta-analysis. *Schizophr Bull*. 2013; 39, 306–318.
- Vancampfort D, Vansteelandt K, Correll CU, et al. Metabolic syndrome and metabolic abnormalities in bipolar disorder: a meta-analysis of prevalence rates and moderators. *Am J Psychiatry*. 2013; 170, 265–274.
- Fernandez-Egea E, Bernardo M, Donner T, et al. Metabolic profile of antipsychotic-naïve individuals with non-affective psychosis. *Br J Psychiatry*. 2009; 194, 434–438.
- Koponen H, Vuononvirta J, Mäki P, et al. No difference in insulin resistance and lipid levels between controls and adolescent subjects who later develop psychosis. *Schizophr Res*. 2008; 104, 31–35.
- Toma S, Fiksenbaum L, Omrin D, Goldstein BI. Elevated familial cardiovascular burden among adolescents with familial bipolar disorder. *Front Psychiatry*. 2019; 10, 8.
- Sobczak S, Honig A, Christophe A, et al. Lower high-density lipoprotein cholesterol and increased omega-6 polyunsaturated fatty acids in first-degree relatives of bipolar patients. *Psychol Med*. 2004; 34, 103–112.
- Dong C, Sanchez LE, Price RA. Relationship of obesity to depression: a family-based study. *Int J Obes Relat Metab Disord*. 2004; 28, 790–795.
- Mannie ZN, Williams C, Diesch J, Steptoe A, Leeson P, Cowen PJ. Cardiovascular and metabolic risk profile in young people at familial risk of depression. *Br J Psychiatry*. 2013; 203, 18–23.
- Huang MH, Chen MH, Huang KL, et al. Increased risk of type 2 diabetes among the siblings of patients with schizophrenia. *CNS Spectr*. 2019; 24, 453–459.
- Kuo CF, Grainge MJ, Valdes AM, et al. Familial aggregation of systemic lupus erythematosus and coaggregation of autoimmune diseases in affected families. *JAMA Intern Med*. 2015; 175, 1518–1526.
- Cheng CM, Chang WH, Chen MH, et al. Co-aggregation of major psychiatric disorders in individuals with first-degree relatives with schizophrenia: a nationwide population-based study. *Mol Psychiatry*. 2018; 23, 1756–1763.
- Chen MH, Lan WH, Hsu JW, et al. Risk of developing type 2 diabetes in adolescents and young adults with autism spectrum disorder: a nationwide longitudinal study. *Diabetes Care*. 2016; 39, 788–793.
- Chen MH, Pan TL, Li CT, et al. Risk of stroke among patients with post-traumatic stress disorder: nationwide longitudinal study. *Br J Psychiatry*. 2015; 206, 302–307.
- Chen MH, Su TP, Chen YS, et al. Attention deficit hyperactivity disorder, tic disorder, and allergy: is there a link? A nationwide population-based study. *J Child Psychol Psychiatry*. 2013; 54, 545–551.
- Liu CY, Hung YT, Chuang YL, Chen YJ, Weng WS, Liu JS. Incorporating development stratification of Taiwan townships into sampling design of large scale health interview survey. *J Health Manage*. 2006; 4, 1–22.
- Natsuaki MN, Ge X, Leve LD, et al. Genetic liability, environment, and the development of fussiness in toddlers: the roles of maternal depression and parental responsiveness. *Dev Psychol*. 2010; 46, 1147–1158.
- Liu L, Li Y, Tollefsbol TO. Gene-environment interactions and epigenetic basis of human diseases. *Curr Issues Mol Biol*. 2008; 10, 25–36.
- Bornstein SR, Schuppenies A, Wong ML, Licinio J. Approaching the shared biology of obesity and depression: the stress axis as the locus of gene-environment interactions. *Mol Psychiatry*. 2006; 11, 892–902.
- Della-Morte D, Guadagni F, Palmirotta R, et al. Genetics of ischemic stroke, stroke-related risk factors, stroke precursors and treatments. *Pharmacogenomics*. 2012; 13, 595–613.
- McCaffery JM, Duan QL, Frasure-Smith N, et al. Genetic predictors of depressive symptoms in cardiac patients. *Am J Med Genet B Neuropsychiatr Genet*. 2009; 150b, 381–388.
- Amare AT, Schubert KO, Klingler-Hoffmann M, Cohen-Woods S, Baune BT. The genetic overlap between mood disorders and cardiometabolic diseases: a systematic review of genome wide and candidate gene studies. *Transl Psychiatry*. 2017; 7, e1007.

34. Abkevich V, Camp NJ, Hensel CH, *et al.* Predisposition locus for major depression at chromosome 12q22–12q23.2. *Am J Hum Genet.* 2003; 73, 1271–1281.
35. Aberg K, Dai F, Sun G, *et al.* A genome-wide linkage scan identifies multiple chromosomal regions influencing serum lipid levels in the population on the Samoan islands. *J Lipid Res.* 2008; 49, 2169–2178.
36. Wilson SG, Adam G, Langdown M, *et al.* Linkage and potential association of obesity-related phenotypes with two genes on chromosome 12q24 in a female dizygous twin cohort. *Eur J Hum Genet.* 2006; 14, 340–348.
37. Sherva R, Miller MB, Pankow JS, *et al.* A whole-genome scan for stroke or myocardial infarction in family blood pressure program families. *Stroke.* 2008; 39, 1115–1120.
38. Muldoon MF, Mackey RH, Williams KV, Korytkowski MT, Flory JD, Manuck SB. Low central nervous system serotonergic responsivity is associated with the metabolic syndrome and physical inactivity. *J Clin Endocrinol Metab.* 2004; 89, 266–271.
39. Muldoon MF, Mackey RH, Sutton-Tyrrell K, Flory JD, Pollock BG, Manuck SB. Lower central serotonergic responsivity is associated with preclinical carotid artery atherosclerosis. *Stroke.* 2007; 38, 2228–2233.
40. Mannie ZN, Harmer CJ, Cowen PJ. Increased waking salivary cortisol levels in young people at familial risk of depression. *Am J Psychiatry.* 2007; 164, 617–621.
41. Vargas J, Junco M, Gomez C, Lajud N. Early life stress increases metabolic risk, HPA axis reactivity, and depressive-like behavior when combined with postweaning social isolation in rats. *PLoS One.* 2016; 11, e0162665.
42. Lemche E, Chaban OS, Lemche AV. Neuroendocrine and epigenetic mechanisms subserving autonomic imbalance and HPA dysfunction in the metabolic syndrome. *Front Neurosci.* 2016; 10, 142.
43. Burford NG, Webster NA, Cruz-Topete D. Hypothalamic-pituitary-adrenal axis modulation of glucocorticoids in the cardiovascular system. *Int J Mol Sci.* 2017; 18.
44. Block A, Schipf S, Van der Auwera S, *et al.* Sex- and age-specific associations between major depressive disorder and metabolic syndrome in two general population samples in Germany. *Nord J Psychiatry.* 2016; 70, 611–620.
45. Gil K, Radziłłowicz P, Zdrojewski T, *et al.* Relationship between the prevalence of depressive symptoms and metabolic syndrome: results of the SOPKARD project. *Kardiol Pol.* 2006; 64, 464–469.
46. Nishina M, Nishina K, Ohira T, Makino K, Iso H. Associations of psychological distress with metabolic syndrome among Japanese urban residents. *J Atheroscler Thromb.* 2011; 18, 396–402.
47. Alemany M. Do the interactions between glucocorticoids and sex hormones regulate the development of the metabolic syndrome? *Front Endocrinol.* 2012; 3, 27.
48. Soares CN, Zitek B. Reproductive hormone sensitivity and risk for depression across the female life cycle: a continuum of vulnerability? *J Psychiatry Neurosci.* 2008; 33, 331–343.



## REVIEW

# Role of gut microbiota in identification of novel TCM-derived active metabolites

Tzu-Lung Lin<sup>1</sup>, Chia-Chen Lu<sup>2,3</sup>, Wei-Fan Lai<sup>4</sup>, Ting-Shu Wu<sup>4,5,6</sup>, Jang-Jih Lu<sup>5,6</sup>, Young-Mao Chen<sup>7</sup>, Chi-Meng Tzeng<sup>8</sup>, Hong-Tao Liu<sup>9</sup>, Hong Wei<sup>10</sup>, Hsin-Chih Lai<sup>1,5,6,11,12</sup>✉

<sup>1</sup> Department of Medical Biotechnology and Laboratory Science, College of Medicine, Chang Gung University, Gueishan, Taoyuan 33302, Taiwan, China

<sup>2</sup> Department of Respiratory Therapy, Fu Jen Catholic University, New Taipei City 24205, Taiwan, China

<sup>3</sup> Department of Chest Medicine, Internal Medicine, Fu Jen Catholic University Hospital, Fu Jen Catholic University, New Taipei City 24205, Taiwan, China

<sup>4</sup> Department of Medicine, Chang Gung University, Taoyuan 33302, Taiwan, China

<sup>5</sup> Department of Laboratory Medicine and Internal Medicine, Linkou Chang Gung Memorial Hospital, Taoyuan 33305, Taiwan, China

<sup>6</sup> Central Research Laboratory, Xiamen Chang Gung Hospital, Xiamen 361026, China

<sup>7</sup> Bachelor Degree Program in Marine Biotechnology, College of Life Sciences, National Taiwan Ocean University, Keelung 20224, Taiwan, China

<sup>8</sup> School of Pharmaceutical Sciences, Xiamen University, Xiamen 361005, China

<sup>9</sup> College of Basic Medicine, Hubei University of Chinese Medicine, Wuhan 430065, China

<sup>10</sup> Central Laboratory, Clinical Medicine Scientific and Technical Innovation Park, Shanghai Tenth People's Hospital, Tongji University, Shanghai 200435, China

<sup>11</sup> Microbiota Research Center and Emerging Viral Infections Research Center, Chang Gung University, Taoyuan 33302, Taiwan, China

<sup>12</sup> Research Center for Chinese Herbal Medicine and Research Center for Food and Cosmetic Safety, College of Human Ecology, Chang Gung University of Science and Technology, Gueishan, Taoyuan 33303, Taiwan, China

✉ Correspondence: hclai@mail.cgu.edu.tw (H.-C. Lai)

Received March 13, 2020 Accepted May 29, 2020

## ABSTRACT

Traditional Chinese Medicine (TCM) has been extensively used to ameliorate diseases in Asia for over thousands of years. However, owing to a lack of formal scientific validation, the absence of information regarding the mechanisms underlying TCMS restricts their application. After oral administration, TCM herbal ingredients frequently are not directly absorbed by the host, but rather enter the intestine to be transformed by gut microbiota. The gut microbiota is a microbial community living in animal intestines, and functions to maintain host homeostasis and health. Increasing evidences indicate that TCM herbs closely affect gut microbiota composition, which is associated with the conversion of herbal components into active metabolites. These may significantly affect the therapeutic

activity of TCMS. Microbiota analyses, in conjunction with modern multiomics platforms, can together identify novel functional metabolites and form the basis of future TCM research.

**KEYWORDS** Traditional Chinese Medicine, herbs, microbiota, transformation, multiomics

## INTRODUCTION

### TCM and herbal formulae

TCM has been used for centuries in China to alleviate symptoms, treat disease, and promote well-being in Chinese patients (Zhao et al., 2014). In contrast to modern Western medicine, research progress made in TCM is often inhibited because of the inherent complexity of herbs as medicine and a comparative lack of modern scientific validation.

Tzu-Lung Lin and Chia-Chen Lu have contributed equally.

Accordingly, TCM research must be modernized by meeting the scientific method.

Historically, recordings that emerged from functional TCM herbal ingredients and aimed at treating specific diseases, eventually evolved into the creating of specific formulae. These formulae were further revised and assembled to create the TCM version of the “Materia Medica”. These manuals established a solid basis and references of TCM for clinical treatment. Among these references, the “*Shennong Bencao Jing*” (literally, *Shennong’s Classic of Materia Medica*) (Jin et al., 2013), “*HuangDi NeiJing*” (literally *The Yellow Emperor’s Classic of Medicine*) (Ni, 1995), and “*Compendium of “Materia Medica”*” (Li et al., 2014; Hao and Jiang, 2015; Gao et al., 2016; Ding et al., 2020) were featured. TCM-derived materia medicas have been rapidly developed and created complicated herbal networks for clinical applications. Each materia medica contained many formulae, with each formula comprising a combination of herbal drugs. Among these, complex components including carbohydrates/polysaccharides (PS), proteins/peptides, glycolipids/glycoproteins, lipids, together with their metabolic derivatives such as glycosides, amines, fatty acids, flavonoids, terpenoids, phenols, and alkaloids intimately interacted with each other and modulated biological responses of immune cells and the hosts (Li and Kan, 2017; Yu et al., 2018b; Zhang et al., 2020c). Differential agonistic, compatible, or antagonistic interactions occur among TCM herbal ingredients. For instance, the Fuzheng Huayu (FZHY) is mainly composed of *Radix Salvia Miltiorrhizae*, *Cordyceps*, *Semen Persicae*, *Gynostemma Pentaphyllum*, *Pollen Pini*, and *Fructus Schisandrae Chinensis*. It is widely administered to ameliorate chronic liver diseases and functions through modulation of multiple signaling pathways in a number of organs (Chen et al., 2019). FZHY effectively regulates immune functions, optimizes systematic amino acid metabolism and endocrine function, and reduces portal vein hypertension (Chen et al., 2019). These alterations lead to improved liver function and antifibrotic effects. Additionally, FZHY also has no serious adverse reactions (Chen et al., 2019). Further, Gegen Qinlian decoction (GQD), composed of four herbs: Gegen (*Radix Puerariae*), Huangqin (*Radix Scutellariae*), Huanglian (*Rhizoma Coptidis*) and Gancao (Honey-fried Licorice Root) is frequently used in TCM for alleviation of type 2 diabetes (Xu et al., 2015). The Qushi Huayu Decoction (QHD), made up of *Herba Artemisiae capillaris*, *Rhizoma Polygoni cuspidati*, *Herba Hyperici Japonici*, *Rhizoma Curcumae longae*, and *Gardenia jasminoides* ameliorates non-alcoholic fatty liver disease (NAFLD) in patients (Feng et al., 2013).

#### Current advances in identification of active components from TCM herbs

The basic principle of scientific exploration in Western medicine has been the discovery of functional compounds

and their corresponding targets in specific signaling pathways within cells. To achieve this understanding, standardized phytochemistry, pharmacology, pharmacokinetics (PK, absorption/distribution/metabolism/excretion, ADME), pharmacodynamics (PD, effects/action/mechanism), and toxicology research procedures are performed (Chen et al., 2020). Currently, platforms for high throughput screening of compounds, together with stringent functional and safety validations are used to better understand the mechanisms of action of functional compounds. Concordantly, for the development of novel therapeutic drugs from TCM-derived herbs, a similar approach was established (Martel et al., 2017a; Jiang et al., 2020). Through this method, many active components in TCM herbs were identified. One famous example was the discovery of artemisinin, a plant-derived compound with anti-malaria and anti-cancer functions (Zhang et al., 2007; Carqueijeiro et al., 2019). Other examples included berberine purified from berberis, capsaicin from chili peppers, caffeine from coffee beans, ephedrine from Ephedra, chitosan from mushrooms, genistein from soybeans, celastrol from thunder god vine, epigallocatechin gallate from green tea, glycyrrhizin from licorice roots, quercetin from various plants, and curcumin from turmeric (Martel et al., 2017b). Besides small chemicals, functional polysaccharides (PS) derived from TCM herbs have also been characterized, such as those from *Ganoderma lucidum* mycelium (Chang et al., 2015), *Hirsutella sinensis* mycelium (Chang et al., 2015; Wu et al., 2019), and *Poria cocos* (Sun et al., 2019).

To improve the efficiency of screening for novel functional TCM herbal components, new approaches using modern technology have been explored. For example, a luciferase-based high-throughput screening (HTS) assay has been used to integrate multiple chemical messages derived from effective TCM healing formulae. This pipeline can expedite the active ingredient discovery process by reducing replicated leads (Yu et al., 2019a). Beyond this screen, a TCM System Pharmacology Database and Analysis Platform (TCMSP) had been established. The TCMSP is a systematic pharmacology database which compiles drug discovery results from previous herbal medicine experiments. This database contains pharmacochemistry, ADME and toxicity properties, drug likeness and targets, associated diseases, and interaction networks. Importantly, this database can be used to unravel active components in TCM herbs and their targeted cellular pathways (Ru et al., 2014; Li et al., 2020). Exploration of this database can be combined with other systems, such as Gene Ontology (GO) predictions and Kyoto Encyclopedia of Genes and Genomes (KEGG) pathway enrichment analyses to identify potential ameliorative mechanisms of key molecules (Yu et al., 2019a). Additionally, interactions between active molecules and their predicted target proteins may be further predicted by “molecular docking” and protein-protein interaction networks, which may enhance understanding of underlying potential interactions. Finally, the TCMSP database enables the linking of identified



compounds to their corresponding targets/pathways involved in disease amelioration. Therefore, through these analyses, axis of component-target-disease (C-T-D) and the corresponding target-pathway (T-P) networks could be established, to further dissect the active compounds, potential targets, and core pathways in treatment of diseases by a specific TCM formula (Li et al., 2020). Subsequently, LC and/or GC-MS/MS can be used to practically monitor the active ingredients of TCMs. This style of pipeline may provide a new, standardized approach to systematically screen TCM herbal components for treatment of diseases (Li et al., 2020). Accordingly, functional molecules in TCMs can be assessed in the context of heterogeneous cell signaling pathways to predict their effects on diseases at immunological, metabolic, and molecular levels (Zhang et al., 2016; Li and Kan, 2017).

Even though many *in vitro* assay-based screening systems are available for high throughput screening, most purified small chemical components directly derived from herbs still suffer from marginal potency, adverse effects, and low bioavailability in animal or clinical studies (Belcher et al., 2019; Liu et al., 2019a; Teijaro et al., 2019). For example, the compound rhein showed beneficial effects on diabetic nephropathy, which is related to reduced levels of TGF- $\beta_1$ , renal fibrosis, metabolism, and oxidative stress status (Hu et al., 2019). However, its adverse effects, such as hepatotoxicity, nephrotoxicity, and embryonic toxicity were also highlighted (Yuan et al., 2016). Further, chemical compounds derived from *Polygonum multiflorum* (also known as Heshouwu) showed ameliorative effects on hair-blackening, liver and kidney-tonifying, anti-aging, as well as neuronal disease treatment (Lin et al., 2015). However, these compounds could induce hepatotoxicity, nephrotoxicity and embryonic toxicity (Lin et al., 2015). Comparatively, the PS purified from TCM herbs showed less toxicity and were frequently modified in the host (Chen et al., 2016). So far the underlying molecular mechanism of PS effects remains poorly understood.

## GUT MICROBIOTA MAINTAINS INTESTINAL HOMEOSTASIS AND PROMOTE HEALTH

The gut microbiota is a collection of microbes colonizing the intestine (Lin et al., 2014; Tsai et al., 2019; Zmora et al., 2019). More than 100 trillion ( $10^{14}$ ) microbes inhabit the human gastrointestinal (GI) tract, which included about 10 times more bacterial cells than the number of human cells, and over 100 times the amount of genetic contents (microbiome) in contrast to the human genome (Thursby and Juge, 2017). Bacteria at the number between  $10^2$ – $10^4$  colony-forming units (CFU)/mL are found in the first section of the small intestine, the duodenum. Generally, the Lactobacilli, Streptococci, Veillonellae, Staphylococci, Actinobacilli and yeasts dominate the duodenum and jejunum (Lin et al., 2014). The GI microbiota changes markedly from the

duodenum to the ileum, with an according increase in bacterial load, reaching up to  $10^6$ – $10^8$  CFU/mL. In the large intestine, commensal bacteria reach high numbers ( $10^7$ – $10^{12}$  CFU/mL) and are extremely diverse. At the same time, the environment of colon is strictly anaerobic. This means that obligate anaerobes that obtain their energy from fermentation dominate. More than 1,500 bacterial species have been identified in the colon of humans (Lin et al., 2014; Chang et al., 2019). However, a large proportion of the GI microbiota bacteria cannot be easily isolated and cultured *in vitro*, necessitating the use of culturomics (Lagier et al., 2018).

Under homeostasis situation, the intestinal microenvironment provides a barrier to prevent the translocation of pathogens or harmful agents (such as the endotoxin LPS) across the intestinal epithelial cells (IECs) into the surrounding lymphoid system and blood (Boyapati et al., 2016). Gut microbiota bacteria maintain host integrity and regulate many important physiological functions, including homeostasis of energy and metabolism, modification of xenobiotics, modulation of intestinal homeostasis, regulation of immunity and protection against pathogens, and even normal host neuronal behavior and cognitive functions (Clemente et al., 2012; Schachter et al., 2018; Lin et al., 2019).

In aberrant physical, chemical, or biological conditions, such as long-term high fat diet, antibiotic treatment, or increased oxidative stress, the composition of gut microbiota changes, lead to GI dysbiosis and disruption of the intestinal mucosa. This dysbiosis results in a damaged intestinal barrier and increased intestinal permeability. Proinflammatory elements, such as pathogen-associated molecular pattern molecules (PAMPS) (mainly the endotoxin, LPS) or damage-associated molecular pattern molecules (DAMPS) (Tang et al., 2012), are increased in intestines and blood, resulting in both local intestinal injury and systemic chronic inflammation (Yan, 2018; Alexandrov et al., 2019). This “leaky gut” phenomenon is closely related to development of chronic inflammation-related diseases. In a broad sense, the gut microbiota appears to be critical in maintaining host homeostasis and health (Lin et al., 2014; Wang et al., 2017a; Gentile and Weir, 2018).

## CLOSE INTERACTION BETWEEN TCM HERBS AND GUT MICROBIOTA IN DISEASES AMELIORATION

TCM herbs closely interact with gut microbiota and affect their composition (Peng et al., 2020). Reciprocally, the gut microbiota also plays essential roles in the conversion of carbohydrates, proteins, lipids, and non-nutritive small chemical compounds from TCM herbs into chemical metabolites that may show beneficial or adverse effects on human health (Blaut and Clavel, 2007; Wang et al., 2013; Yu et al., 2018a; Feng et al., 2019; Lu et al., 2019; Qu et al., 2019; Yue et al., 2019; Zhang et al., 2019a, b, 2020c) (Fig. 1



and Table 1). These results indicated that modulation of gut microbiota composition may contribute to the effects of disease amelioration by TCM treatment. For oral treatment, TCM herbs have mostly been prepared by soaking the ingredients in boiling/hot water to generate a water extract that contains a mixture of chemical components, which was generally named as “decoction” (Zhou et al., 2016; Chi et al., 2019; Deng et al., 2019). While some TCM nutraceuticals may directly affect epithelial and immune cells of the digestive tract; others, such as indigestible PS, polyphenols, and alkaloids, etc., may pass through the stomach and reach small and large intestine. Many herbal ingredients are frequently fermented or converted by local gut microbiota to form bioactive, bioavailable, or even toxic metabolites (Lyu et al., 2017; Liu et al., 2018b; Dey, 2019; Wu and Tan, 2019; Yang and Lao, 2019). Depending on use of different formulae, some transformed metabolites may be functionally novel and not clearly defined (Fig. 1). Both changed microbiota bacteria and transformed TCM metabolites may contribute to control of progression of diseases development. Take the TCM effects on amelioration of diabetes as an example: while almost all bacterial phyla seemed to be affected by

TCM herbs administration, Bacteroidetes, Firmicutes (and therefore the Firmicutes/Bacteroidetes (F/B) ratio), Proteobacteria, Verrucomicrobia, Cyanobacteria, Deferribacteres, and Actinobacteria were mostly reported (Dey, 2019; Zhang et al., 2019a). Further detailed analyses indicated the abundance of potentially beneficial (such as anti-inflammatory, or SCFAs producers) and harmful (proinflammatory and pathogenic) bacteria could be differentially affected by ingestion of different TCM herbs (Chang et al., 2015; Lyu et al., 2017; Tong et al., 2018; Lin et al., 2019; Nie et al., 2019; Wu et al., 2019). Alteration of the gut microbiota composition is therefore closely related to development of differential immune and metabolic activities in the hosts. Roles of these bacteria on health or disease development are species or even strain dependent under different disease situations, which is under intensive study (Lin et al., 2019).

Recent studies have shown a variety of TCM herbal components influence microbial abundance and diversity, which reciprocally is closely related to the efficacy of TCM herbs (Table 1). Among these, effects from PS treatment on obesity, diabetes and related metabolic syndromes seemed to be most intensively studied. For example, treatment with

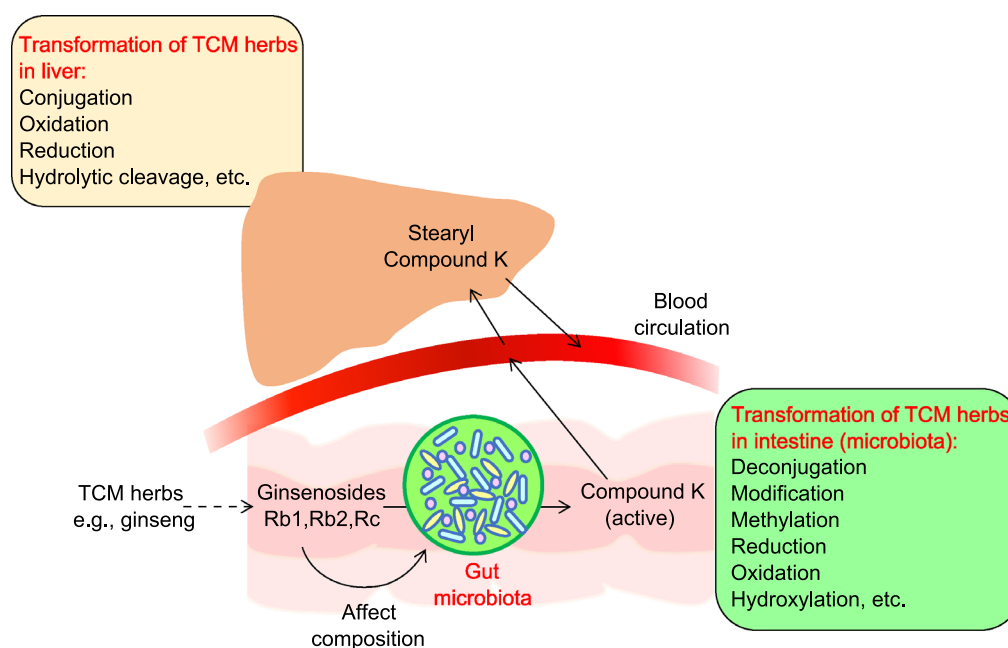


**Figure 1. The transformation of TCM herbal ingredients (ginseng extracts as an example).** Transformation of TCM herbal ingredients into active metabolites in host was contributed both by gut microbiota and liver. Understanding ginseng's pharmacokinetics is important for better medication in patients. After oral administration of ginseng, the bioavailability of ginsenosides is low, and the metabolites transformed by gut microbiota may become biologically active. For example, ginsenosides Rb1, Rb2 and Rc were transformed by gut microbiota to form compound K, followed by absorption into the blood (Qi et al., 2011). Compound K showed higher potency and activity compared with ginsenoside Rb1. Compound K adsorbed into blood metabolized again in liver to form stearyl compound K (Kim, 2018). On the other hand, ginsenoside Rb1 also could modulate the composition of gut microbiota (Wan et al., 2017). Therefore, gut microbiota produces active metabolites and plays an important role in the pharmacological action of orally administered ginseng.

**Table 1. Relationship between TCM herbal ingredients, gut microbiota composition, metabolites produced and targeted diseases.** ND, not clearly defined.

TCM herbal ingredients	Microbiota affected	Metabolites produced	Target diseases	References
<b>Main component: Decoction or Tang</b>				
Daesi ho Tang (DSHT)	Bacteroidetes, Bacteroidetes/Firmicutes ratio	ND	Obesity	(Hussain et al., 2016)
Gegen Qinlian Decoction (GQD)	<i>Faecalibacterium prausnitzii</i>	ND	Type 2 diabetes	(Xu et al., 2015)
Qushi Huayu Decocti (QHD)	Generally affects gut microbiota composition. Does not affect identified Gram-negative bacteria.	ND	NAFLD	(Leng et al., 2020)
Xiexin Tang (XXT)	Adlercreutzia, Alloprevotella, Barnesiella, Ventriosum group, Blautia, Lachnospiraceae UCG-001, Papillibacter, Prevotellaceae NK3B31 group	SCFAs	Type 2 diabetes	(Wei et al., 2018)
Metformin and a specifically designed herbal formula, AMC	Blautia spp., <i>Faecalibacterium</i> spp.	ND	Type 2 diabetes	(Tong et al., 2018)
Huang-Lian-Jie-Du decoction (HLJDD)	Parabacteroides, Blautia, Akkermansia, Aerococcus, Staphylococcus-Corynebacterium	SCFAs	Hyperglycemia and insulin resistance	(Chen et al., 2018b)
Qijian mixture	Mainly Bacteroidetes	55 proteins and related metabolism of galactose, valine, leucine, isoleucine, alanine, aspartate and glutamate. Biosynthesis of aminoacyl-tRNA.	Type 2 diabetes	(Gao et al., 2018)
<b>Main component: TCM polysaccharide</b>				
<i>G. lucidum</i>	Parabacteroides, Roseburia, Eubacterium, Clostridium	ND	Obesity, NAFLD, diabetes mellitus	(Chang et al., 2015)
<i>H. sinensis</i> mycelium	<i>P. goldsteinii</i>	ND	Obesity, NAFLD, diabetes mellitus	(Wu et al., 2019)
Mulberry fruit	Bacteroidales, Lactobacillus, Allobaculum, Bacteroides, Akkermansia	ND	Obesity	(Chen et al., 2018a)
<i>Ganoderma atrum</i>	ND	SCFAs	Intestinal mucosal dysfunction, type 2 diabetes	(Zhu et al., 2016) (Ying et al., 2020)
Stigma maydis	Lactobacillus, Bacteroides			(Wang et al., 2016)

Table 1. continued

TCM herbal ingredients	Microbiota affected	Metabolites produced	Target diseases	References
Main component: Proteins/amino acids				
A variety of different herbs	Multiple phyla in microbiota bacteria	-ammonia -amines -gases (methane, hydrogen gas, H <sub>2</sub> S) -catecholamines and phenols ( <i>p</i> -cresol, <i>p</i> -nitrosophenol, <i>p</i> -diazquinone, indoxyl sulfate, hippuric acid, phenyl sulfate, pyrocatechol sulfate, 4-ethylphenyl sulfate, <i>p</i> -cresol glucuronide, and equol 7-glucuronide) -neuro-active metabolites, such as serotonin, melatonin, kynurenine, quinolinine, indole, IAA, IPA, and tryptamine	Chronic inflammation related diseases	(Baumann and Bisping, 1995; Magee et al., 2000; Blachier et al., 2007; Neis et al., 2015; Liu et al., 2016; Mazzoli and Pessione, 2016; Portune et al., 2016; Velenosi et al., 2016; Lin et al., 2017; Ma et al., 2017; Kaur et al., 2019)
Main component: Lipids/fatty acids				
A variety of different herbs	Multiple phyla in microbiota bacteria	-conjugated essential fatty acids (conjugated linoleic acid) -trimethyl amine (TMA)	Chronic inflammation related diseases	(Devillard et al., 2007; Marques et al., 2015; Rath et al., 2017; Janeiro et al., 2018; Schoeler and Caesar, 2019; Yu et al., 2019b)
Main component: Chemicals and related				
A variety of different herbs	Multiple phyla in microbiota bacteria	-secondary glycosides and/or aglycones -CPT-11 related SN-38-glucuronide -secondary bile acids	Chronic inflammation related diseases	(Dabek et al., 2008; Yang et al., 2011; Yan et al., 2013; Chen et al., 2015; Wahlstrom et al., 2016; Ramirez-Perez et al., 2017; Jia et al., 2018)
Ginsenosides in Du-Shen-Tang (DST)	Enhance the growth of <i>Lactobacillus</i> spp. and <i>Bacteroides</i> spp.	ND	Fatigue, acute cold stress	(Zhou et al., 2016)
Banxia Xiexin decoction (BXD)	ND	Baicalin, baicalin, wogonoside-wogonin, scutellarin, berberine, coptisine, ginsenoside Rb1, ginsenoside Re	Diabetic gastroparesis	(Xu et al., 2018)
Meformin and <i>Houttuynia cordata</i> extract (HCE)	<i>Roseburia</i> , <i>Akkermansia</i> , Gram-negative bacteria including <i>Escherichia coli</i> , <i>Bacteroidetes fragilis</i> .	ND	Insulin resistance and metabolic syndromes	(Wang et al., 2017b; Wang et al., 2018a)
Berberine derived from <i>Coptis chinensis</i>	<i>Bifidobacterium</i> , <i>Escherichia coli</i>	ND	Glucolipid metabolism and insulin resistance in diabetic mice	(Han et al., 2016; Liu et al., 2018b)
Rhein	<i>Bacteroidetes</i>	ND	Antidiabetic effects	(Wang et al., 2018b)

PS purified from *G. lucidum* and *H. sinensis* mycelium significantly reduced obesity through enhancement of a consortium of commensal bacteria, including *Parabacteroides goldsteinii*, *Roseburia*, *Eubacterium* and *Clostridium* spp. (Chang et al., 2015; Wu et al., 2019). Mulberry fruit PS also influenced obesity and modulated gut microbiota (Chen et al., 2018a), while PS from *Ganoderma atrum* ameliorated intestinal mucosal dysfunction and improved liver function in type 2 diabetes (Zhu et al., 2016), and *stigma maydis* PS ameliorated type-2 diabetes (Wang et al., 2016) by changing gut microbial populations and related fermentation functions. Further, the PS and ginsenosides contained in decoction of ginseng, the Du-Shen-Tang (DST), restored fatigue and acute cold stress, and modulates the gut microbiota composition (Zhou et al., 2016). There were many other examples highlighting the microbial change during the treatment of obesity, diabetes and metabolic syndromes (Table 1). These examples include Daesih-Tang (DSHT) that attenuated obesity and significantly increased the relative abundance of Bacteroidetes, B/F ratio, Akkermansia, Bifidobacterium, Lactobacillus, and decreased the level of Firmicutes (Hussain et al., 2016), Gegen Qinlian Decoction (GQD) alleviated Type 2 diabetes and significantly increased *Faecalibacterium prausnitzii* (Xu et al., 2015), while Qushi Huayu Decoction (QHD) reduced HFD-induced non-alcoholic fatty liver disease (NAFLD), and significantly increased the abundance of Parabacteroides and decreased the abundance of Odoribacter, Rikenella, Tyzzerella, Intestini-bacter, Romboutsia and 2 members in Lachnospiraceae (Leng et al., 2020). Other examples related to gut microbiota changes included (Table 1): 20% *Folium Mori* amelioration of diabetes (Zhang et al., 2019a), Xiexin Tang-mediated improvement of type 2 diabetes (Wei et al., 2018), amelioration of human type 2 diabetes by metformin and a traditional Chinese herbal formula, AMC (Tong et al., 2018), Huang-Lian-Jie-Du decoction-mediated treatment of hyperglycemia and insulin resistance (Chen et al., 2018b), improvement of type 2 diabetes by treatment with Qijian (Gao et al., 2018), Banxia Xiexin decoction on diabetic gastroparesis rats (Xu et al., 2018), *Houttuynia cordata* facilitation of metformin on reducing insulin resistance (Wang et al., 2017b), berberine, the main bioactive alkaloid of *Coptis chinensis*, on glucolipid metabolism and insulin resistance in diabetic mice (Han et al., 2016; Liu et al., 2018a), and rhein's role in antidiabetic effects (Wang et al., 2018b). Evidently, efficacy of TCM herbal treatment is closely related to their influence on gut microbiota composition. Therefore, the ingredients of TCM herbs may not only directly regulate host cells activity, but also be metabolized by gut microbiota and affect their structures. Close interaction between TCM and gut microbiota contributes to modulating the host immune and metabolic activities. New research approaches based on gut microbiota-related characterization of clinically applicable TCM components have to be developed (Zhao et al., 2014).

## ROLE OF GUT MICROBIOTA IN FERMENTATION OF TCM PS

TCM PS as well as other plant-derived PS such as vegetables, fruits, and whole grains etc. were shown to play important functions in immune-modulation and disease amelioration (Chang, 2002; Yang et al., 2009; Li et al., 2013; Yu et al., 2018b; Sun et al., 2019). For example, both high (>100 kDa.) and low (<100 kDa.) molecular weight, and neutral and acidic PS prepared from *Panax ginseng* that displayed differential functions affecting cellular and host physiology (Sun, 2011; Kim et al., 2020) were among the many examples. Owing to the limited digestive enzymes encoded by the human genome, PS are frequently undigested until they reach the colon (Baumann and Bisping, 1995). In the colon, fermentable PS, such as  $\beta$ -glucans, were broken down by gut microbes via their saccharolytic machinery to produce important groups of natural bioactive products. Serial digestion of PS resulted in production of a number of short-chain oligosaccharides, comprising varying chain lengths, structural conformations, and number of branches (Tzianabos, 2000; Santa et al., 2014). These varied oligosaccharides may function to enhance growth of probiotics, such as *Bifidobacterium* spp. and *Bacteroides* spp. (Bouhnik et al., 2004). The shorter PS may be further digested to form either monosugars such as mannose (Man), glucose (Glc), galactose (Gal), rhamnose (Rha), arabinose (Ara), and fucose (Fuc) which enhance bacterial growth (Koropatkin et al., 2012; Tremaroli and Backhed, 2012). Monosugars can continuously be catabolized to form metabolites such as short chain fatty acids (SCFAs) (formate, acetate, propionate, butyrate), lactate, hydrogen, and carbon dioxide, which may directly affect host physiology (Schwartz et al., 2010; Simpson and Campbell, 2015; Burokas et al., 2017; Martel et al., 2017a). On the other hand, degraded products such as D-mannose may act as signaling molecules which show differential immunomodulatory effects and functions towards host cells and tissues (Zhang et al., 2017; Zhang et al., 2018).

A consortium of gut bacteria participates in the degradation of TCM-derived PS. For example, a host of bacterial species are involved in butyrate production, including *F. prausnitzii*, *Eubacterium rectale*, *Roseburia* spp. *Clostridium* spp. and many others belonging to Bacteroidetes (Zhang et al., 2018). These functional bacteria were characterized by their displays of several to dozens of enzymes used to degrade PS by targeting specific glycosidic linkages or chemical substituents (Martens et al., 2011). Genetic clusters involved in binding, degradation and importation of various PS include miscellaneous polysaccharide utilization loci (PULs), or starch utilization system (Sus)-like systems in Bacteroidetes (Bayer et al., 2008; Ravcheev et al., 2013). Comparatively, with respect to carbohydrate active enzymes (CAZymes), Bacteroidetes degrade a relatively wide range of polysaccharides, while Firmicutes prefer to catabolize selected polysaccharides (Cockburn and Koropatkin, 2016;

Zhang et al., 2018). Many different bacterial species may involve sequential catabolism of PS, and the functional metagenomics of consortium of bacteria that participate in PS metabolism are currently under intensive study.

### TCM AFFECTS GUT MICROBIOTA THAT PRODUCES FUNCTIONAL AMINO ACIDS METABOLITES

Dietary proteins including those derived from TCM herbs, dietary foods, and other nutraceuticals can be digested by both hosts and gut microbiota, which may further affect gut microbiota structure (Conlon and Bird, 2014; Madsen et al., 2017; Amaretti et al., 2019). At the same time, certain gut bacteria in the distal colon also metabolize amino acids to form unique functional metabolites through specific biochemical pathways (Baumann and Bisping, 1995; Neis et al., 2015; Liu et al., 2016). The metabolic intermediates produced may involve either optimal modulation of energy homeostasis, nutrition metabolism, intestinal health and immunity, or cause inflammation and diseases (Neis et al., 2015; Portune et al., 2016; Lin et al., 2017). Basically, deamination of amino acids results in the production of ammonia, whereas decarboxylation leads to amine production (Baumann and Bisping, 1995). Depending on the amount of proteins up taken, the concentrations of ammonia, trace amines, and gases (methane, hydrogen, H<sub>2</sub>S) related to cytotoxins, genotoxins, and carcinogens produced in colon are altered (Ma et al., 2017). These harmful metabolites may translocate across the intestinal barrier and enter the blood for systematic circulation, resulting diseases development.

Anaerobic fermentation of cysteine and methionine by bacteria results in H<sub>2</sub>S formation. Long term increased sulfide and ammonia concentrations in the colon were shown to promote colitis and tumorigenesis (Baumann and Bisping, 1995; Magee et al., 2000). Also, metabolism of aromatic amino acids may produce a group of uremic toxins, including indoxyl sulfate, *p*-cresyl sulfate, hippuric acid, phenyl sulfate, pyrocatechol sulfate, 4-ethylphenyl sulfate, *p*-cresol glucuronide, and equol 7-glucuronide (Velenosi et al., 2016). These compounds are closely related to the development of chronic kidney disease (CKD), where the gut-plasma-kidney metabolic axis is established (Mishima et al., 2017; Liu et al., 2018b). Furthermore, degradation of "tyrosine" gives rise to catecholamines and phenols, where *p*-cresol, *p*-nitrosophenol and *p*-diazquinone are proposed to show carcinogenic effects (Bone et al., 1976; Kikugawa and Kato, 1988), tyramine is related to hypertension, and DOPA, dopamine and nor-adrenaline can modulate multiple physiological functions (Mazzoli and Pessione, 2016). On the other hand, the anaerobic conversion of "tryptophan" also produces functional metabolites related to the gut-brain axis (GBA). These include neuro-active metabolites, such as serotonin, melatonin, kynurenine, quinolinic acid, indole, IAA, IPA, and tryptamine (Mazzoli and Pessione, 2016; Kaur et al., 2019). Other

neuroactive molecules including histamine, glutamate, and GABA are also synthesized owing to the close interaction between the host and the microbiota (Sharon et al., 2014; Mazzoli and Pessione, 2016). The gut bacteria involved in such metabolism processes were widely categorized into five phyla including Actinobacteria, Firmicutes, Bacteroidetes, Proteobacteria, and Fusobacteria, in which *Clostridium*, *Burkholderia*, *Streptomyces*, *Pseudomonas*, and *Bacillus* were further enriched to be involved in the many tryptophan metabolism pathways (Kaur et al., 2019).

Branched chain amino acids (BCAAs), such as leucine (Leu), isoleucine (Ile), and valine (Val), work both as the substrates for anabolism of nitrogenous compounds and as signaling molecules regulating energy homeostasis via multiple signaling networks, including the phosphoinositide 3-kinase/protein kinase B/mammalian target of rapamycin (PI3K/AKT/mTOR) pathway (Nie et al., 2018). Gut microbiota also participates in fermentation of BCAA and generates a complex mixture of metabolites, including ammonia, SCFAs, and branched-chain fatty acids (valerate, isobutyrate, and isovalerate). These bacterial metabolites have been shown to influence normal mucosal immunity of the host (Blachier et al., 2007).

Generally, the abundance of gut microbiota bacteria that are involved in amino acids metabolism are frequently affected by TCM herbs administration (Chang et al., 2015; Lyu et al., 2017; Tong et al., 2018; Feng et al., 2019; Lin et al., 2019; Nie et al., 2019; Wu et al., 2019; Yue et al., 2019; Zhang et al., 2019a). These included the *Clostridium* clusters, *Bacillus*, *Lactobacillus*, *Streptococcus*, and *Proteobacteria* in human small intestine, and the *Clostridia* and *Peptostreptococci* in large intestine of healthy humans (Neis et al., 2015). More and more bacterial species are expected to be unraveled to be involved in protein metabolism. Therefore, advances with regard to unraveling the protein/amino acid fermentation pathways, the potential novel corresponding metabolites produced by gut microbiota, and modulation of microbiota composition by TCM herbs are essential (Zhang et al., 2019b).

### TCM-AFFECTED GUT MICROBIOTA PRODUCES FUNCTIONAL METABOLITES IN LIPID METABOLISM

Lipids and their derived functional metabolites play multiple physiological roles in the host. Lipids from TCM herbs and daily foods intake have also been shown to affect gut microbial growth and composition, while gut microbiota bacteria are also important players in lipid metabolism in hosts (Marques et al., 2015; Di et al., 2019; Schoeler and Caesar, 2019; Yu et al., 2019b) (Table 1). Besides SCFAs, many other functional metabolites derived from lipid metabolism are also produced by bacteria in the gut. For example, commensal bacteria, including *Roseburia*, *Lactobacillus*, *Butyrivibrio*, and *Megasphaera* participate in fatty acid metabolism to produce an array of conjugated essential fatty



acids (e.g., conjugated linoleic acid) that intricately influence host physiology (Devillard et al., 2007). On the other hand, milk fat increases taurine-conjugation of bile acids, which leads to the further growth of *Bilophila wadsworthia* that then uses the increased availability of amino acid-derived sulfur to produce  $H_2S$  closely related to the incidence rates of colitis (Devkota et al., 2012).

Using key enzyme components of the trimethylamine (TMA)-synthesis pathways such as the choline TMA-lyase (CutC) pathway and carnitine oxygenase (CntA) pathway, gut bacteria such as *Clostridium* XIVa strains and *Eubacterium* spp. catabolize choline and L-carnitine to produce TMA. TMA is converted to trimethylamine-N-oxide (TMAO) in the liver (Rath et al., 2017; Janeiro et al., 2018). Many studies have indicated a close association between TMAO plasma levels and the risk of atherothrombotic cardiovascular disease (CVD) (Canyelles et al., 2018).

Previous studies have highlighted the roles of gut bacteria, such as Akkermansia, Butyrivibrio, Christensenellaceae, Eggerthella, Tenericutes, and Pasteurellaceae, on affecting specific aspects of lipid metabolism and/or distinct classes of lipoproteins (Ghazalpour et al., 2016). At the same time, rapid progresses have been made in unraveling the underlying mechanisms of TCM-mediated regulation of lipid metabolism and amelioration of disease. For instance, TCMs have been shown to inhibit intestinal absorption, reduce de novo biosynthesis, increase catabolism, and enhance secretion in lipids (Bei et al., 2012). The changed gut microbiota composition by TCM herbs administration may contribute to the ameliorative effects on abnormal lipids metabolism (Huang et al., 2019; Zhang et al., 2019a). On the other hand, ginseng extract can enrich *Enterococcus faecalis* that produces an unsaturated long chain fatty acid, myristoleic acid (MA), leading to reducing adiposity by activation of brown adipose tissue (BAT) and formation of beige fat (Quan et al., 2019). Therefore, modulation of gut microbiota bacteria by TCM herbs may produce optimal amounts of beneficial lipid metabolites, which is an effective strategy for promotion of well-being in hosts.

## TRANSFORMATION OF TCM SMALL CHEMICAL MOLECULES BY GUT MICROBIOTA

Different TCM formulae contain an array of small chemical molecules with a number biological functions, including flavonoids, saponins, alkaloids, and anthraquinones, etc. (Xu et al., 2013; Yan et al., 2013; Chen et al., 2015; Zhang et al., 2020b) (Table 1). Both gut microbiota and the liver involve conversion of the xenobiotics ingredients into subsequent metabolites (Fig. 1). In the intestines, these components can be modified/deconjugated by gut microbiota. Alternatively, they can also be absorbed and transported to the liver, where they are also modified/conjugated to increase their water solubility and facilitate excretion. After excretion into the intestinal tract from liver, these metabolites may further

undergo modification/deconjugation by gut microbiota to form secondary metabolites (Wahlstrom et al., 2016; Kim, 2018). Many of the transformed metabolites frequently act as functional compounds directly influencing the curative effects of TCM treatment. For example, herbal glycosides such as saponins, geniposide, iridoid glycosides, and flavone glycosides frequently identified in TCM ingredients are metabolized into secondary glycosides or aglycones by bacterial  $\beta$ -glucosidase (GUS) (Dabek et al., 2008; Yang et al., 2011) (Fig. 1). Such transformation may affect the bioavailability and bioactivity of these molecules (Yang et al., 2011). Additionally, the gut microbial GUS enzymes encoded by a variety of gut bacteria belonging to Firmicutes (60%) and Bacteroidetes (21%) (Humblot et al., 2007; Creekmore et al., 2019) also catalyze hydrolysis of  $\beta$ -D-glucuronic acid from their conjugated compounds and influence drug potency and toxicity. The transformation of ginseng extracts is taken as an example (Fig. 1). After oral administration, ginsenosides such as Rb1, Rb2 and Rc from ginseng extracts were transformed by gut microbiota to form 20-O- $\beta$ -D-glucopyranosyl-20(S)-protopanaxadiol (compound K) which was absorbed into the blood to achieve the pharmacological functions. Compound K showed more potent anti-tumor, anti-inflammatory, and anti-allergic activities more than ginsenoside Rb1 (Wang et al., 2011; Kim et al., 2013). Therefore, the gut microbiota plays an important role in the pharmacological action of orally administered ginseng.

Another example is the CPT-11 which is a potent anti-cancer agent metabolized to the active compound, SN-38 *in vivo*. A balanced SN-38 concentration in patients is essential to maintain optimal efficacy of cancer treatment while reducing toxicity. Intriguingly, both TCM components and gut microbiota are involved in modulation of SN-38 activity. For detoxification, SN-38 is conjugated to SN-38-glucuronide by UDP-glucuronosyltransferase (UGT). However, purified herbal aglycons where the glycosyl group of a glycoside was removed inhibited UGT activity (Yokoi et al., 1995; Ramesh et al., 2010; Bailly, 2019), leading to an increase in toxic SN-38 concentration in the enterohepatic circulation. On the other hand, gut microbiota bacteria also use the *gus* encoded  $\beta$ -glucuronidase for deconjugation of the SN-38-glucuronide. Therefore, the underlying regulatory activities formed a complicated regulatory network (Dabek et al., 2008). How to achieve a balanced SN-38 activity in patients with maximal efficacy of cancer treatment while reducing toxicity is an important issue.

Gut microbiota also transform bile acids and cholesterol, producing a variety of functional metabolites (Gerard, 2013). Among these, primary bile acids are produced in the liver as glycine, taurine, or sulfate conjugates, and after secretion into the intestine, are deconjugated and modified by intestinal bacteria. Through interaction with bile acid farnesoid X receptor (FXR) and G protein-coupled bile acid receptor 1 (TGR5), bile acids signaling controls multiple important physiological behaviors and maintains intestinal homeostasis and a healthy environment (Jia et al., 2018). Bacteria such as

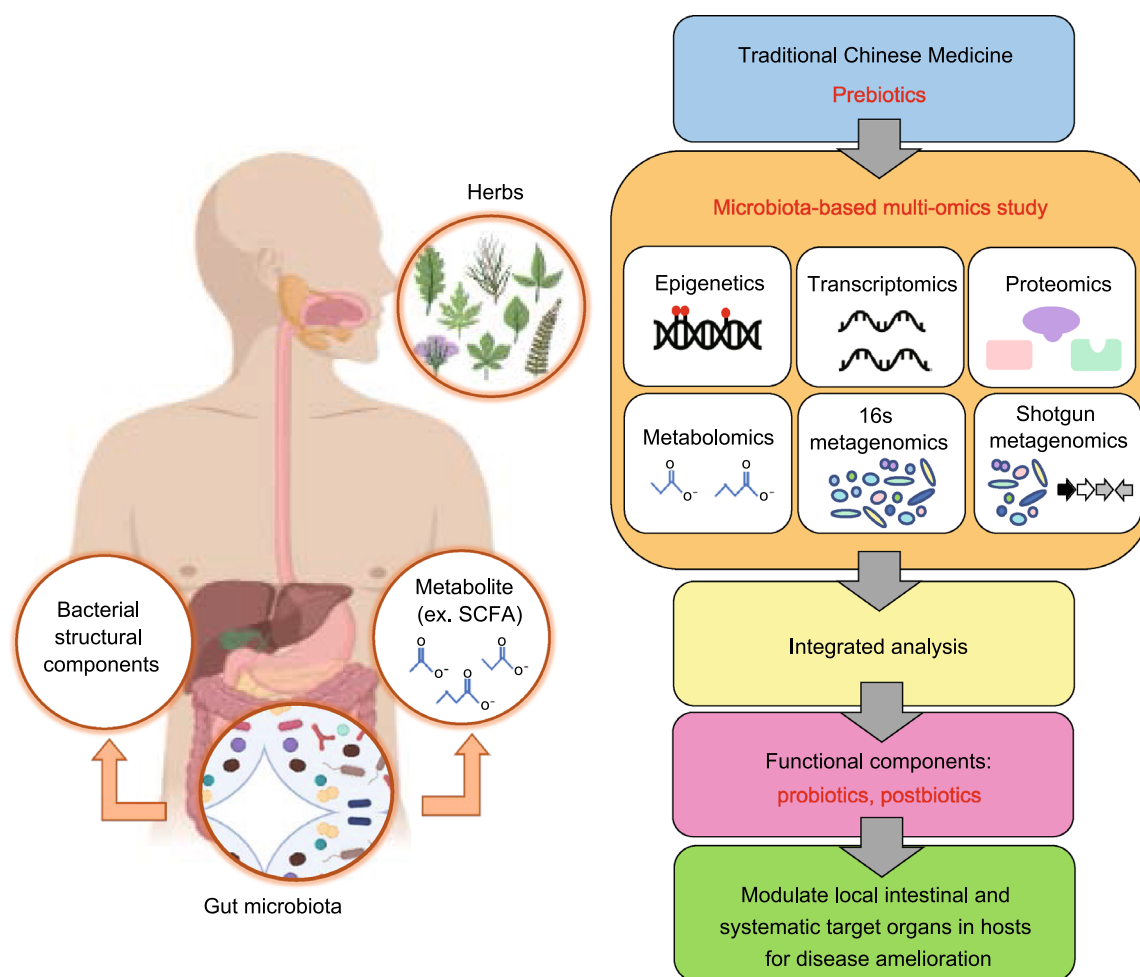


**Figure 2. Microbiota-based integrated multi-omics platforms for TCM-derived herb study.** The basic rationale is to identify TCM herbs related active components after transformation by gut microbiota fermentation. The multiomics platforms such as, epigenetics, 16s metagenomics, shotgun metagenomics, transcriptomics, proteomics, and metabolomics are to be used, followed by the integrated analysis. Such strategy may identify novel TCM prebiotics, bacteria (probiotics) and metabolites (postbiotics) as well as bacterial structural components (paraprobiotics) to modulate local intestine and systematic target organs in hosts for disease amelioration.

Bacteroides, Bifidobacterium, Clostridium, Egghertella, Escherichia, Eubacterium, Fusobacterium, Lactobacillus, Listeria, Peptococcus, Peptostreptococcus, Pseudomonas, and Ruminococcus, use their enzymes in deconjugation, oxidation and epimerization, 7-dehydroxylation, esterification, and desulfatation of the bile acids (Gerard, 2013). Secondary bile acids that might work as tumor promoters are therefore produced after bacterial fermentation in intestine (Wahlstrom et al., 2016; Ramirez-Perez et al., 2017; Jia et al., 2018). Accordingly, the development of disease-treatment strategies using TCM herbs, or use of metabolically engineered bacteria to modify chemicals for maintaining health are warranted (van Duynhoven et al., 2011; Lee et al., 2012; Anlu et al., 2019).

## MICROBIOTA-BASED INTEGRATED MULTIOMICS STUDY-THE NEXT GENERATION TCM HERBAL RESEARCH

Owing to the difficulties encountered in TCM research, one must consider developing novel strategy to characterize TCM herbs related active components. For future TCM-derived herbal studies, use of microbiota-based integrated multiomics platforms seems critical (Fig. 2). The underlying basic rationale is as follows: instead of directly screening functional components from herbal extracts, identifying functional components after transformation by gut microbiota fermentation using multiomics approaches (Fig. 2). Prepared TCM herbal products (such as crude extracts/decoctions or powders), are first fed to animals to evaluate their efficacy of

disease amelioration. If positive results are obtained, the classification and abundance of bacteria in intestine/feces, and their derived metabolites (including bacterial structural components containing potential paraprobiotics) in intestine/feces/blood samples are subsequently quantified. Bacteria and metabolites that show statistical differences between control and experimental groups may be involved in treatment efficacy of the disease in question, and accordingly will be targets of interest. These bacteria (potential probiotics) or compounds (potential postbiotics or paraprobiotics), either singly or in a consortium, will then be systematically assessed for their function and mechanism. To achieve this, cutting-edge analyses platforms, such as next generation sequencing (NGS), proteomics, and metabolomics are to be used.

The experimental design of microbiota-based TCM multiomics research is described as follows (Fig. 2): (i) In preparing TCM herbal products such as decoction, strictly follow the instructions for consistency. (ii) Optimally grouping the animals and humans, followed by observing disease progression and development, and finally evaluating the results by statistics. (iii) The composition of gut microbiota and/or their predicted functions of gut microbiome are analyzed by 16S rRNA gene sequencing, or shotgun sequencing, respectively, followed by bioinformatics analyses on operational taxonomic units (OTUs), and other functional DNA fragments. (iv) Metabolites will be analyzed by metabolomics combined with other analyses such as metatranscriptomics (for gut microbiota), and epigenetics, transcriptomics/single cell RNA sequencing (scRNA seq), and proteomics (for host). This multiomics approach will work in concert with traditional immunological, physiological, and pathological analyses for holistic results. (v) Associations between and among datasets obtained from control and experimental groups are analyzed to identify parameters with significant differences. Potential enriched or decreased biochemical pathways are established by GO and KEGG pathway analyses. Besides, some databases related to TCM and gut microbiota research including the TCM-Mesh, TCMSp, Traditional Chinese Medicines Integrated Database (TCMID), Compound Reference Database (CRD) and HIT, as well as pathogen-host databases (PHI-base and EHFPI) can be used as references of analytical systems for TCM pharmacology network analysis (Zhang et al., 2020a, b). (v) Isolate selected microbiota bacteria and purify or synthesize novel functional metabolites for further evaluation or validation of their safety and efficacy. (vii) Based on the results obtained, evaluate the possibility of further clinical trials.

Critically, after fermentation of TCM ingredients by microbiota, only important elements involved in the regulation of signaling pathways and diseases amelioration are highlighted. These elements are then selected to develop new treatment strategies. Currently, there are many multiomics-based templates that can be recruited as references for use in TCM and microbiota related studies. For instance,

a functional analysis of the gut microbiota ecosystem for better understanding inflammatory bowel disease (IBD) (Lloyd-Price et al., 2019), while the modified ColPortal platform (Esteban-Gil et al., 2019) integrates multiomics studies to understand the relationship between the microbiota and metabolomics in inflammatory bowel disease (IBS) disease model (Liu et al., 2019b). The pipelines described here have the potential to identify novel TCM-based herbal prebiotics, probiotics, and postbiotics for treatment of disease.

## PERSPECTIVE

Recent studies have demonstrated that gut microbiota participate in the metabolism of foods and nutrients and play central roles in the transformation of original TCM herbal components into functional metabolites. Under increasing studies on characterizing the metabolites after administration of various TCM herbs and gut microbiota transformation, together with the help from cutting-edge multiomics research tools, such as the NGS and metabolomics platforms, as well as the advanced bioinformatics analyses, databases, and algorithms, the identification of novel and effective metabolites for safe treatments is possible. Ultimately, a better understanding of the molecular mechanisms TCM function will make great contributions to the effective treatment of the chronic inflammation related diseases.

## ACKNOWLEDGEMENTS

We would like to express our thankfulness for funding provided from CORPD1F0013 and CORPD1J0052 from Chang Gung Memorial Hospital, Microbiota Research Center from Chang Gung University, and the Research Center for Emerging Viral Infections from The Featured Areas Research Center Program within the framework of the Higher Education Sprout Project (MOST109-2634-F-182-001, 109-2320-B-030-010, 109-2327-B-182-001).

## ABBREVIATIONS

ADME, absorption/distribution/metabolism/excretion; Ara, arabinose; BAT, brown adipose tissue; BCAAs, branched chain amino acids; CAZymes, carbohydrate active enzymes; CFU, colony-forming units; CKD, chronic kidney disease; CRD, compound Reference Database; C-T-D, component-target-disease; CVD, cardiovascular disease; DAMPS, damage-associated molecular pattern molecules; DSHT, Daesiho-Tang; DST, Du-Shen-Tang; F/B, Firmicutes/Bacteroidetes; Fuc, Fucose; FZHY, Fuzheng Huayu; Gal, galactose; GI, gastrointestinal; Glc, glucose; GO, Gene Ontology; GQD, Gegen Qinlian decoction; GUS,  $\beta$ -glucosidase; HTS, high-throughput screening; IBD, inflammatory bowel disease; IECs, intestinal epithelial cells; Ile, isoleucine; KEGG, Kyoto Encyclopedia of Genes and Genomes; Leu, leucine; MA, myristoleic acid; Man, mannose; NAFLD, non-alcoholic fatty liver disease; NGS, next generation sequencing; OTUs, operational taxonomic units; PAMPS, pathogen-associated molecular pattern molecules; PD, pharmacodynamics; PK, pharmacokinetics; PS, polysaccharides; PULs, polysaccharide utilization loci; QHD, Qushi Huayu Decoction; Rha, rhamnose;

SCFAs, short chain fatty acids; scRNA seq, single cell RNA sequencing; Sus, starch utilization system; TCM, Traditional Chinese Medicine; TCMID, Traditional Chinese Medicines Integrated Database; TCMSP, TCM System Pharmacology Database and Analysis Platform; TMA, trimethylamine; TMAO, trimethylamine-*N*-oxide; T-P, target-pathway; UGT, UDP-glucuronosyltransferase; Val, valine.

## COMPLIANCE WITH ETHICS GUIDELINES

Tzu-Lung Lin, Chia-Chen Lu, Wei-Fan Lai, Ting-Shu Wu, Jang-Jih Lu, Young-Mao Chen, Chi-Meng Tzeng, Hong-Tao Liu, Hong Wei, and Hsin-Chih Lai declare that they have no conflict of interest.

## OPEN ACCESS

This article is licensed under a Creative Commons Attribution 4.0 International License, which permits use, sharing, adaptation, distribution and reproduction in any medium or format, as long as you give appropriate credit to the original author(s) and the source, provide a link to the Creative Commons licence, and indicate if changes were made. The images or other third party material in this article are included in the article's Creative Commons licence, unless indicated otherwise in a credit line to the material. If material is not included in the article's Creative Commons licence and your intended use is not permitted by statutory regulation or exceeds the permitted use, you will need to obtain permission directly from the copyright holder. To view a copy of this licence, visit <http://creativecommons.org/licenses/by/4.0/>.

## REFERENCES

- Alexandrov P, Zhai Y, Li W, Lukiw W (2019) Lipopolysaccharide-stimulated, NF- $\kappa$ B-, miRNA-146a- and miRNA-155-mediated molecular-genetic communication between the human gastrointestinal tract microbiome and the brain. *Folia Neuropathol* 57:211–219
- Amaretti A, Gozzoli C, Simone M, Raimondi S, Righini L, Perez-Brocal V, Garcia-Lopez R, Moya A, Rossi M (2019) Profiling of protein degraders in cultures of human gut microbiota. *Front Microbiol* 10:2614
- Anlu W, Dongcheng C, He Z, Qiuyi L, Yan Z, Yu Q, Hao X, Keji C (2019) Using herbal medicine to target the “microbiota-metabolism-immunity” axis as possible therapy for cardiovascular disease. *Pharmacol Res* 142:205–222
- Bailey C (2019) Irinotecan: 25 years of cancer treatment. *Pharmacol Res* 148:104398
- Baumann U, Bisping B (1995) Proteolysis during tempe fermentation. *Food Microbiol* 12:39–47
- Bayer EA, Lamed R, White BA, Flint HJ (2008) From cellulosomes to cellulosomes. *Chem Rec* 8:364–377
- Bei WJ, Guo J, Wu HY, Cao Y (2012) Lipid-regulating effect of traditional chinese medicine: mechanisms of actions. *Evid Based Complement Altern Med* 2012:970635
- Belcher SM, Cline JM, Conley J, Groeters S, Jefferson WN, Law M, Mackey E, Suen AA, Williams CJ, Dixon D et al (2019) Endocrine disruption and reproductive pathology. *Toxicol Pathol* 47:1049–1071
- Blachier F, Mariotti F, Huneau JF, Tome D (2007) Effects of amino acid-derived luminal metabolites on the colonic epithelium and physiopathological consequences. *Amino Acids* 33:547–562
- Blaut M, Clavel T (2007) Metabolic diversity of the intestinal microbiota: implications for health and disease. *J Nutr* 137:751S–755S
- Bone E, Tamm A, Hill M (1976) The production of urinary phenols by gut bacteria and their possible role in the causation of large bowel cancer. *Am J Clin Nutr* 29:1448–1454
- Bouhnik Y, Raskine L, Simoneau G, Vicaute E, Neut C, Flourie B, Brouns F, Bornet FR (2004) The capacity of nondigestible carbohydrates to stimulate fecal bifidobacteria in healthy humans: a double-blind, randomized, placebo-controlled, parallel-group, dose-response relation study. *Am J Clin Nutr* 80:1658–1664
- Boyapati RK, Rossi AG, Satsangi J, Ho GT (2016) Gut mucosal DAMPs in IBD: from mechanisms to therapeutic implications. *Mucosal Immunol* 9:567–582
- Burokas A, Arbolea S, Moloney RD, Peterson VL, Murphy K, Clarke G, Stanton C, Dinan TG, Cryan JF (2017) Targeting the microbiota-gut-brain axis: prebiotics have anxiolytic and antidepressant-like effects and reverse the impact of chronic stress in mice. *Biol Psychiatry* 82:472–487
- Canyelles M, Tondo M, Cedo L, Farras M, Escola-Gil JC, Blanco-Vaca F (2018) Trimethylamine N-Oxide: a link among diet, gut microbiota, gene regulation of liver and intestine cholesterol homeostasis and HDL function. *Int J Mol Sci* 19(10):3228
- Carqueijeiro I, Langley C, Grzech D, Koudounas K, Papon N, O'Connor SE, Courdavault V (2019) Beyond the semi-synthetic artemisinin: metabolic engineering of plant-derived anti-cancer drugs. *Curr Opin Biotechnol* 65:17–24
- Chang CJ, Lin CS, Lu CC, Martel J, Ko YF, Ojcius DM, Tseng SF, Wu TR, Chen YY, Young JD et al (2015) *Ganoderma lucidum* reduces obesity in mice by modulating the composition of the gut microbiota. *Nat Commun* 6:7489
- Chang CJ, Lin TL, Tsai YL, Wu TR, Lai WF, Lu CC, Lai HC (2019) Next generation probiotics in disease amelioration. *J Food Drug Anal* 27:615–622
- Chang R (2002) Bioactive polysaccharides from traditional Chinese medicine herbs as anticancer adjuvants. *J Altern Complement Med* 8:559–565
- Chen C, You LJ, Huang Q, Fu X, Zhang B, Liu RH, Li C (2018a) Modulation of gut microbiota by mulberry fruit polysaccharide treatment of obese diabetic db/db mice. *Food Funct* 9:3732–3742
- Chen J, Hu Y, Chen L, Liu W, Mu Y, Liu P (2019) The effect and mechanisms of Fuzheng Huayu formula against chronic liver diseases. *Biomed Pharmacother* 114:108846
- Chen L, Krekels EHJ, Verweij PE, Buil JB, Knibbe CAJ, Bruggemann RJM (2020) Pharmacokinetics and pharmacodynamics of posaconazole. *Drugs* 80:671–695
- Chen M, Liao Z, Lu B, Wang M, Lin L, Zhang S, Li Y, Liu D, Liao Q, Xie Z (2018b) Huang-Lian-Jie-Du-Decoction ameliorates hyperglycemia and insulin resistant in association with gut microbiota modulation. *Front Microbiol* 9:2380



- Chen Q, Xiao S, Li Z, Ai N, Fan X (2015) Chemical and metabolic profiling of Si-Ni decoction analogous formulae by high performance liquid chromatography-mass spectrometry. *Sci Rep* 5:11638
- Chen Y, Yao F, Ming K, Wang D, Hu Y, Liu J (2016) Polysaccharides from traditional Chinese medicines: extraction, purification, modification, and biological activity. *Molecules* 21:1705
- Chi X, Wang S, Baloch Z, Zhang H, Li X, Zhang Z, Zhang H, Dong Z, Lu Y, Yu H et al (2019) Research progress on classical traditional Chinese medicine formula Lily Bulb and Rehmannia Decoction in the treatment of depression. *Biomed Pharmacother* 112:108616
- Clemente JC, Ursell LK, Parfrey LW, Knight R (2012) The impact of the gut microbiota on human health: an integrative view. *Cell* 148:1258–1270
- Cockburn DW, Koropatkin NM (2016) Polysaccharide degradation by the intestinal microbiota and its influence on human health and disease. *J Mol Biol* 428:3230–3252
- Conlon MA, Bird AR (2014) The impact of diet and lifestyle on gut microbiota and human health. *Nutrients* 7:17–44
- Creekmore BC, Gray JH, Walton WG, Biernat KA, Little MS, Xu Y, Liu J, Gharaibeh RZ, Redinbo MR (2019) Mouse gut microbiome-encoded beta-glucuronidases identified using metagenome analysis guided by protein structure. *Systems* 4:e00452-19
- Dabek M, McCrae SI, Stevens VJ, Duncan SH, Louis P (2008) Distribution of beta-glucosidase and beta-glucuronidase activity and of beta-glucuronidase gene gus in human colonic bacteria. *FEMS Microbiol Ecol* 66:487–495
- Deng Z, Jing WG, Wang SH, Jiao MJ, Zhang Q, Zhou HY, Zhang J, Liu A (2019) Discussion and research progress in standard decoction of medicinal slices. *Zhongguo Zhong Yao Za Zhi* 44:242–248
- Devillard E, McIntosh FM, Duncan SH, Wallace RJ (2007) Metabolism of linoleic acid by human gut bacteria: different routes for biosynthesis of conjugated linoleic acid. *J Bacteriol* 189:2566–2570
- Devkota S, Wang Y, Musch MW, Leone V, Fehlner-Peach H, Nadimpalli A, Antonopoulos DA, Jabri B, Chang EB (2012) Dietary-fat-induced taurocholic acid promotes pathobiont expansion and colitis in IL10<sup>-/-</sup> mice. *Nature* 487:104–108
- Dey P (2019) Gut microbiota in phytopharmacology: a comprehensive overview of concepts, reciprocal interactions, biotransformations and mode of actions. *Pharmacol Res* 147:104367
- Di S, Wang Y, Han L, Bao Q, Gao Z, Wang Q, Yang Y, Zhao L, Tong X (2019) The intervention effect of traditional Chinese medicine on the intestinal flora and its metabolites in glycolipid metabolic disorders. *Evid Based Complement Alternat Med* 2019:2958920
- Ding Z, Zhong R, Xia T, Yang Y, Xing N, Wang W, Wang Y, Yang B, Sun X, Shu Z (2020) Advances in research into the mechanisms of Chinese Materia Medica against acute lung injury. *Biomed Pharmacother* 122:109706
- Esteban-Gil A, Perez-Sanz F, Garcia-Solano J, Albuquerque-Gonzalez B, Parreno-Gonzalez MA, Legaz-Garcia MDC, Fernandez-Breis JT, Rodriguez-Braun E, Pimentel P, Tuomisto A et al (2019) ColPortal, an integrative multiomic platform for analysing epigenetic interactions in colorectal cancer. *Sci Data* 6:255
- Feng Q, Gou X-J, Meng S-X, Huang C, Zhang Y-Q, Tang Y-J, Wang W-J, Xu L, Peng J, Hu Y-Y (2013) Qushi Huayu decoction inhibits hepatic lipid accumulation by activating AMP-activated protein kinase in vivo and in vitro. *Evid-Based Complement Alternat Med: eCAM* 2013:184358
- Feng W, Ao H, Peng C, Yan D (2019) Gut microbiota, a new frontier to understand traditional Chinese medicines. *Pharmacol Res* 142:176–191
- Gao K, Yang R, Zhang J, Wang Z, Jia C, Zhang F, Li S, Wang J, Murtaza G, Xie H et al (2018) Effects of Qijian mixture on type 2 diabetes assessed by metabolomics, gut microbiota and network pharmacology. *Pharmacol Res* 130:93–109
- Gao W, Guo SZ, Han LW, Zhang FZ (2016) Analysis of projects funded by NSFC in field of Chinese material medica resource in recent three years. *Zhongguo Zhong Yao Za Zhi* 41:3696–3701
- Gentile CL, Weir TL (2018) The gut microbiota at the intersection of diet and human health. *Science* 362:776–780
- Gerard P (2013) Metabolism of cholesterol and bile acids by the gut microbiota. *Pathogens* 3:14–24
- Ghazalpour A, Cespedes I, Bennett BJ, Allayee H (2016) Expanding role of gut microbiota in lipid metabolism. *Curr Opin Lipidol* 27:141–147
- Han Y, Li C, Huan Y, Sun S, Mu Y, Shen Z (2016) Effects of berberine compatible with stachyose on glucolipid metabolism and gut microbiota in diabetic mice. *Chin J Clin Pharmacol* 32:1121–1124
- Hao YF, Jiang JG (2015) Origin and evolution of China Pharmacopoeia and its implication for traditional medicines. *Mini Rev Med Chem* 15:595–603
- Hu HC, Zheng LT, Yin HY, Tao Y, Luo XQ, Wei KS, Yin LP (2019) A significant association between rhein and diabetic nephropathy in animals: a systematic review and meta-analysis. *Front Pharmacol* 10:1473
- Huang X, Chen W, Yan C, Yang R, Chen Q, Xu H, Huang Y (2019) Gypenosides improve the intestinal microbiota of non-alcoholic fatty liver in mice and alleviate its progression. *Biomed Pharmacother* 118:109258
- Humblot C, Murkovic M, Rigottier-Gois L, Bensaada M, Bouclet A, Andrieux C, Anba J, Rabot S (2007) Beta-glucuronidase in human intestinal microbiota is necessary for the colonic genotoxicity of the food-borne carcinogen 2-amino-3-methylimidazo [4,5-f]quinoline in rats. *Carcinogenesis* 28:2419–2425
- Hussain A, Yadav MK, Bose S, Wang JH, Lim D, Song YK, Ko SG, Kim H (2016) Daesih-Tang is an effective herbal formulation in attenuation of obesity in mice through alteration of gene expression and modulation of intestinal microbiota. *PLoS ONE* 11: e0165483
- Janeiro MH, Ramirez MJ, Milagro FI, Martinez JA, Solas M (2018) Implication of trimethylamine N-Oxide (TMAO) in disease: potential biomarker or new therapeutic target. *Nutrients* 10 (10):1398
- Jia W, Xie G, Jia W (2018) Bile acid-microbiota crosstalk in gastrointestinal inflammation and carcinogenesis. *Nat Rev Gastroenterol Hepatol* 15:111–128
- Jiang Y, Liu M, Liu H, Liu S (2020) A critical review: traditional uses, phytochemistry, pharmacology and toxicology of *Stephania tetrandra* S. Moore (Fen Fang Ji). *Phytochem Rev* 19:449–489
- Jin R, Lin ZJ, Xue CM, Zhang B (2013) An improved association-mining research for exploring Chinese herbal property theory:



- based on data of the Shennong's Classic of Materia Medica. *J Integr Med* 11:352–365
- Kaur H, Bose C, Mande SS (2019) Tryptophan metabolism by gut microbiome and gut-brain-axis: an in silico analysis. *Front Neurosci* 13:1365
- Kikugawa K, Kato T (1988) Formation of a mutagenic diazoquinone by interaction of phenol with nitrite. *Food and Chemical Toxicology* 26:209–214
- Kim DH (2018) Gut microbiota-mediated pharmacokinetics of ginseng saponins. *J Ginseng Res* 42:255–263
- Kim HM, Song Y, Hyun GH, Long NP, Park JH, Hsieh YSY, Kwon SW (2020) Characterization and Antioxidant Activity Determination of Neutral and Acidic Polysaccharides from *Panax Ginseng* C.A. Meyer. *Molecules* 25:791
- Kim KA, Jung IH, Park SH, Ahn YT, Huh CS, Kim DH (2013) Comparative analysis of the gut microbiota in people with different levels of ginsenoside Rb1 degradation to compound K. *PLoS One* 8:e62409
- Koropatkin NM, Cameron EA, Martens EC (2012) How glycan metabolism shapes the human gut microbiota. *Nat Rev Microbiol* 10:323–335
- Lagier JC, Dubourg G, Million M, Cadoret F, Bilen M, Fenollar F, Levasseur A, Rolain JM, Fournier PE, Raoult D (2018) Culturing the human microbiota and culturomics. *Nat Rev Microbiol* 16:540–550
- Lee JW, Na D, Park JM, Lee J, Choi S, Lee SY (2012) Systems metabolic engineering of microorganisms for natural and non-natural chemicals. *Nat Chem Biol* 8:536–546
- Leng J, Huang F, Hai Y, Tian H, Liu W, Fang Y, Hu Y, Peng J (2020) Amelioration of non-alcoholic steatohepatitis by Qushi Huayu decoction is associated with inhibition of the intestinal mitogen-activated protein kinase pathway. *Phytomedicine* 66:153135
- Li C, Du X, Liu Y, Liu QQ, Zhi WB, Wang CL, Zhou J, Li Y, Zhang H (2020) A systems pharmacology approach for identifying the multiple mechanisms of action for the Rougui-Fuzi Herb pair in the treatment of cardiocerebral vascular diseases. *Evid Based Complement Alternat Med* 2020:5196302
- Li G, Wang D, Fang S, Xu M (2014) Textual research on *Costus root* (*Aucklandia lappa* Decne) in the *Sheng nong ben cao jing* (Shennong's Classic of Materia Medica). *Zhonghua Yi Shi Za Zhi* 44:135–137
- Li LC, Kan LD (2017) Traditional Chinese medicine for pulmonary fibrosis therapy: Progress and future prospects. *J Ethnopharmacol* 198:45–63
- Li SP, Wu D-T, Lv G-P, Zhao J (2013) Carbohydrates analysis in herbal glycomics. *TrAC Trends Anal Chem* 52:155–169
- Lin CS, Chang CJ, Lu CC, Martel J, Ojcius DM, Ko YF, Young JD, Lai HC (2014) Impact of the gut microbiota, prebiotics, and probiotics on human health and disease. *Biomed J* 37:259–268
- Lin L, Ni B, Lin H, Zhang M, Li X, Yin X, Qu C, Ni J (2015) Traditional usages, botany, phytochemistry, pharmacology and toxicology of *Polygonum multiflorum* Thunb.: a review. *J Ethnopharmacol* 159:158–183
- Lin R, Liu W, Piao M, Zhu H (2017) A review of the relationship between the gut microbiota and amino acid metabolism. *Amino Acids* 49:2083–2090
- Lin T-L, Shu C-C, Lai W-F, Tzeng C-M, Lai H-C, Lu C-C (2019) Investiture of next generation probiotics on amelioration of diseases—strains do matter. *Med Microecol* 1–2:100002
- Liu C, Li S, Zhang Q, Guo F, Tong M, Martinez M, Wang HH, Zhao Y, Shang D (2019a) Emerging role of chinese herbal medicines in the treatment of pancreatic fibrosis. *Am J Chin Med* 47:709–726
- Liu D, Zhang Y, Liu Y, Hou L, Li S, Tian H, Zhao T (2018a) Berberine modulates gut microbiota and reduces insulin resistance via the TLR4 signaling pathway. *Exp Clin Endocrinol Diabetes* 126:513–520
- Liu M, Wang Y, Liu Y, Ruan R (2016) Bioactive peptides derived from traditional Chinese medicine and traditional Chinese food: a review. *Food Res Int* 89:63–73
- Liu S, Li C, Yu Y, Zhao G, Chen L, Zhao Y, Zhang Z, Li H, Chen Y, Min L et al (2019b) Multi-omics analysis of gut microbiota and metabolites in rats with irritable bowel syndrome. *Front Cell Infect Microbiol* 9:178
- Liu Y, Li J, Yu J, Wang Y, Lu J, Shang EX, Zhu Z, Guo J, Duan J (2018b) Disorder of gut amino acids metabolism during CKD progression is related with gut microbiota dysbiosis and metagenome change. *J Pharm Biomed Anal* 149:425–435
- Lloyd-Price J, Arze C, Ananthakrishnan AN, Schirmer M, Avila-Pacheco J, Poon TW, Andrews E, Ajami NJ, Bonham KS, Brislawn CJ et al (2019) Multi-omics of the gut microbial ecosystem in inflammatory bowel diseases. *Nature* 569:655–662
- Lu Y-M, Xie J-J, Peng C-G, Wang B-H, Wang K-C, Li L-J (2019) Enhancing clinical efficacy through the gut microbiota: a new field of traditional Chinese medicine. *Engineering* 5:40–49
- Lyu M, Wang YF, Fan GW, Wang XY, Xu SY, Zhu Y (2017) Balancing herbal medicine and functional food for prevention and treatment of cardiometabolic diseases through modulating gut microbiota. *Front Microbiol* 8:2146
- Ma N, Tian Y, Wu Y, Ma X (2017) Contributions of the interaction between dietary protein and gut microbiota to intestinal health. *Curr Protein Pept Sci* 18:795–808
- Madsen L, Myrmet LS, Fjaere E, Liaset B, Kristiansen K (2017) Links between dietary protein sources, the gut microbiota, and obesity. *Front Physiol* 8:1047
- Magee EA, Richardson CJ, Hughes R, Cummings JH (2000) Contribution of dietary protein to sulfide production in the large intestine: an in vitro and a controlled feeding study in humans. *Am J Clin Nutr* 72:1488–1494
- Marques TM, Wall R, O'Sullivan O, Fitzgerald GF, Shanahan F, Quigley EM, Cotter PD, Cryan JF, Dinan TG, Ross RP et al (2015) Dietary trans-10, cis-12-conjugated linoleic acid alters fatty acid metabolism and microbiota composition in mice. *Br J Nutr* 113:728–738
- Martel J, Ko YF, Ojcius DM, Lu CC, Chang CJ, Lin CS, Lai HC, Young JD (2017a) Immunomodulatory properties of plants and mushrooms. *Trends Pharmacol Sci* 38:967–981
- Martel J, Ojcius DM, Chang CJ, Lin CS, Lu CC, Ko YF, Tseng SF, Lai HC, Young JD (2017b) Anti-obesogenic and antidiabetic effects of plants and mushrooms. *Nat Rev Endocrinol* 13:149–160
- Martens EC, Lowe EC, Chiang H, Pudlo NA, Wu M, McNulty NP, Abbott DW, Henrissat B, Gilbert HJ, Bolam DN et al (2011) Recognition and degradation of plant cell wall polysaccharides by two human gut symbionts. *PLoS Biol* 9:e1001221




- Mazzoli R, Pessione E (2016) The neuro-endocrinological role of microbial glutamate and GABA signaling. *Front Microbiol* 7:1934
- Mishima E, Fukuda S, Mukawa C, Yuri A, Kanemitsu Y, Matsumoto Y, Akiyama Y, Fukuda NN, Tsukamoto H, Asaji K et al (2017) Evaluation of the impact of gut microbiota on uremic solute accumulation by a CE-TOFMS-based metabolomics approach. *Kidney Int* 92:634–645
- Neis EP, Dejong CH, Rensen SS (2015) The role of microbial amino acid metabolism in host metabolism. *Nutrients* 7:2930–2946
- Ni M (1995) The yellow emperor's classic of medicine: a new translation of the Neijing Suwen with commentary. Shambhala, Boston and London
- Nie C, He T, Zhang W, Zhang G, Ma X (2018) Branched chain amino acids: beyond nutrition metabolism. *Int J Mol Sci* 1:1. <https://doi.org/10.1136/gutjnl-2019-319114>
- Nie Q, Chen H, Hu J, Fan S, Nie S (2019) Dietary compounds and traditional Chinese medicine ameliorate type 2 diabetes by modulating gut microbiota. *Crit Rev Food Sci Nutr* 59:848–863
- Peng Y, Li X, Zhang S, Liu Z, Ji J, Wu C, Yang J (2020) Gut microbiota and Chinese medicine syndrome: altered fecal microbiotas in spleen (Pi)-deficient patients. *J Tradit Chin Med* 40:137–143
- Portune KJ, Beaumont M, Davila A-M, Tomé D, Blachier F, Sanz Y (2016) Gut microbiota role in dietary protein metabolism and health-related outcomes: the two sides of the coin. *Trends Food Sci Technol* 57:213–232
- Qi LW, Wang CZ, Du GJ, Zhang ZY, Calway T, Yuan CS (2011) Metabolism of ginseng and its interactions with drugs. *Curr Drug Metab* 12:818–822
- Qu W, Liu S, Zhang W, Zhu H, Tao Q, Wang H, Yan H (2019) Impact of traditional Chinese medicine treatment on chronic unpredictable mild stress-induced depression-like behaviors: intestinal microbiota and gut microbiome function. *Food Funct* 10:5886–5897
- Quan LH, Zhang C, Dong M, Jiang J, Xu H, Yan C, Liu X, Zhou H, Zhang H, Chen L et al (2019) Myristoleic acid produced by enterococci reduces obesity through brown adipose tissue activation. *Gut* 69(7):1239–1247
- Ramesh M, Ahlawat P, Srinivas NR (2010) Irinotecan and its active metabolite, SN-38: review of bioanalytical methods and recent update from clinical pharmacology perspectives. *Biomed Chromatogr* 24:104–123
- Ramirez-Perez O, Cruz-Ramon V, Chinchilla-Lopez P, Mendez-Sanchez N (2017) The role of the gut microbiota in bile acid metabolism. *Ann Hepatol* 16:s15–s20
- Rath S, Heidrich B, Pieper DH, Vital M (2017) Uncovering the trimethylamine-producing bacteria of the human gut microbiota. *Microbiome* 5:54
- Ravcheev DA, Godzik A, Osterman AL, Rodionov DA (2013) Polysaccharides utilization in human gut bacterium *Bacteroides thetaiotaomicron*: comparative genomics reconstruction of metabolic and regulatory networks. *BMC Genomics* 14:873
- Ru J, Li P, Wang J, Zhou W, Li B, Huang C, Li P, Guo Z, Tao W, Yang Y et al (2014) TCMSPP: a database of systems pharmacology for drug discovery from herbal medicines. *J Cheminform* 6:13
- Santa HSD, Romão PRT, Sovrani V, Oliveira FR, Peres A, Monteiro MC (2014) Dietary polysaccharides and Immune Modulation. In: Ramawat KG, Mérillon J-M (eds) *Polysaccharides: bioactivity and biotechnology*. Springer International Publishing, Cham, pp 1–24
- Schachter J, Martel J, Lin CS, Chang CJ, Wu TR, Lu CC, Ko YF, Lai HC, Ojcius DM, Young JD (2018) Effects of obesity on depression: a role for inflammation and the gut microbiota. *Brain Behav Immun* 69:1–8
- Schoeler M, Caesar R (2019) Dietary lipids, gut microbiota and lipid metabolism. *Rev Endocr Metab Disord* 20:461–472
- Schwiertz A, Taras D, Schafer K, Beijer S, Bos NA, Donus C, Hardt PD (2010) Microbiota and SCFA in lean and overweight healthy subjects. *Obesity (Silver Spring)* 18:190–195
- Sharon G, Garg N, Debelius J, Knight R, Dorrestein PC, Mazmanian SK (2014) Specialized metabolites from the microbiome in health and disease. *Cell Metab* 20:719–730
- Simpson HL, Campbell BJ (2015) Review article: dietary fibre-microbiota interactions. *Aliment Pharmacol Ther* 42:158–179
- Sun SS, Wang K, Ma K, Bao L, Liu HW (2019) An insoluble polysaccharide from the sclerotium of *Poria cocos* improves hyperglycemia, hyperlipidemia and hepatic steatosis in ob/ob mice via modulation of gut microbiota. *Chin J Nat Med* 17:3–14
- Sun Y (2011) Structure and biological activities of the polysaccharides from the leaves, roots and fruits of *Panax ginseng* C.A. Meyer: an overview. *Carbohydrate Polymers - CARBOHYD POLYM* 85:490–499
- Tang D, Kang R, Coyne CB, Zeh HJ, Lotze MT (2012) PAMPs and DAMPs: signal 0s that spur autophagy and immunity. *Immunol Rev* 249:158–175
- Tejaro CN, Adhikari A, Shen B (2019) Challenges and opportunities for natural product discovery, production, and engineering in native producers versus heterologous hosts. *J Ind Microbiol Biotechnol* 46:433–444
- Thursby E, Juge N (2017) Introduction to the human gut microbiota. *Biochem J* 474:1823–1836
- Tong X, Xu J, Lian F, Yu X, Zhao Y, Xu L, Zhang M, Zhao X, Shen J, Wu S et al (2018) Structural alteration of gut microbiota during the amelioration of human type 2 diabetes with hyperlipidemia by metformin and a traditional Chinese herbal formula: a multicenter, randomized, Open label clinical trial. *mBio* 9(3):e02392-17
- Tremaroli V, Backhed F (2012) Functional interactions between the gut microbiota and host metabolism. *Nature* 489:242–249
- Tsai YL, Lin TL, Chang CJ, Wu TR, Lai WF, Lu CC, Lai HC (2019) Probiotics, prebiotics and amelioration of diseases. *J Biomed Sci* 26:3
- Tzianabos AO (2000) Polysaccharide immunomodulators as therapeutic agents: structural aspects and biologic function. *Clin Microbiol Rev* 13:523–533
- van Duynhoven J, Vaughan EE, Jacobs DM, Kemperman RA, van Velzen EJ, Gross G, Roger LC, Possemiers S, Smilde AK, Dore J et al (2011) Metabolic fate of polyphenols in the human superorganism. *Proc Natl Acad Sci USA* 108(Suppl 1):4531–4538
- Velenosi TJ, Hennop A, Feere DA, Tieu A, Kucey AS, Kyriacou P, McCuaig LE, Nevison SE, Kerr MA, Urquhart BL (2016) Untargeted plasma and tissue metabolomics in rats with chronic kidney disease given AST-120. *Sci Rep* 6:22526
- Wahlstrom A, Sayin SI, Marschall HU, Backhed F (2016) Intestinal crosstalk between bile acids and microbiota and its impact on host metabolism. *Cell Metab* 24:41–50

- Wan JY, Wang CZ, Zhang QH, Liu Z, Musch MW, Bissonnette M, Chang EB, Li P, Qi LW, Yuan CS (2017) Significant difference in active metabolite levels of ginseng in humans consuming Asian or Western diet: the link with enteric microbiota. *Biomed Chromatogr.* <https://doi.org/10.1002/bmc.3851>
- Wang B, Yao M, Lv L, Ling Z, Li L (2017a) The human microbiota in health and disease. *Engineering* 3:71–82
- Wang C, Yin Y, Cao X, Li X (2016) Effects of Maydis stigma polysaccharide on the intestinal microflora in type-2 diabetes. *Pharm Biol* 54:3086–3092
- Wang JH, Bose S, Lim SK, Ansari A, Chin YW, Choi HS, Kim H (2017b) *Houttuynia cordata* facilitates metformin on ameliorating insulin resistance associated with gut microbiota alteration in OLETF rats. *Genes (Basel)* 8:239
- Wang JH, Bose S, Shin NR, Chin YW, Choi YH, Kim H (2018a) Pharmaceutical impact of *houltuynia cordata* and metformin combination on high-fat-diet-induced metabolic disorders: link to intestinal microbiota and metabolic endotoxemia. *Front Endocrinol (Lausanne)* 9:620
- Wang L, Liu QM, Sung BH, An DS, Lee HG, Kim SG, Kim SC, Lee ST, Im WT (2011) Bioconversion of ginsenosides Rb(1), Rb(2), Rc and Rd by novel beta-glucosidase hydrolyzing outer 3-O glycoside from *Sphingomonas* sp. 2F2: cloning, expression, and enzyme characterization. *J Biotechnol* 156:125–133
- Wang Q, Kuang H, Su Y, Sun Y, Feng J, Guo R, Chan K (2013) Naturally derived anti-inflammatory compounds from Chinese medicinal plants. *J Ethnopharmacol* 146:9–39
- Wang R, Zang P, Chen J, Wu F, Zheng Z, Ma J, Yang C, Du H (2018b) Gut microbiota play an essential role in the antidiabetic effects of rhein. *Evid Based Complement Alternat Med* 2018:6093282
- Wei X, Tao J, Xiao S, Jiang S, Shang E, Zhu Z, Qian D, Duan J (2018) Xiexin Tang improves the symptom of type 2 diabetic rats by modulation of the gut microbiota. *Sci Rep* 8:3685
- Wu TR, Lin CS, Chang CJ, Lin TL, Martel J, Ko YF, Ojcius DM, Lu CC, Young JD, Lai HC (2019) Gut commensal *Parabacteroides goldsteinii* plays a predominant role in the anti-obesity effects of polysaccharides isolated from *Hirsutella sinensis*. *Gut* 68:248–262
- Wu XM, Tan RX (2019) Interaction between gut microbiota and ethnomedicine constituents. *Nat Prod Rep* 36:788–809
- Xu J, Lian F, Zhao L, Zhao Y, Chen X, Zhang X, Guo Y, Zhang C, Zhou Q, Xue Z et al (2015) Structural modulation of gut microbiota during alleviation of type 2 diabetes with a Chinese herbal formula. *ISME J* 9:552–562
- Xu JD, Mao Q, Shen H, Zhu LY, Li SL, Yan R (2013) Ultra-high performance liquid chromatography coupled with photo-diode array and quadrupole/time-of-flight mass spectrometry based chemical profiling approach to evaluate the influence of preparation methods on the holistic quality of Qiong-Yu-Gao, a traditional complex herbal medicine. *J Chromatogr A* 1304:154–168
- Xu M, Yue RS, Yang MY, Yang X, Wu TC, Li JN (2018) Effects of Banxia Xiexin Decoction on intestinal flora and inflammatory factors of diabetic gastroparesis rats. *Chinese Traditional and Herbal Drugs* 49:3056–3061
- Yan Q (2018) Neuroimmune imbalances and Yin-Yang dynamics in stress, anxiety, and depression. *Methods Mol Biol* 1781:77–85
- Yan Y, Chai CZ, Wang DW, Yue XY, Zhu DN, Yu BY (2013) HPLC-DAD-Q-TOF-MS/MS analysis and HPLC quantitation of chemical constituents in traditional Chinese medicinal formula Ge-Gen Decoction. *J Pharm Biomed Anal* 80:192–202
- Yang M, Lao L (2019) Emerging applications of metabolomics in traditional Chinese medicine treating hypertension: biomarkers. *Pathways and More. Front Pharmacol* 10:158
- Yang M, Sun J, Lu Z, Chen G, Guan S, Liu X, Jiang B, Ye M, Guo DA (2009) Phytochemical analysis of traditional Chinese medicine using liquid chromatography coupled with mass spectrometry. *J Chromatogr A* 1216:2045–2062
- Yang YS, Zhang T, Yu SC, Ding Y, Zhang LY, Qiu C, Jin D (2011) Transformation of geniposide into genipin by immobilized beta-glucosidase in a two-phase aqueous-organic system. *Molecules* 16:4295–4304
- Ying M, Zheng B, Yu Q, Hou K, Wang H, Zhao M, Chen Y, Xie J, Nie S, Xie M (2020) *Ganoderma atrum* polysaccharide ameliorates intestinal mucosal dysfunction associated with autophagy in immunosuppressed mice. *Food Chem Toxicol* 138:111244
- Yokoi T, Narita M, Nagai E, Hagiwara H, Aburada M, Kamataki T (1995) Inhibition of UDP-glucuronosyltransferase by aglycons of natural glucuronides in kampo medicines using SN-38 as a substrate. *Jpn J Cancer Res* 86:985–989
- Yu J, Guo J, Tao W, Liu P, Shang E, Zhu Z, Fan X, Shen J, Hua Y, Zhu KY et al (2018a) Gancan-Gansui combination impacts gut microbiota diversity and related metabolic functions. *J Ethnopharmacol* 214:71–82
- Yu Y, Li Z, Guo R, Qian J, Zhang H, Zhang J, Zhao X, Wang S, Wang Y (2019a) Ononin, sec-O-beta-d-glucosylhamadul and astragaloside I: antiviral lead compounds identified via high throughput screening and biological validation from traditional Chinese medicine Zhongjing formulary. *Pharmacol Res* 145:104248
- Yu Y, Raka F, Adeli K (2019b) The role of the gut microbiota in lipid and lipoprotein metabolism. *J Clin Med* 8(12):2227
- Yu Y, Shen M, Song Q, Xie J (2018b) Biological activities and pharmaceutical applications of polysaccharide from natural resources: a review. *Carbohydr Polym* 183:91–101
- Yuan Y, Zheng J, Wang M, Li Y, Ruan J, Zhang H (2016) Metabolic activation of rhein: insights into the potential toxicity induced by rhein-containing herbs. *J Agric Food Chem* 64:5742–5750
- Yue SJ, Wang WX, Yu JG, Chen YY, Shi XQ, Yan D, Zhou GS, Zhang L, Wang CY, Duan JA et al (2019) Gut microbiota modulation with traditional Chinese medicine: a system biology-driven approach. *Pharmacol Res* 148:104453
- Zhang B, Yue R, Chen Y, Yang M, Huang X, Shui J, Peng Y, Chin J (2019a) Gut microbiota, a potential new target for Chinese herbal medicines in treating diabetes mellitus. *Evid Based Complement Alternat Med* 2019:2634898
- Zhang D, Chia C, Jiao X, Jin W, Kasagi S, Wu R, Konkel JE, Nakatsukasa H, Zanvit P, Goldberg N et al (2017) D-mannose induces regulatory T cells and suppresses immunopathology. *Nat Med* 23:1036–1045
- Zhang D, Yang L, Yang LX, Wang MY, Tu YY (2007) Determination of artemisinin, arteannuin B and artemisinic acid in Herba

- Artemisiae Annuae by HPLC-UV-ELSD. Yao Xue Xue Bao 42:978–981
- Zhang D, Zhang Y, Gao Y, Chai X, Pi R, Chan G, Hu Y (2020a) Translating traditional herbal formulas into modern drugs: a network-based analysis of Xiaoyao decoction. Chin Med 15:25
- Zhang ND, Han T, Huang BK, Rahman K, Jiang YP, Xu HT, Qin LP, Xin HL, Zhang QY, Li YM (2016) Traditional Chinese medicine formulas for the treatment of osteoporosis: Implication for antiosteoporotic drug discovery. J Ethnopharmacol 189:61–80
- Zhang R, Gao X, Bai H, Ning K (2020b) Traditional Chinese medicine and gut microbiome: their respective and concert effects on healthcare. Front Pharmacol 1:1. <https://doi.org/10.3389/fphar.2020.00538>
- Zhang T, Yang Y, Liang Y, Jiao X, Zhao C (2018) Beneficial effect of intestinal fermentation of natural polysaccharides. Nutrients 10 (8):55
- Zhang WJ, Wang S, Kang CZ, Lv CG, Zhou L, Huang LQ, Guo LP (2020c) Pharmacodynamic material basis of traditional Chinese medicine based on biomacromolecules: a review. Plant Methods 16:26
- Zhang YL, Cai LT, Qi JY, Lin YZ, Dai YC, Jiao N, Chen YL, Zheng L, Wang BB, Zhu LX et al (2019b) Gut microbiota contributes to the distinction between two traditional Chinese medicine syndromes of ulcerative colitis. World J Gastroenterol 25:3242–3255
- Zhao CQ, Zhou Y, Ping J, Xu LM (2014) Traditional Chinese medicine for treatment of liver diseases: progress, challenges and opportunities. J Integr Med 12:401–408
- Zhou SS, Xu J, Zhu H, Wu J, Xu JD, Yan R, Li XY, Liu HH, Duan SM, Wang Z et al (2016) Gut microbiota-involved mechanisms in enhancing systemic exposure of ginsenosides by coexisting polysaccharides in ginseng decoction. Sci Rep 6:22474
- Zhu KX, Nie SP, Tan LH, Li C, Gong DM, Xie MY (2016) A polysaccharide from ganoderma atrum improves liver function in type 2 diabetic rats via antioxidant action and short-chain fatty acids excretion. J Agric Food Chem 64:1938–1944
- Zmora N, Suez J, Elinav E (2019) You are what you eat: diet, health and the gut microbiota. Nat Rev Gastroenterol Hepatol 16:35–56

## Research Article

# The Effect of Thermal Processing on the Saponin Profiles of *Momordica charantia* L.

Yi-Jui Liu,<sup>1</sup> Yun-Ju Lai ,<sup>1</sup> Reuben Wang,<sup>2,3</sup> Yi-Chen Lo ,<sup>1</sup> and Chun-Hui Chiu <sup>4,5</sup>

<sup>1</sup>Graduate Institute of Food Science and Technology, National Taiwan University, No. 1 Section 4 Roosevelt Road, Taipei City, Taiwan

<sup>2</sup>Institute of Food Safety and Health, College of Public Health, National Taiwan University, Taipei City, Taiwan

<sup>3</sup>Master of Public Health Degree Program, College of Public Health, National Taiwan University, Taipei City, Taiwan

<sup>4</sup>Graduate Institute of Health-Industry Technology, Research Center for Food and Cosmetic Safety, College of Human Ecology, Chang Gung University of Science and Technology, No. 261 Wenhua 1st Rd., Guishan Dist., Taoyuan City, Taiwan

<sup>5</sup>Department of Traditional Chinese Medicine, Chang Gung Memorial Hospital, Keelung City, Taiwan

Correspondence should be addressed to Yi-Chen Lo; [loyichen@ntu.edu.tw](mailto:loyichen@ntu.edu.tw) and Chun-Hui Chiu; [chchiu@mail.cgust.edu.tw](mailto:chchiu@mail.cgust.edu.tw)

Received 12 June 2020; Revised 12 August 2020; Accepted 14 August 2020; Published 22 September 2020

Academic Editor: Antimo Di Maro

Copyright © 2020 Yi-Jui Liu et al. This is an open access article distributed under the Creative Commons Attribution License, which permits unrestricted use, distribution, and reproduction in any medium, provided the original work is properly cited.

Saponins from *Momordica charantia* L. are a class of triterpenoid glucoside molecules that contribute to the bitter flavour of the plant and possess pharmacological properties. However, little is known about how the bioactivity and bitter flavour of saponins are affected by thermal processing. We established saponin profiles in bitter gourd extracts using a UPLC-ESI-MS/MS method. Seven saponins including momordicoside F<sub>1</sub>, momordicoside F<sub>2</sub>, momordicoside I, momordicoside K, momordicoside L, 3 $\beta$ ,7 $\beta$ ,25-trihydroxycucurbita-5,23(E)-dien-19-al, and momordicine I were monitored for the effects of thermal processing on their stabilities. The results showed that both 3 $\beta$ ,7 $\beta$ ,25-trihydroxycucurbita-5,23(E)-dien-19-al and momordicoside L were extremely sensitive to heat treatment, particularly when they were heated at 100°C for more than 10 mins and under 121°C for 20 mins. Other saponins were reduced significantly by autoclaving, but they remained unchanged at lower temperatures. In conclusion, specific bitter gourd saponins are affected by thermal treatment, which may modify the bioactive components or bitter flavour of the bitter gourd extracts.

## 1. Introduction

Bitter gourd (*Momordica charantia* L.) is a member of the cucurbitaceae family. The most well-known functional properties of *M. charantia* L. are the hypoglycaemic effects and antidiabetic activities [1–5]. In Asian countries, bitter gourds are usually cooked by steaming, microwave, or boiling, while studies have shown these various preparation and cooking processes can affect the nutritional quality of the bitter gourd [6–8]. Shreds of evidence also shown that thermal treatment can alter the nutritional profiles by changing the stability and functionality of the ingredients in vegetables [6, 9]. However, pressure cooking and frying were reported to retain the maximum antioxidant potential of *M. charantia* L. fruit in total phenol content, total flavonoids,

tannin content, carotenoid content, and antioxidant activity measurements, when compared to microwave cooking [8, 9].

Interestingly, the major active components of the *Momordica charantia* L. extracts are cucurbitane-type triterpenes and related glycosides, also known as bitter gourd saponins [10–13]. Currently, more than 100 bitter gourd saponins have been isolated and identified from different parts of this plant, including the fruit, stems, or leaves. It is reported that the bitter gourd fruit is rich in momordicoside I, momordicoside F<sub>2</sub>, and momordicoside F<sub>1</sub> [14]. The antidiabetic component, 3 $\beta$ ,7 $\beta$ ,25-trihydroxycucurbita-5,23(E)-dien-19-al [15], has been used as the functional ingredient for dietary supplements extracted from the bitter gourd [16]. However, only some bitter gourd saponins,



including momordicoside K, momordicoside L, momordicine I, and momordicine II are related to the bitter taste or bitterness of the bitter gourd [17]. The presence of these bitter taste-related saponins may limit the consumption of bitter gourds. Thus, potential food processing methods that could remove some of the bitter taste-related saponins while retaining the functional component could make the bitter gourd acceptable to consumers.

Although saponins are considered the iconic compounds of *M. charantia* L., little is known about the effects of cooking methods on changes in the saponins of the bitter gourd. Tan et al. discussed the effect of food processing, including temperature, time, and water-to-sample ratio, on the stability of saponins in bitter gourds. The results indicated that the total saponin content of the bitter gourd is affected by temperature [18]. Donya et al. specifically explored the effects of six treatments, including frying, blanching, sun drying, oven drying, and freeze-drying on the proximate compositions and contents of momordicoside K and momordicoside L. It was reported that momordicosides K and momordicosides L were not detected by HPLC-ESI/MS in the blanched samples [19]. In addition, momordicoside L, but not momordicoside K, was retained in the hot water ( $98^{\circ}\text{C} \pm 2$ , 3 min).

Due to the complexity of the saponin structure in *M. charantia* L. fruit, the detection of individual cucurbitane-type triterpene glycoside in *M. charantia* fruit is challenging. Recently, Hu et al. developed a method for the quantitative determination of cucurbitane-type triterpenes and triterpene glycosides in bitter gourd juices using UHPLC [20]. Apart from momordicoside K and momordicoside L, there is no literature available regarding the thermal stability of the bitter saponins in *M. charantia* L. Thus, the objective of this study was to establish a UPLC-ESI-MS/MS method to simultaneously determine seven bitter gourd saponins and to evaluate the profile changes of these saponins in *M. charantia* L. var. Hualien No. 3 before and after thermal treatment.

## 2. Materials and Methods

**2.1. Materials and Reagents.** Hualien No. 3 wild bitter gourd was bred through the Hualien District Agricultural Improvement Station, Taiwan. The whole wild bitter gourd fruits purchased from a local farm were dried at  $45^{\circ}\text{C}$  and ground into a fine powder. Bitter gourd powder was vacuum packaged and stored at  $4^{\circ}\text{C}$  in the dark before use. Methanol (LC-MS grade) was purchased from J. T. Baker (Mallinckrodt Baker, Phillipsburg, NJ, USA). Methanol (HPLC grade) was purchased from Macron Fine Chemicals (Center Valley, PA, USA). Formic acid, analytical grade 99.7% purity, was purchased from Riedel-de Haen (Seelze, Germany). Saponin standards, including momordicoside L,  $3\beta,7\beta,25$ -trihydroxycucurbita-5,23(E)-dien-19-al, momordicoside K, momordicine I, momordicoside I, momordicoside F<sub>2</sub>, and momordicoside F<sub>1</sub>, were purchased from Starsci Biotech Co., Ltd.

(Taipei, Taiwan) with purities of 94.3%, 95.6%, 92.3%, 95.2%, 98.1%, 95.3%, and 92.2%, respectively.

**2.2. Sample Preparation.** Bitter gourd powders (0.5 g) were sonicated in 40 mL of 100% methanol for 30 min, followed by centrifugation for 15 min at 4000 rpm. The supernatant was transferred to a flask. This procedure was repeated five more times. The combined supernatants were evaporated in a Rotavapor (BÜCHI Labortechnik AG, Flawil, Switzerland) until dry.

**2.3. Standard Preparation.** Stock solutions of each standard saponin (1.0 mg/mL) were prepared in methanol and stored at  $-30^{\circ}\text{C}$ . Different calibration levels were prepared by diluting the stock solutions with methanol. Seven stock solutions were mixed with methanol to prepare a working solution (1  $\mu\text{g}/\text{mL}$  each). The working solution was further diluted to six concentration levels for the calibration curve within the range of 20–200  $\mu\text{g}/\text{mL}$ .

**2.4. Thermal Stability Test.** Methanol extracts of bitter gourds were dissolved in 40 mL of water and were used as a background control. The aqueous solution (5 mL) was placed in a 50 mL test tube and boiled in a water bath at various temperatures, including  $30^{\circ}\text{C}$ ,  $60^{\circ}\text{C}$ , and  $100^{\circ}\text{C}$  for periods of 5, 10, and 20 mins, respectively. Samples were also autoclaved at  $121^{\circ}\text{C}$  for 20 minutes. After heating, samples were immediately placed in an ice box to cool down.

**2.5. UPLC-ESI-MS/MS Analysis.** Methanol extracts of the bitter gourds and the aqueous solution were purified by reversed-phase C-18 solid-phase-extraction cartridges (Agela, China) using 10–100% methanol as the elution buffer. The total eluted solvent was evaporated until dry. The residues were reconstituted to 1 mL with methanol and filtered using a 0.22  $\mu\text{m}$  nylon membrane filter before UPLC-ESI-MS/MS analysis. UPLC-ESI-MS/MS analysis was performed using a Waters ACQUITY ultra performance LC system (Waters, Milford MA, USA) equipped with a TQS triple quadrupole MS/MS system (Waters, Milford, MA, USA). The reversed-phase Waters BEH RP-18 column (2.1 mm  $\times$  100 mm i.d., particle size 1.7  $\mu\text{m}$ ) (Waters, USA) was maintained at  $35^{\circ}\text{C}$  with the flow rate of 0.3 mL/min. The mobile phase consisted of (A) water and (B) methanol, both containing 0.01% formic acid. Gradient elution was performed as follows: 0–2 min, 20% B; 2–6 min, 70% B; 6–15 min, 70% B; 15–19 min, 72% B; 19–22 min, 72% B; 22–25 min, 80% B; 25–28 min, 80%. Two microliters of the sample were injected by an autosampler. The ESI parameters were set as follows: capillary voltage was 3.0 kV, cone voltage was 39 V, desolvation temperature was  $200^{\circ}\text{C}$ , desolvation gas flow was 800 (L/hr), and cone gas flow was 150 (L/hr). Data were acquired and processed using the Mass Lynx 4.1 software (Waters, Milford, MA, USA).

**2.6. Statistical Analysis.** The data were presented as the mean  $\pm$  standard deviation (SD) from three independent experiments. The data were analysed using one-way ANOVA followed by Tukey's honest significant difference (HSD) test. Statistical significance is determined by  $P < 0.05$ .

### 3. Results

**3.1. Identification and Quantification of Cucurbitane Triterpenoids.** We first established the platform to analyse the specific saponins from the wild bitter gourd and investigated the effect of thermal processing on these functional or bitter taste-related compounds (Figure 1).

Individual saponins were detected using tandem mass spectrometry with the multiple reaction monitoring (MRM) mode. For each compound, the strongest MRM transition was selected as the quantification ion and the other transition was used for qualification. To distinguish compounds with the same MRM transitions, such as  $3\beta,7\beta,25$ -trihydroxycucurbita-5,23(E)-dien-19-al and momordicine I,  $m/z$  495 ( $[M + Na]^+$ )  $> m/z$  477 ( $[M + Na - H_2O]^+$ ), or momordicoside I and momordicoside  $F_2$ ,  $m/z$  641 ( $[M + Na]^+$ )  $> m/z$  337 ( $[M + Na - \text{hexose-side chain}]^+$ ), the retention time of the individual compound was determined according to the corresponding standard (Table 1). These identification profiles of individual saponins helped quantify the bitter gourd saponins.

**3.2. The Specific Saponin Content of the Bitter Gourd.** Calibration curves were established by independently diluting individual stock standard solutions. The concentrations (20–200 ng/mL) of the target saponins were tested. The results showed that linearity was obtained for all analytes throughout the concentration range, and the coefficient of correlation ( $r$ ) was greater than 0.9970 (Table 2). The specific triterpenoid contents in the methanol extract of bitter gourd were analysed and calculated based on the standard curves. The results revealed that the bitter gourd extracts contained high amounts of momordicoside L ( $420.94 \pm 18.17 \mu\text{g/g}$ ) and momordicine I ( $458.78 \pm 35.08 \mu\text{g/g}$ ) compared to other analysed saponins (Table 3). The bitter gourd extracts also contained a high amount of momordicoside  $F_2$  ( $218.28 \pm 26.43 \mu\text{g/g}$ ), momordicoside I ( $200.45 \pm 26.71 \mu\text{g/g}$ ), and  $3\beta,7\beta,25$ -trihydroxycucurbita-5,23(E)-dien-19-al ( $190.00 \pm 9.63 \mu\text{g/g}$ ) (Table 3). Momordicoside K ( $5.23 \pm 0.79 \mu\text{g/g}$ ) and momordicoside  $F_1$  ( $1.91 \pm 0.24 \mu\text{g/g}$ ) were minor components in our extract (Table 3).

**3.3. The Effect of Thermal Processing on the Saponin Content.** To study the effect of thermal processing on the stability of the bitter gourd saponins, we treated the bitter gourd extracts with an extreme autoclaving condition at  $121^\circ\text{C}$  for 20 mins as a control. The results showed that this dramatically reduced the levels of all saponins (Figure 2). We also heated the bitter gourd extracts at various temperatures, including  $30^\circ\text{C}$ ,  $60^\circ\text{C}$ , and  $100^\circ\text{C}$ , and

collected the samples at 5 min intervals for saponin analysis. It was surprising that the levels of momordicoside L, momordicoside K, momordicoside I, and momordicoside  $F_1$  remained stable during the 20 mins of treatment at different temperatures (Figures 2(a)–2(d)). However, heating at  $100^\circ\text{C}$  might change the levels of momordicoside  $F_2$  (Figures 2(e)) compared to those at lower temperatures. The bioactive component,  $3\beta,7\beta,25$ -trihydroxycucurbita-5,23(E)-dien-19-al and the bitter taste compound, momordicine I, were less affected after  $30^\circ\text{C}$  and  $60^\circ\text{C}$  treatment for 20 mins. However, the levels of  $3\beta,7\beta,25$ -trihydroxycucurbita-5,23(E)-dien-19-al were significantly reduced after 5 mins at  $100^\circ\text{C}$  and almost eliminated after 20 mins of high-temperature treatment (Figures 2(f)). Momordicine I was the most sensitive to high temperature. It was barely detected after 10 mins at  $100^\circ\text{C}$  (Figures 2(g)).

### 4. Discussion

In this study, we identified that specific triterpenoids, including the bioactive component,  $3\beta,7\beta,25$ -trihydroxycucurbita-5,23(E)-dien-19-al, and the bitter taste compound, momordicine I, in the methanol extracts of bitter gourd were extremely sensitive to high temperature ( $100^\circ\text{C}$ ) treatment. Others, including momordicoside L, momordicoside K, momordicoside I, and momordicoside  $F_1$ , were relatively stable under the same conditions. We also observed that autoclaving had profound effects on the levels of all 7 saponins studied. Indeed, Tan et al. reported that thermal treatment exceeding  $40^\circ\text{C}$  would decrease total saponin content in the bitter gourd [18], but no specific components were identified. Interestingly, Donya et al. could not detect momordicoside K and momordicoside L from the blanched bitter gourds. It was speculated that momordicosides might increase the loss in the blanching water or be degraded at the high blanching temperatures [19]. Here, we demonstrated that momordicoside K and momordicoside L are less affected by heating at  $100^\circ\text{C}$  for 20 mins, which was more stringent than the blanching in other experimental conditions.

It is known that the bitter gourd fruit is rich in bioactive and bitter flavour-related saponins [15, 16]. The profiles of saponins may vary in different breeds of bitter gourds. In this study, we determined the levels of specific saponins in a hybrid bitter gourd, Hualien No. 3, in Taiwan. Interestingly, we found that momordicoside I and momordicoside L were abundant in our sample. Wang et al. indicated that the amount of momordicoside L was the highest in the Fujian bitter gourd, while kuguaglycoside C and goyaglycoside D were higher in the Guangdong bitter gourd [2]. However, others showed that momordicoside L and momordicoside  $F_2$  were the major components, compared to other saponins, in the bitter gourd extracts [21]. Thus, the content of these saponins in the bitter gourd samples may be related to environmental regions, species [2], or the extraction methods. Notably,  $3\beta,7\beta,25$ -trihydroxycucurbita-5,23(E)-dien-19-al, has been used as the functional

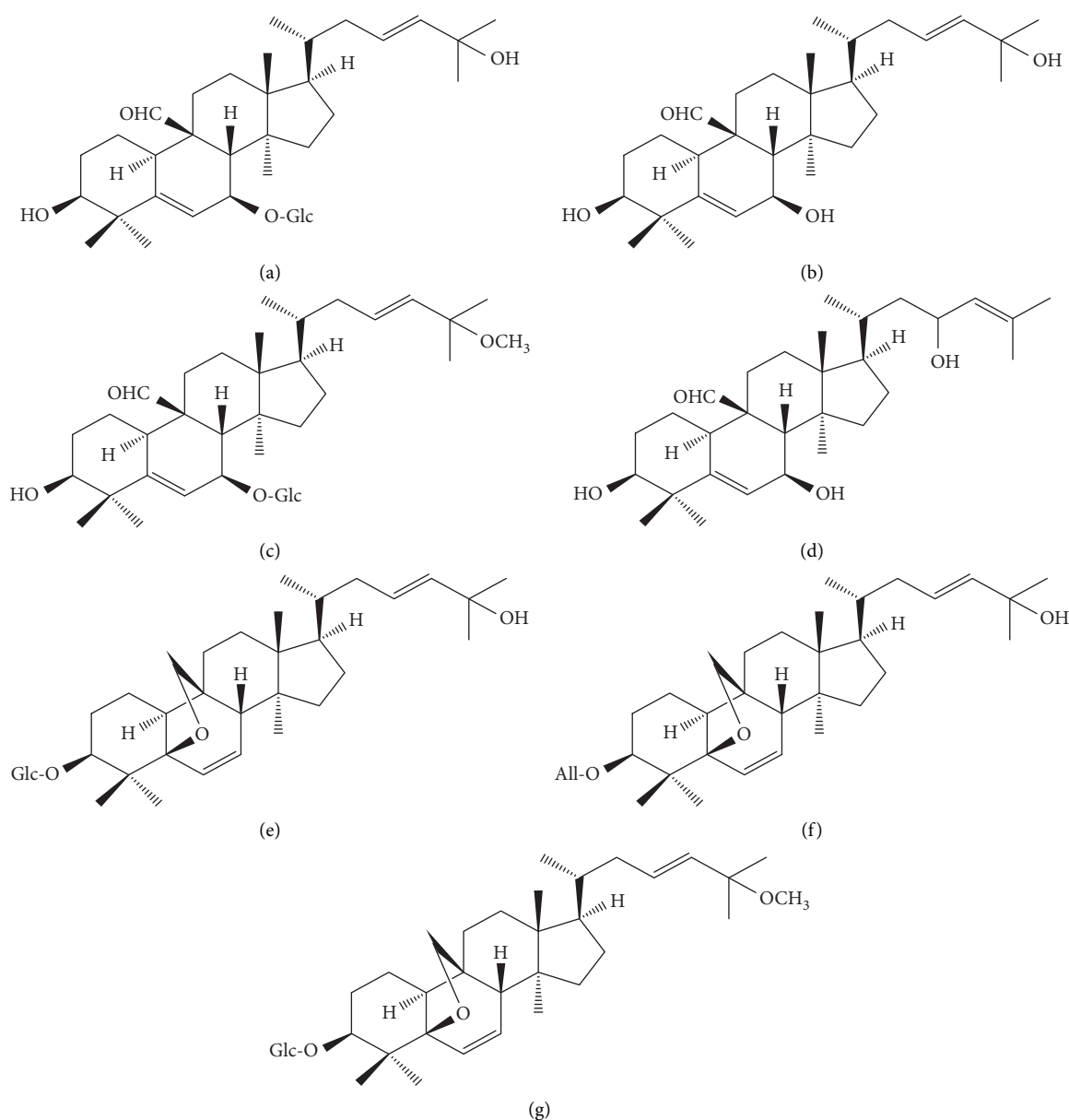


FIGURE 1: Structures of specific bitter melon saponins. (a) Momordicoside L, (b) 3 $\beta$ ,7 $\beta$ ,25-trihydroxycucurbita-5,23(E)-dien-19-al, (c) momordicoside K, (d) momordicine I, (e) momordicoside I, (f) momordicoside F<sub>2</sub>, and (g) momordicoside F<sub>1</sub>. Glc denotes a glucose molecule. All denotes allose. Structures were drawn by MDL ISIS/Draw 2.5.

TABLE 1: Retention times and fragment ions of bitter melon saponins.

Bitter melon saponins	Retention time (min)	MW	Parent ion (m/z) > daughter ion (m/z)	
			Quality	Quantity
Momordicoside L	9.52	634	657 > 203	657 > 477
3 $\beta$ ,7 $\beta$ ,25-trihydroxycucurbita-5,23(E)-dien-19-al	11.51	472	495 > 477	495 > 495
Momordicoside K	14.55	648	671 > 203	671 > 491
Momordicine I	15.24	472	495 > 477	495 > 495
Momordicoside I	15.46	618	641 > 337	641 > 203
Momordicoside F <sub>2</sub>	15.80	618	641 > 337	641 > 203
Momordicoside F <sub>1</sub>	24.03	632	655 > 337	655 > 625

TABLE 2: Calibration curve for specific bitter gourd saponins by UPLC-ESI/MS/MS.

Bitter gourd saponins	Linear range (ng/mL)	Calibration curve	<i>r</i>
Momordicoside L	20–200	$y = 397.55x - 1373.1$	0.9995
3β,7β,25-trihydroxycucurbita-5,23(E)-dien-19-al	20–200	$y = 8175.7x - 160.56$	0.9997
Momordicoside K	20–200	$y = 236.32x - 700.75$	0.9991
Momordicine I	20–200	$y = 1997x - 5541$	0.9988
Momordicoside I	20–200	$y = 27.691x - 149.9$	0.9993
Momordicoside F <sub>2</sub>	20–200	$y = 29.61x - 133$	0.9970
Momordicoside F <sub>1</sub>	20–200	$y = 122.42x - 272.49$	0.9994

TABLE 3: Contents of specific bitter gourd saponins in bitter gourd extracts.

Bitter gourd saponins	Bitter gourd methanol extracts (μg/g)
Momordicoside L	420.94 ± 18.17
3β,7β,25-trihydroxycucurbita-5,23(E)-dien-19-al	190.00 ± 9.63
Momordicoside K	5.23 ± 0.79
Momordicine I	458.78 ± 35.08
Momordicoside I	200.45 ± 26.71
Momordicoside F <sub>2</sub>	218.28 ± 26.43
Momordicoside F <sub>1</sub>	1.91 ± 0.24

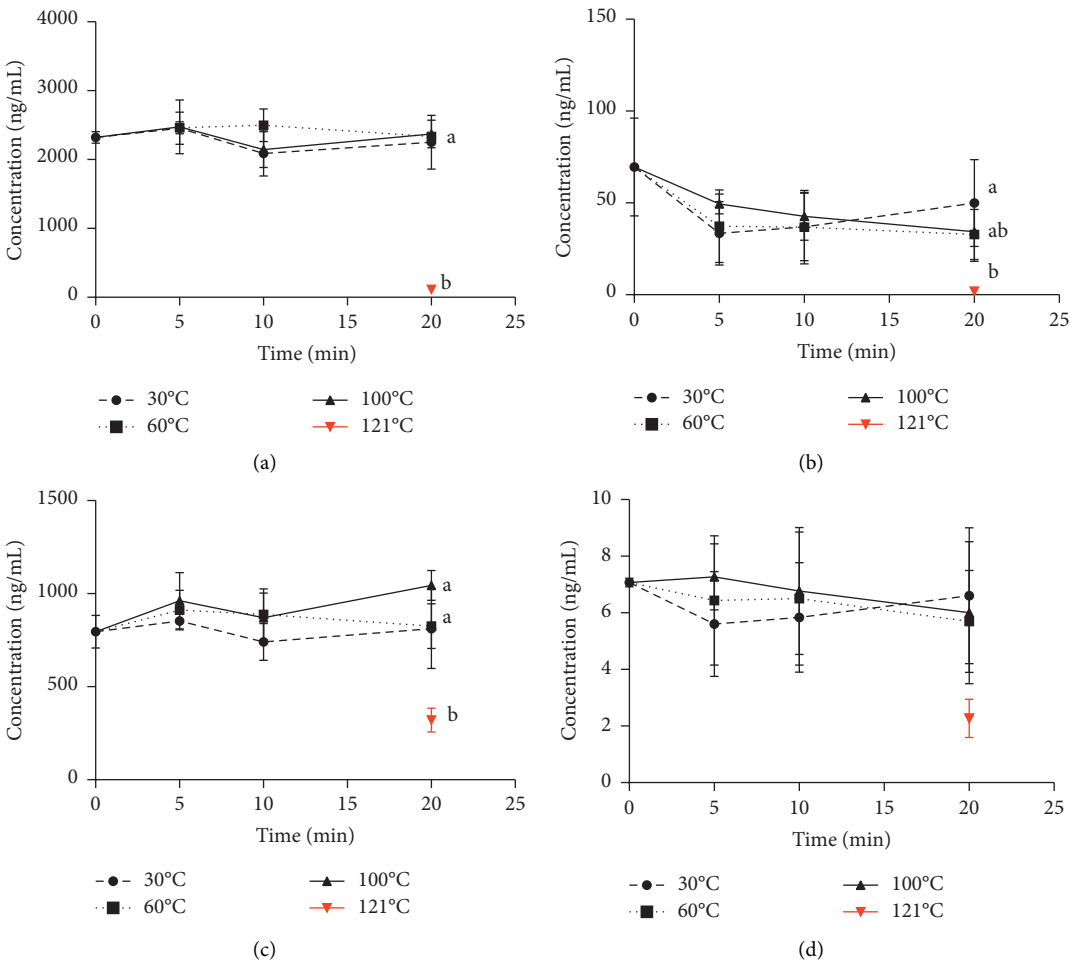


FIGURE 2: Continued.

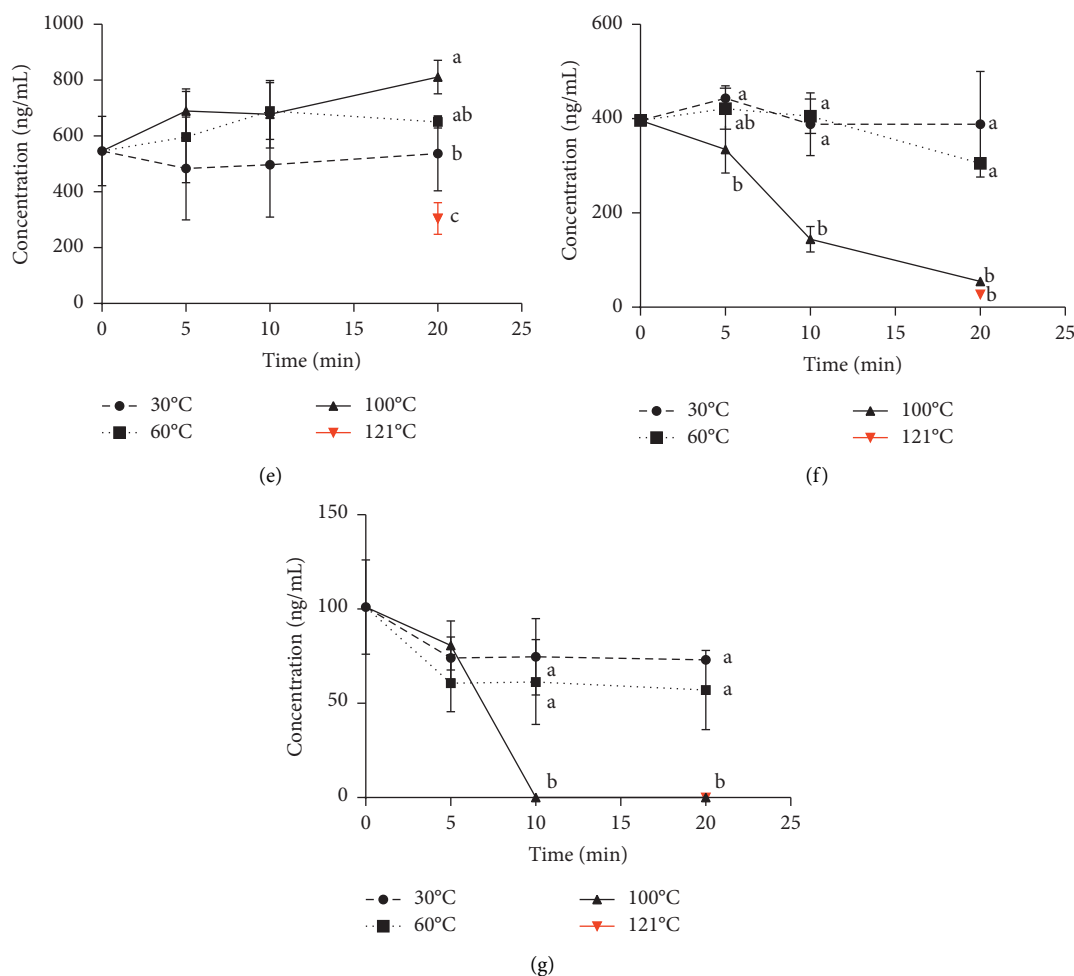


FIGURE 2: The effect of thermal processing on the contents of bitter gourd saponins. Bitter gourd extracts were treated at 30°C (filled circle), 60°C (filled square), 100°C (filled triangle), or 121°C (inverted triangle). (a) momordicoside L, (b) momordicoside K, (c) momordicoside I, (d) momordicoside F<sub>1</sub>, (e) momordicoside F<sub>2</sub>, (f) 3, 7, 25-trihydroxycucurbita-5,23(E)-dien-19-al, and (g) momordicine I were analysed by UPLC-ESI-MS/MS. Different letters represent significant differences. The error bars represent the standard deviation ( $n=3$ ).

ingredient for dietary supplement extracted from the bitter gourd [16]. Our study revealed that 3 $\beta$ ,7 $\beta$ ,25-trihydroxycucurbita-5,23(E)-dien-19-al is unstable after heating at high temperatures or autoclaving. Thus, this compound could be a good indicator of functional ingredients and a quality control for bitter gourd saponins in the future.

## 5. Conclusions

In conclusion, our results demonstrate that cooking at high temperatures may partially eliminate the bitter taste of saponins of bitter gourds. However, it could also result in the reduction of the bioactive components in the bitter gourd. These could provide insights to modify methods for bitter gourd processing in the future.

## Data Availability

The data used to support the findings of this study are included within the article.

## Conflicts of Interest

The authors declare that there are no conflicts of interest.

## Acknowledgments

This research was financially supported by Ministry of Science and Technology, Taiwan, ROC (NSC 102-2313-B-002-057-MY3, MOST105-2320-B-002-026-MY3, and MOST 107-2320-B-255-007).

## References

- [1] H. Y. Lo, T. Y. Ho, C. Lin, C. C. Li, and C. Y. Hsiang, "Momordica charantia and its novel polypeptide regulate glucose homeostasis in mice via binding to insulin receptor," *Journal of Agricultural and Food Chemistry*, vol. 61, no. 10, pp. 2461–2468, 2013.
- [2] B. L. Wang, W. J. Zhang, J. Zhao et al., "Gene cloning and expression of a novel hypoglycaemic peptide from *Momordica charantia*," *Journal of the Science of Food and Agriculture*, vol. 91, no. 13, pp. 2443–2448, 2011.



- [3] M. G. Sridhar, R. Vinayagamoorathi, V. Arul Suyambunathan, Z. Bobby, and N. Selvaraj, "Bitter gourd (*Momordica charantia*) improves insulin sensitivity by increasing skeletal muscle insulin-stimulated IRS-1 tyrosine phosphorylation in high-fat-fed rats," *British Journal of Nutrition*, vol. 99, no. 4, pp. 806–812, 2008.
- [4] Q. Chen, L. L. Y. Chan, and E. T. S. Li, "Bitter melon (*Momordica charantia*) reduces adiposity, lowers serum insulin and normalizes glucose tolerance in rats fed a high fat diet," *The Journal of Nutrition*, vol. 133, no. 4, pp. 1088–1093, 2003.
- [5] J. Virdi, S. Sivakami, S. Shahani, A. C. Suthar, M. M. Banavalikar, and M. K. Biyani, "Antihyperglycemic effects of three extracts from *Momordica charantia*," *Journal of Ethnopharmacology*, vol. 88, no. 1, pp. 107–111, 2003.
- [6] A. D. Fabbri and G. A. Crosby, "A review of the impact of preparation and cooking on the nutritional quality of vegetables and legumes," *International Journal of Gastronomy and Food Science*, vol. 3, pp. 2–11, 2016.
- [7] Z. X. Ng, K. H. Chua, and U. R. Kuppusamy, "Proteomic analysis of heat treated bitter gourd (*Momordica charantia* L. var. Hong Kong Green) using 2D-DIGE," *Food Chemistry*, vol. 148, pp. 155–161, 2014.
- [8] R. Yadav, B. S. Yadav, and R. B. Yadav, "Effect of heat processing treatments and extraction solvents on the phenolic content and antioxidant activity of *Momordica Charantia* fruit," *Journal of Food Processing and Preservation*, vol. 41, no. 4, Article ID.e13037, 2017.
- [9] M. Şengül, H. Yildiz, and A. Kavaz, "The effect of cooking on total polyphenolic content and antioxidant activity of selected vegetables," *International Journal of Food Properties*, vol. 17, no. 3, pp. 481–490, 2014.
- [10] C. I. Chang, C. H. Chou, M. H. Liao et al., "Bitter melon triterpenes work as insulin sensitizers and insulin substitutes in insulin-resistant cells," *Journal of Functional Foods*, vol. 13, pp. 214–224, 2015.
- [11] B. Joseph and D. Jini, "Antidiabetic effects of *Momordica charantia* (bitter melon) and its medicinal potency," *Asian Pacific Journal of Tropical Disease*, vol. 3, no. 2, pp. 93–102, 2013.
- [12] M. J. Tan, J. M. Ye, N. Turner et al., "Antidiabetic activities of triterpenoids isolated from bitter melon associated with activation of the AMPK pathway," *Chemistry & Biology*, vol. 15, no. 3, pp. 263–273, 2008.
- [13] J. K. Grover and S. P. Yadav, "Pharmacological actions and potential uses of *Momordica charantia*: a review," *Journal of Ethnopharmacology*, vol. 93, no. 1, pp. 123–132, 2004.
- [14] Y. H. Wang, B. Avula, Y. Liu, and I. A. Khan, "Determination and quantitation of five cucurbitane triterpenoids in *Momordica charantia* by reversed-phase high-performance liquid chromatography with evaporative light scattering detection," *Journal of Chromatographic Science*, vol. 46, no. 2, pp. 133–136, 2008.
- [15] L. Harinantenaina, M. Tanaka, S. Takaoka et al., "*Momordica charantia* constituents and antidiabetic screening of the isolated major compounds," *Chemical & Pharmaceutical Bulletin*, vol. 54, no. 7, pp. 1017–1021, 2006.
- [16] J. Ma, A. J. Krynetsky, E. Grundel, and J. I. Rader, "Quantitative determination of cucurbitane-type triterpenes and triterpene glycosides in dietary supplements containing bitter melon (*Momordica charantia*) by HPLC-MS/MS," *Journal of AOAC International*, vol. 95, no. 6, pp. 1597–1608, 2012.
- [17] H. Okabe, Y. Miyahara, and T. Yamauchi, "Structures of momordicosides F1, F2, G, I, K and L, novel cucurbitacins in the fruits of L," *Tetrahedron Letters*, vol. 23, no. 1, pp. 77–80, 1982.
- [18] S. P. Tan, Q. V. Vuong, C. E. Stathopoulos, S. E. Parks, and P. D. Roach, "Optimized aqueous extraction of saponins from bitter melon for production of a saponin-enriched bitter melon powder," *Journal of Food Science*, vol. 79, no. 7, pp. E1372–E1381, 2014.
- [19] A. Donya, N. Hettiarachchy, R. Liyanage, J. Lay, P. Chen, and M. Jalaluddin, "Effects of processing methods on the proximate composition and momordicosides K and L content of bitter melon vegetable," *Journal of Agricultural and Food Chemistry*, vol. 55, no. 14, pp. 5827–5833, 2007.
- [20] S. Hu, Y. H. Wang, B. Avula, M. Wang, and I. A. Khan, "Separation of cucurbitane triterpenoids from bitter melon drinks and determination of partition coefficients using vortex-assisted dispersive liquid-phase microextraction followed by UHPLC analysis," *Journal of Separation Science*, vol. 40, no. 10, pp. 2238–2245, 2017.
- [21] B. Yu, B. Ge, Y. Song, D. Li, X. Ma, and M. Wu, "Ultrasound-surfactant synergistic extraction of saponins from balsam pear," *Transactions of the Chinese Society of Agricultural Engineering*, vol. 29, no. 15, pp. 294–300, 2013.



Article

# Docosahexaenoic Acid-Loaded Polylactic Acid Core-Shell Nanofiber Membranes for Regenerative Medicine after Spinal Cord Injury: In Vitro and In Vivo Study

Zhuo-Hao Liu <sup>1</sup> , Yin-Cheng Huang <sup>1</sup>, Chang-Yi Kuo <sup>2</sup>, Chao-Ying Kuo <sup>1</sup>, Chieh-Yu Chin <sup>1</sup>, Ping K. Yip <sup>3</sup> and Jyh-Ping Chen <sup>2,4,5,6,\*</sup>

- <sup>1</sup> Department of Neurosurgery, Chang Gung Memorial Hospital, Linkou, Chang Gung University School of Medicine, Kwei-San, Taoyuan 33305, Taiwan; b8402022@gmail.com (Z.-H.L.); ns3068@gmail.com (Y.-C.H.); recall04729@gmail.com (C.-Y.K.); gobananas929@gmail.com (C.-Y.C.)
  - <sup>2</sup> Department of Chemical and Materials and Materials Engineering, Chang Gung University, Kwei-San, Taoyuan 33302, Taiwan; onesky1997@gmail.com
  - <sup>3</sup> Queen Mary University of London, Barts and The London School of Medicine and Dentistry, Blizard Institute, Centre for Neuroscience, Surgery & Trauma, London E1 2AT, UK; p.yip@qmul.ac.uk
  - <sup>4</sup> Department of Plastic and Reconstructive Surgery and Craniofacial Research Center, Chang Gung Memorial Hospital, Linkou, Kwei-San, Taoyuan 33305, Taiwan
  - <sup>5</sup> Research Center for Food and Cosmetic Safety, Research Center for Chinese Herbal Medicine, College of Human Ecology, Chang Gung University of Science and Technology, Taoyuan 33302, Taiwan
  - <sup>6</sup> Department of Materials Engineering, Ming Chi University of Technology, Tai-Shan, New Taipei City 24301, Taiwan
- \* Correspondence: jpchen@mail.cgu.edu.tw; Tel.: +886-3211-8800 (ext. 5298)

Received: 7 September 2020; Accepted: 23 September 2020; Published: 24 September 2020



**Abstract:** Spinal cord injury (SCI) is associated with disability and a drastic decrease in quality of life for affected individuals. Previous studies support the idea that docosahexaenoic acid (DHA)-based pharmacological approach is a promising therapeutic strategy for the management of acute SCI. We postulated that a nanostructured material for controlled delivery of DHA at the lesion site may be well suited for this purpose. Toward this end, we prepare drug-loaded fibrous mats made of core-shell nanofibers by electrospinning, which contained a polylactic acid (PLA) shell for encapsulation of DHA within the core, for delivery of DHA in situ. In vitro study confirmed sustained DHA release from PLA/DHA core-shell nanofiber membrane (CSNM) for up to 36 days, which could significantly increase neurite outgrowth from primary cortical neurons in 3 days. This is supported by the upregulation of brain-derived neurotrophic factor (BDNF) and neurotrophin-3 (NT-3) neural marker genes from qRT-PCR analysis. Most importantly, the sustained release of DHA could significantly increase the neurite outgrowth length from cortical neuron cells in 7 days when co-cultured with PLA/DHA CSNM, compared with cells cultured with 3  $\mu$ M DHA. From in vivo study with a SCI model created in rats, implantation of PLA/DHA CSNM could significantly improve neurological functions revealed by behavior assessment in comparison with the control (no treatment) and the PLA CSNM groups. According to histological analysis, PLA/DHA CSNM also effectively reduced neuron loss and increased serotonergic nerve sprouting. Taken together, the PLA/DHA CSNM may provide a nanostructured drug delivery system for DHA and contribute to neuroprotection and promoting neuroplasticity change following SCI.

**Keywords:** nanofiber; spinal cord injury; docosahexaenoic acid; regenerative medicine; poly(lactic acid)

## 1. Introduction

Being a very debilitating pathology, spinal cord injury (SCI) may lead to irreversible sensory, motor, and autonomic disabilities in most cases. To date, SCI treatment remains one of the most challenging problems in regenerative medicine with no effective cure. The pathological and pathophysiological changes after SCI include primary injury and subsequent secondary injury [1,2]. As the pathophysiological mechanism of SCI is more than simple mechanical disruption of nerve transmission, multiple treatment interventions have been suggested to fully improve neurological function following SCI. Previous studies have suggested that therapeutic strategies such as bridging the lesion, drug delivery, and cell delivery could be effective for the treatment of SCI. Nonetheless, although direct administration of pharmacological agents or neurotrophic factors to the injury site in SCI is frequently applied, such approaches did not lead to favorable outcomes due to the rapid biological clearance of these agents from the body [3–5]. The nanotechnology-based drug delivery system to the central nervous system (CNS) may provide new opportunities for SCI repair [6].

After adipose tissue, the CNS has the second-highest concentration of lipids, with a high concentration of lipids in the brain being comprised of polyunsaturated fatty acids (PUFAs) [7,8]. Omega-3 PUFAs are important components of cell membranes and are precursors to many other substances in the body, such as those involved in regulating blood pressure and inflammatory responses. The major omega-3 PUFAs in the CNS is docosahexaenoic acid (DHA), composing 10–20% of such fatty acids [9]. Normal CNS function and structure have been proposed to be dependent on an optimal level of omega-3 PUFAs, and if reduced, may lead to neurologic deficits [10] or cognitive changes [11]. Using the transient spinal cord ischemia model in rats, Lang-Lazdunski et al. were the first group to show the beneficial effect of omega-3 PUFAs after SCI [12]. Over the past 10 years, there has been increasing interest in the health benefits of PUFAs, with emerging evidence support that omega-3 PUFAs have significant therapeutic potential in a variety of CNS disorders, including Zellweger syndrome, schizophrenia, depression, and Alzheimer's disease [13]. Most importantly, a number of clinical and pre-clinical studies have shown the neuroprotective effects from diets rich in omega-3 PUFAs [14–16].

The route of administration of DHA after SCI is important for its potential clinical applications. Previous studies have reported that after intravenous injection of radiolabelled fatty acids, PUFAs showed a fast clearance rate from plasma with a half-life less than 1 min. In addition, only 1% of the injected dose was incorporated into brain lipids, particularly phospholipids [17–19]. Accordingly, efficient administration strategies for protecting these highly unsaturated fatty acids against oxidation in addition to their sustained delivery through controlled drug release are necessary in order to avoid the loss of therapeutic effects. In this sense, the electrospinning process is a straightforward and versatile drug encapsulation technique suitable for the production of nanofibers/microfibers containing bioactive compounds. Indeed, lipophilic compounds such as  $\beta$ -carotene and fish oil have been successfully entrapped into nanofibers produced by electrospinning of a zein polymer solution prepared in water/ethanol solutions [20,21].

The coaxial electrospinning is an attractive process that contains a concentric spinneret accommodating two different solutions simultaneously for producing core-shell nanofiber structure with high quality and improved functionality [22]. During coaxial electrospinning, a core solution that usually contains bioactive substances such as drugs, antibiotics, or proteins in solution form, is delivered through the inner needle. The shell solution, usually containing polymeric materials dissolved in an organic solvent, is delivered through the outer needle. Under the action of an applied electric field to the tip of the needle, a liquid jet is ejected from the needle tip above a threshold voltage. After solvent evaporation, core-shell structure nanofibers can be collected with a conductive collector placed at a suitable distance from the needle tip [23]. Core-shell nanofibers have been suggested as controlled drug delivery carriers with several advantages over monolithic nanofibers, such as drug/protein incorporation efficiency in the nanofibers, control of drug release rate, as well as maintenance of structure and activity of bioactive substance [24]. As high and frequent dosing is

required to enhance the performance of drugs for SCI repair due to the low intrinsic potency and short half-lives when manipulated *in vivo*, core-shell nanofibers look attractive as a drug delivery system to achieve a rapid functional recovery of the spinal cord after SCI [25].

Using biodegradable polymers for sustained drug delivery and other biomedical applications has attracted growing attention recently [26]. Consider polymers to be used to prepare DHA-loaded core-shell nanofibers to bridge SCI, polylactic acid (PLA) could be a promising candidate due to its outstanding properties like nontoxicity, biodegradability, and biocompatibility. Indeed, PLA has been considered as one of the most promising biodegradable materials to be widely studied and reported for medical use [27]. The slow degrading nature of PLA is also important for SCI repair *in vivo* as long periods (3–6 months) are usually required for functional regeneration after SCI.

In this study, we intend to use coaxial electrospinning to prepare a DHA-loaded core-shell nanofiber membrane (CSNM) for restoring functional loss after SCI, using PLA as the base polymer (Figure 1). The effects of electrospinning parameters on nanofiber morphology were studied. The optimum PLA/DHA CSNM was characterized for mechanical properties and drug release profile. Finally, efficacies of prompting neurite outgrowth *in vitro*, and recovery of neurologic function with PLA/DHA CSNM treatment *in vivo*, using the SCI model in a rat model, were studied.

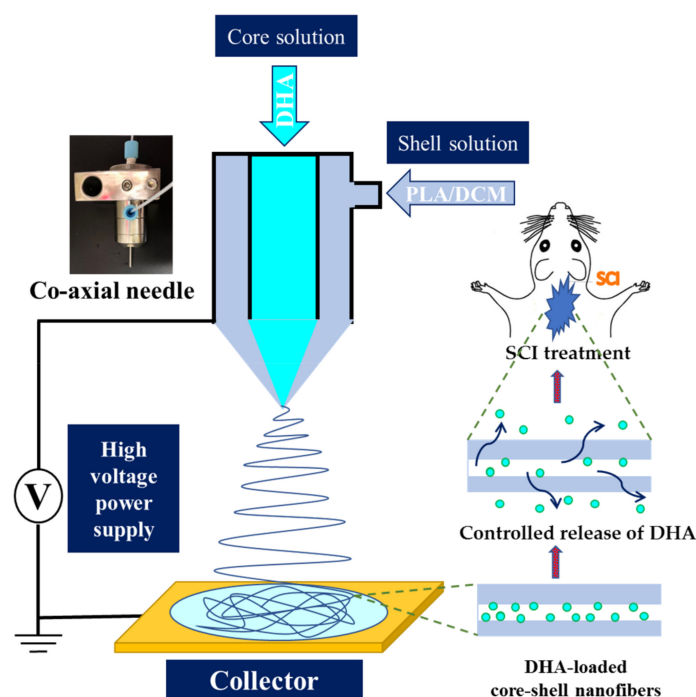


**Figure 1.** The schematic diagram showing the preparation of docosahexaenoic acid (DHA)-loaded core-shell nanofibers using polylactic acid/dichloromethane (PLA/DCM) shell solution for the treatment of spinal cord injury (SCI) in rats.

## 2. Results

### 2.1. Preparation and Characterization of Core-Shell Nanofiber Membrane (CSNM)

We used a 10% (*w/v*) PLA shell solution prepared in dichloromethane (DCM) and a 1 mM DHA core solution (prepared in ethanol) for the fabrication of PLA/DHA CSNM. The voltage and flow rate during electrospinning were reported to be major parameters affecting the morphology and diameter of electrospun nanofibers [28]. Therefore, we studied the effect of voltage and core solution flow rate on nanofiber morphology with a constant shell solution flow rate (1 mL/h). The range of chosen parameters for electrospinning was determined beforehand from pilot runs for the successful formation of the nanofiber membrane. As shown from images taken with a scanning electron microscope

(SEM) in Figure 2, all runs generate nanofibers free of beads-on-string morphology. Although stable nanofiber formation was confirmed within the range of chosen voltage and flow rate, the nanofibers tended to become more irregular and with more uneven morphology at higher voltages (15 kV and 20 kV). Considering the rate of fabricating CSNM, we chose 10 kV and the highest flow rate (0.7 mL/h) to fabricate PLA/DHA CSNM for the following studies, which could provide bead-free nanofibers under the well-controlled electrospinning condition. The average fiber diameter was calculated to be  $644 \pm 106$  nm from SEM images. The membrane thickness was  $136 \pm 10$   $\mu$ m and the loading of DHA was  $6.23 \pm 0.43$   $\mu$ g/mg CSNM after dissolving the membrane in dichloromethane (DCM) and quantified DHA concentration with an enzyme-linked immunosorbent assay (ELISA) kit.

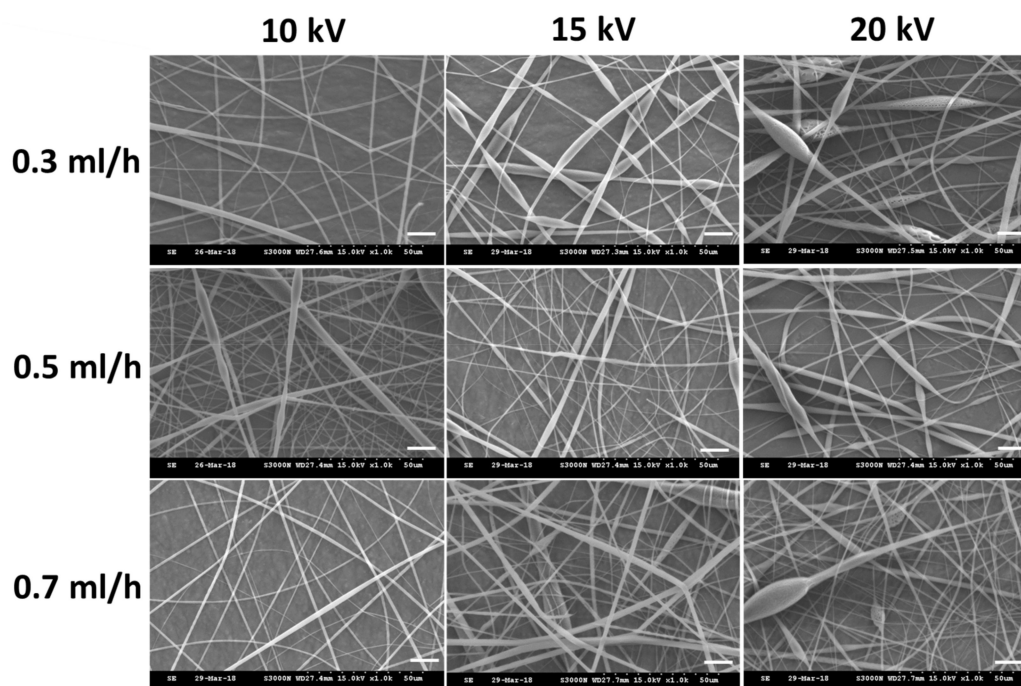


**Figure 2.** The scanning electron microscope (SEM) images of the electrospun polylactic acid/docosahexaenoic acid (PLA/DHA) core-shell nanofibers fabricated under different voltage (in kV) and core solution flow rate (in mL/h).

As demonstrated in Figure 3A, the formation of distinguishable core-shell nanofiber structure could be elucidated by observation under a transmission electron microscope (TEM). Indeed, a sharp boundary separating the shell from the core was confirmed from the TEM image of a single PLA/DHA nanofiber, with  $\sim 300$  nm core diameter and  $\sim 80$  nm shell thickness. To confirm the DHA encapsulation within the CSNM, a fluorescence dye (fluorescein isothiocyanate) was added to label the core solution, followed by the same electrospinning condition to prepare fluorescently labeled nanofibers. As shown in Figure 3B, nanofibers examined by confocal laser scanning microscopy revealed a fluorescent signal within the nanofibers, supporting the successful formation of core-shell nanofibers.

The mechanical properties of a membrane intended for the treatment of SCI is an important design criterion, as matching the mechanical properties of a material to the surrounding native tissue may facilitate cell migration [5]. Therefore, the mechanical properties of PLA/DHA CSNF were fully characterized by tensile mechanical testing. As shown from Figure 4A, a stress-strain curve typical for a ductile material was found for PLA/DHA CSNF, from which parameters of the mechanical property was calculated (Figure 4B). The Young's modulus is a mechanical property that measures the stiffness of a material and calculated from the slope in the stress-strain curve. The toughness represents a material's resistance to fracture when stressed and is determined from the area under the stress-strain curve.



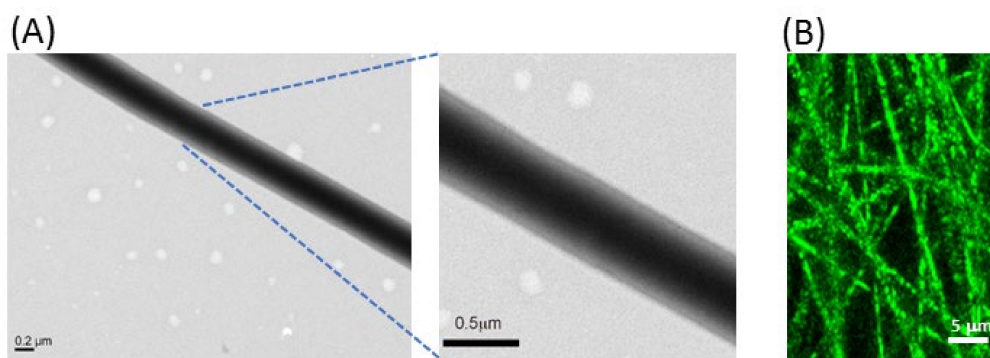


**Figure 3.** The transmission electron microscope (TEM) (A) and the confocal laser scanning microscope (the core solution was labeled with fluorescein isothiocyanate) (B) micrographs of polylactic acid/docosahexaenoic acid (PLA/DHA) core-shell nanofibers.

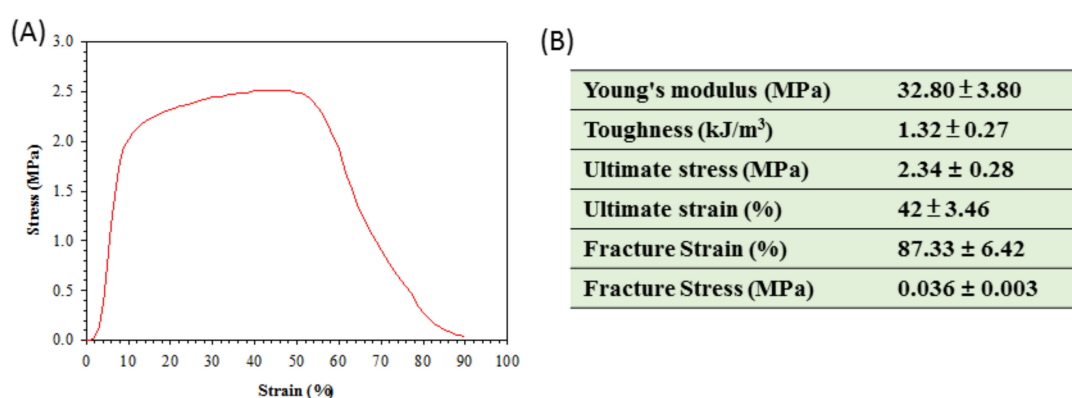


**Figure 4.** A typical tensile stress–strain curve of polylactic acid/docosahexaenoic acid (PLA/DHA) core-shell nanofiber membrane (A) and parameters of mechanical property determined from the stress-strain curves ( $n = 6$ , mean  $\pm$  SD) (B).

The release profile of PLA/DHA CSNM shows the initial burst release of DHA from the membrane, followed by sustained drug behavior extending up to 36 days (Figure 5A). The cumulative DHA release percentage was 55% within 72 h and reached quantitative release at the end of the drug release experiment (Figure 5B).

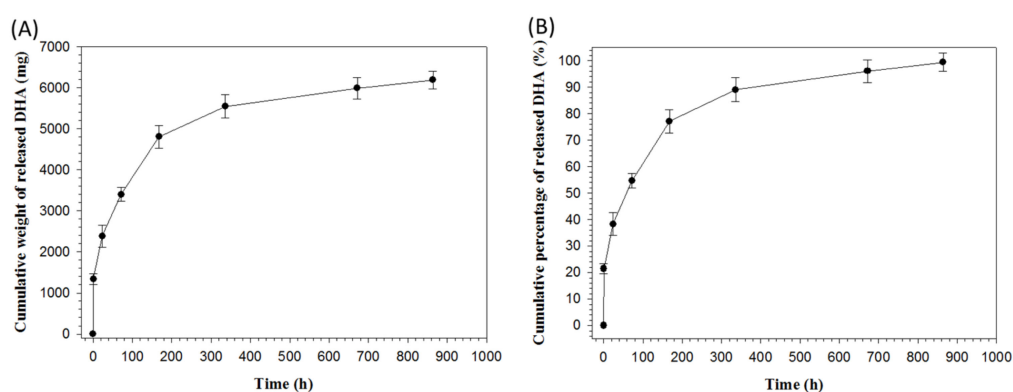


**Figure 5.** The release profiles of docosahexaenoic acid (DHA) from polylactic acid/docosahexaenoic acid (PLA/DHA) core-shell nanofiber membrane determined from the cumulative released weight (A) and cumulative released percentage (normalized to loaded DHA in the membrane) (B) of DHA.

## 2.2. In Vitro Cell Culture

Evaluation of the possible cytotoxicity of CSNMs was carried out according to the ISO10993-5 standard for a medical device using the 24 h extract of a CSNM for cell culture. A PLA CSNM was prepared using the same electrospinning parameters but without DHA in the core solution for comparison. Using 3T3 fibroblasts, the relative cell viability was determined for PLA and PLA/DHA CSNM and compared with cells cultured in fresh cell culture medium (control). The rationale behind the experiment was to analyse whether any of the constituents of the CSNMs or residual organic solvent may have cytotoxic effects. As shown in Figure 6, the relative cell viability of PLA or PLA/DHA is not significantly different from that of the control, endorsing the high biocompatibility of the CSNM fabricated by electrospinning.

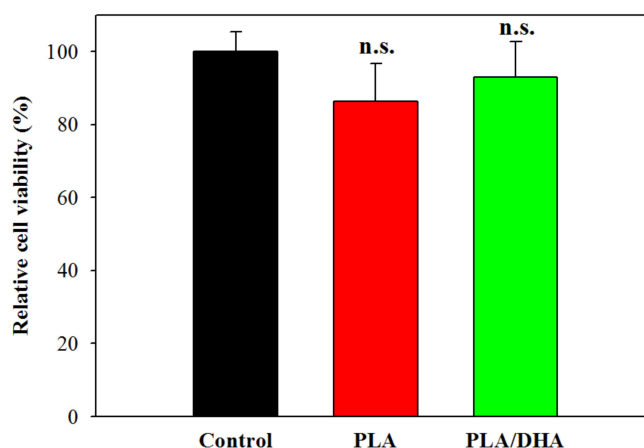


**Figure 6.** Evaluation of the cytotoxicity of core-shell nanofiber membrane toward fibroblasts using the 24 h extraction medium of polylactic acid (PLA) or polylactic acid/docosahexaenoic acid (PLA/DHA) core-shell nanofiber membrane for the culture of fibroblasts ( $n = 6$ , mean  $\pm$  SD). The control is cells cultured with fresh cell culture medium. The cell viability was determined using the MTS assay and normalized to the control. n.s., not significant compared to control ( $p > 0.05$ ).

To determinate whether DHA-load CSNMs directly affected the elongation of existing neurites, we characterized neurite outgrowth from primary cortical neuronal cells under different culture conditions. Neurons were stained with an antibody against  $\beta$ -tubulin-III, a specific marker for the somatodendritic compartment, 3 days after co-cultured with PLA or PLA/DHA CSNM in cell culture medium and compared with control (only cell culture medium) (Figure 7A). In the primary cortical neuron culture, the PLA/DHA group significantly increased the average neurite length per cell body (Figure 7B) and showed greater maximum neurite length per neuron (Figure 7C) when compared with PLA and control groups. No significant difference was noted between the PLA and control groups. This suggests that PLA/DHA CSNM can increase axonal growth and modulate neurogenesis. In order to explore the underlying mechanism that PLA/DHA CSNM promotes neurite outgrowth, primary cortical neurons co-cultured with the membrane for 3 days were subjected to quantitative real-time polymerase chain reaction (qRT-PCR) analysis of gene expression. As shown in Figure 7D,E, the relative mRNA expression of neural marker gene brain-derived neurotrophic factor (BDNF) and neurotrophin-3 (NT-3) were significantly higher in PLA/DHA group compared with the other groups, with no difference found between PLA and control groups. This endorsed the activity of released DHA from PLA/DHA CSNM, which could enhance the neurite outgrowth demonstrated in Figure 6A–C, through modulation of BDNF and NT3 gene expression.

To evaluate the advantage of using PLA/DHA CSNM for temporally and spatially controlled DHA delivery, we further evaluated the time-lapsed neurite outgrowth pattern from primary cortical neuron cells after being co-cultured with PLA/DHA or PLA CSNM in cell culture medium, as well as in cell

culture medium supplement with 3  $\mu\text{M}$  DHA. Primary cortical neuron cells co-cultured with PLA/DHA CSNM presented fewer aggregates than cultured in the presence of free DHA (Figure 8A). However, continuous neurite outgrowth was identified in cortical neuronal cells co-cultured with PLA/DHA CSNM. Significant neurite outgrowth was observed on day 7 among all three groups. Regardless of elapsed culture time, cortical neuron cells co-cultured with PLA/DHA CSNM showed significantly increased average neurite length compared with PLA CSNM. The difference in average neurite length between PLA and PLA/DHA also appeared to increase with culture time, supporting DHA released from PLA/DHA CSNM remains active to promote neurite outgrowth with time (Figure 8B). Comparing PLA/DHA and DHA groups, although the average neurite length was lower for PLA/DHA up to day 5; the trend was reversed on day 7, when the neurite length of PLA/DHA was significantly higher than DHA. This difference underlined the advantage of using PLA/DHA CSNM for controlled DHA delivery over a 3  $\mu\text{M}$  DHA treatment in vitro for neurite outgrowth. Taken together, our results support that the spatio-temporal DHA delivery with PLA/DHA CSNM can increase axonal growth and modulate neurogenesis in vitro.

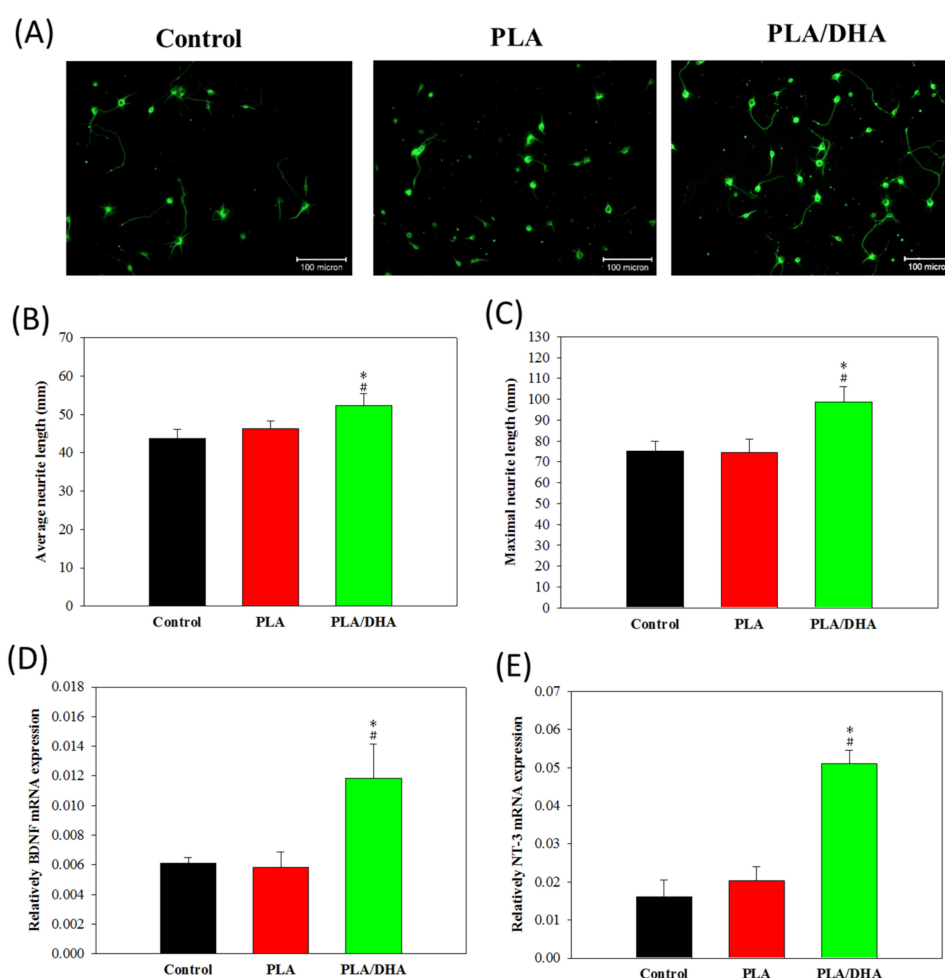


**Figure 7.** The neurite outgrowth was observed from  $\beta$ -tubulin III-positive primary cortical neuron cells under a fluorescent microscope after being co-cultured with polylactic acid (PLA) or polylactic acid/docosaheptaenoic acid (PLA/DHA) core-shell nanofiber membrane in cell culture medium for 3 days (bar = 100  $\mu\text{m}$ ) (A). The control was in the culture medium only. The average neurite length (B) and the maximum neurite length from neurite outgrowth was calculated for each neuron (C) using the ImageJ software ( $n = 3$ , mean  $\pm$  SD). The relative mRNA expression of brain-derived neurotrophic factor (BDNF), (D) and neurotrophin-3 (NT-3) (E) neural marker gene was determined by real-time polymerase chain reaction (qRT-PCR). \*  $p < 0.05$  compared with control, #  $p < 0.05$  compared with PLA.

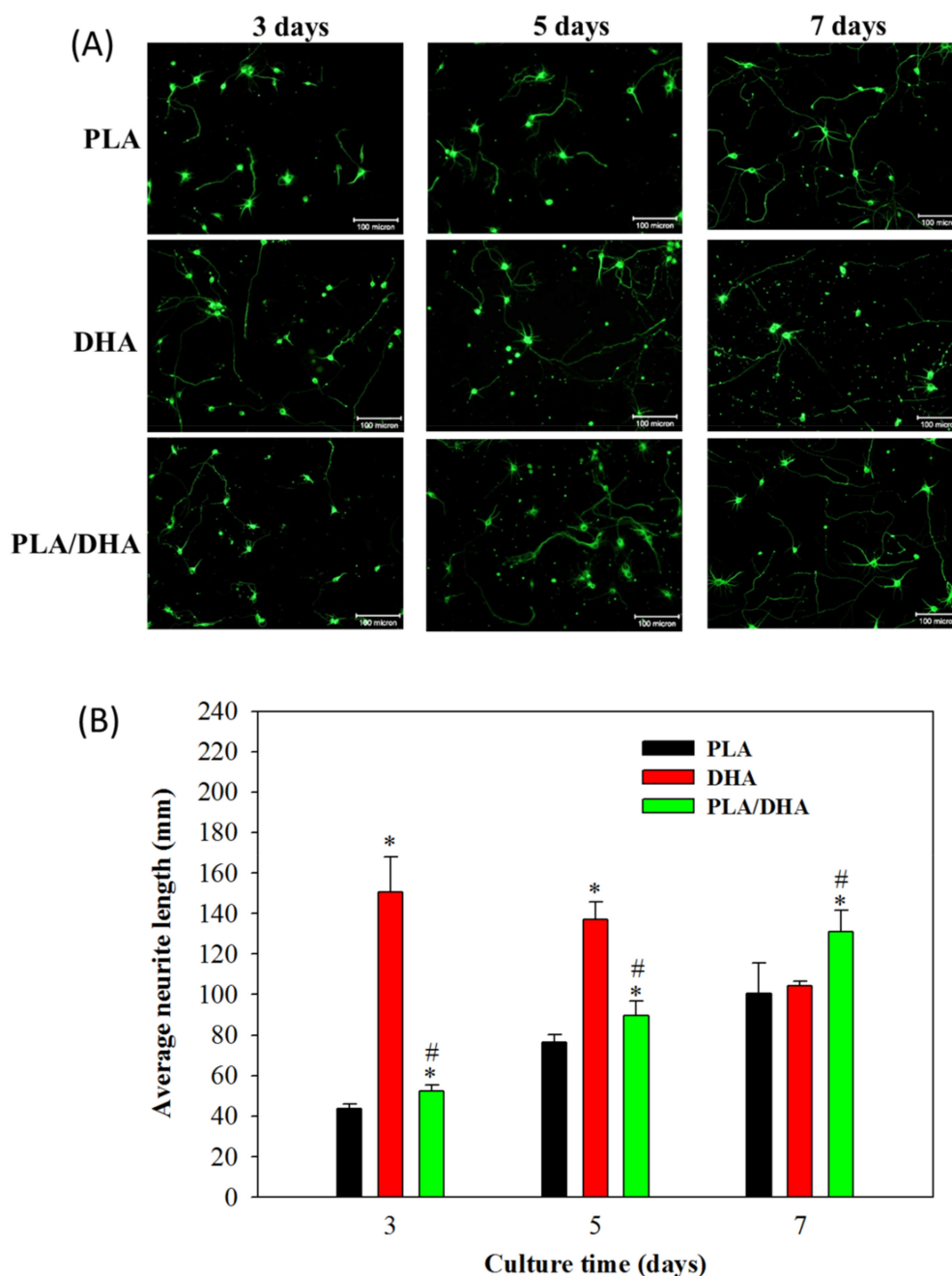


**Figure 8.** (A) The observation of neurite outgrowth from  $\beta$ -tubulin-III-positive primary cortical neuron cells after being co-cultured with polylactic acid (PLA) and polylactic acid/docosahexaenoic acid (PLA/DHA) core-shell nanofiber membrane in culture medium or cultured with 3  $\mu$ M DHA in culture medium for 3, 5, and 7 days (bar = 100  $\mu$ m). (B) The average neurite length due to neurite outgrowth was calculated for each neuron ( $n = 3$ , mean  $\pm$  SD). \*  $p < 0.05$  compared with control, #  $p < 0.05$  compared with PLA.

### 2.3. In Vivo Study

The grid exploration test has been reported to be sensitive enough to evaluate the sensorimotor coordination of the four limbs in the SCI animal model [29,30]. It was used here for the behavioral assessment of rats in control, PLA CSNM-treated, and PLA/DHA CSNM-treated groups, for their ability to accurately place the denervated forepaws following the spinal cord lesion. As shown in Figure 9A, the number of left forelimb slips of the tested animal was significantly less in the PLA/DHA group than the PLA and control groups as early as 1-week post-treatment and showed the same trend

thereafter until the end of the experiment. By 3 weeks post-treatment, the number of foot-slips being made was  $3.6 \pm 0.7$  in the PLA/DHA group compared to  $10.5 \pm 1.2$  in the PLA group and  $13.0 \pm 0.7$  in the control group (Figure 8A). From these data, PLA/DHA CSNM shows a significant effect on the neurological recovery of animals with SCI from the analysis of left forelimb slips.

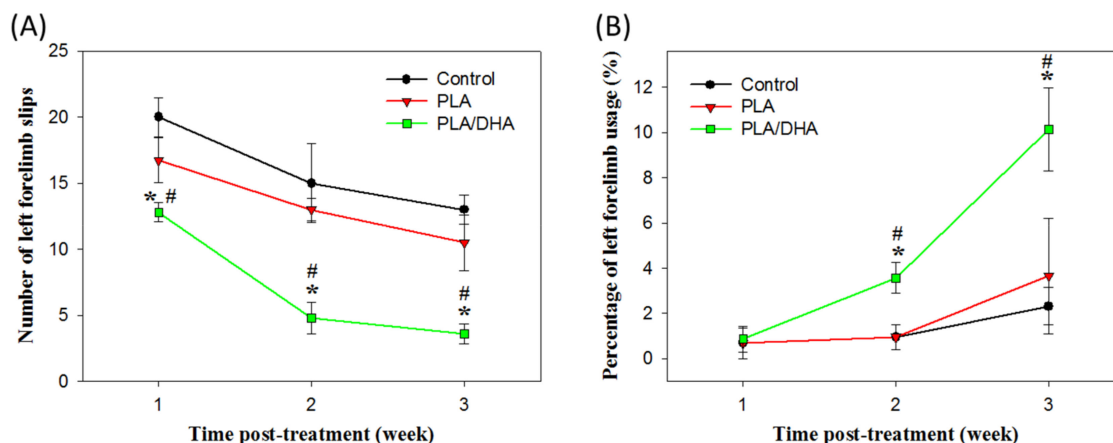


**Figure 9.** The evaluation of the neurological function recovery by the grid exploration test (A) and the cylinder test (B) using a spinal cord injury model in rats. The lesion was covered with a polylactic acid (PLA) or a polylactic acid/docosahexaenoic acid (PLA/DHA) core-shell nanofiber membrane for treatment. The control group received no treatment. \*  $p < 0.05$  compared with control, #  $p < 0.05$  compared with PLA.

Another behavioral assessment was from the cylinder test that measured a rodent's spontaneous forelimb use, which can then be used to evaluate the sensory-motor function in a number of injury models that cause forelimb use to be asymmetrical [31]. At one week following spinal lesion surgery, a marked decrease in the forelimb usage for weight support during vertical exploration of a cylinder was noted for all groups (Figure 9B). However, at 2 and 3 weeks after surgery, the percentage of forelimb usage with the left (lesioned side) forelimb in PLA/DHA group significantly increases over those in PLA and control groups, with no significant difference found between these groups. This pattern indicated that the animals receiving PLA/DHA CSNM implantation could bear weight on the left forelimbs more frequently; supporting that PLA/DHA CSNM treatment improves neurological function recovery after SCI.

From histological analysis, the application of PLA/DHA CSNM leads to significantly improved neuronal survival over PLA CSNM 3 weeks post-spinal injury in rats, as demonstrated by the number of neurons immunostained for the neuronal marker neuronal nuclei (NeuN), around the injury epicentre (Figure 10A–C). In particular, a significantly increased number of neuron cells in PLA/DHA-treated rats compared to PLA-treated and control rats was observed (Figure 10D), which supports that PLA/DHA CSNM can provide protection against neuronal cell loss after a spinal cord lesion. To investigate neuroplasticity changes after treatment, the serotonergic fibers were identified by utilizing serotonin (5-HT) immunohistochemical staining (Figure 10E–G). The number of serotonin fibers was quantified as 5-mm caudal to the lesion site (white arrows). The quantification results reveal robust sprouting and significantly more serotonergic fibers caudal to the lesion in animals received PLA/DHA CSNM treatment compared to PLA and control groups (Figure 10H).



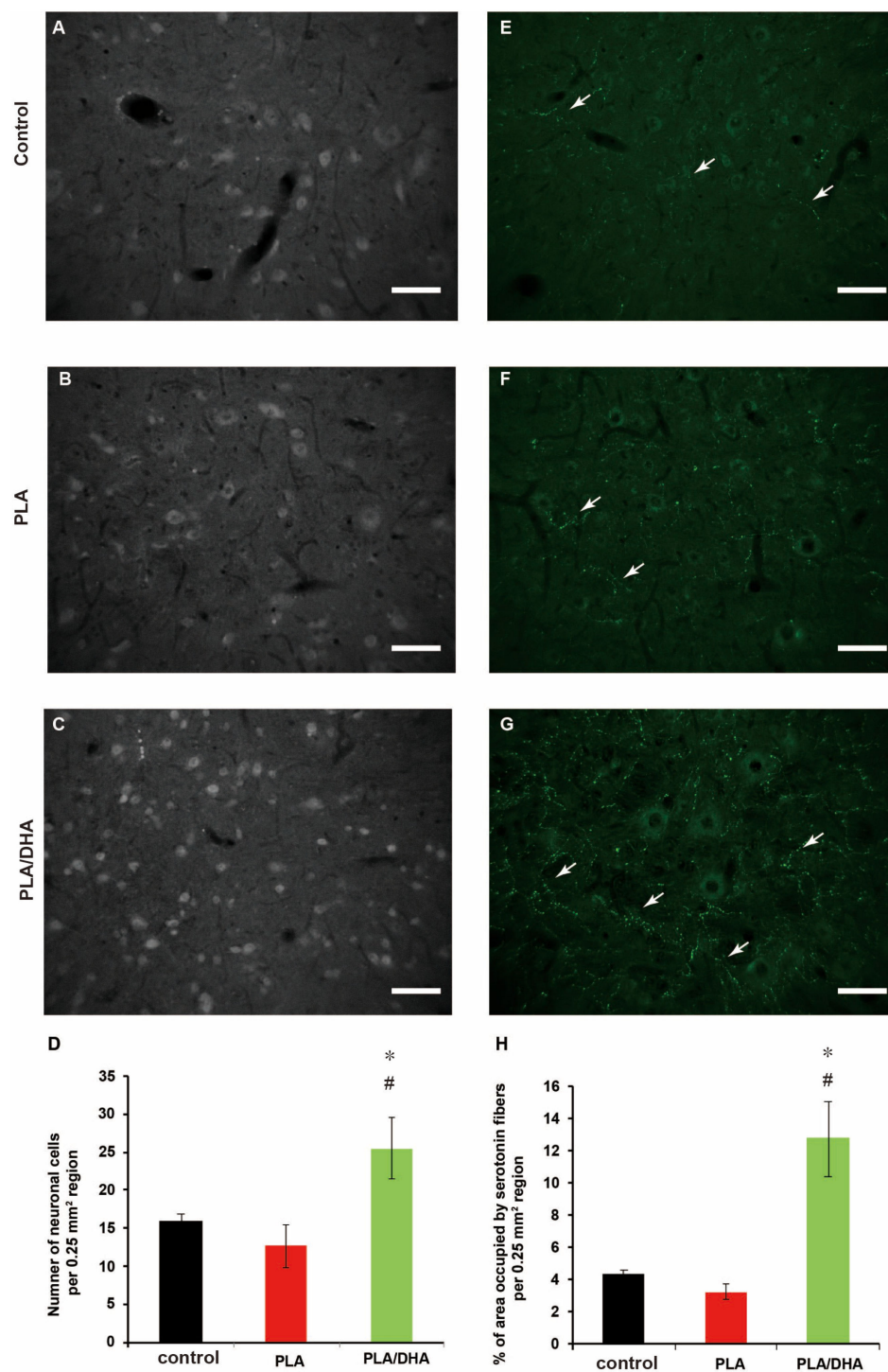


**Figure 10.** The polylactic acid/docosahexaenoic acid (PLA/DHA) core-shell nanofiber membrane (CSNM) prevented neuronal nuclei (NeuN) immunopositive cell loss and increase serotonin (5-HT) positive neurofiber sprouting in the rat after spinal cord injury. (A–C) The sections caudal to the injury site of the contused rat spinal cord were immunostained for NeuN and analyzed (bar = 100 μm). (D) The PLA/DHA CSNM implanted rats show significantly increased NeuN immunolabelled cells when compared to control and PLA groups at 21 days post-injury. (E–G) The sections show serotonergic fibers (white arrows) in the spinal cord tissue caudal to the lesion site after staining with anti-serotonin antibody (bar = 100 μm). (H) The quantification of serotonergic fibers reveals the serotonergic fiber is significantly increased in rats receiving PLA/DHA CSNM implantation. \*  $p < 0.05$  compared with control, #  $p < 0.05$  compared with PLA.

### 3. Discussion

Various strategies have been explored to create adequate biomaterial for nerve regeneration. Electrospun nanofiber membrane may be useful in guiding neuron regeneration in the spinal cord and brain, as well as serving as a scaffold to differentiate and guide transplanted neurons and stem cells in nervous system lesions [32]. Toward the use of nanofiber membrane in nerve regeneration, the mechanical properties of PLGA/DHA CSNM could meet the end of a biomaterial for SCI repair, from both softness and mechanical strength (Figure 4) [33]. Many reports have shown the benefits of using DHA for inducing noticeable functional recovery after SCI [15,16,34,35]. The focus of such studies with omega-3 fatty acids after the CNS traumatic injury was mainly based on their neuroprotective potentials. Nonetheless, the benefits offered by DHA after a central neurological injury may also be related to its role in promoting neuroplasticity. Indeed, DHA has been reported to increase the maximum neurite length and the number of neurites in cortical neuron and embryonic hippocampal cultures [36,37], as well as in primary sensory neurons [38]. In animal studies, oral DHA has been shown to promote the synthesis of components of synaptic membranes and specific presynaptic and postsynaptic proteins [39] and to improve brain learning involving synaptic plasticity [40].

In order to achieve the controlled release of DHA in the lesion site, we develop core-shell structure nanofibers in this study by accommodating DHA within the core region. This design may modulate DHA release to address the needs in suppressing inflammatory responses at the early stage and promoting axon growth at the later stage after SCI. We found that most DHA was released during the first 3 days, followed by continuous and sustained DHA release up to 36 days (Figure 5). With a burst release of close to half of its encapsulated DHA, PLA/DHA CSNM may play a major role in attenuating early inflammation. Following the initial burst DHA release, a low dose of DHA delivery from the PLA/DHA CSNM may effectively stimulate axon growth.

The PLA/DHA CSNM was shown to favor neurite outgrowth from primary neurons on day 3 (Figure 7A–C). Consider the possible mechanisms underlying the effects of DHA on neuroplasticity. Although the exact mechanisms remain unknown, the reasons behind the effects of DHA on neurite outgrowth are likely to involve complex interactions of the structure, function, and gene expression of the neuronal membrane. As a general strategy to promote axonal sprouting and remodeling, the application of exogenous neurotrophic factors, such as BDNF and NT3, was used in several studies [41,42]. As BDNF and NT3 are constantly expressed in the cortex and spinal cord, respectively, they were reported to enhance axonal sprouting from the intact side after SCI in animal models [42,43]. In line with the molecular mechanism for axonal sprouting, only primary cortical neurons co-cultured with DHA/PLA CSNMs showed significantly up-regulated BDNF and NT3 gene expression (Figure 7D,E). Furthermore, not only did the PLA/DHA CSNM favor primary neuron cell growth, time-lapsed study indicated continued neurite outgrowth in neuron cells co-cultured with PLA/DHA CSNM, which even exceed the efficacy offered by a single dose of DHA treatment on day 7 (Figure 8). This endorses the importance of sustained DHA delivery to promote neurite outgrowth. Interestingly, a single dose of DHA treatment was found not to offer better neurite outgrowth compared to the control group at this time point (Figure 8).

In studies on rodent brain, DHA supplementation increased CaM-dependent protein kinase II (CaMKII) and cAMP-responsive element-binding protein (CREB) levels and BDNF secretion to strengthen synaptic plasticity for spatial learning memory formation [44,45]. The BDNF system seems crucial for mediating the action of DHA in the brain, as a diet deficient in DHA has been shown to reduce the activation of tropomyosin receptor kinase B (TrkB) receptors [46]. Furthermore, DHA may also activate transcription factors, such as peroxisome proliferator-activated receptors (PPARs) and retinoid X receptors (RXRs) by altering their gene expression. Previous studies have shown that DHA reduced monocyte chemoattractant protein-1 (MCP-1) expression and lipopolysaccharide-induced nuclear factor-kappaB (NF- $\kappa$ B) activation, through the activation of PPARs [47,48]. Activation of PPARs can also increase BDNF and nerve growth factor (NGF) levels [49] and induce neuronal differentiation by modulating the BDNF/TrkB pathway [50]. An increased BDNF level was also detected in traumatic

brain injury (TBI) [51,52] and cerebral ischemia [53] animal models after DHA supplementation, which could be correlated to functional recovery in the neurological system. Overall, our data is in line with those findings, as shown from the up-regulated BDNF expression and neurogenesis from DHA.

From in vivo study, DHA/PLA treatment produced a marked recovery of neurological function, with significant improvement from 1 week (grid exploration test) and 2 weeks (cylinder test) onwards (Figure 10). In grid exploration tasks, the PLA/DHA group made few foot slips, but PLA-treated lesioned rats and control were severely and significantly impaired throughout testing, albeit with some recovery over time. In the cylinder test, the deficits in ipsilateral forelimb usage were about 1% among the three groups. However, 2 and 3 weeks following injury, the percentage of impair forelimb usage significantly increased compared with PLA and control groups. These findings are consistent with previous studies, which demonstrated DHA could enhance neurological recovery after SCI [30].

DHA was reported to reduce neuronal and oligodendrocyte loss, lesion size, and apoptotic death, which led to the improvement of neurological outcome from the motor score, general balance, and limb coordination [35,54]. In our study, the neuroprotective effect of PLA/DHA is demonstrated by the number of neurons immunostained for the neuronal marker NeuN, around the injury epicenter (Figure 10D). These results show that DHA released from PLA/DHA CSNM can protect against neuronal loss after a spinal cord lesion. In regard to neuroplasticity changes following SCI, several studies have previously reported that rapidly diminished spinal levels of serotonin occur ipsilateral to a spinal lesion following thoracic SCI and cervical SCI [30,55], which is correlated with the severity and recovery of SCI. In our animal study, quantitative analysis revealed a significant increase in the number of serotonin-labeled axons in PLA/DHA group in comparison with PLA and control groups (Figure 10H). These data indicate that serotonin sprouting might contribute to promote functional recovery following PLA/DHA CSNM treatment.

#### 4. Materials and Methods

##### 4.1. Preparation of Core-Shell Nanofiber Membrane (CSNM)

The PLA/DHA CSNM was prepared from two distinct solutions destined respectively for the shell or core part of a nanofiber. The shell solution was prepared by dissolving 0.5 g PLA (poly(L-lactide-co-D,L-lactide), L-lactide:D,L-lactide = 70:30, Resomer® LR 706 S; Evonik, Essen, Germany) in 5 mL of DCM to make a 10% (*w/v*) PLA solution. The core solution was prepared by dissolving 0.654 mg DHA (D2534; Sigma-Aldrich, St. Louis, MO, USA) in 100 mL absolute ethanol to make a 1 mM DHA solution. The CSNM were prepared by electrospinning with a coaxial spinneret at different flow rates (shell flow rate = 1 mL/h, core flow rate = 0.3, 0.5, or 0.7 mL/h). When a high voltage (10, 15, or 20 kV) was applied to the polymer solution, the electrostatic force overcomes the surface tension of the polymer solution at the tip of the needle to form a Taylor cone, which is further elongated into a fluid jet by ejecting the polymer solution from the tip of the needle. Nanofibers formed from the charged fluid jet after solvent evaporation were collected using a collector covered with aluminum foil placed 10 cm from the needle tip. The PLA CSNM was prepared as a control by following the same preparation condition used for PLA/DHA CSNM but with DHA-free core solution. To prepare fluorescently labeled PLA/DHA CSNM, fluorescein isothiocyanate (FITC) fluorescence dye was added to the core solution before electrospinning.

##### 4.2. Characterization of Nanofiber Membrane

The surface morphology of CSNMs was observed using a scanning electron microscope (SEM) (S3000N; Hitachi, Tokyo, Japan). At least 100 fibers randomly chosen from 10 SEM images were selected to measure the fiber diameter. The thickness of all membranes was measured with a dial thickness gauge (TECLOCK SM-1201, Nagano, Japan). A transmission electron microscope (TEM) (JEM-1230, JEOL, Tokyo, Japan) was used to determine the core-shell structure by operating at 75 kV [56]. The fluorescently labeled PLA/DHA CSNM was observed under a confocal laser scanning

microscope (LSM 510 Meta, Zeiss, Oberkochen, Germany) at 364 nm/460 nm excitation/emission wavelength. The tensile properties of CSNM were evaluated using an H1KT mechanical testing machine (Tinius Olsen, Horsham, PA, USA) equipped with a 10 N loading cell. Samples were cut into strips (10 mm × 50 mm) and allowed to undergo tensile elongation at a crosshead speed of 0.3 mm/s and a gauge length of 30 mm. Young's modulus (MPa), fracture strain (%), toughness (kJ/m<sup>3</sup>), ultimate stress (MPa) and ultimate strain (%) were calculated from the tensile stress-strain curves ( $n = 6$ ). To determine the release profile of DHA from PLA/DHA CSNM, the membrane was cut into small pieces, and ~10 mg of sample was immersed in 1 mL of pH 7.4 phosphate buffer solution (PBS) at 37 °C. At predetermined time points, the PBS was completely removed for analysis and 1 mL of fresh PBS was added for continuous incubation up to 36 days. The amount of DHA released at each time point was determined by using an enzyme-linked immunosorbent assay (ELISA) kit for DHA (CEO623Ge, Cloud-Clone Co., Katy, TX, USA), which can detect 12.35–1000 pg/mL DHA based on a competitive inhibition test method. By following the manufacturer suggested procedure, we used 50 µL sample solution and determined the absorbance at 450 nm using an ELISA plate reader (Synergy HT, BioTek, Winooski, VT, USA). By recording the released weight of DHA at each time point, the cumulative released weight of DHA vs. time was reported. The cumulative released percentage of DHA was also calculated after normalizing to the amount of DHA loaded in 10 mg PLA/DHA CSNF. The amount of loaded DHA was determined from completely dissolved PLA/DHA CSNF in DMF for quantification of DHA concentration using a DHA ELISA kit as described before.

#### 4.3. Primary Cortical Cell Culture

Primary cortical neurons were prepared from 18-day-old embryos of Sprague-Dawley rats following protocols approved by the Chang Gung University's Institutional Animal Care and Use Committee [57]. A plastic dish (60 mm diameter) treated with polyethyleneimine was used for cell culture. The plating medium is Minimum Essential Medium (MEM) with Earle's balanced salts and supplemented with 10% fetal bovine serum (FBS), 1 mM pyruvate, 1 mM L-glutamine, 26 mM sodium bicarbonate and 20 mM KCl and (pH 7.2). After 3 to 4 h for cell attachment, the plating medium was replaced with the neurobasal medium containing B-27 supplements, 2 mM L-glutamine, 1 mM 4-(2-hydroxyethyl)-1-piperazineethanesulfonic acid (HEPES) and 0.001% gentamycin sulfate for cell culture.

#### 4.4. Cytotoxicity Evaluation

Cytotoxicity of the CSNMs was examined by the indirect contact method following the biological evaluation of medical devices in ISO 10993-5 [58]. Square shaped CSNMs (1 cm × 1 cm) were sterilized by UV light and immersed in 1 mL of Dulbecco's Modified Eagle Medium (DMEM) containing 10% (v/v) FBS for 24 h. The extraction medium was removed and used for cell culture. 3T3 fibroblasts at  $1 \times 10^4$  cells per well were seeded in a 24-well tissue culture plate for 4 h and cultured with the extract medium for 24 h at 37 °C in a humidified 5% CO<sub>2</sub> environment. Cells cultured with fresh cell culture medium were adopted as the control. The relative cell viability was determined from MTS assay using CellTiter 96® Aqueous One Solution Cell Proliferation Assay from Promega (Madison, WI, USA). The solution absorbance at 492 nm was obtained from an ELISA plate reader (Synergy HT, BioTek, Winooski, VT, USA) and normalizing to that of control.

#### 4.5. Neurite Outgrowth Evaluation

To evaluate the ability of PLA/DHA CSNM to promote neurite outgrow, primary cortical neuronal cells were re-suspended to a cell concentration of  $2.5 \times 10^5$  cells/mL after washing and pelleting, and seeded onto poly-D-lysine coated glass coverslips placed in a 24-well plate for culture in 5% CO<sub>2</sub> incubator at 37 °C ( $n = 3$ ). After culture for 1 day, a CSNM (1 cm × 1 cm) was placed at the bottom of a Corning Transwell® cell culture plate insert (8.0 µm pore size porous membrane) for diffusion of DHA from the CSNM to the seeded cells on the well surface. The CSNM-loaded inserts were



fitted into the 24-well culture plate, and the cell culture medium was added to fully immerse the membrane for co-culture of PLA/DHA CSNM with primary cortical neuron cells. Primary cortical neuronal cells cultured with cell culture medium, cell culture medium supplement with 3  $\mu$ M DHA and co-cultured with PLA CSNM were used for comparison. After culture for 3, 5 or 7 days, the cells were fixed with 4% paraformaldehyde for 20 min, permeabilized with cold methanol and washed with PBS. For immunostaining, cortical neuronal culture was incubated at room temperature for 2 h with anti- $\beta$  tubulin III primary antibody (Sigma-Aldrich, 1:1000). After staining with AlexaFluor 488 conjugated secondary antibody (Invitrogen, 1:1000) at room temperature for 45 min and PBS washing, cells were mounted with FluorSave reagent (Calbiochem) and observed under an inverted fluorescent microscope. Neurite length was analyzed by drawing a line along every neurite for each neuron cell body and analyzed using the ImageJ software (version 1.41, NIH, Bethesda, MD, USA) to calculate the average and maximum neurite length.

#### 4.6. qRT-PCR to Detect BDNF and NT-3 mRNA Expression

To examine axonal outgrowth-related gene expression, the primary cortical neuron cells co-cultured with PLA and PLA/DHA CSNM for 3 days were subject to quantitative real-time polymerase chain reaction (qRT-PCR) analysis and compared with control runs using culture medium only. The expression of neural marker gene brain-derived neurotrophic factor (BDNF) and neurotrophin-3 (NT-3) was analyzed using standard protocols for RNA isolation and cDNA synthesis. Total RNA was extracted from the primary cortical neuron cells using TRIzol<sup>®</sup> reagent (Invitrogen) and reversely transcribed into cDNA by using Total RNA Isolation Kit and Maxime RT PreMix Kit according to the manufacturer's protocols. The qRT-PCR was conducted using an SYBR Green RT-PCR kit in a MiniOpticon<sup>™</sup> real-time PCR detection system (Bio-Rad CFD-3120). Glyceraldehyde 3-phosphate dehydrogenase (GAPDH) acted as the housekeeping gene, and relative mRNA expression of BDNF and NT-3 was determined using the  $2^{-\Delta\Delta C_t}$  relative quantification method. The primers used are listed in Table 1.

**Table 1.** Apoptotic primer sequence used for qRT-PCR analysis.

Genes	Forward Primer (5'→3')	Reverse Primer (5'→3')
NT-3 <sup>1</sup>	CGTGGTGGCGAACAGAACAT	GGCCGATGACTTGTCGGTC
BDNF <sup>2</sup>	CTACGAGACCAAGTGCAATCC	AATCGCCAGCCAATTCTCTTT
GAPDH <sup>3</sup>	GCAAGTTCAAGGCACA	CATTGATGTTAGCGGGAT

<sup>1</sup> NT-3, neurotrophin-3; <sup>2</sup> BDNF, brain-derived neurotrophic factor; <sup>3</sup> GAPDH, glyceraldehyde 3-phosphate dehydrogenase.

#### 4.7. Animal Surgery

Cervical lateral hemisection of the spinal cord was performed in adult female Sprague-Dawley (SD) rats (250–300 g) using methods previously described [30,59]. All animal experiments were conducted according to protocols approved by the Chang Gung University's Institutional Animal Care and Use Committee. Briefly, animals were anesthetized with isoflurane, and a dorsal midline incision was made at cervical level, to expose the cervical vertebrae. A left hemilaminectomy was carried out at C4 and C5, and then a lateral hemisection was made at the C4–5 level using a microblade. A CSNM was put over the lesion site and cover with dura matter. After surgery, the muscles and skin layers were sutured and animals were returned to a warm incubator for recovery. The control animal received only hemisection of cervical spinal without implantation of CSNM. Post-operative care involved sub-cutaneous injection of analgesic and saline twice daily for 3 days following surgery.

#### 4.8. Grid Exploration Test

Animals were placed on a 20-cm raised grid platform (40 cm × 60 cm) containing 5 cm × 5 cm square grids every week post-operatively, to assess the misplaced steps made by the injured left forelimb. A misplacement was recorded when the limb protruded entirely through the grid and



extended below the wire surface. An experimenter blinded to the treatment group scored the number of foot slips out of the first 30 steps taken with the left forelimb. All animals were tested for their baseline performance by subjecting them to the grid exploration test three times prior to surgery.

#### 4.9. Cylinder Test

In this test, the animal was placed in a glass cylinder, and the number of times it rears up and touches the cylinder wall was measured. The footage was later analyzed in slow motion and the number of times the animal reached up and touched the wall with its left forelimb, right forelimb, or both forelimbs was counted. The results are expressed as the percentage of left forelimb usage for weight support relative to the total number of touches.

#### 4.10. Histological Analysis

At the end of the study, animals were sacrificed and flushed with saline transcardially followed by 4% paraformaldehyde. After placing the spinal cord tissues in 20% sucrose for cryoprotection, spinal cord segments containing the hemisected region were cut horizontally at 20  $\mu\text{m}$  using a cryostat and organized as slide series. Slides of the spinal cord section were randomly chosen and washed with gentle agitation in PBS. The sections were incubated in 10% normal donkey or goat serum for 30 min followed by an overnight incubation with primary antibodies (rabbit anti-serotonin, 1:3000; mouse anti-neuronal nuclei (anti-NeuN), 1:1000). The next day, sections were washed three times (5 min each) in PBS before being incubated for 2 h with secondary antibodies conjugated to Alexa Fluor 488 or 594 (1:1000). After another 5-min wash in PBS, sections were counterstained with the fluorescent nuclear dye Hoechst 33342 (2 mg/mL) for 5 min to facilitate the detection of cell nuclei. Slides were mounted in ProLong<sup>TM</sup> Gold antifade reagent.

#### 4.11. Image Analysis of Histological Sections

Image analysis and quantification were carried out with the observer blinded to the group assignment. At least four sections per staining of the corresponding horizontal plane containing the region of interest (e.g., motor neurons) were viewed and captured on a Leica epifluorescence microscope at 20 $\times$  magnification. The depth and distance from the lesion site of the images were taken and analyzed consistently for all animals. Quantitative analysis of the number of serotonin-labeled axons and the number of neuronal cells was conducted by randomly capturing images of the spinal cord 5-mm caudal to the lesion site. The immunoreactivity in captured images was then quantified in a 500  $\mu\text{m}$   $\times$  500  $\mu\text{m}$  measuring frame by using the ImageJ analysis software. The level of immunoreactivity was expressed as the percentage of the area of the measuring frame that contained immunoreactivity.

#### 4.12. Statistical Analysis

All data are expressed as mean  $\pm$  standard deviation (SD). One-way analysis of variance (ANOVA) was used for statistical analysis using post-hoc Tukey HSD test. Significance was found when the *p*-value was less than 0.05.

### 5. Conclusions

We report successful fabrication of electrospun drug-loaded fibrous mats made of core-shell nanofibers, with PLA shell to encapsulate DHA within the core, for controlled release of DHA in situ. This PLA/DHA CSNM is endowed with adequate mechanical properties for sustained release of the biological cue DHA that has been proven to be effective for SCI repair. The PLA/DHA CSNM co-cultured with primary cortical neuron cells successfully promotes neurite outgrowth in vitro, which correlates well with the molecular mechanism of up-regulated neural marker genes BDNF and NT-3. Furthermore, the advantage of using CSNM for DHA delivery is also supported by increased neurite outgrowth length over a single dose of DHA treatment during primary cortical neuron culture.

From the SCI model in rats, animals treated with PLA/DHA CSNM show pronounced neurological function recovery from behavior assessment within 1 or 2 weeks, which is supported by histological analysis. We thus believe this drug-loaded nanostructure may offer mechanical and chemical support for the fabrication of central nerve grafts in the future, either in vitro or in situ. This work may also provide a starting point for the further fabrication of other neural tissues by loading appropriate instructive cues.

**Author Contributions:** Study conception and design of experiments: Z.-H.L., Y.-C.H., C.-Y.K. (Chao-Ying Kuo), and J.-P.C.; acquisition of data: C.-Y.K. (Chang-Yi Kuo), and C.-Y.C.; analysis and interpretation of data: Z.-H.L. and Y.-C.H.; C.-Y.K. (Chang-Yi Kuo), C.-Y.C., P.K.Y., and J.-P.C.; article drafting and revision: Z.-H.L. and J.-P.C. All authors have read and agreed to the published version of the manuscript.

**Funding:** This research was funded by the National Health Research Institutes, Taiwan (NHRI-EX107-10715EC, NHRI-EX107-10815EC and NHRI-EX107-10915EC).

**Acknowledgments:** The authors would like to thank Chang Gung Memorial Hospital (CMRPG3H0461, CMRPD2G0141 and CMRPD2G0142) for financial support of this research. The Microscope Core Laboratory at Chang Gung Memorial Hospital, Linkou are acknowledged for microscopy analysis.

**Conflicts of Interest:** The authors declare no conflict of interest.

## References

- Schwab, M.E. Repairing the injured spinal cord. *Science* **2002**, *295*, 1029–1031. [\[CrossRef\]](#)
- Thuret, S.; Moon, L.D.; Gage, F.H. Therapeutic interventions after spinal cord injury. *Nat. Rev. Neurosci.* **2006**, *7*, 628–643. [\[CrossRef\]](#)
- Pardridge, W.M. Drug transport across the blood-brain barrier. *J. Cereb. Blood Flow Metab.* **2012**, *32*, 1959–1972. [\[CrossRef\]](#) [\[PubMed\]](#)
- Tsintou, M.; Dalamagkas, K.; Seifalian, A.M. Advances in regenerative therapies for spinal cord injury: A biomaterials approach. *Neural Regen. Res.* **2015**, *10*, 726–742. [\[CrossRef\]](#) [\[PubMed\]](#)
- Straley, K.S.; Foo, C.W.; Heilshorn, S.C. Biomaterial design strategies for the treatment of spinal cord injuries. *J. Neurotrauma* **2010**, *27*, 1–19. [\[CrossRef\]](#) [\[PubMed\]](#)
- Saeedi, M.; Eslamifar, M.; Khezri, K.; Dizaj, S.M. Applications of nanotechnology in drug delivery to the central nervous system. *Biomed. Pharmacother.* **2019**, *111*, 666–675. [\[CrossRef\]](#) [\[PubMed\]](#)
- Salem, N., Jr.; Hullin, F.; Yoffe, A.M.; Karanian, J.W.; Kim, H.Y. Fatty acid and phospholipid species composition of rat tissues after a fish oil diet. *Adv. Prostaglandin Thromboxane and Leukot. Res.* **1989**, *19*, 618–622.
- Horrocks, L.A.; Farooqui, A.A. Docosahexaenoic acid in the diet: Its importance in maintenance and restoration of neural membrane function. *Prostaglandins, Leukotrienes and Essential Fatty Acids* **2004**, *70*, 361–372. [\[CrossRef\]](#)
- Michael-Titus, A.T. Omega-3 fatty acids: Their neuroprotective and regenerative potential in traumatic neurological injury. *Clin. Lipidol.* **2009**, *4*, 343–353. [\[CrossRef\]](#)
- Noaghiul, S.; Hibbeln, J.R. Cross-national comparisons of seafood consumption and rates of bipolar disorders. *Am. J. Psychiatry* **2003**, *160*, 2222–2227. [\[CrossRef\]](#)
- Conquer, J.A.; Tierney, M.C.; Zecevic, J.; Bettger, W.J.; Fisher, R.H. Fatty acid analysis of blood plasma of patients with Alzheimer's disease, other types of dementia, and cognitive impairment. *Lipids* **2000**, *35*, 1305–1312. [\[PubMed\]](#)
- Lang-Lazdunski, L.; Blondeau, N.; Jarretou, G.; Lazdunski, M.; Heurteaux, C. Linolenic acid prevents neuronal cell death and paraplegia after transient spinal cord ischemia in rats. *J. Vasc. Surg.* **2003**, *38*, 564–575. [\[PubMed\]](#)
- Calon, F.; Cole, G. Neuroprotective action of omega-3 polyunsaturated fatty acids against neurodegenerative diseases: Evidence from animal studies. *Prostaglandins, Leukotrienes and Essential Fatty Acids* **2007**, *77*, 287–293. [\[CrossRef\]](#)
- Morris, M.C.; Evans, D.A.; Bienias, J.L.; Tangney, C.C.; Bennett, D.A.; Wilson, R.S.; Aggarwal, N.; Schneider, J. Consumption of fish and n-3 fatty acids and risk of incident Alzheimer disease. *Arch. Neurol.* **2003**, *60*, 940–946. [\[CrossRef\]](#) [\[PubMed\]](#)

15. Huang, W.L.; King, V.R.; Curran, O.E.; Dyal, S.C.; Ward, R.E.; Lal, N.; Priestley, J.V.; Michael-Titus, A.T. A combination of intravenous and dietary docosahexaenoic acid significantly improves outcome after spinal cord injury. *Brain* **2007**, *130*, 3004–3019. [\[CrossRef\]](#)
16. Figueroa, J.D.; Cordero, K.; Llan, M.S.; De Leon, M. Dietary omega-3 polyunsaturated fatty acids improve the neurolipidome and restore the DHA status while promoting functional recovery after experimental spinal cord injury. *J. Neurotrauma* **2013**, *30*, 853–868. [\[CrossRef\]](#) [\[PubMed\]](#)
17. Robinson, P.J.; Noronha, J.; DeGeorge, J.J.; Freed, L.M.; Nariai, T.; Rapoport, S.I. A quantitative method for measuring regional in vivo fatty-acid incorporation into and turnover within brain phospholipids: Review and critical analysis. *Brain Res. Brain Res. Rev.* **1992**, *17*, 187–214. [\[CrossRef\]](#)
18. Rapoport, S.I. In vivo fatty acid incorporation into brain phospholipids in relation to plasma availability, signal transduction and membrane remodeling. *J. Mol. Neurosci.* **2001**, *16*, 243–261, discussion 279–284. [\[CrossRef\]](#)
19. Rapoport, S.I. In vivo approaches to quantifying and imaging brain arachidonic and docosahexaenoic acid metabolism. *J. Pediatrics* **2003**, *143*, S26–S34.
20. Moomand, K.; Lim, L.-T. Oxidative stability of encapsulated fish oil in electrospun zein fibres. *Food Res. Int.* **2014**, *62*, 523–532. [\[CrossRef\]](#)
21. Yang, H.; Wen, P.; Feng, K.; Zong, M.H.; Lou, W.Y.; Wu, H. Encapsulation of fish oil in a coaxial electrospun nanofibrous mat and its properties. *Rsc Adv.* **2017**, *7*, 14939–14946. [\[CrossRef\]](#)
22. Song, W.; Yu, X.; Markel, D.C.; Shi, T.; Ren, W. Coaxial PCL/PVA electrospun nanofibers: Osseointegration enhancer and controlled drug release device. *Biofabrication* **2013**, *5*, 035006. [\[CrossRef\]](#) [\[PubMed\]](#)
23. Mickova, A.; Buzgo, M.; Benada, O.; Rampichova, M.; Fisar, Z.; Filova, E.; Tesarova, M.; Lukas, D.; Amler, E. Core/shell nanofibers with embedded liposomes as a drug delivery system. *Biomacromolecules* **2012**, *13*, 952–962. [\[CrossRef\]](#) [\[PubMed\]](#)
24. Zupančič, Š. Core-shell nanofibers as drug delivery systems. *Acta Pharm.* **2019**, *69*, 131–153. [\[CrossRef\]](#)
25. Faccendini, A.; Vigani, B.; Rossi, S.; Sandri, G.; Bonferoni, M.C.; Caramella, C.M.; Ferrari, F. Nanofiber Scaffolds as Drug Delivery Systems to Bridge Spinal Cord Injury. *Pharmaceuticals* **2017**, *10*, 63. [\[CrossRef\]](#)
26. Armentano, I.; Dottori, M.; Fortunati, E.; Mattioli, S.; Kenny, J. Biodegradable polymer matrix nanocomposites for tissue engineering: A review. *Polym. Degrad. Stab.* **2010**, *95*, 2126–2146. [\[CrossRef\]](#)
27. Tian, H.; Tang, Z.; Zhuang, X.; Chen, X.; Jing, X. Biodegradable synthetic polymers: Preparation, functionalization and biomedical application. *Prog. Polym. Sci.* **2012**, *37*, 237–280. [\[CrossRef\]](#)
28. Shalumon, K.T.; Anjana, J.; Mony, U.; Jayakumar, R.; Chen, J.-P. Process study, development and degradation behavior of different size scale electrospun poly(caprolactone) and poly(lactic acid) fibers. *J. Polym. Res.* **2018**, *25*, 82. [\[CrossRef\]](#)
29. Sandrow, H.R.; Shumsky, J.S.; Amin, A.; Houle, J.D. Aspiration of a cervical spinal contusion injury in preparation for delayed peripheral nerve grafting does not impair forelimb behavior or axon regeneration. *Exp. Neurol.* **2008**, *210*, 489–500. [\[CrossRef\]](#)
30. Liu, Z.H.; Yip, P.K.; Adams, L.; Davies, M.; Lee, J.W.; Michael, G.J.; Priestley, J.V.; Michael-Titus, A.T. A Single Bolus of Docosahexaenoic Acid Promotes Neuroplastic Changes in the Innervation of Spinal Cord Interneurons and Motor Neurons and Improves Functional Recovery after Spinal Cord Injury. *J. Neuroscience* **2015**, *35*, 12733–12752. [\[CrossRef\]](#)
31. Schallert, T.; Fleming, S.M.; Leasure, J.L.; Tillerson, J.L.; Bland, S.T. CNS plasticity and assessment of forelimb sensorimotor outcome in unilateral rat models of stroke, cortical ablation, parkinsonism and spinal cord injury. *Neuropharmacology* **2000**, *39*, 777–787. [\[CrossRef\]](#) [\[PubMed\]](#)
32. Corey, J.M.; Gertz, C.C.; Wang, B.S.; Birrell, L.K.; Johnson, S.L.; Martin, D.C.; Feldman, E.L. The design of electrospun PLLA nanofiber scaffolds compatible with serum-free growth of primary motor and sensory neurons. *Acta Biomater.* **2008**, *4*, 863–875. [\[CrossRef\]](#) [\[PubMed\]](#)
33. Liu, S.; Xie, Y.Y.; Wang, B. Role and prospects of regenerative biomaterials in the repair of spinal cord injury. *Neural Regen. Res.* **2019**, *14*, 1352–1363. [\[CrossRef\]](#) [\[PubMed\]](#)
34. Lim, S.N.; Huang, W.; Hall, J.C.; Michael-Titus, A.T.; Priestley, J.V. Improved outcome after spinal cord compression injury in mice treated with docosahexaenoic acid. *Exp. Neurol.* **2013**, *239*, 13–27. [\[CrossRef\]](#)
35. King, V.R.; Huang, W.L.; Dyal, S.C.; Curran, O.E.; Priestley, J.V.; Michael-Titus, A.T. Omega-3 fatty acids improve recovery, whereas omega-6 fatty acids worsen outcome, after spinal cord injury in the adult rat. *J. Neurosci.* **2006**, *26*, 4672–4680. [\[CrossRef\]](#)

36. Calderon, F.; Kim, H.Y. Docosahexaenoic acid promotes neurite growth in hippocampal neurons. *J. Neurochem.* **2004**, *90*, 979–988. [[CrossRef](#)]
37. Cao, D.; Xue, R.; Xu, J.; Liu, Z. Effects of docosahexaenoic acid on the survival and neurite outgrowth of rat cortical neurons in primary cultures. *J. Nutr. Biochem.* **2005**, *16*, 538–546. [[CrossRef](#)]
38. Robson, L.G.; Dyal, S.; Sidloff, D.; Michael-Titus, A.T. Omega-3 polyunsaturated fatty acids increase the neurite outgrowth of rat sensory neurones throughout development and in aged animals. *Neurobiol. Aging* **2010**, *31*, 678–687. [[CrossRef](#)]
39. Wurtman, R.J.; Ulus, I.H.; Cansev, M.; Watkins, C.J.; Wang, L.; Marzloff, G. Synaptic proteins and phospholipids are increased in gerbil brain by administering uridine plus docosahexaenoic acid orally. *Brain Res.* **2006**, *1088*, 83–92. [[CrossRef](#)]
40. Wu, A.; Ying, Z.; Gomez-Pinilla, F. Docosahexaenoic acid dietary supplementation enhances the effects of exercise on synaptic plasticity and cognition. *Neuroscience* **2008**, *155*, 751–759. [[CrossRef](#)]
41. Lu, P.; Tuszynski, M.H. Growth factors and combinatorial therapies for CNS regeneration. *Exp. Neurol.* **2008**, *209*, 313–320. [[CrossRef](#)] [[PubMed](#)]
42. Fouad, K.; Bennett, D.J.; Vavrek, R.; Blesch, A. Long-term viral brain-derived neurotrophic factor delivery promotes spasticity in rats with a cervical spinal cord hemisection. *Front. Neurol.* **2013**, *4*, 187. [[CrossRef](#)] [[PubMed](#)]
43. Zhou, L.; Shine, H.D. Neurotrophic factors expressed in both cortex and spinal cord induce axonal plasticity after spinal cord injury. *J. Neurosci. Res.* **2003**, *74*, 221–226. [[CrossRef](#)]
44. Tanabe, Y.; Hashimoto, M.; Sugioka, K.; Maruyama, M.; Fujii, Y.; Hagiwara, R.; Hara, T.; Hossain, S.M.; Shido, O. Improvement of spatial cognition with dietary docosahexaenoic acid is associated with an increase in Fos expression in rat CA1 hippocampus. *Clin. Exp. Pharmacol. Physiol.* **2004**, *31*, 700–703. [[CrossRef](#)]
45. Cao, D.; Kevala, K.; Kim, J.; Moon, H.S.; Jun, S.B.; Lovinger, D.; Kim, H.Y. Docosahexaenoic acid promotes hippocampal neuronal development and synaptic function. *J. Neurochem.* **2009**, *111*, 510–521. [[CrossRef](#)]
46. Bhatia, H.S.; Agrawal, R.; Sharma, S.; Huo, Y.X.; Ying, Z.; Gomez-Pinilla, F. Omega-3 fatty acid deficiency during brain maturation reduces neuronal and behavioral plasticity in adulthood. *PLoS ONE* **2011**, *6*, e28451. [[CrossRef](#)] [[PubMed](#)]
47. Li, H.; Ruan, X.Z.; Powis, S.H.; Fernando, R.; Mon, W.Y.; Wheeler, D.C.; Moorhead, J.F.; Varghese, Z. EPA and DHA reduce LPS-induced inflammation responses in HK-2 cells: Evidence for a PPAR-gamma-dependent mechanism. *Kidney Int.* **2005**, *67*, 867–874. [[CrossRef](#)]
48. Dyal, S.C.; Michael, G.J.; Michael-Titus, A.T. Omega-3 fatty acids reverse age-related decreases in nuclear receptors and increase neurogenesis in old rats. *J. Neurosci. Res.* **2010**, *88*, 2091–2102. [[CrossRef](#)]
49. Meng, B.; Zhang, Q.; Huang, C.; Zhang, H.T.; Tang, T.; Yang, H.L. Effects of a single dose of methylprednisolone versus three doses of rosiglitazone on nerve growth factor levels after spinal cord injury. *J. Int. Med Res.* **2011**, *39*, 805–814.
50. D'Angelo, B.; Benedetti, E.; Di Loreto, S.; Cristiano, L.; Laurenti, G.; Ceru, M.P.; Cimini, A. Signal transduction pathways involved in PPARbeta/delta-induced neuronal differentiation. *J. Cell. Physiol.* **2011**, *226*, 2170–2180. [[CrossRef](#)]
51. Wu, A.; Ying, Z.; Gomez-Pinilla, F. Dietary omega-3 fatty acids normalize BDNF levels, reduce oxidative damage, and counteract learning disability after traumatic brain injury in rats. *J. Neurotrauma* **2004**, *21*, 1457–1467. [[CrossRef](#)] [[PubMed](#)]
52. Wu, A.; Ying, Z.; Gomez-Pinilla, F. The salutary effects of DHA dietary supplementation on cognition, neuroplasticity, and membrane homeostasis after brain trauma. *J. Neurotrauma* **2011**, *28*, 2113–2122. [[CrossRef](#)] [[PubMed](#)]
53. Blondeau, N.; Nguemini, C.; Debruyne, D.N.; Piens, M.; Wu, X.; Pan, H.; Hu, X.; Gandin, C.; Lipsky, R.H.; Plumier, J.C.; et al. Subchronic alpha-linolenic acid treatment enhances brain plasticity and exerts an antidepressant effect: A versatile potential therapy for stroke. *Neuropsychopharmacology* **2009**, *34*, 2548–2559. [[CrossRef](#)] [[PubMed](#)]
54. Ward, R.E.; Huang, W.; Curran, O.E.; Priestley, J.V.; Michael-Titus, A.T. Docosahexaenoic acid prevents white matter damage after spinal cord injury. *J. Neurotrauma* **2010**, *27*, 1769–1780. [[CrossRef](#)] [[PubMed](#)]
55. Saruhashi, Y.; Matsusue, Y.; Fujimiya, M. The recovery of 5-HT transporter and 5-HT immunoreactivity in injured rat spinal cord. *Arch. Orthop. Trauma Surg.* **2009**, *129*, 1279–1285. [[CrossRef](#)]

56. Chen, C.-H.; Chen, S.-H.; Shalumon, K.T.; Chen, J.-P. Dual functional core–sheath electrospun hyaluronic acid/polycaprolactone nanofibrous membranes embedded with silver nanoparticles for prevention of peritendinous adhesion. *Acta Biomater.* **2015**, *26*, 225–235. [[CrossRef](#)]
57. Lee, R.K.; Wurtman, R.J.; Cox, A.J.; Nitsch, R.M. Amyloid precursor protein processing is stimulated by metabotropic glutamate receptors. *Proc. Natl. Acad. Sci. USA* **1995**, *92*, 8083–8087. [[CrossRef](#)]
58. Li, W.; Zhou, J.; Xu, Y. Study of the in vitro cytotoxicity testing of medical devices. *Biomed. Rep.* **2015**, *3*, 617–620. [[CrossRef](#)]
59. Liu, Z.H.; Yip, P.K.; Priestley, J.V.; Michael-Titus, A.T. a single dose of docosahexaenoic acid increases the functional recovery promoted by rehabilitation after cervical spinal cord injury in the rat. *J. Neurotrauma* **2017**, *34*, 1766–1777. [[CrossRef](#)]



© 2020 by the authors. Licensee MDPI, Basel, Switzerland. This article is an open access article distributed under the terms and conditions of the Creative Commons Attribution (CC BY) license (<http://creativecommons.org/licenses/by/4.0/>).





Article

# Injectable Thermo-Sensitive Chitosan Hydrogel Containing CPT-11-Loaded EGFR-Targeted Graphene Oxide and SLP2 shRNA for Localized Drug/Gene Delivery in Glioblastoma Therapy

Yu-Jen Lu <sup>1,2,3</sup>, Yu-Hsiang Lan <sup>1,4</sup>, Chi-Cheng Chuang <sup>2</sup>, Wan-Ting Lu <sup>3</sup>, Li-Yang Chan <sup>4</sup>, Peng-Wei Hsu <sup>2</sup> and Jyh-Ping Chen <sup>3,5,6,7,\*</sup> 

<sup>1</sup> School of Medicine, Chang Gung University, Kwei-San, Taoyuan 33302, Taiwan; alexlu0416@gmail.com (Y.-J.L.); orange7975@yahoo.com.tw (Y.-H.L.)

<sup>2</sup> Department of Neurosurgery, Chang Gung Memorial Hospital, Linkou, Kwei-San, Taoyuan 33305, Taiwan; ccc2915@cgmh.org.tw (C.-C.C.); ns3096@cgmh.org.tw (P.-W.H.)

<sup>3</sup> Department of Chemical and Materials and Materials Engineering, Chang Gung University, Kwei-San, Taoyuan 33302, Taiwan; s904140328@yahoo.com.tw

<sup>4</sup> Department of Surgery, Chang Gung Memorial Hospital, Linkou, Kwei-San, Taoyuan 33305, Taiwan; mangojoneschan@gmail.com

<sup>5</sup> Department of Plastic and Reconstructive Surgery and Craniofacial Research Center, Chang Gung Memorial Hospital, Linkou, Kwei-San, Taoyuan 33305, Taiwan

<sup>6</sup> Research Center for Food and Cosmetic Safety, Research Center for Chinese Herbal Medicine, College of Human Ecology, Chang Gung University of Science and Technology, Taoyuan 33302, Taiwan

<sup>7</sup> Department of Materials Engineering, Ming Chi University of Technology, Tai-Shan, New Taipei City 24301, Taiwan

\* Correspondence: jpchen@mail.cgu.edu.tw; Tel.: +886-3211-8800 (ext. 5298)

Received: 19 August 2020; Accepted: 25 September 2020; Published: 26 September 2020



**Abstract:** In this study, we aimed to develop a multifunctional drug/gene delivery system for the treatment of glioblastoma multiforme by combining the ligand-mediated active targeting and the pH-triggered drug release features of graphene oxide (GO). Toward this end, we load irinotecan (CPT-11) to cetuximab (CET)-conjugated GO (GO-CET/CPT11) for pH-responsive drug release after endocytosis by epidermal growth factor receptor (EGFR) over-expressed U87 human glioblastoma cells. The ultimate injectable drug/gene delivery system was designed by co-entrapping stomatin-like protein 2 (SLP2) short hairpin RNA (shRNA) and GO-CET/CPT11 in thermosensitive chitosan-g-poly(*N*-isopropylacrylamide) (CPN) polymer solution, which offers a hydrogel depot for localized, sustained delivery of the therapeutics after the in situ formation of CPN@GO-CET/CPT11@shRNA hydrogel. An optimal drug formulation was achieved by considering both the loading efficiency and loading content of CPT-11 on GO-CET. A sustained and controlled release behavior was found for CPT-11 and shRNA from CPN hydrogel. Confocal microscopy analysis confirmed the intracellular trafficking for the targeted delivery of CPT-11 through interactions of CET with EGFR on the U87 cell surface. The efficient transfection of U87 using SLP2 shRNA was achieved using CPN as a delivery milieu, possibly by the formation of shRNA/CPN polyplex after hydrogel degradation. In vitro cell culture experiments confirmed cell apoptosis induced by CPT-11 released from acid organelles in the cytoplasm by flow cytometry, as well as reduced SLP2 protein expression and inhibited cell migration due to gene silencing. Finally, in vivo therapeutic efficacy was demonstrated using the xenograft of U87 tumor-bearing nude mice through non-invasive intratumoral delivery of CPN@GO-CET/CPT11@shRNA by injection. Overall, we have demonstrated the novelty of this thermosensitive hydrogel to be an excellent depot for the co-delivery of anticancer drugs and siRNA. The in situ forming hydrogel will not only provide extended drug release but also combine

the advantages offered by the chitosan-based copolymer structure for siRNA delivery to broaden treatment modalities in cancer therapy.

**Keywords:** hydrogel; drug delivery; cancer therapy; nanomedicine; chitosan; graphene oxide; shRNA

---

## 1. Introduction

Glioblastoma multiforme (GBM) is the most aggressive and lethal brain tumor in adults. It is characterized by rapid proliferation, high infiltration capacity, and chemoresistance. It is also highly recurrent even through multimodal interventions, making it challenging to treat. The prognosis is often bleak, with a median overall survival ranging from 12 to 15 months and a 5-year survival of 6.8% [1,2]. Current standard treatment for GBM is maximal surgical resection, followed by chemotherapy and radiation [3].

Irinotecan (CPT-11), a chemotherapeutic agent sold under the brand name Camptosar®, can be used in treating GBM [4,5]. However, the major obstacle that hinders successful chemotherapy is its lack of selective targeting. Indeed, chemotherapeutic drugs may not be able to distinguish between normal and malignant cells, resulting in attacking healthy cells while killing cancer cells minimally [6]. Furthermore, multi-drug resistance and poor pharmacokinetic properties are other challenges that we are facing in cancer treatment. Therefore, innovative targeting strategies with enhanced cancer selectivity and minimal adverse effects are needed. Graphene oxide (GO) has been widely used as a nanocarrier for drug delivery with advantages such as large surface area, two-dimensional planar structure, chemical and mechanical stability, and biocompatibility [7]. In addition, pH-responsive drug release from drug-loaded GO will provide an efficient intracellular release of therapeutic drugs in acidic organelles after the endocytosis of drug-loaded GO by cancer cells [8]. Nevertheless, limitations still exist in nanocarrier-based drug delivery systems. Nanocarriers tend to undergo rapid elimination from the reticuloendothelial system due to their small size, in addition to lacking a “smart” selectivity for tumor tissues [9]. Therefore, the targeted delivery of anti-tumor drugs for cancer therapy is considered to be more effective than traditional chemotherapy [10]. Indeed, an active targeting strategy could increase the ability of nanocarriers to be specifically recognized by tumor cells through modifying the carrier surface with a ligand, such as a monoclonal antibody [11]. The epidermal growth factor receptor (EGFR) is over-expressed by most brain tumors, but not by normal tissues, which explains the reason why cetuximab (CET), the EGFR monoclonal antibody, was developed specifically for brain tumor targeting [12]. Thus, modifying GO nanocarriers with CET could enhance its intracellular uptake by cancer cells through ligand-mediated targeted drug delivery [13].

On the other hand, a single drug might not be able to efficiently eliminate all cancer cells, either due to the heterogenic nature of malignant tumors or the existence of malignant cells at the disparate cell division or growth stage [14]. Therefore, combination therapy with different molecular targets is a promising strategy to vanquish drug resistance, reduce the possibility of tumor metastasis, and improve treatment outcomes [15]. Gene therapy as a strategy to curb tumor growth and invasion by the insertion of new genes (DNA and RNA) into target cells is an emerging therapeutic strategy for the treatment of GBM [16]. As an efficient method to post-transcriptionally turn off the expression of specific proteins and transcription factors, RNA interference (RNAi) using small interfering RNA (siRNA) emerges as therapeutics for cancer therapy [17]. Combinatorial siRNA delivery to human primary GBM using cancer-selective nanoparticles was demonstrated to be effective for multimodal therapeutic for cancer [18]. However, some hurdles need to be overcome for delivery of the negatively charged naked siRNA, including their biological instability, off-target effects, inability to passively diffuse across the negatively charged cell membranes, and easy degradation by ribonucleases [19]. To overcome these limitations, a number of siRNA delivery systems, including liposomes, polyplexes, and nanoparticles have been developed for siRNA delivery [20]. Nonetheless, as nanocarriers for siRNA delivery could

be easily dispersed *in vivo* to render local delivery to target sites difficult for a prolonged period of time, sustained localized siRNA delivery is more desirable to enhance its clinical applicability.

As a member of the highly conserved stomatin superfamily, stomatin-like protein 2 (STOML2 or SLP2) was found to be widely expressed in mammalian tissues and considered to be a major mitochondrial inner membrane protein. Recently, several studies have reported that SLP2 plays an oncogenic role in tumor occurrence and progression [21,22]. One study found that SLP2 is one of the 16 most up-regulated proteins in super invasive cancer cells, implying that SLP2 might play a role in cancer metastasis [23]. However, the molecular mechanisms of SLP2 in the progression and development of cancer remain largely unknown. Specifically, SLP2 was found to be markedly upregulated in glioma cells and glioma specimens. The up-regulation of SLP2 was shown to be significantly correlated with the World Health Organization (WHO) histological grade of gliomas, while patients with higher SLP2 expression levels had an overall shorter survival time compared to patients with a lower expression of SLP2 [24]. It was also demonstrated that the silencing of SLP2 gene expression could drastically reduce the migration and invasive ability of glioma cells by inhibiting the transcriptional activity of nuclear factor kappa-light-chain-enhancer of activated B cells (NF- $\kappa$ B) and repressing the expression levels of NF- $\kappa$ B target genes, including matrix metalloproteinase 9 [25]. Therefore, SLP2 plays an important role in human glioma progression and pathogenesis.

Hydrogels are outstanding candidates for drug/gene controlled-release delivery systems. Considering hydrogels for the local release of therapeutics, an injectable hydrogel formulation with *in situ* sol-to-gel transition, triggered externally under physiological conditions after injection using light exposure or temperature/pH change, will be preferred over preformed hydrogels considering non-invasive surgical intervention during delivery [26]. Specifically, thermo-responsive hydrogels are one of the most studied classes of stimuli-responsive polymer systems. The self-assembly of these polymers could lead to sol–gel phase transition when the temperature was increased to above the lower critical solution temperature in an aqueous solution of such polymers. For biomedical and pharmaceutical applications, the poly(*N*-isopropylacrylamide) (PNIPAM)-based polymer is one of the most popular thermosensitive polymers intended for such application, with its phase transition temperature being around 32 °C [27]. Taking advantage of this unique property, a drug/gene-loaded thermal-sensitive polymer solution could be non-invasively administered peritumorally or intratumorally into a tumor at room temperature using a syringe needle. After thermally induced phase transition at body temperature, the formed hydrogel will provide a gel depot for controlled drug/gene release in accordance with the degradation rate of the formed hydrogel [14,28,29]. Interestingly, an injectable, thermosensitive hydrogel combined with drug-loaded nanoparticles was shown to provide better control of drug release and proved to be an efficient drug delivery system with sustained drug release around tumor tissues for peritumoral chemotherapy [30]. On the other hand, hydrogels also appear to be a reliable solution to deliver two or more therapeutic agents concurrently. Combination cancer therapy by incorporating anticancer drugs and genes in carriers has the advantages of protecting drug bioactivity, limiting unwanted toxicity, improving hydrophilicity, prolonging duration time, controlling the rate of drug release, and showing synergistic anticancer effects [31,32].

Considering the advantages offered by polysaccharides for the development of hydrogels, the chitosan-based hydrogels play a crucial role in the development of new biomaterials for use in drug/gene delivery for its biocompatible and biodegradable natures. *In situ* forming chitosan-based hydrogels are very attractive for the local delivery of drugs by showing the sustained release of drug to enhance the drug bioavailability and reduce systemic toxicity [33]. Moreover, chitosan has attracted significant attention for siRNA delivery owing to its cationic nature for easy complexation with siRNA [34]. Indeed, chitosan nanoparticles were suggested to be an effective drug/gene delivery system for the treatment of prostate cancer by the co-delivery of irinotecan and Snail siRNA [35]. Previously, we developed a comb-like thermo-responsive polymer chitosan-g-PNIPAM (CPN), using chitosan as the backbone for pendant PNIPAM group grafting, which was accomplished by conjugating

PNIPAM-COOH to chitosan by amide bond linkages. This thermo-responsive copolymer was proved to be biocompatible as a milieu for cell culture and drug delivery [36,37]. We postulate that this copolymer will be an excellent candidate, as an in situ forming hydrogel depot for cancer therapy, by the co-delivery of anticancer drugs and siRNA. To provide extended drug release, entrapping drug-loaded GO within CPN hydrogel should improve the drug release behavior. To further broaden the treatment modalities offered by CPN, siRNA gene delivery could be combined with drug delivery through the advantages offered by this chitosan-based hydrogel. Considering gene delivery, although both siRNAs and short hairpin RNA (shRNA) expression plasmids are common methods that mimic Dicer cleavage for sequence-specific targeting mRNAs, siRNAs are susceptible to nuclease destruction and cannot penetrate the cell membrane because of their highly charged backbone. Therefore, we will construct and use SLP2 shRNA plasmids in this study for effective gene delivery.

Hence, in the present study, we aim to develop a localized, sustained co-delivery strategy of SLP2 shRNA and GO-CET/CPT11 (CPT-11 loaded to GO-CET) by utilizing the biodegradable CPN hydrogel as an injectable hydrogel depot for the treatment of glioblastoma in vitro and in vivo (Figure 1). The CPN hydrogel loaded with GO-CET/CPT11 or SLP2 shRNA was characterized during each preparation step as well as the drug/gene release characteristics. To study the synergistic anti-tumor efficacy of functionalized CPN hydrogel, U87 human glioblastoma cells were used to study cell cytotoxicity, SLP2 gene transfection, gene silencing, and cell apoptosis in vitro. Finally, by intratumoral injection of CPN hydrogel co-loaded with SLP2 shRNA and GO-CET/CPT11 (CPN@GO-CET/CPT11@shRNA) into nude mice bearing human glioblastoma U87 xenografts, the anti-tumor efficiency was also studied in vivo.

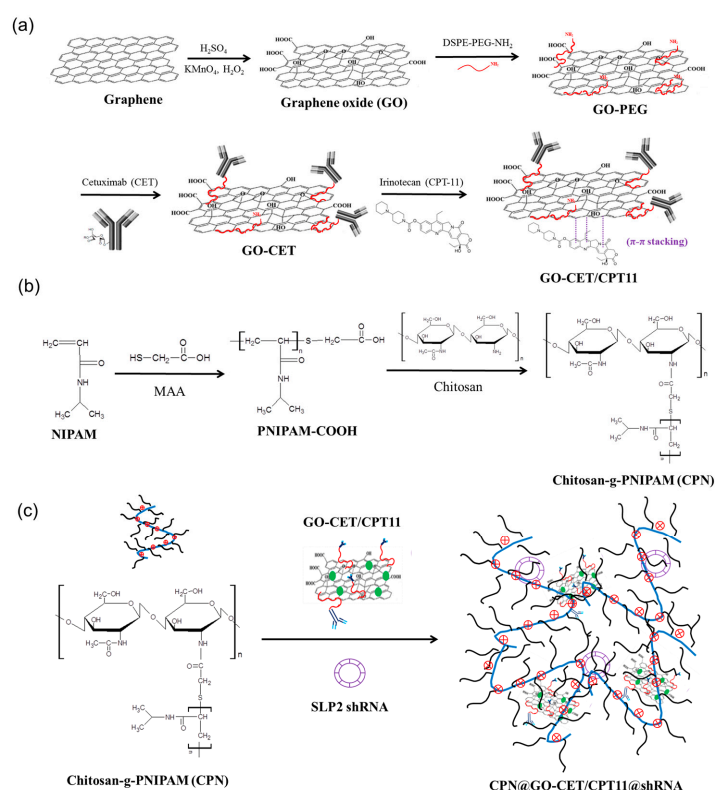


**Figure 1.** The flow diagram for synthesizing irinotecan (CPT-11) to cetuximab (CET)-conjugated graphene oxide (GO) (GO-CET/CPT11) for co-entrapment with stomatin-like protein 2 (SLP2) short hairpin RNA (shRNA) in chitosan-g-poly(*N*-isopropylacrylamide) (CPN). (a) GO produced by the modified Hummers method was modified with *N*-(aminopropyl polyethyleneglycol)carbonyl-distearoylphosphatidyl-ethanolamine 1,2-distearoyl-sn-glycero-3-phosphoethanolamine-*N*-[amino(polyethyleneglycol)] (DSPE-

PEG-NH<sub>2</sub>) to prepare GO-PEG, followed by conjugation with CET to obtain GO-CET. CPT-11 was loaded onto GO-CET via  $\pi$ - $\pi$  stacking interactions to form GO-CET/CPT11. (b) Chitosan-g-poly(*N*-isopropylacrylamide) (CPN) was synthesized by grafting carboxylic acid-ended poly(*N*-isopropylacrylamide) (PNIPAM) (PNIPAM-COOH), prepared by the free radical polymerization of *N*-isopropylacrylamide (NIPAM) and mercaptoacetic acid (MAA), onto chitosan backbone through amide bond linkages. (c) The GO-CET/CPT11 and SLP2 shRNA could be mixed with the thermosensitive CPN hydrogel at room temperature and entrapped within the polymer matrix after sol-gel transition *in situ* to form CPN@GO-CET/CPT11@shRNA.

## 2. Results and Discussion

### 2.1. Synthesis and Characterization of GO, GO-PEG, GO-CET, and GO-CET/CPT11

The GO-based nanocarriers prepared as illustrated in Figure 1a were characterized after each synthesis step. From dynamic light scattering (DLS) analysis of particle size, the average particle diameters determined by DLS were  $201 \pm 1.5$ ,  $213 \pm 0.8$  nm,  $250 \pm 1.6$  nm, and  $279 \pm 1.1$  nm, for GO, GO-PEG, GO-CET, and GO-CET/CPT11, respectively, which could facilitate endocytosis by cancer cells [38]. The morphology of GO, GO-PEG, and GO-CET were observed under transmission electron microscope (TEM). Figure 2a reveals the laminar stacking form of GO with  $\approx 200$  nm size, which is consistent with that from DLS analysis. After PEGylation and CET conjugation modification, GO-PEG and GO-CET show similar surface morphology with slightly larger size as expected. The GO exhibited a highly negative zeta potential value ( $-48.4 \pm 0.59$  mV) due to the presence of abundant oxygen-containing functional groups on its surface. The zeta potential changed to  $-34.4 \pm 0.17$  mV for GO-PEG due to the positive charge of *N*-(aminopropyl polyethyleneglycol)carbonyl-distearoylphosphatidyl-ethanolamine 1,2-distearoyl-sn-glycero-3-phosphoethanolamine-*N*-[amino(polyethyleneglycol)] (DSPE-PEG-NH<sub>2</sub>), indicating the successful PEGylation of GO. The zeta potentials further increased toward the positive side to  $-19.3 \pm 0.64$  mV and  $-11.7 \pm 0.82$  mV for GO-CET, and GO-CET/CPT11, respectively, indicating the successful conjugation of CET onto GO-PEG owing to the slightly positive charge of CET (isoelectric point = 8.5) and CPT-11 [39].

The X-ray diffraction (XRD) patterns of graphene and GO are illustrated in Figure 2b. Graphene showed a diffraction peak at  $2\theta = 26.5^\circ$ , which could be indexed to the (001) plane of a cubic cell (JCPDS no. 75-2078). After oxidation, a new peak corresponding to the (002) plane of GO is formed at  $2\theta = 11.6^\circ$ . The interlayer spacing calculated from the Bragg's equation increased significantly from 0.336 nm for graphene to 0.745 nm for GO, due to the introduction of oxygen-containing functional groups during the oxidation step for exfoliation [40]. Further confirmation of the GO structure was provided by Raman spectroscopy, which is often used for characterizing graphene and its derivatives by studying the disorder and defects in crystal structure. As shown in Figure 2c, the Raman spectrum of graphene displays a single G-band at  $1573\text{ cm}^{-1}$ . In contrast, the Raman spectrum of GO displays two strong peaks at  $1351$  and  $1604\text{ cm}^{-1}$ , corresponding to the D and G-bands, respectively. The G-band is attributed to the first-order scattering of the  $\text{sp}^2$  carbon-carbon bond [41], while the D-band represents the defect sites associated with vacancies and grain boundaries [42]. During the oxygenation of graphene to form  $\text{sp}^3$  carbon atoms, the G-band in GO will shift to a higher wavenumber. On the other hand, a broadened D-band will form after oxygenation due to the reduced  $\text{sp}^2$  domain size by the creation of vacancies, defects, and distortions in GO. The  $I_D/I_G$  of GO was 0.84, which confirms the successful preparation of GO as a starting nanomaterial for drug loading.

The Fourier transform infrared (FTIR) spectra further confirmed the successful preparation of GO-CET (Figure 2d). The FTIR spectrum of GO showed major peaks at  $3400\text{ cm}^{-1}$  (OH),  $1731\text{ cm}^{-1}$  (C=O),  $1640\text{ cm}^{-1}$  (C=C),  $1246\text{ cm}^{-1}$  (C-OH), and  $1060\text{ cm}^{-1}$  (C-O). For GO-PEG, additional peaks at  $1460$  and  $2900\text{ cm}^{-1}$  (C-H bending and stretching vibrations in CH<sub>2</sub>) as well as  $945\text{ cm}^{-1}$  (P-O-C) could be assigned to DSPE-PEG-NH<sub>2</sub> in PEGylated GO. As for GO-CET, a new peak at  $1640\text{ cm}^{-1}$ ,



corresponding to C=N bond formation between the amine groups of DSPE-PEG-NH<sub>2</sub> in GO-PEG and the aldehyde groups of activated CET (Figure 1a), provides strong evidence of successful CET conjugation through amide bond formation. From chemical analysis, the amount of NH<sub>2</sub> in GO-PEG, for conjugation with CET, is estimated to be  $1.2 \times 10^{-4}$  mmol/g GO from 2,4,6-trinitrobenzene sulfonic acid (TNBSA) assays. Using excess CET for reacting with GO-PEG, we successfully synthesize GO-CET with 0.14 mg CET/mg GO-CET from protein assays. This density of CET, an EGFR antibody, is deemed suitable to be recognized by the overexpressed EGFR moiety on the U87 cancer cell surface for active targeting [43].

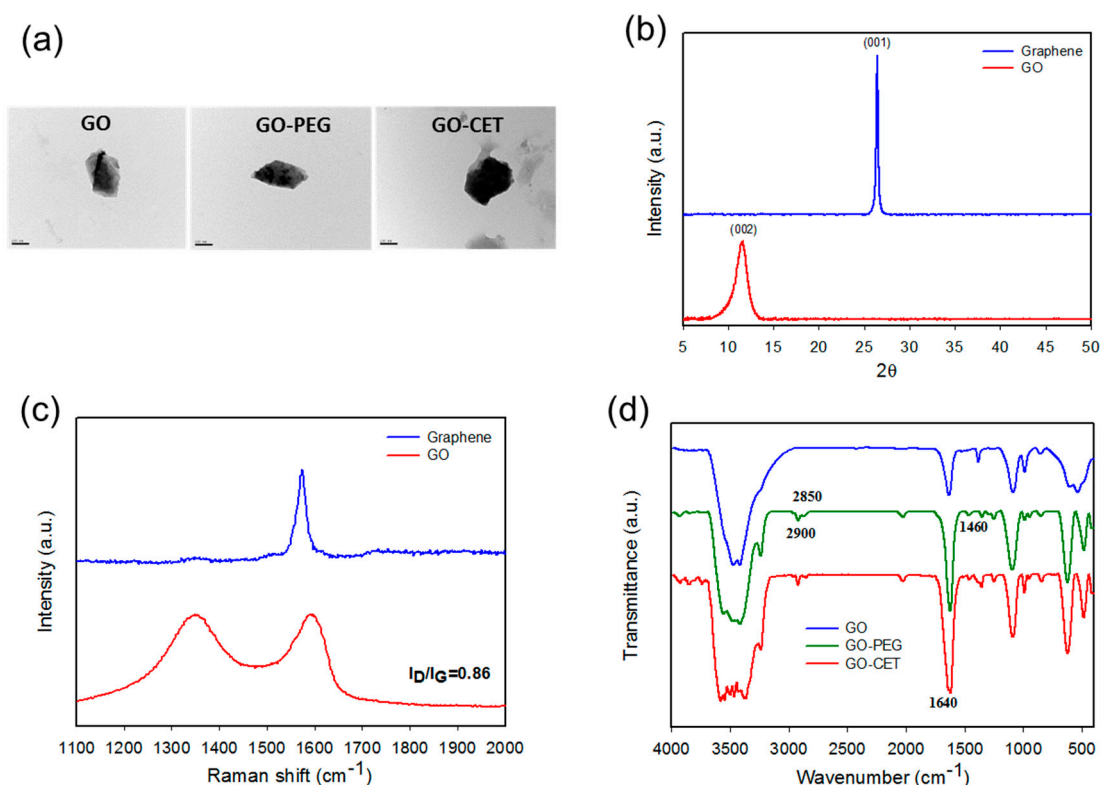


**Figure 2.** Characterization of nanocarriers by transmission electron microscopy (TEM) (bar = 100 nm) (a), X-ray diffraction (XRD) (b), Raman spectroscopy (c), and Fourier transform infrared (FTIR) spectroscopy (d).

## 2.2. Synthesis and Characterization of CPN

The CPN copolymer was prepared according to Figure 1b and characterized. The zeta potential of PNIPAM-COOH displayed a negative surface potential ( $-7.85 \pm 0.39$  mV) due to the dissociation of protons from the -COOH end groups in water. After grafting PNIPAM-COOH to chitosan, the surface potential of CPN turns positive to  $6.14 \pm 0.76$  mV, due to consumption of the negative charges associated with the carboxylate groups during the formation of the neutral amide bonds as well as remnant positive charges associated with protonated primary amine groups in the chitosan backbone. As shown from the FTIR spectra in Figure 3a, PNIPAM-COOH displayed characteristic peaks assigned to amide bonds at  $1654 \text{ cm}^{-1}$  (C=O) and  $1565 \text{ cm}^{-1}$  (N-H) as well as C-H peaks assigned to the isopropyl group at  $1380 \text{ cm}^{-1}$ . The characteristic peaks at  $1100 \text{ cm}^{-1}$ ,  $1565 \text{ cm}^{-1}$ , and  $1654 \text{ cm}^{-1}$  in the spectrum of chitosan could be assigned to the C-O stretching of chitosan skeletal ether bonds, N-H bending vibration of the primary amino group, and the C=O stretching vibration. For CPN, we could use the peak corresponding to C-H in the isopropyl groups at  $1380 \text{ cm}^{-1}$  for the positive identification of PNIPAM in CPN, as characteristic amide bands are overlapping with PNIPAM and chitosan. In addition, the C-O absorption bands of chitosan are clearly observed at  $1100 \text{ cm}^{-1}$  for identifying the chitosan backbone in CPN. From thermogravimetric analysis (TGA), PNIPAM-COOH showed a peak decomposition

temperature at 380 °C with 5.1% residual weight at 500 °C (Figure 3b). By grafting PNIPAM-COOH to chitosan to form CPN, the peak decomposition temperature shifted to 390 °C, together with increased residual weight (11.5%) at 500 °C. Using the difference in the residual weight between PNIPAM-COOH and CPN, the weight percentage of chitosan in CPN could be estimated to be  $\approx 18\%$  considering the residual weight of chitosan (40.7%).

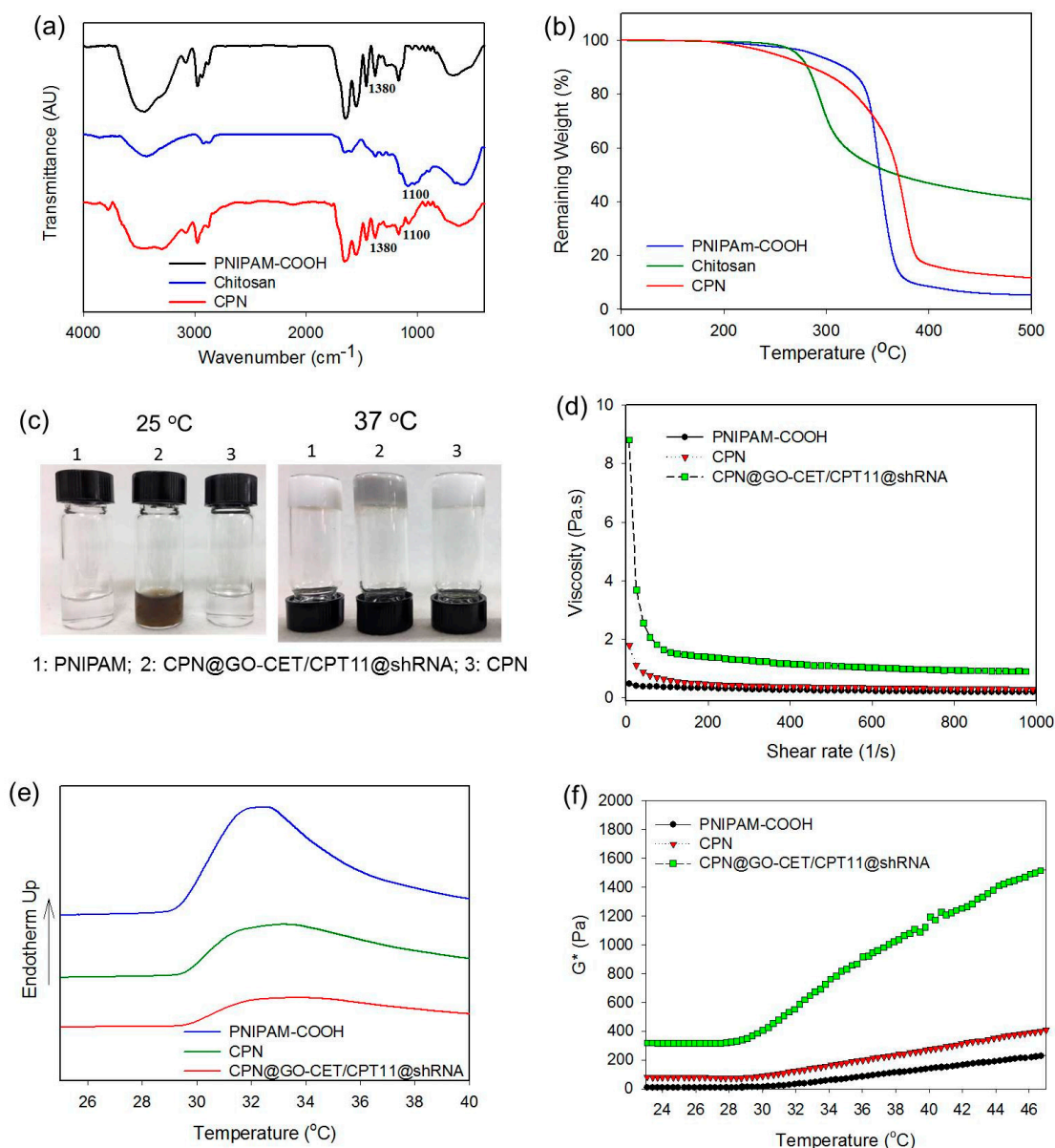


**Figure 3.** Characterization of PNIPAM-COOH, chitosan, and CPN by Fourier transform infrared (FTIR) spectroscopy (a) and thermogravimetric analysis (TGA) (b). (c) Gross view of sol–gel phase transition of 10% (w/v) polymer solution from 25 °C (solution) to 37 °C (gel). (d) The viscosity of 10% (w/v) polymer solution at 25 °C. The sol–gel phase transition was analyzed using a differential scanning calorimeter (DSC) (e) as well as a rheometer to determine the complex shear modulus ( $G^*$ ) (f).

The gross observation of PNIPAM-COOH and CPN polymer solutions indicates both are clear, free-flowing solution and injectable through a syringe needle at 25 °C. At 37 °C, the polymer solution undergoes phase transition from a swollen hydrated state to a shrunken dehydrated state, which forms a rigid hydrogel sticking firmly to the bottom of the inverted vial (Figure 3c). After entrapping GO-CET/CPT11 and shRNA, the CPN polymer solution maintains the same thermo-responsive

characteristic as an injectable delivery vehicle for CPT-11 and shRNA, albeit with a change of appearance color from white to black due to the color of GO (Figure 3c). An ideal injectable hydrogel should offer low resistance to flow after shear, thus a shear thinning behavior. This property is expected to allow the hydrogel solution to be injected with little energy consumption once the plunger starts to move, with the viscosity of the hydrogel solution starting to decrease. In order to determine the hydrogel resistance to flow through a syringe, we studied the effect of shear rate on the viscosity of different polymer solutions at 25 °C. As shown in Figure 3d, PNIPAM-COOH, CPN, and CPN@GO-CET/CPT11@shRNA displayed the desirable shear thinning behavior with decreasing viscosity with increasing shear rate, endorsing the applicability of CPN as an injectable hydrogel vehicle for GO-CET/CPT11 and shRNA delivery.

The phase transition behavior of hydrogel was further subject to differential scanning calorimetry (DSC) analysis. As shown from Figure 3e, the sol–gel phase transition starts at 29.5, 29.6, and 29.6 °C for PNIPAM-COOH, CPN, and CPN@GO-CET/CPT11@shRNA, respectively, with the endothermic peak temperatures at 32.3, 33.0, and 33.3 °C. The endothermic enthalpy change decreased from 2.24 to 1.94 J/g after grafting PNIPAM to chitosan, which further decreased to 1.59 J/g after blending with GO-CET/CPT11 and shRNA. This shift in enthalpy change indicates grafting PNIPAM to chitosan, or the entrapment of GO and shRNA in CPN may facilitate gel formation. To evaluate the temperature-responsive change of hydrogel strength, the complex shear modulus ( $G^*$ ) at different temperatures was determined (Figure 3f). The rise of  $G^*$  values for all samples occurs at around 30 °C, which could be correlated with the sol-to-gel phase transition characteristic of PNIPAM above the lower critical solution temperature. Furthermore, the  $G^*$  were in the order of CPN@GO-CET/CPT11@shRNA >> CPN > PNIPAM, especially after gel formation, indicating the much improved mechanical property of CPN hydrogel. The significantly enhanced mechanical strength of CPN in the presence of GO and shRNA, which is beneficial for maintaining the shape of the implanted composite hydrogel after intratumoral delivery, could be ascribed to the electrostatic interaction between the positively charged CPN and the negatively charged GO-CET/CPT11 and shRNA. Taken together, encapsulating GO-CET/CPT11 and shRNA in CPN not only retains the thermo-responsive natures of CPN for the injectable delivery of therapeutics, it also greatly strengthens the mechanical property of CPN@GO-CET/CPT11@shRNA composite hydrogel formed in situ.

### 2.3. Loading and Release of CPT-11

The loading efficiency and loading content of CPT-11 on GO-CET was reported in Figure 4a, when different amounts of CPT-11 was mixed with 0.5 mg of GO-CET. At higher CPT-11 concentrations for drug loading, the drug loading content (weight of CPT-11 loaded per unit weight of GO-CET) increased from 29.3% to 231%. On the contrary, the loading efficiency (weight percentage of initial CPT-11 loaded on GO-CET) decreased from 73.2% to 44.4%. As space available for CPT-11 binding on GO-CET is limited, the drug loading content increases with drug concentration up to 1.8 mg, after which it shows saturation by approaching the maximum loading capacity. For drug loading efficiency, the trend shown from the drug loading content gives a somewhat flat loading efficiency curve initially, followed by a rapid decrease of loading efficiency after 1.8 mg CPT-11 (Figure 4a). Thus, a dramatic increase in drug loading content led to a detrimental decrease in loading efficiency. To obtain a suitable formulation, an ideal tradeoff between the loading content and loading efficiency should be taken into consideration. Taken together, missing CPT-11 with 0.5 mg GO-CET was deemed the best formulation, which provided 220% loading content and 61.3% loading efficiency. This preparation was used in all studies herewith.

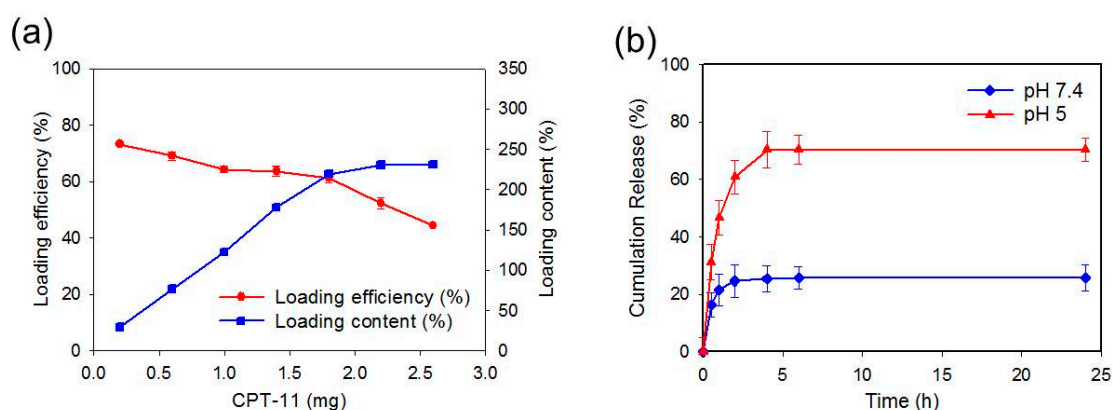


**Figure 4.** (a) Drug loading efficiency (weight percentage of initial CPT-11 loaded on GO-CET) and drug loading content (weight of CPT-11 loaded per unit weight of GO-CET) when a drug solution with different amounts of CPT-11 was reacted with 0.5 mg GO. (b) CPT-11 release from GO-CET/CPT11 at pH 7.4 and pH 5 in PBS (37 °C).

Since the release of CPT-11 from GO-CET/CPT11 is preferable after endocytosis for maximum anticancer efficacy, a pH-dependent drug release behavior for GO-CET should be confirmed, even though GO has been widely reported to be endowed with such characteristics for chemotherapy drugs [8]. The release of drug from GO-CET/CPT11 was evaluated from the cumulative percentage of CPT-11 released at 37 °C in pH 7.4 and pH 5 phosphate-buffered saline (PBS) to simulate the physiological condition and the endosomal environment, respectively. As shown in Figure 4b, a burst release of CPT-11 from GO-CET/CPT11 was observed to be pH-dependent, where the percentage of CPT-11 released at pH 5 (70.4%) in 96 h is 2.7-fold that at pH 7.4 (25.8%). The adsorption of CPT-11 to GO-CET involves hydrogen bonding between  $-\text{COOH}$  of GO-CET and  $-\text{OH}$  of CPT-11. As hydrogen bond formation is pH-dependent, more protons will compete with functional groups responsible for hydrogen bonding at pH 5 than at pH 7.4. This can weaken the interactions between CPT-11 and GO-CET and lead to substantially more released CPT-11 under acidic condition. This pH-sensitive CPT-11 release behavior from GO-CET will facilitate the prompt and enhanced drug release in the acidic endosomal environment, which will cause specific cell killing by poisoning topoisomerase in cancer cells after the endocytosis of released GO-CET/CPT11 from CPN due to shedding of the hydrogel [44].

#### 2.4. Degradation of CPN and Release of CPT-11 and shRNA from CPN

A desired degradation behavior of hydrogels is important for biomedical applications. Furthermore, as the release of CPT-11 and shRNA CPN is dependent on the degradation of CPN, which leads to the release of GO-CET/CPT11 and shRNA, we studied the degradation (dissolution) of CPN based on the residual weight of hydrogel after incubation in PBS (pH 7.4). CPN showed gradual weight loss due to the dissolution of CPN polymer in PBS with about 62% weight loss in 28 days (Figure 5a). This slow degradation leads to the much improved sustained release of CPT-11 from CPN@GO-CET/CPT11@shRNA up to 28 days, in a slower and controlled manner, compared with GO-CET/CPT11 (burst release in 6 h) (Figure 5b) [45]. Therefore, entrapping GO-CET/CPT11 in CPN provided an effective modulation of the burst release of drug at the extracellular environment (physiological pH). After CPN degradation and the shedding of GO-CET/CPT11 that targets cancer cells through CET/EGFR interaction, copious CPT-11 would be released from GO-CET/CPT11 in the acid endosomal environment of cancer cells due to improved drug release at pH 5 (Figure 4b) to exert maximum therapeutic effect.



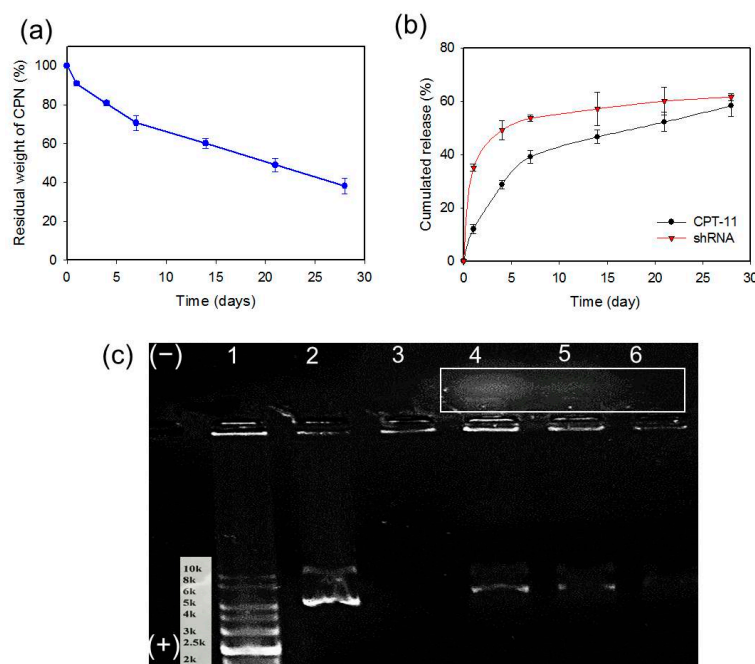


**Figure 5.** The degradation of CPN in pH 7.4 PBS at 37 °C (a) and the release of CPT-11 and SLP2 shRNA from CPN@GO-CET/CPT11@shRNA at pH 7.4 in phosphate-buffered saline (PBS) at 37 °C (b). (c) The agarose gel electrophoresis analysis of released shRNA. 1: marker; 2: shRNA; 3: release solution of CPN@GO on day 21; 4: release solution of CPN@GO-CET-CPT11@shRNA on day 4; 5: release solution of CPN@GO-CET-CPT11@shRNA an day 14; 6: release solution of CPN@GO-CET-CPT11@shRNA on day 21. The rectangle area indicates a population of shRNA/CPN complex (polyplex) migrating toward the negative electrode detected in the release solution of CPN@GO-CET/CPT11@shRNA.

A similar sustained release behavior was also observed for shRNA released from CPN@GO-CET/CPT11@shRNA, but with faster kinetics compared to CPT-11 (Figure 5b). A burst release was observed for 7 days followed by sustained release up to 28 days. The release of shRNA also matches the rate of CPN degradation in PBS at pH 7.4 (Figure 5a), suggesting that the dissolution of CPN polymer from the hydrogel leads to the shedding of shRNA from the hydrogel. It should be noted since the release of drug or shRNA from CPN hydrogel was tested in vitro in PBS, we could expect a much higher release rate of CPT-11 and shRNA with the hydrolysis of chitosan by lysozyme in vivo for timely anticancer effects.

The shRNA release was subject to gel electrophoresis studies by gel retardation assays of shRNA in the release solution. As shown in Figure 5c, shRNA was detected in the release solution up to 21 days, to be consistent with its release curve in Figure 5b. The migration ability of released shRNA from CPN@GO-CET/CPT11@shRNA toward the positive electrode (+) was similar to that of free shRNA as expected in open-circular, linear, or supercoiled forms. Nonetheless, a population of smear shRNA bands was found migrating toward the negative electrode (−), in contrast to shRNA that migrated toward the positive electrode (+) originating from the negative charge associated with the phosphate groups present. We postulated that this positively charged shRNA complex arises due to polyplex formation when shRNA was complexed with CPN in the release solution. As CPN molecules were entangled with shRNA in the release solution in different ratios, their positive charges eventually moved shRNA/CPN complexes to the negative electrode (−) [46]. Indeed, the negatively charged shRNA is inclined to be wrapped around by the positively charged CPN polymer chains due to electrostatic interaction. As CPN forms a polyplex with shRNA with N/P ratios (the ratio between the protonated amines from the chitosan and the negatively charged phosphate groups from nucleic acid) higher than 1, the negative charge of shRNA will be reversed into a positive one and can change the migration direction during gel electrophoresis [47]. Taken together, by incorporating shRNA within CPN, the injectable hydrogel will provide a preferred milieu for shRNA delivery by using the degraded



CPN copolymer in the solution as a favorable nonviral vector for the delivery of plasmid shRNA, which could protect and transport shRNA to the cytoplasm of cancer cells.

### 2.5. Intracellular Uptake

The high expression of EGFR on the U87 glioblastoma cell surface is expected to facilitate the active targeting of U87 cells by using CET, an EGFR antibody, as a ligand. This targeting effect could be visualized through the intracellular uptake of fluorescently labeled GO or GO-CET (green fluorescence) under a confocal microscope (Figure 6). The confocal images confirmed that U87 demonstrated a higher intracellular uptake of GO-CET than GO from the intensity of green fluorescence signals. Without EGFR conjugation, GO still exhibited limited fluorescence signals, as nano-sized GO could enter cells mainly through clathrin-mediated endocytosis [48]. The internalization of GO-CET by U87 was restricted when cells were pre-treated with CET, indicating that CET pretreatment will saturate the EGFR on the U87 surface, rendering their inaccessibility to be recognized by GO-CET. To further confirm the process of endocytosis, the U87 cells were also stained for lysosomes with LysoTracker (red fluorescence) in Figure 6. The enclosure of GO-CET within lysosomes after cellular internalization could be clearly identified with merging of green and red fluorescence signals. Taken together, the confocal microscopy results indicate that the intercellular uptake of GO-CET by U87 cells could be augmented via active targeting by conjugated CET.

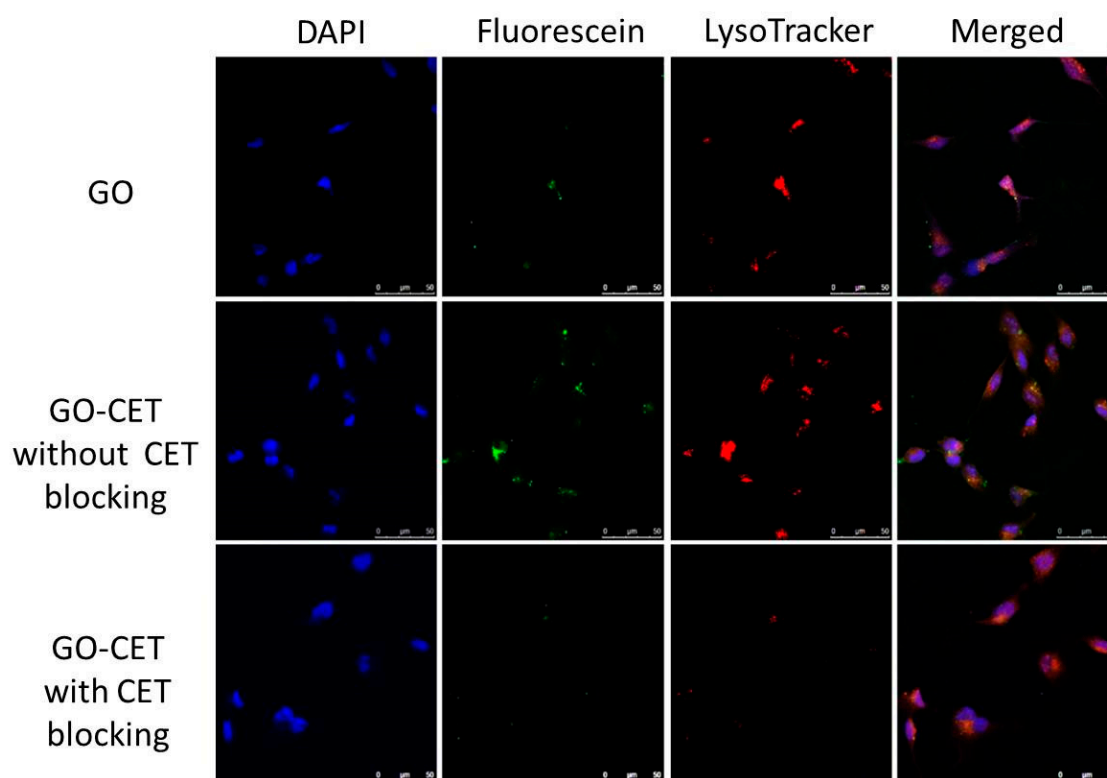


**Figure 6.** The intracellular uptake of fluorescein-labelled GO and GO-CET (with or without CET blocking) by U87 cells was studied by confocal laser scanning microscopy analysis. The cell nuclei showed blue fluorescence after staining with 4',6-diamidino-2-phenylindole dihydrochloride (DAPI) and GO (or GO-CET) showed green fluorescence by labeling with fluorescein, and lysosomes showed red fluorescence after staining with LysoTracker. Bar = 50 µm.

### 2.6. In Vitro Biocompatibility of GO and Cytotoxicity of CPT-11-Loaded GO

The in vitro biocompatibility of the GO was evaluated by the 3-(4,5-dimethylthiazol-2-yl)-5-(3-carboxymethoxyphenyl)-2-(4-sulfophenyl)-2H-tetrazolium (MTS) assays using normal cell line (3T3 fibroblasts). From Figure 7a, we could confirm that GO is biocompatible at a concentration up

100 µg/mL in cell culture medium with relative cell viability (compared to culture medium) higher than 90%. Once confirming the cellular internalization characteristic and the safety of the nanocarriers, we sought to study the drug cytotoxic efficacy with free and GO-bound CPT-11. From Figure 7b, GO-CET/CPT11 exerted the most cytotoxic effect toward U87 with the lowest IC<sub>50</sub> (6.21 µg/mL), in comparison with 32.50 and 94.86 µg/mL for GO/CPT11 and CPT-11, respectively. Undoubtedly, an enhanced cytotoxic effect could be attributed to the CET-mediated active targeting of GO-CET/CPT11 toward the EGFR over-expressed U87 cells. Considering the better performance of GO/CPT11 over CPT-11 at higher drug concentrations, a previous report reported that CPT-11 loaded to GO will lead to higher cytotoxicity in HepG2 and HeLa cell lines due to the limited water solubility of CPT-11, which would be improved by using GO/CPT11 that shows good aqueous solubility [49]. Thus, the difference in cytotoxicity toward U87 cells between CPT-11 and GO/CPT11 was enhanced at higher CPT-11 concentration.

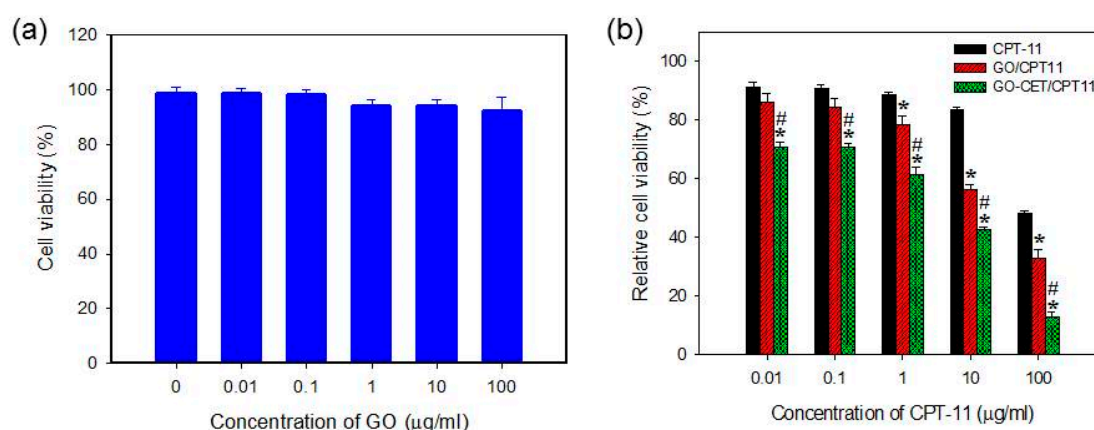


**Figure 7.** The biocompatibility of GO tested with 3T3 fibroblasts (a) and cytotoxicity of CPT-11 toward U87 cancer cells in different formulations (b). \*  $p < 0.05$  compared with CPT-11, #  $p < 0.05$  compared with GO/CPT11.

## 2.7. Gene Delivery, Gene Silencing, and Migration Inhibition of U87 Cells with SLP2 shRNA

The RNA interference (RNAi) is a viable strategy for functional gene silencing in tumor cells by inducing function loss of the targeted gene [50]. To mediate the RNAi effect, both small interfering RNA (siRNA) and short hairpin RNA (shRNA) could be used in addition to bi-functional shRNA. With the simplicity of manufacturing and the transient effect, siRNA is most suited for certain medical disorders such as viral injections. In contrast, optimized shRNA constructs will allow for high and sustainable potency at low copy numbers with the endogenous processing mechanism to result in less off-target effects [51]. A nonviral vehicle for the delivery of shRNA is typically a cationic preparation with its positive charge facilitating complexation with negatively charged nucleic acids. Therefore, we use CPN as the vehicle for the delivery of SLP2 shRNA. After shedding from the CPN vehicle, we expect that the CPN polymer will complex with shRNA to form polyplex due to the electrostatic interactions as supported from Figure 5c. The shRNA/CPN complex will bind to the negatively charged cell membrane to promote endocytosis and once endocytosed, CPN's positive charge could facilitate early escape from the endosome [52]. Once entering the cytoplasm, the shRNA expression vector will be transported into the nucleus for processing into the primary transcripts (pre-shRNAs). The pre-shRNAs will subsequently be transported to the cytoplasm, followed by further processing into mature shRNA to exhibit RNAi function either through translational suppression or mRNA degradation [53].

To confirm that the SLP2 shRNA could be inserted into genes of targeted cancer cells to exert its RNAi function, we proceed to identify the expression of the green fluorescent protein (GFP) in U87 cells after being transfected with different formulations of shRNA by taking advantage of the

reporter GFP gene encoded in SLP2 shRNA plasmids. As shown in Figure 8a, CPN@GO-CET@shRNA exhibited much higher transfection efficiency compared to free shRNA, which shows a minimum expression of GFP protein similar to the vehicle without shRNA (CPN@GO-CET), indicating that SLP2 shRNA plasmid could easily enter the negatively charged cellular membranes after being entrapped in and released from the positively charged CPN. This endorsed our intended use of the chitosan-based hydrogel in gene delivery with chitosan reported to be a desirable nonviral vector with advantages such as low toxicity, low immunogenicity, and excellent biocompatibility [54]. Additionally, there is a continuous time-dependent increase of GFP expression (Figure 8a), coinciding with the sustained release of SLP2 shRNA from the CPN hydrogel (Figure 5b). By comparing with the transfection with shRNA where a minimum expression of GFP was found, we demonstrate that the inefficient gene transfection using free SLP2 shRNA could be drastically improved, possibly by the formation of polyplex between shRNA and CPN before entering cell cytoplasm (Figure 5c) [55].

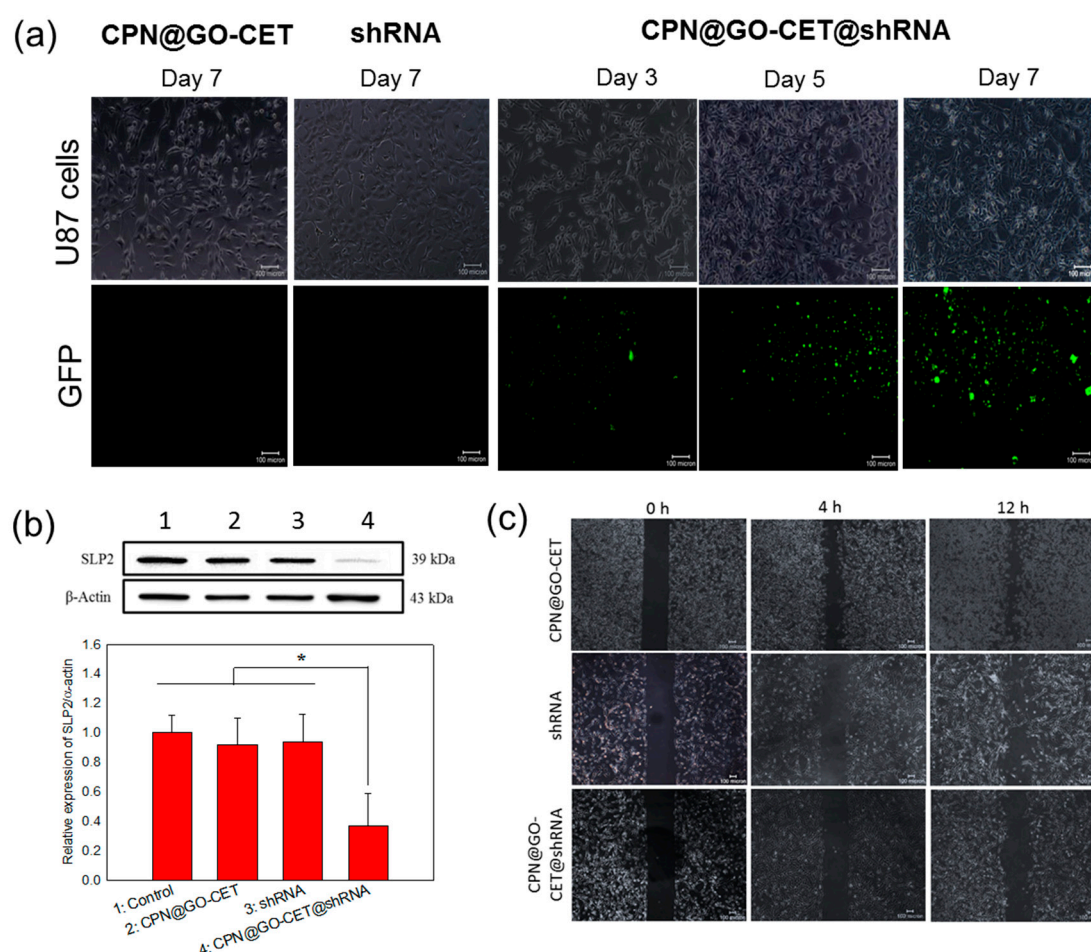


**Figure 8.** Transfections of U87 cancer cells with CPN@GO-CET@shRNA could knockdown SLP2 gene expression and inhibit cancer cell migration. (a) The transfection efficiency was determined from green fluorescent protein (GFP) expression with the fluorescence images shown below the corresponding bright-field images (bar = 100  $\mu$ m). The effects of SLP2 shRNA on SLP2 expression level in U87 cells were examined by Western blot analysis using  $\beta$ -actin as a loading control (b) and wound-healing assays for cell migration ability (bar = 100  $\mu$ m) (c) after U87 cells were transfected with CPN@GO-CET, shRNA and CPN@GO-CET@shRNA for 5 days. \*  $p < 0.05$ .

The confirmation of successful knockdown of the SLP2 gene was undertaken by Western blot analysis of SLP2 protein expression in transfected U87 cells. As shown in Figure 8b, consistent with GFP protein expression, the Western blot analysis clearly demonstrated that SLP2 depletion only

occurred when U87 cells were transfected with CPN@GO-CET@shRNA, which shows significantly lower SLP2 protein expression than other groups. Indeed, the CPN@GO-CET@SLP2shRNA treatment substantially reduced the level of SLP2 protein to 35% compared to cells transfected with free shRNA and the vehicle (CPN@GO-CET). A previous study shows the inhibition of cell proliferation and mobility and some alteration of cell cycle by knockdown of the SLP2 gene, but without a noticeable change of cell apoptosis rate [56]. To confirm that the depletion of SLP2 will lead to such effects, we used the wound-healing assay, which is an integrated process of cell migration and proliferation, to examine the migration ability of transfected U87 cells. The SLP2-depleted U87 cells and control cells were detached from the well surface 5 days post-transfection. After seeding into new 24-well plates with equal cell numbers, the cells were subjected to scratch wounding on the next day after the formation of a confluent monolayer. As shown in Figure 8c, the migration of U87 was inhibited due to the knockdown of the SLP2 gene. Although the cells in shRNA and CPN@GO-CET groups migrated rapidly into the wound area to cause higher wound closure within 12 h, a significant wound closure inhibition was observed in the SLP-2 depleted cells. The recovered wound areas compared with the initial wound area are  $16.7 \pm 1.3\%$  and  $30.7 \pm 2.0\%$  for CPN@GO-CET@shRNA at 4 and 12 h, respectively. These values are significantly less than those for CPN@GO-CET ( $47.5 \pm 2.3\%$  at 4 h and  $59.7 \pm 2.6\%$  at 12 h) and shRNA ( $45.6 \pm 1.2\%$  at 4 h and  $57.9 \pm 3.3\%$  at 12 h), which showed no significance between them.

## 2.8. Cell Cytotoxicity and Apoptosis of CPT-11-Loaded GO in CPN

As a final confirmation of the enhanced cytotoxicity of CPN@GO-CET/CPT11 toward U87 cancer cells, we studied cell cytotoxicity by MTS assays and cell apoptosis by flow cytometry in comparison with the vehicle (CPN@GO and CPN@GO-CET). As shown in Figure 9a, the relative cell viability of CPT-11 loaded CPN (CPN@GO-CET/CPT11) is less than half of that in CPT11-free vehicle (CPN@GO and CPN@GO-CET). The less than 5% cell death in CPN@GO and CPN@GO-CET groups also endorse the biocompatibility of CPN.

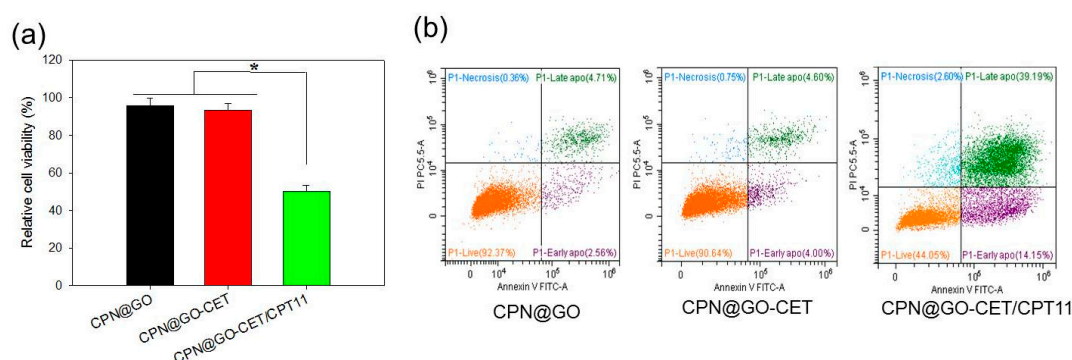


**Figure 9.** Cell cytotoxicity and cell apoptosis induced by different CPN formulation using U87 cells by 3-(4,5-dimethylthiazol-2-yl)-5-(3-carboxymethoxyphenyl)-2-(4-sulfophenyl)-2H-tetrazolium (MTS) assays (a) and flow cytometry (b). \*  $p < 0.05$ .

To further assess the cytotoxic effect of CPN@GO-CET/CPT11, we preformed flow cytometry analysis by staining the cells with Annexin V/propidium iodide (PI) to quantitatively determine the distribution of live, apoptotic, and necrotic cells from the change of cell membrane permeability and integrity (Figure 9b). U87 were co-cultured with CPN@GO-CET and CPN@GO-CET/CPT11 for 48h. The CPN@GO group showed the cell survival and apoptosis rate to be 92.37% and 7.27%, respectively. For CPN@GO-CET, a comparable cell survival (90.64%) and apoptosis rate (8.69%) was observed, supporting the safety and biocompatibility of CPN and GO as before. The slightly higher apoptosis rate in CPN@GO-CET could be attributed to the fact that CET may cause cytotoxicity to EGFR-expressing cancer cells, as CET is a U.S. Food and Drug Administration (FDA)-approved



drug for treating colon and head/neck cancers [57]. However, treatment with CPN@GO-CET/CPT11 revealed the most pronounced decrease of cell survival (44.05%) and the increase of apoptotic rate (53.34%), without a significant change in the ratio of necrotic cells, to be consistent with the anti-tumor mechanism of CPT-11. Taken together, in accordance with the anti-tumor mechanism of CPT-11, our data supported that CPN@GO-CET/CPT11 will lead to enhanced U87 cancer cell killing by the induction of apoptosis [58].

### 2.9. Degradation and Biocompatibility of CPN@GO In Vivo

As the desired degradation behavior and excellent biocompatibility of hydrogels are crucial for biomedical applications, we started the animal study by investigating the biodegradability and biocompatibility of CPN@GO in vivo (Figure 10a). This was accomplished by injection of 0.2 mL 10% (*w/v*) GO-containing CPN hydrogel solution into the subcutaneous pocket in the right flank of a nude mouse to form a rigid gel mass. By continuously monitoring the implanted area, we did not observe any signs when a toxic injectable hydrogel is tested in vivo such as erythematous change around subcutaneous mass, skin necrosis, or even pus formation (Figure 10a) [59]. The gel mass continued to degrade in the subcutaneous layer after implantation, and complete degradation was found after 3 weeks. That CPN hydrogel degraded faster in vivo than in vitro (Figure 5a), which could be due to several factors, is generally in line with previous studies [60]. There was also no significance difference in mouse body weight between the control group without implantation and the CPN@GO group, suggesting that the implantation of CPN@GO might not have a detrimental effect on the mice.

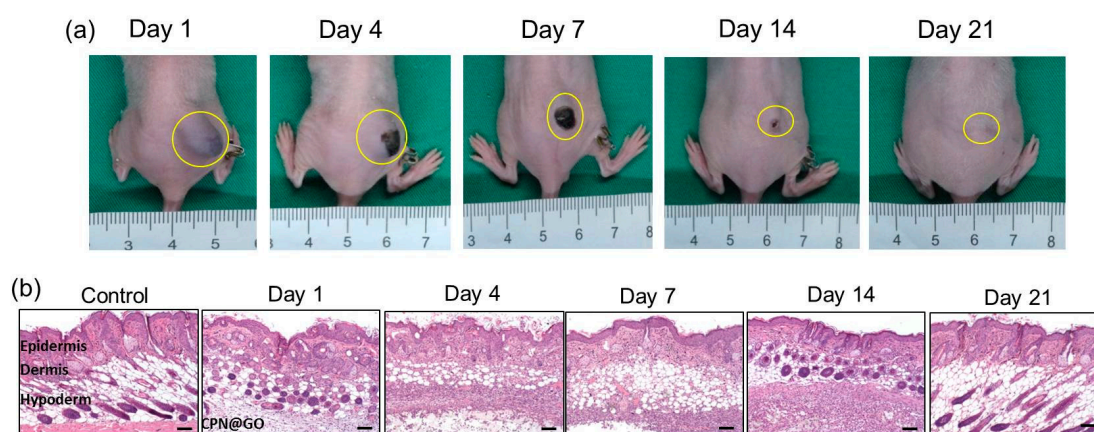


**Figure 10.** The in vivo degradation of CPN@GO hydrogel after the subcutaneous injection of a polymer solution containing 10% (*w/v*) CPN and 0.5% (*w/w*) GO to the right flank of a nude mouse. Gross view images were taken at different time points post-implantation (a), and the tissues surrounding the hydrogels were dissected and subject to hematoxylin–eosin (H&E) stain (b).

The in vivo biocompatibility was further tested by histological examination (hematoxylin–eosin (H&E) staining) of the tissue surrounding the injected hydrogel at given time points (Figure 10b). No significant necrosis, edema, hemorrhaging, and hyperemia were noted in all tissue sections, except for a mild acute inflammation with enhanced neutrophils in tissues 14 days post-injection. Nevertheless, the inflammation was reduced steadily as the hydrogel degraded completely on day 21, demonstrating an acceptable biocompatibility of CPN hydrogel in vivo.

### 2.10. Anticancer Efficacy in Xenograft Nude Mice Animal Model

The CPN hydrogels containing SLP2 shRNA and GO-CET/CPT-11 were studied in a xenograft tumor model in mice to evaluate the in vivo combinatory anti-tumor efficacy. For this purpose, BALB/c mice bearing U87 tumors in the right flank area were divided into three groups ( $n = 6$  in each group) and subject to intratumoral administration of 50  $\mu$ L of PBS (control), 10% (*w/v*)



hydrogel solution (CPN@GO-CET), or 10% (*w/v*) CPT-11 and shRNA co-encapsulated hydrogel solution (CPN@GO-CET/CPT11@shRNA). The body weight of mice and tumor size were continuously monitored up to 12 days post-treatment. Although initial weight loss was noted for the hydrogel groups for up to 5 days, no obvious body weight loss was observed at the end of observation period, demonstrating minimum systemic toxicity though the localized injection of hydrogels with or without GO-CET/CPT-11 and shRNA (Figure 12a). Considering the change of tumor size shown in Figure 12b, mice in hydrogel groups (CPN@GO-CET or CPN@GO-CET/CPT11@shRNA) started showing an abrupt increase of tumor size at the first observation period after treatment (day 1) compared with the control, which could be ascribed to the volume occupied by the intratumorally injected hydrogel mass (Figure 10a). Most importantly, the tumor volume increased rapidly during the time series of observation beyond day 1 in the control and CPN@GO-CET groups, in contrast to the CPN@GO-CET/CPT11@shRNA group, in which the tumor size was maintained at nearly a constant value close to that on day 1 to the end of the observation period. On the final observation day (day 12), the tumor volume in the CPN@GO-CET/CPT11@shRNA treated group ( $335.3 \pm 139.1 \text{ mm}^3$ ) was significantly less than that in control ( $826.2 \pm 80.9 \text{ mm}^3$ ) and CPN@GO-CET groups ( $886.7 \pm 140.5 \text{ mm}^3$ ), which showed no significant difference between them. This was also supported from the gross observation of the explanted tumor mass on day 12 in Figure 12c. Taken together, we can conclude that CPN@GO-CET possesses neither anti-tumor efficacy nor systemic toxicity to the host after injection. Nonetheless, treatment with hydrogels loaded with GO-CET/CPT-11 and shRNA displayed a remarkably anti-tumor efficacy, whose mechanism is fully supported from the *in vitro* experiments. The sustained and controlled release of CPT-11 and SLP2 shRNA from the hydrogel (Figure 5b) will lead to the targeted delivery of CPT-11 (Figure 6) and efficient transfection of U87 (Figure 8a), which results in cell apoptosis by CPT-11 released in the endosomes (Figure 9b) as well as reduced SLP2 protein expression (Figure 8b) and inhibited cell migration (Figure 8c) associated with gene silencing by RNAi.

Bioluminescence imaging (BLI) through an *in vivo* imaging system (IVIS) has been suggested to be a gold standard for evaluating the preclinical efficacy of drug candidates in brain tumor therapy [61]. On the other hand, as the tumor volume might be influenced by injected hydrogel, we sought to confirm the anti-tumor efficacy results from tumor volume measurement with BLI using IVIS. As shown from Figure 12d, the remarkable anti-tumor efficacy of CPN@GO-CET11/CPT11@shRNA treatment manifests itself from the representative IVIS images of tumor-bearing nude mice on day 12. The value of BLI after normalization was calculated after standardization of the bioluminescent signal intensity on day 12 with that on day 0 when the treatment started. The BLI analysis clearly indicated that the CPN@GO-CET/CPT11@shRNA group showed remarkable treatment benefits over control and CPN@GO-CET with a significant reduction of normalized BLI signal intensity, echoing what has been observed from tumor volume measurements.

At day 12, the harvested tumors were subject to histological analysis. As shown in Figure 11, the H&E staining indicates the substantial and mild necrosis of tumor tissue in the CPN@GO-CET/CPT11@shRNA group. However, cell growth was noticed in the control and CPN@GO-CET groups. Indeed, there was no evidence of necrosis in the H&E staining slides for tumor samples in the control and CPN@GO-CET group, whereas significantly more necrosis regions were found in tumors treated with CPN@GO-CET/CPT11@shRNA with a more obvious cavitation phenomenon in coagulative necrosis. These results demonstrated that the intratumoral delivery of CPN@GO-CET/CPT11@shRNA enhanced the anti-tumor efficacy, suggesting it to be an excellent treatment for cancer therapy. Improved tumor therapy should also inhibit the proliferation of cancer cells. The immunohistochemistry (IHC) analysis by staining tumor sections with cell proliferation marker Ki-67 antibody showed high immunoreactivity for control and CPN@GO-CET groups due to the active proliferation of tumor cells in tumor samples retrieved from animals in these groups. In comparison, the tumor sample retrieved from animals subject to CPN@GO-CET/CPT11@shRNA treatment displayed weak Ki-67 immunoreactivity with minimum Ki-67 expression due to the apoptosis of U87 cancer cells (Figure 11). These results could be further supported by staining the apoptosis biomarker phosphorylated extracellular signal-regulated kinases

(pERK) protein in the tumor tissue (Figure 11), which showed an intense expression of pERK protein only in the tumor tissue of CPN@GO-CET/CPT11@shRNA-treated mice. The cancer cells also showed much less SLP2 protein expression after gene knockdown by the efficient delivery of SLP2 shRNA using CPN to confirm successful RNAi therapeutics in vivo (Figure 11).

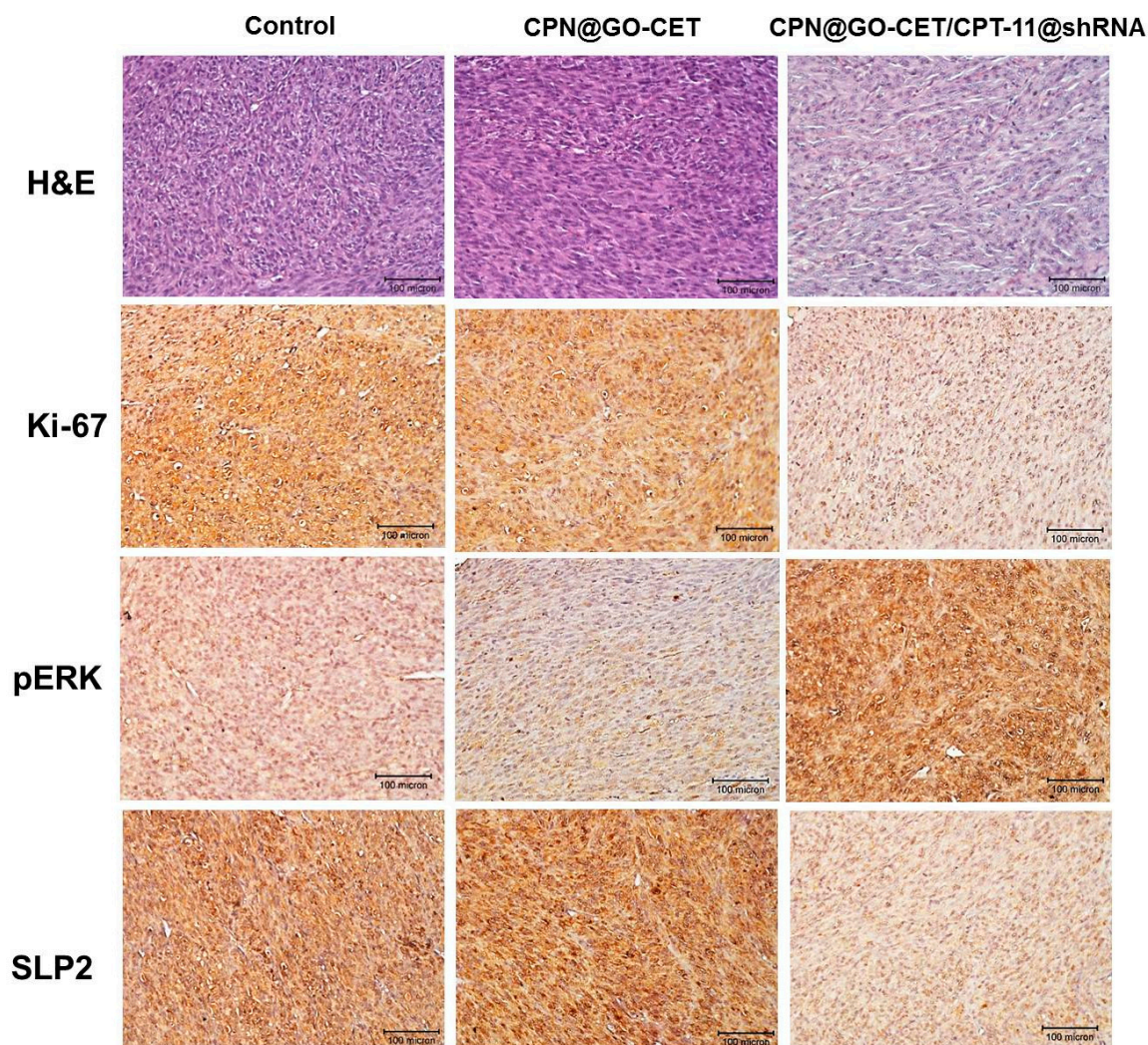


**Figure 11.** The H&E stain and immunohistochemistry (IHC) analysis of Ki-67, phosphorylated extracellular signal-regulated kinases (pERK), and SLP2 of U87 tumors in control group and groups treated with CPN-GO-CET or CPN@GO-CET/CPT11@SLP2shRNA (bar = 100  $\mu$ m).



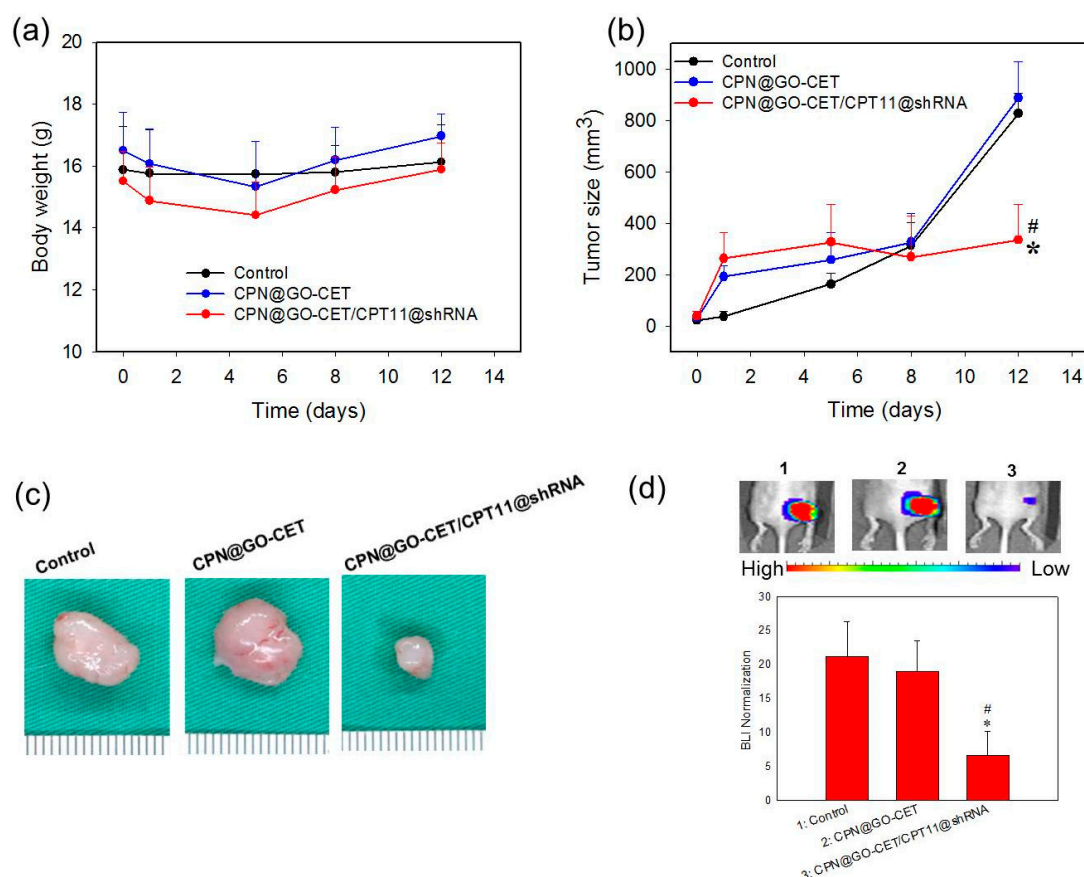


**Figure 12.** The anti-tumor activity induced by the intratumoral delivery of CPT-11 (40 mg/kg) and SLP2 shRNA (3.33 mg/kg) with CPN to U87 tumor bearing nude mice. The treatment was initiated on day 0 and the tumor size was measured on days 1, 5, 8 and 12 post-treatment. The body weight (a) and tumor size (b) at different times points were determined for three treatment groups including PBS (control), CPN@GO-CET (vehicle), and CPN@GO-CET/CPT11@shRNA ( $n = 6$ , mean  $\pm$  SD). (c) The gross view of the explanted tumor 12 days after different treatments. (d) Representative bioluminescence imaging (BLI) obtained by in vivo imaging system (IVIS) and the BLI normalization on day 12 ( $n = 6$ , mean  $\pm$  SD). \*  $p < 0.05$  compared with control, #  $p < 0.05$  compared with CPN@GO-CET.

### 3. Materials and Methods

#### 3.1. Materials

Graphene powder (N002) and *N*-(aminopropyl polyethyleneglycol)carbonyl-distearoylphosphatidyl-ethanolamine 1,2-distearoyl-sn-glycero-3-phosphoethanolamine-*N*-[amino(polyethyleneglycol)] (DSPE-PEG-NH<sub>2</sub>) (PEG chain molecular weight = 2000) were obtained from Angstrom Materials Inc. (Dayton, OH, USA) and NOF Co. (White Plains, NY, USA), respectively. The SLP2 shRNA expression vector was constructed and purchased from BIOTOOLS Co. Ltd. (Taipei, Taiwan). 1-(3-dimethylaminopropyl)-3-ethylcarbodiimide hydrochloride (EDC) and *N*-hydroxysuccinimide (NHS) were purchased from Acros Organics (Geel, Belgium). Cetuximab (CET) was purchased from Merck (Darmstadt, Germany). Chitosan (deacetylation degree = 98%, molecular weight =  $1.5 \times 10^5$  Da), *N*-isopropylacrylamide (NIPAM), azobisisobutyronitrile (AIBN), mercaptoacetic acid (MAA), 2,4,6-trinitrobenzene sulfonic acid (TNBS), 5(6)-carboxyfluorescein *N*-hydroxysuccinimide ester (fluorescein-NHS), 4',6-diamidino-2-phenylindole dihydrochloride (DAPI), CPT-11, and Dulbecco's Modified Eagle's Medium (DMEM) were purchased from Sigma-Aldrich (St. Louis, MO, USA). Hyclone fetal bovine serum (FBS) purchased from Cytiva (Marlborough, MA, USA) was used for cell culture. Potassium salt of D-luciferin was obtained from Gold Biotechnology Inc. (Taipei, Taiwan).

LysoTracker™ Deep Red for staining lysosomes, Annexin V FITC/PI cell apoptosis kit for flow cytometry, and Pierce™ BCA protein assay kit were acquired from Thermo Fisher Scientific (Waltham, MA, USA). The CellTiter 96® AQueous One Solution Cell Proliferation Assay (MTS) kit for determination of the number of viable cells was provided by Promega Co. (Madison, WI, USA).

### 3.2. Preparation of GO, GO-PEG, GO-CET, and Fluorescently Labeled GO

Graphene nano-platelet was subject to modification following a modified Hummers method [62]. One gram of graphene powder was added to 23 mL 98% H<sub>2</sub>SO<sub>4</sub> and stirred on a magnetic stirrer for 12 h, followed by adding 3 g KMnO<sub>4</sub> with continuous stirring for 30 min at 20 °C, 30 min stirring at 40 °C, and 45 min stirring at 65–80 °C. Forty-six milliliters of distilled deionized water (ddH<sub>2</sub>O) was added to the mixture and stirred at 95 °C for 30 min. After cooling for 1 h at room temperature, 140 mL ddH<sub>2</sub>O and 10 mL H<sub>2</sub>O<sub>2</sub> solution (30%) were added, followed by reacting at 40 °C for 5 min. After the reaction, GO was washed with 5% HCl solution and centrifuged at 5000× g to remove the supernatant. This washing process was continued three times, followed by washing with ddH<sub>2</sub>O three times and dialyzed against ddH<sub>2</sub>O until reaching a neutral pH value. The GO was subject to ultrasonication at 500 W for 30 min using a probe sonicator (Qsonica Q700, Newtown, CT, USA), followed by filtering with a 0.2 µm filter to obtain GO nano-platelet for PEGylation. The PEGylation of GO was achieved by modifying the surface of GO with DSPE-PEG-NH<sub>2</sub> through the hydrophobic interaction of heptadecyl end groups of DSPE-PEG-NH<sub>2</sub> with GO. Briefly, 1 mL GO solution prepared in pH 7.4 phosphate-buffered saline (PBS) containing 0.5 mg GO was sonicated for 20 min at 100 W, followed by adding 1.5 mg DSPE-PEG-NH<sub>2</sub> and sonicating for 60 min at 30 W. After centrifugation at 25,000× g for 30 min to remove the supernatant containing unreacted PEG, 1 mL pH 7.4 PBS was added to obtain PEGylated GO (GO-PEG). The amount of DSPE-PEG-NH<sub>2</sub> coated on the GO surface was determined by quantification of its end amine groups using the TNBSA method [63]. This method offers a simple method to determine primary amines by reacting TNBSA with the amine groups to form a chromogenic derivative. By measuring the solution absorbance at 335 nm, the quantification of amines could be achieved by using a standard curve constructed from the amine-containing amino acid glycine.

To conjugate CET onto GO-PEG, amine groups on the GO-PEG surface were reacted with activated CET after oxidation of the carbohydrate moieties in CET (an EGFR antibody) to aldehydes [39]. For this purpose, a 0.1 mg/mL CET solution was prepared in 1 mL ddH<sub>2</sub>O, which was followed by adding 0.2 mL of 0.1 M NaIO<sub>4</sub> dropwise to open the saccharide rings between vicinal diols and leaving two aldehyde groups for spontaneous reaction with the amine groups on GO-PEG. The solution was purified by passing through a PV-10 desalting column (GE Healthcare, Chicago, IL, USA) using sodium acetate solution (pH 4.3) as elution buffer and sodium carbonate solution (pH 9.5) as stopping buffer to obtain purified CET-CHO. The purified CET-CHO (40 µL) was reacted with GO-PEG (0.5 mg/mL) in 1 mL sodium carbonate buffer (pH 9.5) for 1 h, which was followed by mixing with 50 µL 0.4 mg/mL NaBH<sub>4</sub> as a reducing agent to stabilize the covalent bonds. After centrifugation at 40,000× g for 30 min, GO-CET was recovered in the precipitate and washed with pH 7.4 PBS twice. The concentration of CET in the collected supernatant was quantified using the BCA protein assay kit to calculate the amount of CET in GO-CET by mass balance. To visualize the intracellular uptake of GO-CET, fluorescently labeled GO or GO-CET was prepared by separately reacting them with fluorescein-NHS for 1 h at room temperature, during which the NHS groups in fluorescein-NHS will spontaneously react with amine groups in GO or GO-CET. After blocking the unreacted amine groups with 1 M glycine, the fluorescently labeled GO or GO-CET was recovered by centrifugation at 40,000× g for 30 min.

### 3.3. Characterization of GO-Based Nanocarriers

The particles size, polydispersity (PDI), and zeta potential of nanocarriers were determined by dynamic light scattering (DLS) using a Zetasizer (Nano ZA 90, Malvern Instruments, Malvern, UK). A 0.1 mg/mL particle suspension prepared in distilled water (DI water) was used for measurements.

The morphology and size of the particles were observed by transmission electron microscopy (JEOL JEM-2000 EX II, Tokyo, Japan) at 100 kV. Before the observation, the particles were diluted to 0.01 mg/mL in DI water and then dropped onto a 200 mesh carbon-coated copper grid, followed by drying at 25 °C for one day. The Fourier transform infrared (FTIR) spectra were recorded on a Horiba FT-730 FTIR spectrometer (Horiba Ltd., Tokyo, Japan) by mixing samples with KBr powder, and scanned from 1000 to 4000  $\text{cm}^{-1}$  at 2.5 mm/s. The crystal structures of samples were analyzed by X-ray diffraction (XRD) and Raman spectra. For XRD analysis, a D2 Phaser X-ray powder diffractometer (Bruker, Billerica, MA, USA) was used by scanning dried power in the  $2\theta$  range from 5° to 50°. The step size was 0.02° per second. The phases were compared with the JCPDS database for identification. Raman analysis was recorded between 1100 and 2000  $\text{cm}^{-1}$  by a Raman spectrometer (UniD2G, UniNanoTech Inc. Co., Seoul, Korea) with 532 nm laser excitation at 25 mW.

### 3.4. Synthesis of CPN Copolymer

PNIPAM end-capped with a carboxyl group (PNIPAM-COOH) was prepared in benzene by free radical polymerization between NIPAM monomers and MAA using AIBN as an initiator as described before [64]. After the polymerization of NIPAM with MAA under nitrogen atmosphere at 60 °C for 24 h, benzene was removed, and the precipitated polymer was dissolved in acetone and re-precipitated in diethyl ether. This step was repeated 3 times for the purification of synthesized polymer, and the final polymer precipitate was dissolved in water and dialyzed for a week at 4 °C to remove residual reagents and NIPAM. The purified PNIPAM-COOH was lyophilized for storage at room temperature. The CPN copolymer was synthesized by reacting 0.25 g chitosan with 5 g PNIPAM-COOH in 50 mL 2-(N-morpholino)ethanesulfonic acid (MES) buffer (0.1 M, pH 5) containing 0.458 g EDC and 1.375 g NHS for 12 h at 25 °C and purified by thermoprecipitation at 50 °C as detailed in our previous study [36].

### 3.5. Characterization of Hydrogel

The rheological properties of hydrogel were determined using a Discovery HR10 rheometer (TA Instruments, New Castle, DE, USA) with 10% (*w/v*) PNIPAM-COOH or CPN samples. The viscosity was determined as a function of shear rate at 25 °C using a 60 mm cone-and-plate from 0 to 1000  $\text{s}^{-1}$  in 600 s. The complex shear modulus ( $G^*$ ) was determined at different temperatures from 20 to 50 °C using a 60 mm cone-and-plate at 1 Pa shear stress and 5 Hz frequency. Thermogravimetric analysis (TGA) was conducted with a Q50 TGA (TA Instruments, New Castle, DE, USA). Eight milligrams of powder sample were heated under nitrogen atmosphere from room temperature to 500 °C at a 10 °C/min heating rate. For differential scanning calorimetry (DSC) analysis, 10% (*w/v*) CPN hydrogel was put into a DSC aluminum pan and subjected to analysis under 50 mL/min nitrogen using a Q20 DSC (TA Instruments, New Castle, DE, USA) with 5 °C/min heating and cooling rate from 25 to 40 °C. For in vitro hydrogel degradation, 1 mL of 10% (*w/v*) CPN polymer solution containing 0.5 mg GO was prepared by stirring at 4 °C for 1 day. Two hundred microliters of solution prepared above were placed in Millicell cell culture inserts (12  $\mu\text{m}$  pore size) and fitted inside a 24-well cell culture plate and incubated at 37 °C. After the formation of CPN@GO hydrogels, 1.8 mL PBS (pH 7.4) was added to the cell culture plate to fully immerse the hydrogel formed in the cell insert. The plate was incubated at 37 °C by shaking at 50 rpm for the degradation (dissolution) of CPN. At predetermined time points, inserts were removed from the plate, freeze dried, and the residual weight of CPN@GO was determined. For in vivo hydrogel degradation and biocompatibility, a 10% (*w/v*) CPN@GO polymer solution (0.2 mL) was subcutaneously injected into the right dorsal region of a nude mouse by using a 1 mL syringe fitted with a 25-gauge needle. The size of the formed gel in the subcutaneous layer was observed continuously and photographed at given time points. The skin tissues surrounding the gel mass were surgically removed and histologically stained by hematoxylin–eosin (H&E) for the examination of inflammatory response to the implanted materials.



### 3.6. Drug Loading and Release

The loading of CPT-11 onto GO-CET was studied by mixing 0.5 mg GO-CET with different amounts of CPT-11 in 1 mL PBS (pH 7.4) at 4 °C for 12 h, followed by centrifugation (30,000× *g*, 15 min). The amount of loaded drug was calculated from mass balance by determining the concentration of CPT-11 in the supernatant with high-performance liquid chromatography (HPLC) at 370 nm. An Eclipse XDB-C18 column (250 mm × 4.6 mm) was used with 0.01 M pH 4 phosphate/75% acetonitrile in a 4/6 volume ratio as the mobile phase at a 1 mL/min flow rate. The drug loading efficiency (%) is defined as weight of CPT-11 loaded/weight of CPT-11 added × 100; the drug loading content (%) is defined as weight of CPT-11 loaded/weight of GO added × 100.

For drug release, GO-CET/CPT-11 was placed in 1 mL PBS (pH 5.7 or pH 7.4) at 37 °C and shaken at 120 rpm. Centrifugation (30,000× *g*, 15 min) was used to separate GO-CET/CPT11 at predetermined time points, and the precipitate was re-suspended with 1 mL fresh PBS of the same pH value as before. The cumulative amount of CPT-11 released from GO-CET/CPT11 (%) was determined from CPT-11 concentration in the supernatant using HPLC and is defined as cumulative weight of released CPT-11/weight of loaded CPT-11 × 100 [65].

To determine CPT-11 release from hydrogel, 0.1 g CPN was dissolved in 1 mL solution containing 0.5 mg GO-CET/CPT11 and 60 µg shRNA by stirring at 4 °C for 1 day. Two hundred microliters of solution prepared above were placed in Millicell cell culture inserts (12 µm pore size) fitted inside a 24-well cell culture plate and incubated at 37 °C. After the formation of CPN@GO-CET/CPT11@shRNA hydrogel, 1.8 mL PBS (pH 7.4) was added to the cell culture plate to fully immerse the hydrogel formed in the insert. The plate was incubated at 37 °C by shaking at 50 rpm for release of CPT-11. At predetermined time points, the solution in each well was removed for the determination of CPT-11 concentration by using HPLC at 370 nm to calculate the cumulative drug release.

### 3.7. SLP2 shRNA Loading and Release

An improved SLP2 shRNA plasmid (SLP2-shRNA-PGLV3/GFP) vector that co-expresses green fluorescent protein (GFP) and SLP2 shRNA simultaneously to facilitate the analysis of silencing at the level of individual cells as well as siRNA for the specific silencing of SLP2 gene expression was used in this study. The shRNA plasmids consist of the TOOLSilent shRNA vectors pGLV3/H1/GFP/Puro vector plasmid encoding SLP-specific 19 nucleotide shRNA designed to knockdown gene expression with 63,000 Da molecular weight [66]. A CPN@GO-CET/CPT11@shRNA polymer solution was prepared by mixing GO-CET/CPT11 and SLP2 shRNA in 0.2 mL 10% (*w/v*) CPN polymer solution. The polymer solution was placed in Millicell cell culture inserts fitted in a 24-well cell culture plate and incubated at 37 °C for gel formation. To determine SLP2 shRNA release from CPN@GO-CET/CPT11@shRNA, PBS buffer (pH 7.4) was added to each well after gel formation to fully immerse the hydrogel in the insert, and the plate was further incubated at 37 °C by shaking at 50 rpm. At predetermined time points, solution in each well was completely removed for the determination of molar concentration of released shRNA with a NanoDrop 2000c spectrophotometer (Thermo Fisher Scientific, Waltham, MA, USA). The released shRNA was also determined by gel retardation assays using 8% (*w/v*) agarose gel electrophoresis by loading 10 µL sample and 2 µL 6× SYBR Green DNA dye (Invitrogen, Madison, WI, USA). After separating at 100 V for 30 min, the gel was subject to chemiluminescence imaging using MultiGel-21 (TopBio, Taipei, Taiwan).

### 3.8. Cell Line and Cell Culture Condition

A U87 human primary glioblastoma cell line was obtained from American Type Culture Collection (ATCC HTB1, Manassas, VA, USA). The U87 cells were genetically modified by lentiviral infection to express firefly luciferase for in vivo bioluminescence imaging. For cell culture, Dulbecco's Modified Eagle's Medium (DMEM) supplemented with 10% FBS and 1% penicillin/streptomycin was used by incubating at 37 °C in a humidified 5% CO<sub>2</sub> incubator.

### 3.9. Intracellular Uptake

To monitor the intracellular uptake of nanocarriers, U87 cells were seeded in a 24-well cell culture plate at a seeding density of  $1 \times 10^4$  cell/well. After being cultured for 24 h, fluorescently labeled GO or GO-CET (green fluorescence) were separately added to each well and incubated for another 12 h. Treated cells were washed with PBS three times before being fixed in 4% paraformaldehyde. After treating with 0.5 mL 0.1% Triton X-100 and washing, the fixed cells were stained for lysosomes with LysoTracker (red fluorescence) for 30 min and counter-stained for cell nucleus with DAPI (blue fluorescence) for 10 min. To further confirm the ligand-mediated intracellular uptake of GO-CET by binding to EGFR on the U87 surface, CET blocking was performed by pre-treating U87 cells with CET (1 mg/mL) for 1 h before incubating with GO-CET. The samples were observed by a confocal laser scanning microscope (CLSM, BioRad Radiance MRP2100, Hercules, CA, USA) at an excitation wavelength 577/364/340 nm (red/green/blue) and emission wavelength 590/480/488 nm (red/green/blue).

### 3.10. Biocompatibility In Vitro

To evaluate the biocompatibility of GO, 3T3 fibroblasts were seeded in a 96-well cell culture plate at a seeding density of  $2.5 \times 10^3$  cell/well. After removing the culture medium, the cells were treated with different concentrations of GO in 100  $\mu$ L cell culture medium and cultured at 37 °C for another 24 h. The relative cell viability (compared to cell culture medium) was determined from MTS assay by measuring the solution absorbance at 490 nm ( $OD_{490}$ ) with a microplate reader. The biocompatibility of CPN, CPN@GO, and CPN@GO-CET was determined similarly with 3T3 fibroblasts by individually placing 0.2 mL hydrogel solution in a Millicell insert. After gel formation at 37 °C, the insert was fitted in a 24-well cell culture plate seeded with cells at  $2.5 \times 10^3$  cell/well and cultured at 37 °C for 24 h. The relative cell viability (compared to cell culture medium) was determined as before.

### 3.11. Cytotoxicity In Vitro

To determine the cytotoxicity in vitro, U87 cells were seeded in a 96-well cell culture plate at  $2.5 \times 10^3$  cell/well and cultured for 24 h. After washing with PBS (pH 7.4), the cells were incubated with 100  $\mu$ L of CPT-11, GO/CPT11, or GO-CET/CPT11 solution prepared in culture medium with different CPT-11 concentrations to determine the  $IC_{50}$  (half-maximum inhibitory concentration) value. The relative cell viability was determined from MTS assay after culture for 24 h and normalized with the  $OD_{490}$  from cell culture medium (for CPT-11), GO (for GO/CPT11), or GO-CET (for GO-CET/CPT11). To determine the cytotoxicity of CPT-11 released from CPN hydrogel, we performed flow cytometry analysis to determine the apoptosis of U87 cells in the presence of CPN@GO, CPN@GO-CET, or CPN@GO-CET/CPT11. The hydrogel sample was prepared in a Millicell insert at 37 °C as before and tested with  $1 \times 10^4$  U87 cells/well for 48 h. Cells were detached by adding 1 mL trypsin/ethylenediaminetetraacetic acid (EDTA) (0.1%), and the detached cell suspension was reacted with FITC-Annexin V for 30 min and then with propidium iodide (PI) for flow cytometry analysis using a CytoFLEX flow cytometer (Beckman Coulter, Brea, CA, USA).

### 3.12. Transfection of U87 Cells

The GFP gene fragment encoded within SLP2 shRNA allows for the easy monitoring of the fluorescent signal after U87 cells were transfected under different treatments. To investigate SLP2 shRNA transfection, U87 cells were seeded in a 24-well cell culture plate at  $5 \times 10^3$  cells/well and cultured for 24 h. A 10% (*w/v*) CPN polymer solution was used to form CPN@GO-CET or CPN@GO-CET@shRNA (with 12  $\mu$ g shRNA) in Millicell inserts and fitted inside a 24-well cell culture plate for incubation at 37 °C. Transfection with free shRNA was also carried out by directly incubating cells with shRNA at the same gene dosage. After removing the medium and washing each well with PBS at predetermined time points, the gene delivery efficiency was examined by observing the green fluorescence of expressed GFP under an inverted fluorescence microscope (Olympus IX-71, Tokyo, Japan).

### 3.13. Western Blot Analysis

The knockdown of SLP2 gene was determined from Western blot using U87 cells. U87 cells were seeded in a 6-well cell culture plate at a seeding density of  $2 \times 10^5$  cell/well for 24 h. Cultured cells were subject to treatment with CPN@GO-CET, CPN@GO-CET, or CPN@GO-CET@shRNA as before for 5 days at 37 °C. After washing with PBS and harvesting with 0.1% trypsin/EDTA, cells were treated with lysis buffer containing a protease inhibitor cocktail for 30 min on ice to extract the total protein. After centrifugation to remove cell debris, the supernatant was recovered, and the protein concentration was determined by the BCA protein assay kit. The protein was heat-denatured at 95 °C for 10 min in sample buffer and an aliquot of cell lysates ( $\approx 25$  µg total protein/lane) was separated by sodium dodecyl sulfate polyacrylamide gel electrophoresis at 50 V for 30 min and then at 110 V for additional 1 h. The gels were transferred to a polyvinylidene fluoride membrane, blocked with 5% fat-free milk for 1 h for nonspecific binding, and blotted with SLP2 or  $\beta$ -actin antibodies for 12 h at 4 °C. After probing with horseradish peroxidase-conjugated secondary antibody (IgG-HRP) and color development with enhanced chemiluminescence (ECL) Western blotting substrate, the immune complexes were detected using a MultiGel-21 image system. The densitometric analysis of specific bands from Western blot was performed using the ImageJ software.

### 3.14. Xenograft Nude Mice Animal Model

BALB/c nude mice (4–6 weeks old, female) were purchased from BioLASCO (Taipei, Taiwan). All animal experiments were conducted according to protocols that were approved by the Chang Gung University's Institutional Animal Care and Use Committee (IACUC Approval No.: CGU105-034, 2018-01-21). Using a 25-gauge needle, 200 µL cell culture medium containing  $1 \times 10^6$  U87 cells was administered subcutaneously to the right flank of a nude mouse. The tumor size was monitored daily using a caliper, and the tumor volume was calculated from  $\text{length} \times (\text{width})^2/2$ . After 7 days when the tumor size was  $> 30 \text{ mm}^3$ , the tumor-bearing mice were randomly divided into three groups ( $n = 6$  in each group) for treatment.

### 3.15. In Vivo Anti-Tumor Efficacy

Each mouse was subject to intratumoral injection of 50 µL of a tested sample. The study group included the following: 1, PBS (control); 2, CPN@GO-CET (10% CPN, 18.35 mg/kg GO-CET); 3, CPN@GO-CET/CPT11-shRNA (10% CPN, 18.35 mg/kg GO-CET 40 mg/kg CPT-11 and 3.33 mg/kg shRNA). After administration, the tumor size and body weight were monitored on day 1, 5, 8, and 12 post-treatment. On day 12, the mice were anesthetized with 1% isoflurane followed by the injection of 100 µL of D-luciferin solution at a dose of 15 mg luciferin/kg body weight. The bioluminescence imaging (BLI) was performed using a non-invasive in vivo imaging system (IVIS) (Xenogen IVIS-200, Caliper Life Sciences) to determine the peak bioluminescence. The BLI intensity was determined by measuring the total bioluminescent signal intensity in the tumor and BLI normalization was done by dividing the total signal intensity with the total signal intensity when the treatment started (day 0). Tumors were harvested at the end of the observation period, and tumor tissues were fixed immediately in 10% buffered formalin, followed by paraffin embedment and sectioning to 5 µm thickness for hematoxylin and eosin (H&E) staining. As for immunohistochemistry (IHC) analysis, the expression of SLP2, pERK and Ki-67 were detected by incubating tissue slices with rabbit primary antibody against the respective protein for 24 h at 4 °C, followed by incubating with HRP-conjugated anti-rabbit secondary antibody (ImmPRESS® HRP universal antibody, anti-rabbit IgG produced in horse) for 30 min. After color development with ImmPACT® DAB EqV Peroxidase (HRP) Substrate and counterstained with hematoxylin for nucleus, images were taken under an inverted microscope.

### 3.16. Statistical Analysis

All results are presented as the mean  $\pm$  standard deviation (SD). To compare means of different groups, one-way analysis of variance (ANOVA) analysis was carried out using the SPSS software. Differences were considered to be significant at  $p < 0.05$ .

## 4. Conclusions

We presented a strategy by the localized, sustained co-delivery of CPT-11 and SLP2 shRNA with CET-conjugated GO entrapped in thermosensitive CPN hydrogel. The formulation retained the thermo-responsive phase-transition characteristic of PNIPAM at body temperature as well as the pH-sensitive drug release behavior of GO. A combination of positively charged CPN and negatively charged nanocarrier led to the controlled drug release and improved mechanical strength of the in situ formed hydrogel. A sustained release behavior up to 28 days was observed for CPT-11 release from drug-loaded hydrogel, while the complex shear modulus increased five times after entrapping GO-CET in the hydrogel. Furthermore, conjugation with the EGFR-specific antibody CET facilitates the cellular internalization of GO. The formulation provided enhanced in vitro anti-tumor efficacy by inducing 53% apoptotic rate in 2 days. The SLP2 gene knockdown led to a 65% reduction of SLP2 protein expression and 50% reduction of cell migratory ability in 5 days. The therapeutic efficacy was demonstrated with a xenograft tumor model in nude mice through the intratumoral injection of CPN@GO-CET/CPT11@shRNA, which showed 40% tumor size compared with the untreated control group after 12 days. Overall, this multifunctional drug/gene delivery platform is suitable for localized application with enhanced cancer selectivity and minimal adverse effects.

**Author Contributions:** Study conception and design of experiments: Y.-J.L., Y.-H.L., C.-C.C. and J.-P.C.; acquisition of data: W.-T.L., L.-Y.C. and P.-W.H.; analysis and interpretation of data: Y.-J.L., Y.-H.L.; C.-C.C.; P.-W.H. and J.-P.C.; article drafting and revision: Y.-J.L., Y.-H.L. and J.-P.C. All authors have read and agreed to the published version of the manuscript.

**Funding:** This research was funded by Ministry of Science and Technology, Taiwan grant number MOST 106-2221-E-182-056-MY3.

**Acknowledgments:** The authors would like to thank Chang Gung Memorial Hospital (CMRPD2I0041, CMRPD2I0042 and BMRP249) for financial support of this research. The Microscope Core Laboratory and the Image Core Laboratory of Institute for Radiological Research at Chang Gung Memorial Hospital, Linkou are acknowledged for the confocal laser scanning microscopy and IVIS analysis.

**Conflicts of Interest:** The authors declare no conflict of interest.

## Abbreviations

GO	Graphene oxide
CET	Cetuximab
EGFR	Epidermal growth factor receptor
SLP2	Stomatin-like protein 2
shRNA	Short hairpin RNA
siRNA	Small interfering RNA
CPN	Chitosan-g-poly(N-isopropylacrylamide)
GBM	Glioblastoma multiforme
RNAi	RNA interference
WHO	World Health Organization
NF- $\kappa$ B	Nuclear factor kappa-light-chain-enhancer of activated B cells
PNIPAM	Poly(N-isopropylacrylamide)
DSPE	1,2-Distearoyl-sn-glycero-3-phosphorylethanolamine
PEG	Polyethylene glycol
PNIPAM-COOH	Carboxylic acid-ended poly(N-isopropylacrylamide)
NIPAM	N-isopropylacrylamide
MAA	Mercaptoacetic acid

DLS	Dynamic light scattering
XRD	X-ray diffraction
FTIR	Fourier transform infrared
TNBSA	2,4,6-Trinitrobenzene sulfonic acid
DSC	Differential scanning calorimeter
GFP	Green fluorescent protein
PI	Propidium iodide
BLI	Bioluminescence imaging
IHC	Immunohistochemistry
pERK	Phosphorylated extracellular signal-regulated kinases
EDC	1-(3-Dimethylaminopropyl)-3-ethylcarbodiimide hydrochloride
NHS	N-hydroxysuccinimide
DAPI	4',6-Diamidino-2-phenylindole dihydrochloride
DMEM	Dulbecco's Modified Eagle's Medium
FBS	Fetal bovine serum
MES	2-(N-morpholino)ethanesulfonic acid
TGA	Thermogravimetric analysis
H&E	Hematoxylin–eosin
PBS	Phosphate buffered saline
HPLC	High-performance liquid chromatography
CLSM	Confocal laser scanning microscope
EDTA	Ethylenediaminetetraacetic acid

## References

- Koshy, M.; Villano, J.L.; Dolecek, T.A.; Howard, A.; Mahmood, U.; Chmura, S.J.; Weichselbaum, R.R.; McCarthy, B.J. Improved survival time trends for glioblastoma using the SEER 17 population-based registries. *J. Neuro Oncol.* **2011**, *107*, 207–212. [[CrossRef](#)] [[PubMed](#)]
- Ostrom, Q.T.; Cioffi, G.; Gittleman, H.; Patil, N.; Waite, K.; Kruchko, C.; Barnholtz-Sloan, J.S. CBTRUS Statistical Report: Primary Brain and Other Central Nervous System Tumors Diagnosed in the United States in 2012–2016. *Neuro-Oncology* **2019**, *21*, v1–v100. [[CrossRef](#)] [[PubMed](#)]
- Shergalis, A.; Bankhead, A.; Luesakul, U.; Muangsins, N.; Neamati, N. Current Challenges and Opportunities in Treating Glioblastoma. *Pharmacol. Rev.* **2018**, *70*, 412–445. [[CrossRef](#)] [[PubMed](#)]
- Friedman, H.S.; Prados, M.D.; Wen, P.Y.; Mikkelsen, T.; Schiff, D.; Abrey, L.E.; Yung, W.K.; Paleologos, N.; Nicholas, M.K.; Jensen, R.; et al. Bevacizumab Alone and in Combination With Irinotecan in Recurrent Glioblastoma. *J. Clin. Oncol.* **2009**, *27*, 4733–4740. [[CrossRef](#)]
- Prados, M.D.; Lamborn, K.; Yung, W.; Jaeckle, K.; Robins, H.I.; Mehta, M.; Fine, H.A.; Wen, P.Y.; Cloughesy, T.; Chang, S.; et al. A phase 2 trial of irinotecan (CPT-11) in patients with recurrent malignant glioma: A North American Brain Tumor Consortium study1. *Neuro-Oncology* **2006**, *8*, 189–193. [[CrossRef](#)]
- Lu, Y.-J.; Chuang, E.-Y.; Cheng, Y.-H.; Anilkumar, T.; Chen, H.-A.; Chen, J.-P. Thermosensitive magnetic liposomes for alternating magnetic field-inducible drug delivery in dual targeted brain tumor chemotherapy. *Chem. Eng. J.* **2019**, *373*, 720–733. [[CrossRef](#)]
- Liu, J.; Cui, L.; Losic, D. Graphene and graphene oxide as new nanocarriers for drug delivery applications. *Acta Biomater.* **2013**, *9*, 9243–9257. [[CrossRef](#)]
- Huang, Y.-S.; Lu, Y.-J.; Chen, J.-P. Magnetic graphene oxide as a carrier for targeted delivery of chemotherapy drugs in cancer therapy. *J. Magn. Magn. Mater.* **2017**, *427*, 34–40. [[CrossRef](#)]
- Nguyen, K.; Dang, P.N.; Alsberg, E. Functionalized, biodegradable hydrogels for control over sustained and localized siRNA delivery to incorporated and surrounding cells. *Acta Biomater.* **2013**, *9*, 4487–4495. [[CrossRef](#)]
- Lu, Y.-J.; Lin, P.-Y.; Huang, P.-H.; Kuo, C.-Y.; Shalumon, K.T.; Chen, M.-Y.; Chen, J.-P. Magnetic Graphene Oxide for Dual Targeted Delivery of Doxorubicin and Photothermal Therapy. *Nanomaterials* **2018**, *8*, 193. [[CrossRef](#)]
- Attia, M.F.; Anton, H.; Wallyn, J.; Omran, Z.; Vandamme, T.F. An overview of active and passive targeting strategies to improve the nanocarriers efficiency to tumour sites. *J. Pharm. Pharmacol.* **2019**, *71*, 1185–1198. [[CrossRef](#)] [[PubMed](#)]



12. Taylor, T.E.; Furnari, F.; Cavenee, W.K. Targeting EGFR for treatment of glioblastoma: Molecular basis to overcome resistance. *Curr. Cancer Drug Targets* **2012**, *12*, 197–209. [\[CrossRef\]](#) [\[PubMed\]](#)
13. Akhter, H.; Madhav, N.S.; Ahmad, J. Epidermal growth factor receptor based active targeting: A paradigm shift towards advance tumor therapy. *Artif. Cells Nanomed. Biotechnol.* **2018**, *46*, 1188–1198. [\[CrossRef\]](#) [\[PubMed\]](#)
14. Wang, W.; Song, H.; Zhang, J.; Li, P.; Li, C.; Wang, C.; Kong, D.; Zhao, Q. An injectable, thermosensitive and multicompartiment hydrogel for simultaneous encapsulation and independent release of a drug cocktail as an effective combination therapy platform. *J. Control. Release* **2015**, *203*, 57–66. [\[CrossRef\]](#)
15. Dai, X.; Tan, C. Combination of microRNA therapeutics with small-molecule anticancer drugs: Mechanism of action and co-delivery nanocarriers. *Adv. Drug Deliv. Rev.* **2015**, *81*, 184–197. [\[CrossRef\]](#)
16. Zhan, C.; Meng, Q.; Li, Q.; Feng, L.; Zhu, J.; Lu, W. Cyclic RGD-Polyethylene Glycol-Polyethylenimine for Intracranial Glioblastoma-Targeted Gene Delivery. *Chem. Asian J.* **2011**, *7*, 91–96. [\[CrossRef\]](#)
17. Shen, H.; Sun, T.; Ferrari, M. Nanovector delivery of siRNA for cancer therapy. *Cancer Gene Ther.* **2012**, *19*, 367–373. [\[CrossRef\]](#)
18. Kozielski, K.L.; Ruiz-Valls, A.; Tzeng, S.Y.; Guerrero-Cázares, H.; Rui, Y.; Li, Y.; Vaughan, H.J.; Gionet-Gonzales, M.; Vantucci, C.; Kim, J.; et al. Cancer-selective nanoparticles for combinatorial siRNA delivery to primary human GBM in vitro and in vivo. *Biomaterials* **2019**, *209*, 79–87. [\[CrossRef\]](#)
19. Wang, J.; Lu, Z.; Wientjes, M.G.; Au, J.L.-S. Delivery of siRNA Therapeutics: Barriers and Carriers. *AAPS J.* **2010**, *12*, 492–503. [\[CrossRef\]](#)
20. Dong, Y.; Siegwart, D.J.; Anderson, D.G. Strategies, design, and chemistry in siRNA delivery systems. *Adv. Drug Deliv. Rev.* **2019**, *144*, 133–147. [\[CrossRef\]](#)
21. Zhang, L.; Elaraj, D.M.; Weinreich, D.M.; Varghese, S.; Puhlmann, M.; Hewitt, S.M.; Carroll, N.M.; Feldman, E.D.; Turner, E.M.; Alexander, H.R. Stomatin-like Protein 2 Is Overexpressed in Cancer and Involved in Regulating Cell Growth and Cell Adhesion in Human Esophageal Squamous Cell Carcinoma. *Clin. Cancer Res.* **2006**, *12*, 1639–1646. [\[CrossRef\]](#)
22. Chang, D.; Ma, K.; Gong, M.; Cui, Y.; Liu, Z.-H.; Zhou, X.-G.; Zhou, C.-N.; Wang, T.-Y. SLP-2overexpression is associated with tumour distant metastasis and poor prognosis in pulmonary squamous cell carcinoma. *Biomarkers* **2009**, *15*, 104–110. [\[CrossRef\]](#) [\[PubMed\]](#)
23. Dowling, P.; Meleady, P.; Dowd, A.J.; Henry, M.; Glynn, S.A.; Clynes, M. Proteomic analysis of isolated membrane fractions from superinvasive cancer cells. *Biochim. Biophys. Acta (BBA) Proteins Proteom.* **2007**, *1774*, 93–101. [\[CrossRef\]](#) [\[PubMed\]](#)
24. Wang, B.; Xie, J.; He, H.-Y.; Huang, E.-W.; Cao, Q.-H.; Luo, L.; Liao, Y.-S.; Guo, Y. Suppression of CLC-3 chloride channel reduces the aggressiveness of glioma through inhibiting nuclear factor- $\kappa$ B pathway. *Oncotarget* **2017**, *8*, 63788–63798. [\[CrossRef\]](#) [\[PubMed\]](#)
25. Song, L.; Liu, L.; Wu, Z.; Lin, C.; Dai, T.; Yu, C.; Wang, X.; Wu, J.; Li, M.; Li, J. Knockdown of stomatin-like protein 2 (STOML2) reduces the invasive ability of glioma cells through inhibition of the NF- $\kappa$ B/MMP-9 pathway. *J. Pathol.* **2011**, *226*, 534–543. [\[CrossRef\]](#) [\[PubMed\]](#)
26. Norouzi, M.; Nazari, B.; Miller, D.W. Injectable hydrogel-based drug delivery systems for local cancer therapy. *Drug Discov. Today* **2016**, *21*, 1835–1849. [\[CrossRef\]](#)
27. Schild, H. Poly(N-isopropylacrylamide): Experiment, theory and application. *Prog. Polym. Sci.* **1992**, *17*, 163–249. [\[CrossRef\]](#)
28. Wang, X.; Wang, J.; Wu, W.; Li, H. Vaginal delivery of carboplatin-loaded thermosensitive hydrogel to prevent local cervical cancer recurrence in mice. *Drug Deliv.* **2016**, *23*, 1–22. [\[CrossRef\]](#)
29. Yang, Y.; Zhao, H.; Jia, Y.; Guo, Q.; Qu, Y.; Su, J.; Lu, X.; Zhao, Y.; Qian, Z. A novel gene delivery composite system based on biodegradable folate-poly (ester amine) polymer and thermosensitive hydrogel for sustained gene release. *Sci. Rep.* **2016**, *6*, 21402. [\[CrossRef\]](#)
30. Huang, P.; Song, H.; Zhang, Y.; Liu, J.; Zhang, J.; Wang, W.; Liu, J.; Li, C.; Kong, D. Bridging the Gap between Macroscale Drug Delivery Systems and Nanomedicines: A Nanoparticle-Assembled Thermosensitive Hydrogel for Peritumoral Chemotherapy. *ACS Appl. Mater. Interfaces* **2016**, *8*, 29323–29333. [\[CrossRef\]](#)
31. Guo, D.-D.; Hong, S.-H.; Jiang, H.-L.; Kim, J.-H.; Minai-Tehrani, A.; Kim, J.-E.; Shin, J.-Y.; Jiang, T.; Kim, Y.-K.; Choi, Y.-J.; et al. Synergistic effects of Akt1 shRNA and paclitaxel-incorporated conjugated linoleic acid-coupled poloxamer thermosensitive hydrogel on breast cancer. *Biomaterials* **2012**, *33*, 2272–2281. [\[CrossRef\]](#) [\[PubMed\]](#)

32. Ma, H.; He, C.; Cheng, Y.; Li, D.; Gong, Y.; Liu, J.; Tian, H.; Chen, X. PLK1shRNA and doxorubicin co-loaded thermosensitive PLGA-PEG-PLGA hydrogels for osteosarcoma treatment. *Biomaterials* **2014**, *35*, 8723–8734. [[CrossRef](#)] [[PubMed](#)]
33. Bhattarai, N.; Gunn, J.; Zhang, M. Chitosan-based hydrogels for controlled, localized drug delivery. *Adv. Drug Deliv. Rev.* **2010**, *62*, 83–99. [[CrossRef](#)] [[PubMed](#)]
34. Ragelle, H.; Vandermeulen, G.; Préat, V. Chitosan-based siRNA delivery systems. *J. Control. Release* **2013**, *172*, 207–218. [[CrossRef](#)]
35. Afkham, A.; Aghebati-Maleki, L.; Siahmansouri, H.; Sadreddini, S.; Ahmadi, M.; Dolati, S.; Afkham, N.M.; Akbarzadeh, P.; Jadidi-Niaragh, F.; Younesi, V.; et al. Chitosan (CMD)-mediated co-delivery of SN38 and Snail-specific siRNA as a useful anticancer approach against prostate cancer. *Pharmacol. Rep.* **2018**, *70*, 418–425. [[CrossRef](#)]
36. Chen, J.-P.; Cheng, T.-H. Thermo-Responsive Chitosan-graft-poly(N-isopropylacrylamide) Injectable Hydrogel for Cultivation of Chondrocytes and Meniscus Cells. *Macromol. Biosci.* **2006**, *6*, 1026–1039. [[CrossRef](#)]
37. Fang, J.-Y.; Chen, J.-P.; Leu, Y.; Hu, J.-W. The Delivery of Platinum Drugs from Thermosensitive Hydrogels Containing Different Ratios of Chitosan. *Drug Deliv.* **2008**, *15*, 235–243. [[CrossRef](#)]
38. Prabha, S.; Arya, G.; Chandra, R.; Ahmed, B.; Nimesh, S. Effect of size on biological properties of nanoparticles employed in gene delivery. *Artif. Cells Nanomed. Biotechnol.* **2014**, *44*, 83–91. [[CrossRef](#)]
39. Chu, I.-M.; Tseng, S.-H.; Chou, M.-Y. Cetuximab-conjugated iron oxide nanoparticles for cancer imaging and therapy. *Int. J. Nanomed.* **2015**, *10*, 3663–3685. [[CrossRef](#)]
40. Hassan, H.M.A.; Abdelsayed, V.; Khder, A.E.R.S.; Abouzeid, K.M.; Turner, J.; El-Shall, M.S.; Al-Resayes, S.I.; El-Azhary, A.A. Microwave synthesis of graphene sheets supporting metal nanocrystals in aqueous and organic media. *J. Mater. Chem.* **2009**, *19*, 3832–3837. [[CrossRef](#)]
41. Perumbilavil, S.; Sankar, P.; Rose, T.P.; Philip, R. White light Z-scan measurements of ultrafast optical nonlinearity in reduced graphene oxide nanosheets in the 400–700 nm region. *Appl. Phys. Lett.* **2015**, *107*, 051104. [[CrossRef](#)]
42. Kim, N.H.; Kuila, T.; Lee, J.H. Simultaneous reduction, functionalization and stitching of graphene oxide with ethylenediamine for composites application. *J. Mater. Chem. A* **2013**, *1*, 1349–1358. [[CrossRef](#)]
43. Elias, E.R.; Poloukhine, A.; Popik, V.V.; Tsourkas, A. Effect of ligand density, receptor density, and nanoparticle size on cell targeting. *Nanomed. Nanotechnol. Biol. Med.* **2012**, *9*, 194–201. [[CrossRef](#)] [[PubMed](#)]
44. Xu, Y.; Villalona-Calero, M.A. Irinotecan: Mechanisms of tumor resistance and novel strategies for modulating its activity. *Ann. Oncol.* **2002**, *13*, 1841–1851. [[CrossRef](#)] [[PubMed](#)]
45. Yuan, Q.; Shah, J.; Hein, S.; Misra, R. Controlled and extended drug release behavior of chitosan-based nanoparticle carrier. *Acta Biomater.* **2010**, *6*, 1140–1148. [[CrossRef](#)] [[PubMed](#)]
46. Hu, W.-W.; Syu, W.-J.; Chen, W.-Y.; Ruaan, R.-C.; Cheng, Y.-C.; Chien, C.-C.; Li, C.; Chung, C.-A.; Tsao, C.-W. Use of Biotinylated Chitosan for Substrate-Mediated Gene Delivery. *Bioconjugate Chem.* **2012**, *23*, 1587–1599. [[CrossRef](#)] [[PubMed](#)]
47. Santos-Carballal, B.; Fernández, E.F.; Goycoolea, F.M. Chitosan in Non-Viral Gene Delivery: Role of Structure, Characterization Methods, and Insights in Cancer and Rare Diseases Therapies. *Polymers* **2018**, *10*, 444. [[CrossRef](#)]
48. Mu, Q.; Su, G.; Li, L.; Gilbertson, B.O.; Yu, L.H.; Zhang, Q.; Sun, Y.-P.; Yan, B. Size-Dependent Cell Uptake of Protein-Coated Graphene Oxide Nanosheets. *ACS Appl. Mater. Interfaces* **2012**, *4*, 2259–2266. [[CrossRef](#)]
49. Bao, H.; Pan, Y.; Ping, Y.; Sahoo, N.G.; Wu, T.; Li, L.; Li, J.; Gan, L.H. Chitosan-Functionalized Graphene Oxide as a Nanocarrier for Drug and Gene Delivery. *Small* **2011**, *7*, 1569–1578. [[CrossRef](#)]
50. Hannon, G.J. RNA interference. *Nature* **2002**, *418*, 244–251. [[CrossRef](#)]
51. Rao, D.D.; Vorhies, J.S.; Senzer, N.N.; Nemunaitis, J. siRNA vs. shRNA: Similarities and differences. *Adv. Drug Deliv. Rev.* **2009**, *61*, 746–759. [[CrossRef](#)] [[PubMed](#)]
52. Thomas, M.; Klivanov, A.M. Enhancing polyethylenimine's delivery of plasmid DNA into mammalian cells. *Proc. Natl. Acad. Sci. USA* **2002**, *99*, 14640–14645. [[CrossRef](#)] [[PubMed](#)]
53. Moore, C.B.; Guthrie, E.H.; Huang, M.T.-H.; Taxman, D.J. Short Hairpin RNA (shRNA): Design, Delivery, and Assessment of Gene Knockdown. *Methods Mol. Biol.* **2010**, *629*, 139–156. [[CrossRef](#)]
54. Cao, Y.; Tan, Y.F.; Wong, Y.S.; Liew, W.J.M.; Venkatraman, S.S. Recent Advances in Chitosan-Based Carriers for Gene Delivery. *Mar. Drugs* **2019**, *17*, 381. [[CrossRef](#)]

55. Köping-Höggård, M.; Vårnum, K.M.; Issa, M.; Danielsen, S.; Christensen, B.E.; Stokke, B.T.; Artursson, P. Improved chitosan-mediated gene delivery based on easily dissociated chitosan polyplexes of highly defined chitosan oligomers. *Gene Ther.* **2004**, *11*, 1441–1452. [\[CrossRef\]](#)
56. Wang, Y.; Cao, W.; Yu, Z.; Liu, Z. Downregulation of a mitochondria associated protein SLP-2 inhibits tumor cell motility, proliferation and enhances cell sensitivity to chemotherapeutic reagents. *Cancer Biol. Ther.* **2009**, *8*, 1651–1658. [\[CrossRef\]](#)
57. Rivera, F.; Vega-Villegas, M.E.; López-Brea, M.F. Cetuximab, its clinical use and future perspectives. *Anti-Cancer Drugs* **2008**, *19*, 99–113. [\[CrossRef\]](#)
58. Cusack, J.C.; Liu, R.; Baldwin, A.S. Inducible Chemoresistance to 7-Ethyl-10-[4-(1-piperidino)-1-piperidino]carbonyloxycamptothecin (CPT-11) in Colorectal Cancer Cells and a Xenograft Model Is Overcome by Inhibition of Nuclear Factor- $\kappa$ B Activation. *Cancer Res.* **2000**, *60*, 2323–2330.
59. Liao, H.-T.; Chen, C.-T.; Chen, J.-P. Osteogenic Differentiation and Ectopic Bone Formation of Canine Bone Marrow-Derived Mesenchymal Stem Cells in Injectable Thermo-Responsive Polymer Hydrogel. *Tissue Eng. Part C Methods* **2011**, *17*, 1139–1149. [\[CrossRef\]](#)
60. Cheng, Y.; He, C.; Ding, J.; Xiao, C.; Zhuang, X.; Chen, X. Thermosensitive hydrogels based on polypeptides for localized and sustained delivery of anticancer drugs. *Biomaterials* **2013**, *34*, 10338–10347. [\[CrossRef\]](#)
61. Jost, S.C.; Collins, L.; Travers, S.; Piwnica-Worms, D.; Garbow, J.R. Measuring Brain Tumor Growth: A Combined BLI / MRI Strategy. *Mol. Imaging* **2009**, *8*, 245–253. [\[CrossRef\]](#) [\[PubMed\]](#)
62. Sun, X.; Liu, Z.; Welshe, K.; Robinson, J.T.; Goodwin, A.; Zaric, S.; Dai, H. Nano-graphene oxide for cellular imaging and drug delivery. *Nano Res.* **2008**, *1*, 203–212. [\[CrossRef\]](#) [\[PubMed\]](#)
63. Cayot, P.; Tainturier, G. The Quantification of Protein Amino Groups by the Trinitrobenzenesulfonic Acid Method: A Reexamination. *Anal. Biochem.* **1997**, *249*, 184–200. [\[CrossRef\]](#) [\[PubMed\]](#)
64. Chou, P.-Y.; Chen, S.-H.; Chen, C.-H.; Fong, Y.T.; Chen, J.-P.; Chen, S.-H. Thermo-responsive in-situ forming hydrogels as barriers to prevent post-operative peritendinous adhesion. *Acta Biomater.* **2017**, *63*, 85–95. [\[CrossRef\]](#) [\[PubMed\]](#)
65. Fong, Y.T.; Chen, C.-H.; Chen, J.-P. Intratumoral Delivery of Doxorubicin on Folate-Conjugated Graphene Oxide by In-Situ Forming Thermo-Sensitive Hydrogel for Breast Cancer Therapy. *Nanomaterials* **2017**, *7*, 388. [\[CrossRef\]](#)
66. Kojima, S.-I.; Vignjevic, D.M.; Borisy, G.G. Improved silencing vector co-expressing GFP and small hairpin RNA. *Biotechniques* **2004**, *36*, 74–79. [\[CrossRef\]](#)



© 2020 by the authors. Licensee MDPI, Basel, Switzerland. This article is an open access article distributed under the terms and conditions of the Creative Commons Attribution (CC BY) license (<http://creativecommons.org/licenses/by/4.0/>).

RESEARCH

Open Access



# Phloretin ameliorates hepatic steatosis through regulation of lipogenesis and Sirt1/AMPK signaling in obese mice

Chian-Jiun Liou<sup>1,2†</sup>, Shu-Ju Wu<sup>3,4†</sup>, Szu-Chuan Shen<sup>5</sup>, Li-Chen Chen<sup>2</sup>, Ya-Ling Chen<sup>6\*</sup> and Wen-Chung Huang<sup>2,7\*</sup> 

## Abstract

**Background:** Phloretin is isolated from apple trees and could increase lipolysis in 3T3-L1 adipocytes. Previous studies have found that phloretin could prevent obesity in mice. In this study, we investigated whether phloretin ameliorates non-alcoholic fatty liver disease (NAFLD) in high-fat diet (HFD)-induced obese mice, and evaluated the regulation of lipid metabolism in hepatocytes.

**Methods:** HepG2 cells were treated with 0.5 mM oleic acid to induce lipid accumulation, and then treated with phloretin to evaluate the molecular mechanism of lipogenesis. In another experiment, male C57BL/6 mice were fed normal diet or HFD (60% fat, w/w) for 16 weeks. After the fourth week, mice were treated with or without phloretin by intraperitoneal injection for 12 weeks.

**Results:** Phloretin significantly reduced excessive lipid accumulation and decreased sterol regulatory element-binding protein 1c, blocking the expression of fatty acid synthase in oleic acid-induced HepG2 cells. Phloretin increased Sirt1, and phosphorylation of AMP activated protein kinase to suppress acetyl-CoA carboxylase expression, reducing fatty acid synthesis in hepatocytes. Phloretin also reduced body weight and fat weight compared to untreated HFD-fed mice. Phloretin also reduced liver weight and liver lipid accumulation and improved hepatocyte steatosis in obese mice. In liver tissue from obese mice, phloretin suppressed transcription factors of lipogenesis and fatty acid synthase, and increased lipolysis and fatty acid  $\beta$ -oxidation. Furthermore, phloretin regulated serum leptin, adiponectin, triglyceride, low-density lipoprotein, and free fatty acid levels in obese mice.

**Conclusions:** These findings suggest that phloretin improves hepatic steatosis by regulating lipogenesis and the Sirt-1/AMPK pathway in the liver.

**Keywords:** HepG2, Lipogenesis, Lipolysis, Phloretin, non-alcoholic fatty liver disease

## Background

Refined foods and junk food increase the prevalence of obesity, which is a risk factor for chronic diseases, including cardiovascular disease, atherosclerosis, type 2 diabetes, and cancer [1]. Obesity not only increases the lipid accumulation of visceral fat tissue, but also induces excessive lipid accumulation in the liver and causes fatty liver disease [2]. Non-alcoholic fatty liver disease (NAFLD) is a common hepatic disease, and the development of

\*Correspondence: ylchen01@tmu.edu.tw; wchuang@mail.cgu.edu.tw

<sup>†</sup>Chian-Jiun Liou and Shu-Ju Wu contributed equally to the work

<sup>2</sup> Division of Allergy, Asthma, and Rheumatology, Department of Pediatrics, Chang Gung Memorial Hospital, Linkou, Guishan Dist., Taoyuan City 33303, Taiwan

<sup>6</sup> School of Nutrition and Health Sciences, Taipei Medical University, 250 Wu-Hsing Street, Taipei City 11031, Taiwan

Full list of author information is available at the end of the article



© The Author(s) 2020. This article is licensed under a Creative Commons Attribution 4.0 International License, which permits use, sharing, adaptation, distribution and reproduction in any medium or format, as long as you give appropriate credit to the original author(s) and the source, provide a link to the Creative Commons licence, and indicate if changes were made. The images or other third party material in this article are included in the article's Creative Commons licence, unless indicated otherwise in a credit line to the material. If material is not included in the article's Creative Commons licence and your intended use is not permitted by statutory regulation or exceeds the permitted use, you will need to obtain permission directly from the copyright holder. To view a copy of this licence, visit <http://creativecommons.org/licenses/by/4.0/>. The Creative Commons Public Domain Dedication waiver (<http://creativecommons.org/publicdomain/zero/1.0/>) applies to the data made available in this article, unless otherwise stated in a credit line to the data.

NAFLD is considered to be a complex metabolic syndrome of abnormal liver metabolism. Patients with obesity or type 2 diabetes also often suffer from NAFLD. Epidemiological studies indicate that approximately 75% of overweight and obese patients in developed and developing countries have NAFLD [3]. The initial development of NAFLD is excessive lipid accumulation in the liver, which is known as liver steatosis. A total of 5–20% of patients with steatosis will develop a more severe non-alcoholic steatohepatitis (NASH), which is characterized by liver inflammation, fibrosis, and tissue damage [4]. Patients with NASH who do not receive medical treatment and regulate their unhealthy lifestyle and eating habits will develop irreversible liver fibrosis, cirrhosis, liver failure, and liver cancer [5]. In addition, NAFLD is thought to increase the risk of cardiovascular disease (coronary atherosclerosis) [6]. Therefore, treatment of NAFLD could attenuate the incidence of many chronic diseases.

The pathological mechanism of NAFLD is not fully understood. Hepatic steatosis is caused by increased lipid accumulation in the liver and reduced lipid breakdown [6]. However, excessive fat accumulation will also induce liver lipid toxicity, oxidative stress, and inflammation, leading to hepatocyte damage and death [7]. Therefore, excessive accumulation of oil droplets will interfere with the physiological function of the liver. With excessive intake of a high-calorie diet, via digestion and metabolism, high-energy foods will be converted into triglycerides (TGs) in the liver and adipocytes [3]. In the lipid synthesis pathway, activation of transcription factors CCAAT/enhancer-binding protein (C/EBP) and sterol regulatory element binding protein 1c (SREBP-1c) regulates the expression of fatty acid synthase (FAS) to increase the lipid synthesis reaction [8]. Therefore, the expression of SREBP-1c and FAS can be higher in the liver or visceral adipose tissue of obese individuals than normal-weight persons.

Many studies have pointed out that accelerating lipid breakdown in the liver of an obese individual would decrease lipid accumulation in the liver and improve NAFLD [9]. In the liver, TG decomposition requires lipases, including adipose triglyceride lipase (ATGL) and hormone-sensitive lipase (HSL), which can break down TGs to produce free fatty acids and glycerol [10]. ATGL-knockout mice cannot lose significant weight under the conditions of proper exercise and calorie restriction [11]. Obviously, the activation of lipase could assist and improve NAFLD. However, excessive free fatty acids from the breakdown of TGs need to be converted to produce energy by  $\beta$ -oxidation [9]. Therefore, promoting lipolysis can regulate lipid metabolism and improve NAFLD towards normal liver function.

In liver, muscle, and adipose tissue, the AMPK signaling pathway can contribute to maintaining an energy balance and regulate lipid metabolism [12]. Activated AMPK can inhibit the expression of lipid synthesis-related proteins, such as SREBP1, FAS, and CD36, and can also increase expression in the fatty acid  $\beta$ -oxidation pathway and related enzymes (e.g., carnitine palmitoyltransferase 1 [CPT-1] and peroxisome proliferator-activated receptor alpha [PPAR $\alpha$ ]) to decrease lipid accumulation [13]. Previous studies have shown that AMPK activation can protect liver cells from oxidative damage and inflammation, and can inhibit apoptosis and improve the development of NAFLD [14]. AMPK phosphorylation can also stimulate acetyl-CoA carboxylase (ACC) phosphorylation, reducing lipid biosynthesis [13]. Sirtuin 1 (Sirt1) is an NAD<sup>+</sup>-dependent deacetylase that can contribute to regulating intracellular NAD<sup>+</sup> levels for maintaining cellular energy balance [15]. In obese mice, adipocytes and liver cells accumulate excess lipid, which inhibits the activity of Sirt1 and AMPK, inactivating the Sirt1/AMPK pathway and aggravating the development of NAFLD [16]. Resveratrol is a Sirt1 enhancer. The treatment of obese mice with resveratrol could induce the expression of Sirt1 and phosphorylation of AMPK, regulating the molecular pathways of lipid and glucose metabolism in the liver [16, 17]. Therefore, stimulating the activation of the Sirt1/AMPK pathway will reduce lipid accumulation in the liver and improve hepatic steatosis in obese and overweight individuals.

Clinically effective drugs for preventing or treating NAFLD are still lacking [18]. Plant extracts or natural products have been investigated extensively for preventing or improving obesity and NAFLD [19, 20]. Phloretin is isolated from apple trees [21]. Our previous studies found that phloretin can inhibit lipid accumulation in 3T3-L1 adipocytes via inhibition of adipogenesis-related transcription factors and promotion of AMPK phosphorylation [22]. Phloretin can also reduce inflammatory adipokines and increase adiponectin expression in LPS or LPS/CoCl<sub>2</sub>-stimulated 3T3-L1 adipocytes [23]. Other studies have found that phloretin can prevent weight gain and regulate blood glucose in high-fat diet (HFD)-induced obese mice [24]. However, the beneficial effects of phloretin on NAFLD are unclear. In the present study, we investigated whether phloretin regulates lipogenesis in HepG2 hepatocytes *in vitro*, ameliorates NAFLD, and modulates the molecular mechanism underlying lipid metabolism in HFD-induced obese mice.

## Materials and methods

### Cell culture and induced fatty liver cells

The HepG2 hepatocyte cells were cultured in DMEM medium supplemented with 1% penicillin–streptomycin



solution and 10% fetal bovine serum. Phloretin (isolated from apple wood, purity  $\geq 99\%$  by HPLC) was purchased from Sigma–Aldrich (St. Louis, MO, USA). Phloretin were dissolved in DMSO, and for all cell experiments the final culture concentration of DMSO was  $<1\%$ . For cell viability assays, HepG2 cells were treated with various concentrations of phloretin or oleic acid for 48 h to measure cell viability using MTT solution (Sigma) as described previously [25]. The culture plate was treated with isopropanol to evaluate cell viability using a microtiter plate reader (Multiskan FC, Thermo Fisher Scientific) at an absorbance of 550 nm. To detect lipid accumulation in hepatocytes, HepG2 cells were incubated with 0.5 mM oleic acid to stimulate lipid accumulation for 48 h. Cells were treated with vehicle (0.1% DMSO) or phloretin (3–30  $\mu\text{M}$ ) for 24 h to detect the molecular mechanism of lipid metabolism. In other cellular experiments, phloretin-treated HepG2 cells were treated with the AMPK inhibitor compound C (Sigma) to evaluate the molecular expression of lipid metabolism.

#### Oil Red O staining

HepG2 cells were incubated with 0.5 mM oleic acid for 48 h and then treated with or without phloretin for 24 h. The culture plate was washed and cells fixed with formalin. Hepatocytes were stained with Oil Red O solution to observe the distribution of oil droplets in liver cells as described previously [26]. Finally, hepatocytes were treated with isopropanol to assay lipid accumulation using a microplate reader (Multiskan FC) at an absorbance of 490 nm.

#### Western blot analysis

Proteins were separated by 8–10% SDS–PAGE and transferred to polyvinylidene difluoride membrane. The membrane was incubated with specific antibodies overnight at 4 °C, followed by secondary antibodies at room temperature for 1 h. Protein signals were visualized using luminol/enhancer solution and the BioSpectrum 600 system (UVP, Upland, CA, USA). The specific primary antibodies were AMPK $\alpha$ , phosphorylated AMPK $\alpha$  (pAMPK $\alpha$ ), CPT-1, CPT2, FAS, Serbp-1c, Sirt1 (Cell Signaling Technology, MA, USA),  $\beta$ -actin (Sigma), ATGL, acetyl CoA carboxylase-1 (ACC-1), phosphorylated-ACC-1 (pACC-1), C/EBP $\beta$ , HSL, phosphorylated HSL (pHSL), and PPAR- $\alpha$  (Abcam, Cambridge, MA, USA).

#### Animals and treatments

Four-week-old male C57BL/6 mice (National Laboratory Animal Center, Taiwan) were randomly divided into four groups of 10. HFD based on research diet TestDiet 58Y1 (Purina TestDiet, St. Louis, MO, USA) containing 23.1% protein, 34.9% fat, and 25.8% carbohydrates, and

fat supplied 60% of energy. The normal control group (N) and HFD control group (HFD) were fed a standard chow diet or HFD, respectively, and administered DMSO solution by intraperitoneal injection. The PT10 and PT20 groups were fed a HFD and administered 10 mg/kg and 20 mg/kg phloretin by intraperitoneal injection, respectively. The HFD, PT10, and PT20 groups were fed a HFD for 4 weeks. All mice were treated with 50  $\mu\text{l}$  DMSO or phloretin (dissolved in DMSO) twice a week for 12 weeks (Fig. 2a). Dietary intake was recorded per day and body weight measured weekly. Food intake (the weight of consumed food (g)  $\times$  calories in the diet) was recorded each day. Animal experiments were approved by the Laboratory Animal Care Committee of Chang Gung University of Science and Technology (IACUC approval number: 2015–019).

#### Biochemical analysis

Mice were anesthetized with isoflurane and blood collected via the orbital vascular plexus. The blood was centrifuged and the serum collected to detect the free fatty acids and low-density lipoprotein (LDL) using a fatty acid quantitation kit and LDL quantitation kit (Sigma), respectively, according to the manufacturer's protocol as described previously [26]. The serum levels of glutamate oxaloacetate transaminase (GOT), glutamate pyruvate transaminase (GPT), total cholesterol (TC), high-density lipoprotein (HDL), and total TGs were measured using the biochemical analyzer (DRI-CHEM NX500, Fuji, Tokyo, Japan). The day before the end of the experiment, mice fasted for 16 h and were administered glucose by intraperitoneal injection to assay blood glucose levels using the biochemical analyzer (Fuji). Blood insulin was detected using the Insulin EIA Kit (Cayman, Ann Arbor, Michigan, USA) according to the manufacturer's protocol. Liver glycogen was detected using the Glycogen Assay Kit (Cayman) according to the manufacturer's protocol, and the glycogen levels were measured using a microplate reader (Multiskan FC) at an absorbance of 570 nm.

#### Histological analysis

Liver tissues were removed and embedded in paraffin. All tissues were cut into 6- $\mu\text{m}$  sections and stained using hematoxylin and eosin (HE) solution as described previously [27]. Glycogen expression in the liver tissue was detected by periodic acid-Schiff (PAS) solution. All biopsy specimens were observed under a light microscope (Olympus, Tokyo, Japan) and an NAFLD score evaluated as described previously [28]. Furthermore, epididymal and inguinal adipose tissue were removed, weighed, and fixed in formalin solution. Next, adipose tissues were embedded in paraffin as described previously

(See figure on next page.)

**Fig. 1** Phloretin (PT) reduced lipid accumulation in HepG2 cells. **a** Oil Red O staining revealed lipid accumulation. **b** HepG2 cells were treated with isopropanol and lipid accumulation measured using the absorbance at OD 490 nm. Effects of phloretin (PT) on lipid metabolism in oleic acid (OA)-induced HepG2 cells. **c** The expression of transcription factors and FAS and **d** the fold expression were measured relative to  $\beta$ -actin. **e**  $\beta$ -oxidation and **f** the fold expression were measured relative to  $\beta$ -actin. **g** Lipolysis was detected by Western blot and **h** the fold expression measured relative to the expression of  $\beta$ -actin. **i** The Sirt1/AMPK pathway and **j** fold expression measured relative to  $\beta$ -actin. Data are presented as mean  $\pm$  SEM; \* $P < 0.05$ , \*\* $P < 0.01$  compared to the OA group. # $P < 0.05$ , ## $P < 0.01$  compared to the without treated-OA group. Furthermore, **k** HepG2 cells were treated with 0.5 mM OA for 48 h, followed by 30  $\mu$ M phloretin with or without an AMPK inhibitor (compound c) for 24 h. **l** The fold expression was measured relative to  $\beta$ -actin. Three independent experiments were analyzed and the data presented as the mean  $\pm$  SEM. \* $P < 0.05$ , \*\* $P < 0.01$  compared to the compound c group. # $P < 0.05$ , ## $P < 0.01$  compared to the OA group

[26]. In briefly, all adipose tissues were cut into 6- $\mu$ m sections and stained with HE solution to observe and take a photograph with a light microscope (Olympus). Furthermore, the images of adipose tissue choose five fat cells to calculate the cell area using cellSens Standard software (Olympus).

#### Real-time PCR

Liver tissues in TRI reagent (Sigma) were homogenized using a homogenizer (FastPrep-24, MP Biomedicals, Santa Ana, CA, USA). Samples were centrifuged and the supernatant collected to extract total RNA. Next, cDNA was synthesized using the cDNA Synthesis Kit (Life Technologies, Carlsbad, CA) as described previously [29]. Using fluorescently labeled SYBR Green treated with DNA sample solutions, we amplified specific gene expression using a spectrofluorometric thermal cycler (iCycler; Bio-Rad Laboratories, Hercules, CA, USA).

#### Statistical analysis

Statistical analyses were performed by one-way analysis of variance (ANOVA) and a Dunnett post hoc test. All data were investigated in at least three independent experiments, and data are presented as the mean  $\pm$  SEM.  $P < 0.05$  was considered significant.

## Results

#### Cell viability of phloretin in HepG2 cells

The cytotoxicity of phloretin in HepG2 cells was determined using the MTT assay. Phloretin did not demonstrate significant cytotoxic effects at a concentration  $\leq 50$   $\mu$ M, and subsequent experiments used phloretin at 3–30  $\mu$ M concentrations for all cell experiments (data not shown). We also determined that oleic acid concentrations  $\leq 0.5$  mM did not significantly affect cell viability in HepG2 cells (data not shown).

#### Phloretin attenuated lipid accumulation in HepG2 cells

Based on Oil Red O staining, phloretin decreased lipid droplets compared to oleic acid-induced HepG2 cells (Fig. 1a). Using isopropanol to treat hepatocytes

confirmed that phloretin significantly attenuated lipid accumulation in oleic acid-treated hepatocytes (Fig. 1b).

#### Effect of phloretin on lipid metabolism in hepatocytes

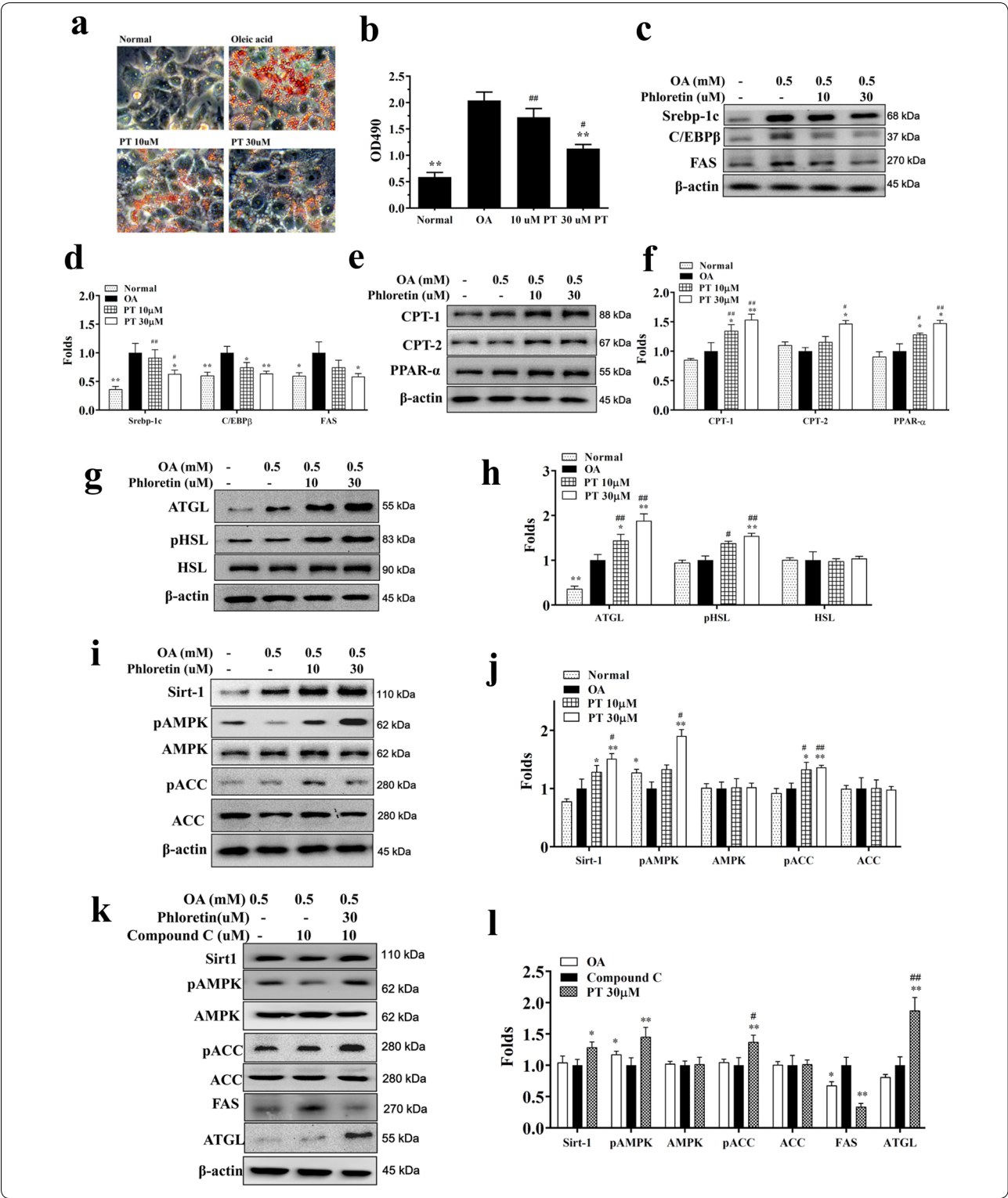
Protein assay demonstrated that phloretin significantly decreased Srebp-1c, C/EBP $\beta$ , and FAS expression compared to oleic acid-induced HepG2 cells (Fig. 1c, d). Phloretin could increase ATGL, pHSL, CPT-1, CPT-2, and PPAR $\alpha$  production in oleic acid-induced HepG2 cells (Fig. 1e–h). Phloretin also significantly increased Sirt-1, phosphorylation of ACC, and phosphorylation of AMPK in a concentration-dependent manner compared to oleic acid-treated HepG2 cells (Fig. 1i, j). In oleic acid-induced HepG2 cells co-treated with 30  $\mu$ M phloretin and compound C, phloretin restored phosphorylated AMPK, phosphorylated ACC, Sirt1, and ATGL, and inhibited FAS expression (Fig. 1k, l).

#### Phloretin reduced HFD-induced obesity in mice

We observed the appearance of the mice at the end of the experiments and found that HFD-induced obese mice were larger and fatter than normal mice (Fig. 2b). Interestingly, PT10 and PT20 mice had significant weight loss compared to HFD mice ( $39.69 \pm 0.36$  g,  $P < 0.05$  and  $37.55 \pm 0.40$  g,  $P < 0.01$  vs.  $43.40 \pm 0.60$  g, respectively; Fig. 2c, d). For obese mice treated with phloretin for 12 weeks, the weight gain in the PT10 and PT20 groups was significantly less than in the HFD group (PT10:  $10.52 \pm 0.73$  g,  $P < 0.05$ ; PT20:  $8.39 \pm 0.50$  g,  $P < 0.01$ ; HFD:  $13.80 \pm 0.78$  g; Fig. 2e). The PT10 and PT20 groups did not have altered food intake compared to the HFD group (Fig. 2f).

#### Phloretin reduced the weight of adipose tissue in obese mice

Using biopsy specimens, we found that phloretin significantly reduced the epididymal (Fig. 2g, h) and inguinal (Fig. 2j, k) adipose tissue weight compared to HFD mice. Phloretin also significantly decreased adipocyte size in the epididymal (Fig. 2i) and inguinal (Fig. 2l) adipose tissue compared to HFD mice.



Phloretin attenuated liver steatosis in obese mice

In HFD-induced obese mice, we found many fat vacuoles and lipid droplets distributed in the liver tissue. Our experiment found that obese mice treated with phloretin had significantly decreased fat vacuoles and fewer lipid droplets compared to HFD-induced obese mice (Fig. 3a,

(See figure on next page.)

**Fig. 2** Phloretin (PT) reduced body weight in mice with HFD-induced obesity. **a** Male mice were fed a HFD (containing 60% fat) for 16 weeks and administered DMSO, 10 mg/kg phloretin (PT10), or 20 mg/kg phloretin (PT20) via intraperitoneal injection (I.P.) twice a week from week 4 to week 16. **b** Appearance of the mice. **c** Body weight was measured for 16 weeks. **d** Body weight was measured in the last week and **e** weight gain measured from the fourth week to the 16th week. **f** Food intake was monitored each day. Phloretin (PT) reduced the epididymal and inguinal adipose tissue weight in HFD-induced obese mice. **g** HE staining of epididymal adipose tissue (200 × magnification). **h** Weight of epididymal adipose tissue. **i** Size of adipocytes in epididymal adipose tissue. **j** HE staining of inguinal adipose tissue (200 × magnification). **k** Weight of inguinal adipose tissue. **l** Size of adipocytes in inguinal adipose tissue. Data are presented as mean ± SEM; n = 10. \* $P < 0.05$ , \*\* $P < 0.01$  compared to HFD group. # $P < 0.05$ , ## $P < 0.01$  compared to the Normal group

b). We also found that phloretin reduced the liver weight compared to obese mice (Fig. 3c). However, obese mice treated with phloretin did not decrease the liver to body weight ratio compared to HFD-induced obese mice (Fig. 3d). Furthermore, HFD mice treated with phloretin had significantly decreased NAFLD scores than the HFD group (Fig. 3e). PAS staining demonstrated that phloretin increased the glycogen distribution in liver tissue compared to HFD-induced obese mice (Fig. 3f). Thus, phloretin significantly recovered the glycogen levels (Fig. 3g) and reduced the levels of TC and TG (Fig. 3h–i) in the livers of mice with HFD-induced obesity.

#### Phloretin regulated adipogenesis in liver tissue

Phloretin suppressed the expression of transcription factors Srebp-1c, C/EBP $\beta$ , and FAS compared to the HFD group (Fig. 4a, b). Phloretin enhanced ATGL, pHSL, CPT-1, CPT-2, and PPAR- $\alpha$  expression in mice with HFD-induced obesity (Fig. 4c–f). Phloretin also increased the phosphorylation of AMPK, Sirt1 and phosphorylation of ACC compared to the HFD group (Fig. 4g, h). Furthermore, phloretin significantly reduced TNF- $\alpha$  levels in the serum of mice with HFD-induced obesity (Fig. 4i). Phloretin also decreased TNF- $\alpha$  gene expression in liver and epididymal adipose tissue compared to HFD-induced obese mice (Fig. 4j, k). However, phloretin did not suppress TNF- $\alpha$  gene expression in inguinal adipose of mice with HFD-induced obesity (Fig. 4l). Next, we investigated the expression of genes involved in lipogenesis. Phloretin significantly decreased Srebp-1c, C/EBP $\beta$ , and FAS, and increased HSL, ATGL, CPT-1, CPT-2, PPAR $\alpha$ , and Sirt1 expression compared to HFD-induced obese mice (Fig. 5).

#### Effects of phloretin on serum lipid metabolism

Phloretin significantly reduced the serum levels of GOT and GPT, recovering liver function in mice with HFD-induced obesity (Fig. 6a, b). Phloretin also significantly suppressed serum free fatty acid, TC, LDL, and TG levels and increased the levels of HDL in HFD-induced obese mice (Fig. 6c–g). We also found that the administration of phloretin significantly inhibited the serum levels of leptin, glucose, and insulin and increased serum

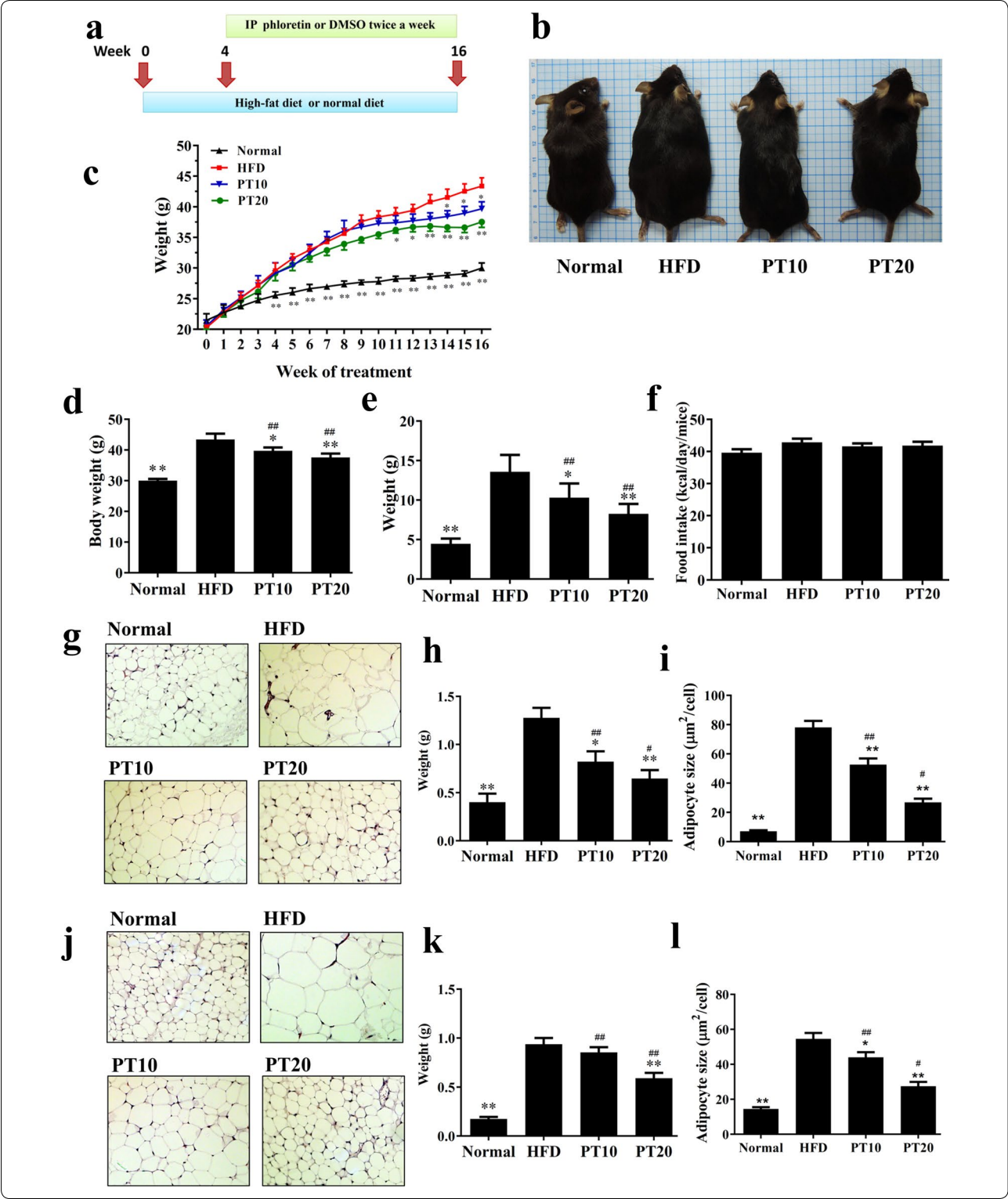
adiponectin levels compared to mice with HFD-induced obesity (Fig. 6h–k).

#### Discussion

Appropriate exercise and adjusted eating habits may improve obesity and NAFLD [4]. In recent years, scholars have pointed out that some pure plant compounds (e.g., resveratrol, curcumin, and maslinic acid) can reduce weight in obese mice and improve NAFLD, mainly by promoting the Sirt1/AMPK signaling pathway [17, 25, 30]. Our previous study found that phloretin can significantly inhibit the accumulation of oil droplets in differentiated 3T3-L1 adipocytes and significantly inhibit the expression of FAS and adipogenesis-related transcription factors. Phloretin can also improve lipolysis by promoting lipases and phosphorylation of AMPK in 3T3-L1 cells [22]. In recent years, some scholars have found that phloretin can prevent obesity and decrease body weight in HFD-induced mice. However, phloretin did not improve body weight or hepatic lipid accumulation in obese mice [24]. In their treatment model, HFD-induced obese mice were fed for 6 weeks and administered 10 mg/kg phloretin by intraperitoneal injection for only 6 weeks. We speculate that prolonging the phloretin treatment period and increasing the dose of phloretin may have reduced the weight in obese mice. Therefore, we designed an experimental procedure to induce obesity for 16 weeks, and treat mice with 10 mg/kg and 20 mg/kg phloretin twice a week for 12 weeks. The 20 mg/kg of phloretin for 12 weeks effectively reduced the weight of obese mice, as well as the weight and lipid accumulation of epididymal and inguinal adipose tissue.

Obesity is an important risk factor for cardiovascular disease and type 2 diabetes [31]. Long-term excessive intake of a refined diet will accelerate the accumulation of excessive energy in the body and lead to excessive weight [32]. Visceral fat tissue plays an important role in supporting and protecting the organs, but excessive accumulation of visceral fat will surround the organs and affect their function [31]. In mice induced by a HFD, visceral and inguinal adipose tissue accumulate large amounts of TGs, which not only increases body weight, but also increases the adipose tissue weight. Previous studies have





found that obese mice do not have reduced adipose tissue weight with intraperitoneal injection of 10 mg/kg phloretin for 6 weeks [24]. However, our experiments found that administration of 10 and 20 mg/kg phloretin by intraperitoneal injection for 12 weeks significantly reduces the weight of epididymal and inguinal adipose



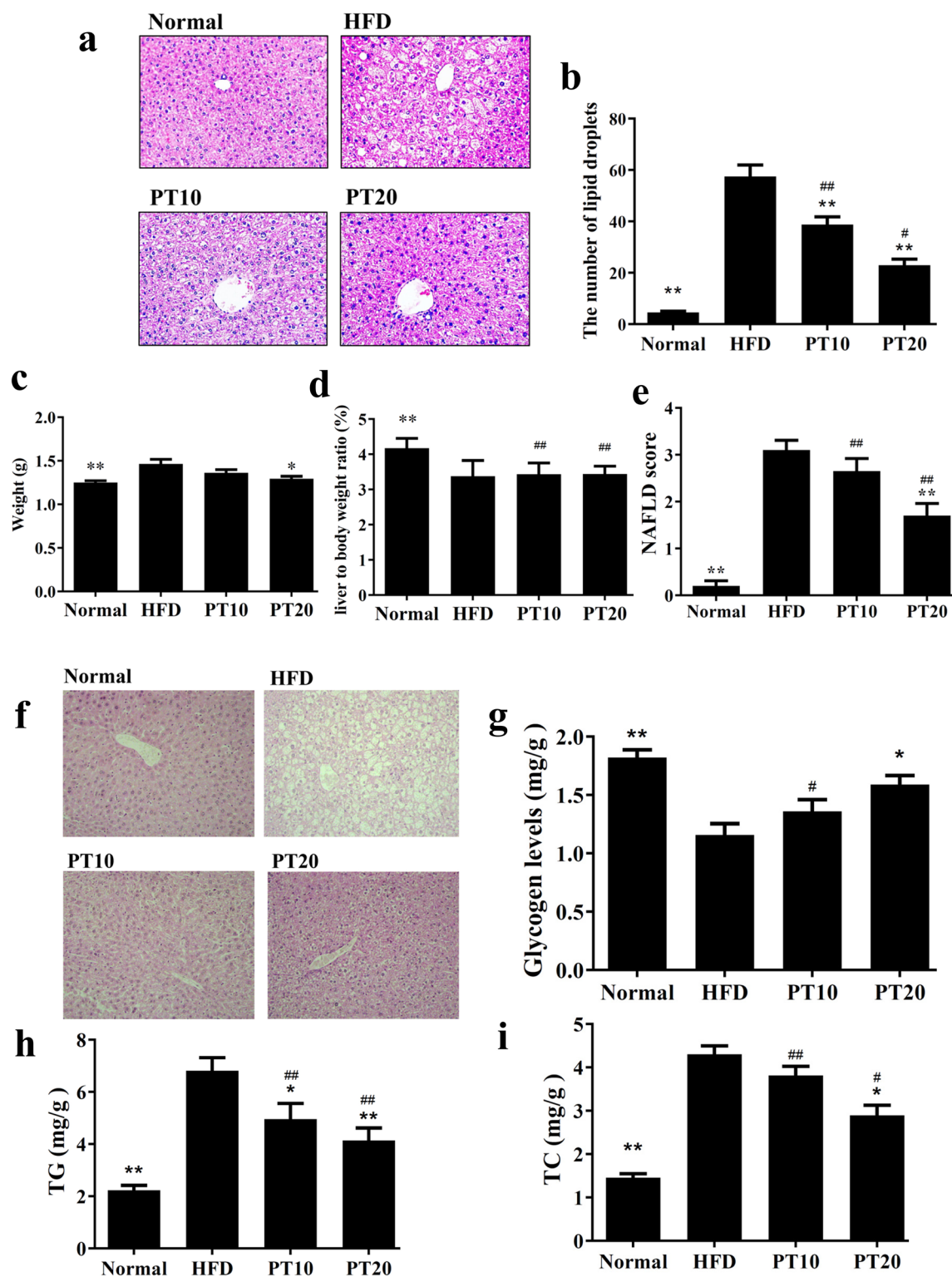


**Fig. 3** Phloretin (PT) ameliorated hepatic steatosis in HFD-induced obese mice. **a** HE staining of liver tissues (200 × magnification). **b** Calculated number of lipid droplets in liver tissue. **c** Liver weight, **d** the ratio of liver weight to body weight and **e** NAFLD scores based on HE staining. **f** PT modulated the glycogen distribution based on PAS staining in the liver (200 × magnification). **g** PT increased glycogen levels and **h** modulated triglyceride (TG) and **i** total cholesterol (TC) levels in the liver tissue. Three independent experiments were analyzed and the data presented as the mean ± SEM; n = 10. \* $P < 0.05$ , \*\* $P < 0.01$  compared to HFD-induced obesity. # $P < 0.05$ , ## $P < 0.01$  compared to the Normal group

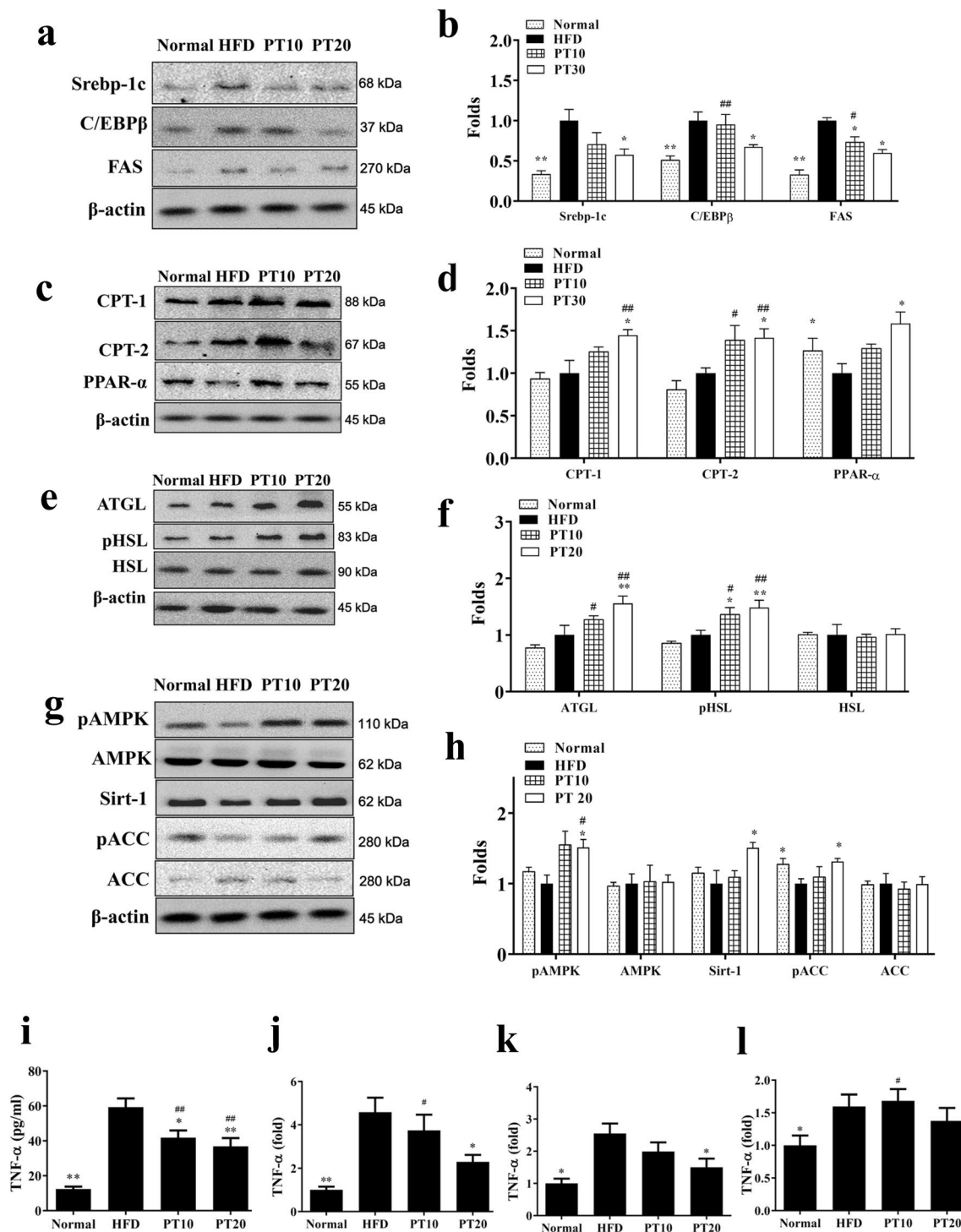


**Fig. 4** Effects of phloretin (PT) on lipid metabolism in mouse liver tissue. **a** The expression of transcription factors and FAS and **b** the fold expression were measured relative to β-actin. **c** β-oxidation and **d** the fold expression were measured relative to β-actin. **e** Lipolysis was detected by Western blot and **f** the fold expression measured relative to β-actin. **g** The Sirt1/AMPK pathway and **h** the fold expression measured relative to β-actin. Effects of phloretin (PT) on TNF-α expression. **i** TNF-α levels in serum from mice and **j** gene expression in the liver, **k** epididymal adipose tissue, and **l** inguinal adipose tissue. Fold-changes in expression were measured relative to β-actin expression levels (internal control). Three independent experiments were analyzed and the data presented as the mean ± SEM; n = 10. \**P* < 0.05, \*\**P* < 0.01 compared to HFD-induced obesity. #*P* < 0.05, ##*P* < 0.01 compared to the Normal group

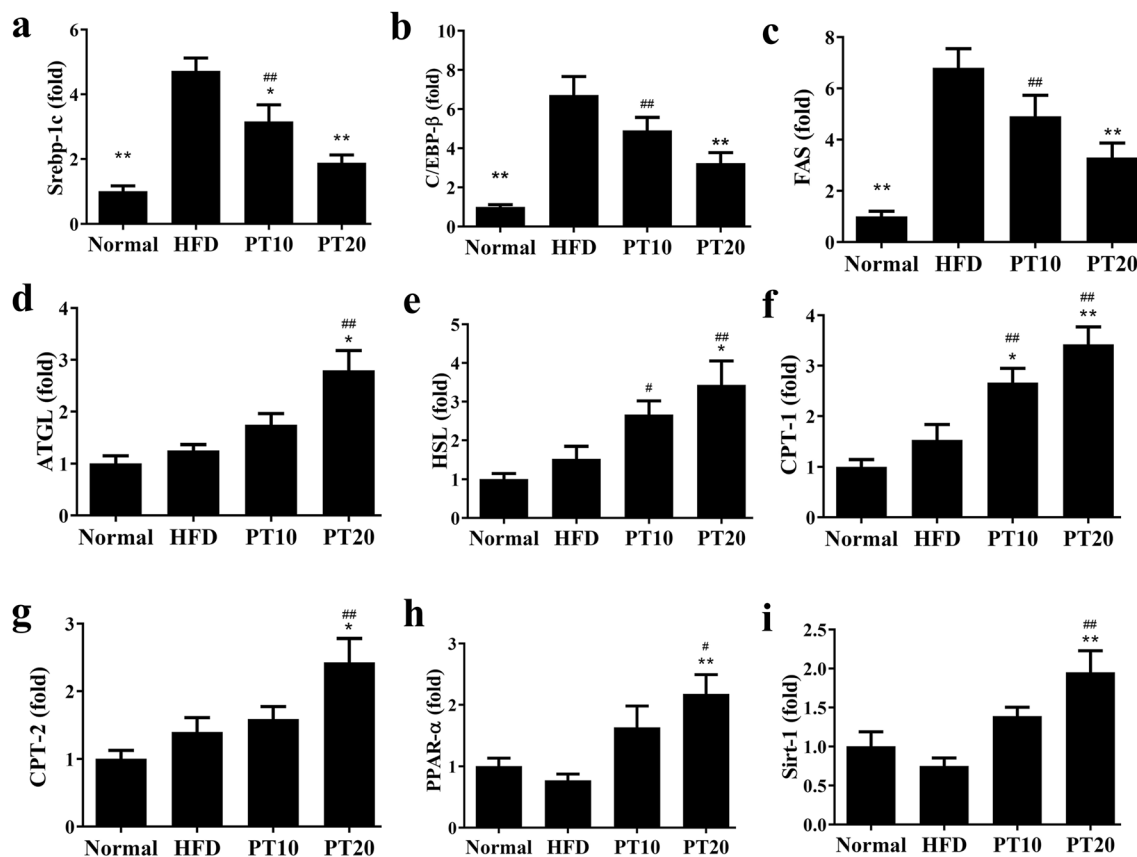


**Fig. 5** Phloretin (PT) modulated lipogenesis and lipolysis gene expression in liver tissue. **a** Expression levels of Srebp-1c, **b** C/EBP $\beta$ , **c** FAS, **d** ATGL, **e** HSL, **f** CPT-1, **g** CPT-2, **h** PPAR- $\alpha$ , and **i** Sirt-1 according to real-time PCR. Fold-changes in expression were measured relative to  $\beta$ -actin expression (internal control). Three independent experiments were analyzed and the data presented as the mean  $\pm$  SEM;  $n = 10$ . \* $P < 0.05$ , \*\* $P < 0.01$  compared to HFD-induced obesity. # $P < 0.05$ , ## $P < 0.01$  compared to the Normal group

tissue in obese mice. Therefore, we conclude that phloretin can not only prevent weight and fat accumulation in obese mice [24], but also improve the adipose tissue weight in obese mice to achieve weight loss.

The liver accumulated more TGs, causing liver steatosis and inducing the development of NAFLD. Fatty liver is defined as excessive accumulation of TGs in liver cells, and the fat content in liver tissue exceeds 5%, or fat vacuole content 10% [33]. The NAFLD score index includes blood biochemical values, fat vacuole number, and macrophage infiltration in liver tissue [28]. The NAFLD score for is significantly higher for HFD-induced obese mice than for normal mice. Phloretin could decrease the liver weight of obese mice, but phloretin did not reduce the ratio of liver weight/ body weight compared to HFD-induced obese mice. We thought that the liver of obese mice increases excessive oil droplets, but liver weight was increased by 1.17 fold in obese mice compared with normal mice. The liver weight was increased by 1.13 fold in obese mice compared with 20 mg/kg phloretin group

mice. Hence, the ratio of liver weight to body weight did not significantly decrease in phloretin-treated obese mice. Furthermore, liver cells can transport glucose into liver cells and convert glucose into glycogen to store energy. However, liver cells of obese people accumulate excessive lipids and interfere with energy metabolism [11]. Liver cells will use glycogen to convert into glucose to provide energy for liver cells. Therefore, fatty liver cells will have less glycogen distribution than normal liver cells. In this current study demonstrated that phloretin was able to recover the glycogen accumulation in liver tissue that reduced in HFD-induced obese mice. Hence, phloretin could regulate glycogen synthesis and maintained the metabolic function in the liver. We found that the TG content and number of fat vacuoles in the livers of phloretin-treated obese mice were significantly reduced compared to obese mice. Obese mice treated with phloretin also have significantly reduced serum GOT and GPT values; therefore, phloretin can restore liver function in obese mice. We think that our

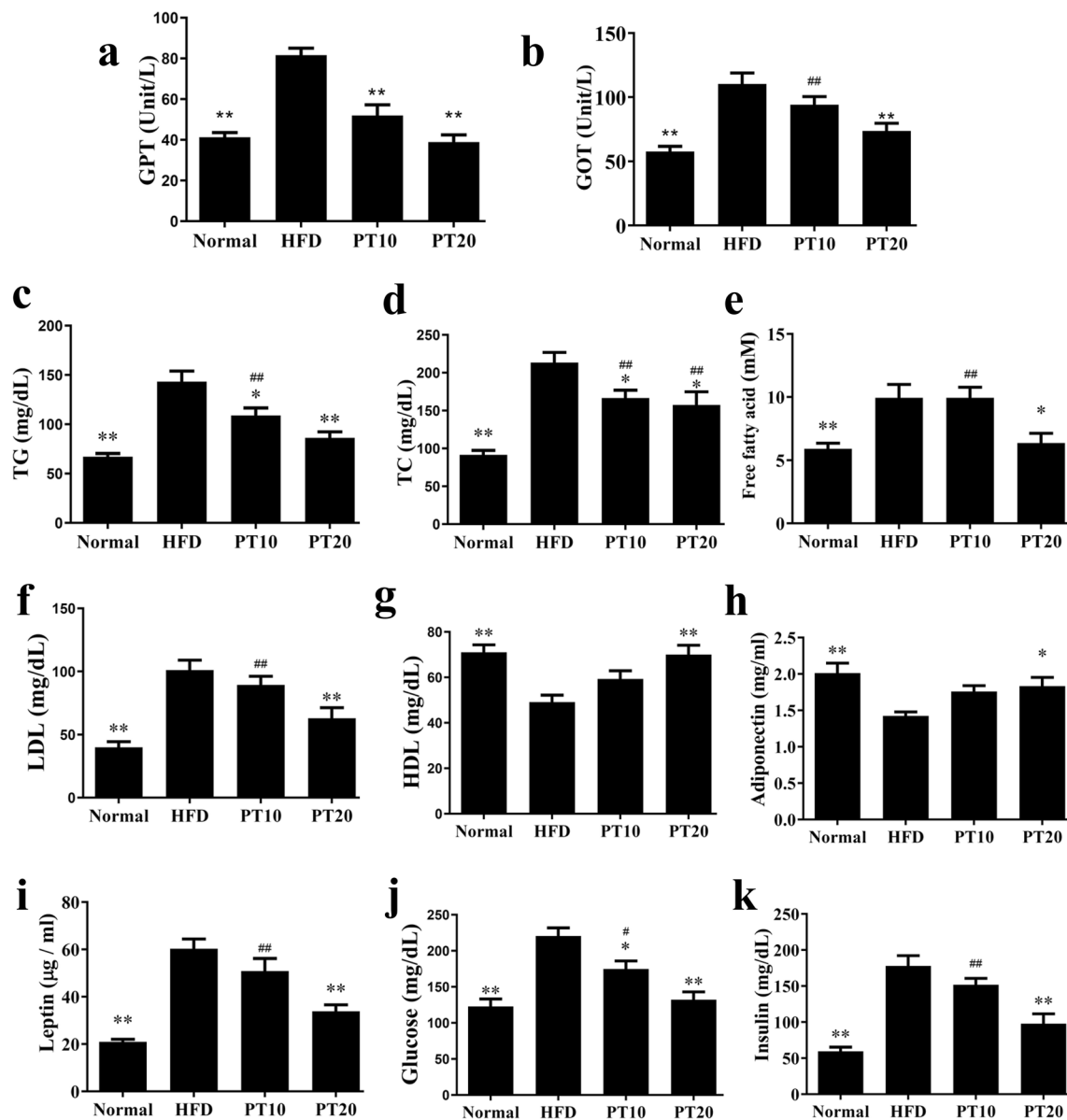


**Fig. 6** Serum biochemical analysis in mice. **a** Expression levels GPT, **b** GOT, **c** TG, **d** TC, **e** free fatty acid, **f** LDL, **g** HDL, **h** adiponectin, **i** leptin, **j** glucose, and **k** insulin. Three independent experiments were analyzed and the data presented as the mean  $\pm$  SEM;  $n = 10$ . \* $P < 0.05$ , \*\* $P < 0.01$  compared to HFD-induced obesity. # $P < 0.05$ , ## $P < 0.01$  compared to the Normal group

experimental results confirm that obese mice given phloretin for 12 weeks have significantly reduced NAFLD scores and improved symptoms of NAFLD.

Excessive accumulation of TGs in the liver will cause hepatic steatosis or NAFLD. The activation of transcription factors (including Srebp-1c and C/EBP $\beta$ ) is important for initiating the expression of genes in the lipid synthesis pathway and activating FAS expression to promote the synthesis of fatty acid chains [34]. Srebp-1c is considered to be the most important transcription

factor regulating lipid synthesis [35]. In the current study, we found that lipid accumulation in HepG2 cells and the fatty livers of obese mice can significantly increase Srebp-1c expression. Both phloretin-treated cells and obese mice have significantly reduced Srebp-1c expression and suppressed FAS productions. FAS is an important enzyme for regulating fatty acid chain synthesis and elongation [8]. A previous study found that HepG2 cells transfected with Srebp-1c siRNA and induced with fatty acid did not express Srebp-1c and excessive oil droplets

[36]. Therefore, we thought that oleic acid-induced HepG2 cells and the hepatocytes of obese mice would accumulate a large number of oil droplets and excessive TC and TGs, which is closely related to the expression of lipid synthesis transcription factors and FAS. We examined the livers of obese mice, and phloretin significantly reduced the expression of C/EBP $\beta$  and Srebp-1c, thereby inhibiting the expression of FAS and the synthesis of fatty acid chains. Therefore, phloretin-treated obese mice have reduced levels of TG and TC in the liver and improved liver steatosis. We used Oil Red O staining to confirm that oleic acid-induced HepG2 hepatocytes have more oil droplets and phloretin can reduce the oil droplet distribution in HepG2 cells. Our cell experiments also found that phloretin has the ability to reduce the expression of Srebp-1c, C/EBP $\beta$ , and FAS in HepG2 cells induced by oleic acid. Therefore, we thought that phloretin has the ability to block liver lipid synthesis by inhibiting transcription factors involved in lipogenesis and FAS expression in obese mice.

Liver or adipose tissue from obese mice has decreased AMPK activation [12, 14]. Sirt-1 regulates AMPK expression and induces AMPK phosphorylation [15]. Resveratrol is considered to be a Sirt1 enhancer, and obese mice treated with resveratrol have improved NAFLD and liver steatosis via promotion of the Sirt1/AMPK pathway [37]. AMPK can be used as a sensor of energy regulation to maintain lipid and sugar metabolism in liver and adipose tissue [13]. Previous studies have confirmed that excessive lipid accumulation in the liver and adipose tissue can inhibit AMPK activity and inhibit AMPK substrate ACC phosphorylation, increasing fatty acid synthesis [38]. Thus, reduced AMPK activity would lead to excessive TG accumulation in the liver, accelerating steatosis and NAFLD. In this study, we found that phloretin can effectively regulate the expression of Sirt1 and phosphorylated AMPK in HepG2 cells induced by oleic acid, and stimulate the phosphorylation of ACC to block FAS expression. An assay of liver protein in obese mice provided the same results as phloretin-treated oleic acid-induced HepG2 cells. In addition, HepG2 cells treated with phloretin and AMPK inhibitors also had restored AMPK phosphorylation and inhibited FAS expression. Therefore, our experimental results confirm that phloretin can reduce the accumulation of lipids in the livers of obese mice by regulating the Sirt1/AMPK pathway.

The excessive lipid accumulation of epididymal and inguinal adipose tissue in an obese individual will interfere with organ functions and induce chronic inflammation and dysfunction [39]. Therefore, increasing the breakdown of excessive TG accumulation will significantly improve liver steatosis and weight loss in obese individuals. TGs can be broken down by ATGL into

free fatty acids and diglycerides, and activated HSL can break down diglycerides into free fatty acids and monoglycerides [40, 41]. Previous studies have found that phloretin treatment for 6 weeks does not decrease the weight of obese mice [24], but they did not analyze the molecular mechanism of lipogenesis and lipolysis, and we do not understand the experimental design regarding the expression of lipid metabolism pathways in phloretin-treated obese mice. However, our experiment was designed to administer phloretin for 12 weeks at an increased dose. Interestingly, our experimental results showed that phloretin can significantly regulate the lipid synthesis and lipolysis pathways of the liver. Therefore, phloretin can effectively improve body weight and hepatic lipid accumulation in obese mice. In this study, we also found that phloretin can increase ATGL and phosphorylated HSL expression in oleic acid-induced HepG2 cells. Interestingly, phloretin can also significantly restore ATGL expression when oleic acid-induced HepG2 cells are co-treated with phloretin and AMPK inhibitor (compound C). Therefore, we confirmed that phloretin can increase lipolysis in fatty liver by regulating the phosphorylation of HSL and ATGL and AMPK expression to achieve weight loss and improve lipid accumulation in the fatty livers of obese mice.

Studies have pointed out that the intestinal bacteria of obese people may stimulate inflammation in the liver and adipose tissue through the intestine and circulatory system, and induce more inflamed macrophages to infiltrate the liver and adipose tissue [42, 43]. Bacterial endotoxin and excess free fatty acids could also stimulate macrophages to release more TNF- $\alpha$  to induce insulin resistance of hepatocytes and adipocytes [44]. Therefore, excessive free fatty acids produced by weight loss people need to generate energy through fatty acid  $\beta$ -oxidation, reducing the inflammation in the liver or adipose tissues caused by free fatty acids. In fatty acid  $\beta$ -oxidation, long-chain fatty acids need to be carried by carnitine to enter the mitochondria [7]. CPT-1 and CPT-2 are important enzymes for liver cells, as they bring free fatty acids from the cytoplasm into the mitochondria [45]. Our results demonstrate that phloretin can significantly increase the expression of CPT-1 and CPT-2 in the livers of obese mice, and phloretin increases the production of CPT-1 and CPT-2 in oleic acid-induced HepG2 cells. Interestingly, animal and cell experiments show that phloretin can also enhance PPAR- $\alpha$  expression in the liver tissues of obese mice and HepG2 cells to increase fatty acid metabolism via the  $\beta$ -oxidation pathway. We also found that phloretin can significantly reduce the levels of serum free fatty acids and TNF- $\alpha$  in obese mice. Furthermore, phloretin reduce the levels of TNF- $\alpha$  in the liver and



epididymal adipose tissue, improving inflammation and insulin resistance.

Adipocytes in overweight and obese individuals secrete more leptin to affect the hypothalamus and suppress appetite, reducing the accumulation of excessive energy in the body [46]. Our experiments show that obese mice treated with phloretin have reduced serum leptin and increased serum adiponectin. However, the food intake of obese mice treated with phloretin was not significantly different from that of control obese mice. Interestingly, phloretin can regulate fasting blood glucose and insulin levels in obese mice. Previous studies have demonstrated that increasing the levels of adiponectin can effectively reduce insulin resistance in obesity [47]. Therefore, we think that phloretin may improve blood sugar levels by regulating the levels of leptin and adiponectin, improving insulin resistance in obese mice.

Previous researchers have concluded that phloretin can prevent obesity in mice [24]. In the current study, our experimental conclusion demonstrated that phloretin can reduce the body weight of obese mice and the adipose tissue weight. Phloretin could also regulate lipid metabolism by increasing the Sirt1/AMPK pathway, improving liver steatosis in obese mice. Therefore, we think that phloretin has potential as a natural anti-obesity agent for treating NAFLD.

#### Abbreviations

ACC-1: Acetyl CoA carboxylase-1; AMPK: AMP-activated protein kinase; ATGL: Adipose triglyceride lipase; C/EBP: CCAAT/enhancer-binding protein; CPT-1: Carnitine palmitoyltransferase 1; CPT-2: Carnitine palmitoyltransferase 2; FAS: Fatty acid synthase; GOT: Glutamate oxaloacetate transaminase; GPT: Glutamate pyruvate transaminase; HDL: High-density lipoprotein; HE: Hematoxylin and eosin; HFD: High-fat diet; HSL: Hormone-sensitive lipase; LDL: Low-density lipoprotein; NAFLD: Non-alcoholic fatty liver disease; OA: Oleic acid; PAS: Periodic acid-Schiff; PPAR: Peroxisome proliferator-activated receptor; PT: Phloretin; Sirt1: Sirtuin 1; SREBP-1c: Sterol regulatory element-binding protein 1c; TG: Triglyceride; TC: Total cholesterol.

#### Acknowledgements

This study was supported in part by grants from Chang Gung Memorial Hospital (CMRPF1J0021, CMRPF1H0023, CMRPF1H0043, and CMRPF1J0061) and the Ministry of Science and Technology in Taiwan (MOST 108-2320-B-255-004, 106-2320-B-255-007-MY3 and 105-2320-B-255-003).

#### Authors' Contributions

Designed the experiments: CJL, YLC, and WCH; Performed the experiments: CJL, SJW, SCS, LCC, and YLC; Analysis and interpretation of data: CJL and SJW; Drafting the manuscript: CJL and WCH. All authors read and approved the final manuscript.

#### Availability of data and materials

Please contact the corresponding author for data on reasonable request.

#### Ethics approval and consent to participate

Animal experiments were approved by the Laboratory Animal Care Committee of Chang Gung University of Science and Technology (IACUC approval number: 2015–019).

#### Competing interests

The authors have no conflicts of interest to declare.

#### Author details

<sup>1</sup> Department of Nursing, Division of Basic Medical Sciences, Research Center for Chinese Herbal Medicine, Chang Gung University of Science and Technology, No.261, Wenhua 1st Rd., Guishan Dist., Taoyuan City 33303, Taiwan. <sup>2</sup> Division of Allergy, Asthma, and Rheumatology, Department of Pediatrics, Chang Gung Memorial Hospital, Linkou, Guishan Dist., Taoyuan City 33303, Taiwan. <sup>3</sup> Department of Nutrition and Health Sciences, Research Center for Chinese Herbal Medicine, Chang Gung University of Science and Technology, No.261, Wenhua 1st Rd., Guishan Dist., Taoyuan City 33303, Taiwan. <sup>4</sup> Aesthetic Medical Center, Department of Dermatology, Chang Gung Memorial Hospital, Linkou, Guishan Dist., Taoyuan 33303, Taiwan. <sup>5</sup> Graduate Program of Nutrition Science, National Taiwan Normal University, 88 Ting-Chow Rd, Sec 4, Taipei City 11676, Taiwan. <sup>6</sup> School of Nutrition and Health Sciences, Taipei Medical University, 250 Wu-Hsing Street, Taipei City 11031, Taiwan. <sup>7</sup> Graduate Institute of Health Industry Technology, Research Center for Food and Cosmetic Safety, Research Center for Chinese Herbal Medicine, College of Human Ecology, Chang Gung University of Science and Technology, No.261, Wenhua 1st Rd., Guishan Dist., Taoyuan City 33303, Taiwan.

Received: 17 June 2020 Accepted: 17 September 2020

Published online: 29 September 2020

#### References

- Shi Z, Wong J, Brooks VL. Obesity: sex and sympathetics. *Biol Sex Differ*. 2020;11(1):10.
- Xin X, Chen C, Hu YY, Feng Q. Protective effect of genistein on nonalcoholic fatty liver disease (NAFLD). *Biomed Pharmacother*. 2019;117:109047.
- Bril F, Cusi K. Nonalcoholic fatty liver disease: the new complication of type 2 diabetes mellitus. *Endocrinol Metab Clin North Am*. 2016;45(4):765–81.
- Glass O, Filozof C, Noureddin M, Berner-Hansen M, Schabel E, Omokaro SO, et al. Standardization of diet and exercise in clinical trials of NAFLD-NASH: recommendations from the liver forum. *J Hepatol*. 2020;27(20):30274–9.
- Kanda T, Goto T, Hirotsu Y, Masuzaki R, Moriyama M, Omata M. Molecular mechanisms: connections between nonalcoholic fatty liver disease, steatohepatitis and hepatocellular carcinoma. *Int J Mol Sci*. 2020;21(4):1525.
- Kitade H, Chen G, Ni Y, Ota T. Nonalcoholic fatty liver disease and insulin resistance: new insights and potential new treatments. *Nutrients*. 2017;9(4):387.
- Khan RS, Bril F, Cusi K, Newsome PN. Modulation of insulin resistance in nonalcoholic fatty liver disease. *Hepatology*. 2019;70(2):711–24.
- Wang Y, Viscarra J, Kim SJ, Sul HS. Transcriptional regulation of hepatic lipogenesis. *Nat Rev Mol Cell Biol*. 2015;16(11):678–89.
- Jarvis H, Craig D, Barker R, Spiers G, Stow D, Anstee QM, et al. Metabolic risk factors and incident advanced liver disease in non-alcoholic fatty liver disease (NAFLD): A systematic review and meta-analysis of population-based observational studies. *PLoS Med*. 2020;17(4):1003100.
- Hodson L, Gunn PJ. The regulation of hepatic fatty acid synthesis and partitioning: the effect of nutritional state. *Nat Rev Endocrinol*. 2019;15(12):689–700.
- Trites MJ, Clugston RD. The role of adipose triglyceride lipase in lipid and glucose homeostasis: lessons from transgenic mice. *Lipids Health Dis*. 2019;18(1):1019–151.
- Day EA, Ford RJ, Steinberg GR. AMPK as a therapeutic target for treating metabolic diseases. *Trends Endocrinol Metab*. 2017;28(8):545–60.
- Lopez M. Hypothalamic AMPK and energy balance. *Eur J Clin Invest*. 2018;48(9):12996.
- Smith BK, Marcinko K, Desjardins EM, Lally JS, Ford RJ, Steinberg GR. Treatment of nonalcoholic fatty liver disease: role of AMPK. *Am J Physiol Endocrinol Metab*. 2016;311(4):E730–E740740.
- Karbasforooshan H, Karimi G. The role of SIRT1 in diabetic retinopathy. *Biomed Pharmacother*. 2018;97:190–4.
- Francini F, Schinella GR, Rios JL. Activation of AMPK by medicinal plants and natural products: its role in type 2 diabetes mellitus. *Mini Rev Med Chem*. 2019;19(11):880–901.
- Tiao MM, Lin YJ, Yu HR, Sheen JM, Lin IC, Lai YJ, et al. Resveratrol ameliorates maternal and post-weaning high-fat diet-induced nonalcoholic

- fatty liver disease via renin-angiotensin system. *Lipids Health Dis.* 2018;17(1):178.
18. Kothari S, Dharmi-Shah H, Shah SR. Antidiabetic drugs and statins in nonalcoholic fatty liver disease. *J Clin Exp Hepatol.* 2019;9(6):723–30.
19. Yao H, Qiao YJ, Zhao YL, Tao XF, Xu LN, Yin LH, et al. Herbal medicines and nonalcoholic fatty liver disease. *World J Gastroenterol.* 2016;22(30):6890–905.
20. Shin JH, Jung JH. Non-alcoholic fatty liver disease and flavonoids: Current perspectives. *Clin Res Hepatol Gastroenterol.* 2017;41(1):17–24.
21. Huang WC, Fang LW, Liou CJ. Phloretin attenuates allergic airway inflammation and oxidative stress in asthmatic mice. *Front Immunol.* 2017;8:134.
22. Huang WC, Chang WT, Wu SJ, Xu PY, Ting NC, Liou CJ. Phloretin and phlorizin promote lipolysis and inhibit inflammation in mouse 3T3-L1 cells and in macrophage-adipocyte co-cultures. *Mol Nutr Food Res.* 2013;57:1803–13.
23. Liddle DM, Kavanagh ME, Wright AJ, Robinson LE. Apple flavonols mitigate adipocyte inflammation and promote angiogenic factors in LPS- and cobalt chloride-stimulated adipocytes, in part by a peroxisome proliferator-activated receptor- $\gamma$ -dependent mechanism. *Nutrients.* 2020;12(5):1386.
24. Alsanea S, Gao M, Liu D. Phloretin prevents high-fat diet-induced obesity and improves metabolic homeostasis. *Aaps J.* 2017;19(3):797–805.
25. Liou CJ, Dai YW, Wang CL, Fang LW, Huang WC. Maslinic acid protects against obesity-induced nonalcoholic fatty liver disease in mice through regulation of the Sirt1/AMPK signaling pathway. *FASEB J.* 2019;33(11):11791–803.
26. Liou CJ, Lee YK, Ting NC, Chen YL, Shen SC, Wu SJ, et al. Protective effects of licochalcone A ameliorates obesity and non-alcoholic fatty liver disease via promotion of the Sirt-1/AMPK pathway in mice fed a high-fat diet. *Cells.* 2019;8(5):447.
27. Liou CJ, Chen YL, Yu MC, Yeh KW, Shen SC, Huang WC. Sesamol alleviates airway hyperresponsiveness and oxidative stress in asthmatic mice. *Antioxidants.* 2020;9(4):295.
28. Kleiner DE, Brunt EM, Van Natta M, Behling C, Contos MJ, Cummings OW, et al. Design and validation of a histological scoring system for nonalcoholic fatty liver disease. *Hepatology.* 2005;41(6):1313–21.
29. Huang WC, Liu CY, Shen SC, Chen LC, Yeh KW, Liu SH, et al. Protective effects of licochalcone A improve airway hyper-responsiveness and oxidative stress in a mouse model of asthma. *Cells.* 2019;8(6):617.
30. Lee DE, Lee SJ, Kim SJ, Lee HS, Kwon OS. Curcumin ameliorates nonalcoholic fatty liver disease through inhibition of O-GlcNAcylation. *Nutrients.* 2019;11(1):2702.
31. Smith GI, Mittendorfer B, Klein S. Metabolically healthy obesity: facts and fantasies. *J Clin Invest.* 2019;129(10):3978–89.
32. Seabrook LT, Borgland SL. The orbitofrontal cortex, food intake and obesity. *J Psychiatry Neurosci.* 2020;45(3):190163.
33. Engin A. Non-alcoholic fatty liver disease. *Adv Exp Med Biol.* 2017;960:443–67.
34. Alves-Bezerra M, Cohen DE. Triglyceride metabolism in the liver. *Compr Physiol.* 2017;8(1):1–8.
35. Moon YA, Liang G, Xie X, Frank-Kamenetsky M, Fitzgerald K, Kotliansky V, et al. The SREBP pathway is essential for developing diabetic fatty liver and carbohydrate-induced hypertriglyceridemia in animals. *Cell Metab.* 2012;15(2):240–6.
36. Zhou Y, Yu S, Cai C, Zhong L, Yu H, Shen W. LXR $\alpha$  participates in the mTOR/S6K1/SREBP-1c signaling pathway during sodium palmitate-induced lipogenesis in HepG2 cells. *Nutr Metab.* 2018;15:31.
37. Tian Y, Ma J, Wang W, Zhang L, Xu J, Wang K, et al. Resveratrol supplement inhibited the NF- $\kappa$ B inflammation pathway through activating AMPK $\alpha$ -SIRT1 pathway in mice with fatty liver. *Mol Cell Biochem.* 2016;422(1–2):75–84.
38. Liou CJ, Wei CH, Chen YL, Cheng CY, Wang CL, Huang WC. Fisetin protects against hepatic steatosis through regulation of the Sirt1/AMPK and fatty acid  $\beta$ -oxidation signaling pathway in high-fat diet-induced obese mice. *Cell Physiol Biochem.* 2018;49(5):1870–84.
39. Wu D, Dawson NA, Levings MK. Obesity-associated adipose tissue inflammation and transplantation. *Am J Transpl.* 2016;16(3):743–50.
40. Steensels S, Ersoy BA. Fatty acid activation in thermogenic adipose tissue. *Biochim Biophys Acta Mol Cell Biol Lipids.* 2019;179:90.
41. Chen W, Jiang Y, Han J, Hu J, He T, Yan T, et al. Atgl deficiency induces podocyte apoptosis and leads to glomerular filtration barrier damage. *FEBS J.* 2017;284(7):1070–81.
42. Gupta B, Liu Y, Chopyk DM, Rai RP, Desai C, Kumar P, et al. Western diet-induced increase in colonic bile acids compromises epithelial barrier in nonalcoholic steatohepatitis. *FASEB J.* 2020;34(5):7089–102.
43. Wang Y, Zhou X, Zhao D, Wang X, Gurley EC, Liu R, et al. Berberine inhibits free fatty acid and LPS-induced inflammation via modulating ER stress response in macrophages and hepatocytes. *PLoS ONE.* 2020;15(5):e0232630.
44. Lefere S, Tacke F. Macrophages in obesity and non-alcoholic fatty liver disease: crosstalk with metabolism. *JHEP Rep.* 2019;1(1):30–433.
45. Longo N, Frigeni M, Pasquali M. Carnitine transport and fatty acid oxidation. *Biochim Biophys Acta.* 2016;1863(10):2422–35.
46. Polyzos SA, Kountouras J, Mantzoros CS. Leptin in nonalcoholic fatty liver disease: a narrative review. *Metabolism.* 2015;64(1):60–78.
47. Adolph TE, Grandner C, Grabherr F, Tilg H. Adipokines and non-alcoholic fatty liver disease: multiple interactions. *Int J Mol Sci.* 2017;18(8):1649.

# Publisher's Note

Springer Nature remains neutral with regard to jurisdictional claims in published maps and institutional affiliations.

**Ready to submit your research? Choose BMC and benefit from:**

- fast, convenient online submission
- thorough peer review by experienced researchers in your field
- rapid publication on acceptance
- support for research data, including large and complex data types
- gold Open Access which fosters wider collaboration and increased citations
- maximum visibility for your research: over 100M website views per year

**At BMC, research is always in progress.**

Learn more [biomedcentral.com/submissions](https://biomedcentral.com/submissions)



# Encapsulation of $\beta$ -Glucosidase within PVA Fibers by CCD-RSM-Guided Coelectrospinning: A Novel Approach for Specific Mogroside Sweetener Production

Virly,<sup>▽</sup> Chun-Hui Chiu,<sup>▽</sup> Tsan-Yu Tsai, Yi-Cheun Yeh, and Reuben Wang\*



Cite This: *J. Agric. Food Chem.* 2020, 68, 11790–11801



Read Online

ACCESS |



Metrics & More



Article Recommendations



Supporting Information

**ABSTRACT:** Siamenoside I is a rare mogroside in *Siraitia grosvenorii* Swingle and has become one of the target ingredients in natural sweetener production. However, the complex structure of siamenoside I has hindered its production in various ways. Here, a yeast cell that produces a specific  $\beta$ -glucosidase for siamenoside I conversion from mogroside V was constructed, and the enzymes were coelectrospun with poly(vinyl alcohol) followed by phenylboronic acid cross-linking to provide potential usage in the batch production process of Siamenoside I. A central composite design (CCD)-response surface methodology (RSM) was used to find the optimum coelectrospinning parameters. The pH stability and sodium dodecyl sulfate tolerance increased for the entrapped enzymes, and positive correlations between the fiber diameter and enzymatic activity were confirmed. The batch process showed an average siamenoside I production rate of  $118 \pm 0.08 \text{ mg L}^{-1} \text{ h}^{-1}$  per gram of fiber. This is the first research article showing specific siamenoside I production on enzyme-loaded electrospun fibers.

**KEYWORDS:** siamenoside I,  $\beta$ -glucosidase, poly(vinyl alcohol), coelectrospinning, CCD-RSM

## INTRODUCTION

Monk fruit or *Luo Han Guo* in Chinese (*Siraitia grosvenorii* Swingle) is one type of Cucurbitaceae fruit found in the southern part of China. It has been used for thousands of years as a traditional Chinese medicine in treating sore throat, high blood pressure, and constipation.<sup>1</sup> The monk fruit extract contains saponin mixtures called mogrosides (MGs) with high sweet intensities<sup>2</sup> and is considered to be a generally recognized as safe (GRAS) ingredient according to the U.S. FDA.<sup>3</sup> Each mogroside molecule comprises one aglycone called mogrol and is attached to several different glucose moieties at its C-3 and C-24 sites. For example, the most abundant mogroside in the fruit extract, mogroside V (MG V), has two and three glucose moieties bound to the C-3 and C-24 sites, respectively (Figure 1A). Meanwhile, both mogroside IV (MG IV) and siamenoside I (S I) have four glucose moieties attached to the mogrol in different patterns.<sup>4–6</sup>

Although there are several kinds of MGs in monk fruit, namely, MG VI, MG V, 11-oxo-MG V, MG IV, S I, MG III E, MG II, and MG I, few kinds are sweet.<sup>2,5</sup> For example, some studies showed that the sweetest mogroside, S I, is 563 times sweeter than 5% sucrose solution, although this compound accounts for less than 5% of total MGs.<sup>2,7,8</sup> Moreover, unlike other types of sweet MGs with sweet profiles varying from that of sucrose,<sup>9</sup> the sweetness characteristics of S I were more similar to those of sucrose, without any aftertaste.<sup>10</sup>

Several attempts have been made to develop procedures for obtaining S I, and most of them have focused on the transformation of MG V into S I. The reason is because MG V accounts for 60% of the total MGs in the fruit without enrichment,<sup>8</sup> and if a 100% conversion rate could be reached, large amounts of S I could be obtained. However, methods

including acid hydrolysis, enzymatic treatment, and in vivo digestion all have shown little effect on generating S I from MG V due to low specificity, as the chemical structures of these two compounds only differ by one glucose moiety, where MG V has one additional glucose on the C-3 position of S I, with a  $\beta$  (1  $\rightarrow$  6) linkage (Figure 1A).<sup>2,11,12</sup> Recently, the transformation of MG V using microbes has shed light on the specific production of S I from MG V. *Saccharomyces cerevisiae* BY4741 wild-type cells were able to produce  $\beta$ -glucosidase (ScExg1), which acts on peripheral glucose with (1  $\rightarrow$  6)- $\beta$ -D-glucosyl linkages at the C-3 and C-24 positions of MG V, generating S I and MG IV as intermediates and MG III E as the end product.<sup>13</sup> Additionally, the  $\beta$ -glucosidase produced by *Dekkera bruxellensis* (DbExg1) alternatively acts only on the peripheral glucose of MG V with (1  $\rightarrow$  6)- $\beta$ -D-glucosyl linkages at the C-3 position, generating only S I from MG V.<sup>14</sup> To the best of our knowledge, to date, no studies have focused on using DbExg1 in the redistribution of mogrosides for S I enrichment.

The high degree of substrate selectivity, energy efficiency, and cost-effectiveness of the enzyme as a biocatalyst have made it widely applied in various applications. Nevertheless, its vulnerability to structural changes caused by un conducive reaction conditions, including extreme pH, temperature, and

**Received:** April 21, 2020

**Revised:** August 6, 2020

**Accepted:** September 29, 2020

**Published:** September 29, 2020



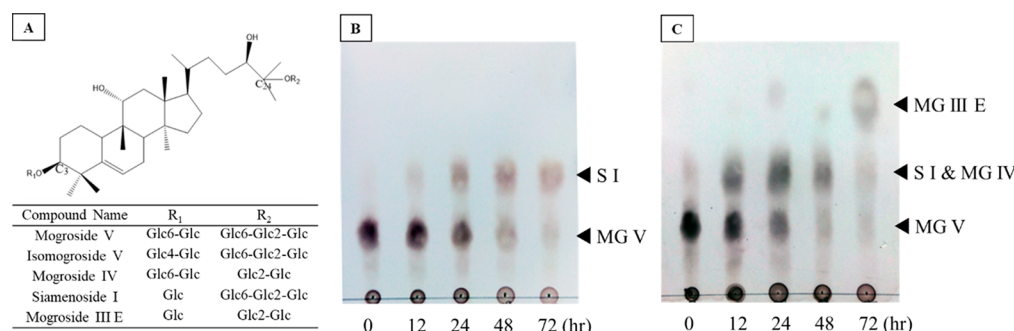


**Figure 1.** Mogrosides redistribution profiles analyzed by TLC. (A) The chemical structure of mogrosides. Mogrosides redistribution in (B) *S. cerevisiae* BY4741 *exg1Δ::DbEXG1* and (C) *S. cerevisiae* BY4741 WT.

the presence of disturbing chemical agents, limits its reusability and application on a larger scale and in a continuous production system.<sup>15,16</sup> To solve the aforementioned constraints of free-form enzymes, an enzyme immobilization technique can be performed.<sup>17,18</sup> Among all the enzyme immobilization techniques, entrapping enzymes in scaffolds has currently gained much attention.

Electrospinning is a method that uses an applied electric force to draw charged polymer solutions in the form of fibers toward a collector, resulting in fibers with high porosity and a high surface-to-volume ratio.<sup>19,20</sup> The coelectrospinning method is a process of combining two different materials and fabricating them into fibers in a single step, which allows minimum usage of chemicals and heat treatment.<sup>21</sup> Additionally, the high voltage applied during the coelectrospinning process has been suggested to have little effect on the tertiary structure of the enzymes.<sup>22</sup> Previously, several studies have demonstrated the suitability of this method in controlling enzyme release,<sup>23</sup> increasing the tolerance to extreme pH and temperature,<sup>24</sup> prolonging the storage stability,<sup>25</sup> increasing the reusability,<sup>26,27</sup> and enhancing the activities of the immobilized enzymes.<sup>28</sup>

In the present study, we endeavored to test the feasibility of S I production in a batch process in which fibers with specific enzymes were submerged in a flask containing MG V as the starting material. Poly(vinyl alcohol) (PVA) was chosen as supporting material of enzymes due to its high biocompatibility and nontoxic characteristics.<sup>23</sup> To achieve this aim, the produced enzyme/PVA fibers were first cross-linked to alter the hydrophilic nature of PVA. By using central composite design-response surface methodology (CCD-RSM), optimization of the electrospinning parameters (i.e., flow rate, applied voltage, and distance between spinneret and collector) was performed to generate a combination of parameters that produced fibers with the highest enzymatic activity as well as to study the relation of the activity to the fiber diameter. Additionally, the potential of the coelectrospinning method in addressing the problem of sustainable S I production was evidenced by demonstrating the reusability and robustness of the enzyme/PVA fibers. Finally, the S I production rate in this batch production process was calculated.

## MATERIALS AND METHODS

### Construction of Yeast Cells with *DbExg1* Secretion Activity.

To create a yeast strain with stable *DbExg1* secretion activity, the gene responsible for the enzyme could be obtained from the *DbEXG1* expression vector using the PCR amplification method.<sup>14</sup> *S. cerevisiae* (BY4741 *exg1Δ::KanMX4*) lacking *URA3* was chosen as the host cell, allowing us to select successfully gene-transformed colonies harboring

*DbEXG1* linked with *URA3* (*DbEXG1-URA3*), which would then appear on Ura<sup>+</sup> plates. However, the source of *DbEXG1*, which originates from the *DbEXG1* expression vector, was not directly linked to *URA3*; instead, there was an antibiotic resistance gene (*ampR*) between *DbEXG1* and *URA3*. Because there were concerns about the presence of antibiotic-resistant genes in the food system, we deleted *ampR* in the *DbEXG1* expression vector before using it as a template for *DbEXG1-URA3* amplification. The deletion of *ampR* was performed by first applying the inverse PCR method with back-to-back primers to amplify part of the *DbEXG1* expression vector, followed by ligation of the linear product to form circular DNA. The circular DNA was then used as the template for amplification of the *DbEXG1-URA3* target gene for DNA transformation. During the strain construction process, we were able to replace the *exg1Δ::KanMX4* gene cassette in BY4741 *exg1Δ* cells with *DbEXG1-URA3* at the chromosomal level through indigenous homologous recombination pathways in yeast. These processes result in cells having exogenous *DbEXG1* and were indicated as *S. cerevisiae* BY 4741 *exg1Δ::DbEXG1* in this study. Figure S1 of the Supporting Information (SI) shows a conceptual schematic of the inverse PCR process for this study, whereas Table S1 and Figure S2A show the primers with the sequence used for obtaining *DbEXG1-URA3* genetic materials and transformation results, respectively.

**Confirmation of Siamenoside I Conversion from Mogroside V in the Gene-Transformed Cells.** The test of MG conversion to S I in newly constructed cells (*S. cerevisiae exg1Δ::DbEXG1*) begins with the inoculation of cells in yeast extract-peptone-dextrose (YPD)-MGs medium. The YPD-MGs medium was prepared by adding 0.5% (w/v) of a commercially available powder of monk fruit extracts containing 80% MG V (Huilin Biotech Co., Ltd., Xi'an city, China) into the YPD medium. The MG conversion was carried out aerobically at 30 °C for 0, 12, 24, 48, and 72 h on an orbital shaker (200 rpm). Samples of cell-free supernatant were obtained after centrifugation (6000g, 10 min, 4 °C). The MGs in the supernatants were then extracted using solid-phase extraction (SPE) cartridges manufactured by Cayman Chemical (C-18, 500 mg/6 mL, FineTech, Taichung, Taiwan). Pure methanol was first infused to activate the cartridge, followed by water to equilibrate the system before sample loading. The unbound impurities and the MGs were eluted using 45% methanol and pure methanol, respectively.

The eluted MGs were first concentrated via a rotary evaporator, and the concentrates were applied onto thin layer chromatography (TLC) silica gel 60 plates (Merck, Germany). The TLC plates were developed in a chamber loaded with the developing solvent containing butanol–acetic acid–water with a 5:4:1 (v/v/v) ratio at the lower phase. After the plate was fully permeated with the developing solvent, the remaining solvent on the plate was allowed to evaporate, and the plate was sprayed with 10% (v/v) H<sub>2</sub>SO<sub>4</sub> to oxidize the mogrosides compound. The visualization of the results was performed after heating the plate on top of a dry incubator at 100 °C for 5 min.<sup>14,29</sup> The MG conversion profile of *S. cerevisiae* BY4741 WT served as a control, following the identical cell cultivation and analysis procedures mentioned above.



Table 1. CCD of Electrospinning Parameters with Enzymatic Activity and Diameter Responses

factors	levels				
	$-\alpha$	$-1$	$0$	$1$	$\alpha$
A: flow rate (mL/min)	0.003	0.004	0.006	0.008	0.009
B: voltage (kV)	12.2	12.5	13.0	13.5	13.8
C: distance (cm)	10.8	12.5	15.0	17.5	19.2
run	A: flow rate (mL/min)	B: voltage (kV)	C: distance (cm)	enzymatic activity ( $\mu$ U/mg)	diameter (nm)
1	0	0	0	213.57 $\pm$ 25.84	254
2	0	0	0	208.21 $\pm$ 26.67	267
3	0	0	0	209.04 $\pm$ 11.94	245
4	0	0	0	209.83 $\pm$ 33.64	240
5	1	1	$-1$	234.02 $\pm$ 22.04	310
6	0	0	$-\alpha$	226.30 $\pm$ 10.01	276
7	$-1$	1	$-1$	136.77 $\pm$ 15.7	273
8	$\alpha$	0	0	243.65 $\pm$ 10.83	343
9	$-\alpha$	0	0	139.64 $\pm$ 3.18	262
10	0	$-\alpha$	0	160.52 $\pm$ 8.82	294
11	$-1$	1	1	136.77 $\pm$ 4.6	246
12	0	0	0	223.49 $\pm$ 9.54	227
13	$-1$	$-1$	1	47.07 $\pm$ 12.76	245
14	1	$-1$	$-1$	265.06 $\pm$ 24.49	351
15	1	$-1$	1	68.19 $\pm$ 6.41	258
16	0	0	0	201.47 $\pm$ 19.42	231
17	0	$\alpha$	0	119.51 $\pm$ 4.23	276
18	1	1	1	91.71 $\pm$ 9.42	225
19	0	0	$\alpha$	32.27 $\pm$ 1.68	179
20	$-1$	$-1$	$-1$	239.11 $\pm$ 42.24	294

**Preparation of the Crude Extract of DbExg1.** To collect the extracellular protein DbExg1, the supernatant from the culture of *S. cerevisiae* *exg1Δ::DbEXG1* cells, which were cultivated in YPD broth at 30 °C for 72 h with orbital shaking (200 rpm), was first collected by centrifugation (6000g for 10 min at 4 °C). These supernatants were frozen at  $-80$  °C and lyophilized using a laboratory-scale freeze-dryer (Kingmech, Model FD4.5-8P-L, Taiwan). To increase the purity of the target protein, the dried supernatant in powder form was resuspended in distilled deionized water (DDW) (10% w/v) and loaded into a 12–14 kDa molecular weight cutoff (MWCO) ultrafiltration membrane, which was then dialyzed three times in DDW with a 1:100 ratio (v/v) at 4 °C for 6 h. The dialyzed suspension was then freeze-dried and kept at  $-80$  °C before further usage.

**DbExg1/PVA (Enzyme/PVA) Fiber Fabrication and Cross-Linking.** The 8% (w/v) PVA (poly(vinyl alcohol); 99% hydrolyzed,  $M_w$  85 000–124 000, Sigma-Aldrich Chemical Co., U.S.A.) solution in acetate buffer (20 mM at pH 5.0) was prepared in a water bath set at 80 °C with magnetic agitation for 3 h. After cooling to room temperature, the freeze-dried enzyme-enriched powder was mixed with the PVA solution with agitation to obtain a homogeneous mixture. The prepared mixtures were filled in a 5 mL Terumo syringe (23 G, 13 mm inside diameter) and delivered to the spinneret with the typical flow rate maintained at 0.006 mL/min controlled by an infusion pump (New Era Pump Systems, Model NE-300, U.S.A.). The spinneret was connected to a high-voltage power supply (Falco, Model FES-HV30, Taiwan) with the applied voltage set at 13.0 kV. The horizontal distance between the tip of the spinneret and the baking paper-covered collector plate was fixed at 15.0 cm. The generated fibers were then stored inside a dry cabinet with 65% relative humidity at 22 °C for 24 h to allow the remaining solvent to evaporate before cross-linking.

The cross-linking of fibers was performed according to Nunes et al. with few modifications.<sup>18</sup> First, the fibers were dipped into a 1% (w/v) phenylboronic acid solution for 2 to 10 min according to different settings. Afterward, the fibers were immersed in citrate-phosphate

buffer adjusted to pH 5.0 for 5 s to eliminate the remaining cross-linking solution and were then air-dried before further analysis.

**Optimization of Electrospinning Parameters Using CCD-RSM.** The main parameters in electrospinning include the flow rate, applied voltage, and distance between the spinneret and collector. These were optimized into a combination of parameters that produced fibers with the highest enzymatic activity. Additionally, the diameter of the produced fibers along with their relationship with enzymatic activity was studied.

First, we wanted to ensure that each of the testing parameters was within a reasonable range for electrospinning. Then, the five-level numbers for each parameter, including the center point, were set within this particular range. The five-level numbers, as well as their combinations of optimization experiments with other parameters, were set by central composite design (CCD) software (Design-Expert 12.0.0). According to this CCD tool, we only needed to include 14 sets of control factor (the three electrospinning parameters) experiments and 6 replicates of the center point to estimate the pure error sum of squares (Table 1). From this experimental design, the diameter of the fibers was set to be the response variable. Then, the data in the diameter of fibers were fitted into the quadratic model shown in eq 1:

$$Y = \beta_0 + \beta_1 X_1 + \beta_2 X_2 + \beta_3 X_3 + \beta_{12} X_1 X_2 + \beta_{13} X_1 X_3 + \beta_{23} X_2 X_3 + \beta_{11} X_1^2 + \beta_{22} X_2^2 + \beta_{33} X_3^2 \quad (1)$$

In addition, the enzymatic activity of fibers obtained from each parameter combination was fitted to the cubic model shown in eq 2:

$$Y = \beta_0 + \beta_1 X_1 + \beta_2 X_2 + \beta_3 X_3 + \beta_{12} X_1 X_2 + \beta_{13} X_1 X_3 + \beta_{23} X_2 X_3 + \beta_{11} X_1^2 + \beta_{22} X_2^2 + \beta_{33} X_3^2 + \beta_{123} X_1 X_2 X_3 + \beta_{112} X_1^2 X_2 + \beta_{122} X_1 X_2^2 \quad (2)$$

In eqs 1 and 2,  $Y$  is the response variable,  $\beta_0$  is the interception coefficient,  $\beta_1$ ,  $\beta_2$ ,  $\beta_3$ ,  $\beta_{12}$ ,  $\beta_{13}$ ,  $\beta_{23}$ ,  $\beta_{11}$ ,  $\beta_{22}$ ,  $\beta_{33}$ ,  $\beta_{123}$ ,  $\beta_{112}$ , and  $\beta_{122}$  are the estimated coefficients of the equation, and  $X_1$ ,  $X_2$ , and  $X_3$  are the manipulated control factors representing the flow rate (A), applied



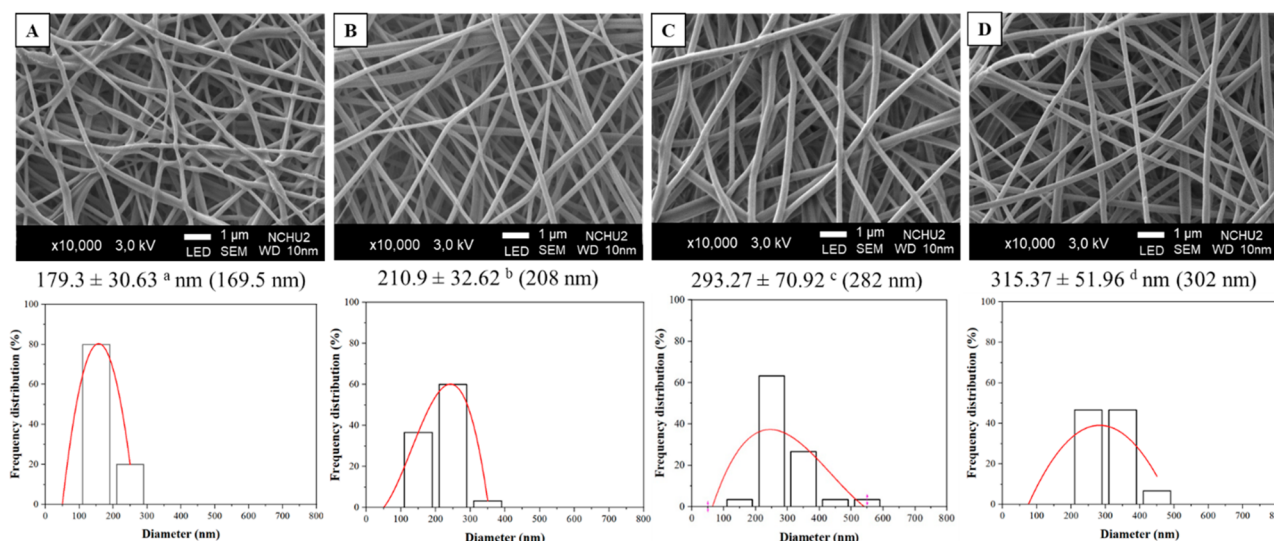


**Figure 2.** SEM micrographs of PVA electrospun fibers loaded with (A) 4%, (B) 5%, (C) 6%, and (D) 7% enzyme and their respective fiber diameters. Average values in diameters that do not share the same letter denote statistical significance ( $p < 0.05$ ). The data were analyzed by one-way ANOVA followed by Duncan's multiple test. Additional numbers in parentheses indicate the median numbers of 30 randomly measured diameter.

voltage (B), and distance between spinneret and collector (C), respectively.

The relations between the response variables ( $Y$ : enzymatic activity and diameter of fiber) and the input control factors ( $X$ : the electrospinning parameters) are shown in the response surfaces. In addition, statistical analysis of the response surface results obtained from response surface methodology (RSM) was performed using the central composite design (CCD) software mentioned above.

**Fiber Characterization.** The morphology and diameter of the produced fibers were analyzed by a scanning electron microscope (JEOL JSM-7800F, Thermal Field Emission Scanning Electron Microscope). The average diameter of the fiber was determined by manually measuring the diameter of 30 independent randomly selected fibers in different parts of the SEM image using ImageJ software (NIH). The types of functional groups in the fibers were analyzed by Fourier transform infrared (FTIR) spectrometry (Bruker Optik, Ettlingen, Germany) over 8 scans in a range 650–4000  $\text{cm}^{-1}$ .

The changes in thermal properties of PVA fiber mats as a result of enzyme loading and cross-linking were analyzed using differential scanning calorimetry (DSC, Mettler-Toledo, Switzerland). DSC analysis was performed in a  $\text{N}_2$  gas-filled chamber with a constant flow rate of 50  $\text{cm}^3 \text{min}^{-1}$  and a heating/cooling rate of 20  $^\circ\text{C min}^{-1}$  in the range of 25 to 250  $^\circ\text{C}$ .

**$\beta$ -Glucosidase Activity Assay.** The  $\beta$ -glucosidase activity of fibers shown in Table 1 was determined by measuring the amount of  $p$ -nitrophenol ( $p$ NP; Sigma-Aldrich) generated from the hydrolysis of 2.5 mg/mL of  $p$ -nitrophenyl- $\beta$ -D-glucopyranoside ( $p$ NPG; Sigma-Aldrich) in citrate-phosphate buffer with pH and temperature settings according to the specified assay conditions. Specifically, each of the free forms of *DbExg1* and *DbExg1*/PVA fibers was immersed in 500  $\mu\text{L}$  of  $p$ NPG and placed in a dry bath incubator for 1 h. The reaction was stopped by removing the fibers followed by the addition of 500  $\mu\text{L}$  of 0.5 M  $\text{Na}_2\text{CO}_3$ . The absorbance of the samples was analyzed using a UV-vis spectrophotometer at a wavelength of 405 nm and calibrated using  $p$ NP standard curves. One unit (U) of enzyme activity was defined as the formation of 1  $\mu\text{mole}$  of  $p$ NP or S I per minute (if the amount of S I was quantitated).

**Bradford Protein Assay.** The amount of protein released from the enzyme/PVA fibers in the cross-linking solution was estimated. After immersing fibers in the solutions for 10 min, 100  $\mu\text{L}$  aliquots were transferred and mixed with 100  $\mu\text{L}$  of Coomassie blue dye (CB Protein Assay reagent, G-Biosciences, U.S.A.). The mixture was incubated for 5 min. The optical density of the final mixture was read

at a wavelength of 595 nm. The absorbance of average test samples was subtracted from the absorbance of average blank samples before calibration using bovine serum albumin (BSA) standards. The final protein concentration results of the solution were expressed in  $\mu\text{g/mL}$ .

**Quantitation of mogrosides using UPLC MS/MS.** Mogroside standards (mogroside V, isomogroside V, siamenside I, mogroside IV, and mogroside III E) were obtained from Chengdu Biopurify Phytochemicals Ltd. (Chengdu, China), and the calibration range was 50–1000 ng/mL. The system included a Waters Acquity UPLC equipped with a pump, column compartment, and autosampler, as well as a Waters TQS mass spectrometer (Waters, Milford, MA, USA) operated in positive electrospray ion ( $\text{ESI}^+$ ) mode. An Acquity UPLC BEH C18 column (130  $\text{\AA}$ , 1.7  $\mu\text{m}$ , 2.1 mm  $\times$  100 mm) was employed and maintained at 35  $^\circ\text{C}$  with a flow rate of 0.3 mL/min and injected with 2  $\mu\text{L}$  of sample. The mobile phase consisted of 5% (A) and 100% methanol (B), both containing 0.01% formic acid. The linear gradient conditions were 45% B (0–1 min), 45–60% B (1–6 min), 60–99% B (6–6.2 min), 99% B (6.2–7 min), 99–45% B (7–8 min), and 45% B (8–10 min). The ESI parameters were set as follows: the capillary voltage was 3.1 kV, cone voltage was 38 V, desolvation temperature was 250  $^\circ\text{C}$ , source temperature was 150  $^\circ\text{C}$ , desolvation gas flow was 800 L/h, cone gas flow was 150 L/h, and nebulizer gas flow was 7.0 bar. The ESI scan range was set from  $m/z$  50 to 1500 Da. All MS/MS data for the analytes were collected by multiple reaction monitoring (MRM) mode and MassLynx4.1 software. The optimized MRM conditions are shown in Table S2.

**Statistical Analysis.** All experiments were performed at least in triplicate. For the enzymatic activity and total protein analyses, all data were expressed as the means  $\pm$  SD. Statistical analysis was performed using one-way ANOVA followed by Duncan's new multiple range test (SPSS for Windows, version 25.0.0.0). A value of  $p < 0.05$  was considered to be statistically significant.

## RESULTS AND DISCUSSION

**Confirmation of MG V Conversion to S I by *S. cerevisiae* *exg1Δ::DbEXG1*.** The *DbExg1* enzyme from *D. bruxellensis* has been found to have S I production specificity from MG V.<sup>14</sup> Nevertheless, the slow growth rate of this organism and its role in wine spoilage have hampered the production of S I through bioconversion.<sup>14</sup> Another kind of yeast, *S. cerevisiae*, with a rather short doubling time, effectively

secretes ScExg1, which converts MG V into S I and MG IV as intermediates and MG III E as the end product.<sup>13</sup> Therefore, to produce DbExg1 more effectively for S I production, the gene of DbExg1 (*DbEXG1*) was incorporated into the chromosome of *S. cerevisiae* which to replace the original ScExg1 controlled under the ScExg1 enzyme promoter (Figures S1 and S2). The self-constructed DbExg1-producing cells (*S. cerevisiae* *exg1Δ::DbEXG1*) were introduced to the S I conversion test. On the basis of the TLC results, it is quite obvious that S I was produced during the bioconversion process (Figure 1B), while the control group, *S. cerevisiae* BY4741 WT cells, first converted MG V to S I and MG IV as intermediates before proceeding to the final production of MG III E (Figure 1C). These results were similar to those of a previous study.<sup>14</sup>

#### Determination of DbExg1 Loading Capacity in Fibers.

When using fibers as a carrier for enzyme immobilization, the best outcome is to load the fibers with high amounts of enzymes while maintaining the fiber morphology.<sup>22</sup> Here, we first tried to determine how many enzymes could be mixed into the material while maintaining the fiber morphology. Through the preparation of PVA solutions with different enzyme loading percentages (4, 5, 6, and 7% w/v) for electrospinning, we found that the Taylor cone was not able to form once the enzyme content increased to 8% (w/v). Therefore, we decreased the amount of enzymes to 4~7% (w/v). The SEM results in Figure 2 show that all fibers had a smooth and bead-free morphology, indicating synergy between the carrier PVA fibers and the DbExg1 enzyme during the fiber fabrication process. Indeed, the diameter of the fiber also increased with increasing enzyme loading, suggesting the homogeneous dispersion of enzymes in PVA and the strong intermolecular interactions between the proteins and PVA.<sup>17,22</sup>

Meanwhile, a significantly lower enzymatic activity was observed in fibers with 4% enzyme loading compared to those with 5% and 7% enzyme loading. However, fibers with 4% and 6% of enzyme loading had a similar enzymatic activity (Figure 3A). These results demonstrate that the increase in enzyme

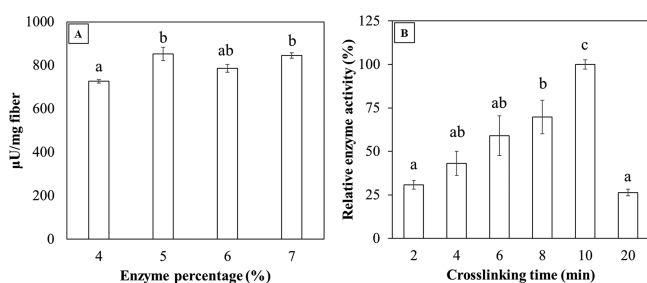


**Figure 3.** (A) Enzymatic activity tests of PVA fibers loaded with different percentages of enzymes. (B) The effect of cross-linking time on the catalytic activities of PVA fibers with 5% enzyme. Bars that do not share similar letters denote statistical significance ( $p < 0.05$ ). The data were analyzed by one-way ANOVA followed by Duncan's multiple test.

loading tends to increase fiber catalytic activity. However, we did notice that the fibers had a maximum overall catalytic activity in high enzyme-loaded fibers. Further increasing of the enzyme loading results in an increased fiber diameter (Figure 2), which we believe will offset the enzymatic activity of fibers because of the decreased mass transfer efficiency in large fibers.<sup>22,23,27,28</sup> Therefore, we proposed that 5% enzyme

loading was enough to produce fibers with acceptable enzymatic activity.

After determining the enzyme amount to be incorporated in the fibers, the cross-linking conditions of the fibers were established. From our results shown in Figure 3B, we suggest that an adequate cross-linking procedure involves the extension of the cross-linking time to prevent the disintegration of PVA fibers and to retain the enzymatic activity of the fibers. These results agree with the literature.<sup>22</sup> As such, 10 min was chosen as the appropriate cross-linking time for the enzyme/PVA fibers. However, 20 min of cross-linking results in lower fiber enzymatic activity.

**Characterization of Enzyme/PVA Fibers.** FTIR analysis was performed to confirm the presence of enzymes (DbExg1) in PVA fibers as well as to investigate the interactions among PVA, DbExg1, and phenylboronic acid (the cross-linker). All fibers shown in Figure 4 have a specific peak at 2939  $\text{cm}^{-1}$ ,

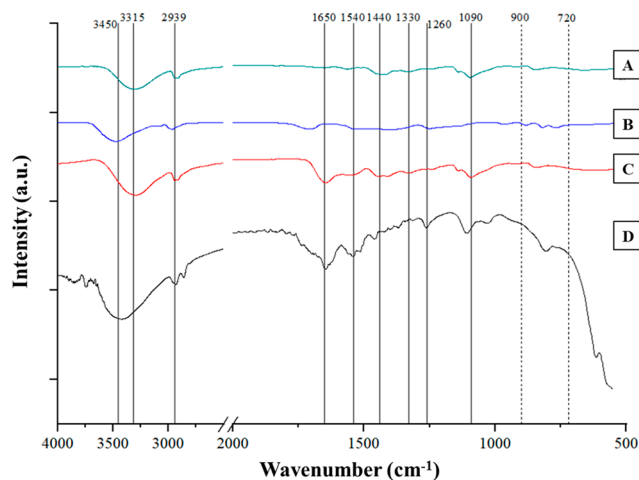


**Figure 4.** FT-IR spectra of (A) PVA fibers, (B) cross-linked PVA fibers, (C) DbExg1/PVA fibers, and (D) cross-linked DbExg1/PVA fibers.

which was characterized as the C–H group of PVA.<sup>30</sup> In the spectra of the noncrosslinked PVA and DbExg1/PVA fibers depicted in Figure 4A and C, the observed peaks at 1090 and 1330  $\text{cm}^{-1}$  represent stretching vibrations of C–O and  $-\text{CH}_2$ , respectively.<sup>27,31</sup> The specific peak at 1440  $\text{cm}^{-1}$  indicates C–C stretching vibrations, and a broad stretching band at approximately 3315  $\text{cm}^{-1}$  are associated with the  $-\text{OH}$  groups of PVA.<sup>22</sup> Meanwhile, a slight shift of peaks from 3315 to 3450  $\text{cm}^{-1}$  in the cross-linked PVA and DbExg1/PVA fibers (Figure 4B and D) might be caused by a diol complexation reaction through covalent boronate ester bonds occurred between two  $-\text{OH}$  groups of PVA and one phenylboronic acid ion during the cross-linking process. The diol complexation reaction also affect the overall structure of PVA which was indicated by the disappearance of peaks at 1090, 1330, and 1440  $\text{cm}^{-1}$  that resemble the C–O,  $-\text{CH}_2$ , and C–C groups of PVA for all cross-linked fibers.<sup>23,32</sup>

The vibrations caused by out-of-plane C–H deformations in the monosubstituted aromatic ring of phenylboronic acid were manifested by the presence of peaks within the range of 900–720  $\text{cm}^{-1}$ .<sup>33</sup> Furthermore, the stretching vibrations of B–O at 1260  $\text{cm}^{-1}$  resulted from the diol complexation reaction between B–OH groups of phenylboronic acid and  $-\text{OH}$

groups of PVA, verifying the cross-linking of PVA and *DbExg1*/PVA fibers using phenylboronic acid (Figure 4B and D).<sup>34,35</sup>

The presence of *DbExg1* was proven by an absorbance peak appearing at 1650 cm<sup>-1</sup> in both cross-linked and non-crosslinked *DbExg1*/PVA fibers (Figure 4C and D), which corresponded to the C=O stretching vibrations around the amide I region.<sup>27,36,37</sup> Although a slight shift of 1650 cm<sup>-1</sup> signal was found in the IR curve of cross-linked *DbExg1*/PVA fibers, which indicated structural changes of enzymes compared to the noncrosslinked fibers,<sup>38</sup> it is still an inevitable and a compromised procedure to prevent the PVA based fiber mat from disintegration when immersed into solutions. Also, the wider stretching bands at 3315 and 3450 cm<sup>-1</sup> for fibers loaded with enzymes were due to the superposition of the stretching vibrations of O–H and N–H bonds, respectively.<sup>28,37</sup>

Further evidence indicating the presence of PVA in fibers was that the melting temperature appeared at 225.5 °C (Figure S3E). This result agrees with the literature value.<sup>39</sup> The cross-linking agent used in this study contains boron, which readily accepts a pair of electrons from the hydroxyl oxygen groups of PVA. This interaction leads to disruption of the crystallinity of PVA fibers due to the decreased electron density of hydroxyl oxygen groups and resulted in the disappearance of the melting temperature (Figure S3D). The change in the melting temperature of each fiber with different treatments is shown in Figure S3.

**Relationship between the Enzymatic Activity and the Diameter of Produced Fibers.** Here, we found that thicker fibers resulted in higher fiber enzymatic activity (Figures 2 and 3B). These results contradict the general idea that fibers with smaller diameters provide a large surface-to-volume ratio, giving higher enzymatic activity than that of large fibers. In this discovery, we refer our results to the existing experiential evidence from Wang and Hsieh,<sup>17</sup> where small fibers offer little accommodation space and dispersion areas for enzyme molecules, which lead to weaker polar intermolecular interactions. As a result, the enzymes could more easily detach from the fibers during cross-linking.

To further extend our aforementioned discoveries and results, we performed a protein leakage test on fibers of different diameters in solutions containing the cross-linking agent phenylboronic acid. As expected, the results shown in Table 2 revealed the inability of small-diameter fibers to retain enzymes within the fiber matrix, as more proteins were detected in the phenylboronic acid solution than when thicker fibers were used. Therefore, we suggest that large-diameter fibers are required to provide stronger intermolecular polar

**Table 2. Protein Concentrations in the Crosslinking Solution of Fibers with Different Diameters**

run <sup>a</sup>	enzymatic activity (μU/mg)	diameter (nm)	protein concentration (μg/mL)
19	32.27 ± 1.68 <sup>b</sup>	201	16.22 ± 2.50 <sup>b</sup>
13	47.07 ± 12.76 <sup>b</sup>	245	10.89 ± 2.00 <sup>b</sup>
20	239.11 ± 42.24 <sup>b</sup>	294	9.33 ± 1.20 <sup>b</sup>
8	243.65 ± 10.83 <sup>b</sup>	343	5.11 ± 2.14 <sup>b</sup>

<sup>a</sup>Electrospinning parameters for each run displayed in Table 1. <sup>b</sup>indicate that values within the same column are significantly different ( $P < 0.05$ ). The data were analyzed by one-way ANOVA followed by Duncan's multiple tests.

interactions between PVA and the enzyme to prevent enzyme leakage during the cross-linking process. For this reason, we aimed to optimize the combination of parameters used in the electrospinning process and to produce fibers with relatively large diameters. Additionally, the relationships between the diameter and the enzymatic activity of individual fibers were investigated again to determine their correlations.

**Optimization of Electrospinning Parameters Using CCD-RSM.** In this part of the experiment, we optimized three essential parameters in electrospinning, namely, (A) flow rate, (B) applied voltage, and (C) distance between spinneret and collector, to generate fibers with different diameters. In addition, we were interested in how those parameters affect the enzyme activity since the fiber diameter played a major role in determining the enzyme activity of the fibers. The fiber diameter and enzyme activity data, which were acquired from experiments based on the central composite design (CCD), are shown in Table 1. According to the data fitting summary, the cubic model and the full quadratic polynomial model were selected as model equations to predict the enzymatic activity (3) and fiber diameter (4) of the produced fibers, respectively. These coded equations are as follows:

$$Y = 210.37 + 34.67A - 12.82B - 57.75C + 0.64AB - 18.39AC + 30.82BC - 6.55A^2 - 26.12B^2 - 27.60C^2 - 17.18ABC + 10.30A^2B - 8.66A^2C - 22.26AB^2 \quad (3)$$

$$Y = 244.42 + 16.60A - 9.36B - 30.56C - 6.75AB - 12.75AC + 3.75BC + 24.50A^2 + 14.83B^2 - 6.83C^2 \quad (4)$$

The results of the analysis of variance (ANOVA) shown in Table 3 revealed that variables  $A$ ,  $B$ ,  $C$ ,  $AC$ ,  $BC$ ,  $A^2$ ,  $B^2$ ,  $C^2$ ,  $ABC$ , and  $AB^2$  significantly influenced the enzymatic activity of fibers ( $p < 0.05$ ). Meanwhile, the lack-of-fit test, which is an evaluation to determine the impact of discrepancies between the actual and predicted values on the pure error among replicates, had a value of 0.1962, which was higher than 0.05, i.e., not significant ( $p$ -value  $< 0.05$ ). In addition, the lack-of-fit  $F$ -value of 2.22 implies that the lack of fit is not significant. There is a 19.62% chance that a lack-of-fit  $F$ -value this large could occur due to noise. Therefore, the cubic model adequately explains the interactions of parameters in the region of experimentation. The goodness of fit of the proposed model for enzyme activity predictions was also determined. Figure 5A–D show enzyme activity values located in a narrow range of normal probability lines, diagonal lines, and two zero-axes, suggesting the adequacy of the model used to predict the experimental results.

The ANOVA (Table 4) shows the diameter of the produced fibers, which were sensitive to all the variations of independent variables ( $A$ ,  $B$ , and  $C$ ), one interactive cross-product coefficient ( $AC$ ), and two quadratic term coefficients ( $A^2$  and  $B^2$ ), with  $p < 0.05$ . In addition, a lack-of-fit  $p$ -value larger than 0.05 indicates the success of the RSM model in predicting the variance in the test and the experimental data. The scattering of diameter values in Figure 5E–H also describes the fitness of the model.

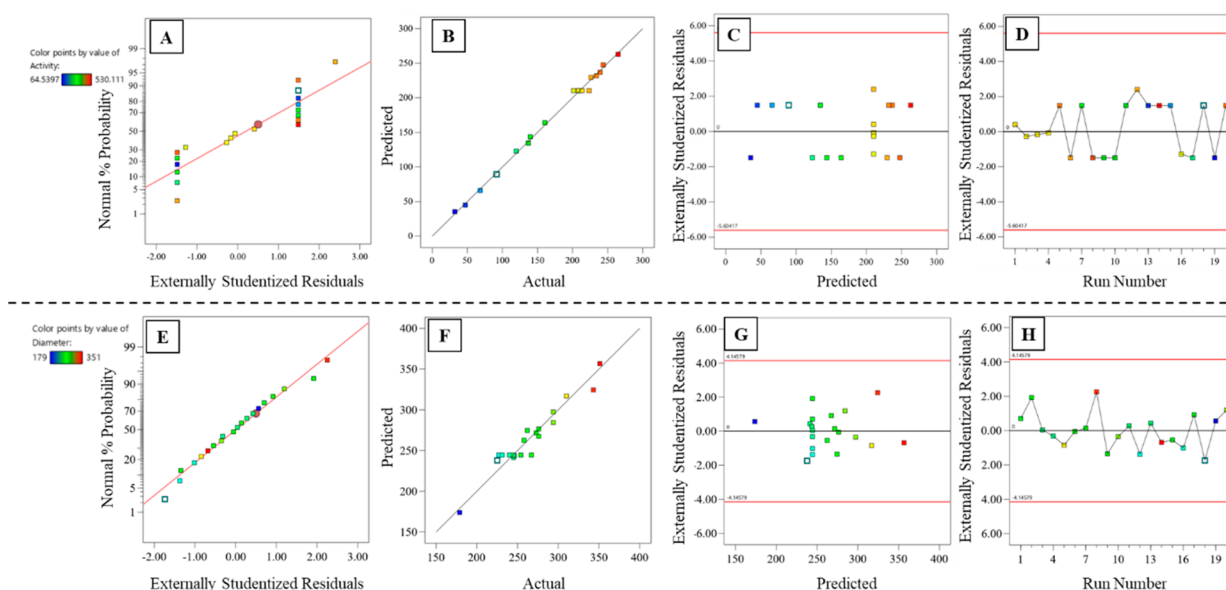
From the response surface plot depicted in Figure 6A and B, we can see that a higher flow resulted in a higher enzymatic activity of fibers. In addition, the sharp curvature of the curve in Figure 6C shows the reciprocal relationships between the distance and enzymatic activity of the fibers. Meanwhile, the optimum value of applied voltage as the driving force to stretch the feed solution worked synergistically with the flow rate and



Table 3. Analysis of Variance (ANOVA) for Enzymatic Activity as the Response<sup>a,b</sup>

source	sum of squares	df	mean square	F-value	p-value	
model	92784.44	13	7137.26	111.29	<0.0001	significant
A, flow rate	5409.04	1	5409.04	84.34	<0.0001	
B, voltage	840.91	1	840.91	13.11	0.0111	
C, distance	18823.82	1	18823.82	293.52	<0.0001	
AB	3.28	1	3.28	0.0512	0.8285	
AC	2706.11	1	2706.11	42.20	0.0006	
BC	7601.18	1	7601.18	118.53	<0.0001	
A <sup>2</sup>	441.76	1	441.76	6.89	0.0393	
B <sup>2</sup>	8479.62	1	8479.62	132.22	<0.0001	
C <sup>2</sup>	11065.68	1	11065.68	172.55	<0.0001	
ABC	2362.44	1	2362.44	36.84	0.0009	
A <sup>2</sup> B	330.89	1	330.89	5.16	0.0635	
A <sup>2</sup> C	247.98	1	247.98	3.87	0.0968	
AB <sup>2</sup>	1427.31	1	1427.31	22.26	0.0033	
residual	384.78	6	64.13			
lack of fit	118.39	1	118.39	2.22	0.1962	not significant
pure error	266.40	5	53.28			
cor total	93169.22	19				

<sup>a</sup>R<sup>2</sup>: 0.9959, Adj. R<sup>2</sup>: 9869, Pred. R<sup>2</sup>: 0.6825, Std. Dev. = 8.01, CV = 4.70%, PRESS = 29 578.50. <sup>b</sup>*p* < 0.05 indicates that the model terms are significant.



**Figure 5.** Diagnostic plots for the enzymatic activity (upper panel) and diameter (lower panel) of fibers: (A, E) normal probability plot on a probit scale, (B, F) predicted versus actual values plot, (C, G) studentized residuals versus predicted values plot, and (D, H) studentized residuals versus run number plot.

distance to promote the production of fibers with the highest enzymatic activity (Figure 6A and C).

The delineated response surface plots depicted in Figure 6D and E showed little change in the diameter when the flow rate was set between 0.004 and 0.006 mL/min, and the diameter started to increase to the highest level when the flow rate increased to 0.007–0.008 mL/min. The increased flow rate resulted in an increased feeding rate at the tip of the spinneret, creating conditions favoring the movement of materials and forming thicker fibers. Additionally, it can be observed from Figure 6D and F that changes in the applied voltage had little effect on the fiber diameter, while Figure 6E and F shows that a decrease in the distance between the spinneret and collector resulted in a linear increase in the fiber diameter.

From the overall CCD-RSM results shown in Table 1, we again proved that fibers with large diameters resulted in higher enzymatic activity and that all the tested parameters had similar trends regarding the fiber diameter and enzymatic activity (Figure 6). However, we found that fibers produced from both the 8<sup>th</sup> and 14<sup>th</sup> runs with a relatively high flow rate and short distance had significantly high values of enzymatic activity as well as diameter. The instability of the electrospinning process caused by the unsuitable parameter combinations in the 14<sup>th</sup> run resulted in fibers with a nonhomogeneous morphology (Figure S4A). Meanwhile, the spinning condition for the 8<sup>th</sup> run generated fibers with a smooth and bead-free morphology (Figure S4B). Considering the information regarding the fiber homogeneity and enzymatic activity, we ultimately chose the parameters of the

Table 4. Analysis of Variance (ANOVA) for Diameter as the Response<sup>a,b</sup>

source	sum of squares	df	mean square	F-value	p-value	
model	28 957.99	9	3217.55	15.33	<0.0001	significant
A, flow rate	3444.50	1	3444.50	16.41	0.0023	
B, voltage	1149.38	1	1149.38	5.48	0.0413	
C, distance	12 741.53	1	12 741.53	60.70	<0.0001	
AB	364.50	1	364.50	1.74	0.2170	
AC	1300.50	1	1300.50	6.20	0.0320	
BC	112.50	1	112.50	0.5359	0.4809	
A <sup>2</sup>	6173.68	1	6173.68	29.41	0.0003	
B <sup>2</sup>	2735.72	1	2735.72	13.03	0.0048	
C <sup>2</sup>	677.93	1	677.93	3.23	0.1025	
residual	2099.21	10	209.92			
lack of fit	995.21	5	199.04	0.9015	0.5439	not significant
pure error	1104.00	5	220.80			
cor total	31057.20	19				

<sup>a</sup>R<sup>2</sup>: 0.9324, Adj. R<sup>2</sup>: 0.8716, Pred. R<sup>2</sup>: 0.7235, Std. Dev. = 14.49, CV = 5.47%, PRESS = 8586.84. <sup>b</sup>p < 0.05 indicates that the model terms are significant.

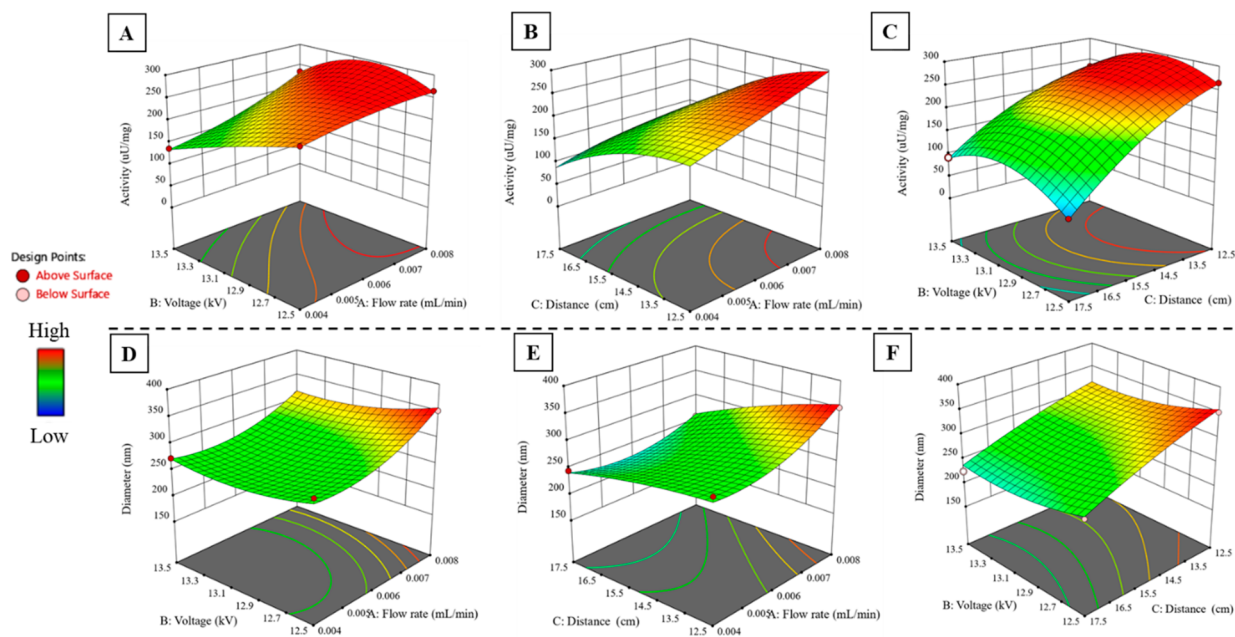


**Figure 6.** Response surface and contour plots for the mutual effects of parameters: (A, D) voltage and flow rate, (B, E) flow rate and distance, and (C, F) voltage and distance on enzymatic activity (upper panel) and diameter (lower panel) of fibers.

8<sup>th</sup> run as the optimum electrospinning parameters (0.009 mL/min, 13.0 kV, and 15.0 cm) for fiber fabrication.

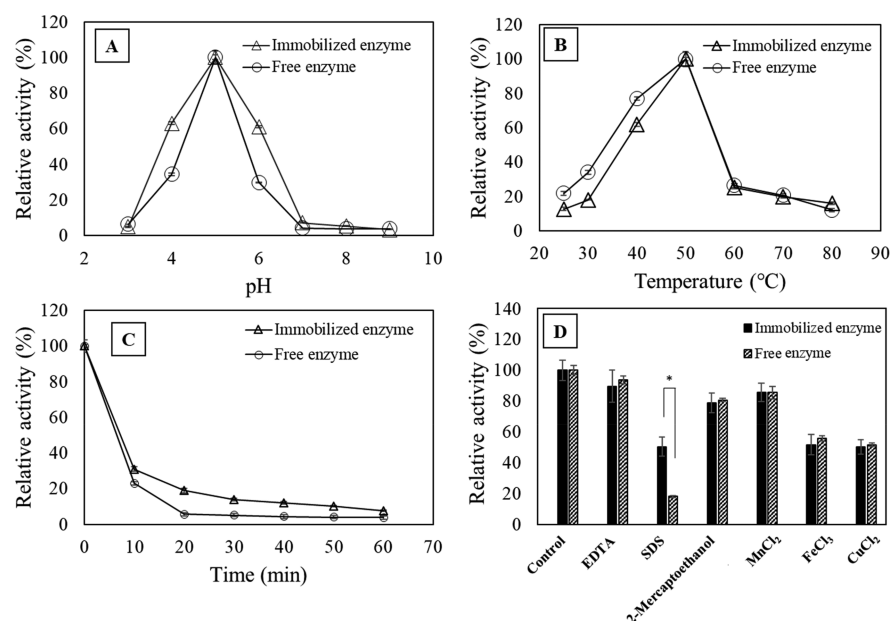
**Characterization of Enzyme Fiber Working Conditions.** The optimum pH working conditions for the enzyme fibers were assessed within the pH range from 3.0 to 9.0 at 50 °C. From Figure 7A, we observed that immobilization did not change the optimum pH of the enzyme but allowed a greater enzymatic activity to be maintained than that of the free enzyme at pH 4 and 6.

Figure 7B shows the enzyme reactivity of fibers at different temperatures from 30 to 80 °C at pH 5.0. Note that there was no significant difference in the relative activity between immobilized and free enzymes at a reaction temperature above 50 °C; this is because DbExg1 was very sensitive to high temperatures and easily became denatured once incubated at temperatures that exceeded its optimum limit.<sup>18</sup> In addition, we realized that immobilization would cause a decrease in the free enzyme activity when the reaction temperature was set

under an optimum working temperature of 50 °C. This result was most likely due to the increased intermolecular interactions of enzymes and the PVA matrix, acting as a physical barrier that inhibited the substrate-enzyme interactions under this less triggering condition.<sup>35</sup> This is also the case because intermolecular interactions decrease the flexibility of the enzyme within PVA molecules that further protect the enzyme under more extreme pH conditions.<sup>22,23</sup>

The thermal stability test of the free enzyme and immobilized enzyme fibers at 60 °C provided additional evidence showing that PVA molecules maintain the stability of the enzyme. The results given in Figure 7C indeed confirm the temperature sensitivity of the enzyme, where extreme losses of enzyme activity occurred during the first 10 min of incubation. However, compared to the free enzyme, the immobilized enzyme was able to maintain a significantly higher catalytic performance during extended 50 min heat exposure. These results were also observed in a previous study.<sup>24</sup>





**Figure 7.** Relative activity of free and immobilized enzymes under different (A) pH values and (B) temperatures when incubated at 50 °C for 1 h and pH 5.0 for 1 h, respectively. (C) The thermostability of free and immobilized enzymes tested at 60 °C and pH 5.0 for 1 h. (D) Effects of chemical agents and metal ions (10 mM) on the relative activity of free and immobilized enzymes. \* Indicates significantly different results from the indicated groups by Student's *t* test with *p*-value <0.05.

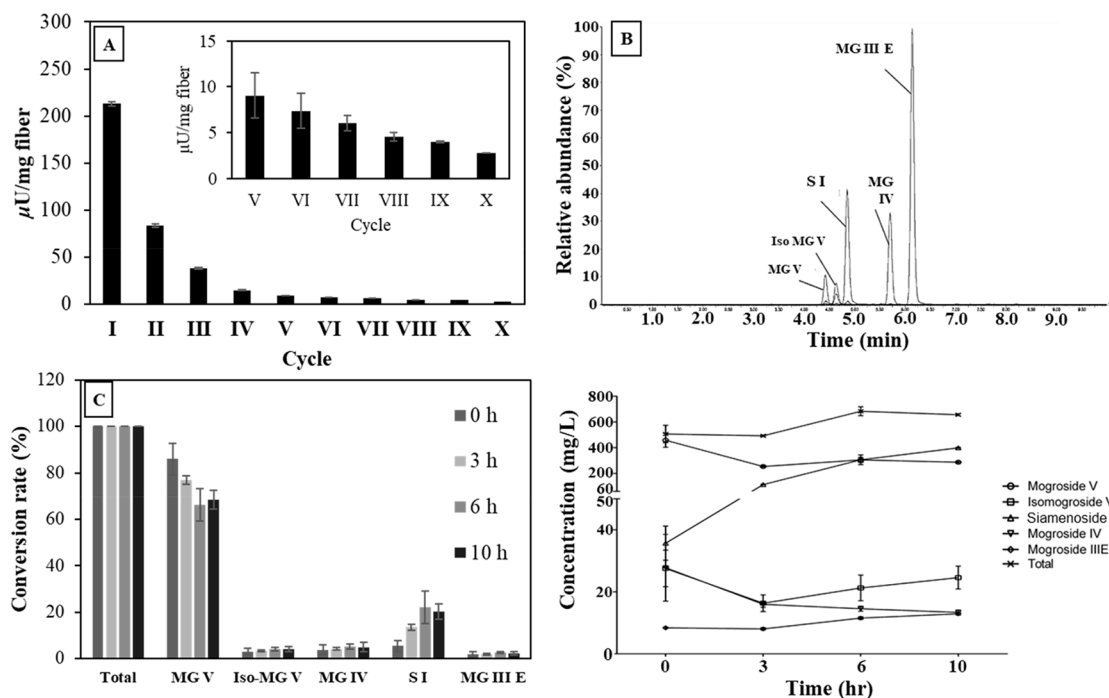


**Figure 8.** Substrate conversion activity of cross-linked enzyme/PVA fibers. (A) pNPG conversion activities during 10 cycles of reuse. (B) A representative mogroside distribution analyzed by UPLC–MS/MS. (C) Time course of the mogroside conversion rate and mogroside content under conditions of 50 °C at pH 5.

Enzymes used in food industries may have the chance to come into contact with chemicals that influence their activity. For example, chemicals including metal ions present in water or from equipment corrosion can work as either activators or inhibitors of enzymes. Meanwhile, chemicals used in the cleaning of equipment, such as detergents, can also damage the tertiary structure of enzymes and lead to decreased enzyme activity. Therefore, several metal ions that have been reported

to be inhibitors of  $\beta$ -glucosidase ( $\text{MnCl}_2$ ,  $\text{FeCl}_3$ , and  $\text{CuCl}_2$ ), as well as other chemicals (EDTA, SDS, and 2-mercaptoethanol) within a concentration of 10 mM, were subjected to a buffer enzymatic activity test to evaluate their influence on the enzymatic activity.<sup>40</sup> The results in Figure 7D show all the metal ions tested in this study had the same level of inhibition toward the enzymatic activity of both free and immobilized enzymes. Similar results were also observed for EDTA and 2-

mercaptoethanol. However, enzymes in fibers were less sensitive than free enzymes toward SDS treatment. These results suggested that the fiber matrices can protect the enzyme hydrophobic segments from being denatured by detergents such as SDS and thus preserve the activity.

**Mogroside Conversion Rate Test in Fibers.** First, the enzymatic activity of the fibers was evaluated for several cycles of reuse via the *p*NPG conversion mentioned previously, but the fibers were rinsed with water before transferring to the next cycle. By measuring the remaining *p*NPG conversion activity in the fibers after each of the 1-h reaction cycles, we showed that the fibers displayed high enzymatic activity in the first cycle, which was  $213.25 \pm 8.25 \mu\text{U}$  per mg of fiber, and that this activity decreased along with the reuse cycles (Figure 8A). The average enzymatic activity toward *p*NPG during those 10 cycles of usage was  $38.25 \pm 3.14 \mu\text{U}$  per mg of fiber. We think that the decrease in enzyme activity in fibers might be caused by the leakage of enzymes or the increase of inaccessibility of the enzyme's active sites toward the substrates due to fiber swelling. Nevertheless, the immobilized enzyme retained approximately 10% of its initial activity after four cycles of reuse, which offers potential for continuous use of the immobilized enzyme in industrial applications.<sup>27</sup>

The ability of fibers to convert MG V into S I was confirmed by incubating 90 mg of a produced fiber mat in 5 mL of monk fruit extract containing 80% MG V for 0, 3, 6, and 10 h at the optimum reaction conditions (citrate-phosphate buffer pH 5.0, 50 °C). UPLC–MS analysis was conducted to quantify the amount of each mogroside (Figure 8B). The overall results show that the amount of MG V gradually decreased from 80% to 60% of the total MGs after 10 h of incubation, while a significant increase in the amount of S I from 5% to 22% of the total MGs was observed (Figure 8C left). In addition, there were no significant changes in the other types of MGs including iso-MG V, MG IV, and MG III E, suggesting a highly specific S I conversion activity of the cross-linked enzyme/PVA fiber (Figure 8C left). An S I production rate of approximately  $118 \pm 0.08 \text{ mg L}^{-1} \text{ h}^{-1}$  per gram of fiber was calculated based on a 5 mL-chamber setting which contains 90 mg of fiber and a net S I production amount of 106.11 g/mL within 10 h (Figure 8C right). Besides, the average enzymatic activity toward S I production was  $11.48 \pm 0.48 \mu\text{U}$  per mg of fiber.

Since batch studies were performed in the MG conversion tests for 10 h, it is likely that the enzymes previously thought to detach from the fiber matrix should still contribute to the MG V conversion in this enclosed 5 mL-chamber system. However, the conversion rate of S I gradually decreased and reached a plateau after 10 h of reaction. We suggest that there was minimal enzyme leakage in the fiber scaffold; otherwise, the amount of S I would continue to go upward as the activity of the free enzyme remains. Hence, the saturated S I conversion result shown in this study was more related to the inaccessibility of the enzyme's active sites toward the substrates, which was caused by the excessive swelling of the hydrophilic PVA fibers in aqueous solutions and a growing diffusion resistance of the fiber.<sup>41</sup> In other words, a decrease in the fiber enzymatic activity toward *p*NPG in each cycle was caused mainly by the aforementioned swelling of fibrous morphology after several reuses and not by the cause of enzyme leakage of fibers although data on enzyme leakage kinetics. Nevertheless, the ability of the cross-linked enzyme/PVA fibers to be used repeatedly proved their potential for

utilization in continuous and larger-scale S I production as long as the swelling can be properly controlled.

In summary, since we calculated the production rate of S I, we can increase the amount of S I production by increasing the operating time, scale, and fiber density in future studies. Accordingly, in this study, the overall illustration of *DbExg1* immobilization using electrospinning certainly presents new insights to overcome the stability and reusability issues encountered in the application of these enzymes to sustainably redistribute mogrosides for use as natural sweeteners.

## ■ ASSOCIATED CONTENT

### Supporting Information

The Supporting Information is available free of charge at <https://pubs.acs.org/doi/10.1021/acs.jafc.0c02513>.

Table S1, sequence of primers used in this study; Table S2, optimized MRM transition and parameters for 5 mogrosides; Figure S1, conceptual schematic showing the inverse PCR procedure; Figure S2, screening of yeast transformants with *exg1Δ::KanMX4* replaced with the *DbExg1-URA3* cassette; Figure S3, DSC curves of the PVA and enzyme/PVA fibers with/without chemical cross-linking; and Figure S4, SEM micrographs of enzyme/PVA fibers produced in the 14<sup>th</sup> and 8<sup>th</sup> runs in the CCD table (PDF)

## ■ AUTHOR INFORMATION

### Corresponding Author

**Reuben Wang** – Institute of Food Safety and Health, College of Public Health and Master of Public Health Program, College of Public Health, National Taiwan University, Taipei City, Taiwan; Department of Food Science, College of Agriculture, Tunghai University, Taichung City, Taiwan; [orcid.org/0000-0002-6328-7331](https://orcid.org/0000-0002-6328-7331); Phone: +886-2-33668084; Email: [reubenwang@ntu.edu.tw](mailto:reubenwang@ntu.edu.tw); Fax: +886-2-33668114

### Authors

**Virly** – Department of Food Science, College of Agriculture, Tunghai University, Taichung City, Taiwan

**Chun-Hui Chiu** – Graduate Institute of Health Industry and Technology, Research Center for Chinese Herbal Medicine and Research Center for Food and Cosmetic Safety, College of Human Ecology, Chang Gung University of Science and Technology, Taoyuan City, Taiwan; Department of Traditional Chinese Medicine, Chang Gung Memorial Hospital, Keelung City, Taiwan

**Tsan-Yu Tsai** – Institute of Polymer Science and Engineering, National Taiwan University, Taipei City, Taiwan

**Yi-Cheun Yeh** – Institute of Polymer Science and Engineering, National Taiwan University, Taipei City, Taiwan

Complete contact information is available at: <https://pubs.acs.org/doi/10.1021/acs.jafc.0c02513>

### Author Contributions

<sup>†</sup>These authors contributed equally to this work.

### Funding

This work is supported by the Ministry of Science and Technology (MOST), Republic of China (Grant No. 106-2218-E-029-002-MY2 and 107-2113-M-002-025-MY4) and Chang Gung University of Science and Technology (ZRRPF3J0071).

## Notes

The authors declare no competing financial interest.

## ACKNOWLEDGMENTS

We thank Dr. Wen-Hsin Chung for technical assistance with the SEM analysis.

## REFERENCES

- (1) Lee, C.-h. Intense sweetener from Lo Han Kuo (*Momordica grosvenori*). *Experientia* **1975**, *31*, 533–534.
- (2) Matsumoto, K.; Kasai, R.; Ohtani, K.; Tanaka, O. Minor cucurbitane-glycosides from fruits of *Siraitia grosvenori* (Cucurbitaceae). *Chem. Pharm. Bull.* **1990**, *38*, 2030–2032.
- (3) Cho, S., Determination of the generally recognized as safe (GRAS) status of *Siraitia grosvenori* Swingle (Luo Han Guo) fruit extract as a food ingredient. 2017, pp 1–140.
- (4) Takemoto, T.; Arihara, S.; Nakajima, T.; Okuhira, M. Studies on the constituents of Fructus momordicae. II. Structure of sapogenin. *Yakugaku Zasshi* **1983**, *103*, 1155–1166.
- (5) Takemoto, T.; Arihara, S.; Nakajima, T.; Okuhira, M. Studies on the constituents of Fructus momordicae. I. on the sweet principle. *Yakugaku Zasshi* **1983**, *103*, 1151–1154.
- (6) Takemoto, T.; Arihara, S.; Nakajima, T.; Okuhira, M. Studies on the constituents of Fructus momordicae. III. structure of mogrosides. *Yakugaku Zasshi* **1983**, *103*, 1167–1173.
- (7) Jia, Z.; Yang, X. A minor, sweet cucurbitane glycoside from *Siraitia grosvenorii*. *Nat. Prod. Commun.* **2009**, *4*, 769–772.
- (8) Qiao, J.; Luo, Z.; Gu, Z.; Zhang, Y.; Zhang, X.; Ma, X. Identification of a Novel Specific Cucurbitadienol Synthase Allele in *Siraitia grosvenorii* Correlates with High Catalytic Efficiency. *Molecules* **2019**, *24* (3), 627.
- (9) Tan, V. W. K.; Wee, M. S. M.; Tomic, O.; Forde, C. G. Temporal sweetness and side tastes profiles of 16 sweeteners using temporal check-all-that-apply (TCATA). *Food Res. Int.* **2019**, *121*, 39–47.
- (10) Zhou, Y.; Amentrout, R. W.; Woodyer, R. D.; Bridges, J. R.; Schunk, T. C.; Fletcher, J. N. Redistribution of mogrol glycoside content (WO 2014/150127). 2014.
- (11) Chen, X. B.; Zhuang, J. J.; Liu, J. H.; Lei, M.; Ma, L.; Chen, J.; Shen, X.; Hu, L. H. Potential AMPK activators of cucurbitane triterpenoids from *Siraitia grosvenorii* Swingle. *Bioorg. Med. Chem.* **2011**, *19*, 5776–5781.
- (12) Murata, Y.; Ogawa, T.; Suzuki, Y. A.; Yoshikawa, S.; Inui, H.; Sugiura, M.; Nakano, Y. Digestion and absorption of *Siraitia grosvenorii* triterpenoids in the rat. *Biosci., Biotechnol., Biochem.* **2010**, *74*, 673–676.
- (13) Chiu, C.-h.; Wang, R.; Lee, C.-c.; Lo, Y.-c.; Lu, T.-j. Biotransformation of mogrosides from *Siraitia grosvenorii* Swingle by *Saccharomyces cerevisiae*. *J. Agric. Food Chem.* **2013**, *61*, 7127–7134.
- (14) Wang, R.; Chen, Y.-c.; Lai, Y.-j.; Lu, T.-j.; Huang, S.-t.; Lo, Y.-C. *Dekkera bruxellensis*, a beer yeast that specifically bioconverts mogrosides into the intense natural sweetener siamenoside I. *Food Chem.* **2019**, *276*, 43–49.
- (15) Chakraborty, S.; Asgerisson, B.; Rao, B. J. A measure of the broad substrate specificity of enzymes based on 'duplicate' catalytic residues. *PLoS One* **2012**, *7* (11), e49313.
- (16) Datta, S.; Christena, L. R.; Rajaram, Y. R. Enzyme immobilization: an overview on techniques and support materials. *3 Biotech* **2013**, *3* (1), 1–9.
- (17) Yushkova, E. D.; Nazarova, E. A.; Matyuhina, A. V.; Noskova, A. O.; Shavronskaya, D. O.; Vinogradov, V. V.; Skvortsova, N. N.; Krivosheina, E. F. Application of Immobilized Enzymes in Food Industry. *J. Agric. Food Chem.* **2019**, *67* (42), 11553–11567.
- (18) Jeong, D. W.; Hyeon, J. E.; Shin, S. K.; Han, S. O. Trienzymatic Complex System for Isomerization of Agar-Derived d-Galactose into d-Tagatose as a Low-Calorie Sweetener. *J. Agric. Food Chem.* **2020**, *68* (10), 3195–3202.
- (19) Reneker, D. H.; Chun, I. Nanometre diameter fibres of polymer, produced by electrospinning. *Nanotechnology* **1996**, *7*, 216–223.
- (20) Pillay, V.; Dott, C.; Choonara, Y. E.; Tyagi, C.; Tomar, L.; Kumar, P.; Du Toit, L. C.; Ndesendo, V. M. K. A review of the effect of processing variables on the fabrication of electrospun nanofibers for drug delivery applications. *J. Nanomater.* **2013**, *2013*, 1–22.
- (21) Wen, P.; Wen, Y.; Zong, M.-H.; Linhardt, R. J.; Wu, H. Encapsulation of Bioactive Compound in Electrospun Fibers and Its Potential Application. *J. Agric. Food Chem.* **2017**, *65* (42), 9161–9179.
- (22) Wang, Y.; Hsieh, Y. L. Immobilization of lipase enzyme in polyvinyl alcohol (PVA) nanofibrous membranes. *J. Membr. Sci.* **2008**, *309* (1), 73–81.
- (23) Nunes, M. A. P.; Martins, S.; Rosa, M. E.; Gois, P. M. P.; Fernandes, P. C. B.; Ribeiro, M. H. L. Improved thermostable polyvinyl alcohol electrospun nanofibers with entangled naringinase used in a novel mini-packed bed reactor. *Bioresour. Technol.* **2016**, *213*, 208–215.
- (24) İspirli Doğan, Y.; Deveci, İ.; Mercimek, B.; Teke, M. A comparative study for lipase immobilization onto alginate based composite electrospun nanofibers with effective and enhanced stability. *Int. J. Biol. Macromol.* **2017**, *96*, 302–311.
- (25) Dai, M.; Jin, S.; Nugen, S. Water-Soluble Electrospun Nanofibers as a Method for On-Chip Reagent Storage. *Biosensors* **2012**, *2*, 388–95.
- (26) Aldahri, M. M.; Almulaiky, Y. Q.; El-Shishtawy, R. M.; Al-Shawafi, W.; Alngadh, A.; Maghrabi, R. Facile Immobilization of Enzyme via Co-Electrospinning: A Simple Method for Enhancing Enzyme Reusability and Monitoring an Activity-Based Organic Semiconductor. *ACS Omega* **2018**, *3* (6), 6346–6350.
- (27) Moreno-Cortez, I. E.; Romero-Garcia, J.; Gonzalez-Gonzalez, V.; Garcia-Gutierrez, D. I.; Garza-Navarro, M. A.; Cruz-Silva, R. Encapsulation and immobilization of papain in electrospun nanofibrous membranes of PVA cross-linked with glutaraldehyde vapor. *Mater. Sci. Eng., C* **2015**, *52*, 306–314.
- (28) dos Santos, J. P.; Zavareze, E. d. R.; Dias, A. R. G.; Vanier, N. L. Immobilization of xylanase and xylanase –  $\beta$ -cyclodextrin complex in polyvinyl alcohol via electrospinning improves enzyme activity at a wide pH and temperature range. *Int. J. Biol. Macromol.* **2018**, *118*, 1676–1684.
- (29) Wang, R.; Lin, P. Y.; Huang, S. T.; Chiu, C. H.; Lu, T. J.; Lo, Y. C. Hyperproduction of beta-Glucanase Exg1 Promotes the Bio-conversion of Mogrosides in *Saccharomyces cerevisiae* Mutants Defective in Mannoprotein Deposition. *J. Agric. Food Chem.* **2015**, *63* (47), 10271–9.
- (30) Wen, P.; Zhu, D.-H.; Wu, H.; Zong, M.-H.; Jing, Y.-R.; Han, S.-Y. Encapsulation of cinnamon essential oil in electrospun nanofibrous film for active food packaging. *Food Control* **2016**, *59*, 366–376.
- (31) Alghunaim, N. S. Optimization and spectroscopic studies on carbon nanotubes/PVA nanocomposites. *Results Phys.* **2016**, *6*, 456–460.
- (32) Nishiyabu, R.; Shimizu, A. Boronic acid as an efficient anchor group for surface modification of solid polyvinyl alcohol. *Chem. Commun.* **2016**, *52* (63), 9765–9768.
- (33) Ermakova, E. N.; Sysoev, S. V.; Nikulina, L. D.; Tsyrendorzhieva, I. P.; Rakhlin, V. I.; Kosinova, M. L. Trimethyl-(phenyl)silane — a precursor for gas phase processes of SiC<sub>x</sub>-H film deposition: Synthesis and characterization. *Modern Electronic Materials* **2015**, *1* (4), 114–119.
- (34) Balachander, L.; Ramadevudu, G.; Shareefuddin, M.; Sayanna, R.; Venudhar, Y. C. IR analysis of borate glasses containing three alkali oxides. *ScienceAsia* **2013**, *39*, 278.
- (35) Ravangave, L.; Devde, G. Structure and Physical Properties of 59B<sub>2</sub>O<sub>3</sub>–10Na<sub>2</sub>O–(30 – x)CdO–xZnO–1CuO (0 ≤ x ≤ 30) Glass System. 2018.
- (36) Barth, A. Infrared spectroscopy of proteins. *Biochim. Biophys. Acta, Bioenerg.* **2007**, *1767* (9), 1073–1101.

- (37) Shoba, E.; Lakra, R.; Kiran, M. S.; Korrapati, P. S. Design and development of papain – urea loaded PVA nanofibers for wound debridement. *RSC Adv.* **2014**, *4*, 60209–60215.
- (38) Secundo, F. Conformational changes of enzymes upon immobilisation. *Chem. Soc. Rev.* **2013**, *42* (15), 6250–61.
- (39) Lemma, S. M.; Scampicchio, M.; Mahon, P. J.; Sbarski, I.; Wang, J.; Kingshott, P. Controlled Release of Retinyl Acetate from  $\beta$ -Cyclodextrin Functionalized Poly (vinyl alcohol) Electrospun Nanofibers. *J. Agric. Food Chem.* **2015**, *63* (13), 3481–3488.
- (40) Kuo, H.-P.; Wang, R.; Huang, C.-Y.; Lai, J.-T.; Lo, Y.-C.; Huang, S.-T. Characterization of an extracellular  $\beta$ -glucosidase from *Dekkera bruxellensis* for resveratrol production. *Journal of Food and Drug Analysis* **2018**, *26* (1), 163–171.
- (41) Ariga, O.; Itoh, K.; Sano, Y.; Nagura, M. Encapsulation of Biocatalyst with PVA Capsules. *J. Ferment. Bioeng.* **1994**, *78* (1), 74–78.





Cite this: RSC Adv., 2020, 10, 38128

# Anti-inflammatory, antiallergic and COVID-19 protease inhibitory activities of phytochemicals from the Jordanian hawksbeard: identification, structure–activity relationships, molecular modeling and impact on its folk medicinal uses†

Sherif S. Ebada,<sup>a</sup> Nariman A. Al-Jawabri,<sup>b</sup> Fadia S. Youssef,<sup>c</sup> Dina H. El-Kashef,<sup>ad</sup> Tim-Oliver Knedel,<sup>e</sup> Amgad Albohy,<sup>f</sup> Michal Korinek,<sup>ghi</sup> Tsong-Long Hwang,<sup>hij</sup> Bing-Hung Chen,<sup>gkl</sup> Guan-Hua Lin,<sup>m</sup> Chia-Yi Lin,<sup>m</sup> Sa'ed M. Aldalaie,<sup>b</sup> Ahmad M. Disi,<sup>n</sup> Christoph Janiak<sup>ib</sup> and Peter Proksch<sup>\*a</sup>

On Wednesday 11<sup>th</sup> March, 2020, the world health organization (WHO) announced novel coronavirus (COVID-19, also called SARS-CoV-2) as a pandemic. Due to time shortage and lack of either a vaccine and/or an effective treatment, many trials focused on testing natural products to find out potential lead candidates. In this field, an edible and folk medicinal Jordanian plant *Crepis sancta* (Asteraceae) was selected for this study. Phytochemical investigation of its enriched polyphenolic extract afforded four eudesmane sesquiterpenes (1–4) together with (6*S*,9*R*)-roseoside (5) and five different methylated flavonols (6–10). Structure elucidation of isolated compounds was unambiguously determined based on HRESIMS, X-ray crystallography, and exhaustive 1D and 2D NMR experiments. All isolated compounds were assessed for their *in vitro* anti-inflammatory, antiallergic and *in silico* COVID-19 main protease (M<sup>Pro</sup>) inhibitory activities. Among the tested compounds, compounds 5–10 revealed potent anti-inflammatory, antiallergic and COVID-19 protease inhibitory activities. Chrysosplenetin (10) is considered as a promising anti-inflammatory and antiallergic lead structure adding to the phytotherapeutic pipeline. Moreover, its inhibitory activity against SARS-CoV-2 M<sup>Pro</sup>, supported by docking and molecular dynamic studies, strengthens its potential as a lead structure paving the way toward finding out a natural remedy to treat and/or to control the current COVID-19 pandemic.

Received 2nd June 2020  
Accepted 5th October 2020

DOI: 10.1039/d0ra04876c

rsc.li/rsc-advances

<sup>a</sup>Institute of Pharmaceutical Biology and Biotechnology, Heinrich-Heine University, D-40225 Düsseldorf, Germany. E-mail: ss\_ebada@mutah.edu.jo; sherif\_elsayed@pharma.asu.edu.eg; Peter.Proksch@hhu.de; Fax: +49-211-81-11923; Tel: +49-211-81-14163

<sup>b</sup>Department of Pharmaceutical Chemistry, Faculty of Pharmacy, Mu'tah University, 61710 Al-Karak, Jordan

<sup>c</sup>Department of Pharmacognosy, Faculty of Pharmacy, Ain-Shams University, Abbasia, 11566 Cairo, Egypt

<sup>d</sup>Department of Pharmacognosy, Faculty of Pharmacy, Minia University, 61519 Minia, Egypt

<sup>e</sup>Institut für Anorganische Chemie und Strukturchemie, Heinrich-Heine-Universität, D-40204 Düsseldorf, Germany

<sup>f</sup>Department of Pharmaceutical Chemistry, Faculty of Pharmacy, The British University in Egypt (BUE), Al-Sherouk City, Cairo-Suez Desert Road, 11837, Egypt

<sup>g</sup>Graduate Institute of Natural Products, College of Pharmacy, Kaohsiung Medical University, Kaohsiung, Taiwan

<sup>h</sup>Department of Biotechnology, College of Life Science, Kaohsiung Medical University, Kaohsiung, Taiwan

<sup>i</sup>Graduate Institute of Natural Products, College of Medicine, Chang Gung University, Taoyuan, Taiwan

<sup>j</sup>Research Center for Chinese Herbal Medicine, Research Center for Food and Cosmetic Safety, Graduate Institute of Health Industry Technology, College of Human Ecology, Chang Gung University of Science and Technology, Taoyuan, Taiwan

<sup>k</sup>Department of Anesthesiology, Chang Gung Memorial Hospital, Taoyuan, Taiwan

<sup>l</sup>Department of Medical Research, Kaohsiung Medical University Hospital, Kaohsiung, Taiwan

<sup>m</sup>The Institute of Biomedical Sciences, National Sun Yat-sen University, Kaohsiung, Taiwan

<sup>n</sup>Department of Basic Pharmaceutical Sciences, Faculty of Pharmacy, Al-Isra University, 11622 Amman, Jordan

† Electronic supplementary information (ESI) available. CCDC 1994762. For ESI and crystallographic data in CIF or other electronic format see DOI: 10.1039/d0ra04876c





## Introduction

Polymorphonuclear neutrophils (PMNs) are a major component of the innate immunity defending the human body against inadvertent entrance of xenobiotics and/or pathogens. PMNs perform their physiological function principally through the production of oxidative free radicals and non-oxidative proteases including neutrophil elastase (NE, a serine protease aka leukocyte elastase).<sup>1</sup> The more PMNs infiltrated, the higher NE levels secreted in response accomplishing their defensive role by demolishing functional proteins of phagocytosed bacterial, fungal and/or viral pathogens. NE is an intracellular enzyme principally stored in azurophilic granules of PMNs. Beside its defensive role against pathogens, they were found to produce devastating effects on elastin-rich connective tissue particularly in the lungs.<sup>2</sup> NE can also split and sever collagen, proteoglycans and other plasma proteins. Hence, its overexpression may result in deleterious effects on permeability barrier integrity between alveolar epithelial and endothelial cells leading to pathologic edematous symptoms in the inflamed lungs undergoing either acute lung injury (ALI), acute respiratory distress syndrome (ARDS) or chronic respiratory disorders such as asthma and chronic obstructive pulmonary disease (COPD).<sup>3</sup> However, ARDS, ALI and COPD are among the leading causes of morbidity and mortality in the intensive care units (ICU) worldwide,<sup>4</sup> some recurrent comorbidities have been reported for COPD with chronic disorders such as hypertension, diabetes, heart diseases, depression and pneumonia.<sup>5</sup>

During the last two decades, two epidemics of zoonotic origins have been introduced into human community, namely, severe acute respiratory syndrome (SARS) commenced at Guangzhou province (China) in 2003 (ref. 6) and Middle East respiratory syndrome (MERS) emerged in Saudi Arabia about 10 years later in 2012.<sup>7</sup> In December 2019 at Wuhan city (China), early reports indicated a group of five patients primarily diagnosed with pneumonia of an unknown etiology featuring ARDS and one of them died later. About six weeks later, the World Health Organization (WHO) announced the onset of a potential coronavirus outbreak caused by SARS-CoV2 (COVID-19, named by WHO on February 11, 2020) and one month later on March 11, 2020, WHO raised alerts and announced this outbreak as a pandemic.<sup>8</sup>

Their causative pathogens belong to betacoronaviruses family and are of zoonotic origins. They all are believed to emerge from the horseshoe bats as a natural reservoir for their immense majority and recently moved through intermediate animal hosts, dromedary camels for MERS and Malayan pangolins for COVID-19, to humans that then adopted human-human transmission leading to epidemics among humans.<sup>9</sup>

Till preparing this manuscript, COVID-19 spread worldwide affecting about 37.1 million patients including more than one million deaths that obliged many governments to implement social distancing together with total lockdown strategies to defend against this pandemic.

Due to the current lack of an effective pharmaceutical and/or an approved vaccine, the major WHO recommendations focus

on infection control measures, improving lifestyle and diet enrichment with more-healthy components. Based on the ongoing research efforts directed toward finding a plausible target for developing a specific antiviral agent, a very recent paper describing COVID-19 virus main protease ( $M^{pro}$ ), a key CoV enzyme mediating viral replication and transcription, that was recognized as a very promising target for drug development.<sup>10</sup>

As a part of our ongoing research and building on the previous notions, we thought of isolating and probing plant natural products as NE and/or COVID-19  $M^{pro}$  inhibitors which may help to ameliorate the clinical manifestations related to ARDS and to cease or even slow down viral replication and transcription granting additional time for the immune system to defend itself against COVID-19.

In this study, we explored an edible and a folk medicinal plant of the genus *Crepis* (aka hawksbeard including about 200 species) belonging to the tribe Cichorieae and family Asteraceae. It is widely eaten and/or used for herbal medicine purposes in different countries and territories within the circumference of the Mediterranean Basin including Italy, Greece and Jordan. The fresh leaves of many *Crepis* species including that discussed in this study, *C. sancta*, are eaten either fresh, boiled or browned in salads by the locals. Traditionally, its decoction has been used for treating different ailments related mainly to respiratory and gastrointestinal systems such as common cold, cough, abdominal colic, constipation, hepatitis along with hypertension and hyperglycemia.<sup>11</sup>

Based on searching the reported literature of the genus *Crepis*, its aerial parts were reported to be rich in both flavonoid aglycones and glycosides<sup>12</sup> in addition to eudesmanes and guaianolides sesquiterpenes present as both aglycone and glycosidic forms.<sup>13</sup> Regarding assessed bioactivities, the extracts of genus *Crepis* have been reported to possess antimicrobial, antiviral and antiproliferative activities together with antioxidant, analgesic, antiulcer and anti-inflammatory.<sup>12,13</sup>

In this study, we report phytochemical exploration of polyphenolic-rich extract of *C. sancta* aerial parts affording ten different compounds belonging to eudesmane sesquiterpenes and methoxylated flavonoids. Structure elucidation of isolated compounds was unambiguously confirmed through HRESIMS, exhaustive 1D, 2D NMR spectroscopy and X-ray crystallography. We also report in this study results of *in vitro* anti-inflammatory and antiallergic activities of isolated compounds in addition to *in silico* COVID-19 main protease ( $M^{pro}$ ) inhibitory activity assessment.

## Materials and methods

### General experimental procedures

Perkin-Elmer-241 MC polarimeter was used for determining optical rotation. LRESIMS and HRESIMS were determined on a LC-MS HP1100 Agilent Finnigan LCQ Deca XP Thermoquest and FTHRMS-Orbitrap (ThermoFinnigan) mass spectrometer, respectively. Chromatographic workups were conducted *via* column chromatography using different stationary phases such as silica gel 60 M (0.04–0.063 mm) and Sephadex LH20. For



screening purposes, ready-made silica gel 60 F<sub>254</sub> TLC plates (Merck, Darmstadt, Germany) were used. For visualizing TLC plates, UV light at 254 and 365 nm wavelengths were applied as non-destructive technique or after spraying with anisaldehyde reagent and heating. For analytical HPLC measurements, a Dionex Ultimate 3000 LC system equipped with a ready-made separation column (125 × 4 mm, *L* × ID), pre-packed with Eurospher-10C<sub>18</sub> (Knauer, Germany) and coupled to a photodiode array (PDA) detector (UVD340S) was implemented, setting up the detection channels at 235, 254, 280 and 340 nm wavelengths. A standard gradient elution was applied using (MeOH, 0.01% formic acid in water): 0 min, 10% MeOH; 5 min, 10% MeOH; 35 min, 100% MeOH; 45 min, 100% MeOH, with a flow rate of 1 mL min<sup>-1</sup>. Preparative HPLC separations were accomplished using a RP-HPLC system of LaChrom-Merck Hitachi equipped with a pump L7100, UV detector L7400 and a column (300 × 8 mm, *L* × ID) prefilled with Euroshper-100C<sub>18</sub> (Knauer, Germany) at a flow rate of 5.0 mL min<sup>-1</sup>. 1D (<sup>1</sup>H and <sup>13</sup>C NMR) and 2D NMR (chemical shifts in ppm) spectra were determined on Bruker AVANCE DMX 600 (Switzerland) using methanol-*d*<sub>4</sub> and DMSO-*d*<sub>6</sub> solvents (Sigma-Aldrich, Germany).

### Plant material

*Crepis sancta* aerial parts were collected in November, 2017 at Al-Basirah region (Al-Tafilah Governorate, southern Jordan). The plant identity was authenticated by Prof. Dr Saleh A. Al-Qur'an at Department of Botany, Faculty of Science, Mu'tah University and a voucher specimen coded CSA-201711 was kept at Department of Pharmaceutical Chemistry, Faculty of Pharmacy, Mu'tah University.

### Extraction, isolation and purification

The freshly collected aerial parts were kept in shade to dry, ground to afford a one-kg net weight that was then extracted by methanol (3 × 1 L). Methanol extract was then concentrated under vacuum till dryness affording a total residue (9.8 g). The total extract was then defatted *via* liquid-liquid fractionation procedure by being dispersed in 90% MeOH (500 mL) and shaken against *n*-hexane (1 L). The two immiscible liquid phases were then separated and the aqueous methanol layer was evaporated till dryness under reduced pressure resulting in a solid residue (5.9 g). Afterwards, the defatted residual solid was chromatographed through vacuum liquid chromatography (VLC) using silica gel stationary phase and implementing a gradient elution system using *n*-hexane : EtOAc and DCM : MeOH with a 20% increment affording 12 fractions (CSV1-CSV12). All obtained fractions were subjected to TLC and analytical HPLC procedures. Fractions CSV2, CSV5-CSV8, CSV11 and CSV12 were chosen for further preparative HPLC purification procedure. Fractions CSV2 (58 mg) and CSV11 (63 mg), eluted with *n*-hexane : EtOAc (8:2) and with DCM : MeOH (2:8), were subjected to preparative HPLC yielding **4** (2.7 mg) and **3** (3.5 mg), respectively. Four fractions (CSV5-CSV8) were collected together and applied on column chromatography using Sephadex LH-20 as stationary phase and methanol as a mobile phase followed by preparative HPLC for final purification to

yield **6** (4.5 mg), **7** (5.7 mg), **8** (6 mg), **9** (8 mg) and **10** (12 mg). Fraction CSV12 (82 mg) eluted by DCM : MeOH (1:4) was further purified using preparative HPLC yielding **1** (1.3 mg), **2** (1.6 mg) and **5** (1.2 mg).

**(6S,7S,10R)-3-Oxo-di-nor-eudesm-4-en-6 $\alpha$ -hydroxy-11-oic acid (1).** Amorphous yellow solid; [ $\alpha$ ]<sub>D</sub><sup>20</sup> +97.6° (*c* 0.02, MeOH); UV (MeOH)  $\lambda_{\text{max}}$  248 nm; <sup>1</sup>H NMR and <sup>13</sup>C NMR see ESI Table S1;† HRESIMS *m/z* 239.1282 [M+H]<sup>+</sup> (calcd for C<sub>13</sub>H<sub>19</sub>O<sub>4</sub>; *m/z* 239.1283) and *m/z* 237.1128 [M-H]<sup>-</sup> (calcd for C<sub>13</sub>H<sub>17</sub>O<sub>4</sub>; *m/z* 237.1127).

**(6S,7S,10R)-3-Oxo-6 $\alpha$ -hydroxy- $\gamma$ -costic acid (2).** Amorphous yellow solid; [ $\alpha$ ]<sub>D</sub><sup>20</sup> +79.0° (*c* 0.02, MeOH); UV (MeOH)  $\lambda_{\text{max}}$  248 nm; <sup>1</sup>H NMR and <sup>13</sup>C NMR see ESI Table S1;† HRESIMS *m/z* 263.1283 [M-H]<sup>-</sup> (calcd for C<sub>15</sub>H<sub>19</sub>O<sub>4</sub>; *m/z* 263.1282).

### Cell viability assay

The mucosal mast-cell derived rat basophilic leukemia cells (RBL-2H3) were obtained from Bioresource Collection and Research Center (Hsin-Chu, Taiwan). The cells were cultured in DMEM containing 10% FBS, 100 U mL<sup>-1</sup> penicillin, and 100  $\mu$ g mL<sup>-1</sup> streptomycin in 10 cm cell culture dishes at 37 °C in a humidified chamber with 5% CO<sub>2</sub> in air. The potential cytotoxic effects of the samples (10 to 100  $\mu$ g mL<sup>-1</sup> for the crude extract and 1 to 400  $\mu$ M for the pure compounds) on RBL-2H3 cells were determined by the methylthiazole tetrazolium (MTT) assay as described previously.<sup>14</sup>

### Superoxide anion generation and elastase release assays by human neutrophils

The human neutrophils were obtained from venous blood of healthy adult volunteers (20–30 years old) following the reported procedure.<sup>15</sup> Measurement of superoxide anion generation by the activated neutrophils was based on the reduction of ferricytochrome c as described before.<sup>15,16</sup> Elastase release by activated neutrophils was determined using *N*-methoxysuccinyl-Ala-Ala-Pro-Val-*p*-nitroanilide as elastase substrate according to the reported method.<sup>16</sup> The concentration was 1 to 10  $\mu$ g mL<sup>-1</sup> for the crude samples and 0.3 to 10  $\mu$ M for the pure compounds. LY294002 was used as the positive control.

### Degranulation assay in mast cells

The level of degranulation in mast cells was evaluated based on A23187- and antigen-induced  $\beta$ -hexosaminidase release in RBL-2H3 cells according to a reported method with some modifications.<sup>14</sup> Briefly, the cells were seeded in a 96-well plate (2 × 10<sup>4</sup> cells per well, for the A23187-induced assay) or a 48-well plate (3 × 10<sup>4</sup> cells per well, for the antigen-induced assay) overnight. At the same time, the cells for the antigen-induced assay were sensitized with anti-DNP IgE (0.5  $\mu$ g mL<sup>-1</sup>; Sigma). RBL-2H3 cells were treated with the samples (0.5, 5 and 50  $\mu$ M) for 30 min in Tyrode's buffer with maximal DMSO dose of 0.5%. For the A23187-induced assay, the cells were activated by adding A23187 (final concentration 0.5  $\mu$ M), while cells for antigen-induced assay were activated by the addition of DNP-BSA (final concentration 100 ng mL<sup>-1</sup>) for 30 min. Azelastine served as a positive control. The amount of  $\beta$ -hexosaminidase



was detected using the method utilizing p-NAG as a substrate according to the procedure described before.<sup>14</sup>

### X-ray crystallographic analysis

Crystals of chrysosplenetin (**10**) have been obtained by crystallization from pure methanol.

Data collection: measurements were done with a Bruker Kappa APEX2 CCD diffractometer with a microfocus tube and Cu K $\alpha$  radiation ( $\lambda = 1.54178$  Å). Data collection, structure solving, refinement and the hydrogen atom positioning were all performed according to the recently reported procedure.<sup>17</sup> The structural data have been deposited in the Cambridge Crystallographic Data Center (CCDC no 1994762†).

### Molecular modeling studies

The proposed binding mode of isolated compounds with neutrophil elastase (NE) and SARS-CoV-2 main protease ( $M^{pro}$ ) was studied using Autodock Vina and a method similar to what we reported earlier.<sup>12</sup> Here, crystal structures of NE (PDB ID: 1H1B) and SARS-CoV-2  $M^{pro}$  (PDB ID: 6LU7) were used. Prepared and co-crystallized ligands were docked in a grid box in the active site ( $25 \times 25 \times 25$  Å<sup>3</sup>, centered on co-crystallized ligand) using exhaustiveness of 16. For each ligand, the top 9 binding poses were ranked according to their binding affinities and the predicted binding interactions were analyzed. The pose with the best binding affinity and binding mood similar to co-crystallized ligand was reported.

### Molecular dynamic (MD) simulation

MD simulations were done using GROMACS 2018.1 molecular dynamics package.<sup>18</sup> CHARMM36 all-atom force field<sup>19</sup> was used for protein simulations while ligands were parameterized using SwissParam.<sup>20</sup> All simulations were performed in TIP3P explicit water<sup>21</sup> in a dodecahedron box and neutralized by Na<sup>+</sup> or Cl<sup>−</sup> ions. Steepest descent algorithm was used for minimization and maximum force was set to less than 1000 kJ mol<sup>−1</sup> nm<sup>−1</sup>. Systems were initially equilibrated using NVT and NPT ensembles for 100 ps each. The temperature was maintained at 300 K using the V-rescale algorithm<sup>22</sup> and pressure was controlled by the Parrinello–Rahman barostat.<sup>23</sup> The LINear Constraint Solver (LINCS) algorithm<sup>24</sup> was used for bond's length constraints and Particle mesh Ewald (PME) method<sup>25</sup> was used for long-range electrostatics calculations. For all simulations 2 fs timestep was used. van der Waals cut-off distance (rwdw) was set to 1.2 nm. Initial coordinates was taken from docking poses or from crystal structure if available.

### Determination of elastase enzymatic activity

The compounds were further tested for direct inhibition of elastase enzymatic activity.<sup>26</sup> The neutrophil suspension ( $6 \times 10^5$  cells per mL) was preheated for 5 min in the presence of CaCl<sub>2</sub> (1 mM) at 37 °C. Priming agent CB ( $1.5 \mu\text{g mL}^{-1}$ ) was added for 2 min, followed by fMLF ( $0.1 \mu\text{M}$ ) for 20 min to release elastase from the cells. After centrifugation at 1000g for 5 min at 4 °C, the supernatant containing elastase was preheated at 37 °C

for 5 min, and the test compounds were added. Then, 0.1 mM of substrate methoxysuccinyl-Ala-Ala-Pro-Val-*p*-nitroanilide was added for 10 min. The effect of the compounds on elastase enzymatic activity was quantified by measuring the absorbance at 405 nm.

### Coronavirus 229E assay

The protective effects of the samples against human coronavirus 229E (HCoV-229) was determined similarly to the previously described method.<sup>27</sup> Huh7 cells (human liver carcinoma cell line) were infected with 9TCID50 (Median Tissue Culture Infectious Dose) of each coronavirus 229E in the presence or absence of the compounds or vehicle. After incubation at 33 °C for 6 days, the surviving cells were then stained with MTT (3-[4,5-dimethylthiazol-2-yl]-2,5-diphenyl tetrazolium bromide). The percentage of surviving cells was then calculated.

## Results and discussion

### Isolation and identification of major metabolites in the plant extract

A careful phytochemical investigation of the plant extract, implementing various chromatographic techniques, MS, 1D, 2D NMR spectroscopic analyses and by comparison with the reported literature, afforded four eudesmane sesquiterpene lactones (**1–4**). Two were unambiguously identified and reported previously as new natural products from the same extract namely, (6*S*,7*S*,10*R*)-3-oxo-di-nor-eudesm-4-en-6 $\alpha$ -hydroxy-11-oic acid (**1**)<sup>28</sup> and (6*S*,7*S*,10*R*)-3-oxo-6 $\alpha$ -hydroxy- $\gamma$ -costic acid (**2**)<sup>28</sup> together with two known congeners, 3-oxo- $\gamma$ -costic acid (**3**)<sup>12,29</sup> and its methyl ester (**4**).<sup>12,30</sup> In addition, (6*S*,9*R*)-roseoside (**5**)<sup>28</sup> and several methoxylated flavonoids namely, jaceidin (**6**),<sup>12,31</sup> kumatakenin (**7**),<sup>12,32</sup> penduletin (**8**),<sup>12,33</sup> pachypodol (**9**)<sup>12,34</sup> and chrysosplenetin (**10**)<sup>12,35</sup> were also isolated. Structure elucidation of the isolated compounds were unambiguously determined based on extensive 1D, 2D NMR analyses together with mass spectrometry (see ESI†).

Compounds (**1** and **2**) were individually purified as white amorphous solids whose molecular formulas were determined to be C<sub>13</sub>H<sub>18</sub>O<sub>4</sub> and C<sub>15</sub>H<sub>20</sub>O<sub>4</sub> based on their HRESIMS spectra that revealed pseudomolecular ion peaks at  $m/z$  237.1128 [ $M-H$ ]<sup>−</sup> and  $m/z$  263.1283 [ $M-H$ ]<sup>−</sup> indicating the existence of five and six degrees of unsaturation, respectively. The larger molecular weight of **2** by 26 atomic units and its additional one degree of unsaturation compared to **1** suggested that the former might have an additional olefin moiety with one of its sp<sup>2</sup> carbons turned into a quaternary one. The 1D NMR spectra of **1** including <sup>1</sup>H and <sup>13</sup>C NMR (see ESI, Table S1†) unravelled a close resemblance to the known natural metabolite 3-oxo-di-nor-eudesma-4-en-11-oic acid with an exocyclic carboxylic acid group ( $\delta_C$  176.8, C-11).<sup>36,37</sup> By careful investigation of extensive 2D NMR spectra such as <sup>1</sup>H–<sup>1</sup>H COSY, HMQC and HMBC, a clear difference was determined in **1** compared to the known metabolite that is the presence of an oxymethine group at  $\delta_H$  5.25 (d, 3.0, 1H,  $\delta_C$  67.6) instead of a methylene group at  $\delta_H$  2.29/ $\delta_H$  2.99 (d, 15.0, 2H,  $\delta_C$  29.2) ascribed for C-6.<sup>37</sup> This notion



**Table 1** Effects of isolated compounds from *Crepis sancta* on superoxide anion generation and elastase release in fMLF/cytochalasin B (CB)-induced human neutrophils

Compound	Superoxide anion generation		Elastase release	
	% Inhibition <sup>a</sup>	IC <sub>50</sub> <sup>b</sup> (μM)	% Inhibition <sup>a</sup>	IC <sub>50</sub> <sup>b</sup> (μM)
(6S,7S,10R)-3-Oxo-di-nor-eudesm-4-en-6α-hydroxy-11-oic acid ( <b>1</b> )	12.05 ± 2.37	>10	2.74 ± 1.90	>10
(6S,7S,10R)-3-Oxo-6α-hydroxy-γ-costic acid ( <b>2</b> )	6.23 ± 3.81	>10	5.89 ± 1.07	>10
3-Oxo-γ-costic acid ( <b>3</b> )	18.46 ± 5.06	>10	3.89 ± 1.91	>10
3-Oxo-γ-costic acid methyl ester ( <b>4</b> )	18.27 ± 4.97	>10	0.70 ± 1.60	>10
(6S,9R)-Roseoside ( <b>5</b> )	9.43 ± 5.12	>10	2.72 ± 1.78	>10
Jaceidin ( <b>6</b> )	80.26 ± 6.22	4.76 ± 0.83	48.22 ± 6.61	>10
Kumatakenin ( <b>7</b> )	24.06 ± 2.75	>10	22.92 ± 4.29	>10
Penduletin ( <b>8</b> )	73.76 ± 5.24	5.66 ± 0.19	33.00 ± 7.94	>10
Pachypodol ( <b>9</b> )	67.46 ± 4.55	6.07 ± 0.65	31.56 ± 5.02	>10
Chrysosplenetin ( <b>10</b> )	92.03 ± 3.95	4.32 ± 0.57	65.82 ± 5.75	6.66 ± 1.03
Genistein	<sup>c</sup>	1.52 ± 0.17	31.57 ± 7.29	16.34 ± 4.26

<sup>a</sup> Percentage of inhibition (Inh%) at 10 μM concentration. <sup>b</sup> Concentration necessary for 50% inhibition (IC<sub>50</sub>). Results are presented as mean ± S.E.M. (*n* = 3–6). \**P* < 0.05, \*\**P* < 0.01, \*\*\**P* < 0.001 compared with the control (0.1% DMSO). <sup>c</sup> Genistein inhibited 67.01 ± 2.38% of superoxide anion generation at 3 μM.

along with other key <sup>1</sup>H–<sup>1</sup>H COSY and HMBC correlations (see ESI, Fig. S3†) confirmed undoubtedly the oxygenation to be at the same position (C-6) in **1**. In addition, <sup>1</sup>H–<sup>1</sup>H COSY and HMQC spectra of **1** distinguished two clear spin systems, one exists between two adjacent methylene moieties at δ<sub>H</sub> 1.72/δ<sub>H</sub>

1.83 (*m*, 2H, δ<sub>C</sub> 39.8) along with the two geminally coupled protons at δ<sub>H</sub> 2.38 (ddd, 17.4, 15.2, 5.2) and at δ<sub>H</sub> 2.66 (ddd, 17.4, 4.5, 2.5) bound to the same carbon peak at δ<sub>C</sub> 34.6 that were assigned for CH<sub>2</sub>-1 and CH<sub>2</sub>-2, respectively. A second spin system can be also featured extending over δ<sub>H</sub> 5.25 (d, 3.0, 1H,

**Table 2** Inhibitory activity of isolated compounds from *Crepis sancta* on A23187- and antigen-induced degranulation

Compound	% Viability, RBL-2H3 <sup>a</sup>	% Inhibition of A23187-induced degranulation <sup>b</sup>				% Inhibition of antigen-induced degranulation <sup>c</sup>			
	100 μM	1 μM	10 μM	100 μM	IC <sub>50</sub> <sup>d</sup> (μM)	1 μM	10 μM	100 μM	IC <sub>50</sub> <sup>d</sup> (μM)
(6S,7S,10R)-3-Oxo-di-nor-eudesm-4-en-6α-hydroxy-11-oic acid ( <b>1</b> )	>90%		2.1 ± 1.8	7.6 ± 6.6			7.7 ± 3.8	11.3 ± 3.6	
(6S,7S,10R)-3-Oxo-6α-hydroxy-γ-costic acid ( <b>2</b> )	>90%		0.2 ± 0.2	0.3 ± 0.3			11.7 ± 4.2	19.8 ± 2.5	
3-Oxo-γ-costic acid ( <b>3</b> )	>90%		2.7 ± 2.3	1.8 ± 1.6			2.8 ± 1.0	0.3 ± 0.2	
3-Oxo-γ-costic acid methyl ester ( <b>4</b> )	>90%		7.2 ± 5.9	61.8 ± 7.4***	80.6		18.2 ± 4.4	36.2 ± 6.5***	
(6S,9R)-Roseoside ( <b>5</b> )	>90%		5.3 ± 4.3	16.8 ± 7.9			19.9 ± 4.3	21.6 ± 1.8	
Jaceidin ( <b>6</b> )	>90%		5.3 ± 4.3	25.5 ± 5.0*			3.9 ± 2.9	46.5 ± 10.2***	
Kumatakenin ( <b>7</b> )	>90%		12.6 ± 9.1	36.8 ± 5.4			11.1 ± 7.6	60.9 ± 8.8***	80.4
Penduletin ( <b>8</b> )	>90%	4.8 ± 3.9	25.1 ± 7.3	<sup>e</sup>		33.9 ± 8.6**	85.8 ± 5.1***	<sup>e</sup>	3.8
Pachypodol ( <b>9</b> )	>90%	3.4 ± 2.8	22.6 ± 3.4	<sup>e</sup>		12.9 ± 6.5	47.2 ± 5.0***	<sup>e</sup>	
Chrysosplenetin ( <b>10</b> )	>90%	7.3 ± 5.9	41.6 ± 9.5***	<sup>e</sup>		12.4 ± 5.1	83.3 ± 7.5***	<sup>e</sup>	5.8
Azelastine <sup>b,c</sup>	>90%				10.9				15.4

<sup>a</sup> The cytotoxicity of samples to RBL-2H3 was evaluated using MTT viability assay. Results are presented as mean (*n* = 3) compared to untreated control (DMSO). All samples were nontoxic towards RBL-2H3 cells. <sup>b</sup> Azelastine (20 μM) was used as a positive control and inhibited 78.4 ± 1.4% \*\*\* of A23187-induced degranulation. The inhibition of degranulation was assessed by A23187-induced β-hexosaminidase release in RBL-2H3 cells. Results are presented as mean ± S.E.M. (*n* = 3); \**P* < 0.05, \*\**P* < 0.01, \*\*\**P* < 0.001 (Prism, ANOVA, Dunnet's test) compared with the control value (A23187 only). <sup>c</sup> Azelastine (20 μM) was used as a positive control and inhibited 66.8 ± 9.8% \*\*\* of antigen-induced degranulation. The inhibition of degranulation was assessed by antigen-induced β-hexosaminidase release in RBL-2H3 cells. Results are presented as mean ± SEM (*n* = 3); \**P* < 0.05, \*\**P* < 0.01, \*\*\**P* < 0.001 (Prism, ANOVA, Dunnet's test) compared with the control value (antigen only). <sup>d</sup> Concentration necessary for 50% inhibition (IC<sub>50</sub>). <sup>e</sup> Compounds **8**, **9** and **10** at concentration of 100 μM formed crystal-like precipitates upon the addition into medium, thus the effects could not be justified.





$\delta_C$  67.6),  $\delta_H$  2.46 (dt, 12.9, 3.0, 1H,  $\delta_C$  49.0) and two methylene groups at  $\delta_H$  2.21 (ddd, 13.4, 12.9, 3.2, 1H) and  $\delta_H$  1.74 (m, 1H) bound to a carbon peak at  $\delta_C$  18.5 in addition to  $\delta_H$  1.39 (dd, 13.3, 3.2) and  $\delta_H$  1.70 (dd, 6.7, 3.0, 1H) bound to a carbon peak at  $\delta_C$  41.4 that were ascribed to  $\underline{CH}$ -6,  $\underline{CH}$ -7,  $\underline{CH}_2$ -8 and  $\underline{CH}_2$ -9, respectively.

A careful exploration of  $^1H$  and  $^{13}C$  NMR spectral data of **2** (see ESI, Table S1†) and by comparison with the reported literature, it was interpreted to be structurally resembling 3-oxo- $\gamma$ -costic acid (**3**)<sup>29</sup> with one additional oxygen atom in **2** as deduced from their molecular formulas. The presence of an additional oxygen atom was explained by comparing 1D and 2D NMR spectral data of **2** (see ESI, Table S1†) and **3** (ref. 19) that confirmed the presence of an oxymethine proton, similar to **1**, at  $\delta_H$  5.52 (d, 6.5, 1H,  $\delta_C$  77.3) in **2** replacing a methylene group at  $\delta_H$  2.83 (br d, 13.5, 1H) and  $\delta_H$  2.02 (br t, 13.5, 1H) bound to a carbon peak at  $\delta_C$  33.3 assigned to C-6 in **3**.<sup>29</sup>

To unambiguously determine the positions of the hydroxyl and carboxylic acid moieties in both **1** and **2**, gHMBC experiments were performed (see ESI, Fig. S3, S9 and S17†). The key HMBC correlations of **1** and **2** (see ESI, Fig. S3†) undoubtedly confirmed the existence of a hydroxyl group at C-6 in both whereas a terminal carboxylic acid group was ascertained to be at C-11 and C-12, respectively.

The relative configuration of **1** was defined by interpreting the coupling constant ( $J$ ) values and by key ROESY correlations (see ESI, Fig. S3†). The determined large  $J$  values for H-7 and H-8a (12.9 Hz) revealed a diaxial orientation, however, a small

coupling constant value (3.0 Hz) for H-7 and H-6 suggested an axial-equatorial orientation, respectively.<sup>36–38</sup> In addition, the ROESY spectrum of **1** disclosed clear correlations (see ESI, Fig. S3 and S11†) namely these from H-6 to H-7 and a singlet methyl group at  $\delta_H$  1.87 (br s, Me-13) together with other key correlations in particular those from a singlet methyl group at  $\delta_H$  1.42 (s, Me-12) to two proton peaks at  $\delta_H$  2.66 (H-2a) and at  $\delta_H$  2.21 (H-8a) indicated that 6-OH and Me-12 are in an axial orientation while 7-COOH adopts an equatorial one. Supported by the results of X-ray crystallography<sup>36</sup> and modified Mosher method<sup>37</sup> for exploring the absolute configuration of biosynthetically related eudesmane-type sesquiterpenes such as 3-oxo-di-nor-eudesma-4-en-11-oic acid and (1*R*,2*S*,6*R*,7*S*,10*S*)-1,2,6-trihydroxyeudesma-4-en-3-one, compound **1** was deduced to have similar absolute configuration to the related congeners<sup>36,37</sup> apart from H-6 which was unambiguously distinguished to be in an equatorial position in **1** rather than an axial orientation in the related congeners. Accordingly, compound **1** was determined to be (6*S*,7*S*,10*R*)-3-oxo-di-nor-eudesma-4-en-6 $\alpha$ -hydroxy-11-oic acid.

The relative and absolute configurations of **2** (see ESI, Fig. S3†) were defined as for **1** based on ROESY spectrum that revealed comparable key correlations to those found in **1** in addition to the  $J$  values analysis that revealed similar orientation pattern of H-6 and H-7 like that noted in **1**. As a conclusion, compound **2** was unambiguously identified as (6*S*,7*S*,10*R*)-3-oxo-6 $\alpha$ -hydroxy- $\gamma$ -costic acid.

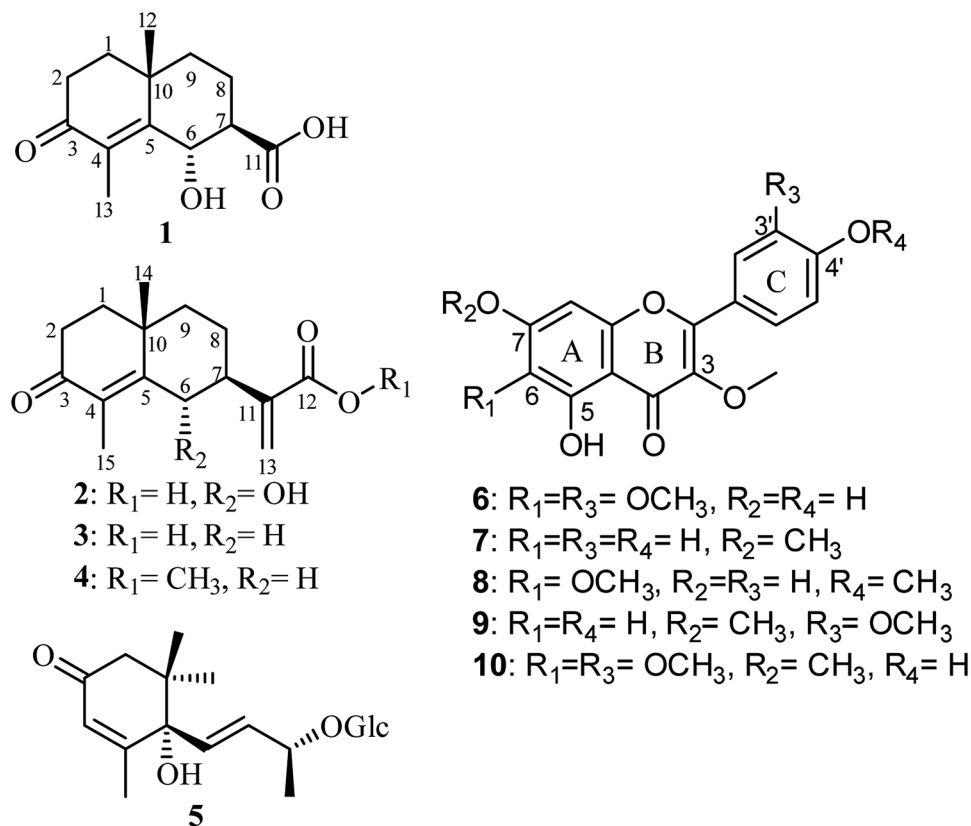


Fig. 1 Chemical structures of isolated compounds **1**–**10**.





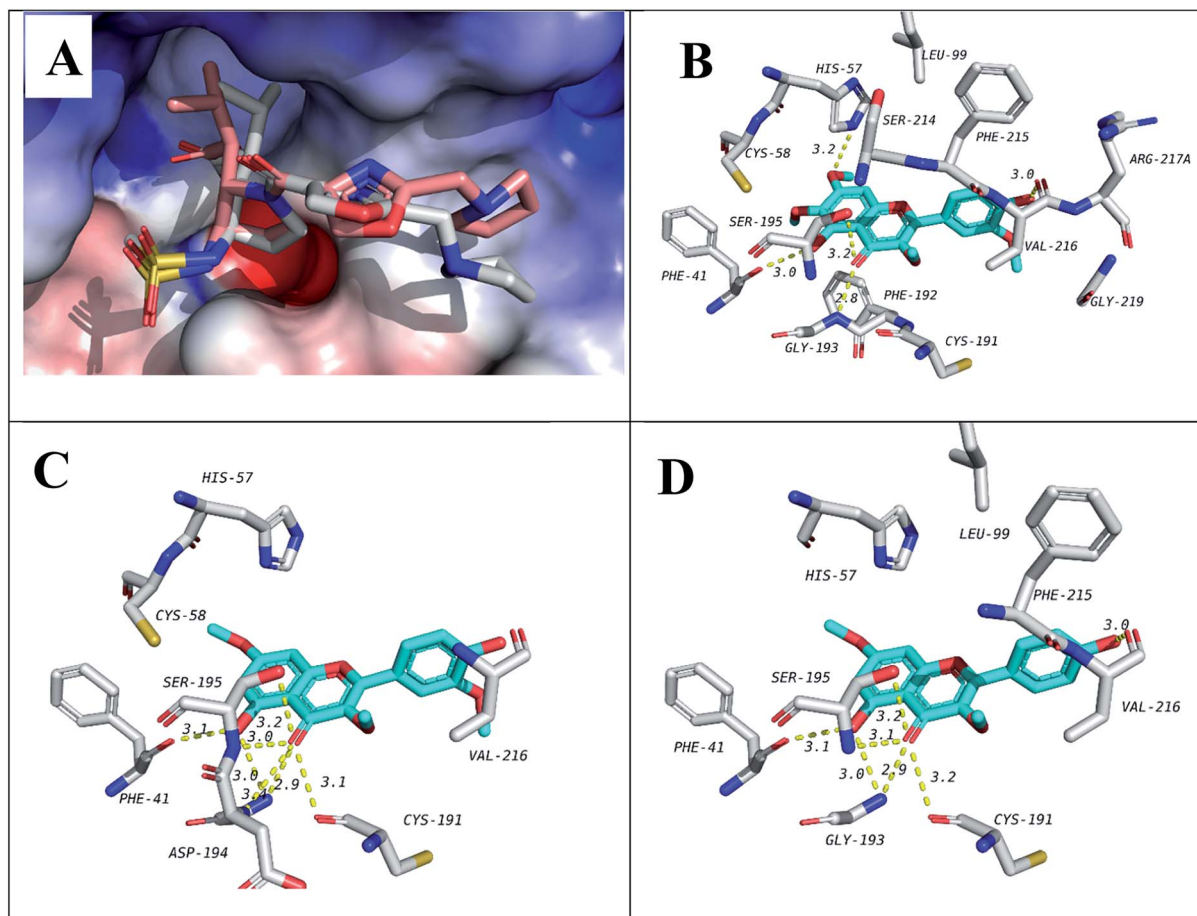


Fig. 2 Docking results of isolated compounds with NE (1H1B). (A) Validation of docking through redocking of the co-crystallized ligand GW475151 (gray) overlaid with the docked structure (pink). (B, C and D) Docking poses of the best docked ligands 10, 9 and 7, respectively.

### Superoxide anion generation and elastase release assays by human neutrophils

Assessment of the anti-inflammatory activity (Table 1) revealed that the isolated flavonols significantly suppressed the superoxide anion generation with  $IC_{50}$  values ranging between  $4.32 \pm 0.57$  and  $6.07 \pm 0.65 \mu\text{M}$ . Flavonoids were previously reported to have potent inhibitory activity against pro-inflammatory mediators such as inducible nitric oxide synthase (iNOS), tumor necrosis factor  $\alpha$  (TNF- $\alpha$ ), interleukin-1 $\beta$  (IL-1 $\beta$ ) and interleukin-6 (IL-6).<sup>39</sup> Among the tested compounds in this study, compound 10 revealed potent inhibitory effect on NE release and superoxide anion generation with  $IC_{50}$  values of  $6.66 \pm 1.03$  and  $4.32 \pm 0.57 \mu\text{M}$ , respectively. The results indicated inhibitory effect on human neutrophils activation. Human neutrophil elastase plays a major role in neutrophils-associated diseases. According to a previous study, structurally similar flavonols including 8 ( $IC_{50} = 65.4 \mu\text{M}$ ) showed inhibitory effect on human neutrophil elastase which correlates with 33.0% inhibitory effect of 8 on NE release in human neutrophils at  $10 \mu\text{M}$ .<sup>40</sup> The obtained results in this study strengthened the previous reports about the anti-inflammatory effects of flavonols combating the respiratory damage and NE release along with plausible antiviral activity as previously reported.<sup>41</sup>

### Degranulation assay in mast cells

All isolated compounds (1–10) were assessed for their toxic effects on normal RBL-2H3 cells up to  $50 \mu\text{M}$ . The results (Table 2) revealed that all tested compounds were non-toxic (viability more than 90%). Antiallergic activity of isolated compounds (1–10) was then tested *via* assessing their inhibitory activities against A23187- and antigen-induced  $\beta$ -hexosaminidase release in RBL-2H3 cells. Calcium ionophore A23187 represents an inducer facilitating calcium transport through mast cells membrane while antigen (IgE plus DNP-BSA) acts *via* Fc $\epsilon$ R1 receptor similar to physiological environment.<sup>15</sup> The obtained results (Table 2) revealed that among eudesmane sesquiterpene lactones (1–4), 3-oxo- $\gamma$ -costic acid methyl ester (4) moderately suppressed A23187-induced degranulation ( $IC_{50}$   $80.6 \mu\text{M}$ ) indicating importance of carboxylic acid esterification for the activity. The obtained results (Table 2) revealed that compounds 8 and 10 displayed potent inhibitory activities against antigen-induced degranulation with  $IC_{50}$  values of 3.8 and  $5.8 \mu\text{M}$ , respectively, exceeding that of azelastine as a standard antiallergic drug ( $IC_{50} = 15.4 \mu\text{M}$ ). Also, compounds 4 and 7 exerted significant effects on antigen-induced degranulation of mast cells. In a previous report, a structurally-related flavonoid aglycone, kaempferol, was found to exert *in vitro* antiallergic actions in RBL-2H3 cells through inducing heme oxygenase-1 (ref.



**Table 3** Binding energy for compounds (1–10) in the active sites of neutrophil elastase (NE) and SARS-CoV-2 main protease ( $M^{Pro}$ ) showing residues forming hydrogen bonds with docked ligands. Energy and interacting residues are for the first pose unless otherwise stated

Compound/ligand	1H1B (elastase)		6LU7 ( $M^{Pro}$ )	
	Binding affinity (kcal mol <sup>-1</sup> )	Interacting residues	Binding affinity (kcal mol <sup>-1</sup> )	Interacting residues
(6 <i>S</i> ,7 <i>S</i> ,10 <i>R</i> )-3-Oxo-di-nor-eudesm-4-en-6 $\alpha$ -hydroxy-11-oic acid (1)	−5.5	Ser195, Val216	−5.9	Gly143
(6 <i>S</i> ,7 <i>S</i> ,10 <i>R</i> )-3-Oxo-6 $\alpha$ -hydroxy- $\gamma$ -costic acid (2)	−6.2	Ser195	−6.1	Gly143, Ser144, His163
3-Oxo- $\gamma$ -costic acid (3)	−5.9	Ser195	−5.9 (4th pose)	Gly143, His163
3-Oxo- $\gamma$ -costic acid methyl ester (4)	−5.9	Ser195	−6.0 (3rd pose)	Gly143, His163
(6 <i>S</i> ,9 <i>R</i> )-Roseoside (5)	−6.4	Phe41, Asn61, Ser195, Val216	−7.2	Thr26, Leu141, Gly143, Ser144, Cys145, His163, Glu166
Jaceidin (6)	−6.2	Cys191, Gly193, Ser195	−7.3	Leu141, Gly143, Ser144, Cys145, Arg188
Kumatakenin (7)	−6.7	Phe41, Cys191, Gly193, Ser195, Val216	−6.8 (3rd pose)	Leu141, Gly143, Ser144
Penduletin (8)	−6.1	Cys191, Gly193, Ser195	−6.7 (4th pose)	Leu141, Gly143, Ser144, Cys145, His163
Pachypodol (9)	−6.7	Phe41, Cys191, Gly193, Asp194, Ser195	−7.1	Gly143, Ser144, Cys145
Chrysosplenetin (10)	−6.5	Phe41, His57, Gly193, Ser195, Val216	−7.1	Leu141, Gly143, Ser144, Cys145
1H1B-ligand	−6.9	Ser195	—	—
6LU7-ligand (N3)	—	—	−7.1 (3rd pose)	Phe140, Gly143, His163, His164, Glu166, Asp187, Thr190

42) which might be a putative mechanism for the antiallergic activity of **8** and **10** as well (Fig. 1).

### X-ray crystallographic analysis

Being unprecedentedly reported and based on the findings obtained from anti-inflammatory and antiallergic assays, we crystallized chrysosplenetin (**10**) using its pure methanol solution. Herein, we report for the first time its crystal structure (see ESI, Fig. S2 and Table S2†). From the single-crystal structure refinement, the structure for chrysosplenetin was obtained, containing two independent molecules in the asymmetric unit, which are connected by a hydrogen bond. Both molecules contain also intramolecular hydrogen bonds.

### Molecular modeling studies

In order to predict the binding mode of the isolated compounds in the active site of NE, compounds were docked using Auto-dock Vina. To validate docking method and parameters, co-crystallized ligand GW475151 was redocked in the active site. When the extracted crystal structure and the docked structure were aligned using DockRMSD server, a root mean square deviation (RMSD) value of 1.317 was obtained which indicates the validity of the method used.<sup>12</sup> Results obtained from docking study of isolated compounds with NE showed that isolated methoxylated flavonols (**6**–**10**) possess better binding in the active site when compared to sesquiterpenes (**1**–**4**). Amongst

flavonols, those with a methoxy group at C-7, compounds **7**, **9** and **10**, demonstrated better binding. This methoxy was found to be in close proximity to His57, one of the catalytic triad of the serine proteases like NE. Another important residue which is also one of the catalytic triad is Ser195 which was found to form hydrogen bond with the C-4 carbonyl group in all the three flavonols. The third residue among the catalytic triad, Asp102 was found to lie at the bottom of the binding site and is positioned beneath the docked flavonols. It is generally accepted that catalytic activity of NE is enhanced by these three residues (catalytic triads; His57, Asp102 and Ser195).<sup>43</sup> The former two residues act as a base to increase nucleophilicity of Ser195 through accepting proton transferred from serine hydroxyl group.<sup>44</sup> In addition to the catalytic triad, docked structures were found to form several hydrogen bonds, represented by dotted yellow line, with residues in the active site as illustrated in Fig. 2 and Table 3. These residues include Phe41, Cys191, Gly 193 and Val216. In addition, hydrophobic interactions between ring A and C from the flavonols with Phe192 and Val216 are observed, respectively. Hydrophobic interaction between ring C and Val216 could explain the differences in dihedral angles between rings B and C in the docked structure and the crystal structure of free flavonols. For example, when we crystallized **10** alone, the dihedral angle between ring B and C was either 0.5° (almost coplanar) or 40° with two independent molecules in the asymmetric unit. On the other hand, when **10** was docked in the



active site of NE a dihedral angle of 85° (almost perpendicular) between rings B and C was obtained due interaction with Val216.

It is worth to mention that docking data has shown good agreement with the elastase release assay in human neutrophils

indicating a possible direct effect on elastase enzymatic activity. To justify this notion, Pearson's correlation coefficient was determined whose value revealed a medium to strong negative association between the inhibition of human elastase release and the docking scores ( $r = -0.5$ ). This indicates that the higher

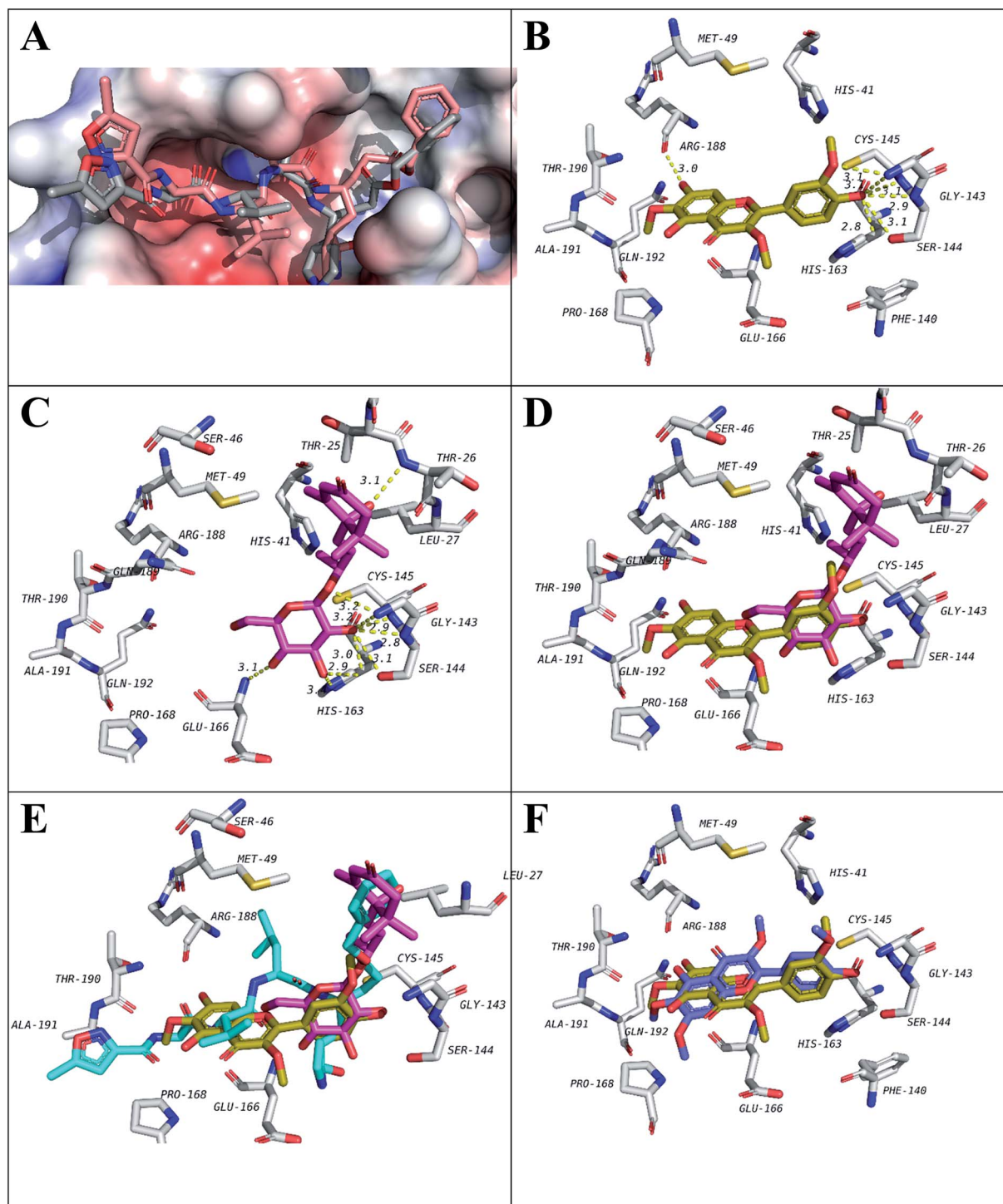


**Fig. 3** Docking results of isolated compounds with SARS-CoV-2 M<sup>pro</sup> (6LU7). (A) Validation of docking through redocking of the co-crystallized ligand N3 (gray) overlaid with the docked structure (pink). (B and C) Docking poses of the best compounds **6** (golden) and **5** (pink) respectively and their overlapping in (D). (E) Docking poses of **5** (pink) and **6** (golden) overlapped with co-crystallized ligand N3 (blue). (F) Docking poses of **6** (golden) and **10** (violet) comparing their binding modes.



Table 4 Coulombic and Lennard-Jones interactions as well as total interaction energy of the complexes studied by MD

Target	Complex	Energy (kJ mol <sup>-1</sup> )		
		Coulombic interaction	Lennard-Jones (L-J) energy	Total interaction energy
Human elastase	1H1B-chrysosplenetin ( <b>10</b> )	-31.12 ± 3.7	-84.81 ± 10	-115.93 ± 10
	1H1B-control	-20.36 ± 3.8	-99.14 ± 6.0	-119.50 ± 7.1
SARS-CoV-2 main protease	6LU7-chrysosplenetin ( <b>10</b> )	-24.29 ± 6.9	-81.58 ± 17	-105.87 ± 18
	6LU7-control	-173.04 ± 5.2	-249.57 ± 2.8	-422.61 ± 5.9
	6LU7-jaceidin ( <b>6</b> )	-43.72 ± 2.0	-113.80 ± 1.7	-157.52 ± 2.6

the inhibitory activity against human elastase release is, the lower the docking score (larger absolute value).

Considering NE as a protease, this encouraged us to assess the binding modes and affinity of the isolated compounds to SARS-CoV-2 main protease (M<sup>Pro</sup>).<sup>10</sup> This enzyme was proposed to be a good target for treatment of COVID-19. Chen and co-workers reported the virtual screening of M<sup>Pro</sup> against a medicinal plant library containing 32 297 compounds including flavonoids.<sup>45</sup>

To test that virtually, the isolated compounds' docking into the active site of M<sup>Pro</sup> was studied. Before running the actual docking, validation was done by redocking of the co-crystallized ligand N3. The docked structure had a RMSD of 1.855 compared to the co-crystallized ligand structure (Fig. 3A).

Among the docked structures, tested flavonols, jaceidin (**6**), pachypodol (**9**) and chrysosplenetin (**10**) along with (6*S*,9*R*)-roseoside (**5**) revealed binding energy values equal or even higher than the co-crystallized ligand (6LU7, Table 3).

Among isolated flavonols, compounds **6**, **9** and **10** feature a similar ring C structure with adjacent methoxy and hydroxyl groups that proved to form hydrogen bond network with residues Cys145, Ser144, Gly143, and Leu141 (Fig. 3B). A very recent report by Zhang and coworkers indicated the inevitable role of Cys145, Ser144 and Gly143 forming the canonical "oxanion hole" of the cysteine protease, in the binding of SARS-CoV-2 M<sup>Pro</sup> inhibitors.<sup>10</sup> In addition, only compound **6** possesses a free hydroxyl group at position 7 of ring A which was found to be involved in a hydrogen bond with Arg188 which may explain the slightly higher binding energy value compared to compounds **9** and **10** (Table 3).

For compound **5** (Fig. 3C), the binding pose is partially overlapped with that of flavonol (**6**) where the glycosidic sugar

moiety in **5** is overlapping with ring C of **6**. The hydroxy groups on the sugar unit in **5** are involved in hydrogen bond network with the same residues similar to **6**, **9** and **10** binding (Cys145, Ser144, Gly143 and Leu141). In addition, hydrogen bonds with His163, Glu166 and Thr26 are also seen. Among those, His163 and Glu166 were reported in Zhang and his fellows' work mentioned above.<sup>10</sup> It will be interesting to synthesize and test a compound that has the aglycon of (6*S*,9*R*)-roseoside linked to 3'-oxygen of **6** (Fig. 3D and E) as a proposed structure for a lead SARS-CoV-2 M<sup>Pro</sup> inhibitor.

### Molecular dynamic simulation

Beside being the best compound in the elastase release assay with IC<sub>50</sub> of 6.66 μM (Table 1), chrysosplenetin (**10**) was among the top compounds that showed the best docking in the active site of human elastase (1H1B) and has shown comparable binding affinity to the co-crystallized ligand in the active site of SARS-CoV-2 main protease (6LU7) as demonstrated in Table 3. These findings encouraged us to further investigate the bonding of **10** with both targets using molecular dynamic simulation studies. Four complexes were studied including **10** in both targets and the co-crystallized ligand corresponding to each target. Using production run trajectories, the average total interaction energy composed of coulombic interaction and Lennard-Jones (L-J) energy was calculated (Table 4).

For elastase complexes, both compound **10** and the co-crystallized ligand have shown comparable average total interaction energy ranging from -115 to -120 kJ mol<sup>-1</sup> supporting its potential activity as elastase inhibitor that was proved by the biological testing. In addition, plotting of RMSD of ligand heavy atoms during the MD production run (Fig. 4A), shows RMSD < 1

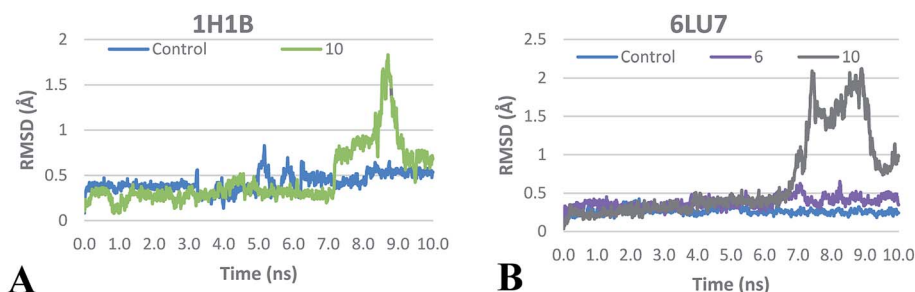


Fig. 4 RMSD plot of ligands heavy atoms in the active sites of (A), human elastase 1H1B and (B), SARS-CoV-2 main protease 6LU7 during the production MD run.



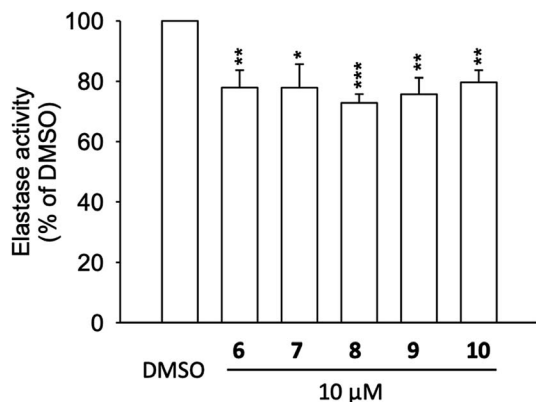


Fig. 5 Elastase enzymatic activity of compounds **6** to **10**. Human neutrophils were incubated with fMLF/CB for 15 min. The elastase supernatant was obtained and incubated with DMSO (as control), or with compounds **6–10** (10  $\mu$ M) for 2 min before the addition of substrate (100  $\mu$ M). Elastase activity was measured at 405 nm. Data are presented as means  $\pm$  S.E.M. ( $n = 4$ ). \* $p < 0.05$ , \*\* $p < 0.01$ , \*\*\* $p < 0.001$  compared with the control group ( $t$ -test).

Å during more than 90% of production run time which suggests the stability of the proposed docking binding mode discussed earlier.

On the other hand, the average total interaction energy between **10** and SARS-CoV-2 main protease was much less than the interaction energy seen in case of the co-crystallized ligand (Table 4). The RMSD plot (Fig. 4B) shows stability of the 6LU7–**10** complex only during the initial MD production run. This suggested that compound **10** could be a lead for the design of compounds targeting main protease but need further improvement. To investigate the last hypothesis, we decided to run MD for 6LU7 complex with **6** whose choice was based on its close structural similarity to **10** and also on its better docking score. In elastase release inhibitory activity, compound **6** was also the second-most potent compound. We found that **6** has better total interaction energy ( $-157 \text{ kJ mol}^{-1}$ ) which resulted from slight structural modification of compound **10**. Moreover, jaceidin (**6**) has also shown less RMSD fluctuation during the MD production run (Fig. 4B). This clearly supports that further improvement can be done in this scaffold to design SARS-CoV-2 main protease inhibitors against COVID-19. This could be done through different medicinal chemistry techniques but it is beyond the scope of this work.

### Elastase enzymatic activity

To address the results from molecular docking and molecular dynamic simulation studies, neutrophil elastase (NE) was extracted from activated neutrophils and cell-free assay on the elastase enzymatic activity was performed (Fig. 5). The results revealed, that compounds **6** to **10** significantly inhibited the activity of elastase enzyme by 20.3 to 27.1% at the concentration of 10  $\mu$ M (Fig. 5). Thus, the effects of **6** to **10** on elastase release (22.9 to 65.8% inhibition at 10  $\mu$ M), could be, at least partly, attributed to the direct interaction with elastase enzyme which is in agreement with the molecular docking of compounds with NE.

### Protective effects against human coronavirus 229E infection

We further tested the compounds that docked well with M<sup>Pro</sup> (compounds **5** to **10**) in the human coronavirus 229E (HCoV-229E) assay *in vitro* (see ESI, Fig. S4†). The cells were infected with HCoV-229E strain (grey) and the protective effects of compounds (**5–10**) were evaluated. None of the tested compounds protected the cells from HCoV-229E infection. However, having no *in vitro* protective activity against viral host cell entry doesn't deny the M<sup>Pro</sup> inhibitory activity that converts viral polyprotein into functional units within host cells to be finally assembled into new viruses.

Recently, natural products have been focused on as a source of inhibitors affecting SARS-CoV-2 M<sup>Pro</sup>, a functional protein considered as a potential target for developing new therapeutics to help combatting the current COVID-19 pandemic. Many natural compounds, belonging to various chemical classes such as alkaloids, coumarins, flavonoids, peptides, terpenoids and tannins, have been assessed for their SARS-CoV-2 M<sup>Pro</sup> inhibitory activity.<sup>46</sup> Many potential M<sup>Pro</sup> inhibitors were chemically belonging to flavonoids such as quercetin, apigenin and luteolin (IC<sub>50</sub> of 20–200  $\mu$ M) in addition to the biflavonoid amentoflavone that was the most potent with IC<sub>50</sub> of 8.3  $\mu$ M.<sup>47</sup> To further investigate and comprehend their M<sup>Pro</sup> inhibitory activity, *in silico* molecular docking and molecular dynamic simulation studies were also conducted.<sup>48,49</sup> In our study, the obtained results enriched potential SARS-CoV-2 M<sup>Pro</sup> inhibitors with some more candidates supported by more details about their binding modes in addition to being proved *in vitro* as inhibitors of human elastase release. These features altogether may also escalate their efficiency in defeating the respiratory distress symptoms triggered by inflammatory responses to SARS-CoV-2 infection.

## Conclusion

Phytochemical investigation of polyphenolic-rich extract of the Jordanian hawksbeard, prescribed by local herbalists for treatment of cough and flu, afforded several eudesmane sesquiterpenes and flavonols. They were assessed for their *in vitro* anti-inflammatory and antiallergic activities. Among the tested compounds, flavonols, in particularly chrysosplenetin (**10**), exhibited potent anti-inflammatory activity that was proved *via in vitro* experimental results through assessing its inhibitory activity against neutrophil elastase release along with further *in silico* molecular modeling that included docking and molecular dynamic simulation studies. By assessing the binding to SARS-CoV-2 (COVID-19) M<sup>Pro</sup> as an important target, chrysosplenetin (**10**) was also found to possess high binding energy comparable to that exhibited by its standard ligand.

These findings are supporting the introduction of chrysosplenetin (**10**) as a potential lead candidate into the phytotherapeutic arena as an anti-inflammatory and antiallergic drug. Moreover, its inhibitory activity against SARS-CoV-2 (COVID-19) M<sup>Pro</sup> will support considering it as a potential lead structure paving the way toward finding out a natural remedy for treatment of the current COVID-19 pandemic.





## Author contributions

SSE and PP: conceptualization, writing, reviewing and editing, SSE, NAA and FSY: Methodology, purification and isolation of pure metabolites; DHEK, TOK and CJ: NMR analysis, data curation and X-ray crystallography; AA: molecular modeling and MD simulation; MK and BHC: antiallergy assay; TLH: anti-inflammatory assay; GHL and CYL: anti-coronavirus 229E assay; SMA, AMD and PP; supervision and editing the manuscript.

## Conflicts of interest

The authors declare that there is no conflict of interest.

## Acknowledgements

S. S. E. acknowledges the Junior Scientist and International Research Center (JUNO) at Heinrich-Heine University (Düsseldorf, Germany) for financial support. P. P. wants to thank Manchot Foundation for their support. The research was supported by the grants from the Ministry of Science and Technology (MOST 106-2320-B-255-003-MY3, MOST 108-2320-B-255-003-MY3, and MOST108-2320-B-037-004), Ministry of Education (EMRPD1G0231 and EMRPD1H0381), Kaohsiung Medical University (KMU-DK109002-3), Chang Gung University of Science and Technology (ZRRPF3H0101 and ZRRPF3H0111), and Chang Gung Memorial Hospital (CMRPF1F0011~3, CMRPF1F0061~3, CMRPF1G0241~3, CMRPF1J0051~3, and BMRP450), Taiwan. The funders had no role in the study design, data collection and analysis, decision to publish, or preparation of the manuscript.

## References

- 1 P. A. Henriksen, The potential of neutrophil elastase inhibitors as anti-inflammatory therapies, *Curr. Opin. Hematol.*, 2014, **21**, 23–28.
- 2 K. Hoenderdos and A. Condliffe, The neutrophil in chronic obstructive pulmonary disease, *Am. J. Respir. Cell Mol. Biol.*, 2013, **48**, 531–539.
- 3 T. J. Moraes, C. W. Chow and G. P. Downey, Proteases and lung injury, *Crit. Care Med.*, 2003, **31**, S189–S194.
- 4 S. Hagiwara, H. Iwasaka, K. Togo and T. Noguchi, A neutrophil elastase inhibitor, sivelestat, reduces lung injury following endotoxin-induced shock in rats by inhibiting HMGB1, *Inflammation*, 2008, **31**, 227–234.
- 5 B. Ställberg, C. Janson, G. Johansson, K. Larsson, G. Stratelis, G. Telg and K. H. Lisspers, Management, morbidity and mortality of COPD during an 11-year period: an observational retrospective epidemiological register study in Sweden (PATHOS), *Prim. Care Respir. J.*, 2014, **23**, 38–45.
- 6 J. S. M. Peiris, Y. Guan and K. Y. Yuen, Severe acute respiratory syndrome, *Nat. Med.*, 2004, **10**, S88–S97.
- 7 A. M. Zaki, S. van Boheemen, T. M. Bestebroer, A. D. Osterhaus and R. A. Fouchier, Isolation of a novel coronavirus from a man with pneumonia in Saudi Arabia, *N. Engl. J. Med.*, 2012, **367**, 1814–1820.
- 8 H. A. Rothan and S. N. Byrareddy, The epidemiology and pathogenesis of coronavirus disease (COVID-19) outbreak, *J. Autoimmun.*, 2020, **108**, 102433, DOI: 10.1016/j.jaut.2020.102433.
- 9 T. T.-Y. Lam, N. Jia, Y.-W. Zhang, M. H.-H. Shum, J.-F. Jiang, H.-C. Zhu, Y.-G. Tong, Y.-X. Shi, X.-B. Ni, Y.-S. Liao, W.-J. Li, B.-G. Jiang, W. Wei, T.-T. Yuan, K. Zheng, X.-M. Cui, J. Li, G.-Q. Pei, X. Qiang, W. Y.-M. Cheung, L.-F. Li, F.-F. Sun, S. Qin, J.-C. Huang, G. M. Leung, E. C. Holmes, Y.-L. Hu, Y. Guan and W.-C. Cao, Identifying SARA-CoV-2 related coronaviruses in Malayan pangolins, *Nature*, 2020, **583**, 282–285.
- 10 L. Zhang, D. Lin, X. Sun, U. Curth, C. Drosten, L. Sauerhering, S. Becker, K. Rox and R. Hilgenfeld, Crystal structure of SARS-Cov-2 main protease provides a basis for design of improved  $\alpha$ -ketamide inhibitors, *Science*, 2020, **368**, 409–412.
- 11 S. Sansanelli and A. Tassoni, Wild food plants traditionally consumed in the area of Bologna (Emilia Romagna region, Italy), *J. Ethnobiol. Ethnomed.*, 2014, **10**(69), 1–11, DOI: 10.1186/1746-4269-10-69.
- 12 S. S. Ebada, N. A. Al-Jawabri, F. S. Youssef, A. Albohy, S. M. Aldalaein, A. M. Disi and P. Proksch, *In vivo* antiulcer activity, phytochemical exploration, and molecular modeling of the polyphenolic-rich fraction of *Crepis sancta* extract, *Inflammopharmacology*, 2020, **28**, 321–331.
- 13 K. Michalska, E. Szneler and W. Kisiel, Structure elucidation of an unusual new sesquiterpene lactone glucoside ester from *Crepis pannonica*, *Magn. Reson. Chem.*, 2016, **54**, 175–177.
- 14 M. Korinek, V. D. Wagh, I.-W. Lo, Y.-M. Hsu, H.-Y. Hsu, T.-L. Hwang, Y.-C. Wu, Y.-B. Cheng, B.-H. Chen and F.-R. Chang, Antiallergic phorbol ester from the seeds of *Aquilaria malaccensis*, *Int. J. Mol. Med.*, 2016, **17**, 398, DOI: 10.3390/ijms17030398.
- 15 M. Korinek, Y. H. Tsai, M. El-Shazly, K. H. Lai, A. Backlund, S. F. Wu, W. C. Lai, T. Y. Wu, S. L. Chen, Y. C. Wu, Y. B. Cheng, T. L. Hwang, B. H. Chen and F. R. Chang, Antiallergic hydroxy fatty acids from *Typhonium blumei* explored through ChemGPS-NP, *Front. Pharmacol.*, 2017, **8**, 356.
- 16 S.-C. Yang, P.-J. Chung, C.-M. Ho, C.-Y. Kuo, M.-F. Hung, Y.-T. Huang, W.-Y. Chang, Y.-W. Chang, K.-H. Chan and T.-L. Hwang, Propofol inhibits superoxide production, elastase release, and chemotaxis in formyl peptide-activated human neutrophils by blocking formyl peptide receptor 1, *J. Immunol.*, 2013, **190**, 6511–6519.
- 17 D. H. El-Kashef, F. S. Youssef, R. Hartmann, T.-O. Knedel, C. Janiak, W. Lin, I. Reimche, N. Teusch, Z. Liu and P. Proksch, Azaphilones from the Red Sea fungus *Aspergillus falconensis*, *Mar. Drugs*, 2020, **18**, 204, DOI: 10.3390/md18040204.
- 18 M. J. Abraham, T. Murtola, R. Schulz, S. Páll, J. C. Smith, B. Hess and E. Lindahl, GROMACS: high performance molecular simulations through multi-level parallelism from laptops to supercomputers, *SoftwareX*, 2015, **1**, 19–25.



- 19 J. Huang and A. D. MacKerell, CHARMM36 all-atom additive protein force field: Validation based on comparison to NMR data, *J. Comput. Chem.*, 2013, **34**, 2135–2145, DOI: 10.1002/jcc.23354.
- 20 V. Zoete, M. A. Cuendet, A. Grosdidier and O. Michielin, SwissParam, a Fast Force Field Generation Tool for Small Organic Molecules, *J. Comput. Chem.*, 2011, **32**, 2359–2368, DOI: 10.1002/jcc.21816 PMID: 21541964.
- 21 P. Mark and L. Nilsson, Structure and dynamics of the TIP3P, SPC, and SPC/E water models at 298 K, *J. Phys. Chem. A*, 2001, **105**, 9954–9960.
- 22 G. Bussi, D. Donadio and M. Parrinello, Canonical sampling through velocity rescaling, *J. Chem. Phys.*, 2007, **126**, 014101.
- 23 M. Parrinello and A. Rahman, Polymorphic transitions in single crystals: a new molecular dynamics method, *J. Appl. Phys.*, 1981, **52**, 7182–7190.
- 24 B. Hess, H. Bekker, H. J. Berendsen and J. G. Fraaije, LINCS: a linear constraint solver for molecular simulations, *J. Comput. Chem.*, 1997, **18**, 1463–1472.
- 25 T. Darden, D. York and L. Pedersen, Particle mesh Ewald: an  $N \log(N)$  method for Ewald sums in large systems, *J. Chem. Phys.*, 1993, **98**, 10089–10092.
- 26 Y. F. Tsai, H. P. Yu, W. Y. Chang, F. C. Liu, Z. C. Huang and T. L. Hwang, Sirtinol inhibits neutrophil elastase activity and attenuates lipopolysaccharide-mediated acute lung injury in mice, *Sci. Rep.*, 2015, **5**, 8347, DOI: 10.1038/srep08347.
- 27 C.-F. Hsieh, J.-R. Jheng, G.-H. Lin, Y.-L. Chen, J. Y. Ho, C.-J. Liu, K.-Y. Hsu, Y.-S. Chen, Y. F. Chan, H.-M. Yu, P.-W. Hsieh, J.-H. Chern and J.-T. Horng, Rosmarinic acid exhibits broad anti-enterovirus A71 activity by inhibiting the interaction between the five-fold axis of capsid VP1 and cognate sulfated receptors, *Emerg. Microb. Infect.*, 2020, **9**, 1194–1205.
- 28 S. S. Ebada, D. H. El-Kashef, W. E. G. Müller and P. Proksch, Cytotoxic eudesmane sesquiterpenes from *Crepis sancta*, *Phytochem. Lett.*, 2019, **33**, 46–48.
- 29 F. R. Garcez, W. S. Garcez, L. Hamerski and A. C. de M. Miranda, Eudesmane and rearranged eudesmane sesquiterpenes from *Nectandra cissiflora*, *Quím. Nova*, 2010, **33**, 1739–1742.
- 30 M.-E. F. Hegazy, H. Matsuda, S. Nakamura, T. A. Hussein, M. Yoshikawa and P. W. Paré, Chemical constituents and their antibacterial and antifungal activity from the Egyptian herbal medicine *Chiliadenus montanus*, *Phytochemistry*, 2014, **103**, 154–161.
- 31 G. Flamini, E. Antognoli and I. Morelli, Two flavonoids and other compounds from the aerial parts of *Centaurea bracteata* from Italy, *Phytochemistry*, 2001, **57**, 559–564.
- 32 J.-H. Woo, J.-H. Ahn, D.-S. Jang, K.-T. Lee and J.-H. Choi, Effect of kumatakenin isolated from cloves on the apoptosis of cancer cells and the alternative activation of tumor-associated macrophages, *J. Agric. Food Chem.*, 2017, **65**, 7893–7899.
- 33 S. E. Sajjadi, S. M. Ghanadian, M. Rabbani and F. Tahmasbi, Isolation and identification of secondary metabolites from the aerial parts of *Stachys lavandulifolia* Vahl, *Iran, J. Pharm. Res.*, 2017, **16**, 58–63.
- 34 H.-A. Ali, A. K. A. Chowdhury, A. K. M. Rahman, T. Borkowski, L. Nahar and S. D. Sarker, Pachypodol, a flavonol from the leaves of *Calycotris floribunda*, inhibits the growth of Caco 2 colon cancer cell line *in vitro*, *Phytother. Res.*, 2008, **22**, 1684–1687.
- 35 X.-Y. Xie, R. Wang and Y.-P. Shi, Flavonoids from the flowers of *Matricaria chamomilla*, *Chem. Nat. Compd.*, 2014, **50**, 910–911.
- 36 E. Fattorusso, F. U. Santelia, G. Appendino, M. Ballero and O. Tagliatela-Scafati, Polyoxygenated eudesmanes and trans-chrysanthemanes from the aerial parts of *Santolina insularis*, *J. Nat. Prod.*, 2004, **67**, 37–41.
- 37 G.-C. Wang, G.-Q. Li, H.-W. Geng, T. Li, J.-J. Xu, F. Ma, X. Wu, W.-C. Ye and Y.-L. Li, Eudesmane-type sesquiterpene derivatives from *Laggera alata*, *Phytochemistry*, 2013, **96**, 201–207.
- 38 M.-E. F. Hegazy, A. A. El-Beih, A. R. Hamed, A. A. Abd El Aty, N. S. Mohamed and P. W. Paré, 3-Oxo- $\gamma$ -cortic acid fungal-transformation generates eudesmane sesquiterpenes with *in vitro* tumor-inhibitory activity, *Bioorg. Med. Chem. Lett.*, 2017, **27**, 3825–3828.
- 39 R. Chen, Y. Yang, J. Xu, Y. Pan, W. Zhang, Y. Xing, H. Ni, Y. Sun, Y. Hou and N. Li, *Tamarix hohenackeri* Bung exerts anti-inflammatory effects on lipopolysaccharide activated microglia *in vitro*, *Phytomedicine*, 2018, **40**, 10–19.
- 40 Z. Uddin, Z. Li, Y. H. Song, J. Y. Kim and K. H. Park, Visconata: a rare flavonol having long chain fatty acid from *Dodonaea viscosa* which inhibits human neutrophil elastase (HNE), *Tetrahedron Lett.*, 2017, **58**, 2507–2511.
- 41 V. S. Somerville, A. J. Braakhuis and W. G. Hopkins, Effect of flavonoids on upper respiratory tract infections and immune function: A systematic review and meta-analysis, *Adv. Nutr.*, 2016, **7**, 488–497, DOI: 10.3945/an.115.010538.
- 42 E. Hirose, M. Matsushima, K. Takagi, Y. Ota, K. Ishigami, T. Hirayama, Y. Hayashi, T. Nakamura, N. Hashimoto, K. Imaizumi, K. Baba, Y. Hasegawa and T. Kawabe, Involvement of heme oxygenase-1 in kaempferol-induced antiallergic actions in RBL-2H3 cells, *Inflammation*, 2009, **32**, 99–108.
- 43 L. Crocetti, I. A. Schepetkin, A. Cilibrizzi, A. Graziano, C. Vergelli, D. Giomi, A. I. Khlebnikov, M. T. Quinn and M. P. Giovannoni, Optimization of *N*-benzoylindazole derivatives as inhibitors of human neutrophil elastase, *J. Med. Chem.*, 2013, **56**, 6259–6272.
- 44 I. M. Ayoub, M. Korinek, T.-L. Hwang, B.-H. Chen, F.-R. Chang, M. El-Shazly and A. N. B. Singab, Probing the antiallergic and anti-inflammatory activity of biflavonoids and dihydroflavonols from *Dietes bicolour*, *J. Nat. Prod.*, 2018, **81**, 243–253.
- 45 M. T. ul Qamar, S. M. Alqahtani, M. A. Alamri and L.-L. Chen, Structural basis of SARS-CoV-2 3CL<sup>pro</sup> and anti-COVID-19 drug discovery from medicinal plants, *J. Pharm. Sci.*, 2020, **10**, 313–319.
- 46 A. M. Sayed, A. R. Khattab, A. M. AboulMagd, H. M. Hassan, M. E. Rateb, H. Zaid and U. R. Abdelmohsen, Nature as a treasure trove of potential anti-SARS-CoV drug leads:



- a structural/mechanistic rationale, *RSC Adv.*, 2020, **10**, 19790–19802.
- 47 Y. B. Ryu, H. J. Jeong, J. H. Kim, Y. M. Kim, J. Y. Park, D. Kim, T. T. Nguyen, S. J. Park, J. S. Chang, K. H. Park, M. C. Rho and W. S. Lee, Biflavonoids from *Torreya nucifera* displaying SARS-CoV 3CL(pro) inhibition, *Bioorg. Med. Chem.*, 2010, **18**, 7940–7947.
- 48 R. S. Joshi, S. S. Jagdale, S. B. Bansode, S. S. Shankar, M. B. Tellis, V. K. Pandya, A. Chugh, A. P. Giri and M. J. Kulkarni, Discovery of potential multi-target-directed ligands by targeting host-specific SARS-CoV-2 structurally conserved main protease, *J. Biomol. Struct. Dyn.*, 2020, **38**, DOI: 10.1080/07391102.2020.1760137.
- 49 D. S. N. B. K. Prasanth, M. Murahari, V. Chandramohan, S. P. Panda, L. R. Atmakuri and C. Guntupalli, *In silico* identification of potential inhibitors from *Cinnamon* against main protease and spike glycoprotein of SARS-CoV-2, *J. Biomol. Struct. Dyn.*, 2020, **38**, DOI: 10.1080/07391102.2020.1779129.



# Polyethylene Glycol-Coated Graphene Oxide Loaded with Erlotinib as an Effective Therapeutic Agent for Treating Nasopharyngeal Cancer Cells

This article was published in the following Dove Press journal:  
International Journal of Nanomedicine

Ming-Ying Lan<sup>1,2</sup>

Yen-Bin Hsu<sup>1,2</sup>

Ming-Chin Lan<sup>3,4</sup>

Jyh-Ping Chen<sup>5-8</sup>

Yu-Jen Lu<sup>9</sup>

<sup>1</sup>Department of Otolaryngology-Head and Neck Surgery, Taipei Veterans General Hospital, Taipei, Taiwan; <sup>2</sup>School of Medicine, National Yang-Ming University, Taipei, Taiwan; <sup>3</sup>Department of Otolaryngology-Head and Neck Surgery, Taipei Tzu Chi Hospital, Buddhist Tzu Chi Medical Foundation, New Taipei City, Taiwan; <sup>4</sup>School of Medicine, Tzu Chi University, Hualien, Taiwan; <sup>5</sup>Department of Chemical and Materials Engineering, Chang Gung University, Taoyuan, Taiwan;

<sup>6</sup>Department of Plastic and Reconstructive Surgery and Craniofacial Research Center, Chang Gung Memorial Hospital, Taoyuan, Taiwan; <sup>7</sup>Research Center for Food and Cosmetic Safety, Research Center for Chinese Herbal Medicine, College of Human Ecology, Chang Gung University of Science and Technology, Taoyuan, Taiwan;

<sup>8</sup>Department of Materials Engineering, Ming Chi University of Technology, Taipei, Taiwan; <sup>9</sup>Department of Neurosurgery, Chang Gung Memorial Hospital Linkou Medical Center and College of Medicine, Chang Gung University, Taoyuan, Taiwan

Correspondence: Yu-Jen Lu  
Department of Neurosurgery, Chang Gung Memorial Hospital Linkou Medical Center and College of Medicine, Chang Gung University, Taoyuan, Taiwan  
Email alexlu0416@gmail.com

Jyh-Ping Chen  
Department of Chemical and Materials Engineering, Chang Gung University, Taoyuan, Taiwan  
Email jpchen@mail.cgu.edu.tw

**Introduction:** Nasopharyngeal carcinoma (NPC) is a common cancer in southern China and Taiwan, and radiation therapy combined with or without chemotherapy is its mainstay treatment. Although it is highly sensitive to radiotherapy, local recurrence and distant metastasis remain difficult unsolved problems. In recent years, graphene oxide (GO) has been found to be a promising novel anticancer drug carrier. Here, we present our designed functionalized GO, polyethylene glycol-coated GO (GO-PEG), as a drug carrier, which was loaded with erlotinib and showed promising anticancer effects on NPC cells.

**Methods:** The effects of GO-PEG-erlotinib on the proliferation, migration, and invasion of NPC cells were investigated by WST-8 assay, wound healing assay, and invasion assay, respectively. RNA sequencing was conducted and analyzed to determine the molecular mechanisms by which GO-PEG-erlotinib affects NPC cells.

**Results:** Our results showed that GO-PEG-erlotinib reduced NPC cell viability in a dose-dependent manner and also inhibited the migration and invasion of NPC cells. The RNA sequencing revealed several related molecular mechanisms.

**Conclusion:** GO-PEG-erlotinib effectively suppressed NPC cell proliferation, migration, and invasion, likely by several mechanisms. GO-PEG-erlotinib may be a potential therapeutic agent for treating NPC in the future.

**Keywords:** nasopharyngeal carcinoma, anti-cancer, graphene oxide, erlotinib, drug carrier

## Introduction

Nasopharyngeal carcinoma (NPC) is very rare in western countries but is one of the most common cancers in southern Asian with annual incidence around 20–30/100,000.<sup>1,2</sup> Due to its deep location inside the nasal cavity and vague symptoms, most NPC patients have been diagnosed at an advanced stage.<sup>2</sup> The etiology of NPC has been proved to be closely related to several factors, including genetic, Epstein-Barr virus exposure, environmental, and dietary factors.<sup>1–4</sup> During development of the disease, viral infection and multiple somatic genetic and epigenetic changes synergistically disrupt normal cell function, thus contributing to NPC pathogenesis.<sup>3–8</sup> Radiotherapy is the foundation of curative treatment for NPC, and chemotherapy is usually combined with radiotherapy for advanced cases.<sup>9</sup> Although NPC is highly radiosensitive and chemosensitive with an optimal 5-year survival of over 80%, the treatment of patients with locoregionally advanced disease remains problematic due to locoregional failure and distant metastasis. Besides, patients often suffer from systemic toxicity or related complications of

chemotherapy. To reach a better outcome for NPC treatment, the refinement of current treatment modalities is of importance.

The recent development of novel materials, especially nanoparticles, having the advantages of large surface area-to-volume ratio and small size, enables them to carry small compounds with high efficiency. Graphene and its derivatives have drawn much attention in pharmaceutical sciences as carriers for targeted drug delivery in cancer diagnosis and treatment.<sup>10–13</sup> Graphene is an allotrope of carbon in the form of a one-atom-thick, two-dimensional, atomic-scale, hexagonal lattice, with high thermal conductivity, excellent mechanical properties, and large surface areas.<sup>14</sup> There are several members of the graphene family, including graphene oxide (GO), reduced graphene oxide (RGO), and graphene quantum dots (GQDs), that have been used in materials science, nanotechnology, and biomedicine. The combination of biomolecules, such as DNA, peptides, proteins, enzymes, carbohydrates, and viruses, with graphene-based materials offers a promising method to fabricate novel graphene-biomolecule hybrid nanomaterials with unique functions in drug delivery, cancer treatment, tissue engineering, biosensors, bioimaging, energy materials, and other nanotechnological applications.<sup>15–20</sup>

Erlotinib, a tyrosine kinase inhibitor (TKI) acting on the epidermal growth factor receptor (EGFR), was demonstrated in 2004 to be effective for locally advanced or metastatic non-small cell lung cancer (NSCLC) and, in combination with gemcitabine, for locally advanced or metastatic pancreatic cancer.<sup>21</sup> Currently, there is little information regarding its usage in NPC. Previously, an *in vitro* study showed that erlotinib has a role as an enhancer of radiation therapy in NPC.<sup>22</sup> However, a Phase II trial conducted on patients with recurrent and/or metastatic NPC revealed no efficacy of erlotinib as maintenance therapy after gemcitabine-platinum chemotherapy.<sup>23</sup>

Our previous works have prioritized several crucial NPC targets and identified many potential drugs for treating NPC.<sup>24,25</sup> Erlotinib is one of our potential drugs and was selected to be loaded on specific functionalized graphene to investigate its anticancer effect. The RNA sequencing was conducted to reveal related molecular mechanisms. The goal is to develop drugs with better anticancer activity but lower toxicity for possible future clinical applications in NPC patients.

## Materials and Methods

### Preparation of Graphene Oxide (GO)

The raw materials of graphite platelet (model xGnP) measuring 100  $\mu\text{m}$  in width and 5–15 nm in thickness were obtained from XG Sciences Inc (East Lansing, MI). Acrylic acid, potassium persulfate, sulfuric acid ( $\text{H}_2\text{SO}_4$ , 98%), sodium sulfate ( $\text{Na}_2\text{SO}_4$ ), potassium permanganate ( $\text{KMnO}_4$ ), hydrogen peroxide solution ( $\text{H}_2\text{O}_2$ ), and ammonia solution were purchased from Showa Chemical Co (Tokyo, Japan). Preparation of GO followed the modified Hummers' method (Figure 1).<sup>26</sup> One gram of graphite platelet and 23 mL of  $\text{H}_2\text{SO}_4$  (98%) were added into a 250 mL flask under magnetic stirring for 12 hours, followed by slow addition of 3 g of  $\text{KMnO}_4$  in an ice bath while keeping the temperature below 20°C. After stirring for 30 minutes, the flask was heated to 35–40°C and continually stirred for 30 minutes. The temperature of the solution was increased to 65–80°C with continued stirring for 45 minutes, followed by addition of 46 mL of deionized water. Then, the temperature of the solution was increased to 98–105°C and stirred for 30 minutes. After cooling for 1 hour at room temperature, 140 mL of deionized water and 10 mL 10%  $\text{H}_2\text{O}_2$  were added to the solution and incubated for 5 minutes at 35–40°C. The solution was centrifuged at 10,000 rpm and washed using 5% HCl solution 2–3 times. Then, deionized water was used to wash the precipitate several times to neutralize it. The precipitate was collected and subject to ultrasonication using an Ultrasonic Liquid Processor 2020 from Misonix (Farmingdale, NY) and filtered with Acrodisc 25 mm syringe filters (0.2  $\mu\text{m}$  Supor membrane). GO collected in the filtrate was subjected to further modification.

### Preparation of PEGylated GO (GO-PEG)

GO-polyethylene glycol (GO-PEG) was made following the method below. Briefly, the PBS was added to GO solution and sonicated for 1 hour. After cooling at room temperature, DSPE-PEG- $\text{CH}_3$  was added to the solution. The solution was then sonicated for 1 hour in an ice bath. Finally, the solution was centrifuged at high speed for 1 hour and the supernatant was removed. All GO materials were then dispersed in sterilized deionized water to prepare the stock solution (0.5 or 1 mg/mL) for later characterization and experiments.

### Characterization of GO Materials

(i) Fourier transform infrared spectroscopy (FTIR)



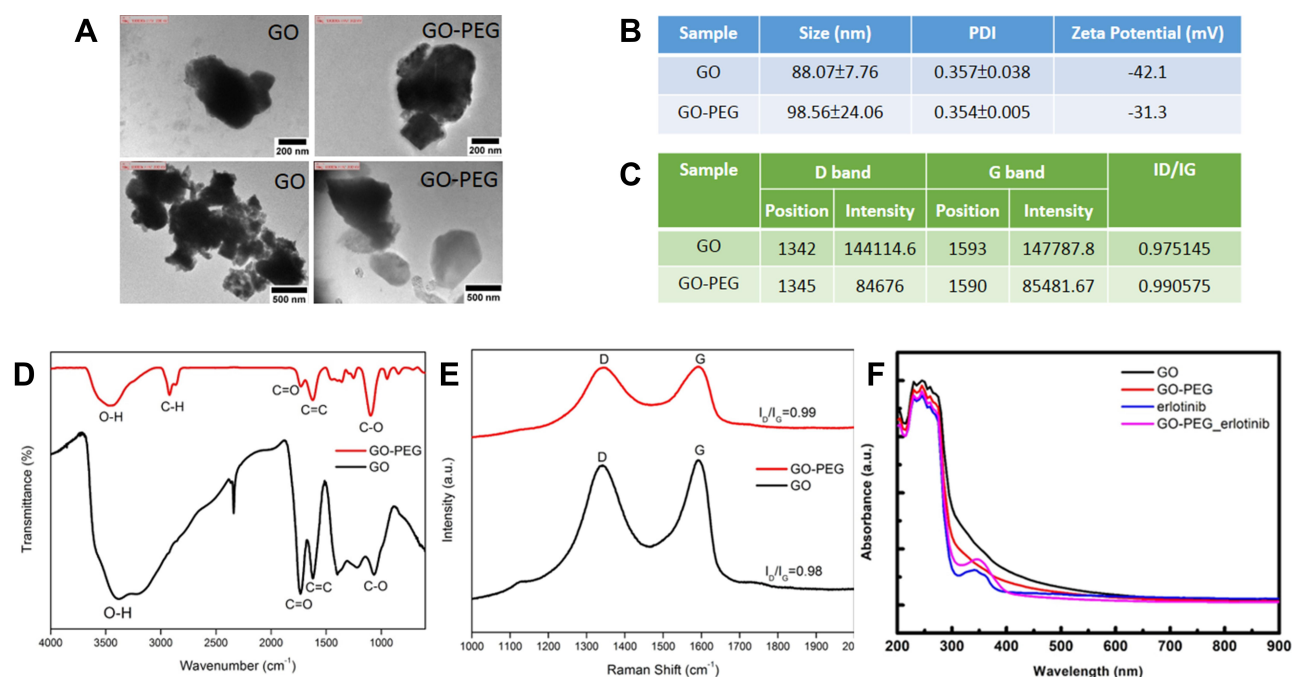


**Figure 1** Characterizations of GO and GO-PEG. **(A)** TEM images of GO and GO-PEG. **(B)** The table lists the measurements of size and zeta potential of GO and GO-PEG analyzed by DLS. **(C)** The intensity of D and G band of GO and GO-PEG in Raman spectra. **(D)** The infrared spectrum of GO and GO-PEG by FTIR shows that PEG was successfully conjugated on GO. **(E)** Raman spectra of GO and GO-PEG. **(F)** Absorbance of GO, GO-PEG, erlotinib, and GO-PEG-erlotinib analyzed by UV-Vis spectrophotometer.

**Abbreviation:** PDI, polydispersity index.

FTIR (Bruker Tensor 27) was used to obtain an infrared spectrum of absorption or emission of the GO and functionalized GO materials.

#### (ii) Dynamic light scattering (DLS) and zeta potential

The sizes of GO and GO-PEG were respectively measured by the zetasizer (Zetasizer Nano ZS90, Malvern).

#### (iii) TEM

Transmission electron microscopy (TEM; JEM-2100, JEOL, Japan) was utilized to determine the structure of the GO materials. The TEM samples were prepared by depositing a small drop of solution onto a carbon-coated copper electron microscopy grid and then dried at room temperature.

#### (iv) Raman spectroscopy

Raman spectra were collected using a Micro-Raman Spectrometer (PTT-EL) equipped with a 532nm laser and a 10X objective. The Raman spectra integration time was 20 sec for each location.

## Drug Loading Study

To prepare GO-PEG loaded with erlotinib (GO-PEG-erlotinib), 200 µg erlotinib was mixed with different concentrations of GO-PEG in 1 mL ddH<sub>2</sub>O. The suspension was rotated at 35 rpm at room temperature overnight and then centrifuged for 1 hour. The supernatant was removed and the concentration of erlotinib in the solution was analyzed by UV-Vis Spectrophotometer (Beckman Coulter DU730) at 735, 333, and 371 nm. The weight of drug loaded on GO-PEG was calculated by mass balance from the amount of drug initially added and the amount of drug in the supernatant. The drug entrapment efficiency (EE) (%) is defined as (weight of drug loaded on GO-PEG / weight of drug initially added) × 100. The drug loading efficiency (LE) (%) is defined as (weight of drug loaded on GO-PEG / weight of GO-PEG) × 100.

## Drug Release Study

GO-PEG-erlotinib was placed into the microtubes with 1 mL phosphate-buffered saline (PBS) at pH 7.4 and 5.5, respectively. The drug release was assumed to start as soon as the microtubes were placed into the incubator at 37°C. The microtube was under constant shaking. At particular time intervals, all supernatant was withdrawn from the

microtube for characterization after centrifugation and washing. The microtube was replenished with the same volume of PBS to continue the drug release study. The concentration of erlotinib released from the functionalized GO-PEG-erlotinib complex was determined using a UV-Vis Spectrophotometer (Beckman Coulter DU730). The drug release percentage was calculated from the cumulative amount of drug released after normalizing with amount of loaded drug.

## Cellular Uptake Study

To determine intracellular uptake of GO-PEG, NPC TW01 cells (10,000 cells/mL) were cultured in 2 mL DMEM supplemented with 10% FBS in 35 mm diameter plates. Cells were grown in a humidified incubator at 37°C under 5% CO<sub>2</sub> for 48 hours. To prepare fluorescent GO-PEG, 95  $\mu$ L of 2 mg/mL FITC-NHS (5/6-carboxyfluorescein succinimidyl ester) was mixed with 1 mL of 1 mg/mL GO-PEG solution and then vortexed at 25°C for 1 hour in the dark. The above solution was then mixed with 19  $\mu$ L of 42mM Glycine and then vortexed at 25°C for 60 minutes in the dark. After centrifugation and washing with 1x PBS, GO-PEG-FITC was re-dispersed in 1 mL ddH<sub>2</sub>O. Cells were then incubated with GO-PEG-FITC (20  $\mu$ L) in 100  $\mu$ L of minimum essential medium for 6 hours. The medium was then removed, and the cells were washed with 1 mL of Hank's balanced salt solution and then fixed with fresh ethanol for 5 minutes at room temperature. The cells were washed three times with Hank's balanced salt solution and analyzed by a laser confocal microscope (Olympus FV10i).

## NPC Cell Culture

The NPC cell line TW01 was kindly provided by Dr. Lin CT (Department of Pathology and Graduate Institute of Pathology, College of Medicine, National Taiwan University, Taiwan). The cell line was derived from primary nasopharyngeal tumors of Chinese patients with de novo NPC.<sup>27,28</sup> The use of the NPC cell line was approved by the institutional review board of the Taipei Veterans General Hospital. The NPC cell line was maintained in DMEM with 10% FBS at 37°C under 5% CO<sub>2</sub>.

## In vitro Cytotoxicity Assay

Cell viability of the exposed cells was determined using the Cell Counting Kit-8 (Sigma-Aldrich, St. Louis, USA), according to the manufacturer's instructions. After seeding cells at a concentration of 2000 cells/well in 100  $\mu$ L

culture medium in a 96-well microplate for 24 hours, cells were washed with PBS twice and exposed with GO, GO-PEG, erlotinib, and GO-PEG-erlotinib for various concentrations in a humidified atmosphere (37°C and 5% CO<sub>2</sub>) for 2–3 days. Then, the cells were incubated with 10  $\mu$ L CCK-8 cell proliferation reagent for 2 hours. Optical density was measured using a microplate reader (Spectral Max250) at 450 nm.

## Wound Healing Assay

Cells were plated in 6-well plates. When the cells grew into full confluency, a wound was created on the monolayer cells by scraping a gap using a micropipette tip after cells had been treated with control and GO-PEG-erlotinib for 20 hours. The speed of wound closure was compared between GO-PEG-erlotinib treated groups and the control group. Photographs were taken under 100 $\times$  magnifications using phase contrast microscopy immediately after wound incision and at 20 hours later.

## Cell Invasion Assay

A Transwell cell culture chamber (Millipore, Bedford, MA, USA) with a 6.5-mm-diameter polycarbonate filter (8  $\mu$ m pore size) was coated with Matrigel, dried, and reconstituted at 37°C with culture medium. Culture medium containing 10% FBS was placed in the lower chamber (24-well plates). Then, the cells at  $1 \times 10^5$  cells per chamber were added to the upper chamber in serum-free DMEM. After 48 hours of incubation with control, GO-PEG, erlotinib or GO-PEG-erlotinib at 37°C, the suspended media in the lower chamber were removed. The cells that had invaded the lower side of the filter were fixed in methanol and stained with DAPI. The number of cells that passed through the pores into the lower chamber was counted under a fluorescent microscope (five fields per chamber).

## RNA-Seq Analysis

Total RNA from NPC cell lines treated with or without GO-PEG-erlotinib (2.15  $\mu$ g/mL) for 72 hours was extracted with RNeasy Mini Kit (Qiagen, Germany) according to the manufacturer's protocol. RNA was subjected to RNA-Seq analysis on BGISEQ-500 system by Tri-I Biotech, Inc. Briefly, the RNA was sheared and reverse transcribed using random primers to obtain cDNA used for library construction. We performed sequencing on prepared library<sup>29</sup> and filtered all the generated raw sequencing reads to get clean reads stored as

FASTQ format.<sup>30</sup> We used Bowtie2 and HISAT to map clean reads to reference genes and genome, respectively.<sup>31,32</sup> Gene expression level (FPKM) was quantified by RSEM.<sup>33</sup> We used the DEseq2 method to screen out differentially expressed genes between two groups with fold change  $\geq 2$  and adjusted P value  $\leq 0.05$ .<sup>34</sup> Gene ontology (GO) and pathway annotation and enrichment analyses were based on the GO Database (<http://www.geneontology.org/>) and KEGG pathway database (<http://www.genome.jp/kegg/>), respectively. We then used the Ingenuity Pathway Analysis (IPA) to assign biological functions to genes and network analysis using the Ingenuity Pathways Knowledge Base (Ingenuity Systems, Inc., Redwood City, CA, USA).

## Statistical Analysis

All experiments were carried out in triplicate, and at least three independent experiments were performed. The results are presented as the means  $\pm$  SDs. Statistical comparisons of multigroup data were analyzed by ANOVA, followed by Scheffe's post-test using SPSS 12.0 software (SPSS Inc. Chicago, IL). A value of  $p < 0.05$  indicated statistical significance.

## Results

We prepared GO and GO-PEG from the raw materials of graphite platelet followed the modified Hummers' method. We characterized the GO and GO-PEG using several tools, including the TEM, FTIR, DLS, and Raman spectroscopy. The TEM images showed the irregular morphology of GO and GO-PEG (Figure 1A) in the solution. Compared to GO-PEG, GO forms small clusters more readily in the solution. From the TEM images, GO-PEG showed better dispersibility in water. Moreover, no contaminating particles were found on the surface of both GO and GO-PEG, which revealed great purity of these two materials in the solution (data not shown). We further used the DSL to measure the size of GO and GO-PEG, which were 88 nm and 96 nm in average, respectively (Figure 1B). DLS is a technique in physics that can be used to determine the size-distribution profile of small particles in suspension or polymers in solution. The polydispersity index (PDI) is used to describe the degree of "non-uniformity" of a distribution. PDI between 0 and 0.35 means narrow size-distribution of particles. The PDI of GO and GO-PEG were 0.357 and 0.354, respectively. ZP (zeta potential) measurements represent the surface charge of the materials. The ZP of GO and GO-PEG were  $-42.1$  and  $-31.1$ ,

respectively (Figure 1B). The FTIR was used to obtain an infrared spectrum of absorption or emission of the GO and functionalized GO materials, which revealed that PEG was successfully conjugated on GO (Figure 1D). Raman spectroscopy was performed using a Micro-Raman Spectrometer (PTT-EL) equipped with a 532nm laser. Raman spectroscopy can provide substantial information about nanostructure defect type, domain size, impurity element, etc. A G-band at around  $1575\text{cm}^{-1}$  in the Raman spectra represents the  $\text{sp}^2$ -hybridized carbon structure of GO, while a D-band at around  $1355\text{cm}^{-1}$  appears when the carbon structure exhibits small defects or edges. The intensity ratio (intensity of the D-band/intensity of the G-band, ID/IG) represents the structural integrity of GO. GO and GO-PEG had similar ID/IG values, indicating that PEGylation did not destroy the aromatic structures of GO (Figure 1C and E). Absorbance of GO, GO-PEG, erlotinib, and GO-PEG-erlotinib analyzed by UV-Vis spectrophotometer is shown in Figure 1F.

We then conducted the drug loading and release studies, which are essential for evaluating a drug delivery system. The drug loading efficiency (LE) and encapsulation efficiency (EE) of erlotinib-loaded GO-PEG were about 80%, and 38%, respectively (Figure 2A). On average,  $46.5 \pm 9.58$   $\mu\text{g}$  erlotinib was loaded on  $141.39 \pm 9.45$   $\mu\text{g}$  GO-PEG when 200  $\mu\text{g}$  erlotinib was mixed with 200  $\mu\text{g}$  GO-PEG. In regard to drug release testing, the release rate of GO-PEG-erlotinib at pH 5 at 5 hours was 93.01%; at 24 hours was 95.88%; and at 72 hours was 98.99%. The release rate of GO-PEG-erlotinib at pH 7 at 5 hours was 63.38%; at 24 hours was 68.33%; and at 72 hours was 76.74% (Figure 2A). In order to duplicate the physiological temperature, a temperature of  $37^\circ\text{C}$  was selected for the drug release response. A pH of 7.4 corresponds to the physiological pH of normal cells, while a pH of 5.5 corresponds to acidic cancer environments, and also within endosomes after internalization. Figure 2B shows that the cumulative release profile of erlotinib from the GO-PEG is pH-dependent, in which erlotinib release is enhanced at pH 5.5.

To determine intracellular uptake of GO-PEG, NPC TW01 cells were cultured and incubated with FITC-labeled GO-PEG suspension for 6 hours. The identification of GO-PEG was made possible by the green fluorescence signals from FITC-labeled GO-PEG (Figure 3). The green fluorescence of FITC-labeled GO-PEG mostly appears in the cytoplasm of NPC TW01 cells. It is supposed that GO-PEG accumulating in the cytoplasm is via endocytosis.

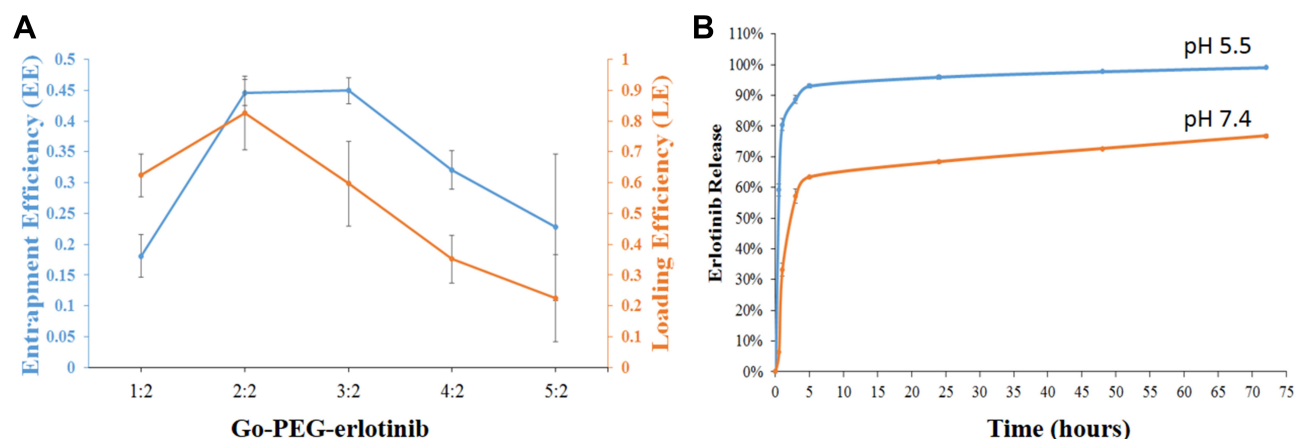


**Figure 2 (A)** The drug loading efficiency (LE) and encapsulation efficiency (EE) of erlotinib-loaded GO-PEG. **(B)** The drug release test of GO-PEG-erlotinib in pH 7.4 and 5.5.

We then tested the GO and GO-PEG on NPC cells. Both GO and GO-PEG showed mild cytotoxicity on NPC cells at a concentration below 10  $\mu\text{g/mL}$ . The erlotinib was further tested for cytotoxicity. Erlotinib seems to have little cytotoxicity effect on NPC cells; the  $\text{IC}_{50}$  at 72 hours is around 100  $\mu\text{g/mL}$  (data not shown). However, GO-PEG-erlotinib has great cytotoxicity with the  $\text{IC}_{50}$  at 72 hours being 2.12  $\mu\text{g/mL}$  (Figure 4). This indicates that GO-PEG might be a promising drug delivery vehicle for erlotinib in NPC treatment.

The migration of NPC TW01 cells with or without GO-PEG-erlotinib was assessed by a wound healing assay. More cells migrated to the denuded area of the wound in the control group than to the cells treated with 0.7 and 2.15  $\mu\text{g/mL}$  GO-PEG-erlotinib at 20 hours after the creation of the wound (Figure 5). The results indicated that GO-PEG-erlotinib inhibited the migration of NPC cells. To investigate whether GO-PEG-erlotinib could inhibit cell invasion, cell invasion assays were conducted. The number of migrating cells was significantly reduced after treatment with 2.15  $\mu\text{g/mL}$  GO-PEG-erlotinib (Figure 6).

To identify differentially expressed genes, the RNA-Seq of the NPC cell lines treated with and without 2.15  $\mu\text{g/mL}$  GO-PEG-erlotinib for 72 hours were compared. A p-value  $<0.05$  was considered statistically significant. In regard to GO-PEG-erlotinib, a total of 1455 genes were differentially expressed by at least two-fold, with 623 upregulated and

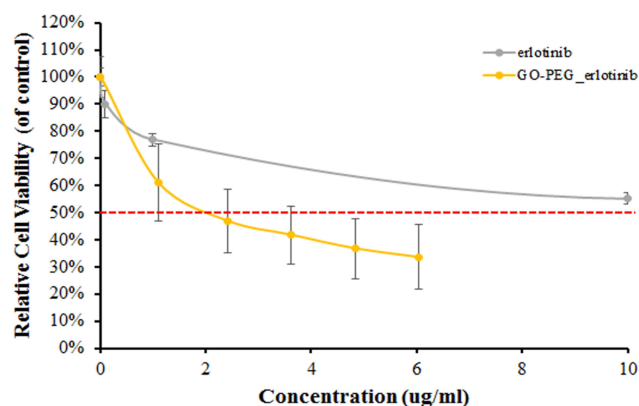


**Figure 4** Cell viability of NPC TW01 after treatment with erlotinib and GO-PEG-erlotinib at various concentrations. Cell viability was determined after incubating with erlotinib or GO-PEG-erlotinib for 72 hours.

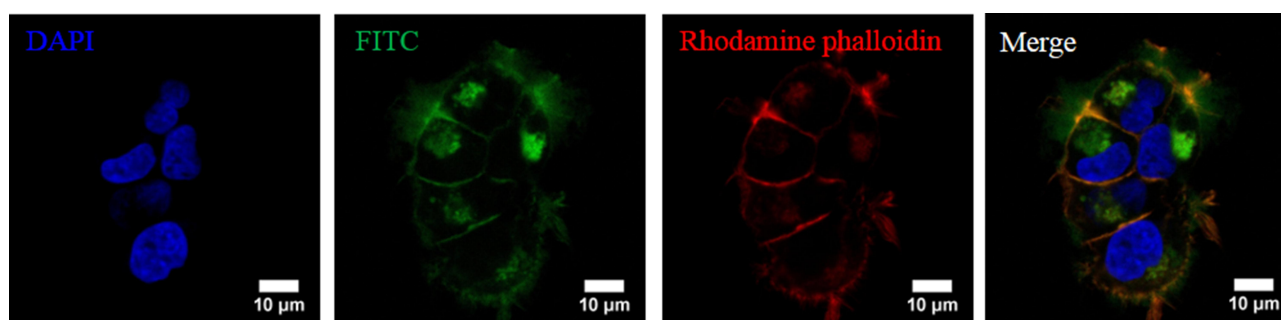


**Figure 3** Confocal microscopy images of NPC TW01 cells after treatment with FITC-labeled GO-PEG for 6 hours.



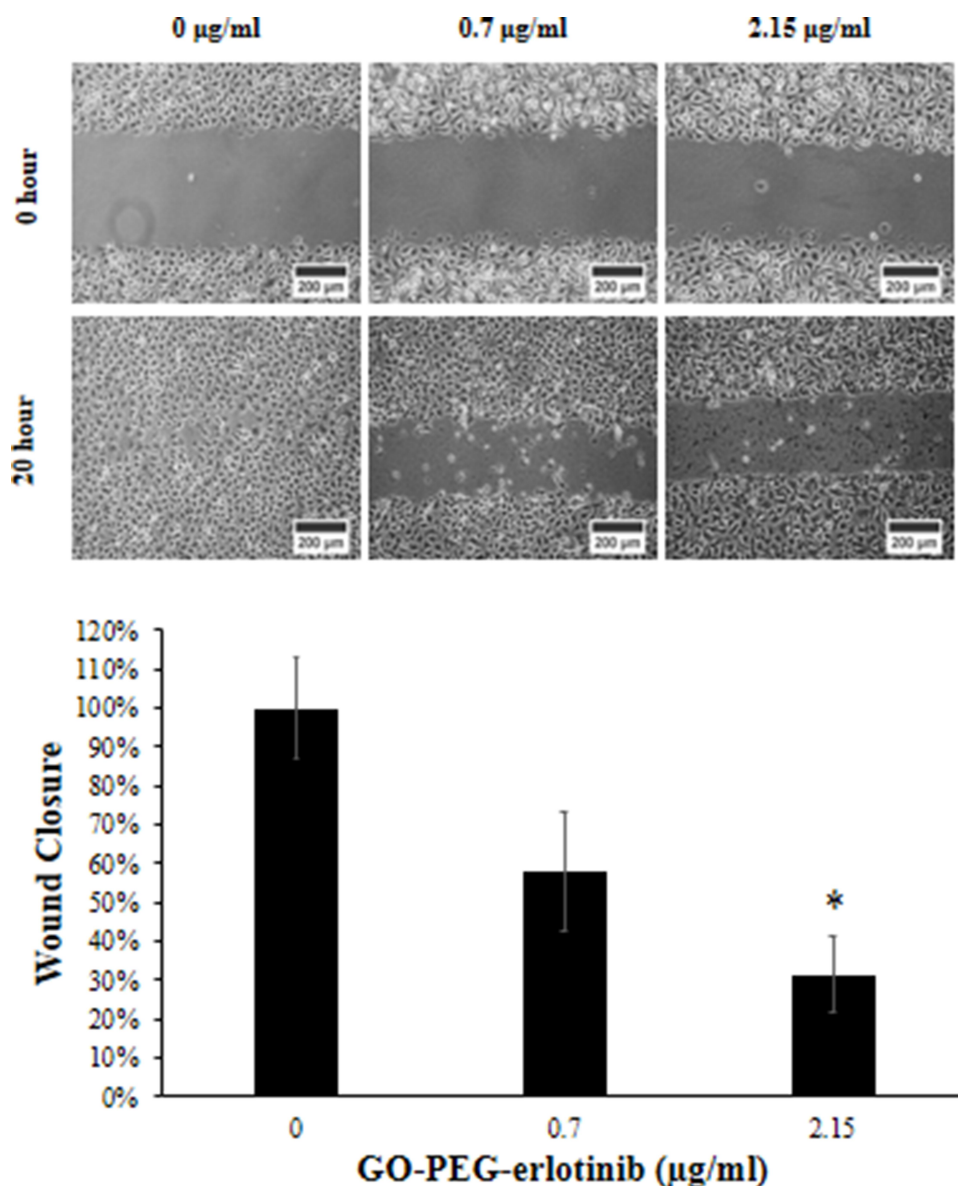


**Figure 5** GO-PEG-erlotinib reduces cell migration in NPC TW01 cells. More cells migrated to the denuded area of the wound in the control group (left) compared to the cells treated with 0.7 µg/mL GO-PEG-erlotinib (middle) and 2.15 µg/mL GO-PEG-erlotinib (right) at 20 hours after the creation of the wound. \* $p < 0.05$  compared with the control group by ANOVA.

832 downregulated genes. The data were then analyzed using the IPA functional analysis tool. Several networks and interactomes were created according to the biological functions of the genes and were ranked by the number of significantly expressed genes they contained. The top 10 upregulated and downregulated molecules and the top 10 upstream regulators in RNA-Seq analysis of NPC cells treated with GO-PEG-erlotinib are listed in Table 1. Further study of these top molecules will be conducted in the future to elucidate their roles in the mechanism of GO-PEG-erlotinib on NPC cells. Table 2 lists the top 5 associated networks of genes involved in the effect of GO-PEG-

erlotinib on NPC cells. Figure 7 shows the top-ranked network identified by IPA analysis in GO-PEG-erlotinib.

The KEGG pathway analysis of GO-PEG-Erlotinib on NPC cells is shown in Figure 8. There are seven branches for KEGG pathways: cellular processes, environmental information processing, genetic information processing, human disease (for animals only), metabolism, and organismal systems.

## Discussion

EGFR has been found to be overexpressed in 73% to 89% of NPC patients, which causes decreased overall



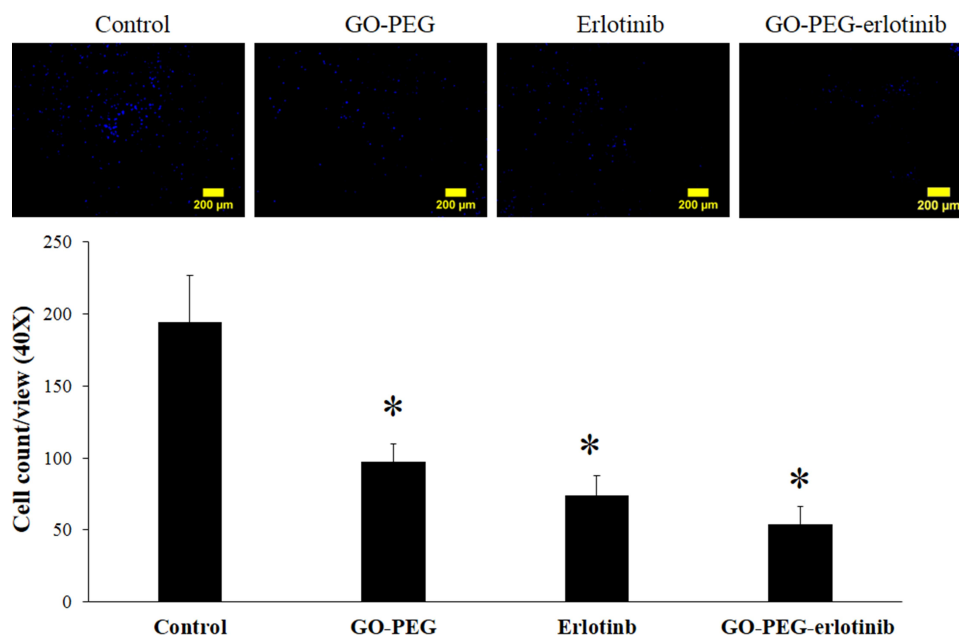


**Figure 6** GO-PEG-erlotinib inhibits cell invasion in NPC TW01 cells. Matrigel invasion assays of NPC TW01 cells showed that the invasion ability of NPC cells was reduced after treatment with 2.15  $\mu\text{g/mL}$  GO-PEG-erlotinib, 2.15  $\mu\text{g/mL}$  erlotinib, and 6.45  $\mu\text{g/mL}$  GO-PEG for 48 hours. \* $p < 0.05$  compared with the control group by ANOVA.

survival and an increased risk of metastasis.<sup>35–37</sup> Several studies have shown that high EGFR expression is correlated with poor locoregional control and overall survival, but not distant metastasis-free survival (DMFS).<sup>38,39</sup> Erlotinib, an EGFR inhibitor, has been shown to be effective for NSCLC and pancreatic cancer, but without much study regarding its effect in head and neck cancer patients or in NPC patients.<sup>21</sup> A randomized phase II trial showed that the addition of erlotinib to cisplatin and radiotherapy did not confer additional tumor response or patient survival of 204 late-stage HNSCC patients.<sup>40</sup> Previously, a phase II trial conducted on patients with recurrent and/or metastatic NPC revealed

no efficacy of erlotinib as maintenance therapy after gemcitabine-platinum chemotherapy.<sup>23</sup>

Zheng et al recently identified serine protease inhibitor Kazal-type 6 (SPINK6) as a functional regulator of NPC metastasis via EGFR signaling, and erlotinib was revealed to reverse SPINK6-induced NPC cell migration and invasion in vitro, as well as inhibiting SPINK6-induced metastasis in vivo.<sup>41</sup> In our study, we found erlotinib has little cytotoxicity effect on NPC cells with the IC<sub>50</sub> at 72 hours being around 100  $\mu\text{g/mL}$ , which may explain the relative unresponsiveness of erlotinib in clinical NPC patients. However, GO-PEG-erlotinib indeed showed good cytotoxicity on NPC cells with the IC<sub>50</sub> at 72 hours being

**Table 1** The Top 10 Upregulated and Downregulated Genes and Their Corresponding Upstream Regulators in RNA-Seq Analysis of NPC Cells Treated with GO-PEG-Erlotinib

Rank	Upregulated Gene	Expression Value	Downregulated Gene	Expression Value
1	<i>CHAC1</i>	4.279	<i>SNAIL</i>	−4.054
2	<i>RGPD4</i>	3.225	<i>ART5</i>	−3.982
3	<i>KRCC1</i>	3.046	<i>NPTX1</i>	−3.880
4	<i>ELAC1</i>	2.941	<i>HIST1H2BJ</i>	−3.774
5	<i>BORCS8-MEF2B</i>	2.755	<i>ART1</i>	−3.474
6	<i>CYP1A1</i>	2.755	<i>SLC6A12</i>	−3.434
7	<i>FGFBP3</i>	2.592	<i>SLC17A7</i>	−3.313
8	<i>C7orf25</i>	2.576	<i>KCNE1B</i>	−3.311
9	<i>SPRN</i>	2.483	<i>KLHL41</i>	−3.261
10	<i>MAGI2</i>	2.478	<i>SUCNR1</i>	−3.232

**Table 2** The Top 5 Associated Networks Involved in the Effect of GO-PEG-Erlotinib on NPC Cells Identified by IPA

Rank	Molecules	Associated Network Functions
1	34	Cardiovascular Disease, Hematological Disease, Hereditary Disorder
2	34	Cellular Development, Embryonic Development, Hair and Skin Development and Function
3	32	Cell Death and Survival, Cell-mediated Immune Response, Cellular Function and Maintenance
4	31	Reproductive System Development and Function, Cancer, Organismal Injury and Abnormalities
5	31	Endocrine System Development and Function, Molecular Transport, Small Molecule Biochemistry

2.12 ug/mL. We calculated the drug LE and EE of erlotinib-loaded GO-PEG was about 80%, and 38%, respectively, and the release rate of GO-PEG-erlotinib was enhanced at pH 5.5, corresponding to the acidic cancer environments in endosomes after internalization. Most tumor cells have high metabolic activity, which contributes to their more acidic intracellular pH.<sup>42</sup> Thus, an internalized graphene-based drug with pH-responsive characteristics, like GO-PEG-erlotinib in our study, can specifically release the drug at tumor sites.<sup>11</sup> Moreover, our results

show that GO-PEG-erlotinib not only reduced NPC cell viability in a dose-dependent manner but also inhibited the migration and invasion of NPC cells. The relatively moderate drug loading and the pH-sensitive release of erlotinib suggest that GO-PEG is a potential drug delivery vehicle for cancer therapy,<sup>43,44</sup> and that GO-PEG is a promising drug delivery vehicle for erlotinib in NPC treatment.

Graphene-based materials immobilize various biomolecules through either noncovalent adsorption, such as  $\pi$ - $\pi$  stacking, hydrogen bonds, and electrostatic interaction; or

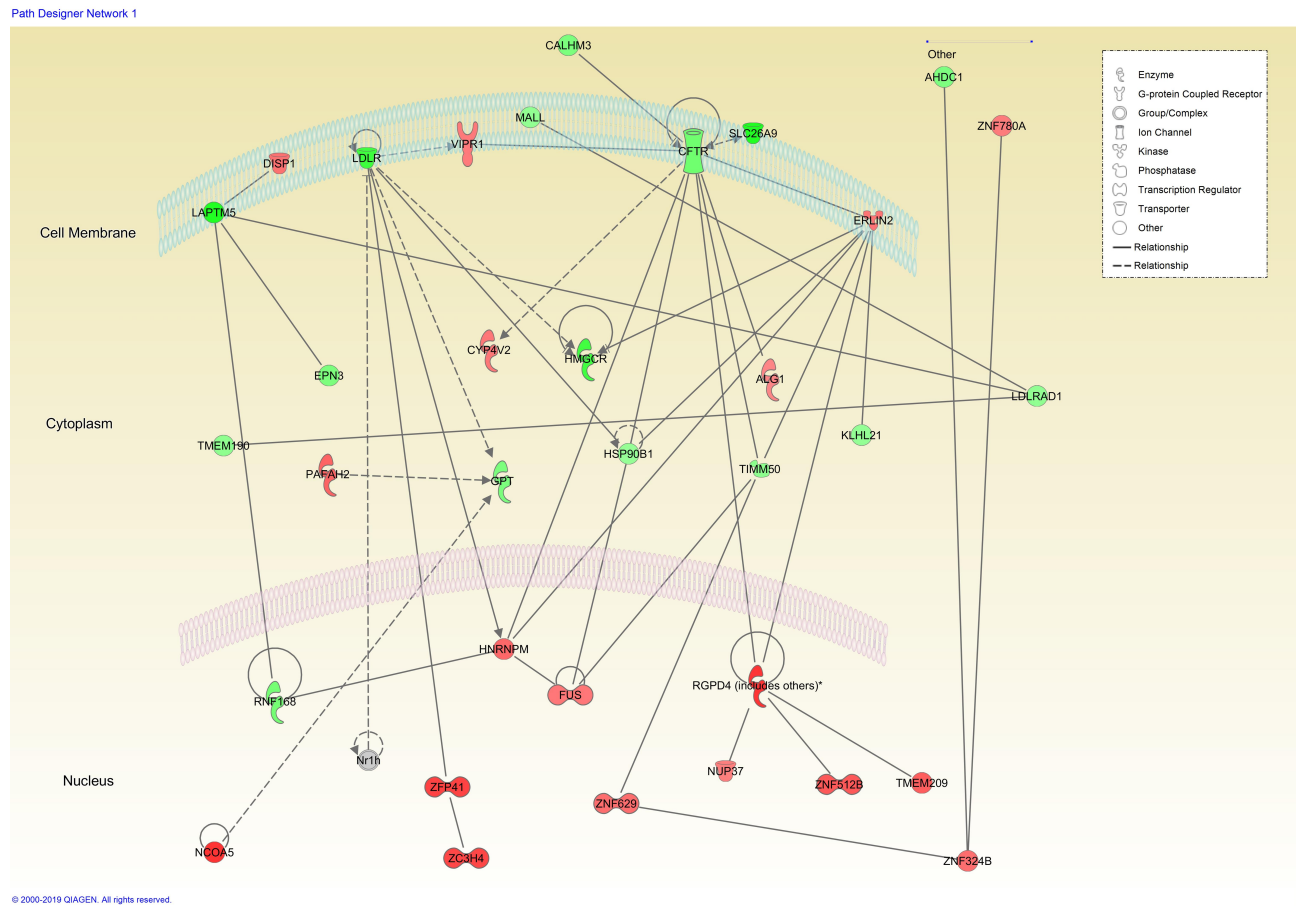


**Figure 7** The top-ranked network identified by IPA analysis in GO-PEG-erlotinib study. The top-ranked network, which includes 34 genes, is related to cardiovascular disease, hematological disease, and hereditary disorder. The genes shaded in red are upregulated, and genes shaded in green are downregulated. All shaded genes are statistically significant, as indicated by the statistical analysis. A dotted line indicates an indirect interaction between the two gene products, and a solid line represents a direct interaction.

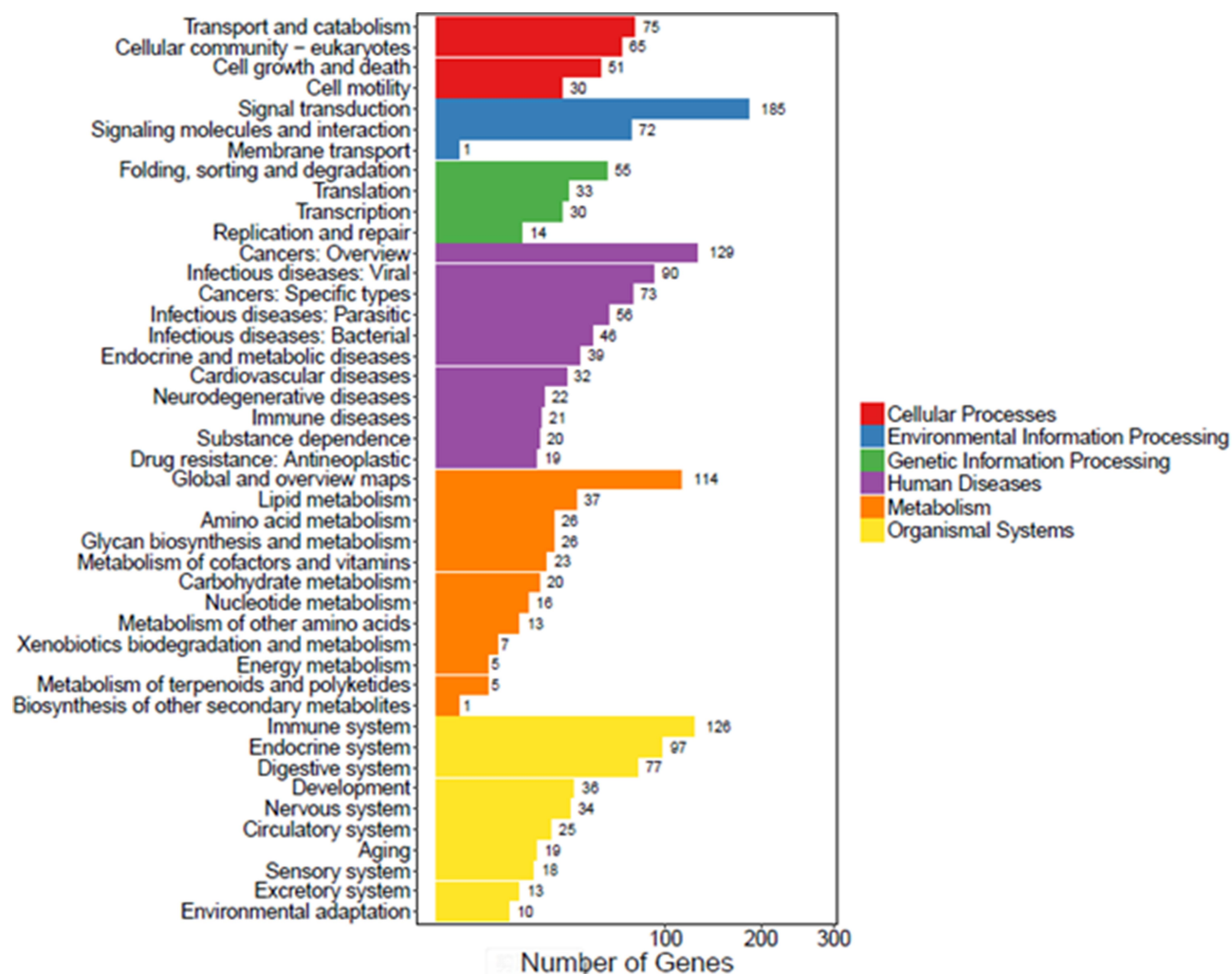


**Figure 8** KEGG pathway analysis of GO-PEG-erlotinib on NPC cells. There are seven branches for KEGG pathways: cellular processes, environmental information processing, genetic information processing, human disease, metabolism, and organismal systems.

covalent binding by their enriched oxygen functional groups.<sup>15</sup> They offer a high surface to weight ratio, a high possibility for surface modification, high drug-loading efficiency, a pH-responsive drug-delivery mechanism, and photothermal effects compared to other drug delivery systems.<sup>18,45,46</sup> Graphene is characterized by a pure carbon, an aromatic network providing an open surface for noncovalent interaction with biomolecules, while GO has many epoxides, carboxyl, and hydroxyl groups on its basal plane and edges which can bind with biomolecules via covalent, electrostatic, and hydrogen bond interactions.<sup>43,44</sup>

Most drugs binding on GO are based on noncovalent interactions. For example, chemotherapeutic drugs possessing aromatic ring structures, such as doxorubicin, camptothecin, and SN-38, bind on GO through  $\pi$ - $\pi$  stacking.<sup>47</sup> Various methods have been developed to

functionalize GO for improving its drug carrier function. Lui et al found that GO functionalized with polyethylene glycol (PEG) can carry water-insoluble cancer drugs such as camptothecin and SN38 and showed pH-dependent drug release behavior.<sup>48</sup> Besides, functionalized GO can enter mammalian cells, and thus it is a reasonable drug carrier. Moreover, the hydrophilic groups on both sides of GO make it stable in physiologic solutions while carrying drugs. In our study, intracellular uptake of FITC-labeled GO-PEG in NPC cells was clearly observed under confocal microscopy, which suggested that GO-PEG accumulating in the cytoplasm is via endocytosis. Finally, GO-PEG-erlotinib showed much better cytotoxicity on NPC cells than erlotinib alone, demonstrating that GO-PEG is a promising drug carrier for possible usage in NPC treatment in the future.

In recent years, several studies have focused on graphene and its derivatives as potential drug carriers for cancer therapy. Yang et al used a chemical coprecipitation method, not only adding Fe<sub>3</sub>O<sub>4</sub> magnetic nanoparticles onto graphene but also decorating it with folic acid as a targeting ligand. The drug-loaded graphene selectively killed breast cancer cells with released doxorubicin.<sup>45</sup> Zhang et al designed the drug carrier with low drug resistance rate but high cytotoxic efficacy by adding positive-charged polyethylenimine (PEI) onto the doxorubicin-loaded graphene which can adsorb negative-charged Bcl-2 siRNA.<sup>49</sup> Lu et al modified the GO surface with abundant polyacrylic acid (PAA) chains, which can react with BCNU through carbodiimide-mediated amide bond formation to increase drug loading. The PAA-GO-BCNU showed promising anticancer efficacy in in vitro study.<sup>47</sup> Yin et al functionalized GO with PEI and (PEG) as a plasmid-based Stat3 siRNA carrier, which showed a significant regression in tumor growth and tumor weight of mouse malignant melanoma growth in vivo.<sup>50</sup> Yang et al developed epidermal growth factor receptor (EGFR) antibody-conjugated PEGylated nanographene oxide (PEG-NGO) carrying epirubicin (EPI) that was able to target the tumor and kill the cancer cells by its triple-therapeutics (growth signal blocking, chemotherapy, photothermal therapy). The synergistic-targeted treatment simultaneously enhances the local drug concentration and performs ultra-efficient tumor suppression to significantly prolong survival in mice. This novel drug delivery platform overcomes the problems of low accumulation of most chemotherapeutic agents in tumor tissue and multidrug resistance (MDR) in current cancer treatment.<sup>51</sup> Recently, Pei et al developed cisplatin and doxorubicin dual-drug-loaded PEGylated nano-graphene oxide which exhibited significantly increased anticancer effect than the single drug delivery system.<sup>52</sup> Wang et al synthesized folate-modified GO/PEI siRNA nanocomplexes which successfully targeted ovarian cancer cells in vitro.<sup>53</sup> Shirvalilou et al developed magnetic NGO as a drug carrier for improving glioma-targeted iodo-2-deoxyuridine (IUDR) delivery and imaging.<sup>54</sup>

By conducting RNA-Seq analysis and following IPA analysis, the top 10 upregulated and top 10 downregulated molecules after GO-PEG-erlotinib treatment on NPC cells were identified (Table 1). Some of these molecules have been reported to be associated with carcinogenesis and prognosis in other types of cancers. CHAC1 (ChaC glutathione-specific gamma-glutamylcyclotransferase 1) plays a role in the regulation of glutathione levels and oxidative

balance in cells and is also a proapoptotic component of the unfolded protein response (UPR).<sup>55,56</sup> Activation of CHAC1 has been reported to induce cell apoptosis and decrease cell proliferation in human head and neck squamous cell cancer cell lines.<sup>57</sup> CYP1A1 (cytochrome P450 family 1 subfamily A member 1) is located at the endoplasmic reticulum. It can metabolize some polycyclic aromatic hydrocarbons to carcinogenic intermediates. This gene has been found to be associated with lung, prostate, and cervical cancer risks.<sup>58–60</sup> SNAI1 (snail family transcriptional repressor 1) proteins primarily act as transcriptional repressors.<sup>61</sup> It can induce epithelial-to-mesenchymal transition (EMT) in colorectal and lung cancer cells.<sup>62,63</sup> NPTX1 (neuronal pentraxin 1) belongs to the long pentraxin family of protein and is highly expressed in the central nervous system.<sup>64</sup> It is also involved in the regulation of apoptosis in some types of cells.<sup>65,66</sup> Recently, some studies found that NPTX1 may be involved in the progression of lung, pancreatic, and colon cancers.<sup>67–69</sup>

Recently, several ligands have been used in cancer targeted therapies, such as biotin, transferrin, and folate.<sup>70,71</sup> Montazerabadi et al functionalized curcumin-loaded dendritic magnetite nanocarriers with folate, which generated a thermo-chemotherapeutic effect on folate receptor-expressed cancer cells.<sup>72</sup> Zeiniazade et al used folate-conjugated gold nanoparticles for targeted nano-photo-thermal therapy.<sup>73</sup> Because of the high surface-area-to-volume ratio of nanocarriers, designing novel drug carriers with multiple targeting ligands are feasible ways to increase their antitumor effect.<sup>71</sup> In the future, we will further modify GO-PEG-erlotinib with specific ligands to induce selective cancer cell death.

Our study revealed that GO-PEG is a promising drug carrier for erlotinib with the advantages of high drug loading and pH-dependent controlled release. GO-PEG-erlotinib reduced NPC cell viability in a dose-dependent manner, and also inhibited the migration and invasion of NPC cells. The RNA sequencing revealed important molecules and several related molecular mechanisms. Further studies will be needed in the future.

## Conclusion

GO-PEG-erlotinib effectively suppressed NPC cell proliferation, migration, and invasion, and presented a better anticancer effect than free drugs. Several molecules and mechanisms were involved. GO-PEG-erlotinib may be a potential therapeutic agent for treating NPC in the future.



## Acknowledgments

This research was supported by grants from the Ministry of Science and Technology (MOST106-2314-B-075-035-MY3-2) to MYL and (MOST107-2314-B-182-020) to YJL. The authors thank the Clinical Research Core Laboratory at Taipei Veterans General Hospital for facility support.

## Disclosure

The authors report no conflicts of interest for this work.

## References

1. Cho WC. Nasopharyngeal carcinoma: molecular biomarker discovery and progress. *Mol Cancer*. 2007;6:1.
2. Lu JJ, Cooper JS, Lee AW. *Nasopharyngeal Cancer: Multidisciplinary Management*. Springer Science & Business Media; 2010.
3. Tao Q, Chan AT. Nasopharyngeal carcinoma: molecular pathogenesis and therapeutic developments. *Expert Rev Mol Med*. 2007;9(12):1–24.
4. Chou J, Lin YC, Kim J, et al. Nasopharyngeal carcinoma—review of the molecular mechanisms of tumorigenesis. *Head Neck*. 2008;30(7):946–963. doi:10.1002/hed.20833
5. Lee YC, Hwang YC, Chen KC, et al. Effect of Epstein-Barr virus infection on global gene expression in nasopharyngeal carcinoma. *Funct Integr Genomics*. 2007;7(1):79–93. doi:10.1007/s10142-006-0035-2
6. Chen X, Liang S, Zheng W, Liao Z, Shang T, Ma W. Meta-analysis of nasopharyngeal carcinoma microarray data explores mechanism of EBV-regulated neoplastic transformation. *BMC Genomics*. 2008;9:322. doi:10.1186/1471-2164-9-322
7. Bruce JP, Yip K, Bratman SV, Ito E, Liu FF. Nasopharyngeal cancer: molecular landscape. *J Clin Oncol*. 2015;33(29):3346–3355. doi:10.1200/JCO.2015.60.7846
8. Dai W, Zheng H, Cheung AK, Lung ML. Genetic and epigenetic landscape of nasopharyngeal carcinoma. *China Clin Oncol*. 2016;5(2):16. doi:10.21037/cco.2016.03.06
9. Gooi Z, Richmon J, Agrawal N, et al. AHNS series - Do you know your guidelines? Principles of treatment for nasopharyngeal cancer: a review of the national comprehensive cancer network guidelines. *Head Neck*. 2017;39(2):201–205. doi:10.1002/hed.24635
10. Ghanbarzadeh S, Hamishehkar H. Application of graphene and its derivatives in cancer diagnosis and treatment. *Drug Res (Stuttg)*. 2017;67(12):681–687. doi:10.1055/s-0042-115638
11. Gu Z, Zhu S, Yan L, Zhao F, Zhao Y. Graphene-based smart platforms for combined cancer therapy. *Adv Mater*. 2019;31(9):e1800662. doi:10.1002/adma.201800662
12. Liu J, Dong J, Zhang T, Peng Q. Graphene-based nanomaterials and their potentials in advanced drug delivery and cancer therapy. *J Control Release*. 2018;286:64–73. doi:10.1016/j.jconrel.2018.07.034
13. de Melo-diogo D, Lima-Sousa R, Alves CG, Costa EC, Louro RO, Correia IJ. Functionalization of graphene family nanomaterials for application in cancer therapy. *Colloids Surf B Biointerfaces*. 2018;171:260–275. doi:10.1016/j.colsurfb.2018.07.030
14. Novoselov KS, Geim AK, Morozov SV, et al. Electric field effect in atomically thin carbon films. *Science*. 2004;306(5696):666–669. doi:10.1126/science.1102896
15. Li D, Zhang W, Yu X, Wang Z, Su Z, Wei G. When biomolecules meet graphene: from molecular level interactions to material design and applications. *Nanoscale*. 2016;8(47):19491–19509. doi:10.1039/C6NR07249F
16. Gurunathan S, Kim JH. Synthesis, toxicity, biocompatibility, and biomedical applications of graphene and graphene-related materials. *Int J Nanomedicine*. 2016;11:1927–1945.
17. Rahmanian N, Eskandani M, Barar J, Omid Y. Recent trends in targeted therapy of cancer using graphene oxide-modified multifunctional nanomedicines. *J Drug Target*. 2017;25(3):202–215.
18. Yang K, Feng L, Liu Z. Stimuli responsive drug delivery systems based on nano-graphene for cancer therapy. *Adv Drug Deliv Rev*. 2016;105(Pt B):228–241. doi:10.1016/j.addr.2016.05.015
19. Zhang B, Wang Y, Zhai G. Biomedical applications of the graphene-based materials. *Mater Sci Eng C Mater Biol Appl*. 2016;61:953–964. doi:10.1016/j.msec.2015.12.073
20. Gulzar A, Yang P, He F, et al. Bioapplications of graphene constructed functional nanomaterials. *Chem Biol Interact*. 2017;262:69–89. doi:10.1016/j.cbi.2016.11.019
21. Xu MJ, Johnson DE, Grandis JR. EGFR-targeted therapies in the post-genomic era. *Cancer Metastasis Rev*. 2017;36(3):463–473. doi:10.1007/s10555-017-9687-8
22. Zhang HH, Yuan TZ, Li J, et al. Erlotinib: an enhancer of radiation therapy in nasopharyngeal carcinoma. *Exp Ther Med*. 2013;6(4):1062–1066. doi:10.3892/etm.2013.1245
23. You B, Le Tourneau C, Chen EX, et al. A Phase II trial of erlotinib as maintenance treatment after gemcitabine plus platinum-based chemotherapy in patients with recurrent and/or metastatic nasopharyngeal carcinoma. *Am J Clin Oncol*. 2012;35(3):255–260. doi:10.1097/COC.0b013e31820dbdce
24. Lan MY, Chen CL, Lin KT, et al. From NPC therapeutic target identification to potential treatment strategy. *Mol Cancer Ther*. 2010;9(9):2511–2523.
25. Lan MY, Yang WL, Lin KT, et al. Using computational strategies to predict potential drugs for nasopharyngeal carcinoma. *Head Neck*. 2014;36(10):1398–1407.
26. Hummers Jr WS, Offeman RE. Preparation of graphitic oxide. *J Am Chem Soc*. 1958;80(6):1339.
27. Lin CT, Wong CI, Chan WY, et al. Establishment and characterization of two nasopharyngeal carcinoma cell lines. *Lab Invest*. 1990;62(6):713–724.
28. Lin CT, Chan WY, Chen W, et al. Characterization of seven newly established nasopharyngeal carcinoma cell lines. *Lab Invest*. 1993;68(6):716–727.
29. Huang J, Liang X, Xuan Y, et al. A reference human genome dataset of the BGISEQ-500 sequencer. *Gigascience*. 2017;6(5):1–9.
30. Cock PJ, Fields CJ, Goto N, Heuer ML, Rice PM. The Sanger FASTQ file format for sequences with quality scores, and the Solexa/Illumina FASTQ variants. *Nucleic Acids Res*. 2010;38(6):1767–1771.
31. Kim D, Langmead B, Salzberg SL. HISAT: a fast spliced aligner with low memory requirements. *Nat Methods*. 2015;12(4):357–360. doi:10.1038/nmeth.3317
32. Langmead B, Salzberg SL. Fast gapped-read alignment with Bowtie 2. *Nat Methods*. 2012;9(4):357–359. doi:10.1038/nmeth.1923
33. Su CY, Fu D, Lu AY, et al. Transfer printing of graphene strip from the graphene grown on copper wires. *Nanotechnology*. 2011;22(18):185309. doi:10.1088/0957-4484/22/18/185309
34. Love MI, Huber W, Anders S. Moderated estimation of fold change and dispersion for RNA-seq data with DESeq2. *Genome Biol*. 2014;15(12):550.
35. Chua DT, Nicholls JM, Sham JS, Au GK. Prognostic value of epidermal growth factor receptor expression in patients with advanced stage nasopharyngeal carcinoma treated with induction chemotherapy and radiotherapy. *Int J Radiat Oncol Biol Phys*. 2004;59(1):11–20. doi:10.1016/j.ijrobp.2003.10.038
36. Sheen TS, Huang YT, Chang YL, et al. Epstein-Barr virus-encoded latent membrane protein 1 co-expresses with epidermal growth factor receptor in nasopharyngeal carcinoma. *Jpn J Cancer Res*. 1999;90(12):1285–1292. doi:10.1111/j.1349-7006.1999.tb00710.x



37. Ma BB, Poon TC, To KF, et al. Prognostic significance of tumor angiogenesis, Ki 67, p53 oncoprotein, epidermal growth factor receptor and HER2 receptor protein expression in undifferentiated nasopharyngeal carcinoma—a prospective study. *Head Neck*. 2003;25(10):864–872. doi:10.1002/hed.10307
38. Ooft ML, Braunius WW, Heus P, et al. Prognostic significance of the EGFR pathway in nasopharyngeal carcinoma: a systematic review and meta-analysis. *Biomark Med*. 2015;9(10):997–1010. doi:10.2217/bmm.15.68
39. Sun W, Long G, Wang J, Mei Q, Liu D, Hu G. Prognostic role of epidermal growth factor receptor in nasopharyngeal carcinoma: a meta-analysis. *Head Neck*. 2014;36(10):1508–1516.
40. Martins RG, Parvathaneni U, Bauman JE, et al. Cisplatin and radiotherapy with or without erlotinib in locally advanced squamous cell carcinoma of the head and neck: a randomized phase II trial. *J Clin Oncol*. 2013;31(11):1415–1421. doi:10.1200/JCO.2012.46.3299
41. Zheng LS, Yang JP, Cao Y, et al. SPINK6 promotes metastasis of nasopharyngeal carcinoma via binding and activation of epithelial growth factor receptor. *Cancer Res*. 2017;77(2):579–589. doi:10.1158/0008-5472.CAN-16-1281
42. Kato Y, Ozawa S, Miyamoto C, et al. Acidic extracellular microenvironment and cancer. *Cancer Cell Int*. 2013;13(1):89. doi:10.1186/1475-2867-13-89
43. Zhu Y, Murali S, Cai W, et al. Graphene and graphene oxide: synthesis, properties, and applications. *Adv Mater*. 2010;22(35):3906–3924.
44. Wang Y, Li Z, Wang J, Li J, Lin Y. Graphene and graphene oxide: biofunctionalization and applications in biotechnology. *Trends Biotechnol*. 2011;29(5):205–212. doi:10.1016/j.tibtech.2011.01.008
45. Yang X, Wang Y, Huang X, et al. Multi-functionalized graphene oxide based anticancer drug-carrier with dual-targeting function and pH-sensitivity. *J Mater Chem*. 2011;21(10):3448–3454. doi:10.1039/C0JM02494E
46. Yang K, Zhang S, Zhang G, Sun X, Lee ST, Liu Z. Graphene in mice: ultrahigh in vivo tumor uptake and efficient photothermal therapy. *Nano Lett*. 2010;10(9):3318–3323. doi:10.1021/nl100996u
47. Lu YJ, Yang HW, Hung SC, et al. Improving thermal stability and efficacy of BCNU in treating glioma cells using PAA-functionalized graphene oxide. *Int J Nanomedicine*. 2012;7:1737–1747.
48. Liu Z, Robinson JT, Sun X, Dai H. PEGylated nanographene oxide for delivery of water-insoluble cancer drugs. *J Am Chem Soc*. 2008;130(33):10876–10877.
49. Zhang L, Lu Z, Zhao Q, Huang J, Shen H, Zhang Z. Enhanced chemotherapy efficacy by sequential delivery of siRNA and anticancer drugs using PEI-grafted graphene oxide. *Small*. 2011;7(4):460–464. doi:10.1002/smll.201001522
50. Yin D, Li Y, Lin H, et al. Functional graphene oxide as a plasmid-based Stat3 siRNA carrier inhibits mouse malignant melanoma growth in vivo. *Nanotechnology*. 2013;24(10):105102. doi:10.1088/0957-4484/24/10/105102
51. Yang HW, Lu YJ, Lin KJ, et al. EGRF conjugated PEGylated nanographene oxide for targeted chemotherapy and photothermal therapy. *Biomaterials*. 2013;34(29):7204–7214. doi:10.1016/j.biomaterials.2013.06.007
52. Pei X, Zhu Z, Gan Z, et al. PEGylated nano-graphene oxide as a nanocarrier for delivering mixed anticancer drugs to improve anticancer activity. *Sci Rep*. 2020;10(1):2717. doi:10.1038/s41598-020-59624-w
53. Wang Y, Sun G, Gong Y, Zhang Y, Liang X, Yang L. Functionalized folate-modified graphene oxide/PEI siRNA nanocomplexes for targeted ovarian cancer gene therapy. *Nanoscale Res Lett*. 2020;15(1):57. doi:10.1186/s11671-020-3281-7
54. Shirvalilou S, Khoei S, Khoei S, Raoufi NJ, Karimi MR, Shakeri-Zadeh A. Development of a magnetic nano-graphene oxide carrier for improved glioma-targeted drug delivery and imaging: in vitro and in vivo evaluations. *Chem Biol Interact*. 2018;295:97–108. doi:10.1016/j.cbi.2018.08.027
55. Mungrue IN, Pagnon J, Kohannim O, Gargalovic PS, Lusis AJ. CHAC1/MGC4504 is a novel proapoptotic component of the unfolded protein response, downstream of the ATF4-ATF3-CHOP cascade. *J Immunol*. 2009;182(1):466–476. doi:10.4049/jimmunol.182.1.466
56. Crawford RR, Prescott ET, Sylvester CF, et al. Human CHAC1 protein degrades glutathione, and mRNA induction is regulated by the transcription factors ATF4 and ATF3 and a Bipartite ATF/CRE regulatory element. *J Biol Chem*. 2015;290(25):15878–15891.
57. Joo NE, Ritchie K, Kamarajan P, Miao D, Kapila YL. Nisin, an apoptogenic bacteriocin and food preservative, attenuates HNSCC tumorigenesis via CHAC1. *Cancer Med*. 2012;1(3):295–305. doi:10.1002/cam4.35
58. Liu Y, Li X, Zhang B, et al. CYP1A1 methylation mediates the effect of smoking and occupational polycyclic aromatic hydrocarbons co-exposure on oxidative DNA damage among Chinese coke-oven workers. *Environ Health*. 2019;18(1):69. doi:10.1186/s12940-019-0508-0
59. Zhu W, Liu H, Wang X, et al. Associations of CYP1 polymorphisms with risk of prostate cancer: an updated meta-analysis. *Biosci Rep*. 2019;39(3). doi:10.1042/BSR20181876.
60. Sengupta D, Guha U, Mitra S, Ghosh S, Bhattacharjee S, Sengupta M. Meta-analysis of polymorphic variants conferring genetic risk to cervical cancer in indian women supports CYP1A1 as an important associated locus. *Asian Pac J Cancer Prev*. 2018;19(8):2071–2081.
61. Jagle S, Busch H, Freihen V, et al. SNAIL1-mediated downregulation of FOXA proteins facilitates the inactivation of transcriptional enhancer elements at key epithelial genes in colorectal cancer cells. *PLoS Genet*. 2017;13(11):e1007109. doi:10.1371/journal.pgen.1007109
62. Ye X, Tam WL, Shibue T, et al. Distinct EMT programs control normal mammary stem cells and tumour-initiating cells. *Nature*. 2015;525(7568):256–260. doi:10.1038/nature14897
63. You J, Li M, Cao LM, et al. Snail1-dependent cancer-associated fibroblasts induce epithelial-mesenchymal transition in lung cancer cells via exosomes. *QJM*. 2019;112(8):581–590. doi:10.1093/qjmed/hcz093
64. Schlimgen AK, Helms JA, Vogel H, Perin MS. Neuronal pentraxin, a secreted protein with homology to acute phase proteins of the immune system. *Neuron*. 1995;14(3):519–526. doi:10.1016/0896-6273(95)90308-9
65. Schvartz D, Coute Y, Brunner Y, Wollheim CB, Sanchez JC. Modulation of neuronal pentraxin 1 expression in rat pancreatic beta-cells submitted to chronic glucotoxic stress. *Mol Cell Proteomics*. 2012;11(8):244–254. doi:10.1074/mcp.M112.018051
66. Guzeloglu-Kayisli O, Basar M, Shapiro JP, et al. Long-acting progestin-only contraceptives enhance human endometrial stromal cell expressed neuronal pentraxin-1 and reactive oxygen species to promote endothelial cell apoptosis. *J Clin Endocrinol Metab*. 2014;99(10):E1957–1966. doi:10.1210/jc.2014-1770
67. Zhou C, Qin Y, Xie Z, et al. NPTX1 is a novel epigenetic regulation gene and associated with prognosis in lung cancer. *Biochem Biophys Res Commun*. 2015;458(2):381–386. doi:10.1016/j.bbrc.2015.01.124
68. Yue W, Wang T, Zachariah E, et al. Transcriptomic analysis of pancreatic cancer cells in response to metformin and aspirin: an implication of synergy. *Sci Rep*. 2015;5:13390. doi:10.1038/srep13390
69. Mori Y, Oлару AV, Cheng Y, et al. Novel candidate colorectal cancer biomarkers identified by methylation microarray-based scanning. *Endocr Relat Cancer*. 2011;18(4):465–478. doi:10.1530/ERC-11-0083
70. Mehdizadeh A, Pandesh S, Shakeri-Zadeh A, et al. The effects of folate-conjugated gold nanorods in combination with plasmonic photothermal therapy on mouth epidermal carcinoma cells. *Lasers Med Sci*. 2014;29(3):939–948. doi:10.1007/s10103-013-1414-2

71. Pérez-Herrero E, Fernández-Medarde A. Advanced targeted therapies in cancer: drug nanocarriers, the future of chemotherapy. *Eur J Pharm Biopharm.* 2015;93:52–79. doi:10.1016/j.ejpb.2015.03.018
72. Montazerabadi A, Beik J, Irajirad R, et al. Folate-modified and curcumin-loaded dendritic magnetite nanocarriers for the targeted thermo-chemotherapy of cancer cells. *Artif Cells Nanomed Biotechnol.* 2019;47(1):330–340. doi:10.1080/21691401.2018.1557670
73. Zeinizade E, Tabei M, Shakeri-Zadeh A, et al. Selective apoptosis induction in cancer cells using folate-conjugated gold nanoparticles and controlling the laser irradiation conditions. *Artif Cells Nanomed Biotechnol.* 2018;46(sup1):1026–1038. doi:10.1080/21691401.2018.1443116

### International Journal of Nanomedicine

Dovepress

### Publish your work in this journal








The International Journal of Nanomedicine is an international, peer-reviewed journal focusing on the application of nanotechnology in diagnostics, therapeutics, and drug delivery systems throughout the biomedical field. This journal is indexed on PubMed Central, MedLine, CAS, SciSearch®, Current Contents®/Clinical Medicine,

Journal Citation Reports/Science Edition, EMBase, Scopus and the Elsevier Bibliographic databases. The manuscript management system is completely online and includes a very quick and fair peer-review system, which is all easy to use. Visit <http://www.dovepress.com/testimonials.php> to read real quotes from published authors.

Submit your manuscript here: <https://www.dovepress.com/international-journal-of-nanomedicine-journal>

## Article

# Qualitative and Quantitative Analysis of Ukrainian *Iris* Species: A Fresh Look on Their Antioxidant Content and Biological Activities

Olha Mykhailenko <sup>1,†</sup> , Michal Korinek <sup>2,3,4,†</sup> , Liudas Ivanauskas <sup>5</sup>, Ivan Bezruk <sup>1</sup> , Artem Myhal <sup>1</sup>, Vilma Petrikaitė <sup>6,7,8</sup> , Mohamed El-Shazly <sup>9,10</sup>, Guan-Hua Lin <sup>11</sup>, Chia-Yi Lin <sup>11</sup>, Chia-Hung Yen <sup>12</sup> , Bing-Hung Chen <sup>2,13,14</sup>, Victoriya Georgiyants <sup>1,\*</sup>  and Tsong-Long Hwang <sup>3,4,15,16,\*</sup> 

<sup>1</sup> Department of Pharmaceutical Chemistry, National University of Pharmacy, 4-Valentynivska st., 61168 Kharkiv, Ukraine; mykhailenko.farm@gmail.com (O.M.); vania.bezruk@gmail.com (I.B.); artem.migal@gmail.com (A.M.)

<sup>2</sup> Department of Biotechnology, College of Life Science, Kaohsiung Medical University, Kaohsiung 80708, Taiwan; mickorinek@hotmail.com (M.K.); bhchen@kmu.edu.tw (B.-H.C.)

<sup>3</sup> Graduate Institute of Natural Products, College of Medicine, Chang Gung University, Taoyuan 33302, Taiwan

<sup>4</sup> Research Center for Chinese Herbal Medicine, Research Center for Food and Cosmetic Safety, and Graduate Institute of Health Industry Technology, College of Human Ecology, Chang Gung University of Science and Technology, Taoyuan 33302, Taiwan

<sup>5</sup> Department of Analytical and Toxicological Chemistry, Lithuanian University of Health Sciences, A. Mickevičiaus g. 9, LT 44307 Kaunas, Lithuania; liudas.ivanaukas@lsmuni.lt

<sup>6</sup> Laboratory of Drug Targets Histopathology, Institute of Cardiology, Lithuanian University of Health Sciences, Sukilelių pr. 13, LT-50162 Kaunas, Lithuania; vilma.petrikaite@lsmuni.lt

<sup>7</sup> Institute of Physiology and Pharmacology, Faculty of Medicine, Lithuanian University of Health Sciences, Mickevičiaus g. 9, LT-44307 Kaunas, Lithuania

<sup>8</sup> Institute of Biotechnology, Life Sciences Centre, Vilnius University, Saulėtekio al. 7, LT-10257 Vilnius, Lithuania

<sup>9</sup> Department of Pharmaceutical Biology, Faculty of Pharmacy and Biotechnology, the German University in Cairo, Cairo 11835, Egypt; mohamed.elshazly@pharma.asu.edu.eg

<sup>10</sup> Department of Pharmacognosy, Faculty of Pharmacy, Ain Shams University, African Union Organization Street, Abbassia, Cairo 11566, Egypt

<sup>11</sup> Department of Biochemistry and Molecular Biology, College of Medicine, Chang Gung University, Taoyuan 33302, Taiwan; cherrylin20170723@gmail.com (G.-H.L.); joyce950509@gmail.com (C.-Y.L.)

<sup>12</sup> Graduate Institute of Natural Products, College of Pharmacy, Kaohsiung Medical University, Kaohsiung 80708, Taiwan; chyen@kmu.edu.tw

<sup>13</sup> Department of Medical Research, Kaohsiung Medical University Hospital, Kaohsiung 80708, Taiwan

<sup>14</sup> The Institute of Biomedical Sciences, National Sun Yat-sen University, Kaohsiung 80424, Taiwan

<sup>15</sup> Department of Anesthesiology, Chang Gung Memorial Hospital, Taoyuan 33305, Taiwan

<sup>16</sup> Chinese Herbal Medicine Research Team, Healthy Aging Research Center, Chang Gung University, Taoyuan 33302, Taiwan

\* Correspondence: vgeor@nuph.edu.ua (V.G.); htl@mail.cgu.edu.tw (T.-L.H.); Tel.: +380572-67-91-97 (V.G.); +886-3-2118800 (ext. 5523) (T.-L.H.)

† These authors contributed equally to this work.

Academic Editors: Michal Tomczyk and Francesco Cacciola

Received: 31 August 2020; Accepted: 2 October 2020; Published: 8 October 2020



**Abstract:** The major groups of antioxidant compounds (isoflavonoids, xanthenes, hydroxycinnamic acids) in the rhizome methanol extracts of four Ukrainian *Iris* sp. (*Iris pallida*, *Iris hungarica*, *Iris sibirica*, and *Iris variegata*) were qualitatively and quantitatively analyzed using HPLC-DAD and UPLC-MS/MS. Gallic acid, caffeic acid, mangiferin, tectoridin, irigenin, iristectorigenin B, irisolidone, 5,6-dihydroxy-7,8,3',5'-tetramethoxyisoflavone, irisolidone-7-O-β-D-glucopyranoside, germanaism B, and nigricin were recognized by comparing their UV/MS spectra, chromatographic retention time (tR) with those of standard reference compounds. *I. hungarica* and *I. variegata* showed the highest total

amount of phenolic compounds. Germanaism B was the most abundant component in the rhizomes of *I. variegata* ( $7.089 \pm 0.032$  mg/g) and *I. hungarica* ( $6.285 \pm 0.030$  mg/g). The compound analyses showed good calibration curve linearity ( $r^2 > 0.999$ ) and low detection and quantifications limit. These results validated the method for its use in the simultaneous quantitative evaluation of phenolic compounds in the studied *Iris* sp. *I. hungarica* and *I. variegata* rhizomes exhibited antioxidant activity, as demonstrated by the HPLC-ABTS system and NRF2 expression assay and anti-inflammatory activity on respiratory burst in human neutrophils. Moreover, the extracts showed anti-allergic and cytotoxic effects against cancer cells. Anti-coronavirus 229E and lipid formation activities were also evaluated. In summary, potent antioxidant marker compounds were identified in the examined *Iris* sp.

**Keywords:** *Iris* rhizomes; HPLC-DAD; UPLC-MS/MS; phenolic compounds; HPLC-ABTS; antioxidant; anti-inflammatory; anti-allergic; cytotoxic; coronavirus 229E

## 1. Introduction

Oxidative stress and inflammation are pathophysiological processes that usually accompany various chronic diseases [1]. Oxidative stress and inflammatory processes are intertwined and affect each other through the activation of a plethora of molecular pathways. Oxidative stress promotes the prognosis of many diseases including inflammation, metabolic and liver diseases. The antioxidant scavenging process is an important process to prevent the harmful effect of free radicals [2]. Recently, nuclear factor erythroid 2-related factor 2 (NRF2), an antioxidant and cytoprotective factor, has received great attention because it exhibits interesting anti-inflammatory and hepatoprotective effects [3]. The uncontrolled generation of superoxide anions by human neutrophils plays a crucial role in the development of inflammatory and autoimmune disorders related to oxidative stress [4]. Thus, the use of drugs with antioxidant and/or anti-inflammatory activity is necessary to treat many oxidative stress-related diseases [5]. Most of the used antioxidants are of natural origin such as phenolics and vitamins. Phenolics are widely distributed in the plant kingdom. They can be found in many foods and medicinal plants and possess potent antioxidant properties rendering them ideal candidates for the development of antioxidant drug leads [6].

*Iris* L. (Iridaceae Juss.) is one of the largest genera of perennial herbaceous plants that comprises 1800 species [7]. *Iris* sp. are distributed in Europe, northern Africa, Asia, and the Middle East [8]. Rhizomes of various *Iris* sp. (*I. germanica* L., *I. pallida* Lam., and *I. florentina* L.) serve as a source of essential oils, which are widely used in cosmetics and perfumery [9]. The underground parts of several *Iris* sp. have been used in traditional European medicine for centuries [10]. Purified and dried rhizomes of *I. germanica*, *I. florentina*, or *I. pallida* are collectively known as *Rhizoma iridis*. They are commonly used because of their cathartic, emetic, stimulant, and expectorant properties. Dry rhizomes were used as an ingredient in tooth powders and as a chewing agent to promote teething in children. *I. germanica* is used to treat liver and spleen diseases in traditional medicinal systems [11].

Previous chemical and pharmacological studies on *Iris* sp. indicated that the plants contain several classes of secondary metabolites such as flavonoids, isoflavones, and their glycosides, C-glucosylxanthones, quinones, triterpenoids, and stilbene glycosides [12–14]. These compounds contribute to the observed immunomodulatory [15,16], estrogenic [17,18], antioxidative [19–21], antibacterial [22,23] and anticholinesterase [24], cytotoxic [11,25], and anti-osteoporotic activities [26]. Experimental results indicate a direct correlation between *Iris* phenolic compounds (hydroxycinnamic acids, isoflavones, flavones, xanthones) and their pharmacological activity, especially the antioxidant activity [20,27–29].

The global distribution of *Iris* sp. along with their potent biological activities have encouraged many research groups to study their metabolic profiles. Several reports have discussed the isolation and purification of new isoflavones from *Iris* rhizomes [25,30–33]. Scientists had to purify the new

compounds using tedious chromatographic techniques and to identify the structures of the compounds using several spectroscopic techniques. These techniques are time-consuming, labor-intensive, and use excessive amounts of solvents [34,35]. Since the 1990s, new methods were developed to provide a direct approach to identify plant constituents in complex herbal extracts.

Liquid chromatography (LC) coupled with MS/MS facilitates the characterization of various compounds based on the molecular formula, exact mass, and fragmentation pattern [36,37]. HPLC-DAD-ESI-MS/MS was used for the qualitative identification of the main constituents in the rhizomes of *I. crocea*, *I. germanica*, and *I. spuria* from Kashmir (India) [38]. This method showed high sensitivity and allowed the identification of substances present in the raw materials in minor quantities. Sajad et al. developed an HPLC-UV-DBP method for the rapid identification and quantification of tectorigenin in *Iris* sp. growing in Kashmir [39]. The quantitative determination of tectorigenin indicated its presence in 1.08% to 8.84%. In another study, HPLC-DAD-CL and HPLC-ESI-Q-TOF-MS/MS were used for the identification of xanthones, isoflavonoid glycosides, and their aglycones, flavones, and other phenolic compounds in the rhizomes of *Belamcanda chinensis* (*I. domestica*), *I. tectorum*, and *I. dichotoma* grown in China [27]. However, most of these methods allowed the qualitative or quantitative determination of one or a few compounds but failed to present the full metabolic profile of the plants of interest.

In the last few years, several groups have used HPLC-DAD-ESI-MS<sup>n</sup> for the identification of the metabolic profile of several medicinal plants [40–42]. This method was used by Wei et al. for the identification of known isoflavones in the rhizomes of *I. tectorum* and *I. dichotoma* grown in China. HPLC-DAD-ESI-MS<sup>n</sup> can simultaneously provide UV and mass spectra, necessary for the identification of known components by comparing the chromatographic data of authentic compounds to the on-line detected chromatograms of the target compounds. It provided fragmentation pathways of the known compounds that can assist in elucidating the unknown structures based on the tandem mass [27,28,43]. Currently, HPLC coupled with several detectors is the optimal chromatographic method for the quick, simple, and quantitative identification of secondary metabolites in plant extracts [44]. Our previous phytochemical investigations on *Iris* sp. resulted in the isolation of flavones, isoflavones, xanthones, hydroxycinnamic acids, and coumarins by column chromatography. However, the qualitative and quantitative determination of phenolic compounds in certain *Iris* sp. using HPLC was never carried before. Thus, this study aimed to qualitatively and quantitatively compare the phenolic compounds in the rhizomes of four Ukrainian *Iris* sp. (*I. pallida*, *I. hungarica*, *I. sibirica*, *I. variegata*) by HPLC-DAD and UPLC-MS/MS. Furthermore, we analyzed the samples' antioxidant capacity using the HPLC-ABTS system and NRF2 expression for the first time. We also conducted related pharmacological in vitro assays for *I. hungarica* and *I. variegata* crude extracts, including anti-inflammatory, anti-allergic, cytotoxic, hepatoprotective, and human coronavirus 229E (HCoV-229E) bioassays.

## 2. Results and Discussion

### 2.1. Optimization of the HPLC-DAD and UPLC-MS/MS Conditions

In the current research, we applied certain modifications to an HPLC method developed for the simultaneous determination of phenolic compounds in the rhizomes of *I. dichotoma* [41]. The applied modifications resulted in a better separation of compounds with good peak symmetry. In our study, we used methanol as the extraction solvent and an ultrasonic bath to enhance the extraction efficacy. Chromatographic separation of the extracts was carried out using a Shimadzu HPLC system equipped with an ACE C<sub>18</sub> column. Gradient elution was applied with 0.1% acetic acid in water-acetonitrile and acetonitrile with increasing polarity from 5% to 95%. Similar polyphenolic compounds were detected in the extracts of *I. pallida*, *I. hungarica*, *I. sibirica*, and *I. variegata* rhizomes as demonstrated by HPLC-DAD and UPLC-MS/MS analyses. Compound identification was based on their co-elution with reference compounds previously isolated from the rhizomes of *I. pseudacorus* [45] and *I. hungarica* [13,46,47],



as well as based on the UV/MS spectroscopic data. For the qualitative analysis of phenolic compounds, a more selective and sensitive negative ionization mode method was selected for the crude plants [48].

## 2.2. Validation of the Methodology

The developed method was fully validated. The calibration curve, limits of detection (LOD), limits of quantification (LOQ), and the linear range for each analyte are provided in Table 1. All compounds showed good linearity ( $r^2 \geq 0.9993$ ) within the tested ranges. The repeatability was expressed as the relative standard deviation (%RSD) of the major constituents' content and the RSD ranged from 0.3% to 1.3%, which was satisfactory. The determination of the main compounds in the tested solutions was done by comparing the peaks retention times and the UV-spectrum obtained from the chromatogram of the standard solution (Table 2 and Table S1). All results revealed repeatability, accuracy, high sensitivity and good linearity of the method.

## 2.3. Qualitative Analysis of the Samples

The retention times and fragmentation pattern of the investigated compounds  $[M - H]^-$  in the negative mode ( $MS^n$  spectra) were compared with the spectra of the standards. Eleven peaks were thus identified, including gallic acid (1), mangiferin (2), caffeic acid (3), tectoridin (4), germanism B (or nigricin 4'-O- $\beta$ -D-glucopyranoside) (5), irisolidone-7-O- $\beta$ -D-glucopyranoside (6), iristectorigenin B (7), nigricin (or irisolone) (8), irigenin (9), 5,6-dihydroxy-7,8,3',5'-tetramethoxyisoflavone (10), and irisolidone (11). All these polyphenolic compounds were qualitatively and quantitatively determined in the rhizomes of *I. pallida*, *I. hungarica*, and *I. variegata*. For *I. sibirica*, only six constituents were identified, including five isoflavonoids (4, 5, 7, 8, and 9), mangiferin (2), and caffeic acid (3). These compounds were detected in the studied *I.* species for the first time. The chromatograms of all reference standards were recorded at 269 nm (Figure 1). The sum of all major peaks area accounted for more than 90% of the total peak area in all chromatograms. The highest content of phenolic compounds was detected in the extracts of *I. variegata* and *I. hungarica* rhizomes compared with other tested *Iris* sp. (Figure 2).

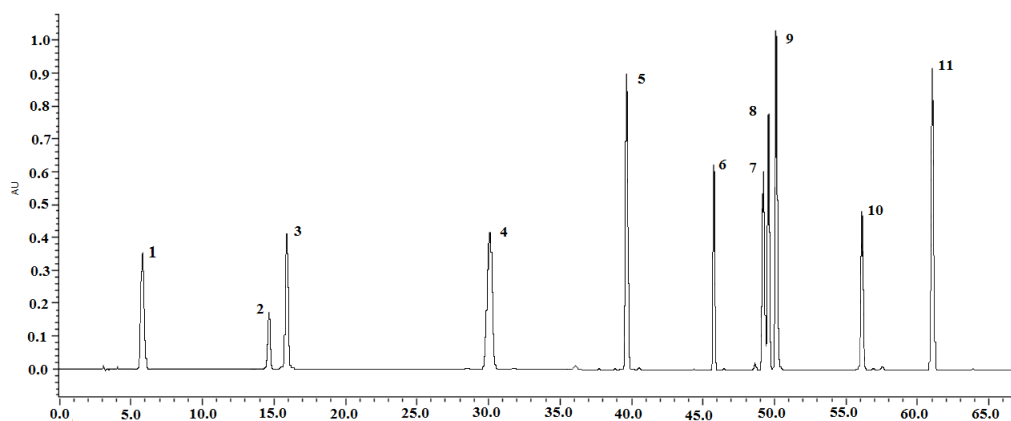


**Figure 1.** HPLC-DAD chromatograms recorded at 269 nm of the mixed reference compounds: Gallic acid (1), mangiferin (2), caffeic acid (3), tectoridin (4), germanism B (5), irisolidone-D-glucoside (6), iristectorigenin B (7), nigricin (8), irigenin (9), 5,6-dihydroxy-7,8,3',5'-tetramethoxyisoflavone (10), and irisolidone (11).

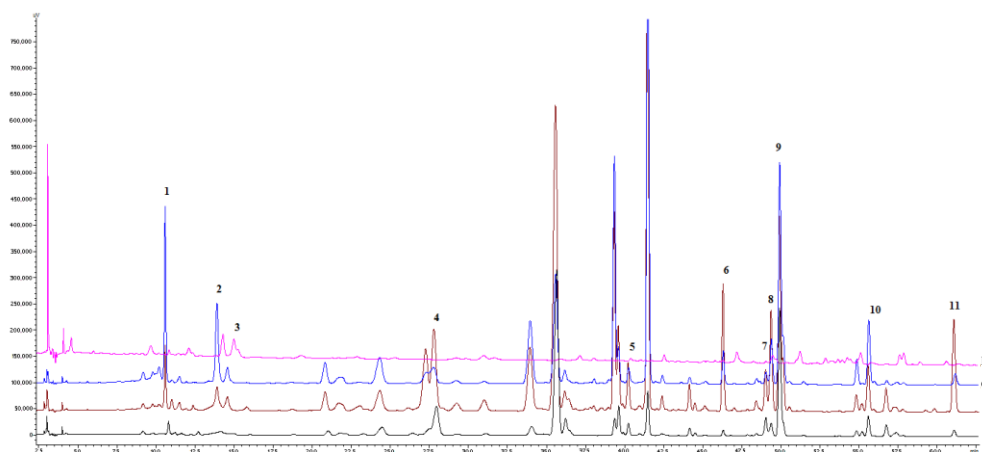


**Figure 2.** The HPLC-DAD chromatograms of the methanolic extracts of *I. pallida* (A), *I. hungarica* (B), *I. variegata* (C), *I. sibirica* (D): Gallic acid (1), mangiferin (2), caffeic acid (3), tectoridin (4), germanism B (5), irisolidone-D-glucoside (6); iristectorigenin B (7), nigricin (8), irigenin (9), 5,6-dihydroxy-7,8,3',5'-tetramethoxyisoflavone (10), and irisolidone (11).

Compound 1 was identified as gallic acid according to the absorbance maxima at 217 nm and 271 nm, characteristic of the hydroxycinnamic group of compounds. The presence of a molecular ion at  $m/z$  169 further confirmed its nature [49]. Gallic acid is formed through the shikimic acid pathway and is a major component of many phenolic compounds [50]. Compound 3 also showed absorbance maxima at 236 nm and 324 nm corresponding to the hydroxycinnamic group of the compound. Compound 3 was eluted at  $t_R$  3.92 min and showed fragment ions at  $m/z$  179, 161, and 135 in the negative-ion mode, suggesting a caffeic acid structure. It is known that caffeic acid possesses potent antioxidant, anti-inflammatory, and antineoplastic properties [51,52] so its presence in the *Iris* raw materials supports their use in folk medicine targeting inflammatory-related disorders.

Compound 2 showed typical maximum absorption peaks at 240 (shoulder peak), 257, 318, and 365 nm, which are characteristic UV features of xanthenes (mangiferin). Compounds 4–11 demonstrated maximum absorption peaks at 218–322 nm (shoulder peak) and 218–264 nm which are characteristic peaks of isoflavones (Table S1). MS data were measured in the negative ion mode and the mass spectroscopic data of all compounds are listed in Table 3. The detected compounds demonstrated regular MS fragmentation behavior, which was useful in providing information on their chemical structures. For the flavonoid glycosides, the MS spectra showed an ion at  $m/z$   $[(M-H) - 120]^-$  which represents a characteristic ion of C-glycosides, such as mangiferin (2). Mangiferin was the only C-glycosidic xanthone derivative identified in *Iris* sp. by this method. The MS spectra of flavonoid glycosides exhibited a loss of 162 Da, suggesting the presence of one hexose residue. This fragmentation pattern was characteristic of O-glycosides, such as tectoridin (4) and irisolidone-D-glucoside (6). The loss of a methyl radical ion (15 Da) was the predominant fragmentation pattern for most of the compounds, owing to the loss of a methoxy group. For example, iristectorigenin B (7) exhibited an ion peak at  $m/z$  329 in the negative ion mode. The mass data showed a fragment ion at  $m/z$  314 indicating the loss of a methyl residue. Irogenin (9) lost three methyl groups showing fragments at  $m/z$  344 and  $m/z$  329. All the LC chromatograms of the identified compounds are depicted in Figure 3. The chromatograms of the methanolic extract of *I. hungarica*, *I. variegata*, *I. pallida*, and *I. sibirica* rhizomes are illustrated in Figures S1–S4. The pseudomolecular ion signals for germanism B (5) and nigricin (8) were not observed in the negative ion mode utilizing the Retro-Diels-Alder (RDA) diagnostic [40], thus, for the detection of 5 and 8, it was necessary to apply the positive ion mode [43].

**Table 1.** Calibration curves, LOD, and LOQ data of eleven phenolic reference compounds.

Peak No	Compound	Calibration Curve <sup>a</sup>	Correlation Coefficient $r^2$ ( $n = 6$ )	Linear Range ( $\mu\text{g/mL}$ )	RSD (%)	LOD <sup>b</sup> (ng/mL)	LOQ <sup>c</sup> (ng/mL)
1	Gallic acid	$y = 32880.6x - 612.983$	0.9999718	0.48–61.08	1.31	30	100
2	Mangiferin	$y = 29263.5x + 13863.9$	0.9997952	0.28–145.00	1.32	310	940
3	Caffeic acid	$y = 57646.8x - 3853.48$	0.9999218	0.72–91.92	1.56	20	60
4	Tectoridin	$y = 76104.4x + 114152$	0.9995802	0.51–260.00	0.55	130	400
5	Germanaism B	$y = 60944.8x + 123042$	0.9993218	0.58–298.00	0.46	50	160
6	Irisolidone	$y = 29507.2x + 5569.89$	0.999981	0.49–63.1	0.98	30	90
7	D-glucoside						
8	Iristectorigenin B	$y = 109562x + 68062.7$	0.9996806	0.23–120.00	0.85	50	150
9	Nigrinin	$y = 89415.4x + 103288$	0.9994037	0.35–181.00	0.30	40	130
10	Irogenin	$y = 81832.6x + 137668$	0.9994881	0.54–277.00	0.64	50	160
11	5,6-Dihydroxy-7,8,3',5'-tetramethoxyisoflavone	$y = 86268.5x + 59193.5$	0.9996879	0.26–132.00	0.54	70	210
	Irisolidone	$y = 54297.4x + 9147.67$	0.999988	0.54–69.77	1.26	10	30

<sup>a</sup> compound concentration (mg/mL); y, peak area; <sup>b</sup> LOD, limit of detection (S/N = 3); <sup>c</sup> LOQ, limit of quantification (S/N = 10).

**Table 2.** Precision and stability of the eleven quantified compounds.

Peak No.	Compound	Concentration ( $\mu\text{g/mL}$ )	Precision				Repeatability	
			Intra-Day ( $n = 3$ )		Inter-Day ( $n = 3$ )		Recovery (%)	RSD (%)
			RSD (%)	Accuracy (%)	RSD (%)	Accuracy (%)		
1	Gallic acid	7.65	0.57	99.81	0.75	101.37	101.07	0.65
		30.35	0.78	99.56	0.24	102.14	99.69	0.56
		61.20	1.02	101.53	0.38	101.32	100.09	0.94
2	Mangiferin	9.06	0.33	100.46	0.29	100.41	100.29	0.25
		36.25	0.24	99.66	0.32	100.45	100.03	0.39
		145	0.22	100.32	1.10	98.45	99.58	0.99
3	Caffeic acid	11.49	1.05	102.02	0.52	98.49	100.01	0.46
		45.96	1.08	98.78	0.67	99.73	99.39	0.99
		91.92	0.64	100.35	0.95	98.17	100.17	0.37
4	Tectoridin	16.25	1.35	101.93	1.57	102.24	101.39	0.98
		65	1.13	101.92	0.72	101.03	100.98	0.95
		260	0.30	99.57	0.03	99.96	99.84	0.23
5	Germanaism B	18.62	0.65	100.92	0.16	100.23	100.38	0.48
		74.5	1.07	101.52	1.50	102.15	101.22	0.99
		298	0.64	99.09	0.93	98.69	99.26	0.68

Table 2. Cont.

Peak No.	Compound	Concentration (µg/mL)	Precision				Repeatability	
			Intra-Day (n = 3)		Inter-Day (n = 3)		Recovery (%)	RSD (%)
			RSD (%)	Accuracy (%)	RSD (%)	Accuracy (%)		
6	Irisolidone-D-glucoside	0.49	1.07	98.35	0.92	101.64	100.34	1.05
		7.88	0.95	101.38	0.73	99.32	98.07	0.97
		31.55	1.02	100.44	0.94	99.78	100.74	0.31
7	Iristectorigenin B	7.5	1.23	101.76	1.64	102.35	101.36	0.97
		30	1.01	102.88	1.23	101.76	101.54	1.01
		120	0.07	99.90	0.33	99.53	99.81	0.25
8	Nigracin	11.31	1.19	101.70	1.21	101.73	101.14	0.98
		45.25	0.37	99.47	1.19	101.70	100.39	0.96
		181	0.57	99.19	0.48	99.33	99.50	0.43
9	Irigenin	17.31	1.08	101.54	1.29	101.84	101.12	0.98
		69.25	0.80	101.14	1.16	101.65	100.93	0.84
		277	0.33	99.53	0.20	99.71	99.74	0.24
10	5,6-Dihydroxy-7,8,3',5'-tetramethoxyisoflavone	8.25	0.43	100.61	0.77	101.09	100.56	0.54
		33	0.06	100.08	0.52	100.74	100.27	0.41
		132	0.18	99.74	0.80	98.88	99.54	0.59
11	Irisolidone	0.54	1.07	98.74	0.52	98.24	100.06	0.52
		8.72	1.12	101.20	0.67	99.41	99.69	0.85
		34.88	0.42	100.29	0.95	100.86	100.77	0.20

Table 3. Chromatographic, UV, and mass spectroscopic data of the reference compounds.

Peak No	t <sub>R</sub> (min)	UV λ <sub>max</sub> (nm)	Mol. Formula	Calculated m/z	Compound	[M – H] <sup>–</sup> (m/z)	Fragment Ions (–)
1	5.96	214, 271	C <sub>7</sub> H <sub>6</sub> O <sub>5</sub>	170.12	Gallic acid	169	125
2	14.18	240, 318, 257, 365	C <sub>19</sub> H <sub>18</sub> O <sub>11</sub>	422.33	Mangiferin	421	403, 331, 301, 271
3	14.48	217, 236, 324	C <sub>9</sub> H <sub>8</sub> O <sub>4</sub>	180.16	Caffeic acid	179	135
4	29.48	263, 328	C <sub>22</sub> H <sub>22</sub> O <sub>11</sub>	462.41	Tectoridin	461	446, 428, 341, 299
5	41.08	260, 322	C <sub>23</sub> H <sub>22</sub> O <sub>11</sub>	474.42	Germanaism B	473	ND*
6	45.91	260, 330	C <sub>23</sub> H <sub>23</sub> O <sub>11</sub>	476.13	Irisolidone D-glucoside	475	313, 298
7	49.15	218, 265	C <sub>17</sub> H <sub>14</sub> O <sub>7</sub>	330.29	Iristectorigenin B	329	314, 311, 299, 271, 255, 164
8	49.50	262, 322	C <sub>17</sub> H <sub>12</sub> O <sub>6</sub>	312.28	Nigracin	311	ND*
9	50.03	264, 218	C <sub>19</sub> H <sub>16</sub> O <sub>8</sub>	360.32	Irigenin	359	344, 329, 314, 286, 258
10	56.03	222, 265	C <sub>19</sub> H <sub>18</sub> O <sub>8</sub>	374.35	5,6-Dihydroxy-7,8,3',5'-tetramethoxyisoflavone	373	358, 135
11	61.24	259, 322	C <sub>14</sub> H <sub>14</sub> O <sub>6</sub>	314.08	Irisolidone	313	298

\* ND—compound was not detected in the negative ion mode.

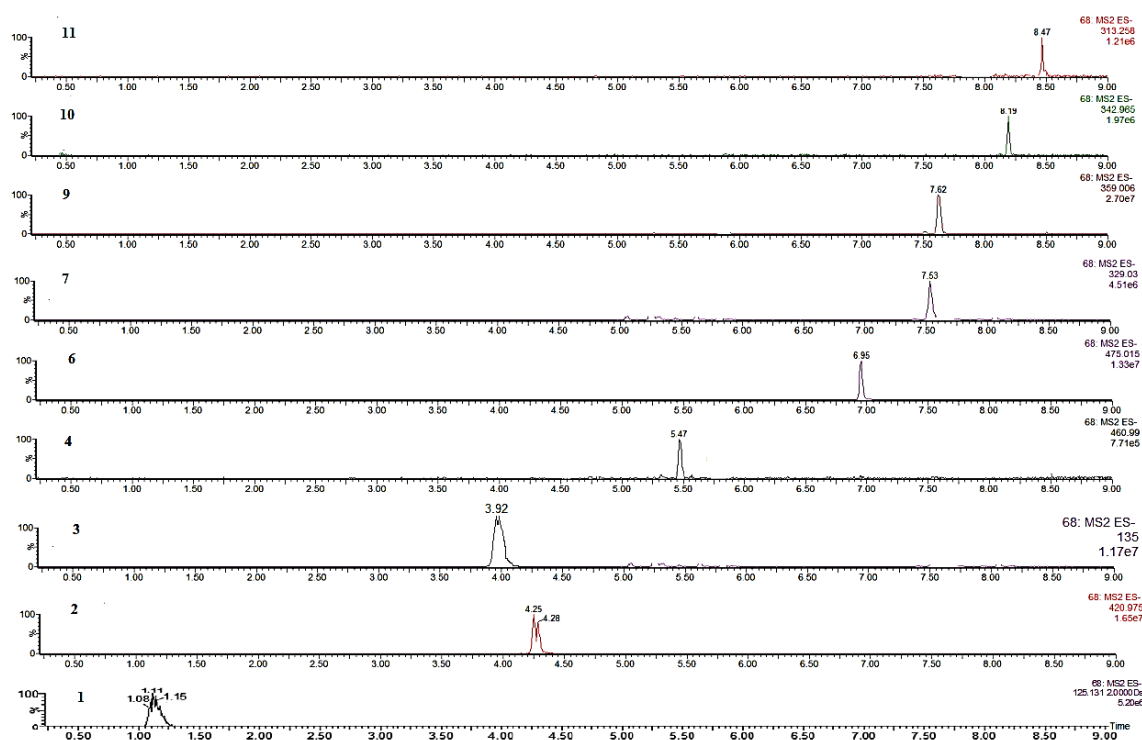


**Figure 3.** UPLC-MS chromatograms of compounds in the negative ion mode: Gallic acid (1) (1.14 min), mangiferin (2) (4.21 min), caffeic acid (3) (3.92 min), tectoridin (4) (5.47 min), irisolidone D-glucoside (6) (6.95 min), iristectorigenin B (7) (7.53 min), irigenin (9) (7.62 min), 5,6-dihydroxy-7,8,3',5'-tetramethoxyisoflavone (10) (8.19 min), and irisolidone (11) (8.47 min).

In a previous report, tectoridin was identified in *I. crocea* and *I. tectorum* rhizomes by HPLC-DAD-ESI-MS/MS [38]. The presence of mangiferin and irigenin in *I. germanica* rhizomes was also demonstrated by the same authors. Also, isoflavonoids such as mangiferin, tectoridin, tectorigenin, irigenin, iristectorin A, iristectorin B, iridinirisflorentin, dichotomitin, and irilone were identified in the rhizomes of *I. dichotoma* grown in China [27]. However, the quantitative analysis of these compounds was never carried out. In the current investigation, gallic acid was only identified in *I. variegata* and *I. hungarica* rhizomes, while caffeic acid was observed in all analyzed samples.

Mangiferin is the most widespread C-glycosylxanthone in *Iris* sp. [53]. It was identified in 47 *Iris* sp. and subspecies, whereas its isomer isomangiferin was detected in 41 species [54]. Mangiferin possesses a chemotaxonomic value for *Iris* plants on the tribe, subgenus, section, and series levels. The Irideae and Tigrideae tribes may be distinguished from other Iridaceae tribes by the presence of mangiferin. In general, isoflavones were detected as the major components and could be considered as chemotaxonomic markers for these *Iris* sp.

#### 2.4. Quantitative Analysis of the Samples

To estimate the potential pharmacological activities of the examined raw material, comparative quantitative analysis of each of the phenolic compounds content was carried out. The results of the HPLC quantitative analysis of the phenolic compounds in the rhizomes of each *Iris* sp. are presented in Table 4.



**Table 4.** Phenolic compounds content of *I. pallida*, *I. hungarica*, *I. sibirica*, and *I. variegata* rhizomes (mg/g).

Peak No	Compound	<i>I. pallida</i>	<i>I. hungarica</i>	<i>I. sibirica</i>	<i>I. variegata</i>
1	Gallic acid	-	2.362 ± 0.076	-	3.729 ± 0.134
2	Mangiferin	0.849 ± 0.029	2.368 ± 0.023	0.267 ± 0.002	5.747 ± 0.080
3	Caffeic acid	0.227 ± 0.033	1.515 ± 0.005	0.288 ± 0.012	1.236 ± 0.005
4	Tectoridin	1.642 ± 0.023	3.921 ± 0.071	0.038 ± 0.001	0.989 ± 0.006
5	Germanaism B	0.534 ± 0.015	6.285 ± 0.030	0.012 ± 0.000	7.089 ± 0.032
6	Irisolidone-D-glucoside	0.325 ± 0.030	7.353 ± 0.025	0.115 ± 0.005	7.507 ± 0.005
7	Iristectorigenin B	0.354 ± 0.004	0.750 ± 0.003	-	0.204 ± 0.005
8	Nigrinin	0.317 ± 0.003	2.267 ± 0.003	0.079 ± 0.002	0.990 ± 0.010
9	Irigenin	3.199 ± 0.034	4.892 ± 0.038	0.069 ± 0.000	5.518 ± 0.031
10	5,6-Dihydroxy-7,8,3',5'-tetramethoxyisoflavone	0.457 ± 0.003	1.056 ± 0.002	-	1.512 ± 0.013
11	Irisolidone	0.264 ± 0.004	4.025 ± 0.005	-	0.437 ± 0.030

Data are expressed as mean ± S.D. For each sample *n* = 2.

According to our results, *I. sibirica* rhizome extract can be distinguished from other extracts by having low amounts of phenolic compounds. The amounts of mangiferin (2) ( $0.267 \pm 0.002$  mg/g) and caffeic acid (3) ( $0.288 \pm 0.012$ ) were the highest among other identified compounds in this *Iris* rhizome. However, the content of all compounds including tectoridin (4) ( $0.038 \pm 0.001$  mg/g), germanaism B (5) ( $0.012 \pm 0.000$  mg/g), irisolidone-D-glucoside (6) ( $0.115 \pm 0.005$  mg/g), nigricin (8) ( $0.079 \pm 0.002$  mg/g), and irigenin (9) ( $0.069 \pm 0.000$  mg/g) was much lower in comparison with the other species. Compounds 1, 7, 10, and 11 were absent in the extract of *I. sibirica* rhizomes which was predictable because they are considered minor metabolites of *Iris* plants.

Studies on *I. pallida* from Ukraine indicated that it does not contain a high quantity of phenolic compounds compared with other species. According to the published data [55], this species contains isoflavones irigenin, iristectorigenin A, nigricin, nigricanin, irisflorentin, iriskumaonin methyl ether, irilone, iriflogenin, and *cis*- and *trans*- $\alpha$ -irone. In the current investigation, high amounts of irigenin (9) ( $3.199 \pm 0.034$  mg/g) and tectoridin (4) ( $1.642 \pm 0.023$  mg/g) were detected. According to our knowledge, tectoridin, germanaism B, irisolidone-D-glucoside, iristectorigenin B, irisolidone, and 5,6-dihydroxy-7,8,3',5'-tetramethoxyisoflavone, were identified for the first time in *I. pallida* by HPLC analysis.

The amounts of germanaism B (5) and irisolidone-D-glucoside (6) were the highest in the methanolic extracts of *I. variegata* and *I. hungarica* rhizomes (7.089 to 6.285 mg/g and 7.507 to 7.353 mg/g, respectively). The concentrations of irigenin (9) ( $5.518 \pm 0.031$  mg/g) and xanthone mangiferin (2) ( $5.747 \pm 0.080$  mg/g) in *I. variegata* were also high in comparison with the other tested *Iris* sp. According to the conducted HPLC analysis, every *Iris* sp. contained mangiferin with its amounts varying from 0.267 (*I. sibirica*) to 5.747 mg/g (*I. variegata*). These amounts were higher compared with the previous reports. For example, the amount of mangiferin in *I. dichotoma* rhizomes from different regions in China was 0.86–2.03 mg/g which was almost three times less compared with *I. variegata* from Ukraine [41]. Mangiferin has a wide range of pharmacological activities such as antiviral [56], antitumor, immunomodulating [57], antioxidant [58], and antituberculosis effects [59], thus its identification and quantification in *Iris* raw materials are important from a therapeutic perspective. Among hydroxycinnamic acids, gallic acid (1) was found in the extracts of *I. variegata* ( $3.729 \pm 0.134$  mg/g) and *I. hungarica* ( $2.362 \pm 0.076$  mg/g).

The most common isoflavonoid-O-glucosides in *I. hungarica* rhizomes were tectoridin (4), germanaism B (5), irisolidone-D-glucoside (6), as well as nigricin (8), irigenin (9), and irisolidone (11). The obtained results illustrated that the amount of tectoridin (3) ( $3.921 \pm 0.071$  mg/g), nigricin (8) ( $2.267 \pm 0.003$  mg/g) and iristectorigenin B (7) ( $0.750 \pm 0.003$  mg/g) in *I. hungarica* rhizomes was remarkably high in comparison with other species. However, the average content of tectoridin in *I. dichotoma* rhizomes obtained from different regions of China was reported to be 9.31 mg/g by HPLC analysis [41]. The highest amount of tectoridin ( $12.85 \pm 0.06$  mg/g) was detected in *Belamcanda chinensis* (*I. domestica*) rhizomes from Hubei Province in China [60], which significantly exceeded the content of tectoridin in *Iris* sp. from Ukraine. On the other hand, an average content of irigenin was detected in *I. domestica* from China  $0.89 \pm 0.08$  mg/g, which was three times less than the detected amount in *I. pallida* ( $3.199 \pm 0.034$  mg/g) and *I. hungarica* ( $4.892 \pm 0.038$  mg/g) from Ukraine, and the content of irigenin in *I. variegata* exceeded five folds the reported content in *I. domestica*.

To the best of our knowledge, there was no previous report on the qualitative and quantitative determination of isoflavones such as iristectorigenin B, germanaism B, irisolidone-D-glucoside, its aglycone, nigricin, and 5,6-dihydroxy-7,8,3',5'-tetramethoxyisoflavone in *Iris* raw materials. In a previous study, 5,6-dihydroxy-7,8,3',5'-tetramethoxyisoflavone (10), a new natural compound, was isolated from *I. pseudacorus* [41]. In the current study, this compound was also identified in the other *Iris* sp. Its amount varied from  $1.056 \pm 0.002$  mg/g in *I. hungarica*,  $0.457 \pm 0.003$  mg/g in *I. pallida* to the highest amount ( $1.512 \pm 0.013$  mg/g) in *I. variegata*. Caffeic acid (3) was found in all species with the amount ranging from 0.227 to 1.515 mg/g, and the highest content was detected in *I. hungarica* rhizomes.

Out of the eleven compounds, **2**, **3**, **4**, **5**, **6**, **8**, and **9** were identified in all *Iris* sp., irisolidone-D-glucoside (**6**) was found in three species, except *I. sibirica*. The amounts of **2**, **4**, **5**, **6**, **8**, and **9** were the highest among all identified compounds in the studied *Iris* sp. Compounds **5**, **6**, **8**, and **9** were previously isolated only from *I. germanica* rhizomes [61] and were found in other *Iris* sp. [14,43,54]. These findings supported the importance of **2**, (mangiferin), **4** (tectordin), **5** (germanaism B), **6** (irisolidone-D-glucoside), **8** (nigricin), and **9** (irigenin) as marker compounds of *Iris* sp.

According to the results of the qualitative and quantitative analysis of the phenolic antioxidant compounds in *Iris* sp. growing in Ukraine, it can be concluded that these plants were not inferior to *Iris* sp. grown in other places around the globe. The presence and high content of phenolic compounds in *I. variegata* and *I. hungarica* encouraged us to subject these two species to intensive pharmacological investigations.

## 2.5. Pharmacology Investigation of *I. variegata* and *I. hungarica* Extracts

Phenolic compounds are known to act as antioxidants with beneficial effects on various diseases. Phenolics can prevent the development of cardiovascular diseases, cataracts, cancers, reduce fat absorption, and positively affect metabolism [62]. The potential antioxidant capacity, as well as other pharmacological activities of *Iris* rhizomes crude extracts, were evaluated in several bioassays reflecting the traditional use of *Iris* rhizomes against infection, liver, and inflammatory diseases.

### 2.5.1. Antioxidant Activity

The HPLC-ABTS co-elution system represents a convenient method to analyze the antioxidant components in the plant crude extract [63]. The radical scavenging activities, which were expressed as Trolox equivalent antioxidant capacity (TEAC), varied among the *Iris* rhizomes water and ethanol extracts (Table 5). The antioxidant activity of *I. variegata* water extracts was the lowest (TEAC  $2.92 \pm 0.07$   $\mu\text{mol/g}$ ) (Figure 4a). On the other hand, *I. hungarica* showed a potent antioxidant capacity for the water extract (TEAC  $23.11 \pm 0.90$   $\mu\text{mol/g}$ ) (Figure 4b), and the ethanol extract showed the highest total antioxidant capacity (TEAC  $50.32 \pm 1.09$   $\mu\text{mol/g}$ ) (Figure 4c). The antioxidant activity of the identified compounds (TEAC values, Trolox  $\mu\text{mol/g}$ ) is displayed in Table 5. The extracts possessed antioxidant activity due to the presence of gallic acid, mangiferin, and caffeic acid. This can be explained by the fact that phenolic compounds are potent antioxidants [50,64,65] due to their high redox potential allowing them to become hydrogen donors and singlet oxygen quenchers [66]. The established antioxidant activity of the extracts was correlated with the content of the identified compounds. The higher the content of mangiferin, caffeic acid, and gallic acid, the higher the antioxidant activity (Figure 4). Higher amounts of mangiferin in *I. hungarica* together with gallic acid in the ethanolic extract accounted for more potent antioxidant capacity of the plant extract in comparison with water extracts. The obtained results were in good agreement with the previous studies [28,37].

**Table 5.** The radical scavenging activity of individual compounds of *I. variegata* and *I. hungarica* extracts expressed as TEAC ( $\mu\text{mol/g}$ ) using the ABTS post-column assay.

Peak No.	Component	Retention Time	<i>I. variegata</i> Rhizomes Extract (H <sub>2</sub> O)	<i>I. hungarica</i> Rhizomes Extract (H <sub>2</sub> O)	<i>I. hungarica</i> Rhizomes Extract (70% EtOH)
1	Gallic acid	5.78	$0.52 \pm 0.01$	$2.83 \pm 0.14$	$3.13 \pm 0.14$
2	Mangiferin	12.68	$2.40 \pm 0.06$	$18.01 \pm 0.87$	$20.55 \pm 1.01$
3	Caffeic acid	15.80	-	$2.27 \pm 0.10$	$26.64 \pm 1.28$
	Total		$2.92 \pm 0.07$	$23.11 \pm 0.90$	$50.32 \pm 1.09$

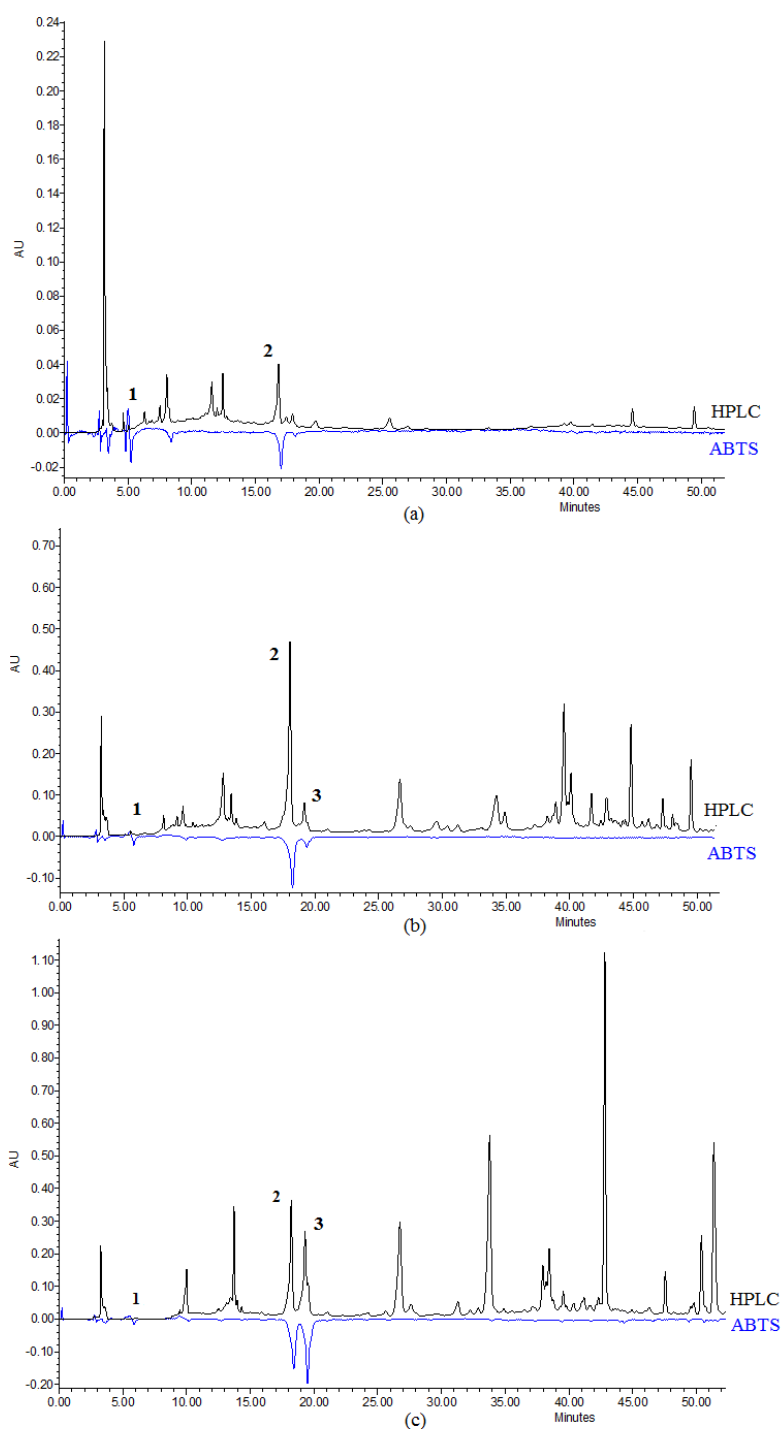


**Figure 4.** HPLC-ABTS chromatograms of (a) *I. variegata* rhizomes extract (H<sub>2</sub>O) at 247 nm (HPLC, black) and 650 nm (ABTS, blue); (b) *I. hungarica* rhizomes extract (H<sub>2</sub>O) at 255 nm/650 nm, and (c) *I. hungarica* rhizomes extract (70% EtOH) at 314 nm/650 nm. Gallic acid (1), mangiferin (2), and caffeic acid (3).

#### 2.5.2. Anti-Inflammatory Activity of *Iris* sp. Extracts against Respiratory Burst and Degranulation by Human Neutrophils

The respiratory burst and degranulation of neutrophils are important processes in the maintenance of human health, but they need careful regulation to prevent the development of chronic and auto-immune diseases. Superoxide is a major radical produced by neutrophils and its excessive amount contributes to several acute and chronic diseases, including lung injury, sepsis, or arthritis [4].

We evaluated the effects of *Iris* extracts on superoxide anion generation and elastase release triggered by fMLF in CB-primed human neutrophils. The results revealed that the water extracts of *I. variegata* and *I. hungarica* rhizomes showed anti-inflammatory potential and inhibited superoxide anion generation at 10 µg/mL by 41.0% and 45.7%, respectively (Table 6). Interestingly, both the ethanolic and water extracts of *I. hungarica* rhizomes showed enhancing effects on elastase release by human neutrophils and thus may have immune-promoting effects related to degranulation. The observed effects of *Iris* water extracts may be correlated to the abundant isoflavone content.

**Table 6.** Anti-inflammatory activity of *Iris* sp.

Sample Description	Superoxide Anion Generation	Elastase Release
	Inh% (10 µg/mL)	Inh% (10 µg/mL)
<i>I. variegata</i> rhizomes (H <sub>2</sub> O)	41.0 ± 0.6 ***	13.8 ± 5.1
<i>I. hungarica</i> rhizomes (H <sub>2</sub> O)	45.7 ± 1.4 ***	enhancing <sup>a</sup>
<i>I. hungarica</i> rhizomes (70% C <sub>2</sub> H <sub>5</sub> OH)	23.6 ± 1.3 ***	enhancing <sup>a</sup>

Percentage of inhibition (Inh%) at 10 µg/mL concentration. Results are presented as mean ± S.E.M. (*n* = 3). \*\*\* *p* < 0.001 compared with the control (fMLF/CB). Genistein served as the positive control and inhibited 99.7 ± 0.6% of superoxide anion generation at 10 µg/mL and 101.2 ± 6.3% of elastase release at 30 µg/mL. <sup>a</sup> *I. hungarica* rhizomes (H<sub>2</sub>O, 10 µg/mL) and *I. hungarica* rhizomes (C<sub>2</sub>H<sub>5</sub>OH, 10 µg/mL) induced elastase release in the presence of cytochalasin B by 59.6 ± 8.1% and 42.4 ± 7.1%. Results are presented as mean ± S.E.M. (*n* = 3). Cell responses induced by fMLF/CB were expressed as 100%.

### 2.5.3. Antioxidant Capacity Expressed as NRF2 Activity

Nuclear factor erythroid 2-related factor 2 (NRF2) is a nuclear transcription factor usually activated in response to reactive oxygen species (ROS). NRF2 increases the antioxidant capability of all cells in response to stress, thus its activation is beneficial for health. It is also known that the level of NRF2 indicates the antioxidant capacity of the cells and its increase is linked with the enhanced ability to scavenge radicals [67]. Plants phenolic rich extracts were previously shown to exert a cytoprotective effect by increasing heme oxygenase-1 (HO-1) together with NRF2 [68]. In the current study, NRF2 activity was evaluated in HacaT normal skin cell line. *I. variegata* rhizomes showed a mild enhancing effect on NRF2 activity by 72.7% in normal skin cells indicating cytoprotective effects (Table 7), however, the effect did not correlate with the phenolics content (Section 2.5.1).

**Table 7.** Antioxidant capacity expressed as NRF2 activity and lipid droplets activity of *Iris* extracts.

Sample Description	Relative NRF2 Activity <sup>a</sup> in HacaT Cells <sup>b</sup>	Lipid Droplet Inhibition Activity <sup>c</sup>
<i>I. variegata</i> rhizomes (H <sub>2</sub> O)	172.7	95.1 ± 11.6
<i>I. hungarica</i> rhizomes (H <sub>2</sub> O)	119.9	64.9 ± 8.1
<i>I. hungarica</i> rhizomes (70% C <sub>2</sub> H <sub>5</sub> OH)	130.8	101.5 ± 6.8

<sup>a</sup> Relative luciferase activity was calculated by normalizing luciferase activity to cell viability and is presented as the fold to solvent control. <sup>b</sup> HacaT, a normal skin cell line. The drug concentration was 100 µg/mL. TBHQ, 2-(1,1-dimethylethyl)-1,4-benzenediol (10 µM), was used as the positive control for NRF2 activation and showed 684.3 ± 37.7% of NRF2 activity. <sup>c</sup> Lipid droplet count. The average lipid droplet counts/cells of oleic acid were used as the standard representing 100% of lipid loading in Huh7 liver cell line, % mean ± S.E.M. Triacsin C (1 µM), an inhibitor of long-chain acyl-CoA synthetase, was used as the positive control and showed 16.3 ± 0.1% of lipid formation.

### 2.5.4. Assessment of the Anti-Allergic Activity by the Inhibition of RBL-2H3 Cells Degranulation

The incidence of allergic diseases is dramatically increasing and the search for new drugs from natural sources is of great importance. We used a degranulation assay to evaluate the anti-allergic effect of *Iris* sp. To ascertain non-false positive effects of the samples that could be caused by the inhibition of cell viability, all samples were evaluated for toxicity against RBL-2H3 (rat basophilic leukemia cells) using MTT viability assay. The samples were found to be nontoxic (viability was over 96% compared with the control) at 100 µg/mL (Table 8). Samples were then evaluated for the anti-allergic activity using degranulation assay (β-hexosaminidase release detection assay) induced either by calcium ionophore



(A23187) or antigen (anti-DNP IgE plus DNP-BSA). Calcium ionophore serves as a direct activator by facilitating calcium influx into the cell, while antigen mimics the physiological conditions of IgE-antigen complex binding to the FcεRI receptor on the mast cell membrane [69]. The results revealed that the water extract of *I. variegata* rhizomes (100 µg/mL) inhibited the degranulation of mast cells stimulated by A23187 or antigen with 38.3% and 27.0%, respectively, and the ethanolic extract of *I. hungarica* rhizomes (100 µg/mL) 22.0% and 46.7%, respectively (Table 8). Dexamethasone, a positive control, inhibited A23187- or antigen-induced β-hexosaminidase release by 65.7% and 66.3%, respectively.

**Table 8.** Anti-allergic activity of *Iris* sp.

Sample Description	% Viability, RBL-2H3 <sup>a</sup>	% Inhibition of A23187-Induced Degranulation <sup>b</sup>		% Inhibition of Antigen-Induced Degranulation <sup>b</sup>	
	100 µg/mL	10 µg/mL	100 µg/mL	10 µg/mL	100 µg/mL
<i>I. variegata</i> rhizomes (H <sub>2</sub> O)	96.3 ± 0.7	12.7 ± 0.3	38.3 ± 3.5 ***	10.7 ± 3.3	27.0 ± 4.5 *
<i>I. hungarica</i> rhizomes (H <sub>2</sub> O)	96.7 ± 1.7	3.7 ± 3.0	3.3 ± 2.0	4.0 ± 3.3	12.7 ± 1.7
<i>I. hungarica</i> rhizomes (70% C <sub>2</sub> H <sub>5</sub> OH)	96.3 ± 1.9	7.3 ± 2.0	22.0 ± 5.0 *	4.7 ± 3.8	46.7 ± 2.1 ***

<sup>a</sup> The cytotoxicity of samples to RBL-2H3 was evaluated using MTT viability assay. Results are presented as mean ± S.E.M. ( $n = 3$ ) compared with the untreated control (DMSO). Samples with viability above 85% were considered nontoxic towards RBL-2H3 cells. <sup>b</sup> Inhibition of the degranulation was assessed by A23187-induced and antigen-induced β-hexosaminidase release in RBL-2H3 cells. Results are presented as mean ± S.E.M. ( $n = 3$ ); \*  $p < 0.05$ , \*\*  $p < 0.01$ , \*\*\*  $p < 0.001$  (Prism, ANOVA, Dunnet's test) compared with the control value (A23187 or antigen only). Dexamethasone (10 nM) was used as the positive control and inhibited 65.7 ± 5.4% \*\*\* of A23187-induced and 66.3 ± 4.8% \*\*\* of antigen-induced degranulation.

#### 2.5.5. Cytotoxic Activity of *Iris* sp. Extracts

*I. variegata* and *I. hungarica* rhizomes aqueous extracts reduced the viability of melanoma (IGR39) (IC<sub>50</sub> 0.53 and 1.15 mg/mL, respectively) and triple-negative breast cancer (MDA-MB-231) (IC<sub>50</sub> 0.33 and 0.57 mg/mL, respectively) cell lines (Figure 5). *I. hungarica* rhizomes 70% ethanolic extract showed comparable efficacy to *I. variegata* water extract. Amin et al. established similar EC<sub>50</sub> values for the methanolic extract of *I. kashmiriana* rhizomes from Kashmir against epithelial cancer cell lines including lung cancer A549 (IC<sub>50</sub> 0.13 mg/mL) and colon cancer Caco-2: (IC<sub>50</sub> 0.24 mg/mL) [70].

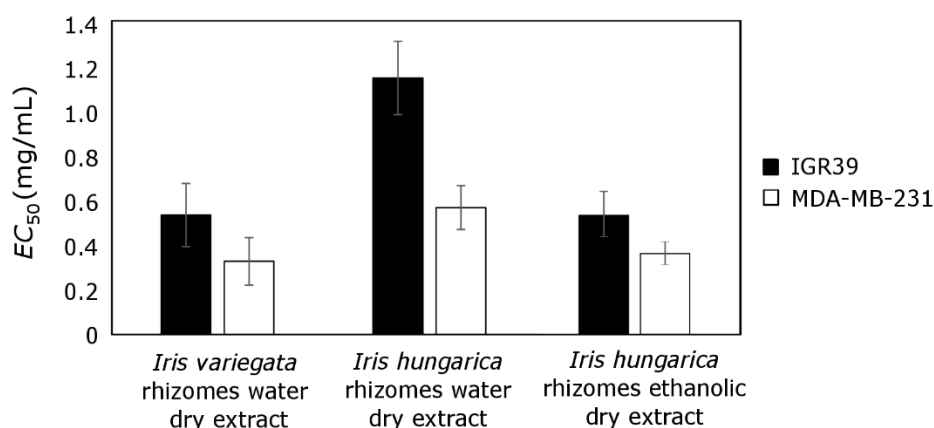


**Figure 5.** Cytotoxic effect of the tested extracts against melanoma (IGR39) and triple-negative breast cancer (MDA-MB-231) cell lines. *I. variegata* rhizomes water extract, *I. hungarica* rhizomes water extract and *I. hungarica* rhizomes ethanolic (70% EtOH) extract were tested. The values are expressed as EC<sub>50</sub> values, indicating concentrations causing a 50% reduction in viability of the cells ( $n = 3$ ).

All extracts demonstrated lower activity against melanoma cells. Triple-negative breast cancer cells were 1.5–2 times more sensitive. It is a very interesting finding, as these cells do not possess receptors for estrogen, progesterone, and HER-2 receptors, and are usually characterized by a more

aggressive nature compared with other cancer cell lines [71]. Comparing the cytotoxic effect of the aqueous and ethanolic extracts obtained from *I. hungarica* rhizomes, ethanolic extract was more effective against both melanoma (IGR39) and triple-negative breast cancer (MDA-MB-231) cells.

### 2.5.6. Lipid Formation Activity

Non-alcoholic fatty liver disease is a common liver disease caused mainly by obesity and metabolic syndrome [72]. Lipid droplets are intracellular fat storage organelles found in most cells and are essential for all organisms. Dysregulated accumulation of lipids in cells leads to many health disorders including non-alcoholic steatohepatitis (fatty liver), obesity, type 2 diabetes, and even facilitates hepatitis type C virus infection [73]. Lipid droplets formation plays a role not only in the fatty liver but also in the process of atherosclerosis, where triacsin C, the long-chain fatty acyl CoA synthetase inhibitor, demonstrated profound effects [74]. According to our results, the water extract of *I. hungarica* rhizomes showed a 35.1% inhibitory effect on the lipid droplets in Huh7 liver cells (Table 7).

*Iris* plants are rich in isoflavonoids and xanthones, which possess a wide range of biological activity, including anti-inflammatory, antioxidant, and antitumor properties. Phytochemical and pharmacological studies provide new insights into the possible therapeutic uses of these plants.

### 2.5.7. Human Coronavirus 229E Activity

Human coronavirus 229E (HCoV-229E) is a strain of coronavirus family viruses, that causes upper respiratory syndrome [75]. In the screening for anti-coronavirus activity, *I. hungarica* and *I. variegata* did not show any protective effects against human coronavirus 229E (HCoV-229E) infection at 10 µg/mL (Figure 6).

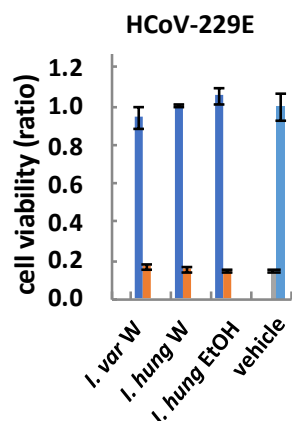


**Figure 6.** Human coronavirus 229E (HCoV-229E) protective activity of *Iris* rhizomes extracts. The cells infected by HCoV-229E were treated with the samples (orange) or vehicle (grey), any difference between them would indicate protective effects against HCoV-229E infection. The uninfected cells were also treated with the samples (dark blue) or vehicle only (light blue), serving as a control for cell viability after the treatment with the samples or vehicle. *I. var W*, *I. variegata* rhizomes (water extract); *I. hung W*, *I. hungarica* rhizomes (water extract); *I. hung EtOH*, *I. hungarica* rhizomes (ethanolic extract).

## 3. Materials and Methods

### 3.1. Chemicals and Reagents

Nine reference compounds, including mangiferin, nigracin, germanaism B, irisolidone-7-O-β-D-glucopyranoside, iristectorigenin B, tectoridin, irisolidone, irigenin, and 5,6-dihydroxy-7,8,3',5'-tetramethoxyisoflavone were previously isolated from the rhizomes of *I. hungarica* and *I. pseudacorus*. The compounds were obtained by column chromatography (silica gel), identified spectroscopically and their purity was determined using UV, IR, and HPLC-MS methods. HPLC grade methanol and acetonitrile were used for the HPLC analysis. Gallic acid, and caffeic acid (purity ≥ 98.0%)

(Sigma-Aldrich GmbH, Buchs, Switzerland), and HPLC grade glacial acetic acid (Fluka Chemie, Buchs, Switzerland) were used in the experiments. Other solvents and chemicals were of analytical grade.

### 3.2. Plant Materials

The rhizomes of *I. hungarica* Waldst. et Kit., *I. pallida* Lam., *I. sibirica* L. and *I. variegata* L. were obtained from the collections of M.M. Gryshko National Botanical Garden of the National Academy of Sciences of Ukraine (Kyiv, Ukraine) in October 2018. They were identified and authenticated by Dr. Buidin (Department of the Ornamental Plants, National Botanical Garden). Voucher specimens (CWN0056548, CWN0056549, CWN0056545, CWN0056534) were identified by Dr. Gamulya and were deposited at Herbarium of V.M. Karazin Kharkiv National University (Kharkiv, Ukraine).

### 3.3. Sample Preparation

The air-dried materials were ground to a fine powder using a laboratory mill. The powdered materials of *Iris* rhizomes (0.1 g, 60 mesh) were weighed into a volumetric flask, and methanol (10 mL) was used for extraction. The flask was placed in an ultrasonic bath at room temperature ( $20 \pm 2$  °C) for 30 min. The solutions were filtered through a membrane filter (0.45 µm) into vials made of glass. An aliquot of 20 µL was injected twice into the HPLC system for analysis. The reference compounds were used to prepare the standard solutions at a concentration of 1.0 mg/mL in methanol and were used for calibration. The samples were stored at 4 °C before use.

### 3.4. HPLC Conditions

The separation of phenolic compounds was carried out using an ACE C<sub>18</sub> column (250 mm × 4.6 mm, 5.0 µm; Zorbax Eclipse Plus, Agilent, Santa Clara, CA, USA). The flow rate of elution was 1 mL/min. The solvent system comprised solvent A (0.1% acetic acid in water) and solvent B (acetonitrile). An ultrasonic bath was used for degassing, then all solvents were filtered using a filter with a 0.22 µm membrane. A linear gradient program was applied: 0–8 min, 5–15% B; 8–30 min, 15–20% B; 30–48 min, 20–40% B; 48–58 min, 40–50% B; 58–65 min, 50%; 65–66 min, 50–95% B. The temperature of the column was constant at 25 °C. The injection volume of the sample solution was adjusted at 20 µL. The chromatograms were recorded at 269 nm (Figure 1).

### 3.5. Chromatographic Conditions for the UPLC-MS Method

Separation of the samples' components was carried out with the ACQUITY H-class UPLC system (Waters, Milford, MA, USA) equipped with ACQUITY UPLC BEH C18 (50 × 2.1 mm, particle size 1.7 µm) (Merck Millipore, Darmstadt, Germany). Gradient elution was performed with 0.1% formic acid water solution (solvent A) and acetonitrile (solvent B), the flow rate at 0.5 mL/min. The following proportions of the solvent system were applied using a linear gradient profile B: Initial 5%, 3 min. 30%, 7 min. 50%, 7 to 8 min. 95%, 15 to 16 min. 5%. Xevo TQD triple quadrupole mass spectrometer detector (Waters) was used to obtain MS/MS data. Positive electrospray ionization was applied with the following settings: Capillary voltage was 1.5 kV, source temperature was 150 °C, desolvation temperature was 350 °C, with a desolvation gas flow 650 l/h, cone gas flow was 25 l/h. Collision energy and cone voltage were optimized for each compound separately. Collision energy varied in the range from 6 eV to 20 eV and cone voltage was selected from 8 V to 38 V.

### 3.6. Identification of the Peaks and Peak Purity

The identification of the compounds 1–11 was achieved by HPLC analysis. The retention time (Rt), UV, MS/MS spectra of the peaks in the samples were compared with those of the authentic reference compounds. The purity of the compounds was evaluated by a diode array detector coupled with the HPLC system. The UV spectra of each peak were compared with those of the authentic reference compounds and/or by assessment of the MS/MS spectra.

### 3.7. Quantitative Determination of the Constituents

The compound concentration in the plant extract was calculated (mg/g) by the following formula:

$$X \left( \frac{\text{mg}}{\text{g}} \right) = \frac{S \times m_{\text{st}} \times V}{S_{\text{st}} \times m \times V_{\text{st}}} \quad (1)$$

where S—phenolic compound peaks average area calculated from the parallel chromatograms of the sample solution;  $S_{\text{st}}$ —reference compound peaks average area calculated from the parallel chromatograms of the standard solution;  $m$ —powdered raw materials weights in g;  $m_{\text{st}}$ —reference compound weights in mg;  $V$ —volumetric flask volume of the test extract in mL and  $V_{\text{st}}$ —volumetric flask volume of the reference compounds in mL. The results are summarized in Table 4.

### 3.8. Quantitative Analysis Validation Procedures

Following the United States Pharmacopeia (USP) recommendations, there are various analytical method validation parameters, including the limit of quantification (LOQ), the limit of detection (LOD), linearity, accuracy, and repeatability [76]. The responses' linearity range of the standards was obtained using ten concentration levels with two injections for each level. The seven analytes were dissolved in methanol and the stock solutions were prepared. The stock solutions were diluted to a series of appropriate concentrations to construct the calibration curves. All calibration curves were recorded using the solutions of the reference compounds with an injection volume of 2.2  $\mu\text{L}$ . The working solution with the lowest concentration was diluted with methanol to various concentrations. These solutions were then used for the determination of the limits of detection (LOD) and limits of quantification (LOQ) at a signal-to-noise ratio (S/N) of 3 and 10 for each compound. The repeatability was evaluated by analyzing six replicates of each preparation using HPLC (repeatability on the real sample). The main peak areas of two repeated chromatograms were used to calculate the relative standard deviation (RSD). The results are presented in Tables 1 and 2.

### 3.9. HPLC-PDA Conditions and HPLC Post-Column Assay

HPLC-PDA and HPLC-ABTS were done using a Waters Alliance 2695 separation module system as previously described by Marksa et al. with some modifications [77]. Details are described in the Supplementary Materials section.

### 3.10. Instruments

Separation of the compounds was achieved using a Nexera X2 LC-30AD HPLC system (Shimadzu, Kyoto, Japan). The system comprises an on-line degasser, a quaternary pump, SIL-30AC autosampler (Shimadzu), CTO-20AC thermostat (Shimadzu), a column temperature controller and a SPD-M20A diode array detector (DAD). Other instruments used in the investigation were an Ultrasonic Cleaner Set (Wise Clean WUC-A06H, Witeg Labortechnik GmbH, (Wertheim Germany), Libra UniBloc AUW120D (Shimadzu Analytical Scale, Kyoto, Japan); pH-meter—Knick Electronic Battery-operated pH Meter 911 PH (Portameß, Berlin, Germany), and class A analytical vials that meet requirements of the State Pharmacopoeia of Ukraine (SPhU, 2015).

### 3.11. Extraction Procedure of *Iris* sp. for Bioassay

*I. variegata* and *I. hungarica* rhizomes were dried, ground, and the powder was extracted with distilled water in a water bath at 100 °C (100 g, 1 L, 60 min  $\times$  3) or 70% ethanol at room temperature (100 g, 1 L, 60 min  $\times$  3). The extracts were concentrated to dryness.

### 3.12. In-Vitro Assessment of NRF2 Activity

The activity of NRF2 reporter cells was evaluated [78]. The cell line HaCaT/ARE (antioxidant response element) was developed using a HaCaT stable cell line carrying a fragment derived from

pGL4.37[luc2P/ARE/Hygro] plasmid and the luciferase reporter gene luc2P. Details are described in the Supplementary Materials section.

### 3.13. Lipid Droplet Assay

Lipid droplet assay was performed by treating Huh7 cells with BSA-conjugated oleic acid as described previously [72]. The details are described in the Supplementary Materials section.

### 3.14. Assessment of Anti-Allergic Activity Using In Vitro Assay

A methylthiazole tetrazolium (MTT) assay [79] was used to measure the possible toxic effects of the samples on RBL-2H3 cells and the experiment was performed as previously described [80].  $\beta$ -Hexosaminidase activity assay was used to determine the degree of A23187-induced [81,82] and antigen-induced [83] degranulation in RBL-2H3 cells as previously described. The details of the assays are presented in the Supplementary Materials section.

### 3.15. Assessment of Anti-Inflammatory Activity Using In Vitro Assay

Blood was taken from healthy human donors using a protocol approved by the Chang Gung Memorial Hospital review board. Neutrophils were isolated according to the standard procedure described before [84]. The inhibition of superoxide anion generation was measured by the reduction of ferricytochrome *c* as previously described [85]. Elastase release representing the degranulation from azurophilic granules was evaluated as described before [86]. Details can be found in the Supplementary Materials section.

### 3.16. In Vitro Assessment of Cytotoxic Activity

The potential cytotoxic effect of *Iris* extracts on certain cell lines was determined by a MTT viability assay as described before [87]. Details can be found in the Supplementary Materials section.

### 3.17. Coronavirus 229E Assay

The protective effects of the samples against human coronavirus 229E (HCoV-229) was determined based on the previously described method [88]. The Huh7 cells line (human liver carcinoma cell line) was obtained from Dr. Rei-Lin Kuo (Chang Gung University, Taoyuan, Taiwan). The cells were infected with nine times the Median Tissue Culture Infectious Dose (TCID<sub>50</sub>) of each coronavirus 229E in the presence or absence of the compounds or vehicle. After incubation at 33 °C for 6 days, the surviving cells were then stained with MTT (3-[4,5-dimethylthiazol-2-yl]-2,5-diphenyl tetrazolium bromide). The percentage of surviving cells was then calculated.

### 3.18. Statistical Analysis

The processing of HPLC data was carried out using the LabSolutions Analysis Data System (Shimadzu). Statistical analysis was performed using one-way analysis of variance (ANOVA) followed by Tukey's multiple comparison using Prism v.5.04 (GraphPad Software Inc., La Jolla, CA, USA, chemical composition), by Dunnet's test (GraphPad Prism 6.0, GraphPad Software Inc., San Diego, CA, USA, anti-allergic assay), or Student's *t*-test (SigmaPlot, Systat Software Inc., San Jose, CA, USA, anti-inflammatory assay). Values with *p*-values below 0.05 were considered statistically significant. The results were expressed as means  $\pm$  SD (chemical analysis) or S.E.M (anti-inflammatory, anti-allergic, and antioxidant assays) values of at least three independent measurements unless otherwise specified. Two definitions were carried out in the chemical analysis.

## 4. Conclusions

In the present study, quantitative and qualitative analyses of the methanol extracts of four *Iris* sp. (*I. pallida*, *I. hungarica*, *I. sibirica*, and *I. variegata*) rhizomes were performed using a new HPLC method.



Eleven phenolic compounds were identified. The identification was based on co-chromatography with reference compounds and UV/MS data. According to our analysis, mangiferin, tectoridin, germanaism B, irigenin, irisolidone-D-glucoside, and irisolidone were the major compounds of *Iris* sp. and can be proposed as chemical markers suitable for the development of quality control protocols of these species. This is the first report on the detailed analysis of the chemical composition of *I. pallida*, *I. hungarica*, *I. sibirica*, and *I. variegata*. Biological evaluation of the *Iris* sp. extracts revealed that *I. hungarica* rhizomes extract exhibited a potent antioxidant effect. The antioxidant activity was attributed to gallic acid and mangiferin content. *I. hungarica* and *I. variegata* rhizomes were for the first time shown to inhibit superoxide anion generation in fMLF-induced human neutrophils and increase the NRF2 expression. The phytochemical and pharmacological results indicated that *I. hungarica* and *I. variegata* rhizomes extract contain a balanced mixture of phenolic compounds with antioxidant, anti-inflammatory and anti-allergic biological activities.

**Supplementary Materials:** The following materials are available online, Figure S1: MS-chromatogram of *I. hungarica*, Figure S2: MS-chromatogram of *I. variegata*, Figure S3: MS-chromatogram of *I. pallida*, Figure S4: MS-chromatogram of *I. sibirica* rhizomes. Table S1: The specificity of eleven quantified compounds and their chemical structures. Details on the Methodology.

**Author Contributions:** Conceptualization, O.M. and M.K.; Data curation, O.M. and M.K.; Funding acquisition, L.I., V.G. and T.-L.H.; Investigation, O.M., M.K., V.P., C.-H.Y. and B.-H.C.; Methodology, O.M., M.K., L.I., V.P., G.-H.L., C.-Y.L., C.-H.Y. and B.-H.C.; Supervision, V.G. and T.-L.H.; Validation, I.B., A.M. and M.E.-S.; Visualization, O.M. and M.K.; Writing—original draft, O.M. and M.K.; Writing—review & editing, M.E.-S., V.G. and T.-L.H. All authors have read and agreed to the published version of the manuscript.

**Funding:** This research was funded by the grants from the Ministry of Science and Technology (MOST 106-2320-B-255-003-MY3, MOST 108-2320-B-255-003-MY3, MOST 108-2320-B-037-004, MOST 109-2327-B-255-001 and MOST 109-2327-B-182-002), Taiwan; Ministry of Education (EMRPD1G0231 and EMRPD1H0381), Kaohsiung Medical University (KMU-DK109002-3), Chang Gung University of Science and Technology (ZRRPF3H0101 and ZRRPF3H0111), and Chang Gung Memorial Hospital (CMRPF1F0011~3, CMRPF1F0061~3, CMRPF1G0241~3, CMRPF1J0051~3, and BMRP450), Taiwan.

**Acknowledgments:** The authors would like to thank the Head of the Department of the Ornamental plants, Senior Researcher of the M.M. Gryshko National Botanical Garden National Academy of Sciences of Ukraine (Kyiv), and Dr. Buidin for their help in the identification and characterization of the plants. The authors would like to thank the Center for Research Resources and Development, Kaohsiung Medical University for providing instrumentation support.

**Conflicts of Interest:** The authors declare no conflict of interest.

## Abbreviations

ABTS	2,2'-azino-bis (3-ethylbenzothiazoline-6-sulfonic acid) diammonium salt
CB	cytochalasin B
DMEM	Dulbecco's modified Eagle's medium
DMSO	dimethyl sulfoxide
DNP-BSA	dinitrophenyl-conjugated bovine serum albumin
FBS	fetal bovine serum
fMLF	formyl-methionyl-leucyl-phenylalanine
HPLC-DAD	high-performance liquid chromatography coupled with diode array detector
NRF2	nuclear factor erythroid 2-related factor 2
RBL	rat basophilic leukemia
UPLC-MS/MS	ultra-performance liquid chromatography coupled with tandem mass spectrometry

## References

1. Kruk, J.; Aboul-Enein, H.Y.; Kladna, A.; Bowser, J.E. Oxidative stress in biological systems and its relation with pathophysiological functions: The effect of physical activity on cellular redox homeostasis. *Free. Radic. Res.* **2019**, *53*, 497–521. [[CrossRef](#)]

2. Ahmadinejad, F.; Geir Moller, S.; Hashemzadeh-Chaleshtori, M.; Bidkhor, G.; Jami, M.S. Molecular mechanisms behind free radical scavengers function against oxidative stress. *Antioxidants* **2017**, *6*, 51. [CrossRef]
3. Paunkov, A.; Chartoumpekis, D.V.; Ziros, P.G.; Sykiotis, G.P. A bibliometric review of the Keap1/Nrf2 pathway and its related antioxidant compounds. *Antioxidants* **2019**, *8*, 353. [CrossRef]
4. Yang, S.C.; Chen, P.J.; Chang, S.H.; Weng, Y.T.; Chang, F.R.; Chang, K.Y.; Chen, C.Y.; Kao, T.I.; Hwang, T.L. Luteolin attenuates neutrophilic oxidative stress and inflammatory arthritis by inhibiting RAF1 activity. *Biochem. Pharmacol.* **2018**, *154*, 384–396. [CrossRef]
5. Nguyen, T.H.; Le, H.D.; Kim, T.N.T.; The, H.P.; Nguyen, T.M.; Cornet, V.; Lambert, J.; Kestemont, P. Anti-inflammatory and antioxidant properties of the ethanol extract of *Clerodendrum cyrtophyllum* Turcz in copper sulfate-induced inflammation in zebrafish. *Antioxidants* **2020**, *9*, 192. [CrossRef] [PubMed]
6. Xie, K.; He, X.; Chen, K.; Chen, J.; Sakao, K.; Hou, D.X. Antioxidant properties of a traditional vine tea, *Ampelopsis grossedentata*. *Antioxidants* **2019**, *8*, 295. [CrossRef] [PubMed]
7. The Plant List. Available online: <http://www.theplantlist.org/> (accessed on 22 February 2020).
8. Goldblatt, P.; Manning, J.C. *The Iris Family: Natural History and Classification*; Timber Press: Portland, OR, USA, 2008.
9. Panda, H. *The Complete Technology Book on Herbal Perfumes & Cosmetics*, 2nd ed.; NIIR Project Consultancy Services: Delhi, India, 2012.
10. Adams, M.; Berset, C.; Kessler, M.; Hamburger, M. Medicinal herbs for the treatment of rheumatic disorders—A survey of European herbals from the 16th and 17th century. *J. Ethnopharmacol.* **2009**, *121*, 343–359. [CrossRef] [PubMed]
11. Lim, T.K. *Iris Germanica. Edible Medicinal and Non-Medicinal Plants: Vol. 11, Modified Stems, Roots, Bulbs*; Springer International Publishing: Cham, Switzerland, 2016.
12. Singab, A.N.B.; Ayoub, I.M.; El-Shazly, M.; Korinek, M.; Wu, T.-Y.; Cheng, Y.-B.; Chang, F.-R.; Wu, Y.-C. Shedding the light on Iridaceae: Ethnobotany, phytochemistry and biological activity. *Ind. Crops Prod.* **2016**, *92*, 308–335. [CrossRef]
13. Mykhailenko, O.O.; Kovalyov, V.M.; Kovalyov, S.V.; Krechun, A.V. Biologically active compounds from the rhizomes of *Iris hungarica*. *J. Org. Pharm. Chem.* **2016**, *14*, 4. [CrossRef]
14. Wang, H.; Cui, Y.; Zhao, C. Flavonoids of the genus *Iris* (Iridaceae). *Mini Rev. Med. Chem.* **2010**, *10*, 643–661. [CrossRef] [PubMed]
15. Nazir, N.; Koul, S.; Qurishi, M.A.; Taneja, S.C.; Ahmad, S.F.; Khan, B.; Bani, S.; Qazi, G.N. Immunomodulatory activity of isoflavones isolated from *Iris germanica* (Iridaceae) on T-lymphocytes and cytokines. *Phytother. Res.* **2009**, *23*, 428–433. [CrossRef] [PubMed]
16. Orhan, I.; Nasim, S.; Sener, B.; Ayanoglu, F.; Ozguven, M.; Choudhary, M.I.; ur-Rahman, A. Two isoflavones and bioactivity spectrum of the crude extracts of *Iris germanica* rhizomes. *Phytother. Res.* **2003**, *17*, 575–577. [CrossRef] [PubMed]
17. Seidlová-Wuttke, D.; Hesse, O.; Jarry, H.; Rimoldi, G.; Thelen, P.; Christoffel, V.; Wuttke, W. *Belamcanda chinensis* and the thereof purified tectorigenin have selective estrogen receptor modulator activities. *Phytomedicine* **2004**, *11*, 392–403. [CrossRef] [PubMed]
18. Kim, J.L.; Li, H.M.; Kim, Y.H.; Lee, Y.J.; Shim, J.H.; Lim, S.S.; Kang, Y.H. Osteogenic activity of yellow flag iris (*Iris pseudacorus*) extract modulating differentiation of osteoblasts and osteoclasts. *Am. J. Chin. Med.* **2012**, *40*, 1289–1305. [CrossRef]
19. Moein, M.R.; Khan, S.I.; Ali, Z.; Ayatollahi, S.A.; Kobarfard, F.; Nasim, S.; Choudhary, M.I.; Khan, I.A. Flavonoids from *Iris songarica* and their antioxidant and estrogenic activity. *Planta Med.* **2008**, *74*, 1492–1495. [CrossRef]
20. Huwaitat, S.; Al-Khateeb, E.; Finjan, S.; Maraqa, A. Antioxidant and antimicrobial activities of *Iris nigricans* methanolic extracts containing phenolic compounds. *Eur. Sci. J.* **2013**, *9*, 83–91.
21. Basgedik, B.; Ugur, A.; Sarac, N. Antimicrobial, antioxidant, antimutagenic activities, and phenolic compounds of *Iris germanica*. *Ind. Crops Prod.* **2014**, *61*, 526–530. [CrossRef]
22. Sofiane, G.; Wafab, N.; Loubna, A. Evaluation of antioxidant and antifungal activities of methanolic aerial part extract of *Iris unguicularis* Poiret. *Asian J. Plant Sci. Res.* **2016**, *6*, 18–23.

23. Ochensberger, S.; Alperth, F.; Mitic, B.; Kunert, O.; Mayer, S.; Mourao, M.F.; Turek, I.; Luca, S.V.; Skalicka-Wozniak, K.; Males, Z.; et al. Phenolic compounds of *Iris adriatica* and their antimycobacterial effects. *Acta. Pharm.* **2019**, *69*, 673–681. [[CrossRef](#)]
24. Hacıbekiroğlu, I.; Kolak, U. Screening antioxidant and anticholinesterase potential of *Iris albicans* extracts. *Arab. J. Chem.* **2015**, *8*, 264–268. [[CrossRef](#)]
25. Wollenweber, E.; Stevens, J.F.; Klimo, K.; Knauf, J.; Frank, N.; Gerhauser, C. Cancer chemopreventive in vitro activities of isoflavones isolated from *Iris germanica*. *Planta Med.* **2003**, *69*, 15–20. [[CrossRef](#)] [[PubMed](#)]
26. Choudhary, D.; Alam, A. Pharmacology and phytochemistry of isoflavonoids from *Iris* species. *J. Pharmacol. Clin. Res.* **2017**, *3*, 1–6.
27. Xie, G.Y.; Zhu, Y.; Shu, P.; Qin, X.Y.; Wu, G.; Wang, Q.; Qin, M.J. Phenolic metabolite profiles and antioxidants assay of three Iridaceae medicinal plants for traditional Chinese medicine "She-gan" by on-line HPLC-DAD coupled with chemiluminescence (CL) and ESI-Q-TOF-MS/MS. *J. Pharm. Biomed. Anal.* **2014**, *98*, 40–51. [[CrossRef](#)] [[PubMed](#)]
28. Kostic, A.Z.; Gasic, U.M.; Pesic, M.B.; Stanojevic, S.P.; Barac, M.B.; Macukanovic-Jocic, M.P.; Avramov, S.N.; Tesic, Z.L. Phytochemical analysis and total antioxidant capacity of rhizome, above-ground vegetative parts and flower of three *Iris* species. *Chem. Biodivers.* **2019**, *16*, e1800565. [[CrossRef](#)]
29. Bisognin, D.A.; Luz, L.V.d.; Lencina, K.H.; Santos, C.O.d.; Sautter, C.K. Contents of total phenolics and flavonoids in and antioxidant activity of *Ilex paraguariensis* leaves. *Pesqui. Agropecu. Bras.* **2019**, *54*. [[CrossRef](#)]
30. Wu, Z.; Ren, S.; Chen, T.; Hui, A.; Zhang, W. Separation and purification of six isoflavones from *Iris tectorum* Maxim by macroporous resin-based column chromatography coupled with preparative high-performance liquid chromatography. *Sep. Sci. Technol.* **2020**, *55*, 1686–1694. [[CrossRef](#)]
31. Alam, A.; Jaiswal, V.; Akhtar, S.; Jayashree, B.S.; Dhar, K.L. Isolation of isoflavones from *Iris kashmiriana* Baker as potential anti proliferative agents targeting NF-kappaB. *Phytochemistry* **2017**, *136*, 70–80. [[CrossRef](#)]
32. Huwaitat, S.; Al-Khateeb, E.; Finjan, S. Isolation and identification of some phytochemical compounds from different parts of *Iris nigricans*. *Eur. Sci. J.* **2013**, *9*, 213–218.
33. Conforti, F.; Menichini, F.; Rigano, D.; Senatore, F. Antiproliferative activity on human cancer cell lines after treatment with polyphenolic compounds isolated from *Iris pseudopumila* flowers and rhizomes. *Z. Naturforsch. C J. Biosci.* **2009**, *64*, 490–494. [[CrossRef](#)]
34. Blicharski, T.; Oniszczuk, A. Extraction methods for the isolation of isoflavonoids from plant material. *Open Chem.* **2017**, *15*, 34–45. [[CrossRef](#)]
35. Kukula-Koch, W.; Sieniawska, E.; Widelski, J.; Urjin, O.; Glowniak, P.; Skalicka-Wozniak, K. Major secondary metabolites of *Iris* spp. *Phytochem. Rev.* **2015**, *14*, 51–80. [[CrossRef](#)]
36. Kumar, S.; Singh, A.; Kumar, B. Identification and characterization of phenolics and terpenoids from ethanolic extracts of *Phyllanthus* species by HPLC-ESI-QTOF-MS/MS. *J. Pharm. Anal.* **2017**, *7*, 214–222. [[CrossRef](#)] [[PubMed](#)]
37. Gouveia-Figueira, S.C.; Castilho, P.C. Phenolic screening by HPLC–DAD–ESI/MS<sup>n</sup> and antioxidant capacity of leaves, flowers and berries of *Rubus grandifolius* Lowe. *Ind. Crops Prod.* **2015**, *73*, 28–40. [[CrossRef](#)]
38. Bhat, G.; Shawl, A.S.; Shah, Z.; Tantry, M. HPLC-DAD-ESI-MS/MS identification and characterization of major constituents of *Iris crocea*, *Iris germanica* and *Iris spuria* growing in Kashmir Himalayas, India. *J. Anal. Bioanal. Tech.* **2014**, *5*, 1000223. [[CrossRef](#)]
39. Sajad, H.W.; Amin, A.; Sofi, S.N.; Mokhdomi, T.A.; Bukhari, S.; Hassan, Q.P.; Shoiab, B.; Qazi, P.H.; Raies, A.Q. RP-HPLC facilitated quantitative analysis of tectorigenin in the different species of *Iris* plant and evaluation of its in vitro anticancer potential. *Int. J. Curr. Res.* **2013**, *5*, 206–211.
40. Shu, P.; Hong, J.-L.; Wu, G.; Yu, B.-Y.; Qin, M.-J. Analysis of flavonoids and phenolic acids in *Iris tectorum* by HPLC-DAD-ESI-MS<sup>n</sup>. *Chin. J. Nat. Med.* **2010**, *8*, 202–207. [[CrossRef](#)]
41. Wei, Y.; Shu, P.; Hong, J.; Qin, M. Qualitative and quantitative evaluation of phenolic compounds in *Iris dichotoma* Pall. *Phytochem. Anal.* **2012**, *23*, 197–207. [[CrossRef](#)]
42. Li, M.; Hou, X.F.; Zhang, J.; Wang, S.C.; Fu, Q.; He, L.C. Applications of HPLC/MS in the analysis of traditional Chinese medicines. *J. Pharm. Anal.* **2011**, *1*, 81–91. [[CrossRef](#)]
43. Alperth, F.; Mitic, B.; Mayer, S.; Males, Z.; Kunert, O.; Hrusevar, D.; Bucar, F. Metabolic profiling of rhizomes of native populations of the strictly endemic Croatian species *Iris adriatica*. *Plant Biosyst.* **2019**, *153*, 317–324. [[CrossRef](#)]
44. Boligon, A.A.; Athayde, M.L. Importance of HPLC in analysis of plants extracts. *Austin Chromatogr.* **2014**, *1*, 2.

45. Isaey, D.I.; Cerimov, Y.B.; Kovalyov, S.V.; Zatylnikova, O.A. Isoflavones of the rhizomes of *Iris imbricata* and *Iris pseudacorus*. *Farmacom* **2010**, *1*, 38–42.
46. Kovalev, V.N.; Zatylnikova, O.A.; Kovalev, S.V. A new isoflavone from *Iris pseudacorus*. *Chem. Nat. Compd.* **2013**, *49*, 34–35. [[CrossRef](#)]
47. Mykhailenko, O.; Kovalyov, V.; Kovalyov, S.; Krechun, A. Isoflavonoids from the rhizomes of *Iris hungarica* and antibacterial activity of the dry rhizomes extract. *Ars Pharm.* **2017**, *58*, 39–45.
48. Fabre, N.; Rustan, I.; de Hoffmann, E.; Quetin-Leclercq, J. Determination of flavone, flavonol, and flavanone aglycones by negative ion liquid chromatography electrospray ion trap mass spectrometry. *J. Am. Soc. Mass Spectrom.* **2001**, *12*, 707–715. [[CrossRef](#)]
49. Fernandes, F.H.; Salgado, H.R. Gallic acid: Review of the methods of determination and quantification. *Crit. Rev. Anal. Chem.* **2016**, *46*, 257–265. [[CrossRef](#)]
50. Rafiee, S.A.; Farhoosh, R.; Sharif, A. Antioxidant activity of gallic acid as affected by an extra carboxyl group than pyrogallol in various oxidative environments. *Eur. J. Lipid Sci. Technol.* **2018**, *120*, 1800319. [[CrossRef](#)]
51. Jiang, R.W.; Lau, K.M.; Hon, P.M.; Mak, T.C.; Woo, K.S.; Fung, K.P. Chemistry and biological activities of caffeic acid derivatives from *Salvia miltiorrhiza*. *Curr. Med. Chem.* **2005**, *12*, 237–246. [[CrossRef](#)]
52. Ru, W.; Pang, Y.; Gan, Y.; Liu, Q.; Bao, J. Phenolic compounds and antioxidant activities of potato cultivars with white, yellow, red and purple flesh. *Antioxidants* **2019**, *8*, 419. [[CrossRef](#)]
53. Mykhailenko, O.; Gudzinskas, Z.; Kovalyov, V.; Desenko, V.; Ivanauskas, L.; Bezruk, I.; Georgiyants, V. Effect of ecological factors on the accumulation of phenolic compounds in *Iris* species from Latvia, Lithuania and Ukraine. *Phytochem. Anal.* **2020**. [[CrossRef](#)]
54. Iwashina, T.; Otani, S. Flavonoids of the genus *Iris*: Structures, distribution and function (review). *Ann. Tsukuba Bot. Gard.* **1998**, *17*, 147–183.
55. Roger, B.; Jeannot, V.; Fernandez, X.; Cerantola, S.; Chahboun, J. Characterisation and quantification of flavonoids in *Iris germanica* L. and *Iris pallida* Lam. resinoids from Morocco. *Phytochem. Anal.* **2012**, *23*, 450–455. [[CrossRef](#)] [[PubMed](#)]
56. Zheng, M.S.; Lu, Z.Y. Antiviral effect of mangiferin and isomangiferin on herpes simplex virus. *Chin. Med. J.* **1990**, *103*, 160–165. [[PubMed](#)]
57. Rajendran, P.; Jayakumar, T.; Nishigaki, I.; Ekambaram, G.; Nishigaki, Y.; Vetriselvi, J.; Sakthisekaran, D. Immunomodulatory effect of mangiferin in experimental animals with benzo(a)pyrene-induced lung carcinogenesis. *Int. J. Biomed. Sci.* **2013**, *9*, 68–74. [[PubMed](#)]
58. Pan, J.; Yi, X.; Zhang, S.; Cheng, J.; Wang, Y.; Liu, C.; He, X. Bioactive phenolics from mango leaves (*Mangifera indica* L.). *Ind. Crops Prod.* **2018**, *111*, 400–406. [[CrossRef](#)]
59. Saha, S.; Sadhukhan, P.; Sil, P.C. Mangiferin: A xanthonoid with multipotent anti-inflammatory potential. *Biofactors* **2016**, *42*, 459–474. [[CrossRef](#)]
60. Zhu, Y.; Pu, B.Q.; Xie, G.Y.; Tian, M.; Xu, F.Y.; Qin, M.J. Dynamic changes of flavonoids contents in the different parts of rhizome of *Belamcanda chinensis* during the thermal drying process. *Molecules* **2014**, *19*, 10440–10454. [[CrossRef](#)]
61. Atta Ur, R.; Nasim, S.; Baig, I.; Ara Jahan, I.; Sener, B.; Orhan, I.; Choudhary, M.I. Isoflavonoid glycosides from the rhizomes of *Iris germanica*. *Chem. Pharm. Bull.* **2002**, *50*, 1100–1102. [[CrossRef](#)]
62. Xu, Z.; Meenu, M.; Chen, P.; Xu, B. Comparative study on phytochemical profiles and antioxidant capacities of chestnuts produced in different geographic area in China. *Antioxidants* **2020**, *9*, 190. [[CrossRef](#)]
63. Marksa, M.; Zymone, K.; Ivanauskas, L.; Radusiene, J.; Pukalskas, A.; Raudone, L. Antioxidant profiles of leaves and inflorescences of native, invasive and hybrid *Solidago* species. *Ind. Crops Prod.* **2020**, *145*, 112123. [[CrossRef](#)]
64. Liu, T.; Li, Z.; Li, R.; Cui, Y.; Zhao, Y.; Yu, Z. Composition analysis and antioxidant activities of the *Rhus typhina* L. stem. *J. Pharm. Anal.* **2019**, *9*, 332–338. [[CrossRef](#)]
65. Ksouda, G.; Hajji, M.; Sellimi, S.; Merlier, F.; Falcimaigne-Cordin, A.; Nasri, M.; Thomasset, B. A systematic comparison of 25 Tunisian plant species based on oil and phenolic contents, fatty acid composition and antioxidant activity. *Ind. Crops Prod.* **2018**, *123*, 768–778. [[CrossRef](#)]
66. Babbar, N.; Oberoi, H.S.; Sandhu, S.K. Therapeutic and nutraceutical potential of bioactive compounds extracted from fruit residues. *Crit. Rev. Food Sci. Nutr.* **2015**, *55*, 319–337. [[CrossRef](#)] [[PubMed](#)]
67. Vargas-Mendoza, N.; Morales-Gonzalez, A.; Madrigal-Santillan, E.O.; Madrigal-Bujaidar, E.; Alvarez-Gonzalez, I.; Garcia-Melo, L.F.; Anguiano-Robledo, L.; Fregoso-Aguilar, T.; Morales-Gonzalez, J.A.



- Antioxidant and adaptative response mediated by NRF2 during physical exercise. *Antioxidants* **2019**, *8*, 196. [CrossRef] [PubMed]
68. Molagoda, I.M.N.; Lee, K.T.; Choi, Y.H.; Kim, G.Y. Anthocyanins from *Hibiscus syriacus* L. inhibit oxidative stress-mediated apoptosis by activating the NRF2/HO-1 signaling pathway. *Antioxidants* **2020**, *9*, 42. [CrossRef]
  69. Chen, B.H.; Kilmon, M.A.; Ma, C.; Caven, T.H.; Chan-Li, Y.; Shelburne, A.E.; Tombes, R.M.; Roush, E.; Conrad, D.H. Temperature effect on IgE binding to CD23 versus FCεRI. *J. Immunol.* **2003**, *170*, 1839–1845. [CrossRef]
  70. Amin, A.; Wani, S.H.; Mokhdomi, T.A.; Bukhari, S.; Wafai, A.H.; Mir, J.I.; Hassan, Q.P.; Qadri, R.A. Investigating the pharmacological potential of *Iris kashmiriana* in limiting growth of epithelial tumors. *Pharmacogn. J.* **2013**, *5*, 170–175. [CrossRef]
  71. Lee, K.L.; Kuo, Y.C.; Ho, Y.S.; Huang, Y.H. Triple-negative breast cancer: Current understanding and future therapeutic breakthrough targeting cancer stemness. *Cancers* **2019**, *11*, 1334. [CrossRef]
  72. Yen, C.H.; Chang, H.S.; Yang, T.H.; Wang, S.F.; Wu, H.C.; Chen, Y.C.; Lin, K.J.; Wang, S. High-content screening of a taiwanese indigenous plant extract library identifies *Syzygium simile* leaf extract as an inhibitor of fatty acid uptake. *Int. J. Mol. Sci.* **2018**, *19*, 2130. [CrossRef]
  73. Rohwedder, A.; Zhang, Q.; Rudge, S.A.; Wakelam, M.J. Lipid droplet formation in response to oleic acid in Huh-7 cells is mediated by the fatty acid receptor FFAR4. *J. Cell Sci.* **2014**, *127*, 3104–3115. [CrossRef]
  74. Matsuda, D.; Namatame, I.; Ohshiro, T.; Ishibashi, S.; Omura, S.; Tomoda, H. Anti-atherosclerotic activity of triacsin C, an acyl-CoA synthetase inhibitor. *J. Antibiot.* **2008**, *61*, 318–321. [CrossRef]
  75. Zumla, A.; Chan, J.F.; Azhar, E.I.; Hui, D.S.; Yuen, K.Y. Coronaviruses-drug discovery and therapeutic options. *Nat. Rev. Drug Discov.* **2016**, *15*, 327–347. [CrossRef] [PubMed]
  76. Q2 (R1) Validation of Analytical Procedures: Text and Methodology. Available online: <https://www.fda.gov/regulatory-information/search-fda-guidance-documents/q2-r1-validation-analytical-procedures-text-and-methodology> (accessed on 22 February 2020).
  77. Marks, M.; Radusiene, J.; Jakstas, V.; Ivanauskas, L.; Marksiene, R. Development of an HPLC post-column antioxidant assay for *Solidago canadensis* radical scavengers. *Nat. Prod. Res.* **2016**, *30*, 536–543. [CrossRef] [PubMed]
  78. Chen, Y.S.; Lai, C.C.; Kuo, Y.P.; Chang, H.S.; Chen, I.S.; Yen, C.H. Identification of compound isolated from *Beilschmiedia tsangii* as a liver cancer specific NRF2 inhibitor. In: Proceedings of the American Association for Cancer Research Annual Meeting 2017; 2017 Apr 1–5; Washington, DC. Philadelphia (PA): AACR. *Cancer Res.* **2017**, *77*, Abstract nr 190.
  79. Marks, D.C.; Belov, L.; Davey, M.W.; Davey, R.A.; Kidman, A.D. The MTT cell viability assay for cytotoxicity testing in multidrug-resistant human leukemic cells. *Leuk. Res.* **1992**, *16*, 1165–1173. [CrossRef]
  80. Korinek, M.; Chen, K.M.; Jiang, Y.H.; El-Shazly, M.; Stocker, J.; Chou, C.K.; Hwang, T.L.; Wu, Y.C.; Chen, B.H.; Chang, F.R. Anti-allergic potential of *Typhonium blumei*: Inhibition of degranulation via suppression of PI3K/PLCγ2 phosphorylation and calcium influx. *Phytomedicine* **2016**, *23*, 1706–1715. [CrossRef] [PubMed]
  81. Chen, B.H.; Wu, P.Y.; Chen, K.M.; Fu, T.F.; Wang, H.M.; Chen, C.Y. Antiallergic potential on RBL-2H3 cells of some phenolic constituents of *Zingiber officinale* (ginger). *J. Nat. Prod.* **2009**, *72*, 950–953. [CrossRef]
  82. Ayoub, I.M.; Korinek, M.; Hwang, T.-L.; Chen, B.-H.; Chang, F.-R.; El-Shazly, M.; Singab, A.N.B. Probing the antiallergic and anti-inflammatory activity of biflavonoids and dihydroflavonols from *Dietes bicolor*. *J. Nat. Prod.* **2018**, *81*, 243–253. [CrossRef]
  83. Korinek, M.; Tsai, Y.H.; El-Shazly, M.; Lai, K.H.; Backlund, A.; Wu, S.F.; Lai, W.C.; Wu, T.Y.; Chen, S.L.; Wu, Y.C.; et al. Anti-allergic hydroxy fatty acids from *Typhonium blumei* explored through ChemGPS-NP. *Front. Pharmacol.* **2017**, *8*, 356. [CrossRef]
  84. Boyum, A. Isolation of mononuclear cells and granulocytes from human blood. Isolation of mononuclear cells by one centrifugation, and of granulocytes by combining centrifugation and sedimentation at 1 g. *Scand. J. Clin. Lab. Invest. Suppl.* **1968**, *97*, 77–89.
  85. Yang, S.C.; Chung, P.J.; Ho, C.M.; Kuo, C.Y.; Hung, M.F.; Huang, Y.T.; Chang, W.Y.; Chang, Y.W.; Chan, K.H.; Hwang, T.L. Propofol inhibits superoxide production, elastase release, and chemotaxis in formyl peptide-activated human neutrophils by blocking formyl peptide receptor 1. *J. Immunol.* **2013**, *190*, 6511–6519. [CrossRef]



86. Hwang, T.L.; Su, Y.C.; Chang, H.L.; Leu, Y.L.; Chung, P.J.; Kuo, L.M.; Chang, Y.J. Suppression of superoxide anion and elastase release by C18 unsaturated fatty acids in human neutrophils. *J. Lipid Res.* **2009**, *50*, 1395–1408. [[CrossRef](#)] [[PubMed](#)]
87. Ceponyte, U.; Paskeviciute, M.; Petrikaite, V. Comparison of NSAIDs activity in COX-2 expressing and non-expressing 2D and 3D pancreatic cancer cell cultures. *Cancer Manag. Res.* **2018**, *10*, 1543–1551. [[CrossRef](#)] [[PubMed](#)]
88. Hsieh, C.F.; Jheng, J.R.; Lin, G.H.; Chen, Y.L.; Ho, J.Y.; Liu, C.J.; Hsu, K.Y.; Chen, Y.S.; Chan, Y.F.; Yu, H.M.; et al. Rosmarinic acid exhibits broad anti-enterovirus A71 activity by inhibiting the interaction between the five-fold axis of capsid VP1 and cognate sulfated receptors. *Emerg. Microbes Infect.* **2020**, *9*, 1194–1205. [[CrossRef](#)] [[PubMed](#)]

**Sample Availability:** Samples of the compounds gallic acid, mangiferin, caffeic acid, tectoridin, germanaism B, irisolidone-7-O- $\beta$ -D-glucopyranoside, iristectorigenin B, nigricin, irigenin, 5,6-dihydroxy-7,8,3',5'-tetramethoxyisoflavone, and irisolidone are available from the authors.



© 2020 by the authors. Licensee MDPI, Basel, Switzerland. This article is an open access article distributed under the terms and conditions of the Creative Commons Attribution (CC BY) license (<http://creativecommons.org/licenses/by/4.0/>).



# Targeting Neutrophils to Treat Acute Respiratory Distress Syndrome in Coronavirus Disease

Chih-Chao Chiang<sup>1,2†</sup>, Michal Korinek<sup>3,4,5†</sup>, Wei-Jen Cheng<sup>1,6,7†</sup>  
and Tsong-Long Hwang<sup>3,4,6,8,9\*</sup>

<sup>1</sup> Graduate Institute of Clinical Medical Sciences, College of Medicine, Chang Gung University, Taoyuan, Taiwan, <sup>2</sup> Puxin Fengze Chinese Medicine Clinic, Taoyuan, Taiwan, <sup>3</sup> Graduate Institute of Natural Products, College of Medicine, Chang Gung University, Taoyuan, Taiwan, <sup>4</sup> Research Center for Chinese Herbal Medicine, Research Center for Food and Cosmetic Safety, and Graduate Institute of Health Industry Technology, Chang Gung University of Science and Technology, Taoyuan, Taiwan, <sup>5</sup> Department of Biotechnology, College of Life Science, Kaohsiung Medical University, Kaohsiung, Taiwan, <sup>6</sup> School of Traditional Chinese Medicine, College of Medicine, Chang Gung University, Taoyuan, Taiwan, <sup>7</sup> Center for Traditional Chinese Medicine, Chang Gung Memorial Hospital, Taoyuan, Taiwan, <sup>8</sup> Department of Anesthesiology, Chang Gung Memorial Hospital, Taoyuan, Taiwan, <sup>9</sup> Department of Chemical Engineering, Ming Chi University of Technology, New Taipei City, Taiwan

## OPEN ACCESS

### Edited by:

Siddappa N. Byreddy,  
University of Nebraska Omaha,  
United States

### Reviewed by:

Betsy J. Barnes,  
Feinstein Institute for Medical  
Research, United States  
Hitendra S. Chand,  
Florida International University,  
United States

### \*Correspondence:

Tsong-Long Hwang  
htl@mail.cgu.edu.tw

<sup>†</sup>These authors have contributed  
equally to this work

### Specialty section:

This article was submitted to  
Inflammation Pharmacology,  
a section of the journal  
Frontiers in Pharmacology

**Received:** 12 June 2020

**Accepted:** 11 September 2020

**Published:** 09 October 2020

### Citation:

Chiang C-C, Korinek M, Cheng W-J  
and Hwang T-L (2020) Targeting  
Neutrophils to Treat Acute  
Respiratory Distress Syndrome  
in Coronavirus Disease.  
*Front. Pharmacol.* 11:572009.  
doi: 10.3389/fphar.2020.572009

This review describes targeting neutrophils as a potential therapeutic strategy for acute respiratory distress syndrome (ARDS) associated with coronavirus disease 2019 (COVID-19), a pandemic caused by severe acute respiratory syndrome coronavirus 2 (SARS-CoV-2). Neutrophil counts are significantly elevated in patients with COVID-19 and significantly correlated with disease severity. The neutrophil-to-lymphocyte ratio can serve as a clinical marker for predicting fatal complications related to ARDS in patients with COVID-19. Neutrophil-associated inflammation plays a critical pathogenic role in ARDS. The effector functions of neutrophils, acting as respiratory burst oxidants, granule proteases, and neutrophil extracellular traps, are linked to the pathogenesis of ARDS. Hence, neutrophils can not only be used as pathogenic markers but also as candidate drug targets for COVID-19 associated ARDS.

**Keywords:** coronavirus disease 2019, severe acute respiratory syndrome coronavirus 2, acute respiratory distress syndrome, neutrophils, neutrophil extracellular trap

## INTRODUCTION

Severe acute respiratory syndrome coronavirus 2 (SARS-CoV-2), an enveloped, nonsegmented, positive-sense RNA  $\beta$ -coronavirus, is the cause of the ongoing coronavirus disease 2019 (COVID-19) pandemic (Guo et al., 2020). SARS-CoV-2 is primarily transmitted by respiratory droplets and airway secretions through close contact with infected individuals (Lee and Hsueh, 2020). The main manifestations of COVID-19 are fever, cough, dyspnea, sore throat, fatigue, diarrhea (Guan et al., 2020), headache, nausea, vomiting (Li Y. C. et al., 2020), anosmia (loss of smell), and ageusia (loss of taste) (Vaira et al., 2020). Severe complications include acute respiratory distress syndrome (ARDS), septic shock, coagulation dysfunction, and multiple organ failure (Wang et al., 2020). The elderly (>65 years of age) and individuals with underlying secondary diseases, such as chronic obstructive pulmonary disease (COPD), cardiovascular disease, hypertension, and diabetes mellitus, tend to

have severe complications and higher mortality rates (Yang et al., 2020). An effective therapy for COVID-19 remains under investigation (Lu, 2020).

Neutrophils are pivotal effector cells in the innate immune defense against infections in humans. Neutrophils migrate to infected tissues in multiple ways including rolling, adhesion, crawling, and transmigration. Subsequently, they are activated and exert inflammatory responses, such as phagocytosis, respiratory burst with superoxide anion production, degranulation with protease release, and NETosis with neutrophil extracellular trap (NET) formation (Liew and Kubes, 2019). Neutrophil inflammatory responses may be considered a double-edged sword; although they protect against infection, they also cause severe tissue damage. Activated neutrophils are involved in many acute and chronic inflammatory diseases as well as autoimmune disorders, such as respiratory diseases (ARDS, COPD, and asthma), cardiovascular diseases (atherosclerosis and thrombosis) (Németh et al., 2020), gastrointestinal diseases (inflammatory bowel disease and autoimmune hepatitis) (Honda and Kubes, 2018), neurological diseases (multiple sclerosis and Alzheimer's disease) (Dong et al., 2018; Woodberry et al., 2018), skin diseases (psoriasis and Behçet's disease) (Safi et al., 2018; Chiang et al., 2019), and metabolic diseases (diabetes mellitus and obesity) (Talukdar et al., 2012; Brotfain et al., 2015).

During the incubation period and nonsevere stage of COVID-19, the host immune system successfully destroys the virus and protects against disease progression. However, in the severe stage, SARS-CoV-2 replicates rapidly and causes massive tissue damage, particularly in the lungs. Thereafter, the destroyed cells cause a dysregulated inflammatory response and cytokine storm, leading to ARDS and other severe complications (Shi H. et al., 2020). Therefore, therapeutic strategies targeting hyperactivated neutrophils may be useful for treating COVID-19 associated ARDS. It has been suggested that a combination of antiviral and anti-inflammatory therapies effectively inhibit SARS-CoV-2 activity and reduce dysregulated immune reactions in COVID-19 (Stebbing et al., 2020).

In this review, we describe the roles of neutrophils in COVID-19 associated ARDS and provide an overview of suitable therapeutic strategies for targeting neutrophils. The particular focus is on clinical drugs and clinical trial drugs shown to affect neutrophil function (Table 1).

## GENERAL CHARACTERISTICS OF COVID-19 ASSOCIATED ARDS

ARDS is a critical noncardiogenic pulmonary edema caused by alveolar infection or inflammation. Patients who develop ARDS suffer from a series of nonspecific manifestations, such as cough, shortness of breath, dyspnea, tachycardia, or cyanosis of the nail bed (Sweeney and Mcauley, 2016). If respiratory failure occurs, patients require endotracheal intubation and mechanical ventilation. The mortality rate is approximately 30%–40% (Stevens et al., 2018). ARDS is diagnosed using the Berlin

criteria, i.e., acute onset or worsening within one week, bilateral lung infiltrates upon chest X-ray or computed tomography scan, origin exclusive of heart failure or volume overload, disease severity based on desaturation values (severe: arterial oxygen tension/inspired oxygen fraction ( $\text{PaO}_2/\text{FiO}_2$ )  $\leq 100$  mmHg, moderate:  $\text{PaO}_2/\text{FiO}_2$  100 to  $\leq 200$  mmHg, and mild:  $\text{PaO}_2/\text{FiO}_2$  200 to  $\leq 300$  mmHg), and minimum positive end-expiratory pressure (PEEP) of 5 cm  $\text{H}_2\text{O}$  for mechanical ventilation (Figure 1) (Ranieri et al., 2012). Patients with pneumonia, sepsis, gastric aspiration, or chest trauma may readily develop ARDS. Respiratory viruses, such as influenza virus, Middle East respiratory syndrome-related coronavirus (MERS), SARS-CoV, rhinovirus, respiratory syncytial virus, parainfluenza virus, human metapneumovirus, and adenoviruses may cause viral pneumonia and severe ARDS (Shah and Wunderink, 2017). SARS-CoV-2 emerged in 2019 and caused the COVID-19 outbreak. Patients with COVID-19 may experience lethal pneumonia and ARDS (Badraoui et al., 2020; Zhou P. et al., 2020). Matthay et al. provided a list of recommended treatments for patients with ARDS caused by COVID-19 including adjustment of the tidal volume to 6 ml/kg predicted weight, maintenance of the plateau airway pressure at  $<30$  cm  $\text{H}_2\text{O}$ , neuromuscular blockade for patient-ventilator dyssynchrony, maintenance of a prone position during ventilation for severe ARDS, maintenance of a negative fluid balance of 0.5–1.0 L/day, and antibiotic administration for secondary bacterial and fungal infections (Matthay et al., 2020). Extracorporeal membrane oxygenation (ECMO) for ARDS related to COVID-19 requires careful patient selection, intensive care, and secondary infection prevention to rescue lung injury in severe cases of ARDS (Mi et al., 2018; Ramanathan et al., 2020).

## CONTRIBUTION OF NEUTROPHILS TO COVID-19 ASSOCIATED ARDS

SARS-CoV-2 employs human angiotensin-converting enzyme 2 (hACE2) as an entry receptor for invading host (Zhou P. et al., 2020). The hACE2 receptor is abundant in the respiratory airway, blood vessels, kidney, and intestine (Li Y. C. et al., 2020). Viral RNAs serve as pathogen-associated molecular patterns (PAMPs) and are sensed by Toll-like receptors (TLRs) such as TLR3, TLR7, TLR8, and TLR9. This results in the production of interferon  $\alpha$  and  $\beta$ , along with various proinflammatory cytokines (Kawai and Akira, 2010). Lung inflammation initiated by proinflammatory macrophages and neutrophils causes ARDS, a critical issue in the severe form of COVID-19 (Shi H. et al., 2020). Patients with severe COVID-19 exhibit dysregulated immune responses, such as decreased lymphocyte levels, but increased neutrophil levels (Qin et al., 2020). The neutrophil count in patients with pneumonia was found higher than in patients with only mild acute respiratory disease related to COVID-19 (Lai et al., 2020). The remarkably elevated neutrophil count was found to serve as a marker for poor prognosis in a retrospective review of 25 deaths related to

TABLE 1 | Drugs targeting neutrophils.

Drug	Neutrophil Target	Clinical Stage	Approved Indication (Approved target)	Clinical Trial (Disease, Phase)	Clinical Trial for COVID-19 (Phase) <sup>1</sup>	Reference
<b>Sivelestat (Elaspol, ONO 5046)</b>	<b>NE</b>	Korea and Japan-approved	Acute lung injury, ARDS (elastase)			(Aikawa and Kawasaki, 2014)
<b>Alvelestat (AZD9668)</b>	<b>NE</b>	Clinical trial		NCT03636347 (COPD, phase 2)		(Barnes et al., 2020)
<b>BAY 85-8501</b>	<b>NE</b>	Clinical trial		NCT01818544 (non-CF bronchiectasis, phase 2)		(Watz et al., 2019)
<b>Lonolestat (POL6014)</b>	<b>NE</b>	Clinical trial		NCT03748199 (CF, phase 1)		(Barth et al., 2020)
<b>CHF6333</b>	<b>NE</b>	Clinical trial		NCT03056326, NCT04010799 (non-CF bronchiectasis, phase 1)		(Gramaglia et al., 2017)
<b>Elafin</b>	<b>NE</b>	Clinical trial		NCT02944279 (ARDS, phase 1)		(Barnes et al., 2020)
<b>N-Acetylcysteine</b>	<b>Respiratory burst and ROS</b>	FDA-approved	Mucolytic (glutathione synthetase)		NCT04419025 (phase 4) NCT04455243 (phase 3) NCT04374461 (phase 2) and 3 more EudraCT 2020-001643-13 (phase 3)	(Allegra et al., 2002; Zhang et al., 2017; Andreou et al., 2020)
<b>Brensocatib (AZD7986)</b>	<b>DPP1</b>	Clinical trial		NCT03218917 (non-CF bronchiectasis, phase 2)		(Palmer et al., 2018)
<b>Dipyridamole</b>	<b>PDEs</b>	FDA-approved	Prevention of postoperative thromboembolism, stroke (PDEs, adenosine receptor)		NCT04410328 (phase 3) NCT04424901 (phase 2) NCT04391179 (phase 2) NCT04433988 (phase 1 and 2)	(Ali et al., 2019; Liu et al., 2020)
<b>Pentoxifylline</b>	<b>PDEs</b>	FDA-approved	Blood flow (PDEs, adenosine receptor)			(Hendry et al., 2020)
<b>Roflumilast</b>	<b>PDE4</b>	FDA-approved	COPD (PDE4)			(Phillips, 2020)
<b>Apremilast</b>	<b>PDE4</b>	FDA-approved	Psoriasis		NCT04488081 (phase 2)	(Queiro Silva et al., 2020)
<b>CHF6001</b>	<b>PDE4</b>	Clinical trial		NCT02986321 (COPD, phase 2), NCT01689571 (asthma, phase 2)		(Singh et al., 2019; Phillips, 2020)
<b>Crisaborole</b>	<b>PDE4</b>	FDA-approved	Atopic dermatitis			(Hashim et al., 2020)
<b>Enfisentrine (RPL554)</b>	<b>PDE4</b>	Clinical trial		NCT04027439 (COPD, phase 2)		(Cazzola et al., 2019)
<b>Disulfiram</b>	<b>GSDMD (NETs)</b>	FDA-approved	Chronic alcoholism (aldehyde dehydrogenase)		NCT04485130 (phase 2)	(Lobo-Galo et al., 2020)
<b>Dornase alfa (Pulmozyme, rhDNase I)</b>	<b>DNase (NETs)</b>	FDA-approved	CF (DNA)		NCT04402970 (phase 3) NCT04359654 (phase 2) NCT04355364 (phase 3) EudraCT 2020-001492-33 (phase 3) and 5 more	(Weber et al., 2020)

(Continued)

TABLE 1 | Continued

Drug	Neutrophil Target	Clinical Stage	Approved Indication (Approved target)	Clinical Trial (Disease, Phase)	Clinical Trial for COVID-19 (Phase) <sup>1</sup>	Reference
<b>BMS-986253 (Humax IL-8)</b>	<b>IL-8</b> (mAb)	Clinical trial		NCT03400332 (cancer, phase 1 and 2)	NCT04347226 (phase 2)	(Bilusic et al., 2019)
<b>AZD5069</b>	<b>CXCR2</b> (receptor for IL-8)	Clinical trial		NCT01255592 (bronchiectasis, phase 2)		(Nicholls et al., 2015; Cullberg et al., 2018)
<b>Danirixin (GSK1325756)</b>	<b>CXCR2</b> (receptor for IL-8)	Clinical trial		NCT03034967 (COPD, phase 2)		(Madan et al., 2019; Barth et al., 2020; Lazaar et al., 2020)
<b>Navarixin (SCH527123)</b>	<b>CXCR2</b> (receptor for IL-8)	Clinical trial		NCT00688467 (allergen-induced asthma, phase 2)		(Holz et al., 2010; Todd et al., 2016)
<b>Ixekizumab</b>	<b>IL-17A</b> (mAb)	FDA-approved	Psoriasis (IL-17A)			(Bulat et al., 2020)
<b>Secukinumab</b>	<b>IL-17A</b> (mAb)	FDA-approved	Autoimmune diseases, RA, and psoriasis (IL-17A)		NCT04403243 (phase 2) EudraCT 2020-001246-18 (phase 4)	(Bulat et al., 2020)
<b>Brodalumab</b>	<b>IL-17A receptor</b> (mAb)	FDA-approved	Autoimmune diseases, RA, and psoriasis (IL-17A receptor)			(Bulat et al., 2020)
<b>Anakinra</b>	<b>IL-1 receptor</b> (mAb)	FDA-approved	Autoimmune diseases (IL-1)		NCT04330638 (phase 3) NCT04364009 (phase 3) EudraCT 2020-001963-10 (phase 3) and 14 more	(Van De Veerdonk and Netea, 2020)
<b>Canakinumab</b>	<b>IL-1<math>\beta</math></b> (mAb)	FDA-approved	Autoimmune diseases (IL-1)		NCT04362813 (phase 3) EudraCT 2020-001370-30 (phase 3) and 4 more	(Prieto-Peña and Dasgupta, 2020)
<b>Rilonacept</b>	<b>IL-1<math>\beta</math></b> (mAb)	FDA-approved	Autoimmune diseases (IL-1)			(Prieto-Peña and Dasgupta, 2020)
<b>Tocilizumab</b>	<b>IL-6 receptor</b> (mAb)	FDA-approved	Autoimmune diseases (IL-6 receptor)		NCT04317092 (phase 2) NCT04320615 (phase 3) EudraCT 2020-001903-17 (phase 3) and 38 more	(Guaraldi et al., 2020)
<b>Sarilumab (Kevzara)</b>	<b>IL-6 receptor</b> (mAb)	FDA-approved	RA (IL-6 receptor)		NCT04315298 (phase 2 and 3) EudraCT 2020-001531-27 (phase 2) and 10 more	(Lu et al., 2020)

<sup>1</sup>Updated on 1<sup>st</sup> September 2020 via <https://clinicaltrials.gov> (US national clinical trials) and <https://www.clinicaltrialsregister.eu> (EU clinical trials). Additional completed or ongoing clinical trial studies in COVID-19 using the drug as main intervention are indicated. ARDS, acute respiratory distress syndrome; CF, cystic fibrosis; COPD, chronic obstructive pulmonary disease; CXCR2, chemokine receptor 2; DPP1, dipeptidyl peptidase 1; GSDMD, gasdermin D; IL, interleukin; mAb, monoclonal antibody; NE, neutrophil elastase; NET, neutrophil extracellular trap; PDE, phosphodiesterase; RA, rheumatic arthritis; ROS, reactive oxygen species.



## Targeting neutrophils for COVID-19 associated ARDS

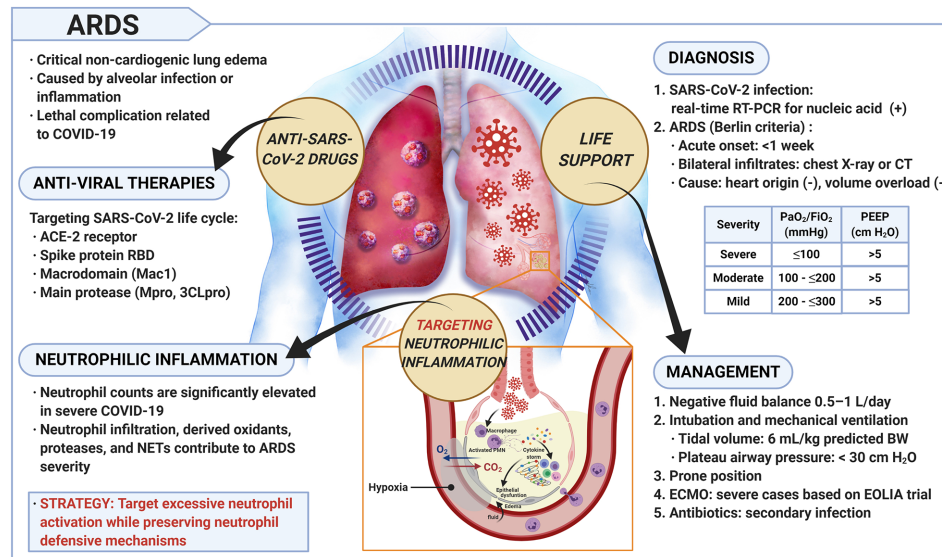


**FIGURE 1 |** Targeting neutrophils for COVID-19 associated ARDS. Precise diagnosis of SARS-CoV-2 infection and effective management of COVID-19 are important. Application of antiviral therapy together with suppression of overly active neutrophilic inflammation appears to be a promising strategy for treating patients with COVID-19 associated ARDS. ARDS, acute respiratory distress syndrome; BW, body weight; COVID-19, coronavirus disease 2019; CT, computed tomography; ECMO, extracorporeal membrane oxygenation; EOLIA, ECMO to rescue lung injury in severe ARDS; FIO<sub>2</sub>, inspired oxygen fraction; ACE2, angiotensin-converting enzyme 2; NET, neutrophil extracellular trap; PaO<sub>2</sub>, arterial oxygen tension; PEEP, positive end-expiratory pressure; PMN, polymorphonuclear leukocyte; RBD, receptor binding domain; RT-PCR, reverse transcription polymerase chain reaction; SARS-CoV-2, severe acute respiratory syndrome coronavirus 2.

SARS-CoV-2 (Li X. et al., 2020). In another retrospective analysis of 95 patients with COVID-19, an increased neutrophil count was related to disease severity and reflected an overt inflammatory response causing complications (Zhang et al., 2020). The neutrophil-to-lymphocyte ratio was significantly elevated in patients with severe COVID-19 based on a meta-analysis. Furthermore, this ratio could be used as a marker for predicting whether more severe complications such as ARDS would arise (Lagunas-Rangel, 2020). Finally, neutrophils are suggested as a target for immunopathologic complications in severe COVID-19 patients (Tomar et al., 2020). The elevated neutrophil count in COVID-19 patients and its significant correlation with disease severity indicates the importance of neutrophils in the management of COVID-19. The elevated neutrophil count is not only an abnormal laboratory finding but also a characteristic feature that should be further evaluated to develop treatments for patients infected with SARS-CoV-2.

Cellular invasion of SARS-CoV-2 reduces hACE2 expression, thereby promoting the recruitment of neutrophils (Tomar et al., 2020). Possible strategies for developing anti-SARS-CoV-2 drugs include targeting the ACE2 receptor, the spike (S) protein receptor binding domain, the macrodomain (Mac1), and the main protease (Mpro, 3CLpro) (Alhammad et al., 2020; Ton et al., 2020; Zhu et al., 2020). Neutrophils were widespread in the alveoli in COVID-19 patients (Zuo et al., 2020). In rats, excessive neutrophil migration to the lungs caused severe lung hemorrhage and increased microvascular permeability. Therefore,

neutrophils participate in viral clearance while contributing to pathological symptoms in rat respiratory coronavirus infection (Haick et al., 2014). Moreover, neutrophils play a pivotal role in the cytokine storm (Tisoncik et al., 2012). In COVID-19 patients, neutrophils secrete interleukin (IL)-6 via a TLR8-mediated mechanism leading to a cytokine storm and subsequent lung damage (Mohamed et al., 2020). IL-1 $\beta$  and NETs form a feedback loop, which contribute to the pathogenesis of ARDS in COVID-19 patients (Yaqinuddin and Kashir, 2020). SARS-CoV-2 may invade nerves and aggravate respiratory failure (Li Y.C. et al., 2020). Neutrophil reactive oxygen species (ROS) and NETs participate in demyelination of the central neural system in mice with neurological diseases and coronavirus infection (Cheng et al., 2019). Therefore, treatments targeting excessive neutrophil activation may improve pathological neutrophilic inflammation during COVID-19 infection complicated by ARDS and nerve invasion.

## TARGETING NEUTROPHILS MAY IMPROVE THE TREATMENT OF ARDS CAUSED BY SARS-COV-2 INFECTION

Neutrophil infiltration is the defining hallmark of ARDS (Zemans and Matthay, 2017). Elevated neutrophils and neutrophil-derived microparticles are found in bronchoalveolar

lavage fluid from patients with ARDS (Nakos et al., 1998; Guervilly et al., 2011). In ARDS patients, macrophages secrete CXCL8 (IL-8) to activate a circulating neutrophil recruitment cascade *via* C-X-C chemokine receptor 1 (CXCR1) receptors. CXCL8 levels are also correlated with the severity and outcome of ARDS (Miller et al., 1992; Groeneveld et al., 1995). CXC chemokines including CXCL1/2, CXCL8, CXCL5, CXCL12, and CXCL15 are responsible for neutrophil recruitment to the lungs during lung injury. However, their blockade would not completely prevent neutrophil recruitment, which indicates a rather complicated mechanism operating during immune activation (Zemans and Matthay, 2017). The SARS-CoV S protein stimulates lung epithelial cells to release IL-8 *via* activation of MAPK and AP-1, the IL-8 promoter (Chang et al., 2004). Epithelial membrane protein 2 (Emp2) of alveolar epithelial type 1 cells is important for the regulation of neutrophil migration in ARDS. Emp2 knock-out mice displayed decreased neutrophil influx to the lungs and an improved survival rate of bacterial pneumonia (Lin et al., 2020). Therefore, anti-EMP2 diabodies may be helpful in treating ARDS by mitigating neutrophil infiltration. Moreover, CCL2 (monocyte chemoattractant protein-1, MCP-1) and CCL7 are increased in the lungs of patients with ARDS (Bhatia et al., 2012; Mercer et al., 2014). Extravasated neutrophils exhibit elevated CCL2 and CCL7 binding to CCR2 receptors. Proteinase-activated receptors (PARs) are present on epithelial cells, monocytes, macrophages, and vascular endothelial cells, and their activation leads to the release of proinflammatory mediators including the cytokines TNF, IL-1 $\beta$ , IL-2, and IL-6, and the chemokines CXCL8 (IL-8) and CCL2, all of which are associated with ARDS pathogenesis. Modulating the CC chemokine response *via* antagonism of PAR1 signaling or by blocking these chemokines directly, may represent a treatment model for excessive neutrophilia and tissue damage associated with ARDS (Mercer et al., 2014). The level of neutrophil-derived calprotectin, along with other acute inflammatory markers, is correlated with pulmonary severity caused by SARS-CoV-2, which indicates that neutrophils are drivers of the thrombo-inflammatory storm, not just bystanders (Shi Y. et al., 2020). Mitochondrial formyl peptides are elevated in ARDS patients (Dorward et al., 2017) and formyl peptides are known to drive neutrophils in ARDS. Formyl peptide receptors (FPRs) play an important role in the activation of neutrophils (Yang and Hwang, 2016; Chen et al., 2017), and FPR-1 expression is elevated in lung injury and fibrosis (Leslie et al., 2020). Several FPR1 antagonists were discovered previously in our lab including the clinical drug propofol (Yang et al., 2013; Liu et al., 2017; Yang et al., 2017; Chen et al., 2018) that may have potential in the development of the treatment for COVID-19 associated ARDS.

NETs are composed of sticky chromatin decorated with various granular components (Zawrotniak and Rapala-Kozik, 2013). Interestingly, sputum viscosity is correlated with the level of NETs (Papayannopoulos et al., 2011; Manzenreiter et al., 2012). Mucokinetic drugs that preserve viscoelasticity, not

mucolytics, were recommended for the management of cystic fibrosis (Henke and Ratjen, 2007). This could also be applied to ARDS in COVID-19 patients. NET level was found related to the polarization of proinflammatory M1 macrophages in ARDS patients; furthermore, NET inhibitors repressed NET formation and reduced M1 macrophage markers in a mouse model of acute lung injury (Song et al., 2019). Phagocytosis of NETs by macrophages is impaired in ARDS (Grégoire et al., 2018). Activation of the AMP-activated protein kinase (AMPK) pathway stimulates macrophage efferocytosis (Bae et al., 2011). Therefore, drugs interacting with AMPK, such as metformin, may reduce ARDS severity (Grégoire et al., 2018). Moreover, NET levels in the plasma are known to be correlated with ARDS mortality (Lefrançois et al., 2018). NETs consist of neutrophil-extruded DNA coated with histones, neutrophil elastase (NE), and myeloperoxidase (MPO). Peptidylarginine deiminase 4 (PAD4), NE, and gasdermin D along with free DNA, all participate in the NET formation (Nathan, 2020). NETs are prevalent in blood, trachea, and lung specimens of COVID-19 patients (Veras et al., 2020). Moreover, SARS-CoV-2 stimulates neutrophils from healthy donors into forming NETs, which can cause apoptosis in respiratory epithelial cells *in vitro* (Oubihi and Wang, 2020). High levels of plasma MPO-DNA complex and aberrant NET formation are correlated with severe ARDS in COVID-19 (Middleton et al., 2020; Zuo et al., 2020). Also, elevated levels of cell-free DNA were observed in COVID-19 patients (n = 50), as well as highly specific markers of NETs, such as MPO-DNA and citrullinated histone H3 (Cit-H3), along with other typical markers (C-reactive protein, D-dimer, neutrophil count, etc.) (Zuo et al., 2020). NETs contributed to microthrombi through platelet-neutrophil interactions in COVID-19 associated ARDS, and neonatal NET-Inhibitory Factor (nNIF) could block NET formation induced by COVID-19 plasma. This represents a potential therapeutic intervention for COVID-19 (Middleton et al., 2020). PAD4 is a predominant driver of histone citrullination in NETs (Wong and Wagner, 2018). Currently, several PAD4 inhibitors were demonstrated to inhibit NET formation *in vitro*. Among them, Cl-amidine (Kusunoki et al., 2016), GSK484 (Lewis et al., 2015), and BMS-P5 (Li M. et al., 2020) may have future development potential. Therefore, inhibition of neutrophil activation and NET formation may be beneficial in COVID-19-associated ARDS.

## DRUGS TARGETING NEUTROPHILS FOR COVID-19 ASSOCIATED ARDS

Currently, there are several clinical drugs indicated for use in respiratory diseases that affect neutrophil function, but other drugs should also be considered for the treatment of ARDS in COVID-19. A summary of commercially available approved drugs or those in clinical trials, allocated to different groups based on their specific target in neutrophils, is provided (Figure 2, Table 1).

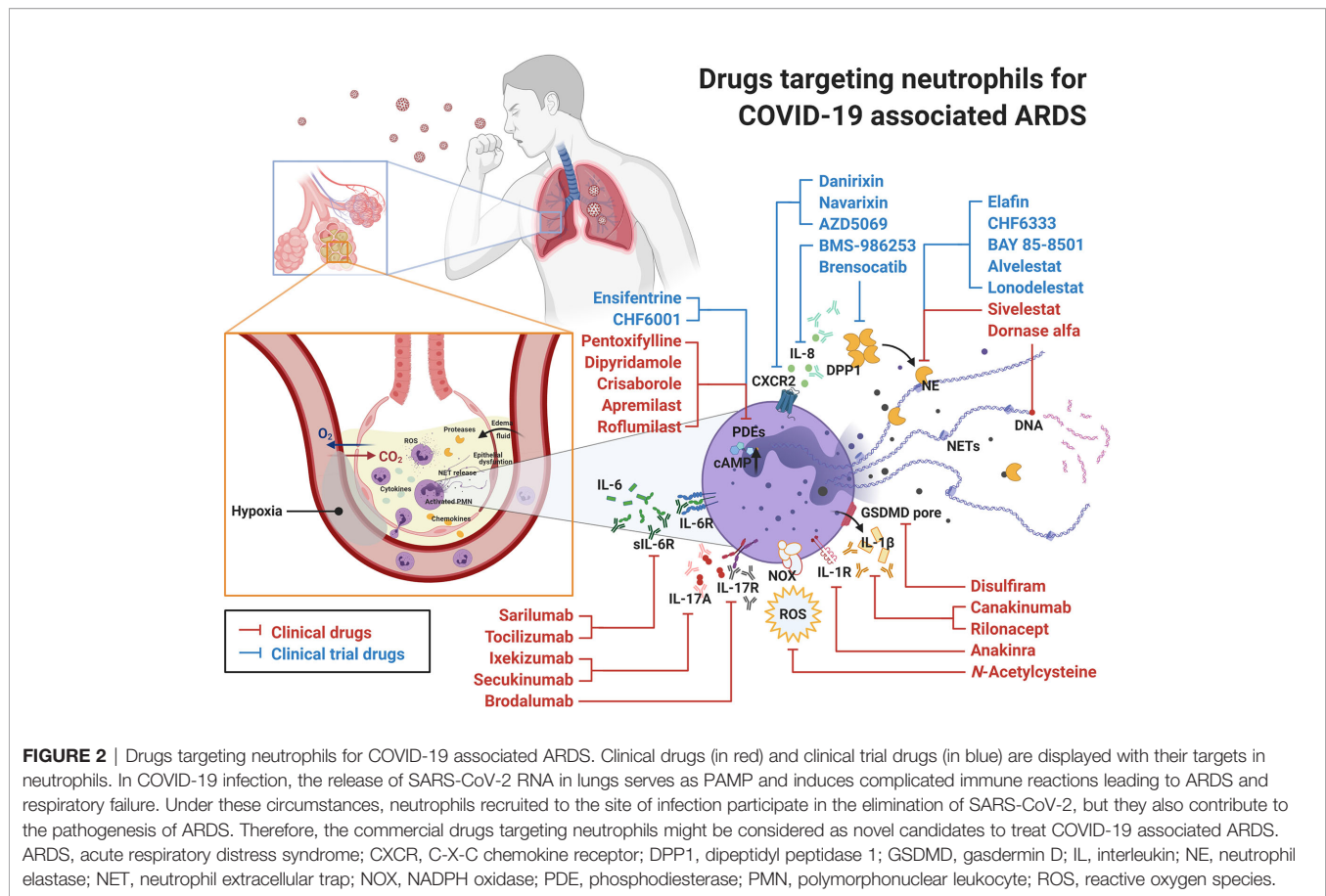


**FIGURE 2 |** Drugs targeting neutrophils for COVID-19 associated ARDS. Clinical drugs (in red) and clinical trial drugs (in blue) are displayed with their targets in neutrophils. In COVID-19 infection, the release of SARS-CoV-2 RNA in lungs serves as PAMP and induces complicated immune reactions leading to ARDS and respiratory failure. Under these circumstances, neutrophils recruited to the site of infection participate in the elimination of SARS-CoV-2, but they also contribute to the pathogenesis of ARDS. Therefore, the commercial drugs targeting neutrophils might be considered as novel candidates to treat COVID-19 associated ARDS. ARDS, acute respiratory distress syndrome; CXCR2, C-X-C chemokine receptor; DPP1, dipeptidyl peptidase 1; GSDMD, gasdermin D; IL, interleukin; NE, neutrophil elastase; NET, neutrophil extracellular trap; NOX, NADPH oxidase; PDE, phosphodiesterase; PMN, polymorphonuclear leukocyte; ROS, reactive oxygen species.

## Neutrophil Elastase Inhibitors

Neutrophil elastase (NE) contributes to the invasion of SARS-CoV-2 into host cells and can also damage lung tissue directly, thus participating in the pathogenesis of COVID-19 associated ARDS (Thierry, 2020). Moreover, NE is an important component and plays an important role in NETosis. For instance, the administration of elastase inhibitors such as sivelestat (Kim et al., 2014) and BAY 85-8501 (Von Nussbaum et al., 2015) ameliorated acute lung injury in mice. Currently, sivelestat is the only approved NE inhibitor for the treatment of ARDS in Korea and Japan (Aikawa and Kawasaki, 2014). There are several other NE inhibitors in different stages of clinical trials including alvelestat (AZD9668, COPD, phase 2, US national clinical trial number NCT03636347) (Stockley et al., 2013), BAY 85-8501 (noncystic fibrosis bronchiectasis, phase 2, NCT01818544), (Watz et al., 2019), lonodelestat (POL6014, cystic fibrosis, phase 1, NCT03748199) (Barth et al., 2020), CHF6333 (noncystic fibrosis bronchiectasis, phase 1, NCT03056326, NCT04010799) (Gramegna et al., 2017), and elafin (ARDS, phase 1, NCT02944279) (Barnes et al., 2020). In a meta-analysis study, sivelestat failed to improve the survival of patients with ARDS (Tagami et al., 2014). However, a retrospective cohort study with 66 ARDS patients demonstrated that sivelestat treatment yields positive outcomes (Maki et al., 2020). In particular, aerosol- or nebulizer-dosed NE inhibitors

significantly improved their efficacy and lowered adverse effects (Barth et al., 2020). Thus, prompt administration of NE inhibitors may be helpful in severe COVID-19 patients with ARDS (Mohamed et al., 2020).

## Respiratory Burst Inhibitor

N-Acetylcysteine is a potential therapeutic in the treatment of COVID-19 (Andreou et al., 2020). It is a mucolytic drug with antioxidant activity that is used in respiratory diseases (Mokhtari et al., 2017) and skin diseases (Adil et al., 2018), as well as an antidote in acetaminophen overdose (Mokhtari et al., 2017). Moreover, N-acetylcysteine inhibited the respiratory burst in activated neutrophils *in vitro* (Allegra et al., 2002) and in patients in the intensive care unit (Heller et al., 2001). Furthermore, N-acetylcysteine alleviated acute lung injury *in vivo* under various conditions (Alkan et al., 2006; Chuang et al., 2007; Liu et al., 2008; Yubero et al., 2012; Guo et al., 2019), and inhibited lung fibrosis *in vivo* (Kulshrestha et al., 2020) with limited patient outcomes, according to a meta-analysis study (Sun et al., 2016). In another meta-analysis study, N-acetylcysteine treatment of ARDS patients shortened their stay in the intensive care unit (Zhang et al., 2017). Finally, it has also been suggested that N-acetylcysteine should be used in combination with other drugs to manage ARDS (Guo et al., 2019; Andreou et al., 2020; Horowitz and Freeman, 2020). Currently, several clinical trials with



*N*-acetylcysteine to treat COVID-19 (NCT04419025, NCT04455243, NCT04374461, etc.) are ongoing. Based on the above, we believe that *N*-acetylcysteine may be helpful in treating ARDS caused by SARS-CoV-2 *via* its antioxidant and anti-respiratory burst activity.

### Dipeptidyl Peptidase 1 Inhibitor

Dipeptidyl peptidase 1 (DPP1), also known as cathepsin C, is a cysteine dipeptidyl aminopeptidase that activates serine proteases such as NE during maturation of neutrophils. Excessive serine protease activity causes various inflammatory lung diseases such as ARDS and contributes to COPD and asthma. Brensocatib (also called INS1007 or AZD7986), a DPP1 inhibitor, was found to reduce NE activity in healthy humans (Palmér et al., 2018) and is now in clinical trials for bronchiectasis (NCT03218917) and COVID-19 (EU clinical trial number EudraCT 2020-001643-13). The administration of DPP1 inhibitors may prevent ARDS progression caused by SARS-CoV-2 (Korkmaz et al., 2020). Thus, DPP1 inhibitors are of interest in treating COVID-19 associated ARDS.

### PDE4 Inhibitors

Phosphodiesterases (PDEs) belong to the class of enzymes that metabolize the intracellular second messenger cyclic adenosine monophosphate (cAMP) and cyclic guanosine monophosphate (cGMP). In particular, cAMP-specific PDE4 type is widely present in immune cells including neutrophils and contributes to neutrophil-mediated lung inflammation (Baillie et al., 2019). There are currently three FDA-approved PDE4 inhibitors: roflumilast for COPD (Phillips, 2020), apremilast for psoriasis (Queiro Silva et al., 2020), and crisaborole for atopic dermatitis (Hashim et al., 2020). Other drugs such as CHF6001 (NCT02986321 for COPD and NCT01689571 for asthma) (Singh et al., 2019), and ensifentrine (RPL554, NCT04027439 for COPD) (Cazzola et al., 2019) are awaiting phase 3 clinical trials. However, many of the experimental drugs were discontinued in clinical trials due to side effects (Phillips, 2020). Several PDE inhibitors have been proposed to be suitable drugs for COVID-19 treatment (Giorgi et al., 2020). Thus, we suggest their clinical consideration in COVID-19 associated ARDS. In light of the above, clinical trials targeting COVID-19 using apremilast (NCT04488081) or ensifentrine (NCT04527471) have been initiated.

Dipyridamole is an FDA-approved nonspecific PDE inhibitor used for thrombosis and was discovered to inhibit NET formation (Ali et al., 2019). Dipyridamole acts by increasing intracellular cAMP levels and blocking adenosine reuptake in cells, thereby leading to its antiplatelet and vasodilatory effects (Tan et al., 2019). In a trial including 31 COVID-19 patients, dipyridamole showed improvement in severe cases with significantly reduced D-dimer levels (Liu et al., 2020). Currently, several COVID-related trials are ongoing for dipyridamole (NCT04410328, NCT04424901, NCT04391179). Another FDA-approved nonspecific PDE inhibitor, pentoxifylline, is a derivative of caffeine. Pentoxifylline stimulates blood flow, inhibits platelets, and has immunomodulatory and anti-inflammatory properties. Pentoxifylline also inhibits neutrophil adhesion (Bone, 1992). It is

currently in ongoing clinical trials for COVID-19 (NCT04433988). Along with specific PDE4 inhibitors, dipyridamole and pentoxifylline may represent suitable candidates for further anti-COVID-19 development (Hendry et al., 2020).

### Gasdermin D Inhibitor

Disulfiram, an FDA-approved gasdermin D inhibitor, blocks SARS-CoV-2 replication *in silico* (Lobo-Galo et al., 2020). Moreover, disulfiram was shown to abrogate gasdermin D pore formation by covalent bonding to Cys191/Cys192 (Hu et al., 2020). Gasdermin D is important in the formation of NETs (Sollberger et al., 2018). Therefore, disulfiram has the potential to reduce NET-related pathogenesis in ARDS caused by SARS-CoV-2. Currently, a clinical trial is ongoing on the potential use of disulfiram in COVID-19 (NCT04485130).

### DNase Inhibitors

Application of DNase I to mice with severe bacterial pneumonia and acute lung injury reduced NET formation and improved their survival rate (Lefrançois et al., 2018). Administration of dornase alfa, an FDA-approved recombinant human DNase I, using a nebulizer in severe COVID-19 associated ARDS patients may help lyse the sputum and improve disease progression (Barnes et al., 2020; Weber et al., 2020). Currently, there are several COVID-19 clinical trials using dornase alfa (NCT04402970, NCT04359654, NCT04355364, EudraCT 2020-001492-33, etc.) (Desilles et al., 2020). Another promising DNase inhibitor, AIR DNase<sup>TM</sup>, is currently undergoing phase 2 clinical trials in cystic fibrosis patients (NCT02605590, NCT02722122).

### Chemokine-Related Drugs (IL-8, IL-17, IL-1β and IL-6)

IL-8 secreted by macrophages and lung epithelial cells is a neutrophil chemoattractant. Moreover, IL-8 contributes to neutrophil activation and NET formation after binding to CXCR2 on neutrophils, thereby causing hyperinflammation. Interestingly, anti-IL-8 monoclonal antibody BMS-986253 (Humax IL-8), developed as an anti-tumor treatment (Bilusic et al., 2019), is currently in clinical trial for COVID-19 (NCT04347226). AZD5069 (Nicholls et al., 2015; Cullberg et al., 2018), danirixin (Madan et al., 2019; Lazaar et al., 2020), and navarixin (SCH527123) (Holz et al., 2010; Todd et al., 2016) are available CXCR2 inhibitors that ameliorate neutrophil activation in pulmonary diseases including bronchiectasis, virus-associated lung infection, COPD and asthma. Therefore, they may represent valuable drugs for the treatment of ARDS in COVID-19 patients (Narasaraju et al., 2020). However, the development of the CXCR2 antagonist QBM076 was terminated for safety reasons (NCT01972776).

IL-17A is a proinflammatory cytokine involved in inflammation and immune responses; thus, blocking its effect is beneficial in treating neutrophilic inflammatory diseases. Ixekizumab (NCT03099538) and secukinumab (NCT03099980) are monoclonal antibodies (mAb) against IL-17A that prevent its interaction with the IL-17A receptor. In particular, IL-17A antagonists have been used for the treatment of rheumatoid arthritis and psoriasis (Chiang et al., 2019). Brodalumab

(NCT04249713) binds with a high affinity to interleukin IL-17 receptor A, thereby inhibiting IL-17 proinflammatory cytokines (Bulat et al., 2020). Secukinumab is currently tested in coronavirus trials (NCT04403243, EudraCT 2020-001246-18).

Anakinra is a IL-1 receptor inhibitor, while canakinumab and rilonacept are IL-1 $\beta$  inhibitors (Prieto-Peña and Dasgupta, 2020). Anakinra was reported in the treatment of COVID-19 (Van De Veerdonk and Netea, 2020). Subcutaneous administration of anakinra reduced mortality and lowered the need for advanced respiratory support in severe COVID-19 patients (Huet et al., 2020); however, several limitations were observed (Khan et al., 2020). There are currently several clinical trials in relation to COVID-19 on anakinra (NCT04330638, NCT04364009, etc.) and canakinumab (NCT04362813, etc.).

Tocilizumab, an IL-6 receptor inhibitor, reduced the level of serum C-reactive protein and ameliorated pulmonary computed tomography appearances in patients with COVID-19 (Guaraldi et al., 2020; Soy et al., 2020; Xu et al., 2020). A plethora of clinical trials using tocilizumab is currently ongoing in relation to COVID-19 (Actemra, Roche, NCT04317092, NCT04320615, etc.). Similarly, several clinical trials for another IL-6 receptor inhibitor, sarilumab (Kevzara, Regeneron, NCT04315298, etc.), have been initiated (Lu et al., 2020).

## Other Drugs

Corticosteroids are recommended by the US National Institutes of Health (NIH) for use in COVID-19 patients who are being mechanically ventilated or require oxygen supplementation (<https://www.covid19treatmentguidelines.nih.gov>). However, there are several concerns, and corticoids were previously not recommended in patients with ARDS related to viral pneumonia (Ni et al., 2019). Corticosteroids also reduce the level of neutrophil-derived secreted IL-1 receptor antagonist (sIL-1Ra), which leads to increased IL-1 $\beta$  expression (Langereis et al., 2011). Hence, corticosteroids have proinflammatory effects in neutrophils. Corticosteroids are generally thought to weakly suppress neutrophilic inflammation, although several research groups reported them to inhibit the neutrophil respiratory burst and interfere with neutrophil recruitment (Strausbaugh and Rosen, 2001; Ronchetti et al., 2018; Ricci et al., 2019). For instance, corticosteroids do not improve neutrophilic inflammation in corticosteroid-resistant asthma or COPD (Yang et al., 2012; Ronchetti et al., 2018).

Dapsone, colchicine, and olanzapine were suggested as potential adjuvant therapies in ARDS caused by SARS-CoV-2 (Altschuler and Kast, 2020). Dapsone has anti-neutrophilic activity through its inhibition of IL-8 mediated chemotaxis and thus may be therapeutic in COVID-19 associated ARDS (Farouk and Salman, 2020; Kast, 2020). Colchicine, a neutrophil microtubule polymerization inhibitor, reduces IL-1 production and is undergoing several clinical trials for COVID-19 (NCT04322682 and 18 more) (Soy et al., 2020). Olanzapine is an antipsychotic drug targeting the histamine 1 receptor, thereby reducing IL-6 generation (Altschuler and Kast, 2020).

Hydroxychloroquine and azithromycin were reported as effective anti-SARS-CoV-2 agents (Ohe et al., 2020; Zhou D.

et al., 2020). Fujita et al. demonstrated that hydroxychloroquine significantly inhibited IL-1 $\beta$  production in activated human neutrophils *in vitro* (Fujita et al., 2019). Hydroxychloroquine inhibited NET formation and ameliorated the hypercoagulation state in mice with orthotopic pancreatic adenocarcinoma. A chemotherapy regimen with hydroxychloroquine prior to surgery improved the rate of perioperative venous thromboembolism in a clinical trial (Boone et al., 2018). With respect to the effect of azithromycin on neutrophils, Bystrzycka et al. revealed that azithromycin decreased NET release in activated neutrophils *in vitro* (Bystrzycka et al., 2017). Anderson et al. demonstrated that azithromycin inhibited neutrophil migration in dextran sulfate sodium-induced mice (Anderson et al., 2019). However, Cavalcanti et al. showed that hydroxychloroquine and azithromycin did not alter disease progression in patients with mild-to-moderate COVID-19 (Cavalcanti et al., 2020). The World Health Organization does not recommend the use of hydroxychloroquine and azithromycin due to the controversial outcomes of several trials.

## CONCLUSION

ARDS is the most lethal complication of COVID-19. Neutrophils, although involved in the elimination of SARS-CoV-2, also participate in the pathogenesis of COVID-19 associated ARDS. Suppression of aberrant neutrophil activation may provide an effective strategy for treating COVID-19 associated ARDS. Several clinical drugs that target neutrophils can be chosen for further therapeutic use in ARDS associated with SARS-CoV-2 infection.

## AUTHOR CONTRIBUTIONS

C-CC, MK, and W-JC wrote the manuscript. T-LH conceived the study and edited the manuscript. All authors contributed to the article and approved the submitted version.

## FUNDING

This work was supported by grants from the Ministry of Science and Technology (MOST 108-2320-B-255-003-MY3, MOST 109-2327-B-255-001, and MOST 109-2327-B-182-002) and Chang Gung Memorial Hospital (BMRP450, and CORPG5K0031). The funding sources had no role in the study design; in the collection, analysis and interpretation of data; in the writing of the report; or in the decision to submit the article for publication.

## ACKNOWLEDGMENTS

This manuscript was edited by Editage. The figures were supported by BioRender.



## REFERENCES

- Adil, M., Amin, S. S., and Mohtashim, M. (2018). N-acetylcysteine in dermatology. *Indian J. Dermatol. Venereol. Leprol.* 84, 652–659. doi: 10.4103/ijdv.IJDVL\_33\_18
- Aikawa, N., and Kawasaki, Y. (2014). Clinical utility of the neutrophil elastase inhibitor sivelestat for the treatment of acute respiratory distress syndrome. *Ther. Clin. Risk Manage.* 10, 621–629. doi: 10.2147/TCRM.S65066
- Alhammad, Y. M. O., Kashipathy, M. M., Roy, A., Johnson, D. K., McDonald, P., Battaille, K. P., et al. (2020). The SARS-CoV-2 conserved macrodomain is a highly efficient ADP-ribosylhydrolase enzyme. *bioRxiv* 2020.05.11.089375. doi: 10.1101/2020.05.11.089375
- Ali, R. A., Gandhi, A. A., Meng, H., Yalavarthi, S., Vreede, A. P., Estes, S. K., et al. (2019). Adenosine receptor agonism protects against NETosis and thrombosis in antiphospholipid syndrome. *Nat. Commun.* 10, 1916. doi: 10.1038/s41467-019-09801-x
- Alkan, A., Eroglu, F., Eroglu, E., Ergin, C., Cerçi, C., and Alsancak, G. (2006). Protective effects of N-acetylcysteine and erdosteine on hemorrhagic shock-induced acute lung injury. *Eur. J. Emerg. Med.* 13, 281–285. doi: 10.1097/00063110-200610000-00007
- Allegra, L., Dal Sasso, M., Bovio, C., Massoni, C., Fonti, E., and Braga, P. C. (2002). Human neutrophil oxidative bursts and their in vitro modulation by different N-acetylcysteine concentrations. *Arzneimittelforschung* 52, 669–676. doi: 10.1055/s-0031-1299949
- Altschuler, E. L., and Kast, R. E. (2020). Dapsone, colchicine and olanzapine as treatment adjuncts to prevent COVID-19 associated adult respiratory distress syndrome (ARDS). *Med. Hypotheses* 141, 109774. doi: 10.1016/j.mehy.2020.109774
- Anderson, S. J., Lockhart, J. S., Estaki, M., Quin, C., Hirota, S. A., Alston, L., et al. (2019). Effects of azithromycin on behavior, pathologic signs, and changes in cytokines, chemokines, and neutrophil migration in C57BL/6 mice exposed to dextran sulfate sodium. *Comp. Med.* 69, 4–15. doi: 10.30802/AALAS-CM-18-000001
- Andreou, A., Trantza, S., Filippou, D., Sipsas, N., and Tsiodras, S. (2020). COVID-19: The potential role of copper and N-acetylcysteine (NAC) in a combination of candidate antiviral treatments against SARS-CoV-2. *In Vivo* 34, 1567–1588. doi: 10.21873/in vivo.11946
- Badraoui, R., Alrashedi, M. M., El-May, M. V., and Bardakci, F. (2020). Acute respiratory distress syndrome: a life threatening associated complication of SARS-CoV-2 infection inducing COVID-19. *J. Biomol. Struct. Dyn.*, 1–10. doi: 10.1080/07391102.2020.1803139 Online ahead of print.
- Bae, H. B., Zmijewski, J. W., Deshane, J. S., Tadie, J. M., Chaplin, D. D., Takashima, S., et al. (2011). AMP-activated protein kinase enhances the phagocytic ability of macrophages and neutrophils. *FASEB J.* 25, 4358–4368. doi: 10.1096/fj.11-190587
- Baillie, G. S., Tejeda, G. S., and Kelly, M. P. (2019). Therapeutic targeting of 3',5'-cyclic nucleotide phosphodiesterases: inhibition and beyond. *Nat. Rev. Drug Discovery* 18, 770–796. doi: 10.1038/s41573-019-0033-4
- Barnes, B. J., Adrover, J. M., Baxter-Stoltzfus, A., Borczuk, A., Cools-Lartigue, J., Crawford, J. M., et al. (2020). Targeting potential drivers of COVID-19: Neutrophil extracellular traps. *J. Exp. Med.* 217 (6), e20200652. doi: 10.1084/jem.20200652
- Barth, P., Bruijnzeel, P., Wach, A., Sellier Kessler, O., Hoofman, L., Zimmermann, J., et al. (2020). Single dose escalation studies with inhaled POL6014, a potent novel selective reversible inhibitor of human neutrophil elastase, in healthy volunteers and subjects with cystic fibrosis. *J. Cyst. Fibros.* 19, 299–304. doi: 10.1016/j.jcf.2019.08.020
- Bhatia, M., Zemans, R. L., and Jayaseelan, S. (2012). Role of chemokines in the pathogenesis of acute lung injury. *Am. J. Respir. Cell Mol. Biol.* 46, 566–572. doi: 10.1165/rcmb.2011-0392TR
- Bilusic, M., Heery, C. R., Collins, J. M., Donahue, R. N., Palena, C., Madan, R. A., et al. (2019). Phase I trial of HuMax-IL8 (BMS-986253), an anti-IL-8 monoclonal antibody, in patients with metastatic or unresectable solid tumors. *J. Immunother. Cancer* 7, 240. doi: 10.1186/s40425-019-0706-x
- Bone, R. C. (1992). Inhibitors of complement and neutrophils: a critical evaluation of their role in the treatment of sepsis. *Crit. Care Med.* 20, 891–898. doi: 10.1097/00003246-199206000-00029
- Boone, B. A., Murthy, P., Miller-Ocuin, J., Doerfler, W. R., Ellis, J. T., Liang, X., et al. (2018). Chloroquine reduces hypercoagulability in pancreatic cancer through inhibition of neutrophil extracellular traps. *BMC Cancer* 18, 678. doi: 10.1186/s12885-018-4584-2
- Brotfain, E., Hadad, N., Shapira, Y., Avinoah, E., Zlotnik, A., Raichel, L., et al. (2015). Neutrophil functions in morbidly obese subjects. *Clin. Exp. Immunol.* 181, 156–163. doi: 10.1111/cei.12631
- Bulat, V., Situm, M., Azdajic, M. D., and Likic, R. (2020). Potential role of IL-17 blocking agents in the treatment of severe COVID-19? *Br. J. Clin. Pharmacol.* doi: 10.1111/bcp.14437 Online ahead of print.
- Bystrzycka, W., Manda-Handzik, A., Sieczkowska, S., Moskalik, A., Demkow, U., and Ciepiela, O. (2017). Azithromycin and chloramphenicol diminish neutrophil extracellular traps (NETs) release. *Int. J. Mol. Sci.* 18 (12), 2666. doi: 10.3390/ijms18122666 Online ahead of print.
- Cavalcanti, A. B., Zampieri, F. G., Rosa, R. G., Azevedo, L. C. P., Veiga, V. C., Avezum, A., et al. (2020). Hydroxychloroquine with or without azithromycin in mild-to-moderate Covid-19. *N. Engl. J. Med.* doi: 10.1056/NEJMoa2019014
- Cazzola, M., Calzetta, L., Rogliani, P., and Matera, M. G. (2019). Ensifentrine (RPL554): an investigational PDE3/4 inhibitor for the treatment of COPD. *Expert Opin. Investig. Drugs* 28, 827–833. doi: 10.1080/13543784.2019.1661990
- Chang, Y. J., Liu, C. Y., Chiang, B. L., Chao, Y. C., and Chen, C. C. (2004). Induction of IL-8 release in lung cells via activator protein-1 by recombinant baculovirus displaying severe acute respiratory syndrome-coronavirus spike proteins: identification of two functional regions. *J. Immunol.* 173, 7602–7614. doi: 10.4049/jimmunol.173.12.7602
- Chen, K., Bao, Z., Gong, W., Tang, P., Yoshimura, T., and Wang, J. M. (2017). Regulation of inflammation by members of the formyl-peptide receptor family. *J. Autoimmun.* 85, 64–77. doi: 10.1016/j.jaut.2017.06.012
- Chen, C. Y., Tsai, Y. F., Huang, W. J., Chang, S. H., and Hwang, T. L. (2018). Propofol inhibits endogenous formyl peptide-induced neutrophil activation and alleviates lung injury. *Free Radic. Biol. Med.* 129, 372–382. doi: 10.1016/j.freeradbiomed.2018.09.048
- Cheng, Y., Skinner, D. D., and Lane, T. E. (2019). Innate immune responses and viral-induced neurologic disease. *J. Clin. Med.* 8 (1), 3. doi: 10.3390/jcm8010003
- Chiang, C. C., Cheng, W. J., Korinek, M., Lin, C. Y., and Hwang, T. L. (2019). Neutrophils in psoriasis. *Front. Immunol.* 10, 2376. doi: 10.3389/fimmu.2019.02376
- Chuang, I. C., Liu, D. D., Kao, S. J., and Chen, H. I. (2007). N-acetylcysteine attenuates the acute lung injury caused by phorbol myristate acetate in isolated rat lungs. *Pulm. Pharmacol. Ther.* 20, 726–733. doi: 10.1016/j.pupt.2006.08.010
- Cullberg, M., Arvidsson, C., Larsson, B., Malmgren, A., Mitchell, P., Wahlby Hamren, U., et al. (2018). Pharmacokinetics of the oral selective CXCR2 antagonist AZD5069: a summary of eight phase I studies in healthy volunteers. *Drugs R. D.* 18, 149–159. doi: 10.1007/s40268-018-0236-x
- Desilles, J. P., Gregoire, C., Le Cossec, C., Lambert, J., Mophawe, O., Losser, M. R., et al. (2020). Efficacy and safety of aerosolized intra-tracheal dornase alfa administration in patients with SARS-CoV-2-induced acute respiratory distress syndrome (ARDS): a structured summary of a study protocol for a randomised controlled trial. *Trials* 21, 548. doi: 10.1186/s13063-020-04488-8
- Dong, Y., Lagarde, J., Xicota, L., Corne, H., Chantran, Y., Chaigneau, T., et al. (2018). Neutrophil hyperactivation correlates with Alzheimer's disease progression. *Ann. Neurol.* 83, 387–405. doi: 10.1002/ana.25159
- Dorward, D. A., Lucas, C. D., Doherty, M. K., Chapman, G. B., Schofield, E. J., Conway Morris, A., et al. (2017). Novel role for endogenous mitochondrial formylated peptide-driven formyl peptide receptor 1 signalling in acute respiratory distress syndrome. *Thorax* 72, 928–936. doi: 10.1136/thoraxjnl-2017-210030
- Farouk, A., and Salman, S. (2020). Dapsone and doxycycline could be potential treatment modalities for COVID-19. *Med. Hypotheses* 140, 109768. doi: 10.1016/j.mehy.2020.109768
- Fujita, Y., Matsuoka, N., Temmoku, J., Furuya, M. Y., Asano, T., Sato, S., et al. (2019). Hydroxychloroquine inhibits IL-1 $\beta$  production from amyloid-stimulated human neutrophils. *Arthritis Res. Ther.* 21, 250. doi: 10.1186/s13075-019-2040-6
- Giorgi, M., Cardarelli, S., Ragusa, F., Saliola, M., Biagioni, S., Poiana, G., et al. (2020). Phosphodiesterase inhibitors: could they be beneficial for the treatment of COVID-19? *Int. J. Mol. Sci.* 21, 5338. doi: 10.3390/ijms21155338

- Gramegna, A., Amati, F., Terranova, L., Sotgiu, G., Tarsia, P., Miglietta, D., et al. (2017). Neutrophil elastase in bronchiectasis. *Respir. Res.* 18, 211–211. doi: 10.1186/s12931-017-0691-x
- Grégoire, M., Uhel, F., Lesouhaitier, M., Gacouin, A., Guirriec, M., Mourcin, F., et al. (2018). Impaired efferocytosis and neutrophil extracellular trap clearance by macrophages in ARDS. *Eur. Respir. J.* 52, 1702590. doi: 10.1183/13993003.02590-2017
- Groeneveld, A. B., Raijmakers, P. G., Hack, C. E., and Thijs, L. G. (1995). Interleukin 8-related neutrophil elastase and the severity of the adult respiratory distress syndrome. *Cytokine* 7, 746–752. doi: 10.1006/cyto.1995.0089
- Guan, W. J., Ni, Z. Y., Hu, Y., Liang, W. H., Ou, C. Q., He, J. X., et al. (2020). Clinical characteristics of coronavirus disease 2019 in China. *N. Engl. J. Med.* 382, 1708–1720. doi: 10.1056/NEJMoa2002032
- Guaraldi, G., Meschiari, M., Cozzi-Lepri, A., Milic, J., Tonelli, R., Menozzi, M., et al. (2020). Tocilizumab in patients with severe COVID-19: a retrospective cohort study. *Lancet Rheumatol.* 2, e474–e484. doi: 10.1016/S2665-9913(20)30173-9
- Guervilly, C., Lacroix, R., Forel, J. M., Roch, A., Camoin-Jau, L., Papazian, L., et al. (2011). High levels of circulating leukocyte microparticles are associated with better outcome in acute respiratory distress syndrome. *Crit. Care* 15, R31. doi: 10.1186/cc9978
- Guo, D. W., Wang, C. Y., and Shih, H. C. (2019). N-acetylcysteine and atorvastatin alleviates lung injury due to ischemia-reperfusion injury in rats. *J. Chin. Med. Assoc.* 82, 909–914. doi: 10.1097/JCMA.0000000000000193
- Guo, Y. R., Cao, Q. D., Hong, Z. S., Tan, Y. Y., Chen, S. D., Jin, H. J., et al. (2020). The origin, transmission and clinical therapies on coronavirus disease 2019 (COVID-19) outbreak - an update on the status. *Mil. Med. Res.* 7, 11. doi: 10.1186/s40779-020-00240-0
- Haick, A. K., Rzepka, J. P., Brandon, E., Balemba, O. B., and Miura, T. A. (2014). Neutrophils are needed for an effective immune response against pulmonary rat coronavirus infection, but also contribute to pathology. *J. Gen. Virol.* 95, 578–590. doi: 10.1099/vir.0.061986-0
- Hashim, P. W., Chima, M., Kim, H. J., Bares, J., Yao, C. J., Singer, G., et al. (2020). Crisaborole 2% ointment for the treatment of intertriginous, anogenital, and facial psoriasis: A double-blind, randomized, vehicle-controlled trial. *J. Am. Acad. Dermatol.* 82, 360–365. doi: 10.1016/j.jaad.2019.06.1288
- Heller, A. R., Groth, G., Heller, S. C., Breitkreutz, R., Nebe, T., Quintel, M., et al. (2001). N-acetylcysteine reduces respiratory burst but augments neutrophil phagocytosis in intensive care unit patients. *Crit. Care Med.* 29, 272–276. doi: 10.1097/00003246-200102000-00009
- Hendry, B. M., Stafford, N., Arnold, A. D., Sangwaiya, A., Manglam, V., Rosen, S. D., et al. (2020). Hypothesis: pentoxifylline is a potential cytokine modulator therapeutic in COVID-19 patients. *Pharmacol. Res. Perspect.* 8, e00631. doi: 10.1002/prp2.631
- Henke, M. O., and Ratjen, F. (2007). Mucolytics in cystic fibrosis. *Paediatr. Respir. Rev.* 8, 24–29. doi: 10.1016/j.prrv.2007.02.009
- Holz, A. R., Khalilieh, S., Ludwig-Sengpiel, A., Watz, H., Stryczak, P., Soni, P., et al. (2010). SCH527123, a novel CXCR2 antagonist, inhibits ozone-induced neutrophilia in healthy subjects. *Eur. Respir. J.* 35, 564–570. doi: 10.1183/09031936.00048509
- Honda, M., and Kubes, P. (2018). Neutrophils and neutrophil extracellular traps in the liver and gastrointestinal system. *Nat. Rev. Gastroenterol. Hepatol.* 15, 206–221. doi: 10.1038/nrgastro.2017.183
- Horowitz, R. I., and Freeman, P. R. (2020). Three novel prevention, diagnostic, and treatment options for COVID-19 urgently necessitating controlled randomized trials. *Med. Hypotheses* 143, 109851. doi: 10.1016/j.mehy.2020.109851
- Hu, J. J., Liu, X., Xia, S., Zhang, Z., Zhang, Y., Zhao, J., et al. (2020). FDA-approved disulfiram inhibits pyroptosis by blocking gasdermin D pore formation. *Nat. Immunol.* 21, 736–745. doi: 10.1038/s41590-020-0669-6
- Huet, T., Beaussier, H., Voisin, O., Jouveshomme, S., Dauriat, G., Lazareth, I., et al. (2020). Anakinra for severe forms of COVID-19: a cohort study. *Lancet Rheumatol.* 2, e393–e400. doi: 10.1016/S2665-9913(20)30164-8
- Kast, R. E. (2020). Dapsone as treatment adjunct in ARDS. *Exp. Lung Res.* 46, 157–161. doi: 10.1080/01902148.2020.1753266
- Kawai, T., and Akira, S. (2010). The role of pattern-recognition receptors in innate immunity: update on Toll-like receptors. *Nat. Immunol.* 11, 373–384. doi: 10.1038/ni.1863
- Khan, A. R., Soneja, M., George, N., and Wig, N. (2020). Anakinra for severe forms of COVID-19. *Lancet Rheumatol.* doi: 10.1016/S2665-9913(20)30271-X
- Kim, D. H., Chung, J. H., Son, B. S., Kim, Y. J., and Lee, S. G. (2014). Effect of a neutrophil elastase inhibitor on ventilator-induced lung injury in rats. *J. Thorac. Dis.* 6, 1681–1689. doi: 10.3978/j.issn.2072-1439.2014.11.10
- Korkmaz, B., Lesner, A., Marchand-Adam, S., Moss, C., and Jenne, D. E. (2020). Lung protection by cathepsin C inhibition: a new hope for COVID-19 and ARDS? *J. Med. Chem.* 7, 2020. doi: 10.1021/acs.jmedchem.0c00776
- Kulshrestha, R., Pandey, A., Jaggi, A., and Bansal, S. (2020). Beneficial effects of N-acetylcysteine on protease-antiprotease balance in attenuating bleomycin-induced pulmonary fibrosis in rats. *Iran. J. Basic Med. Sci.* 23, 396–405. doi: 10.22038/IJBMS.2020.39031.9261
- Kusunoki, Y., Nakazawa, D., Shida, H., Hattanda, F., Miyoshi, A., Masuda, S., et al. (2016). Peptidylarginine deiminase inhibitor suppresses neutrophil extracellular trap formation and MPO-ANCA production. *Front. Immunol.* 7:227. doi: 10.3389/fimmu.2016.00227
- Lagunas-Rangel, F. A. (2020). Neutrophil-to-lymphocyte ratio and lymphocyte-to-C-reactive protein ratio in patients with severe coronavirus disease 2019 (COVID-19): A meta-analysis. *J. Med. Virol.* doi: 10.1002/jmv.25819
- Lai, C. C., Liu, Y. H., Wang, C. Y., Wang, Y. H., Hsueh, S. C., Yen, M. Y., et al. (2020). Asymptomatic carrier state, acute respiratory disease, and pneumonia due to severe acute respiratory syndrome coronavirus 2 (SARS-CoV-2): facts and myths. *J. Microbiol. Immunol. Infect.* 53, 404–412. doi: 10.1016/j.jmii.2020.02.012
- Langereis, J. D., Oudijk, E. J., Schweizer, R. C., Lammers, J. W., Koenderman, L., and Ulfman, L. H. (2011). Steroids induce a disequilibrium of secreted interleukin-1 receptor antagonist and interleukin-1 $\beta$  synthesis by human neutrophils. *Eur. Respir. J.* 37, 406–415. doi: 10.1183/09031936.00170409
- Lazaar, A. L., Miller, B. E., Donald, A. C., Keeley, T., Ambery, C., Russell, J., et al. (2020). CXCR2 antagonist for patients with chronic obstructive pulmonary disease with chronic mucus hypersecretion: a phase 2b trial. *Respir. Res.* 21, 149. doi: 10.1186/s12931-020-01401-4
- Lee, P. I., and Hsueh, P. R. (2020). Emerging threats from zoonotic coronaviruses—from SARS and MERS to 2019-nCoV. *J. Microbiol. Immunol. Infect.* 53, 365–367. doi: 10.1016/j.jmii.2020.02.001
- Lefrançois, E., Mallavia, B., Zhuo, H., Calfee, C. S., and Looney, M. R. (2018). Maladaptive role of neutrophil extracellular traps in pathogen-induced lung injury. *JCI Insight* 3 (3), e98178. doi: 10.1172/jci.insight.98178
- Leslie, J., Millar, B. J., Del Carpio Pons, A., Burgoyne, R. A., Frost, J. D., Barksby, B. S., et al. (2020). FPR-1 is an important regulator of neutrophil recruitment and a tissue-specific driver of pulmonary fibrosis. *JCI Insight* 5 (4), e125937. doi: 10.1172/jci.insight.125937
- Lewis, H. D., Liddle, J., Coote, J. E., Atkinson, S. J., Barker, M. D., Bax, B. D., et al. (2015). Inhibition of PAD4 activity is sufficient to disrupt mouse and human NET formation. *Nat. Chem. Biol.* 11, 189–191. doi: 10.1038/nchembio.1735
- Li, M., Lin, C., Deng, H., Strnad, J., Bernabei, L., Vogl, D. T., et al. (2020). A novel peptidylarginine deiminase 4 (PAD4) inhibitor BMS-P5 blocks formation of neutrophil extracellular traps and delays progression of multiple myeloma. *Mol. Cancer Ther.* 19, 1530–1538. doi: 10.1158/1535-7163.MCT-19-1020
- Li, X., Wang, L., Yan, S., Yang, F., Xiang, L., Zhu, J., et al. (2020). Clinical characteristics of 25 death cases infected with COVID-19 pneumonia: a retrospective review of medical records in a single medical center, Wuhan, China. *Int. J. Infect. Dis.* 94, 128–132. doi: 10.1016/j.ijid.2020.03.053
- Li, Y. C., Bai, W. Z., and Hashikawa, T. (2020). The neuroinvasive potential of SARS-CoV2 may play a role in the respiratory failure of COVID-19 patients. *J. Med. Virol.* 92, 552–555. doi: 10.1002/jmv.25728
- Liew, P. X., and Kubes, P. (2019). The neutrophil's role during health and disease. *Physiol. Rev.* 99, 1223–1248. doi: 10.1152/physrev.00012.2018
- Lin, W. C., Gowdy, K. M., Madenspacher, J. H., Zemans, R. L., Yamamoto, K., Lyons-Cohen, M., et al. (2020). Epithelial membrane protein 2 governs transepithelial migration of neutrophils into the airspace. *J. Clin. Invest.* 130, 157–170. doi: 10.1172/JCI127144
- Liu, D. D., Kao, S. J., and Chen, H. I. (2008). N-acetylcysteine attenuates acute lung injury induced by fat embolism. *Crit. Care Med.* 36, 565–571. doi: 10.1097/01.CCM.0000299737.24338.5C
- Liu, F. C., Yu, H. P., Syu, Y. T., Fang, J. Y., Lin, C. F., Chang, S. H., et al. (2017). Honokiol suppresses formyl peptide-induced human neutrophil activation by

- blocking formyl peptide receptor 1. *Sci. Rep.* 7, 6718. doi: 10.1038/s41598-017-07131-w
- Liu, X., Li, Z., Liu, S., Sun, J., Chen, Z., Jiang, M., et al. (2020). Potential therapeutic effects of dipyrindamole in the severely ill patients with COVID-19. *Acta Pharm. Sin. B* 10 (7), 1205–1215. doi: 10.1016/j.apsb.2020.04.008
- Lobo-Galo, N., Terrazas-López, M., Martínez-Martínez, A., and Díaz-Sánchez, A. G. (2020). FDA-approved thiol-reacting drugs that potentially bind into the SARS-CoV-2 main protease, essential for viral replication. *J. Biomol. Struct. Dyn.* 1–9. doi: 10.1080/07391102.2020.1764393
- Lu, C. C., Chen, M. Y., Lee, W. S., and Chang, Y. L. (2020). Potential therapeutic agents against COVID-19: What we know so far. *J. Chin. Med. Assoc.* 83, 534–536. doi: 10.1097/JCMA.0000000000000318
- Lu, H. (2020). Drug treatment options for the 2019-new coronavirus, (2019-nCoV). *Biosci. Trends* 14, 69–71. doi: 10.5582/bst.2020.01020
- Madan, A., Chen, S., Yates, P., Washburn, M. L., Roberts, G., Peat, A. J., et al. (2019). Efficacy and safety of danirixin (GSK1325756) co-administered with standard-of-care antiviral (oseltamivir): a phase 2b, global, randomized study of adults hospitalized with influenza. *Open Forum Infect. Dis.* 6, ofz163. doi: 10.1093/ofid/ofz163
- Maki, C., Inoue, Y., Ishihara, T., Hirano, Y., Kondo, Y., Sueyoshi, K., et al. (2020). Evaluation of appropriate indications for the use of sivelestat sodium in acute respiratory distress syndrome: a retrospective cohort study. *Acute Med. Surg.* 7, e471. doi: 10.1002/ams2.471
- Manzenreiter, R., Kienberger, F., Marcos, V., Schilcher, K., Krautgartner, W. D., Obermayer, A., et al. (2012). Ultrastructural characterization of cystic fibrosis sputum using atomic force and scanning electron microscopy. *J. Cyst. Fibros.* 11, 84–92. doi: 10.1016/j.jcf.2011.09.008
- Matthay, M. A., Aldrich, J. M., and Gotts, J. E. (2020). Treatment for severe acute respiratory distress syndrome from COVID-19. *Lancet Respir. Med.* 8, 433–434. doi: 10.1016/S2213-2600(20)30127-2
- Mercer, P. F., Williams, A. E., Scotton, C. J., José, R. J., Sulikowski, M., Moffatt, J. D., et al. (2014). Proteinase-activated receptor-1, CCL2, and CCL7 regulate acute neutrophilic lung inflammation. *Am. J. Respir. Cell Mol. Biol.* 50, 144–157. doi: 10.1165/rcmb.2013-0142OC
- Mi, M. Y., Matthay, M. A., and Morris, A. H. (2018). Extracorporeal membrane oxygenation for severe acute respiratory distress syndrome. *N. Engl. J. Med.* 379, 884–887. doi: 10.1056/NEJMclde1804601
- Middleton, E. A., He, X. Y., Denorme, F., Campbell, R. A., Ng, D., Salvatore, S. P., et al. (2020). Neutrophil extracellular traps contribute to immunothrombosis in COVID-19 acute respiratory distress syndrome. *Blood* 136 (10), 1169–1179. doi: 10.1182/blood.2020007008
- Miller, E. J., Cohen, A. B., Nagao, S., Griffith, D., Maunder, R. J., Martin, T. R., et al. (1992). Elevated levels of NAP-1/interleukin-8 are present in the airspaces of patients with the adult respiratory distress syndrome and are associated with increased mortality. *Am. Rev. Respir. Dis.* 146, 427–432. doi: 10.1164/ajrccm/146.2.427
- Mohamed, M. M. A., El-Shimy, I. A., and Hadi, M. A. (2020). Neutrophil elastase inhibitors: a potential prophylactic treatment option for SARS-CoV-2-induced respiratory complications? *Crit. Care* 24, 311. doi: 10.1186/s13054-020-03023-0
- Mokhtari, V., Afsharian, P., Shakhosini, M., Kalantar, S. M., and Moini, A. (2017). A review on various uses of N-acetyl cysteine. *Cell J.* 19, 11–17. doi: 10.22074/cellj.2016.4872
- Nakos, G., Kitsioulis, E. I., Tsangaris, I., and Lekka, M. E. (1998). Bronchoalveolar lavage fluid characteristics of early intermediate and late phases of ARDS. Alterations in leukocytes, proteins, PAF and surfactant components. *Intensive Care Med.* 24, 296–303. doi: 10.1007/s001340050571
- Narasaraju, T., Tang, B. M., Herrmann, M., Muller, S., Chow, V. T. K., and Radic, M. (2020). Neutrophilia and NETopathy as key pathologic drivers of progressive lung impairment in patients with COVID-19. *Front. Pharmacol.* 11:870. doi: 10.3389/fphar.2020.00870
- Nathan, C. (2020). Neutrophils and COVID-19: Nots, NETs, and knots. *J. Exp. Med.* 21 (9), e20201439.7. doi: 10.1084/jem.20201439
- Németh, T., Sperandio, M., and Mócsai, A. (2020). Neutrophils as emerging therapeutic targets. *Nat. Rev. Drug Discovery* 19, 253–275. doi: 10.1038/s41573-019-0054-z
- Ni, Y. N., Chen, G., Sun, J., Liang, B. M., and Liang, Z. A. (2019). The effect of corticosteroids on mortality of patients with influenza pneumonia: a systematic review and meta-analysis. *Crit. Care* 23, 99. doi: 10.1186/s13054-019-2395-8
- Nicholls, D. J., Wiley, K., Dainty, I., Macintosh, F., Phillips, C., Gaw, A., et al. (2015). Pharmacological characterization of AZD5069, a slowly reversible CXCR2 chemokine receptor 2 antagonist. *J. Pharmacol. Exp. Ther.* 353, 340–350. doi: 10.1124/jpet.114.221358
- Ohe, M., Shida, H., Jodo, S., Kusunoki, Y., Seki, M., Furuya, K., et al. (2020). Macrolide treatment for COVID-19: will this be the way forward? *Biosci. Trends* 14, 159–160. doi: 10.5582/bst.2020.03058
- Oubihi, Z., and Wang, L. (2020). Caught by NETs. *Nat. Rev. Immunol.* 20, 462. doi: 10.1038/s41577-020-0384-4
- Palmér, R., Mäenpää, J., Jauhiainen, A., Larsson, B., Mo, J., Russell, M., et al. (2018). Dipeptidyl Peptidase 1 inhibitor AZD7986 induces a sustained, exposure-dependent reduction in neutrophil elastase activity in healthy subjects. *Clin. Pharmacol. Ther.* 104, 1155–1164. doi: 10.1002/cpt.1053
- Papayannopoulos, V., Staab, D., and Zychlinsky, A. (2011). Neutrophil elastase enhances sputum solubilization in cystic fibrosis patients receiving DNase therapy. *PLoS One* 6, e28526. doi: 10.1371/journal.pone.0028526
- Phillips, J. E. (2020). Inhaled phosphodiesterase 4 (PDE4) inhibitors for inflammatory respiratory diseases. *Front. Pharmacol.* 11, 259. doi: 10.3389/fphar.2020.00259
- Prieto-Peña, D., and Dasgupta, B. (2020). Biologic agents and small-molecule inhibitors in systemic autoimmune conditions: an update. *Pol. Arch. Intern. Med.* doi: 10.20452/pamw.15438
- Qin, C., Zhou, L., Hu, Z., Zhang, S., Yang, S., Tao, Y., et al. (2020). Dysregulation of immune response in patients with COVID-19 in Wuhan, China. *Clin. Infect. Dis.* 71, 762–768. doi: 10.1093/cid/ciaa248
- Queiro Silva, R., Armesto, S., González Vela, C., Naharro Fernández, C., and González-Gay, M. A. (2020). COVID-19 patients with psoriasis and psoriatic arthritis on biologic immunosuppressant therapy vs apremilast in North Spain. *Dermatol. Ther.* e13961. doi: 10.1111/dth.13961
- Ramanathan, K., Antognini, D., Combes, A., Paden, M., Zakhary, B., Ogino, M., et al. (2020). Planning and provision of ECMO services for severe ARDS during the COVID-19 pandemic and other outbreaks of emerging infectious diseases. *Lancet Respir. Med.* 8, 518–526. doi: 10.1016/S2213-2600(20)30121-1
- Ranieri, V. M., Rubenfeld, G. D., Thompson, B. T., Ferguson, N. D., Caldwell, E., Fan, E., et al. (2012). Acute respiratory distress syndrome: the Berlin Definition. *JAMA* 307, 2526–2533. doi: 10.1001/jama.2012.5669
- Ricci, E., Ronchetti, S., Gabrielli, E., Pericolini, E., Gentili, M., Roselletti, E., et al. (2019). GILZ restrains neutrophil activation by inhibiting the MAPK pathway. *J. Leukoc. Biol.* 105, 187–194. doi: 10.1002/JLB.3AB0718-255R
- Ronchetti, S., Ricci, E., Migliorati, G., Gentili, M., and Riccardi, C. (2018). How glucocorticoids affect the neutrophil life. *Int. J. Mol. Sci.* 19 (12), 4090. doi: 10.3390/ijms19124090
- Safi, R., Kallas, R., Bardawil, T., Mehanna, C. J., Abbas, O., Hamam, R., et al. (2018). Neutrophils contribute to vasculitis by increased release of neutrophil extracellular traps in Behçet's disease. *J. Dermatol. Sci.* 92, 143–150. doi: 10.1016/j.jdermsci.2018.08.010
- Shah, R. D., and Wunderink, R. G. (2017). Viral pneumonia and acute respiratory distress syndrome. *Clin. Chest Med.* 38, 113–125. doi: 10.1016/j.ccm.2016.11.013
- Shi, H., Zuo, Y., Yalavarthi, S., Gockman, K., Zuo, M., Madison, J. A., et al. (2020). Neutrophil calprotectin identifies severe pulmonary disease in COVID-19. *Medrxiv Preprint Server Health Sci.* 2020. doi: 10.1101/2020.05.06.20093070
- Shi, Y., Wang, Y., Shao, C., Huang, J., Gan, J., Huang, X., et al. (2020). COVID-19 infection: the perspectives on immune responses. *Cell Death Differ.* 27 (5), 1451–1454. doi: 10.1038/s41418-020-0530-3
- Singh, D., Beeh, K. M., Colgan, B., Kornmann, O., Leaker, B., Watz, H., et al. (2019). Effect of the inhaled PDE4 inhibitor CHF6001 on biomarkers of inflammation in COPD. *Respir. Res.* 20, 180. doi: 10.1186/s12931-019-1142-7
- Sollberger, G., Choidas, A., Burn, G. L., Habenberger, P., Di Lucrezia, R., Kordes, S., et al. (2018). Gasdermin D plays a vital role in the generation of neutrophil extracellular traps. *Sci. Immunol.* 3 (26), eaar6689. doi: 10.1126/sciimmunol.aar6689
- Song, C., Li, H., Li, Y., Dai, M., Zhang, L., Liu, S., et al. (2019). NETs promote ALI/ARDS inflammation by regulating alveolar macrophage polarization. *Exp. Cell Res.* 382, 111486. doi: 10.1016/j.yexcr.2019.06.031



- Soy, M., Keser, G., Atagündüz, P., Tabak, F., Atagündüz, I., and Kayhan, S. (2020). Cytokine storm in COVID-19: pathogenesis and overview of anti-inflammatory agents used in treatment. *Clin. Rheumatol.* 39, 2085–2094. doi: 10.1007/s10067-020-05190-5
- Stebbing, J., Phelan, A., Griffin, I., Tucker, C., Oechsle, O., Smith, D., et al. (2020). COVID-19: combining antiviral and anti-inflammatory treatments. *Lancet Infect. Dis.* 20, 400–402. doi: 10.1016/S1473-3099(20)30132-8
- Stevens, J. P., Law, A., and Giannakoulis, J. (2018). Acute respiratory distress syndrome. *JAMA* 319, 732. doi: 10.1001/jama.2018.0483
- Stockley, R., De Soyza, A., Gunawardena, K., Perrett, J., Forsman-Semb, K., Entwistle, N., et al. (2013). Phase II study of a neutrophil elastase inhibitor (AZD9668) in patients with bronchiectasis. *Respir. Med.* 107, 524–533. doi: 10.1016/j.rmed.2012.12.009
- Strausbaugh, H. J., and Rosen, S. D. (2001). A potential role for annexin 1 as a physiologic mediator of glucocorticoid-induced L-selectin shedding from myeloid cells. *J. Immunol.* 166, 6294–6300. doi: 10.4049/jimmunol.166.10.6294
- Sun, T., Liu, J., and Zhao De, W. (2016). Efficacy of N-acetylcysteine in idiopathic pulmonary fibrosis: a systematic review and meta-analysis. *Med. (Baltimore)* 95, e3629. doi: 10.1097/MD.0000000000003629
- Sweeney, R. M., and McAuley, D. F. (2016). Acute respiratory distress syndrome. *Lancet* 388, 2416–2430. doi: 10.1016/S0140-6736(16)00578-X
- Tagami, T., Tosa, R., Omura, M., Fukushima, H., Kaneko, T., Endo, T., et al. (2014). Effect of a selective neutrophil elastase inhibitor on mortality and ventilator-free days in patients with increased extravascular lung water: a post hoc analysis of the PiCCO Pulmonary Edema Study. *J. Intensive Care* 2, 67. doi: 10.1186/s40560-014-0067-y
- Talukdar, S., Oh, D. Y., Bandyopadhyay, G., Li, D., Xu, J., Mcnelis, J., et al. (2012). Neutrophils mediate insulin resistance in mice fed a high-fat diet through secreted elastase. *Nat. Med.* 18, 1407–1412. doi: 10.1038/nm.2885
- Tan, M. K. X., Heng, T. Y. J., and Mak, A. (2019). The potential use of metformin, dipyrindamole, N-acetylcysteine and statins as adjunctive therapy for systemic lupus erythematosus. *Cells* 8 (4), 323. doi: 10.3390/cells8040323
- Thierry, A. R. (2020). Anti-protease treatments targeting plasmin(ogen) and neutrophil elastase may be beneficial in fighting COVID-19. *Physiol. Rev.* 100, 1597–1598. doi: 10.1152/physrev.00019.2020
- Tisoncik, J. R., Korth, M. J., Simmons, C. P., Farrar, J., Martin, T. R., and Katze, M. G. (2012). Into the eye of the cytokine storm. *Microbiol. Mol. Biol. Rev.* 76, 16–32. doi: 10.1128/MMBR.05015-11
- Todd, C. M., Salter, B. M., Murphy, D. M., Watson, R. M., Howie, K. J., Milot, J., et al. (2016). The effects of a CXCR1/CXCR2 antagonist on neutrophil migration in mild atopic asthmatic subjects. *Pulm. Pharmacol. Ther.* 41, 34–39. doi: 10.1016/j.pupt.2016.09.005
- Tomar, B., Anders, H. J., Desai, J., and Mulay, S. R. (2020). Neutrophils and neutrophil extracellular traps drive necroinflammation in COVID-19. *Cells* 9 (6), 1383. doi: 10.3390/cells9061383
- Ton, A. T., Gentile, F., Hsing, M., Ban, F., and Cherkasov, A. (2020). Rapid Identification of Potential Inhibitors of SARS-CoV-2 Main Protease by Deep Docking of 1.3 Billion Compounds. *Mol. Inform.* 39 (8), e2000028. doi: 10.1002/minf.202000028
- Vaira, L. A., Salzano, G., Deiana, G., and De Riu, G. (2020). Anosmia and ageusia: common findings in COVID-19 patients. *Laryngoscope* 130, 1787. doi: 10.1002/lary.28692
- Van De Veerdonk, F. L., and Netea, M. G. (2020). Blocking IL-1 to prevent respiratory failure in COVID-19. *Crit. Care* 24, 445. doi: 10.1186/s13054-020-03166-0
- Veras, F. P., Pontelli, M. C., Silva, C. M., Toller-Kawahisa, J. E., De Lima, M., Nascimento, D. C., et al. (2020). SARS-CoV-2-triggered neutrophil extracellular traps mediate COVID-19 pathology. *J. Exp. Med.* 217 (12), e20201129. doi: 10.1084/jem.20201129
- Von Nussbaum, F., Li, V. M., Allerheiligen, S., Anlauf, S., Bärfacker, L., Bechem, M., et al. (2015). Freezing the Bioactive Conformation to Boost Potency: The Identification of BAY 85-8501, a Selective and Potent Inhibitor of Human Neutrophil Elastase for Pulmonary Diseases. *ChemMedChem* 10, 1163–1173. doi: 10.1002/cmdc.201500131
- Wang, D., Hu, B., Hu, C., Zhu, F., Liu, X., Zhang, J., et al. (2020). Clinical characteristics of 138 hospitalized patients with 2019 novel coronavirus-infected pneumonia in Wuhan, China. *JAMA* 323 (11), 1061–1069. doi: 10.1001/jama.2020.1585
- Watz, H., Nagelschmitz, J., Kirsten, A., Pedersen, F., Van Der Mey, D., Schwes, S., et al. (2019). Safety and efficacy of the human neutrophil elastase inhibitor BAY 85-8501 for the treatment of non-cystic fibrosis bronchiectasis: a randomized controlled trial. *Pulm. Pharmacol. Ther.* 56, 86–93. doi: 10.1016/j.pupt.2019.03.009
- Weber, A. G., Chau, A. S., Egeblad, M., Barnes, B. J., and Janowitz, T. (2020). Nebulized in-line endotracheal dornase alfa and albuterol administered to mechanically ventilated COVID-19 patients: a case series. *medRxiv* 2020.05.13.20087734. doi: 10.1101/2020.05.13.20087734
- Wong, S. L., and Wagner, D. D. (2018). Peptidylarginine deiminase 4: a nuclear button triggering neutrophil extracellular traps in inflammatory diseases and aging. *FASEB J.* 32 (12), 6358–6370. doi: 10.1096/fj.201800691R
- Woodberry, T., Bouffler, S. E., Wilson, A. S., Buckland, R. L., and Brüstle, A. (2018). The emerging role of neutrophil granulocytes in multiple sclerosis. *J. Clin. Med.* 7 (12):511. doi: 10.3390/jcm7120511
- Xu, X., Han, M., Li, T., Sun, W., Wang, D., Fu, B., et al. (2020). Effective treatment of severe COVID-19 patients with tocilizumab. *Proc. Natl. Acad. Sci. U.S.A.* 117, 10970–10975. doi: 10.1073/pnas.2005615117
- Yang, S. C., and Hwang, T. L. (2016). The potential impacts of formyl peptide receptor 1 in inflammatory diseases. *Front. Biosci. (Elite Ed.)* 8, 436–449.
- Yang, I. A., Clarke, M. S., Sim, E. H., and Fong, K. M. (2012). Inhaled corticosteroids for stable chronic obstructive pulmonary disease. *Cochrane Database Syst. Rev.* (7), Cd002991. doi: 10.1002/14651858.CD002991.pub3
- Yang, S. C., Chung, P. J., Ho, C. M., Kuo, C. Y., Hung, M. F., Huang, Y. T., et al. (2013). Propofol inhibits superoxide production, elastase release, and chemotaxis in formyl peptide-activated human neutrophils by blocking formyl peptide receptor 1. *J. Immunol.* 190, 6511–6519. doi: 10.4049/jimmunol.1202215
- Yang, S. C., Chang, S. H., Hsieh, P. W., Huang, Y. T., Ho, C. M., Tsai, Y. F., et al. (2017). Dipeptide HCH6-1 inhibits neutrophil activation and protects against acute lung injury by blocking FPR1. *Free Radic. Biol. Med.* 106, 254–269. doi: 10.1016/j.freeradbiomed.2017.02.038
- Yang, X., Yu, Y., Xu, J., Shu, H., Xia, J., Liu, H., et al. (2020). Clinical course and outcomes of critically ill patients with SARS-CoV-2 pneumonia in Wuhan, China: a single-centered, retrospective, observational study. *Lancet Respir. Med.* 8, 475–481. doi: 10.1016/S2213-2600(20)30079-5
- Yaqinuddin, A., and Kashir, J. (2020). Novel therapeutic targets for SARS-CoV-2-induced acute lung injury: targeting a potential IL-1beta/neutrophil extracellular traps feedback loop. *Med. Hypotheses* 143, 109906. doi: 10.1016/j.mehy.2020.109906
- Yubero, S., Ramudo, L., Manso, M. A., Colliá, F., and De Dios, I. (2012). Evaluation of N-acetylcysteine treatment in acute pancreatitis-induced lung injury. *Inflamm. Res.* 61, 699–705. doi: 10.1007/s00011-012-0462-6
- Zawrotniak, M., and Rapala-Kozik, M. (2013). Neutrophil extracellular traps (NETs) - formation and implications. *Acta Biochim. Pol.* 60, 277–284. doi: 10.18388/abp.2013\_1983
- Zemans, R. L., and Matthay, M. A. (2017). What drives neutrophils to the alveoli in ARDS? *Thorax* 72, 1–3. doi: 10.1136/thoraxjnl-2016-209170
- Zhang, Y., Ding, S., Li, C., Wang, Y., Chen, Z., and Wang, Z. (2017). Effects of N-acetylcysteine treatment in acute respiratory distress syndrome: A meta-analysis. *Exp. Ther. Med.* 14, 2863–2868. doi: 10.3892/etm.2017.4891
- Zhang, G., Zhang, J., Wang, B., Zhu, X., Wang, Q., and Qiu, S. (2020). Analysis of clinical characteristics and laboratory findings of 95 cases of 2019 novel coronavirus pneumonia in Wuhan, China: a retrospective analysis. *Respir. Res.* 21, 74. doi: 10.1186/s12931-020-01338-8
- Zhou, D., Dai, S. M., and Tong, Q. (2020). COVID-19: a recommendation to examine the effect of hydroxychloroquine in preventing infection and progression. *J. Antimicrob. Chemother.* 75, 1667–1670. doi: 10.1093/jac/dkaa114
- Zhou, P., Yang, X. L., Wang, X. G., Hu, B., Zhang, L., Zhang, W., et al. (2020). A pneumonia outbreak associated with a new coronavirus of probable bat origin. *Nature* 579, 270–273. doi: 10.1038/s41586-020-2012-7
- Zhu, Y., Li, J., and Pang, Z. (2020). Recent insights for the emerging COVID-19: drug discovery, therapeutic options and vaccine development. *Asian J. Pharm. Sci.* doi: 10.1016/j.ajps.2020.06.001

Zuo, Y., Yalavarthi, S., Shi, H., Gockman, K., Zuo, M., Madison, J. A., et al. (2020). Neutrophil extracellular traps in COVID-19. *JCI Insight* 5 (11), e138999. doi: 10.1172/jci.insight.138999

**Conflict of Interest:** The authors declare that the research was conducted in the absence of any commercial or financial relationships that could be construed as a potential conflict of interest.





*Copyright © 2020 Chiang, Korinek, Cheng and Hwang. This is an open-access article distributed under the terms of the Creative Commons Attribution License (CC BY). The use, distribution or reproduction in other forums is permitted, provided the original author(s) and the copyright owner(s) are credited and that the original publication in this journal is cited, in accordance with accepted academic practice. No use, distribution or reproduction is permitted which does not comply with these terms.*





## Article

# ***Salvia sclarea* L. Essential Oil Extract and Its Antioxidative Phytochemical Sclareol Inhibit Oxytocin-Induced Uterine Hypercontraction Dysmenorrhea Model by Inhibiting the $\text{Ca}^{2+}$ –MLCK–MLC20 Signaling Cascade: An Ex Vivo and In Vivo Study**

Jennifer Wong <sup>1</sup>, Yi-Fen Chiang <sup>1,†</sup>, Yin-Hwa Shih <sup>2</sup>, Chun-Hui Chiu <sup>3,4</sup>, Hsin-Yuan Chen <sup>1</sup> , Tzong-Ming Shieh <sup>5,6,†</sup>, Kai-Lee Wang <sup>7</sup> , Tsui-Chin Huang <sup>8</sup> , Yong-Han Hong <sup>9</sup> and Shih-Min Hsia <sup>1,10,11,12,\*</sup> 

<sup>1</sup> School of Nutrition and Health Sciences, College of Nutrition, Taipei Medical University, Taipei 11031, Taiwan; jenniferwong21@hotmail.com (J.W.); yvonne840828@gmail.com (Y.-F.C.); hsin246@gmail.com (H.-Y.C.)

<sup>2</sup> Department of Healthcare Administration, Asia University, Taichung 41354, Taiwan; s875008@gmail.com

<sup>3</sup> Graduate Institute of Health Industry and Technology, Research Center for Food and Cosmetic Safety, College of Human Ecology, Chang Gung University of Science and Technology, Taoyuan City 33303, Taiwan; chchiu@mail.cgust.edu.tw

<sup>4</sup> Department of Traditional Chinese Medicine, Chang Gung Memorial Hospital, Keelung City 20401, Taiwan

<sup>5</sup> School of Dentistry, College of Dentistry, China Medical University, Taichung 40402, Taiwan; tmshieh@mail.cmu.edu.tw

<sup>6</sup> Department of Dental Hygiene, College of Health Care, China Medical University, Taichung 40402, Taiwan

<sup>7</sup> Department of Nursing, Ching Kuo Institute of Management and Health, Keelung City 20301, Taiwan; kellywang@tmu.edu.tw

<sup>8</sup> Graduate Institute of Cancer Biology and Drug Discovery, College of Medical Science and Technology, Taipei Medical University, Taipei 11031, Taiwan; tsuichin@tmu.edu.tw

<sup>9</sup> Department of Nutrition, I-Shou University, Kaohsiung City 82445, Taiwan; yonghan@isu.edu.tw

<sup>10</sup> Graduate Institute of Metabolism and Obesity Sciences, College of Nutrition, Taipei Medical University, Taipei 11031, Taiwan

<sup>11</sup> School of Food Safety, College of Nutrition, Taipei Medical University, Taipei 11031, Taiwan

<sup>12</sup> Nutrition Research Center, Taipei Medical University Hospital, Taipei 11031, Taiwan

\* Correspondence: bryanhsia@tmu.edu.tw; Tel.: +886-273-61661-6558

† Equal contribution as first author.

Received: 1 September 2020; Accepted: 12 October 2020; Published: 14 October 2020



**Abstract:** *Salvia sclarea* essential oil is used as an aromatic therapy for dysmenorrhea. Sclareol—one of the natural products isolated from *S. sclarea*—displays anti-inflammatory and antioxidant activities; however, researchers have not yet evaluated the mechanism related to the pain-relieving effect of sclareol. In the present study, we aimed to investigate the potential effect of sclareol in ex vivo and in vivo dysmenorrhea models, as well as its possible mechanism. In the ex vivo study of uterine tissue from Sprague Dawley (SD) rats, the uterine contraction amplitude was observed and recorded. In the in vivo study, we measured the uterine contraction pressure of SD rats and performed writhing tests on mice. The uterine tissues from the writhing test subjects were collected and analyzed by Western blot. The results demonstrated that sclareol inhibited prostaglandin (PG)  $\text{F}_{2\alpha}$ -, oxytocin-, acetylcholine-, carbachol-, KCl-, and Bay K 8644-induced uterine contraction and possessed an analgesic effect in the writhing test. Sclareol affects the  $\text{Ca}^{2+}$  level and regulates oxytocin receptor (OTR), myosin light chain kinase (MLCK), extracellular signal-regulated kinase, p-p38, cyclooxygenase-2 (COX-2), and phospho-myosin light chain 20 (p-MLC20) protein

expression. Integrating these results, we suggest that sclareol is a potential alternative supplement for dysmenorrhea.

**Keywords:** sclareol; *Salvia sclarea* essential oil; dysmenorrhea; uterine contraction; writhing test

## 1. Introduction

Dysmenorrhea is the most common gynecological disease affecting reproductive women globally, with a 16–91% prevalence [1,2]. Instances of dysmenorrhea, leading to absence from school or work, affect performance, as well as causing economic losses [3]. Dysmenorrhea refers to when women undergo lower abdominal pain, who may present with associated symptoms, such as headache, diarrhea, and vomiting [1,4]. However, the reason for dysmenorrhea is still unclear, and most theories have been directed toward the high level of prostaglandin (PG) F<sub>2α</sub> in the menstrual phase [5]. PG is produced by cyclooxygenase-2 (COX-2) and it can stimulate vasoconstriction of the uterus, leading to ischemia [6]. PG can also cause sensitization of afferent nerves, resulting in the painful symptoms of dysmenorrhea [7].

The pain of dysmenorrhea is caused by uterine hyper-contraction. Calcium is one of the most important manipulators of this contraction [8]. Contractions occur in the smooth muscle upon calcium influx through the calcium channel, where calcium and calmodulin form a complex which activates myosin light chain kinase (MLCK) to induce the extracellular signal-regulated kinase (ERK)/p38 signaling pathway. Furthermore, phosphorylated myosin light chain 20 (MLC-20) is combined with actin, resulting in cross-bridge cycling and uterine contraction [9].

Aromatherapy has been used as a form of pain-relief therapy [10], using essential oils, such as clary sage, marjoram, and lavender oils. Sclareol is one of the compounds found in *Salvia sclarea* essential oil, isolated from *Salvia sclarea* flowers or leaves, and it is classified as a bicyclic diterpene alcohol [11]. It has been noted that sclareol displays antitumor, anti-inflammation, antioxidant, and immune-regulation activity both in vivo and in vitro [12–15]. The condition of chronic inflammation is highly correlated with pain [16], also indicating that chronic inflammation is related to uterine pain behavior in an endometriosis model [17]. Several natural compounds show high antioxidant and anti-inflammation effects, such as extra virgin olive oil (EVOO) [18–20] and resveratrol [21], which can decrease inflammatory cytokine levels and prevent oxidative-related cell death. Sclareol can regulate inflammation by affecting the protein expression of COX-2 [12,13], as well as antioxidant enzyme activity. These reasons indicate that sclareol has the potential to improve dysmenorrhea. In this study, we investigated the anti-dysmenorrhea activities of sclareol in ex vivo and in vivo dysmenorrhea models, as well as its possible mechanism.

## 2. Materials and Methods

### 2.1. Reagent Preparation

Sclareol (CAS: 515-03-7, 98%), oxytocin, sodium bicarbonate, carbachol, acetylcholine (ACh), mannitol, glucose, potassium chloride, potassium phosphate, magnesium sulfate, calcium chloride, estradiol, and dimethyl sulfoxide (DMSO) were purchased from (Sigma-Aldrich, St. Louis, MO, USA). PGF<sub>2α</sub> and Bay K 8644 were purchased from (Cayman Chemical Company, Ann Arbor, MI, USA).

### 2.2. Ultra-Performance Liquid Chromatography–Mass Spectrometry (UPLC–MS) Analysis of Total Sclareol Content of *Salvia sclarea* Essential Oil

The *Salvia sclarea* L. essential oil (Can June International Inc., Taipei, Taiwan) was diluted to an appropriate concentration with ethanol and filtrated using a nylon filter (0.22 μm) before being injected into the ultra-performance liquid chromatography–mass spectrometry (UPLC–MS)

system. Standard stock solutions of sclareol standard (Sigma-aldrich, St. Louis, MO, USA) were dissolved in ethanol and the calibration range was 20–150 ng/mL with a correlation coefficient of 0.999. The system included a Waters Acquity UPLC equipped with a pump, column compartment, autosampler, and Waters TQS mass spectrometer (Waters, Milford, MA, USA) operated in positive electrospray ion (ESI<sup>+</sup>) mode. The Acquity UPLC HSS T3 (1.8 µm; 2.1 mm × 100 mm) column was employed and maintained at 35 °C with a flow rate at 0.3 mL/min and injection of 2 µL. The mobile phase consisted of 10% (A) and 90% methanol (B), both containing 5 mM ammonium acetate and 0.1% formic acid. The linear gradient conditions were as follows: 1–99% A (0–10 min), 99% B (10–12 min). The ESI parameters were set as follows: capillary voltage, 3.0 kV; cone voltage, 15 V; desolvation temperature, 400 °C; source temperature, 150 °C; desolvation gas flow, 850 L/h; cone gas flow, 150 L/h; nebulizer gas flow, 7.0 bar. Selected ion recording (SIR) mode was used to monitor sclareol at  $m/z$  331 [M + Na]<sup>+</sup>. All data were collected using MassLynx 4.1 software spectrometer (Waters, Milford, MA, USA).

### 2.3. Cell Culture

Human uterine smooth muscle cells were obtained from promo cells and were cultured in Dulbecco's modified Eagle's medium, nutrient Mixture F-12 (DMEM F12) (Caisson, Taichung City, Taiwan) supplemented with 10% fetal bovine serum (FBS) (Gibco, Grand Island, NY, USA) and 100× penicillin–streptomycin solution (Corning, Manassas, VA, USA) at 37 °C in a humidified 5% CO<sub>2</sub> incubator.

### 2.4. Reactive Oxygen Species (ROS) Measurement

For treatments, cells were cultured in 96-well plates (1000 cells/well), treated with 1 µM PGF<sub>2α</sub> and sclareol for 30 min, and incubated with 25 µM 2',7'-dichlorofluorescein diacetate (DCFDA) for 30 min. A fluorescence microscope was used to capture the fluorescence. We used ImageJ to quantify the ROS density.

### 2.5. Animals

Female imprinting control region (ICR) mice (18–22 g) and Sprague Dawley (SD) rats (200–300 g) were housed in a temperature-controlled and 12 h/12 h artificial illumination room, given *ad libitum* access to food and water. All animal studies were conducted according to the protocols approved by the IACUC of Taipei Medical University (Permit No. LAC-2019-0350, LAC-2019-0351 and LAC-2019-0645).

### 2.6. Uterine Tissue Preparations and Measurement of Uterine Contraction *Ex Vivo*

Preparation and measurement were carried out according to previously studies [21,22]. SD rats were sacrificed by CO<sub>2</sub> and the uterus was surgically removed. Uterine tissue was placed in a container that contained Krebs solution (113 mM NaCl, 4.8 mM KCl, 2.5 mM CaCl<sub>2</sub>, 18 mM NaHCO<sub>3</sub>, 1.2 mM KH<sub>2</sub>PO<sub>4</sub>, 1.2 mM MgSO<sub>4</sub>, 5.5 mM glucose, and 30 mM mannitol; pH 7.4), adherent fat, and connective tissue guardedly removed from the uterus. Each piece of uterine tissue was cut at the same length and set in an isolated organ bath which contained Krebs solution, bubbled with 95% O<sub>2</sub> and 5% CO<sub>2</sub> at 37 °C. We preloaded 1 g and equilibrated after at least 30 min. After equilibration, uterine tissue contractions were stimulated using different drugs (10<sup>−6</sup> M PGF<sub>2α</sub>, 10<sup>−6</sup> M oxytocin, 10<sup>−5</sup> M carbachol, 10<sup>−6</sup> M Ach, 50 mM KCl, and 10<sup>−6</sup> M Bay K 8644). Sclareol (10, 25, 50, 75 and 100 µM), *Salvia sclarea* essential oil (10, 25, 50, 75, and 100 ppm), or DMSO (solvent control) was added to the organ bath at 10 min intervals. The contraction tension was detecting by force displacement transducers and recorded using LabScribe. To revise for variations between individual uterine contractions, the mean amplitude vales of the pretreatment intervals were expressed as a percentage of control values and taken as 100%.

### 2.7. Measurement of Uterine Contraction Pressure in the In Vivo Study

The method for the measurement of uterine contraction in vivo was modified from previous studies [21,22]. SD rats were anesthetized. We then made a ventral incision at the abdomen and uterus. We put a thin catheter into the uterus, and the catheter was connected to a transducer to detect pressure transformations, which were recorded using LabScribe software. The rat was injected with oxytocin (1 IU) intraperitoneally (ip) to stimulate uterine hypercontraction, with an ip injection of sclareol (5, 10, or 15 mg/kg) at 20 min intervals. The mean amplitude values of the pretreatment intervals were expressed as a percentage of control values and taken as 100%.

### 2.8. Measurement of Uterine Tissue under $\text{Ca}^{2+}$ -Dependent Contractions

This study method was modified from [23]. The uterine tissue was placed in an organ bath containing  $\text{Ca}^{2+}$ -free Krebs solution. After equilibration, sclareol (100  $\mu\text{M}$ ) was added; then, the  $\text{Ca}^{2+}$ -free Krebs solution was supplied with increasing concentrations of  $\text{Ca}^{2+}$ , from 0.5 to 5 mM, to restore spontaneous contraction. In another study, the uterine tissues were placed in an organ bath containing  $\text{Ca}^{2+}$ -free Krebs solution. After equilibration, oxytocin ( $10^{-6}$  M) was added to the organ bath to induce intracellular  $\text{Ca}^{2+}$  release from the sarcoplasmic reticulum to produce contractions; then, sclareol (10, 25, 50, 75, and 100  $\mu\text{M}$ ) or DMSO (solvent control) was added to the organ bath at 10 min intervals.

### 2.9. Acetic Acid-Induced Writhing Test

Forty-eight female ICR mice were randomly separated into six groups (control, model control, 50 mg/kg sclareol, 100 mg/kg sclareol, and 150 mg/kg sclareol,  $n = 8/\text{group}$ ) and were orally pretreated with PBS (control and model control group) and sclareol (50, 100, or 150 mg/kg) 15 min before induction. After pretreatment, all animals received an ip injection of PBS (only control group) or acetic acid (0.6%, 10 mL/kg). The number of writhes was recorded in the 30 min after the ip injection. Analgesia (%) = (model control writhing times – (sclareol writhing times))/model control writhing times.

### 2.10. Oxytocin-Induced Writhing Test

The oxytocin-induced writhing test was carried out according to previous studies [24–26]. Forty-eight female ICR mice were randomly separated into six groups ( $n = 4\text{--}8/\text{group}$ ): control, model control, 50 mg/kg sclareol, 100 mg/kg sclareol, and 150 mg/kg sclareol. All mice were pretreated with estradiol ( $\text{E}_2$ , ip, 1 mg/kg) for seven consecutive days. Different doses of sclareol (50, 100, or 150 mg/kg) were administered orally for three days before ip injection  $\text{E}_2$ . On day 7, oxytocin (70 IU/kg) was given as an ip injection after pretreatment for 15 min. The number of writhes was recorded in the 30 min after the ip injection. After the test, mice were sacrificed, and uterine tissue was collected for further analysis. Analgesia (%) = (model control writhing times – (sclareol writhing times))/model control writhing times.

### 2.11. Lipid Peroxidation Determination

The lipid peroxidation was measured using the level of malondialdehyde (MDA) in the serum. We used a 2-thiobarbituric acid-reacting substances test (TBARS) assay kit and followed the manufacturer's instructions. Results were measured on a 532 nm plate using a VERSA Max microplate reader (Molecular Devices, San Jose, CA, USA).

### 2.12. Western Blotting Analysis

Tissue proteins were homogenized by means of a radioimmunoprecipitation assay buffer containing protease inhibitor and phosphatase inhibitor (Roche Mannheim, Baden-Württemberg, Germany). Protein samples were quantitated using the bicinchoninic acid assay (BCA) (T-Pro Biotechnology, Dublin, UK). In total, 40–60  $\mu\text{g}$  of protein in the sample was separated by 10–12%

SDS-PAGE. The protein was transferred to 0.22  $\mu\text{m}$  poly (vinylidene fluoride) (PVDF) membranes and blocked with 5% bovine serum albumin (BSA) for 1 h at room temperature (RT). The membrane was incubated with primary antibodies, including oxytocin receptor (OTR) (1:500, sc-8103, Santa Cruz), myosin light-chain kinase (MLCK) (1:1000, sc-25428, Santa Cruz), cyclooxygenase-2 (COX-2) (1:200, 160126, Cayman), phosphorylated extracellular signal-regulated kinase (p-ERK) (1:1000, #9101, Cell signaling), ERK (1:1000, #9102, Cell signaling), p-p38 (1:1000, #9211, Cell signaling), p38 (1:1000, #9212, Cell signaling), phosphorylated myosin light chain-20 (p-MLC20) (1:1000, #3675, Cell signaling), MLC20 (1:1000, sc-28319, Santa Cruz), and  $\alpha$ -actin (1:5000, sc-32251, Santa Cruz) overnight at 4 °C. Then, the membranes were incubated with a secondary horseradish peroxidase (HRP) -conjugated antibody (anti-mouse or anti-rabbit, 1:10000 or anti-goat, 1:500, RT, 2 h) and visualized using enhanced chemiluminescence (ECL) (T-Pro Biotechnology). Results were quantitated using ImageJ software.

### 2.13. Statistical Analysis

All results are expressed as the means  $\pm$  standard error of the mean (SEM), analyzed using GraphPad Prism version 5.0 software (GraphPad, San Diego, CA, USA). Calculation of statistically significant differences was performed using one-way analysis of variance (ANOVA) with Tukey's post hoc test or the Mann–Whitney U test. A Student's unpaired *t*-test was used for comparison between two groups. Significance was accepted at  $p < 0.05$ .

## 3. Results

### 3.1. Effect of *Salvia sclarea* L. Essential Oil on $\text{PGF}_{2\alpha}$ -Induced Uterine Contractions

To explore whether *Salvia sclarea* L. essential oil had the potential to inhibition uterine contraction, we first used  $\text{PGF}_{2\alpha}$  to induce uterine contraction, as  $\text{PGF}_{2\alpha}$  is the major factor leading to dysmenorrhea. Figure 1A,B show that  $\text{PGF}_{2\alpha}$  ( $10^{-6}$  M) significantly increased the contraction amplitude, and, when exposed to *Salvia sclarea* essential oil (at 10, 25, 50, 75, and 100 ppm), the contraction amplitude was inhibited in a dose-dependent manner; at 25–100 ppm, it was significantly inhibited. This verifies that *Salvia sclarea* essential oil has the potential to inhibit uterine contraction.

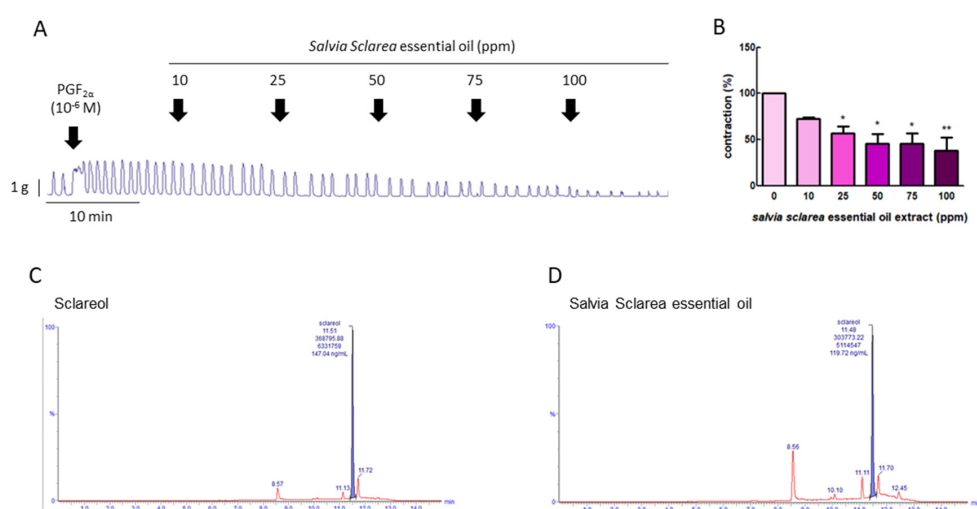


**Figure 1.** Effect of *Salvia sclarea* L. essential oil on prostaglandin (PG)  $\text{F}_{2\alpha}$ -induced uterine contraction and total sclareol content in *Salvia sclarea* L. essential oil. (A) Representative recordings of rat uterine tissue were induced with  $\text{PGF}_{2\alpha}$  ( $10^{-6}$  M) along with exposure of rat uterine smooth muscles to essential oil (at 10, 25, 50, 75, and 100 ppm.) (B) Dose-dependent effects of essential oil on the mean peak amplitude. Each column represents the mean  $\pm$  standard error of the mean (SEM);  $n = 4$ ; \*  $p < 0.05$ , \*\*  $p < 0.001$  compared to 0. (C) Ultra-performance liquid chromatography (UPLC)–MS/MS chromatogram of sclareol standard. (D) UPLC–MS/MS chromatogram of *Salvia sclarea* essential oil.



### 3.2. Total Sclareol Content of *Salvia sclarea* L. Essential Oil

To evaluate the effective compound in *Salvia sclarea* L. essential oil, the total sclareol content of *Salvia sclarea* essential oil was analyzed using UPLC-MS/MS. We found that the retention time of sclareol was 11.51 min, and that of clary sage oil was 11.48 min. The sclareol content in clary sage oil was 0.239%, according to the calibration curve (Figure 1C,D).

### 3.3. Effect of Sclareol on Oxytocin-Induced Uterine Contraction In Vivo

To confirm the inhibitive effect of sclareol in vivo, we examined the uterine contraction pressure of rats. The rats were ip injected with oxytocin (1 IU) to induce uterine contraction, and then ip injected with 5, 10, or 15 mg/kg sclareol. The intervention of sclareol was able to significantly reduce the uterine contraction pressure, proving that sclareol is able to affect the uterine contractions in vivo (Figure 2).

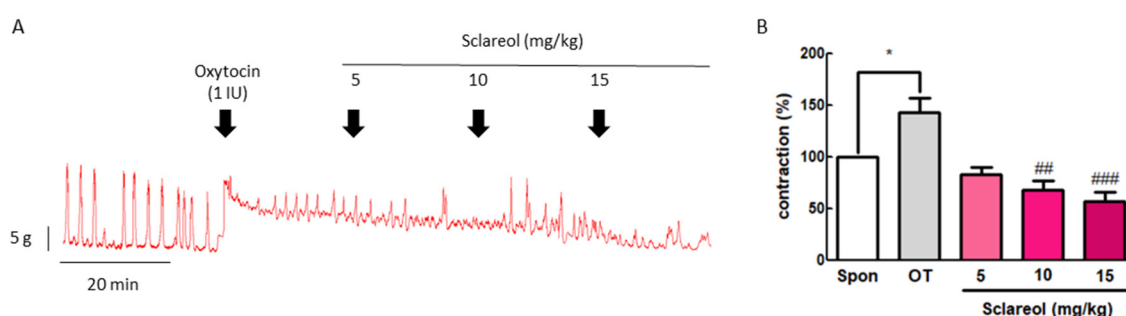


**Figure 2.** Effect of sclareol on oxytocin-induced uterine contraction in vivo and its possible mechanism. (A) Effect of sclareol (5, 10, or 15 mg/kg) on oxytocin-induced (1 IU) uterine contractions in vivo. The rats were ip injected with oxytocin combined with sclareol (5, 10, or 15 mg/kg), and the contractions were recorded. (B) The effects of sclareol on the mean peak amplitude. \*  $p < 0.05$  compared to spontaneous contraction (Spon), ##  $p < 0.01$  compared to oxytocin, ###  $p < 0.001$  compared to oxytocin. Each column represents the mean  $\pm$  SEM;  $n = 7$ .

### 3.4. Effect of Sclareol on $\text{PGF}_{2\alpha}$ -, Oxytocin-, Acetylcholine-, and Carbachol-Induced Uterine Contractions

Since sclareol is contained in *Salvia sclarea* L. essential oil, we further examined the effect of sclareol on uterine contractions, to investigate whether sclareol can affect uterine contractions via different pathways. We, thus, examined the effect of sclareol on  $\text{PGF}_{2\alpha}$ -, oxytocin-, acetylcholine-, and carbachol-induced uterine contractions.  $\text{PGF}_{2\alpha}$  is the main reason for the increase in dysmenorrhea. Oxytocin, acetylcholine, and carbachol are intended to release intracellular stored  $\text{Ca}^{2+}$ . As a result,  $\text{PGF}_{2\alpha}$  ( $10^{-6}$  M) can significantly increase the contraction amplitude, and, at concentrations of 25–100  $\mu\text{M}$ , sclareol was significantly inhibited, showing that sclareol can possibly be used to treat uterine hypercontraction (Figure 3A). Sclareol significantly decreased oxytocin-, acetylcholine-, and carbachol-induced uterine contraction in different dosages (Figure 3B,D). The vehicle (DMSO) did not affect oxytocin-, acetylcholine-, and carbachol-induced uterine contraction.

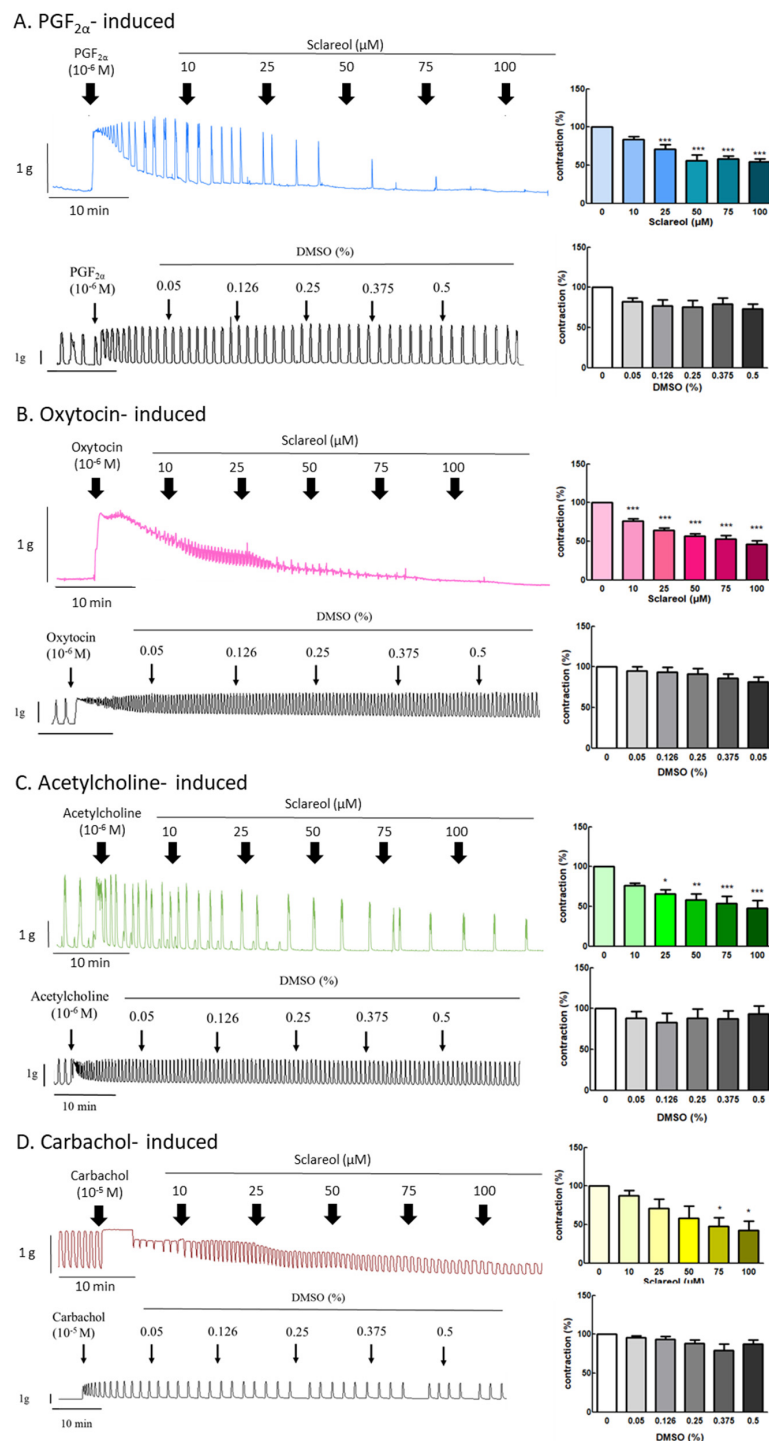


**Figure 3.** Effect of sclareol on drug-induced uterine contraction. Representative recordings of rat uterine tissues were induced with (A) 10<sup>-6</sup> M PGF<sub>2α</sub>, (B) 10<sup>-6</sup> M oxytocin, (C) 10<sup>-5</sup> M carbachol, and (D) 10<sup>-6</sup> M acetylcholine Ach, with exposure of rat uterine smooth muscles to sclareol (10, 25, 50, 75, and 100 μM). Dose-dependent effects of sclareol on the mean peak amplitude. Each column represents the mean ± SEM; n = 4–8. \* p < 0.05, \*\* p < 0.01 and \*\*\* p < 0.001 compared to 0 (drug-induced only).

### 3.5. Effect of Sclareol on KCl- and Bay K 8644-Induced Uterine Contractions

To explore the effect of extracellular calcium on uterine contraction, we used KCl to create High-K<sup>+</sup> conditions due to membrane depolarization, causing extracellular Ca<sup>2+</sup> entry through the voltage-dependent calcium channel. Bay K 8644 is an L-type Ca<sup>2+</sup>-channel activator that increases

the entry of extracellular  $\text{Ca}^{2+}$ . Administration of sclareol along with KCl (10–100  $\mu\text{M}$ ) or Bay K 8644 (75–100  $\mu\text{M}$ ) resulted in a dose-dependent decrease in uterine contractions (Figure 4A,B).

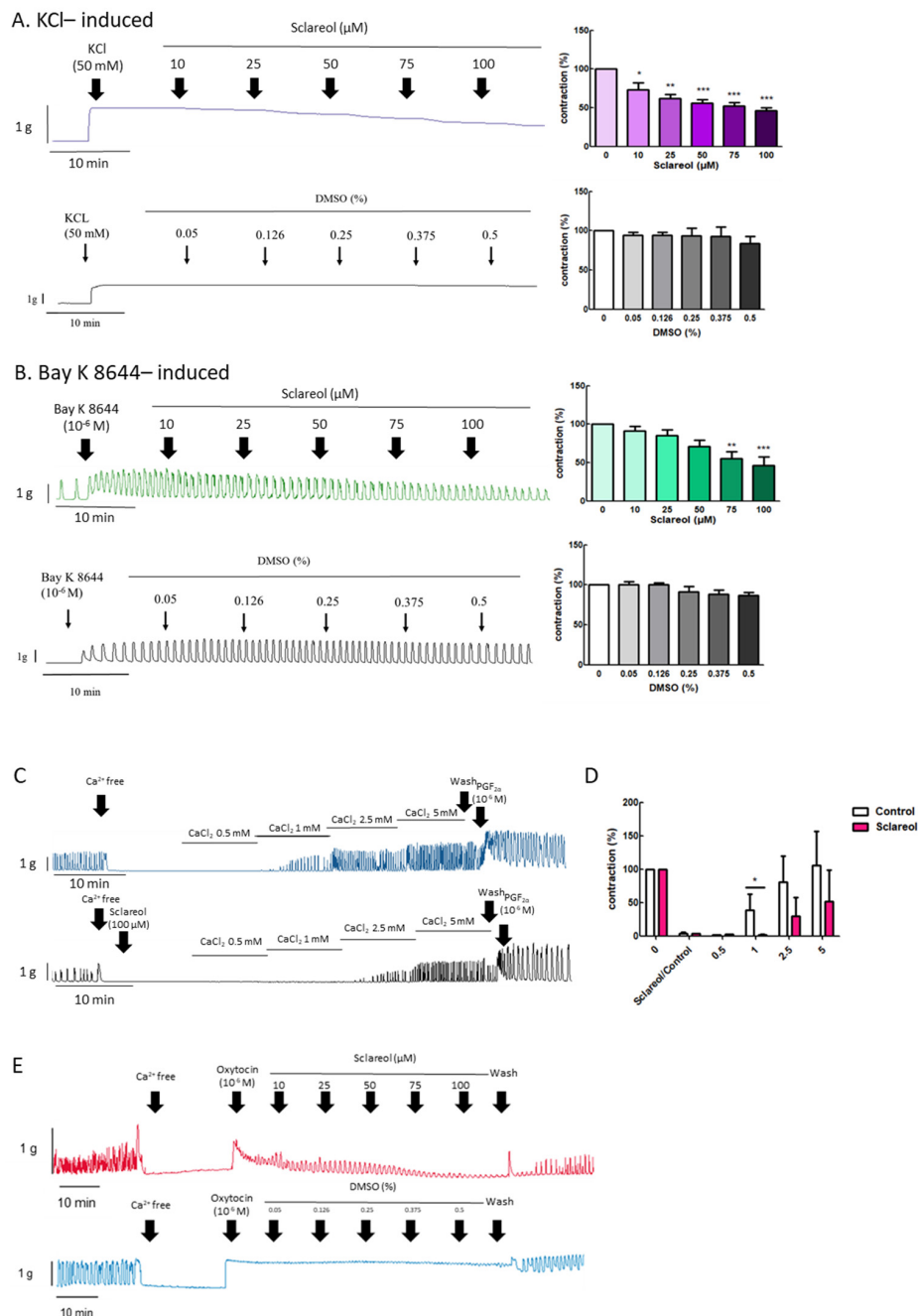


**Figure 4.** Effect of sclareol on  $\text{Ca}^{2+}$ -dependent contractile responses. Representative recordings of rat uterine contractions were induced with (A) 50 mM KCl and (B)  $10^{-6}$  M Bay K 8644, with exposure of rat uterine smooth muscles to sclareol (10, 25, 50, 75, and 100  $\mu\text{M}$ ). Dose-dependent effects of sclareol on the mean peak amplitude. Each column represents the mean  $\pm$  SEM;  $n = 4$ –8. \*  $p < 0.05$ , \*\*  $p < 0.01$  and \*\*\*  $p < 0.001$  compared to 0 (drug-induced only). Inhibitory actions of sclareol on  $\text{Ca}^{2+}$ -dependent contractile responses. (C) Muscle segments were initially pretreated in a  $\text{Ca}^{2+}$ -free medium containing calcium (0.5–5 mM) only or plus sclareol (100  $\mu\text{M}$ ), and calcium was then cumulatively applied to trigger muscle contraction. (D) Inhibitory effect of sclareol on the mean peak amplitude. \*  $p < 0.05$  compared to control;  $n = 3$ . (E) Rat uterine contractions were induced with oxytocin (OT) ( $10^{-6}$  M) and exposure to sclareol (10, 25, 50, 75, and 100  $\mu\text{M}$ ) or DMSO (0.05%, 0.126%, 0.25%, 0.375%, and 0.5%).

### 3.6. Effect of Sclareol on $\text{Ca}^{2+}$ -Dependent Contractions

When uterine tissue is in  $\text{Ca}^{2+}$  free conditions, the spontaneous contractions were invalidated. Along with an increase in  $\text{Ca}^{2+}$  concentrations, the spontaneous contractions were recovered. To test the calcium-dependent contraction, we used a calcium-free solution for further examination. When in the  $\text{Ca}^{2+}$ -free Krebs solution combined with sclareol treatment, the contractions declined (Figure 4C,D). As shown in Figure 4E, oxytocin ( $10^{-6}$  M) was added to an organ bath to increase the calcium influx, which recovered the uterine contraction, and sclareol showed the inhibition of calcium influx-induced contraction. This demonstrates that sclareol can effectively decrease calcium-dependent contractions.

### 3.7. Effect of Sclareol on $\text{PGF}_{2\alpha}$ -Induced Uterine Contraction-Related Protein Expression

To examine the possible mechanism of sclareol's inhibition of uterine contractions, we used Western blot analysis to observe the uterine contraction-related protein expression. Uterine tissue was collected after treatment with  $\text{PGF}_{2\alpha}$  or in combination with sclareol (100  $\mu\text{M}$ ) for 30 min. Uterine tissue that was treated with the sclareol combination presented significantly lower protein expression of COX-2, MLCK, p-ERK, p-p38, and p-MLC20 compared with the uterine tissue treated with  $\text{PGF}_{2\alpha}$ , illustrating that sclareol inhibited uterine contraction by affecting calcium-related signaling and protein expression (Figure 5B,F).

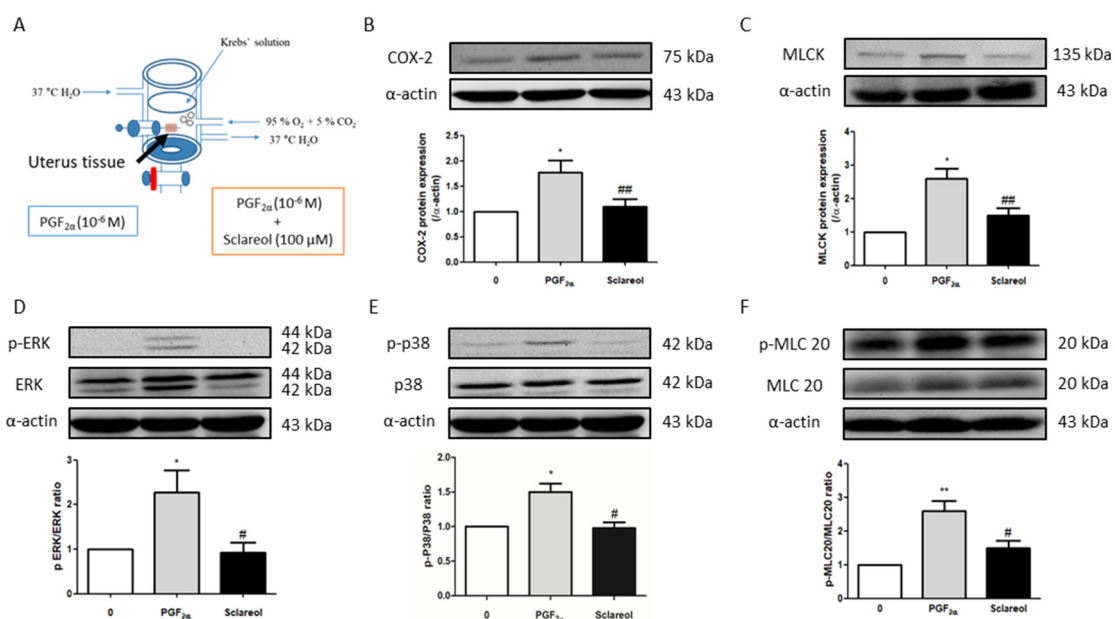


**Figure 5.** Possible mechanism underlying the effect of sclareol on  $\text{PGF}_{2\alpha}$ -induced uterine contraction. (A) Tissue collection method. After  $\text{PGF}_{2\alpha}$ -induced uterine contraction in the presence of 0 and 100  $\mu\text{M}$  sclareol, the uterus was taken out (at 30 min). (B–F) Protein expression of cyclooxygenase-2 (COX-2), myosin light-chain kinase (MLCK), phosphorylated extracellular signal-regulated kinase (p-ERK), ERK, p-p38, p38, phosphorylated myosin light chain 20 (p-MLC20), MLC20, and  $\alpha$ -actin during  $\text{PGF}_{2\alpha}$ -induced contraction at 30 min in rat uterus;  $n = 3$ –6; \*  $p < 0.05$ , \*\*  $p < 0.001$  compared to 0; #  $p < 0.05$ , ###  $p < 0.01$  compared to  $\text{PGF}_{2\alpha}$ . Each column represents the mean  $\pm$  SEM.

### 3.8. Effect of Sclareol on Acetic Acid-Induced Writhing Test

To evaluate analgesic effects, we used the acetic acid-induced writhing model. The acetic acid solution significantly increased writhing times in the model control group and attained 62.5 times more writhing in 30 min. On the other hand, intervention with sclareol (at 50, 100, and 150 mg/kg) was able to significantly reduce the writhing times compared to the model control group, demonstrating that sclareol possesses analgesic effects (Table 1).

**Table 1.** Effect of sclareol on acetic acid- and oxytocin-induced writhing tests.

Model	Acetic Acid- Induced		Oxytocin-Induced(Pretreat Sclareol)	
Group	Writhing Times /30 min	Analgesia (%)	Writhing Times /30 min	Analgesia (%)
Control	0.0 ± 0.0	-	0.0 ± 0.0	-
Model control (MC)	62.5 ± 18.6 ***	-	17.4 ± 5.6 ***	-
Sclareol (mg/kg)	50	24.6 ± 16.5 ##	60.7	4.0 ± 3.3 ###
	100	30.4 ± 11.0 ##	51.3	3.5 ± 2.8 ###
	150	36.2 ± 19.8 #	42.1	1.8 ± 1.7 ###

Analgesia (%) = (Model control writhing times—(sclareol writhing times))/model control writhing times. \*\*\*  $p < 0.001$  compared to control group, #  $p < 0.05$  compared to model control group, ##  $p < 0.01$  compared to model group, ###  $p < 0.001$  compared to model group. Each column represents the mean ± SEM;  $n = 4-8$ .

### 3.9. Effect of Sclareol on Oxytocin-Induced Writhing Test

To further evaluate the inhibition of uterine hypercontraction pain, we used an oxytocin-induced writhing model. The injection of oxytocin could significantly increase writhing times in model control groups, and the administration of sclareol (at 50, 100, and 150 mg/kg) could significantly decrease the writhing times in 30 min. This demonstrates that sclareol has the potential to improve dysmenorrhea (Table 1).

### 3.10. Effect of Sclareol on Oxidative Stress in Uterine Smooth Muscle Cell and Dysmenorrhea Mice

A significant increase in the serum MDA level was observed in the oxytocin-treated group compared with the control group. As treatment with sclareol decreased significantly, oxytocin-induced oxidative stress increased. We used an in vitro method to examine the ROS fluorescence density. The results showed that the PGF2 $\alpha$ -induced group had a significantly higher ROS density, and a high dose of sclareol could eliminate the increase in ROS density. This shows that the high antioxidant ability of sclareol plays an important role in the inhibition of dysmenorrhea (Figure 6).

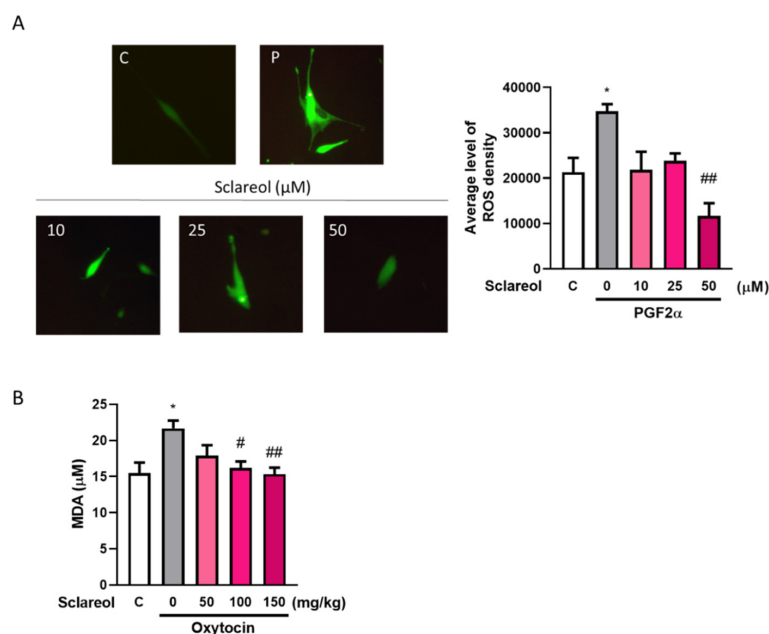


**Figure 6.** Effect of sclareol on oxidative stress in uterine smooth muscle cell and dysmenorrhea mice. (A) Reactive oxygen species (ROS) density in in vitro study. \*  $p < 0.05$  compared with control group, ##  $p < 0.01$  compared with sclareol 0  $\mu$ M group; C, control group. (B) Serum MDA concentration in oxytocin-induced writhing test. \*  $p < 0.05$  compared with control group; #  $p < 0.05$ , ##  $p < 0.01$  compared with sclareol 0 mg/kg group;  $n = 3-8$ ; the graph was captured at 20 $\times$  magnification.



### 3.11. Effect of Sclareol on Oxytocin-Induced Uterine Contraction-Related Protein Expression

To investigate the possible mechanism underlying sclareol's improvement of writhing times in the oxytocin-induced writhing test, we used Western blot analysis to observe the uterine contraction-related protein expression. We found that the intervention of sclareol resulted in a lower protein expression of p-MLC20/MLC20, p-ERK/ERK, p-p38/p38, COX-2, MLCK, and OTR. These results, as well as those of the earlier Western blot study from rat uterine tissue, prove that sclareol improves dysmenorrhea by affecting calcium-related signaling and protein expression (Figure 7).

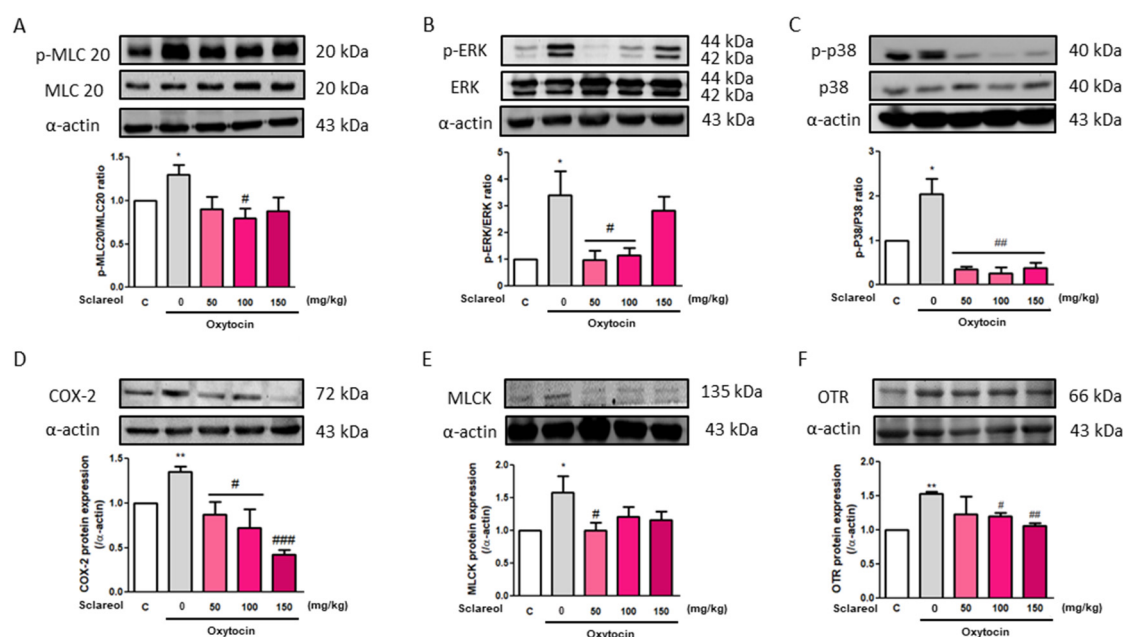


**Figure 7.** Effect of sclareol on uterine contraction-related protein expression in oxytocin-induced writhing test model. The (A) p-MLC20/MLC20, (B) p-ERK/ERK, (C) p-p38/p38, (D) COX-2, (E) MLCK, and (F) oxytocin receptor (OTR) levels were detected by Western blot. C, Control; 0, model control group; 50, sclareol 50 mg/kg; 100, sclareol 100 mg/kg; 150, sclareol 150 mg/kg;  $n = 4-6$ ; \*  $p < 0.05$ , \*\*  $p < 0.01$  compared to C; #  $p < 0.05$ , ##  $p < 0.01$ , ###  $p < 0.001$  compared to the sclareol 0 mg/kg group. Each column represents the mean  $\pm$  SEM;  $n = 3-5$ .

## 4. Discussion

Sclareol is a labdane-type diterpenes compound, which was first extracted from the plant *Salvia sclarea* L. (Lamiaceae). Sclareols are widely used in the food and cosmetic industries and as supplements. Recently, it has been widely used in anticancer [27] and anti-inflammation experiments [12]. Sclareol inhibited lipopolysaccharide-induced lung injury via the inhibition of p-ERK and p-p38 protein expression to reduce the mitogen-activated protein kinase (MAPK) signaling transduction pathway, further inhibiting COX-2 expression and having an antioxidant effect, decreasing the number of reactive oxygen species (ROS) and inflammation [12]. Furthermore, in cancer research, it was shown that sclareol has an outstanding effect on the inhibition of the ERK-related signaling pathway [28]. These effects of sclareol demonstrate the capacity for *Salvia sclarea* essential oil to be used for the improvement of dysmenorrhea symptoms [29]. It has been used as an abdominal massage oil, and it was proven to be effective in decreasing the severity of dysmenorrhea [30]. The results of the present study demonstrate that *Salvia sclarea* essential oil reduced uterine contractions in a PGF<sub>2α</sub>-induced rat uterine contraction model, illustrating that *Salvia sclarea* essential oil can improve dysmenorrhea via the reduction of uterine hypercontraction.

In this study, we used different agents to induce uterine contraction, and those agents acted on different receptors, such as PGF<sub>2α</sub> acting on the FP receptor, oxytocin acting on OTR [31], acetylcholine

and carbachol acting on the muscarinic acetylcholine receptor (M3) receptor [32], and Bay K 8644 and KCl affecting the voltage-gated calcium channels (VDCC) [33,34]. Although uterotonic hormones (PGF<sub>2α</sub>, oxytocin, acetylcholine, and carbachol) act on different receptors, they all induce uterine contraction via increases in extracellular Ca<sup>2+</sup> entry and intracellular Ca<sup>2+</sup> release. Moreover, Bay K 8644 (a Ca<sup>2+</sup> channel activator) and KCl solution (which creates high K<sup>+</sup> conditions, leading to membrane depolarization) increase extracellular Ca<sup>2+</sup> via the VDCC [21]. In addition, when the uterine tissue is in Ca<sup>2+</sup>-free Krebs solution, oxytocin can induce contraction via intracellular Ca<sup>2+</sup> release from the sarcoplasmic reticulum [23]. Obviously, sclareol showed inhibitory effects in this study, demonstrating that the relaxation effect induced by sclareol can take place via several receptors, thus affecting Ca<sup>2+</sup> level.

Phosphorylated MLC20 (p-MLC20) plays a pivotal role in regulating uterine smooth muscle contraction, and it is the only known physiological substrate of MLCK [35]. Phosphorylated ERK is one of the proteins that can active MLCK [25,36]. p-ERK also acts as a signaling trigger in several pathways. Previous studies showed that sclareol can significantly decrease the activity of the p38-AMPK signaling pathway [37]. In cancer research, sclareol not only showed an anticancer effect, but also had the ability to target the mitogen-activated protein kinase (MAPK)/extracellular signal-regulated kinase (ERK) signaling pathway [28], showing that sclareol can modulate the ERK/p38 signaling pathway. This is the first study to claim the effect of sclareol on the calcium-related muscle contraction signaling pathway. Our results showed that p-ERK, MLCK, and p-MLC20 protein expression was increased in PGF<sub>2α</sub>-induced rat uterine tissue, and that intervention with sclareol was able to reduce the expression of those proteins, indicating that the effect of sclareol on uterine contraction may take place by affecting p-ERK, MLCK, and p-MLC20 protein expression.

PGF<sub>2α</sub> is a critical factor in dysmenorrhea and a product of COX-2. Hence, nonsteroidal anti-inflammatory drugs (NSAIDs) have been used as a first-line therapy for treating dysmenorrhea. NSAIDs are a cyclooxygenase inhibitor; they can inhibit COX, reducing prostaglandin production. However, NSAIDs have around a 30% failure rate [38], and disorders of the liver, kidney, and digestive system can occur when using them in the long term. In a previous study, it was shown that p-p38 is a protein that can regulate Phospholipase A2 (PLA<sub>2</sub>) activity, decreasing the production of arachidonic acid and PGH<sub>2</sub> [39], which is the first intermediate in the biosynthesis of all PGs [6]. In our study, we found that p-p38 protein expression was increased in PGF<sub>2α</sub>-induced rat uterine tissue, suggesting that sclareol potentially improves inflammatory conditions in dysmenorrhea by affecting p-p38 protein expression.

The acetic acid-induced writhing test has been used as a screening tool for peripheral analgesic or anti-inflammatory new substances [40]. When mice are ip injected with acetic acid solutions, proinflammatory substances are released, activating peripheral nociceptors, leading to pain and writhing responses [24]. Compared to the control group, a significant reduction in writhing times is considered an antinociceptive response [41]. Sclareol produced significant reductions in writhing times, suggesting that sclareol exerts a peripheral analgesic effect. Although it did not show a dose-dependent result, this can be explained by the suggestion that a low dose of sclareol exerted central control at the brain or spinal cord level to provide an analgesic effect [42]. A high dose of sclareol can provide an anti-inflammatory effect; however, it takes more than 15 min to act.

To further explore the possibility of using sclareol to relieve dysmenorrhea, an oxytocin-induced writhing test was carried out. The oxytocin-induced writhing test is a reliable model for primary dysmenorrhea [43]. This model reflects the clinical features and pathogenesis of dysmenorrhea, such as uterine contraction, PG synthesis, pain, and Ca<sup>2+</sup> entry [26]. Pretreatment with estrogen could increase the oxytocin receptor (OTR) protein expression and increase the writhing responses induced by oxytocin [44]. In this study, oxytocin significantly increased writhing times and OTR protein expression, as in previous studies, and the intervention with sclareol attenuated writhing times and OTR protein expression. Equally, sclareol inhibited oxytocin-induced uterine contraction *ex vivo*. These findings imply that sclareol can reduce dysmenorrhea.

## 5. Conclusions

Our findings suggest that sclareol is a potential natural product that can treat primary dysmenorrhea. In fact, this is the first study showing the relationship between sclareol and dysmenorrhea. Furthermore, sclareol improved dysmenorrhea via downregulating the protein expression of OTR, MLCK, COX-2, p-ERK, p-p38, and p-MLC20 and regulating the concentration of intracellular calcium. Hence, sclareol may ameliorate primary dysmenorrhea and inflammation (Figure 8).

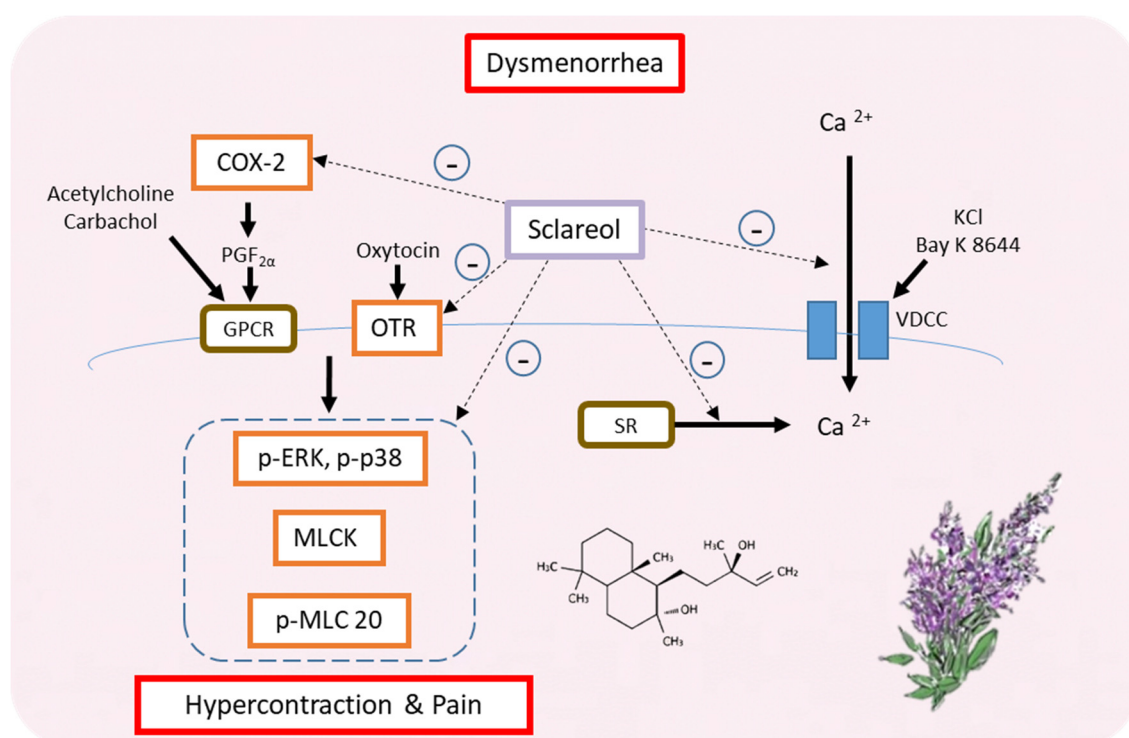


**Figure 8.** Possible model for the regulation of dysmenorrhea by sclareol in ex vivo and in vivo dysmenorrhea models. In summary, sclareol can downregulate the protein expression of OTR, MLCK, COX-2, p-ERK, p-p38, and p-MLC20 and can regulate the concentration of intracellular calcium, thus having the potential to regulate dysmenorrhea.

**Author Contributions:** Conceptualization, J.W., Y.-F.C., H.-Y.C., and S.-M.H.; experimentation, J.W., Y.-F.C., H.-Y.C., C.-H.C., T.-M.S., K.-L.W., T.-C.H., and S.-M.H.; data analysis and figure preparation, J.W., and Y.-F.C.; methodology and resources Y.-H.S., H.-Y.C., C.-H.C., T.-M.S., K.-L.W., Y.-H.H., T.-C.H., and S.-M.H.; writing—original draft preparation, J.W., Y.-F.C., H.-Y.C., and S.-M.H. writing—review and editing, J.W., Y.-F.C. and S.-M.H.; editing and approval of the final version of the manuscript, S.-M.H. All authors have read and agreed to the published version of the manuscript.

**Funding:** This study was supported by the grants MOST109-2314-B-038-059, 109-2628-B-038-015, 108-2314-B-039-009-MY3, 109-2320-B-254-001 and 107-2320-B-25 -001 from the Ministry of Science and Technology, Taiwan, Republic of China. The study was supported by the grants CMU109-MF-32 from China Medical University, Taiwan, Republic of China.

**Acknowledgments:** The authors gratefully acknowledge aromatherapist Hung-Lin Huang (Can June International Inc.) for giving the clinical advices of dysmenorrhea improvement.

**Conflicts of Interest:** The authors declare no conflict of interest.

## References

- Ju, H.; Jones, M.; Mishra, G. The Prevalence and Risk Factors of Dysmenorrhea. *Epidemiologic Rev.* **2014**, *36*, 104–113. [[CrossRef](#)] [[PubMed](#)]
- French, L. Dysmenorrhea. *Am. Fam. Physician* **2005**, *71*, 285–291. [[PubMed](#)]
- Dawood, M. Nonsteroidal anti-inflammatory drugs and changing attitudes toward dysmenorrhea. *Am. J. Med.* **1988**, *84*, 23–29. [[CrossRef](#)]
- Burnett, M.; Lemyre, M. No. 345-Primary Dysmenorrhea Consensus Guideline. *J. Obstet. Gynaecol. Can.* **2017**, *39*, 585–595. [[CrossRef](#)]
- Iacovides, S.; Avidon, I.; Baker, F.C. What we know about primary dysmenorrhea today: A critical review. *Hum. Reprod. Updat.* **2015**, *21*, 762–778. [[CrossRef](#)]
- Hanna, V.S.; Hafez, E.A.A. Synopsis of arachidonic acid metabolism: A review. *J. Adv. Res.* **2018**, *11*, 23–32. [[CrossRef](#)]
- Chen, L.; Yang, G.; Grosser, T. Prostanoids and inflammatory pain. *Prostaglandins Other Lipid Mediat.* **2013**, *104–105*, 58–66. [[CrossRef](#)]
- Wray, S.; Jones, K.; Kupittayanant, S.; Li, Y.; Matthew, A.; Monir-Bishty, E.; Noble, K.; Pierce, S.J.; Quenby, S.; Shmygol, A.V. Calcium signaling and uterine contractility. *J. Soc. Gynecol. Investig.* **2003**, *10*, 252–264. [[CrossRef](#)]
- Ulrich, C.C.; Quillici, D.R.; Schegg, K.; Woolsey, R.; Nordmeier, A.; Buxton, I.L.O. Uterine smooth muscle S-nitrosylproteome in pregnancy. *Mol. Pharmacol.* **2011**, *81*, 143–153. [[CrossRef](#)]
- Ou, M.-C.; Hsu, T.-F.; Lai, A.C.; Lin, Y.-T.; Lin, C.-C. Pain relief assessment by aromatic essential oil massage on outpatients with primary dysmenorrhea: A randomized, double-blind clinical trial. *J. Obstet. Gynaecol. Res.* **2012**, *38*, 817–822. [[CrossRef](#)]
- Zhong, Y.; Huang, Y.; Santoso, M.B.; Wu, L.D. Sclareol exerts anti-osteoarthritic activities in interleukin-1 $\beta$ -induced rabbit chondrocytes and a rabbit osteoarthritis model. *Int. J. Clin. Exp. Pathol.* **2015**, *8*, 2365–2374.
- Hsieh, Y.-H.; Deng, J.-S.; Pan, H.-P.; Liao, J.-C.; Huang, S.-S.; Huang, G.-J. Sclareol ameliorate lipopolysaccharide-induced acute lung injury through inhibition of MAPK and induction of HO-1 signaling. *Int. Immunopharmacol.* **2017**, *44*, 16–25. [[CrossRef](#)]
- Tsai, S.-W.; Hsieh, M.-C.; Li, S.; Lin, S.-C.; Wang, S.-P.; Lehman, C.W.; Lien, C.Z.; Lin, C.-C. Therapeutic Potential of Sclareol in Experimental Models of Rheumatoid Arthritis. *Int. J. Mol. Sci.* **2018**, *19*, 1351. [[CrossRef](#)] [[PubMed](#)]
- Noori, S.; Hassan, Z.M.; Mohammadi, M.; Habibi, Z.; Sohrabi, N.; Bayanolhagh, S. Sclareol modulates the Treg intra-tumoral infiltrated cell and inhibits tumor growth in vivo. *Cell. Immunol.* **2010**, *263*, 148–153. [[CrossRef](#)] [[PubMed](#)]
- Zhang, T.; Wang, T.; Cai, P. Sclareol inhibits cell proliferation and sensitizes cells to the antiproliferative effect of bortezomib via upregulating the tumor suppressor caveolin-1 in cervical cancer cells. *Mol. Med. Rep.* **2017**, *15*, 3566–3574. [[CrossRef](#)] [[PubMed](#)]
- Peritore, A.F.; Siracusa, R.; Crupi, R.; Cuzzocrea, S. Therapeutic Efficacy of Palmitoylethanolamide and Its New Formulations in Synergy with Different Antioxidant Molecules Present in Diets. *Nutrients* **2019**, *11*, 2175. [[CrossRef](#)]
- Fusco, R.; D’Amico, R.; Cordaro, M.; Gugliandolo, E.; Siracusa, R.; Peritore, A.F.; Crupi, R.; Impellizzeri, D.; Cuzzocrea, S.; Di Paola, R. Absence of formyl peptide receptor 1 causes endometriotic lesion regression in a mouse model of surgically-induced endometriosis. *Oncotarget* **2018**, *9*, 31355–31366. [[CrossRef](#)]
- Liang, J.; Bonvino, N.P.; Hung, A.; Karagiannis, T.C. In silico characterisation of olive phenolic compounds as potential cyclooxygenase modulators. Part 1. *J. Mol. Graph. Model* **2020**, *101*, 107719. [[CrossRef](#)]
- Jimenez-Lopez, C.; Carpena, M.; Lourenço-Lopes, C.; Gallardo-Gomez, M.; Lorenzo, J.M.; Barba, F.J.; Prieto, M.A.; Simal-Gandara, J. Bioactive Compounds and Quality of Extra Virgin Olive Oil. *Foods* **2020**, *9*, 1014. [[CrossRef](#)]
- Angeloni, C.; Malaguti, M.; Barbalace, M.C.; Hrelia, S. Bioactivity of Olive Oil Phenols in Neuroprotection. *Int. J. Mol. Sci.* **2017**, *18*, 2230. [[CrossRef](#)]
- Hsia, S.M.; Wang, K.L.; Wang, P.S. Effects of resveratrol, a grape polyphenol, on uterine contraction and Ca<sup>2+</sup>-mobilization in rats in vivo and in vitro. *Endocrinology* **2011**, *152*, 2090–2099. [[CrossRef](#)]



22. Wu, C.-H.; Shieh, T.-M.; Wang, K.-L.; Huang, T.-C.; Hsia, S.-M. Quercetin, a main flavonoid in onion, inhibits the PGF2 $\alpha$ -induced uterine contraction in vitro and in vivo. *J. Funct. Foods* **2015**, *19*, 495–504. [\[CrossRef\]](#)
23. Hsu, C.S.; Yang, J.K.; Yang, L.L. Effect of “Dang-Qui-Shao-Yao-San” a Chinese medicinal prescription for dysmenorrhea on uterus contractility in vitro. *Phytomedicine* **2006**, *13*, 94–100. [\[CrossRef\]](#)
24. Zendehdel, M.; Torabi, Z.; Hassanpour, S. Antinociceptive mechanisms of Bunium persicum essential oil in the mouse writhing test: Role of opioidergic and histaminergic systems. *Veterinárni Med.* **2016**, *60*, 63–70. [\[CrossRef\]](#)
25. Peng, Y.; Zheng, X.; Fan, Z.; Zhou, H.; Zhu, X.; Wang, G.; Liu, Z. Paeonol alleviates primary dysmenorrhea in mice via activating CB2R in the uterus. *Phytomedicine* **2020**, *68*, 153151. [\[CrossRef\]](#)
26. Yang, L.; Cao, Z.; Yu, B.; Chai, C. An in vivo mouse model of primary dysmenorrhea. *Exp Anim.* **2015**, *64*, 295–303. [\[CrossRef\]](#)
27. Chen, H.L.; Gong, J.Y.; Lin, S.-C.; Li, S.; Chiang, Y.-C.; Hung, J.-H.; Yen, C.-C.; Lin, C.-C. Effects of Sclareol Against Small Cell Lung Carcinoma and the Related Mechanism: In Vitro and In Vivo Studies. *Anticancer Res.* **2020**, *40*, 4947–4960. [\[CrossRef\]](#)
28. Li, W.; Ping, Z.; Xuemei, G.; Minglian, L.; Hongjuan, M.; Yi, H.; Zhongxiang, Z. Naturally Occurring Sclareol Diterpene Augments the Chemosensitivity of Human Hela Cervical Cancer Cells by Inducing Mitochondrial Mediated Programmed Cell Death, S-Phase Cell Cycle Arrest and Targeting Mitogen-Activated Protein Kinase (MAPK)/Extracellular-Signal-Regulated Kinase (ERK) Signaling Pathway. *Med. Sci. Monit.* **2020**, *26*, e920248.
29. Mahboubi, M. Clary sage essential oil and its biological activities. *Adv. Tradit. Med.* **2020**, 1–12. [\[CrossRef\]](#)
30. Han, S.-H.; Hur, M.-H.; Buckle, J.; Choi, J.; Lee, M.S. Effect of Aromatherapy on Symptoms of Dysmenorrhea in College Students: A Randomized Placebo-Controlled Clinical Trial. *J. Altern. Complement. Med.* **2006**, *12*, 535–541. [\[CrossRef\]](#)
31. Sun, L.; Liu, L.-N.; Li, J.-C.; Lv, Y.-Z.; Zong, S.-B.; Zhou, J.; Wang, Z.-Z.; Kou, J.-P.; Xiao, W. The essential oil from the twigs of Cinnamomum cassia Presl inhibits oxytocin-induced uterine contraction in vitro and in vivo. *J. Ethnopharmacol.* **2017**, *206*, 107–114. [\[CrossRef\]](#)
32. Kitazawa, T.; Hirama, R.; Masunaga, K.; Nakamura, T.; Asakawa, K.; Cao, J.; Teraoka, H.; Unno, T.; Komori, S.-I.; Yamada, M.; et al. Muscarinic receptor subtypes involved in carbachol-induced contraction of mouse uterine smooth muscle. *Naunyn Schmiedeberg Arch. Pharmacol.* **2007**, *377*, 503–513. [\[CrossRef\]](#)
33. Alotaibi, M.F. The effect of cinnamon extract on isolated rat uterine strips. *Reprod. Biol.* **2016**, *16*, 27–33. [\[CrossRef\]](#)
34. Ratz, P.H.; Berg, K.M.; Urban, N.H.; Miner, A.S. Regulation of smooth muscle calcium sensitivity: KCl as a calcium-sensitizing stimulus. *Am. J. Physiol. Physiol.* **2005**, *288*, C769–C783. [\[CrossRef\]](#)
35. Deng, M.; Ding, W.; Min, X.; Xia, Y. MLCK-independent phosphorylation of MLC20 and its regulation by MAP kinase pathway in human bladder smooth muscle cells. *Cytoskeleton* **2010**, *68*, 139–149. [\[CrossRef\]](#)
36. Tanimura, S.; Takeda, K. ERK signalling as a regulator of cell motility. *J. Biochem.* **2017**, *162*, 145–154. [\[CrossRef\]](#)
37. Signoretto, E.; Laufer, S.A.; Lang, F. Stimulating Effect of Sclareol on Suicidal Death of Human Erythrocytes. *Cell Physiol. Biochem.* **2016**, *39*, 554–564. [\[CrossRef\]](#)
38. Proctor, M.; Farquhar, C. Diagnosis and management of dysmenorrhoea. *BMJ* **2006**, *332*, 1134–1138. [\[CrossRef\]](#)
39. Kumar, S.; Boehm, J.; Lee, J.C. p38 MAP kinases: Key signalling molecules as therapeutic targets for inflammatory diseases. *Nat. Rev. Drug Discov.* **2003**, *2*, 717–726. [\[CrossRef\]](#)
40. Ho, Y.-L.; Chang, Y.-S. Studies on the antinociceptive, anti-inflammatory and antipyretic effects of Isatis indigotica root. *Phytomedicine* **2002**, *9*, 419–424. [\[CrossRef\]](#)
41. Ganeshpurkar, A.; Rai, G. Experimental evaluation of analgesic and anti-inflammatory potential of Oyster mushroom Pleurotus florida. *Indian J. Pharmacol.* **2013**, *45*, 66–70. [\[CrossRef\]](#)
42. Munir, M.A.; Enany, N.; Zhang, J.-M. Nonopioid Analgesics. *Med. Clin. N. Am.* **2007**, *91*, 97–111. [\[CrossRef\]](#)



43. Ma, H.; Su, S.-L.; Duan, J.-A.; Tang, Y.-P.; Zhou, J.; Guo, J.-M.; Zhan, Z. Evaluation of the analgesic activities of the crude aqueous extract and fractions of Shao Fu Zhu Yu decoction. *Pharm. Biol.* **2010**, *49*, 137–145. [[CrossRef](#)]
44. Nissenson, R.; Flouret, G.; Hechter, O. Opposing effects of estradiol and progesterone on oxytocin receptors in rabbit uterus. *Proc. Natl. Acad. Sci. USA* **1978**, *75*, 2044–2048. [[CrossRef](#)]

**Publisher’s Note:** MDPI stays neutral with regard to jurisdictional claims in published maps and institutional affiliations.



© 2020 by the authors. Licensee MDPI, Basel, Switzerland. This article is an open access article distributed under the terms and conditions of the Creative Commons Attribution (CC BY) license (<http://creativecommons.org/licenses/by/4.0/>).

## Research Article

# Luteolin Attenuates IL-1 $\beta$ -Induced THP-1 Adhesion to ARPE-19 Cells via Suppression of NF- $\kappa$ B and MAPK Pathways

Wen-Chung Huang<sup>1,2</sup>, Chian-Jiun Liou<sup>2,3</sup>, Szu-Chuan Shen<sup>4</sup>, Cindy Hu<sup>5,6</sup>,  
Chien-Yu Hsiao<sup>6,7</sup> and Shu-Ju Wu<sup>6,7</sup>

<sup>1</sup>Graduate Institute of Health Industry Technology, Research Center for Food and Cosmetic Safety, College of Human Ecology, Chang Gung University of Science and Technology, Taoyuan City 33303, Taiwan

<sup>2</sup>Division of Allergy, Asthma, and Rheumatology, Department of Pediatrics, Chang Gung Memorial Hospital, Linkou, Taoyuan City 33303, Taiwan

<sup>3</sup>Department of Nursing, Division of Basic Medical Sciences, Research Center for Chinese Herbal Medicine, and Graduate Institute of Health Industry Technology, Chang Gung University of Science and Technology, Taoyuan 33303, Taiwan

<sup>4</sup>Graduate Program of Nutrition Science, National Taiwan Normal University, 88 Ting-Chow Rd, Sec 4, Taipei, Taiwan

<sup>5</sup>Department of Cosmetic Science, College of Human Ecology, Chang Gung University of Science and Technology, Guishan Dist., Taoyuan City 33303, Taiwan

<sup>6</sup>Department of Dermatology, Aesthetic Medical Center, Chang Gung Memorial Hospital, Linkou, Taoyuan City 33303, Taiwan

<sup>7</sup>Department of Nutrition and Health Sciences, Research Center for Chinese Herbal Medicine, College of Human Ecology, Chang Gung University of Science and Technology, Taoyuan City 33303, Taiwan

Correspondence should be addressed to Chien-Yu Hsiao; [nulycopene@gmail.com](mailto:nulycopene@gmail.com) and Shu-Ju Wu; [sjwu@mail.cgust.edu.tw](mailto:sjwu@mail.cgust.edu.tw)

Received 8 June 2020; Revised 23 July 2020; Accepted 4 August 2020; Published 16 October 2020

Academic Editor: Carla Sipert

Copyright © 2020 Wen-Chung Huang et al. This is an open access article distributed under the Creative Commons Attribution License, which permits unrestricted use, distribution, and reproduction in any medium, provided the original work is properly cited.

Cytokine-induced endothelial dysfunction leads to inflammation and vascular adhesion molecule production in retinal pigment epithelium (RPE) cells. Inflammation is a critical mediator in retinal degeneration (RD) diseases, including age-related macular degeneration (AMD), and RD progression may be prevented through anti-inflammatory activity in RPE cells. The flavonoid polyphenol luteolin (LU) has anti-inflammatory and antidiabetes activities, but its effects regarding retinal protection remain unknown. Here, we examined the ability of luteolin to alleviate markers of inflammation related to RD in cytokine-primed ARPE-19 cells. We found that luteolin decreased the levels of interleukin- (IL-) 6, IL-8, soluble intercellular adhesion molecule-1 (sICAM-1), and monocyte chemoattractant protein-1 (MCP-1) and attenuated adherence of the human monocytic leukemia cell line THP-1 to IL-1 $\beta$ -stimulated ARPE-19 cells. Luteolin also increased anti-inflammatory protein heme oxygenase-1 (HO-1) levels. Interestingly, luteolin induced protein kinase B (AKT) phosphorylation, thus inhibiting nuclear factor- (NF-)  $\kappa$ B transfer from cytoplasm into the nucleus and suppressing mitogen-activated protein kinase (MAPK) inflammatory pathways. Furthermore, cotreatment with MAPK inhibitors and luteolin decreased inflammatory cytokine and chemokine levels, and further suppressed THP-1 adhesion. Overall, these results provide evidence that luteolin protects ARPE-19 cells from IL-1 $\beta$ -stimulated increases of IL-6, IL-8, sICAM-1, and MCP-1 production by blocking the activation of MAPK and NF- $\kappa$ B signaling pathways, thus ameliorating the inflammatory response.

## 1. Introduction

The retinal pigment epithelium (RPE) is a single layer of pigment cells, which is in close contact with photoreceptors and maintains visual function [1]. RPE exposure to ultraviolet/

visible light leads to oxidative stress and chronic inflammation in the retinal tissue. Inflammation clearly plays a role in the development of age-related macular degeneration (AMD), which is a cause of severe irreversible visual impairment in elderly persons and in diabetic retinopathy [2, 3]. A

variety of factors promote retinal tissue degeneration and AMD progression, including genetic and environmental factors, aging, and oxidative stress [4]. AMD involves reduced photoreceptor cells and retinal pigment epithelium dysfunction in the macula and can be classified as “dry AMD” or “wet/exudative/neovascular AMD.” Compared to neovascular AMD, dry AMD has a higher incidence, but involves less vision degradation and is thus less frequently a cause of “blindness” [5, 6]. Neovascular AMD is characterized by excessive choroidal neovascularization (CNV) under the retina, leading to retinal edema and even detachment, thereby causing vision loss. Notably, dry AMD can potentially evolve into neovascular AMD, leading to irreversible vision loss [7, 8]. Therefore, the best means of avoiding vision deterioration in elderly persons and cases of diabetic retinopathy is to prevent macular degeneration.

Available data suggest that a number of inflammatory cytokines and chemokines are elevated in the serum or ocular tissue of AMD patients—including interleukin-6 (IL-6), IL-8, monocyte chemoattractant protein (MCP-1), and intercellular adhesion molecule (ICAM-1) [9–11]. Notably, IL-6 levels are increased in the intraocular fluids of patients with neovascular AMD compared to controls, and findings suggest that IL-6 and IL-8 are proangiogenic in AMD progression [12, 13]. Intraocular MCP-1 is a chemokine for monocyte recruitment, and ICAM-1 is an adhesion molecule that facilitates leukocyte transmigration. Studies have reported that elevated MCP-1 levels contribute to subfoveal neovascular membrane development and the degree of macular edema in eyes with exudative AMD and that elevated soluble ICAM-1 (sICAM-1) levels are correlated with choroidal neovascularization [13, 14]. Inflammatory mediators, including chemokines and cytokines, can upregulate ICAM-1 expression. IL-6 could directly or indirectly activate the leukocytes to induce retinal inflammation. It has been found that MCP-1 recruits leukocytes to sites of injury and activates ICAM-1; thus, ICAM-1 induced leukocyte-endothelial interactions and promoted leukocyte migration into extravascular locations involved in the inflammatory response [14, 15]. More studies found that IL-8 and MCP-1 could attract neutrophils and monocytes to migrate into inflammatory tissues. IL-1 $\beta$  is a proinflammatory cytokine and promotes the upregulation of chemokines in RPE as model of focal retinal degeneration [15]. In the present study, we evaluated the ability of the luteolin to modulate inflammation in ARPE-19 cells-THP-1 monocytes interactions. The levels of the inflammatory cytokines IL-6, IL-8, MCP-1, and ICAM-1 in ocular tissue are significantly associated with exudative AMD occurrence and progression [4]. Moreover, IL-1 $\beta$  activates inflammatory-related pathways, including nuclear factor- (NF-)  $\kappa$ B and mitogen-activated protein kinase (MAPK) signaling, thus enhancing the production of the proinflammatory mediators MCP-1, IL-6, cyclooxygenase-2 (COX-2), and inducible nitric oxide synthase (iNOS). Proinflammatory mediators are closely associated with the development and progression of retinal degenerative diseases [15, 16].

Luteolin (Lu), 3',4',5,7-tetrahydroxyflavone, is a flavonoid polyphenolic compound found in numerous vegetables

(e.g., celery, carrots, broccoli, and peppers), fruits (e.g., apple, mango, blueberry, peaches, and prunes), and herbs (e.g., chrysanthemum flowers and *Taraxacum mongolicum*) [17–20]. In previous studies, it was demonstrated that luteolin shows anti-inflammatory, anticancer, neuroprotective, and antiviral properties in vitro and in animal models [21–25]. Thus, luteolin has been investigated for potential use in the treatment of obesity [26] and obesity-related diseases and for antidiabetic [27–29] and neuroprotective therapies [30, 31]. In ophthalmological research, luteolin protects against oxidative stress-related damage and decreases inflammation in ARPE-19 cells [32, 33]. Luteolin is protective against diabetes-induced progression of retinopathy and reportedly inhibits expressions of the inflammation-related markers NF- $\kappa$ B and IL-1 $\beta$ , decreases levels of the lipid peroxidation product malondialdehyde (MDA), and increases the antioxidant glutathione (GSH) in diabetes-induced oxidative stress in the retina [34]. These findings indicate the potential to use luteolin for prevention and treatment of retinal inflammatory diseases.

Based on the available data, we speculate that IL-6, IL-8, MCP-1, and sICAM-1 could be target molecules for AMD therapy or prevention. In the present study, we aimed to assess the mechanisms underlying the luteolin-induced anti-inflammatory effects in ARPE-19 cells stimulated by the proinflammatory cytokine IL-1 $\beta$  (Figure 1).

## 2. Materials and Methods

**2.1. Materials.** Luteolin ( $\geq 98\%$  purity by TLC), cell counting kit-8 assays (CCK-8), and DAPI solution were purchased from Sigma-Aldrich (St. Louis, MO, USA). Human recombinant proinflammatory cytokine IL-1 $\beta$  and enzyme-linked immunosorbent assay (ELISA) kits were purchased from R&D Systems (Minneapolis, MN, USA). The inhibitors PD98059, SP600125, SB202190, and Bay 117082 were purchased from Enzo Life Sciences (Farmingdale, NY, USA). Antibodies against  $\beta$ -actin, COX-2, iNOS, HO-1, AKT, and phosphorylated- (phospho-) AKT were purchased from Santa Cruz Biotechnology (Santa Cruz, CA, USA). Antibodies against JNK, ERK, p38, phospho-JNK, phospho-ERK, and phospho-p38 were purchased from Millipore (Billerica, MA, USA).

**2.2. Preparation of Luteolin and Cell Culture.** Luteolin was dissolved in dimethyl sulfoxide (DMSO) to prepare a 100 mM stock solution, which was stored at  $-20^{\circ}\text{C}$ . The final culture medium had a DMSO concentration of  $\leq 0.1\%$ , as previously described [16]. The ARPE-19 human retinal pigment epithelial cell line was purchased from Bioresource Collection and Research Center (BCRC, Taiwan) and cultured in Dulbecco's modified Eagle's medium (DMEM)/F-12 medium (Invitrogen-Gibco, Paisley, Scotland) containing 10% heat-inactivated fetal bovine serum (FBS; Invitrogen-Gibco) and penicillin G (100 U/mL), streptomycin (100  $\mu\text{g/mL}$ ), and gentamycin (50 ng/mL). Cells were subcultured every 2–3 days at  $37^{\circ}\text{C}$  in a humidified atmosphere of 5%  $\text{CO}_2$ . ARPE-19 cells ( $2 \times 10^5$ ) were pretreated with or without various luteolin concentrations (1–30  $\mu\text{M}$ ) for 1 h,

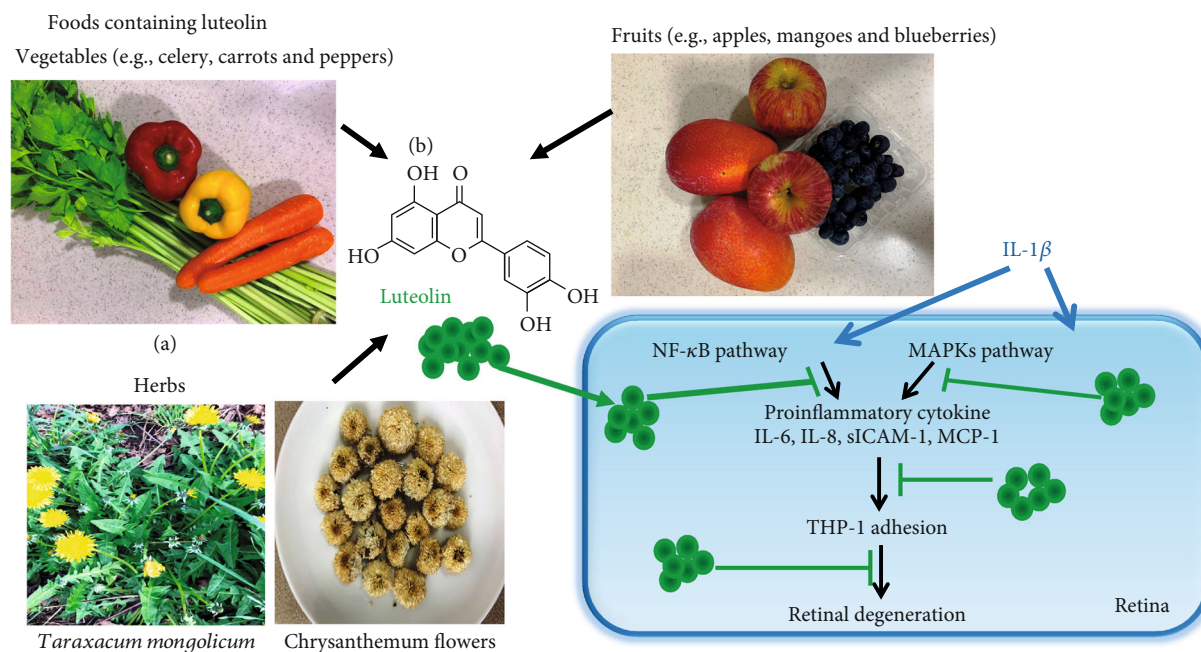


FIGURE 1: Experimental abstract. (a) Foods containing luteolin. (b) The structure of luteolin. (c) Pathways likely related to the anti-inflammatory activity of luteolin in IL-1 $\beta$ -stimulated ARPE-19 cells.

and then, IL-1 $\beta$  (1  $\mu$ g/mL) was added. After 24 h, the ARPE-19 cells were lysed for western blot analysis, and the media samples were subjected to ELISA analysis. The THP-1 human monocytic leukemia cell line was obtained from American Type Culture Collection (Manassas, VA, USA). THP-1 cells were cultured in RPMI 1640 medium (Gibco) containing FBS (10%) at 37°C in a humidified atmosphere of 5% CO<sub>2</sub> and subcultured every 3–4 days.

**2.3. Cell Viability Assay.** We assessed the inhibitory effect of luteolin on cell viability using CCK-8 kits (Sigma-Aldrich) as described previously [35]. Cells were seeded at 10<sup>5</sup> cells/well into 96-well plates and treated with luteolin at concentrations of 1–100  $\mu$ M for 24 h. After treatment, the CCK-8 solution was added, and the plates were incubated at 37°C for 2 h. Finally, cell viability was measured at 450 nm using a microplate reader (Multiskan FC; Thermo, Waltham, MA, USA). The CCK-8 assay with each concentration was carried out in triplicate, and cell viability was reported as a percentage relative to the cells without luteolin treatment.

**2.4. ELISA Assay.** ARPE-19 cells (10<sup>5</sup> cells/mL) were pretreated without or with various luteolin concentrations (1–30  $\mu$ M) in 24-well plates for 1 h. Then IL-1 $\beta$  (1 ng/mL) was added, and the cells were cultured for 24 h. Specific ELISA kits were used to measure the levels of IL-6, IL-8, MCP-1, and ICAM-1 in the supernatants, following the manufacturers' instructions. The OD at 450 nm was determined using a microplate reader (Multiskan FC; Thermo).

**2.5. Preparation of Total Proteins.** ARPE-19 cells (8 cells/mL) were pretreated with or without luteolin (1–30  $\mu$ M) for 1 h. In 6-well plates, the cells were then stimulated with or without IL-1 $\beta$  (1 ng/mL) for 24 h to evaluate total protein content,

or for 30 min to evaluate phosphorylated protein content. Cells were harvested with 300  $\mu$ L lysis buffer (50 mM Tris-HCl, pH 7.4; 1 mM EDTA; 150 mM NaCl; 1 mM DTT; 0.5% NP40; and 0.1% sodium dodecyl sulfate (SDS)) containing protease inhibitor cocktail and phosphatase inhibitors (Sigma, St. Louis, MO, USA). The BCA assay kit (Pierce) was used to quantitate all protein concentrations.

**2.6. Western Blot Analysis.** Protein samples were separated on 10% SDS polyacrylamide gels and then transferred to polyvinylidene fluoride (PVDF) membranes (Millipore, Billerica, MA, USA). Next, the PVDF membranes were incubated overnight at 4°C with specific primary antibodies against  $\beta$ -actin (Sigma), COX-2, iNOS, HO-1, AKT, pAKT (Santa Cruz, CA, USA), JNK, pJNK, p38, and pp38 (Cell Signaling Technology, Danvers, MA, USA). Then, the membranes were washed three times with tris-buffered saline with Tween 20 (TBST) buffer and incubated with secondary antibodies at room temperature for 1 h. Proteins were detected using Luminol/Enhancer solution (Millipore), and signals were detected using the BioSpectrum 600 system (UVP, Upland, CA, USA) to quantitate protein bands.

**2.7. Monocyte Adhesion Assay.** In the first step, AREP19 cells (2  $\times$  10<sup>5</sup> cells/mL) were pretreated with luteolin (1, 3, 10, and 30  $\mu$ M) or inhibitors (10  $\mu$ M SP600125, 10  $\mu$ M PD98059, 10  $\mu$ M SB202190, or 5  $\mu$ M Bay 11-7082) for 1 h in DMEM medium. THP-1 cells (5  $\times$  10<sup>5</sup> cells/mL) were labeled with fluorescent dye (5  $\mu$ M calcein-AM) in RPMI-1640 medium at 37°C for 30 min in the dark and then washed by centrifugation. Second, the labeled THP-1 cells were cocultured with the ARPE-19 cells in plates for 1 h, and then, the cells were washed three times with PBS to remove nonadherent THP-1



cells. Finally, the extent of adhesion of THP-1 cells to ARPE19 cells was observed under fluorescence microscope (4 per view; magnification,  $\times 200$ ; Olympus Corporation, Tokyo, Japan). The control groups were treated with IL-1 $\beta$  alone, and all experiments were repeated three times.

**2.8. Immunofluorescence Staining.** ARPE19 cells were seeded into 6-well plates until reaching 50–60% confluence and pretreated with or without luteolin (1, 3, 10, and 30  $\mu\text{M}$ ) for 1 h, followed by addition of IL-1 $\beta$  for 15 min. Then, the medium was suctioned out, and the cells were washed with PBS. The cells were fixed with 4% (*w/v*) paraformaldehyde and incubated with anti-NF- $\kappa\text{B}$  p65 antibody overnight at 4°C. The next day, the medium was removed, and the cells were washed with PBS and then incubated with secondary antibodies at room temperature for 1 h. Then, the cells were washed 2–3 times with PBS, followed by the addition of fluorescent dye (BODIPY493/503 or BODIPY581/591). The cells were again washed with PBS to remove the dye, and 4',6-diamidino-2-phenylindole (DAPI; Sigma) was added to stain the nucleus. Finally, images were acquired using a fluorescence microscope (Olympus, Tokyo, Japan).

**2.9. Statistical Analysis.** Image Lab software (Bio-Rad) was used to quantify the intensity of western blot bands, and ImageJ software (W. Rasband, NIH, USA) to determine the numbers of THP-1 cells in the adhesion assay. Data were presented as the mean  $\pm$  standard deviation (SD) from at least three independent experiments. Statistical analyses included one-way analysis of variance (ANOVA) followed by the Tukey's post hoc test. A *p* value of  $< 0.05$  was considered significant.

### 3. Results

**3.1. Luteolin Inhibited Inflammatory Mediator Expression and Increased Anti-Inflammatory Protein HO-1 Expression in IL-1 $\beta$ -Stimulated ARPE19 Cells.** First, we performed a CCK-8 assay to assess luteolin cytotoxicity in ARPE-19 cells. Luteolin concentrations of  $\leq 50 \mu\text{M}$  showed no significant cytotoxicity in ARPE-19 cells, while cell numbers were significantly reduced at concentrations of  $\geq 100 \mu\text{M}$  (Figure 2(a)). Therefore, all subsequent experiments were performed using 1–30  $\mu\text{M}$  luteolin. ARPE-19 cells were seeded in 6-well plates, treated with luteolin, and then stimulated with 1 ng/mL IL-1 $\beta$ . Compared with IL-1 $\beta$  alone, additional treatment with luteolin at  $\geq 1 \mu\text{M}$  significantly inhibited expression of the inflammatory mediator iNOS (Figures 2(b) and 2(c)) but did not significantly inhibit COX-2 expression (data not shown). Notably, compared with IL-1 $\beta$  alone, treatment with 1 and 30  $\mu\text{M}$  luteolin significantly increased expression of the anti-inflammatory protein HO-1 (Figures 2(d) and 2(e)). Previous studies have indicated that AKT activation may contribute to inhibiting the NF- $\kappa\text{B}$  inflammatory pathway in inflammation-related diseases [36]. Our results showed that luteolin at  $\geq 1 \mu\text{M}$  enhanced the expression of phosphorylated AKT proteins in IL-1 $\beta$ -stimulated ARPE19 cells compared with in cells treated with IL-1 $\beta$  alone (Figures 2(f) and 2(g)).

**3.2. Luteolin Inhibited Inflammation-Related Cytokines and Attenuated THP-1 Cell Adherence to IL-1 $\beta$ -Stimulated ARPE-19 Cells.** ARPE-19 cells were pretreated with luteolin (1, 3, 10, or 30  $\mu\text{M}$ ) for 1 h, and then, 1 ng/mL IL-1 $\beta$  was added for 24 h. IL-1 $\beta$  treatment alone significantly stimulated ARPE19 cells to release cytokines and chemokines compared with control cells. Luteolin at concentrations of 10 and 30  $\mu\text{M}$  significantly inhibited the IL-1 $\beta$ -induced release of IL-6 and IL-8 and decreased the levels of the cell adhesion molecule sICAM-1. Additionally, treatment with 30  $\mu\text{M}$  luteolin significantly decreased MCP-1 levels compared to treatment with IL-1 $\beta$  alone (Figures 3(a)–3(d)). Since luteolin concentrations of  $\geq 10 \mu\text{M}$  strongly inhibited sICAM-1 levels, we further investigated whether luteolin attenuated THP-1 cell adhesion to IL-1 $\beta$ -stimulated ARPE-19 cells. Pretreatment with luteolin significantly inhibited THP-1 cell adherence to IL-1 $\beta$ -stimulated ARPE-19 cells, compared to samples treated with IL-1 $\beta$  alone (Figures 3(e) and 3(f)).

**3.3. Luteolin Inhibited NF- $\kappa\text{B}$  Activation to Suppress THP-1 Cell Adherence to IL-1 $\beta$ -Stimulated ARPE-19 Cells.** We observed that luteolin significantly increased AKT activation (Figures 2(f) and 2(g)), and pAKT has previously been associated with inhibition of the NF- $\kappa\text{B}$  inflammatory pathway [37]. Therefore, we evaluated whether luteolin inhibited NF- $\kappa\text{B}$  in relation to the suppression of THP-1 cell adherence to IL-1 $\beta$ -stimulated ARPE-19 cells. Cells were pretreated with or without luteolin (1–30  $\mu\text{M}$ ) for 1 h, then stimulation with IL-1 $\beta$  (1 ng/mL) for 15 min, to investigate whether luteolin inhibited NF- $\kappa\text{B}$  p65 translocation. Immunofluorescence staining revealed that luteolin at  $\geq 10 \mu\text{M}$  suppressed NF- $\kappa\text{B}$  p65 translocation from the cytoplasm into the nucleus and that the p65 subunit was retained in the cytoplasm in IL- $\beta$ -activated ARPE-19 cells (Figure 4(a)). Then, we evaluated whether luteolin inhibited I $\kappa\text{B}$  phosphorylation. Treatment with luteolin at  $\geq 1 \mu\text{M}$  significantly inhibited phosphorylated I $\kappa\text{B}$  expression, compared with IL-1 $\beta$  alone (Figure 4(b)). We further investigated whether luteolin decreased THP-1 cell adherence to ARPE-19 cells via inhibition of NF- $\kappa\text{B}$  p65 activation. First, ARPE-19 cells were pretreated with either luteolin (10  $\mu\text{M}$ ) or Bay 11-7082 (5  $\mu\text{M}$ ) for 1 h and then stimulated with IL-1 $\beta$ . Second, these pretreated ARPE-19 cells were cocultured with labeled THP-1 cells. Our results showed that both luteolin and Bay 11-7082 pretreatment significantly inhibited THP-1 cell adherence to IL-1 $\beta$ -stimulated ARPE-19 cells compared to cells treated with IL-1 $\beta$  alone (Figures 4(b) and 4(c)).

**3.4. Luteolin Blocked MAPK Inflammatory Pathways and MAPK Inhibitors Decreased THP-1 Cell Adherence to IL-1 $\beta$ -Stimulated ARPE-19 Cells.** We next evaluated whether luteolin inhibited MAPK phosphorylation and if this was related to the decreased THP-1 cell adherence to IL-1 $\beta$ -stimulated ARPE-19 cells. First, cells were pretreated with luteolin (1–30  $\mu\text{M}$ ) for 1 h and then incubated with IL-1 $\beta$  (1 ng/mL) for 30 min or 24 h to evaluate the expression of MAPK signaling proteins. Our results showed that luteolin at  $\geq 3 \mu\text{M}$  significantly decreased phosphorylated c-JUN N-



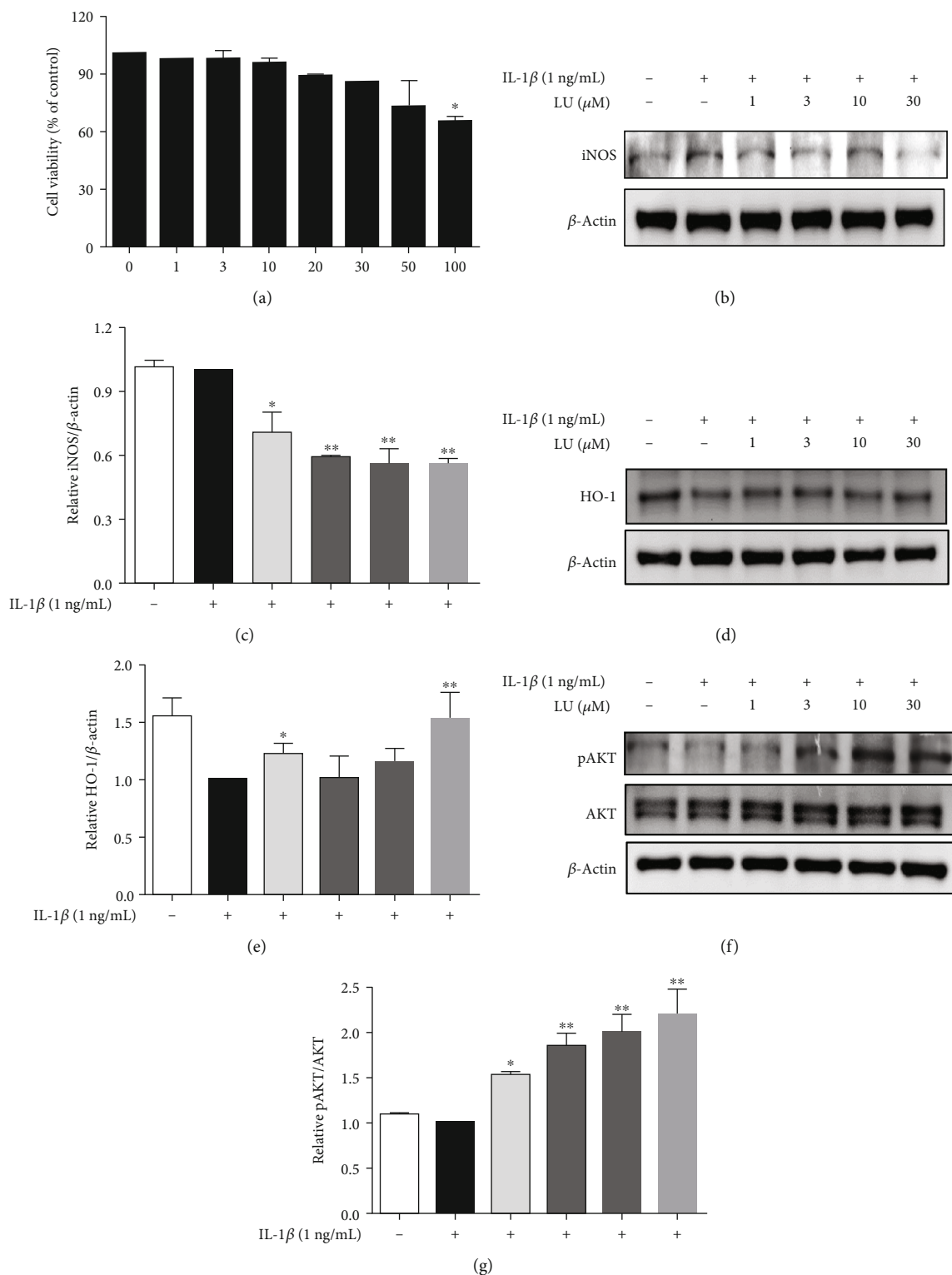


FIGURE 2: Luteolin inhibited inflammatory mediator expression and increased anti-inflammatory protein HO-1 expression in IL-1 $\beta$ -stimulated ARPE19 cells. (a) Cell viability of ARPE19 cells treated with various luteolin (LU) concentrations (0–100  $\mu$ M). Cells were pretreated with luteolin for 1 h, then stimulated with IL-1 $\beta$  (1 ng/mL) for 24 h. (b) Cells were pretreated with different LU doses and then incubated with IL-1 $\beta$  (1 ng/mL) for 30 min or 24 h. Western blots show iNOS protein expression. (c) The fold-change in iNOS protein expression was measured relative to  $\beta$ -actin expression. (d) Western blots show HO-1 protein expression. (e) The fold-change in HO-1 protein expression was measured relative to  $\beta$ -actin expression. (f) Western blots show phosphorylated AKT protein expression. (g) The fold-change in pAKT protein expression was measured relative to AKT expression. Data represent the mean  $\pm$  SD. \* $p$  < 0.05, \*\* $p$  < 0.01, compared to ARPE-19 cells stimulated with IL-1 $\beta$  alone.

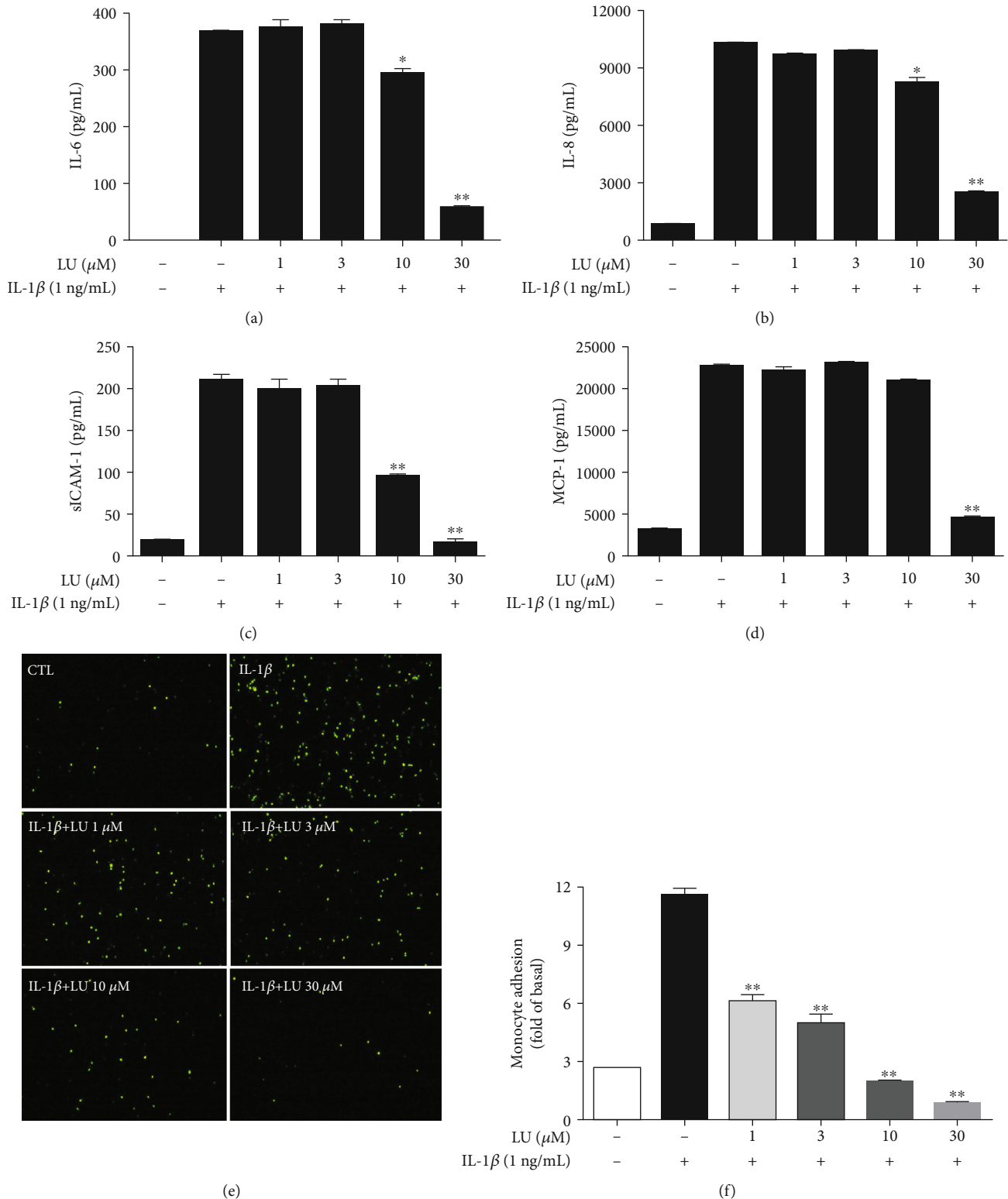


FIGURE 3: Luteolin inhibited inflammation-related cytokine expression and attenuated THP-1 cell adherence to IL-1 $\beta$ -stimulated ARPE-19 cells. Cells were pretreated with different doses of luteolin (LU) and then incubated with IL-1 $\beta$  (1 ng/mL) for 24 h. ELISA results showed the levels of (a) IL-6, (b) IL-8, (c) sICAM-1, and (d) MCP-1. (e) LU significantly suppressed THP-1 cell adherence to IL-1 $\beta$ -stimulated ARPE-19 cells. Fluorescent-labeled THP-1 cells (green) were cocultured with control (CTL) or IL-1 $\beta$ -stimulated ARPE-19 cells in the absence or presence of the indicated LU concentrations. (f) The fluorescence intensity revealed THP-1 cell adherence to IL-1 $\beta$ -stimulated ARPE-19 cells, which was used to quantify calcein-AM fluorescence. The data represent the mean  $\pm$  SD. \* $p$  < 0.05, \*\* $p$  < 0.01, compared to ARPE-19 cells stimulated with IL-1 $\beta$  alone.

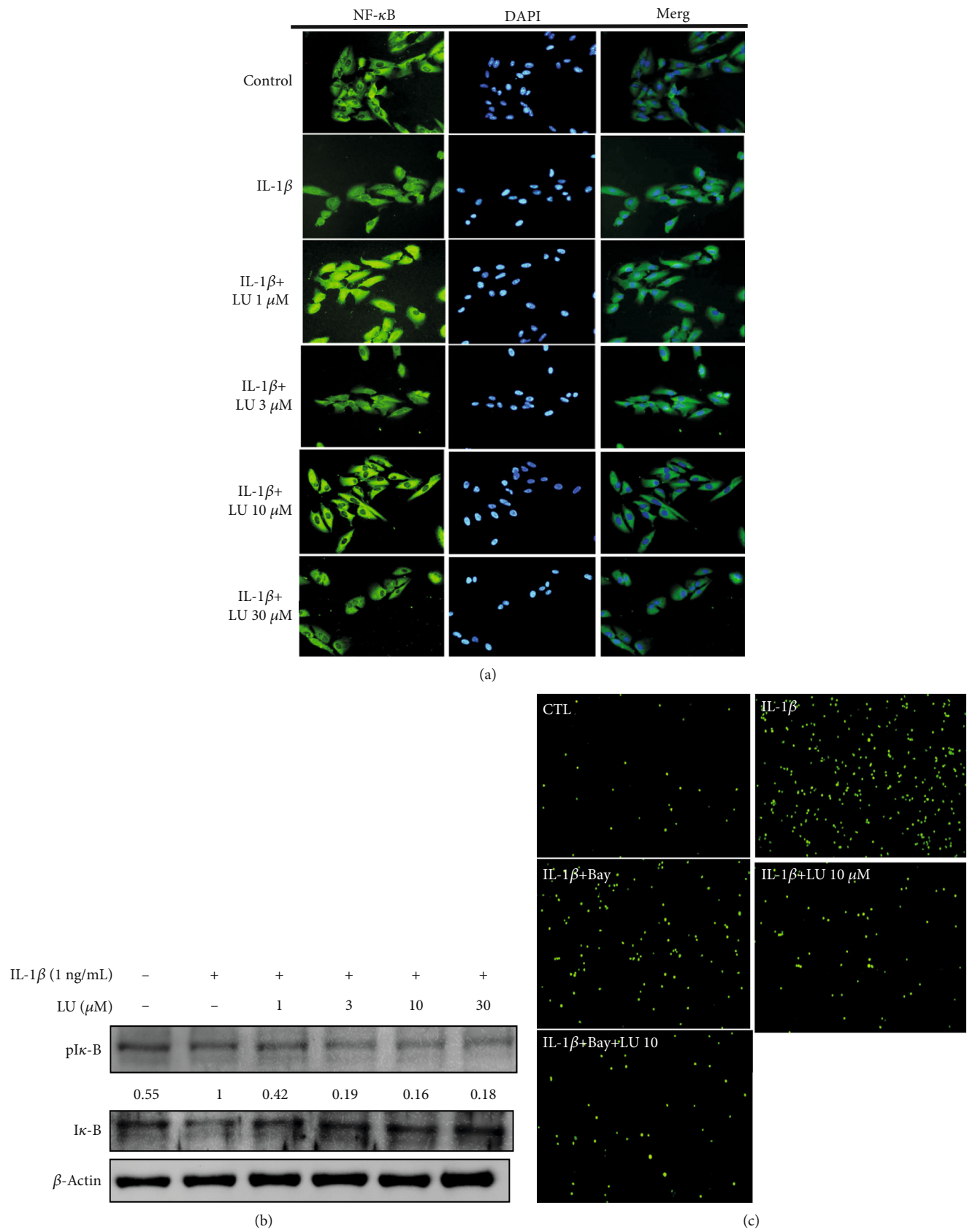


FIGURE 4: Continued.

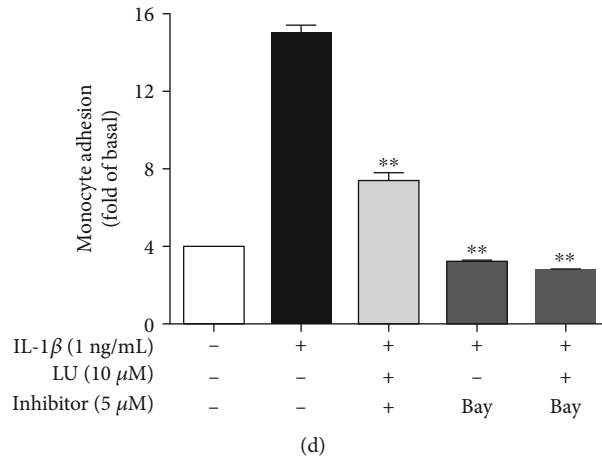


FIGURE 4: Luteolin inhibited NF- $\kappa$ B activation and thereby suppressed THP-1 cell adherence to IL-1 $\beta$ -stimulated ARPE-19 cells. Cells were pretreated with different doses of luteolin (LU) and then incubated with IL-1 $\beta$  (1 ng/mL) for 15 min. NF- $\kappa$ B p65 translocation was evaluated by immunofluorescence staining. Green: location of the p65 subunit. Blue: DAPI for nuclear staining. (a) DAPI staining revealed that luteolin attenuated NF- $\kappa$ B p65 translocation in IL-1 $\beta$ -stimulated ARPE-19 cells. (b) Western blots show the levels of phosphorylated I $\kappa$ B protein expression. (c) Luteolin suppressed THP-1 adhesion. ARPE-19 cells were pretreated with 10  $\mu$ M luteolin or 5  $\mu$ M Bay 117082 for 1 h and then cocultured with labeled THP-1 cells. (d) Fluorescence intensity showed THP-1 cell adhesion to IL-1 $\beta$ -stimulated ARPE-19 cells, which was used to quantify calcein-AM fluorescence. Data represent the mean  $\pm$  SD. \*\* $p$  < 0.01, compared to ARPE-19 cells stimulated with IL-1 $\beta$  alone.

terminal kinase (pJNK) 1/2 expression, luteolin at  $\geq 10$   $\mu$ M significantly decreased phosphorylated extracellular signal-regulated kinase (pERK) 1/2 expression, and luteolin at  $\geq 3$   $\mu$ M significantly decreased phosphorylated p38 protein expression (Figures 5(a), 5(b), 6(a), 6(b), 7(a), and 7(b)). We further evaluated whether the MAPK-inhibiting effects of luteolin were associated with decreased THP-1 adherence to ARPE-19 cells. ARPE-19 cells were pretreated with 10  $\mu$ M luteolin and/or 10  $\mu$ M of the JNK inhibitor SP60012, the ERK1/2 inhibitor PD98059, or the p38 inhibitor SB202190 for 1 h, followed by incubation with IL-1 $\beta$  (1 ng/mL) for 24 h. All tested pretreatments decreased THP cell adherence to ARPE-19 cells. Moreover, combined pretreatment with luteolin plus SP60012 or luteolin plus SB202190 resulted in significantly greater reductions of THP-1 adhesion compared to treatment with any of these agents alone (Figures 5(c), 5(d), 6(c), 6(d), 7(c), and 7(d)).

**3.5. MAPK Inhibitors Mediated the Levels of Cytokines and Chemokines in IL-1 $\beta$ -Stimulated ARPE-19 Cells.** We observed that luteolin significantly decreased the release of IL-6, IL-8, sICAM-1, and MCP-1 in IL-1 $\beta$ -stimulated ARPE-19 cells (Figures 3(a)–3(d)), as well as significantly suppressed MAPK pathways (Figures 5(a), 5(b), 6(a), 6(b), 7(a), and 7(b)). Next, we investigated whether MAPK inhibitors could attenuate the IL-1 $\beta$ -stimulated production of the inflammatory cytokines IL-6, IL-8, and MCP-1. ARPE-19 cells were pretreated with luteolin and/or MAPK inhibitors (10  $\mu$ M SB202190, 10  $\mu$ M PD98059, or 10  $\mu$ M SP600125) for 1 h and then incubated with 1 ng/mL IL-1 $\beta$  for 24 h. Interestingly, the pretreatment with MAPK inhibitors and luteolin significantly reduced the levels of IL-6, IL-8, sICAM-1, and MCP-1 in IL-1 $\beta$ -stimulated ARPE-19 cells (Figures 8(a)–8(d)). These results suggested that in IL-1 $\beta$ -stimulated ARPE-19 cells, luteolin suppressed the expression

of IL-6, IL-8, sICAM-1, and MCP-1 by influencing the phosphorylation of p38, ERK1/2, and JNK1/2.

#### 4. Discussion

In many retinal degenerative (RD) diseases, the pathogenesis is inflammation-induced, involving the recruitment and activation of microglia and macrophages, the expression of inflammatory mediators (COX-2 and iNOS), and photoreceptor cell death. The proinflammatory cytokine IL-1 $\beta$  triggers inflammatory responses and attracts inflammatory cells to migrate into the retina, promoting retinal impairment and degeneration in RD diseases [38, 39]. Numerous studies reported that IL-1 $\beta$  activates the expression of other proinflammatory cytokines and modulates chemokine expression. Proinflammatory cytokines can target and induce retinal inflammation in RD pathogenesis [36, 37] and the phytochemical luteolin has excellent anti-inflammatory properties [32, 33]. Therefore, here we performed a detailed exploration of the anti-inflammatory effects of luteolin in IL-1 $\beta$ -stimulated ARPE19 cells.

Prior studies have indicated that the cytokines IL-6 and IL-8 are proangiogenic, while the chemokine MCP-1 and cell adhesion molecule ICAM-1 facilitate leukocyte transmigration into ocular tissue, in AMD development and progression [4, 12–14]. Elevated IL-1 $\beta$  levels in the vitreous or retina lead to photoreceptor cell death in retinal detachment patients and in a mouse model, while reduced IL-1 $\beta$  levels inhibit photoreceptor cell death [40]. In the present study, we demonstrated that luteolin significantly inhibited cytokine and chemokine release in IL-1 $\beta$ -stimulated ARPE-19 cells (Figures 3(a)–3(d)). Prior studies have also shown that ICAM-1 is upregulated in response to inflammatory mediators and mediates leukocyte adhesion and transmigration on the RPE, while decreased ICAM-1 levels can suppress

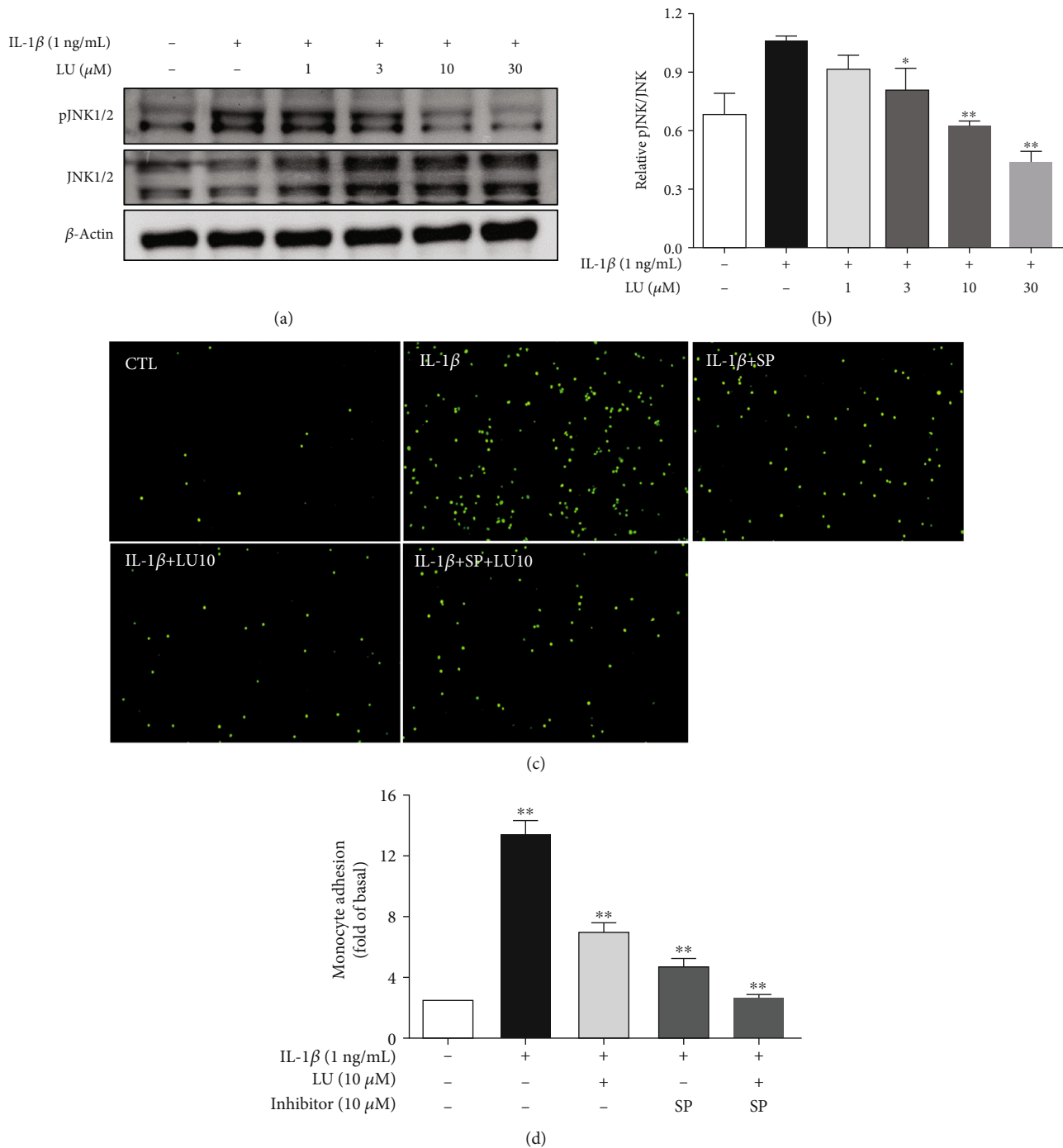


FIGURE 5: Luteolin blocked JNK phosphorylation, and the JNK inhibitor SP60012 (SP) decreased THP-1 cell adherence to IL-1 $\beta$ -stimulated ARPE-19 cells. (a) Western blots show the levels of phosphorylated JNK protein expression. (b) The fold-change in pJNK protein expression was measured relative to JNK expression. (c) ARPE-19 cells were pretreated with 10  $\mu$ M luteolin or JNK inhibitor (SP600125) for 1 h and then cocultured with labeled THP-1 cells. (d) The fluorescence intensity was used to quantify calcein-AM fluorescence. Data represent the mean  $\pm$  SD. \* $p$  < 0.05, \*\* $p$  < 0.01, compared to ARPE-19 cells stimulated with IL-1 $\beta$  alone.

monocyte adhesion in RPE cells [41, 42]. Here, we demonstrated that luteolin inhibited sICAM-1 levels and attenuated THP-1 cell adhesion to IL-1 $\beta$ -stimulated ARPE-19 cells (Figure 3(e)). We also found that luteolin significantly inhibited iNOS protein expression and increased HO-1 protein expression (Figures 2(b) and 2(d)). These findings support

that luteolin is indeed an anti-inflammatory phytochemical that can attenuate proinflammatory cytokine-induced inflammation in ARPE-19 cells.

IL-1 $\beta$  activation of NF- $\kappa$ B signaling is closely associated with RD diseases [15, 16] and pAKT is related to inhibition of the NF- $\kappa$ B inflammatory pathway [36]. Previous studies



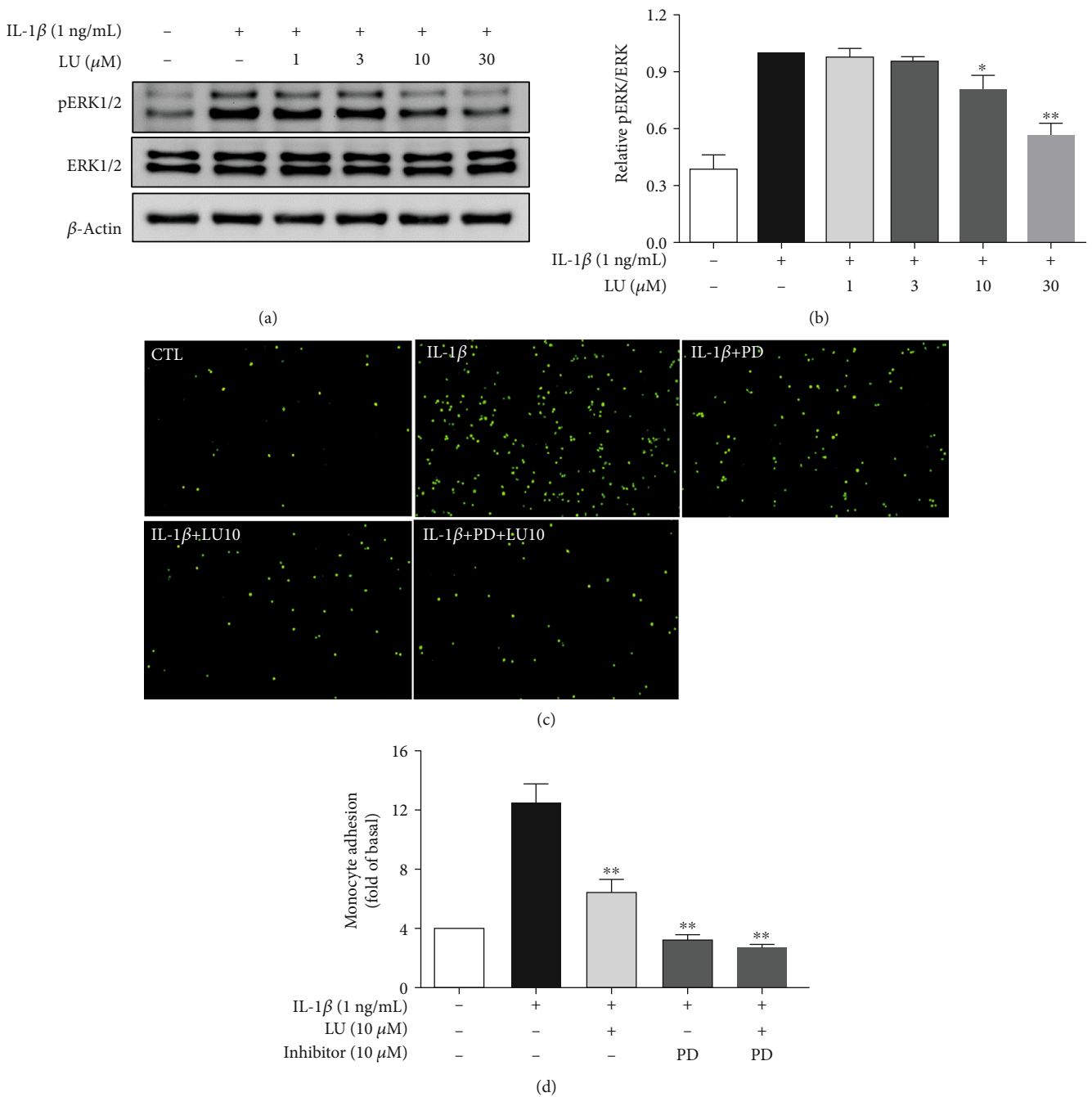


FIGURE 6: Luteolin blocked ERK phosphorylation and the ERK inhibitor PD98059 (PD) decreased THP-1 cell adherence to IL-1 $\beta$ -stimulated ARPE-19 cells. (a) Western blots show levels of phosphorylated ERK protein expression. (b) The fold-change in pERK protein expression was measured relative to ERK expression. (c) ARPE-19 cells were pretreated with 10  $\mu$ M luteolin or ERK inhibitor (PD98059) for 1 h and then cocultured with labeled THP-1 cells. (d) The fluorescence intensity was used to quantify calcein-AM fluorescence. Data represent the mean  $\pm$  SD. \* $p$  < 0.05, \*\* $p$  < 0.01, compared to ARPE-19 cells stimulated with IL-1 $\beta$  alone.

show that IL-1 $\beta$ -activates NF- $\kappa$ B, resulting in its translocation from the cytoplasm into the nucleus, followed by induction of cytokine and chemokine expressions in ARPE-19 cells [43]. Our present results showed that luteolin promoted AKT phosphorylation (Figures 2(f) and 2(g)), inhibited NF- $\kappa$ B p65 activation, and suppressed THP-1 cell adhesion (Figure 4). These findings suggest that luteolin promotes

AKT phosphorylation to block NF- $\kappa$ B p65 activation and thereby suppresses THP-1 cell adherence to IL-1 $\beta$ -stimulated ARPE-19 cells. Many studies have indicated that MAPK signaling plays an important role in AMD [44]. We observed that luteolin decreased the expression levels of IL-6, IL-8, sICAM-1, and MCP-1 in IL-1 $\beta$ -stimulated ARPE-19 cells. Thus, we further investigated whether luteolin attenuated

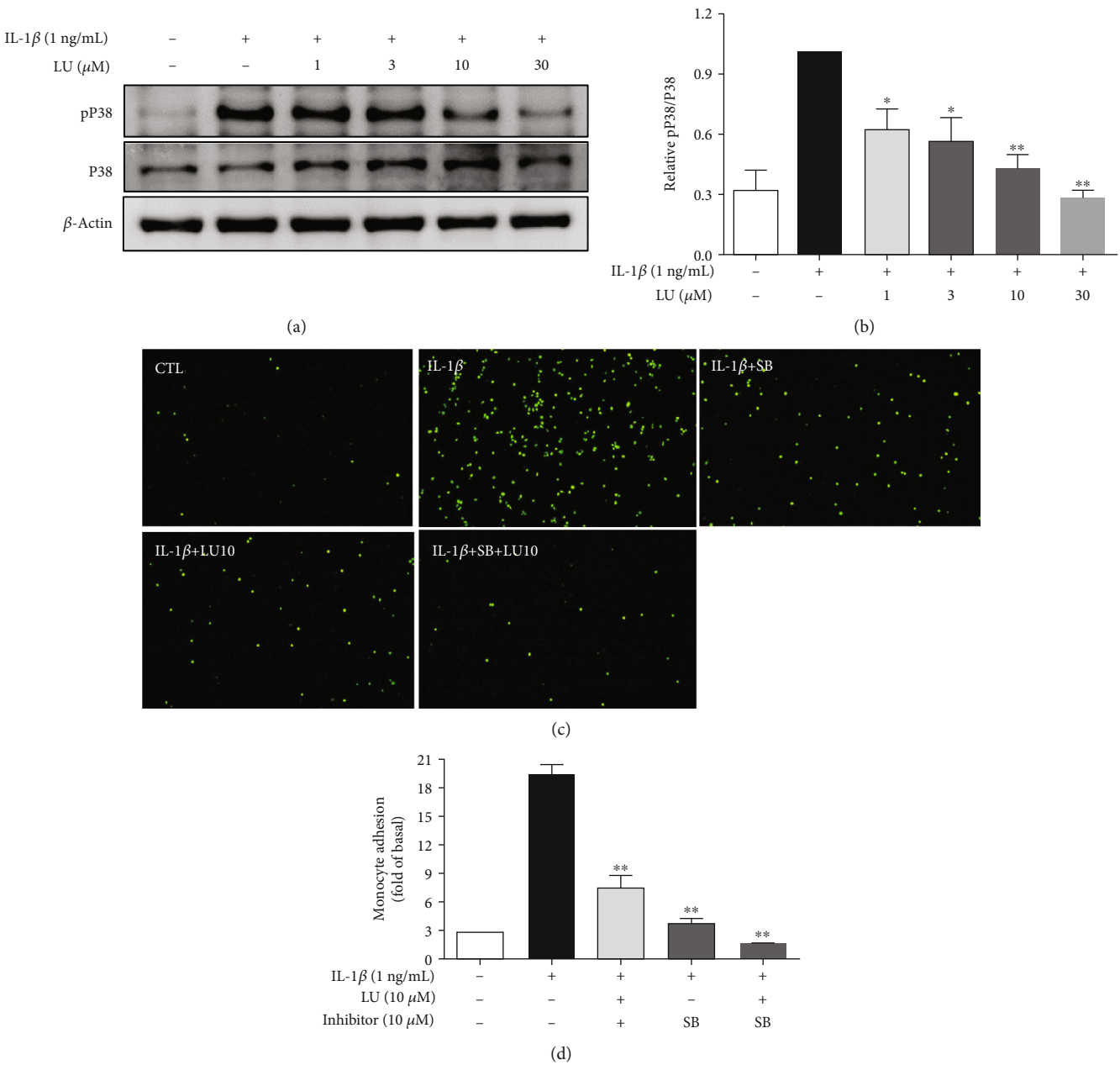


FIGURE 7: Luteolin blocked P38 phosphorylation, and the P38 inhibitor SB202190 (SB) decreased THP-1 cell adherence to IL-1 $\beta$ -stimulated ARPE-19 cells. (a) Western blots show levels of phosphorylated P38 protein expression. (b) The fold-change in pP38 protein expression was measured relative to P38 expression. (c) ARPE-19 cells were pretreated with 10  $\mu$ M luteolin or P38 inhibitor (SB203580) for 1 h and then cocultured with labeled THP-1 cells. (d) The fluorescence intensity was used to quantify calcein-AM fluorescence. Data represent the mean  $\pm$  SD. \* $p < 0.05$ , \*\* $p < 0.01$ , compared to ARPE-19 cells stimulated with IL-1 $\beta$  alone.

inflammation by suppressing MAPK pathways. Our results demonstrated that luteolin significantly inhibited the phosphorylation of the MAPKs JNK 1/2, ERK 1/2, and p38, supporting that luteolin may block MAPK pathways to decrease production of IL-6, IL-8I, sICAM-1, and MCP-1 (Figures 5(a), 5(b), 6(a), 6(b), 7(a), and 7(b)).

Human and animal studies have demonstrated that specific MAPK inhibitors may be potential therapeutic targets for RD disease treatment [44]. To explore the importance of individual MAPKs, we used the MAPK inhibitors SP600125 (JNK 1/2 inhibitor), PD98059 (ERK 1/2 inhibitor),

and SB202190 (P38), individually and as cotreatments with luteolin in IL-1 $\beta$ -stimulated ARPE-19 cells. We found that luteolin and MAPK inhibitors decreased THP-1 cell adherence to IL-1 $\beta$ -stimulated ARPE-19 cells (Figures 5(c), 5(d), 6(c), 6(d), 7(c), and 7(d)). We further found that these MAPK inhibitors attenuated the IL-1 $\beta$ -stimulated production of the inflammatory cytokines IL-6, IL-8, sICAM-1, and MCP-1 (Figures 8(a)–8(d)). These results suggested that luteolin blocked MAPK pathways and inhibited the expression of inflammation-related cytokines—thereby suppressing THP-1 adhesion.

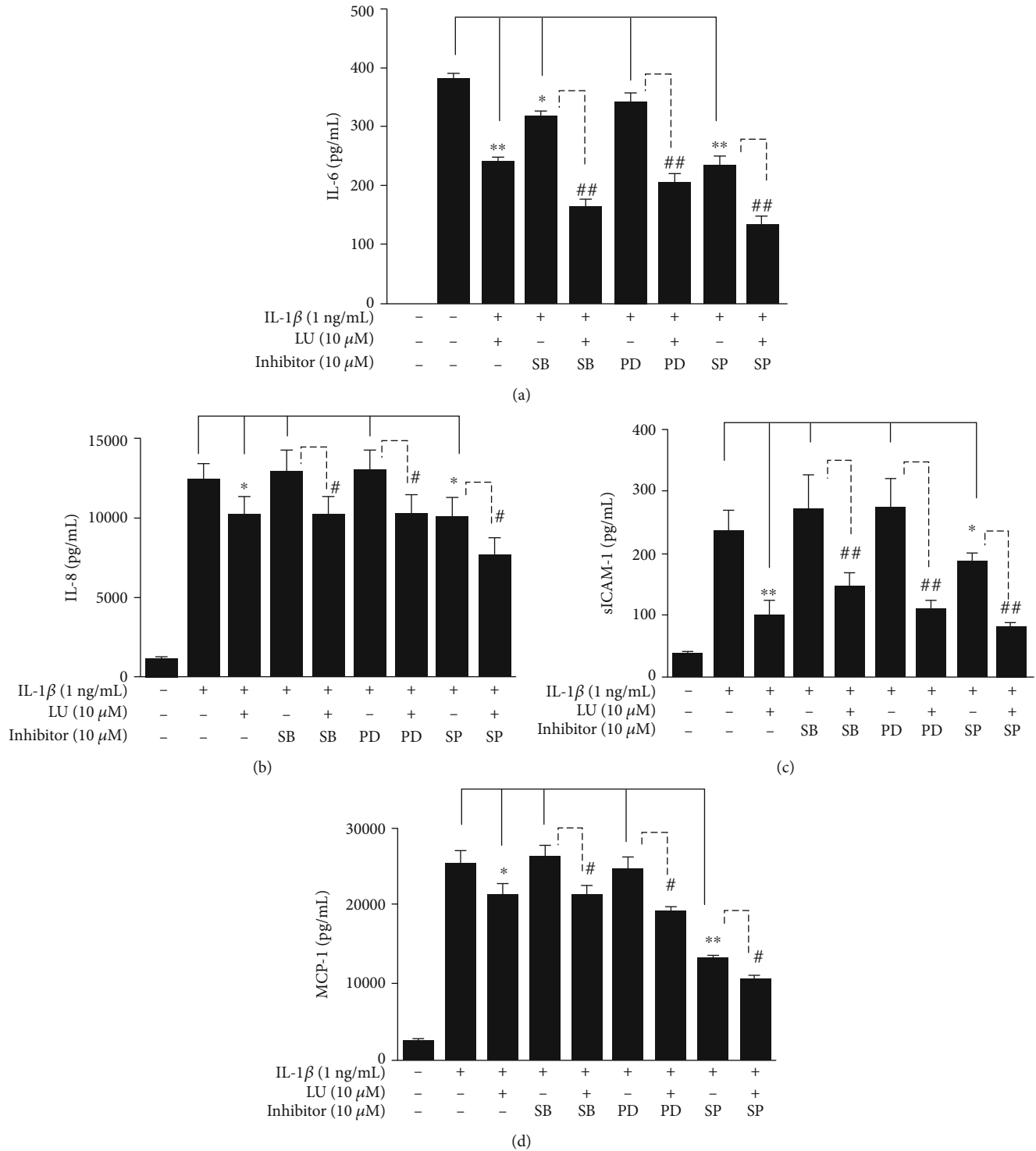


FIGURE 8: MAPK inhibitors mediated the expression levels of cytokines and chemokines in IL-1 $\beta$ -stimulated ARPE-19 cells. ARPE-19 cells were treated with MAPK inhibitors (10  $\mu$ M SB203580 (SB), 10  $\mu$ M PD98059 (PD), or 10  $\mu$ M SP600125 (SP)) with or without 10  $\mu$ M luteolin and then incubated with IL-1 $\beta$  for 24 h. ELISA results showed the levels of (a) IL-6, (b) IL-8, (c) sICAM-1, and (d) MCP-1. Data represent the mean  $\pm$  SD. \* $p$  < 0.05, \*\* $p$  < 0.01, compared to ARPE-19 cells stimulated with IL-1 $\beta$  alone. # $p$  < 0.05, ## $p$  < 0.01, compared to IL-1 $\beta$ -stimulated ARPE-19 cells pretreated with only MAPK inhibitor.

## 5. Conclusions

Our present data demonstrate that luteolin suppressed pro-inflammatory cytokine-induced retinal pigment epithelium

(RPE) inflammation via inactivation of the NF- $\kappa$ B pathway in IL-1 $\beta$ -stimulated ARPE-19 cells. Moreover, cotreatment with MAPK inhibitors plus luteolin attenuated THP-1 cell adhesion to IL-1 $\beta$ -stimulated ARPE-19 cells. Importantly,

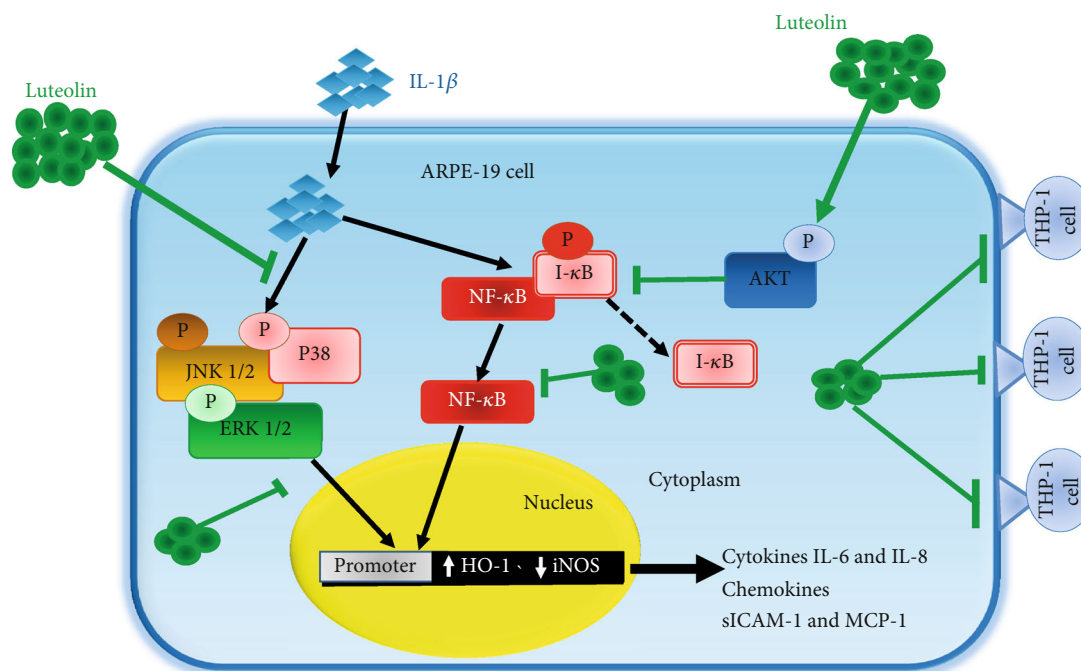


FIGURE 9: Model explaining the mechanisms via which luteolin inhibits IL-1 $\beta$ -induced inflammation in ARPE-19 cells. Luteolin promotes AKT phosphorylation, thus mediating the NF- $\kappa$ B and MAPK pathways, leading to decreased release of inflammatory-related cytokines, and thereby suppressing THP-1 cell adhesion to IL-1 $\beta$ -stimulated ARPE-19 cells. Luteolin also increases expression of the anti-inflammatory protein HO-1 and inhibits iNOS protein expression.

luteolin significantly reduced the expression levels of IL-6, IL-8, sICAM-1, and MCP-1 in IL-1 $\beta$ -stimulated ARPE-19 cells. Taken together, our findings suggest that luteolin blocks MAPK pathways, thus decreasing the expression levels of IL-6, IL-8, sICAM-1, and MCP-1, and thereby suppressing THP-1 cell adhesion to IL-1 $\beta$ -stimulated ARPE-19 cells (Figure 9). We conclude that the natural agent luteolin may ameliorate inflammation-induced retinal degeneration-related disorders via inhibition of the NF- $\kappa$ B and MAPK pathways in IL-1 $\beta$ -stimulated ARPE19 cells.

## Abbreviations

RPE:	Retinal pigment epithelium cells
RD:	Retinal degeneration
AMD:	Age-related macular degeneration
ARPE-19 cells:	Human retinal pigment epithelial cells
LU:	Luteolin
IL-1 $\beta$ :	Interleukin-1 $\beta$
IL-6:	Interleukin-6
IL-8:	Interleukin-8
sICAM-1:	Soluble intercellular adhesion molecule-1
MCP-1:	Monocyte chemoattractant protein-1
HO-1:	Heme oxygenase-1
AKT:	Protein kinase B
iNOS:	Inducible nitric oxide synthase
NF- $\kappa$ B:	Nuclear factor- $\kappa$ B
MAPK:	Mitogen-activated protein kinase
ELISA:	Enzyme-linked immunosorbent assay
JNK:	c-JUN N-terminal kinase
ERK:	Extracellular signal-regulated kinase.

## Data Availability

The data used to support the findings of this study are available from the corresponding author upon request.

## Conflicts of Interest

The authors declare that there is no conflict of interests regarding the publication of this paper.

## Authors' Contributions

Wen-Chung Huang and Chian-Jiun Liou are equal contributors to the work.

## Acknowledgments

This research was supported by grants from the Chang Gung Memorial Hospital (CMRPF1G0203, CMRPF1J0041), Ministry of Science and Technology (MOST 108-2320-B-255-004-), and Chang Gung University of Science and Technology (ZRRPF3J0081) of Taiwan.

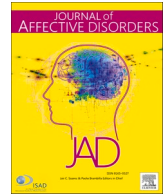
## References

- [1] O. Strauss, "The retinal pigment epithelium in visual function," *Physiological Reviews*, vol. 85, no. 3, pp. 845–881, 2005.
- [2] S. Datta, M. Cano, K. L. Ebrahimi, L. Wang, and J. T. Handa, "The impact of oxidative stress and inflammation on RPE degeneration in non-neovascular AMD," *Progress in Retinal and Eye Research*, vol. 60, pp. 201–218, 2017.

- [3] H. Xu, M. Chen, and J. V. Forrester, "Para-inflammation in the aging retina," *Progress in Retinal and Eye Research*, vol. 28, no. 5, pp. 348–368, 2009.
- [4] J. E. Knickelbein, C. C. Chan, H. N. Sen, F. L. Ferris, and R. B. Nussenblatt, "Inflammatory mechanisms of age-related macular degeneration," *International Ophthalmology Clinics*, vol. 55, no. 3, pp. 63–78, 2015.
- [5] W. al-Zamil and S. A. Yassin, "Recent developments in age-related macular degeneration: a review," *Clinical Interventions in Aging*, vol. 12, pp. 1313–1330, 2017.
- [6] R. Chou, T. Dana, C. Bougatsos, S. Grusing, and I. Blazina, "Screening for impaired visual acuity in older adults: updated evidence report and systematic review for the US Preventive Services Task Force," *JAMA*, vol. 315, no. 9, pp. 915–933, 2016.
- [7] S. Hajar, A. al Hazmi, M. Wasli, A. Mousa, and M. Rabi, "Prevalence and causes of blindness and diabetic retinopathy in Southern Saudi Arabia," *Saudi Medical Journal*, vol. 36, no. 4, pp. 449–455, 2015.
- [8] A. Biesemeier, T. Taubitz, S. Julien, E. Yoeuruk, and U. Schraermeyer, "Choriocapillaris breakdown precedes retinal degeneration in age-related macular degeneration," *Neurobiology of Aging*, vol. 35, no. 11, pp. 2562–2573, 2014.
- [9] S. Cao, A. Ko, M. Partanen et al., "Relationship between systemic cytokines and complement factor H Y402H polymorphism in patients with dry age-related macular degeneration," *American Journal of Ophthalmology*, vol. 156, no. 6, pp. 1176–1183, 2013.
- [10] R. Klein, C. E. Myers, K. J. Cruickshanks et al., "Markers of inflammation, oxidative stress, and endothelial dysfunction and the 20-year cumulative incidence of early age-related macular degeneration: the Beaver Dam Eye Study," *JAMA Ophthalmology*, vol. 132, no. 4, pp. 446–455, 2014.
- [11] J. M. Seddon, S. George, B. Rosner, and N. Rifai, "Progression of age-related macular degeneration: prospective assessment of C-reactive protein, interleukin 6, and other cardiovascular biomarkers," *Archives of Ophthalmology*, vol. 123, no. 6, pp. 774–782, 2005.
- [12] H. Miao, Y. Tao, and X. X. Li, "Inflammatory cytokines in aqueous humor of patients with choroidal neovascularization," *Molecular Vision*, vol. 18, pp. 574–580, 2012.
- [13] J. B. Jonas, R. A. Jonas, M. Neumaier, and P. Findeisen, "Cytokine concentration in aqueous humor of eyes with diabetic macular edema," *Retina*, vol. 32, no. 10, pp. 2150–2157, 2012.
- [14] J. B. Jonas, Y. Tao, M. Neumaier, and P. Findeisen, "Monocyte chemoattractant protein 1, intercellular adhesion molecule 1, and vascular cell adhesion molecule 1 in exudative age-related macular degeneration," *Archives of Ophthalmology*, vol. 128, no. 10, pp. 1281–1286, 2010.
- [15] E. Brint, T. Kamradt, and S. L. Doyle, "Editorial: IL-1 family members in health and disease," *Frontiers in Immunology*, vol. 10, no. 2596, 2019.
- [16] Y. Dong, C. Qian, G. Wan, P. Yan, S. Liang, and J. Wang, "Schizandrin A protects human retinal pigment epithelial cell line ARPE-19 against HG-induced cell injury by regulation of miR-145," *Molecular Therapy - Nucleic Acids*, vol. 19, pp. 42–49, 2020.
- [17] A. K. Pandurangan and N. M. Esa, "Luteolin, a bioflavonoid inhibits colorectal cancer through modulation of multiple signaling pathways: a review," *Asian Pacific Journal of Cancer Prevention*, vol. 15, no. 14, pp. 5501–5508, 2014.
- [18] K. H. Miesan and S. Mohamed, "Flavonoid (myricetin, quercetin, kaempferol, luteolin, and apigenin) content of edible tropical plants," *Journal of Agricultural and Food Chemistry*, vol. 49, no. 6, pp. 3106–3112, 2001.
- [19] T. Sun, Z. Xu, C.-T. Wu, M. Janes, W. Prinyawiwatkul, and H. K. No, "Antioxidant activities of different colored sweet bell peppers (*Capsicum annuum* L.)," *Journal of Food Science*, vol. 72, no. 2, pp. S98–102, 2007.
- [20] Y. Luo, P. Shang, and D. Li, "Luteolin: a flavonoid that has multiple cardio-protective effects and its molecular mechanisms," *Frontiers in Pharmacology*, vol. 8, 2017.
- [21] N. Aziz, M. Y. Kim, and J. Y. Cho, "Anti-inflammatory effects of luteolin: a review of in vitro, in vivo, and in silico studies," *Journal of Ethnopharmacology*, vol. 225, pp. 342–358, 2018.
- [22] M. Imran, A. Rauf, T. Abu-Izneid et al., "Luteolin, a flavonoid, as an anticancer agent: a review," *Biomedicine & Pharmacotherapy*, vol. 112, article 108612, 2019.
- [23] S. F. Nabavi, N. Braid, O. Gortzi et al., "Luteolin as an anti-inflammatory and neuroprotective agent: a brief review," *Brain Research Bulletin*, vol. 119, pp. 1–11, 2015.
- [24] T. C. Theoharides, "COVID-19, pulmonary mast cells, cytokine storms, and beneficial actions of luteolin," *BioFactors*, vol. 46, no. 3, pp. 306–308, 2020.
- [25] H. Yan, L. Ma, H. Wang et al., "Luteolin decreases the yield of influenza A virus in vitro by interfering with the coat protein I complex expression," *Journal of Natural Medicines*, vol. 73, no. 3, pp. 487–496, 2019.
- [26] C. Horvath and C. Wolfrum, "Feeding brown fat: dietary phytochemicals targeting non-shivering thermogenesis to control body weight," *The Proceedings of the Nutrition Society*, vol. 15, pp. 1–19, 2020.
- [27] Y. Zhang, Y. Wang, X. Li et al., "WSF-7 inhibits obesity-mediated PPAR $\gamma$  phosphorylation and improves insulin sensitivity in 3T3-L1 adipocytes," *Biological and Pharmaceutical Bulletin*, vol. 43, no. 3, pp. 526–532, 2020.
- [28] Y. Baek, M. N. Lee, D. Wu, and M. Pae, "Luteolin reduces adipose tissue macrophage inflammation and insulin resistance in postmenopausal obese mice," *The Journal of Nutritional Biochemistry*, vol. 71, pp. 72–81, 2019.
- [29] Q. Zhang, E. Gonzalez de Mejia, D. Luna-Vital et al., "Relationship of phenolic composition of selected purple maize (*Zea mays* L.) genotypes with their anti-inflammatory, anti-adipogenic and anti-diabetic potential," *Food Chemistry*, vol. 289, pp. 739–750, 2019.
- [30] S. Park, D. S. Kim, S. Kang, and H. J. Kim, "The combination of luteolin and l-theanine improved Alzheimer disease-like symptoms by potentiating hippocampal insulin signaling and decreasing neuroinflammation and norepinephrine degradation in amyloid- $\beta$ -infused rats," *Nutrition Research*, vol. 60, pp. 116–131, 2018.
- [31] F. Ali and Y. H. Siddique, "Bioavailability and pharmacotherapeutic potential of luteolin in overcoming Alzheimer's disease," *CNS & Neurological Disorders - Drug Targets (Formerly Current Drug Targets - CNS & Neurological Disorders)*, vol. 18, no. 5, pp. 352–365, 2019.
- [32] M. Hytti, N. Piippo, E. Korhonen, P. Honkakoski, K. Kaarniranta, and A. Kauppinen, "Fisetin and luteolin protect human retinal pigment epithelial cells from oxidative stress-induced cell death and regulate inflammation," *Scientific Reports*, vol. 5, article 17645, no. 1, 2016.



- [33] M. Hytti, D. Szabó, N. Piippo et al., "Two dietary polyphenols, fisetin and luteolin, reduce inflammation but augment DNA damage-induced toxicity in human RPE cells," *The Journal of Nutritional Biochemistry*, vol. 42, pp. 37–42, 2017.
- [34] H. Lu, Y. Chen, X. B. Sun, B. Tong, and X. H. Fan, "Effects of luteolin on retinal oxidative stress and inflammation in diabetes," *RSC Advances*, vol. 5, no. 7, pp. 4898–4904, 2015.
- [35] W. C. Huang, H. H. Su, L. W. Fang, S. J. Wu, and C. J. Liou, "Licochalcone A inhibits cellular motility by suppressing E-cadherin and MAPK signaling in breast cancer," *Cells*, vol. 8, no. 3, p. 218, 2019.
- [36] Y. Wooff, S. M. Man, R. Aggio-Bruce, R. Natoli, and N. Fernando, "IL-1 family members mediate cell death, inflammation and angiogenesis in retinal degenerative diseases," *Frontiers in Immunology*, vol. 10, p. 1618, 2019.
- [37] Y. C. Lin, H. C. Kuo, J. S. Wang, and W. W. Lin, "Regulation of inflammatory response by 3-methyladenine involves the coordinative actions on Akt and glycogen synthase kinase  $\beta$  rather than autophagy," *The Journal of Immunology*, vol. 189, no. 8, pp. 4154–4164, 2012.
- [38] X. He, D. Sun, S. Chen, and H. Xu, "Activation of liver X receptor delayed the retinal degeneration of rd1 mice through modulation of the immunological function of glia," *Oncotarget*, vol. 8, no. 19, pp. 32068–32082, 2017.
- [39] C. A. Dinarello, "Overview of the IL-1 family in innate inflammation and acquired immunity," *Immunological Reviews*, vol. 281, no. 1, pp. 8–27, 2018.
- [40] K. Kataoka, H. Matsumoto, H. Kaneko et al., "Macrophage- and RIP3-dependent inflammasome activation exacerbates retinal detachment-induced photoreceptor cell death," *Cell Death & Disease*, vol. 6, no. 4, article e1731, 2015.
- [41] P. Thichanpiang, S. J. Harper, K. Wongprasert, and D. O. Bates, "TNF- $\alpha$ -induced ICAM-1 expression and monocyte adhesion in human RPE cells is mediated in part through autocrine VEGF stimulation," *Molecular Vision*, vol. 20, pp. 781–789, 2014.
- [42] L. Yang, R. M. Froio, T. E. Sciuto, A. M. Dvorak, R. Alon, and F. W. Luscinskas, "ICAM-1 regulates neutrophil adhesion and transcellular migration of TNF- $\alpha$ -activated vascular endothelium under flow," *Blood*, vol. 106, no. 2, pp. 584–592, 2005.
- [43] X. Chen, R. Han, P. Hao et al., "Nepetin inhibits IL-1 $\beta$  induced inflammation via NF- $\kappa$ B and MAPKs signaling pathways in ARPE-19 cells," *Biomedicine & Pharmacotherapy*, vol. 101, pp. 87–93, 2018.
- [44] S. V. Kyosseva, "Targeting MAPK signaling in age-related macular degeneration," *Ophthalmology and Eye Diseases*, vol. 8, pp. 23–30, 2016.



## Research paper

# Bidirectional association between migraine and depression among probands and unaffected siblings: A nationwide population-based study

Mu-Hong Chen<sup>a,b,1</sup>, Tai-Long Pan<sup>f,g,h,1</sup>, Wei-Chen Lin<sup>a,b</sup>, Kai-Lin Huang<sup>a,b</sup>, Ju-Wei Hsu<sup>a,b,\*</sup>, Cheng-Ta Li<sup>a,b</sup>, Shih-Jen Tsai<sup>a,b</sup>, Tung-Ping Su<sup>a,b,e</sup>, Tzeng-Ji Chen<sup>c,d</sup>, Ya-Mei Bai<sup>a,b,\*</sup>

<sup>a</sup> Department of Psychiatry, Taipei Veterans General Hospital, Taipei, Taiwan

<sup>b</sup> Division of Psychiatry, School of Medicine, National Yang-Ming University, Taipei, Taiwan

<sup>c</sup> Department of Family Medicine, Taipei Veterans General Hospital, Taipei, Taiwan

<sup>d</sup> Institute of Hospital and Health Care Administration, National Yang-Ming University, Taipei, Taiwan

<sup>e</sup> Department of Psychiatry, General Cheng Hsin Hospital

<sup>f</sup> School of Traditional Chinese Medicine, Chang Gung University, Taoyuan, Taiwan

<sup>g</sup> Research Center for Chinese Herbal Medicine and Research Center for Food and Cosmetic Safety, College of Human Ecology, Chang Gung University of Science and Technology, Taoyuan, Taiwan

<sup>h</sup> Liver Research Center, Chang Gung Memorial Hospital, Taoyuan, Taiwan

## ARTICLE INFO

## Keywords:

Migraine

Depression

Familial coaggregation

Taiwan National Health Insurance Research

Database

## ABSTRACT

**Background:** Evidence suggests a bidirectional association between migraine and depression in individuals and in twins. However, whether a bidirectional association between migraine and depression also occurs among siblings (probands and unaffected nontwin siblings) remains unknown.

**Methods:** Using the Taiwan National Health Insurance Research Database, we examined the data of 1504 probands with migraine, 1595 unaffected siblings, and 6380 nonmigrainous controls born before 2000 to identify new-onset depression for the period between 1996 and 2011. Conversely, 31824 probands with depression, 34325 unaffected siblings, and 137300 nondepressive controls were examined for the identification of new-onset migraine.

**Results:** Logistic regression analyses demonstrated that compared with the controls, patients with migraine (odds ratio [OR]: 4.09; 95% confidence interval [CI]: 3.75–4.46) and unaffected siblings (OR: 1.40; 95% CI: 1.24–1.58) were more likely to develop depression during the follow-up period. Moreover, patients with depression and unaffected siblings had a 4.13-fold (95% CI: 3.18–5.36) and 1.45-fold (95% CI: 1.03–2.05) increased risk of migraine.

**Discussion:** The bidirectional association between migraine and depression among probands and unaffected siblings suggests a familial coaggregation of these two conditions. Additional studies are required to investigate the genetic and environmental etiologies for this coaggregation.

Migraine and depression are common complex disorders that result in considerable societal and economic burdens measured by years lived with disability (Disease et al., 2018). Longitudinal studies have reported a bidirectional relationship between migraine and depression, with one disorder increasing the relative risk for the other (Modgill et al., 2012, Breslau et al., 1994). However, the definite pathophysiology of migraine and depression remains unclear; the confluence and interactions of various genetic and environmental risk factors lead to a spectrum of neurobiological vulnerability to these two disorders.

Increasing evidence indicates that migraine and depression commonly occur together and that they may share overlapping genetic factors (Yang et al., 2018, Yang et al., 2016). Using single-nucleotide polymorphism (SNP) and gene-based analyses of genome-wide association study (GWAS) genotype data (comprising 59674 patients with migraine and 9240 with depression), Yang et al. (Yang et al., 2018) found a significant SNP-based heritability for both migraine ( $h^2 = 12\%$ ) and depression ( $h^2 = 19\%$ ) and a significant cross-disorder genetic correlation ( $r_G = 0.25$ ;  $p < .05$ ). Furthermore, Peroutka et al. (Peroutka

\* Corresponding authors. Department of Medical Research, Taipei Veterans General Hospital, No. 201, Sec. 2, Shih-Pai Road, Taipei 112, Taiwan  
E-mail addresses: [jwhsu@vghtpe.gov.tw](mailto:jwhsu@vghtpe.gov.tw) (J.-W. Hsu), [ymbi@mail2000.com.tw](mailto:ymbi@mail2000.com.tw) (Y.-M. Bai).

<sup>1</sup> equally contributed.

<https://doi.org/10.1016/j.jad.2020.10.056>

Received 19 August 2020; Received in revised form 22 October 2020; Accepted 26 October 2020

Available online 29 October 2020

0165-0327/© 2020 Elsevier B.V. All rights reserved.

et al., 1998) reported that polymorphisms of dopamine D2 receptor (DRD2) NcoI alleles may contribute to the comorbidity of migraine and depression. An Australian twin study conducted on 5319 twin pairs revealed that the relative risk (RR) for migraine in cotwins of probands reporting depression was 2.23 and 1.55 in monozygotic and dizygotic pairs, respectively; additionally, the RR for depression in cotwins of probands reporting migraine was 1.35 and 1.06 in monozygotic and dizygotic pairs, respectively (Yang et al., 2016). However, whether familial coaggregation of migraine and depression also exists between probands and their unaffected nontwin siblings remains unknown. In addition, such familial coaggregation of these two conditions in Asian populations requires further investigation.

In the current longitudinal follow-up study, we investigated the bidirectional temporal association of migraine and depression between probands and their unaffected nontwin siblings by using data from the Taiwan National Health Insurance Research Database (NHIRD). We hypothesized that probands with migraine or depression and unaffected siblings would have a higher likelihood of developing new-onset depression or migraine, respectively, during the follow-up period compared with nonmigrainous or nondepressive controls.

## 1. Methods

### 1.1. Data source

Taiwan's National Health Insurance (NHI) is a mandatory universal health insurance program and was implemented in 1995. It offers comprehensive medical care coverage to all Taiwanese residents.

The National Health Research Institute (NHRI) audits and releases the NHI research database (NHIRD) for scientific and study purposes. The NHRI Claims data of subjects included in the NHIRD are anonymous to maintain individual privacy. Comprehensive information on insured subjects is included in the database, including demographic data, dates of clinical visits, and disease diagnoses. Using a unique personal identification number assigned to each resident in Taiwan, all of the medical information were linked together. Following Chen et al.'s and Cheng et al.'s methods, the recorded family kinships in the NHIRD were used for genealogy reconstruction (Chen et al., 2019, Cheng et al., 2018). The diagnostic codes used were based on the International Classification of Diseases, 9th Revision, Clinical Modification (ICD-9-CM). The NHIRD has been used extensively in many epidemiologic studies in Taiwan (Chen et al., 2019, Cheng et al., 2018, Chen et al., 2016, Huang et al., 2020). This study was approved by the Institutional Review Board of Taipei Veterans General Hospital. The study flowcharts were shown in figure 1.

### 1.2. Study population, exposure, and outcome

A bidirectional case-control cohort study design was used to

investigate the temporal and coaggregated association between migraine and depression. The study subjects (probands, nontwin unaffected siblings, and controls) included individuals who were born before 2000 from the NHIRD, and followed up from January 1996 until the primary outcome, death, or December 2011.

### 1.3. Study 1: Migraine → depression

Patients with migraine and their unaffected siblings were enrolled in the study 1. Migraine was diagnosed by board-certificated neurologists or pain specialists at least twice based on ICD-9-CM code of 346. The primary outcome assessed was new-onset depression (ICD-9-CM codes: 296.2, 296.3, 300.4, 311) given by board-certificated psychiatrists at least twice. In order to identify the incidence of depression, patients with migraine who had a depression diagnosis prior to migraine were excluded.

### 1.4. Study 2: Depression → Migraine

In study 2, subjects with depression and their unaffected siblings were enrolled. Depression was diagnosed by board-certificated psychiatrists at least twice based on ICD-9-CM codes of 296.2, 296.3, 300.4, and 311. The primary outcome assessed was new-onset migraine (ICD-9-CM code: 346) given by board-certificated neurologists or pain specialists at least twice. Likewise, in order to identify incident migraine, patients with a migraine diagnosis prior to depression were excluded.

## 2. Matched controls

For each unaffected sibling of probands with migraine or depression, four matched controls were randomly selected from the NHIRD based on age, sex, monthly income, and residence after those with migraine or any major psychiatric and depressive disorder were excluded, respectively. Level of urbanization (level 1 to level 5; level 1: most urbanized region; level 5: least urbanized region) was also assessed for our study (Liu et al., 2006). Monthly income and urbanization levels were used to represent socioeconomic status. Charlson Comorbidity Index was used for clinical prognosis and comorbidity adjustment (Charlson et al., 1987).

### 2.1. Statistical analysis

For between-group comparisons, the F test was used for continuous variables and Pearson's  $\chi^2$  test for nominal variables, where appropriate. Logistic regression models with the adjustment of demographic data (age, sex, monthly income, and residence) and CCI scores were used to examine the odds ratios (ORs) and 95% confidence intervals (CIs) of new-onset depression or migraine in the study 1 and study 2 cohorts, respectively. Logistic regression stratified by sex was performed to

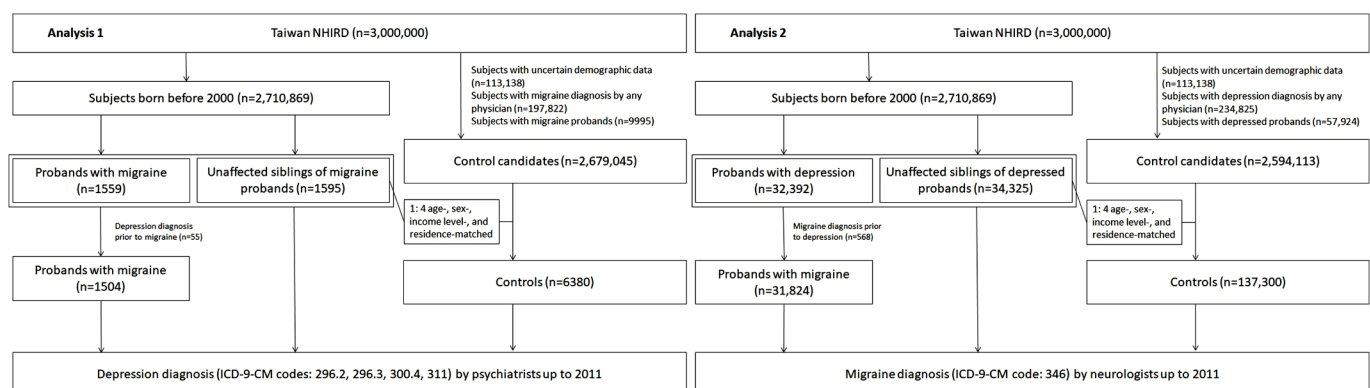


Figure 1. Study flowcharts

investigate the role of sex in the bidirectional association between migraine and depression. A 2-tailed *P*-value of less than 0.05 was considered statistically significant. All data processing and statistical analyses were performed with Statistical Package for Social Science (SPSS) version 19 software (SPSS Inc.) and Statistical Analysis Software (SAS) version 9.1 (SAS Institute, Cary, NC).

### 3. Results

#### 3.1. Study 1: Migraine → depression

There were 1504 patients with migraine, 1595 unaffected siblings, and 6380 controls in this study. Age, sex, monthly income, and residence were matched and did not have between-group differences among unaffected siblings and controls (Table 1). Overall, 8.2% of patients with migraine (*n* = 124) and 2.9% of the unaffected siblings (*n* = 46) developed depression as compared to 1.9% of the controls (*n* = 122). Logistical regression analysis with the adjustment of demographic data and CCI scores determined that patients with migraine (OR: 4.09, 95% CI: 3.75–4.46) and the unaffected siblings (OR: 1.40, 95% CI: 1.24–1.58) were more likely to develop depression during the follow-up period than the control group (Table 3). The association between migraine and depression risk remained significant when we stratified the subjects by sex (Table 4).

#### 3.2. Study 2: Depression → Migraine

Overall, 31824 patients with depression, 34325 unaffected siblings, and 137300 controls were included in study 2 (Table 2). During the study period, 3.6% of the depression probands (*n* = 1146) and 1.1% of the unaffected siblings (*n* = 364) developed migraine as compared to 0.7% of the controls (*n* = 1021). After adjusting for potential confounders (age, sex, monthly income, urbanization, and CCI scores), patients with depression and unaffected siblings had 4.13-fold (95% CI: 3.18–5.36) and 1.45-fold (95% CI: 1.03–2.05) increased risk for migraine compared with the control group, respectively (Table 3). After the stratification of subjects by sex, the association between depression and migraine risk remained significant for men (Table 4). However, unaffected siblings of depressed probands were not related to the migraine risk (OR: 1.12, 95% CI: 0.69–1.82), but unaffected siblings of migraine probands were associated with the depression risk (OR: 1.35, 95% CI: 1.17–1.57) (Table 4).

### 4. Discussion

The study findings support our hypothesis that probands with migraine or depression and unaffected siblings would have a higher likelihood of developing new-onset depression or migraine, respectively, later in life compared with controls without either condition. We also found similar risk levels (approximately 1.4-fold in the unaffected siblings and 4-fold in the probands) between migraine increasing depression and depression increasing migraine, suggesting equal coaggregation between migraine and depression among siblings.

To our knowledge, our study is the first to suggest a familial coaggregation of migraine and depression between probands and unaffected nontwin siblings. In general, affective spectrum disorders, including particular mental disorders (i.e., anxiety disorders, depression, and stress-related disorders) and certain physical disorders (i.e., irritable bowel syndrome and migraine), have been suggested to have shared, but as yet unknown, neurophysiologic and etiologically specific abnormalities (Scharin et al., 2012). Previous studies have reported that affective spectrum disorders commonly co-occur among individuals within families and may respond to the same type of pharmacological treatment, such as serotonin or norepinephrine modulators (Scharin et al., 2012). Genetic studies of migraine and depression have determined that polymorphisms in several specific genes, such as *DRD2* NcoI and *SLC6A4*, underlie the common pathophysiology of migraine and depression (Yang et al., 2018; Ghosh et al., 2013; Zhang et al., 2019), although the pure forms of these two conditions may still be genetically distinct, according to the study by Ligthart et al. (Ligthart et al., 2014).

Beyond the overlapping genetic factors, migraine and depression probands may share common environmental risks, such as psychological stress and social adversities (Zhang et al., 2019; Baksa et al., 2017; Deligianni et al., 2012). Swanson et al. (Scharin et al., 2012) demonstrated that such stressors, including change in social support, childhood trauma, chronic stress, recent household financial problems, recent marital problems, recent unemployment, and work stress, mediated the bidirectional association between migraine and depression. Modgill et al. (Modgill et al., 2012) further confirmed that stress and childhood trauma intensified the bidirectional relationship between migraine and depression, particularly among those with depression developing new-onset migraine. Considering the preceding pieces of evidence overall, our study expanded the observation of familial coaggregation of migraine and depression from twins to their nontwin siblings. Specifically, we demonstrated that unaffected nontwin siblings and probands with migraine or depression were more likely to develop new-onset depression or migraine later in life compared with nonmigrainous or

**Table 1**  
Demographic data and incidence of depression among patients with migraine and their unaffected siblings

	A Patients with migraine (n=1504)	B Unaffected siblings (n=1595)	C. Controls (n=6380)	p-value	post-hoc
Age (years, SD)	31.83 (8.48)	31.01 (9.40)	31.02 (9.42)	0.008	A>B~C
Sex (n, %)				<0.001	A>B~C
Male	429 (28.5)	813 (51.0)	3252 (51.0)		
Female	1075 (71.5)	782 (49.0)	3128 (49.0)		
Level of urbanization (n, %)				0.753	
1 (most urbanized)	375 (24.9)	390 (24.5)	1560 (24.5)		
2	504 (33.5)	544 (34.1)	2176 (34.1)		
3	242 (16.1)	228 (14.3)	912 (14.3)		
4	167 (11.1)	179 (11.2)	716 (11.2)		
5 (most rural)	216 (14.4)	254 (15.9)	1016 (15.9)		
Income (n, %)				0.020	A>B~C
≤ 15,840 NTD/month	474 (31.5)	575 (36.1)	2300 (36.1)		
15,841–25,000NTD/month	524 (34.8)	509 (31.9)	2036 (31.9)		
≥ 25,001NTD/month	506 (33.6)	511 (32.0)	2044 (32.0)		
CCI scores (SD)	1.00 (1.17)	0.70 (1.10)	0.56 (0.92)	<0.001	A>B>C
Incidence of depression					
Event (n, %)	124 (8.2)	46 (2.9)	122 (1.9)	<0.001	A>B>C
Age of diagnosis (years, SD)	26.72 (7.45)	26.89 (9.15)	26.96 (7.56)	0.969	

SD: standard deviation; NTD: new Taiwan dollar; CCI: Charlson Comorbidity Index.

The F test was used for continuous variables and Pearson's  $\chi^2$  test for nominal variables, where appropriate.

**Table 2**

Demographic data and incidence of migraine among patients with depression and their unaffected siblings

	Patients with depression (n=31824)	Unaffected siblings (n=34325)	Controls (n=137300)	p-value	post-hoc
Age (years, SD)	32.05 (8.81)	30.91 (96.8)	30.91 (96.8)	<0.001	A>B~C
Sex (n, %)				<0.001	A>B~C
Male	12437 (39.1)	17700 (51.6)	70800 (51.6)		
Female	19387 (60.9)	16625 (48.4)	66500 (48.4)		
Level of urbanization (n, %)				<0.001	B~C>A
1 (most urbanized)	8593 (27.0)	9094 (26.5)	36376 (26.5)		
2	10628 (33.4)	11588 (33.8)	46352 (33.8)		
3	4445 (14.0)	4678 (13.6)	18712 (13.6)		
4	3310 (10.4)	3296 (9.6)	13184 (9.6)		
5 (most rural)	4848 (15.5)	5669 (16.5)	22676 (16.5)		
Income (n, %)				<0.001	B~C>A
≤ 15,840 NTD/month	12709 (39.9)	13072 (38.1)	52288 (38.1)		
15,841–25,000NTD/month	10925 (34.4)	10277 (29.9)	41108 (29.9)		
≥ 25,001NTD/month	8190 (25.7)	10976 (32.0)	43904 (32.0)		
CCI scores (SD)	0.96 (1.21)	0.65 (0.97)	0.57 (0.93)	<0.001	A>B>C
Incidence of migraine					
Event (n, %)	1146 (3.6)	364 (1.1)	1021 (0.7)	<0.001	A>B>C
Age of diagnosis (years, SD)	27.67 (8.70)	24.81 (7.52)	26.68 (8.78)	<0.001	A>C>B

SD: standard deviation; NTD: new Taiwan dollar; CCI: Charlson Comorbidity Index.

The F test was used for continuous variables and Pearson's  $\chi^2$  test for nominal variables, where appropriate.**Table 3**

Risk of migraine and depression among probands and unaffected siblings\*

	Depression risk (OR, 95% CI)	Migraine risk (OR, 95% CI)
Group		
Controls	1 (ref.)	1 (ref.)
Unaffected siblings	<b>1.40 (1.24–1.58)</b>	<b>1.45 (1.03–2.05)</b>
Probands	<b>4.09 (3.75–4.46)</b>	<b>4.13 (3.18–5.36)</b>
CCI scores	<b>1.26 (1.23–1.30)</b>	<b>1.27 (1.16–1.38)</b>

CCI: Charlson Comorbidity Index; OR: odds ratio; CI: confidence interval.

**Bold** type indicates statistical significance.

\*logistic regression models with the adjustment of demographic data (age, sex, monthly income, and residence) and CCI scores were used to examine the ORs and 95% CIs.

**Table 4**

Risk of migraine and depression among probands and unaffected siblings, stratified by sex\*

	Depression risk (OR, 95% CI)	Migraine risk (OR, 95% CI)
Male		
Group		
Controls	1 (ref.)	1 (ref.)
Unaffected siblings	<b>1.51 (1.23–1.87)</b>	<b>2.00 (1.22–3.30)</b>
Probands	<b>4.52 (3.83–5.33)</b>	<b>3.65 (2.22–6.01)</b>
CCI scores	<b>1.18 (1.12–1.24)</b>	<b>1.38 (1.20–1.59)</b>
Female		
Group		
Controls	1 (ref.)	1 (ref.)
Unaffected siblings	<b>1.35 (1.17–1.57)</b>	1.12 (0.69–1.82)
Probands	<b>3.93 (3.55–4.35)</b>	<b>3.76 (2.74–5.15)</b>
CCI scores	<b>1.31 (1.26–1.35)</b>	<b>1.21 (1.09–1.36)</b>

CCI: Charlson Comorbidity Index; OR: odds ratio; CI: confidence interval.

**Bold** type indicates statistical significance.

\* logistic regression models with the adjustment of demographic data (age, monthly income, and residence) and CCI scores were used to examine the ORs and 95% CIs.

nondepressive controls. Overlapping genetic and environmental risk factors may synergistically contribute to migraine and depression within families.

Regarding the coaggregation of depression and migraine between probands and unaffected siblings, the clinical issues of treating the condition of dual diagnoses and reducing the likelihoods of depression and migraine in the high-risk siblings were of concern. Evidence suggested that optimal modulation of serotonergic, dopaminergic and

$\gamma$ -aminobutyric acid-ergic systems and supplement of brain-derived neurotrophic factor (BDNF) remained strong candidates for treatment and prevention of migraine and depression (Yang et al., 2016, Karatas et al., 2018). As mentioned, serotonin or norepinephrine modulators should be considered in the condition of dual diagnoses (Scharin et al., 2012). However, whether optimal exercise and calorie restriction, which increased BDNF levels in the brain and reduced systemic low-grade inflammation, may be beneficial to reduce the likelihoods of depression and migraine in the high-risk individuals, such as unaffected siblings of migraine/depression probands, would need further investigation (Amin et al., 2018, Pitts et al., 2020, Manchishi et al., 2018, Araya et al., 2008, Di Lorenzo et al., 2019).

Several study limitations should be addressed here. First, the incidence of migraine and depression may have been underestimated because only patients who sought medical help and consultation were examined. However, because diagnoses of both disorders were made by board-certified neurologists, pain specialists, or psychiatrists, diagnostic validity was enhanced. Second, because data concerning education, engagement in physical activity, environmental factors, occupation, and personal lifestyle are not available in the Taiwan NHIRD, we could not examine the influence of these factors.

In conclusion, probands with migraine or depression and unaffected siblings were more prone to developing new-onset depression or migraine during the follow-up period, respectively, compared with nonmigrainous or nondepressive controls. The bidirectional association of migraine and depression among siblings may indicate a familial coaggregation of these two conditions. Additional studies are required to elucidate the underlying genetic and environmental mechanisms that contribute to this coaggregation.

## Funding Source

The study was supported by grant from Taipei Veterans General Hospital (V103E10-001, V104E10-002, V105E10-001-MY2-1, V105A-049, V106B-020, V107B-010, V107C-181, V108B-012), Yen Tjing Ling Medical Foundation (CI-109-21, CI-109-22) and Ministry of Science and Technology, Taiwan (107-2314-B-075-063-MY3, 108-2314-B-075-037). The funding source had no role in any process of our study.

## Financial Disclosure

All authors have no financial relationships relevant to this article to disclose.



## Contributions

Dr MHC, Dr JWH, Prof TLP, and Dr YMB designed the study, wrote the protocol and manuscripts, Dr WCL, Dr KLH, Dr SJT, Dr CTL, and Dr TPS assisted with the preparation and proof-reading of the manuscript, and Dr TJC, Dr YMB, and Dr MHC provided the advices on statistical analysis.

## Declaration of Competing Interest

No conflict of interest.

## Acknowledgement


We thank Mr I-Fan Hu for his friendship and support.

## References

- Disease, GBD, Injury, I, Prevalence, C, 2018. Global, regional, and national incidence, prevalence, and years lived with disability for 354 diseases and injuries for 195 countries and territories, 1990–2017: a systematic analysis for the Global Burden of Disease Study 2017. *Lancet* 392, 1789–1858.
- Modgill, G, Jette, N, Wang, JL, Becker, WJ, Patten, SB, 2012. A population-based longitudinal community study of major depression and migraine. *Headache* 52, 422–432.
- Breslau, N, Davis, GC, Schultz, LR, Peterson, EL, 1994. Joint 1994 Wolff Award Presentation. Migraine and major depression: a longitudinal study. *Headache* 34, 387–393.
- Yang, Y, Zhao, H, Boomsma, DI, Ligthart, L, Belin, AC, Smith, GD, Esko, T, Freilinger, TM, Hansen, TF, Ikram, MA, Kallela, M, Kubisch, C, Paraskevi, C, Strachan, DP, Wessman, M, 2018. International Headache Genetics C, van den Maagdenberg A, Terwindt GM, Nyholt DR. Molecular genetic overlap between migraine and major depressive disorder. *Eur J Hum Genet* 26, 1202–1216.
- Yang, Y, Zhao, H, Heath, AC, Madden, PA, Martin, NG, Nyholt, DR, 2016. Shared Genetic Factors Underlie Migraine and Depression. *Twin Res Hum Genet* 19, 341–350.
- Peroutka, SJ, Price, SC, Wilhoit, TL, Jones, KW, 1998. Comorbid migraine with aura, anxiety, and depression is associated with dopamine D2 receptor (DRD2) NcoI alleles. *Mol Med* 4, 14–21.
- Yang, Y, Zhao, H, Heath, AC, Madden, PA, Martin, NG, Nyholt, DR, 2016. Familial Aggregation of Migraine and Depression: Insights From a Large Australian Twin Sample. *Twin Res Hum Genet* 19, 312–321.
- Chen, MH, Hsu, JW, Huang, KL, Su, TP, Li, CT, Lin, WC, Tsai, SJ, Cheng, CM, Chang, WH, Pan, TL, Chen, TJ, Bai, YM, 2019. Risk and coaggregation of major psychiatric disorders among first-degree relatives of patients with bipolar disorder: a nationwide population-based study. *Psychol Med* 49, 2397–2404.
- Cheng, CM, Chang, WH, Chen, MH, Tsai, CF, Su, TP, Li, CT, Tsai, SJ, Hsu, JW, Huang, KL, Lin, WC, Chen, TJ, Bai, YM, 2018. Co-aggregation of major psychiatric disorders in individuals with first-degree relatives with schizophrenia: a nationwide population-based study. *Mol Psychiatry* 23, 1756–1763.
- Chen, MH, Lan, WH, Hsu, JW, Huang, KL, Su, TP, Li, CT, Lin, WC, Tsai, CF, Tsai, SJ, Lee, YC, Chen, YS, Pan, TL, Chang, WH, Chen, TJ, Bai, YM, 2016. Risk of Developing Type 2 Diabetes in Adolescents and Young Adults With Autism Spectrum Disorder: A Nationwide Longitudinal Study. *Diabetes Care* 39, 788–793.
- Huang, MH, Cheng, CM, Tsai, SJ, Bai, YM, Li, CT, Lin, WC, Su, TP, Chen, TJ, Chen, MH, 2020. Familial coaggregation of major psychiatric disorders among first-degree relatives of patients with obsessive-compulsive disorder: a nationwide study. *Psychol Med* 1–8.
- Liu, CY, Hung, Y.T., Chuang, Y.L., Chen, Y.J., Weng, W.S., Liu, J.S., 2006. Incorporating development stratification of Taiwan townships into sampling design of large scale health interview survey. *J Health Management (Chin)* 4, 1–22.
- Charlson, ME, Pompei, P, Ales, KL, MacKenzie, CR, 1987. A new method of classifying prognostic comorbidity in longitudinal studies: development and validation. *J Chronic Dis* 40, 373–383.
- Scharin, M, Archer, T, Hellstrom, P, 2012. Affective spectrum disorders in an urban Swedish adult psychiatric unit: a descriptive study. *Depress Res Treat* 2012, 527827.
- Ghosh, J, Pradhan, S, Mittal, B, 2013. Identification of a novel ANKK1 and other dopaminergic (DRD2 and DBH) gene variants in migraine susceptibility. *Neuromolecular Med* 15, 61–73.
- Zhang, Q, Shao, A, Jiang, Z, Tsai, H, Liu, W, 2019. The exploration of mechanisms of comorbidity between migraine and depression. *J Cell Mol Med* 23, 4505–4513.
- Ligthart, L, Hottenga, JJ, Lewis, CM, Farmer, AE, Craig, IW, Breen, G, Willemsen, G, Vink, JM, Middeldorp, CM, Byrne, EM, Heath, AC, Madden, PA, Pergadia, ML, Montgomery, GW, Martin, NG, Penninx, BW, McGuffin, P, Boomsma, DI, Nyholt, DR, 2014. Genetic risk score analysis indicates migraine with and without comorbid depression are genetically different disorders. *Hum Genet* 133, 173–186.
- Baksa, D, Gonda, X, Juhasz, G, 2017. Why are migraineurs more depressed? A review of the factors contributing to the comorbidity of migraine and depression. *Neuropsychopharmacol Hung* 19, 37–44.
- Deligianni, CI, Vekelis, M, Mitsikostas, DD, 2012. Depression in headaches: chronification. *Curr Opin Neurol* 25, 277–283.
- Yang, Y, Ligthart, L, Terwindt, GM, Boomsma, DI, Rodriguez-Acevedo, AJ, Nyholt, DR, 2016. Genetic epidemiology of migraine and depression. *Cephalalgia* 36, 679–691.
- Karatas, H, Yemisci, M, Eren-Kocak, E, Dalkara, T, 2018. Brain Peptides for the Treatment of Neuropsychiatric Disorders. *Curr Pharm Des* 24, 3905–3917.
- Amin, FM, Aristidou, S, Baraldi, C, Czapinska-Ciepiela, EK, Ariadni, DD, Di Lenola, D, Fenech, C, Kampouris, K, Karagiorgis, G, Braschinsky, M, Linde, M, 2018. European Headache Federation School of Advanced S. The association between migraine and physical exercise. *J Headache Pain* 19, 83.
- Pitts, BL, Wen, V, Whealin, JM, Fogle, BM, Southwick, SM, Esterlis, I, Pietrzak, RH, 2020. Depression and Cognitive Dysfunction in Older U.S. Military Veterans: Moderating Effects of BDNF Val66Met Polymorphism and Physical Exercise. *Am J Geriatr Psychiatry* 28, 959–967.
- Manchishi, SM, Cui, RJ, Zou, XH, Cheng, ZQ, Li, BJ, 2018. Effect of caloric restriction on depression. *J Cell Mol Med* 22, 2528–2535.
- Araya, AV, Orellana, X, Espinoza, J, 2008. Evaluation of the effect of caloric restriction on serum BDNF in overweight and obese subjects: preliminary evidences. *Endocrine* 33, 300–304.
- Di Lorenzo, C, Pinto, A, Ienca, R, Coppola, G, Sirianni, G, Di Lorenzo, G, Parisi, V, Serrao, M, Spagnoli, A, Vestri, A, Schoenen, J, Donini, LM, Pierelli, F, 2019. A Randomized Double-Blind, Cross-Over Trial of very Low-Calorie Diet in Overweight Migraine Patients: A Possible Role for Ketones? *Nutrients* 11.

## Article

# Co-Delivery of CPT-11 and Panobinostat with Anti-GD2 Antibody Conjugated Immunoliposomes for Targeted Combination Chemotherapy

Gils Jose <sup>1,†</sup>, Yu-Jen Lu <sup>2,†</sup>, Jung-Tung Hung <sup>3</sup>, Alice L. Yu <sup>3</sup> and Jyh-Ping Chen <sup>1,4,5,6,\*</sup> 

<sup>1</sup> Department of Chemical and Materials Engineering, Chang Gung University, Kwei-San, Taoyuan 33302, Taiwan; D0523015@stmail.cgu.edu.tw

<sup>2</sup> Department of Neurosurgery, Chang Gung Memorial Hospital, Linkou, Kwei-San, Taoyuan 33305, Taiwan; luyj@cgmh.org.tw

<sup>3</sup> Institute of Stem Cell & Translational Cancer Research, Chang Gung Memorial Hospital, Linkou, Kwei-San, Taoyuan 33305, Taiwan; flixht@cgmh.org.com (J.-T.H.); aiylu@health.ucsd.edu (A.L.Y.)

<sup>4</sup> Department of Plastic and Reconstructive Surgery and Craniofacial Research Center, Chang Gung Memorial Hospital, Linkou, Kwei-San, Taoyuan 33305, Taiwan

<sup>5</sup> Research Center for Food and Cosmetic Safety, Research Center for Chinese Herbal Medicine, College of Human Ecology, Chang Gung University of Science and Technology, Taoyuan 33305, Taiwan

<sup>6</sup> Department of Materials Engineering, Ming Chi University of Technology, Tai-Shan, New Taipei City 24301, Taiwan

\* Correspondence: jpchen@mail.cgu.edu.tw; Tel.: +886-3-211-8800

† These authors contributed equally to this paper.

Received: 30 September 2020; Accepted: 29 October 2020; Published: 31 October 2020



**Simple Summary:** In targeted cancer therapies, liposomes conjugated with antibody (Ab) can selectively deliver drugs to antigen-expressing cancer cells through active targeting and improve anti-cancer efficacy. Many glioblastoma cell lines and primary biopsies express high levels of disialoganglioside GD2 antigen, making it an excellent candidate for targeted cancer therapy. In this study, we prepared anti-GD2 Ab conjugated immunoliposomes (ImmuLipCP) for co-delivery of CPT-11 and panobinostat, which is intended for combination targeted chemotherapy. To compare the GD2 targeting mechanism, we used glioma cells with low GD2 expression (U87MG) and its drug-resistant variant with high GD2 expression (U87 DR). We demonstrate that ImmuLipCP show enhanced cytotoxicity against U87DR through Ab-mediated intracellular trafficking and drug delivery, for synergistic cancer cell killing effects. Using a xenograft tumor model by subcutaneous implantation of U87DR in nude mice, we also validate the targeting and anti-cancer efficacy of ImmuLipCP in vivo.

**Abstract:** The consistent expression of disialoganglioside GD2 in neuroblastoma tumor cells and its restricted expression in normal tissues open the possibility to use it for molecularly targeted neuroblastoma therapy. On the other hand, immunoliposomes combining antibody-mediated tumor recognition with liposomal delivery of chemotherapeutics have been proved to enhance therapeutic efficacy in brain tumors. Therefore, we develop immunoliposomes (ImmuLipCP) conjugated with anti-GD2 antibody, for targeted co-delivery of CPT-11 and panobinostat in this study. U87MG human glioma cell line and its drug resistant variant (U87DR), which were confirmed to be associated with low and high expression of cell surface GD2, were employed to compare the targeting efficacy. From in vitro cytotoxicity assay, CPT-11 showed synergism drug interaction with panobinostat to support co-delivery of both drugs with ImmuLipCP for targeted synergistic combination chemotherapy. The molecular targeting mechanism was elucidated from intracellular uptake efficacy by confocal microscopy and flow cytometry analysis, where 6-fold increase in liposome and 1.8-fold increase in drug uptake efficiency was found using targeted liposomes. This enhanced intracellular trafficking for drug delivery endows ImmuLipCP with pronounced cytotoxicity toward U87DR cells in vitro, with 1.6-fold increase of apoptosis rate. Using xenograft nude mice model with

subcutaneously implanted U87DR cells, we observe similar biodistribution profile but 5.1 times higher accumulation rate of ImmuLip from in vivo imaging system (IVIS) observation of Cy5.5-labelled liposomes. Taking advantage of this highly efficient GD-2 targeting, ImmuLipCP was demonstrated to be an effective cancer treatment modality to significantly enhance the anti-cancer therapeutic efficacy in U87DR tumors, shown from the significant reduced tumor size in and prolonged survival time of experiment animals as well as diminished expression of cell proliferation and enhanced expression of apoptosis marker proteins in tumor section.

**Keywords:** liposome; targeted delivery; antibody; cancer therapy; drug delivery system; CPT-11; panobinostat; nanomedicine

## 1. Introduction

Malignant gliomas, the most common and aggressive subtype of primary brain tumor, are receiving considerable attention from physicians and researchers mainly because of their incurable nature [1]. Although various therapeutic inventions are increasingly emerging, the recurrence of malignant cells within a few months has enabled the definition of such tumor as the most difficult neoplasms to treat [2]. The highly proliferative and infiltrative nature of brain glioma cells and its resistive nature towards many chemotherapeutic agents further enhances the complexity of glioma treatment [3]. Even though various chemotherapy drugs are available for clinical applications, the poor capability of these drugs to penetrate the blood brain barrier and to attain desired doses of systemic chemotherapeutics demands the development of novel drug delivery system for effective glioma therapy [4].

Nano-sized drug carriers made of various materials, such as polymers, metal particles, lipids and so forth, have entered into the pharmaceutical market with the aim of enhancing the therapeutic properties of various drugs [5,6]. Due to the characteristic features of nanocarriers to store the drugs within themselves and to release the desirable amount of drug in the right place, nanoparticle-based drug delivery system (DDS) shows higher potentials in overcoming drawbacks of current chemotherapy drugs, including unwanted side effects due to non-specificity and low availability [7,8]. Owing to the unique characteristics such as biodegradability, biocompatibility and amphiphilic nature, liposomes have shown enormous potential as a drug carrier for cancer therapy [9]. Liposomes are unilamellar or multilamellar vesicles with interior aqueous space, composed of self-assembled lipid molecules and can carry both hydrophobic and hydrophilic drugs [10,11]. As liposomes can act as a long circulating nanocarriers, drug-loaded liposomes can lead to site-specific accumulation of drugs [12]. Moreover, liposomes may provide a consistent level exposure of the targeted tissue to the drug, due to its sustained release characteristics [11]. So far various formulations of liposomes, containing both hydrophilic and hydrophobic chemotherapeutics, are available for research and clinical studies [13]. Among these, CPT-11 (irinotecan)-loaded liposomes has received tremendous attention for the treatment of various cancers through the inhibition of the DNA eukaryotic enzyme topoisomerase I [14].

The CPT-11, 7-ethyl-10-[4-(1-piperidino)-1-piperidino]-carbonyloxy-camptothecin, has long been known for its auspicious role in the treatment of various cancers [15]. As a topoisomerase I inhibitor, CPT-11 is capable to inhibit DNA replication and thereby exerts cytotoxicity towards cancer cells [16,17]. When irinotecan comes in contact with glioma cells, it undergoes carboxylesterase mediated breakdown and produces the metabolite called SN-38, which is known to be 100–1000 times more potent as an inhibitor of topoisomerase [18,19]. Although CPT-11 is capable of crossing the blood brain barrier, studies have shown that the response rate attained from CPT-11 single drug chemotherapy was in between 0 and 44% with a survival rate of 2 to 11 months [20]. Therefore, combination therapy using CPT-11 with some other drugs was introduced and shown to offer a better option for enhancing the chemotherapeutic efficacy [21]. Panobinostat (Farydak®) is a Food and Drug Administration (FDA) approved histone deacetylase inhibitor for multiple myeloma treatment [22]. As a potent inhibitor

of histone deacetylase, panobinostat prevents the deacetylation of histone and nonhistone proteins and results in cellular differentiation, cell-cycle progression and regulation of gene transcription and apoptosis [23]. Chemically, this deacetylase (DAC) inhibitor is capable to induce apoptosis in multiple myeloma cells even at low concentrations. Compared to other DAC inhibitors, panobinostat leads to elongated hyperacetylation of the histone protein and prominent alterations of gene expressions in tumor cells in contrast to healthy cells [24].

The anticancer properties of the commercially available drugs were well explored in combination with nanotechnology [25]. Due to the introduction of nanoparticle-based drug delivery system (DDS), we were able to overcome the drawbacks of most of the chemotherapeutics including non-specific targeting and related drug toxicity, which is being considered as the main obstacle of conventional chemotherapy [26]. Although nanocarrier-based DDS offers many advantages over conventional chemotherapy, poor accessibility of antineoplastic agents to the tumor results in lower drug dosage and the resultant transient responses [27]. Hence, targeting tumors by means of active targeting, by conjugating the nanocarriers with a ligand that can specifically bind to the receptor expressed on tumor cell surface, could be envisioned as a viable means to enhance the cancer treatment efficiency [28]. Toward this end, a number of targeting ligands were investigated for the development of targeted liposomes in drug delivery, including peptides, carbohydrates and antibodies [29]. Among them, antibody-conjugated liposomes (immunoliposomes), that can target antigen-expressing cancer cells, have attracted considerable attention for targeted cancer therapies as they can selectively deliver drugs to tumor cells with improved anti-cancer efficacy and reduced toxicity [30].

The GD2 is a disialoganglioside that is consistently expressed on tumors of neuroectodermal origin such as human neuroblastoma. Besides neuroblastoma, several neuroectoderm-derived neoplasms, including glioblastoma and sarcomas express high levels of the tumor-associated antigen GD2 [31]. Similar to several pediatric and adult solid tumors, a variety of glioblastoma cell lines and primary biopsies commonly express high levels of GD2 antigen [32]. Due to its high density on tumor cells as well as its restricted expression on normal tissue, GD2 is an excellent candidate for targeted cancer therapy [33,34]. As a matter of fact, the National Cancer Institute has ranked GD2 as the 12th most important cancer antigen from its pilot program for prioritization of cancer antigens [35]. Specifically, immunoliposomes conjugated with whole or fragment of anti-GD2 antibody (Ab) have been explored for targeted delivery of doxorubicin [34,36], antisense oligodeoxynucleotides [37], fenretinide [38] and survivin inhibitor [39] to tumor cells.

In this study, we prepared anti-GD2 Ab conjugated immunoliposomes (ImmuLipCP) for co-delivery of CPT-11 and panobinostat (Figure 1). We hypothesized that ImmuLipCP will show enhanced cytotoxicity against tumor cells overexpressing GD2, through anti GD2 Ab-mediated intracellular trafficking and drug delivery, for synergistic cancer cell killing effects (Figure 1). This hypothesis will be tested by comparing the targeting efficiency of liposomes without anti-GD2 Ab (Lip) or liposomes modified with low (ImmuLip-L) or high (ImmuLip) density of anti-GD2 Ab. To elucidate the GD2 targeting mechanism, we explored the use of glioma cells with low GD2 (U87MG) and high GD2 expression (U87 DR, a drug-resistant cell line derived from U87MG) in this study. Finally, we conduct a proof-of-concept study using a xenograft tumor model by subcutaneous implantation of U87DR in nude mice to validate the targeting and anti-cancer efficacy of ImmuLipCP.

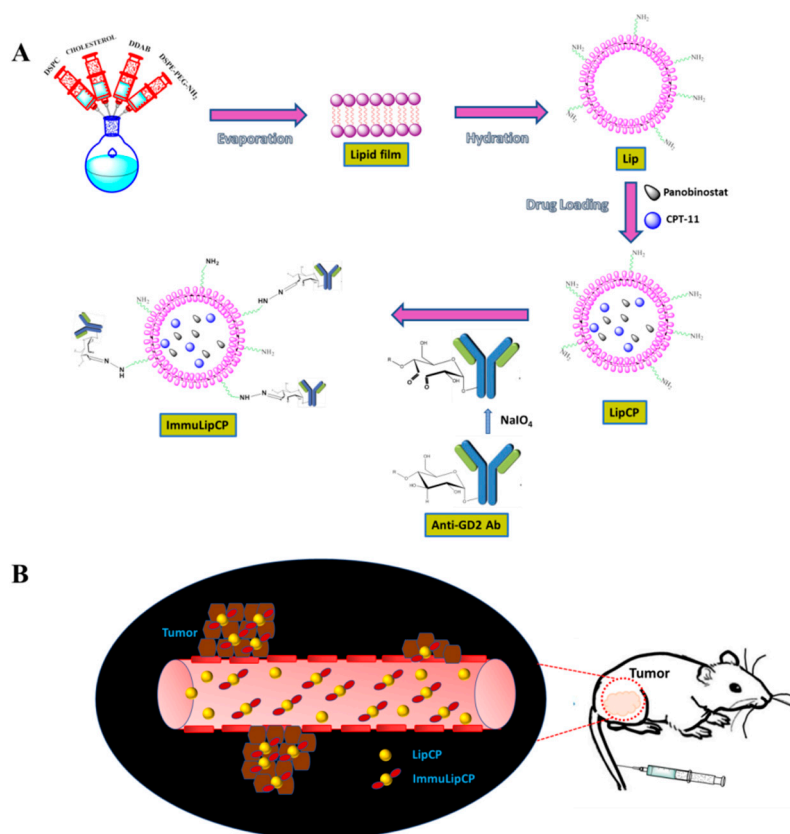


**Figure 1.** (A) The liposomes (Lip) were formed from 1,2-distearoyl-sn-glycero-3-phosphocholine (DSPC), dimethyldioctadecylammonium bromide (DDAB), cholesterol and N-(aminopropyl polyethyleneglycol)carbonyl-distearoylphosphatidyl-ethanolamine (DSPE-PEG-NH<sub>2</sub>) using the thin film hydration method. The drugs were loaded into liposomes by repeated freeze-thaw cycles to prepare CPT-11 and panobinostat-loaded liposomes (LipCP). The LipCP was surface conjugated with anti-GD2 Ab by forming covalent bonds between surface amine groups in liposomes and aldehyde groups in activated anti-GD2 Ab that is formed after NaIO<sub>4</sub>-catalyzed ring opening of the sugar moiety in the Ab. (B) The ImmuLipCP could show enhanced cytotoxicity toward tumor cells overexpressing GD2 over LipCP.

## 2. Results and Discussion

### 2.1. Physico-Chemical Characterization of Liposomes

We prepare blank liposomes in this study by the thin-film hydration method, followed by drug loading through repeated freeze-thaw cycles (Figure 1A). After conjugation of anti-GD2 Ab to liposomes through spontaneous covalent bonds formed between aldehyde groups in activated Ab and amine groups on liposome surface, we obtain the drug-loaded immunoliposome (ImmuLipCP) (Figure 1A). Using 4 mg anti-GD2 Ab for conjugation with 5 mg Lip, 65% Ab conjugation efficiency was found for the Ab, which translates to 0.52 mg GD2/mg liposome. The average particle size from dynamic light scattering (DLS) as well as zeta potential were determined for various liposomal formulation. As shown in Table 1, the particle size of all prepared liposomes was below 200 nm, with significant increase of hydrodynamic diameter originated from Ab conjugation to liposome surface with the high molecular weight of immunoglobulins. Nonetheless, loading of drugs within the aqueous core of liposome did not lead to significant change of particle size as expected. The polydispersity index (PDI) is below 0.30 for all preparations, indicating a homogenous distribution of the lipid vesicles as well as a stable suspension of liposomes [40]. The average zeta potentials are 13.3 and 14.7 mV and show no significant difference between Lip and LipCP from electrophoretic mobility measurements due to



the presence of cationic lipid dimethyldioctadecylammonium bromide (DDAB) in the lipid bilayer (Table 1). The zeta potential also shows no significant difference between blank and drug-loaded immunoliposomes (ImmuLip vs ImmuLipCP). Nonetheless, the zeta potential decreased (9.6 and 8.3 mV) after conjugation with ligand, arising from the slightly net negative charge associated with anti-GD2 Ab (isoelectric point = 7.3) and the consumption of the amine groups on liposome surface during the conjugation step.

**Table 1.** Size and zeta potentials values ( $n = 3$ , mean  $\pm$  SD).

Samples <sup>1</sup>	Size From DLS (nm) <sup>2</sup>	PDI <sup>3</sup>	Zeta Potential (mV)
Lip	130.9 $\pm$ 5.2	0.188 $\pm$ 0.03	14.7 $\pm$ 1.1
LipCP	147.5 $\pm$ 3.0	0.196 $\pm$ 0.02	13.3 $\pm$ 0.6
ImmuLip	168.4 $\pm$ 9.8 *	0.275 $\pm$ 0.02	9.6 $\pm$ 0.7
ImmuLipCP	160.3 $\pm$ 7.1 #	0.081 $\pm$ 0.04	8.3 $\pm$ 1.0

<sup>1</sup> Lip: liposomes, LipCP: liposomes loaded with CPT-11 and panobinostat, ImmuLip: immunoliposomes, ImmuLipCP: immunoliposomes loaded with CPT-11 and panobinostat. <sup>2</sup> The average particle diameter measured from dynamic light scattering (DLS). <sup>3</sup> PDI: polydispersity index. \*  $p < 0.05$  compared with Lip, #  $p < 0.05$  compared with LipCP.

To determine the in vivo-relevant colloidal stability of drug-loaded immunoliposomes, the particle size of ImmuLipCP was determined in 10% fetal bovine serum (FBS) diluted in 90% phosphate buffered saline (PBS) at different time points using nanoparticle tracking analysis (NTA). As shown in Figure 2A, the peak particle size of liposome apparently increased with incubation time. However, decrease of peak particle concentration was noted with simultaneous appearance of some smaller diameter liposome population, possibly due to destruction of liposomes. Nonetheless, no liposome with size above 300 nm was detected even after 12 h incubation. The stability of liposomes depends on many factors and particle aggregation may lead to increase in size and decrease of counts from NTA analysis [41]. Overall, the stability of ImmuLipCP determined from NTA endorses their capability for targeted drug delivery and intracellular uptake by cancer cells. We further determined the morphology of liposomes by observation with a cryo-transmission electron microscope (cryo-TEM). As shown in Figure 2B, the morphology of liposomes (Lip) and immunoliposomes (ImmuLip) were spherical in shape with an aqueous core enclosed by lipid bilayer. The particle size in the range of 50 to 200 nm, which is consistent with the hydrodynamic particle diameter measured from DLS analysis. Most liposomes are unilamellar vesicles as shown from the cryo-TEM image with minimum multilamellar vesicles after the extrusion process [42]. With higher internal aqueous volume, the unilamellar liposomes may be more efficient in encapsulating hydrophilic drugs such CPT-11 and panobinostat than multilamellar liposomes.

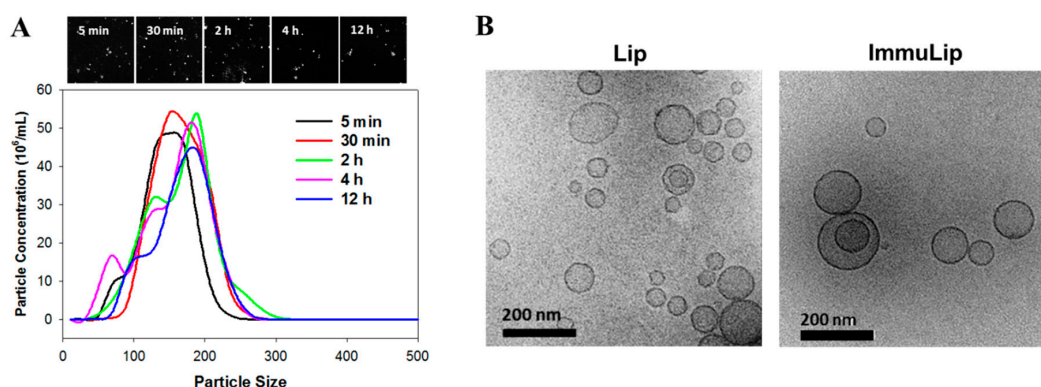


**Figure 2.** (A) The stability of CPT-11 and panobinostat-loaded immunoliposomes (ImmuLipCP) in 10% fetal bovine serum (FBS)/90% phosphate buffered saline (PBS) solution as determined by nanoparticle tracking analysis (NTA) with the screenshot images showing the light scattering particles. (B) The morphology of liposomes (Lip) and immunoliposomes (ImmuLip) from cryo-transmission electron microscopy (cryo-TEM) analysis (Bar = 200 nm).

## 2.2. Drug Loading and Release

The encapsulation efficiency (EE) of drugs into immunoliposomes was studied based on pilot experiments conducted to optimize the ratio between CPT-11 and panobinostat. Using 2 mg/mL CPT-11 and 0.5 mg/mL panobinostat for drug loading, we achieved the optimum EE of both drugs, which is  $57.8 \pm 7.2\%$  (CPT-11) and  $63.7 \pm 12.3\%$  (panobinostat) (Figure 3A). These values could be compared with the EE when each drug was encapsulated separately in the liposomes, which are  $61.5 \pm 5.8\%$  and  $66.8 \pm 11.4\%$  for CPT-11 and panobinostat, respectively. As no significant difference was found between the EE when a drug was loaded either alone or in the presence of the other drug, we conclude that minimum interference between drugs exists during drug loading, which might hamper the EE during co-encapsulation of both drugs. This underlines the feasibility to co-encapsulate both drugs within the aqueous core of ImmuLipCP for co-delivery of CPT-11 and panobinostat. The final preparation of ImmuLipCP with 0.06 mg CPT-11/mg liposome and 0.26 mg panobinostat/mg liposome were used for following studies. We postulate that ImmuLipCP could show synergistic cancer cell killing effects by co-delivery of CPT-11 and panobinostat at this drug concentration.

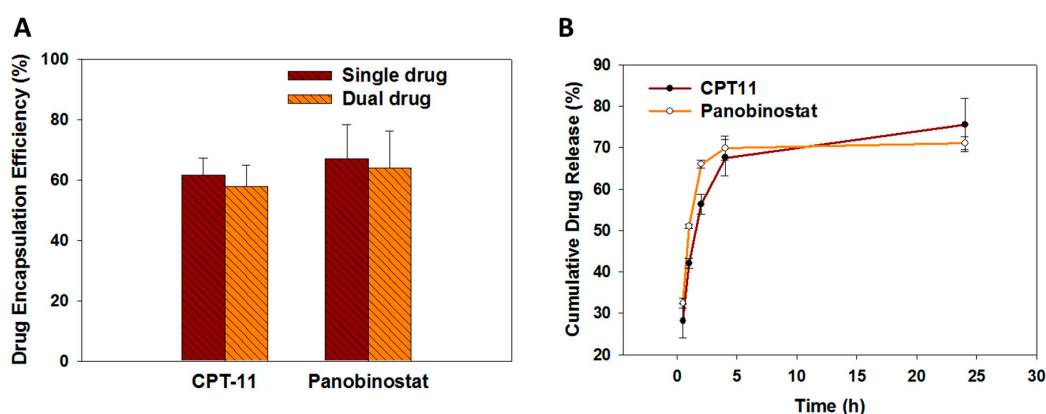


**Figure 3.** (A) The drug encapsulation efficiency of CPT-11 (single drug), panobinostat (single drug) or CPT-11 + panobinostat (dual drug) in immunoliposomes ( $n = 5$ ). (B) The drug release profiles from CPT-11 and panobinostat-loaded immunoliposomes (ImmuLipCP) at 37 °C in PBS (pH 7.4) ( $n = 5$ ).

The release profiles of CPT-11 and panobinostat from ImmuLipCP were evaluated in phosphate buffered saline (pH 7.4) at 37 °C. As shown in Figure 3B, both drugs exhibit a biphasic drug release profile that was consistent with drug release from liposomes [43]. A burst release of each drug from liposomes was observed up to 5 h with faster release rate of panobinostat than CPT-11. The release percentages of both drugs reached 70–75% after 24 h with no significant difference found between them.

## 2.3. In Vitro Experiments

### 2.3.1. Glioma Cell Lines with Different GD2 Expression and Intracellular Uptake of Immunoliposomes

In order to study the effect of GD2 expression level on targeting efficacy of ImmuLip, we first develop palbociclib-resistant glioma cells (U87DR) with higher GD2 expression than U87MG in this study. Using a gradient of palbociclib concentration from 0.2  $\mu\text{M}$  to 1  $\mu\text{M}$ , we observed morphological change of U87MG to its variant U87DR within 3 months (Supplementary Figure S1). The exact nature of GD2 expression was determined from flow cytometry analysis, which gave 16.1% and 43.9% GD2-positive cells and 136 and 542 mean fluorescence intensity for U87MG and U87DR cell lines, respectively. We thus achieve the goal of obtaining a high GD2 expressing glioma cell line by using a drug-resistant variant of U87MG after screening with palbociclib. The four times higher expression of GD2 in U87DR glioma cells justify its use for following in vitro and in vivo studies to elucidate the effect of anti GD2 Ab-mediated targeted drug delivery by ImmuLipCP.

Intracellular uptake of liposomes fluorescently labelled with 5(6)-carboxyfluorescein N-hydroxysuccinimide ester (fluorescein NHS) was first evaluated qualitatively by incubating U87DR cells separately with Lip or ImmuLip for 24 h (Figure 4). The uptake efficiency of green fluorescence-producing liposomes was examined using a confocal laser scanning microscope after staining the cell cytoskeleton with red fluorescence-producing phalloidin-tetramethylrhodamine B isothiocyanate and the nucleus with blue fluorescence-producing Hoechst 33342. To elucidate the effect of ligand density on cellular trafficking, a different immunoliposome (ImmuLip-L) was prepared by following the same procedure as ImmuLip but by reacting 1 mg anti-GD2 Ab (1/4 of ImmuLip) with 5 mg Lip. The ImmuLip was prepared with 61% Ab conjugation efficiency and 0.12 mg GD2/mg liposome. As shown in Figure 4, the fluorescence intensity obtained for ImmuLip was significantly stronger in comparison to both Lip and ImmuLip-L. It is clear from the confocal image that, the internalization efficiency of liposomes by U87DR, as revealed from the green fluorescence signal area associated with liposome, is in the order of  $\text{ImmuLip} \gg \text{ImmuLip-L} > \text{Lip}$ . As the difference in intracellular uptake is correlated with the presence and density of ligand, we ascribe this effect to be originated from anti-GD2 Ab conjugated to the liposome surface. Taken together, our study underlines the importance of ligand density on antigen-Ab mediated intracellular trafficking and endorse the preference of using ImmuLip for targeted drug delivery.

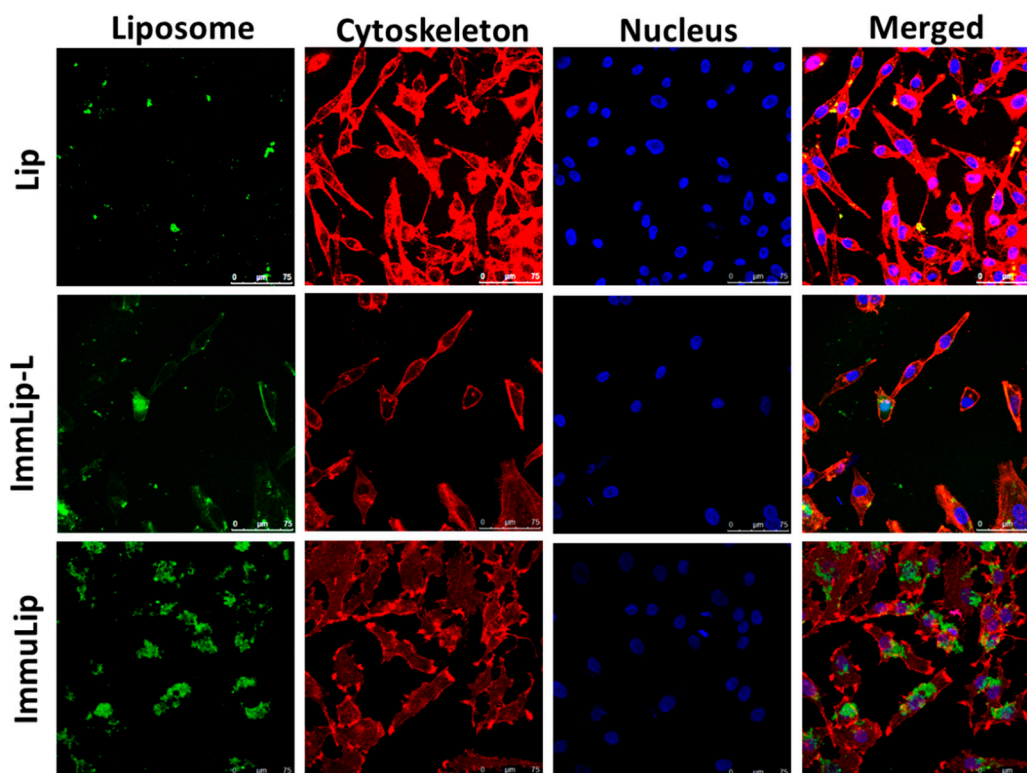


**Figure 4.** The intracellular uptake of liposomes (Lip), immunoliposomes (ImmuLip) and immunoliposomes prepared with 1/4 of anti-GD2 Ab used for ImmuLip (ImmuLip-L) by U87DR cells in 24 h from confocal laser scanning microscopy analysis (bar = 75  $\mu\text{m}$ ). Liposomes were labelled with 5(6)-carboxyfluorescein N-hydroxysuccinimide ester (green), cytoskeleton labelled with phalloidin-tetramethylrhodamine B isothiocyanate (red) and nuclei counterstained with Hoechst (blue).

The intracellular uptake efficiency of different liposomes into U87DR was further subject to quantitatively analysis using flow cytometry, which can determine the intracellular fluorescence signal intensity associated with fluorescein-labelled liposomes. As shown from Figure 5A, the geometric mean fluorescence intensities after 24 h incubation with U87DR from fluorescence-activated cell sorting (FACS) analysis are 5945, 8743 and 35,918 for Lip, ImmuLip-L and ImmuLip, respectively. In line with

the trends observed from confocal microscopy analysis (Figure 4), ImmuLip is shown with 6 times higher targeting efficacy than Lip through the action of abundant anti-GD2 Ab on liposome surface for mediating cellular trafficking.

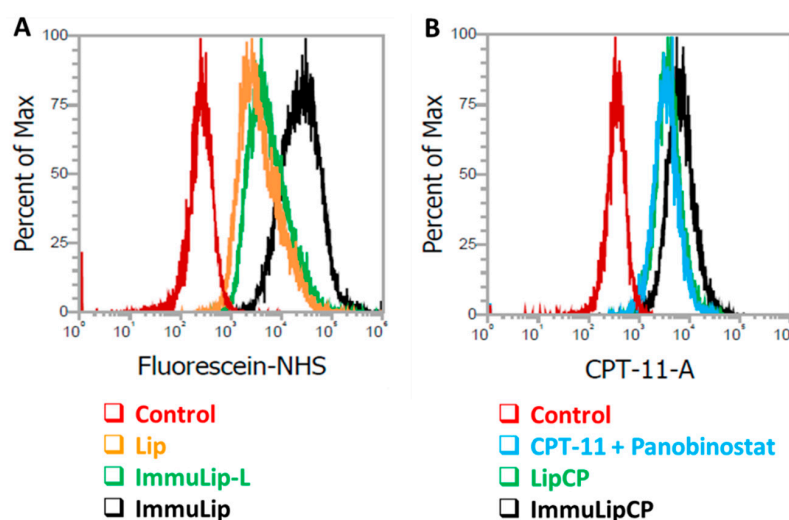


**Figure 5.** (A) The intracellular liposome uptake efficiency from flow cytometry analysis after incubating U87DR cells with fluorescein-labelled Lip, ImmuLip-L and ImmuLip for 24 h. (B) The intracellular drug uptake efficiency of from flow cytometry analysis of CPT-11 blue fluorescence after incubating U87DR cells with free drugs (CPT-11 + panobinostat), LipCP and ImmuLipCP for 24 h.

As cytotoxicity toward cancer cells is related to the intracellular drug concentration, the effectiveness of ImmuLipCP as a DDS was further examined from flow cytometry analysis. This was accomplished by taking advantage of the blue fluorescence signal associated with CPT-11 when U87DR cells were treated with free drugs, LipCP or ImmuLipCP for 24 h (Figure 5B). As in particle uptake, concomitant increase of intracellular CPT-11 fluorescence intensity was found for ImmuLipCP vs. LipCP, with the geometric mean intensities being 7294 and 4255, respectively. That similar drug uptake efficiency with merged peaks in Figure 5B found between free drugs (CPT-11 + panobinostat) (geometric mean intensity = 4064) and LipCP indicates drug delivery with non-targeted liposomal formulation could not improve the passive delivery of drugs into cancer cells. This further underlines the importance of targeted drug delivery by using anti-GD2 Ab as a ligand to enhance the cytotoxicity toward GD2 overexpressing U87DR. It should be noted the 1.8-fold increase in the drug uptake efficacy using ImmuLip over Lip is lower than the 6-fold increase shown in particle uptake efficacy. The difference between particle and drug uptake efficiency may be due to premature drug release before intracellular uptake of liposomes. Nonetheless, ImmuLip could be deemed as an efficient DDS for targeted drug delivery to enhance cytotoxicity toward GD2-overexpressing U87DR cell line.

### 2.3.2. In Vitro Cytotoxicity of Free Drugs

To support co-delivery of CPT-11 and panobinostat using liposomes, we determine the synergism of the drug combination toward U87DR cells with different concentrations of CPT-11 and/or panobinostat. The cytotoxicity was determined from relative cell viability using (3-(4,5-dimethylthiazol-2-yl)-5-(3-carboxymethoxyphenyl)-2-(4-sulfophenyl)-2H-tetrazolium) (MTS) assays, which is a calorimetric method for the sensitive quantification of viable cells when NAD(P)H-dependent dehydrogenase enzymes present in viable cells converting the MTS tetrazolium compound to a soluble and colored formazan product [44]. As shown in Figure 6A, the cytotoxicity of CPT-11 increases as the concentration of the drug increases from 1  $\mu$ M to 40  $\mu$ M. In comparison to 24 h incubation, the cytotoxicity shows an increasing trend when cells were incubated with the drug for longer durations at 48 h and 72 h. The IC<sub>50</sub> values were in the order of 40  $\mu$ M, 20  $\mu$ M and 5  $\mu$ M for 24 h, 48 h and 72 h respectively.

Similarly, panobinostat also shows an increase in cytotoxicity when its concentration increases from 10 nM to 80 nM (Figure 6A). Although the cytotoxicity of panobinostat was not predominant after 24 h incubation within the tested concentrations, a rapid decrease of cell viability was noted at longer incubation duration (48 h and 72 h).

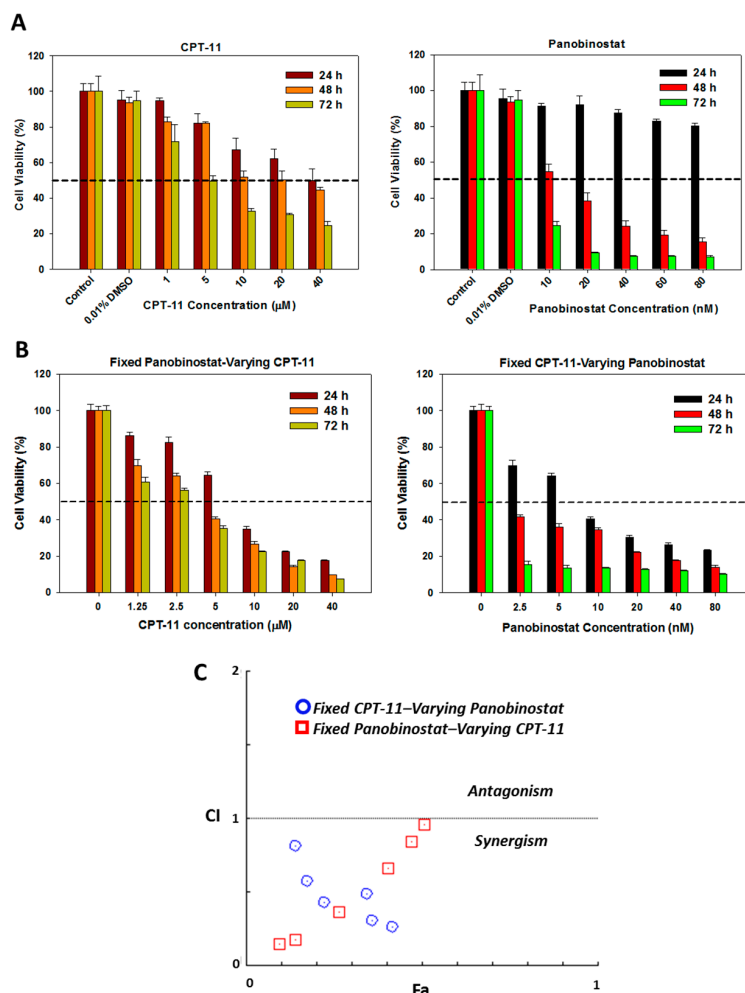


**Figure 6.** The cytotoxicity of single drug (CPT-11 or panobinostat) (A) and dual drug (CPT-11 and panobinostat) (B) toward U87DR at different time points ( $n = 5$ ). (C) The synergistic effect of drug combination was analyzed by CompuSyn software with results taken from (B), from which the combination index (CI) value could be used to categorize the drug interaction into synergism ( $\text{CI} < 1$ ), additive ( $\text{CI} = 1$ ) and antagonism ( $\text{CI} > 1$ ).

Combination of panobinostat and CPT-11 at different ratios leads to further decrease in cell viability (Figure 6B). As expected, the relative cell viability using dual drug by either fixing panobinostat concentration (20 nM panobinostat) or fixing CPT-11 concentration (2  $\mu\text{M}$ ) shows drastic decline when compared to those obtained by using single drug. Most importantly, the dual drug cytotoxicity data offer the possibility to determine the synergistic effect of drug combination, as analyzed from the CompuSyn software with the non-constant ratio combination method (Figure 6C). This software was used to calculate the combination index (CI) value from results in Figure 6B, based on which the drug interaction could be categorized into synergism ( $\text{CI} < 1$ ), additive ( $\text{CI} = 1$ ) or antagonism ( $\text{CI} > 1$ ) effect [45]. As shown in Figure 6C, the CI values obtained for all combinations of panobinostat and CPT-11 are between zero and one, thereby confirming the combination of these two drugs will lead to drug synergism for synergistic cancer cell killing effect toward U87DR. It also supports the rational to use ImmuLipCP for co-delivery of CPT-11 and panobinostat in synergistic cancer chemotherapy.



### 2.3.3. Biocompatibility of Liposomes and Apoptosis Induced by Drug-Loaded Liposomes

To study the apoptosis induced by drug-loaded liposomes, we first confirm the biocompatibility of ImmuLip by determining the relative cell viability using MTS assays when U87DR were treated with different concentrations of liposome for 24 h. As shown in Figure 7A, there is no significant difference in cell viability up to 40  $\mu\text{g/mL}$  liposome concentration, highlighting the excellent biocompatibility of ImmuLip. It is important that the concentration of ImmuLipCP for following in vivo study was below the cytotoxicity window shown in Figure 7A. As both CPT-11 and panobinostat were reported to exhibit a cancer cell killing effect by causing cell apoptosis [46,47], we test the cytotoxicity of drugs delivered through liposomes using flow cytometry for cell apoptosis assays. The U87DR cells treated with LipCP or ImmuLipCP were labelled with Annexin V/PI and represented separately in Q1, Q2, Q3 and Q4 quadrants as necrotic, late apoptotic, viable and early apoptotic cells (Figure 7B). The cell death mechanism is confirmed to be mainly due to late apoptosis, with the total apoptosis rate from targeted (ImmuLipCP) or non-targeted (LipCP) liposomes being at 45.5% and 29.2%, respectively. Undoubtedly, the mechanism responsible for the observed elevated apoptosis rate is associated with the pronounced increase of intracellular uptake of ImmuLip and the improved intracellular accumulation of drugs (Figure 5). Overall, the enhanced cancer cell killing effect originated from Ab-mediated targeted co-delivery of CPT-11 and panobinostat to GD-2 overexpressed cancer cells suggests the use of ImmuLipCP for in vivo anti-cancer therapy.

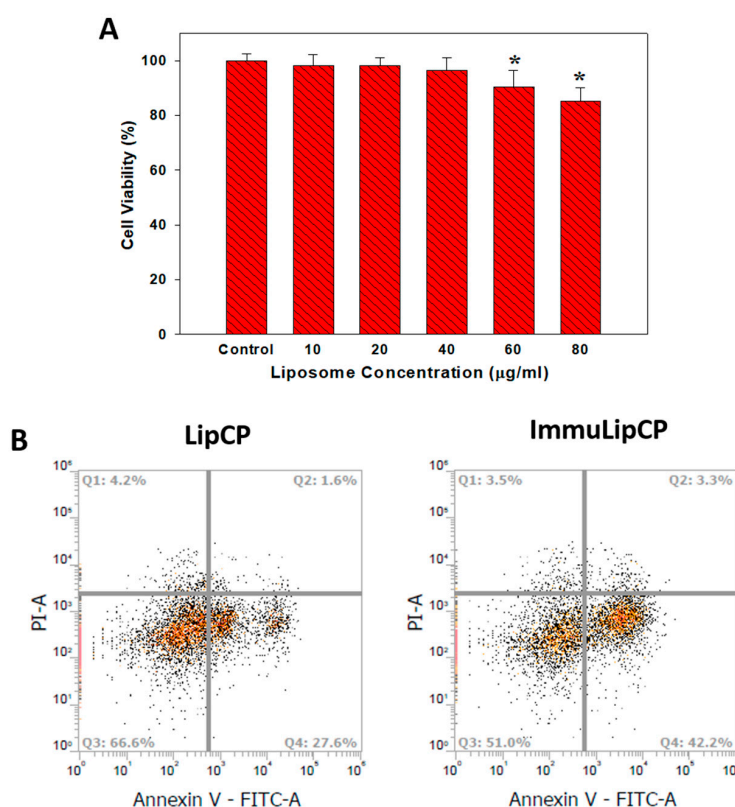


**Figure 7.** (A) Biocompatibility of ImmuLip by determining the relative cell viability using MTS assays when U87DR cells were treated with different concentrations of liposome for 24 h ( $n = 5$ ). \*  $p < 0.05$  compared with control. (B) The flow cytometry analysis for cell apoptosis after 24 h incubation of U87DR with drug-loaded non-targeted liposomes (LipCP) and targeted liposomes (ImmuLipCP) at 37 °C. The cells were stained with Annexin V/PI and apoptotic and necrotic cells were visualized (Q1: necrotic; Q2: late apoptotic; Q3: live; Q4: early apoptotic). The concentration of panobinostat and CPT-11 were fixed as 5 nM and 2  $\mu\text{M}$  for each experiment group.

### 2.3.4. In Vitro Hemocompatibility

With the growing number of studies reporting the hemocompatibility of liposomal formulation for drug delivery, it is important to evaluate the impact of systematic administration of immunoliposomes on blood components before animal experiments [48]. This was assessed by determining whether ImmuLip will cause any damage to red blood cells (RBCs) from in vitro haemocompatibility assays. After incubating diluted RBCs with ImmuLip prepared in PBS for 2 h at 37 °C, we collected the supernatant to evaluate its absorption spectra. In addition to liposomes, diluted RBCs were incubated with PBS and water, which were used as the negative and positive controls, respectively. From Figure 8A, it is clear that the absorption spectra of all liposome samples were similar to that in PBS, which confirms that ImmuLip will not cause any damage to RBCs. In contrast, the absorption spectra of the supernatant collected after incubating RBCs with water shows strong absorption peaks at 540 nm and 570 nm, corresponding to the release of oxyhemoglobin caused by bursting of RBCs in water. The gross views of all samples shown in the insert of Figure 8A further confirms the absorption spectra observed. The results were further quantified in terms of hemolysis ratio, which is the ratio of the difference in OD<sub>570</sub> (absorbance at 570 nm) between the sample and the negative control (PBS) divided by the difference between the positive control (water) and the negative control (PBS). As shown in Figure 8B, the hemolysis ratio obtained for ImmuLip up to 0.5 mg/mL were lower than 2%, indicating negligible hemolysis. However, RBCs incubated in water shows more than 90% hemolysis ratio. With the excellent biocompatibility and hemocompatibility, ImmuLip is ready to be used in the following animal study as a nanocarrier for CPT-11 and panobinostat to evaluate anti-cancer efficacy in vivo [49].

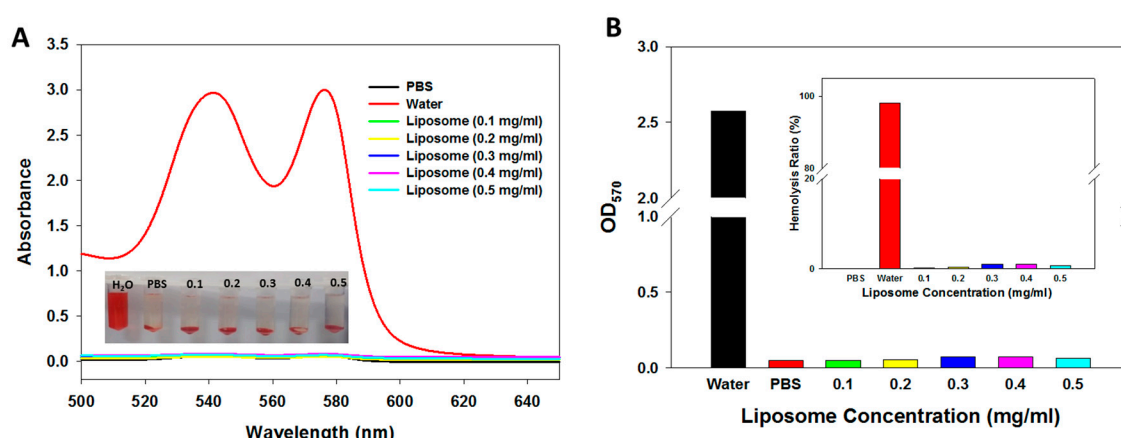


**Figure 8.** (A) Haemocompatibility of ImmuLip determined from the hemolysis assay after incubating ImmuLip with diluted red blood cells in phosphate buffered saline (PBS) at 37 °C for 2 h. Water and PBS were used as the positive and the negative controls, respectively. The full-wavelength absorption spectra of the supernatant as well as gross views of the samples (insert) are shown. (B) The absorbance at 570 nm (OD<sub>570</sub>) were used to calculate the hemolysis ratio shown in the insert.

## 2.4. In Vitro Experiments

### 2.4.1. Biodistribution and Tumor Targeting In Vivo

With in vitro studies, we have illustrated the importance of anti-GD2 Ab density on targeting efficiency of ImmuLip to U87DR cell line, as mediated by the overexpressed GD2 on cell surface. To confirm the targeting effects in vivo, ImmuLip was labelled with Cy5.5 and injected intravenously (via the tail vein) into nude mice bearing high GD2-expression U87DR tumor by subcutaneously implanting U87DR cells in the right flank. Four hours after administration of Cy5.5-labelled ImmuLip (100 µg dose), the animal was subject to in vivo imaging system (IVIS) observation for biodistribution and tumor targeting. To conduct biodistribution assay, the mouse was sacrificed, followed by harvesting the organs to visualize the accumulation of liposomes in each organ by IVIS (Figure 9A). The distribution

of Lip or ImmuLip among organs was calculated from the fluorescence intensity in each organ from the ex vivo images. As shown in Figure 9B, the particle is mainly accumulated in liver, kidney and lungs with no difference shown between Lip and ImmuLip. More than half of the administrated ImmuLip was accumulated in the liver as hepatic clearance represents the primary route of excretion for nanoparticles that do not undergo renal clearance [50]. The biodistribution study also suggests the in vivo stability of ImmuLip as more and more nanoparticles will be entrapped within the liver and spleen when the size of liposomes was increased beyond 150 nm [51]. The presence of fluorescence signal in kidney is reminiscent of appearance of liposomes with 50–100 nm size in diluted serum within 4 h (Figure 2A), as nanoparticles with size within that range were reported to be filtered out by the kidney [50]. The effect of GD2 targeting is demonstrated in the ex vivo tumor images in Figure 9C, which show 5.1 times higher fluorescence intensity of Cy5.5-labelled ImmuLip than Lip in U87DR tumors. The in vivo tumor targeting study thus matches the drastically enhanced intracellular uptake efficiency shown from the confocal microscopy (Figure 4) and flow cytometry analysis (Figure 5A) in vitro. Taken together, ImmuLip will be an excellent candidate for drug delivery to GD2-overexpressed tumors.

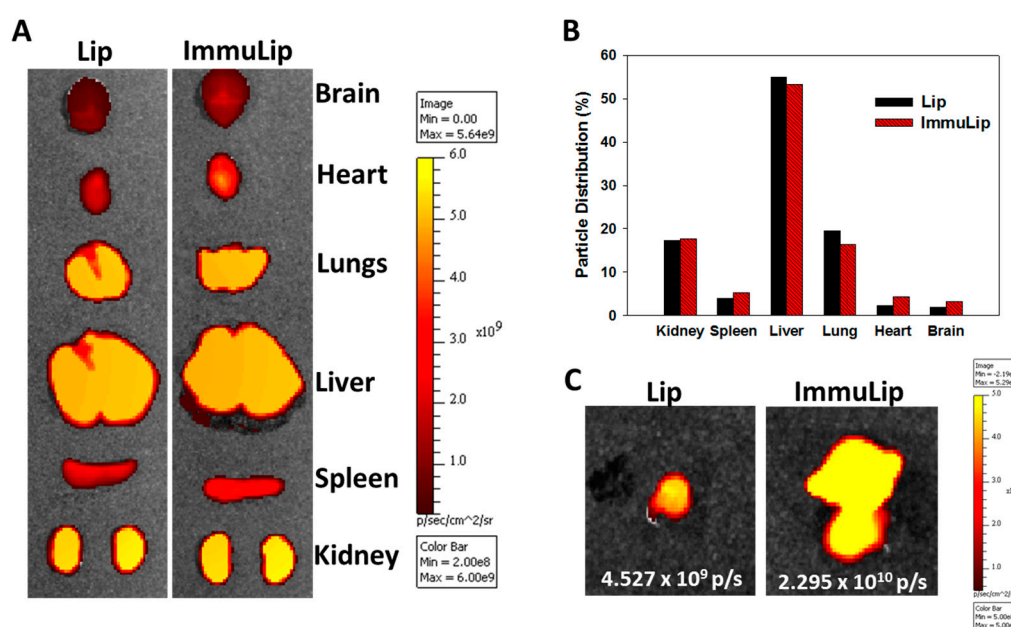


**Figure 9.** The biodistribution of Lip and ImmuLip in U87 tumor-bearing nude mice by injecting 100  $\mu$ L solution containing Cy5.5 labelled liposomes (2 mg/mL) through the tail vein. The in vivo imaging system (IVIS) was used for ex vivo imaging of harvested organs after 4 h (A) and quantification of distribution of liposomes in each organ was calculated based on fluorescence intensity in each organ (B). The targeting effects of ImmuLip vs Lip was shown from the ex vivo IVIS imaging of explanted tumors (C).

#### 2.4.2. In Vivo Anti-Tumor Efficacy

To determine in vivo anti-tumor efficacy, we used a xenograft tumor model created in nude mice with subcutaneously implanted U87DR cells. Six days after tumor cell implantation, the mice were divided into three groups and treated by intravenous injection of PBS (control), LipCP and ImmuLipCP. Additional treatments were conducted on day 8, 10 and 12. The tumor size was monitored every two days and tumor volume was calculated as  $\text{length} \times \text{width} \times \text{width} \div 2$ . The mouse was sacrificed when the tumor volume exceeds 1000  $\text{mm}^3$ . The representative gross view image of explanted tumors on day 14 is shown in Figure 10A. It is clear from the image that tumors treated with ImmuLipCP demonstrated significant reduction in tumor size compared with other groups. The tumor growth curve in the xenograft model is shown in Figure 10B. The tumor volume of mice in the control group

increased rapidly; followed by the group treated with LipCP. In contrast, the ImmuLipCP group showed significantly slower increase of tumor size. Indeed, due to the presence of targeting ligand, ImmuLipCP will be accumulated in the tumor more than LipCP (Figure 9B), which could lead to higher anti-tumor efficacy manifest from the slowest increase of tumor volume. Hence, passive targeting through the enhanced permeability and retention phenomenon with the nano-sized liposomes could be augmented by anti-GD2 Ab directed active targeting to improve the completeness of tumor destruction [52].

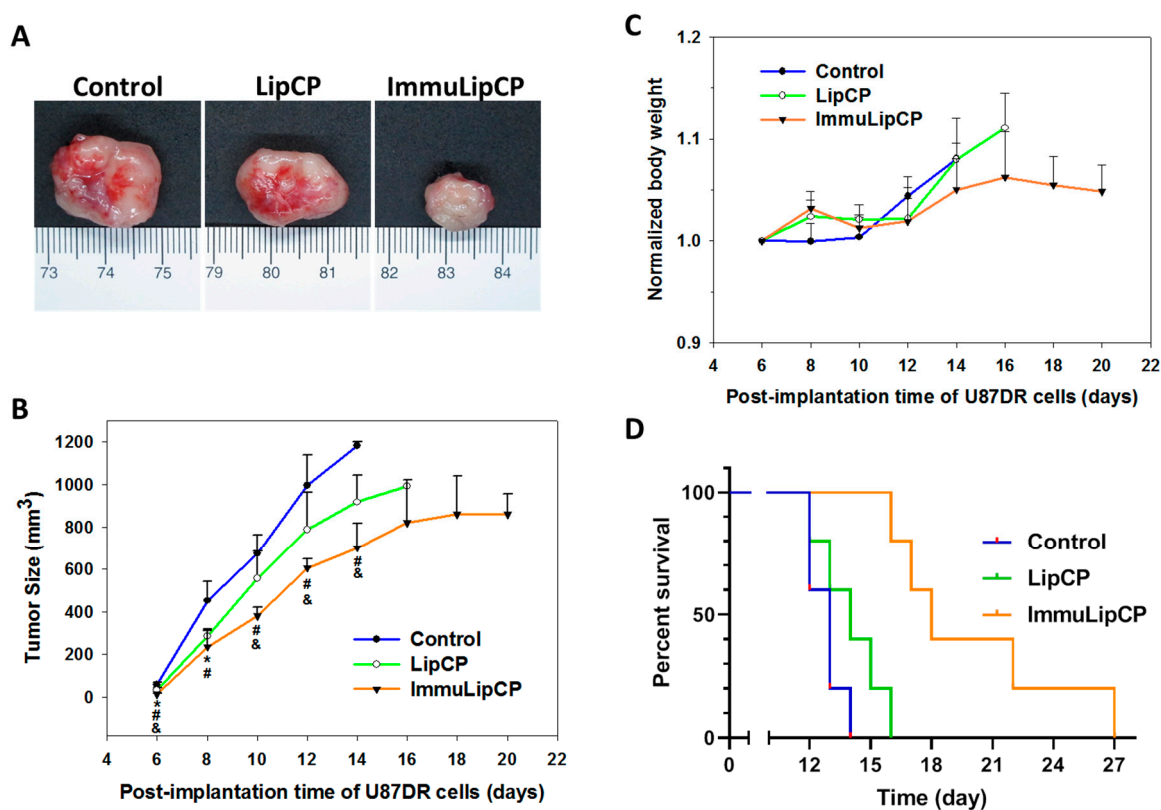


**Figure 10.** The in vivo anti-tumor efficacy was studied using a xenograft tumor model in nude mice by subcutaneous implantation of U87DR cells. The mice were divided into 3 groups and subject to intravenous injection of 100  $\mu$ L of PBS (control), LipCP (7 mg/mL) or ImmuLipCP (7 mg/mL) on day 6, 8, 10 and 12. (A) The gross view of tumors retrieved on day 14. (B) The efficacy of treatment was evaluated from change of tumor size with time ( $n = 5$ ). \*  $p < 0.05$ , LipCP vs control; #  $p < 0.05$  ImmuLipCP vs control; &  $p < 0.05$  ImmuLipCP vs LipCP. (C) The change of body weight with time ( $n = 5$ ). (D) The survival curve as obtained from the survival time of mice by sacrificing the animal when the tumor volume exceeds 1000 mm<sup>3</sup> ( $n = 5$ ).

In addition to tumor volume measurements, we measured mouse body weight to assess chemotherapy-induced weight loss. The change of body weight was normalized to that on day 6 when the treatment starts and presented in Figure 10C. No significant changes in body weight were noted among all groups, indicating no adverse effect using dual drug-loaded liposomes. A survival curve of mice was constructed by setting 1000 mm<sup>3</sup> tumor volume as the time for sacrificing the animal (Figure 10D). The mice in ImmuLipCP group showed prolonged median survival time (18 days) over mice in LipCP (14 days) and control (13 days) groups (Table 2). The survival time in the ImmuLipCP group is also significantly higher than that in LipCP and control groups (Table 2). Overall, the trend observed from mice survival is consistent with that from tumor volume and endorse the use of ImmuLipCP for cancer therapy in xenograft tumor model created with GD2 overexpressed U87DR cells.

**Table 2.** Survival times for U87DR tumor-bearing mice after different treatments.

Group <sup>1</sup>	Median Survival Time (days)	Survival Times (days) <sup>2</sup>
Control	13	12.8 ± 0.7
LipCP	14	14.0 ± 1.4 *
ImmuLipCP	18	20.0 ± 4.0 *,#

<sup>1</sup> Control: treated with PBS, LipCP: treated with liposomes loaded with CPT-11 and panobinostat, ImmuLipCP: treated with immunoliposomes loaded with CPT-11 and panobinostat. <sup>2</sup> Mean ± SD, *n* = 5. \* *p* < 0.05 compared with control, # *p* < 0.05 compared with LipCP.

#### 2.4.3. Histological Analysis

The therapeutic efficiencies of different treatments were further evaluated with a histological analysis of tumor sections from samples retrieved on day 14 (Figure 11A). The H&E staining of tumor tissue will contain irregular voids with purple outlines corresponding to the cells. This could be observed from the sample collected from the control group, which exhibits relatively higher cell intensity than the groups treated with drug-loaded liposomes. The ImmuLipCP treatment also shows much lower cell density than LipCP, corresponding to an increase in cell death with treatment. This was further confirmed from the immunohistochemical (IHC) staining of the cell proliferation marker Ki-67. The IHC images of tissue stained with Ki-67 antibody confirms the presence of actively proliferating cells in the control group, similar to the result obtained from H&E staining. However, when tumor bearing mice were subject to LipCP treatment, proliferation of tumor cell was arrested to result in less Ki-67 immunoreactivity than the control group due to apoptosis of U87DR cells. Most importantly, the tumor treated with ImmuLipCP shows the weakest immunoreactivity of Ki-67 and the most effective inhibition of cancer cell proliferation. As less cell proliferation marker was expressed in tumors treated with ImmuLipCP, more cellular apoptosis could be suggested to be induced through targeted delivery of CPT-11 and panobinostat.

The trend seen in both H&E and Ki-67 staining was further supported by staining the apoptosis protein marker, cleaved caspase 3 and phospho-ERK (pERK), in the tumor tissue, which were reported to be reliable indicators of cell apoptosis caused by CPT-11 [43]. The activation of caspase 3 is a key event in cell apoptosis and a reliable indicator of apoptosis [53]. When cancer cells are treated with chemotherapeutics, activation of stress-related signaling pathways is an important outcome at the cellular level and a signaling pathway involving the pERK protein could lead to endoplasmic reticular stress-induced apoptosis [54]. As shown from Figure 11A, we could observe the most pronounced expression of cleaved caspase 3 and pERK protein in the tumor tissue section of ImmuLipCP-treated mice (Figure 10A). Moreover, the trend was similar for the other cell apoptosis marker pERK. The IHC staining of apoptosis marker proteins in tumors from in vivo study thus is consistent with the in vitro apoptosis result obtained from the flow cytometry analysis.

The qualitative results for the IHC analysis were further quantified by Pax-It image analysis software from 5 different areas in the enlarged histological image. As shown in Figure 11B, the positively stained areas, shown as percent of region of interest (ROI) for Ki-67 is 57.4%, 40.2% and 26.6%, respectively, for mice treated with PBS, LipCP and ImmuLipCP. The less than half Ki-67-positive area identified from the histological image of the ImmuLip group compared with the control strongly supports the use of this DDS in arresting the cell proliferation of tumor cells. In contrast, the results obtained for both apoptosis marker proteins, cleaved caspase 3 and pERK, clearly show a reverse order as expected. Compared to the control group, the percent of ROI corresponding to cleaved caspase 3 (or pERK) of ImmuLipCP were ~5 times that of control and 3.2 (or 1.6) times that of LipCP, due to a significantly higher cell apoptosis rate.



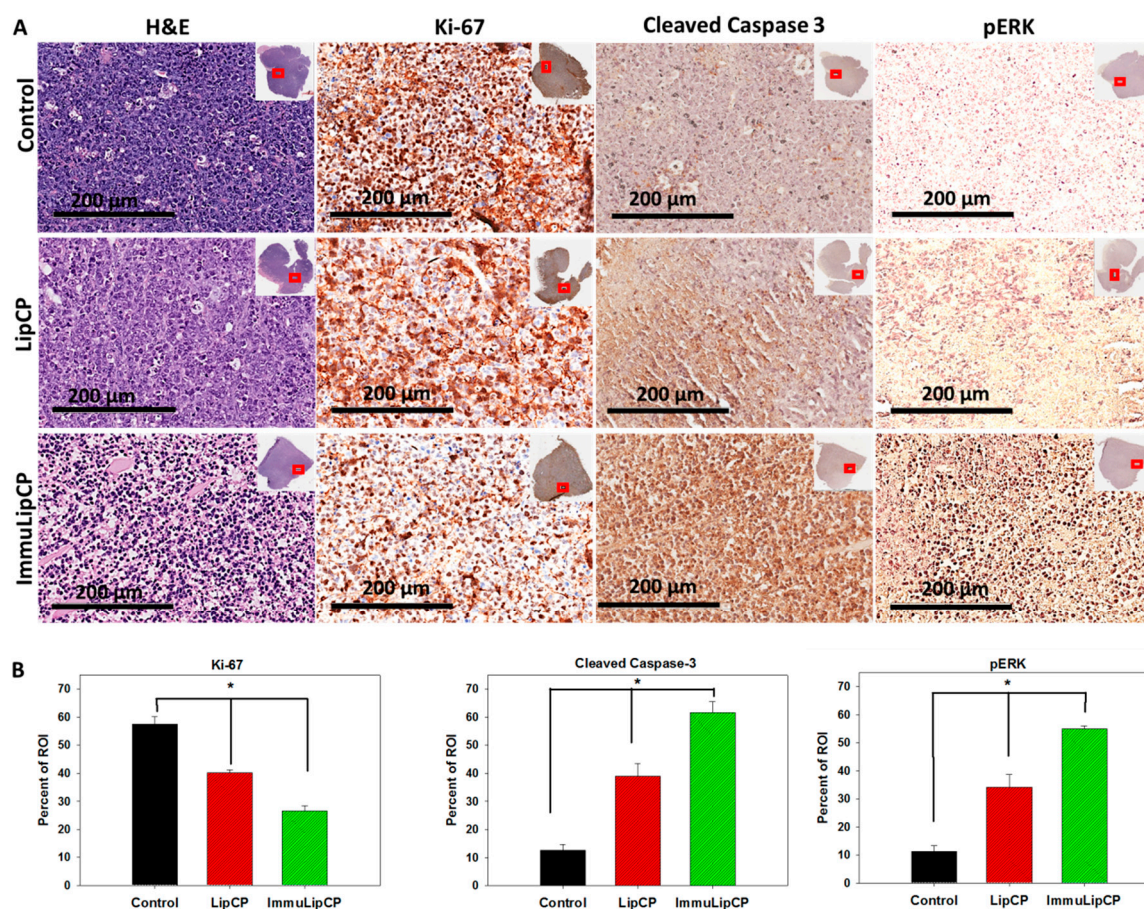


**Figure 11.** (A) The H&E and immunohistochemical (IHC) staining of Ki-67, cleaved caspase 3 and pERK after treatment with PBS (control), LipCP and ImmuLipCP (bar = 200  $\mu$ m). The image was an enlarged view of the red square shown in the insert for each tumor section. (B) The quantitative analysis of IHC staining results ( $n = 5$ ).

#### 2.4.4. Hematological Analysis

The *in vivo* toxicities of the treatment groups were tested from hematological and biochemistry analysis of blood samples collected from sacrificed mice ( $n = 5$ ). As shown in Table 3, the administration of LipCP or ImmuLipCP did not significantly alter the level of blood counts and hepatic or renal functions from hematologic study when compared with the control group ( $p > 0.05$ ). The non-significant change of blood urea nitrogen (BUN) and creatinine level indicates that treatment with drug-loaded liposomes causes no significant toxicity towards mice to influence kidney functions. Similarly, the non-toxicity shown from the liver functions was confirmed from the unaltered values of aspartate transaminase (AST), alanine transaminase (ALT). Thereby, as in body weight change shown in Figure 10C, co-delivery of CPT-11 and panobinostat by LipCP or ImmuLipCP will not lead to significant adverse effects from hematological analysis, which has been a prime concern of free drug delivery.

**Table 3.** Blood analysis for evaluation of systemic toxicity ( $n = 5$ , mean  $\pm$  SD).

Analysis	Item <sup>1</sup>	Unit	Control	LipCP	ImmuLipCP
Hematology	WBC	10 <sup>3</sup> cells/ $\mu$ L	3.2 $\pm$ 0.35	3.1 $\pm$ 1.62	3.2 $\pm$ 0.45
	RBC	10 <sup>6</sup> cells/ $\mu$ L	7.9 $\pm$ 0.33	7.3 $\pm$ 0.28	7.4 $\pm$ 0.25
	HGB	g/dL	12.5 $\pm$ 0.82	11.8 $\pm$ 0.83	11.7 $\pm$ 0.43
	HCT	%	37.6 $\pm$ 1.38	35.0 $\pm$ 1.17	32.7 $\pm$ 2.04
	PLT	10 <sup>3</sup> cells/ $\mu$ L	992 $\pm$ 174.9	1041.3 $\pm$ 140.5	1038.7 $\pm$ 277.8
Clinical Chemistry	AST	U/L	428.3 $\pm$ 75.9	440.3 $\pm$ 100	375 $\pm$ 184.6
	ALT	U/L	53.3 $\pm$ 13.9	55.7 $\pm$ 11.0	53.7 $\pm$ 20.7
	BUN	mg/dL	31.0 $\pm$ 1.73	33.7 $\pm$ 2.49	31.5 $\pm$ 2.49
	CREA	mg/dL	0.23 $\pm$ 0.06	0.27 $\pm$ 0.05	0.25 $\pm$ 0.01

<sup>1</sup> WBC: white blood cell; RBC: red blood cell; HGB: hemoglobin; HCT: hematocrit; PLT: platelet; AST: aspartate transaminase; ALT: alanine transaminase; BUN: blood urea nitrogen; CREA: creatinine Values are means  $\pm$  standard deviation (SD) of four independent measurements.

### 3. Materials and Methods

#### 3.1. Materials

1,2-Distearoyl-sn-glycero-3-phosphocholine (DSPC) was procured from Avanti Polar Lipids (Alabaster, AL, USA). Dimethyldioctadecylammonium bromide (DDAB), cholesterol and Triton X-100 were obtained from Sigma-Aldrich (St. Louis, MO, USA). N-(aminopropyl polyethyleneglycol)carbonyl-distearoylphosphatidyl-ethanolamine with 5000 PEG chain molecular weight (DSPE-PEG-NH<sub>2</sub>) was purchased from NOF Co. (Tokyo, Japan). 5(6)-Carboxyfluorescein N-hydroxysuccinimide ester (fluorescein NHS) was acquired from Nanocs Inc. (New York, NY, USA) while cyanine 5.5-NHS (Cy5.5-NHS) was from Lumiprobe Co. (Hunt Valley, MD, USA). Panobinostat and CPT-11 (irinotecan hydrochloride salt) were purchased from AdooQ BioScience (Irving, CA, USA) and LC Laboratories (Woburn, MA, USA), respectively. The U87MG human glioblastoma cell line (ATCC HTB1) was obtained from the American Type Culture Collection (Manassas, VA, USA). The anti-GD2 Ab (14G2a) was isolated and purified from hybridoma cell culture supernatant using a protein G column (HiTrap Protein G HP, Cytiva, Marlborough, MA, USA).

#### 3.2. Preparation of Liposomes (Lip)

The liposomes were prepared by the thin film hydration method in phosphate buffered saline (PBS), as described in our previous work [10]. In brief, DSPC, cholesterol, DDAB and DSPE-PEG-NH<sub>2</sub> with 6:4:1:0.5 molar ratios were dissolved in a 100 mL round-bottom flask containing 3 mL of chloroform/methanol (2:1(v/v)) mixture to prepare a 10 mM lipid solution. The lipid solution was converted into a lipid film using a roto-evaporator (EYELA N-1200AVF, Tokyo, Japan) working at 100 psi and 55 °C. After 20 min evaporation, the film formed on the wall of the round-bottom flask was further dried overnight in a vacuum oven, for complete removal of trace organic solvents. Subsequently, the lipid film was hydrated for 20 min at 55 °C with 10 mL PBS in the round-bottom flask and the resultant liposome suspension was sonicated for 20 min using a Q700 ultrasonicator (Qsonica, Newtown, CT, USA) maintained at 30% amplitude and 5 s pulse on/off cycles. By extrusion of liposomes through a polycarbonate filter of 220 nm pore size in an Avanti® Mini Extruder (Avanti Polar Lipids, Inc., Alabaster, AL, USA), we produced small unilamellar vesicles (SUVs) or large unilamellar vesicles (LUVs) from multilamellar vesicles (MLVs). Compared to the MLVs, the SUVs and LUVs are more stable and could achieve higher drug encapsulation efficiency.

#### 3.3. Preparation of Drug-Loaded Liposomes (LipCP)

Various approaches, including active and passive methods, were used to develop drug-loaded liposomal formulations [55]. As the freeze-thaw method has been shown to increase drug encapsulation capacity in liposomes by decreasing the lamellarity of formed liposomal particles, we adopted this

method for the co-encapsulation of CPT-11 and panobinostat in this study [56,57]. This method is an active method for drug loading by alternatively exposing the liposome sample to different temperatures in high gradients. For this purpose, the liposomal solution prepared above in PBS was mixed with a drug solution containing panobinostat (2 mg/mL) and/or CPT-11 (0.5 mg/mL). The mixture was incubated in a 60 °C water bath for 30 min, followed by freezing in a −20 °C refrigerator for 1 h and thawing again at 60 °C for 30 min. This freeze-thaw cycle was repeated five times and finally the solution was centrifuged at 35,000× g for 30 min to remove unencapsulated drugs in the supernatant. To determine the drug encapsulation efficiency (EE), drug-loaded liposomes were treated with a lysis buffer (0.1% Triton X-100 in PBS, pH 7.4) at 37 °C for 30 min. The solution was centrifuged at 35,000× g for 30 min and the supernatant was collected for analysis of drug concentration by high performance liquid chromatography (HPLC). A Thermo Finnigan Surveyor HPLC System was used, with a Hypersil™ ODS C18 column (5 µm) and 1:1(v/v) 0.1% orthophosphoric acid/acetonitrile as the mobile phase and operating at 0.3 mL/min flow rate. The concentration of CPT-11 and panobinostat were detected with an UV detector at 370 nm and 270 nm, respectively. The drug encapsulation efficiency (%) is weight of encapsulated drug ÷ weight of drug initially added × 100 ( $n = 5$ ).

### 3.4. Preparation of Immunoliposomes (ImmuLip) and Drug-Loaded Immunoliposomes (ImmuLipCP)

The immunoliposomes with (ImmuLipCP) or without (ImmuLip) the drug were fabricated by conjugating anti-GD2 Ab to LipCP or Lip following procedures reported before with some modifications [38,58]. We used the -NH<sub>2</sub> functional group on liposome surface originated from DSPE-PEG-NH<sub>2</sub> in the lipid bilayer, for conjugating with the -CHO groups in anti-GD2 Ab by spontaneous covalent bond formation (Figure 1A). To activate anti-GD<sub>2</sub> Ab for reactivity towards the -NH<sub>2</sub> group, sodium periodate (NaIO<sub>4</sub>) solution (0.1 M) was added dropwise into an anti-GD2 Ab solution and stirred for 20 min in dark. During this step, the sugar-based anti-GD<sub>2</sub> Ab undergoes ring opening to produce reactive aldehyde groups (Figure 1A). The activated anti-GD<sub>2</sub> Ab was purified by passing through a PV-10 desalting column and diluted with 0.2 M sodium carbonate buffer (pH 9.5) to 40 µL/mL. Five hundred microliter of Lip or ImmuLip solution (5 mg/mL) was added slowly into the above mixture and allowed to react for 5 min to conjugate anti-GD<sub>2</sub> Ab to liposome surface by forming covalent bonds. Subsequently, the covalent bonds were stabilized by adding NaBH<sub>4</sub> to reach 4 mg/mL final concentration and incubated at 4 °C for 1 h. The liposomes were recovered by centrifugation at 40,000× g for 30 min and the concentration of unconjugated Ab in the supernatant was analyzed quantitatively using Pierce™ BCA protein assay kit (Thermo Fisher Scientific, Waltham, MA, USA) using a calibration curve constructed with the anti-GD2 Ab.

### 3.5. Physico-Chemical Characterization of Liposomes and Drug Release

The Lip and ImmuLip were characterized for morphology using a cryo-transmission electron microscope (Cryo-TEM). To prepare the cryo-TEM sample, 2 µL of liposome suspension (100 µg/mL) was dropped on a holey carbon grid that has been treated by glow discharge [59]. Following incubation for 20 s, the grid was blotted quickly and plunged in precooled liquid ethane. The grid was transferred into a cryo-TEM holder in presence of liquid nitrogen and visualized under a JEOL JEM 2100 Plus Cryo-TEM. The particle size from dynamic light scattering (DLS) and the zeta potential were analyzed by Zetasizer (Nano ZS 90, Malvern, UK) using a 50 µg/mL liposome suspension in PBS (pH 7.4) ( $n = 3$ ). To determine the in vitro stability of liposomes mimicking the in vivo condition, a 5 µg/mL ImmuLipCP solution was prepared in 10% FBS/90% PBS and filtered through a 220 nm filter. After incubating at 37 °C for predetermined times, the solution was analyzed by nanoparticle tracking analysis (NTA) using NanoSight LM10 (Malvern Panalytical, Malvern, UK) equipped with a 405 nm laser. Based on Brownian motion, the scattered light intensity from the particle upon laser exposure could determine the concentration and diameter of liposomes [60,61].

The drug release profile from liposomes was determined in 1 mL PBS (pH 7.4) in a shaking water bath at 37 °C. After shaken at 100 rpm for predetermined times, the solution was centrifuged at 30000× g



for 30 min and the supernatant was collected for analysis of drug concentration by HPLC as described before. Fresh PBS was added to replenish the volume of removed supernatant and the drug release experiment was continued. The cumulative drug release (%) is cumulative weight of drug released from liposomes  $\div$  weight of drug encapsulated in the liposomes  $\times 100$  ( $n = 5$ ).

### 3.6. In Vitro Experiments

#### 3.6.1. Establishing Drug-Resistant Glioma Cell Line (U87DR) with High GD2 Expression

Most of the tumor cells are characterized by the abnormal cell proliferation resulting from the cyclin-dependent kinases (CDKs) activation [62]. Preventing tumor cell division and proliferation by blocking CDK4 and CDK6 with the help of a CDK4/6 inhibitor like palbociclib is a potential way for cancer therapy. However, palbociclib-resistant cell line was reported to hamper this approach [63]. To develop a high GD2 expression glioma cell line (U87DR), we adopted methods reported before for establishing palbociclib-resistant estrogen receptor positive breast cancer cells and carried out a long-term culture of U87MG cells in the presence of palbociclib [64,65]. In brief, the U87MG cells were cultured in the Dulbecco's Modified Eagle's Medium-High Glucose (DMEM-high glucose) containing 10% fetal bovine serum (FBS) and 0.2  $\mu$ M of palbociclib. The medium was changed every 3 days. After observing cell growth, an increasing gradient of palbociclib concentration up to 1  $\mu$ M was used for culture to make develop drug resistant U87MG variant. The palbociclib-resistant U87DR cell line could be established this way within 3 months, which was maintained in 1  $\mu$ M palbociclib. The morphological changes of cells were monitored to confirm the conversion of U87MG to U87DR and flow cytometry analysis was performed to determine the difference of GD2 expression between those cell lines.

#### 3.6.2. GD2 Expression on U87MG and U87DR Cell Surface by Flow Cytometry

The expression of GD2 antigen on U87MG and U87DR surface was analyzed by flow cytometry analysis using anti-GD2 Ab (14G2a). To perform this assay, cells were trypsinized and detached from the culture plates. The cells were collected and washed with PBS for incubation with unlabeled anti-GD2 Ab (1  $\mu$ g per  $10^6$  cells) for 1 h. Followed by this, the cells were washed in PBS containing 1%FBS and 0.02% sodium azide. Subsequently, the cells were incubated with fluorescein isothiocyanate (FITC)-labeled anti-mouse IgG (1:1000) for 40 min and washed twice in PBS. The samples were then analyzed using FACS instrument (SONY SA3800 spectral cell analyzer) where 10,000 events were collected for each sample. The data so obtained were further analyzed using the FlowJo software to determine the extent of GD2 expression.

#### 3.6.3. Intracellular Particle and Drug Uptake

The intracellular uptake of Lip and ImmuLip were determined from confocal microscopy and flow cytometry analysis, for analyzing cell trafficking and targeting efficiency mediated by anti-GD2 Ab. To perform the qualitative analysis, U87DR cells were seeded on a 15 mm coverslip in a 24-well culture plate at  $5 \times 10^4$  cells per well and cultured in cell culture medium (DMEM supplemented with 10% FBS) for 24 h in a humidified CO<sub>2</sub> incubator at 37 °C under 5% CO<sub>2</sub>. After washing with PBS, the cells were incubated with green fluoresce-producing liposomes (50  $\mu$ g/mL in cell culture medium) that were prepared by labelling liposomes with fluorescein NHS through reaction between -NH<sub>2</sub> groups of liposomes and -NHS group of fluorescein NHS. After 24 h incubation, the cells were washed with PBS and fixed with 4% paraformaldehyde. Subsequently, the cells were further treated with Triton X-100 (0.1% in PBS) for 10 min at room temperature and the cell cytoskeleton was stained with red fluorescence-producing phalloidin-tetramethylrhodamine B isothiocyanate (1%, Sigma-Aldrich, St. Louis, MO, USA). In the next step, the cell nuclei were visualized by counterstaining with blue fluorescence-producing Hoechst 33342 (1  $\mu$ g/mL, Thermo Fisher Scientific). The intracellular uptake of liposomes was observed under a confocal laser scanning microscope (Zeiss LSM 510 Meta) at

excitation/emission wavelength of 350 nm/451 nm for blue, 492 nm/517 nm for green and 577 nm/590 nm for red fluorescence signal. All three fluorescence were visualized individually at its corresponding wavelengths and then merged together to visualize the cellular internalization of liposomes. To study the effect of anti-GD2 Ab density on targeting efficiency, we also used immunoliposome (ImmuLip-L) prepared with 20% of the anti-GD2 Ab concentration used for preparing ImmuLip and observe its intracellular uptake by confocal microscopy.

The intracellular uptake of Lip (liposomes without anti-GD2 Ab), ImmuLip-L (liposome with low anti-GD2 Ab) and ImmuLip (liposome with high anti-GD2 Ab) was also determined quantitatively by flow cytometry analysis using fluorescein-labelled liposomes. To perform this analysis, U87DR cells were seeded in T-25 tissue culture flasks with a cell density of  $5 \times 10^5$  cells per flask and incubated at 37 °C under 5% CO<sub>2</sub> atmosphere. Subsequently, the cells were treated separately with Lip, ImmuLip-L or ImmuLip at 50 µg/mL final liposome concentration for 24 h. After washing with PBS, the cells were trypsinized and centrifuged at 2000× g for 5 min for collecting the cell pellet. The cell pellet was re-suspended in 500 µL binding buffer, followed by determining the fluorescence intensity corresponding to intracellularly accumulated liposome using a FACS instrument (Attune NxT Flow cytometer, Life Technologies) with a 530 nm emission filter.

To confirm the carrier-dependent accumulation of drugs, the intracellular drug uptake efficiency was also analyzed by flow cytometry analysis through the blue fluorescence intensity from CPT-11. To perform this experiment, cells in a T-25 cell culture flask ( $5 \times 10^5$  cells per flask) were treated with LipCP, ImmuLipCP or free CPT-11/panobinostat at the same drug dosage (20 µg/mL CPT-11). After 24 h incubation, the cell pellet was collected and analyzed for fluorescence intensity of CPT-11 at 405/450 nm using the same protocol established for liposome uptake [6]. The flow cytometry analysis of particle and drug uptake was duplicated to confirm reproducibility of the data and representative images are shown.

### 3.6.4. In Vitro Cytotoxicity

The cell viability of U87DR cells after different treatments in vitro was determined using the MTS cell proliferation assay from the solution absorbance of metabolites of 3-(4,5-dimethylthiazol-2-yl)-5-(3-carboxymethoxyphenyl)-2-(4-sulfophenyl)-2H-tetrazolium (MTS) salt [66]. The biocompatibility of ImmuLip was determined by seeding U87DR cells in 96-well cell culture plate at  $2.5 \times 10^3$  cells/well and incubated for 12 h. The cells were separately treated with different concentrations of ImmuLip (up to 80 µg/mL) for 24 h or 48 h at 37 °C. Subsequently, the cell culture medium was replaced with 100 µL PBS and 20 µL MTS reagent for incubation at 37 °C for 3 h. The solution absorbance was analyzed using an enzyme-linked immunosorbent assay (ELISA) plate reader (BioTek Synergy HT) at 490 nm wavelength to detect the product produced from reduction of MTS reagent through the mitochondria activity of live cells. The analysis was performed five times for each group and the average values obtained were then normalized to those obtained for the control group using cell culture medium alone, which was taken as 100% ( $n = 5$ ).

The in vitro cytotoxicity of CPT-11 and/or panobinostat was evaluated in a similar way using U87DR cells to determine the synergistic effect of drug combination. The cells were seeded in 96-well culture plate and incubated with different concentrations of CPT-11 (1 µM to 40 µM), panobinostat (10 nM to 80 nM) or combinations of CPT-11 and panobinostat (with fixed panobinostat concentration or fixed CPT-11 concentration). After 24, 48 and 72 h incubation, the relative cell viability was determined by the MTS assay as before ( $n = 5$ ). The cell viability obtained for single drug and dual drug was analyzed using the CompuSyn software (ComboSyn Inc., Paramus, NJ, USA) for the evaluation of the combined effects of CPT-11 and panobinostat [67].

The cytotoxicity of drug-loaded liposomes (LipCP and ImmuLipCP) was determined from flow cytometry analysis of the apoptosis rates of U87DR cells using an apoptosis detection kit (Thermo Fischer Scientific) that contains fluorescein isothiocyanate-labeled Annexin V (Annexin V-FITC) and propidium iodide (PI). In brief, the cells were seeded in T-25 culture flask at a cell density of



$5 \times 10^5$  cells/flask and incubated with LipCP and ImmuLipCP at 5 nM panobinostat and 2  $\mu$ M CPT-11 dosages for 24 h. The cells were trypsinized and centrifuged at  $2000 \times g$  for 5 min. The collected cell pellet was incubated with Annexin V-FITC for 30 min to label the live cells and early apoptotic cells. After labelling the late apoptotic and necrotic cells with PI, cells were analyzed for the fluorescence emission at 530 nm/570 nm using a FACS instrument (Attune NxT Flow cytometer, Life Technologies, USA). The flow cytometry analysis of cytotoxicity was duplicated to confirm the reproducibility and representative images are shown.

### 3.6.5. In Vitro Hemocompatibility

The blood compatibility of was analyzed by evaluating possible hemolysis induced by ImmuLip [68]. Briefly, whole blood sample collected from rats was diluted ten times with PBS and 0.3 mL diluted blood sample was mixed with 1.2 mL test sample and incubated at 37 °C for 2 h. The diluted blood sample treated with deionized water and PBS were used as the positive and negative controls, respectively. The mixture was centrifuged and the absorbance of the supernatant was recorded at 540 nm ( $OD_{540}$ ) using a UV-Vis spectrophotometer. The hemolysis ratio was calculated by dividing the difference in  $OD_{540}$  between the sample and the negative control by the difference in  $OD_{540}$  between the positive control and the negative control.

### 3.7. In Vivo Experiments

All in vivo experiments were performed as per protocols that have been approved by the Chang Gung University's Institutional Animal Care and Use Committee (IACUC Approval No.: CGU108-214). The biodistribution and in vivo targeting efficiency of ImmuLip and Lip was performed in nude mice bearing U87DR tumor by subcutaneous injection of  $10^5$  U87DR cells to the right flank of 6–8 week old mouse. To perform the biodistribution study, Lip and ImmuLip were labelled with Cy5.5 using Cy5.5-NHS. One hundred microliter of Cy5.5-labelled liposomes (1.92  $\mu$ g/mL) was administered intravenously via tail vein. Four hours after administration, the mice were sacrificed and organs including kidney, spleen, liver, lungs, heart and brain were harvested to visualize the accumulation of particle in each organ with an in vivo imaging system (IVIS) (Xenogen IVIS 200, Caliper Life Sciences, Hopkinton, MA, USA). The tumor tissue was explanted from each mouse and analyzed by IVIS to compare the accumulation of Lip and ImmuLip in vivo for targeting efficiency.

The in vivo antitumor efficacy was studied in U87DR tumor bearing mice prepared as before. Six days after U87DR cell implantation, the mice were randomly divided into 3 groups and subject to intravenous injection of 100  $\mu$ L of PBS (control), 100  $\mu$ L of 7 mg/mL LipCP or 100  $\mu$ L of 7 mg/mL ImmuLipCP at 12 mg/kg panobinostat and 7 mg/kg CPT-11 drug dose ( $n = 5$ , each group). All mice were treated similarly again on day 8, 10 or 12. The tumor size and the mouse body weight were recorded. The tumor was explanted from one mouse on day 14 for gross observation. The tumor size was measured using a caliper and tumor volume was calculated from length  $\times$  width  $\times$  width  $\div$  2. Mice were sacrificed when the tumor volume exceeded 1000 mm<sup>3</sup>, from which survival time of the animal was determined.

For histology, tumor tissues were collected after euthanizing the mice and fixed in 12% formaldehyde. The tissues were sectioned into 5- $\mu$ m thickness on glass slide after paraffin-embedding. Samples were then subject to hematoxylin and eosin (H&E) staining following standard protocols. Another set of slides were allowed to undergo immunohistochemical (IHC) staining using rabbit primary antibody for Ki-67 (Cell Signaling anti-Ki-67, 1:400), pERK (Cell Signaling anti-phospho-p44/42 MAPK, 1:400) and cleaved caspase-3 (Cell Signaling anti-cleaved caspase-3, 1:600). After incubating with anti-rabbit secondary antibody (ImmPRESS® HRP universal antibody) for color development counterstained with hematoxylin for nucleus, images were taken under Aperio ScanScope® XT and analyzed by the ImageScope software. The immunoreactivity in captured images was then quantified in a 70  $\mu$ m  $\times$  150  $\mu$ m measuring frame by using the PAX-it image analysis software. The protein expression from the level of immunoreactivity was expressed as the percentage of the area in the region

of interest (ROI) of the measuring frame that contained immunoreactivity. Five different areas from an image were selected for the quantification ( $n = 5$ ).

To evaluate systemic toxicity, blood samples from sacrificed mice ( $n = 5$ ) were collected in BD Microtainer® blood collection tubes with K2EDTA (Becton, Dickinson and Company, Franklin Lakes, NJ, USA). The collected blood was subject to hematologic analysis of white blood cell (WBC), red blood cell (RBC), platelet (PLT), hemoglobin (HGB) and hematocrit (HCT), as well as biochemical analysis of major organ functions from aspartate transaminase (AST), alanine transaminase (ALT), blood urea nitrogen (BUN) and creatinine (CRE).

### 3.8. Statistical Analysis

All quantitative results were expressed as mean  $\pm$  standard deviation (SD). To compare means of different groups, the one-way analysis of variance (ANOVA) analysis with Tukey's HSD post-hoc test was used for statistical analysis. Differences were considered to be significant at  $p < 0.05$ .

## 4. Conclusions

In this study, we demonstrated active targeting of GD2 overexpressed U87DR glioma cells by anti-GD2 Ab conjugated liposomes (ImmuLip). By finding the drug concentrations for synergism interaction, we successfully used this nanostructured vehicle for co-delivery of CPT-11 and panobinostat (ImmuLipCP) for targeted synergistic combination chemotherapy. Due to the overexpression of GD2 on U87DR cell line, ImmuLipCP results in active tumor targeting and effective chemotherapy. The *in vitro* experiments confirm the effective intracellular uptake of ImmuLip by U87DR, which shows 6-fold increase of uptake efficiency over non-targeted Lip and dependent on conjugated Ab density on liposome surface. Endowed with efficient active targeting ability, ImmuLipCP provides impressive enhancement of intracellular drug concentration to provide enhanced *in vitro* cytotoxicity by inducing cell apoptosis with synergistic action of CPT-11 and panobinostat. Moreover, the biocompatibility and hemocompatibility test ImmuLip supports its use for *in vivo* experiments. In xenograft model with U87DR tumor bearing nude mice, the 5.1-fold higher accumulation rate of targeted liposomes over non-targeted ones supports the *in vitro* targeting efficacy for drug delivery. The tumor bearing mice treated with ImmuLipCP showed similar body weight change and hematologic analysis results with the control and LipCP group, suggesting a highly compatible tumor treatment modality. Most importantly, mice treated with ImmuLipCP showed significantly reduced tumor growth rate and prolonged survival time. Overall, the results confirm that ImmuLipCP was an effective GD2-targeted cancer treatment modality to significantly enhance the anti-cancer therapeutic efficacy in U87DR tumors. The Ab-mediated liposome-based drug delivery system could provide a paradigm for targeted delivery of chemotherapeutics into tumor cells.

**Supplementary Materials:** The following are available online at <http://www.mdpi.com/2072-6694/12/11/3211/s1>, Figure S1. The cell morphology and the expression levels of GD2 of U87MG and U87DR cell lines from flow cytometry analysis (bar = 100  $\mu$ m).

**Author Contributions:** Study conception and design of experiments: Y.-J.L., A.L.Y. and J.-P.C.; acquisition of data: G.J. and J.-T.H.; analysis and interpretation of data: G.J., Y.-J.L., J.-T.H. and J.-P.C.; article drafting and revision: G.J., J.-T.H. and J.-P.C. All authors have read and agreed to the published version of the manuscript.

**Funding:** This research was funded by the Ministry of Science and Technology, Taiwan (MOST106-2221-E-182-056-MY3 and MOST108-2314-B-182-018-MY2). The authors would like to thank Chang Gung Memorial Hospital (CMRPD2G0081 and CMRPD2G0082) for financial support of this research.

**Acknowledgments:** The Microscope Core Laboratory at Chang Gung Memorial Hospital, Linkou is acknowledged for microscopy analysis.

**Conflicts of Interest:** The authors declare no conflict of interest.

## References

1. D'Angelo, M.; Castelli, V.; Benedetti, E.; Antonosante, A.; Catanesi, M.; Dominguez-Benot, R.; Pitari, G.; Ippoliti, R.; Cimini, A. Theranostic Nanomedicine for Malignant Gliomas. *Front. Bioeng. Biotechnol.* **2019**, *7*, 325. [\[CrossRef\]](#) [\[PubMed\]](#)
2. Krauze, M.T.; Noble, C.O.; Kawaguchi, T.; Drummond, D.; Kirpotin, D.B.; Yamashita, Y.; Kullberg, E.; Forsayeth, J.; Park, J.W.; Bankiewicz, K.S. Convection-enhanced delivery of nanoliposomal CPT-11 (irinotecan) and PEGylated liposomal doxorubicin (Doxil) in rodent intracranial brain tumor xenografts. *Neuro Oncol.* **2007**, *9*, 393–403. [\[CrossRef\]](#) [\[PubMed\]](#)
3. Li, X.-T.; Tang, W.; Xie, H.-J.; Liu, S.; Song, X.-L.; Xiao, Y.; Wang, X.; Cheng, L.; Chen, G.-R. The efficacy of RGD modified liposomes loaded with vinorelbine plus tetrandrine in treating resistant brain glioma. *J. Liposome Res.* **2017**, *29*, 21–34. [\[CrossRef\]](#) [\[PubMed\]](#)
4. Zhang, C.-X.; Zhao, W.-Y.; Liu, L.; Ju, R.-J.; Mu, L.-M.; Zhao, Y.; Zeng, F.; Xie, H.-J.; Yan, Y.; Lu, W.-L. A nanostructure of functional targeting epirubicin liposomes dually modified with aminophenyl glucose and cyclic pentapeptide used for brain glioblastoma treatment. *Oncotarget* **2015**, *6*, 32681–32700. [\[CrossRef\]](#) [\[PubMed\]](#)
5. Aghabati-Maleki, L.; Dolati, S.; Ahmadi, M.; Baghbanzhadeh, A.; Asadi, M.; Fotouhi, A.; Yousefi, M. Nanoparticles and cancer therapy: Perspectives for application of nanoparticles in the treatment of cancers. *J. Cell. Physiol.* **2019**, *235*, 1962–1972. [\[CrossRef\]](#) [\[PubMed\]](#)
6. Casadó, A.; Mora, M.; Sagristá, M.L.; Rello-Varona, S.; Acedo, P.; Stockert, J.C.; Cañete, M.; Villanueva, A. Improved selectivity and cytotoxic effects of irinotecan via liposomal delivery: A comparative study on Hs68 and HeLa cells. *Eur. J. Pharm. Sci.* **2017**, *109*, 65–77. [\[CrossRef\]](#)
7. Karra, N.; Benita, S. The ligand nanoparticle conjugation approach for targeted cancer therapy. *Curr. Drug Metab.* **2012**, *13*, 22–41. [\[CrossRef\]](#)
8. Senapati, S.; Mahanta, A.K.; Kumar, S.; Maiti, P. Controlled drug delivery vehicles for cancer treatment and their performance. *Signal Transduct. Target. Ther.* **2018**, *3*, 7. [\[CrossRef\]](#)
9. Voinea, M.; Simionescu, M. Designing of 'intelligent' liposomes for efficient delivery of drugs. *J. Cell. Mol. Med.* **2007**, *6*, 465–474. [\[CrossRef\]](#)
10. Jose, G.; Lu, Y.-J.; Chen, H.-A.; Hsu, H.-L.; Hung, J.-T.; Anilkumar, T.; Chen, J.-P. Hyaluronic acid modified bubble-generating magnetic liposomes for targeted delivery of doxorubicin. *J. Magn. Magn. Mater.* **2019**, *474*, 355–364. [\[CrossRef\]](#)
11. Drummond, D.C.; Noble, C.O.; Hayes, M.E.; Park, J.W.; Kirpotin, D.B. Pharmacokinetics and in vivo drug release rates in liposomal nanocarrier development. *J. Pharm. Sci.* **2008**, *97*, 4696–4740. [\[CrossRef\]](#)
12. Yuan, F.; Leunig, M.; Huang, S.K.; Berk, D.A.; Papahadjopoulos, D.; Jain, R.K. Microvascular permeability and interstitial penetration of sterically stabilized (stealth) liposomes in a human tumor xenograft. *Cancer Res.* **1994**, *54*, 3352–3356. [\[PubMed\]](#)
13. Hardiansyah, A.; Yang, M.-C.; Liu, T.-Y.; Kuo, C.-Y.; Huang, L.-Y.; Chan, T.-Y. Hydrophobic drug-loaded PEGylated magnetic liposomes for drug-controlled release. *Nanoscale Res. Lett.* **2017**, *12*, 355. [\[CrossRef\]](#) [\[PubMed\]](#)
14. Rougier, P.; Bugat, R. CPT-11 in the treatment of colorectal cancer: Clinical efficacy and safety profile. *Semin. Oncol.* **1996**, *23*, 34–41.
15. Wu, M.H.; Yan, B.; Humerickhouse, R.; Dolan, M.E. Irinotecan activation by human carboxylesterases in colorectal adenocarcinoma cells. *Clin. Cancer Res.* **2002**, *8*, 2696–2700.
16. Pommier, Y.; Tanizawa, A.; Kohn, K.W. Mechanisms of topoisomerase I inhibition by anticancer drugs. *Adv. Pharmacol.* **1994**, *29*, 73–92. [\[CrossRef\]](#)
17. Garcia-Carbonero, R.; Supko, J.G. Current perspectives on the clinical experience, pharmacology, and continued development of the camptothecins. *Clin. Cancer Res.* **2002**, *8*, 641–661.
18. Chen, T.C.; Su, S.; Fry, D.; Liebes, L. Combination therapy with irinotecan and protein kinase C inhibitors in malignant glioma. *Cancer* **2003**, *97*, 2363–2373. [\[CrossRef\]](#)
19. Innocenti, F. UGT1A1 genotyping in patients undergoing treatment with irinotecan. *Clin. Adv. Hematol. Oncol.* **2005**, *3*, 843–844.

20. Gawley, M.; Almond, L.; Daniel, S.; Lastakchi, S.; Kaur, S.; Detta, A.; Cruickshank, G.; Miller, R.; Hingtgen, S.; Sheets, K.; et al. Development and in vivo evaluation of Irinotecan-loaded Drug Eluting Seeds (iDES) for the localised treatment of recurrent glioblastoma multiforme. *J. Control. Release* **2020**, *324*, 1–16. [\[CrossRef\]](#)
21. Ge, J.-J.; Li, C.; Qi, S.-P.; Xue, F.-J.; Gao, Z.-M.; Yu, C.; Zhang, J.-P. Combining therapy with recombinant human endostatin and cytotoxic agents for recurrent disseminated glioblastoma: A retrospective study. *BMC Cancer* **2020**, *20*, 24–28. [\[CrossRef\]](#)
22. Moore, D. Panobinostat (Farydak): A novel option for the treatment of relapsed or relapsed and refractory multiple myeloma. *P T Peer-Rev. J. Formul. Manag.* **2016**, *41*, 296–300.
23. Andreu-Vieyra, C.V.; Berenson, J.R. The potential of panobinostat as a treatment option in patients with relapsed and refractory multiple myeloma. *Ther. Adv. Hematol.* **2014**, *5*, 197–210. [\[CrossRef\]](#) [\[PubMed\]](#)
24. Singh, A.; Patel, V.K.; Jain, D.K.; Patel, P.; Rajak, H. Panobinostat as pan-deacetylase inhibitor for the treatment of pancreatic cancer: Recent progress and future prospects. *Oncol. Ther.* **2016**, *4*, 73–89. [\[CrossRef\]](#) [\[PubMed\]](#)
25. Gad, A.; Kydd, J.; Piel, B.; Rai, P. Targeting cancer using polymeric nanoparticle mediated combination chemotherapy. *Int. J. Nanomed. Nanosurgery* **2016**, *2*. [\[CrossRef\]](#)
26. Pourgholi, F.; Hajivalili, M.; Farhad, J.-N.; Kafil, H.S.; Yousefi, M. Nanoparticles: Novel vehicles in treatment of Glioblastoma. *Biomed. Pharmacother.* **2016**, *77*, 98–107. [\[CrossRef\]](#) [\[PubMed\]](#)
27. Jang, S.H.; Wientjes, M.G.; Lu, D.; Au, J.L. Drug delivery and transport to solid tumors. *Pharm. Res.* **2003**, *20*, 1337–1350. [\[CrossRef\]](#)
28. Vasir, J.K.; Labhasetwar, V. Targeted drug delivery in cancer therapy. *Technol. Cancer Res. Treat.* **2005**, *4*, 363–374. [\[CrossRef\]](#)
29. Noble, G.T.; Stefanick, J.F.; Ashley, J.D.; Kiziltepe, T.; Bilgicer, B. Ligand-targeted liposome design: Challenges and fundamental considerations. *Trends Biotechnol.* **2014**, *32*, 32–45. [\[CrossRef\]](#)
30. Wang, D.; Sun, Y.; Liu, Y.; Meng, F.; Lee, R.J. Clinical translation of immunoliposomes for cancer therapy: Recent perspectives. *Expert Opin. Drug Deliv.* **2018**, *15*, 893–903. [\[CrossRef\]](#)
31. Suzuki, M.; Cheung, N.-K.V. Disialoganglioside GD2 as a therapeutic target for human diseases. *Expert Opin. Ther. Targets* **2015**, *19*, 349–362. [\[CrossRef\]](#) [\[PubMed\]](#)
32. Longee, D.C.; Wikstrand, C.J.; He, X.; Fuller, G.N.; Bigner, S.H.; Fredman, P.; Svennerholm, L.; Bigner, D.D. Disialoganglioside GD2 in human neuroectodermal tumor cell lines and gliomas. *Acta Neuropathol.* **1991**, *82*, 45–54. [\[CrossRef\]](#) [\[PubMed\]](#)
33. Tivnan, A.; Orr, W.S.; Gubala, V.; Nooney, R.; Williams, D.E.; McDonagh, C.; Prenter, S.; Harvey, H.; Domingo-Fernández, R.; Bray, I.M.; et al. Inhibition of neuroblastoma tumor growth by targeted delivery of microRNA-34a using anti-disialoganglioside GD2 coated nanoparticles. *PLoS ONE* **2012**, *7*, e38129. [\[CrossRef\]](#) [\[PubMed\]](#)
34. Pastorino, F.; Brignole, C.; Marimietri, D.; Sapra, P.; Moase, E.H.; Allen, T.M.; Ponzoni, M. Doxorubicin-loaded Fab' fragments of anti-disialoganglioside immunoliposomes selectively inhibit the growth and dissemination of human neuroblastoma in nude mice. *Cancer Res.* **2003**, *63*, 86–92. [\[PubMed\]](#)
35. Cheever, M.A.; Allison, J.P.; Ferris, A.S.; Finn, O.J.; Hastings, B.M.; Hecht, T.T.; Mellman, I.; Prindiville, S.A.; Viner, J.L.; Weiner, L.M.; et al. The prioritization of cancer antigens: A national cancer institute pilot project for the acceleration of translational research. *Clin. Cancer Res.* **2009**, *15*, 5323–5337. [\[CrossRef\]](#)
36. Brignole, C.; Marimietri, D.; Gambini, C.; Allen, T.M.; Ponzoni, M.; Pastorino, F. Development of Fab' fragments of anti-GD (2) immunoliposomes entrapping doxorubicin for experimental therapy of human neuroblastoma. *Cancer Lett.* **2003**, *197*, 199–204. [\[CrossRef\]](#)
37. Pagnan, G.; Stuart, D.D.; Pastorino, F.; Raffaghello, L.; Montaldo, P.G.; Allen, T.M.; Calabretta, B.; Ponzoni, M. Delivery of c-myc antisense oligodeoxynucleotides to human neuroblastoma cells via disialoganglioside GD2-targeted immunoliposomes: Antitumor effects. *J. Natl. Cancer Inst.* **2000**, *92*, 253–261. [\[CrossRef\]](#)
38. Pagnan, G.; Montaldo, P.G.; Pastorino, F.; Raffaghello, L.; Kirchmeier, M.; Allen, T.M.; Ponzoni, M. GD2-mediated melanoma cell targeting and cytotoxicity of liposome-entrapped fenretinide. *Int. J. Cancer* **1999**, *81*, 268–274. [\[CrossRef\]](#)
39. Gholizadeh, S.; Dolman, E.M.; Wieriks, R.; Sparidans, R.W.; Hennink, W.E.; Kok, R. Anti-GD2 immunoliposomes for targeted delivery of the survivin inhibitor sepantronium bromide (YM155) to neuroblastoma tumor cells. *Pharm. Res.* **2018**, *35*, 1–15. [\[CrossRef\]](#)

40. Danaei, M.; Dehghankhold, M.; Ataei, S.; Davarani, F.H.; Javanmard, R.; Dokhani, A.; Khorasani, S.; Mozafari, M.R. Impact of particle size and polydispersity index on the clinical applications of lipidic nanocarrier systems. *Pharmaceutics* **2018**, *10*, 57. [\[CrossRef\]](#)
41. Ribeiro, L.N.D.M.; Couto, V.M.; Fraceto, L.F.; De Paula, E. Use of nanoparticle concentration as a tool to understand the structural properties of colloids. *Sci. Rep.* **2018**, *8*, 982. [\[CrossRef\]](#) [\[PubMed\]](#)
42. Chattopadhyay, S.; Modesto-López, L.B.; Venkataraman, C.; Biswas, P. Size distribution and morphology of liposome aerosols generated by two methodologies. *Aerosol Sci. Technol.* **2010**, *44*, 972–982. [\[CrossRef\]](#)
43. Lu, Y.-J.; Chuang, E.-Y.; Cheng, Y.-H.; Anilkumar, T.; Chen, H.-A.; Chen, J.-P. Thermosensitive magnetic liposomes for alternating magnetic field-inducible drug delivery in dual targeted brain tumor chemotherapy. *Chem. Eng. J.* **2019**, *373*, 720–733. [\[CrossRef\]](#)
44. Rai, Y.; Pathak, R.; Kumari, N.; Sah, D.K.; Pandey, S.; Kalra, N.; Soni, R.; Dwarakanath, B.S.; Bhatt, A.N. Mitochondrial biogenesis and metabolic hyperactivation limits the application of MTT assay in the estimation of radiation induced growth inhibition. *Sci. Rep.* **2018**, *8*, 1–15. [\[CrossRef\]](#)
45. Chou, T.-C.; Talalay, P. Quantitative analysis of dose-effect relationships: The combined effects of multiple drugs or enzyme inhibitors. *Adv. Enzym. Regul.* **1984**, *22*, 27–55. [\[CrossRef\]](#)
46. Jeon, Y.-J.; Ko, S.M.; Cho, J.H.; Chae, J.-I.; Shim, J.-H. The HDAC inhibitor, panobinostat, induces apoptosis by suppressing the expression of specificity protein 1 in oral squamous cell carcinoma. *Int. J. Mol. Med.* **2013**, *32*, 860–866. [\[CrossRef\]](#)
47. Nakatsu, S.; Kondo, S.; Kondo, Y.; Yin, D.; Peterson, J.W.; Kaakaji, R.; Morimura, T.; Kikuchi, H.; Takeuchi, J.; Barnett, G.H. Induction of apoptosis in multi-drug resistant (MDR) human glioblastoma cells by SN-38, a metabolite of the camptothecin derivative CPT-11. *Cancer Chemother. Pharmacol.* **1997**, *39*, 417–423. [\[CrossRef\]](#)
48. Kuznetsova, N.R.; Sevrin, C.; Lespineux, D.; Bovin, N.V.; Vodovozova, E.L.; Mészáros, T.; Szebeni, J.; Grandfils, C. Hemocompatibility of liposomes loaded with lipophilic prodrugs of methotrexate and melphalan in the lipid bilayer. *J. Control. Release* **2012**, *160*, 394–400. [\[CrossRef\]](#)
49. Gentile, P.; Chiono, V.; Carmagnola, I.; Hatton, P.V. An overview of poly(lactic-co-glycolic) acid (PLGA)-based biomaterials for bone tissue engineering. *Int. J. Mol. Sci.* **2014**, *15*, 3640–3659. [\[CrossRef\]](#)
50. Longmire, M.; Choyke, P.L.; Kobayashi, H. Clearance properties of nano-sized particles and molecules as imaging agents: Considerations and caveats. *Nanomedicine* **2008**, *3*, 703–717. [\[CrossRef\]](#)
51. Blanco, E.; Shen, H.; Ferrari, M. Principles of nanoparticle design for overcoming biological barriers to drug delivery. *Nat. Biotechnol.* **2015**, *33*, 941–951. [\[CrossRef\]](#) [\[PubMed\]](#)
52. Attia, M.F.; Anton, N.; Wallyn, J.; Omran, Z.; Vandamme, T.F. An overview of active and passive targeting strategies to improve the nanocarriers efficiency to tumour sites. *J. Pharm. Pharmacol.* **2019**, *71*, 1185–1198. [\[CrossRef\]](#) [\[PubMed\]](#)
53. Porter, A.G.; Jänicke, R.U. Emerging roles of caspase-3 in apoptosis. *Cell Death Differ.* **1999**, *6*, 99–104. [\[CrossRef\]](#) [\[PubMed\]](#)
54. Arai, K.; Van Leyen, K.; Kurose, H.; Lo, E.H.; Lee, S.-R. Involvement of ERK MAP kinase in endoplasmic reticulum stress in SH-SY5Y human neuroblastoma cells. *J. Neurochem.* **2004**, *89*, 232–239. [\[CrossRef\]](#)
55. Gubernator, J. Active methods of drug loading into liposomes: Recent strategies for stable drug entrapment and increased in vivo activity. *Expert Opin. Drug Deliv.* **2011**, *8*, 565–580. [\[CrossRef\]](#) [\[PubMed\]](#)
56. Sriwongsitanont, S.; Ueno, M. Effect of a PEG lipid (DSPE-PEG2000) and freeze-thawing process on phospholipid vesicle size and lamellarity. *Colloid Polym. Sci.* **2004**, *282*, 753–760. [\[CrossRef\]](#)
57. Llu, L.; Yonetani, T. Preparation and characterization of liposome-encapsulated haemoglobin by a freeze-thaw method. *J. Microencapsul.* **1994**, *11*, 409–421. [\[CrossRef\]](#)
58. Kirpotin, D.; Park, J.W.; Hong, K.; Zalipsky, S.; Li, W.-L.; Carter, P.; Benz, A.C.C.; Papahadjopoulos, D. Sterically stabilized anti-HER2 immunoliposomes: Design and targeting to human breast cancer cells in vitro. *Biochemistry* **1997**, *36*, 66–75. [\[CrossRef\]](#)
59. Almgren, M.; Edwards, K.; Karlsson, G. Cryo transmission electron microscopy of liposomes and related structures. *Colloids Surf. A Physicochem. Eng. Asp.* **2000**, *174*, 3–21. [\[CrossRef\]](#)
60. Kestens, V.; Bozatzidis, V.; De Temmerman, P.-J.; Ramaye, Y.; Roebben, G. Validation of a particle tracking analysis method for the size determination of nano- and microparticles. *J. Nanoparticle Res.* **2017**, *19*, 1–16. [\[CrossRef\]](#)




61. Dragovic, R.A.; Gardiner, C.; Brooks, A.S.; Tannetta, D.S.; Ferguson, D.J.; Hole, P.; Carr, B.; Redman, C.W.; Harris, A.L.; Dobson, P.J.; et al. Sizing and phenotyping of cellular vesicles using nanoparticle tracking analysis. *Nanomed. Nanotechnol. Biol. Med.* **2011**, *7*, 780–788. [[CrossRef](#)]
62. Xu, X.-Q.; Pan, X.-H.; Wang, T.-T.; Wang, J.; Yang, B.; He, Q.-J.; Ding, L. Intrinsic and acquired resistance to CDK4/6 inhibitors and potential overcoming strategies. *Acta Pharmacol. Sin.* **2020**. [[CrossRef](#)]
63. Herrera-Abreu, M.T.; Palafox, M.; Asghar, U.; Rivas, M.A.; Cutts, R.J.; Garcia-Murillas, I.; Pearson, A.; Guzman, M.; Rodriguez, O.; Grueso, J.; et al. Early adaptation and acquired resistance to CDK4/6 Inhibition in estrogen receptor–positive breast cancer. *Cancer Res.* **2016**, *76*, 2301–2313. [[CrossRef](#)]
64. Lypova, N.; Lanceta, L.; Gipson, A.; Vega, S.; Garza-Morales, R.; McMasters, K.M.; Chesney, J.; Gomez-Gutierrez, J.G.; Imbert-Fernandez, Y.; Gibson, A. Targeting palbociclib-resistant estrogen receptor-positive breast cancer cells via oncolytic virotherapy. *Cancers* **2019**, *11*, 684. [[CrossRef](#)]
65. Pancholi, S.; Ribas, R.; Simigdala, N.; Schuster, E.; Nikitorowicz-Buniak, J.; Ressa, A.; Gao, Q.; Leal, M.F.; Bhamra, A.; Thornhill, A.; et al. Tumour kinome re-wiring governs resistance to palbociclib in oestrogen receptor positive breast cancers, highlighting new therapeutic modalities. *Oncogene* **2020**, *39*, 4781–4797. [[CrossRef](#)] [[PubMed](#)]
66. Curran, C.S.; Evans, M.D.; Bertics, P.J. GM-CSF Production by glioblastoma cells has a functional role in eosinophil survival, activation, and growth factor production for enhanced tumor cell proliferation. *J. Immunol.* **2011**, *187*, 1254–1263. [[CrossRef](#)] [[PubMed](#)]
67. Chou, T.-C. Theoretical basis, experimental design, and computerized simulation of synergism and antagonism in drug combination studies. *Pharmacol. Rev.* **2006**, *58*, 621–681. [[CrossRef](#)]
68. Chen, H.-A.; Ma, Y.-H.; Hsu, T.-Y.; Chen, J.-P. Preparation of peptide and recombinant tissue plasminogen activator conjugated poly (lactic-Co-glycolic acid) (PLGA) magnetic nanoparticles for dual targeted thrombolytic therapy. *Int. J. Mol. Sci.* **2020**, *21*, 2690. [[CrossRef](#)]

**Publisher’s Note:** MDPI stays neutral with regard to jurisdictional claims in published maps and institutional affiliations.



© 2020 by the authors. Licensee MDPI, Basel, Switzerland. This article is an open access article distributed under the terms and conditions of the Creative Commons Attribution (CC BY) license (<http://creativecommons.org/licenses/by/4.0/>).

# Antimetabolite pemetrexed primes a favorable tumor microenvironment for immune checkpoint blockade therapy

Chia-Sing Lu,<sup>1</sup> Ching-Wen Lin,<sup>2</sup> Ya-Hsuan Chang,<sup>3</sup> Hsuan-Yu Chen,<sup>3</sup> Wei-Chia Chung,<sup>2</sup> Wei-Yun Lai,<sup>2</sup> Chao-Chi Ho,<sup>1</sup> Tong-Hong Wang,<sup>4</sup> Chi-Yuan Chen,<sup>4</sup> Chen-Lin Yeh,<sup>1</sup> Sean Wu,<sup>2</sup> Shu-Ping Wang,<sup>2</sup> Pan-Chyr Yang <sup>1,2,5</sup>

**To cite:** Lu C-S, Lin C-W, Chang Y-H, *et al.* Antimetabolite pemetrexed primes a favorable tumor microenvironment for immune checkpoint blockade therapy. *Journal for ImmunoTherapy of Cancer* 2020;**8**:e001392. doi:10.1136/jitc-2020-001392

► Additional material is published online only. To view, please visit the journal online (<http://dx.doi.org/10.1136/jitc-2020-001392>).

C-SL and C-WL contributed equally.

Accepted 09 November 2020



© Author(s) (or their employer(s)) 2020. Re-use permitted under CC BY. Published by BMJ.

For numbered affiliations see end of article.

## Correspondence to

Dr Pan-Chyr Yang;  
pcyang@ntu.edu.tw

Dr Shu-Ping Wang;  
spwang@ibms.sinica.edu.tw

## ABSTRACT

**Background** The immune checkpoint blockade (ICB) targeting programmed cell death-1 (PD-1) and its ligand (PD-L1) has been proved beneficial for numerous types of cancers, including non-small-cell lung cancer (NSCLC). However, a significant number of patients with NSCLC still fail to respond to ICB due to unfavorable tumor microenvironment. To improve the efficacy, the immune-chemotherapy combination with pemetrexed, cis/carboplatin and pembrolizumab (anti-PD-1) has been recently approved as first-line treatment in advanced NSCLCs. While chemotherapeutic agents exert beneficial effects, the underlying antitumor mechanism(s) remains unclear.

**Methods** Pemetrexed, cisplatin and other chemotherapeutic agents were tested for the potential to induce PD-L1 expression in NSCLC cells by immunoblotting and flow cytometry. The ability to prime the tumor immune microenvironment was then determined by NSCLC/T cell coculture systems and syngeneic mouse models. Subpopulations of NSCLC cells responding differently to pemetrexed were selected and subjected to RNA-sequencing analysis. The key signaling pathways were identified and validated in vitro and in vivo.

**Results** Pemetrexed induced the transcriptional activation of *PD-L1* (encoded by *CD274*) by inactivating thymidylate synthase (TS) in NSCLC cells and, in turn, activating T-lymphocytes when combined with the anti-PD-1/PD-L1 therapy. Nuclear factor  $\kappa$ B (NF- $\kappa$ B) signaling was activated by intracellular reactive oxygen species (ROS) that were elevated by pemetrexed-mediated TS inactivation. The TS–ROS–NF- $\kappa$ B regulatory axis actively involves in pemetrexed-induced PD-L1 upregulation, whereas when pemetrexed fails to induce PD-L1 expression in NSCLC cells, NF- $\kappa$ B signaling is unregulated. In syngeneic mouse models, the combinatory treatment of pemetrexed with anti-PD-L1 antibody created a more favorable tumor microenvironment for the inhibition of tumor growth.

**Conclusions** Our findings reveal novel mechanisms showing that pemetrexed upregulates PD-L1 expression and primes a favorable microenvironment for ICB, which provides a mechanistic basis for the combinatory chemoimmunotherapy in NSCLC treatment.

## BACKGROUND

Lung cancer is the leading cause of cancer-related death worldwide.<sup>1</sup> Among non-small-cell lung cancer (NSCLC) represents a heterogeneous group of lung tumors based on histology and accounts for approximately 85% of lung cancers. Since the development of immune checkpoint blockade (ICB), immunotherapy has been state of the art in the treatment pipeline for patients with NSCLC in different stages of the disease.<sup>2,3</sup> Several humanized monoclonal antibodies targeting programmed cell death-1 (PD-1) (eg, pembrolizumab and nivolumab) and programmed death-ligand 1 (PD-L1; eg, atezolizumab) have been approved by the US Food and Drug Administration (FDA) and been shown promising potencies as immunotherapeutic agents for NSCLC treatments.<sup>4–6</sup> Although the PD-1/PD-L1 blockade therapy significantly improves the durable response rate and prolongs long-term survival for patients with NSCLC that lack targetable mutations, nearly 70% of patients in advanced stages of NSCLC are still unresponsive; especially those with low or no tumor PD-L1 expression.<sup>7–10</sup> With impaired PD-L1 expression, tumors usually display a lack of T cell activation and/or infiltration in the surrounding tumor microenvironment.<sup>11,12</sup> This kind of non-T-cell-inflamed tumor microenvironment has been characterized as ‘non-inflamed’ or ‘cold’ tumors. Thus, the clinical benefit from the PD-1/PD-L1 blockade therapy in NSCLC treatment is limited, and the reactivation of PD-L1 expression in tumor cells could be a key factor for turning the cold tumor microenvironment into a ‘hot’ one.<sup>13</sup> In this regard, identifying specific agents that show potentials to reactivate tumor PD-L1

expression may be critical in designing effective combinatory therapy regimens.<sup>12</sup>

The combination chemotherapy has long been the standard treatment for patients in advanced stages of NSCLC. Among the chemotherapeutic combinations, most commonly used are platinum-based agents, such as cisplatin or carboplatin, along with other chemotherapeutics. Emerging evidence indicates that modulation of the immune response through the PD-1/PD-L1 blockade can be enhanced by the potential immunogenic effects of cytotoxic chemotherapy, including increased tumor cell immunogenicity and repressed immunosuppressive circuitries.<sup>14–15</sup> In accord with this view, several clinical trials are underway to evaluate the efficacy of the combination strategy with chemotherapeutics and immune checkpoint inhibitors.<sup>16</sup> Pemetrexed (PEM), an antimetabolite that affects the folate pathway, is known to exert less side effects than cisplatin and carboplatin and is commonly used in the cisplatin/carboplatin-based combinatory chemotherapy for multiple solid tumors.<sup>17</sup> In recent years, pemetrexed also shows huge potential in combination with immunotherapies.<sup>18–20</sup> The combination of pemetrexed plus anti-PD-1 antibody (pembrolizumab), particularly in the presence of carboplatin-based chemotherapy, has been shown to improve the overall survival (OS) of patients with advanced stage NSCLC in KEYNOTE-021<sup>19</sup> and KEYNOTE-189 trials.<sup>20</sup> Recently, the IMpower132 trial also shows increased OS in the combination of pemetrexed plus anti-PD-L1 antibody (atezolizumab) in the presence of cisplatin or carboplatin.<sup>21</sup> These improvements have led to the approval of the combination of pemetrexed, pembrolizumab (anti-PD-1), and platinum-based chemotherapeutics as the first-line treatment for patients with advanced non-squamous NSCLC. Nevertheless, it remains unclear how these chemotherapeutics enhance effects of cancer immunotherapy.

Here, we screen the effects of front-line NSCLC chemotherapeutic agents on PD-L1 expression in NSCLC cell lines and activation of tumor-infiltrating T-lymphocytes (TILs) in combination with ICB therapy. We find that sublethal doses of antimetabolites, pemetrexed and 5-fluorouracil (5-FU), can upregulate PD-L1 expression in NSCLC cells and modulate activities of TILs, priming a favorable tumor microenvironment for ICB therapy. By dissecting the mechanisms underlying the crosstalk between pemetrexed and ICB therapy, we further show that thymidylate synthase (TS) plays as a critical hub for connecting pemetrexed to the activation of NF- $\kappa$ B signaling pathway. Pemetrexed inhibits the activity of TS and in turn promotes the elevation of intracellular reactive oxygen species (ROSs), which enhances the phosphorylation of inhibitor of NF- $\kappa$ B (I $\kappa$ B) and subsequent activation of NF- $\kappa$ B signaling pathway. Thereby, this leads to the re-expression of PD-L1 in tumor cells, the augment and/or activation of TILs when combined with the PD-1/PD-L1 blockade, and the concomitant conversion of a cold tumor immune microenvironment to a hot state. These results provide mechanistic insights of pemetrexed

in enhancing the anti-PD-1/PD-L1 therapy for NSCLC treatment.

## METHODS

### Cell culture and inhibitors

The H1299 and A549 human lung cancer cell lines and the T47D human breast cancer cell line were obtained from the American Type Culture Collection (Manassas, Virginia) and cultured in Dulbecco's Modified Eagle Medium containing 10% fetal bovine serum (FBS). The PC9 human lung cancer cell line was a gift from Dr C.-H. Yang (Graduate Institute of Oncology, Cancer Research Center, National Taiwan University). The CL141 and CL1-5 human lung cancer cell lines, derived from clinical patients, were established in our laboratory<sup>22–23</sup> and maintained in Roswell Park Memorial Institute (RPMI) medium containing 10% FBS. Human peripheral blood mononuclear cells (PBMCs) were isolated from healthy blood donors. Isolation of PBMC in the buffy coats of fresh whole blood samples was performed by density gradient centrifugation on Ficoll-Paque Premium (GE Healthcare). Human PBMCs and Jurkat leukemia T cell line were cultured in RPMI medium containing 10% heat-inactivated FBS.

The I $\kappa$ B kinase (IKK) inhibitor BAY 11-7082 was acquired from MCE (MedChemExpress). Cell viability was analyzed by sulforhodamine B assay according to the manufacturer's instructions. Further details about immunoblot analysis, real-time reverse transcriptase PCR, flow cytometry analysis, RNA interference and luciferase reporter assay are fully provided in the online supplemental materials.

### Xenograft tumor formation assay

CL1-5 cells ( $1 \times 10^6$ ) were subcutaneously injected into the right flanks of 6-week-old nude mice, followed by intraperitoneal pemetrexed (50 mg/kg) every 4 days for two cycles. Tumors were collected 1 week after the final treatment. The isolated tumors were cut into small pieces, which were lysed with Radioimmunoprecipitation assay buffer (RIPA buffer, 1% Nonidet P-40, 0.5% sodium deoxycholate and 0.1% SDS) containing complete protease inhibitor cocktail (Roche). Protein samples were subjected to immunoblotting with antibodies against PD-L1 (#13684, Cell Signaling) and anti- $\beta$ -actin (Sigma-Aldrich), the latter being the internal control.

### Interleukin-2 (IL-2) secretion by activated Jurkat T cells and PBMCs

CL1-5, CL141 and H1299 lung cancer cells were pretreated with chemotherapeutic drugs for 24 hours. These cells were subsequently cocultured with Jurkat T-cells or PBMCs at the cancer cell to T cell ratio of 5:1 (CL1-5 cells) or 10:1 (CL141 cells) for additional 48 hours in the presence of  $1 \times$  T Cell Stimulation Cocktail (eBioscience). Coculture mediums were kept containing  $1 \times$  T Cell Stimulation Cocktail and

chemotherapeutic drugs. For blockade of the PD-1/PD-L1 pathway, 10 µg/mL of anti-PD-L1 antibody or control mouse IgG was added to the coculture medium. The culture supernatants were harvested at 48 hours after coculture and the concentrations of IL-2 were assessed by IL-2 Human ELISA Kit (Catalog # 88-7025-88, Thermo Scientific).

### Intracellular cytokine staining assays

For intracellular cytokine staining (ICS), monensin (3 µM) was added into coculture media for blocking cytokine secretion. Human Jurkat T-cells or PMBCs were harvested and washed with ice-cold PBS. Cells were then stained with specific antibodies for surface markers, CD45 (Biolegend, #368511) and CD69 (Biolegend, #310903), in cell staining buffer (Biolegend, #420201) for 30 min on ice in accordance with the manufacturer's protocols. The intracellular staining of IL-2 (Biolegend, #500306) was performed with Cyto-Fast Fix/Perm buffer set (Biolegend, #426803). Afterwards, cells were washed twice with ice-cold PBS/FBS, resuspended, then analyzed by Fluorescence-activated cell sorting (FACS) analysis using a FACS Calibur system. FACS data analysis was performed using FlowJo software (Tree Star, Ashland, Oregon).

### T cell-mediated killing assay

CL141 lung cancer cells stably expressing NucLight red fluorescence protein (RFP) (#4476, Essen Bioscience) were seeded into 96-well plates and treated with anti-PD-L1 antibody (10 µg/mL) and/or pemetrexed (100 nM) for 24 hours. Cells were subsequently cocultured with activated Jurkat T-cells at the cancer cell to T cell ratio of 1:5. The fluorescence signals were detected by a SpectraMax iD3 fluorescence spectrometer (Molecular Devices).

### Syngeneic tumor model

For the CT26 tumor model, BALB/c mice aged 6–8 weeks were inoculated subcutaneously with murine CT26 ( $2 \times 10^5$ ) colon cancer cells. For the LL2 tumor model, C57BL/6 mice aged 6–8 weeks were inoculated subcutaneously with murine LL2 ( $2 \times 10^5$ ) lung cancer cells. Tumor volumes were measured at 4 or 5 days after inoculation using the formula:  $L \times D^2/2$ , where L and D are the long and short dimensions, respectively, of the tumor. Mice were injected intraperitoneally every 4 days with 3 mg/kg of antimouse PD-L1 antibody (10F.9G2, Bio X cell) or control rat IgG2b (LTF-2, Bio X cell). Mice were also injected intraperitoneally with 100 mg/kg of pemetrexed every 2 days for 2 weeks. Tumors were harvested on day 20 and fixed in formaldehyde for the immunohistochemistry (IHC) staining.

To assess the activation and/or infiltration of CD4<sup>+</sup> and CD8<sup>+</sup> TILs surrounding tumor tissues, tumors treated by monotherapy or combination therapy were harvest and analyzed by IHC staining. Details of analysis methods are fully provided in the online supplemental materials.

### RNA sequencing of the CL1-5 subclones

Using the limited dilution method, the parental CL1-5 lung cancer cells were seeded in the 96-well plate with an average of one cell per well. After 20 days of culture, subclones were expanded in RPMI-1640 medium supplemented with 10% FBS. Twenty single-cell colonies were selected as CL1-5 subclones and then treated with a sublethal dose of pemetrexed (50 nM). After 48 hours of treatment, the levels of PD-L1 protein were detected by immunoblotting. In treatment with pemetrexed (PEM), the CL1-5 subclones exhibiting elevated PD-L1 protein levels were defined as pemetrexed responders (PEM-R) while the subclones exhibiting no significant PD-L1 upregulation were defined as non-responders (PEM-NR).

For RNA sequencing and gene expression analysis, total RNA was extracted from pemetrexed-treated CL1-5 subclones. rRNA was depleted by the rRNA depletion method. Library preparation was followed by the manual protocol and paired-end reads with 150 bps were sequenced by Illumina HiSeq 4000 (Illumina). Sequencing quality and adaptor contamination were further evaluated by FASTQC (v0.11.7). Raw reads were cleaned by Trimmomatic (v0.33) for removal of adaptor sequences and lower quality bases (average quality score of 4-bases wide sliding window <20). Trimmed paired-end reads were aligned to human reference genome GRC37/hg19 using STAR2 (STAR-2.6.0c). Based on ensemble GRC37 gene annotation, gene expression was quantified by raw read counts using the htseq-count algorithm.

Before identifying differentially expressed genes between experiment groups, several preprocess steps were applied to avoid system errors. The read throughput difference was first adjusted by the trimmed mean of M-values algorithm of edgeR (R package). Next, count per million (CPM) was as gene expression unit. Genes with CPM<1 and not detected in at least two samples were excluded. Finally, logarithm 2 transformation and quantile normalization were applied before data analysis. For statistical analysis, the Log2 ratio of gene expression between the experiment and the corresponding control group was calculated. A two-sample t-test was used to identify differentially expressed genes. All tests were two-tailed and p values<0.05 were considered significant.

### ROS detection

Cells were trypsinized and resuspended in PBS containing 10 µM CM-H2DCFDA (#C6827; Invitrogen). After incubation at 37°C for 30 min in the dark, intracellular ROS levels were assessed by flow cytometry using a FACS Calibur system.

### Statistical analysis

Data are presented as the mean±SD; statistical significance was assessed via GraphPad Prism Software V.7.0; groups were compared using the t-test, with p<0.05 considered significant.



## RESULTS

### Antimetabolites, pemetrexed and 5-FU, induce PD-L1 expression in NSCLC cells in vitro and in vivo

Antitumor therapy becomes more successful when it can induce an immunogenic form of tumor cell death (ICD) that elicits a strong immune response.<sup>24,25</sup> Recently, monotherapy of the frontline NSCLC chemotherapeutics, such as pemetrexed, carboplatin and paclitaxel (PTX), have been shown to induce ICD in syngeneic mouse models with various degrees while, interestingly, only the folate antimetabolite pemetrexed show the greater potential to synergize with PD-1/PD-L1 blockade.<sup>26</sup> Although pemetrexed exerts the strongest immunogenic effects on tumor and immune cells, we noticed that pemetrexed also induced substantial levels of PD-L1 upregulation.<sup>26</sup> Knowing that higher PD-L1 expression on tumor cells associated with better responses to ICB therapy,<sup>27</sup> we attempted to assess the potential PD-L1 priming ability of pemetrexed and other frontline NSCLC chemotherapeutics in NSCLC cell lines. The half-maximal inhibitory concentration ( $IC_{50}$ ) of pemetrexed (PEM), 5-FU, cisplatin, and PTX were initially determined in the commonly used NSCLC cell lines CL1-5, CL141 and H1299<sup>22,23</sup> (online supplemental table S1). To avoid triggering massive tumor cell death, these NSCLC cell lines were treated with the corresponding sublethal doses of chemotherapeutics for 72 hours and examined for their PD-L1 levels. Interestingly, we found that protein levels of PD-L1 were elevated by pemetrexed or 5-FU in a dose-dependent manner (figure 1A), while treatment with cisplatin or PTX did not increase PD-L1 expression (online supplemental figure S1A). We further confirmed that upregulation of PD-L1 (encoded by *CD274*) by either pemetrexed or 5-FU was initiated at the transcriptional level (figure 1B). To assess whether the pemetrexed and 5-FU-induced *PD-L1* gene upregulation produces functionally and clinically targetable PD-L1 proteins, we detected the membrane-bound PD-L1 protein by anti-PD-L1 flow cytometry antibodies. NSCLC cells treated with pemetrexed or 5-FU displayed a significant increase in PD-L1 levels on the cell surface (figure 1C,D), whereas cisplatin and PTX did not give such PD-L1 priming effects (online supplemental figure S1C,D). To further confirm this indication, we assessed the pemetrexed-mediated PD-L1 priming effect in human xenograft tumors. Human CL1-5 lung cancer cells were implanted into nude mice to form subcutaneous tumors followed by the injection of pemetrexed. We found that mice treated with pemetrexed displayed a substantial increase in PD-L1 levels in the CL1-5 xenograft tumor (figure 1E), suggesting that pemetrexed may stimulate certain signaling(s) in NSCLC tumors that drive the upregulation of PD-L1. Collectively, these results suggest that the sublethal dose of antimetabolic chemotherapeutics, such as pemetrexed and 5-FU, is capable of inducing PD-L1 expression in NSCLC cells whether in vitro or in vivo.

### Pemetrexed and PD-1/PD-L1 blockade induce T-cell activation in cocultured NSCLC and T cells

The chemoimmunotherapy combination of pemetrexed, cis/carboplatin and immune checkpoint inhibitors (anti-PD-1/anti-PD-L1) has recently been approved as first-line treatment in advanced NSCLCs.<sup>19–21</sup> However, which chemotherapeutics in the chemoimmunotherapy combination exert beneficial effects and the underlying antitumor mechanism(s) still remain obscure. T-cell activation is a key indicator of ICB therapy, which can be assessed by monitoring well-known surface markers (eg, CD69) and cytokine molecules (eg, IL-2, IFN- $\gamma$ ) enriched in activated T cells in human cytotoxic T lymphocyte (CTL) or Jurkat leukemia T cell coculture systems.<sup>28</sup> To evaluate whether treatment of NSCLC cells with frontline NSCLC chemotherapeutics can modulate T-cell activation, we measured the levels of secreted IL-2 and IFN- $\gamma$  in human Jurkat T-cells or PBMCs, which include CD3<sup>+</sup> T-lymphocytes, incubated either alone or in coculture with NSCLC cells. The ELISA showed that activated Jurkat T-cells or PBMCs secreted high amounts of IL-2 and IFN- $\gamma$  into the coculture medium, whereas the ability of the T cells to produce these antitumor cytokines was substantially suppressed when cocultured with CL1-5 or CL141 cells (figure 2A–D). This is consistent with previous findings that tumor cells may hijack the immune checkpoints to inhibit or exhaust T-cell activities through the PD-1/PD-L1 pathway.<sup>29</sup> Indeed, CL1-5 and CL141 cells pretreated with pemetrexed or 5-FU displayed greater abilities to inhibit Jurkat T-cell or CTL-mediated cytokine secretion (figure 2A–D), supporting the idea that these antimetabolic chemotherapeutics are capable of inducing PD-L1 expression in tumor cells and the following T-cell suppression. In contrast, there were no detectable changes in IL-2 secretion in T cells when NSCLC cells were pretreated with chemotherapeutics (ie, cisplatin and PTX) showing no effects on PD-L1 upregulation (online supplemental figure S2A). The ICS assays further confirmed that NSCLC cells pretreated with pemetrexed or 5-FU greatly suppressed the levels of CD69 and intracellular IL-2 in human Jurkat T-cells (figure 2E–G and online supplemental figure S2C,D). To further test whether pemetrexed in combination with ICB therapy could exert antitumor activities through T-cell activation, we evaluated effects of the combined treatment of pemetrexed and anti-PD-1 antibody on T-cell activation in the NSCLC/T-cell coculture system. We found that addition of anti-PD-1 antibody or anti-PD-L1 antibody in pemetrexed-treated coculture system greatly reinvigorates the exhausted T cells by blocking the PD-1/PD-L1 interactions (online supplemental figure S2B). The effects of the combined treatment of pemetrexed and anti-PD-L1 antibody on the tumor-killing activity of T cells were also tested. CL141 cells stably expressing a nuclear RFP, NucLight RFP, were cocultured with activated Jurkat T-cells in the presence of pemetrexed and/or anti-PD-L1 antibody. By measuring the RFP signals, which represent cell viability, we found that sublethal dose of



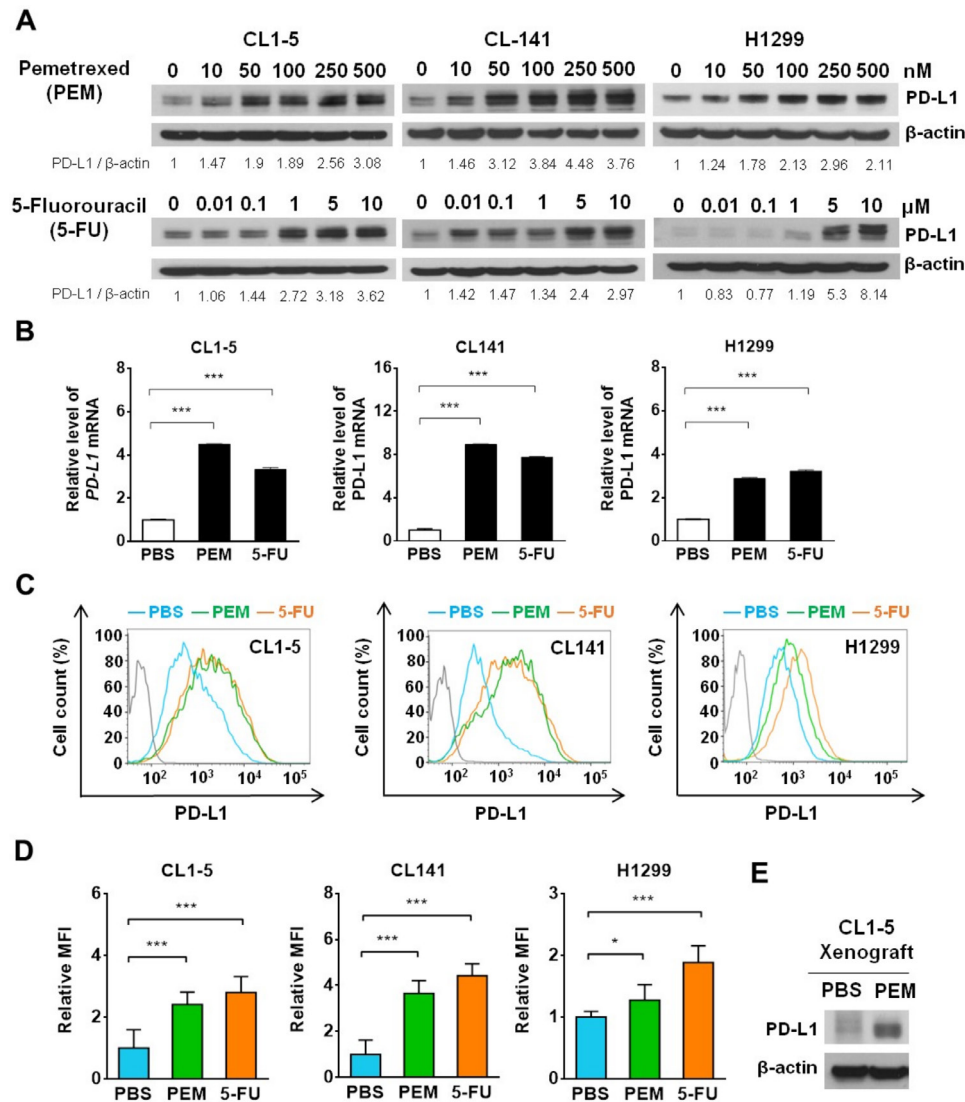


**Figure 1** Pemetrexed (PEM) and 5-fluorouracil (5-FU) upregulate programmed cell death-ligand 1 (PD-L1) expression in non-small-cell lung cancer (NSCLC) cell lines and xenograft tumors. (A) Detection of PD-L1 in NSCLC cell lines CL1-5, CL141 and H1299 treated with sublethal concentrations of PEM, 5-FU, or the vehicle control (PBS) for 72 hours by immunoblotting. The expression of β-actin serves as a loading control. The ratios between the intensity of the bands corresponding to programmed death-ligand 1 (PD-L1) and those corresponding to β-actin were calculated. (B–D) CL1-5, CL141 and H1299 cells were treated with PBS, 100 nM PEM or 5 μM 5-FU for 72 hours. Relative *PD-L1* mRNA expression levels, determined by qRT-PCR, are shown in (B). Representative histograms for PD-L1 expression levels on the cell surface of NSCLC cells obtained by flow cytometry are shown in (C). Relative mean fluorescence intensity for PD-L1 expression levels is shown in (D). (E) CL1-5 cells were subcutaneously inoculated into nude mice and intravenously injected with PEM. The tumors were harvested and PD-L1 expression levels were assessed by immunoblotting. All the data are shown as means and s.e.m. for three independent experiments (n=3). \*P<0.005 and \*\*\*p<0.001 by Student's t test.

pemetrexed only caused partial suppression of tumor cell viability (figure 2H). However, the combined treatment of pemetrexed and anti-PD-L1 antibody resulted in the synergistic inhibition of tumor cell growth (figure 2H). These findings indicate that while pemetrexed could only exert minor cytotoxic effects on tumor cells, pemetrexed-induced PD-L1 upregulation plus the subsequent PD-1/PD-L1 blockade could sensitize tumor cells to the T cell-mediated tumor cell killing. Altogether, our data suggest that pemetrexed or 5-FU-induced PD-L1 upregulation in NSCLC cells can modulate T-cell activation when combined with PD-1/PD-L1 blockade, while addition of

cisplatin or PTX did not have such immunomodulatory effects.

### Pemetrexed and PD-1/PD-L1 blockade synergistically inhibit tumor growth, increase PD-L1 expression, recruit TILs, and restore exhausted T-cell activities

The observed immunomodulatory effects of pemetrexed in combination with PD-1/PD-L1 blockade in the in vitro system prompted us to evaluate this chemioimmunotherapy combination in immunocompetent syngeneic mouse tumor models. We chose the commonly used murine Lewis lung carcinoma (LL2) and colorectal cancer cell (CT26)

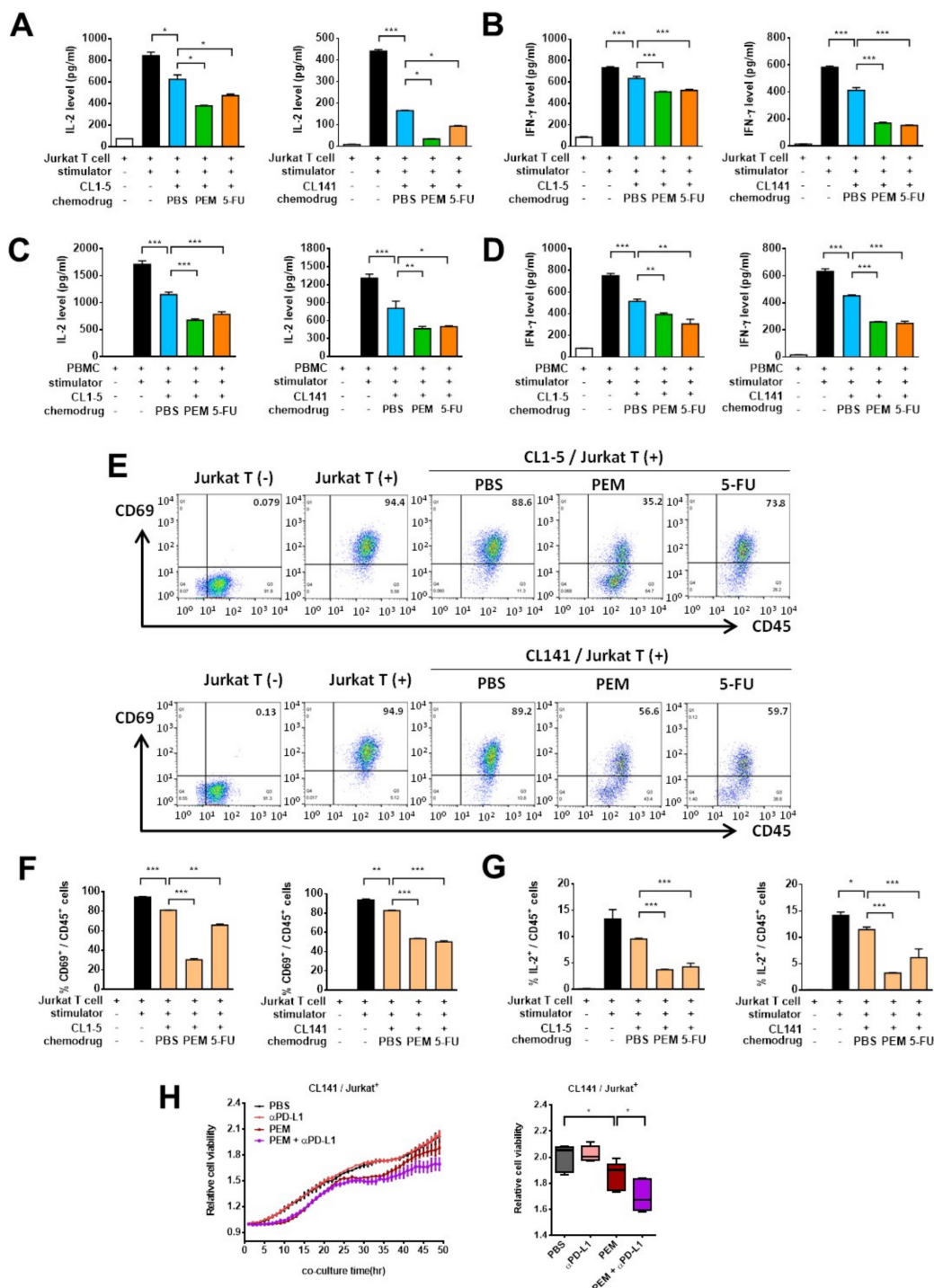


**Figure 2** Pemetrexed (PEM) and 5-fluorouracil (5-FU) suppress the production of interleukin-2 (IL-2) and interferon (IFN)- $\gamma$  by activated T cells in the non-small-cell lung cancer (NSCLC) and T cell coculture system. (A–D) CL1-5 or CL141 cells were preincubated with 100 nM PEM, 5  $\mu$ M 5-FU or the vehicle control (PBS) for 48 hours, and subsequently cocultured with activated Jurkat T-cells (A, B) or PBMCs (C, D) at different cancer to T cell ratios in the presence of 1 $\times$  T cell stimulation cocktail for additional 48 hours. The levels of IL-2 and IFN- $\gamma$  were measured by ELISA. Data are shown as means and SD for three independent experiments (n=3). (E–G) CL1-5 or CL141 cells were preincubated with 100 nM PEM, 5  $\mu$ M 5-FU or the vehicle control (PBS) for 48 hours, and subsequently cocultured with activated Jurkat T-cells in the presence of 1 $\times$  T cell stimulation cocktail for additional 48 hours. The levels of CD69 and intracellular IL-2 produced by Jurkat T-cells were measured by flow cytometry. (E) Representative dot plots for the indicated cell percentages determined by flow cytometry. (F, G) Quantitative plots for the CD69 and intracellular IL-2 staining in CD45<sup>+</sup> T-cells. (H) T-cell-mediated killing of PD-L1-expressing CL141 NSCLC cells. CL141 cells stably expressing nuclear RFP protein were pretreated with or without 50 nM PEM for 48 hours and cocultured with activated Jurkat T-cells with or without 10  $\mu$ g/mL of anti-PD-L1 antibody for additional 48 hours. Relative cell viability was measured by RFP signaling after 48 hours of cocultivation and the results were normalized at the zero-time point. Data are shown as means and s.e.m. for three independent experiments (n=3). \*P<0.005, \*\*p<0.01 and \*\*\*p<0.001 by Student's t-test.

lines and confirmed that both cell lines respond to the treatment with pemetrexed or 5-FU by membrane-bound PD-L1 protein upregulation (online supplemental figure S3A). To test the effects of pemetrexed on increasing the efficacy of ICB therapy in the mouse tumor models, we cocultured mouse LL2 or CT26 cancer cell lines with primary splenocytes derived from the mouse spleen and measured the levels of secreted IL-2 and IFN- $\gamma$  in the coculture system. Similar to the effects in human NSCLC/T cell coculture systems, we found that pemetrexed treatment significantly suppresses the splenocyte-mediated cytokine secretion (figure 3A,B). Notably, the addition of anti-PD-L1 antibody in pemetrexed-treated coculture system greatly induced splenocyte activation (figure 3A,B), confirming that the effects of the pemetrexed/anti-PD-L1 antibody combinational therapy can also be observed in the mouse tumor models. Moreover, the number of CD3<sup>+</sup> T-lymphocytes, which contains CD4<sup>+</sup> helper and CD8<sup>+</sup> cytotoxic T-cells, in the splenocyte population was greatly increased in the combinational treatment of pemetrexed and anti-PD-L1 antibody (online supplemental figure S3B). The effects of the pemetrexed/anti-PD-L1 antibody combinational therapy on tumor growth were further evaluated by monitoring the tumor sizes and the surrounding tumor microenvironment in mouse syngeneic tumor models. Although treatment with pemetrexed or anti-PD-L1 antibody showed significant tumor growth hindrance in both mouse models (ie, LL2 and CT26), the combined treatment exerted far more superior tumor suppressive effects (figure 3C,D). The tumors were harvested and assessed for PD-L1 expression and the recruitment and/or activation of CD4<sup>+</sup> and CD8<sup>+</sup> TILs. The IHC staining in tumor specimens showed substantial PD-L1 signals in tumors receiving pemetrexed (online supplemental figure 3C,D). IHC staining of CD4 in tumor specimens showed that pemetrexed treatment induced a significant increase in the number of CD4<sup>+</sup> TILs in tumor areas (figure 3E), suggesting that the tumor cytotoxic effects of pemetrexed may trigger the activation and/or recruitment of CD4<sup>+</sup> T helper cells to the tumors. Through the IHC staining, we also found that the anti-PD-L1 antibody triggered the activation and/or infiltration of CD8<sup>+</sup> T cells into tumors (figure 3E), consistent with the concept of ICB therapy. Interestingly, the combined treatment of pemetrexed and anti-PD-L1 antibody synergistically amplified the numbers of both CD4<sup>+</sup> and CD8<sup>+</sup> TILs even more in the tumor surroundings (figure 3E), indicating that the immunosuppressive tumor microenvironment has been altered through this combinational treatment. To further confirm this idea, we detected the expression levels of various anti-tumor cytokines, tumor necrosis factor (TNF)- $\alpha$ , IFN- $\gamma$  and IL-2, that have been shown to lose their expressions in exhausted TILs<sup>30 31</sup> and found that this combinational treatment induced much higher levels of IL-2, TNF- $\alpha$  and IFN- $\gamma$  in tumor areas than individual drug treatments (figure 3F).

To test the therapeutic effect platinum-based chemotherapy has when combined with pemetrexed and ICB

therapy in NSCLC treatment, we investigated whether the addition of cisplatin into the combinational treatment of pemetrexed and anti-PD-L1 antibody would exhibit an enhanced effect on the suppression of lung tumor growth in vivo. Although monotherapy with pemetrexed, cisplatin, or anti-PD-L1 antibody all showed significant tumor growth inhibition in the LL2 mouse lung tumor model, the combined treatment of pemetrexed and anti-PD-L1 antibody exerted far more superior tumor suppressive effects (figure 3G). Interestingly, there seems to be no advantage of cisplatin in the combination therapy of pemetrexed and anti-PD-L1 antibody for LL2 lung cancer treatment (figure 3G). Thus, our results indicate that the combination of antimetabolic chemotherapeutics (eg, pemetrexed) with PD-1/PD-L1 blockade (eg, anti-PD-L1 antibody) could further enhance the antitumor immune responses and restore exhausted T-cell activities, thereby priming a favorable tumor microenvironment for cancer immunotherapy.

### RNA-sequencing for NSCLC subpopulations identifies NF- $\kappa$ B signaling involved in pemetrexed-induced PD-L1 upregulation

Increasing evidence indicates that the intratumoral heterogeneity is a critical factor that leads to chemoresistance.<sup>32</sup> We speculate that the tumor heterogeneity caused different response rates to chemotherapeutics, which may also account for the failure of ICB therapy.<sup>33 34</sup>

To investigate whether NSCLC cells respond to pemetrexed treatment differently and generate drug-resistant subpopulations, we selected CL1-5-derived subclones that displayed different pemetrexed responses and classified them into two groups, PEM-R and non-responder (PEM-NR) (figure 4A,B). Interestingly, we found that the PEM-NR cell clones expressed extremely low levels of PD-L1 at both the mRNA and protein levels, and had little response, if any, to the pemetrexed-induced PD-L1 upregulation (figure 4A,B). This suggests that pemetrexed might fail to stimulate certain signaling(s) in this subpopulation that lost the ability to drive the transcriptional activation of *PD-L1* gene (ie, *CD274*). To dissect the molecular mechanisms by which pemetrexed may render distinct regulations on *PD-L1* expression depending on different cellular contexts, we performed RNA-sequencing (RNA-seq) for each CL1-5 subclone (PEM-R1, R2, NR1, or NR2) and compared transcriptome profiles between the PEM-R and PEM-NR groups. An estimate of 337 genes, which matched our criteria for upregulation in the PEM-R group and downregulation in the PEM-NR group, were identified (online supplemental figure S4A). Gene ontology enrichment analysis further identified that the NF- $\kappa$ B regulatory pathway and its related genes have significant changes in their expressions in response to pemetrexed treatment (figure 4C,D). This encouraged us to investigate the potential regulation of pemetrexed in the NF- $\kappa$ B signaling pathway.

NF- $\kappa$ B activation is tightly controlled by IKK-mediated phosphorylation of I $\kappa$ B, which normally sequesters NF- $\kappa$ B in the cytosol.<sup>35</sup> On the phosphorylation by IKK,

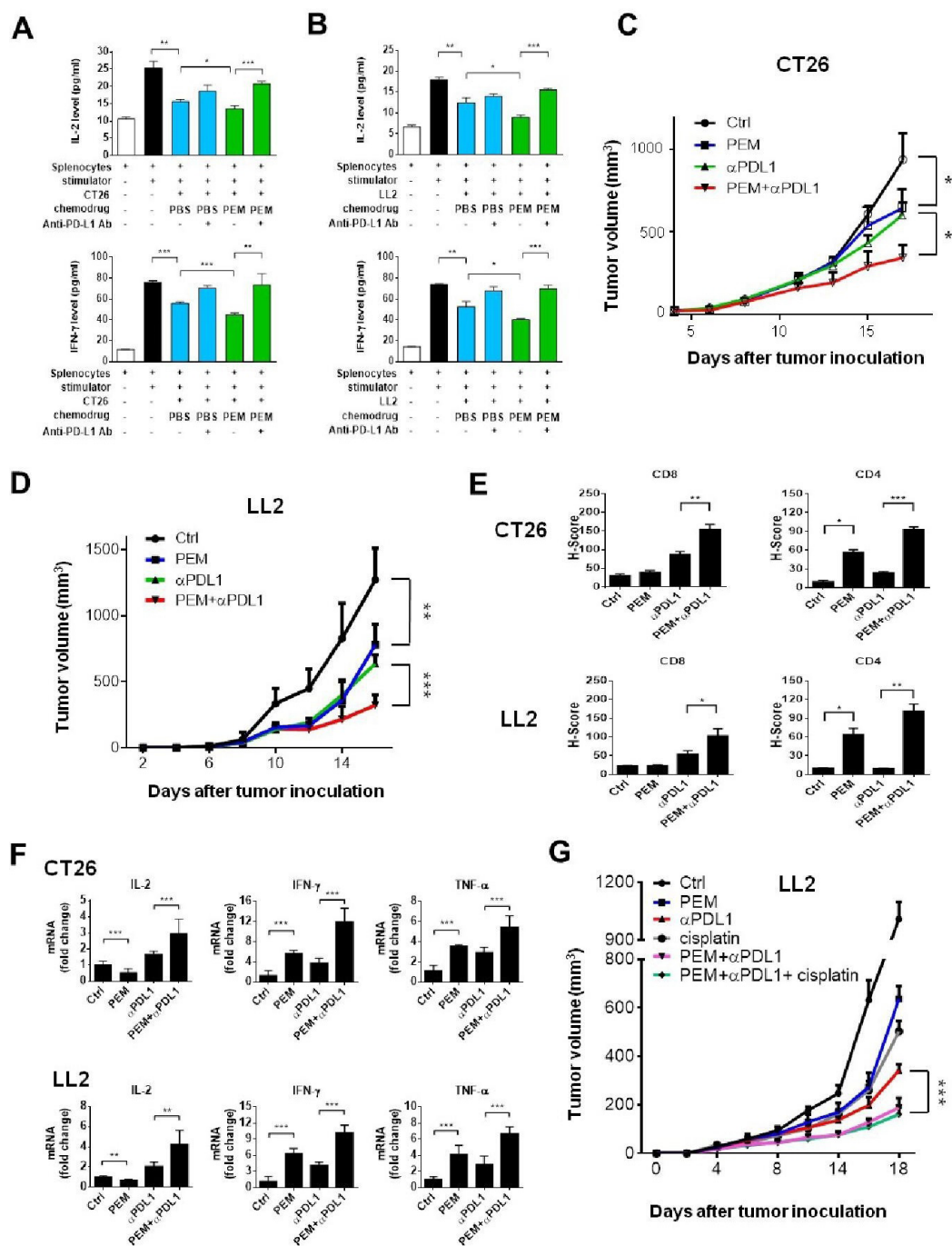


**Figure 3** Pemetrexed (PEM) promotes the efficacy of anti-programmed death-ligand 1 (PD-L1) antibody in tumor cell killing in mouse syngeneic tumor models. (A, B) Spleen was removed from wild mouse immediately after killing; erythrocytes were then lysed, and the spleen-derived lymphocytes from each mouse were then resuspended in RPMI 1640 with 10% heat-inactivated fetal bovine serum. CT26 and LL2 cells were preincubated with 100 nM PEM or the vehicle control (PBS) for 48 hours, and subsequently cocultured with activated spleen-derived lymphocytes in the presence of 1 $\times$  T cell stimulation cocktail with or without anti-programmed cell death-ligand 1 (PD-L1) antibody (10  $\mu$ g/mL) for additional 48 hours. The levels of interleukin-2 (IL-2) and interferon (IFN)- $\gamma$  were measured by ELISA. Data are shown as means and SD for three independent experiments (n=3). (C–F) The combinational treatment of PEM and anti-PD-L1 antibody inhibits tumor growth in the CT26 and LL2 mouse tumor models. Murine CT26 cells were implanted into Balb/c mice and LL2 cells were implanted into C57BL/6 mice based on their origins. Tumor volumes were measured at the indicated time points and shown in C (CT26) and D (LL2). The positive staining signals from the immunohistochemistry of CD4 and CD8 in serial sections of tumor specimens were quantified by the H-score system and shown in (E). (F) Relative mRNA expression levels of antitumor cytokines IL-2, tumor necrosis factor (TNF)- $\alpha$  and IFN- $\gamma$  in the tumor area. Total RNA was extracted from tumors in each group and relative mRNA expression levels of IL-2, TNF- $\alpha$  and IFN- $\gamma$  were determined by qRT-PCR. Data are shown as means and SD for three independent experiments (n=3). (G) Effects of different combinations of PEM (100 mg/kg), cisplatin (4 mg/kg), and anti-PD-L1 antibody (3 mg/kg) on tumor growth in the LL2 mouse tumor model.



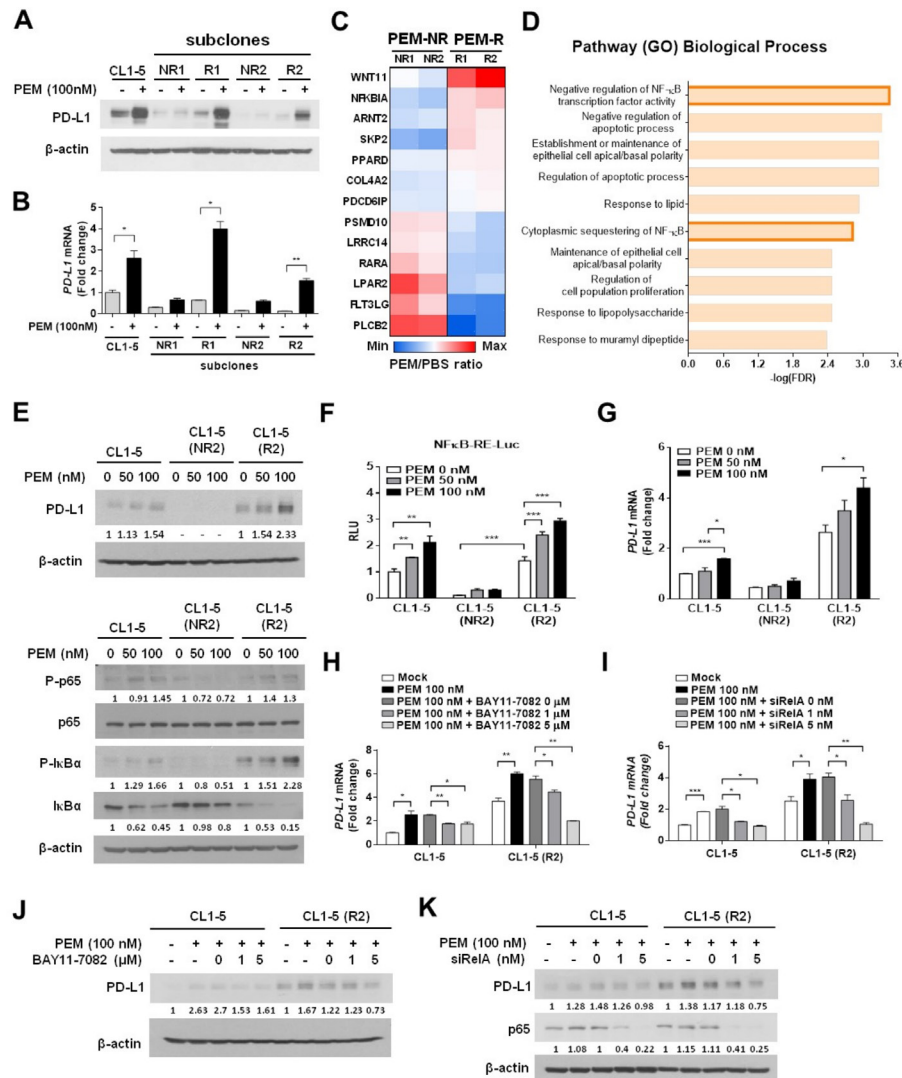


**Figure 4** NF-κB signaling acts downstream of pemetrexate (PEM) to induce the transcriptional activation of programmed death-ligand 1 (*PD-L1*) in non-small-cell lung cancer (NSCLC) cells. (A, B) *PD-L1* expression levels in two groups of CL1-5 cell subclones, PEM responder (PEM-R) and PEM non-responder (PEM-NR), in response to PEM incubation. CL1-5 subclonal cells were treated with 100nM PEM or the vehicle control (PBS) for 72 hours. The protein levels of *PD-L1* were detected by immunoblotting and shown in (A). The levels of β-actin serve as a loading control. Relative *PD-L1* mRNA expression levels, determined by qRT-PCR, are shown in B. Data are shown as means and s.e.m. for three independent experiments (n=3). (C) Heat map of representative cancer-related genes (p<0.05) from RNA-seq results between PEM-R and PEM-NR groups were identified using Kyoto Encyclopedia of Genes and Genomes (KEGG) analysis. Red and blue colors indicate increased and decreased levels, respectively. (D) The top 10 most significant terms or pathways were revealed by Search Tool for the Retrieval of Interacting Genes/Proteins (STRING) analysis. The bars represent the adjusted p value (FDR). (E) CL1-5, CL1-5/NR2 and CL1-5/R2 cells were treated with 50 or 100nM PEM or the vehicle control (PBS) for 72 hours. The expression of the indicated total or phosphorylated proteins was evaluated by immunoblotting. The levels of β-actin serve as a loading control. (F) Transcriptional activation of a NF-κB reporter gene in PEM-treated parental and subclonal CL1-5 cells. NF-κB—Luc, a NF-κB responsive promoter—reporter construct, was transfected into each CL1-5 cell clone as indicated. The luminescence signal from the NF-κB—Luc reporter (firefly luciferase) was normalized to that of cotransfected pRL-TK vector (Renilla luciferase) to control for transfection efficiency and was expressed as relative light units. Data are shown as means and SD for three independent experiments (n=3). (G) Relative mRNA expression levels of *PD-L1*, determined by qRT-PCR, in each CL1-5 cell clone in response to PEM. (H) Inhibition of NF-κB signaling impairs the PEM-induced *PD-L1* upregulation. Each CL1-5 cell clone was cotreated with PEM (100nM) and different doses of the IKK inhibitor (BAY117082) for 3 days. Total RNA was isolated and relative *PD-L1* mRNA levels were determined by qRT-PCR. The same experiment was performed and the protein levels of *PD-L1* were evaluated with immunoblotting (J). Numbers below the respective panels of the immunoblots indicate the densitometric values normalized with the relative β-actin value. (I) Knockdown of NF-κB p65 reverses the effects of PEM on the expression of *PD-L1*. CL1-5 or CL1-5/PEM-R2 cells were transfected with control-siRNA (siCtrl) or *RelA*-siRNA (siRelA) oligonucleotides for 24 hours and followed by treatment with 100nM PEM or the vehicle control (PBS) for additional 72 hours. Cells were lysed and analyzed by qRT-PCR (I) or immunoblotting (K). Data are shown as means and SD for three independent experiments (n=3). \*P<0.005, \*\*p<0.01 and \*\*\*p<0.001 by Student's t-test.



I $\kappa$ B is degraded through proteasome-mediated mechanisms, thereby releasing NF- $\kappa$ B and enabling it to enter the nucleus for its transactivation function.<sup>35,36</sup> We first investigated the effects of pemetrexed on NF- $\kappa$ B signaling by monitoring the phosphorylation status of I $\kappa$ B- $\alpha$ . Interestingly, we observed that the phosphorylated I $\kappa$ B- $\alpha$  can only be detected in pemetrexed-responsive CL1-5 subclones but not in non-responsive subclones (figure 4E and online supplemental figure S4B). The pemetrexed-induced I $\kappa$ B- $\alpha$  phosphorylation was accompanied by a significant loss of I $\kappa$ B- $\alpha$  protein and the phosphorylation of NF- $\kappa$ B p65; both events facilitate NF- $\kappa$ B to enter the nucleus and bind to the promoters of target genes.<sup>37</sup> These data strongly suggest that pemetrexed triggers the activation of NF- $\kappa$ B signaling, and thereby transactivates *PD-L1* gene expression. Supporting the idea, luciferase reporter experiments in CL1-5 subclones demonstrated that pemetrexed induced the transactivation activity of NF- $\kappa$ B in a dose-dependent manner, which is only detectable in pemetrexed-responsive CL1-5 subclones (figure 4F and online supplemental figure S4C). The mRNA expression levels of *PD-L1* in each group of CL1-5 subclones also displayed the same patterns with corresponding protein expression levels when cells responded to pemetrexed treatment (figure 4G and online supplemental figure S4D). To further confirm that the NF- $\kappa$ B signaling pathway acts downstream of pemetrexed to transactivate *PD-L1* expression, we treated the pemetrexed-responsive CL1-5 subclones with an IKK inhibitor, BAY11-7082, to suppress the phosphorylation of I $\kappa$ B- $\alpha$ . As expected, the treatment of BAY11-7082 significantly repressed the pemetrexed-induced PD-L1 expression at both the mRNA and protein levels (figure 4H,J and online supplemental figure S4E). Moreover, silencing the major subunit of NF- $\kappa$ B p65 (encoded by *RelA*) by siRNA oligonucleotides (siRelA) could also recapitulate the effects of BAY11-7082 on the pemetrexed-responsive CL1-5 subclones; as we found that the knockdown of p65 greatly suppressed the ability of pemetrexed to induce PD-L1 upregulation (figure 4I,K and online supplemental figure S4F). Taken together, we demonstrated that pemetrexed induces *PD-L1* expression through the engagement of NF- $\kappa$ B-mediated transactivation activity in NSCLC cells.

### Pemetrexed induces *PD-L1* gene transcription through the TS-ROS-NF- $\kappa$ B regulatory axis

We next sought to trace the direct target(s) of pemetrexed that is required for its PD-L1 priming activity. Since the JAK1/2 kinase family has been reported to mediate PD-L1 expression on extracellular stimulation in tumor cells,<sup>38</sup> we first investigated the effects of ruxolitinib (a JAK inhibitor) on the expression of PD-L1 in pemetrexed-treated CL1-5 and CL141 cells. Our results showed that ruxolitinib did not have any effect on pemetrexed-dependent upregulation of PD-L1 (online supplemental figure S5), suggesting that pemetrexed might regulate PD-L1 expression through a different target(s). It is also known that pemetrexed and 5-FU can inhibit DNA biosynthesis

processes by suppressing the activity of TS, an enzyme that catalyzes the transformation of deoxyuridine monophosphate to deoxythymidine monophosphate for the maintenance of DNA replication and repair, thereby inducing DNA damage in tumor cells through TS inhibition.<sup>17,39</sup> Although there is no evidence showing TS being involved in gene regulation, we tried to evaluate the possibility that TS might be the direct target of pemetrexed for regulating *PD-L1* gene expression. We performed RNAi silencing approaches to knock down the endogenous TS expression in CL1-5 and CL141 cells. We found that both mRNA and protein expression of PD-L1 significantly elevated on the knockdown of TS (figure 5A,C), suggesting that TS is capable of regulating *PD-L1* gene expression. Essentially, knockdown of TS greatly elevated membrane-bound PD-L1 levels in CL1-5 and CL141 cells (figure 5B), thereby enhancing the ability of tumor cells to suppress Jurkat T-cell or CTL activation (figure 5G). Thus, these results suggest that pemetrexed may upregulate *PD-L1* expression through the inactivation of the TS-dependent DNA synthesis pathway. The elevated PD-L1 levels on the cell surface of NSCLC cells, in turn, diminish immune responses by suppressing T-cell activation (eg, IL-2 secretion).

Since we identified that the conventional pemetrexed target TS as well as the NF- $\kappa$ B signaling, both involved in *PD-L1* gene expression, we explored whether the TS-dependent DNA synthesis pathway can crosstalk with the NF- $\kappa$ B signaling pathway. Knockdown of TS significantly induced the phosphorylation of I $\kappa$ B- $\alpha$  and NF- $\kappa$ B p65 in CL1-5 and CL141 cells, indicating that TS is capable of cross-regulating the NF- $\kappa$ B activity (figure 5D). To further confirm this idea and verify whether TS acts upstream of the NF- $\kappa$ B pathway to regulate *PD-L1* expression, we co-silenced the expression of TS and *RelA* by specific siRNA oligonucleotides in CL1-5 and CL141 cells. We found that knockdown of TS by TS-siRNA induced PD-L1 upregulation at both the mRNA and protein levels, while the effects of TS-siRNA on PD-L1 expression were abolished by the treatment of *RelA*-siRNA (figure 5E,F). This confirms that the NF- $\kappa$ B pathway acts downstream of TS for the control of PD-L1 expression.

High level of ROS in tumor cells has been connected to the activation of NF- $\kappa$ B signaling in tumor inflammation.<sup>40–42</sup> The intracellular ROS may enhance the phosphorylation of I $\kappa$ B and lead to the proteasomal degradation of I $\kappa$ B, which in turn induces the release and translocation of NF- $\kappa$ B to the nucleus to initiate transcription. Interestingly, the inhibition of TS by TS inhibitors has also been shown to increase the intracellular level of ROS.<sup>43</sup> To explore whether pemetrexed-mediated TS inhibition could increase the intracellular level of ROS and result in the activation of NF- $\kappa$ B signaling pathway, we detected intracellular levels of ROS in CL1-5 and CL141 cells on the inhibition of TS. As expected, we found that intracellular levels of ROS were significantly elevated on inhibition of TS by either pemetrexed or TS knockdown (figure 6A,B). Luciferase reporter experiments in CL1-5

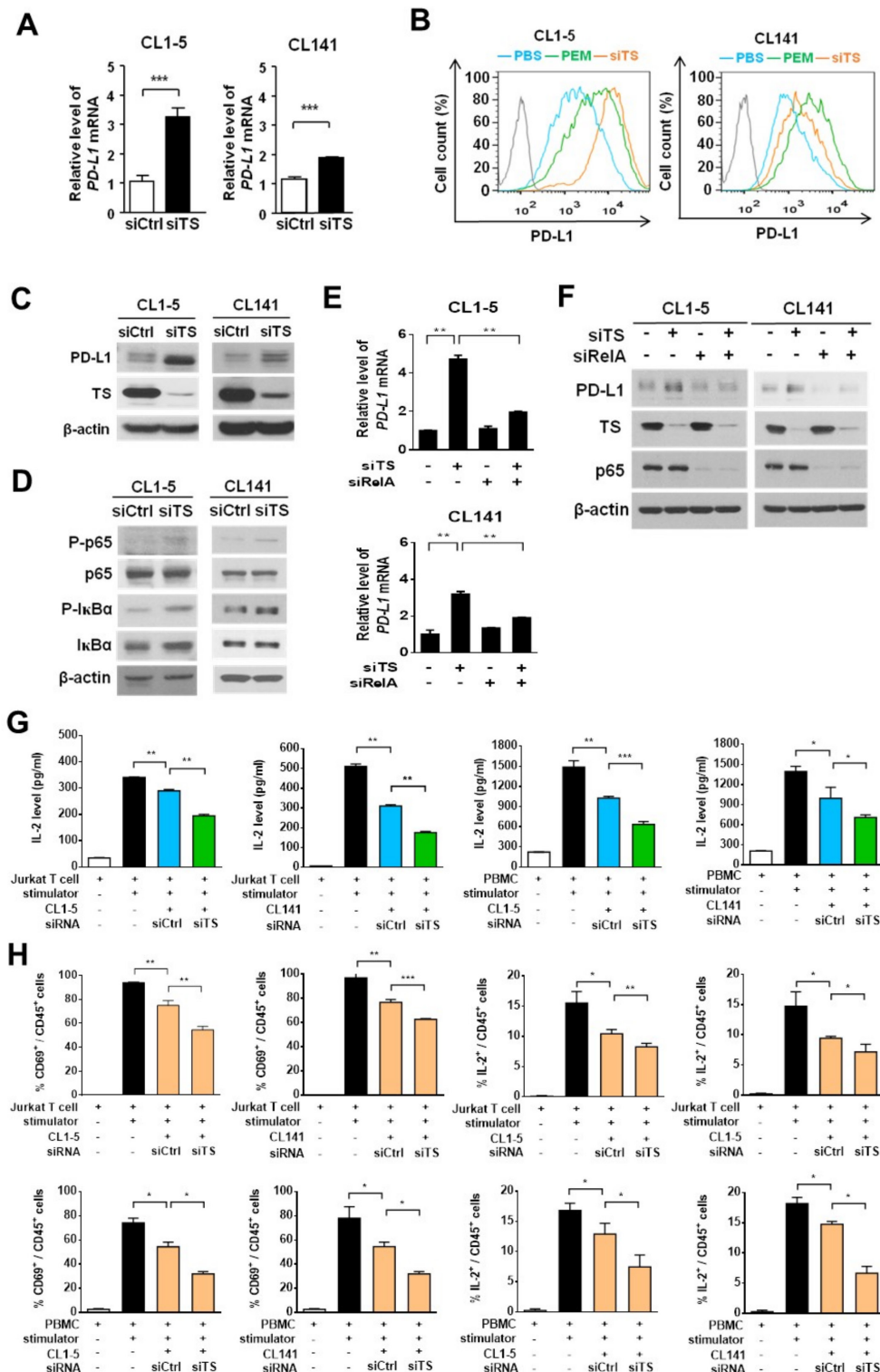


**Figure 5** Knockdown of thymidylate synthase (TS) induces programmed death-ligand 1 (PD-L1) expression in non-small-cell lung cancer (NSCLC) cells and decreases the production of interleukin-2 (IL-2) by activated T cells in the NSCLC and T cell coculture system. (A–D), CL1-5 or CL141 cells transfected with control-siRNA (siCtrl) or TS-siRNA (siTS) oligonucleotides were lysed and analyzed by qRT-PCR (A), flow cytometry (B), or immunoblotting (C, D) 72 hours after transfection. Data are shown as means and SD for three independent experiments (n=3). (E, F) CL1-5 or CL141 cells transfected with control-siRNA (siCtrl), TS-siRNA (siTS) and RelA-siRNA (siRelA) oligonucleotides in different combination were lysed and analyzed by qRT-PCR (E) or immunoblotting (F), 72 hours after transfection. (G, H) CL1-5 or CL141 cells were transfected with siCtrl or siTS siRNA oligonucleotides for 24 hours and followed by cocultured with Jurkat T-cells or PBMCs at different cancer to T cell ratios in the presence of the 1×T cell stimulation cocktail for additional 48 hours. (G) IL-2 levels were measured by ELISA. (H) The levels of CD69 and intracellular IL-2 produced by Jurkat T-cells or PBMCs were measured by flow cytometry. \*\*P<0.01 and \*\*\*p<0.001 by Student's t test.

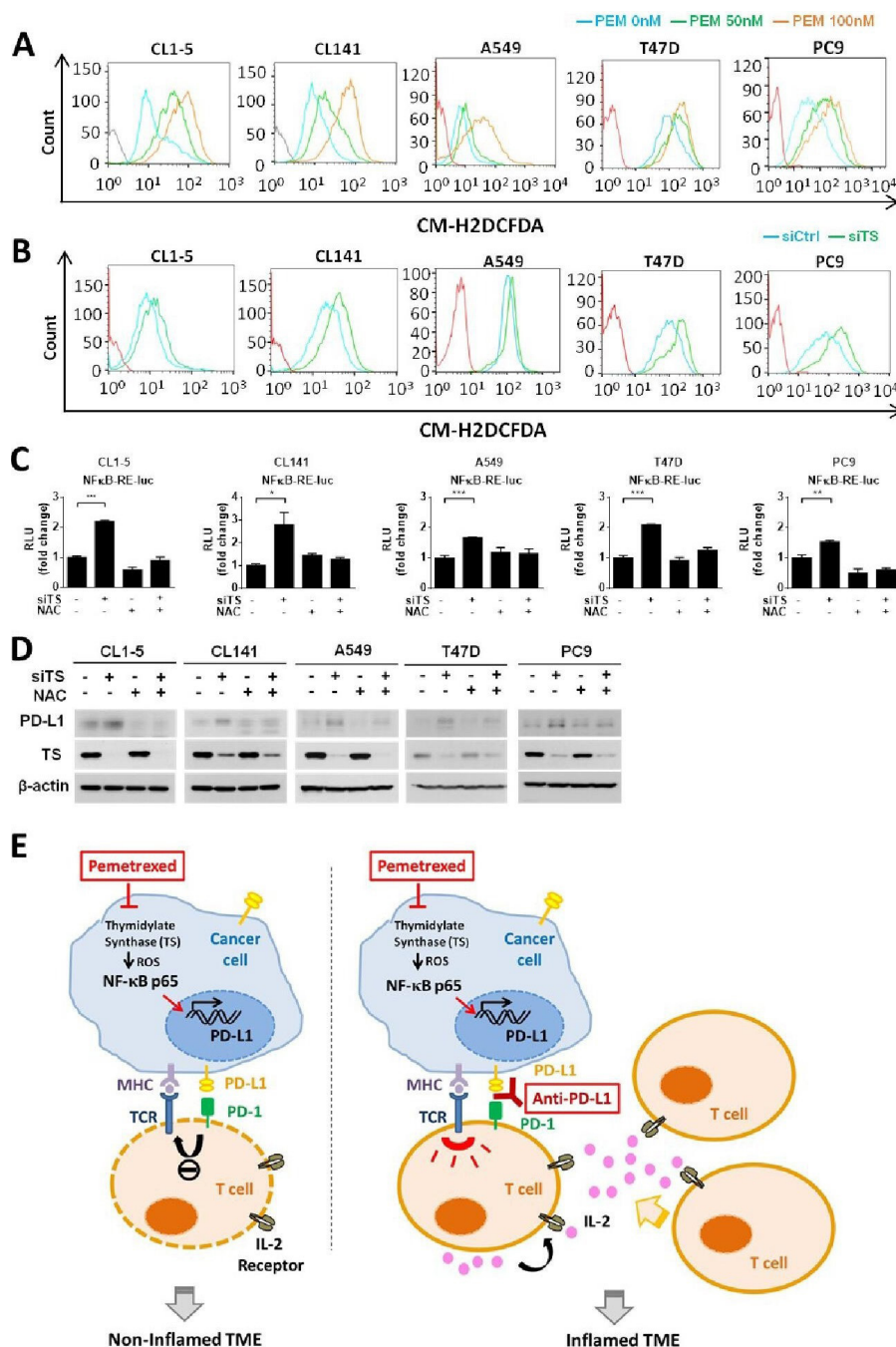


**Figure 6** The thymidylate synthase (TS)–reactive oxygen species (ROS)–NF-κB regulatory axis mediates pemetrexed (PEM)-induced programmed death-ligand 1 (PD-L1) upregulation. (A, B) CL1-5, CL141, A549, T47D or PC9 cells were treated with PEM (50 or 100 nM) alone or in combination with control siRNA (siCtrl) or TS-siRNA (siTS) for 24 hours, followed by incubation with the DCFDA fluorogenic dye (10 μM) for 30 min. The levels of ROS were assessed by flow cytometry. (C) CL1-5, CL141, A549, T47D or PC9 cells transfected with the NF-κB–Luc reporter plasmid in combination with control siRNA (siCtrl) or TS-siRNA (siTS) were treated with N-acetylcysteine (NAC) (5 mM) or left untreated, for 72 hours. The luminescence signal from the NF-κB–Luc reporter (firefly luciferase) was normalized to that of cotransfected pRL-TK vector (Renilla luciferase) to control for transfection efficiency and was expressed as relative light units. Data are shown as means and SD for three independent experiments (n=3). (D) CL1-5, CL141, A549, T47D or PC9 cells transfected with control siRNA (siCtrl) or TS-siRNA (siTS) were treated with NAC (5 mM) or left untreated, for 72 hours. Cells were lysed and analyzed by immunoblotting with the indicated antibodies. (E) Proposed model illustrating the molecular basis of the combinational treatment of PEM and anti-PD-L1 antibody in non-small-cell lung cancer (NSCLC). PEM induces the inhibition of TS, which in turn increases intracellular levels of ROS and results in the activation of NF-κB signaling pathway. NF-κB then transactivates *PD-L1* expression and increases the levels PD-L1 on the cell surface of tumor cells. The upregulation of PD-L1 expression in tumor cells may suppress T-cell activation through the PD-L1/PD-1 engagement and lead to non-T-cell-inflamed tumor microenvironment (left). However, the combinational treatment of PEM and anti-PD-1/PD-L1 antibodies reactivates T-cell activities and improves effector function (right). MHC, major histocompatibility complex; TCR, T-cell receptor; IL-2, Interleukin-2; TME, tumor microenvironment.



and CL141 cells further demonstrated that knockdown of TS induced the transactivation activity of NF- $\kappa$ B, while the effects of TS-knockdown on NF- $\kappa$ B could be rescued when the intracellular ROS was effectively scavenged by the antioxidant, N-acetylcysteine (NAC) (figure 6C). Additionally, we demonstrated that 5-FU, an antimetabolic chemotherapeutic that is also known to target TS and inhibit DNA biosynthesis, has the potential to increase the intracellular level of ROS and result in the activation of NF- $\kappa$ B signaling pathway in NSCLC cells (online supplemental figure 6A-C). These data indicate that anti-metabolites, pemetrexed and 5-FU, can induce the activation of NF- $\kappa$ B signaling by regulating the activity of TS and the intracellular level of ROS. To further confirm that this TS-ROS-NF- $\kappa$ B regulatory axis contributes to the upregulation of PD-L1 in NSCLC cells, we checked the PD-L1 level in this scenario. Indeed, knockdown of TS promoted PD-L1 upregulation in CL1-5 and CL141 cells, while the effects can be abolished if the intracellular ROS is reduced effectively by NAC (figure 6D). To further confirm that the TS-ROS-NF- $\kappa$ B regulatory axis is actively involved in the activation of *PD-L1* transcription in tumor cells, we selected A549, PC9 human lung cancer and T47D human breast cancer cell lines that are known not to express PD-L1<sup>44 45</sup> (online supplemental figure S7A), and tested the effects of TS inhibition on these tumor cells by either pemetrexed or TS knockdown. We found that pemetrexed greatly induced the intracellular level of ROS in A549, PC9 and T47D cells (figure 6A). Consistently, knockdown of TS induced the intracellular level of ROS, the transactivation activity of NF- $\kappa$ B, as well as PD-L1 levels in these cancer cell lines while the effects of TS inhibition could be significantly abolished by the antioxidant NAC (figure 6B-D and online supplemental figure S7B). These results strongly support a general function of the TS-ROS-NF- $\kappa$ B regulatory axis in transcriptional regulation of *PD-L1* in tumor cells.

In conclusion, our results indicate that pemetrexed can induce PD-L1 upregulation in human NSCLC cells by regulating the TS-ROS-NF- $\kappa$ B regulatory axis and prime a favorable tumor microenvironment for ICB therapy (figure 6E).

## DISCUSSION

The folate antimetabolite pemetrexed is one of the most commonly used chemotherapeutics in NSCLC treatment. Recently, the combination of pemetrexed-based chemotherapy and ICB therapy has demonstrated persuasive clinical activity in patients with NSCLC with cancer metastasis. These clinical results led to the initial accelerated approval of this chemoimmunotherapy combination for patients with advanced NSCLC.<sup>19 20</sup> Although this novel combinatory therapy has become first-line treatment in advanced NSCLC, very little is known about the underlying antitumor mechanisms of pemetrexed in combination with immunotherapy. In the present study, we show that pemetrexed, but not the other commonly used

chemotherapeutics (eg, cisplatin and PTX), is capable of inducing PD-L1 expression in NSCLC cells that further primes the tumor microenvironment favorable to the ICB therapy. We find that pemetrexed and anti-PD-1/PD-L1 antibody synergistically induce T-cell activation in vitro and in vivo, mainly through restoring the exhausted T-cell activities. Additionally, we reveal a novel molecular mechanism of how pemetrexed induces PD-L1 upregulation in tumor cells. Pemetrexed suppresses the activity of TS and in turn increases the intracellular level of ROS, which further triggers the NF- $\kappa$ B signaling pathway and the following activation of *PD-L1* gene transcription in NSCLC cells. Interestingly, pemetrexed fails to trigger *PD-L1* transcriptional activation in a subpopulation of NSCLC cells where the NF- $\kappa$ B signaling pathway is unregulated. Thus, the role of pemetrexed in the aforementioned chemoimmunotherapy may need to be reinterpreted by the thought that pemetrexed can exert immunomodulatory effects through multiple pathways (discussed next). Furthermore, the differential responses of tumor cells from individual patients to the pemetrexed-induced PD-L1 expression may need to be analyzed for the pemetrexed-based immunotherapy.

It is now clear that tumor cells escape immune surveillance and attack by upregulating the expression of PD-L1, which can interact with the immunosuppressive molecule PD-1 on T cells to inhibit the function of T cells and induce T-cell exhaustion.<sup>11 46</sup> Through the inhibition of PD-1/PD-L1 interaction, monoclonal antibodies targeting PD-1 or PD-L1 have shown potent efficacy in reducing immunosuppressive signals within the tumor microenvironment and in increasing T cell-mediated antitumor immunity.<sup>47</sup> Here, we demonstrate that the beneficial effects of pemetrexed in the FDA approval chemoimmunotherapy<sup>19-21</sup> are mediated, at least in part, by its ability to upregulate the expression of PD-L1 in NSCLC cells and synergize with PD-1/PD-L1 blockade to restore exhausted T-cell activities. TILs, CD4<sup>+</sup> and CD8<sup>+</sup> T cells, can secrete antitumor cytokines such as IL-2, TNF- $\alpha$  and IFN- $\gamma$ , while the effector activities for producing these cytokines could be extinguished due to T-cell exhaustion.<sup>30 31</sup> Our data from the NSCLC/T cell coculture systems and syngeneic mouse models indicate that pemetrexed alone suppresses the ability of T cells to produce IL-2 and IFN- $\gamma$  because of PD-L1 upregulation, while the levels of IL-2 and IFN- $\gamma$  can be restored or even further enhanced in the combinational treatment of pemetrexed and anti-PD-1/PD-L1 antibodies. We also demonstrate that pemetrexed can synergize with PD-1/PD-L1 blockade to enhance the production of IL-2, TNF- $\alpha$  and IFN- $\gamma$  within the tumor microenvironment in the mouse syngeneic models. Interestingly, pemetrexed alone is capable of inducing the production of IL-2, TNF- $\alpha$  and IFN- $\gamma$  in the tumor area, suggesting that the cytotoxic effects of pemetrexed on tumor cells may also activate antigen-presenting cells (APCs), such as macrophages and dendritic cells, or other effector cells, such as natural killer cells, that are known to produce TNF- $\alpha$

and IFN- $\gamma$ .<sup>48 49</sup> More interestingly, our data indicates that platinum-based chemotherapy, for example, cisplatin, cannot induce the expression of PD-L1 in NSCLC cells and provides no advantage in the combinatory therapy of pemetrexed and anti-PD-L1 antibody for lung cancer treatment. This strongly suggests that pemetrexed can possibly be combined with ICB therapy without platinum-based chemotherapy. Further clinical investigations are therefore needed to test the potential of pemetrexed alone in combination with ICB therapy.

Although we show that pemetrexed primes a favorable tumor microenvironment for ICB therapy via inducing PD-L1 expression in tumor cells, another possible mechanism can be attributed to the cytotoxic effects of pemetrexed in inducing immunogenic cell death (ICD). ICD induces the chronic exposure of immune-stimulating factors from dying tumor cells, which activates APCs to induce T-cell priming and antitumor adaptive immunity.<sup>24 25</sup> Indeed, Schaer *et al* recently reported that pemetrexed monotherapy resulted in upregulation of multiple immune-related genes and increased T-cell activation in mouse MC38 and Colon26 colorectal tumor models via inducing ICD in mouse tumor cells.<sup>26</sup> Consistent with previous observations, our data show that pemetrexed induces significant increase in the number of CD4<sup>+</sup> cells infiltrating the tumors in mouse CT26 colorectal and LL2 lung tumor models. Additionally, our RNA-seq data finds the level of MHC class II genes, for example, HLA-DQB1 and HLA-DMA, being upregulated in pemetrexed-responsive CL1-5 subclones (data not shown). Thus, our findings indicate that pemetrexed could also induce ICD and trigger CD4<sup>+</sup> T helper cells to infiltrate tumors. The ICD induction could also be attributed to the pemetrexed-induced ROS production, which is known to target the endoplasmic reticulum (ER) and induce ER stress.<sup>50</sup> More importantly, we find that the pemetrexed-induced ROS production triggers NF- $\kappa$ B signaling and induces the transcriptional activation of *PD-L1* gene. Our findings therefore suggest that pemetrexed may exert a dual role in facilitating ICB therapy; pemetrexed can induce ICD to activate APCs and trigger the tumor infiltration of CD4<sup>+</sup> T helper cells, and also induce the expression of PD-L1 in tumor cells that boosts the effects of ICB on the activation of CD8<sup>+</sup> cytotoxic T cells.

Several studies indicate that high expression of the conventional pemetrexed target, TS, is associated with pemetrexed resistance.<sup>51–53</sup> However, these observations cannot fully explain the phenomena observed in clinical NSCLC samples,<sup>54</sup> raising the possibility that other mechanism(s) might exist, which can be responsible for pemetrexed resistance. We demonstrate here that the NF- $\kappa$ B signaling pathway plays an essential role in the transcriptional activation of *PD-L1* in NSCLC cells, and such signaling regulation can be triggered by the pemetrexed-induced ROS production. Interestingly, we also identify a subpopulation of lung cancer cells that does not respond to the pemetrexed-induced PD-L1 upregulation with its

NF- $\kappa$ B signaling pathway unregulated. The unregulated NF- $\kappa$ B signaling might be due to the dysfunction of IKK, an upstream kinase for the phosphorylation of I $\kappa$ B and the subsequent proteasomal degradation, in such lung cancer subpopulation where the I $\kappa$ B level is relatively high and the phosphorylation of I $\kappa$ B cannot be induced on pemetrexed stimulation (figure 4E and online supplemental figure S4B). Thus, the potential role of IKK or other upstream regulators of NF- $\kappa$ B signaling in the pemetrexed-resistance mechanism may be considered and warrants further investigation.

Although the pemetrexed-induced ROS accumulation might also cause cellular DNA damage and affect the stages of cell cycle, we found that there is no significant change in the cell stages of NSCLC cells (eg, H1299, CL141, CL1-5 parental, R1, R2, NR1, and NR2) in response to pemetrexed (online supplemental figure S8A). Our data indicate that the sublethal dose (50 or 100 nM) of pemetrexed may only cause the induction of *PD-L1* transcription via the TS-ROS-NF- $\kappa$ B regulatory axis but not affect cell stages, such as cell apoptosis and cell cycle arrest. Interestingly, we found that the stages of the cell cycle in pemetrexed non-responsive CL1-5 subclones (PEM-NR1, NR2) are different to that in pemetrexed-responsive subclones (PEM-R1, R2). Our results showed an increased percentage of cells in G1 phase and a decreased percentage of cells in S phase in non-responsive subclones (NR1, NR2) as compared with the responsive subclones (R1, R2) (online supplemental figure S8B). It is consistent with previous findings that NF- $\kappa$ B is capable of promoting G1/S transition while overexpression of I $\kappa$ B- $\alpha$  or inactivation of NF- $\kappa$ B causes a retarded G1/S transition.<sup>55 56</sup> Although we found that cell cycle regulation of the pemetrexed-responsive and non-responsive NSCLC subpopulations may be different due to differential NF- $\kappa$ B activities, whether pemetrexed effects differentially to a specific cell stage of NSCLC might warrant further investigation.

The roles of NF- $\kappa$ B signaling in cancer have been linked to cancer progression via its function in preventing apoptosis and enhancing cell proliferation.<sup>57 58</sup> Our data reveal that antimetabolites, pemetrexed and 5-FU, are capable of inducing the transcriptional activation of *PD-L1* via the TS-ROS-NF- $\kappa$ B regulatory axis in NSCLC cells, providing an additional linkage between NF- $\kappa$ B signaling and chemotherapy-induced immunosuppression. Consistent with our findings, Peng *et al* reported that PTX and gemcitabine can upregulate *PD-L1* gene expression in ovarian cancer cells via increasing cellular NF- $\kappa$ B p65 protein, which fosters consequently an immunosuppressive tumor microenvironment in ovarian cancer.<sup>59</sup> Together our results indicate that NF- $\kappa$ B can exert its transactivation function to activate *PD-L1* gene expression in cancer cells, while the mechanism of action of chemotherapeutic agents in the induction of NF- $\kappa$ B signaling could be variant and dependent on specific cellular contexts.



Our findings provide new insights into the molecular mechanism by which pemetrexed induces PD-L1 upregulation in tumor cells through the TS-ROS-NF- $\kappa$ B regulatory axis. It also offers an indication to avoid unnecessary treatments for lung cancer patients due to cisplatin providing no advantage in the combinatory therapy of pemetrexed and anti-PD-L1 antibody.

## CONCLUSIONS

In this study, we found that pemetrexed, instead of the platinum analog cisplatin, can improve PD-L1 expression in advanced NSCLC cells through the inactivation of TS follow by the accumulation of intracellular ROSs and activation of the NF- $\kappa$ B pathway. By using syngeneic tumor models, we confirmed that the combinatory treatment of pemetrexed (without cisplatin) with PD-1/PD-L1 blockage antibodies is sufficient to inhibit tumor growth through the activation and/or recruitment of tumor-infiltrating CD4 and CD8 T-lymphocytes. Our results provide fundamental insights into the regulatory mechanism of pemetrexed in the improvement of ICB therapy in lung cancer treatment.

## Author affiliations

<sup>1</sup>Department of Internal Medicine, National Taiwan University Hospital, National Taiwan University College of Medicine, Taipei, Taiwan

<sup>2</sup>Institute of Biomedical Sciences, Academia Sinica, Taipei, Taiwan

<sup>3</sup>Institute of Statistical Science, Academia Sinica, Taipei, Taiwan

<sup>4</sup>Tissue Bank, Chang Gung Memorial Hospital; Graduate Institute of Health Industry Technology and Research Center for Industry of Human Ecology, College of Human Ecology, Chang Gung University of Science and Technology, Taoyuan, Taiwan

<sup>5</sup>Institute of Biomedical Sciences and Genomics Research Center, Academia Sinica, Taipei, Taiwan

**Contributors** S-PW and P-CY directed the project, wrote the paper and contributed equally to this work. C-SL and C-WL performed and analyzed most of the experiments, and contributed equally to this work. Y-HC, H-YC, W-CC, W-YL, C-CH, T-HW, C-YC, and C-LY provided reagents and materials, and performed data analysis. The first draft of the manuscript was written by C-SL and C-WL with review and revision by S-PW, P-CY and SW.

**Funding** This work was supported by grants from Ministry of Science and Technology (MOST-108-3114-Y-001-002, MOST-109-2314-B-002-254, MOST-109-2314-B-002-277, MOST-108-2320-B-001-007-MY2, MOST-108-2319-B-492-001, MOST-109-0210-01-18-02) and Academia Sinica (AS-SUMMIT-109, AS-KPQ-109-BioMed, 2325-1080010) in Taiwan.

**Competing interests** None declared.

**Patient consent for publication** Not required.

**Ethics approval** The protocol was approved by the Institutional Review Board at National Taiwan University Hospital. All animal experiments were performed in accordance with the animal guidelines of the Department of Animal Care, Institute of Biomedical Sciences, Academia Sinica, Taipei, Taiwan (Approve No. 2011099).

**Provenance and peer review** Not commissioned; externally peer reviewed.

**Data availability statement** Data are available upon reasonable request.

**Supplemental material** This content has been supplied by the author(s). It has not been vetted by BMJ Publishing Group Limited (BMJ) and may not have been peer-reviewed. Any opinions or recommendations discussed are solely those of the author(s) and are not endorsed by BMJ. BMJ disclaims all liability and responsibility arising from any reliance placed on the content. Where the content includes any translated material, BMJ does not warrant the accuracy and reliability of the translations (including but not limited to local regulations, clinical guidelines, terminology, drug names and drug dosages), and is not responsible for any error and/or omissions arising from translation and adaptation or otherwise.

**Open access** This is an open access article distributed in accordance with the Creative Commons Attribution 4.0 Unported (CC BY 4.0) license, which permits others to copy, redistribute, remix, transform and build upon this work for any purpose, provided the original work is properly cited, a link to the licence is given, and indication of whether changes were made. See <https://creativecommons.org/licenses/by/4.0/>.

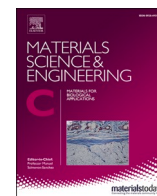
## ORCID iD

Pan-Chyr Yang <http://orcid.org/0000-0001-6330-6048>

## REFERENCES

- 1 Siegel RL, Miller KD, Jemal A. Cancer statistics, 2019. *CA Cancer J Clin* 2019;69:7–34.
- 2 Darvin P, Toor SM, Sasidharan Nair V, Nair S V, *et al.* Immune checkpoint inhibitors: recent progress and potential biomarkers. *Exp Mol Med* 2018;50:1–11.
- 3 Camidge DR, Doebele RC, Kerr KM. Comparing and contrasting predictive biomarkers for immunotherapy and targeted therapy of NSCLC. *Nat Rev Clin Oncol* 2019;16:341–55.
- 4 Kazandjian D, Suzman DL, Blumenthal G, *et al.* Fda approval summary: nivolumab for the treatment of metastatic non-small cell lung cancer with progression on or after platinum-based chemotherapy. *Oncologist* 2016;21:634–42.
- 5 Pai-Scherf L, Blumenthal GM, Li H, *et al.* Fda approval summary: pembrolizumab for treatment of metastatic non-small cell lung cancer: first-line therapy and beyond. *Oncologist* 2017;22:1392–9.
- 6 Suzman DL, Agrawal S, Ning Y-M, *et al.* Fda approval summary: Atezolizumab or pembrolizumab for the treatment of patients with advanced urothelial carcinoma ineligible for cisplatin-containing chemotherapy. *Oncologist* 2019;24:563–9.
- 7 Herbst RS, Soria J-C, Kowanetz M, *et al.* Predictive correlates of response to the anti-PD-L1 antibody MPDL3280A in cancer patients. *Nature* 2014;515:563–7.
- 8 Hirano F, Kaneko K, Tamura H, *et al.* Blockade of B7-H1 and PD-1 by monoclonal antibodies potentiates cancer therapeutic immunity. *Cancer Res* 2005;65:1089–96.
- 9 Herbst RS, Baas P, Kim D-W, *et al.* Pembrolizumab versus docetaxel for previously treated, PD-L1-positive, advanced non-small-cell lung cancer (KEYNOTE-010): a randomised controlled trial. *Lancet* 2016;387:1540–50.
- 10 Garon EB, Rizvi NA, Hui R, *et al.* Pembrolizumab for the treatment of non-small-cell lung cancer. *N Engl J Med* 2015;372:2018–28.
- 11 Konishi J, Yamazaki K, Azuma M, *et al.* B7-H1 expression on non-small cell lung cancer cells and its relationship with tumor-infiltrating lymphocytes and their PD-1 expression. *Clin Cancer Res* 2004;10:5094–100.
- 12 Fehrenbacher L, Spira A, Ballinger M, *et al.* Atezolizumab versus docetaxel for patients with previously treated non-small-cell lung cancer (poplar): a multicentre, open-label, phase 2 randomised controlled trial. *Lancet* 2016;387:1837–46.
- 13 van der Woude LL, Gorris MAJ, Halilovic A, *et al.* Migrating into the tumor: a roadmap for T cells. *Trends Cancer* 2017;3:797–808.
- 14 Bracci L, Schiavoni G, Sistigu A, *et al.* Immune-Based mechanisms of cytotoxic chemotherapy: implications for the design of novel and rationale-based combined treatments against cancer. *Cell Death Differ* 2014;21:15–25.
- 15 Heinhuis KM, Ros W, Kok M, *et al.* Enhancing antitumor response by combining immune checkpoint inhibitors with chemotherapy in solid tumors. *Ann Oncol* 2019;30:219–35.
- 16 Yan Y, Kumar AB, Finnes H, *et al.* Combining immune checkpoint inhibitors with conventional cancer therapy. *Front Immunol* 2018;9:9.
- 17 Hanauske AR, Chen V, Paoletti P, *et al.* Pemetrexed disodium: a novel antifolate clinically active against multiple solid tumors. *Oncologist* 2001;6:363–73.
- 18 Stinchcombe TE, Borghaei H, Barker SS, *et al.* Pemetrexed with platinum combination as a backbone for targeted therapy in non-small-cell lung cancer. *Clin Lung Cancer* 2016;17:1–9.
- 19 Langer CJ, Gadgil SM, Borghaei H, *et al.* Carboplatin and pemetrexed with or without pembrolizumab for advanced, non-squamous non-small-cell lung cancer: a randomised, phase 2 cohort of the open-label KEYNOTE-021 study. *Lancet Oncol* 2016;17:1497–508.
- 20 Gandhi L, Rodríguez-Abreu D, Gadgeel S, *et al.* Pembrolizumab plus chemotherapy in metastatic non-small-cell lung cancer. *N Engl J Med* 2018;378:2078–92.
- 21 Papadimitrakopoulou V, Cobo M, Bordon R, *et al.* OA05.07 IMPower132: pfs and safety results with 1L Atezolizumab +

- Carboplatin/Cisplatin + pemetrexed in stage IV non-squamous NSCLC. *J Thorac Oncol* 2018;13:S332–3.
- 22 Yeh C-T, Wu ATH, Chang PM-H, *et al.* Trifluoperazine, an antipsychotic agent, inhibits cancer stem cell growth and overcomes drug resistance of lung cancer. *Am J Respir Crit Care Med* 2012;186:1180–8.
  - 23 Chu YW, Yang PC, Yang SC, *et al.* Selection of invasive and metastatic subpopulations from a human lung adenocarcinoma cell line. *Am J Respir Cell Mol Biol* 1997;17:353–60.
  - 24 Green DR, Ferguson T, Zitvogel L, *et al.* Immunogenic and tolerogenic cell death. *Nat Rev Immunol* 2009;9:353–63.
  - 25 Galluzzi L, Buqué A, Kepp O, *et al.* Immunogenic cell death in cancer and infectious disease. *Nat Rev Immunol* 2017;17:97–111.
  - 26 Schaer DA, Geeganage S, Amaladas N, *et al.* The folate pathway inhibitor pemetrexed pleiotropically enhances effects of cancer immunotherapy. *Clin Cancer Res* 2019;25:7175–88.
  - 27 Reck M, Rodríguez-Abreu D, Robinson AG, *et al.* Pembrolizumab versus chemotherapy for PD-L1-positive non-small-cell lung cancer. *N Engl J Med* 2016;375:1823–33.
  - 28 Schwarz EM, Salgame P, Bloom BR. Molecular regulation of human interleukin 2 and T-cell function by interleukin 4. *Proc Natl Acad Sci U S A* 1993;90:7734–8.
  - 29 Zou W, Chen L. Inhibitory B7-family molecules in the tumour microenvironment. *Nat Rev Immunol* 2008;8:467–77.
  - 30 Wherry EJ. T cell exhaustion. *Nat Immunol* 2011;12:492–9.
  - 31 Yi JS, Cox MA, Zajac AJ. T-Cell exhaustion: characteristics, causes and conversion. *Immunology* 2010;129:474–81.
  - 32 Pribluda A, de la Cruz CC, Jackson EL. Intratumoral heterogeneity: from diversity comes resistance. *Clin Cancer Res* 2015;21:2916–23.
  - 33 Seth S, Li C-Y, Ho I-L, *et al.* Pre-Existing functional heterogeneity of tumorigenic compartment as the origin of chemoresistance in pancreatic tumors. *Cell Rep* 2019;26:1518–32.
  - 34 Jia Q, Wu W, Wang Y, *et al.* Local mutational diversity drives intratumoral immune heterogeneity in non-small cell lung cancer. *Nat Commun* 2018;9:5361.
  - 35 Beg AA, Baldwin AS. The I kappa B proteins: multifunctional regulators of rel/NF-kappa B transcription factors. *Genes Dev* 1993;7:2064–70.
  - 36 Karin M, Yamamoto Y, Wang QM. The IKK NF-kappa B system: a treasure trove for drug development. *Nat Rev Drug Discov* 2004;3:17–26.
  - 37 Pahl HL. Activators and target genes of Rel/NF-kappaB transcription factors. *Oncogene* 1999;18:6853–66.
  - 38 Garcia-Diaz A, Shin DS, Moreno BH, *et al.* Interferon receptor signaling pathways regulating PD-L1 and PD-L2 expression. *Cell Rep* 2017;19:1189–201.
  - 39 Longley DB, Harkin DP, Johnston PG. 5-Fluorouracil: mechanisms of action and clinical strategies. *Nat Rev Cancer* 2003;3:330–8.
  - 40 Morgan MJ, Liu Z-gang, Liu ZG. Crosstalk of reactive oxygen species and NF-κB signaling. *Cell Res* 2011;21:103–15.
  - 41 Nakanishi C, Toi M. Nuclear factor-kappaB inhibitors as sensitizers to anticancer drugs. *Nat Rev Cancer* 2005;5:297–309.
  - 42 Nathan C, Cunningham-Bussell A. Beyond oxidative stress: an Immunologist's guide to reactive oxygen species. *Nat Rev Immunol* 2013;13:349–61.
  - 43 Ozer U, Barbour KW, Clinton SA, *et al.* Oxidative stress and response to thymidylate Synthase-Targeted antimetabolites. *Mol Pharmacol* 2015;88:970–81.
  - 44 Chen N, Fang W, Zhan J, *et al.* Upregulation of PD-L1 by EGFR activation mediates the immune escape in EGFR-Driven NSCLC: implication for optional immune targeted therapy for NSCLC patients with EGFR mutation. *J Thorac Oncol* 2015;10:910–23.
  - 45 Qin G, Wang X, Ye S, *et al.* Npm1 upregulates the transcription of PD-L1 and suppresses T cell activity in triple-negative breast cancer. *Nat Commun* 2020;11:1669.
  - 46 Blank C, Gajewski TF, Mackensen A. Interaction of PD-L1 on tumor cells with PD-1 on tumor-specific T cells as a mechanism of immune evasion: implications for tumor immunotherapy. *Cancer Immunol Immunother* 2005;54:307–14.
  - 47 Alsaab HO, Sau S, Alzhrani R, *et al.* Pd-1 and PD-L1 checkpoint signaling inhibition for cancer immunotherapy: mechanism, combinations, and clinical outcome. *Front Pharmacol* 2017;8:561.
  - 48 Showalter A, Limaye A, Oyer JL, *et al.* Cytokines in immunogenic cell death: applications for cancer immunotherapy. *Cytokine* 2017;97:123–32.
  - 49 Chen G, Emens LA. Chemoimmunotherapy: reengineering tumor immunity. *Cancer Immunol Immunother* 2013;62:203–16.
  - 50 Cao SS, Kaufman RJ. Endoplasmic reticulum stress and oxidative stress in cell fate decision and human disease. *Antioxid Redox Signal* 2014;21:396–413.
  - 51 Zhang D, Ochi N, Takigawa N, *et al.* Establishment of pemetrexed-resistant non-small cell lung cancer cell lines. *Cancer Lett* 2011;309:228–35.
  - 52 Ozasa H, Oguri T, Uemura T, *et al.* Significance of thymidylate synthase for resistance to pemetrexed in lung cancer. *Cancer Sci* 2010;101:161–6.
  - 53 Shimizu T, Nakagawa Y, Takahashi N, *et al.* Thymidylate synthase gene amplification predicts pemetrexed resistance in patients with advanced non-small cell lung cancer. *Clin Transl Oncol* 2016;18:107–12.
  - 54 Liang J, Lu T, Chen Z, *et al.* Mechanisms of resistance to pemetrexed in non-small cell lung cancer. *Transl Lung Cancer Res* 2019;8:1107–18.
  - 55 Kaltschmidt B, Kaltschmidt C, Hehner SP, *et al.* Repression of NF-kappaB impairs HeLa cell proliferation by functional interference with cell cycle checkpoint regulators. *Oncogene* 1999;18:3213–25.
  - 56 Ledoux AC, Perkins ND. NF-κB and the cell cycle. *Biochem Soc Trans* 2014;42:76–81.
  - 57 Karin M. Nuclear factor-kappaB in cancer development and progression. *Nature* 2006;441:431–6.
  - 58 Hong S, Lee C, Kim S-J. Smad7 sensitizes tumor necrosis factor induced apoptosis through the inhibition of antiapoptotic gene expression by suppressing activation of the nuclear factor-kappaB pathway. *Cancer Res* 2007;67:9577–83.
  - 59 Peng J, Hamanishi J, Matsumura N, *et al.* Chemotherapy induces programmed cell Death-Ligand 1 overexpression via the nuclear factor-κB to foster an immunosuppressive tumor microenvironment in ovarian cancer. *Cancer Res* 2015;75:5034–45.



# A bioactive multi-functional heparin-grafted aligned poly (lactide-co-glycolide)/curcumin nanofiber membrane to accelerate diabetic wound healing

Han Tsung Liao<sup>a,b</sup>, Yu-Tin Lai<sup>a</sup>, Chang-Yi Kuo<sup>a</sup>, Jyh-Ping Chen<sup>a,b,c,d,\*</sup>

<sup>a</sup> Department of Chemical and Materials Engineering, Chang Gung University, Kwei-San, Taoyuan 33302, Taiwan, ROC

<sup>b</sup> Department of Plastic and Reconstructive Surgery and Craniofacial Research Center, Chang Gung Memorial Hospital, Chang Gung University School of Medicine, Kwei-San, Taoyuan 33305, Taiwan, ROC

<sup>c</sup> Research Center for Food and Cosmetic Safety, Research Center for Chinese Herbal Medicine, Chang Gung University of Science and Technology, Kwei-San, Taoyuan 33302, Taiwan, ROC

<sup>d</sup> Department of Materials Engineering, Ming Chi University of Technology, Tai-Shan, New Taipei City 24301, Taiwan, ROC

## ARTICLE INFO

### Keywords:

Wound healing  
Nanofibers  
Curcumin  
Heparin  
Wound dressing  
Poly(lactide-co-glycolide)

## ABSTRACT

Curcumin is reported to possess excellent efficacy to treat wounds that exhibit impaired healing. Heparin shows high affinity for many growth factors that are key biological mediators during the wound healing process. In this study, we aimed to prepare wound dressing membranes, for sustained release of an exogenous factor curcumin as well as sequestering endogenous growth factors at the wound site, to promote wound healing in diabetic rats. Toward this end, we prepared aligned curcumin-loaded poly(lactide-co-glycolide) (PLGA) nanofiber membranes (PC NFMs), followed by high density surface grafting of heparin to fabricate PLGA/curcumin (PCH) NFMs. Both PC and PCH NFMs show high tensile strength, low cytotoxicity and suitable water vapor transmission rate for application as wound dressings. Nonetheless, the PCH NFM shows higher curcumin release rate than PC due to enhanced hydrophilicity, which leads to higher cell migration rate and induced oxidative stress protection of HS68 fibroblast cells in vitro. In vivo study indicated the PCH exhibits the fastest wound closure rate among all membranes with accelerated re-epithelization rate, higher angiogenesis rate and more collagen deposition at the wound site. The accelerated and better skin tissue regeneration could be suggested to correlate with the multi-functionality of nanofibers, where grafted heparin attracting and stabilizing the growth factors important for wound healing in situ, together with relieving the high oxidative stress and the inflammatory cascade from released curcumin during diabetic wound healing.

## 1. Introduction

A wound dressing may provide physical protection, antibacterial function, exudate management and healing acceleration of the wound. However, conventional dressing materials may restrict wound healing from the secondary trauma during dressing removal or infection caused by excessive exudate [1]. In contrast, nanofiber membranes (NFMs) with their high surface area and microporous structure may attract fibroblasts toward the wound bed to start the wound healing signaling pathway, where cells can excrete collagen, angiogenic factors and growth factors for repair of damaged tissue [2]. In addition, the open structure offered by microporous NFMs provides good drainage of exudates and reduces the risk of secondary infection [3].

The electrospinning process can directly process biocompatible polymers into nanofibers by using an electrical charge to draw very fine fibers from a polymer solution [4]. The characteristic of electrospun NFMs could be manipulated by controlling process parameters such as voltage, flow rate, polymer concentration and solvent composition [5]. In order to provide physical cues for cell attachment, an aligned fiber orientation could replace the random orientation of typical electrospun nanofibers. Indeed, aligned nanofiber scaffold represent a unique group of fibrous scaffolds that could induce a particular cell orientation response, which will be suitable for regeneration of tendons, skin, muscle and nerve tissues with the anisotropic structure of these tissues [6,7]. From in vitro cell culture, aligned nanofiber scaffolds were found to exhibit higher cell proliferation rate compared with the random ones

\* Corresponding author at: Department of Chemical and Materials Engineering, Chang Gung University, Kwei-San, Taoyuan 33302, Taiwan, ROC.

E-mail address: [jpchen@mail.cgu.edu.tw](mailto:jpchen@mail.cgu.edu.tw) (J.-P. Chen).

<https://doi.org/10.1016/j.msec.2020.111689>

Received 21 April 2020; Received in revised form 23 October 2020; Accepted 27 October 2020

Available online 1 November 2020

0928-4931/© 2020 Elsevier B.V. All rights reserved.

with fiber alignment strengthening the interactions between cells and fibers in the longitudinal fiber direction [8]. The substrate morphology could also change the expression of matrix components (elastin, collagen and fibronectin) of fibroblasts [9]. For wound healing, it is thus possible to affect the process of wound closure in a spatial manner, using topographical cues offered by aligned NFMs, to result in faster wound closure rate [10]. A previous study showed that aligned nanofibers promote cell migration and wound healing, where contact guidance of cytoskeletal filaments via aligned nanostructure was postulated to be responsible for change in cell behavior [11].

After physical or chemical damage to the skin, the wound healing process involves four steps including hemostasis, inflammation, cell proliferation and remodeling [12]. In the hemostatic phase, the blood vessels contract to accelerate hemostasis and coagulation. Platelets and fibrin during blood clotting release platelet-derived growth factor (PDGF) and transforming growth factor beta 1 (TGF- $\beta$ 1) to recruit fibroblasts, endothelial cells and macrophages [12]. Macrophages are then stimulated to secrete cytokines, including fibroblast growth factor 2 (FGF-2). The production of FGF-2 is essential for angiogenesis during the wound healing process [13]. During the inflammation phase, vascular contraction promotes vascular permeability, leading to the intrusion of neutrophils, macrophages, and lymphocytes as well as eliminating the bacteria and necrotic tissue by reactive oxygen species (ROS) [14]. Excessive ROS causes damage to normal cells, which places endogenous antioxidants such as superoxide dismutase (SOD) and glutathione peroxidase (GPx) to play a critical role in ROS homeostasis. It is generally agreed that fibroblasts are widely required to secrete collagen for cell proliferation and neovascular formation [15]. The collagen at the wound is rearranged and the angiogenesis process is terminated afterward during the remodeling phase. In addition, the recycle of collagen is subsequently mediated by collagenase, with excessive collagen at the injured site prone for rigid scar formation in the end.

Poly(lactic-co-glycolic acid) (PLGA) is one of the polymers that are approvable by the U.S. Food and Drug Administration (FDA) for clinical use in wound dressing materials due to its biocompatibility and biodegradability. Previously, PLGA powder was found to promote angiogenesis and accelerate healing of excisional skin wounds, which was ascribed to sustained local release of exogenous lactate from PLGA [16]. Nonetheless, surface modification of PLGA is deemed necessary to improve its hydrophilicity for biomedical applications [17]. Specifically, surface grafting of bioactive molecules to fiber surface could enhance the hydrophilicity in addition to increase the functionality of PLGA NFMs [18].

Curcumin is a polyphenolic compound obtained from tumeric, the powdered root of *Curcuma longa*. It has been used for the treatment of common cold, skin diseases, abdominal spasms and inflammation, and is also employed as a dietary herbal supplement [19]. Specifically, a PLGA/curcumin nanofiber membrane has been reported to be effective for the treatment of carcinoma [20]. Recently, various topical formulations of curcumin have been developed to deliver curcumin at wounded sites and showed excellent efficacy to promote impaired wound healing [21]. The accelerated wound healing was suggested to be due to enhanced migratory ability of cells in the wound bed, improved neovascularization and efficient free radical scavenging activity [22]. Previous studies also show that curcumin has anti-inflammatory and anti-tumor activity by regulating the expression of interleukin-8, tumor necrosis factor- $\alpha$ , cyclooxygenase and lipoxygenase [23]. In addition, increasing number of studies indicate that curcumin decreases ROS and inflammation both in vitro and in vivo through mediation of the nuclear factor- $\kappa$ B (NF $\kappa$ B) pathway [24,25]. Taking advantage of the antioxidant and anti-inflammatory properties, curcumin-loaded nanofiber was shown to increase the wound closure rate in diabetic mice [26]. An additional benefit offered by curcumin for accelerated wound healing was suggested to be due to the regulation of collagen synthesis [27]. Furthermore, polyethyleneimine-carboxymethyl chitosan/pDNA-

angiogenin nanoparticles/cellulose nanocrystals/curcumin/PLGA composite NFMs were prepared to prevent local infection and promote skin regeneration in infected full-thickness burn wounds [28].

The extracellular matrix (ECM), with glycoaminoglycans (GAGs) as primary components, is a natural reservoir of many growth factors, where GAGs can bind, stabilize and promote the actions of various growth factors [29]. For instance, heparan sulfate in the ECM could bind with heparin-binding growth factors, which is critical for accumulation of growth factors in cell vicinity, protection of growth factors from degradation and proper cell signaling functions. In particular, heparin, a highly sulfated GAG, possesses structural domains exhibiting affinity to various growth factors. Heparin is well known for its capabilities to bind and enhance the functions of pro-angiogenic growth factors such as vascular endothelial growth factor (VEGF) and fibroblast growth factor 2 (FGF-2) through their heparin-binding domains [30]. With this growth factor binding activity, nanofiber surface decorated with heparin chains was found to induce new blood vessel formation in a rat model, which could not be achieved using bolus heparin injections or heparin delivered by using collagen gel matrix [31]. As supplement growth factors have been incorporated in many matrices (including nanofibers) to accelerate wound healing [32], endogenous growth factors secreted during different phases of wound healing could be also sequestered and stabilized by heparin at the wound bed for better wound healing outcomes. This was demonstrated in a previous study where soluble heparin/chitosan complex was reported to recruit the growth factor to the epidermis and subsequently enhance wound healing [33]. Therefore, nanofiber surface grafted with heparin may also be used as a physical cue to attract the locally produced growth factors and fortify the activity of endogenous growth factors by sequestering and localizing these growth factors produced in situ. Conjugating heparin moieties to a wound dressing material for sequestering the endogenous growth factors may lead to a new therapeutic angiogenesis modality to promote wound healing without exogenous proteins delivery by maximizing the action of endogenous pro-angiogenic growth factors at the wound site [34].

In this study, we start by hypothesizing a multi-functional wound dressing could be designed as a mechanical support to accelerate diabetic wound healing. Toward this end, we first prepared aligned PLGA/curcumin (PCH) NFMs, followed by surface grafting of high density heparin to provide bio-guidance for attracting endogenous growth factors as well as facilitating curcumin release, which could serve as an exogenous factor for wound healing. We first investigate the physico-chemical characteristics of the NFMs, followed by in vitro cell culture, and finally carry out diabetic wound healing in rats to study the mechanism and the efficacy of wound healing exerted by the designed NFMs.

## 2. Experimental section

### 2.1. Materials

Poly(lactic-co-glycolic acid) (PLGA) with a lactide-to-glycolide ratio of 50:50 (intrinsic viscosity = 0.42 dL/g) was provided by Green Chemical Inc. (Taipei, Taiwan). Poly(ethylene glycol) diamine HCl salt (PEG diamine, H<sub>2</sub>N-PEG-NH<sub>2</sub>, M<sub>w</sub> = 3500) was purchased from JenKem Company (Plano, TX, USA). Curcumin, 1-(3-dimethylaminopropyl)-3-ethylcarbodiimide (EDC), N-hydroxysuccinimide (NHS), heparin sodium salt from porcine intestinal mucosa and mouse anti- $\beta$ -actin monoclonal antibody were purchased from Sigma-Aldrich (St. Louis, MO, USA). N, N-Dimethylformamide (DMF) and tetrahydrofuran (THF) were purchased from Tedia (Fairfield, OH, USA). CellTiter 96® AQueous One Solution Cell Proliferation Assay Kits was obtained from Promega Co. (Madison, WI, USA). 2-(N-morpholino)ethanesulfonic acid, Dulbecco's modified Eagle's medium (DMEM), HyClone fetal bovine serum (FBS), penicillin/streptomycin, Ultra V Block, DAB Quanto Chromogen and Absolute q-PCR SYBR Green Mix were purchased from Thermo



Fisher Scientific (Waltham, MA, USA). Total RNA Isolation Kit was purchased from GeneDireX Corporation (Miaoli, Taiwan). Maxime RT PreMix Kit was purchased from iNtRON Biotechnology Co. (Kyungki-Do, Korea). DC™ Protein Assay kit was purchased from Bio-Rad (Hercules, CA, USA).

## 2.2. Preparation of NFMs

Electrospun PLGA NFMs and PLGA/curcumin (PC) NFMs were prepared using 27%(w/w) PLGA and 26%(w/w) PLGA/1.3%(w/w) curcumin in a mixed solvent system of DMF and THF (1:1 volume ratio). The polymer solution was pumped from a syringe fitted with a 23-gauge needle (internal diameter = 0.37 mm) at 0.7 mL/h. The applied voltages were 15 kV and 20 kV for PLGA and PC NFMs, respectively. Aligned nanofibers were collected with a grounded rotational drum rotating at 3500 rpm. The drum surface was covered with an aluminum foil and placed 10 cm from the needle tip for collecting the electrospun nanofibers. The environment during electrospinning was controlled at ~25 °C and ~40% relative humidity. The PLGA/curcumin/heparin (PCH) NFM was prepared with EDC/NHS as the coupling agent for covalent binding of heparin to plasma-treated PC (PC-plasma) NFM, which contained abundant carboxyl (-COOH) groups on fiber surface [35]. In brief, PC was subjected to plasma treatment with a DC-pulsed O<sub>2</sub> plasma reactor using a SPIK 1000A oxygen plasma generator (MELEC GmbH, Baden, Germany) at 200 mTorr and 600 V for 60 s to obtain PC-plasma NFMs. PEG diamine was subsequently grafted by reacting PC-plasma NFM with EDC (6.4 M), NHS (4.3 M) and PEG diamine in pH 7 MES buffer (0.5 M) for 24 h (NH<sub>2</sub>/COOH molar ratio = 5) to obtain PC-NH<sub>2</sub> NFMs. Heparin was subsequently grafted to PC-NH<sub>2</sub> using similar EDC/NHS coupling chemistry in pH 7 MES buffer with 12.5 nmol heparin per mg of NFM-NH<sub>2</sub> to obtain PCH NFMs.

## 2.3. Characterization of NFMs

### 2.3.1. Determination of carboxylic acid group, primary amine group and heparin in NFMs

The amount of carboxylic groups introduced to PC-plasma NFM after plasma treatment was determined from the Toluidine Blue O (TBO) assay, assuming TBO complexed with carboxyl groups in 1:1 molar ratio. A 1 × 1 cm NFM was weighed and reacted with 1 mL TBO solution (0.5 mM) for 5 h at room temperature. After washing with 0.1 mM NaOH, the NFM was dried completely in a vacuum oven at 37 °C. The TBO complexed to -COOH was desorbed with 2 mL 50% acetic acid and the solution absorbance was determined at 633 nm using a UV-VIS spectrophotometer. The amount of -COOH was determined from a standard curve prepared from solutions with known TBO concentrations. The amount of primary amine groups introduced to PC-NH<sub>2</sub> NFM by grafting PEG diamine was determined by the o-phthalaldehyde (OPA) method using a UV-VIS spectrophotometer at 340 nm [36]. The amount of heparin conjugated to PCH was determined using a 5 µg/mL TBO solution prepared in 0.01 M HCl at 632 nm [37].

### 2.3.2. X-ray photoelectron spectroscopy (XPS) analysis

The surface chemical composition of NFMs was detected by a PHI 1600 ESCA photoelectron spectrometer (Physical Electronics; Chanhassen, MN, USA) equipped with a multichannel detector and a spherical capacitor analyzer to perform high-resolution X-ray photoelectron spectroscopy (XPS). The X-ray source was a magnesium anode operated at 15 kV and 400 W, and the pressure in the analysis chamber was maintained at  $2 \times 10^{-6}$  Pa. Using symmetrical Gaussian peak shapes and integrated background subtraction, the relative percentages of carbon atoms in different carbon functional groups was determined from the high resolution C1s spectra by fixing the peak positions according to tabulated chemical shifts during the curve fitting process.

### 2.3.3. Electron microscopy analysis

Scanning electron microscopy (SEM) (JEOL LSM 5410) was used to determine the orientation and the diameters of nanofibers. The diameters were calculated from 100 fibers chosen randomly from 10 SEM images using the ImageJ software (NIH, Bethesda, MD, USA). The orientation of nanofibers was calculated from the distribution of fiber angles of 100 fibers, which was obtained fiber orientation relative to a defined vertical direction (taken as 0°) within -90 to 90°. A field emission scanning electron microscope (FE-SEM) (Hitachi S5000) was used to study the detailed surface morphology of the nanofibers.

### 2.3.4. Water contact angle and water vapor transmission rate

The water contact angle of a NFM was determined at 25 °C using a FTA-125 contact angle/surface tension instrument (First Ten Angstroms; Portsmouth, VA, USA). The NFM was cut into 1 × 1 dimensions and loaded into a specimen holder. The images were taken within 3 s when a water drop was dropped on NFM surface, from both parallel and perpendicular directions to the axis of the aligned fiber. All reported contact angles were averaged over three measurements for three replicate NFM samples using distilled deionized (DDI) water.

The water vapor transmission rate (WVTR) was determined using a custom-made evaporimeter following ASTM E96-90 [38]. Briefly, a closed glass chamber in a 37 °C incubator was maintained at a relative humidity within  $73 \pm 5\%$  using saturated magnesium chloride solution in the chamber. A cup filled with 10 g of deionized (DI) water was covered by a NFM and placed in the chamber. Evaporation of water through the NFM was monitored from the lost weight of water in the cup due to permeation of water vapor through the membrane, from which WVTR (g/m<sup>2</sup>/day) was calculated.

### 2.3.5. Mechanical tensile testing

The mechanical properties of NFMs were evaluated by uniaxial tensile testing with a Tinius Olsen H1KT universal tensile testing machine. Each sample was in 50 × 10 mm rectangular dimension and vertically mounted by holding ends with two mechanical grippers and leaving a 3-cm gauge length for mechanical loading. The load-deformation value was recorded using a 10 N load cell at 5 mm/min deforming rate up to 30 mm maximum elongation length. The tensile stress at break, tensile strain at break and Young's modulus were calculated from the recorded stress-strain curve.

### 2.3.6. Curcumin release rates

The release of curcumin from NFMs was determined by immersing ~100 mg NFM discs (0.5 cm × 0.5 cm) in a 10 mL sample vial filled with 5 mL phosphate buffered saline (PBS) or 70% PBS/30% ethanol. The vial was shaken at 150 rpm in a 37 °C incubator. At predetermined time, the solution was completely removed from the vial and replenished with equal volume of fresh solution as before to continue the drug release study. The amount of curcumin released was determined from the solution absorbance (OD) by an ELISA microplate reader (BioTek, Winooski, VT) at 420 nm using a standard curve prepared from solutions with known curcumin concentrations.

## 2.4. In vitro studies

### 2.4.1. Cytotoxicity

Human skin fibroblast cell (HS68) purchased from the Bioresource Collection and Research Centre (Taiwan) was used for cell culture. Cytotoxicity of the material was examined from cell viability test by following ISO 10993-5. A 2 × 2 cm NFM was extracted with 1 mL of cell culture medium (DMEM with 10% FBS and 1% penicillin/streptomycin) at 37 °C for 24 h. HS68 fibroblasts were seeded ( $2.5 \times 10^3$  cells/well) in 24-well tissue culture plate and cultured with the extract at 37 °C and 5% CO<sub>2</sub>. Cell viability was monitored on day 1 and 3 from MTS assays using CellTiter 96® Aqueous One Solution Cell Proliferation Assay Kits. Fresh cell culture medium was used as a control.



#### 2.4.2. Cellular response of fibroblasts to NFMs

HS68 fibroblasts were seeded onto disk-shaped NFMs (1.5 cm diameter) in 24-well culture plates at a density of  $1 \times 10^5$  cells/well and cultured with cell culture medium (90% DMEM with 10% FBS and 1% penicillin/streptomycin) at 37 °C in a humidified CO<sub>2</sub> incubator. On day 3, the morphology of cells was observed by SEM and cell viability was examined by Live/Dead cell viability assays. The cell-seeded NFM was washed with PBS and cells were stained with the Live/Dead Viability/Cytotoxicity kit for mammalian cells (Thermo Fisher Scientific) and observed under a confocal laser scanning microscope (Zeiss LSM 510 Meta) at 490/515 nm for live cells and 535/617 nm for dead cells. For SEM observation, the cell-seeded NFMs were rinsed by PBS, followed by fixation with 2.5% glutaraldehyde at 4 °C for 2 h. The sample went through a stepwise dehydration process using 50%, 70%, 80%, 90% and 95% ethanol before immersing in absolute ethanol for 30 min. After drying, the sample was coated with gold and subject to SEM analysis.

#### 2.4.3. Migration of fibroblasts for wound healing

A NFM (2 × 2 cm) was extracted with 1 mL of cell culture medium at 37 °C for 48 h and the extract was collected for in vitro wound healing assays. Human fibroblast HS68 ( $2 \times 10^3$  cells) were seeded into a Culture-Insert 2 Well in  $\mu$ -Dish (IB 80206, ibidi GmbH, Martinsried, Germany) placed in a 35-mm culture dish. After cell attachment for 24 h, the Culture-Insert was removed to create a cell-free gap for observation of cell migration. For in vitro wound healing/migration assay, the medium was replaced by the extraction medium and cell migration into the gap was monitored by taking photos under an inverted microscope after 24 and 48 h. To analyze the gap closure rate, the sample was fixed in 100% formaldehyde for 1 h prior to staining with 0.04% (w/v) Giemsa solution for 30 min. The gap closure rate was calculated from the cell-free gap area determined by the PAX-it software (Villa Park, IL, USA), with relative cell migrated area (%) =  $(1 - GA_t/GA_0) \times 100$ , where  $GA_0$  and  $GA_t$  denote the initial gap area and the gap area at time  $t$ , respectively.

#### 2.4.4. Cytoprotective effects under high oxidative stress

After extracting a NFM (2 × 2 cm) with 1 mL cell culture medium at 37 °C for 48 h, the extract was collected to determine the cytoprotective effects of curcumin-loaded NFM under conditions of high oxidative stress environment occurred at a diabetic wound site. HS68 cells were seeded in 24-well culture plates at a density of  $2.5 \times 10^3$  cells/well and cultured with 1 mL extract medium containing 1% H<sub>2</sub>O<sub>2</sub> and cultured in a 5% CO<sub>2</sub> incubator at 37 °C for 24 h. At the end of the incubation time, the viability of cells was evaluated using the MTS assay. The cell viability was normalized to the blank sample without adding hydrogen peroxide in each group, which was taken as 100%.

### 2.5. In vivo studies

#### 2.5.1. Wound model and wound closure rates

All animal protocols were approved by the Institutional Animal Care and Use Committee of Chang Gung University. The streptozotocin-induced diabetic wound model in Sprague-Dawley (SD) rats was used for in vivo evaluation of wound closure. Male fifteen-week-old SD rats (LASCO, Taipei, Taiwan) weighing ~250 g were made hyperglycemic by intraperitoneal injections of 80 mg/kg body weight of streptozotocin (in pH 4.5 sodium citrate buffer). Whole blood was withdrawn from the tail vein on day 3, 10 and 17 after injection and the plasma glucose concentration was monitored using a blood glucose monitor. Only rats that had two consecutive fasting blood glucose levels higher than 250 mg/dL on day 10 and 17 were considered diabetic and used in the study. After complete anesthetization by intraperitoneal injection of Zoletil-50 and Rompun, two full-thickness wounds were created on each side of the dorsal area of a SD rat. A full-thickness wound to the deep fascia was made by excising the skin using a sterile square template in 1.5 cm × 1.5 cm dimension. The aseptic technique was followed throughout the

entire experiment period. Each wound created was covered with a 2 cm × 2 cm UV-sterilized gauze (control), or PLGA, PC or PCH NFMs. Afterward, the wounded area was covered with Tegaderm (3 M, USA) and adhesive fabric tape (BSN medical, France) was applied to prevent the rat from removing the NFM or gauze. All rats were returned to the housing and maintained with normal food and water. On day 3, 7 and 14 post-treatment, dressings were removed from four rats and animals were sacrificed with an overdose of intravenous sodium pentobarbital. The wounds were digitally photographed by maintaining identical optical zoom throughout the experiments. For quantitative evaluation, the wounds were replicated on a transparent tracing paper after tracing the wound border covered with epithelium. The paper was scanned, followed by analyzing the wound size with the ImageJ software (National Institute of Health, Bethesda, MD, USA). The wound closure rate was calculated based on the percentage closure of the original wound as relative wound size (%) =  $WA_t/WA_0 \times 100$ , where  $WA_0$  and  $WA_t$  denote the initial wound area and the wound area at time  $t$ , respectively. Dorsal skin tissue was dissected from the sacrificed rat and subject to histological and qPCR analysis. The granulation tissue in the wound and the sub-epidermal tissue in normal skin were used for the qPCR analysis.

#### 2.5.2. Histology and immunohistochemistry

The excised skin tissue of rat sacrificed on day 14 was harvested for hematoxylin-eosin (H&E), Masson's trichrome and immunohistochemical (IHC) analysis. For histological analysis, samples were immersed in 10% formaldehyde, followed by dehydration and embedding in paraffin. The samples were sectioned into 4- $\mu$ m thickness and subject to H&E, Masson's trichrome and  $\alpha$ -smooth muscle actin ( $\alpha$ -SMA) IHC staining after deparaffinization. For IHC staining, Ultra V Block was used to diminish nonspecific binding for 5 min, followed by incubation with 1:200 diluted  $\alpha$ -SMA primary antibody (rabbit anti- $\alpha$ -SMA polyclonal antibody, Abcam ab5694) for 24 h at 4 °C. Samples were then rinsed with PBST and incubated with N-Histofine simple stain rat MAX PO (MULTI) for 30 min at room temperature. The color was developed with DAB reagent (30  $\mu$ L of DAB Quanto Chromogen in 1 mL of DAB Quanto Substrate) prior to counterstaining by hematoxylin. The images were taken under an IX-71 inverted optical microscope and semi-quantitative analysis was carried out with the PAX-it software based on stained area. Six randomly selected fields from microscopic observation were examined and used to calculate the area percentage of  $\alpha$ -SMA positive vessels.

#### 2.5.3. Quantitative real-time polymerase chain reaction (qRT-PCR) analysis

The RNA of tissue samples was extracted and reverse transcribed into cDNA by using Total RNA Isolation Kit and Maxime RT PreMix Kit according to manufacturer's protocols. The cDNA was mixed with the SYBR Green RT-PCR kit before using a CFX-3120 Mini Option detection system (Bio-Rad, Hercules, CA, USA) for quantitative real-time polymerase chain reaction (qRT-PCR). Glyceraldehyde 3-phosphate dehydrogenase (GAPDH) was used as the housekeeping gene. The relative mRNA expression of GPx and NF- $\kappa$ B was determined using the  $2^{-\Delta\Delta Ct}$  relative quantification method.

### 2.6. Statistical analysis

All results were presented as mean  $\pm$  standard deviation (SD). One-way analysis of variance (ANOVA) LSD test was used for statistical analysis and significant level was set at  $p < 0.05$ .

## 3. Results and discussion

### 3.1. Characterization of PLGA, PC and PCH NFMs

To achieve the goal of engineering a multi-functional nanofibrous wound dressing, we prepared aligned PLGA, PC and PCH NFMs under well-controlled electrospinning conditions, including optimized flow

rate, voltage, tip-to-collector distance and collector rotational speed. To achieve high heparin grafting ratio, PC NFMs were successively subjected to plasma treatment (PC-plasma NFMs), one-ended conjugation with PEG diamine (PC-NH<sub>2</sub> NFMs) and heparin grafting (PCH NFMs) as shown schematically in Fig. 1A. By choosing appropriate electrospinning parameters, aligned PLGA or PC with uniform and bead-free nanofibers could be obtained with similar surface morphology to PCH NFMs as shown from SEM images (Fig. 1B). The membrane thickness of PLGA, PC and PCH NFMs were  $190 \pm 24$  nm,  $185 \pm 6$  nm and  $220 \pm 16$  nm, respectively. The average fiber diameter and fiber orientation (average fiber angle) showed no significant difference among PLGA, PC and PCH NFMs (Table 1).

As the water contact angle is expected to be anisotropy for aligned fibers, the water contact angles were measured from two different orientations, parallel or perpendicular to the axis of aligned fibers (Fig. 1C). In contrast to randomly oriented nanofibers, where water wetting is isotropic, aligned nanofibers in uniaxial arrays leads to an asymmetric surface topography and consequently to different water contact angle measured along a direction parallel or perpendicular to the oriented fiber longitudinal axis (Table 1) [39]. The low contact angle from direction perpendicular to the fiber orientation is a result of preferential spreading of the droplet along the nanofibers due to roughness enhanced wetting as there are no barriers to the contact line motion that would cause pinning [40]. The water contact angle of PCH NFM from each direction decreased significantly when compared with that of PLGA or PC (Table 1), with no significant difference between them. This indicates that heparin grafting increased membrane hydrophilicity by introducing abundant hydrophilic heparin molecules to fiber surface (Fig. 1A). Furthermore, the difference in contact angles measured from different directions only changed substantially for PCH due to its higher hydrophilicity compared with PLGA or PC NFMs (Table 1).

Chemical analysis was used to confirm successful chemical change after the chemical modification of nanofibers as shown in Fig. 1A. After plasma treatment,  $2.99 \pm 0.09$  nmol -COOH was found per mg of PC-plasma NFM. Using excess PEG diamine to react with -COOH on PC-plasma, we can assure one-ended covalent binding of PEG diamine to

**Table 1**

The fiber diameter, fiber angle, water contact angle and water vapor transmission rate of NFMs. The water contact angles are shown for direction parallel or perpendicular to the fiber alignment axis.

NFM	Average fiber diameter (nm)	Average fiber angle (°)	Contact angle (°)		Water vapor transmission rate (g/m <sup>2</sup> /d)
			Parallel	Perpendicular	
PLGA	$461 \pm 109$	$90 \pm 7$	$94.3 \pm 4.6$	$93.9 \pm 3.3$	$456.5 \pm 10.1$
PC	$459 \pm 105$	$91 \pm 5$	$100.6 \pm 4.9$	$87.7 \pm 3.7$	$452.5 \pm 12.8$
PCH	$479 \pm 129$	$91 \pm 13$	$64.3 \pm 7.8^{*,\&}$	$35.8 \pm 9.8^{*,\&}$	$450.4 \pm 7.8$

\*  $p < 0.05$  compared to PLGA.

&  $p < 0.05$  compared to PC.

PC-plasma, leaving the other -NH<sub>2</sub> end group to react with -COOH in heparin. The amount of -NH<sub>2</sub> introduced to PC-NH<sub>2</sub> was determined to be  $1.06 \pm 0.14$  nmol/mg NFM using the OPA method to quantitatively determine the primary amine groups on fiber surface. The last step in Fig. 1A is critical to conjugate abundant heparin for exerting binding affinity toward endogenous growth factors. Using an optimal solution pH and heparin concentration during the conjugation step, we successfully achieved high loading of heparin on fiber surface at  $1.14 \pm 0.06$  nmol/mg NFM. This value was at least one order of magnitude higher than those reported before for heparin immobilization to different PLGA scaffolds, which was 0.096 pmol/mg for PLGA microspheres [41] and  $0.069 \pm 0.004$   $\mu$ mol/mg for PLGA yarn [42]. This high grafting density of heparin on PCH would facilitate guiding endogenous growth factors to the wound bed to promote wound healing..

Undoubtedly, more sophisticated morphological and chemical analyses of NFMs are needed. To meet this need, we use FE-SEM to observe the fiber surface morphology change from PC to PCH. As shown in Fig. 2, the original PC nanofibers showed smooth surface morphology. Plasma treatment introduced change of fiber surface morphology in PC nanofiber as expected. Nonetheless, further grafting with PEG diamine and

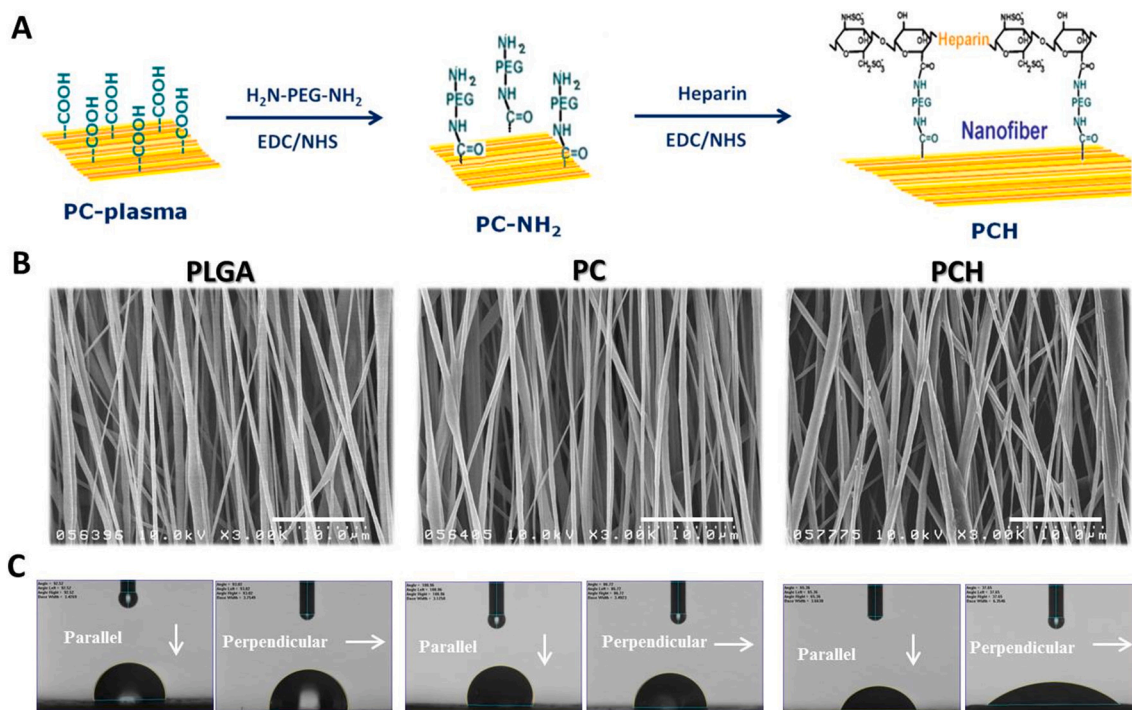


**Fig. 1.** (A) The schematic diagram showing the steps involved in preparing PCH NFMs. The SEM images (bar = 10  $\mu$ m) (B) and optical micrographs of water droplets in direction parallel and perpendicular to the fiber alignment axis of PLGA, PC and PCH nanofibers (C).

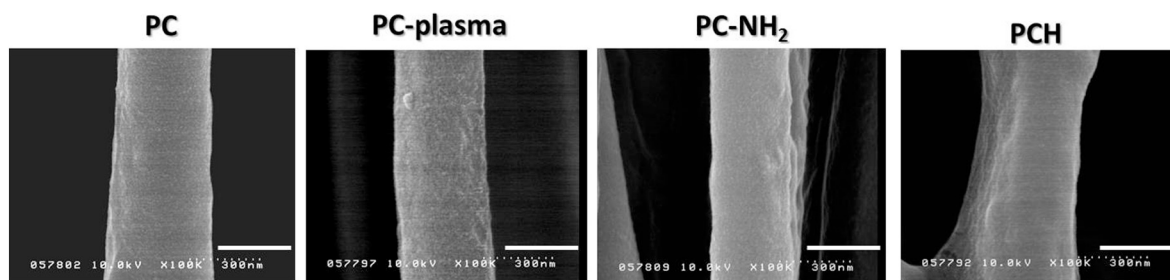


Fig. 2. The FE-SEM micrographs of PC, PC-plasma, PC-NH<sub>2</sub> and PCH NFMs. Bar = 300 nm.

heparin immobilization resulted in change of surface morphology of PC-NH<sub>2</sub> and PCH back to the smooth surface observed for PC. This is due to masking of surface roughness from grafted macromolecules on fiber surface, albeit with little change of fiber diameter. This surface morphology change is different from our previous report when gelatin was immobilized to plasma-treated PLLA nanofibers using the same crosslinking agent (EDC), which showed scattered particles of gelatin molecules distributed along the nanofiber surface as well as increased fiber diameter and surface roughness [35]. Although the average fiber diameter did not significantly change after heparin grafting from SEM images (Table 1), we could still observe a distinctive thin surface layer outside of PCH fiber from the FE-SEM image (Fig. 2). Undoubtedly, such difference could be attributed to different chemical structure between heparin and gelatin. Unlike gelatin, heparin molecules could not be crosslinked with each other on fiber surface using EDC/NHS (Fig. 1A), which leads to a thin coating of heparin on PCH fiber surface and smooth fiber surface morphology.

The surface chemical composition of NFMs was studied by XPS. As shown from the survey scan spectra in Fig. 3A, the XPS spectra had two separated peaks corresponding to C1s (285 eV) and O1s (532 eV). A distinct N1s peak at 400 eV in the spectrum of PC-NH<sub>2</sub> indicates that amine groups were successfully introduced onto fiber surface with the N atomic percentage being 2.2%. The N1s peak also appeared in PCH as expected with increased N atomic percentage (4.0%) due to nitrogen atoms in heparin. Additional Na1s, S2s and S2p peaks appeared in PCH NFMs (0.9% Na and 0.9% S atomic percentage) with the use of sodium heparin in this study. Furthermore, high resolution XPS C1s spectra are shown for all NFMs in Fig. 3B–F and the fractions of different carbon functional groups are given in Table 2. The spectrum from PLGA shows three components at 285, 286.8 and 289.9 eV, corresponding to C–C, C–O and O=C–O bonds in the chain (Fig. 3B) [43]. From the spectrum for PC, same peaks exist but the C–C peak increased while the C–O peak decreased as curcumin is less abundant in O (Fig. 3C). For PC-plasma, the saturated hydrocarbon C–C C1s peak decreased after plasma treatment, with concomitant increase in the peak intensity of C–O (from 33.7% to 35.2%) and O=C–O (from 28.2% to 32.7%), which could be attributed to the increase in carboxyl groups and the introduction of oxygen functionalities on fiber surface (Fig. 3D) [35]. Both PC-NH<sub>2</sub> (Fig. 3E) and PCH (Fig. 3F) revealed a new peak at 286.3 eV, which corresponds to the amide carbon in NH–C=O. This was accompanied by a decrease in the O=C–O peak from 32.7% to 11.5% for PC-NH<sub>2</sub> and further to 6.2% for PCH. Taken together, the XPS analysis confirms introduction of primary amine groups on fiber surface, which react with carboxyl groups of heparin for amide bond formation.

### 3.2. Water vapor permeation and mechanical properties of NFMs

Maintaining moisture is important during wound healing and a potential wound dressing should provide a suitable water vapor transmission rate (WVTR) to prevent excessive dehydration during wound healing. Toward this end, water loss from a NFM was determined in a well-controlled environment (Fig. 4A), from which the WVTR was

calculated within 2 h to 30 h. A similar WVTR was observed among all NFMs (Table 1), suggesting PLGA, PC and PCH NFMs are endowed with similar capability to maintain suitable moisture with the microporous structure of 1 to 2  $\mu\text{m}$  pore size (Fig. 1B). The water vapor permeability of a wound dressing should prevent both excessive dehydration as well as buildup of exudate. Therefore, the dressing material should control the water loss from a wound due to evaporation at an optimal rate [44]. It has been reported that the evaporative water losses for normal skin, burns and granulating wounds at close to skin temperature (35 °C) are  $204 \pm 12$ ,  $279 \pm 26$  and  $5138 \pm 202$  g/m<sup>2</sup> per day, respectively [45]. It could be also noted from Table 1 that the WVTR of all NFMs are  $\sim 450$  g/m<sup>2</sup> per day, which is close to the value for wet human skin (350 g/m<sup>2</sup>/day) and dry human skin (215 g/m<sup>2</sup>/day) [46]. Comparing with the WVTRs of commercial sponge-type wound dressings, such as Biobrane II (1565 g/m<sup>2</sup>/day) and HYAFF 11p75 (2327 g/m<sup>2</sup>/day), the functional NFM could reduce WVTR. On the other hand, the NFM has higher WVTR from its macroporous fiber structure when compared with a commercial film type PU wound dressing (Tegaderm®, WVTR = 62 g/m<sup>2</sup>/day). Taken together, the NFMs engineered here are deemed suitable to provide adequate moisture control for the wound and prevent excessive wound dehydration for an appropriate milieu during wound healing.

A wound dressing material should also provide good mechanical strength to withstand stretching and abrasion during application. From tensile mechanical testing, typical stress vs. strain curves are shown in Fig. 4B, from which the tensile strain at break, tensile stress at break and Young's modulus was compared in Table 3 for different NFMs. Overall, the incorporation of curcumin (PC) significantly raised the mechanical strength (ultimate stress and Young's modulus) of the NFM without influencing its flexibility and stretchability (ultimate strain). Even subject to further plasma treatment and grafting reactions, PCH is evident to retain or improve the preferred mechanical property of PC, to be useful as a membrane-type material for wound dressing application.

### 3.3. Release of curcumin and biocompatibility of NFMs

The release profile of curcumin from PC and PCH NFMs was first studied in PBS solution. As shown in Fig. 5A, slow release of curcumin was found for both NFMs and the cumulative release was only 13.5% (PC) and 21% (PCH) after 500 h due to the sparingly soluble nature of curcumin in water ( $\sim 0.6$   $\mu\text{g/mL}$ ) [47]. Nonetheless, the drug release from PCH is consistently and significantly higher, which could be correlated with the higher hydrophilic nature of PCH, as shown from the contact angle difference in Table 1. To confirm that curcumin could reach quantitative release disregarding the solubility limit, we also tested curcumin release in 70% PBS/30% ethanol solutions (Fig. 5B). A distinctive burst release was observed with 49% and 62% cumulative release of curcumin in 12 h was found for PCH and PC, respectively. The release percentage increased with time and plateaued at 95% for PCH and 92% for PC, without showing significant difference as expected.

In order to determine whether the released curcumin exerted any cytotoxicity, human HS68 fibroblasts were cultured in 24 h extraction medium of a NFM and the relative cell viability was determined by MTS

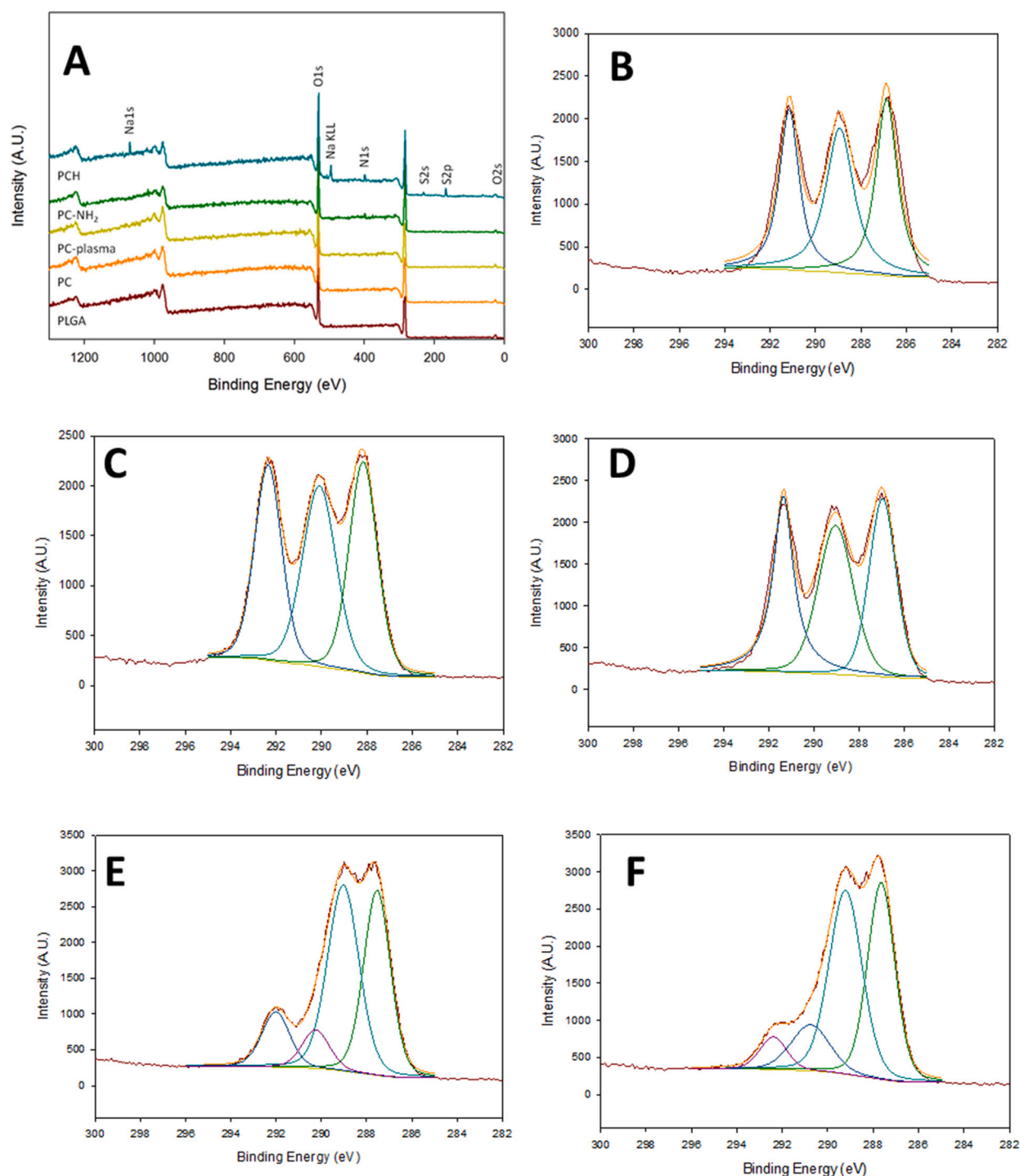


Fig. 3. The XPS survey scan spectra of different NFMs (A) and the XPS C1s spectra of PLGA (B), PC (C), PC-plasma (D), PC-NH<sub>2</sub> (E) and PCH (F) NFMs.

**Table 2**  
Fraction of carbon functional groups from high resolution C1s XPS peaks.

NFM	C—H ~285 eV (%)	C—O ~286.8 eV (%)	O—C=O ~289.9 eV (%)	NH—C=O ~286.3 eV (%)
PLGA	34.4	36.7	28.9	0.0
PC	38.1	33.7	28.2	0.0
PC-plasma	32.1	35.2	32.7	0.0
PC-NH <sub>2</sub>	36.9	43.7	11.5	7.9
PCH	38.2	43.0	6.2	12.6

assays. Fig. 6A shows cells cultured in the extraction medium of PC and PCH showed significantly reduced relative cell viability compared to curcumin-free PLGA NFM. No significant difference in cell viability was found between PC and PCH, since similar curcumin concentration was expected in the 24 h extraction medium from the drug release study in PBS (Fig. 5A). Curcumin is known to exhibit a wide range of pharmacological effects including anti-inflammatory, antioxidant and anti-carcinogenic activities, which is known to be concentration dependent. In a dose-dependent manner, curcumin can induce apoptosis in a wide variety of cells and down-regulate transcription factors such as NFκB [48]. Previous studies indicate that the cytotoxic effect of



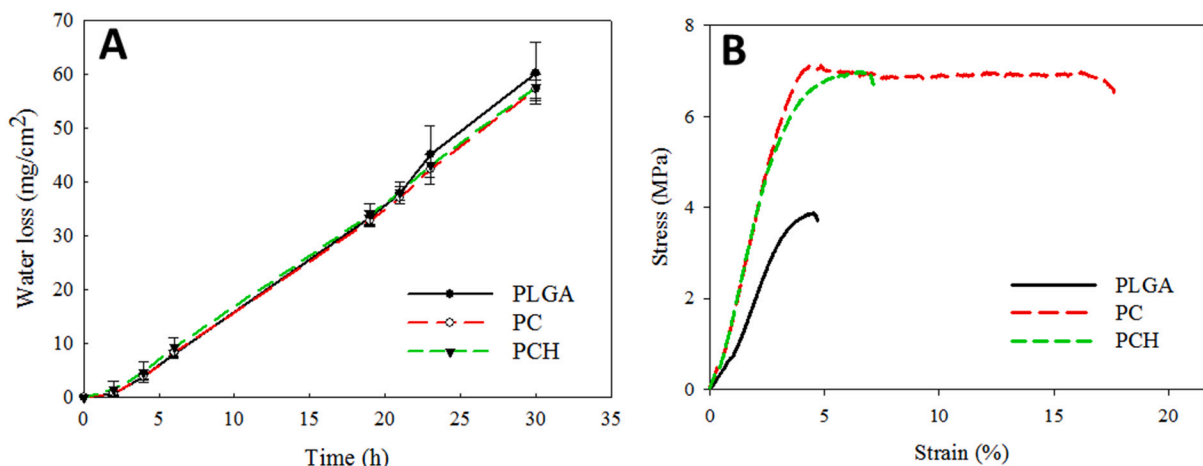


Fig. 4. The water vapor transmission rates (A) and the stress vs. strain curves (B) of PLGA, PC and PCH NFMs from tensile mechanical testing.

Table 3

The mechanical properties of PLGA, PC and PCH NFMs.

NFM	Tensile stress at break (MPa)	Tensile strain at break (%)	Young's modulus (MPa)
PLGA	3.82 ± 0.56	4.60 ± 0.19	125.95 ± 24.45
PC	7.04 ± 0.76*	4.81 ± 0.20	181.45 ± 20.31*
PCH	7.25 ± 0.65*	5.93 ± 0.57*,&	198.97 ± 16.98*

\*  $p < 0.05$  compared to PLGA.

&  $p < 0.05$  compared to PC.

curcumin was exhibited only at high concentrations (~25  $\mu\text{M}$ ) where less than 50% cell survival was found [49]. However, with more than 70% viable cells shown in Fig. 6A, we could confirm the low cytotoxicity of both curcumin-loaded NFMs, which is also consistent with a previous report that gradual release of curcumin from NFMs induced low cytotoxicity to fibroblasts [50].

Further experiments followed to elucidate membrane biocompatibility by seeding HS68 fibroblasts on different NFMs and cultured for 72 h before Live/Dead staining and SEM observation. As expected, fibroblasts showed high cell viability when cultured on all NFMs with minimum dead cells (red) distributed within a large number of viable cells (green) (Fig. 6B). More dead cells were found in PCH as more curcumin was released in 72 h (Fig. 5A). From SEM observation, there was no discernible change in cell morphology, with well-spread cells showing flat and spindle-like morphology and lamellipodia, endorsing the high biocompatibility of NFMs toward HS68 cell even when loaded with

curcumin (Fig. 6C). It could be also confirmed that attached cells were oriented in the direction of fiber alignment with elongated shape when cells proliferated in the direction of fiber alignment (Fig. 6B and C). Previous studies indicated aligned nanofiber scaffold could shorten the time for wound healing during skin tissue reconstruction due to the “contact-guided” effects of nanofiber orientation on cells [51]. In addition, aligned electrospun nanofibers also improve type I collagen expression with a higher degree of organization of collagen fibers secreted by fibroblast cells attached to aligned nanofibers [52].

#### 3.4. Migration of fibroblasts and protective effects under high oxidative stress

To confirm the released curcumin could promote cell migration, in vitro wound healing test was studied. Fig. 7A illustrates the curcumin-loaded NFMs (PC and PCH) enhanced HS68 migration at both time points compared with the control (medium) and the curcumin-free PLGA NFMs. Specifically, the quantitative analysis results shown in Fig. 7B indicate the area occupied by migrated cells in PC and PCH group increased by 3.1 and 5.6 folds, respectively, compared to control after 24 h. Similarly, PC and PCH groups showed 1.3 to 1.4 folds increase in recovered area after 48 h. Comparing PC and PCH, the faster curcumin release profile of PCH in PBS leads to higher curcumin in the 48 h extraction medium and significantly enhanced cell migration rate at 24 h (Fig. 5A). No significant difference between PC and PCH was found at 48 h as it is close to the end of the wound healing assay. Cells cultured with the extraction medium of PLGA did not show any significant effect

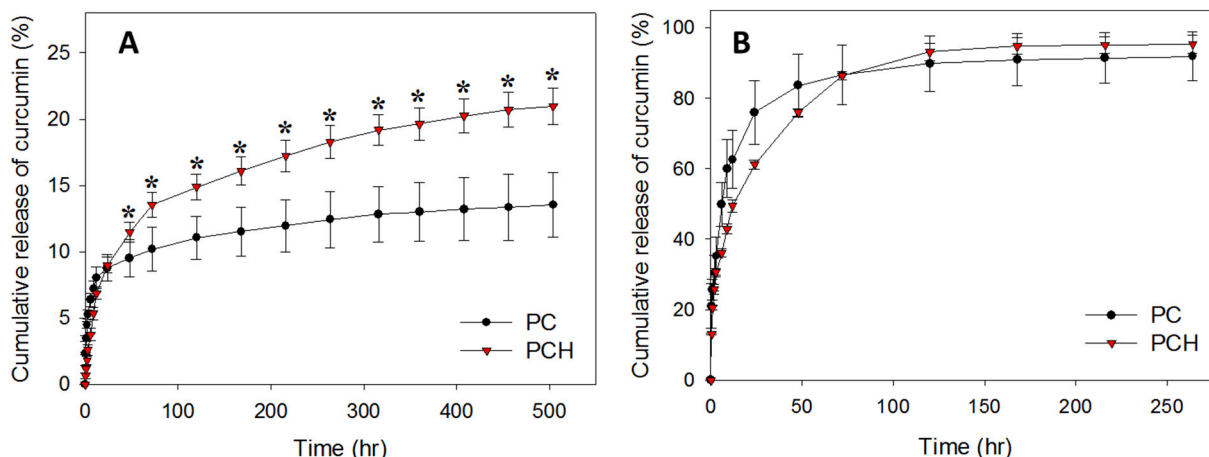
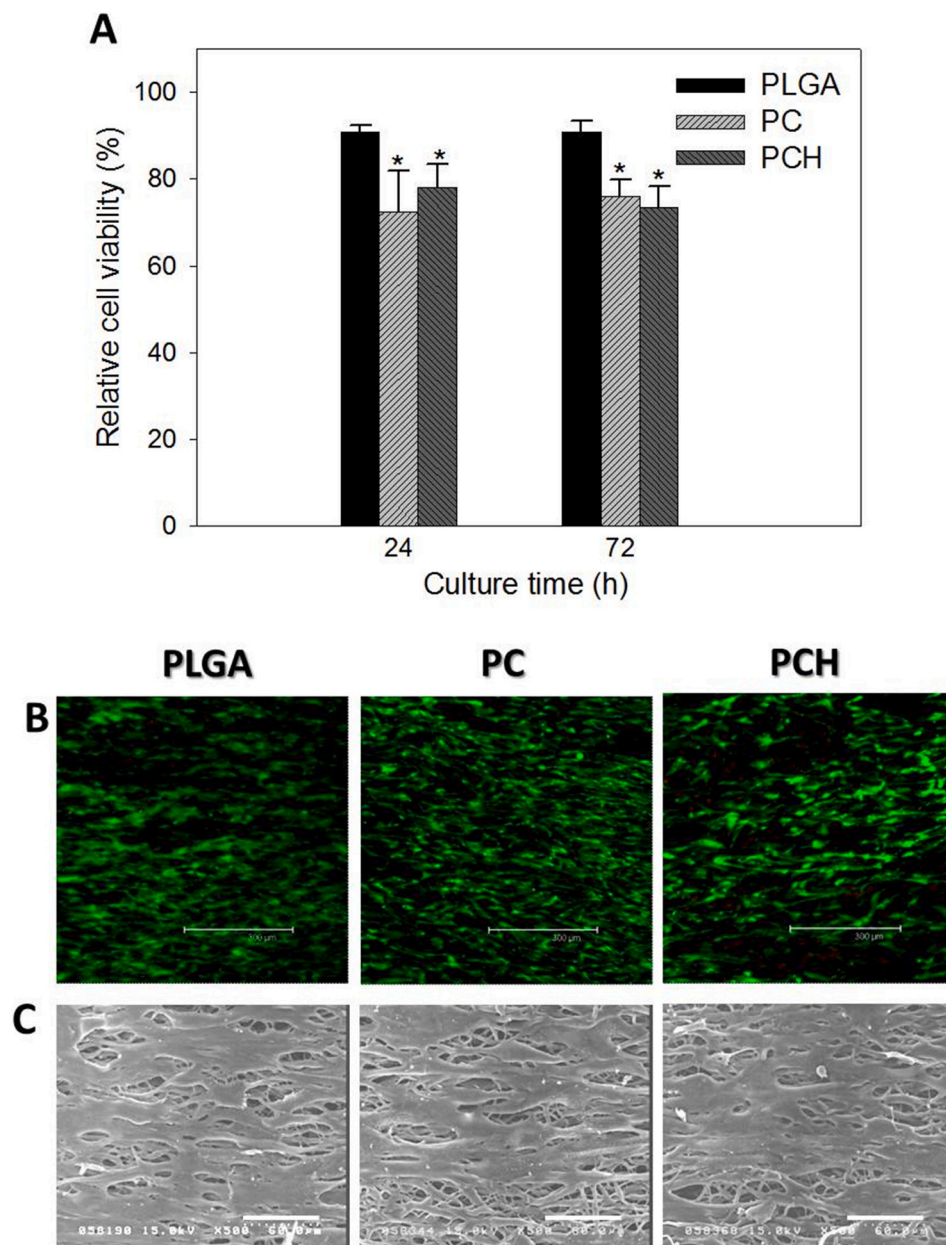


Fig. 5. The release profiles of curcumin from PC and PCH NFMs in PBS (A) and 70% PBS/30% ethanol (B). \* $p < 0.05$  compared with PC.





**Fig. 6.** Biocompatibility of NFMs by culture of fibroblasts with 24 h extraction medium of NFMs for 1 and 3 days (A) and culture of fibroblasts on NFMs for 3 days and subject to Live/Dead staining (B, bar = 300  $\mu$ m) or SEM observation (C, bar = 60  $\mu$ m). The cell viability in (A) was determined by MTS assays and reported as relative cell viability with cell culture medium taken as 100%. \* $p < 0.05$  compared with PLGA. (For interpretation of the references to color in this figure, the reader is referred to the web version of this article.)

to promote cell migration when compared to the control at both time points. These results are consistent with a recent study where wound healing capability was measured with human fibroblasts using curcumin-loaded gelatin nanofibers. The wound closure rate of human fibroblasts from wound scratch assay in vitro was found to be 26.6 and 14.4% for control and 0.003% curcumin after 48 h, respectively [53]. Taken together, the cell migration results suggest that curcumin released from PC and PCH will retain its bioactivity to enhance cell migration in vitro and also endorse the use of PCH over PC to shorten the required time for wound healing in vivo.

To evaluate the anti-oxidant effect and the free radical-quenching ability of curcumin-loaded nanofibers in reference to the beneficial effect on diabetic wound healing, we further evaluate the inhibition of cell death due to the oxidative stress induced by hydrogen peroxide. HS68 fibroblasts were cultured in 48 h extraction medium of NFM and supplemented with 1%  $H_2O_2$  to simulate the high oxidative stress. The cell viability determined by MTS assays in Fig. 7C shows the  $H_2O_2$ -induced oxidative stress caused damage to cells and reduced the relative cell viability to ~53% in both control and PLGA groups when compared to

the non-oxidative stress condition in the absence of hydrogen peroxide. However, the  $H_2O_2$ -induced oxidative stress damage was effectively alleviated, and the cell viability drastically elevated in the PC and PCH groups. Indeed, the relative cell viability in both PC and PCH groups was above 80% and significantly higher than those in the control and PLGA groups. The PCH also significantly enhanced the protective effect over PC due to more pronounced power to alleviate the oxidative stress, which improves cell viability under the high oxidative stress, as more curcumin was released in the 48 h extraction medium (Fig. 5A). Hydrogen peroxide is known to elicit excessive intracellular ROS, which lead to mitochondria and cell membrane damage and eventually cell apoptosis. The pronounced protective effect of PCH on proliferative fibroblasts, which are damaged by  $H_2O_2$ -induced supra-oxidative stress in vitro, underlines the modality of PCH to accelerate re-epithelialization during diabetes wound healing in vivo [54].

### 3.5. Diabetic wound healing in rats

To further verify whether aligned NFMs could accelerate diabetes

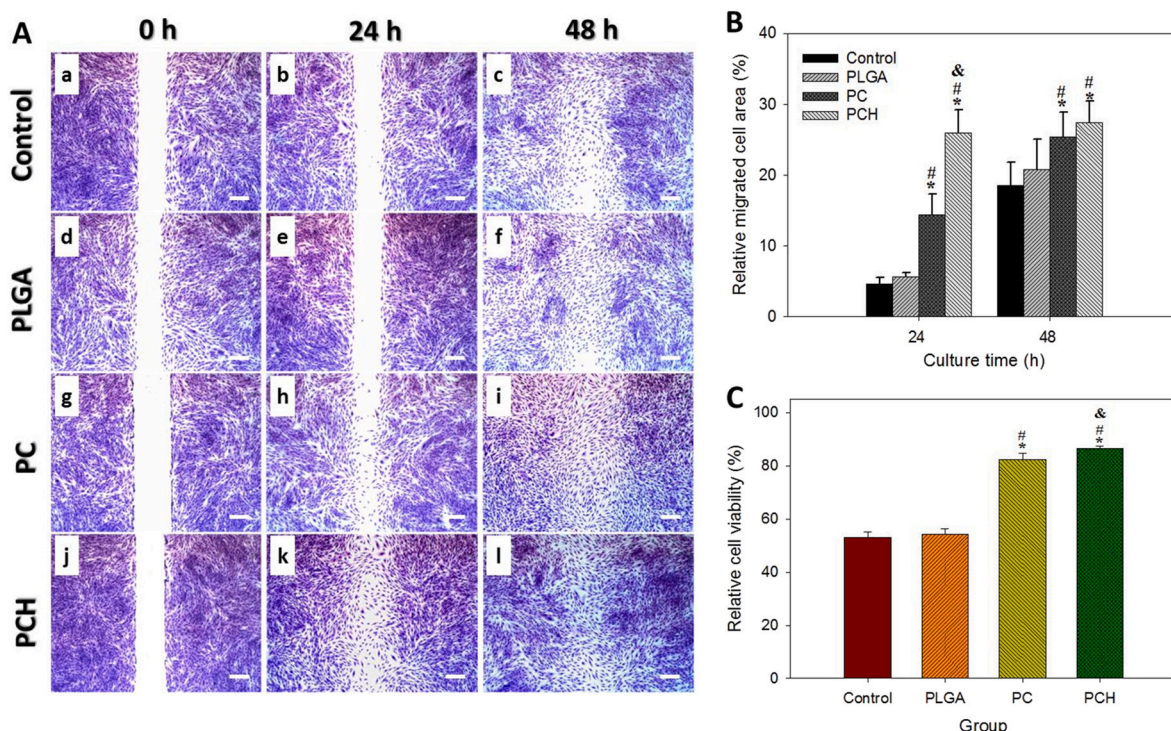


**Fig. 7.** In vitro wound healing assays from migration of HS68 fibroblasts after cultured with cell culture medium (control, a–c), 48 h extraction medium of PLGA (d–f), PC (g–i) or PCH NFM (j–l). The microscopic images of stained cells after cultured with the extraction medium for 24 and 48 h are shown in (A) (bar = 200  $\mu$ m), from which the relative migrated cell area was quantified using an image analysis software based on initial wound area at 0 h (B). (C) The relative cell viability of HS68 fibroblasts by MTS assays after cultured in cell medium (control), 48 h extraction medium of PLGA, PC or PCH NFM for 24 h in the presence of 1% hydrogen peroxide. The cell viability was taken as 100% in the absence of hydrogen peroxide for each group. \* $p < 0.05$  relative to control, # $p < 0.05$  relative to PLGA, & $p < 0.05$  relative to PC.

wound healing and to explore whether the combination of heparin grafting and curcumin controlled release could promote wound healing, an in vivo wound healing study was carried out using streptozotocin-induced diabetic SD rats. The healing rates of critical size wounds created in diabetic SD rats were evaluated after individually covering the wound with gauze (control), PLGA, PC or PCH NFMs (Fig. S1A, supplementary materials). The dressing was removed from the wound at day 3, 7 and 14 post-treatment for gross observation of wounds (Fig. S1B, supplementary materials). The wound area was estimated by image analysis from the gross view images taken from the wound area (Fig. 8A). The wound closure rate was compared among treatment groups using NFMs and the control group using gauze after normalizing the remaining wound size with the respective initial wound size. In accordance with the significant effect of curcumin-loaded NFMs in vitro, the diabetic wounds treated with PC and PCH showed faster wound healing rate compared with control and PLGA groups, with PCH NFM providing the best outcomes of wound healing. As shown in Fig. 8B, as early as 3 days post-treatment, PCH and PC significantly decrease the area of the wound to  $58.3 \pm 5.5\%$  and  $58.1 \pm 3.6\%$ , respectively, which are significantly less than the control ( $66.2 \pm 4.9\%$ ). The wound healing effect of all NFM-treated groups showed significant improvement over the control on day 7 with the PCH NFM group starting to show significant difference from the PLGA group. On day 14, the combined effect of curcumin and heparin manifest themselves in the PCH group, which significantly improved the wound healing rate over PC (with curcumin only). The wound size is in the order of PCH ( $13.9 \pm 6.6\%$ ) < PC ( $20.5 \pm 0.9\%$ ) < PLGA ( $27.4 \pm 4.4\%$ ) < gauze ( $37.1 \pm 6.6\%$ ), with significant difference among groups.

Interestingly, the PLGA NFM shows improved wound healing with significant contraction of wound size when compared with control gauze after day 7, which is in accordance with a previous report that released lactate from PLGA could promote wound healing [27]. It is also possible

the aligned nanofiber orientation can facilitate migration of fibroblasts and keratinocytes from the wound area peripheral to the center and promote re-epithelization and collagen deposition to shorten the wound healing time [55]. Encapsulation of curcumin in nanomaterials were shown to be an efficient and promising approach to maximize wound healing efficacy of curcumin [56]. Various topical formulations of curcumin such as films, fibers, emulsion, hydrogels and different nano-formulations were shown to deliver curcumin in a sustained way at the wounded site to improve the therapeutic effects [57]. Curcumin-loaded poly( $\epsilon$ -caprolactone) (PCL) nanofibers was demonstrated to increase the rate of wound closure in a diabetic mice model [58]. Mice treated with curcumin-loaded PCL nanofibers showed 80% wound closure, compared with only 60% wound closure in mice treated with PCL nanofibers on day 10. PLGA nanoparticles encapsulating curcumin could accelerate the wound healing in a full thickness excisional wound healing mouse model where PLGA–curcumin nanoparticles showed a two-fold higher wound healing activity compared to that of PLGA or curcumin [59]. Using electrospun curcumin-loaded PCL/gum tragacanth nanofibers for wound healing in diabetic rats, the pathological study showed that the nanofibers lead to markedly faster wound closure rate. Well-formed granulation tissues dominated by fibroblast proliferation, collagen deposition, complete early regenerated epithelial layer and formation of sweat glands and hair follicles were found after 15 days [60].

Although PC and PCH NFMs showed better wound healing due to their respective therapeutic activities, PCH accelerated the healing more profoundly than PC due to additive activity of released curcumin and add-on growth factor sequestering ability of heparin. These data suggested accelerated wound healing with aligned PLGA nanofibers compared with the control from the early phase of wound healing, which could be further improved by incorporating the exogenous therapeutic factor curcumin. Overall, the multi-functional PCH NFM is deemed as the most effective treatment for the diabetic wound to



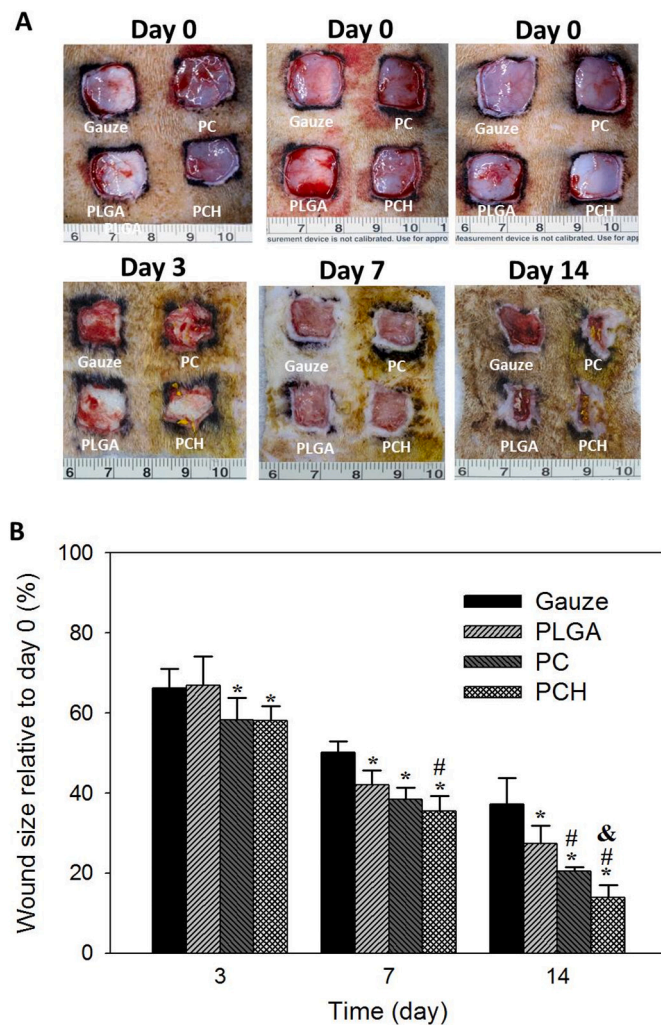


**Fig. 8.** (A) Wound closure for diabetic rats treated with gauze (control), PLGA, PC or PCH NFMs on day 0, 3, 7 and 14. (B) The relative wound size was determined from image analysis of the wound area from traced wound border covered with epithelium for each treatment and normalized to the initial wound area on day 0 ( $n = 4$ ). \* $p < 0.05$  relative to control, # $p < 0.05$  relative to PLGA, & $p < 0.05$  relative to PC.

effectively accelerate wound healing by reducing wound size to less than 14% of its original size in diabetic rats within 14 days. Undoubtedly, this trend is in accordance with our original objective by sequestering endogenous growth factors around the wound area through the action of grafted heparin in NFM, which must be subject to further examination through protein expression analysis of the healed wound tissues.

### 3.6. Histological analysis of wounds

At the final time point (day 14), skin tissue samples were harvested and examined by hematoxylin and eosin (H&E) staining for general observation of skin layers, Masson's trichrome staining to study the extent of collagen deposition and immunohistochemistry (IHC) analysis of  $\alpha$ -SMA expression (Fig. 9). Representative wound histology from HE stains for all groups showed clear differences in the extent of re-epithelialization and granulation tissue formation in the wounds after different treatments. The stratum corneum, stratum spinosum and stratum basale were differentiable in the PC and PCH groups, suggesting that the skin had partially recovered from the injury (Fig. 9A). Specifically, complete re-epithelialization and differentiated epithelium characterized by well-developed epidermis layers were shown in

wounds subjected to PCH NFM treatment, which clearly differed from less-differentiated epidermis in wounds treated with PC or epithelial incompleteness accompanied by fibrinous debris in wounds of control group and PLGA groups (Fig. 9A). Indeed, a loose crust of dermal layers and poor epithelium were evident in the control and PLGA groups while PC and PCH groups demonstrated a varied degree of migration of the epithelium over the dermis, granulation tissue formation and dermal remodeling. The PCH group showed complete re-epithelialization of the wound with well-formed and differentiated epithelium and significant increased deposition of connective tissue. Furthermore, more stratified epidermal layers were observed in PCH where papilla basement membrane was also observed as signs of well-defined dermal-epidermal junctions. The PCH group also showed neo-vascular structure compared to other groups.

The Masson trichrome stain could reveal the extent of collagen deposition in addition to the alignment of collagen fiber after wound healing. When stained with Masson's trichrome, keratin and muscle fiber were stained in red while collagen in blue. The Masson's trichrome staining clearly indicates increased collagen expression in the PCH group, with a dermal layer much closer in appearance to that of normal skin (Fig. 9B). Furthermore, neovascular structure was also visualized in PCH group from the H&E and Masson's trichrome staining. The neo-vessel formation in the newly formed skin tissue is expected to promote the vascularization in the damaged tissue for faster wound healing.

$\alpha$ -SMA is a marker for myofibroblasts that are largely responsible for wound contraction and production of ECM components such as collagen [61]. TGF- $\beta$ 1 is considered to be the major growth factor directly promoting myofibroblast development by inducing expression of  $\alpha$ -SMA, which are "fine-tuned" by cooperative or antagonistic growth factors [62]. Besides myofibroblasts,  $\alpha$ -SMA is also expressed by pericytes, which wrap around the endothelial cells lining the capillaries and are required for the maturation of blood vessels [63]. Therefore, the expression of  $\alpha$ -SMA marker in wounded tissue is deemed important for blood vessel maturation and wound contraction [64]. Increased  $\alpha$ -SMA expression by myofibroblasts and pericytes is shown for all groups from IHC staining of  $\alpha$ -SMA on day 14 (Fig. 9C). Indeed,  $\alpha$ -SMA-positive myofibroblasts in PCH group arranged more orderly and compactly than other groups, indicating the early differentiation of fibroblasts into myofibroblasts. The vascularization of wounds examined from IHC staining for  $\alpha$ -SMA also revealed extensive staining of blood vessel walls in the PCH treated wounds, indicating early blood vessel formation not present in other groups (Fig. 9C). Quantitative analysis of IHC staining images from image analysis indicated the area percentage of  $\alpha$ -SMA positive vessels in PCH group ( $17.4 \pm 4.0\%$ ) is significant higher than that associated with other groups, which is 5.8, 3.6 and 1.9 folds that of gauze ( $3.0 \pm 0.8\%$ ), PLGA ( $4.9 \pm 2.0\%$ ) and PC ( $9.4 \pm 0.9\%$ ) (Fig. 9D). As the vascularized area was significantly increased after PCH treatment, this heparin grafted membrane would be beneficial for critical wound healing originated from its growth factor sequestering ability. It could be suggested that PCH may enhance vessel formation and accelerate diabetic wound healing by sequestering and stabilizing growth factors such as TGF- $\beta$ 1 and FGF-2. By high density grafting heparin onto the surface of biodegradable nanofibers, sequestering, stabilization and release of endogenous growth factors could be expected in the wound as the matrix degrades in vivo.

### 3.7. Anti-inflammatory effect from qRT-PCR

Diabetic wounds are characterized by prolonged inflammation and oxidative stress originated from the hyperglycemic microenvironment, which will prevent the diabetic wound from transferring to the next proliferation phase with the prolonged inflammation phase [65]. The high oxidative stress environment in diabetic wounds also impair macrophage and neutrophil function in the inflammation phase, impair keratinocytes for delayed re-epithelialization and impair fibroblasts and vascular endothelial cells for insufficient granulation tissue and

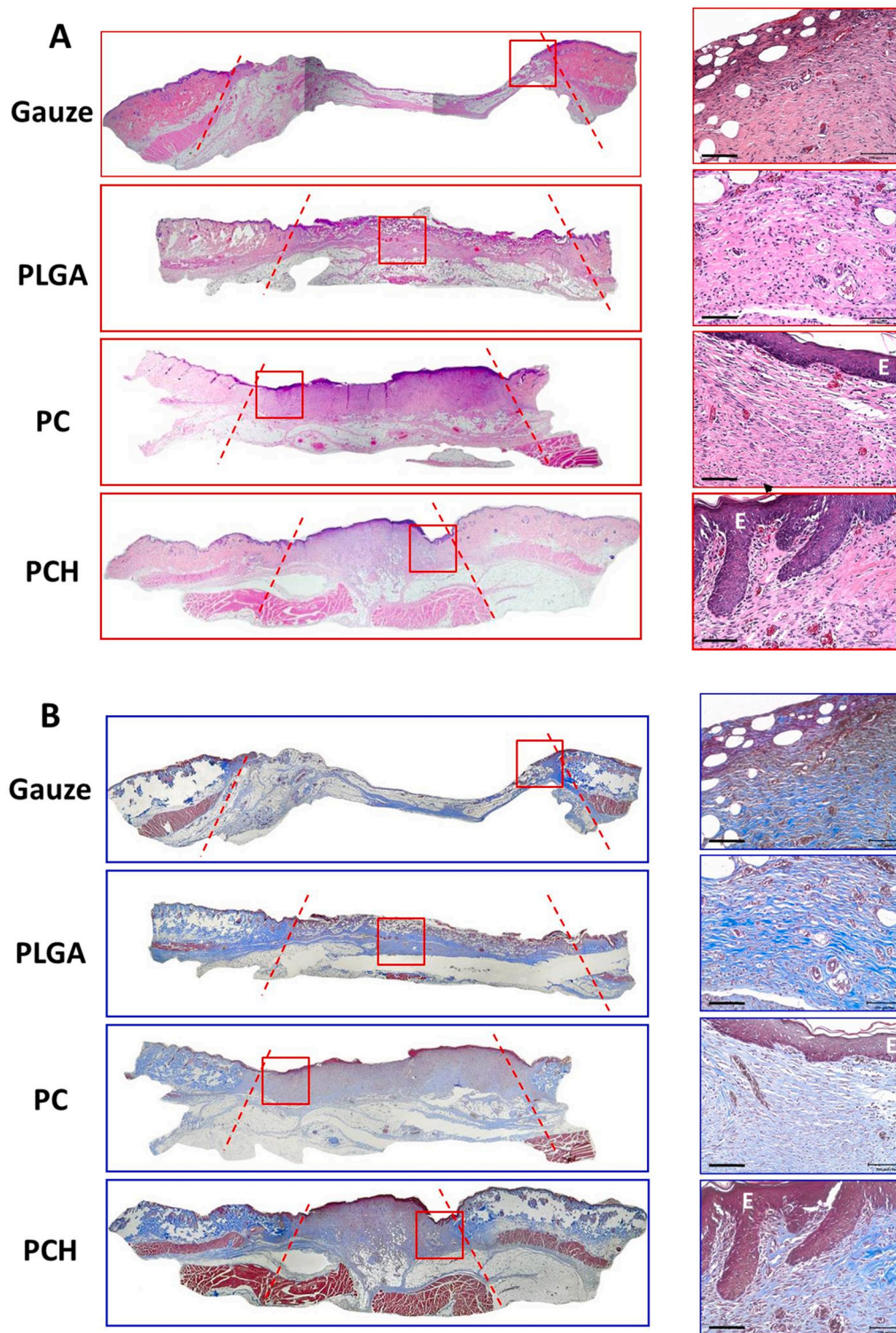


**Fig. 9.** Histological evaluation of wounds treated with gauze (control), PLGA, PC and PCH NFMs for 14 days by H&E (A) and Masson's trichrome staining (B) (bar = 100  $\mu$ m, E, epidermis). A low power image of each wound is shown with dotted lines indicating the boundary of created wound. A high power image taken from the rectangle in the low power image is shown to the right. White arrows in (A) indicate vessels perfused by blood. Images of immunohistochemical (IHC) staining (C) and the area percentage of  $\alpha$ -SMA positive vessels (D) on day 14 (bar = 100  $\mu$ m, V, vessel, L, lumen, M, myofibroblast, \* $p < 0.05$ ; \*\* $p < 0.01$ ). (For interpretation of the references to color in this figure, the reader is referred to the web version of this article.)

ischemia. As a dressing material for diabetic wound treatment must have anti-oxidative stress and anti-inflammation function, we evaluate the relative mRNA expression of the anti-oxidative enzyme glutathione peroxidase (GPx) and the transcription factor involved in cellular

inflammation response (NF $\kappa$ B) in wound tissues by qRT-PCR. This could verify whether released curcumin from PC or PCH NFM could retain its function in vivo for accelerated diabetic wound healing. As shown in Fig. 10, significant down regulation of GPx and NF $\kappa$ B gene expression



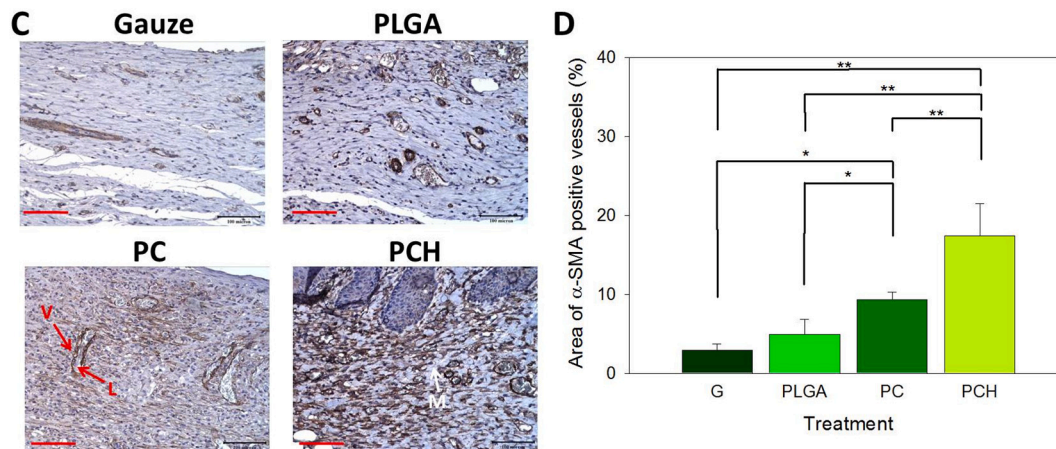


Fig. 9. (continued).

were found for PC and PCH compared to control and PLGA, which showed no significant difference between them on day 3 and 14 post-treatment. This reveals the sustained release of curcumin from the curcumin-containing PC and PCH NFMs can successfully quench ROS to enable reduction of GPx expression and mediate inflammation by regulating the PI3K/AKT/NFκB pathway.

Oxidative stress is a part of the wound physiology arising from the high cellular proliferation, migration and infiltration activities. The anti-oxidative enzymes like GPx can regulate the peroxidation rate and ROS generation at wounded area [66]. The low expression of GPx suggested that curcumin in PC and PCH NFMs may directly reduce the ROS level and indirectly inhibit the synthesis of endogenous antioxidant, which is consistent with previous findings [24,27]. Inflammation phase of the injury produced tremendous ROS, and it is possible to induce damage and lead to neoplastic transformation [67]. The successful quenching of ROS by released curcumin thus also leads to down-regulation of NFκB, which is a well-known transcription factor triggering the production of inflammatory cytokines by enhancing the inflammation pathway. Therefore, the results of GPx and NFκB relative mRNA expression underline the importance of sustained release of curcumin from PC to reduce inflammation throughout the wound healing process. This effect was further augmented, shown from accelerated wound closure in PCH, after additional benefit provided by heparin to justify the choice of PCH NFM as the best multi-functional wound dressing membrane. Overall, the PCH NFM exhibited the highest wound healing rate by

downregulating anti-oxidative enzymes and inflammatory marker gene expression and accelerating re-epithelialization, angiogenesis and collagen deposition in diabetes wound sites. The underlying mechanism may relate to the anti-oxidative stress and anti-inflammation effects of PCH, which demonstrates improved curcumin release rate after heparin grafting, for alleviating non-healing diabetic wounds. This will transfer the long-term inflammation phase into the proliferation phase to promote wound healing during diabetes wound healing [68]. The overall microenvironment change at wound sites induced by PCH therefore promoted a faster healing process for diabetic wounds.

#### 4. Conclusions

In this study, we employ nanotechnology-based engineering strategy to design electrospun NFMs as a multi-functional wound dressing material to accelerate diabetic wound healing. By taking advantage of the combined effects of curcumin and heparin, we designed functional aligned nanofibers by combining the exogenous effect from controlled delivery of curcumin and the endogenous effect from sequestered growth factors. The PC NFM is endowed with the intrinsic wound healing benefits provided by the base material PLGA, the aligned fiber orientation and the drug curcumin. This could be further programmed to provide specific binding sites for endogenous growth factors by surface grafting of high density heparin to fiber surface in PCH NFM to accelerate diabetic wound healing. With the high tensile strength, low

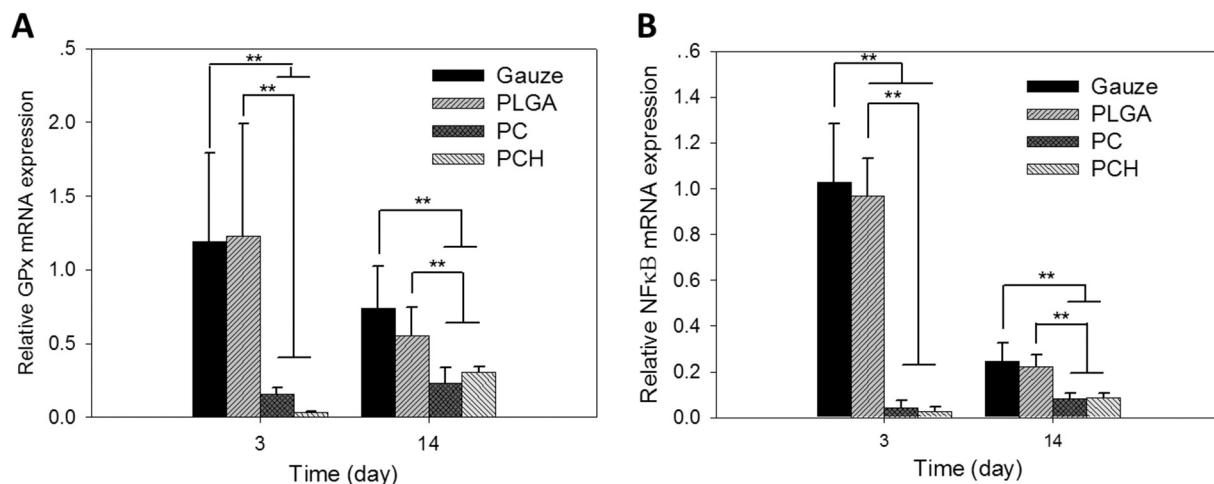


Fig. 10. Quantitative real-time PCR analysis of anti-inflammatory markers GPx (A) and NFκB (B) relative mRNA levels in skin tissue extracts of healed wounds of diabetic rats on day 3 and day 14 after treatment with gauze (control), PLGA, PC and PCH NFMs. Values are means  $\pm$  SD (n = 4). \* $p$  < 0.05, \*\* $p$  < 0.01.



cytotoxicity and suitable water vapor transmission rate, the PCH NFM was deemed as a suitable wound dressing material. Furthermore, as heparin surface grafting leads to higher curcumin release rate, PCH provides additional advantage such as higher migration ability and higher induced oxidative stress protection of HS68 fibroblast cells in vitro. In vivo study indicated the PCH NFM exhibits the fastest wound closure rate among all NFMs with accelerated re-epithelization, higher angiogenesis and collagen deposition at the wound site. Overall, this study suggests a promising nanofiber membrane to improve the clinical efficacy of diabetic wound healing by combining the heparin-induced endogenous factor (growth factors) and the exogenous factor (curcumin), which is expected to provide a basis for future development of material-based therapeutics.

Supplementary data to this article can be found online at <https://doi.org/10.1016/j.msec.2020.111689>.

### Declaration of competing interest

The authors declare that they have no known competing financial interests or personal relationships that could have appeared to influence the work reported in this paper.

### Acknowledgments

The authors would like to thank the Ministry of Science and Technology of Taiwan (ROC) (MOST106-2314-B-182-013-MY2) and Chang Gung Memorial Hospital (CMRPD2I0041, CMRPD2I0042 and BMRP249) for financially supporting this research.




### References

- J.S. Boateng, K.H. Matthews, H.N. Stevens, G.M. Eccleston, Wound healing dressings and drug delivery systems: a review, *J. Pharm. Sci.* 97 (8) (2008) 2892–2923.
- J.-P. Chen, G.-Y. Chang, J.-K. Chen, Electrospun collagen/chitosan nanofibrous membrane as wound dressing, *Colloids Surf. A Physicochem. Eng. Asp.* 313–314 (2008) 183–188.
- J.P. Chen, Y. Chiang, Bioactive electrospun silver nanoparticles-containing polyurethane nanofibers as wound dressings, *J. Nanosci. Nanotechnol.* 10 (11) (2010) 7560–7564.
- S.-H. Chen, Y. Chang, K.-R. Lee, J.-Y. Lai, A three-dimensional dual-layer nano/microfibrous structure of electrospun chitosan/poly(D,L-lactide) membrane for the improvement of cytocompatibility, *J. Membr. Sci.* 450 (2014) 224–234.
- M.S. Khil, D.I. Cha, H.Y. Kim, I.S. Kim, N. Bhattarai, Electrospun nanofibrous polyurethane membrane as wound dressing, *J. Biomed. Mater. Res. B Appl. Biomater.* 67 (2) (2003) 675–679.
- J. Xie, M.R. MacEwan, A.G. Schwartz, Y. Xia, Electrospun nanofibers for neural tissue engineering, *Nanoscale* 2 (1) (2010) 35–44.
- C.H. Chen, S.H. Chen, C.Y. Kuo, M.L. Li, J.P. Chen, Response of dermal fibroblasts to biochemical and physical cues in aligned polycaprolactone/silk fibroin nanofiber scaffolds for application in tendon tissue engineering, *Nanomaterials* (Basel, Switzerland) 7 (8) (2017).
- S. Zhong, W.E. Teo, X. Zhu, R.W. Beuerman, S. Ramakrishna, L.Y. Yung, An aligned nanofibrous collagen scaffold by electrospinning and its effects on in vitro fibroblast culture, *J. Biomed. Mater. Res.* A 79 (3) (2006) 456–463.
- K.D. Andrews, J.A. Hunt, Upregulation of matrix and adhesion molecules induced by controlled topography, *J. Mater. Sci. Mater. Med.* 19 (4) (2008) 1601–1608.
- M. Ottosson, A. Jakobsson, F. Johansson, Accelerated wound closure - differently organized nanofibers affect cell migration and hence the closure of artificial wounds in a cell based in vitro model, *PLoS One* 12 (1) (2017), e0169419.
- S. Patel, K. Kurpinski, R. Quigley, H. Gao, B.S. Hsiao, M.M. Poo, S. Li, Bioactive nanofibers: synergistic effects of nanotopography and chemical signaling on cell guidance, *Nano Lett.* 7 (7) (2007) 2122–2128.
- T. Velnar, T. Bailey, V. Smrkolj, The wound healing process: an overview of the cellular and molecular mechanisms, *J. Int. Med. Res.* 37 (5) (2009) 1528–1542.
- S. Werner, A novel enhancer of the wound healing process: the fibroblast growth factor-binding protein, *Am. J. Pathol.* 179 (5) (2011) 2144–2147.
- T. Kurahashi, J. Fujii, Roles of antioxidative enzymes in wound healing, *J. Dev. Biol.* 3 (2) (2015) 57.
- R.F. Diegelmann, M.C. Evans, Wound healing: an overview of acute, fibrotic and delayed healing, *Front. Biosci.* 9 (2004) 283–289.
- P.E. Porporato, V.L. Payen, C.J. De Saedeleer, V. Pr  at, J.-P. Thissen, O. Feron, P. Sonveaux, Lactate stimulates angiogenesis and accelerates the healing of superficial and ischemic wounds in mice, *Angiogenesis* 15 (4) (2012) 581–592.
- H. Park, K.Y. Lee, S.J. Lee, K.E. Park, W.H. Park, Plasma-treated poly(lactic-co-glycolic acid) nanofibers for tissue engineering, *Macromol. Res.* 15 (3) (2007) 238–243.
- J. Sharma, M. Lizu, M. Stewart, K. Zygula, Y. Lu, R. Chauhan, X. Yan, Z. Guo, E. Wujcik, S. Wei, Multifunctional Nanofibers towards active biomedical therapeutics, *Polymers* 7 (2) (2015) 186.
- S.J. Hewlings, D.S. Kalman, Curcumin: a review of its effects on human health, *Foods* (Basel, Switzerland) 6 (10) (2017).
- M. Sampath, R. Lakra, P. Korrapati, B. Sengottuvelan, Curcumin loaded poly(lactic-co-glycolic) acid nanofiber for the treatment of carcinoma, *Colloids Surf. B: Biointerfaces* 117 (2014) 128–134.
- D. Akbik, M. Ghadiri, W. Chrzanowski, R. Rohanizadeh, Curcumin as a wound healing agent, *Life Sci.* 116 (1) (2014) 1–7.
- X. Dai, J. Liu, H. Zheng, J. Wichmann, U. Hopfner, S. Sudhop, C. Prein, Y. Shen, H.-G. Machens, A.F. Schilling, Nano-formulated curcumin accelerates acute wound healing through Dkk-1-mediated fibroblast mobilization and MCP-1-mediated anti-inflammation, *NPG Asia Materials* 9 (3) (2017) e368.
- K.M. Shanmugam, G. Rane, M.M. Kanchi, F. Arfuso, A. Chinnathambi, E.M. Zayed, A.S. Alharbi, K.B. Tan, P.A. Kumar, G. Sethi, The multifaceted role of curcumin in cancer prevention and treatment, *Molecules* 20 (2) (2015).
- C. Mohanty, M. Das, S.K. Sahoo, Sustained wound healing activity of curcumin loaded oleic acid based polymeric bandage in a rat model, *Mol. Pharm.* 9 (10) (2012) 2801–2811.
- C. Buhrmann, A. Mobasher, F. Busch, C. Aldinger, R. Stahlmann, A. Montaseri, M. Shakibaei, Curcumin modulates nuclear factor kappaB (NF-kappaB)-mediated inflammation in human tenocytes in vitro: role of the phosphatidylinositol 3-kinase/Akt pathway, *J. Biol. Chem.* 286 (32) (2011) 28556–28566.
- N. Fereydouni, M. Darroudi, J. Movaffagh, A. Shahroodi, A.E. Butler, S. Ganjali, A. Sahebkar, Curcumin nanofibers for the purpose of wound healing, *J. Cell. Physiol.* 234 (2019) 5537–5554.
- M. Panchatcharam, S. Miriyala, V.S. Gayathri, L. Suguna, Curcumin improves wound healing by modulating collagen and decreasing reactive oxygen, *Mol. Cell. Biochem.* 290 (2006) 87–96.
- Y. Mo, Y. Zhang, B. Cheng, Y. Ahang, Controlled dual delivery of angiogenin and curcumin by electrospun nanofibers for skin regeneration, *Tissue Eng. A* 23 (13–14) (2017) 597–608.
- R. Sasisekharan, R. Raman, V. Prabhakar, Glycomics approach to structure-function relationships of glycosaminoglycans, *Annu. Rev. Biomed. Eng.* 8 (1) (2006) 181–231.
- D.L. Rabenstein, Heparin and heparan sulfate: structure and function, *Nat. Prod. Rep.* 19 (3) (2002) 312–331.
- K. Rajangam, H.A. Behanna, M.J. Hui, X. Han, J.F. Hulvat, J.W. Lomasney, S. I. Stupp, Heparin binding nanostructures to promote growth of blood vessels, *Nano Lett.* 6 (9) (2006) 2086–2090.
- H.J. Lai, C.H. Kuan, H.C. Wu, J.C. Tsai, T.M. Chen, D.J. Hsieh, T.W. Wang, Tailored design of electrospun composite nanofibers with staged release of multiple angiogenic growth factors for chronic wound healing, *Acta Biomater.* 10 (10) (2014) 4156–4166.
- D.K. Kweon, S.B. Song, Y.Y. Park, Preparation of water-soluble chitosan/heparin complex and its application as wound healing accelerator, *Biomaterials* 24 (9) (2003) 1595–1601.
- Y. Niu, Q. Li, Y. Ding, L. Dong, C. Wang, Engineered delivery strategies for enhanced control of growth factor activities in wound healing, *Adv. Drug Deliv. Rev.* 146 (2018) 190–208.
- J.P. Chen, C.H. Su, Surface modification of electrospun PLLA nanofibers by plasma treatment and cationized gelatin immobilization for cartilage tissue engineering, *Acta Biomater.* 7 (1) (2011) 234–243.
- J.P. Chen, P.C. Yang, Y.H. Ma, S.J. Tu, Y.J. Lu, Targeted delivery of tissue plasminogen activator by binding to silica-coated magnetic nanoparticle, *Int. J. Nanomedicine* 7 (2012) 5137–5149.
- G. Rohman, S.C. Baker, J. Southgate, N.R. Cameron, Heparin functionalisation of porous PLGA scaffolds for controlled, biologically relevant delivery of growth factors for soft tissue engineering, *J. Mater. Chem.* 19 (48) (2009) 9265–9273.
- H.M. Jeong, B.K. Ahn, B.K. Kim, Temperature sensitive water vapour permeability and shape memory effect of polyurethane with crystalline reversible phase and hydrophilic segments, *Polym. Int.* 49 (12) (2000) 1714–1721.
- H. Wu, R. Zhang, Y. Sun, D. Lin, Z. Sun, W. Pan, P. Downs, Biomimetic nanofiber patterns with controlled wettability, *Soft Matter* 4 (12) (2008) 2429–2433.
- G. Morello, R. Manco, M. Moffa, L. Persano, A. Camposeo, D. Pisignano, Multifunctional polymer nanofibers: UV emission, optical gain, anisotropic wetting, and high hydrophobicity for next flexible excitation sources, *ACS Appl. Mater. Interfaces* 7 (39) (2015) 21907–21912.
- H.J. Chung, H.K. Kim, J.J. Yoon, T.G. Park, Heparin immobilized porous PLGA microspheres for angiogenic growth factor delivery, *Pharm. Res.* 23 (8) (2006) 1835–1841.
- S. Bae, M.J. DiBalsi, N. Meilinger, C. Zhang, E. Beal, G. Korneva, R.O. Brown, K. G. Kornev, J.S. Lee, Heparin-eluting electrospun nanofiber yarns for antithrombotic vascular sutures, *Appl. Mater. Interfaces* 10 (10) (2018) 8426–8435.
-   . Kiss, I. Bert  ti, E.I. Vargha-Butler, XPS and wettability characterization of modified poly(lactic acid) and poly(lactic/glycolic acid) films, *J. Colloid Interface Sci.* 245 (1) (2002) 91–98.
- F.L. Mi, S.S. Shyu, Y.B. Wu, S.T. Lee, J.Y. Shyong, R.N. Huang, Fabrication and characterization of a sponge-like asymmetric chitosan membrane as a wound dressing, *Biomaterials* 22 (2) (2001) 165–173.
- L.O. Lamke, G.E. Nilsson, H.L. Reithner, The evaporative water loss from burns and the water-vapour permeability of grafts and artificial membranes used in the treatment of burns, *Burns* 3 (3) (1977) 159–165.

- [46] L. Ruiz-Cardona, Y.D. Sanzgiri, L.M. Benedetti, V.J. Stella, E.M. Topp, Application of benzyl hyaluronate membranes as potential wound dressings: evaluation of water vapour and gas permeabilities, *Biomaterials* 17 (16) (1996) 1639–1643.
- [47] G.H. Shin, J. Li, J.H. Cho, J.T. Kim, H.J. Park, Enhancement of curcumin solubility by phase change from crystalline to amorphous in Cur-TPGS nanosuspension, *J. Food Sci.* 81 (2) (2016) N494–N501.
- [48] M. Notoya, H. Nishimura, J.T. Woo, K. Nagai, Y. Ishihara, H. Hagiwara, Curcumin inhibits the proliferation and mineralization of cultured osteoblasts, *Eur. J. Pharmacol.* 534 (1–3) (2006) 55–62.
- [49] A. Scharstuhl, H.A. Mutsaers, S.W. Pennings, W.A. Szarek, F.G. Russel, F. A. Wagener, Curcumin-induced fibroblast apoptosis and in vitro wound contraction are regulated by antioxidants and heme oxygenase: implications for scar formation, *J. Cell. Mol. Med.* 13 (4) (2009) 712–725.
- [50] M.J. G. M.S. W. T. Lu, L.C. T. C.A. F. N.L. S, Curcumin-loaded poly( $\epsilon$ -caprolactone) nanofibres: diabetic wound dressing with anti-oxidant and anti-inflammatory properties, *Clin. Exp. Pharmacol. Physiol.* 36 (12) (2009) 1149–1156.
- [51] H.N. Kim, Y. Hong, M.S. Kim, S.M. Kim, K.Y. Suh, Effect of orientation and density of nanotopography in dermal wound healing, *Biomaterials* 33 (34) (2012) 8782–8792.
- [52] J. Xie, M.R. Macewan, W.Z. Ray, W. Liu, D.Y. Siewe, Y. Xia, Radially aligned, electrospun nanofibers as dural substitutes for wound closure and tissue regeneration applications, *ACS Nano* 4 (9) (2010) 5027–5036.
- [53] S.K. Sukumaran, R.J. Vadakkettikal, H. Kanakath, Comparative evaluation of the effect of curcumin and chlorhexidine on human fibroblast viability and migration: an in vitro study, *Journal of Indian Society of Periodontology* 24 (2) (2020) 109–116.
- [54] S. Patel, S. Srivastava, M.R. Singh, D. Singh, Mechanistic insight into diabetic wounds: pathogenesis, molecular targets and treatment strategies to pace wound healing, *Biomed. Pharmacother.* 112 (2019) 108615.
- [55] H. Hasmad, M.R. Yusof, Z.R. Mohd Razi, R.B. Hj Idrus, S.R. Chowdhury, Human amniotic membrane with aligned electrospun fiber as scaffold for aligned tissue regeneration, *Tissue Engineering. Part C, Methods* 24 (6) (2018) 368–378.
- [56] Z. Hussain, H.E. Thu, S.-F. Ng, S. Khan, H. Katas, Nanoencapsulation, an efficient and promising approach to maximize wound healing efficacy of curcumin: a review of new trends and state-of-the-art, *Colloids Surf. B: Biointerfaces* 150 (2017) 223–241.
- [57] C. Mohanty, S.K. Sahoo, Curcumin and its topical formulations for wound healing applications, *Drug Discov. Today* 22 (10) (2017) 1582–1592.
- [58] J.G. Merrell, S.W. McLaughlin, L. Tie, C.T. Laurencin, A.F. Chen, L.S. Nair, Curcumin-loaded poly( $\epsilon$ -caprolactone) nanofibres: diabetic wound dressing with anti-oxidant and anti-inflammatory properties, *Clin. Exp. Pharmacol. Physiol.* 36 (12) (2009) 1149–1156.
- [59] K.K. Cherredy, R. Coco, P.B. Memvanga, B. Ucar, A. des Rieux, G. Vandermeulen, V. Pr  at, Combined effect of PLGA and curcumin on wound healing activity, *J. Control. Release* 171 (2) (2013) 208–215.
- [60] M. Ranjbar-Mohammadi, S. Rabbani, S.H. Bahrami, M.T. Joghataei, F. Moayer, Antibacterial performance and in vivo diabetic wound healing of curcumin loaded gum tragacanth/poly( $\epsilon$ -caprolactone) electrospun nanofibers, *Mater. Sci. Eng. C* 69 (2016) 1183–1191.
- [61] I.A. Darby, B. Laverdet, F. Bont  , A. Desmouli  re, Fibroblasts and myofibroblasts in wound healing, *Clin. Cosmet. Investig. Dermatol.* 7 (2014) 301–311.
- [62] B. Hinz, Formation and function of the myofibroblast during tissue repair, *J. Investig. Dermatol.* 127 (3) (2007) 526–537.
- [63] G. Bergers, S. Song, The role of pericytes in blood-vessel formation and maintenance, *Neuro-Oncology* 7 (4) (2005) 452–464.
- [64] R.J. Bodnar, L. Satish, C.C. Yates, A. Wells, Pericytes: a newly recognized player in wound healing, *Wound Repair Regen.* 24 (2) (2016) 204–214.
- [65] C.-C.E. Lan, C.-S. Wu, S.-M. Huang, I.H. Wu, G.-S. Chen, High-glucose environment enhanced oxidative stress and increased interleukin-8 secretion from keratinocytes: new insights into impaired diabetic wound healing, *Diabetes* 62 (7) (2013) 2530–2538.
- [66] A.M. Rasik, A. Shukla, Antioxidant status in delayed healing type of wounds, *Int. J. Exp. Pathol.* 81 (4) (2000) 257–263.
- [67] H. Steiling, B. Munz, S. Werner, M. Brauchle, Different types of ROS-scavenging enzymes are expressed during cutaneous wound repair, *Exp. Cell Res.* 247 (2) (1999) 484–494.
- [68] Y. Han, Y. Jiang, Y. Li, M. Wang, T. Fan, M. Liu, Q. Ke, H. Xu, Z. Yi, An aligned porous electrospun fibrous scaffold with embedded asiatic acid for accelerating diabetic wound healing, *J. Mater. Chem. B* 7 (40) (2019) 6125–6138.

## Article

# Novel Caryophyllane-Related Sesquiterpenoids with Anti-Inflammatory Activity from *Rumphella antipathes* (Linnaeus, 1758)

Yu-Chia Chang <sup>1,†</sup> , Chih-Chao Chiang <sup>2,†</sup>, Yuan-Shiun Chang <sup>3</sup>, Jih-Jung Chen <sup>4</sup> , Wei-Hsien Wang <sup>5</sup>, Lee-Shing Fang <sup>5,6,7</sup>, Hsu-Ming Chung <sup>8,\*</sup>, Tsong-Long Hwang <sup>1,9,10,11,12,\*</sup> , and Ping-Jyun Sung <sup>5,13,14,15,16,\*</sup> 

- <sup>1</sup> Research Center for Chinese Herbal Medicine, Graduate Institute of Healthy Industry Technology, College of Human Ecology, Chang Gung University of Science and Technology, Taoyuan 333324, Taiwan; ycchang03@mail.cgu.edu.tw
  - <sup>2</sup> Graduate Institute of Clinical Medical Sciences, College of Medicine, Chang Gung University, Taoyuan 333323, Taiwan; D0600501@cgu.edu.tw
  - <sup>3</sup> Department of Chinese Pharmaceutical Sciences and Chinese Medicine Resources, College of Chinese Medicine, China Medical University, Taichung 404333, Taiwan; yschang@mail.cmu.edu.tw
  - <sup>4</sup> Faculty of Pharmacy, School of Pharmaceutical Sciences, National Yang-Ming University, Taipei 112304, Taiwan; chenjj@ym.edu.tw
  - <sup>5</sup> Department of Marine Biotechnology and Resources, College of Marine Sciences, National Sun Yat-sen University, Kaohsiung 804201, Taiwan; whw@mail.nsysu.edu.tw (W.-H.W.); lsfang@gcloud.csu.edu.tw (L.-S.F.)
  - <sup>6</sup> Center for Environmental Toxin and Emerging-Contaminant Research, Cheng Shiu University, Kaohsiung 833301, Taiwan
  - <sup>7</sup> Super Micro Mass Research and Technology Center, Cheng Shiu University, Kaohsiung 833301, Taiwan
  - <sup>8</sup> Department of Applied Chemistry, College of Science, National Pingtung University, Pingtung 900393, Taiwan
  - <sup>9</sup> Graduate Institute of Natural Products, College of Medicine, Chang Gung University, Taoyuan 333323, Taiwan
  - <sup>10</sup> Department of Anesthesiology, Chang Gung Memorial Hospital, Taoyuan 333423, Taiwan
  - <sup>11</sup> Department of Chemical Engineering, College of Environment and Resources, Ming Chi University of Technology, New Taipei City 243303, Taiwan
  - <sup>12</sup> Research Center for Food and Cosmetic Safety, College of Human Ecology, Chang Gung University of Science and Technology, Taoyuan 333324, Taiwan
  - <sup>13</sup> National Museum of Marine Biology and Aquarium, Pingtung 944401, Taiwan
  - <sup>14</sup> Graduate Institute of Marine Biology, College of Marine Sciences, National Dong Hwa University, Pingtung 944401, Taiwan
  - <sup>15</sup> Chinese Medicine Research and Development Center, China Medical University Hospital, Taichung 404394, Taiwan
  - <sup>16</sup> Graduate Institute of Natural Products, College of Pharmacy, Kaohsiung Medical University, Kaohsiung 807378, Taiwan
- \* Correspondence: shiuanmin@mail.nptu.edu.tw (H.-M.C.); htl@mail.cgu.edu.tw (T.-L.H.); pjsung@nmmba.gov.tw (P.-J.S.); Tel.: +886-8-766-3800 (ext. 33253) (H.-M.C.); +886-3-211-8800 (T.-L.H.); +886-8-882-5037 (P.-J.S.); Fax: +886-8-723-0305 (H.-M.C.); +886-3-211-8506 (T.-L.H.); +886-8-882-5087 (P.-J.S.)
- † These authors contributed equally to this work.

Received: 21 September 2020; Accepted: 2 November 2020; Published: 6 November 2020



**Abstract:** Two previously undescribed caryophyllane-related sesquiterpenoids, antipacids A (1) and B (2), with a novel bicyclo[5.2.0] core skeleton, and known compound clovane-2 $\beta$ ,9 $\alpha$ -diol (3), along with rumphellolide L (4), an esterified product of 1 and 3, were isolated from the organic extract of octocoral *Rumphella antipathes*. Their structures, including the absolute configurations were elucidated by spectroscopic and chemical experiments. In vivo anti-inflammatory activity analysis indicated

that antipacid B (2) inhibited the generation of superoxide anions and the release of elastase by human neutrophils, with  $IC_{50}$  values of 11.22 and 23.53  $\mu M$ , respectively, while rumphellolide L (4) suppressed the release of elastase with an  $IC_{50}$  value of 7.63  $\mu M$ .

**Keywords:** *Rumphella antipathes*; antipacid; caryophyllane; clovane; rumphellolide; superoxide anion; elastase

## 1. Introduction

*Rumphella* (family Gorgoniidae) is a genus of soft coral consisting of four species, *R. aggregata*, *R. antipathes*, *R. suffruticosa*, and *R. torta*, the center of marine diversity of this genus being found in the Indo-Pacific Ocean. Corals were described by Shi-Zhen Li in his ancient herbal *Compendium of Chinese Materia Medica*, published in 1596, as “sweet, neutral and non-toxic; used to remove eye vision obstruction; clear abiding static blood; blow the powder to nose to stop nose bleeding; brighten the eye and calm the spirit; stop epileptic seizure; apply to the eye to improve floater.” Previous studies showed that the *Rumphella* genus exhibited extensive bioactivities, including antiproliferative [1], cytotoxic [2–4], antifungal [5], antibacterial [6–9], and anti-inflammatory [10–18] activities. Studies of the chemical constituents of octocorals of the *Rumphella* genus have led to the isolation of a series of compounds, including caryophyllanes [2,6–12,16–22], clovanes [13–15,23], steroids [3–5,24,25], glycerols [5], and fatty acids and lipids [25–29]. Our continuing studies of the constituents of the same extract from *R. antipathes* (Figure 1) resulted in the isolation of two novel caryophyllane-related sesquiterpenoids, antipacids A (1) and B (2), featuring a bicyclo[5.2.0] carbon core; a known sesquiterpenoid, clovane-2 $\beta$ ,9 $\alpha$ -diol (3); and rumphellolide L (4), an esterified product of 1 and 3 (Figure 1). This paper describes the isolation, structure determination, biosynthetic pathway analysis, and anti-inflammatory properties of sesquiterpenoids 1–4.

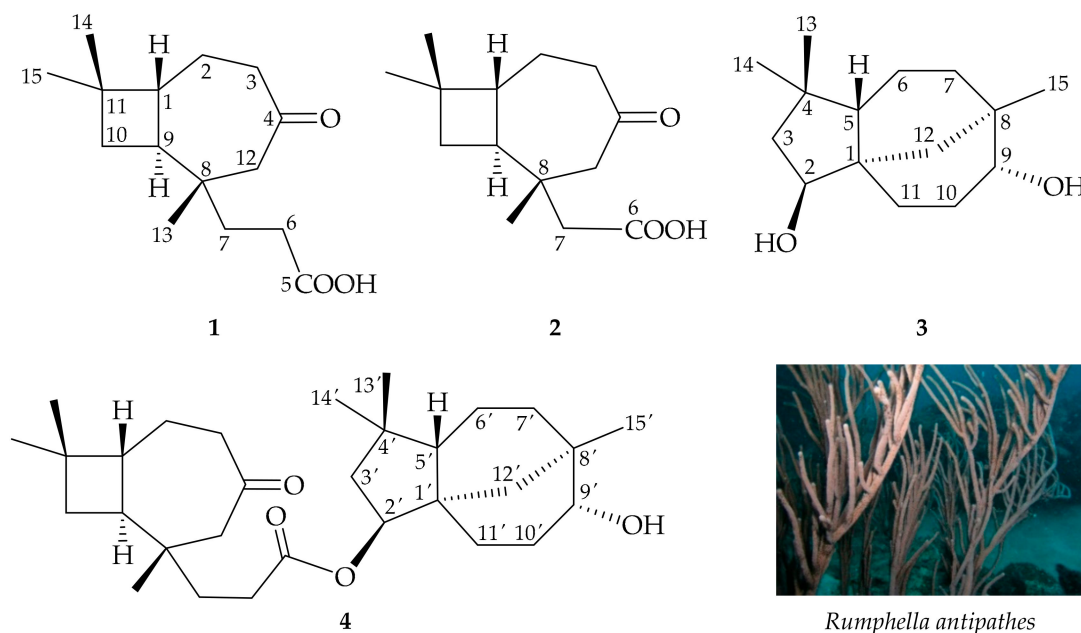


**Figure 1.** Structures of antipacids A (1) and B (2), clovane-2 $\beta$ ,9 $\alpha$ -diol (3), and rumphellolide L (4), and an image of *Rumphella antipathes*.

## 2. Results and Discussion

Antipacid A (1) was obtained as a colorless colloid, showing an electrospray ionization mass spectrum (ESIMS) quasimolecular ion peak at  $m/z$  253, and was found to have the molecular formula

$C_{15}H_{24}O_3$  by analysis of  $^{13}C$  and  $^1H$  NMR data (Table 1); this conclusion was confirmed by a positive-mode high-resolution-ESIMS ([+]-HRESIMS) peak at  $m/z$  253.1792  $[M + H]^+$  (calcd. for  $C_{15}H_{24}O_3 + H$ , 253.1789), with four indexes of hydrogen deficiency. The IR spectrum showed absorption bands at 3600–2400 (carboxyl group) and  $1708\text{ cm}^{-1}$  (ketonic carbonyl). From the  $^{13}C$  NMR data of **1** (Table 1), ketonic ( $\delta_C$  212.8, C-4) and carboxyl ( $\delta_C$  179.1, C-5) groups were deemed present. Thus, **1** was identified as a bicyclic compound.  $^1H$ - $^1H$  correlation spectroscopy (COSY) enabled identification of two spin systems,  $H_2$ -10/ $H$ -9/ $H$ -1/ $H$ -2/ $H$ -3 and  $H_2$ -6/ $H$ -7 (Figure 2). These findings, together with the  $^2J$ - and  $^3J$ - $^1H$ - $^{13}C$  long-range correlations between protons and non-protonated carbons, such as  $H_2$ -3,  $H_2$ -12/C-4;  $H_2$ -6,  $H_2$ -7/C-5;  $H_2$ -6,  $H_2$ -7,  $H$ -9,  $H_2$ -10,  $H_2$ -12,  $H_3$ -13/C-8; and  $H$ -1,  $H_2$ -10,  $H_3$ -14,  $H_3$ -15/C-11 in the heteronuclear multiple-bond coherence (HMBC) experiment (Figure 2), permitted elucidation of the main carbon skeleton of **1**.

**Table 1.**  $^1H$  (400 MHz,  $CDCl_3$ ) and  $^{13}C$  (100 MHz,  $CDCl_3$ ) NMR data of **1** and **2**.

C/H	1		2	
	$\delta_H$ (J in Hz)	$\delta_C$ , Type	$\delta_H$ (J in Hz)	$\delta_C$ , Type
1	1.77 ddd (10.4, 10.4, 3.6)	45.3, CH	1.81 ddd (10.8, 10.8, 3.6)	44.9, CH
2a/b	1.70 m; 1.64 m	23.7, $CH_2$	1.71 m; 1.62 m	23.7, $CH_2$
3a/b	2.48 m; 2.41 m	43.8, $CH_2$	2.49 m	43.7, $CH_2$
4	-	212.8, C	-	212.5, C
5	-	179.1, C	-	-
6	2.27 m	29.3, $CH_2$	-	176.0, C
7a/b	1.72 m; 1.53 m	36.5, $CH_2$	2.29 d (13.6); 2.28 d (13.6)	44.7, $CH_2$
8	-	35.0, C	-	34.9, C
9	1.87 ddd (10.4, 10.4, 8.0)	46.3, CH	1.98 ddd (10.8, 10.8, 8.4)	46.2, CH
10a/b	1.57 dd (10.4, 8.0); 1.49 dd (10.4, 10.4)	35.5, $CH_2$	1.56 dd (10.8, 8.4); 1.48 dd (10.8, 10.8)	34.9, $CH_2$
11	-	34.4, C	-	33.9, C
12a/b	2.35 d (11.2); 2.30 d (11.2)	54.8, $CH_2$	2.60 d (11.2); 2.49 d (11.2)	54.1, $CH_2$
13	0.92 s	20.5, $CH_3$	1.08 s	21.2, $CH_3$
14	1.01 s	30.1, $CH_3$	1.02 s	30.1, $CH_3$
15	1.01 s	22.1, $CH_3$	1.01 s	22.1, $CH_3$

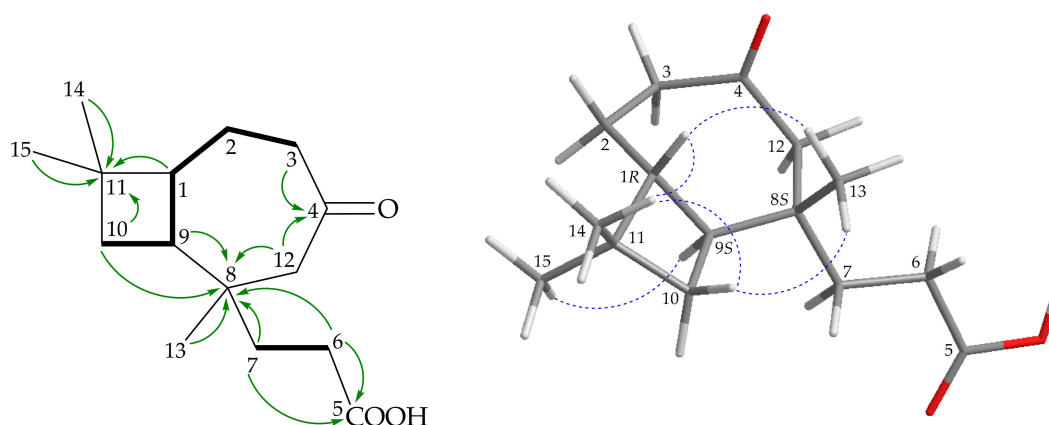


**Figure 2.** (A) Key COSY (—), HMBC (—), and (B) NOESY (---) correlations of **1**.

The relative configuration of **1** was assigned from the results of a nuclear Overhauser effect spectroscopy (NOESY) experiment (Figure 2) and vicinal coupling constants. The *trans* geometries of  $H$ -9 ( $\delta_H$  1.87) and  $H$ -1 ( $\delta_H$  1.77) were indicated by a large coupling constant ( $J = 10.4\text{ Hz}$ ) between these two ring juncture protons, and  $H$ -9 and  $H$ -1 were  $\alpha$ - and  $\beta$ -oriented, respectively.  $H$ -1 exhibited a correlation with  $H_3$ -13, setting Me-13 at C-8 on the  $\beta$  face. Based on the above findings, the stereogenic carbons of **1** were elucidated as (1*R*\*,8*S*\*,9*S*\*). Antipacids A (**1**) and B (**2**) were isolated along with natural



products rumphellaone A, a novel 4,5-*seco*-caryophyllane [2], and (8*R*,9*R*)-isocaryolane-8,9-diol [21,30] (the numbering system used in reference [30] was different to that in this study) from the same target organism, *R. antipathes* [2,21]. The structures, including the absolute configurations, of rumphellaone A [31–33] and (8*R*,9*R*)-isocaryolane-8,9-diol [30], were confirmed by synthetic methods. Based on these findings and previous studies [2,6–12,16–22], all marine-origin naturally occurring caryophyllane-type sesquiterpenoids have the H-9 *trans* to H-1, which are assigned as  $\alpha$ - and  $\beta$ -oriented, respectively. Therefore, it is reasonable on biogenetic grounds to suggest that **1** and **2** have the same absolute configuration as rumphellaone A and (8*R*,9*R*)-isocaryolane-8,9-diol, tentatively, and the configurations of the stereogenic carbons of **1** can be elucidated as (1*R*,8*S*,9*S*) (Supplementary Materials, Figures S1–S7).

Antipacid B (**2**) was isolated as a colorless colloid that showed a sodiated adduct ion peak in (+)-HRESIMS at  $m/z$  261.1468  $[M + Na]^+$ , which accounted for the molecular formula,  $C_{14}H_{22}O_3$  (calcd. for  $C_{14}H_{22}O_3 + Na$ , 261.1467), with 4 degrees of unsaturation. The spectroscopic data of **2** resembled those of **1** (Table 1). The one-dimensional (1D) and two-dimensional (2D) NMR spectra revealed that the signals corresponding to the propanoic acid moiety in **1** were replaced by those of an acetic acid in **2** (Figure 3). Therefore, **2** was assigned as having a structure with the same stereochemistry as **1** because of the stereogenic carbons that **2** had in common with **1** by correlations observed in the NOESY spectrum (Figure 3); therefore, the configurations of the stereogenic carbons of **2** were elucidated as (1*R*,8*S*,9*S*) (Supplementary Materials, Figures S8–S14).

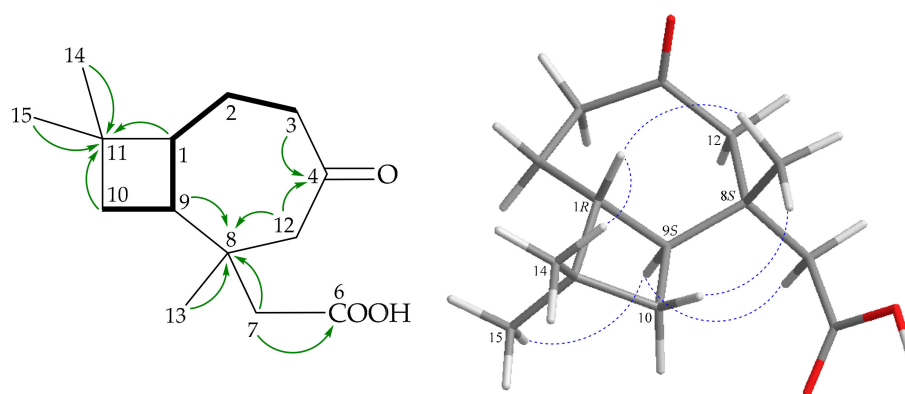
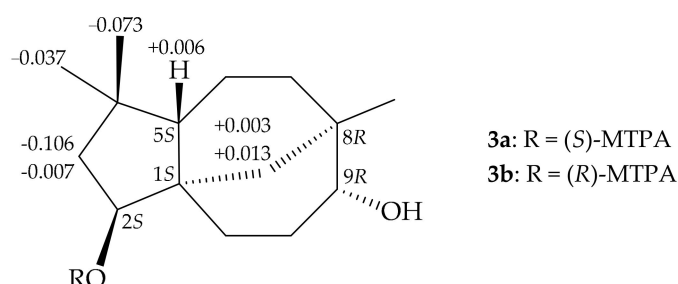


Figure 3. Key COSY (—), HMBC (—), and NOESY (---) correlations of **2**.

Compound **3** was identified by comparison of its spectroscopic data with those of clovane-2 $\beta$ ,9 $\alpha$ -diol, which had been previously isolated from terrestrial plants *Dipterocarpus pilosus* [34], *Salvia canariensis* [35], *Viguiera excelsa* [36], *Viguiera linearis* [37], and *Sindora sumatrana* [38]. This was the first occasion in which this metabolite was obtained from a marine source. Clovane **3** was treated with (*R*)-(-)- and (*S*)-(+)-MTPA chloride to yield (*S*)- and (*R*)-MTPA esters **3a** and **3b**, respectively. A comparison of the  $^1H$  NMR chemical shifts of **3a** and **3b** ( $\Delta\delta$  values shown in Figure 4) led to the assignment of the *S*-configuration at C-2 (Supplementary Materials, Figures S15–S16). Therefore, the absolute configurations of the stereogenic centers of **3** were determined as (1*S*,2*S*,5*S*,8*R*,9*R*).



**Figure 4.**  $^1\text{H}$  NMR chemical shift differences  $\Delta\delta$  ( $\delta_S - \delta_R$ ) in ppm for the MPTA esters of **3**.

Rumphellolide L (**4**) was isolated as a colorless colloid that showed a sodiated adduct ion peak  $[\text{M} + \text{Na}]^+$  at  $m/z$  495.3447 in (+)-HRESIMS. The result revealed that this compound had a molecular formula of  $\text{C}_{30}\text{H}_{48}\text{O}_4$  (calcd. for  $\text{C}_{30}\text{H}_{48}\text{O}_4 + \text{Na}$ , 495.3450), with 7 degrees of unsaturation. Strong bands at 3485, 1731, and  $1704\text{ cm}^{-1}$  in the IR spectrum indicated the presence of hydroxy, ester, and ketonic groups. The  $^{13}\text{C}$  NMR and distortionless enhancement by polarization transfer (DEPT) spectra revealed that **4** had 30 carbons (Table 2), including six methyls, twelve methylenes, five methines (including two oxymethines), five  $\text{sp}^3$  quaternary carbons, an ester carbonyl, and a ketonic carbonyl. Therefore, **4** was identified as having five rings.

**Table 2.**  $^1\text{H}$  (400 MHz,  $\text{CDCl}_3$ ) and  $^{13}\text{C}$  (100 MHz,  $\text{CDCl}_3$ ) NMR data for **4**.

C/H	$\delta_{\text{H}}$ (J in Hz)	$\delta_{\text{C}}$ , Type	C/H	$\delta_{\text{H}}$ (J in Hz)	$\delta_{\text{C}}$ , Type
1	1.77 m	45.2, CH	1'	-	44.5, C
2	1.64 m	23.6, $\text{CH}_2$	2'	4.83 dd (8.8, 6.0)	82.1, CH
3a/b	2.48 ddd (12.4, 7.6, 4.0); 2.39 m	43.7, $\text{CH}_2$	3'a/b	1.78 dd (12.0, 6.0); 1.51 m	44.3, $\text{CH}_2$
4	-	212.2, C	4'	-	38.0, C
5	-	173.6, C	5'	1.48 m	50.3, CH
6	2.21 t (7.6)	29.8, $\text{CH}_2$	6'	1.46 m	20.8, $\text{CH}_2$
7	1.73 m	36.7, $\text{CH}_2$	7'	1.40 m	33.0, $\text{CH}_2$
8	-	35.1, C	8'	-	34.6, C
9	1.87 ddd (10.8, 10.8, 8.4)	46.4, CH	9'	3.31 br s	74.9, CH
10	1.54 m	35.5, $\text{CH}_2$	10'a/b	2.00 m; 1.65 m	26.3, $\text{CH}_2$
11	-	34.4, C	11'	1.58 m	27.3, $\text{CH}_2$
12	2.31 s	54.9, $\text{CH}_2$	12'a/b	1.53 m; 1.01 m	35.4, $\text{CH}_2$
13	0.90 s	20.5, $\text{CH}_3$	13'	1.05 s	31.4, $\text{CH}_3$
14	1.02 s	30.1, $\text{CH}_3$	14'	0.91 s	25.3, $\text{CH}_3$
15	1.00 s	22.1, $\text{CH}_3$	15'	0.94 s	28.2, $\text{CH}_3$

From the  $^1\text{H}$ - $^1\text{H}$  COSY spectrum, the data differentiated the spin systems  $\text{H}_2$ -10/ $\text{H}$ -9/ $\text{H}$ -1/ $\text{H}_2$ -2/ $\text{H}_2$ -3,  $\text{H}_2$ -6/ $\text{H}_2$ -7,  $\text{H}$ -2'/ $\text{H}_2$ -3',  $\text{H}$ -5'/ $\text{H}_2$ -6'/ $\text{H}_2$ -7', and  $\text{H}$ -9'/ $\text{H}_2$ -10'/ $\text{H}_2$ -11' (Figure 5), and these findings together with the results of key HMBC correlations shown in Figure 5 confirmed the carbon skeleton of **4**. An HMBC correlation between  $\text{H}$ -2' ( $\delta_{\text{H}}$  4.83), an oxymethine proton, and the C-5 ester carbonyl carbon ( $\delta_{\text{C}}$  173.6) was found, which proved the existence of an ester linkage in **4**. It was found that the NMR data were similar to those of **1** and **3**, and this compound was proven to be the dehydrated product of **1** and **3**. Due to the absolute configurations of **1** and **3** having been determined, the absolute configurations of the stereogenic carbons of **4** were assigned as (1*R*,8*S*,9*S*,1'*S*,2'*S*,5'*S*,8'*R*,9'*R*) (Supplementary Materials, Figures S17–S23).

The proposed biogenetic pathway of sesquiterpenoids **1–4** is outlined in Scheme 1. The ring-opening reaction might be rationally derived from (8*R*,9*R*)-isocaryolane-8,9-diol [30] (the numbering system used in reference [30] was different to that in this study), which had also been isolated from *R. antipathes* [21], and might subsequently, under oxidation, produce the carbon skeletons of **1** and **2**.

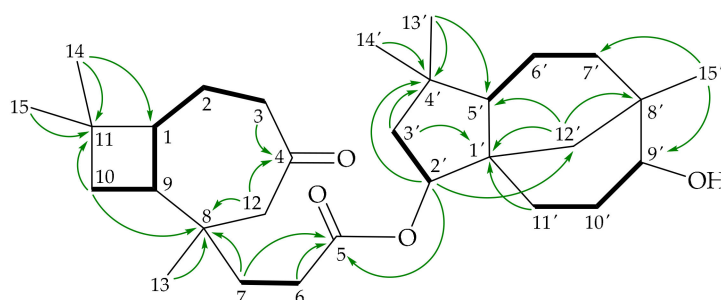
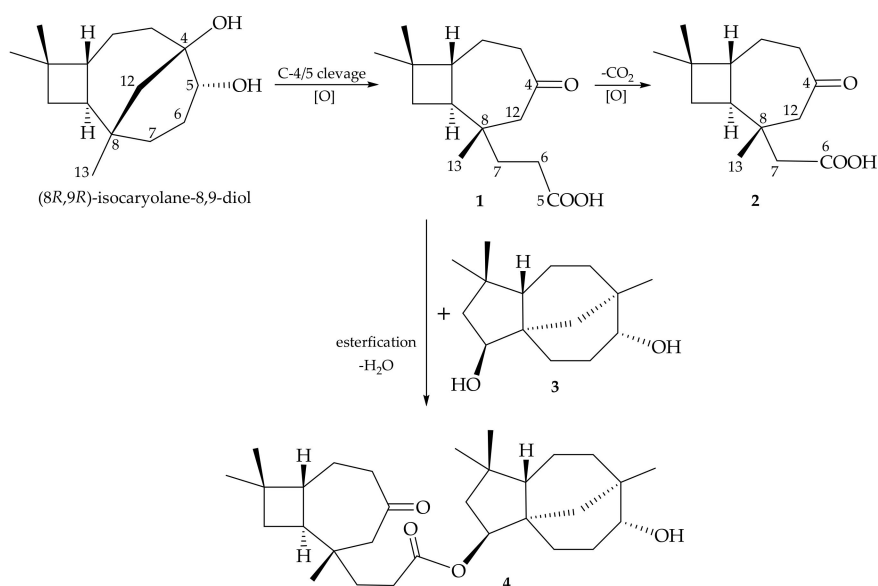


Figure 5. Key COSY (—) and HMBC (—) correlations of 4.



Scheme 1. Plausible biogenetic pathway of 1–4.

The *in vitro* anti-inflammatory effects of 1–4 were assessed (Table 3). Antipacid B (2) displayed inhibitory effects on the generation of superoxide anions and the release of elastase by human neutrophils ( $IC_{50}$  = 11.22 and 23.53  $\mu$ M, respectively). Antipacid A (1) did not show activity, implying that the presence of a large substituent at C-8 weakens the activity in comparison with the structure and anti-inflammatory activities of 2. Although 1 and 3 were not active, rumphellolide L (4), the dehydrated product of 1 and 3 with esterification, showed activity in inhibiting the release of elastase ( $IC_{50}$  = 7.63  $\mu$ M).

**Table 3.** Inhibitory effects of sesquiterpenoids 1–4 on superoxide anion generation and elastase release by human neutrophils in response to *N*-Formyl-L-methionyl-L-leucyl-L-phenylalanine/ Cytochalasin B (fMLF/CB).

Compound	Superoxide Anion		Elastase	
	$IC_{50}$ ( $\mu$ M) <sup>a</sup>	Inh % <sup>b</sup>	$IC_{50}$ ( $\mu$ M) <sup>a</sup>	Inh % <sup>b</sup>
1	-	11.89 $\pm$ 5.13	-	13.69 $\pm$ 2.33 *
2	11.22	-	23.53	-
3	-	22.92 $\pm$ 4.27 *	-	35.33 $\pm$ 6.40 *
4	-	19.57 $\pm$ 3.69 **	7.63	-

<sup>a</sup> Concentration necessary for 50% inhibition ( $IC_{50}$ ). <sup>b</sup> Percentage of inhibition (Inh %) at 10  $\mu$ g/mL. Results are presented as means  $\pm$  S.E.M (standard error of the mean) ( $n$  = 3). \*  $p$  < 0.05, \*\*  $p$  < 0.01 compared with the control (solvent, dimethyl sulfoxide-DMSO).

### 3. Materials and Methods

#### 3.1. General Experimental Procedures

Optical rotations were recorded on a JASCO-P1010 polarimeter (Japan Spectroscopic Corporation, Tokyo, Japan). IR spectra were obtained on a Varian Digilab FTS 1000 FT-IR spectrometer (Varian Inc., Palo Alto, CA, USA). NMR spectra were recorded on a Varian Mercury Plus 400 spectrometer (400 MHz for  $^1\text{H}$  and 100 MHz for  $^{13}\text{C}$ ) (Varian Inc.) using the residual  $\text{CHCl}_3$  ( $\delta_{\text{H}}$  7.26 ppm) and  $\text{CDCl}_3$  ( $\delta_{\text{C}}$  77.1 ppm) signals as internal references for  $^1\text{H}$  and  $^{13}\text{C}$  NMR, respectively.

Chemical shifts are shown in  $\delta$  (ppm) and coupling constants ( $J$ ) are given in Hz. ESIMS and HRESIMS data were recorded using a Bruker APEX II FTMS system (Bremen, Germany). Silica gel (230–400 mesh, Merck, Darmstadt, Germany) was used for column chromatography. Thin-layer chromatography (TLC) was performed on plates precoated with Kieselgel 60 F<sub>254</sub> (0.25-mm-thick, Merck), then sprayed with 10%  $\text{H}_2\text{SO}_4$  solution followed by heating to visualize the spots. Normal-phase HPLC (NP-HPLC) (Hitachi L-7100 series using a L-7455 photodiode array detector, Hitachi Ltd., Tokyo, Japan; and a semi-preparative Hibar 250 mm  $\times$  10 mm, LiChrospher Si 60, 5  $\mu\text{m}$  column, Merck) was employed.

#### 3.2. Animal Material

The octocoral *R. antipathes* (Linnaeus, 1758) was collected by hand by self-contained underwater breathing apparatus (SCUBA) divers off the coast of South Taiwan in May 2004. The samples were stored in a  $-20^\circ\text{C}$  freezer until used for extraction. Identification of the species of this organism was performed by comparison as described in previous studies [39,40]. A voucher specimen (no.: NMMBA-TWGC-010) was deposited in the National Museum of Marine Biology and Aquarium, Taiwan.

#### 3.3. Extraction and Isolation

*R. antipathes* (wet/dry weight = 402/144 g) was sliced and then extracted with a solvent mixture of MeOH and dichloromethane (DCM) (1:1). The extract was partitioned between ethyl acetate (EtOAc) and  $\text{H}_2\text{O}$ . The EtOAc layer (1.23 g) was then applied on silica gel column and eluted with gradients of hexanes/EtOAc (from 25:1 to 100% EtOAc) to furnish 29 subfractions. Fraction 18 was purified by NP-HPLC using a solvent mixture of *n*-hexane/EtOAc (5:1; at a flow rate = 3.0 mL/min) to yield **4** (3.5 mg, 5:1). Fraction 22 was separated by NP-HPLC using a mixture of DCM and EtOAc (10:1; at a flow rate = 5.0 mL/min) to afford **2** (3.5 mg). Fraction 24 was separated by NP-HPLC using a mixture of *n*-hexane and EtOAc (1:1; at a flow rate = 5.0 mL/min) to afford **1** (5.8 mg) and **3** (60.1 mg), respectively.

Antipacid A (**1**): Colorless colloid;  $[\alpha]_{25\text{D}} -9.2$  ( $c$  0.29,  $\text{CHCl}_3$ ); IR (neat)  $\nu_{\text{max}}$  3600–2400 (broad), 1708  $\text{cm}^{-1}$ ;  $^1\text{H}$  and  $^{13}\text{C}$  NMR data, see Table 1; ESIMS:  $m/z$  253  $[\text{M} + \text{H}]^+$ ; HRESIMS:  $m/z$  253.1792  $[\text{M} + \text{H}]^+$  (calcd. for  $\text{C}_{15}\text{H}_{24}\text{O}_3 + \text{H}$ , 253.1789).

Antipacid B (**2**): Colorless colloid;  $[\alpha]_{25\text{D}} -9.4$  ( $c$  0.18,  $\text{CHCl}_3$ ); IR (neat)  $\nu_{\text{max}}$  3600–2600 (broad), 1710  $\text{cm}^{-1}$ ;  $^1\text{H}$  and  $^{13}\text{C}$  NMR data, see Table 1; ESIMS:  $m/z$  261  $[\text{M} + \text{Na}]^+$ ; HRESIMS:  $m/z$  261.1468  $[\text{M} + \text{Na}]^+$  (calcd. for  $\text{C}_{14}\text{H}_{22}\text{O}_3 + \text{Na}$ , 261.1467).

Clovane-2 $\beta$ ,9 $\alpha$ -diol (**3**): Amorphous powder;  $[\alpha]_{23\text{D}} +3.5$  ( $c$  1.82,  $\text{CHCl}_3$ ) (ref. [38]  $[\alpha]_{\text{D}} +3.19$  ( $c$  2.27,  $\text{CHCl}_3$ )); IR (neat)  $\nu_{\text{max}}$  3378  $\text{cm}^{-1}$ ;  $^1\text{H}$  (400 MHz,  $\text{CDCl}_3$ ) and  $^{13}\text{C}$  (100 MHz,  $\text{CDCl}_3$ ) NMR data were found to be in complete agreement with a previous report [37]; ESIMS:  $m/z$  261  $[\text{M} + \text{Na}]^+$ .

Rumphellolide L (**4**): Colorless colloid;  $[\alpha]_{25\text{D}} -7.5$  ( $c$  0.18,  $\text{CHCl}_3$ ); IR (neat)  $\nu_{\text{max}}$  3485, 1731, 1704  $\text{cm}^{-1}$ ;  $^1\text{H}$  and  $^{13}\text{C}$  NMR data, see Table 2; ESIMS:  $m/z$  495  $[\text{M} + \text{Na}]^+$ ; HRESIMS:  $m/z$  495.3447  $[\text{M} + \text{Na}]^+$  (calcd. for  $\text{C}_{30}\text{H}_{48}\text{O}_4 + \text{Na}$ , 495.3450).

#### 3.4. (S)- and (R)-MTPA Esters of **3**

To a solution of **3** (10.0 mg) in pyridine (0.4 mL) (–)- $\alpha$ -methoxy- $\alpha$ -(trifluoromethyl)-phenylacetyl (MTPA) chloride was added (25.0  $\mu\text{L}$ ) at  $25^\circ\text{C}$  for 4–5 h. The mixture was dried and purified by a silica gel column with *n*-hexane/EtOAc (10:1) to give (S)-MTPA ester **3a** (8.5 mg). The (R)-MTPA ester

**3b** (0.2 mg) was prepared from (+)-MTPA chloride by the same method (10 mg compound **3** was used). Selected  $\Delta\delta$  values are shown in Figure 4.

### 3.5. Superoxide Anion Generation and Elastase Release by Human Neutrophils

The proinflammatory suppression assay was employed to assess the activities of isolated compounds **1–4** against the generation of superoxide anions and the release of elastase by human neutrophils according to the protocols described in the literature [41].

## 4. Conclusions

The current work illustrated the anti-neutrophilic inflammatory properties of caryophyllane-related sesquiterpenoids, and two metabolites with novel structures, antipacids A and B (**1** and **2**), clovane-2 $\beta$ ,9 $\alpha$ -diol (**3**), and rumphellolide L (**4**), an esterified product of **1** and **3**, were isolated from *R. antipathes*. Compound **2** displayed inhibitory effects on the generation of superoxide anions and the release of elastase, and **4** showed activity in suppressing the release of elastase. These results indicated a structural-dependent specificity of C-8 in **1**, **2**, and **4** in neutrophilic targets, which will motivate future research examining this specificity, as well as clarify the molecular mechanisms of the active leads.

**Supplementary Materials:** The following are available online at <http://www.mdpi.com/1660-3397/18/11/554/s1>, Figure S1: HRESIMS spectrum of **1**; Figures S2–S7:  $^1\text{H}$  NMR (400 MHz),  $^{13}\text{C}$  NMR (100 MHz), HMQC,  $^1\text{H}$ - $^1\text{H}$  COSY, HMBC and NOESY Spectrum of **1** in  $\text{CDCl}_3$ ; Figure S8: HRESIMS spectrum of **2**; Figures S9–S14:  $^1\text{H}$  NMR (400 MHz),  $^{13}\text{C}$  NMR (100 MHz), HMQC,  $^1\text{H}$ - $^1\text{H}$  COSY, HMBC and NOESY Spectrum of **2** in  $\text{CDCl}_3$ ; Figure S15:  $^1\text{H}$  NMR (S)-MTPA ester of **3** in  $\text{CDCl}_3$ ; Figure S16:  $^1\text{H}$  NMR (R)-MTPA ester of **3** in  $\text{CDCl}_3$ ; Figure S17: HRESIMS spectrum of **4**; Figures S18–S23:  $^1\text{H}$  NMR (400 MHz),  $^{13}\text{C}$  NMR (100 MHz), HMQC,  $^1\text{H}$ - $^1\text{H}$  COSY, HMBC and NOESY Spectrum of **4** in  $\text{CDCl}_3$ .

**Author Contributions:** Conceptualization, H.-M.C., T.-L.H., and P.-J.S.; investigation, Y.-C.C., C.-C.C., Y.-S.C., J.-J.C., W.-H.W., L.-S.F., and H.-M.C.; writing—original draft preparation, Y.-C.C., H.-M.C., and P.-J.S.; writing—review and editing, Y.-C.C., H.-M.C., T.-L.H., and P.-J.S. All authors have read and agreed to the published version of the manuscript.

**Funding:** This research was supported by grants from the NMMBA; and the Ministry of Science and Technology, Taiwan (Grant Nos: MOST 107-2320-B-291-001-MY3 and 109-2320-B-291-001-MY3) awarded to P.-J. Sung.

**Acknowledgments:** This research was supported by grants from the National Museum of Marine Biology and Aquarium; and the Ministry of Science and Technology (Grant Nos MOST 106-2320-B-291-001-MY3, 107-2320-B-291-001-MY3, and 109-2320-B-291-001-MY3), Taiwan, awarded to P.-J.S.

**Conflicts of Interest:** The authors declare no conflict of interest.

## References

1. Nourry, M.; Urvois, A.P.; Tomasoni, C.; Biard, J.F.; Verbist, J.F.; Roussakis, C. Antiproliferative effects of a product isolated from the gorgonian *Rumphella aggregata*. *Anticancer. Res.* **1999**, *19*, 1881–1885.
2. Chung, H.-M.; Chen, Y.-H.; Lin, M.-R.; Su, J.-H.; Wang, W.-H.; Sung, P.-J. Rumphellaone A, a novel caryophyllane-related derivative from the gorgonian coral *Rumphella antipathes*. *Tetrahedron Lett.* **2010**, *51*, 6025–6027. [CrossRef]
3. Liu, C.-X.; Li, P.-L.; Tang, X.-L.; Li, G.-Q. Studies on chemical constituents of the South China Sea gorgonian *Rumphella aggregata*. *Chin. J. Mar. Drugs* **2012**, *31*, 5–10.
4. Yin, F.-Z.; Yang, M.; Li, S.-W.; Wu, M.-J.; Huan, X.-J.; Miu, Z.-H.; Wang, H.; Guo, Y.-W. Two new hydroperoxy steroids from the South China Sea gorgonian *Rumphella* sp. *Steroids* **2020**, *155*, 108558. [CrossRef] [PubMed]
5. Alarif, W.M. Glycerol Derivatives and Steroid Constituents from the Soft Coral *Rumphella aggregata* (Gorgoniidae) of Saudi Red Sea Water. *J. King Abdulaziz Univ. Sci.* **2012**, *23*, 57–67. [CrossRef]
6. Sung, P.-J.; Chuang, L.-F.; Kuo, J.; Chen, J.-J.; Fan, T.-Y.; Li, J.-J.; Fang, L.-S.; Wang, W.-H. Rumphellolides A–F, six new caryophyllane-related derivatives from the Formosan gorgonian coral *Rumphella antipathes*. *Chem. Pharm. Bull.* **2007**, *55*, 1296–1301. [CrossRef]



7. Sung, P.-J.; Chuang, L.-F.; Kuo, J.; Fan, T.-Y.; Hu, W.-P. Rumphellatin A, the first chloride-containing caryophyllane-type norsesquiterpenoid from *Rumphella antipathes*. *Tetrahedron Lett.* **2007**, *48*, 3987–3989. [\[CrossRef\]](#)
8. Sung, P.-J.; Chuang, L.-F.; Hu, W.-P. Rumphellatins B and C, two new caryophyllane-type hemiketal norsesquiterpenoids from the Formosan gorgonian coral *Rumphella antipathes*. *Bull. Chem. Soc. Jpn.* **2007**, *80*, 2395–2399. [\[CrossRef\]](#)
9. Chuang, L.-F.; Fan, T.-Y.; Li, J.-J.; Kuo, J.; Fang, L.-S.; Wang, W.-H.; Sung, P.-J. Isokobusone, a caryophyllane-type norsesquiterpenoid from the gorgonian coral *Rumphella antipathes* (Gorgoniidae). *Platax* **2007**, *4*, 61–67.
10. Sung, P.-J.; Su, Y.-D.; Hwang, T.-L.; Chuang, L.-F.; Chen, J.-J.; Li, J.-J.; Fang, L.-S.; Wang, W.-H. Rumphellatin D, a novel chlorinated caryophyllane from gorgonian coral *Rumphella antipathes*. *Chem. Lett.* **2008**, *37*, 1244–1245. [\[CrossRef\]](#)
11. Hwang, T.-L.; Su, Y.-D.; Hu, W.-P.; Chuang, L.-F.; Sung, P.-J. Rumphellolide H, a new natural caryophyllane from the gorgonian *Rumphella antipathes*. *Heterocycles* **2009**, *78*, 1563–1567.
12. Sung, P.-J.; Su, Y.-D.; Hwang, T.-L.; Chuang, L.-F.; Chung, H.-M.; Chen, J.-J.; Li, J.-J.; Fang, L.-S.; Wang, W.-H. Rumphellolide I, a novel caryophyllane-related tetrahydropyran norsesquiterpenoid from gorgonian coral *Rumphella antipathes*. *Chem. Lett.* **2009**, *38*, 282–283. [\[CrossRef\]](#)
13. Chung, H.-M.; Hwang, T.-L.; Chen, Y.-H.; Su, J.-H.; Lu, M.-C.; Chen, J.-J.; Li, J.-J.; Fang, L.-S.; Wang, W.-H.; Sung, P.-J. Rumphellcloveane B, a novel clovane analogue from the gorgonian coral *Rumphella antipathes*. *Bull. Chem. Soc. Jpn.* **2011**, *84*, 119–121. [\[CrossRef\]](#)
14. Chung, H.-M.; Su, J.-H.; Hwang, T.-L.; Li, J.-J.; Chen, J.-J.; Chen, Y.-H.; Chang, Y.-C.; Su, Y.-D.; Chen, Y.-H.; Fang, L.-S.; et al. Rumphellcloveanes C–E, new clovane-type sesquiterpenoids from the gorgonian coral *Rumphella antipathes*. *Tetrahedron* **2013**, *69*, 2740–2744. [\[CrossRef\]](#)
15. Chung, H.-M.; Wang, W.-H.; Hwang, T.-L.; Wu, Y.-C.; Sung, P.-J. Natural clovanes from the gorgonian coral *Rumphella antipathes*. *Nat. Prod. Commun.* **2013**, *8*, 1037–1040.
16. Chung, H.-M.; Wang, W.-H.; Hwang, T.-L.; Li, J.-J.; Fang, L.-S.; Wu, Y.-C.; Sung, P.-J. Rumphellaones B and C, new 4,5-seco-caryophyllane sesquiterpenoids from *Rumphella antipathes*. *Molecules* **2014**, *19*, 12320. [\[CrossRef\]](#)
17. Chung, H.-M.; Wang, W.-H.; Hwang, T.-L.; Fang, L.-S.; Wen, Z.-H.; Chen, J.-J.; Wu, Y.-C.; Sung, P.-J. Rumphellaic acid A, a novel sesquiterpenoid from the Formosan gorgonian coral *Rumphella antipathes*. *Mar. Drugs* **2014**, *12*, 5856. [\[CrossRef\]](#)
18. Chung, H.-M.; Wang, W.-H.; Hwang, T.-L.; Chen, J.-J.; Fang, L.-S.; Wen, Z.-H.; Wang, Y.-B.; Wu, Y.-C.; Sung, P.-J. Rumphellols A and B, New Caryophyllene Sesquiterpenoids from a Formosan Gorgonian Coral, *Rumphella antipathes*. *Int. J. Mol. Sci.* **2014**, *15*, 15679. [\[CrossRef\]](#)
19. Chuang, L.-F.; Fan, T.-Y.; Li, J.-J.; Sung, P.-J. Kobusone: Occurrence of a norsesquiterpenoid in the gorgonian coral *Rumphella antipathes* (Gorgoniidae). *Biochem. Syst. Ecol.* **2007**, *35*, 470–471. [\[CrossRef\]](#)
20. Sung, P.-J.; Chuang, L.-F.; Fan, T.-Y.; Chou, H.-N.; Kuo, J.; Fang, L.-S.; Wang, W.-H. Rumphellolide G, a new caryophyllane-type tetrahydropyran norsesquiterpenoid from the gorgonian coral *Rumphella antipathes* (Gorgoniidae). *Chem. Lett.* **2007**, *36*, 1322–1323. [\[CrossRef\]](#)
21. Chung, H.-M.; Wang, W.-H.; Hwang, T.-L.; Wu, Y.-C.; Sung, P.-J. Natural caryophyllane sesquiterpenoids from *Rumphella antipathes*. *Nat. Prod. Commun.* **2015**, *10*, 835–838.
22. Lin, C.-C.; Chung, H.-M.; Su, Y.-D.; Peng, B.-R.; Wang, W.-H.; Hwang, T.-L.; Wu, Y.-C.; Sung, P.-J. Rumphellolide J, an ester of 4 $\beta$ ,9 $\beta$ -epoxycaryophyllan-5-ol and rumphellaic acid A, from the gorgonian *Rumphella antipathes*. *Nat. Prod. Commun.* **2017**, *12*, 1835–1837.
23. Chung, H.-M.; Chen, Y.-H.; Hwang, T.-L.; Chuang, L.-F.; Wang, W.-H.; Sung, P.-J. Rumphellcloveane A, a novel clovane-related sesquiterpenoid from the gorgonian coral *Rumphella antipathes*. *Tetrahedron Lett.* **2010**, *51*, 2734–2736. [\[CrossRef\]](#)
24. Ciereszko, L.S.; Johnson, M.A.; Schmidt, R.W.; Koons, C.B. Chemistry of coelenterates—VI. Occurrence of gorgosterol, A C30 sterol, in coelenterates and their zooxanthellae. *Comp. Biochem. Physiol.* **1968**, *24*, 899–904. [\[CrossRef\]](#)
25. Kader, N.A.A.; Habib, E.S.; Hasanean, H.A.; Ahmed, S.A.E.; Abdelhameed, R.F.; Ibrahim, A.K. B: Chemical Investigation of the Red Sea Gorgonian Coral *Rumphella torta*. *Rec. Pharm. Biomed. Sci.* **2020**, *4*, 16–24.
26. Joseph, J.D. Lipid composition of marine and estuarine invertebrates: Porifera and cnidaria. *Prog. Lipid Res.* **1979**, *18*, 1–30. [\[CrossRef\]](#)

27. Urvois, P.A.; Barnathan, G.; Biard, J.F.; Debitus, C.; Verbist, J.F. Fatty acid composition of the New Caledonian gorgonian *Rumphella aggregata*: Identification of 9-methyl-6,9-heptadecadienoic acid. In *Proceedings of Marine Lipids, Brest, France, 19–20 November 1988*; Baudimant, G., Guézennec, J., Roy, P., Samain, J.F., Eds.; IFREMER: Plouzané, France, 2000; pp. 44–49.
28. Bergé, J.-P.; Barnathan, G. Fatty Acids from Lipids of Marine Organisms: Molecular Biodiversity, Roles as Biomarkers, Biologically Active Compounds, and Economical Aspects. *Aestivation* **2005**, *96*, 49–125.
29. Imbs, A.B.; Demidkova, D.A.; Dautova, T.N.; Latyshev, N.A. Fatty Acid Biomarkers of Symbionts and Unusual Inhibition of Tetracosapolyenoic Acid Biosynthesis in Corals (Octocorallia). *Lipids* **2008**, *44*, 325–335. [[CrossRef](#)] [[PubMed](#)]
30. Racero, J.C.; Macías-Sánchez, A.J.; Hernández-Galán, R.; Hitchcock, P.B.; Hanson, J.R.; Collado, I.G. Novel Rearrangement of an Isocaryolane Sesquiterpenoid under Mitsunobu Conditions. *J. Org. Chem.* **2000**, *65*, 7786–7791. [[CrossRef](#)]
31. Hirokawa, T.; Kuwahara, S. Synthesis of rumphellaone A via epoxy nitrile cyclization. *Tetrahedron* **2012**, *68*, 4581–4587. [[CrossRef](#)]
32. Ranieri, B.; Obradors, C.; Mato, M.; Echavarren, A.M. Synthesis of Rumphellaone A and Hushinone by a Gold-Catalyzed [2 + 2] Cycloaddition. *Org. Lett.* **2016**, *18*, 1614–1617. [[CrossRef](#)]
33. Beck, J.C.; Lacker, C.R.; Chapman, L.M.; Reisman, S.E. A modular approach to prepare enantioenriched cyclobutanes: Synthesis of (+)-rumphellaone A. *Chem. Sci.* **2019**, *10*, 2315–2319. [[CrossRef](#)] [[PubMed](#)]
34. Gupta, A.S.; Dev, S. Studies in sesquiterpenes—XLVI. Sesquiterpenes from the oleoresin of *Dipterocarpus pilosus*: Humulene epoxide-III, caryophyllenol-I and caryophyllenol-II. *Tetrahedron* **1971**, *27*, 635–644. [[CrossRef](#)]
35. González, A.G.; Fraga, B.M.; Luis, J.G.; Ravelo, A.G. Componentes de la “*Salvia canariensis* L.”. *An. Quim.* **1975**, *71*, 701–705.
36. Delgado, G.; Cárdenas, H.; Peláez, G.; De Vivar, A.R.; Pereda-Miranda, R. Terpenoids From *Viguiera excelsa* and *Viguiera oaxacana*. *J. Nat. Prod.* **1984**, *47*, 1042–1045. [[CrossRef](#)]
37. Delgado, G.; Alvarez, L.; De Vivar, A.R. 15-Hydroxy-acetylerioflorin and other constituents from *Viguiera linearis*. *Phytochem.* **1985**, *24*, 2736–2738. [[CrossRef](#)]
38. Heymann, H.; Tezuka, Y.; Kikuchi, T.; Supriyatna, S. Constituents of *Sindora sumatrana* MIQ. I. Isolation and NMR Spectral Analysis of Sesquiterpenes from the Dried Pods. *Chem. Pharm. Bull.* **1994**, *42*, 138–146. [[CrossRef](#)]
39. Bayer, F.M. Key to the genera of octocorallia exclusive of Pennatulacea (Coelenterata: Anthozoa), with diagnoses of new taxa. *Proc. Biol. Soc. Wash.* **1981**, *94*, 902–947.
40. Dai, C.-F.; Chin, C.-H. *Octocoral Fauna of Kenting National Park*; Kenting National Park Headquarters: Kenting, Pingtung, Taiwan, 2019; pp. 484–485.
41. Chen, P.-J.; Ko, I.-L.; Lee, C.-L.; Hu, H.-C.; Chang, F.-R.; Wu, Y.-C.; Leu, Y.-L.; Wu, C.-C.; Lin, C.-Y.; Pan, C.-Y.; et al. Targeting allosteric site of AKT by 5,7-dimethoxy-1,4-phenanthrenequinone suppresses neutrophilic inflammation. *EBioMedicine* **2019**, *40*, 528–540. [[CrossRef](#)] [[PubMed](#)]

**Publisher’s Note:** MDPI stays neutral with regard to jurisdictional claims in published maps and institutional affiliations.



© 2020 by the authors. Licensee MDPI, Basel, Switzerland. This article is an open access article distributed under the terms and conditions of the Creative Commons Attribution (CC BY) license (<http://creativecommons.org/licenses/by/4.0/>).

## Article

# Anti-Inflammatory Cembranoids from a Formosa Soft Coral *Sarcophyton cherbonnieri*

Chia-Chi Peng <sup>1,†</sup>, Chiung-Yao Huang <sup>1,†</sup>, Atallah F. Ahmed <sup>2,3</sup> , Tsong-Long Hwang <sup>4,5,6</sup>  and Jyh-Horng Sheu <sup>1,7,8,\*</sup>

<sup>1</sup> Department of Marine Biotechnology and Resources, National Sun Yat-sen University, Kaohsiung 804, Taiwan; Chia-Chi.Peng@hki-jena.de (C.-C.P.); huangcy@mail.nsysu.edu.tw (C.-Y.H.)

<sup>2</sup> Department of Pharmacognosy, College of Pharmacy, King Saud University, Riyadh 11451, Saudi Arabia; afahmed@ksu.edu.sa

<sup>3</sup> Department of Pharmacognosy, Faculty of Pharmacy, Mansoura University, Mansoura 35516, Egypt

<sup>4</sup> Graduate Institute of Natural Products, College of Medicine, Chang Gung University, Taoyuan 333, Taiwan; htl@mail.cgu.edu.tw

<sup>5</sup> Research Center for Industry of Human Ecology and Graduate Institute of Health Industry Technology, Chang Gung University of Science and Technology, Taoyuan 333, Taiwan

<sup>6</sup> Department of Anesthesiology, Chang Gung Memorial Hospital, Taoyuan 333, Taiwan

<sup>7</sup> Graduate Institute of Natural Products, Kaohsiung Medical University, Kaohsiung 807, Taiwan

<sup>8</sup> Department of Medical Research, China Medical University Hospital, China Medical University, Taichung 404, Taiwan

\* Correspondence: sheu@mail.nsysu.edu.tw; Tel.: +886-7-525-2000 (ext. 5030); Fax: +886-7-525-5020

† These authors contributed equally to this work.

Received: 25 September 2020; Accepted: 13 November 2020; Published: 19 November 2020



**Abstract:** The present investigation on chemical constituents of the soft coral *Sarcophyton cherbonnieri* resulted in the isolation of seven new cembranoids, cherbonolides F–L (1–7). The chemical structures of 1–7 were determined by spectroscopic methods, including infrared, one- and two-dimensional (1D and 2D) NMR (COSY, HSQC, HMBC, and NOESY), MS experiments, and a chemical reduction of hydroperoxide by triphenylphosphine. The anti-inflammatory activities of 1–7 against neutrophil proinflammatory responses were evaluated by measuring their inhibitory ability toward *N*-formyl-methionyl-leucyl-phenylalanine/cytochalasin B (fMLF/CB)-induced superoxide anion generation and elastase release in primary human neutrophils. The results showed that all isolates exhibited moderate activities, while cherbonolide G (2) and cherbonolide H (3) displayed a more active effect than others on the inhibition of elastase release (48.2% ± 6.2%) and superoxide anion generation (44.5% ± 4.6%) at 30 µM, respectively.

**Keywords:** *Sarcophyton cherbonnieri*; cembranoid; anti-inflammatory activity; elastase release; superoxide anion generation

## 1. Introduction

Series of cembranoidal secondary metabolites from soft corals have been shown to exhibit attractive biological activities including cytotoxicity [1–14] and anti-inflammatory ability [6,7,9,11,13–18]. From previous investigations of exploring bioactive natural products from soft corals, many cembranoids were discovered from organisms of the genera *Sarcophyton*, [1–8,16], *Sinularia* [9–12,17,18], and *Lobophyton* [13–15]. In some cases, two cembranoid units could be linked to produce biscembranoids via various reactions [18–24], marking the high diversity and complexity in chemical structures of cembrane-related soft coral natural products.

Many studies have revealed that soft corals of the genus *Sarcophyton* are important sources of various types of natural products, some of them with notable bioactivities [25–28]. Our previous chemical study on *Sarcophyton cherbonnieri* led to the isolation of six new cembranoids cherbonolides A–E and one biscembranoid bischerbolide peroxide, along with a known compound, isosarcophine [24]. In continuation of our effort on discovery of new and bioactive compounds from marine animals, we further explored the chemical constituents of *S. cherbonnieri*. This investigation again led to the discovery of new cembranoids, cherbonolides F–L (1–7). The structures of 1–7 (Figure 1) were determined by spectroscopic analysis, including two-dimensional (2D) NMR experiments and a chemical reaction. Compounds 2 and 4 were elucidated as cembranoids possessing an allylic peroxy group. Cembranoids of isosarcophine-type have been reported frequently [24,27–30].

The screening of the *in vitro* anti-inflammatory activities through the inhibition of superoxide anion generation and elastase release in *N*-formyl-methionyl-leucyl-phenylalanine/cytochalasin B (fMLF/CB)-induced primary human neutrophils was also performed in order to unveil the anti-inflammatory ability of these compounds. We report herein the isolation, structure determination, and bioactivity of the new metabolites 1–7.

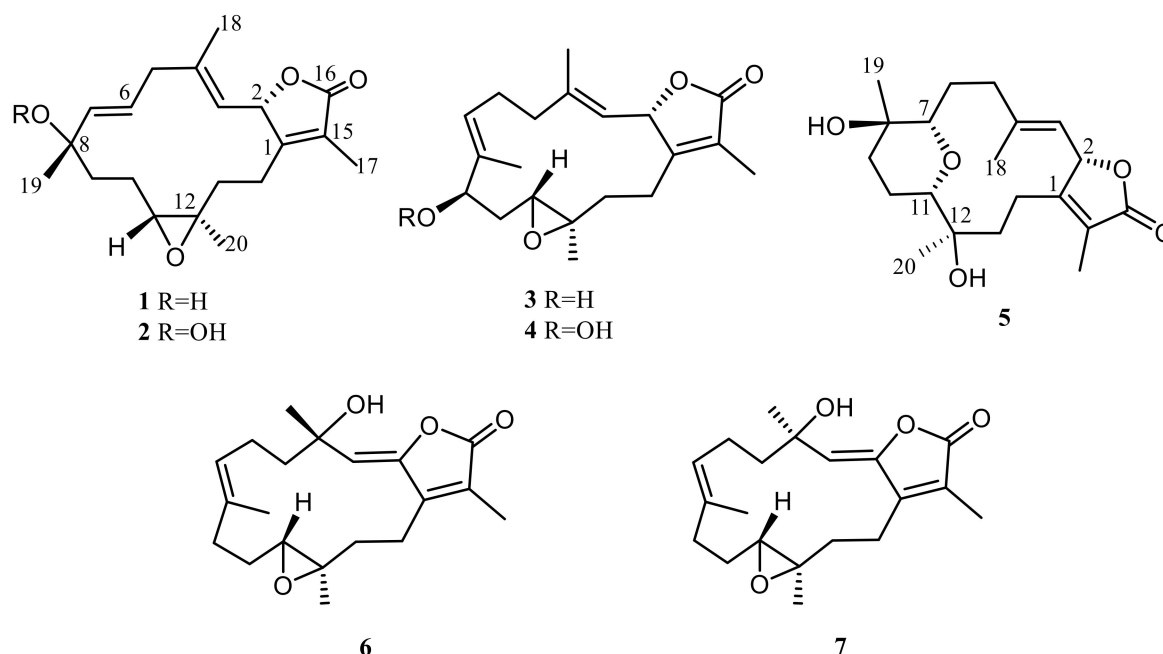


Figure 1. New cembranoids isolated from *Sarcophyton cherbonnieri*.

## 2. Results and Discussion

Solvent-free residue of the ethyl acetate extract of the soft coral *S. cherbonnieri* was separated and further purified by chromatographic methods to yield metabolites 1–7. The structures were established by extensive analyses of MS and NMR spectra (Figures S1–S49, Supplementary Materials).  $^{13}\text{C}$ - and  $^1\text{H}$ -NMR data which were essential for structure determination of 1–7 are listed in Tables 1–3.

Cherbonolide F (1) was obtained as a colorless oil. The molecular formula of 1,  $\text{C}_{20}\text{H}_{28}\text{O}_4$ , was established by high-resolution electrospray ionization mass spectrometry (HR-ESI-MS) ( $m/z$  calculated 355.1880; found 355.1879,  $[\text{M} + \text{Na}]^+$ ), implying seven degrees of unsaturation. The IR spectrum of 1 revealed the absorptions of a hydroxy ( $\nu_{\text{max}}$  3460  $\text{cm}^{-1}$ ) and a lactonic carbonyl group ( $\nu_{\text{max}}$  1748  $\text{cm}^{-1}$ ). The  $^{13}\text{C}$ -NMR spectrum of 1 showed 20 signals which were assigned to four methyls, five  $sp^3$  methylenes, two  $sp^3$  oxygenated methines, three  $sp^2$  methines, and two  $sp^3$  and four  $sp^2$  nonprotonated carbon atoms (Table 1) with the assistance of distortionless enhancement by polarization transfer (DEPT) spectra. Carbon signals resonating at  $\delta_{\text{C}}$  173.9 (C), 160.5 (C), 123.6 (C), 78.6 (CH), and 9.0 ( $\text{CH}_3$ ) and proton signals resonating at  $\delta_{\text{H}}$  4.95 (1H, dd,  $J = 10.0, 1.6$  Hz) and  $\delta_{\text{H}}$

1.66 (3H, s) were attributed to signals of an  $\alpha$ -methyl- $\alpha,\beta$ -unsaturated- $\gamma$ -lactone ring by comparing the NMR data of the  $\gamma$ -lactone ring of the known compound isosarcophine (7). Signals at  $\delta_C$  61.2 (CH), 60.2 (C), and  $\delta_H$  2.54 (1H, dd,  $J = 6.0, 6.0$  Hz) showed the appearance of a trisubstituted epoxide. One trisubstituted and one disubstituted double bond were identified by NMR signals resonating at  $\delta_C$  120.9 (CH), 142.4 (C) and  $\delta_H$  4.54 (1H, dd,  $J = 10.0, 0.8$  Hz), and at  $\delta_C$  140.3 (CH), 124.5 (CH) and  $\delta_H$  5.32 (1H, d,  $J = 16.0$  Hz) and 5.38 (1H, ddd,  $J = 16.0, 6.8, 6.8$  Hz), respectively.  $^1\text{H}$ - $^1\text{H}$  correlation spectroscopy (COSY) correlations established four separate proton sequences, which were connected by heteronuclear multiple bond correlation (HMBC) correlations (Figure 2). Essential HMBC correlations from H-2 to C-1 and C-4, H<sub>2</sub>-14 to C-1 and C-2, H<sub>3</sub>-17 to C-1, C-15, and C-16, H<sub>3</sub>-18 to C-3, C-4, and C-5, H<sub>3</sub>-19 to C-7, C-8, and C-9, and H<sub>3</sub>-20 to C-11, C-12, and C-13 established the 14-membered ring carbon skeleton of **1**, which also indicated the presence of a hydroxyl at C-8.

Furthermore, analysis of nuclear Overhauser effect (NOE) correlations was applied to establish the relative configuration of **1**, as shown in Figure 3. It was revealed that H-2 showed NOE correlation with H<sub>3</sub>-18, but not with H-3; therefore, assuming the  $\beta$ -orientation of H-2, H<sub>3</sub>-18 should be located on the  $\beta$  face. Moreover, H<sub>3</sub>-18 exhibited NOE correlation with H-7, but not with H-6, revealing the  $\beta$ -orientation of H-7 and the  $\alpha$ -orientation of H-6. Both H-6 and H-7 exhibited NOE interactions with H<sub>3</sub>-19, thus established the  $\beta$ -orientation of H<sub>3</sub>-19 as shown in Figure 3. One methylene proton at C-13 exhibited NOE correlation with H-2 and was characterized as H-13 $\beta$  ( $\delta_H$  0.99, m), while the other proton was assigned as H-13 $\alpha$  ( $\delta_H$  1.49, m). NOE correlations of H-13 $\beta$  with H-11 and H-13 $\alpha$  with H<sub>3</sub>-20 reflected the  $\beta$ -orientation of H-11 and the  $\alpha$ -orientation of H<sub>3</sub>-20. The *E* geometries of the trisubstituted C-3/C-4 and C-6/C-7 double bonds were also assigned from the NOE correlations of H<sub>3</sub>-18 ( $\delta_H$  1.35, s) with H-2, but not with H-3, as well as the large coupling constant  $J = 16.0$  Hz between H-6 and H-7, and the observed more shielded signal of C-18 ( $\delta_C$  16.7). According to the above observations, the relative configuration of this compound was established. As **1** was isolated together with the previous reported compounds isosarcophine and cherbonolides A–E [24] from the same organism, it should possess the same (2*S*,8*S*,11*R*,12*R*)-configuration from the shared biosynthetic pathway.

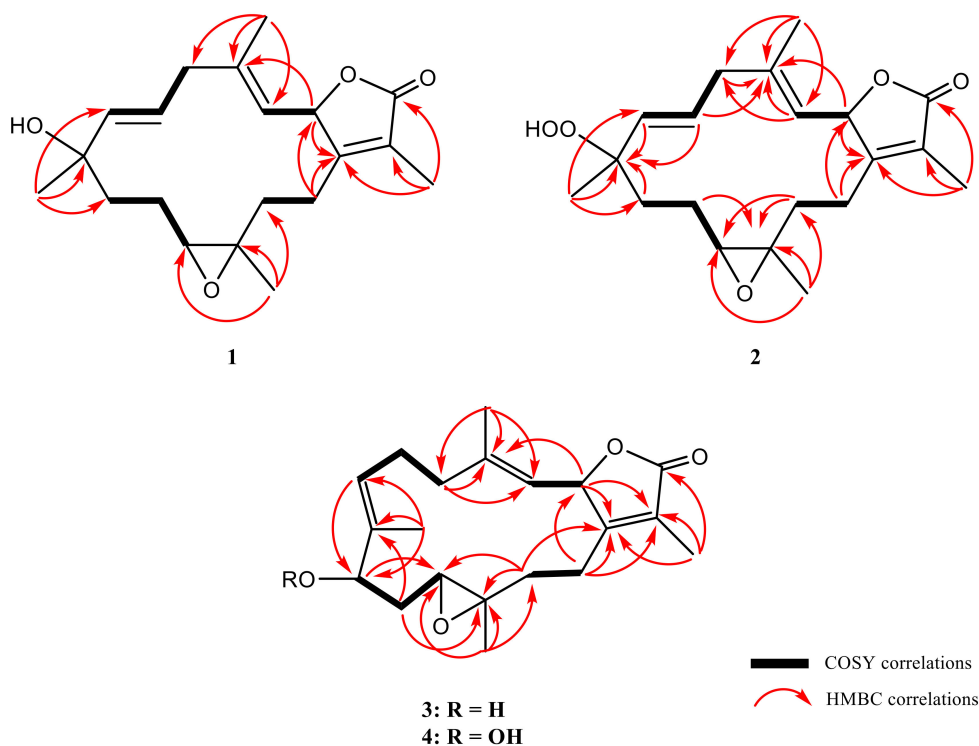


**Figure 2.** The selected COSY and HMBC correlations of **1**–**4**.



**Table 1.**  $^{13}\text{C}$ -NMR spectroscopic data of compounds 1–7.

Position	1 <sup>a</sup>	2 <sup>a</sup>	3 <sup>a</sup>	4 <sup>c</sup>	5 <sup>a</sup>	6 <sup>d</sup>	7 <sup>d</sup>
1	160.5 (C)	160.4 (C)	159.9 (C)	160.2 (C)	162.4 (C)	151.2 (C)	151.2 (C)
2	78.6 (CH) <sup>b</sup>	78.5 (CH)	77.7 (CH)	78.0 (CH)	79.5 (CH)	147.2 (C)	147.2 (C)
3	120.9 (CH)	121.2 (CH)	121.8 (CH)	122.3 (CH)	120.7 (CH)	116.2 (CH)	116.1 (CH)
4	142.4 (C)	142.1 (C)	143.2 (C)	143.4 (C)	143.2 (C)	72.7 (C)	72.6 (C)
5	41.5 (CH <sub>2</sub> )	41.9 (CH <sub>2</sub> )	38.4 (CH <sub>2</sub> )	38.7 (CH <sub>2</sub> )	36.4 (CH <sub>2</sub> )	42.5 (CH <sub>2</sub> )	42.2 (CH <sub>2</sub> )
6	124.5 (CH)	128.6 (CH)	23.9 (CH <sub>2</sub> )	24.4 (CH <sub>2</sub> )	24.7 (CH <sub>2</sub> )	23.1 (CH <sub>2</sub> )	23.2 (CH <sub>2</sub> )
7	140.3 (CH)	135.9 (CH)	127.3 (CH)	130.9 (CH)	84.1 (CH)	127.2 (CH)	126.5 (CH)
8	71.7 (C)	83.7 (C)	137.1 (C)	133.8 (C)	69.4 (C)	133.9 (C)	133.8 (C)
9	39.7 (CH <sub>2</sub> )	35.7 (CH <sub>2</sub> )	76.2 (CH)	88.9 (CH)	40.7 (CH <sub>2</sub> )	36.3 (CH <sub>2</sub> )	36.2 (CH <sub>2</sub> )
10	24.3 (CH <sub>2</sub> )	24.2 (CH <sub>2</sub> )	32.4 (CH <sub>2</sub> )	28.4 (CH <sub>2</sub> )	23.5 (CH <sub>2</sub> )	24.4 (CH <sub>2</sub> )	24.3 (CH <sub>2</sub> )
11	61.3 (CH)	61.1 (CH)	59.2 (CH)	59.4 (CH)	80.1 (CH)	60.5 (CH)	60.5 (CH)
12	60.2 (C)	60.2 (C)	60.1 (C)	60.6 (C)	72.6 (C)	60.2 (C)	60.3 (C)
13	35.7 (CH <sub>2</sub> )	35.6 (CH <sub>2</sub> )	36.9 (CH <sub>2</sub> )	37.3 (CH <sub>2</sub> )	37.2 (CH <sub>2</sub> )	35.1 (CH <sub>2</sub> )	35.1 (CH <sub>2</sub> )
14	23.2 (CH <sub>2</sub> )	22.9 (CH <sub>2</sub> )	23.6 (CH <sub>2</sub> )	24.0 (CH <sub>2</sub> )	20.2 (CH <sub>2</sub> )	19.6 (CH <sub>2</sub> )	19.8 (CH <sub>2</sub> )
15	123.6 (C)	123.6 (C)	123.7 (C)	124.1 (C)	123.4 (C)	123.6 (C)	123.7 (C)
16	173.9 (C)	173.9 (C)	173.8 (C)	174.2 (C)	174.4 (C)	169.5 (C)	169.8 (C)
17	9.0 (CH <sub>3</sub> )	8.9 (CH <sub>3</sub> )	8.7 (CH <sub>3</sub> )	9.1 (CH <sub>3</sub> )	8.9 (CH <sub>3</sub> )	9.1 (CH <sub>3</sub> )	9.0 (CH <sub>3</sub> )
18	16.7 (CH <sub>3</sub> )	16.2 (CH <sub>3</sub> )	14.4 (CH <sub>3</sub> )	14.7 (CH <sub>3</sub> )	16.2 (CH <sub>3</sub> )	29.9 (CH <sub>3</sub> )	29.4 (CH <sub>3</sub> )
19	28.0 (CH <sub>3</sub> )	21.6 (CH <sub>3</sub> )	9.6 (CH <sub>3</sub> )	10.3 (CH <sub>3</sub> )	20.4 (CH <sub>3</sub> )	15.3 (CH <sub>3</sub> )	15.5 (CH <sub>3</sub> )
20	16.7 (CH <sub>3</sub> )	16.9 (CH <sub>3</sub> )	16.0 (CH <sub>3</sub> )	16.2 (CH <sub>3</sub> )	23.7 (CH <sub>3</sub> )	17.5 (CH <sub>3</sub> )	17.4 (CH <sub>3</sub> )

<sup>a</sup> Spectra recorded in  $\text{C}_6\text{D}_6$  at 100 MHz at 25 °C. <sup>b</sup> Attached protons were deduced by distortionless enhancement by polarization transfer (DEPT) experiments. <sup>c</sup> Spectra recorded in  $\text{C}_6\text{D}_6$  at 125 MHz. <sup>d</sup> Spectra recorded in  $\text{CDCl}_3$  at 100 MHz.

**Table 2.**  $^1\text{H}$ -NMR spectral data for compounds 1–4.

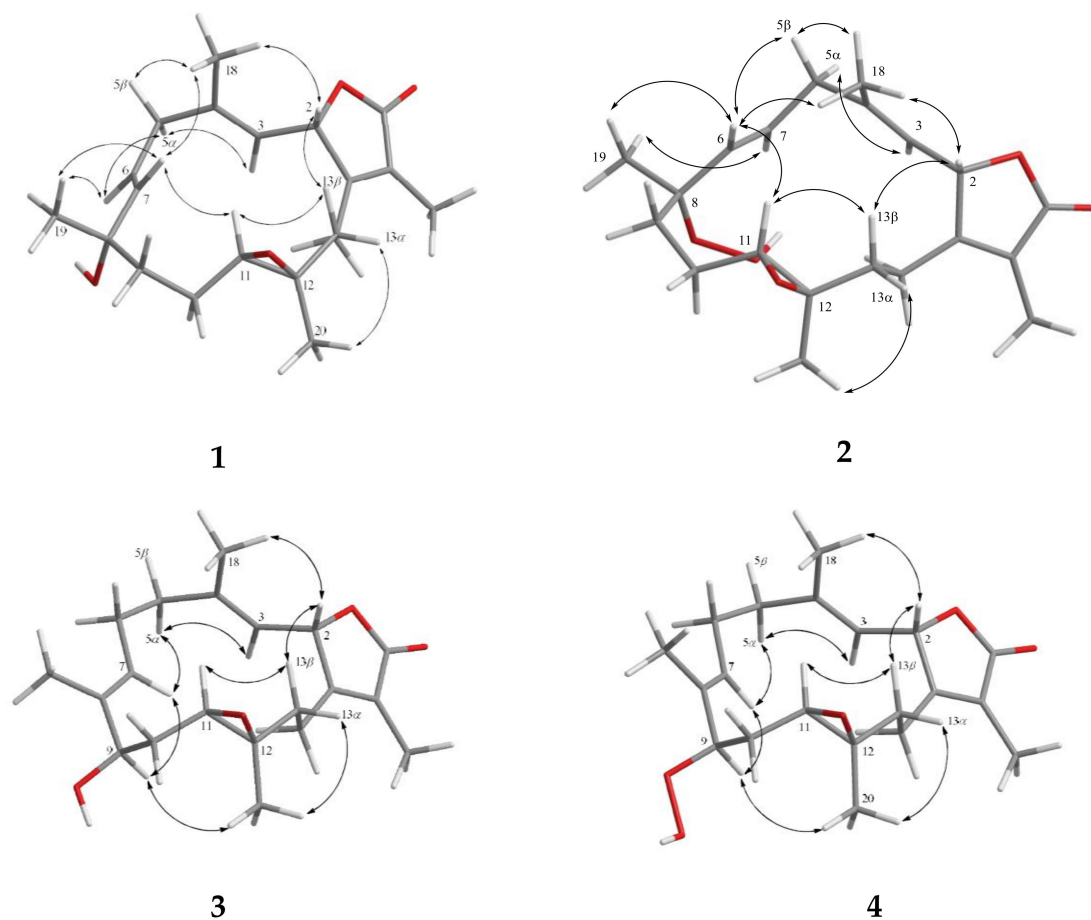
Position	1 <sup>a</sup>	2 <sup>a</sup>	3 <sup>a</sup>	4 <sup>b</sup>
2	4.95, dd (10.0, 1.6) <sup>c</sup>	4.92, dd (10.0, 1.6)	4.99, dd (10.4, 1.6)	4.96, d (10.5)
3	4.54, dd (10.0, 0.8)	4.47, d (10.0)	4.49, d (10.4)	4.47, d (10.5)
5	2.40, dd (13.2, 6.8)	2.41, dd (13.6, 7.2)	1.84, dd (13.2, 4.4)	1.80, dd (13.5, 4.5)
6	2.26, dd (13.2, 6.8)	2.27, dd (13.6, 7.2)	1.92, m	1.91, m
	5.38, ddd (16.0, 6.8, 6.8)	5.47, ddd (16.8, 7.2, 7.2)	1.73, m	1.75, m
			2.03, m	2.02, m
7	5.32, d (16.0)	5.35, d (16.8)	4.74, dd (10.0, 1.2)	4.91, d (9.5)
9	1.52, m	1.57, m	3.68, dd (11.6, 4.0)	4.06, dd (12.0, 4.0)
10	1.59, m	1.59, m		
	1.43, m	1.56, m	1.47, m	1.53, m
	1.71, m	1.56, m	2.16, ddd	2.03, m
11	2.54, dd (6.0, 6.0)	2.44, dd (6.4, 6.4)	2.03, m	2.09, dd (10.5, 3.0)
13	1.49, m	1.69, m	1.59, dd (13.2, 5.6)	1.56, m
14	0.99, m	0.99, m	0.72, ddd (13.2, 13.2, 2.8)	0.69, dd (13.5, 13.5, 2.5)
	1.81, m	1.78, m	1.93, m	1.89, m
	1.67, m	1.68, m	1.49, m	1.43, m
17	1.66, s	1.66, s	1.65, s	1.65, s
18	1.35, s	1.29, s	1.13, s	1.11, s
19	1.05, s	1.19, s	1.37, s	1.37, s
20	1.03, s	1.02, s	1.03, s	1.01, s

<sup>a</sup> Spectra recorded in  $\text{C}_6\text{D}_6$  at 400 MHz at 25 °C. <sup>b</sup> Spectra recorded in  $\text{C}_6\text{D}_6$  at 500 MHz at 25 °C. <sup>c</sup> Coupling constants (*J* values) in Hz are shown in parentheses.

**Table 3.**  $^1\text{H}$ -NMR spectral data for compounds 5–7.

Position	5 <sup>a</sup>	6 <sup>b</sup>	7 <sup>b</sup>
2	4.92, d (11.2) <sup>c</sup>		
3	4.85, d (11.2)	5.50, s	5.52, s
5	2.07, m	1.83, m	1.94, m
	1.93, m	1.98, m	1.94, m
6	1.31, m	2.41, m	2.46, m
	1.70, m	2.21, m	2.14, m
7	2.79, dd (10.0, 2.4)	5.26, dd (6.0, 6.0)	5.25, dd (7.2, 7.2)
9	1.59, m	2.28, m	2.26, m
	1.31, m	2.08, m	2.06, m
10	1.22, m	1.53, m	1.54, m
	1.50, m	1.85, m	1.86, m
11	2.96, d (11.2)	2.71, dd (6.8, 5.6)	2.73, dd (7.6, 4.6)
13	1.59, m	2.16, m	2.19, m
	1.21, m	1.63, m	1.62, m
14	2.16, ddd (12.4, 12.4, 6.4)	2.26, m	2.24, m
	1.59, m	2.42, m	2.45, m
17	1.72, s	1.95, s	1.92, s
18	1.47, s	1.41, s	1.51, s
19	0.94, s	1.66, s	1.65, s
20	0.89, s	1.30, s	1.28, s

<sup>a</sup> Spectra recorded in  $\text{C}_6\text{D}_6$  at 400 MHz at 25 °C. <sup>b</sup> Spectra recorded in  $\text{CDCl}_3$  at 400 MHz at 25 °C. <sup>c</sup> Coupling constants ( $J$  values) in Hz are shown in parentheses.

**Figure 3.** Key NOE correlations for 1–4.

The molecular formula of cherbonolide G (**2**) was found to be  $C_{20}H_{28}O_5$  by analysis of HR-ESI-MS ( $m/z$  calculated 371.1829; found 371.1830,  $[M + Na]^+$ ), revealing that **2** possesses an additional oxygen atom to that of **1**. Moreover, both **1** and **2** showed the very similar  $^1H$ - and  $^{13}C$ -NMR data (Table 1), except that the chemical shift of C-8 was shifted from  $\delta_C$  71.7 of **1** to  $\delta_C$  83.7 of **2**. The very similar COSY, HMBC (Figure 2), and NOE (Figure 3) correlations of **1** and **2** also revealed the very close structures for both compounds. However, the hydroxy group of **1** at C-8 was replaced by a hydroperoxy group in **2**, with a broad singlet appearing at  $\delta_H$  6.72 and the downfield shift of C-8. Accordingly, the molecular skeleton and the (2*S*,8*S*,11*R*,12*R*)-configuration of **2** were determined.

Cherbonolide H (**3**) has the same molecular formula as that of **1**, as determined by HR-ESI-MS experiment. Moreover, most of the  $^1H$ - $^1H$  COSY and HMBC correlations (Figure 2) of **3** were similar to those of isosarcophine except for the presence of a hydroxyl at C-9 leading to the shift of CH-9 to lower field ( $\delta_C$  76.2;  $\delta_H$  3.68), and the shift of C-6/C-7 double bond of **1** to C-7/C-8 double bond of **3**. Analysis of NOE correlations (Figure 3) showed that the  $\beta$ -oriented H-2 exhibited NOE interactions with both H<sub>3</sub>-18 and H-13 $\beta$ , but not with H-3, assigning the *E*-geometry of the trisubstituted C-3/C-4 double bond. These results, along with the found NOE correlations (Figure 3) of H-13 $\alpha$ /H<sub>3</sub>-20, H<sub>3</sub>-20/H-9, led to the assignment of the  $\alpha$ -orientation of H-9.

Cherbonolide I (**4**) was found to contain one additional oxygen atom than **3**, according to HR-ESI-MS experiment. These two compounds also showed very similar  $^1H$ - $^1H$  COSY and HMBC correlations, revealing the identical molecular framework of both compounds. NMR data of **3** and **4** were similar (Table 1), except for those of CH-9, suggesting that **4** is possibly the C-9 hydroperoxy derivative of **3**. By analysis of NOE correlations (Figure 3), the *E* geometries of both C-3/C-4 and C-7/C-8 double bonds of **4** and the (2*S*,9*R*,11*R*,12*R*)-configuration were also established. Reduction of **4** by triphenylphosphine yielded **3**, further confirming the structure of **4**.

Cherbonolide J (**5**) was given as a colorless oil with a molecular formula  $C_{20}H_{30}O_5$  on the basis of HR-ESI-MS data ( $m/z$  calculated for  $C_{20}H_{30}O_5Na$  373.1986; found 373.1984), revealing six degrees of unsaturation. The IR absorptions at 3443 and 1748  $cm^{-1}$  were due to hydroxy and ester carbonyl groups, respectively. The  $^{13}C$ - and  $^1H$ -NMR spectroscopic data (Tables 1 and 3) of **5** measured at  $C_6D_6$  were very close to a known compound sarcophylide E [29], and the 2D NMR (COSY, HSQC, and HMBC) correlation analysis revealed that both compounds had the same molecular framework (Figure 4). Detailed analysis of the NOE correlations (Figure 5) showed that both compounds possessed the same relative configuration. However, the  $[\alpha]_{25}^D$  values in  $CHCl_3$  (−6 for **5** and +4.4 for sarcophylide E) were close but with different signs, suggesting that **5** is the enantiomer of this known compound. The absolute configurations of **5** and sarcophylide E were deduced by comparison of the circular dichroism (CD) spectroscopic data. As shown in Figure 6, the negative Cotton effect at 247 nm and positive effect at 228 nm for **5** in comparison with the positive and negative Cotton effects at 252 and 226 nm for sarcophylide E [29], respectively, confirmed that **5** is the newly found enantiomer of sarcophylide E.

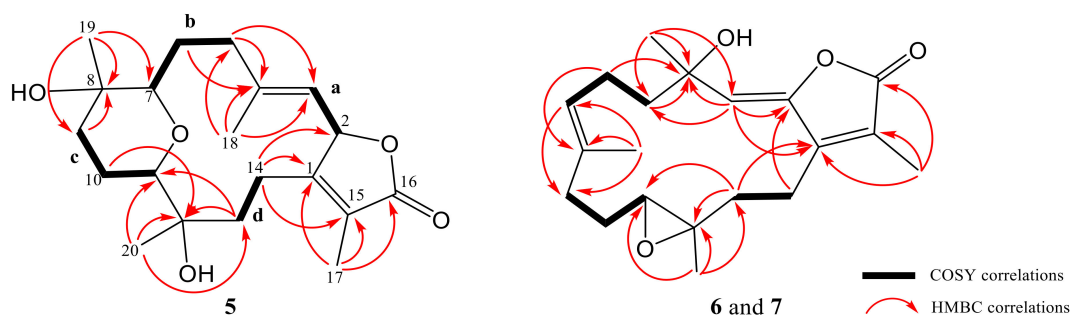
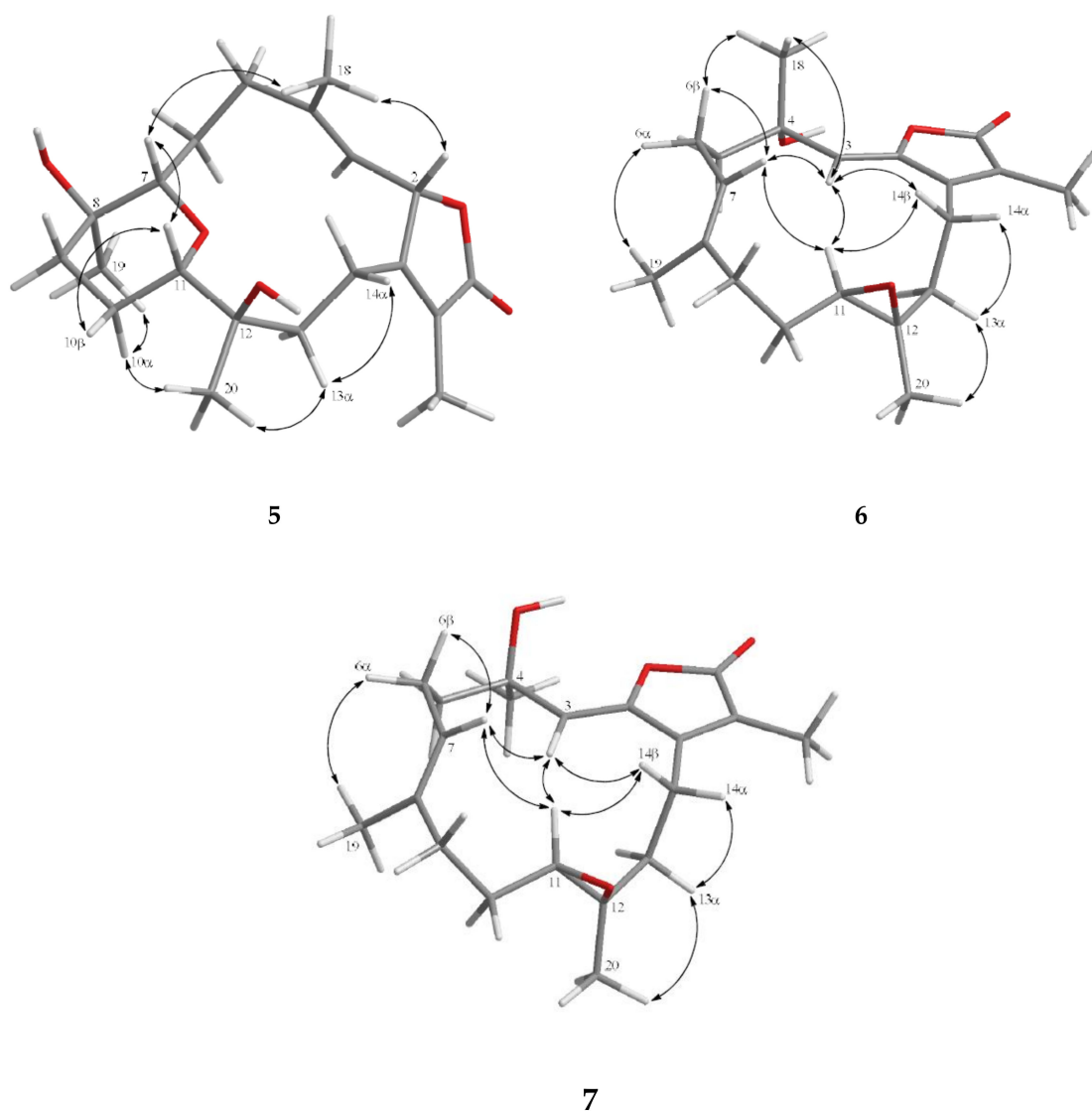
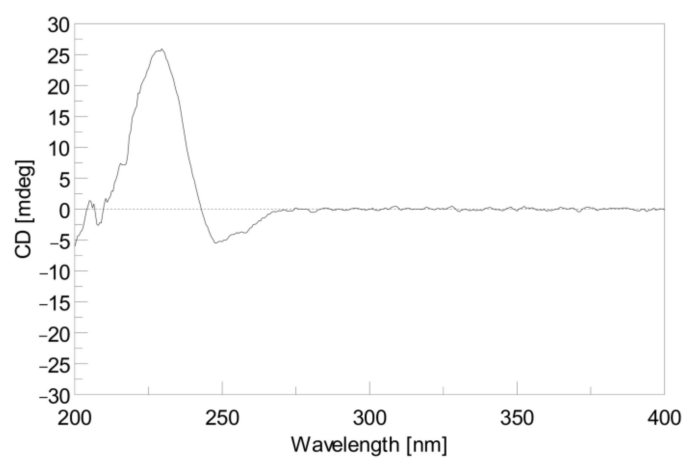


Figure 4. Selected COSY and HMBC correlations of **5**–**7**.



**Figure 5.** Selected NOE correlations for 5–7.



**Figure 6.** the CD spectrum of 5 ( $1.2 \times 10^{-4}$  M, MeOH).

Cherbonolide K (6) is a colorless oil which was shown to have the molecular formula  $C_{20}H_{28}O_4$  by HR-ESI-MS experiment, appropriate for seven degrees of unsaturation. The infrared (IR) spectrum

of **6** showed peaks of hydroxy and estercarbonyl groups at 3444 and 1763  $\text{cm}^{-1}$ , respectively.  $^{13}\text{C}$ -NMR data (Table 1) with signals at  $\delta_{\text{C}}$  151.2 (C), 147.2 (C), 116.2 (CH), 72.7 (C), 123.6 (C), 169.5 (C), 9.1 ( $\text{CH}_3$ ), and 29.9 ( $\text{CH}_3$ ) and  $^1\text{H}$  NMR data (Table 3) with signals at  $\delta_{\text{H}}$  5.50 (s, 1H), 1.95 (s, 3H), and 1.41 (s, 3H) were attributed to the cembranoidal  $\alpha$ -methyl- $\alpha,\beta$ -unsaturated- $\gamma$  lactone ring with a conjugated 2,3-double bond that further connected with the methyl and hydroxyl substituted C-4. The above results were supported by HMBC correlations of **6** (Figure 4) from H-3 ( $\delta_{\text{H}}$  5.50) to C-1 ( $\delta_{\text{C}}$  151.2), C-2 ( $\delta_{\text{C}}$  147.2), and C-4 ( $\delta_{\text{C}}$  72.7), H<sub>3</sub>-17 ( $\delta_{\text{H}}$  1.95) to C-1, C-15 ( $\delta_{\text{C}}$  123.6), and C-16 ( $\delta_{\text{C}}$  169.5), and H<sub>3</sub>-18 ( $\delta_{\text{H}}$  1.41) to C-3 ( $\delta_{\text{C}}$  116.2) and C-4 ( $\delta_{\text{C}}$  72.6). The remainder of the structure from C-5 to C-14 was found to be identical to isosarcophine [24]. Thus, the planar structure of **6** was established. Furthermore, the NOE correlation analysis shown in Figure 5 revealed the  $\alpha$ -orientations of 4-OH and 12- $\text{CH}_3$ ,  $\beta$ -orientation of H-11, (Z)-2,3-double bond, and (E)-7,8-double bond. An isomer of **6**, cherbonolide L (**7**), was also subsequently isolated. The metabolite **7** had nearly the same NMR data as **6** except for  $\text{CH}_2$ -5 and  $\text{CH}_2$ -6. Thus, it can be assumed that **7** is the C-4 epimer of **6**. Analysis of the 2D NMR correlations of **7** (Figures 4 and 6) further supported this assumption.

For the screening of bioactivities, the anti-inflammation activities of **1–7** toward inhibition of N-formyl-methionyl-leucyl-phenylalanine/cytochalasin B (fMLF/CB)-induced generation of superoxide anion ( $\text{O}_2^{\bullet-}$ ) and release of elastase in primary human neutrophils were measured. The results (Table 4) showed that, although none of the isolates exhibited strong inhibitory activities in the assay, **2** and **3** were found to display notable ability to inhibit the elastase release ( $48.2\% \pm 6.2\%$ ) and superoxide anion generation ( $44.5\% \pm 4.6\%$ ) at 30  $\mu\text{M}$ , respectively. In comparison with (+)-isosarcophine, cherbonolides A–E, and bischerbonolide peroxide discovered previously from *S. cherbonnieri* [24], it was found that, although **2** and **3** exhibited weaker activities than bischerbonolide peroxide, they displayed comparable activities to those of cherbonolides A and C. In general, allylic oxidation at the 7,8-double bond of (+)-isosarcophine might be able to produce derivatives with stronger bioactivities.

**Table 4.** Inhibitory effects of metabolites **1–7** against elastase release and superoxide anion generation in N-formyl-methionyl-leucyl-phenylalanine/cytochalasin B (fMLF/CB)-induced primary human neutrophils.  $\text{IC}_{50}$ , half maximal inhibitory concentration.

Compound	Superoxide Anion		Elastase Release	
	$\text{IC}_{50}$ ( $\mu\text{M}$ ) <sup>a</sup>	Inh <sup>b</sup> %	$\text{IC}_{50}$ ( $\mu\text{M}$ ) <sup>a</sup>	Inh <sup>b</sup> %
<b>1</b>	>30	11.0 $\pm$ 8.7	>30	35.1 $\pm$ 10.6 ***
<b>2</b>	>30	29.8 $\pm$ 9.8 **	>30	48.2 $\pm$ 12.5 ***
<b>3</b>	>30	44.5 $\pm$ 7.9 ***	>30	35.6 $\pm$ 10.7 ***
<b>4</b>	>30	6.4 $\pm$ 7.3	>30	27.6 $\pm$ 12.8 **
<b>5</b>	>30	6.2 $\pm$ 5.5	>30	29.7 $\pm$ 11.1 **
<b>6</b>	>30	12.9 $\pm$ 11.4	>30	16.7 $\pm$ 10.2 *
<b>7</b>	>30	17.1 $\pm$ 11.6 *	>30	27.6 $\pm$ 12.0 **
<b>Idelalisib</b>	0.07 $\pm$ 0.03	102.8 $\pm$ 5.4 ***	0.07 $\pm$ 0.02	99.6 $\pm$ 10.3 ***

<sup>a</sup> Concentration necessary for 50% inhibition ( $\text{IC}_{50}$ ). <sup>b</sup> Percentage of inhibition (Inh %) at 30  $\mu\text{M}$ . Results presented as mean  $\pm$  S.D. The anti-inflammatory assays were performed with eight biological replicates. \*  $p < 0.05$ , \*\*  $p < 0.01$ , and \*\*\*  $p < 0.001$  compared with the control.

### 3. Materials and Methods

#### 3.1. General Experimental Procedures

Values of the specific optical rotation of the isolates were measured with a JASCO P-1020 polarimeter (JASCO Corporation, Tokyo, Japan). Infrared spectra were recorded using a JASCO FT/IR-4100 infrared spectrophotometer (JASCO Corporation, Tokyo, Japan). The CD spectrum was recorded on a Jasco J-815 circular dichroism (CD) spectropolarimeter (JASCO, Tokyo, Japan) in MeOH.  $^1\text{H}$ - and  $^{13}\text{C}$ -NMR spectra were acquired on a Varian 400MR FT-NMR (or Varian Unity INOVA500 FT-NMR) instrument (Varian Inc., Palo Alto, CA, USA) at 400 MHz (or 500 MHz) and 100 MHz (or



125 MHz), respectively, in  $\text{CDCl}_3$  or  $\text{C}_6\text{D}_6$ . LR-ESI-MS and HR-ESI-MS experiments were carried out using a Bruker APEX II (Bruker, Bremen, Germany) mass spectrometer. Silica gel (230–400 mesh) was used as the adsorbent for normal-phase column chromatography. Thin-layer chromatography (TLC) analyses were performed with precoated silica gel plates (Kieselgel 60 F-254, 0.2 mm, Merck, Darmstadt, Germany). Further purification of impure fractions or compounds was further achieved by high-performance liquid chromatography on a Hitachi L-7100 HPLC instrument (Hitachi Ltd., Tokyo, Japan) with a Merck Hibar Si-60 column (250 mm  $\times$  21 mm, 7  $\mu\text{m}$ ; Merck, Darmstadt, Germany) and on a Hitachi L-2455 HPLC apparatus (Hitachi, Tokyo, Japan) with a Supelco C18 column (250 mm  $\times$  21.2 mm, 5  $\mu\text{m}$ ; Supelco, Bellefonte, PA, USA).

### 3.2. Animal Materials

The marine organism *S. cherbonnieri* was collected and preserved as described previously [24].

### 3.3. Extraction and Isolation

By using the procedure reported previously, 1.2 kg (wet weight) of organism *S. cherbonnieri* was dehydrated, minced, extracted, and concentrated to afford 10.2 g of residue. The residue was fractionated by chromatography to yield 19 fractions [24]. Fraction 10, eluting with *n*-hexane–acetone (4:1), was further purified over silica gel using *n*-hexane–acetone (6:1) to afford seven subfractions (A1–A7). Subfraction A3 was further separated by reverse-phase HPLC using acetonitrile– $\text{H}_2\text{O}$  (1:1.1) to afford **2** (1.4 mg). Subfraction A4 was purified by reverse-phase HPLC using acetonitrile– $\text{H}_2\text{O}$  (1:1.2) to afford **4** (8.8 mg), and subfraction A6 was purified by reverse-phase HPLC acetonitrile– $\text{H}_2\text{O}$  (2:1) to afford **5** (3.1 mg). Fractions 11 and 12, obtained by eluting with *n*-hexane–acetone 3:1 and 2:1, respectively, were combined and further eluted with acetone by a Sephadex LH-20 column to afford six subfractions (B1–B6). The purification of subfractions B4 and B5 using reverse-phase HPLC by elution of acetonitrile– $\text{H}_2\text{O}$  (1:1.3) and  $\text{MeOH}$ – $\text{H}_2\text{O}$  (3:2) afforded **6** (12.4 mg) and **7** (33.1 mg), respectively. Fraction 13, eluting with *n*-hexane–acetone (1:1), was purified by eluting with acetone on Sephadex LH-20 to yield five subfractions (C1–C5). Subfraction C2 was further separated by reverse-phase HPLC using acetonitrile– $\text{H}_2\text{O}$  (1:1.4) to afford **1** (3.3 mg) and **3** (10.8 mg).

Cherbonolide F (**1**): colorless oil;  $[\alpha]_{25}^{\text{D}} +177$  (c 0.50,  $\text{CHCl}_3$ ); IR (neat)  $\nu_{\text{max}}$  3460, 2967, 2928, 2864, 1748, 1677, 1452, 1385, 1096, 984, and 755  $\text{cm}^{-1}$ ; for  $^{13}\text{C}$ - and  $^1\text{H}$ -NMR data (400 MHz;  $\text{C}_6\text{D}_6$ ), see Tables 1 and 2; ESI-MS  $m/z$  355  $[\text{M} + \text{Na}]^+$ ; HR-ESI-MS  $m/z$  355.1879  $[\text{M} + \text{Na}]^+$  (calculated for  $\text{C}_{20}\text{H}_{28}\text{O}_4\text{Na}$ , 355.1880).

Cherbonolide G (**2**): colorless oil;  $[\alpha]_{25}^{\text{D}} +25$  (c 0.33,  $\text{CHCl}_3$ ); IR (neat)  $\nu_{\text{max}}$  3419, 2925, 2855, 1748, 1678, 1454, 1387, 1096, 987, and 755  $\text{cm}^{-1}$ ; for  $^{13}\text{C}$ - and  $^1\text{H}$ -NMR data (400 MHz;  $\text{C}_6\text{D}_6$ ), see Tables 1 and 2; ESI-MS  $m/z$  371  $[\text{M} + \text{Na}]^+$ ; HR-ESI-MS  $m/z$  371.1830  $[\text{M} + \text{Na}]^+$  (calculated for  $\text{C}_{20}\text{H}_{28}\text{O}_5\text{Na}$ , 371.1829).

Cherbonolide H (**3**): colorless oil;  $[\alpha]_{25}^{\text{D}} +41$  (c 1.00,  $\text{CHCl}_3$ ); IR (neat)  $\nu_{\text{max}}$  3445, 2928, 2864, 1747, 1679, 1455, 1387, 1094, 996, and 755  $\text{cm}^{-1}$ ; for  $^{13}\text{C}$ - and  $^1\text{H}$ -NMR data (400 MHz;  $\text{C}_6\text{D}_6$ ), see Tables 1 and 2; ESI-MS  $m/z$  355  $[\text{M} + \text{Na}]^+$ ; HR-ESI-MS  $m/z$  355.1878  $[\text{M} + \text{Na}]^+$  (calculated for  $\text{C}_{20}\text{H}_{28}\text{O}_4\text{Na}$ , 355.1880).

Cherbonolide I (**4**): colorless oil;  $[\alpha]_{25}^{\text{D}} +13$  (c 1.00,  $\text{CHCl}_3$ ); IR (neat)  $\nu_{\text{max}}$  3420, 2925, 2855, 1747, 1541, 1390, 992, and 756  $\text{cm}^{-1}$ ; for  $^{13}\text{C}$ - and  $^1\text{H}$ -NMR data (500 MHz;  $\text{C}_6\text{D}_6$ ), see Tables 1 and 2; ESI-MS  $m/z$  371  $[\text{M} + \text{Na}]^+$ ; HR-ESI-MS  $m/z$  371.1828  $[\text{M} + \text{Na}]^+$  (calculated for  $\text{C}_{20}\text{H}_{28}\text{O}_5\text{Na}$ , 371.1829).

Cherbonolide J (**5**): white powder;  $[\alpha]_{25}^{\text{D}} -6$  (c 0.50,  $\text{CHCl}_3$ ); IR (neat)  $\nu_{\text{max}}$  3443, 2937, 2860, 1755, 1675, 1381, 1076, 990, and 755  $\text{cm}^{-1}$ ; CD ( $1.2 \times 10^{-4}$  M,  $\text{MeOH}$ )  $\lambda_{\text{max}}$  ( $\Delta\epsilon$ ) 247 (−5.2), and 228 (+26.5) nm; for  $^{13}\text{C}$ - and  $^1\text{H}$ -NMR data (400 MHz;  $\text{C}_6\text{D}_6$ ), see Tables 1 and 3; ESI-MS  $m/z$  373  $[\text{M} + \text{Na}]^+$ ; HR-ESI-MS  $m/z$  373.1984  $[\text{M} + \text{Na}]^+$  (calculated for  $\text{C}_{20}\text{H}_{30}\text{O}_5\text{Na}$ , 373.1986).

Cherbonolide K (6): yellow oil;  $[\alpha]_{25}^D +12$  (c 1.00,  $\text{CHCl}_3$ ); IR (neat)  $\nu_{\text{max}}$  3444, 2927, 1763, 1435, 1386, 1241, 1083, 931, and  $756\text{ cm}^{-1}$ ; for  $^{13}\text{C}$ - and  $^1\text{H}$ -NMR data (400 MHz;  $\text{CDCl}_3$ ), see Tables 1 and 3; ESI-MS  $m/z$  355  $[\text{M} + \text{Na}]^+$ ; HR-ESI-MS  $m/z$  355.1880  $[\text{M} + \text{Na}]^+$  (calculated for  $\text{C}_{20}\text{H}_{28}\text{O}_4\text{Na}$ , 355.1880).

Cherbonolide L (7): yellow oil;  $[\alpha]_{25}^D +33$  (c 1.00,  $\text{CHCl}_3$ ); IR (neat)  $\nu_{\text{max}}$  3445, 2929, 2872, 1752, 1665, 1455, 1384, 1050, 927, and  $756\text{ cm}^{-1}$ ; for  $^{13}\text{C}$ - and  $^1\text{H}$ -NMR data (400 MHz;  $\text{CDCl}_3$ ), see Tables 1 and 3; ESI-MS  $m/z$  355  $[\text{M} + \text{Na}]^+$ ; HR-ESI-MS  $m/z$  355.1877  $[\text{M} + \text{Na}]^+$  (calculated for  $\text{C}_{20}\text{H}_{28}\text{O}_4\text{Na}$ , 355.1880).

### 3.4. Reduction of Cherbonolide I (4)

The solution of compound 4 (1.4 mg) in diethyl ether (5.0 mL) was added to an excess amount of triphenylphosphine (1.3 mg), and the mixture was stirred at room temperature for 4 h. The solvent of the solution was evaporated under reduced pressure to afford a residue, which was purified by silica gel column chromatography using *n*-hexane–acetone (3:1) as an eluent to yield 3 (1.0 mg, 75%).

### 3.5. In Vitro Anti-Inflammatory Assay

#### 3.5.1. Primary Human Neutrophils

Blood was obtained from the elbow vein of healthy adult volunteers (with ages 20–30). Neutrophils were enriched by means of dextran sedimentation, Ficoll–Hypaque centrifugation, and hypotonic lysis. Neutrophils were incubated in an ice-cold  $\text{Ca}^{2+}$ -free Hank's Balanced Salt Solution (HBSS buffer, pH 7.4) [31]. The research protocol was granted approval by the institutional review board of Chang Gung Memorial Hospital (IRB No: 201601307A3, 20161124-20191123; 201902217A3, 20200501-20240630). All subjects gave their informed consent for inclusion before they participated in the study. The study was conducted in accordance with the Declaration of Helsinki.

#### 3.5.2. Superoxide Anion Generation

Neutrophils ( $6 \times 10^5\text{ cells}\cdot\text{mL}^{-1}$ ) incubated in HBSS with ferricytochrome *c* ( $0.5\text{ mg}\cdot\text{mL}^{-1}$ ) and  $\text{Ca}^{2+}$  (1 mM) at  $37\text{ }^\circ\text{C}$  were treated with dimethyl sulfoxide (DMSO), as control, or with the tested compound for 5 min. Neutrophils were primed by cytochalasin B (CB,  $1\text{ }\mu\text{g}\cdot\text{mL}^{-1}$ ) for 3 min before activating fMLF (100 nM) for 10 min (fMLF/CB). The change in superoxide anion generation was spectrophotometrically measured at 550 nm (U-3010, Hitachi, Tokyo, Japan) [32,33].

#### 3.5.3. Elastase Release

Neutrophils ( $6 \times 10^5\text{ cells}\cdot\text{mL}^{-1}$ ) incubated in HBSS with MeO-Suc-Ala-Ala-Pro-Val-*p*-nitroanilide (100  $\mu\text{M}$ ) and  $\text{Ca}^{2+}$  (1 mM) at  $37\text{ }^\circ\text{C}$  were treated with DMSO or the tested compound for 5 min. Neutrophils were challenged by fMLF (100 nM)/CB ( $0.5\text{ }\mu\text{g}\cdot\text{mL}^{-1}$ ) for 10 min. The change in elastase release was spectrophotometrically measured at 405 nm (U-3010, Hitachi, Tokyo, Japan) [32].

#### 3.5.4. Statistical Analysis

Data were displayed as the mean  $\pm$  SD, and comparisons were performed by one-way ANOVA with Dunnett analysis. All results were obtained from eight biological replicates. A probability value of 0.05 or less was considered to be significant. The Prism software (Version 5.0, GraphPad Software, San Diego, CA, USA) was used for the statistical analysis.

## 4. Conclusions

Our present examination of the chemical constituents of the soft coral *S. cherbonnieri* led to the discovery of new cembranoid compounds 1–7. All compounds were found to possess anti-inflammatory activity by exhibiting inhibitory effects on the generation of superoxide anion and elastase release in fMLF/CB-induced primary human neutrophils, and cherbonolides G and H (2 and 3) were found to be the most active in the inhibition of elastase release and superoxide anion generation, respectively.

As the marine environment is an important source of bioactive substances, and due to the high chemical diversity and specimen diversity of the *Sarcophyton* genus [27,28,34,35], it can be expected that new natural products and activities from soft corals of this genus can be continuously discovered in the future.

**Supplementary Materials:** The following are available online at <http://www.mdpi.com/1660-3397/18/11/573/s1>. HR-ESI-MS,  $^1\text{H}$ -NMR,  $^{13}\text{C}$ -NMR, DEPT, HMQC, COSY, HMBC, and NOESY spectra of new compounds 1–7 are available online at <http://www.mdpi.com/1660-3397/16/8/276/s1>. Figure S1: HR-ESI-MS spectrum of 1; Figure S2.  $^1\text{H}$ -NMR spectrum of 1 in  $\text{C}_6\text{D}_6$ ; Figure S3.  $^{13}\text{C}$ -NMR spectrum of 1 in  $\text{C}_6\text{D}_6$ ; Figure S4. HSQC spectrum of 1 in  $\text{C}_6\text{D}_6$ ; Figure S5.  $^1\text{H}$ – $^1\text{H}$  COSY spectrum of 1 in  $\text{C}_6\text{D}_6$ ; Figure S6. HMBC spectrum of 1 in  $\text{C}_6\text{D}_6$ ; Figure S7. NOESY spectrum of 1 in  $\text{C}_6\text{D}_6$ ; Figure S8. HR-ESI-MS spectrum of 2; Figure S9.  $^1\text{H}$ -NMR spectrum of 2 in  $\text{C}_6\text{D}_6$ ; Figure S10.  $^{13}\text{C}$ -NMR spectrum of 2 in  $\text{C}_6\text{D}_6$ ; Figure S11. HSQC spectrum of 2 in  $\text{C}_6\text{D}_6$ ; Figure S12.  $^1\text{H}$ – $^1\text{H}$  COSY spectrum of 2 in  $\text{C}_6\text{D}_6$ ; Figure S13. HMBC spectrum of 2 in  $\text{C}_6\text{D}_6$ ; Figure S14. NOESY spectrum of 2 in  $\text{C}_6\text{D}_6$ ; Figure S15. HR-ESI-MS spectrum of 3; Figure S16.  $^1\text{H}$ -NMR spectrum of 3 in  $\text{C}_6\text{D}_6$ ; Figure S17.  $^{13}\text{C}$ -NMR spectrum of 3 in  $\text{C}_6\text{D}_6$ ; Figure S18. HSQC spectrum of 3 in  $\text{C}_6\text{D}_6$ ; Figure S19.  $^1\text{H}$ – $^1\text{H}$  COSY spectrum of 3 in  $\text{C}_6\text{D}_6$ ; Figure S20. HMBC spectrum of 3 in  $\text{C}_6\text{D}_6$ ; Figure S21. NOESY spectrum of 3 in  $\text{C}_6\text{D}_6$ ; Figure S22. HR-ESI-MS spectrum of 4; Figure S23.  $^1\text{H}$ -NMR spectrum of 4 in  $\text{C}_6\text{D}_6$ ; Figure S24.  $^{13}\text{C}$ -NMR spectrum of 4 in  $\text{C}_6\text{D}_6$ ; Figure S25. HSQC spectrum of 4 in  $\text{C}_6\text{D}_6$ ; Figure S26.  $^1\text{H}$ – $^1\text{H}$  COSY spectrum of 4 in  $\text{C}_6\text{D}_6$ ; Figure S27. HMBC spectrum of 4 in  $\text{C}_6\text{D}_6$ ; Figure S28. NOESY spectrum of 4 in  $\text{C}_6\text{D}_6$ ; Figure S29. HR-ESI-MS spectrum of 5; Figure S30.  $^1\text{H}$ -NMR spectrum of 5 in  $\text{C}_6\text{D}_6$ ; Figure S31.  $^{13}\text{C}$ -NMR spectrum of 5 in  $\text{C}_6\text{D}_6$ ; Figure S32. HSQC spectrum of 5 in  $\text{C}_6\text{D}_6$ ; Figure S33.  $^1\text{H}$ – $^1\text{H}$  COSY spectrum of 5 in  $\text{C}_6\text{D}_6$ ; Figure S34. HMBC spectrum of 5 in  $\text{C}_6\text{D}_6$ ; Figure S35. NOESY spectrum of 5 in  $\text{C}_6\text{D}_6$ ; Figure S36. HR-ESI-MS spectrum of 6; Figure S37.  $^1\text{H}$ -NMR spectrum of 6 in  $\text{CDCl}_3$ ; Figure S38.  $^{13}\text{C}$ -NMR spectrum of 6 in  $\text{CDCl}_3$ ; Figure S39. HSQC spectrum of 6 in  $\text{CDCl}_3$ ; Figure S40.  $^1\text{H}$ – $^1\text{H}$  COSY spectrum of 6 in  $\text{CDCl}_3$ ; Figure S41. HMBC spectrum of 6 in  $\text{CDCl}_3$ ; Figure S42. NOESY spectrum of 6 in  $\text{CDCl}_3$ ; Figure S43. HR-ESI-MS spectrum of 7; Figure S44.  $^1\text{H}$ -NMR spectrum of 7 in  $\text{CDCl}_3$ ; Figure S45.  $^{13}\text{C}$ -NMR spectrum of 7 in  $\text{CDCl}_3$ ; Figure S46. HSQC spectrum of 7 in  $\text{CDCl}_3$ ; Figure S47.  $^1\text{H}$ – $^1\text{H}$  COSY spectrum of 7 in  $\text{CDCl}_3$ ; Figure S48. HMBC spectrum of 7 in  $\text{CDCl}_3$ ; Figure S49. NOESY spectrum of 7 in  $\text{CDCl}_3$ .

**Author Contributions:** Conceptualization, J.-H.S.; investigation, C.-C.P.; analysis, C.-C.P. and C.-Y.H.; writing—original draft, C.-Y.H., J.-H.S., and A.F.A.; writing—review and editing, J.-H.S.; anti-inflammatory assay, T.-L.H. All authors read and agreed to the published version of the manuscript.

**Funding:** Financial support of this work from the Ministry of Science and Technology of Taiwan (MOST 104-2313-M-110-006, 104-2320-B-110-001-MY2, and 107-2320-B-110-001-MY3) to J.-H.S. and further funding from the Deanship of Scientific Research at King Saud University through research group RG-1440-127.

**Conflicts of Interest:** The authors declare no conflict of interest.

## References

- Farag, M.A.; Fekry, M.I.; Al-Hammady, M.A.; Khalil, M.N.; El-Seedi, H.R.; Meyer, A.; Porzel, A.; Westphal, H.; Wessjohann, L.A. Cytotoxic effects of *Sarcophyton* sp. soft corals—is there a correlation to their NMR fingerprints? *Mar. Drugs* **2017**, *15*, 211. [CrossRef]
- Chao, C.H.; Li, W.L.; Huang, C.Y.; Ahmed, A.F.; Dai, C.F.; Wu, Y.C.; Lu, M.C.; Liaw, C.C.; Sheu, J.H. Isoprenoids from the soft coral *Sarcophyton glaucum*. *Mar. Drugs* **2017**, *15*, 202. [CrossRef]
- Hegazy, M.E.F.; Elshamy, A.I.; Mohamed, T.A.; Hamed, A.R.; Ibrahim, M.A.A.; Ohta, S.; Paré, P.W. Cembrene diterpenoids with ether linkages from *Sarcophyton ehrenbergi*: An anti-proliferation and molecular-docking assessment. *Mar. Drugs* **2017**, *15*, 192. [CrossRef]
- Elkhateeb, A.; El-Beih, A.A.; Gamal-Eldeen, A.M.; Alhammady, M.A.; Ohta, S.; Paré, P.W.; Hegazy, M.E.F. New terpenes from the Egyptian soft coral *Sarcophyton ehrenbergi*. *Mar. Drugs* **2014**, *12*, 1977–1986. [CrossRef]
- Eltahawy, N.A.; Ibrahim, A.K.; Radwan, M.M.; ElSohly, M.A.; Hassanean, H.A.; Hassanean, H.A.; Ahmed, S.A. Cytotoxic cembranoids from the Red Sea soft coral, *Sarcophyton auritum*. *Tetrahedron Lett.* **2014**, *55*, 3984–3988. [CrossRef]
- Lin, W.Y.; Lu, Y.; Su, J.H.; Wen, Z.H.; Dai, C.F.; Kuo, Y.H.; Sheu, J.H. Bioactive cembranoids from the dongsha atoll soft coral *Sarcophyton crassocaule*. *Mar. Drugs* **2011**, *9*, 994–1006. [CrossRef]
- Lin, W.Y.; Su, J.H.; Lu, Y.; Wen, Z.H.; Dai, C.F.; Kuo, Y.H.; Sheu, J.H. Cytotoxic and anti-inflammatory cembranoids from the Dongsha Atoll soft coral *Sarcophyton crassocaule*. *Bioorg. Med. Chem.* **2010**, *18*, 1936–1941. [CrossRef]

8. Hassan, H.M.; Rateb, M.E.; Hassan, M.H.; Sayed, A.M.; Shabana, S.; Raslan, M.; Amin, E.; Behery, F.A.; Ahmed, O.M.; Bin Muhsinah, A.; et al. New antiproliferative cembrane diterpenes from the Red Sea *Sarcophyton* species. *Mar. Drugs* **2019**, *17*, 411. [\[CrossRef\]](#)
9. Huang, C.Y.; Tseng, Y.J.; Chokkalingam, U.; Hwang, T.L.; Hsu, C.H.; Dai, C.F.; Sung, P.J.; Sheu, J.H. Bioactive isoprenoid-derived natural products from a Dongsha Atoll soft coral *Sinularia erecta*. *J. Nat. Prod.* **2016**, *79*, 1339–1346. [\[CrossRef\]](#)
10. Tseng, Y.J.; Yang, Y.C.; Wang, S.K.; Duh, C.Y. Numerosol A–D, new cembranoid diterpenes from the soft coral *Sinularia numerosa*. *Mar. Drugs* **2014**, *12*, 3371–3380. [\[CrossRef\]](#)
11. Lillsunde, K.-E.; Festa, C.; Adel, H.; De Marino, S.; Lombardi, V.; Tilvi, S.; Nawrot, D.A.; Zampella, A.; D'Souza, L.; D'Auria, M.V.; et al. Bioactive cembrane derivatives from the Indian Ocean soft coral, *Sinularia kavarattiensis*. *Mar. Drugs* **2014**, *12*, 4045–4068. [\[CrossRef\]](#)
12. Li, G.; Zhang, Y.; Deng, Z.; van Ofwegen, L.; Proksch, P.; Lin, W. Cytotoxic cembranoid diterpenes from a soft coral *Sinularia gibberosa*. *J. Nat. Prod.* **2005**, *68*, 649–652. [\[CrossRef\]](#)
13. Cheng, S.Y.; Wen, Z.H.; Wang, S.K.; Chiou, S.F.; Hsu, C.H.; Dai, C.F.; Chiang, M.Y.; Duh, C.Y. Unprecedented hemiketal cembranolides with anti-inflammatory activity from the soft coral *Lobophytum durum*. *J. Nat. Prod.* **2009**, *72*, 152–155. [\[CrossRef\]](#)
14. Chao, C.H.; Wen, Z.H.; Wu, Y.C.; Yeh, H.C.; Sheu, J.H. Cytotoxic and anti-inflammatory cembranoids from the soft coral *Lobophytum crassum*. *J. Nat. Prod.* **2008**, *71*, 1819–1824. [\[CrossRef\]](#)
15. Lai, K.H.; You, W.J.; Lin, C.C.; El-Shazly, M.; Liao, Z.J.; Su, J.H. Anti-inflammatory cembranoids from the soft coral *Lobophytum crassum*. *Mar. Drugs* **2017**, *15*, 327. [\[CrossRef\]](#) [\[PubMed\]](#)
16. Lin, K.H.; Tseng, Y.J.; Chen, B.W.; Hwang, T.L.; Chen, H.Y.; Dai, C.F.; Sheu, J.H. Tortuosenes A and B, new diterpenoid metabolites from the Formosan soft coral *Sarcophyton tortuosum*. *Org. Lett.* **2014**, *16*, 1314–1317. [\[CrossRef\]](#)
17. Chao, C.H.; Wu, C.Y.; Huang, C.Y.; Wang, H.C.; Dai, C.F.; Wu, Y.C.; Sheu, J.H. Cubitanoids and cembranoids from the soft coral *Sinularia nanolobata*. *Mar. Drugs* **2016**, *14*, 150. [\[CrossRef\]](#)
18. Chen, B.W.; Chao, C.H.; Su, J.H.; Huang, C.Y.; Dai, C.F.; Wen, Z.H.; Sheu, J.H. A novel symmetric sulfur-containing biscembranoid from the Formosan soft coral *Sinularia flexibilis*. *Tetrahedron Lett.* **2010**, *51*, 764–766. [\[CrossRef\]](#)
19. Huang, C.Y.; Sung, P.J.; Uvarani, C.; Su, J.H.; Lu, M.C.; Hwang, T.L.; Dai, C.F.; Wu, S.L.; Sheu, J.H. Glaucumolides A and B, biscembranoids with new structural type from a cultured soft coral *Sarcophyton glaucum*. *Sci. Rep.* **2015**, *5*, 15624. [\[CrossRef\]](#)
20. Jia, R.; Kurtan, T.; Mandi, A.; Yan, X.H.; Zhang, W.; Guo, Y.W. Biscembranoids formed from an  $\alpha$ ,  $\beta$ -unsaturated gamma-lactone ring as a dienophile: Structure revision and establishment of their absolute configurations using theoretical calculations of electronic circular dichroism spectra. *J. Org. Chem.* **2013**, *78*, 3113–3119. [\[CrossRef\]](#)
21. Kusumi, T.; Igari, M.; Ishitsuka, M.O.; Ichikawa, A.; Itezono, Y.; Nakayama, N.; Kakisawa, H. A novel chlorinated biscembranoid from the marine soft coral *Sarcophyton glaucum*. *J. Org. Chem.* **1990**, *55*, 6286–6289. [\[CrossRef\]](#)
22. Tseng, Y.J.; Ahmed, A.F.; Dai, C.F.; Chiang, M.Y.; Sheu, J.H. Sinulochmodins A–C, three novel terpenoids from the soft coral *Sinularia lochmodes*. *Org. Lett.* **2005**, *7*, 3813–3816. [\[CrossRef\]](#) [\[PubMed\]](#)
23. Li, Y.; Pattenden, G. Biomimetic syntheses of ineleganolide and sinulochmodin C from 5-episinuleptolide via sequences of transannular Michael reactions. *Tetrahedron* **2011**, *67*, 10045–10052. [\[CrossRef\]](#)
24. Peng, C.C.; Huang, C.Y.; Ahmed, A.F.; Hwang, T.L.; Dai, C.F.; Sheu, J.H. New cembranoids and a iscembranoid peroxide from the soft coral *Sarcophyton cherbonnieri*. *Mar. Drugs* **2018**, *16*, 276. [\[CrossRef\]](#) [\[PubMed\]](#)
25. Sang, V.T.; Dat, T.; Vinh, L.B.; Cuong, L.; Oanh, P.; Ha, H.; Kim, Y.H.; Anh, H.; Yang, S.Y. Coral and coral-associated microorganisms: A prolific source of potential bioactive natural products. *Mar. Drugs* **2019**, *17*, 468. [\[CrossRef\]](#) [\[PubMed\]](#)
26. Rodrigues, I.G.; Miguel, M.G.; Mnif, W. A brief review on new naturally occurring cembranoid diterpene derivatives from the soft corals of the genera *Sarcophyton*, *Sinularia*, and *Lobophytum* since 2016. *Molecules* **2019**, *24*, 781. [\[CrossRef\]](#) [\[PubMed\]](#)
27. Elkhawas, Y.A.; Elissawy, A.M.; Elnaggar, M.S.; Mostafa, N.M.; Al-Sayed, E.; Bishr, M.M.; Singab, A.N.B.; Salama, O.M. Chemical diversity in species belonging to soft coral genus *Sarcophyton* and its impact on biological activity: A review. *Mar. Drugs* **2020**, *18*, 41. [\[CrossRef\]](#)

28. Maloney, K.N.; Botts, R.T.; Davis, T.S.; Okada, B.K.; Maloney, E.M.; Leber, C.A.; Alvarado, O.; Brayton, C.; Caraballo-Rodríguez, A.M.; Chari, J.V.; et al. Cryptic species account for the seemingly idiosyncratic secondary metabolism of *Sarcophyton glaucum* specimens collected in Palau. *J. Nat. Prod.* **2020**, *83*, 693–705. [[CrossRef](#)]
29. Xi, Z.; Bie, W.; Chen, W.; Liu, D.; van Ofwegen, L.; Proksch, P.; Lin, W. Sarcophyolides B–E, new cembranoids from the soft coral *Sarcophyton elegans*. *Mar. Drugs* **2013**, *11*, 3186–3196. [[CrossRef](#)]
30. Kusumi, T.; Yamada, K.; Ishitsuka, M.O.; Fujita, Y.; Kakisawa, H. New cembranoids from the Okinawan soft coral *Sinularia mayi*. *Chem. Lett.* **1990**, *19*, 1315–1318. [[CrossRef](#)]
31. Hwang, T.L.; Su, Y.C.; Chang, H.L.; Leu, Y.L.; Chung, P.J.; Kuo, L.M.; Chang, Y.J. Suppression of superoxide anion and elastase release by C18 unsaturated fatty acids in human neutrophils. *J. Lipid Res.* **2009**, *50*, 1395–1408. [[CrossRef](#)] [[PubMed](#)]
32. Yang, S.C.; Chung, P.J.; Ho, C.M.; Kuo, C.Y.; Hung, M.F.; Huang, Y.T.; Chang, W.Y.; Chang, Y.W.; Chan, K.H.; Hwang, T.L. Propofol inhibits superoxide production, elastase release, and chemotaxis in formyl peptide-activated human neutrophils by blocking formyl peptide receptor 1. *J. Immunol.* **2013**, *190*, 6511–6519. [[CrossRef](#)] [[PubMed](#)]
33. Yu, H.P.; Hsieh, P.W.; Chang, Y.J.; Chung, P.J.; Kuo, L.M.; Hwang, T.L. 2-(2-Fluorobenzamido) benzoate ethyl ester (EFB-1) inhibits superoxide production by human neutrophils and attenuates hemorrhagic shock-induced organ dysfunction in rats. *Free Radic. Biol. Med.* **2011**, *50*, 1737–1748. [[CrossRef](#)] [[PubMed](#)]
34. Wei, W.-C.; Sung, P.-J.; Duh, C.-Y.; Chen, B.-W.; Sheu, J.-H.; Yang, N.-S. Anti-inflammatory activities of natural products isolated from soft corals of Taiwan between 2008 and 2012. *Mar. Drugs* **2013**, *11*, 4083–4126. [[CrossRef](#)] [[PubMed](#)]
35. Ahmad, B.; Shah, M.; Choi, S. Oceans as a source of immunotherapy. *Mar. Drugs* **2019**, *17*, 282. [[CrossRef](#)] [[PubMed](#)]

**Publisher's Note:** MDPI stays neutral with regard to jurisdictional claims in published maps and institutional affiliations.



© 2020 by the authors. Licensee MDPI, Basel, Switzerland. This article is an open access article distributed under the terms and conditions of the Creative Commons Attribution (CC BY) license (<http://creativecommons.org/licenses/by/4.0/>).





# Novel regulator role of CIL-102 in the epigenetic modification of TNFR1/TRAIL to induce cell apoptosis in human gastric cancer

Chih-Chuan Teng<sup>a,b</sup>, Shui-Yi Tung<sup>c,d</sup>, Ko-Chao Lee<sup>e,f</sup>, Kam-Fai Lee<sup>g</sup>, Wen-Shih Huang<sup>d,h</sup>, Chien-Heng Shen<sup>c</sup>, Meng-Chiao Hsieh<sup>h,i</sup>, Cheng-Yi Huang<sup>h</sup>, Jiunn-Ming Sheen<sup>j</sup>, Hsing-Chun Kuo<sup>a,b,k,l,\*</sup>

<sup>a</sup> Department of Nursing, Division of Basic Medical Sciences, Chang Gung University of Science and Technology, Chiayi, Taiwan

<sup>b</sup> Chang Gung Memorial Hospital, Chiayi, Taiwan

<sup>c</sup> Department of Hepato-Gastroenterology, Chang Gung Memorial Hospital, Chiayi, Taiwan

<sup>d</sup> Chang Gung University College of Medicine, Taoyuan, Taiwan

<sup>e</sup> Division of Colorectal Surgery, Department of Surgery, Chang Gung Memorial Hospital, Kaohsiung Medical Center, Chang Gung University College of Medicine, Kaohsiung, Taiwan

<sup>f</sup> Department of Information Management & College of Liberal Education, Shu-Te University, Kaohsiung, Taiwan

<sup>g</sup> Department of Pathology, Chang Gung Memorial Hospital at Chiayi, Taiwan

<sup>h</sup> Division of Colon and Rectal Surgery, Department of Surgery, Chang Gung Memorial Hospital Chiayi, Taiwan

<sup>i</sup> Graduate Institute of Clinical Medical Sciences, College of Medicine, Chang Gung University, Taiwan

<sup>j</sup> Department of Pediatrics, Chiayi Chang Gung Memorial Hospital and Chang Gung University College of Medicine, Chiayi, Taiwan

<sup>k</sup> Research Center for Industry of Human Ecology, Chang Gung University of Science and Technology, Taoyuan, Taiwan

<sup>l</sup> Chronic Diseases and Health Promotion Research Center, CGUST, Chiayi, Taiwan

## ARTICLE INFO

### Keywords:

CIL-102  
Gastric cancer cells  
Apoptosis  
Death receptors  
H3K4me3

## ABSTRACT

CIL-102 (1-[4-(furo [2,3-b]quinolin-4-ylamino)phenyl]ethanone) is a major active agent and an alkaloid derivative of *Camptotheca acuminata*, which has valuable biological properties, including anti-tumorigenic activity. However, the molecular mechanisms of CIL-102 related to inductive apoptosis in human gastric cancer remain unclear. By using diphenyltetrazolium bromide (MTT), annexin-V-fluorescein-isothiocyanate (FITC)/propidium iodide staining and a 2',7'-dichlorofluorescein diacetate (DCFDA), a Fluo-3 fluorescence staining assay, the cell death and cell viability in gastric cancer cells and an in vivo xenograft mouse model, with or without the addition of CIL-102, were measured, respectively. Furthermore, signaling pathways and apoptotic molecules were also detected by western blots and an immunohistochemical assay. Our results demonstrated that CIL-102 treatment significantly induced the cell apoptosis of gastric cancer cells, along with increased ROS production and increased intracellular Ca<sup>2+</sup> levels. In addition, through the inactivation of CDK1/cyclin B1, CIL-102 treatment induced the cell cycle G2/M arrest of gastric cancer cells. Moreover, our data revealed that multiple signaling pathways were involved in the H3K4 trimethylation of TNFR1 and TRAIL proteins by CIL-102, including ROS-derived and JNK/mTOR/p300 pathways in gastric cancer AGS cells. The CIL-102 treatment also consistently inhibited tumor growth and increased tumor apoptosis, as measured by TUNEL assay in an in vivo xenograft mouse model. An immunohistochemical analysis revealed that the upregulation of the TNFR1 and TRAIL proteins and the downregulation of PCNA and CDK1 proteins were found in the CIL-102-treated gastric cancer xenograft mouse model, compared to that of the saline control. Together, this study sheds light on the novel mechanism associated with CIL-102 for inducing gastric cancer apoptosis.

## 1. Introduction

Stomach cancer, also known as gastric cancer, originally develops

from the stomach lining. Epidemiological investigations in 2018 revealed that this cancer is the fifth leading type of stomach cancer (8.2%) mortality across 20 world regions (Jemal et al., 2011). At a later stage, gastric cancer spreads from the stomach to other parts of the body,

\* Corresponding author. Chang Gung Memorial Hospital, Institute of Nursing and Department of Nursing, Chang Gung Institute of Technology, Chia-Yi Campus, Taiwan.

E-mail address: [kuohc@mail.cgu.edu.tw](mailto:kuohc@mail.cgu.edu.tw) (H.-C. Kuo).

<https://doi.org/10.1016/j.fct.2020.111856>

Received 21 June 2020; Received in revised form 2 November 2020; Accepted 6 November 2020

Available online 25 November 2020

0278-6915/© 2020 Published by Elsevier Ltd.

particularly to the liver, lungs, bones, the lining of the abdomen, as well as the lymph nodes (Herszenyi and Tulassay, 2010). As many therapeutic interventions for gastric cancer have been developed, such as the

### Abbreviations

CIL-102	1-[4-(furo[2,3-b]quinolin-4-ylamino)phenyl]ethanone
PI	Propidium iodide
MTT	3-(4,5-dimethylthiazol-2-yl)-2,5-diphenyltetrazolium bromide
NAC	N-acetyl cysteine
H <sub>2</sub> DCFDA	2,7-dichlorodihydrofluorescein diacetate
DHE	Dihydroethidium
H3	Ac-Histone H3
DMEM	Dulbecco's modified Eagle's medium
DAPI	4',6-diamidino-2-phenylindole
SDS	sodium deoxycholate, 0.1% sodium dodecyl sulfate
OD	optical density
EGCG	epigallocatechin-3-gallate
HMTs	histone methyltransferases
HDMs	histone demethylases

surgery, chemotherapy, and/or radiation therapy (Ogino et al., 2019), death rates due to gastric cancer have been decreasing since 1930 in many areas of the world (Balakrishnan et al., 2017). However, the occurrence and death rates of gastric cancer was still high in 2018, with patients being affected annually and deaths occurring. Many risk factors have been considered for the development of gastric cancer, including infections, smoking, dietary aspects and obesity (Wagner et al., 2010). On the other hand, chemo-preventive compounds that are present in dietary foods, such as fruits, mushrooms, garlic, soybeans, and green onions have been reported to decrease the risk of stomach cancer development (Ranjan et al., 2019; Woo et al., 2014). Thus, establishing the anti-cancer effects of the novel dietary compounds seems to be a promising therapeutic strategy for the prevention and treatment of gastric cancer.

The 9-anilino-furoquinoline derivative, CIL-102, which is used as an antiseptic drug, can be found in the bark and stem of *Camptotheca acuminata* (Chen et al., 2003). Recent studies have reported that the anti-cancer and chemo-preventive properties of CIL-102 help to inhibit the proliferation of tumor cells (Chen et al., 2005; Huang et al., 2005). Our previous study has also shown that CIL-102 decreases the proliferation and invasiveness of glioma cells through multiple signaling pathways, such as ERK1/2 and Cdc25c<sup>216</sup>, as well as by ROS generation (Teng et al., 2012). In colorectal cancer, CIL-102 treatment has shown a strong anti-cancer effect and it activates intracellular signals for the induction of cancer cell apoptosis (Teng et al., 2013). CIL-102 treatment works well to induce cell apoptosis in other type of cancers, such as gastric cancer; however, its mechanism related to signal transduction remains unclear.

With regards to cancer therapy, it has been observed that the induction of cell apoptosis not only inhibits cancer growth, but it also disrupts cell viability in cancer-affected cells (Hanahan and Weinberg, 2000). In fact, cell apoptosis is an important physiological process that leads to cell death (Feitelson et al., 2015). Usually, this process happens during the normal developmental process. Once the dysregulation of cell apoptosis occurs, the cells become immortal and proliferative (uncontrolled cell division), which initiates the process of carcinogenesis (Hsu et al., 2020; Wong, 2011). In general, there are two signaling pathways that are involved in the process of cell apoptosis. In response to an intrinsic apoptotic stimulus, the release of cytochrome *c* from the mitochondria further sequentially increases the activity of caspase-9 and

caspase-3, resulting in the induction of cell apoptosis (Chen and Chien, 2014). Conversely, the activity of caspase-8, -9 and -3 can also be activated by extracellular ligands, such as Fas-L, for inducing cell apoptosis, while binding to their corresponding receptors (death receptors) (Reed, 2000). In addition, the production of ROS, the second messengers that are sensitive to oxidative damage-mediated cell apoptosis, is a critical event that plays a significant role during an intrinsic or extrinsic apoptotic stimulus (Li-Weber, 2013). Interestingly, some studies have demonstrated that epigenetic modification also contributes to the regulation of cell apoptosis in cancer cells (Cheng et al., 2019). For instance, the upregulation of the death-receptor-related gene by histone H3 methylation occurs under ROS production-mediated cell apoptosis (Elmallah and Micheau, 2019; Savva et al., 2016). In this study, our results have shown that a novel mechanism is associated with CIL-102 that induces gastric cancer cell apoptosis through the involvement of the epigenetic histone H3 methylation-mediated upregulation of TNFR1 and TRAIL signals.

## 2. Materials and Methods

### 2.1. Chemical reagents and antibodies

All culture materials were purchased from Gibco (Grand Island, NY, USA). 1-[4-(Furo [2,3-b]quinolin-4-ylamino)phenyl] ethanone (CIL-102), 3-(4,5-dimethylthiazol-2-yl)-2,5-diphenyltetrazolium bromide (MTT), ROS scavenger (N-acetyl cysteine [NAC]), 2,7-dichlorodihydrofluorescein diacetate (H<sub>2</sub>DCFDA), dihydroethidium (DHE), ERK inhibitor (PD98059), c-Jun N-terminal kinase (JNK1/2) inhibitor (SP600125), p300/CBP inhibitor (C646), and mTOR inhibitor (rapamycin), were purchased from Sigma (St. Louis, MO, USA). Mouse monoclonal antibodies against cyclin A, cyclin D1, cyclin E, cyclin B1, histone H3 trimethylation at lysine 4 (H3K4me3), cytochrome *c* and  $\beta$ -actin, respectively, were purchased from Santa Cruz Biotechnology (Santa Cruz, CA, USA). Rabbit polyclonal antibodies against cdk1, ERK1/2<sup>Thr<sup>202</sup>Tyr<sup>204</sup></sup>, p70S6K<sup>Thr<sup>389</sup>Tyr<sup>182</sup></sup>, and JNK1/2<sup>Thr<sup>183</sup>Tyr<sup>185</sup></sup> mouse monoclonal PCNA, Cdk1, cyclin B, Bcl-2, p300/CBP, p50, GADD45, TNFR1 and TRAIL, cleavage caspase-3 and -9 antibodies, were purchased from Cell Signaling Technology (Beverly, MA, USA). SDS, NP-40, sodium deoxycholate, and protease inhibitor cocktails were purchased from Sigma (St Louis, MO, USA). The TdT-mediated dUTP Nick End Labeling (TUNEL) kits were purchased from Roche (Mannheim, Germany).

### 2.2. Cell culture

The human gastric cancer cell line AGS (CRL-1739) and TSGH 9201 were purchased from the American Type Culture Collection (ATCC). Cells were cultured in Dulbecco's modified Eagle's medium (DMEM) and supplemented with 10% fetal calf serum (Gibco), non-essential amino acids, 1 mM sodium pyruvate and 1% antibiotics (100 units/mL penicillin and 100  $\mu$ g/mL streptomycin). All experiments were performed in plastic tissue culture flasks, dishes, or in microplates (Nunc, Naperville, Denmark). Incubation was carried out at 37 °C in a humidified atmosphere of 5% CO<sub>2</sub> and 95% oxygen. Passage Number 1 of normal human colonic epithelial cells (HCoEpiC) was purchased from ScienCell Research Laboratories (Carlsbad, CA) and the cells were grown. Both cell types were maintained at 37 °C in a humidified 5% CO<sub>2</sub> incubator (Lee et al., 2017).

### 2.3. Cell growth and proliferation assay in gastric cancer cells

The MTT quantitative colorimetric assay is a method used for the determination of cell viability, as previously described. The cells were incubated with MTT (0.5 mg/mL) for 4 h. After the solubilization of the MTT-treated cells with isopropanol, the production of formazan was spectrophotometrically measured at 563 nm, which was directly

proportional to the number of viable cells (Huang et al., 2016).

#### 2.4. Apoptosis assay in gastric cancer cells

The morphological characteristics of the cells stained with 4',6-diamidino-2-phenylindole (DAPI) were observed under fluorescence microscopy. Firstly, the cells were fixed with 4% paraformaldehyde for 30 min at room temperature and were then permeabilized in 0.2% Triton X-100 in phosphate-buffered saline three times for 15 min. After PBS washing, the cells were incubated with 1 µg/mL of DAPI for 30 min. The percentage of the apoptotic nuclei in the field of the 200–300 cells was observed and scored. According to a previous report, a fluorescent microscope with a 340/380 nm excitation filter was used under 200 × magnification, (Lu et al., 2016).

Co-staining with Annexin V-FITC and propidium iodide (Biosource International, USA) was used to measure cell apoptosis, as described in a previous study. After staining, the cells were subjected to a FACS analysis (Attune NxT Flow Cytometer, Thermo Fisher Scientific Inc.) and the number of apoptotic cells (V+/PI-) were quantified and analyzed by using software. The data of the fluorescent intensity were represented as a percentage of the untreated control group, in three independent experiments.

#### 2.5. Protein extraction and immunoblot analysis in gastric cancer cells

The cells were lysed with a buffer comprising of 1% NP-40, 0.5% sodium deoxycholate, 0.1% sodium dodecyl sulfate (SDS) and a protease-inhibitor mixture (phenylmethylsulfonyl fluoride, aprotinin and sodium orthovanadate); the protein lysates were obtained, as described in a previous study. Following the SDS-polyacrylamide gel electrophoresis (PAGE) (12% running and 4% stacking), once it was transferred to the PVDF member, protein expression was detected by using specific antibodies in the Western-light chemiluminescent detection system (Bio-Rad, Hercules, CA, USA) and the quantitative assay (Fujifilm Image Gauge program), as previously described (Lu et al., 2016).

#### 2.6. Chromatin immunoprecipitation (ChIP) analysis in gastric cancer cells

We then examined the regulation of the JNK1/2 MAPK and mTOR/p300 pathways in CIL-102-mediated AGS cells, while cells were incubated for 2 h with the specific ROS scavenger NAC (1 mM), JNK inhibitor SP600125 (10 µM), and mTOR inhibitor Rapamycin (50 nM), as well as p300/CBP inhibitor C646 (10 µM) and solvent control (0.05% DMSO), and were then treated with CIL-102. AGS cells were incubated with 1% formaldehyde at room temperature to generate a DNA-protein cross-link and then, 10 min later, 125 mM glycine was added to the cells for 5 min. The cells were scraped into a sodium dodecyl sulfate (SDS) lysis buffer (50 mM Tris-HCl [pH 8.1], 1% SDS and 10 mM EDTA) and rotated with specific antibodies against the histone H3K4me3 and 2 µl of non-immunized rabbit IgG, which were kept overnight at 4 °C in the presence of protease inhibitors (1 µg/mL leupeptin, aprotinin and pepstatin A, 1 mM phenylmethylsulfonyl fluoride [PMSF]). After the elution was done with an elution buffer (50 mM Tris-HCl [pH 7.5], 1 mM EDTA, 1% SDS), the cross-linked immunoprecipitated complexes were reversed at a temperature of 65 °C and were incubated for at least 2 h. DNA fragments were purified using a ChIP DNA Clean & Concentrator Kit (Zymo), and a quantitative PCR analysis was then performed to amplify the promoter region of the TNFR1 and TRAIL genes, by using specific primers (Table 1) under the following conditions: 40 cycles of denaturation at 94 °C, primer annealing at 60 °C, and extension at 72 °C. Dissociation curves were generated after each PCR, to ensure that a single PCR product of the amplified appropriate length ran in the electrophoresis. In addition, the mean CT ± SE was calculated from an individual CT value, which was obtained from triplicate determinations at

**Table 1**

The specific primers.

<b>TRAIL</b>	
5'- TGCATGGATCCTGA GGGCAAGG -3'	
5'-TTGAACCTGCAACTGTCCTCC-3'	
<b>TNFR1</b>	
5'-GAT TGG GTT GGG GGC ACA -3'	
5'-ATT AAA GCA GAG AGG GGA GAG A -3'	

each stage. The normalized mean CT was estimated as ΔCT by subtracting the mean CT of the input from that of the individual region among the untreated control group and the drug treatment groups. Specific genes were calculated by using the ΔΔCt method [24]:  $2^{(-\Delta\Delta C_t)}$  [treatment/control], where  $\Delta\Delta C_t$  [treatment/control] = ( $\Delta C_t$  [treatment]) - ( $\Delta C_t$  [control]). The results were statistically analyzed by using the Student's paired *t*-test. A *P*-value of <0.05 was considered to be statistically significant (Lee et al., 2019).

#### 2.7. In vivo xenograft mouse model

The animal care and general protocols for performing animal experiments, as used in this study, were approved by the Institutional Animal Care and Use Committee of the Chang Gung Memorial Hospital, Chiayi, Animal Ethics Research Board (IACUC approval: 2017110202). Male BALB/c-nu nude mice, 4–6 weeks old (18–20 g), were purchased from the National Laboratory Animal Center located in Taiwan and were maintained under specific pathogen-free (SPF) conditions, with sterilized food and water. The AGS cells ( $10^6$  cells/0.2 mL) were injected subcutaneously into the flanks of 4–6-week-old female athymic BALB/c-nu mice. After the tumor inoculation, the mice were randomly divided into four groups (*n* = 8 per group). The control group animals were treated daily with 0.1 mL DMSO control group (0.25%; i.p.); the test animals were treated with CIL-102 at different concentrations, ranging from 1 to 5 mg/day, i.p. for 5 days. Tumor volumes were monitored and measured after every 4 days, using calipers. The calculation of tumor volumes was based on the following formula: length × width  $2 \times \pi/6$ . The body weight of the mice was measured every week to monitor the drug toxicity. After 18 days of drug treatment, the mice were euthanized and their tumors and organs, including the liver, lungs and kidneys, were collected. In addition, a pathology doctor examined the organs of each mouse, including the liver, lung, and kidney (Lu et al., 2016).

#### 2.8. Histochemistry and immunohistochemistry analysis

Tumor tissue sections were fixed in 4% formaldehyde and were then embedded in paraffin blocks. After staining with hematoxylin and eosin, these tissue slides were mounted for microscopic examination. For the immunohistochemical analysis, 5-µm-thick sections of each subcutaneous tumor specimen were incubated with monoclonal anti-TNFR1 and TRAIL antibodies (Santa Cruz, CA, USA) overnight, at 4 °C after blocking, and they were then incubated with 1:100 diluted biotinylated horse anti-mouse IgG for 1 h. After the PBS wash, the tissue sections were reacted with a 1:100 diluted avidin-biotin peroxidase mixture (Vectastain Universal Elite ABC Kit) for 30 min. Following a thorough PBS wash, these slides were counterstained with hematoxylin, dehydrated and mounted for microscopic examination. The digital images were captured by using a digital camera (Canon A640), and the positive area and Optical Density (OD) of the immunoreactive cells (brown) were analyzed in three randomly-selected microscopic fields (200 × magnification) for each slide. In accordance with previous reports, the IHC index was defined as having an average integral optical density (AIOD; positive area × OD/total area) (Kuo et al., 2016).

#### 2.9. Statistical analysis

All data, expressed as the mean ± standard deviation, were

compared between the groups, using the Student's t-test, or one-way Analysis of Variance (ANOVA), with Tukey's Multiple Comparison Test. The statistically-significant difference between the values was set at  $P < 0.05$  (Lee et al., 2019).

### 3. Results

#### 3.1. Induction of cell apoptosis by CIL-102 in human gastric cancer cells

We aimed to determine whether CIL-102 treatment induced any cell toxicity in gastric cancer cells. MTT assay revealed that the cell viability of TSGH-9201 and AGS cells were dose-dependently decreased in 24 h. The CIL-102 treatment was compared with the untreated cells at concentrations of 1, 2 and 5  $\mu\text{M}$  (Fig. 1A). In contrast, no effect was seen on the viability of normal epithelial HCoEpiC cells under CIL-102 treatment (data not shown). Furthermore, treatment with CIL-102 at 1 and 2  $\mu\text{M}$  concentrations induced the early apoptotic chromatin condensation that was shown by DAPI staining in AGS and TSGH-9201 cells (Fig. 1B).

Moreover, by using a flow cytometry analysis for Annexin-V and PI, our results revealed that an increased percentage of annexin V-positive cells was found in all untreated and CIL-102-treated AGS cells in a dose-dependent manner, and shown as 7%, 26%, and 29%. (Fig. 2A). The increased intracellular ROS through the ROS production by 1.3 and 1.6-fold (Fig. 2B), compared to the cells that did not receive the CIL-102 treatment control. Fluo-3 fluorescence staining was used to measure the rate of intracellular  $\text{Ca}^{2+}$  release, as an index of the mitochondria-mediated cell apoptosis in AGS cells (Honorio-Franca et al., 2016). Our data showed that AGS cells presented with a low spontaneous intracellular  $\text{Ca}^{2+}$  release, under normal conditions. Under CIL-102 treatment, the intracellular  $\text{Ca}^{2+}$  level of these AGS cells was increased to 1.3 and 1.6-fold (Fig. 2C). On the other hand, a higher portion of AGS cells treated with CIL-102 was arrested in the G2/M stage of the cell cycle (G2/M arrest), as 32%, 75% and 78% (Fig. 2D). Overall, our results have demonstrated the functional role of CIL-102 treatment in gastric cancer cells, including the induction of cell apoptosis, the blockage of cell proliferation and the upregulation of ROS production.

#### 3.2. Growth inhibition of gastric cancer cells by CIL-102 in a nude mouse xenograft model

An in vivo nude mouse model of a gastric cancer cell xenograft was performed to further verify the in vitro findings on the anti-cancer effects of CIL-102. Our results showed that the tumor volume, body weight and tumor weight of the AGS xenograft in nude mice decreased after the CIL-102 treatment via a dose-dependent manner (Fig. 3,  $*p < 0.05$ ). Consistent with the in vitro findings, the CIL-102 treatment showed inhibitory effects on the cell growth of gastric cancer in vivo. We further detected the expression of PCNA (a marker for cell proliferation), cdk1 (a key regulator for the cell cycle G2/M), TNFR1 (a marker for extrinsic cell apoptosis) and TRAIL (a marker for extrinsic cell apoptosis) at protein level in these animals, by using immunohistochemistry staining (Fig. 4). The reduction of PCNA and cdk1 expression were significantly decreased to 5% and 5%, as well as 25% and 10% in the animals after CIL-102 treatments (1 and 5 mg/kg doses of CIL-102), compared with the control group ( $p < 0.05$ ) (Fig. 4). In contrast, the CIL-102 treatment significantly increased the protein levels of TNFR1 and TRAIL to 45% and 50%, as well as 45% and 60%, compared with the control group ( $p < 0.05$ ) (Fig. 4). In addition, the TUNEL assay revealed the induction of cell apoptosis of the AGS xenograft to 50% and 55% by the using the CIL-102 treatment in these nude mice (Fig. 4). Similar to the in vitro data, the CIL-102 treatment showed impressive anti-cancer effects on gastric cancer cell xenografts. In addition, no signs of toxicity were observed in the body weight (Fig. 3) and microscopic examination of individual organs (data not shown) in all nude mice.

#### 3.3. Regulation of the intrinsic signals by CIL-102 in AGS cells

A Western blot was performed to measure the protein levels of Bcl-2, the cleavage of caspase 9 and caspase 3, TRAIL and TNFR1, which are classically considered as the hallmarks for representing apoptotic cell death (Ivanova et al., 2019) in AGS cells treated with or without CIL-102. Our results showed that the active form of caspase-3 and -9 was increased in the cells after the CIL-102 treatment (Fig. 5A). Furthermore, their upstream proteins, TRAIL and FasL, were also upregulated by the CIL-102 treatment (Fig. 5A). In addition, the CIL-102 treatment decreased the levels of anti-apoptotic Bcl-2 and the G2/M checkpoint CDK1/Cyclin B protein in AGS cells (Fig. 5A). Moreover, the phosphorylation of JNK1/2 Thr<sup>183</sup>/Tyr<sup>185</sup>, for 6 h, 12 h and 24 h, was increased in CIL-102-treated AGS cells in a time-dependent manner (Fig. 5B). The activation of p70S6K Thr<sup>389</sup> kinases by CIL-102 was also observed at an early time point and markedly sustained for at least 24 h (Fig. 5B). Similarly, the NF $\kappa$ B p50/p300/CBP pathway was constitutively activated for a certain time period after the CIL-102 treatment (Fig. 5B). Therefore, our data showed that a novel biological property of CIL-102 is involved in extrinsic cell apoptosis and cell cycle pathways to regulate the multiple-protein network.

#### 3.4. Regulatory mechanism of histone H3 methylation by CIL-102

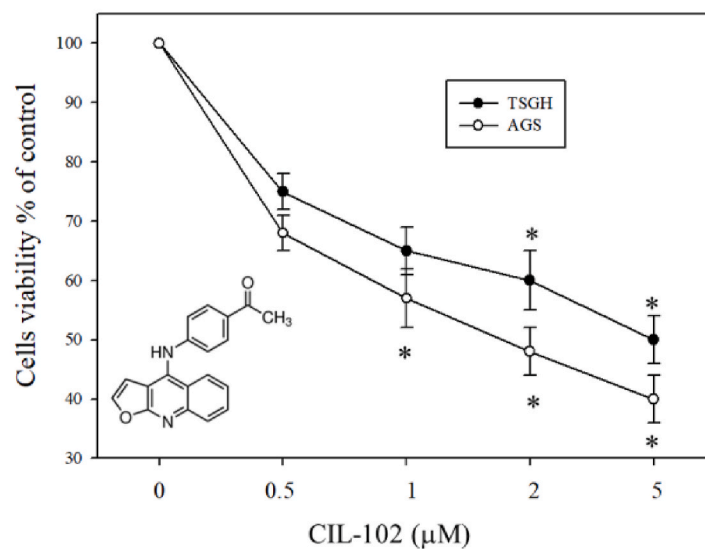
Some evidence has demonstrated that the trimethylation of histone H3 is a key event that upregulates TNFR1 and TRAIL expression during cell apoptosis (Elmallah and Micheau, 2019; Ghare et al., 2014; Savva et al., 2016). Thus, we determined whether the effect of CIL-102 treatment can regulate the histone H3 trimethylation (H3K4me3) binding activities of the TNFR1 and TRAIL promoter regions. The results from the ChIP assay showed that the trimethylation of histone H3 on the promoter region of both TNFR1 and TRAIL genes was increased in the cells that had undergone CIL-102 treatment (Fig. 6). Later, we also determined that signaling molecules were involved in this epigenetic modification (Knight et al., 2001; Shilatifard, 2008). Our data revealed that the CIL-102-mediated histone H3 trimethylation was reversed by the inhibitors, and was associated with ROS production and multiple-protein kinase, such as JNK, p70S6K and p300/CBP (Fig. 6). These results all suggest that the novel mechanism of CIL-102, which plays a significant role in stimulating the transcriptional activation of the histone H3K4me3 binding of the TNFR1 and TRAIL promoters via ROS-derived and JNK/mTOR/p300 pathways, are involved in gastric cancer apoptosis.

### 4. Discussion

Many drugs have been tested by conducting animal experiments and clinical trials for the treatment of gastric cancer (Tan et al., 2018). However, gastric cancer remains one of the most common causes of cancer-related death worldwide, especially in East-Asian countries, such as China and Japan (Herszenyi and Tulassay, 2010; Ogino et al., 2019). Recent studies have reported that some dietary foods can be considered as a potential source of bioactive safe compounds, due to their chemo-preventive properties related to cancer formation (Link et al., 2010). The results of this study have demonstrated the novel role of CIL-102 for inhibiting the viability of the AGS and TSGH 9201 cells, as well as in an in vivo xenograft mouse model (Figs. 1–4). Dietary-food-derived bioactive compounds have displayed strong anti-cancer effects, including the regulation of cell motility and adhesion, the inhibition of cancer growth and the induction of tumor apoptosis via ROS-mediated JNK/mTOR/p300 pathways, and have caused damage to DNA and apoptotic signals (Kuo et al., 2017; Li-Weber, 2009; Raman et al., 2007; Zhu et al., 2007). One of the functions of ROS (a class of oxygen-containing and associated active species) is to facilitate the activation of tyrosine kinases and tyrosine phosphatases, which results in the induction of cellular apoptosis (Loo,



A



B

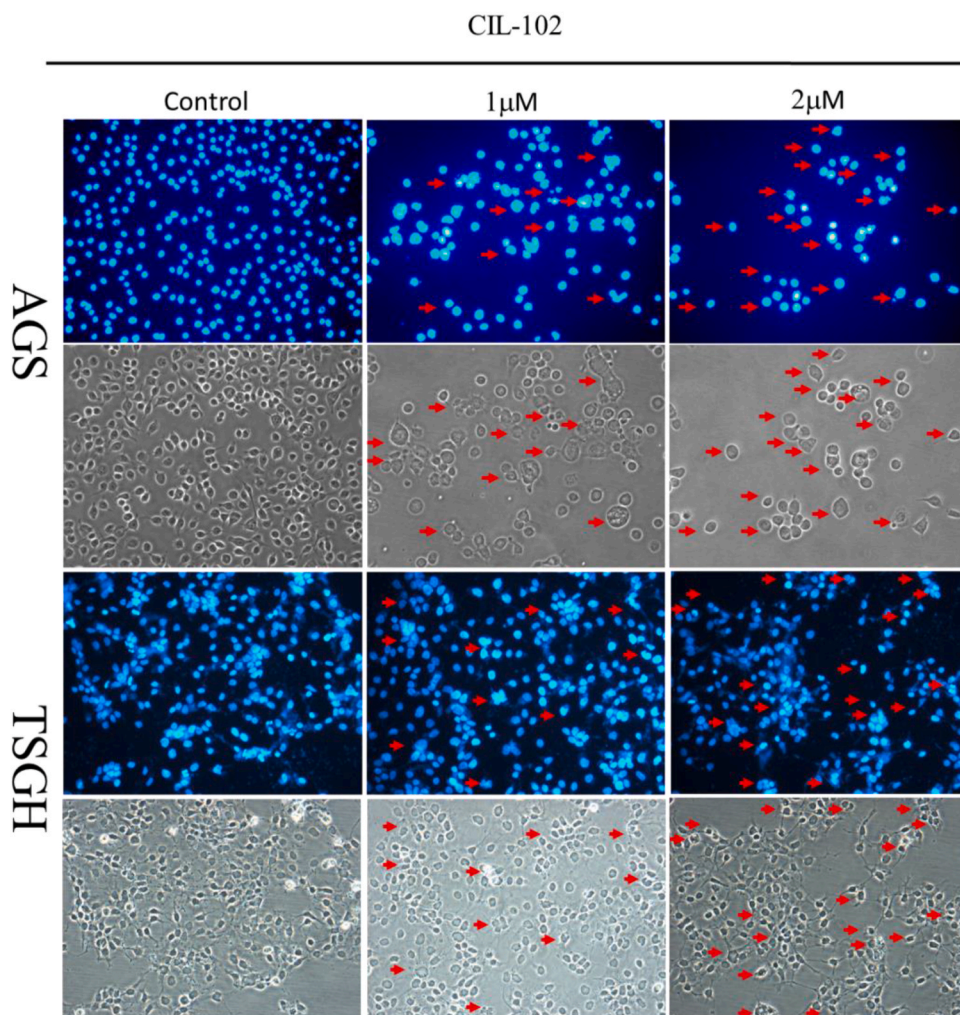


**Fig. 1.** CIL-102 decreases cell viability in gastric cancer cell lines (A). The cell viability of AGS and TSGH-9201 cells treated with either 0.1% DMSO (as control) or CIL-102 (1–2 μM) for 24 h was measured by the MTT assay. (B) After 24 h of vehicle or CIL-102 treatment, the apoptotic cells (changes in nuclei) were measured by DAPI staining in these AGS and TSGH-9201 cells under fluorescence microscopy. The data are expressed as the mean  $\pm$  SD obtained from three independent experiments. They are presented as the mean of three repeats from one independent experiment. \* $P < 0.05$ .



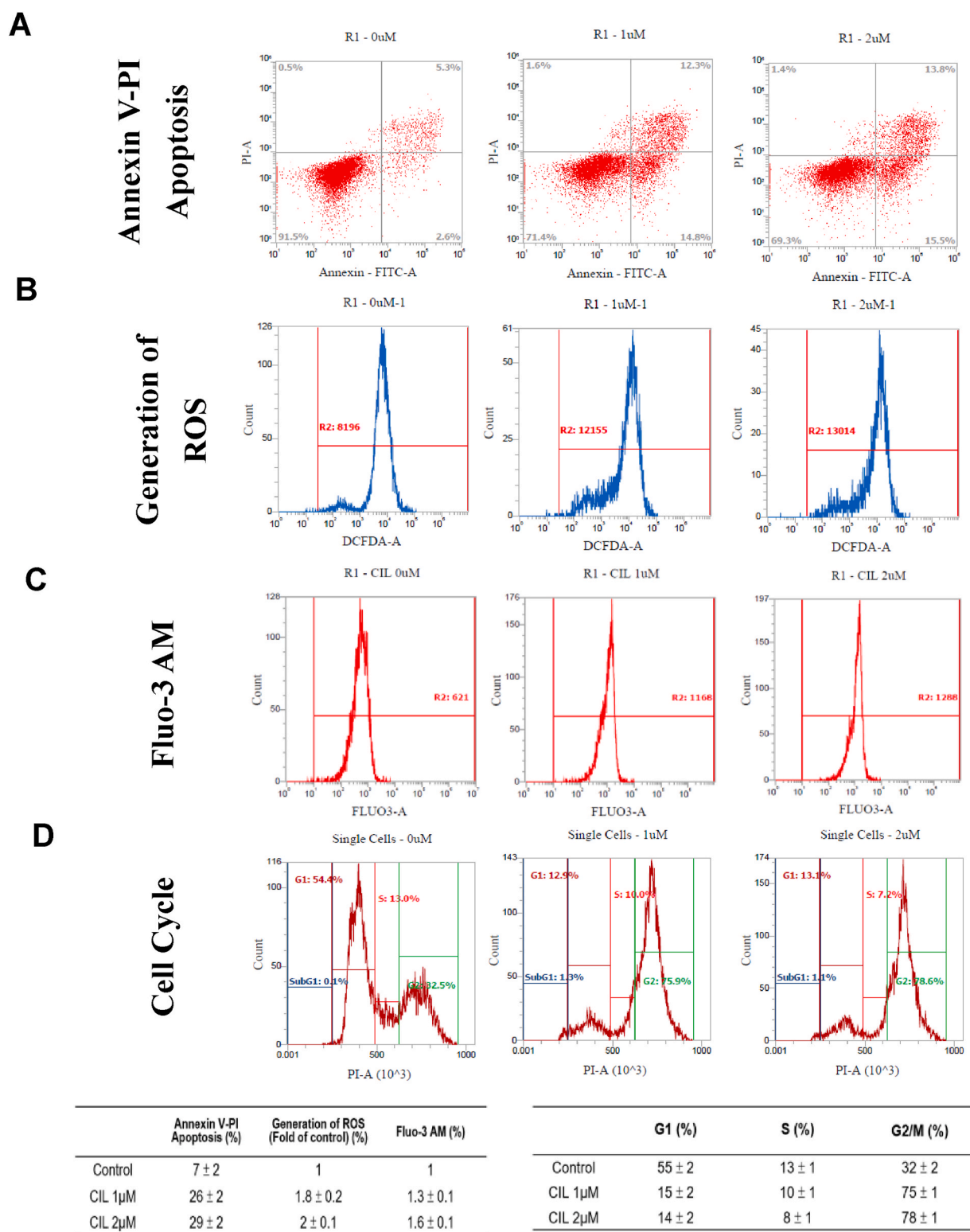


**Fig. 2.** CIL-102 induces cell apoptosis, G2 arrest and ROS production in AGS cells. (A) After 24 h of CIL-102 treatment, the AGS cells were stained with FITC-conjugated Annexin-V and PI for a flow cytometry analysis, as described in the Materials and Methods section. After receiving individual treatment, the percentage of the apoptotic cells is shown in each frame, as indicated. (B) After treatment with CIL-102 for 24 h, the AGS cells were fixed and stained with propidium iodide for analyzing the status of the cell cycle (DNA content: G1, S and G2/M) by flow cytometry (FACS). The percentage of the cell number involved in each cell cycle phase (G1, S, and G2/M) during treatment was calculated and expressed in the panels (C). The intracellular ROS of AGS cells treated with CIL-102 for 24 h was measured by using a FACS analysis, as described in the Materials and Methods section. Representative histograms of typical H2DCFDA profiles are shown. The production of ROS was expressed as the fold of the control group. (D) The CIL-102-treated AGS cells kept for 24 h were stained with Fluo-4 AM (for what kind propose to run this experiment) for a flow cytometry analysis. Data are presented, based on three independent experiments, as mean ± S.D.

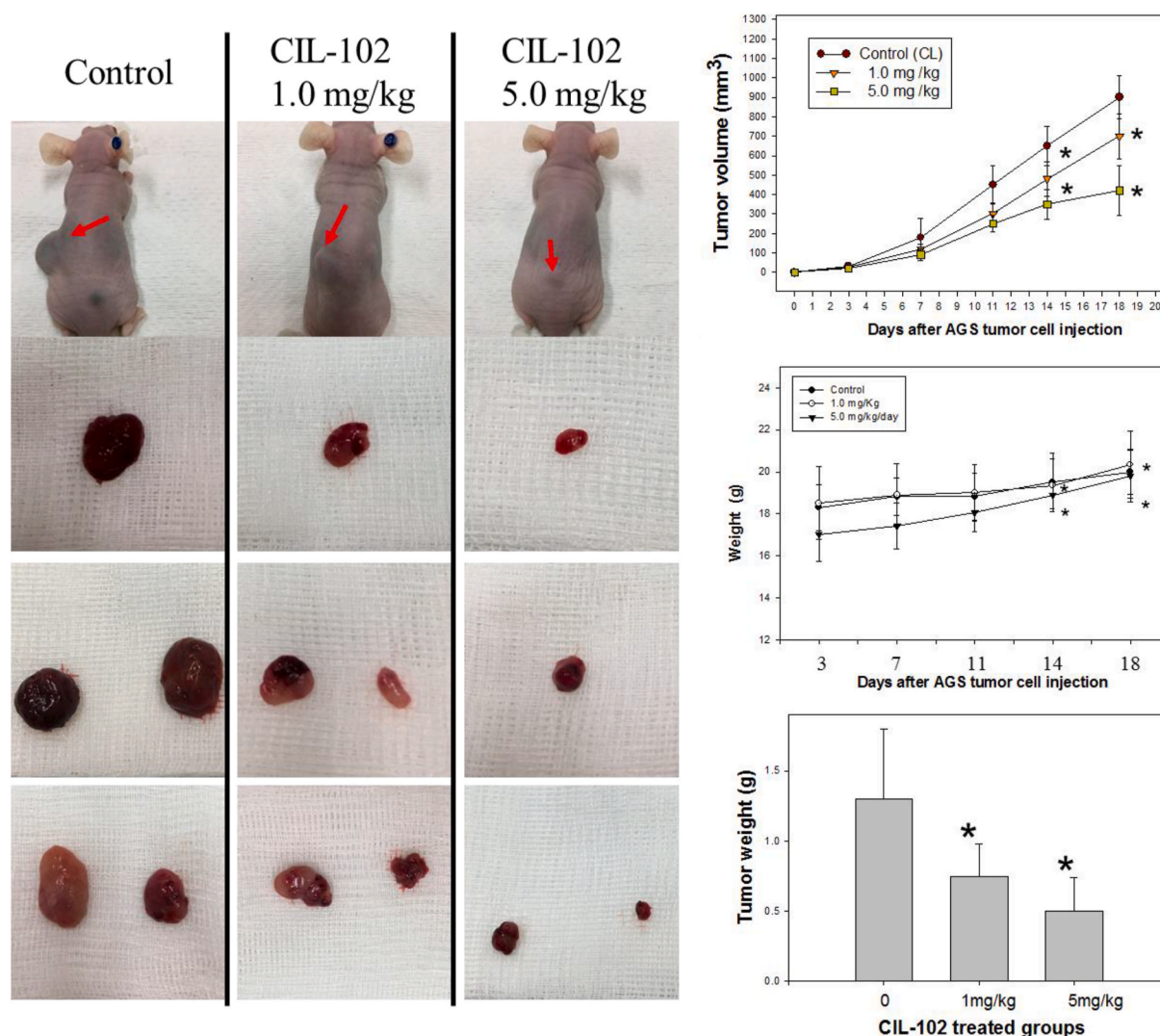


**Fig. 3.** CIL-102 inhibits the growth of gastric cancer cells in the in vivo xenograft mouse model. Five nude mice were injected subcutaneously with  $1 \times 10^7$  cells/mouse for each of the indicated AGS cell lines. Upper panels: the tumor volume of these animals, with the indicated treatments, was measured, at intervals of 0, 3, 7, 11, 14 and 18d, after the tumor cells were implanted. Bottom panels: the results show the images of nude mice implanted with gastric cancer cells, with or without CIL-102 treatment, the tumor volume, body weight and tumor weight of the quantitative data. Data were expressed as mean  $\pm$  S.D. ( $n = 6$ /group). \* $P < 0.05$ , compared with the control group.

2003). On the other hand, ROS also alters intracellular  $\text{Ca}^{2+}$  influx in human cells, causing cell damage via the activation of cell death pathways. Some signaling molecules, including JNK, mTOR and p300/CBP, have been reported to trigger the antioxidant of phytochemicals (Lee et al., 2019).

Our results have also indicated that treatment with CIL-102 can increase the production of ROS and the level of intracellular  $\text{Ca}^{2+}$  release, and that it can cause the arrest of the cell cycle at the G2/M stage in the gastric cancer cells (Fig. 2). Subsequently, we also observed the time-dependent induction of apoptosis in the AGS and TSGH 9201 under the CIL-102 treatment. Our previous study has highlighted that treatment with the 9-anilino-furoquinoline derivative in colorectal cancer also exhibited similar outcomes, as shown after CIL-102 treatment, as the activation of ROS-mediated JNK1/2, NF $\kappa$ B p50, p300/CBP signaling molecules and p21 and GADD45 expression occurred to inhibit the formation of human colorectal cancer cells (Huang et al., 2017). Although the ERK1/2, MAPK, and Cdc25c pathways, which lead to cdk1/cyclin B inactivation and increase cell cycle arrest, are considered as the upstream signals associated with the ROS accumulation (Lee et al., 2013; Lu et al., 2016; Rajendran et al., 2011), the details of the signaling network involving CIL-102 still remain unclear. At the same

time, it is still an open question as to whether different subtypes of bioactive CIL-102 share the same anti-cancer properties or not. A consistently-significant reduction of the tumor volume (tumor size and weight) of the AGS xenograft was found in nude mice, by using intraperitoneal injections with CIL-102 (1 or 5 mg/kg/day) (Fig. 3). Furthermore, the level of PCNA and CDK1 in the tumor region of the AGS xenograft in nude mice was decreased, after intraperitoneal injections with CIL-102. On the contrary, intraperitoneal injections with CIL-102 increased the expression of TNFR1 and TRAIL (Fig. 4). Moreover, CIL-102 induced gastric cancer cell apoptosis via both death-receptor-mediated extrinsic apoptosis (caspase 9, caspase 3, TNFR1 and TRAIL) and the mitochondria-mediated apoptotic pathway (Bcl-2) (Fig. 5A). The assembly of cell-cycle-related protein (decreased CDK1, Cyclin B activation) and intracellular calcium was also altered by CIL-102 treatment during cell death. In addition, there was an increase in the cellular levels of the phospho-JNK MAPK/p70S6K/p300 pathways, TNFR1 and TRAIL in the CIL-102-induced apoptosis (Fig. 5B).

Several studies have demonstrated that many natural phytochemicals may cause aberrant epigenetic alterations, in order to trigger sustainable DNA damage and cell apoptosis in vitro and in vivo (Rajendran et al., 2011). Modified histones, in turn, may alter the process of



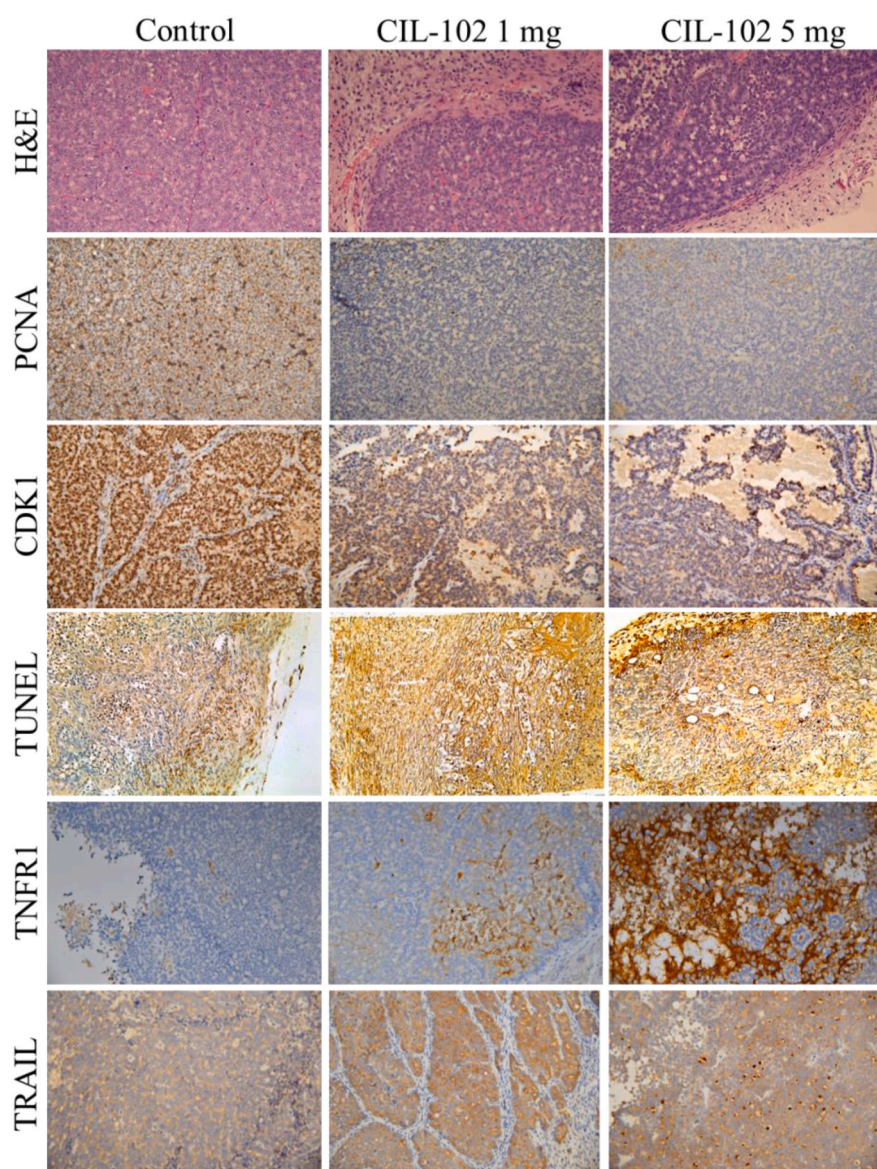
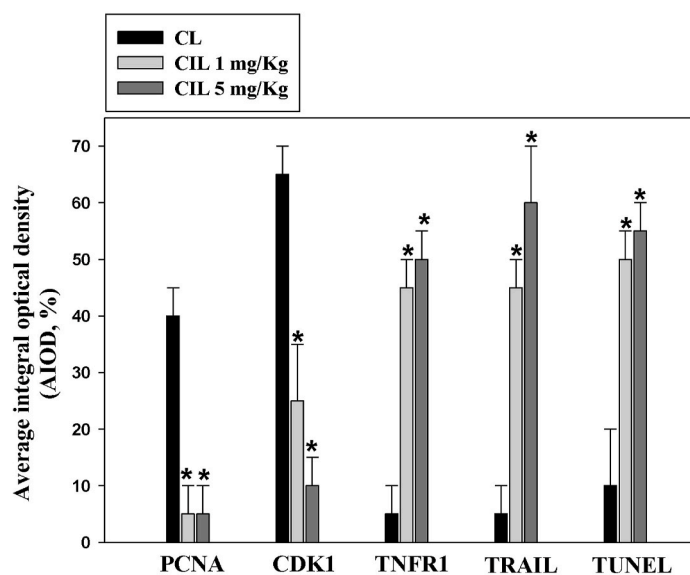
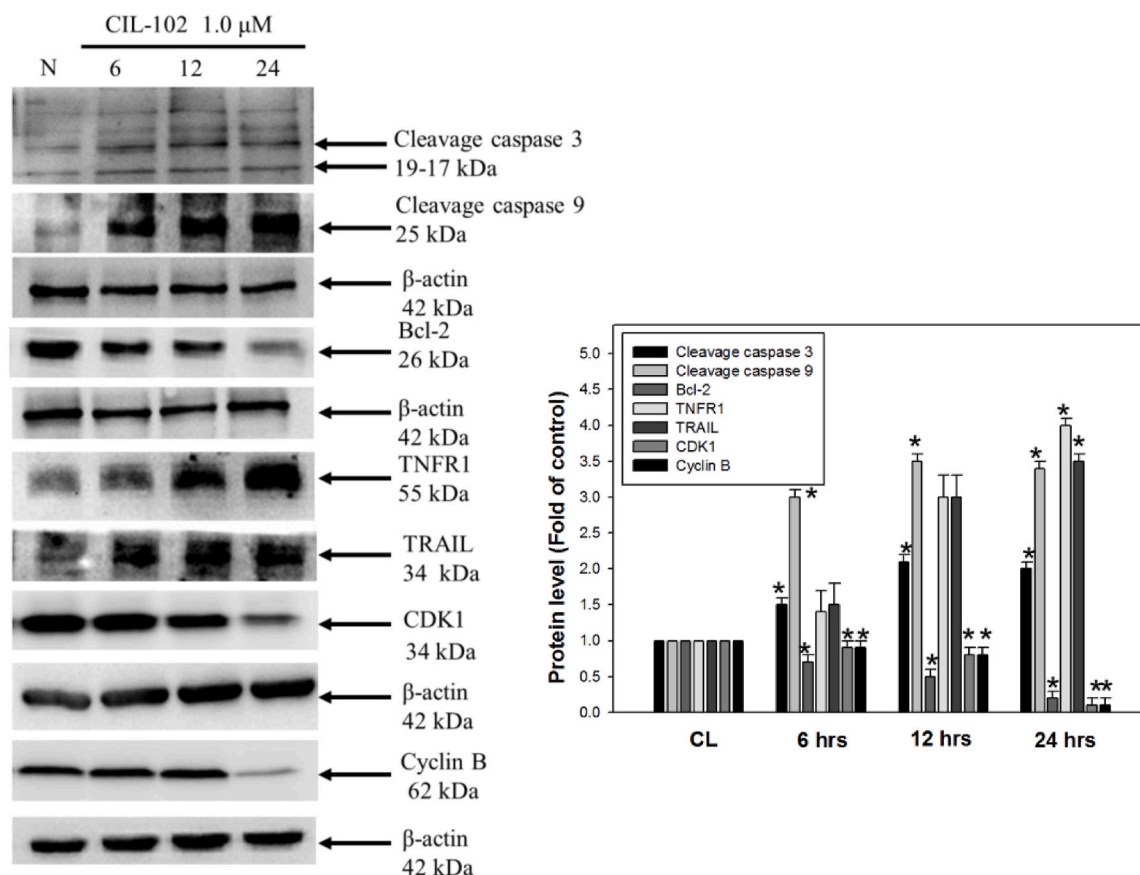


**Fig. 4.** CIL-102 alters the level of proliferative and apoptotic proteins associated with gastric cancer cells in the in vivo xenograft mouse model. The tumors of the nude mice, with the indicated treatment, were harvested and prepared for H&E staining (1st row, upper panel), the measurement of the protein levels of PCNA (2nd row, upper panel), CDK1 (3rd row, upper panel), TNFR1 (5th row, upper panel) and TRAIL (6th row, upper panel), by using an immunohistochemical analysis, and the detection of cell apoptosis, by using the TUNEL stain (4th row, upper panel). Bottom panel: Quantitative immunohistochemical proteins, PCNA, CDK1, TNFR1, TRAIL, and TUNEL stain, were evaluated by calculating the Average of Integrated Optical Density (AIOD). Multiple tumor fields were evaluated per treatment group. The positive stained area was evaluated from three randomly-selected observational fields of each section. The data were expressed as mean  $\pm$  SD. (n = 6/group). \*P < 0.05, compared with the control group, at a magnification of  $\times 200$ .



A



B

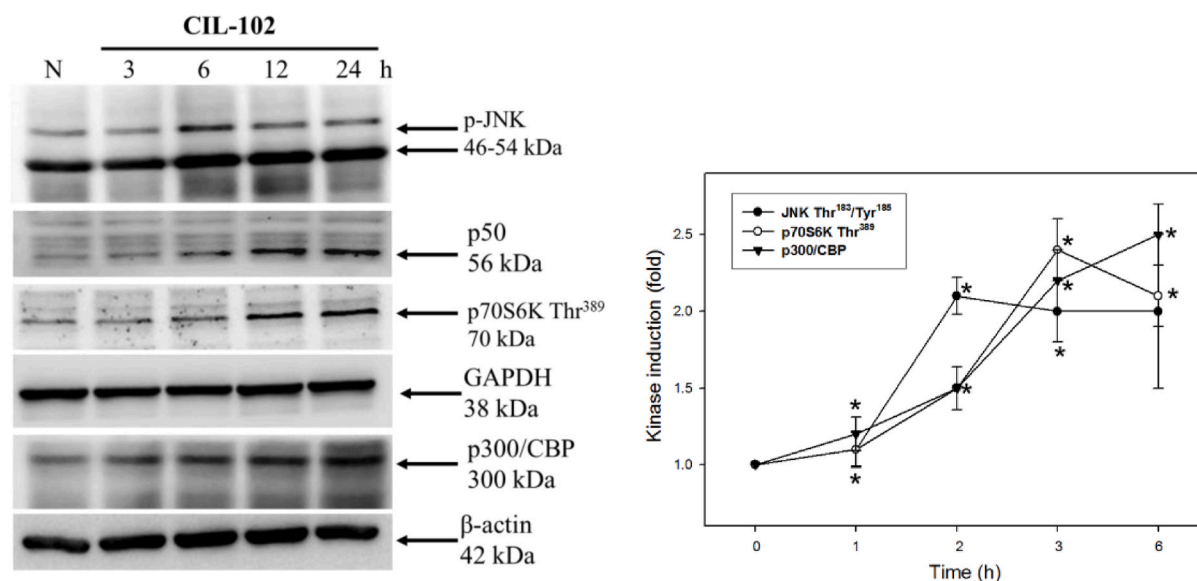


**Fig. 5.** The effect of CIL-102 on the protein level of the molecules-related to cell death, the cell cycle and JNK/p70S6K/p300 pathways in AGS cell lines. The protein level of CIL-102 (1 μM)-treated AGS cell for 0–24 h were detected by Western blot, including Bcl-2, cleavage caspase 9, cleavage caspase 3, TNFR1, TRAIL and CDK1, Cyclin B (A) and JNK, p70S6K and p300 (B). Here, β-actin served as an internal control. Protein levels were quantified by a densitometric analysis, with the control being set at 100%; β-actin was used for equal loading as the control. Data are presented as the means ± SD of three independent experiments. \*P < 0.05, when compared with the untreated control group.

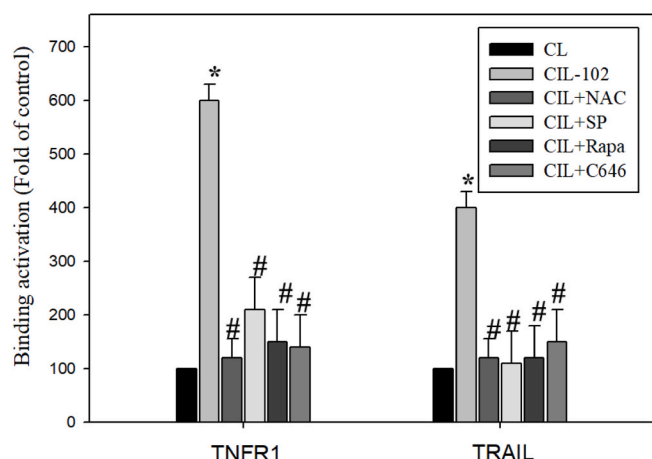


**Fig. 6.** The histone H3 trimethylation of the TNFR1 and TRAIL genes by CIL-102 via multiple signaling. The status of histone H3 trimethylation at lysine 4 (H3K4me3) on TNFR1 and TRAIL promoters in the AGS cells, with or without CIL-102 (1  $\mu$ M) treatment, after 24-h, in the presence of several chemical or kinase inhibitors (NAC for ROS scavenger, SP600125 for JNK inhibitor, Rapa for p70S6K inhibitor, or C646 for the P300 inhibitor), were measured by a chromatin immunoprecipitation (ChIP) assay. The amount of immunoprecipitated DNA in each sample is represented as a normalized signal to the negative control ChIP. The normalized mean CT was estimated as  $\Delta$ CT by subtracting the mean CT of the input from that of the individual region among the untreated control group. The effect of the CIL-102 treatment on specific genes was calculated by using the  $\Delta\Delta$ CT method. The data are presented as the mean  $\pm$  SD of three independent experiments. # $P < 0.01$ , is compared to the control group; \* $P < 0.01$ , is compared to the CIL-102 -treated group.

transcription by directly affecting the chromatin structures; for example, the two modifications that are closely correlated with gene activation are H3 acetylation and H3K4 methylation (Kumar et al., 2019; Patel and Wang, 2013). The aberrant methylation of histone 3 lysine 4 (H3K4), a critical feature of the active promoter state, occurs in human cancer cells (Kumar et al., 2019). For instance, the post-translational modification of histone H3 and H4 can potentially inhibit tumor necrosis and factor-related apoptosis-inducing ligand (TRAIL)-induced apoptosis (Ghare et al., 2014). The association of the induction of TNFR1 and TRAIL genes with histone H3 methylation is regulated by protein kinases, such as JNK, mTOR and P300/CBP (Alam et al., 2015; Elmallah and Micheau, 2019; Savva et al., 2016; Zhang et al., 2003). Similarly, our data demonstrate that CIL-102 treatment altered the transcriptional activation of the histone H3 methylation (H3K4me3) of the TNFR1 and TRAIL promoters, via multiple signaling pathways (ROS and JNK/mTOR/p300 CBP signaling, Fig. 6). Oxidative ROS influences histone modification in various ways and thus affects a number of chromatin-regulated processes (Kreuzet et al., 2016). Future research needs to focus on directly demonstrating how CIL-102-induced chromatin changes impact on gastric cancer cells apoptosis, and the molecular mechanism of CIL-102 induction associated with ROS, as the second messenger, by H3K4 methylation, needs to be investigated. In fact, many natural phytochemicals (polyphenols, isothiocyanates, epigallocatechin-3-gallate (EGCG), curcumin, resveratrol, sulforaphane, isoflavones, quercetin, genistein, caffeine and anacardic acid) have shown that they are capable of undergoing epigenetic modification (Rosato et al., 2003; Spangle et al., 2016). Our results may establish an interaction network between ROS and JNK/mTOR/p300 CBP that causes a synergistic function in H3K4 methylation and transcription activation, and overall, it provides an insight into the underlying mechanisms. Additional studies are still needed to elucidate the action mechanisms of these natural phytochemicals, including CIL-102, that are associated with these epigenetic modifications, by either modulating histone methyltransferases (HMTs) or demethylases (HDMs), and the

linkage between their epigenetic modifications to demonstrate the anti-cancer effects.

In conclusion, this study demonstrated the novel possible usage of CIL-102 in cancer therapy for human gastric cancer and its underlying mechanisms. Our data have shown that the modulation of histone modification (H3K4me3) of the binding TNFR1 and TRAIL promoters by CIL-102 is a key event that triggers the cell death of gastric cancer via activating the both the ROS-derived and JNK/mTOR/p300 CBP pathways (Fig. 7). Our findings associated with CIL-102 treatment may be applied to different types of cancer therapy.

#### Authors' contributions

C.T. Provision of study material, collection and assembly of data and histopathological evaluation and manuscript writing, S.-Y.T. and K.-C.L. Design, collection, assembly of data, K.-F.L. Conception, histopathological evaluation. W.-S.H., C.-H.S. and C.-Y.H. Provision of study material or animals, M.-C.H. Provision of study material, collection, and assembly of data, J.-M.S. Administrative support, collection, and assembly of data (flow cytometry), H-CK Conception and design, financial support, administrative support, manuscript writing, final approval of manuscript. All authors read and approved the final manuscript.

#### Availability of data and materials

All relevant data are within the paper. The raw data supporting the conclusions of this manuscript will be made available by the authors, without undue reservation, to any qualified researcher.

#### Consent for publication

Not applicable.

#### Ethics approval and consent to participate

Animal care and the general protocols for animal use were approved

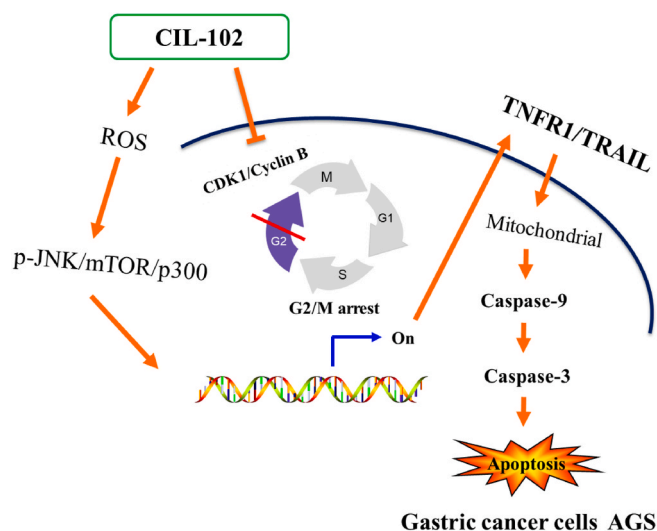


**Fig. 7.** A schematic illustration of the molecular mechanism underlying CIL-102-induced cell apoptosis, ROS production and the G2/M arrest of gastric cancer cells. Through multiple signaling pathways and ROS, CIL-102 treatment modulates histone H3 trimethylation at the promoter region of death receptors of TNFR1 and TRAIL results in the elevation of their protein level. Subsequently, the activation of TNFR1 and TRAIL by CIL-102 is critical for an apoptotic pathway to either activate or downregulate caspase-3 and 9, or to inhibit anti-apoptotic Bcl-2 protein. On the other hand, the downregulation of CDK1/cyclin B by the CIL-102 treatment may lead to the cell cycle G2/M arrest of AGS cells.



by the Institutional Animal Care and Use Committee of Chang Gung Memorial Hospital, Chiayi, Animal Ethics Research Board (IACUC approval: 2017110202). All procedures and the reporting thereof comply with the Institutional Animal Care and Use Committee (IACUC) guidelines.

## Declaration of competing interest

The authors declare that they have no known competing financial interests or personal relationships that could have appeared to influence the work reported in this paper.

## Acknowledgments

The Funding for this study was provided in part by research grants from the Chang Gung Memorial Hospital, Chiayi, Taiwan. This study was supported by grants BMRPD42, CLRPG8G0591, CMRPF6H0011, CMRPF6H0012, CMRPF6H0013, CMRPF6J0081, CMRPF6K0071 from Chang Gung Memorial Hospital, Chiayi, Taiwan, and Chang Gung University of Science and Technology, Chia-Yi Campus, Taiwan, and by the Ministry of Science and Technology, Taiwan (MOST 107-2320-B-255-001-MY3 and MOST 108-2622-B-255-001-CC3). The authors thank Dr. Chun-Hsien Chu (Institute of Molecular Medicine, College of Medicine, National Cheng Kung University) for the assistance with scientific consulting and manuscript editing. We thank the "Tissue Bank, Chang Gung Memorial Hospital, Chiayi and Laboratory Animal Center, Chang Gung Memorial Hospital, Chiayi, Taiwan" for their technical services.







## References

- Alam, H., Gu, B., Lee, M.G., 2015. Histone methylation modifiers in cellular signaling pathways. *Cell. Mol. Life Sci.* 72, 4577–4592.
- Balakrishnan, M., George, R., Sharma, A., Graham, D.Y., 2017. Changing trends in stomach cancer throughout the world. *Curr. Gastroenterol. Rep.* 19, 36.
- Chen, F.P., Chien, M.H., 2014. Phytoestrogens induce apoptosis through a mitochondria/caspase pathway in human breast cancer cells. *Climacteric* 17, 385–392.
- Chen, I.L., Chen, Y.L., Tzeng, C.C., 2003. An efficient synthesis of antitumor 4-anilino-furo [2,3-b]quinoline derivatives. *Chin. Pharmaceut. J.* 55, 49–53.
- Chen, Y.L., Chen, I.L., Wang, T.C., Han, C.H., Tzeng, C.C., 2005. Synthesis and anticancer evaluation of certain 4-anilino-furo[2,3-b]quinoline and 4-anilino-furo[3,2-c]quinoline derivatives. *Eur. J. Med. Chem.* 40, 928–934.
- Cheng, Y., He, C., Wang, M., Ma, X., Mo, F., Yang, S., Han, J., Wei, X., 2019. Targeting epigenetic regulators for cancer therapy: mechanisms and advances in clinical trials. *Signal Transduct Target Ther* 4, 62.
- Elmallah, M.I.Y., Micheau, O., 2019. Epigenetic regulation of TRAIL signaling: implication for cancer therapy. *Cancers* 11.
- Feitelson, M.A., Arzumanyan, A., Kulathinal, R.J., Blain, S.W., Holcombe, R.F., Mahajna, J., Marino, M., Martinez-Chantar, M.L., Nawroth, R., Sanchez-Garcia, I., Sharma, D., Saxena, N.K., Singh, N., Vlachostergios, P.J., Guo, S., Honoki, K., Fujii, H., Georgakilas, A.G., Bilsland, A., Amedei, A., Nicolai, E., Amin, A., Ashraf, S., Boosani, C.S., Guha, G., Ciriolo, M.R., Aquilano, K., Chen, S., Mohammed, S.I., Azmi, A.S., Bhakta, D., Halicka, D., Keith, W.N., Nowsheen, S., 2015. Sustained proliferation in cancer: mechanisms and novel therapeutic targets. *Semin. Canc. Biol.* 35 (Suppl. 1), S25–S54.
- Ghare, S.S., Joshi-Barve, S., Moghe, A., Patil, M., Barker, D.F., Gobejishvili, L., Brock, G. N., Cave, M., McClain, C.J., Barve, S.S., 2014. Coordinated histone H3 methylation and acetylation regulate physiologic and pathologic fas ligand gene expression in human CD4+ T cells. *J. Immunol.* 193, 412–421.
- Hanahan, D., Weinberg, R.A., 2000. The hallmarks of cancer. *Cell* 100, 57–70.
- Herszenyi, L., Tulassay, Z., 2010. Epidemiology of gastrointestinal and liver tumors. *Eur. Rev. Med. Pharmacol. Sci.* 14, 249–258.
- Honorio-Franca, A.C., Nunes, G.T., Fagundes, D.L., de Marchi, P.G., Fernandes, R.T., Franca, J.L., Franca-Botelho Ado, C., Moraes, L.C., Varotti Fde, P., Franca, E.L., 2016. Intracellular calcium is a target of modulation of apoptosis in MCF-7 cells in the presence of IgA adsorbed to polyethylene glycol. *OncoTargets Ther.* 9, 617–626.
- Hsu, F.T., Chiang, I.T., Wang, W.S., 2020. Induction of apoptosis through extrinsic/intrinsic pathways and suppression of ERK/NF-kappaB signalling participate in anti-glioblastoma of imipramine. *J. Cell Mol. Med.* 24, 3982–4000.
- Huang, W.S., Hsieh, M.C., Huang, C.Y., Kuo, Y.H., Tung, S.Y., Shen, C.H., Hsieh, Y.Y., Teng, C.C., Lee, K.F., Chen, T.C., Lee, K.C., Kuo, H.C., 2016. The association of CXC receptor 4 mediated signaling pathway with oxaliplatin-resistant human colorectal cancer cells. *PLoS One* 11, e0159927.
- Huang, W.S., Kuo, Y.H., Kuo, H.C., Hsieh, M.C., Huang, C.Y., Lee, K.C., Lee, K.F., Shen, C. H., Tung, S.Y., Teng, C.C., 2017. CIL-102-Induced cell cycle arrest and apoptosis in colorectal cancer cells via upregulation of p21 and GADD45. *PLoS One* 12, e0168989.
- Huang, Y.T., Huang, D.M., Guh, J.H., Chen, I.L., Tzeng, C.C., Teng, C.M., 2005. CIL-102 interacts with microtubule polymerization and causes mitotic arrest following apoptosis in the human prostate cancer PC-3 cell line. *J. Biol. Chem.* 280, 2771–2779.
- Ivanova, S., Polajnar, M., Narbona-Perez, A.J., Hernandez-Alvarez, M.I., Frager, P., Slobodnyuk, K., Plana, N., Nebreda, A.R., Palacin, M., Gomis, R.R., Behrends, C., Zorzano, A., 2019. Regulation of death receptor signaling by the autophagy protein TP53INP2. *EMBO J.* 38.
- Jemal, A., Bray, F., Center, M.M., Ferlay, J., Ward, E., Forman, D., 2011. Global cancer statistics. *CA Cancer J Clin* 61, 69–90.
- Knight, M.J., Riffkin, C.D., Muscat, A.M., Ashley, D.M., Hawkins, C.J., 2001. Analysis of FasL and TRAIL induced apoptosis pathways in glioma cells. *Oncogene* 20, 5789–5798.
- Kumar, A., Kumari, N., Nallabelli, N., Prasad, R., 2019. Pathogenic and therapeutic role of H3K4 family of methylases and demethylases in cancers. *Indian J. Clin. Biochem.* 34, 123–132.
- Kuo, H.C., Kuo, Y.R., Lee, K.F., Hsieh, M.C., Huang, C.Y., Hsieh, Y.Y., Lee, K.C., Kuo, H.L., Lee, L.Y., Chen, W.P., Chen, C.C., Tung, S.Y., 2017. A comparative proteomic analysis of erinacine A's inhibition of gastric cancer cell viability and invasiveness. *Cell. Physiol. Biochem.* 43, 195–208.
- Kuo, H.C., Lu, C.C., Shen, C.H., Tung, S.Y., Hsieh, M.C., Lee, K.C., Lee, L.Y., Chen, C.C., Teng, C.C., Huang, W.S., Chen, T.C., Lee, K.F., 2016. Hericium erinaceus mycelium and its isolated erinacine A protection from MPTP-induced neurotoxicity through the ER stress, triggering an apoptosis cascade. *J. Transl. Med.* 14, 78.
- Lee, J.H., Khor, T.O., Shu, L., Su, Z.Y., Fuentes, F., Kong, A.N., 2013. Dietary phytochemicals and cancer prevention: nrf2 signaling, epigenetics, and cell death mechanisms in blocking cancer initiation and progression. *Pharmacol. Ther.* 137, 153–171.
- Lee, K.C., Kuo, H.C., Shen, C.H., Lu, C.C., Huang, W.S., Hsieh, M.C., Huang, C.Y., Kuo, Y. H., Hsieh, Y.Y., Teng, C.C., Lee, L.Y., Tung, S.Y., 2017. A proteomics approach to identifying novel protein targets involved in erinacine A-mediated inhibition of colorectal cancer cells' aggressiveness. *J. Cell Mol. Med.* 21, 588–599.
- Lee, K.C., Lee, K.F., Tung, S.Y., Huang, W.S., Lee, L.Y., Chen, W.P., Chen, C.C., Teng, C. C., Shen, C.H., Hsieh, M.C., Kuo, H.C., 2019. Induction apoptosis of erinacine A in human colorectal cancer cells involving the expression of TNFR, fas, and fas ligand via the JNK/p300/p50 signaling pathway with histone acetylation. *Front. Pharmacol.* 10, 1174.
- Li-Weber, M., 2009. New therapeutic aspects of flavones: the anticancer properties of Scutellaria and its main active constituents Wogonin, Baicalein and Baicalin. *Canc. Treat Rev.* 35, 57–68.
- Li-Weber, M., 2013. Targeting apoptosis pathways in cancer by Chinese medicine. *Canc. Lett.* 332, 304–312.
- Link, A., Balaguer, F., Goel, A., 2010. Cancer chemoprevention by dietary polyphenols: promising role for epigenetics. *Biochem. Pharmacol.* 80, 1771–1792.
- Loo, G., 2003. Redox-sensitive mechanisms of phytochemical-mediated inhibition of cancer cell proliferation (review). *J. Nutr. Biochem.* 14, 64–73.
- Lu, C.C., Huang, W.S., Lee, K.F., Lee, K.C., Hsieh, M.C., Huang, C.Y., Lee, L.Y., Lee, B.O., Teng, C.C., Shen, C.H., Tung, S.Y., Kuo, H.C., 2016. Inhibitory effect of Erinacines A on the growth of DLD-1 colorectal cancer cells is induced by generation of reactive oxygen species and activation of p70S6K and p21. *J. Funct. Foods* 21, 474–484.
- Ogino, I., Watanabe, S., Misumi, T., Hata, M., Kunisaki, C., 2019. Lymph node metastases diagnosed by (18)F-FDG-PET/CT in esophageal squamous cell cancer treated with concurrent chemoradiotherapy. *Anticancer Res.* 39, 4977–4985.
- Patel, D.J., Wang, Z., 2013. Readout of epigenetic modifications. *Annu. Rev. Biochem.* 82, 81–118.
- Rajendran, P., Ho, E., Williams, D.E., Dashwood, R.H., 2011. Dietary phytochemicals, HDAC inhibition, and DNA damage/repair defects in cancer cells. *Clin. Epigenet.* 3, 4.
- Raman, M., Chen, W., Cobb, M.H., 2007. Differential regulation and properties of MAPKs. *Oncogene* 26, 3100–3112.
- Ranjana, A., Ramachandran, S., Gupta, N., Kaushik, I., Wright, S., Srivastava, S., Das, H., Srivastava, S., Prasad, S., Srivastava, S.K., 2019. Role of phytochemicals in cancer prevention. *Int. J. Mol. Sci.* 20.
- Reed, J.C., 2000. Mechanisms of apoptosis. *Am. J. Pathol.* 157, 1415–1430.
- Rosato, R.R., Almenara, J.A., Dai, Y., Grant, S., 2003. Simultaneous activation of the intrinsic and extrinsic pathways by histone deacetylase (HDAC) inhibitors and tumor necrosis factor-related apoptosis-inducing ligand (TRAIL) synergistically induces mitochondrial damage and apoptosis in human leukemia cells. *Mol. Canc. Therapeut.* 2, 1273–1284.
- Savva, C.G., Totokotsopoulos, S., Nicolaou, K.C., Neophytou, C.M., Constantinou, A.I., 2016. Selective activation of TNFR1 and NF-kappaB inhibition by a novel biouyanagin analogue promotes apoptosis in acute leukemia cells. *BMC Canc.* 16, 279.
- Shilatfard, A., 2008. Molecular implementation and physiological roles for histone H3 lysine 4 (H3K4) methylation. *Curr. Opin. Cell Biol.* 20, 341–348.
- Spangle, J.M., Dreijerink, K.M., Groner, A.C., Cheng, H., Ohlson, C.E., Reyes, J., Lin, C.Y., Bradner, J., Zhao, J.J., Roberts, T.M., Brown, M., 2016. PI3K/AKT signaling regulates H3K4 methylation in breast cancer. *Cell Rep.* 15, 2692–2704.
- Tan, A.C., Chan, D.L., Faisal, W., Pavlakis, N., 2018. New drug developments in metastatic gastric cancer. *Therap. Adv. Gastroenterol.* 11, 1756284818808072.
- Teng, C.C., Kuo, H.C., Cheng, H.C., Wang, T.C., Sze, C.I., 2012. The inhibitory effect of CIL-102 on the growth of human astrocytoma cells is mediated by the generation of reactive oxygen species and induction of ERK1/2 MAPK. *Toxicol. Appl. Pharmacol.* 263, 73–80.

- Teng, C.C., Kuo, H.C., Sze, C.I., 2013. Quantitative proteomic analysis of the inhibitory effects of CIL-102 on viability and invasiveness in human glioma cells. *Toxicol. Appl. Pharmacol.* 272, 579–590.
- Wagner, A.D., Unverzagt, S., Grothe, W., Kleber, G., Grothey, A., Haerting, J., Fleig, W. E., 2010. Chemotherapy for advanced gastric cancer. *Cochrane Database Syst. Rev.*, CD004064.
- Wong, R.S., 2011. Apoptosis in cancer: from pathogenesis to treatment. *J. Exp. Clin. Canc. Res.* 30, 87.
- Woo, H.D., Park, S., Oh, K., Kim, H.J., Shin, H.R., Moon, H.K., Kim, J., 2014. Diet and cancer risk in the Korean population: a meta- analysis. *Asian Pac. J. Cancer Prev. APJCP* 15, 8509–8519.
- Zhang, X.D., Gillespie, S.K., Borrow, J.M., Hersey, P., 2003. The histone deacetylase inhibitor suberic bishydroxamate: a potential sensitizer of melanoma to TNF-related apoptosis-inducing ligand (TRAIL) induced apoptosis. *Biochem. Pharmacol.* 66, 1537–1545.
- Zhu, J.Y., Lavrik, I.N., Mahlkecht, U., Giaisi, M., Proksch, P., Krammer, P.H., Li-Weber, M., 2007. The traditional Chinese herbal compound rocaglamide preferentially induces apoptosis in leukemia cells by modulation of mitogen-activated protein kinase activities. *Int. J. Canc.* 121, 1839–1846.

## Article

# Aqueous Extract of Kan-Lu-Hsiao-Tu-Tan Ameliorates Collagen-Induced Arthritis in Mice by Inhibiting Oxidative Stress and Inflammatory Responses

Chih-Chao Chiang <sup>1,2</sup>, Yi-Rong Li <sup>3</sup>, Kuei-Hung Lai <sup>4,5</sup> , Wei-Jen Cheng <sup>1,6,7</sup> ,  
Shih-Chao Lin <sup>8,9</sup> , Yi-Hsuan Wang <sup>10</sup>, Po-Jen Chen <sup>11</sup> , Sien-Hung Yang <sup>1,6,7,\*</sup>,  
Chi-Chien Lin <sup>12,13,14,\*</sup>  and Tsong-Long Hwang <sup>4,10,15,16,\*</sup> 

- <sup>1</sup> Graduate Institute of Clinical Medical Sciences, College of Medicine, Chang Gung University, Taoyuan 333, Taiwan; moonlight0604@hotmail.com or d0600501@cgu.edu.tw (C.-C.C.); misterarren@gmail.com or misterarren@mail.cgu.edu.tw (W.-J.C.)
- <sup>2</sup> Puxin Fengze Chinese Medicine Clinic, Taoyuan 326, Taiwan
- <sup>3</sup> Changhua Christian Hospital, Thoracic Medicine Research Center, Changhua 500, Taiwan; peanutsnoopyemmali@gmail.com or 181065@cch.org.tw
- <sup>4</sup> Research Center for Chinese Herbal Medicine, Research Center for Food and Cosmetic Safety, and Graduate Institute of Health Industry Technology, Chang Gung University of Science and Technology, Taoyuan 333, Taiwan; mos19880822@gmail.com or kueihunglai@tmu.edu.tw
- <sup>5</sup> Graduate Institute of Pharmacognosy, College of Pharmacy, Taipei Medical University, Taipei 110, Taiwan
- <sup>6</sup> Center for Traditional Chinese Medicine, Chang Gung Memorial Hospital, Taoyuan 333, Taiwan
- <sup>7</sup> School of Traditional Chinese Medicine, Chang Gung University, Taoyuan 333, Taiwan
- <sup>8</sup> National Center for Biodefense and Infectious Diseases, School of Systems Biology, George Mason University, Manassas, VA 20110, USA; slin20@gmu.edu
- <sup>9</sup> Bachelor Degree Program in Marine Biotechnology, National Taiwan Ocean University, Keelung 202, Taiwan
- <sup>10</sup> Graduate Institute of Natural Products, College of Medicine, Chang Gung University, Taoyuan 333, Taiwan; e0919133641@gmail.com or d0901501@cgu.edu.tw
- <sup>11</sup> Department of Cosmetic Science, Providence University, Taichung 433, Taiwan; litlep@hotmail.com or pjchen@pu.edu.tw
- <sup>12</sup> Institute of Biomedical Science, College of Life Sciences, National Chung-Hsing University, 250 Guoguang Road, Taichung 402, Taiwan
- <sup>13</sup> Department of Pharmacology, College of Medicine, Kaohsiung Medical University, Kaohsiung 807, Taiwan
- <sup>14</sup> Department of Medical Research, China Medical University Hospital, Taichung 404, Taiwan
- <sup>15</sup> Department of Anesthesiology, Chang Gung Memorial Hospital, Taoyuan 333, Taiwan
- <sup>16</sup> Department of Chemical Engineering, Ming Chi University of Technology, New Taipei City 243, Taiwan
- \* Correspondence: dryang@mail.cgu.edu.tw (S.-H.Y.); lincc@dragon.nchu.edu.tw (C.-C.L.); htl@mail.cgu.edu.tw (T.-L.H.)

Received: 26 October 2020; Accepted: 24 November 2020; Published: 27 November 2020



**Abstract:** Background: Kan-Lu-Hsiao-Tu-Tan (KLHTT) exhibits anti-psoriatic effects through anti-inflammatory activity in mice. However, the therapeutic effects of KLHTT on rheumatoid arthritis (RA), another significant autoimmune inflammatory disorder, have not been elucidated. Herein, we explored the anti-arthritis effects of KLHTT on collagen-induced arthritis (CIA) in mice. Methods: KLHTT was extracted by boiling water and subjected to spectroscopic analysis. Chicken collagen type II (CII) with complete Freund's adjuvant was intradermally injected to induce CIA in DBA/1J mice. Anti-CII antibody, cytokines, malondialdehyde (MDA), and hydrogen peroxide (H<sub>2</sub>O<sub>2</sub>) were measured using ELISA, thiobarbituric acid reactive substances, and a hydrogen peroxide assay kit. Splenocyte proliferation was tested using thymidine incorporation. Th1 and Th17 cells were analyzed by flow cytometry. Results: Oral KLHTT treatment (50 and 100 mg/kg) ameliorated mouse CIA by decreasing the levels of interleukin (IL)-1 $\beta$ , IL-6, IL-17A, and tumour necrosis factor- $\alpha$  in the paw homogenates and serum. KLHTT also suppressed anti-CII antibody formation, splenocyte proliferation, and splenic Th1 and Th17 cell numbers. Additionally, KLHTT showed antioxidant

activity by reducing the concentrations of MDA and H<sub>2</sub>O<sub>2</sub> in paw tissues. Conclusions: The therapeutic effects of KLHTT in CIA mice were through regulating oxidative stress and inflammatory responses. Our results suggest that KLHTT has potential to treat RA.

**Keywords:** Kan-Lu-Hsiao-Tu-Tan; collagen-induced arthritis; inflammation; immunity; Chinese medicine

## 1. Introduction

Rheumatoid arthritis (RA) is an autoimmune disease affecting approximately 1% of the global population, which is characterised by synovitis, cartilage damage, and bone resorption in the joint [1]. Moreover, RA is associated with fatigue [2], cervical spine disease, carpal tunnel syndrome [3], interstitial lung disease [4], cardiovascular disease [5], depression [6], and sleep disorders [7]. RA can cause personal and emotional problems, and impose a significant socio-economic burden [8,9]. The medical treatment of RA includes biological disease-modifying anti-rheumatic drugs, conventional disease-modifying anti-rheumatic drugs, and analgesics. However, these available therapies cannot treat the disease completely and exert significant side effects. Therefore, the development of new therapeutics for RA is needed [10,11].

RA is characterised by synovitis accompanied by the infiltration of immune cells [12], including T cells, B cells, dendritic cells [13], neutrophils [14], and macrophages [15]. Studies have indicated that anti-citrullinated protein antibodies (ACPAs) and inflammatory cytokines, such as interleukin (IL)-1 $\beta$ , IL-6, IL-17, and tumour necrosis factor- $\alpha$  (TNF- $\alpha$ ), are pivotal mediators in RA [16]. ACPAs are also a specific diagnostic biomarker for RA [17]. Furthermore, oxidative stress caused by reactive oxygen species (ROS) is crucial in joint inflammation, and RA patients exhibit high level of ROS in serum [18,19]. Hence, antioxidant drugs may be effective in treating RA [20]. Collagen-induced arthritis (CIA) in mice recapitulates the clinical and pathogenic characteristics of human RA, and they are widely used to study RA [21].

Kan-Lu-Hsiao-Tu-Tan (KLHTT), a Chinese medicine (CM), has been used to treat inflammatory conditions such as RA, systemic lupus erythematosus, dermatomyositis [22], sinusitis, gingivitis, gastritis, hepatitis [23], and dermatitis [24]. Our previous study demonstrated that KLHTT exerts ROS scavenging ability and anti-inflammatory activity in human neutrophils and exhibits anti-psoriatic activity in mice [25]. However, the pharmacologic effects of KLHTT on RA, another significant autoimmune inflammatory disorder, have not yet been elucidated. Herein, in this study, we aimed to investigate the anti-arthritis effects of KLHTT in CIA mice and evaluate its value in the treatment of RA.

## 2. Materials and Methods

### 2.1. Reagents

KLHTT (batch number: 0503-2-403-01) was supplied by Sun Ten Pharmaceutical Corporation, New Taipei City, Taiwan. Chicken collagen type II (CII) was purchased from Chondrex, Inc., Woodinville, WA, USA. Mycobacterium tuberculosis H37RA was bought from Difco Laboratories Inc., Detroit, MI, USA. Methotrexate (MTX) and EDTA were ordered from Bio Basic Inc., Toronto, ON, Canada. Enzyme-linked immunosorbent assay (ELISA) kits (for IL-1 $\beta$ , IL-6, and TNF- $\alpha$ ) were obtained from eBioscience, San Diego, CA, USA. An IL-17A ELISA kit was purchased from R&D Systems Inc., Minneapolis, MN, USA. A hydrogen peroxide assay kit was purchased from Cell Biolabs, Inc., San Diego, CA, USA. Goat anti-mouse IgG1 and goat anti-mouse IgG2a secondary antibodies were purchased from Jackson ImmunoResearch Laboratories, West Grove, PA, USA. 2,2'-Azinobis [3-ethylbenzothiazoline-6-sulfonic acid]-diammonium salt (ABTS) substrate solution was ordered from Roche Diagnostic Systems, South San Francisco, CA, USA. A <sup>3</sup>H labelled thymidine was purchased

from Amersham Pharmacia Biotech, Arlington Heights, IL, USA. Brefeldin A and Freund's adjuvant were bought from Sigma-Aldrich, St. Louis, MO, USA. Phycoerythrin (PE)-conjugated anti-mouse CD4 (clone GK1.5), FITC-conjugated anti-mouse IL-17A (clone TC11-18H10.1), and FITC-conjugated anti-mouse interferon (IFN)- $\gamma$  (clone XMG1.2) antibodies were ordered from Biolegend, San Diego, CA, USA. Formalin was bought from AVANTOR, Center Valley, PA. Bovine serum albumin (BSA) was purchased from EMD Millipore, Billerica, MA, USA. Tween 20 was obtained from EMD Millipore, Alsace, France.

## 2.2. KLHTT Preparation

The herbs of KLHTT were purchased and identified by Sun Ten Pharmaceutical Corporation, New Taipei City, Taiwan. A total of 27.93 g of herbs (6.25 g Soapstone, 4.58 g *Artemisia capillaris* Thunb. (seedling), 4.17 g *Scutellaria baicalensis* Georgi (root), 2.50 g *Acorus gramineus* Soland. (rhizome), 2.08 g *Clematis armandii* Franch. (rattan and stem), 2.08 g *Fritillaria cirrhosa* D. Don (bulb), 1.67 g *Pogostemon cablin* (Blanco) Benth. (plant shoot), 1.67 g *Forsythia suspensa* (Thunb.) Vahl (fruits), 1.67 g *Anomum kravanh* Pierre ex Gagnep. (fruits), 1.67 g *Mentha haplocalyx* Briq. (stem and leaf plot), and 1.67 g *Belamcanda chinensis* (L.) DC (rhizome)) was extracted by boiling water (12 times the weight of the herbs) for 1 h, and then concentrated to a voucher specimen (CGU\_KLHTT-01) by the freeze dryer (LABCONCO, Kansas City, MO, USA) [25]. The voucher specimen complied with Chang Gung University guidelines.

## 2.3. Ultra-Performance Liquid Chromatography-Tandem Mass Spectrometry

The chemical profile of KLHTT extract was obtained using ultra-performance liquid chromatography-tandem mass spectrometry (UPLC-MS/MS) comprising an LC-30AD pump, SIL-30AC auto-sampler, CTO-20AC column, and SPD-M20A photodiode array detector (Nexera X2, Shimadzu, Kyoto, Japan). Prior to being loaded onto the UPLC column, 1 mg of KLHTT extract was first dissolved in 1 mL of methanol and filtered through a 0.45  $\mu$ m membrane. Sample injections of 1  $\mu$ L were then performed automatically. Liquid chromatography was performed using a CORTECS UPLC C18 column (90 $\text{\AA}$ , 1.6  $\mu$ m, 2.1 mm  $\times$  100 mm) (Waters, Milford, MA, USA). The mobile phase was a mixture of MeCN (A) and water (W, containing 0.1% formic acid). A gradient sequence was executed as follows: 0–10 min, 10–20% A; 10–14 min, 20–25% A; 14–24 min, 25–30% A; 24–28 min, 30–40% A; 28–33 min, 40–50% A; 33–38 min, 50–75% A; 38–40 min, 75–100% A; and 40–43 min, 100% A. The column temperature was set at 35  $^{\circ}$ C. The flow rate was at 0.4 mL/min. The range of detection wavelengths was fixed in the 190–500 nm.

Multiple reaction monitoring (MRM) experiments (in negative) were carried out using Shimadzu LCMS-8045 triple quadrupole mass spectrometry to identify the constituents of KLHTT extract. The precursor ion settings of the corresponding profiling peaks were determined using the full scan experiment (50–1000 amu). The product ions were settled according to previously reported data. The dwell time was fixed at 100 ms and the collision energy was set at 25–45 eV. All MS data were acquired and processed using LCMS LabSolutions software Version 5.93 (Shimadzu, Kyoto, Japan).

## 2.4. Experimental Animals

DBA/1J mice (male, six- to eight-week old, weight 20–22 g) were purchased from Jackson Laboratories (Bar Harbor, ME, USA) and maintained at 20–25  $^{\circ}$ C with half day light/dark cycle under a specific pathogen-free condition. All mice were treated according to the guidelines of the Institutional Animal Care and Use Committee of National Chung Hsing University (NCHU). The study protocol was approved by NCHU ethics committee (approval code: 109-115).

## 2.5. CIA Model Establishment

CIA was induced by active immunisation with chicken CII [26]. Briefly, 2 mg/mL CII was dissolved in 10 mM acetic acid solution and emulsified with an equal volume of complete Freund's adjuvant



containing *Mycobacterium tuberculosis* H37RA (250 µg/mouse). The mixture (200 µL/mouse) was intradermally injected at the base of the tail. Incomplete Freund's adjuvant and CII were administered as booster injections to the mice on day 21 after the first immunisation. ddH<sub>2</sub>O, KLHTT, or MTX was administered orally once a day from day 21 to 42. Mice were divided into four groups ( $n = 6/\text{group}$ ) randomly as follows: Group I, Normal; Group II, Vehicle (ddH<sub>2</sub>O) + CII; Group III, KLHTT (50 mg/kg) + CII; Group IV, KLHTT (100 mg/kg) + CII. MTX (0.5 mg/kg) was used as a positive control. Mice were euthanized with CO<sub>2</sub> exposure (100% CO<sub>2</sub> for 5 min) by experienced experimenters humanely on day 42. The arthritis severity score was recorded every 3 days after the treatment of drugs. The biochemical and histological assays were performed on day 42.

## 2.6. Assessment of Clinical Arthritis Severity

The body weight and arthritis severity score were obtained [26]. The arthritis severity score was evaluated as: 0, no swelling nor redness; 1, mild swelling and redness restricted to the tarsals or the ankle joint; 2, mild swelling and redness from the tarsals to the ankle; 3, moderate swelling and redness extending to the metatarsal joints; 4, severe swelling and redness from the ankle to the foot and the digits, or limb ankyloses. In addition, paw volume was measured using a plethysmometer 37,140 (Ugo Basile SRL, Comerio, VA, Italy).

## 2.7. Assessment of Histological Arthritis Severity

After the mice were humanely sacrificed, the hind limbs were fixed in 10% buffered formalin, decalcified in 15% EDTA, and embedded in paraffin. Serial paraffin sections (5 µm) were stained with haematoxylin and eosin. The severity of histopathological lesions was scored [26] as follows: 0, normal appearance; 1, mild infiltration of inflammatory cells, mild pannus front, and minimal cartilage damage; 2, moderate infiltration of inflammatory cells, erosive pannus front, and moderate cartilage damage; 3, diffuse infiltration of inflammatory cells, severe cartilage damage and bone resorption.

## 2.8. Measurement of Pro-Inflammatory Cytokine Levels

Hind paw was dissected and homogenised in ice-cold saline using a tissue homogeniser. After being centrifuged at 3000 rpm (4 °C, 10 min, twice), the hind paw homogenates were harvested. Blood was collected from the heart. The levels of cytokines in hind paw homogenates and serum were measured by ELISA [16].

## 2.9. Measurement of the Concentrations of Oxidative Markers

Malondialdehyde (MDA) concentration was determined by thiobarbituric acid reactive substances assay at 532 nm. The standard curve was obtained using 1,1,3,3-tetramethoxypropane. Hydrogen peroxide (H<sub>2</sub>O<sub>2</sub>) concentration was measured using a colorimetric OxiSelect™ hydrogen peroxide assay kit at 560 nm [16].

## 2.10. Anti-Collagen Type II Antibody Analysis

Serum samples were diluted 1:250 for IgG1 or 1:125 for IgG2a in Tris-buffered saline (1% BSA and 0.5% Tween 20, pH 8.0), and then transferred to CII (10 µg/mL) pre-coated 96-well plates (Microtiter™, Thermo Fisher Scientific, Roskilde, Denmark) at 4 °C overnight. The plates were washed and incubated with goat anti-mouse secondary antibodies IgG1 (1:500 dilution) or IgG2a (1:500 dilution) at 25–27 °C for 1 h. After being washed, ABTS substrate was added and the reactions were stopped by adding H<sub>2</sub>SO<sub>4</sub>. The level of IgG1 and IgG2a was measured at 450 nm by an ELISA reader (Sunrise, Tecan Inc., Männedorf, Switzerland) [16].

### 2.11. Splenocyte Proliferation Assay

Splenocytes ( $4 \times 10^5$  cells/well) were cultured with chicken CII (50  $\mu\text{g/mL}$ ) at 37 °C for 40 h, and then incubated with  $^3\text{H}$  for 8 h. Cell proliferation was evaluated by radioactive thymidine incorporation [16].

### 2.12. Intracellular Staining

Splenocytes ( $1 \times 10^6$  cells/well) were cultured with chicken CII (50  $\mu\text{g/mL}$ ) at 37 °C for 48 h, and then brefeldin A (5  $\mu\text{g/mL}$ ) was added for 6 h. Cells were harvested and extracellularly stained with PE-conjugated anti-mouse CD4 antibodies. After being fixed and permeabilised with Cytofix/Cytoperm solution (BD Pharmingen), cells were then intracellularly labelled with FITC-conjugated anti-mouse IL-17A and anti-mouse IFN- $\gamma$  antibodies. Splenocytes were detected by an Accuri C5 flow cytometer (Accuri Cytometers, Ann Arbor, MI, USA) and analysed by BD Accuri™ C6 Plus software [26].

### 2.13. Statistical Analysis

Data are presented as mean  $\pm$  SD. Statistical analyses were performed using one- or two-way ANOVA followed by Tukey's honest significant difference test. A  $p$ -value  $< 0.05$  was considered statistically significant.

## 3. Results

### 3.1. Identification of Flavone Derivatives in KLHTT Extract

In this study, qualitative analysis of flavonoid-derived constituents was performed by UPLC-MS/MS under 330 nm. The most significant components of the KLHTT extract were flavonoid derivatives (Figure 1A). It has been reported that flavone glycosides are the major constituents of the KLHTT aqueous extract [27]. Moreover, some of the flavonoids and their glycosides such as baicalin and baicalein were found to display significant anti-inflammatory properties [25]. Therefore, we conducted tandem mass (MS/MS) spectrometry experiments to identify the constituents of KLHTT for flavonoids and their glycosides specifically. The specific mass fragmentations were compared with previous references [28–34], and eight flavonoids were identified: chrysin 6-C-arabinoside-8-C-glucoside (1), chrysin 6-C-glucoside-8-C-arabinoside (2), baicalin (3), norwogonin-7-O- $\beta$ -D-glucuronide (4), chrysin 7-O- $\beta$ -D-glucuronide (5), oroxylin A 7-O- $\beta$ -D-glucuronide (6), wogonoside (7), and baicalein (8) (Figure 1B) (Table 1).

**Table 1.** UV and multi-stage mass spectrometry data for the identification of the constituents of Kan-Lu-Hsiao-Tu-Tan extract.

No.	$T_R$ (Min)	Formula	(–)-ESI-MS/MS Fragment Ions	$\lambda_{\text{max}}$ (Nm)	Identification
1	7.269	$\text{C}_{26}\text{H}_{28}\text{O}_{13}$	547, 487, 457, 427, 367, 337	271, 317	Chrysin 6-C-arabinoside-8-C-glucoside
2	8.249	$\text{C}_{26}\text{H}_{28}\text{O}_{13}$	547, 457, 427, 367, 337	271, 317	Chrysin 6-C-glucoside-8-C-arabinoside
3	12.674	$\text{C}_{21}\text{H}_{18}\text{O}_{11}$	445, 269, 251, 223, 197, 113	276, 316	Baicalin
4	14.321	$\text{C}_{21}\text{H}_{18}\text{O}_{11}$	445, 269, 241, 225, 171	278, 347	Norwogonin-7-O- $\beta$ -D-glucuronide
5	15.209	$\text{C}_{21}\text{H}_{18}\text{O}_{10}$	429, 253, 209, 143, 113	267	Chrysin 7-O- $\beta$ -D-glucuronide
6	15.455	$\text{C}_{22}\text{H}_{20}\text{O}_{11}$	459, 283, 268	271, 311	Oroxylin A 7-O- $\beta$ -D-glucuronide
7	16.345	$\text{C}_{22}\text{H}_{20}\text{O}_{11}$	459, 283, 268	273, 340	Wogonoside
8	19.220	$\text{C}_{15}\text{H}_{10}\text{O}_5$	269, 251, 241, 223, 195, 169, 136	275, 324	Baicalein

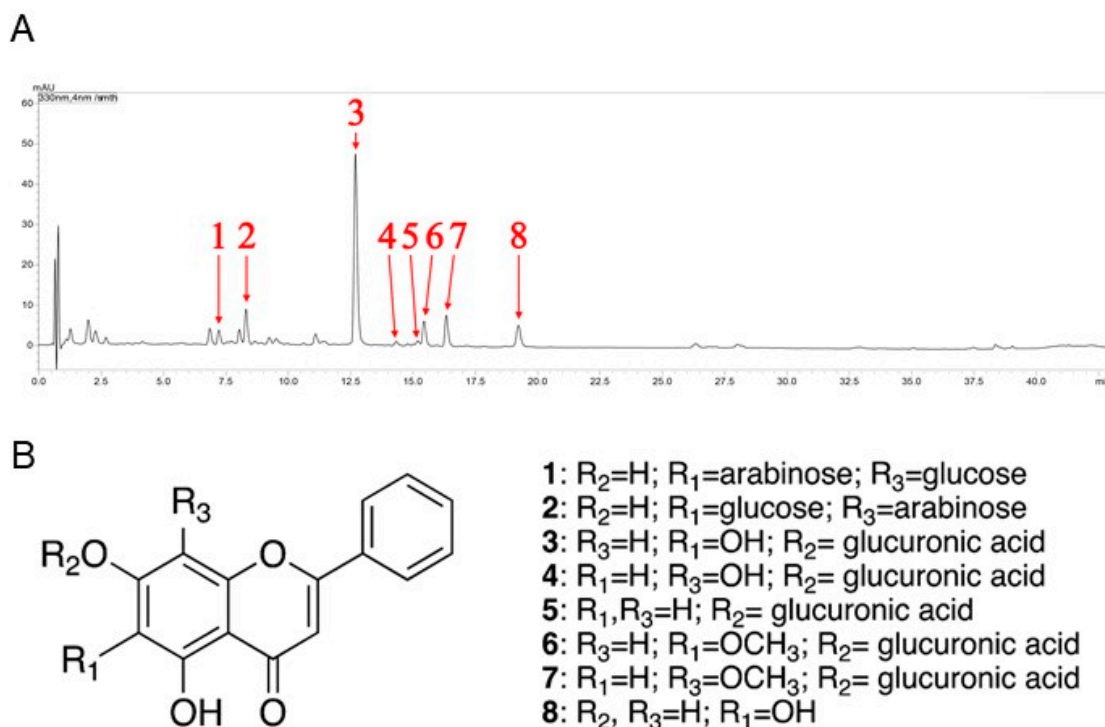


**Figure 1.** The chemical fingerprint of KLHTT. (A) Ultra-performance liquid chromatography with photodiode array detector chromatogram ( $\lambda = 330$  nm) of KLHTT extract. (B) The flavonoid derivatives in KLHTT extract were identified by comparing specific liquid chromatography-tandem mass spectrometry monitoring fragmentations with previously reported data, and were determined to be: chrysin 6-C-arabinoside-8-C-glucoside (1), chrysin 6-C-glucoside-8-C-arabinoside (2), baicalin (3), norwogonin-7-O- $\beta$ -D-glucuronide (4), chrysin 7-O- $\beta$ -D-glucuronide (5), oroxylin A 7-O- $\beta$ -D-glucuronide (6), wogonoside (7), and baicalein (8). KLHTT, Kan-Lu-Hsiao-Tu-Tan.

### 3.2. KLHTT Exerts Anti-Arthritic Effects in CIA Mice

The CIA mouse model is a well-established and commonly used model mimicking the clinical symptoms and immunopathogenesis of human RA [35]. Immunisation of mice with CII induced increases in clinical arthritis scores, paw volume, and histopathological damage. The normal group exhibited no gross or histological changes. KLHTT (50 and 100 mg/kg) showed inhibitory effects on arthritis severity (Figure 2A) and paw erythema and swelling (Figure 2B,C). The body weight loss in CIA mice was also restored by KLHTT (Figure 2D).

Histopathological analysis of the CIA mice revealed inflammatory cell infiltration into articular tissues, exudates within the synovial space, synovial hyperplasia, and cartilage erosion. KLHTT-treated mice demonstrated well-preserved joint spaces with minimal inflammatory exudates, normal cartilage structure, and clear synovial spaces, along with improved histological arthritis severity scores (Figure 3). MTX (0.5 mg/kg) was used as a positive control and showed comparable inhibitory effects with KLHTT in CIA mice (Figures 2 and 3).

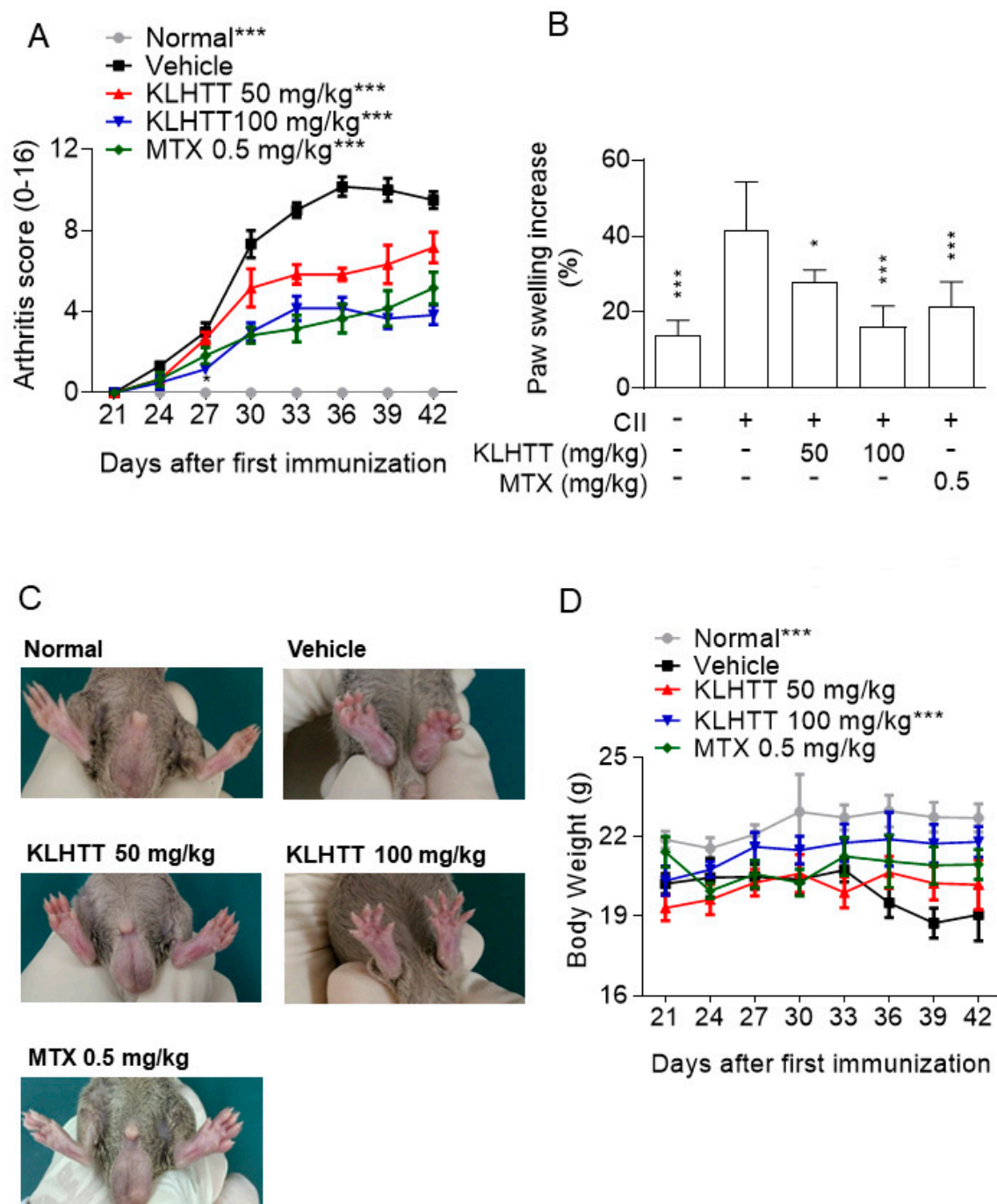


**Figure 2.** KLHTT ameliorates CIA severity. CIA was induced by active immunisation with chicken CII in DBA/1J mice. Drugs were administered orally once a day from day 21 to 42. (A) Arthritis score was monitored every 3 days after the treatment of drugs. Data are expressed as mean  $\pm$  SD ( $n = 6$ ). \*\*\*  $p < 0.001$  versus vehicle-treated CIA control mice; two-way ANOVA. (B) Paw swelling was assessed using a plethysmometer on day 42. Data are expressed as mean  $\pm$  SD ( $n = 6$ ). \*  $p < 0.05$  and \*\*\*  $p < 0.001$  versus vehicle-treated CIA control mice; one-way ANOVA. (C) Representative pictures of hind paws on day 42 are showed. (D) Body weight was monitored after the booster immunisation. \*\*\*  $p < 0.001$  versus vehicle-treated CIA control mice; two-way ANOVA. CIA, collagen-induced arthritis; CII, collagen type II; KLHTT, Kan-Lu-Hsiao-Tu-Tan; MTX, methotrexate.



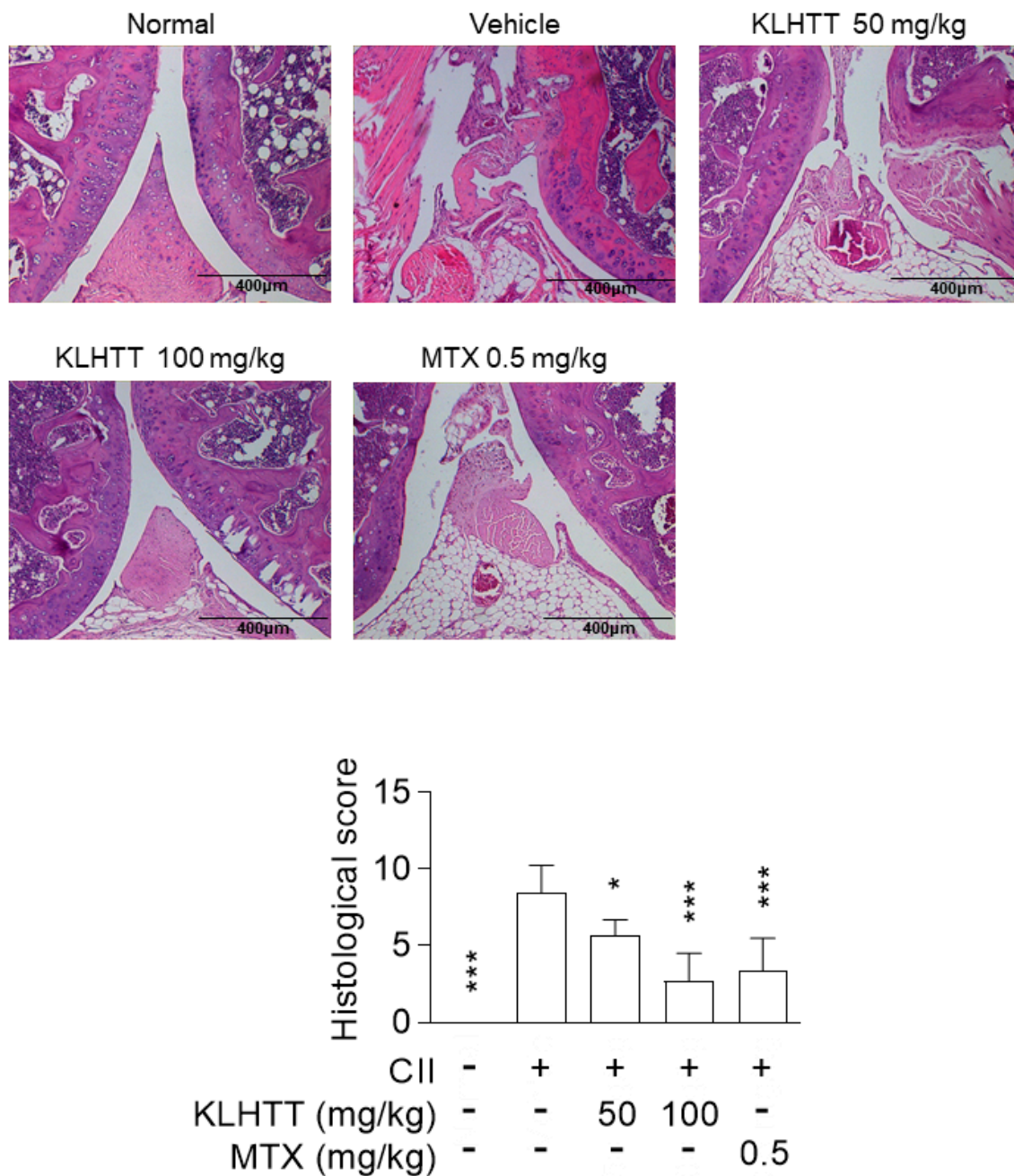


**Figure 3.** KLHTT reduces joint damage in CIA mice. CIA was induced by active immunisation with chicken CII in DBA/1J mice. Drugs were administered orally once a day from day 21 to 42. Haematoxylin and eosin-stained joint sections from mice of different groups were prepared and pathogenic scores were determined. Original magnification 100 $\times$ . Bar = 400  $\mu$ m. Data are expressed as mean  $\pm$  SD ( $n = 6$ ). \*  $p < 0.05$  and \*\*\*  $p < 0.001$  versus vehicle-treated CIA control mice; one-way ANOVA. CIA, collagen-induced arthritis; CII, collagen type II; KLHTT, Kan-Lu-Hsiao-Tu-Tan; MTX, methotrexate.

### 3.3. KLHTT Inhibits Cytokine Production in CIA Mice

The pathogenesis of RA involves activated T cells promoting macrophages to release pro-inflammatory cytokines [35]. Therefore, the levels of TNF- $\alpha$ , IL-1 $\beta$ , IL-6, and IL-17 in hind paw homogenates and serum samples were measured by sandwich ELISA. KLHTT (50 and 100 mg/kg) treatment inhibited the levels of IL-1 $\beta$ , IL-6, IL-17, and TNF- $\alpha$  in paw homogenates (Figure 4A) and serum samples (Figure 4B) in CIA mice. These results indicated that KLHTT effectively attenuates inflammation in CIA mice.



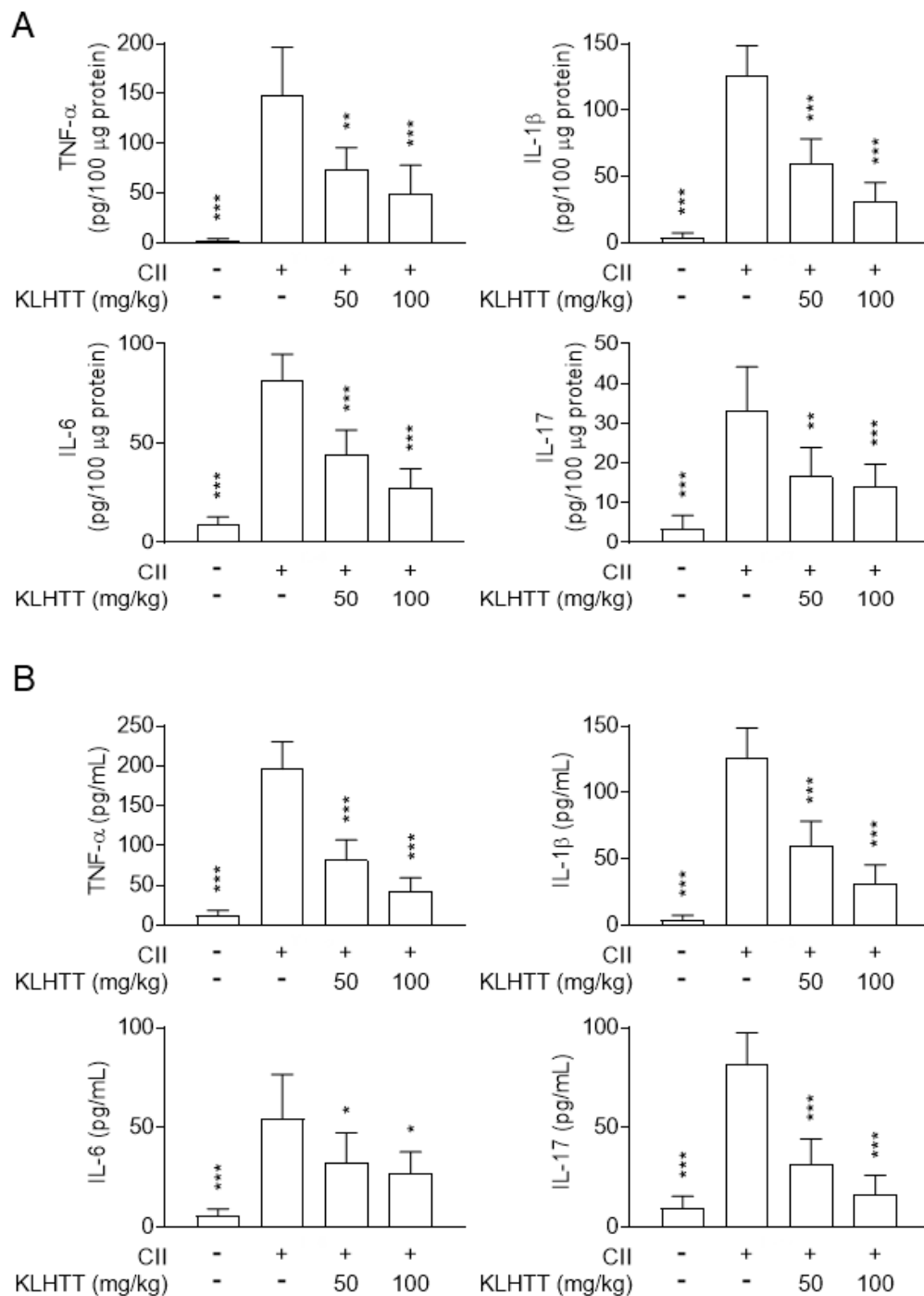


**Figure 4.** KLHTT inhibits pro-inflammatory cytokine production in CIA mice. CIA was induced by active immunisation with chicken CII in DBA/1J mice. Drugs were administered orally once a day from day 21 to 42. The levels of cytokines in hind paw homogenates (A) and serum (B) from CIA mice were measured on day 42 by enzyme-linked immunosorbent assay. Data are expressed as mean  $\pm$  SD ( $n = 6$ ). \*  $p < 0.05$ , \*\*  $p < 0.01$ , and \*\*\*  $p < 0.001$  versus vehicle-treated CIA control mice; one-way ANOVA. CIA, collagen-induced arthritis; CII, collagen type II; IL, interleukin; KLHTT, Kan-Lu-Hsiao-Tu-Tan; TNF- $\alpha$ , tumour necrosis factor- $\alpha$ .

### 3.4. KLHTT Reduces Oxidative Stress in CIA Mice

RA patients exhibit high level of oxidative stress, which correlates with joint inflammation and may contribute to the chronicity of RA [36]. Significantly elevated levels of MDA and  $H_2O_2$  were

noted in the hind paw homogenates of CIA mice. KLHTT (50 and 100 mg/kg) significantly reduced the levels of MDA (Figure 5A) and  $H_2O_2$  (Figure 5B). These data show that KLHTT protects mice from oxidative damage, which may have contributed to the amelioration of CIA.

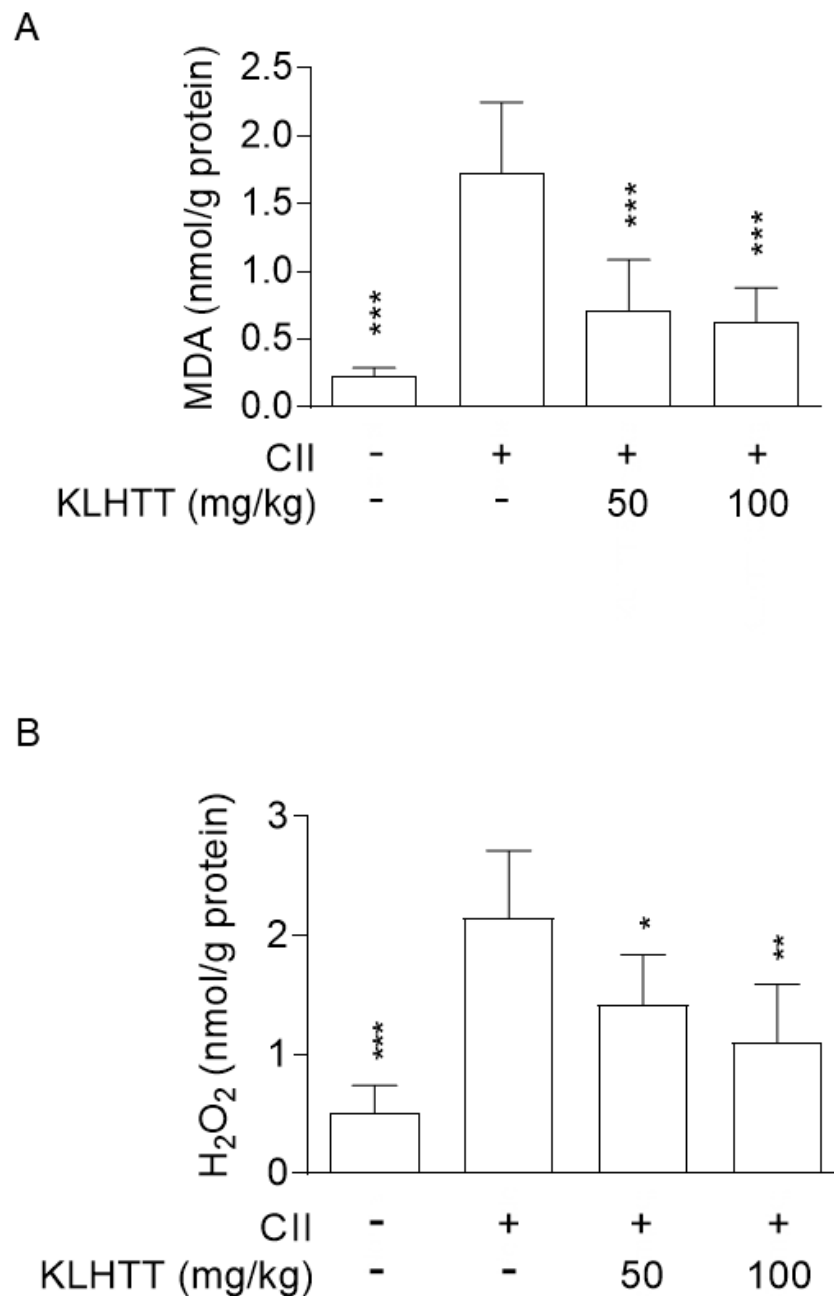


**Figure 5.** KLHTT reduces the levels of MDA and  $H_2O_2$  in CIA mice. CIA was induced by active immunisation with chicken CII in DBA/1J mice. Drugs were administered orally once a day from day 21 to 42. (A) MDA (a lipid peroxidation marker) and (B)  $H_2O_2$  (an ROS marker) were determined on day 42 by the thiobarbituric acid reactive substances assay and the hydrogen peroxide assay kit, respectively. Data are expressed as mean  $\pm$  SD ( $n = 6$ ). \*  $p < 0.05$ , \*\*  $p < 0.01$ , and \*\*\*  $p < 0.001$  versus vehicle-treated CIA control mice; one-way ANOVA. CIA, collagen-induced arthritis; CII, collagen type II;  $H_2O_2$ , hydrogen peroxide; KLHTT, Kan-Lu-Hsiao-Tu-Tan; MDA, malondialdehyde; ROS, reactive oxygen species.

### 3.5. KLHTT Inhibits CII-Specific Antibody Production and Splenocyte Proliferation in CIA Mice

Autoantibodies targeting IgG play a major role in RA. Similarly, elevated levels of IgG1 and IgG2a antibodies were detected in serum samples from CIA mice. KLHTT significantly suppressed IgG1 and IgG2a antibody production (Figure 6A). Furthermore, KLHTT significantly inhibited the proliferation of CII-induced splenocytes (Figure 6B).

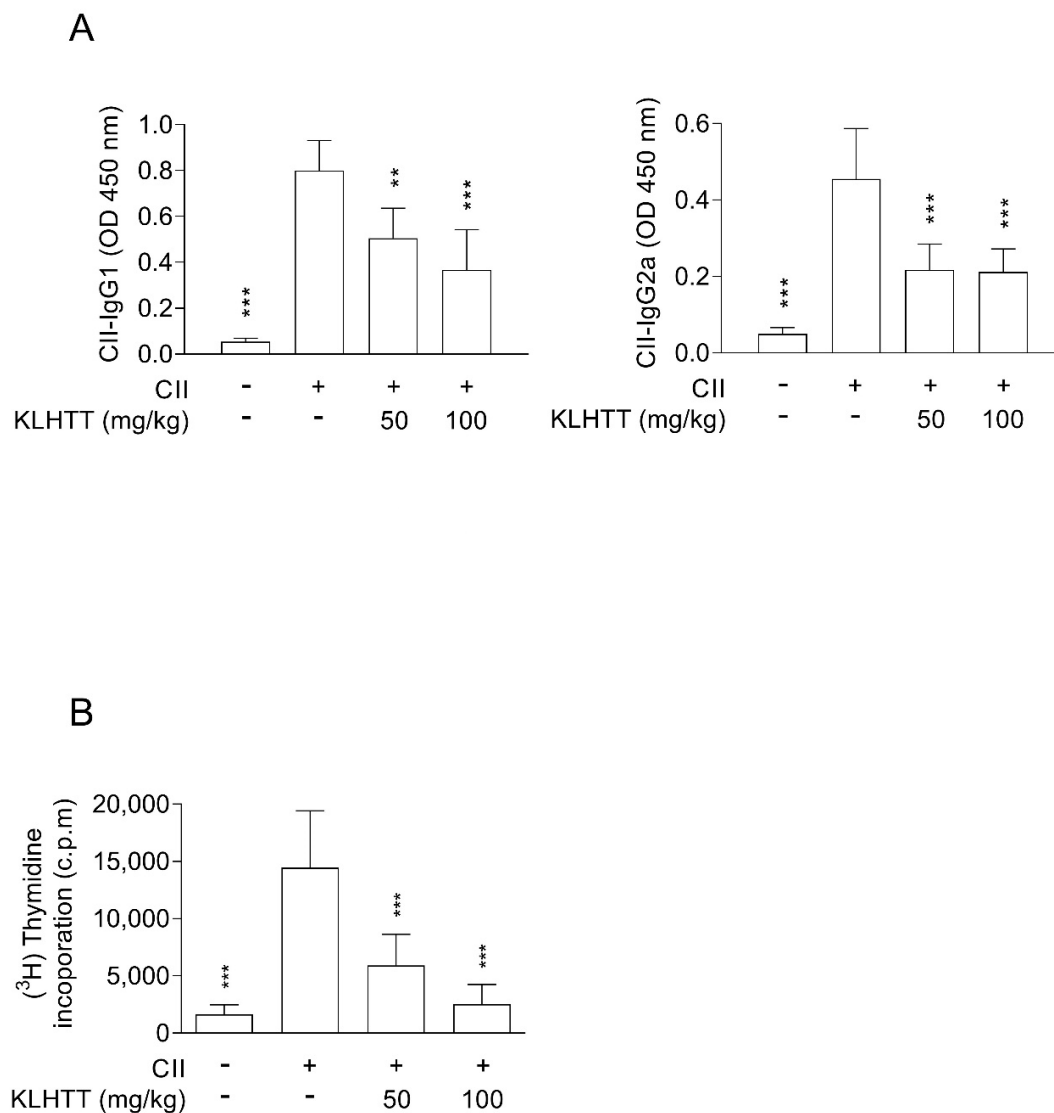


**Figure 6.** KLHTT inhibits anti-IgG CII antibody production and splenocyte proliferation in CIA mice. CIA was induced by active immunisation with chicken CII in DBA/1J mice. Drugs were administered orally once a day from day 21 to 42. (A) The levels of anti-CII IgG1 and IgG2a antibodies were detected on day 42 using enzyme-linked immunosorbent assay. (B) Splenocytes were cultured with CII for 40 h, and then cell proliferation was measured by incorporation of (<sup>3</sup>H)-thymidine. Data are expressed as mean  $\pm$  SD ( $n = 6$ ). \*\*  $p < 0.01$ , and \*\*\*  $p < 0.001$  versus vehicle-treated CIA control mice; one-way ANOVA. CIA, collagen-induced arthritis; CII, collagen type II; KLHTT, Kan-Lu-Hsiao-Tu-Tan.

### 3.6. KLHTT Reduces the Levels of Splenic Th1 and Th17 Cells in CIA Mice

The pro-inflammatory Th1 and Th17 cell axes play crucial roles in RA. The levels of splenic Th1 and Th17 cells were higher after CII induction. KLHTT significantly decreased the numbers of CD4<sup>+</sup> IFN $\gamma$ <sup>+</sup>Th1 and CD4<sup>+</sup>IL17A<sup>+</sup>Th17 cells (Figure 7). KLHTT also mitigated the levels of pro-inflammatory cytokines in CIA mice (Figure 4). These results indicated that KLHTT decreases splenic pro-inflammatory Th1 and Th17 cells in CIA mice.

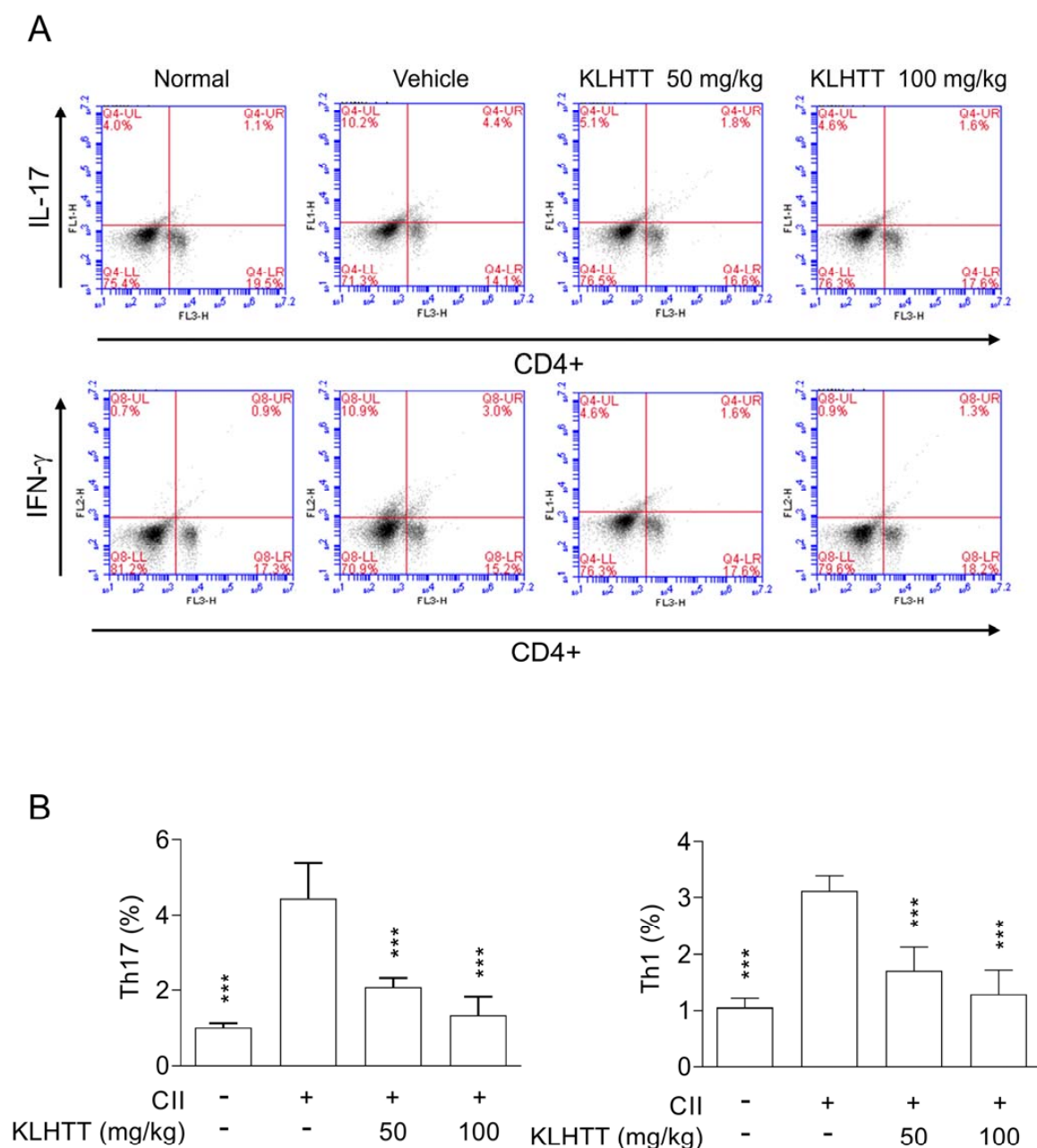


**Figure 7.** KLHTT reduces the levels of splenic Th1 and Th17 cells in CIA mice. CIA was induced by active immunisation with chicken CII in DBA/1J mice. Drugs were administered orally once a day from day 21 to 42. **(A)** On day 42, splenocytes were cultured with CII for 2 d, and then stained with PE-conjugated anti-CD4 antibodies followed by FITC-conjugated anti-IL-17A or anti-IFN- $\gamma$  antibodies. Samples were analysed by flow cytometry. **(B)** Bars display the mean  $\pm$  SD ( $n = 6$ ). \*\*\*  $p < 0.001$  versus vehicle-treated CIA control mice; one-way ANOVA. CIA, collagen-induced arthritis; CII, collagen type II; FITC, fluorescein isothiocyanate; IL-17, interleukin 17; IFN- $\gamma$ , interferon gamma; KLHTT, Kan-Lu-Hsiao-Tu-Tan; PE, phycoerythrin.

#### 4. Discussion

RA is a chronic autoimmune inflammatory disease [1]. Patients with RA have systemic inflammatory comorbidities. The therapeutic armamentarium for RA has expanded from analgesics and nonsteroidal anti-inflammatory drugs to biological disease-modifying anti-rheumatic drugs and conventional disease-modifying anti-rheumatic drugs; however, these available therapies may cause

adverse reactions and fail to achieve long-term remission [37]. Therefore, the development of new drugs is required to improve the treatment of RA.

KLHTT is a well-known CM and has been used to treat inflammatory diseases [22]. In this study, we investigated the anti-arthritis effect of KLHTT in CIA mice. Mice actively immunised with CII develop CIA, which closely resembles human RA. CIA mice showed paw erythema and swelling, synovitis, cartilage damage, and bone erosion [35]. KLHTT reduced arthritis severity scores and paw swelling, and restored body weight in CIA mice. KLHTT also decreased inflammatory cell infiltration. Both in CIA and human RA, pro-inflammatory cytokines such as TNF- $\alpha$ , IL-1 $\beta$ , IL-6, and IL-17 trigger autoimmune reactions and enhance chronic inflammation in synovial tissues [38,39]. These pro-inflammatory cytokines activate synovial fibroblasts and chondrocytes to produce enzymes which degrade collagen and proteoglycans, thus damaging adjacent joint tissues [40]. KLHTT significantly reduced the levels of TNF- $\alpha$ , IL-1 $\beta$ , IL-6, and IL-17 in serum samples and joint homogenates. Therefore, KLHTT exerts local and systemic anti-inflammatory effects, which may explain its anti-arthritis activity.

Autoantibodies such as rheumatoid factor and ACPAs can be detected in 50–80% of RA patients. Increased levels of anti-CII IgG correlate with elevated TNF- $\alpha$  and IL-6 in RA patients [41]. In CIA mice, anti-CII antibodies initiate arthritis and CII-reactive T cells promote the progression of the disease [42]. In this study, KLHTT reduced the levels of anti-CII IgG1 and IgG2a in serum samples from CIA mice. Anti-CII IgG2 autoantibodies are the predominant subclass of autoantibodies in CIA mice [35]. Additionally, KLHTT inhibited CII-induced splenocyte proliferation and reduced the levels of splenic Th1 and Th17 cells. These results indicate that KLHTT has immunomodulatory effects in CIA.

Oxidative stress is involved in the pathogenesis of RA [36,43]. In this study, KLHTT significantly decreased the levels of H<sub>2</sub>O<sub>2</sub> (an ROS marker) and MDA (a lipid peroxidation marker) in joint homogenates from CIA mice. MDA-related reactions are highly immunogenic. MDA levels correlate with RA severity and can be used to predict RA severity [43]. In addition, autoreactive T cells such as Th1 and Th17 cells are crucial in the pathogenesis of RA [44]. The newly diagnosed RA patients have higher levels of serum Th1 and Th17 cells [45]. RA patients show increased Th17 cell infiltration in the synovium [46,47]. Infliximab, an anti-TNF- $\alpha$  antibody, promotes Th1 cell apoptosis in RA patients, thus impeding RA progression [48]. Adalimumab, another anti-TNF- $\alpha$  drug, mitigates the homing of Th17 cells to the synovium, consequently improving joint damage [49]. In this study, KLHTT decreased the levels of splenic Th1 and Th17 cells. The levels of pro-inflammatory cytokines, such as IL-1 $\beta$ , IL-6, IL-17, and TNF- $\alpha$ , were also inhibited by KLHTT. Therefore, we suggest that the regulation of Th1 and Th17 cells is also involved in the anti-arthritis effects of KLHTT.

We identified eight flavonoids from KLHTT, including chrysin 6-C-arabinoside-8-C-glucoside, chrysin 6-C-glucoside-8-C-arabinoside, baicalin, norwogonin-7-O- $\beta$ -D-glucuronide, chrysin 7-O- $\beta$ -D-glucuronide, oroxylin A 7-O- $\beta$ -D-glucuronide, wogonoside, and baicalein. Previous studies have reported that baicalin ameliorated CIA in mice by down-regulating Janus kinase 1/signal transducer and activator of transcription 3 signalling and inhibiting IL-17-mediated joint inflammation [50,51]. Baicalein also suppressed human RA fibroblast-like synoviocyte proliferation, induced by IL-1 $\beta$  [52]. Intraperitoneal administration of oroxylin A ameliorated CIA in mice and reduced the levels of IL-1 $\beta$  and IL-6 in human RA fibroblast-like synoviocyte stimulated by TNF- $\alpha$  [53]. Chrysin suppressed nuclear factor- $\kappa$ B and high-mobility group box chromosomal protein in human osteoarthritis chondrocytes stimulated by IL-1 $\beta$  [54,55]. The pathogenesis factors of RA are very complex. A CM formulation that contains various herbs may exhibit synergistic effects [56]. Observably, the anti-arthritis effects of KLHTT were comparable to those of MTX. However, more research is required to prove the synergistic effects of KLHTT in treating RA.



## 5. Conclusions

In summary, our results indicate that KLHTT, a CM formulation, shows significant anti-inflammatory effects, antioxidant activities, and immunomodulatory functions in CIA mice. The present study also demonstrates that KLHTT has potential to treat RA.

**Author Contributions:** Conceptualisation: C.-C.L. and T.-L.H.; conducting experiments: C.-C.C., Y.-R.L., K.-H.L., Y.-H.W. and P.-J.C.; data curation: C.-C.L. and T.-L.H.; formal analysis: C.-C.L. and T.-L.H.; funding acquisition: T.-L.H.; investigation: C.-C.C. and W.-J.C.; methodology: C.-C.C., K.-H.L., Y.-H.W., P.-J.C. and T.-L.H.; project administration: C.-C.L. and T.-L.H.; resources: C.-C.C. and Y.-R.L.; software: C.-C.C. and Y.-R.L.; supervision: C.-C.L. and T.-L.H.; validation: T.-L.H. and S.-H.Y.; visualisation: T.-L.H.; writing—original draft: C.-C.C., W.-J.C. and S.-C.L.; writing—review and editing: C.-C.C., C.-C.L. and T.-L.H. All authors have read and agreed to the published version of the manuscript.

**Funding:** This study was supported by grants from the Ministry of Science Technology (MOST 106-2320-B-255-003-MY3 and MOST 104-2320-B-255-004-MY3), Chang Gung University of Science and Technology (ZRRPF3H0101 and ZRRPF3H0111), and Chang Gung Memorial Hospital (CMRPF1F0011~3, CMRPF1F0061~3, CMRPF1G0241~3, CMRPG3K0161, and BMRP450), Taiwan. The funders had no role in this research.

**Acknowledgments:** The authors thank Ingrid Kuo at the Center for Big Data Analytics and Statistics (Grant CLRPG 3D0045) of Chang Gung Memorial Hospital for help in creating the illustrations.

**Conflicts of Interest:** The authors declare no conflict of interest.

## References

1. Van der Woude, D.; Van der Helm-van Mil, A.H.M. Update on the epidemiology, risk factors, and disease outcomes of rheumatoid arthritis. *Best Pract. Res. Clin. Rheumatol.* **2018**, *32*, 174–187. [[CrossRef](#)] [[PubMed](#)]
2. Katz, P. Causes and consequences of fatigue in rheumatoid arthritis. *Curr. Opin. Rheumatol.* **2017**, *29*, 269–276. [[CrossRef](#)] [[PubMed](#)]
3. DeQuattro, K.; Imboden, J.B. Neurologic Manifestations of Rheumatoid Arthritis. *Rheum. Dis. Clin. N. Am.* **2017**, *43*, 561–571. [[CrossRef](#)] [[PubMed](#)]
4. Krause, A.; Rubbert-Roth, A. Pulmonary involvement in rheumatoid arthritis. *Z. Rheumatol.* **2019**, *78*, 228–235. [[CrossRef](#)]
5. Sinnathurai, P.; Capon, A.; Buchbinder, R.; Chand, V.; Henderson, L.; Lassere, M.; March, L. Cardiovascular risk management in rheumatoid and psoriatic arthritis: Online survey results from a national cohort study. *BMC Rheumatol.* **2018**, *2*, 25. [[CrossRef](#)]
6. Sruamsiri, R.; Kaneko, Y.; Mahlich, J. The underrated prevalence of depression in Japanese patients with rheumatoid arthritis—Evidence from a Nationwide survey in Japan. *BMC Rheumatol.* **2017**, *1*, 5. [[CrossRef](#)]
7. Turk, S.A.; Rasch, L.A.; van Schaardenburg, D.; Lems, W.F.; Sanberg, M.; Van Tuyl, L.H.D.; Ter Wee, M.M. Pain, sleep and emotional well-being explain the lack of agreement between physician- and patient-perceived remission in early rheumatoid arthritis. *BMC Rheumatol.* **2018**, *2*, 16. [[CrossRef](#)]
8. Fazal, S.A.; Khan, M.; Nishi, S.E.; Alam, F.; Zarin, N.; Bari, M.T.; Ashraf, G.M. A Clinical Update and Global Economic Burden of Rheumatoid Arthritis. *Endocr. Metab. Immune Disord. Drug Targets* **2018**, *18*, 98–109. [[CrossRef](#)]
9. Toye, F.; Seers, K.; Barker, K.L. Living life precariously with rheumatoid arthritis—A mega-ethnography of nine qualitative evidence syntheses. *BMC Rheumatol.* **2019**, *3*, 5. [[CrossRef](#)]
10. Yasuda, K.; Takeuchi, Y.; Hirota, K. The pathogenicity of Th17 cells in autoimmune diseases. *Semin. Immunopathol.* **2019**, *41*, 283–297. [[CrossRef](#)]
11. Yayikci, Y.I.; Karadağ, A. Effects of Conventional and Biological Drugs Used for the Treatment of Rheumatoid Arthritis on the Quality of Life and Depression. *Eurasian J. Med.* **2019**, *51*, 12–16. [[CrossRef](#)] [[PubMed](#)]
12. Smolen, J.S.; Aletaha, D.; McInnes, I.B. Rheumatoid arthritis. *Lancet* **2016**, *388*, 2023–2038. [[CrossRef](#)]
13. Hu, X.X.; Wu, Y.J.; Zhang, J.; Wei, W. T-cells interact with B cells, dendritic cells, and fibroblast-like synoviocytes as hub-like key cells in rheumatoid arthritis. *Int. Immunopharmacol.* **2019**, *70*, 428–434. [[CrossRef](#)] [[PubMed](#)]
14. Cecchi, I.; De La Rosa, I.A.; Menegatti, E.; Roccatello, D.; Collantes-Estevez, E.; Lopez-Pedraza, C.; Barbarroja, N. Neutrophils: Novel key players in Rheumatoid Arthritis. Current and future therapeutic targets. *Autoimmun. Rev.* **2018**, *17*, 1138–1149. [[CrossRef](#)]

15. Siouti, E.; Andreakos, E. The many facets of macrophages in rheumatoid arthritis. *Biochem. Pharmacol.* **2019**, *165*, 152–169. [[CrossRef](#)]
16. Wang, S.P.; Lin, S.C.; Li, S.; Chao, Y.H.; Hwang, G.Y.; Lin, C.C. Potent Antiarthritic Properties of Phloretin in Murine Collagen-Induced Arthritis. *Evid. Based Complement. Altern. Med.* **2016**, *2016*, 9831263. [[CrossRef](#)]
17. Aletaha, D.; Neogi, T.; Silman, A.J.; Funovits, J.; Felson, D.T.; Bingham, C.O., III; Birnbaum, N.S.; Burmester, G.R.; Bykerk, V.P.; Cohen, M.D.; et al. 2010 Rheumatoid arthritis classification criteria: An American College of Rheumatology/European League Against Rheumatism collaborative initiative. *Arthritis Rheumatol.* **2010**, *62*, 2569–2581. [[CrossRef](#)]
18. Hadjigogos, K. The role of free radicals in the pathogenesis of rheumatoid arthritis. *Painminerva Med.* **2003**, *45*, 7–13.
19. Ali, A.M.; Habeeb, R.A.; El-Azizi, N.O.; Khattab, D.A.; Abo-Shady, R.A.; Elkabarity, R.H. Níveis de óxido nítrico mais elevados estão associados à atividade da doença em pacientes egípcios com artrite reumatoide. *Rev. Bras. Reumatol.* **2014**, *54*, 446–451. [[CrossRef](#)]
20. Mateen, S.; Rehman, T.; Shahzad, S.; Naeem, S.S.; Faizy, A.F.; Khan, A.Q.; Khan, M.S.; Husain, F.M.; Moin, S. Anti-oxidant and anti-inflammatory effects of cinnamaldehyde and eugenol on mononuclear cells of rheumatoid arthritis patients. *Eur. J. Pharmacol.* **2019**, *852*, 14–24. [[CrossRef](#)]
21. Caplazi, P.; Baca, M.; Barck, K.H.; Carano, R.A.D.; Devoss, J.; Lee, W.P.; Bolon, B.; Diehl, L. Mouse Models of Rheumatoid Arthritis. *Vet. Pathol.* **2015**, *52*, 819–826. [[CrossRef](#)] [[PubMed](#)]
22. Sun, Y.-W.; Yin, H.-B.; Chen, Y.-G.; Zhang, L. Kan-Lu-Hsiao-Tu-Tan treats rheumatism: 4 cases reports (Print in Chinese). *Int. J. Tradit. Chin. Med.* **2015**, *37*, 461–462. [[CrossRef](#)]
23. Wei, S.-C.; Yue, D.-H.; Yu, L.-H.; Wei, J.; Teng, S.-Y.; Bi, Y. Research Overview of Ganlu Xiaodu Pills in Treating Disease with Syndrome of Damp-heat. *Clin. J. Tradit. Chin. Med.* **2017**, *29*, 735–738. [[CrossRef](#)]
24. Xu, Y. Variant Ganlu Xiaodu Dan treating chronic dermatitis in 47 cases (Print in Chinese). *Clin. J. Tradit. Chin. Med.* **2010**, *22*, 514–515.
25. Chiang, C.-C.; Cheng, W.-J.; Lin, C.-Y.; Lai, K.-H.; Ju, S.-C.; Lee, C.; Yang, S.-H.; Hwang, T.-L. Kan-Lu-Hsiao-Tu-Tan, a traditional Chinese medicine formula, inhibits human neutrophil activation and ameliorates imiquimod-induced psoriasis-like skin inflammation. *J. Ethnopharmacol.* **2020**, *246*, 112246. [[CrossRef](#)]
26. Chen, D.Y.; Lin, C.C.; Chen, Y.M.; Chao, Y.H.; Yang, D.H. Dextromethorphan Exhibits Anti-inflammatory and Immunomodulatory Effects in a Murine Model of Collagen-Induced Arthritis and in Human Rheumatoid Arthritis. *Sci. Rep.* **2017**, *7*, 11353. [[CrossRef](#)]
27. Hsieh, Y.J.; Yen, M.H.; Chiang, Y.W.; Yeh, C.F.; Chiang, L.C.; Shieh, D.E.; Yeh, I.; Chang, J.S. Gan-Lu-Siao-Du-yin, a prescription of traditional Chinese medicine, inhibited enterovirus 71 replication, translation, and virus-induced cell apoptosis. *J. Ethnopharmacol.* **2016**, *185*, 132–139. [[CrossRef](#)]
28. Zhi, H.-J.; Zhu, H.-Y.; Zhang, Y.; Lu, Y.; Li, H.; Chen, D.-F. In vivo effect of quantified flavonoids-enriched extract of *Scutellaria baicalensis* root on acute lung injury induced by influenza A virus. *Phytomedicine* **2019**, *57*, 105–116. [[CrossRef](#)]
29. Xu, J.; Yu, Y.; Shi, R.; Xie, G.; Zhu, Y.; Wu, G.; Qin, M. Organ-Specific Metabolic Shifts of Flavonoids in *Scutellaria baicalensis* at Different Growth and Development Stages. *Molecules* **2018**, *23*, 428. [[CrossRef](#)]
30. Sameena, Y.; Chandrasekaran, S.; Enoch, I.V.M.V. Inclusion complexation between baicalein and  $\beta$ -cyclodextrin and the influence of  $\beta$ -cyclodextrin on the binding of baicalein with DNA: A spectroscopic approach. *J. Biomol. Struct. Dyn.* **2016**, *34*, 1395–1408. [[CrossRef](#)]
31. Qiao, X.; Li, R.; Song, W.; Miao, W.-J.; Liu, J.; Chen, H.-B.; Guo, D.-A.; Ye, M. A targeted strategy to analyze untargeted mass spectral data: Rapid chemical profiling of *Scutellaria baicalensis* using ultra-high performance liquid chromatography coupled with hybrid quadrupole orbitrap mass spectrometry and key ion filtering. *J. Chromatogr. A* **2016**, *1441*, 83–95. [[CrossRef](#)] [[PubMed](#)]
32. Yu, C.; Zhang, Z.; Zhang, H.; Zhen, Z.; Calway, T.; Wang, Y.; Yuan, C.S.; Wang, C.Z. Pretreatment of baicalin and wogonoside with glycoside hydrolase: A promising approach to enhance anticancer potential. *Oncol. Rep.* **2013**, *30*, 2411–2418. [[CrossRef](#)] [[PubMed](#)]
33. Ye, G.; Tang, Y.H.; Wang, G.Y.; Li, Z.X.; Zhu, H.Y.; Ma, C.H.; Sun, Z.L.; Huang, C.G. Characterization of the multiple absorbed constituents in rats after oral administration of Chai-Huang decoction by liquid chromatography coupled with electrospray-ionization mass spectrometry. *Chem. Biodivers.* **2010**, *7*, 2917–2930. [[CrossRef](#)] [[PubMed](#)]

34. Singh, R.; Wu, B.; Tang, L.; Liu, Z.; Hu, M. Identification of the Position of Mono-O-glucuronide of Flavones and Flavonols by Analyzing Shift in Online UV Spectrum ( $\lambda_{\text{max}}$ ) Generated from an Online Diode Array Detector. *J. Agric. Food Chem.* **2010**, *58*, 9384–9395. [\[CrossRef\]](#) [\[PubMed\]](#)
35. Miyoshi, M.; Liu, S. Collagen-Induced Arthritis Models. *Methods Mol. Biol.* **2018**, *1868*, 3–7. [\[CrossRef\]](#)
36. Mateen, S.; Moin, S.; Khan, A.Q.; Zafar, A.; Fatima, N. Increased Reactive Oxygen Species Formation and Oxidative Stress in Rheumatoid Arthritis. *PLoS ONE* **2016**, *11*, e0152925. [\[CrossRef\]](#)
37. McInnes, I.B.; O'Dell, J.R. State-of-the-art: Rheumatoid arthritis: Figure 1. *Ann. Rheum. Dis.* **2010**, *69*, 1898–1906. [\[CrossRef\]](#)
38. Noack, M.; Miossec, P. Selected cytokine pathways in rheumatoid arthritis. *Semin. Immunopathol.* **2017**, *39*, 365–383. [\[CrossRef\]](#)
39. Feldmann, M.; Maini, S.R.N. Role of cytokines in rheumatoid arthritis: An education in pathophysiology and therapeutics. *Immunol. Rev.* **2008**, *223*, 7–19. [\[CrossRef\]](#)
40. Lubberts, E.; van den Berg, W.B. Cytokines in the pathogenesis of rheumatoid arthritis and collagen-induced arthritis. *Adv. Exp. Med. Biol.* **2003**, *520*, 194–202. [\[CrossRef\]](#)
41. Kim, W.U.; Yoo, W.H.; Park, W.; Kang, Y.M.; Kim, I.S.; Park, J.H.; Lee, S.S.; Joo, Y.S.; Min, J.K.; Hong, Y.S.; et al. IgG antibodies to type II collagen reflect inflammatory activity in patients with rheumatoid arthritis. *J. Rheumatol.* **2000**, *27*, 575–581. [\[PubMed\]](#)
42. Nandakumar, K.S.; Bäcklund, J.; Vestberg, M.; Holmdahl, R. Collagen type II (CII)-specific antibodies induce arthritis in the absence of T or B cells but the arthritis progression is enhanced by CII-reactive T cells. *Arthritis Res. Ther.* **2004**, *6*, R544–R550. [\[CrossRef\]](#) [\[PubMed\]](#)
43. Quinonez-Flores, C.M.; Gonzalez-Chavez, S.A.; Del Rio Najera, D.; Pacheco-Tena, C. Oxidative Stress Relevance in the Pathogenesis of the Rheumatoid Arthritis: A Systematic Review. *BioMed Res. Int.* **2016**, *2016*, 6097417. [\[CrossRef\]](#) [\[PubMed\]](#)
44. Damsker, J.M.; Hansen, A.M.; Caspi, R.R. Th1 and Th17 cells: Adversaries and collaborators. *Ann. N. Y. Acad. Sci.* **2010**, *1183*, 211–221. [\[CrossRef\]](#)
45. Bazzazi, H.; Aghaei, M.; Memarian, A.; Asgarian-Omran, H.; Behnampour, N.; Yazdani, Y. Th1-Th17 Ratio as a New Insight in Rheumatoid Arthritis Disease. *Iran. J. Allergy Asthma Immunol.* **2018**, *17*, 68–77.
46. Awasthi, A.; Kuchroo, V.K. Th17 cells: From precursors to players in inflammation and infection. *Int. Immunol.* **2009**, *21*, 489–498. [\[CrossRef\]](#)
47. Kotake, S.; Udagawa, N.; Takahashi, N.; Matsuzaki, K.; Itoh, K.; Ishiyama, S.; Saito, S.; Inoue, K.; Kamatani, N.; Gillespie, M.T.; et al. IL-17 in synovial fluids from patients with rheumatoid arthritis is a potent stimulator of osteoclastogenesis. *J. Clin. Investig.* **1999**, *103*, 1345–1352. [\[CrossRef\]](#)
48. Herman, S.; Zurgil, N.; Machlav, S.; Shinberg, A.; Langevitz, P.; Ehrenfeld, M.; Deutsch, M. Distinct Effects of Anti-Tumor Necrosis Factor Combined Therapy on TH1/TH2 Balance in Rheumatoid Arthritis Patients. *Clin. Vaccine Immunol.* **2011**, *18*, 1077–1082. [\[CrossRef\]](#)
49. Aerts, N.E.; De Knop, K.J.; Leysen, J.; Ebo, D.G.; Bridts, C.H.; Weyler, J.J.; Stevens, W.J.; De Clerck, L.S. Increased IL-17 production by peripheral T helper cells after tumour necrosis factor blockade in rheumatoid arthritis is accompanied by inhibition of migration-associated chemokine receptor expression. *Rheumatology* **2010**, *49*, 2264–2272. [\[CrossRef\]](#)
50. Yang, X.; Yang, J.; Zou, H. Baicalin inhibits IL-17-mediated joint inflammation in murine adjuvant-induced arthritis. *Clin. Dev. Immunol.* **2013**, *2013*, 268065. [\[CrossRef\]](#)
51. Wang, C.; Song, Y.; Wang, X.; Mao, R.; Song, L. Baicalin Ameliorates Collagen-Induced Arthritis Through the Suppression of Janus Kinase 1 (JAK1)/Signal Transducer and Activator of Transcription 3 (STAT3) Signaling in Mice. *Med Sci. Monit.* **2018**, *24*, 9213–9222. [\[CrossRef\]](#) [\[PubMed\]](#)
52. Chen, S.; Yang, Y.; Feng, H.; Wang, H.; Zhao, R.; Liu, H. Baicalein inhibits interleukin-1 $\beta$ -induced proliferation of human rheumatoid arthritis fibroblast-like synoviocytes. *Inflammation* **2014**, *37*, 163–169. [\[CrossRef\]](#) [\[PubMed\]](#)
53. Wang, Y.-L.; Gao, J.-M.; Xing, L.-Z. Therapeutic potential of Oroxylin A in rheumatoid arthritis. *Int. Immunopharmacol.* **2016**, *40*, 294–299. [\[CrossRef\]](#)
54. Zhang, C.; Yu, W.; Huang, C.; Ding, Q.; Liang, C.; Wang, L.; Hou, Z.; Zhang, Z. Chrysin protects human osteoarthritis chondrocytes by inhibiting inflammatory mediator expression via HMGB1 suppression. *Mol. Med. Rep.* **2018**, *19*, 1222–1229. [\[CrossRef\]](#) [\[PubMed\]](#)

55. Zheng, W.; Tao, Z.; Cai, L.; Chen, C.; Zhang, C.; Wang, Q.; Ying, X.; Hu, W.; Chen, H. Chrysin Attenuates IL-1 $\beta$ -Induced Expression of Inflammatory Mediators by Suppressing NF- $\kappa$ B in Human Osteoarthritis Chondrocytes. *Inflammation* **2017**, *40*, 1143–1154. [[CrossRef](#)] [[PubMed](#)]
56. Ho, L.J.; Chang, W.L.; Chen, A.; Chao, P.; Lai, J.H. Differential immunomodulatory effects by Tripterygium wilfordii Hook f-derived refined extract PG27 and its purified component PG490 (triptolide) in human peripheral blood T cells: Potential therapeutics for arthritis and possible mechanisms explaining in part Chinese herbal theory “Junn-Chenn-Zuou-SS”. *J. Transl. Med.* **2013**, *11*, 294. [[CrossRef](#)]

**Publisher’s Note:** MDPI stays neutral with regard to jurisdictional claims in published maps and institutional affiliations.



© 2020 by the authors. Licensee MDPI, Basel, Switzerland. This article is an open access article distributed under the terms and conditions of the Creative Commons Attribution (CC BY) license (<http://creativecommons.org/licenses/by/4.0/>).



# Electrochemical immunosensor for serum parathyroid hormone using voltammetric techniques and a portable simulator

Guan-Cheng Chen<sup>a</sup>, Chi-Hsien Liu<sup>a, b, c, d, \*</sup>, Wei-Chi Wu<sup>d, e</sup>

<sup>a</sup> Department of Chemical and Materials Engineering, Chang Gung University, 259 Wen-Hwa First Road, Kwei-Shan, Tao-Yuan, 333, Taiwan

<sup>b</sup> Research Center for Chinese Herbal Medicine and Research Center for Food and Cosmetic Safety, College of Human Ecology, Chang Gung University of Science and Technology, 261 Wen-Hwa First Road, Taoyuan, Taiwan

<sup>c</sup> Department of Chemical Engineering, Ming Chi University of Technology, 84 Gung-Juan Road, New Taipei City, Taiwan

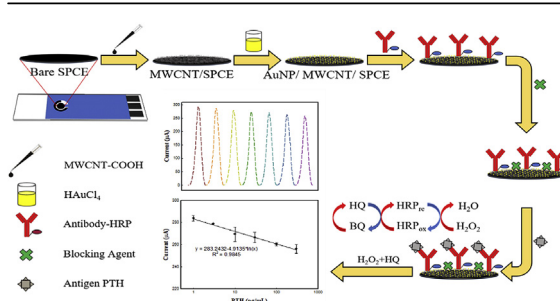
<sup>d</sup> Department of Ophthalmology, Chang Gung Memorial Hospital, Linkou, 5 Fu-Hsing Street, Taoyuan, Taiwan

<sup>e</sup> College of Medicine, Chang Gung University, 259 Wen-Hwa First Road, Taoyuan, Taiwan

## HIGHLIGHTS

- Immunosensors based on screen-printed electrodes were explored to detect human parathyroid hormone (PTH).
- A quick analysis of PTH can be applied as the electrochemical immunosensing platform for point-of-care testing.
- This PTH immunosensor had a PTH detection limit of 0.065 pg/ml using the square wave voltammetry.

## GRAPHICAL ABSTRACT



## ARTICLE INFO

### Article history:

Received 27 October 2020

Received in revised form

25 November 2020

Accepted 27 November 2020

Available online 30 November 2020

### Keywords:

Parathyroid hormone

Immunosensor

Voltammetry

## ABSTRACT

An electrochemical platform based on a screen-printed carbon electrode (SPCE) is developed to detect parathyroid hormone (PTH). A nanocomposite of multi-walled carbon nanotube (MWCNT) and gold nanoparticles (AuNP) was deposited on the SPCE to immobilize antibodies and horseradish peroxidase (HRP). MWCNT improved the stability and conductivity of the immunosensor because of its good electron-transfer ability and tubular structure. The AuNP not only provided a large surface area for antibody immobilization, but it also enhanced the electrochemical signal for enzyme-linked immunosensing. Cyclic voltammetry showed both electron transfer and the effective surface area were increased on the modified electrode. The characteristics of the modified SPCE were assayed by Raman spectroscopy, scanning electron microscopy, atomic force microscopy, and electrochemical techniques. The linear detection range of this PTH immunosensor was within 1–300 pg/ml, and the electrochemical performance was not affected by interference from protein components in human serum. After storage at 4 °C for 28 days, 85% PTH sensing ability of this immunosensor was maintained compared to the freshly prepared one using the SWV and DPV methods. The relative standard deviations of all measurements were within 3–8% for both voltammetric methods. These results indicated the developed immunosensor had good stability and reproducibility. This PTH immunosensor had a detection limit of 0.886 and 0.065 pg/ml for the differential pulse voltammetry and square wave voltammetry, respectively. We

\* Corresponding author. Department of Chemical and Materials Engineering, Chang Gung University, 259 Wen-Hwa First Road, Kwei-Shan, Tao-Yuan, 333, Taiwan.

E-mail address: [CHL@mail.cgu.edu.tw](mailto:CHL@mail.cgu.edu.tw) (C.-H. Liu).



provided a quick analysis of serum PTH which might be used as an electrochemical immunosensing platform for point-of-care testing.

© 2020 Elsevier B.V. All rights reserved.

## 1. Introduction

Electrochemical immunosensors combine the ability to recognize targets with electrochemical transduction [1]. Amplifying the enzymatic signal using peroxidase or phosphatase in the immunosensor can generate a redox reaction for quantitative assay. One popular targeting strategy is to use a “sandwich” with two capture- and detection-antibodies [2]. However, a single antibody-enzyme complex on the electrode has been reported to recognize the target and amplify the current signal at the same time [3]. The formation of the target-antibody complex results in a stereo hindrance of the electron transfer between the enzyme and electrode surface, causing a decreased current and increased impedance [4]. The target binding to the antibody-enzyme complex also alters the enzyme conformation, and it reduces catalytic activity, thus providing a sensing response [5,6]. Moreover, antibody immobilization and signal amplification are two key factors in immunosensing targets at ultra-low concentrations. Nanomaterials can amplify the electrochemical signal using different mechanisms, including a large active surface, extraordinary electron-transfer ability, and multivalent affinity with the enzyme and antibody [7,8].

Parathyroid hormone (PTH) is an important factor in maintaining the concentrations of calcium, phosphate, and vitamin D metabolites in blood and regulating the activity of bone cells. Intact PTH is the 84 amino acid peptide. Full-length PTH and its metabolized fragments, including N-terminal, C-terminal, and other length fragments, circulate in the body. However, fragments of PTH accumulate in patients with cardiovascular disease, chronic kidney diseases, and several cancers. PTH testing is routinely performed to monitor patients with chronic kidney disease and mineral and bone disorders [9]. However, a discrepancy between PTH assays has been reported. This could be attributed to different technologies and instruments [10,11]. The immunological detection of PTH has been investigated using radioimmunoassay [12], magnetic nanoparticle and actuation [13], liquid chromatography-mass spectrometry [14], and capillary electrophoresis-electrospray ionization-mass spectrometry [15], and electrochemical sensors [16]. Mass spectrometry is a sensitive and accurate test that provides repeated performance. However, the drawbacks include the need for trained personnel and expensive instruments. Alternatively, electrochemical biosensors provide fast, low-cost, efficient, and on-site testing. Screen-printed carbon electrodes (SPCEs) are also mass-produced and disposable. A few electrochemical methods for PTH detection have been reported recently [17–22]. Applying SPCE technology in point-of-care testing is attractive because of its miniaturization and affordable cost [23,24].

Voltammetric techniques alter the electrode potential, using a specific waveform to measure the current signal in the reaction. Differential pulse voltammetry (DPV) and square wave voltammetry (SWV) generate the potential pattern using two steps: pre-concentration and dissolution [25]. The SWV provides waveforms similar to those from DPV, except that the pre-concentration and pulse period are of equal duration in DPV [26]. Voltammetry is one of the most popular technologies used in electrochemical immunosensors. The voltammetric methods adjust the decay rates of the charging and faradaic currents, and they scan the potential using different waveforms. This increased ratio of faradaic to non-

faradaic current allows for a lower detection limit and higher sensitivity in reversible and irreversible reactions [27]. Differential pulse methods require a few seconds for an assay; while electrochemical impedance methods might need several minutes or longer to generate signals. The voltammetric device is also cost-effective, compared to the impedance device [28]. We systematically developed and characterized PTH immunosensors using a nanocomposite on the SPCE surface. The performance of this immunosensor was evaluated by using DPV and SWV techniques in the physiological PTH range.

## 2. Experimental section

### 2.1. Reagents and materials

Potassium ferricyanide ( $K_3Fe(CN)_6$ ), sodium phosphate dibasic ( $Na_2HPO_4$ , 99%), sodium phosphate monobasic ( $NaH_2PO_4$ ), gold (III) chloride trihydrate (99%), bovine serum albumin, glucose, Insulin, human immunoglobulin, lysozyme, hydroquinone (HQ), 1-Ethyl-3-(3-dimethylaminopropyl) carbodiimide hydrochloride (EDC) and N-hydroxysuccinimide (NHS),  $\alpha$ -terpineol and ascorbic acid were purchased from Sigma-Aldrich (St. Louis, Missouri, USA). The human serum was collected from male donors within USA and purchased from Sigma-Aldrich (H4522). Carboxylated MWCNTs (10–30  $\mu m$ , UniRegion, Taipei, Taiwan) and  $H_2O_2$  (30%, Fluka, MI, USA) were used in this study. Polyclonal rabbit anti-human PTH antibody (AB51516), goat antibody to rabbit IgG conjugated horseradish peroxidase (HRP) (AB6721) and human PTH (AB51234) were from Abcam (MA, USA). Disposable SPCEs (TE-100) were purchased from Zensor (Taichung, Taiwan). PTH ELISA kit (SEK13192), anti-PTH capture antibody (13192-MM02), anti-PTH detection antibody (13192-T08), and recombinant PTH (aa 32–65, GST Tag, 13192-H09E) were purchased from Sino Biological (Beijing, China). Phosphate buffered saline (0.1 M PBS, pH 7.4) and ultrapure water with  $18.2 M\Omega cm^{-1}$  resistance (Leifei, Taoyuan City, Taiwan) were used in this study. All reagents are used without further purification.

### 2.2. Apparatus

A contact angle analyzer (Phoenix mini, Surface Electro Optics, Seoul, Korea) used the sessile drop method at room temperature with ultrapure water droplets to determine the hydrophobicity of the surfaces on the modified SPCE. The surfaces of SPCEs were investigated by using a metallurgical microscope (Leica, DM2700 M, Wetzlar, Germany) and an atomic force microscope (Park systems, XE-Series, South Korea). The elemental analysis was investigated by using a scanning electron microscope (HITACHI S-4700, Tokyo, Japan) equipped with an energy-dispersive spectrometer (Bruker, XFlash Detector 5030, Berlin, Germany). The D and G bands of carbon on the surfaces of SPCEs were analyzed by the Raman mapping system (UninanoTech, Yongin, South Korea). The electrochemical properties of the immunosensing SPCEs were analyzed using an ECAS 100 Electrochemical Simulator (Zensor).

### 2.3. Fabrication of PTH biosensor

MWCNTs and  $\alpha$ -terpineol were used to modify the SPCE surface. MWCNTs (10 mg/ml) were well dispersed in  $\alpha$ -terpineol with vortex and a probe-type sonicator. MWCNT in  $\alpha$ -terpineol (1  $\mu$ L) was coated on the SPCE surface and dried at 50 °C for 15 h [29]. 100  $\mu$ L of 10 mM of HAuCl<sub>4</sub> in 0.1 M PBS was loaded on the SPCE for the nanocomposite preparation. The controlled potential and duration of the electrodeposition were set at –200 mV and 300 s. After the modified SPCE was washed with ultrapure water, it was ready for antibody immobilization. The biotinized antibody (220 ng/ml) and streptavidin-HRP (500-fold dilution) were mixed at 4 °C for 30 min to form an antibody-HRP complex. The working electrodes were treated for 30 min at 4 °C using a mixture of 2.5  $\mu$ L of 64 mg/ml EDC, 2.5  $\mu$ L of 128 mg/ml NHS, and 5  $\mu$ L of antibody-HRP. After they were rinsed, the SPCEs were incubated for 30 min with 100  $\mu$ L blocking reagents. Finally, the immuno-electrodes were rinsed and stored at 4 °C for further experiments. All measurements were performed in triplicate to obtain the standard deviation.

### 2.4. PTH immunosensing procedure

Human serum spiked with PTH was used to evaluate the performance of the PTH immunosensors. The PTH sample was loaded onto two electrodes, incubated at room temperature for 30 min, and rinsed with water. DPV and SWV techniques were applied to determine the effects of the PTH dosage on electrochemical signals by using 100  $\mu$ L of 5 mM H<sub>2</sub>O<sub>2</sub>/5 mM HQ mixture in pH 7.4 PBS. DPV was carried out using the following parameters: modulation time = 0.09 s, interval time = 0.15 s, initial potential = 0.4 V, end potential = –0.35 V, step potential = 0.0125 V, modulation amplitude = 0.3 V, and standby potential = 0 V. The setting condition of SWV was as follows: modulation time = 0.15 s, interval time = 0.3 s, initial potential = 0.3 V, end potential = –0.6 V, step potential = 0.0125 V, modulation amplitude = 0.3 V, standby potential = 0 V. Assays were performed in triplicate. An ELISA assay was performed according to the manufacturer's protocol. The claimed detection range was between 0.3 ng/ml and 20 ng/ml. The limit of detection (LOD) was calculated using the following equation: LOD = 3  $\times$  SD/m; where m is the slope of the calibration curve, and standard deviation (SD) is from the peak current of the blank with three repeats.

### 2.5. Characterization of the electrochemical properties of the electrodes

#### 2.5.1. Measurement of electron transfer rate constant by CV

The effective surface area (A) can be obtained using the Randles-Sevcik equation.

$$I_p = 0.4463 (n^3 F^3 v D_0 / RT)^{1/2} A C_0 \quad (1)$$

where  $I_p$  refers to the peak current;  $D_0$  is the diffusion coefficient ( $7.0 \times 10^{-6}$  cm<sup>2</sup> s<sup>–1</sup>);  $C$  is the concentration of ferricyanide (mol cm<sup>–3</sup>);  $v$  is the scan rate (mV s<sup>–1</sup>). The electron transfer rate constant ( $k_s$ , cm s<sup>–1</sup>) of the SPCEs was estimated by CV scanning over a potential range from –500 to +600 mV at different scan rates varying from 10 to 100 mV s<sup>–1</sup> in 3 mM ferricyanide. The calculation of  $k_s$  by CV data is based on the Nicholson method as shown in Eqs. (2) and (3) [30].

$$\Psi = (-0.6288 + 0.021\Delta E_p)/(1 - 0.017\Delta E_p) \quad (2)$$

$$\Psi = k_s [\pi D n v F / (RT)]^{-1/2} \quad (3)$$

where  $\Psi$ , a dynamic parameter, is a function of the peak potential difference ( $\Delta E_p$ );  $D$  is the diffusion coefficient;  $n$  is the number of electrons transferred in the reaction;  $F$  is the Faraday constant;  $V$  is the scanning rate;  $R$  is the gas constant; and  $T$  is the temperature in Kelvin.

#### 2.5.2. IT estimation of rate constant (Kcat) between HRP and H<sub>2</sub>O<sub>2</sub>/HQ

To prove the hypothesis that immune-complex of antibody-HRP and PTH would decrease the activity of HRP, chronoamperometry was applied for the evaluation of the catalytic rate constant ( $K_{cat}$ , M<sup>–1</sup> s<sup>–1</sup>). The current density ( $j$ ) is proportional to the square roots of time and  $K_{cat}$  in the following equation [31,32].

$$j_{cat}/j_d = (\pi C K_{cat})^{1/2} t^{1/2} \quad (4)$$

where  $j_{cat}$  and  $j_d$  are the current density in the presence and absence of H<sub>2</sub>O<sub>2</sub>/HQ, respectively. The catalytic activity of HRP ( $K_{cat}$ ) can be obtained from the slope of  $t^{1/2}$  versus  $j_{cat}/j_d$  in the linear fitting equation. The apparent Michaelis–Menten constant ( $K_{app}^M$ ), an indication of the enzyme–substrate kinetics, was obtained according to Lineweaver–Burk plot [33]:

$$1/I_{ss} = 1/I_{max} + K_{app}^M / I_{max} C \quad (5)$$

The steady state currents ( $I_{ss}$ ) were obtained using five different H<sub>2</sub>O<sub>2</sub>/HQ concentrations ( $C$ ) loaded on SPCE surface. The theoretical maximum current ( $I_{max}$ ) and the  $K_{app}^M$  value were obtained by analysis of the slope and the intercept in Lineweaver–Burk plot ( $1/I_{ss}$  versus  $1/C$ ).

## 3. Results and discussion

### 3.1. Characterization of prepared SPCE

Fig. 1 shows the procedure for fabricating the immunosensor by nanomaterials, antibody and enzymes. The microscopic surface images of modified SPCEs from FE-SEM showed their nanostructure and morphological characteristics. The working electrode was coated using MWCNTs suspended in terpeneol. Depositing AuNP on the bare SPCE created a petal-like gold structure that ranged between 300 nm and 400 nm by using HAuCl<sub>4</sub> dissolved in the 0.1 M PBS. In contrast, AuNP on the MWCNT-modified SPCE formed the isolated nanoparticles with 100 nm–200 nm on the tubular structure. The small-size AuNP provided more surface area for antibody binding and more transfer sites for electrons in the redox reaction. The energy dispersive spectrometer showed that MWCNT (carbon) and gold nanoparticles were successfully modified on the surfaces (Fig. 2). Finally, the gold- and MWCNT-modified SPCEs were chosen for further experiments. The D/G ratio in the Raman spectrum indicated the graphite ( $sp^2$ ) content in the working electrodes. Raman spectra of bare SPCE, AuNP/SPCE, and MWCNT-AuNP/SPCE are shown in Fig. 2(D). The bare SPCE containing graphite represented the typical Raman spectrum. G-band at 1576 cm<sup>–1</sup> resulted from in-plane vibrations of carbon atoms bonded with  $sp^2$ . The peak, which appeared at 1347 cm<sup>–1</sup>, is known as the D-band. It is caused by out-of-plane vibration of  $sp^3$  carbon atoms [34]. Fig. 2(I) shows that the G/D ratio of AuNP/SPCE was slightly lower than the ratio obtained from bare SPCE and AuNP/MWCNT/SPCE. The p-doping effects of AuNP may hinder the plane  $sp^2$  vibration of C=C bonds and reduced the G/D ratio. After coating the surface of the electrode with MWCNT, the G/D ratio changed from 0.96 to 1.03. This indicated that coating with MWCNT slightly increased the  $sp^2$  vibration on the electrode. Finally, the band shift of D-band because of the p-doping effect imposed by AuNP has

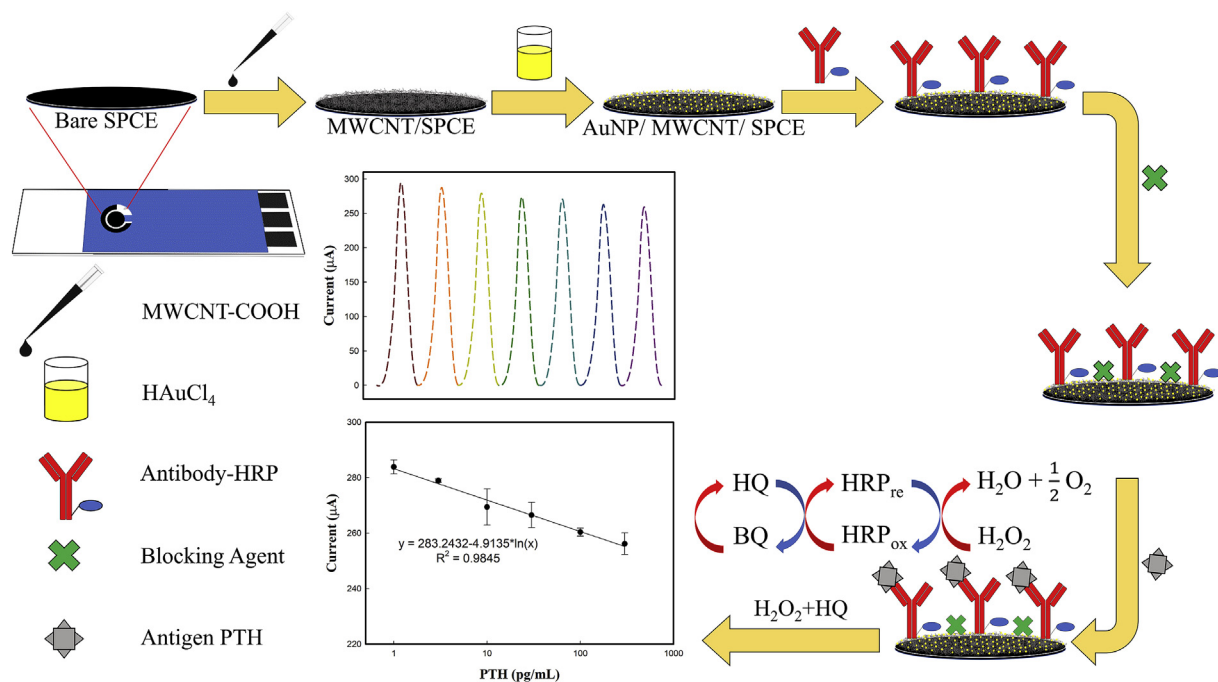


Fig. 1. Schematic diagram showing the fabrication process and immuno-electrochemical reaction on the PTH immunosensor.

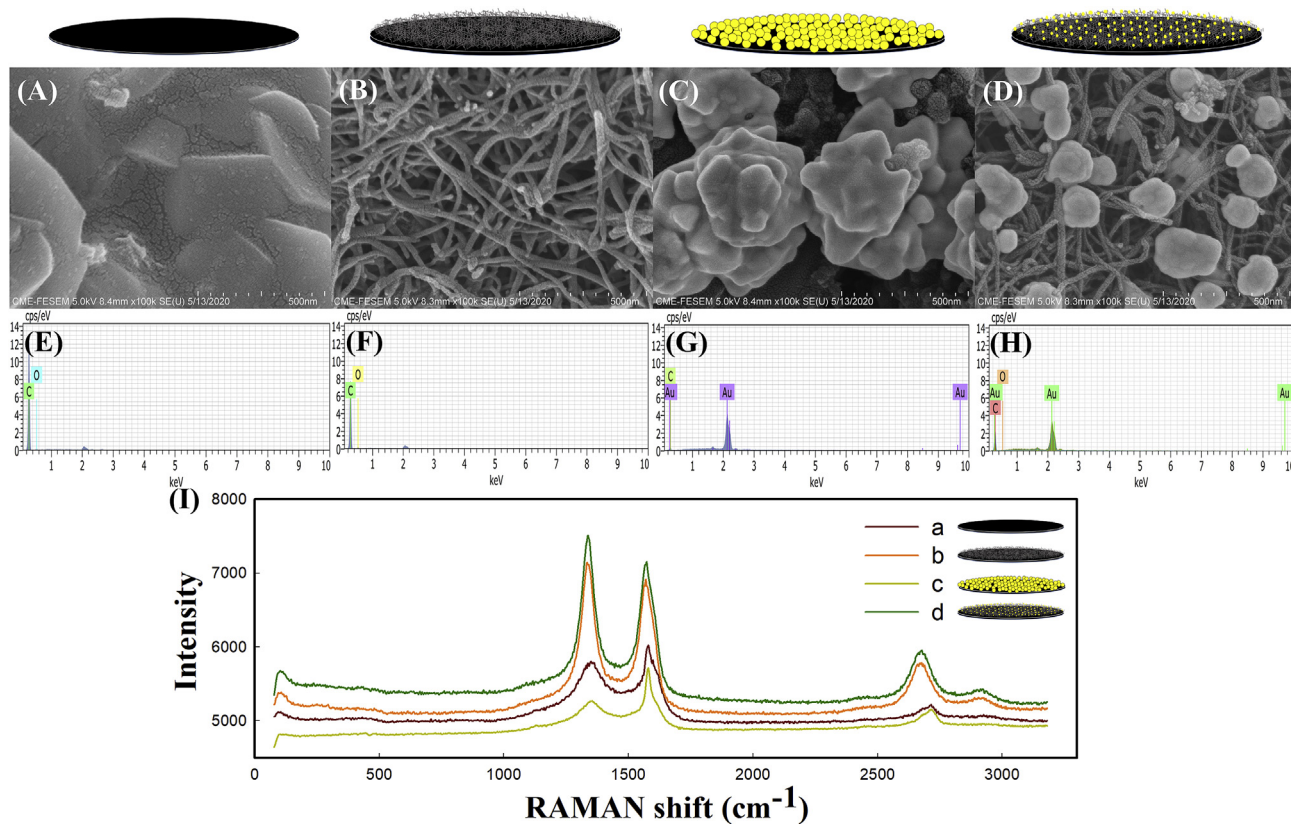


Fig. 2. SEM images of bare and modified SPCE. (A) Bare SPCE, (B) MWCNT/SPCE, (C) AuNP/SPCE, (D) AuNP/MWCNT/SPCE, scale bar: 0.5 μm. Energy dispersive X-Ray spectroscopy results: (E) Bare SPCE, (F) MWCNT/SPCE, (G) AuNP/SPCE, (H) MWCNT-AuNP/SPCE show the elemental mapping of modified SPCE surfaces for 'C' and 'Au' elements. The inclusion of MWCNT enhanced the carbon content from 7 to 47% and the Au content was 53%. (I) Raman spectra on the modified SPCE surfaces: (a) Bare SPCE, (b) MWCNT/SPCE, (c) AuNP/SPCE, (d) AuNP/MWCNT/SPCE.



been reported [35]. SPCEs modified at every step were analyzed to evaluate their physicochemical and electrochemical properties. Anti-HRP antibody and HRP were used to detect, quantify, and amplify the PTH in serum using DPV and SWV methods, as described in the next section.

### 3.2. Electrochemical characterization of modified SPCE

#### 3.2.1. Optimization and characterization of SPCE modification

The electrochemical behaviors of the prepared SPCEs are summarized in Table S1. Fig. 3(A) and (B) show that AuNP/MWCNT/SPCE had a higher peak current than that of AuNP/SPCE. After AuNP was deposited on the MWCNT surfaces, the potential change ( $\Delta E_p$ ) of the redox peaks decreased slightly and the peak current increased. This indicated that the structure of AuNP/MWCNT/SPCE not only increased the effective surface area but it also enhanced the electron transfer between the redox probe and the electrode surface. Compared with a bare SPCE, the electrodes modified with AuNP and MWCNT had more electrical conductivity and they could transfer more redox probes. This enhanced performance might be because AuNP provided a larger surface area, while MWCNTs enhanced network connectivity and enabled faster electronic transmission.

Cyclic voltammograms showed the symmetric current pattern of AuNP/MWCNT/SPCE at different scan rates (Fig. 3). The symmetric peaks in the shape of CV indicated a reversible electrochemical reaction. The scan rate of voltammetry can be used to evaluate the charge transfer process involved in the electrode-

electrolyte interface. The square root of the scan rate was plotted against the peak current in Fig. 3 (D). This reversible behavior indicated the fast kinetics of electron transfer using redox-active ferricyanide on the electrode. The data included the linear relationship of scan rate current, and the symmetric voltammograms indicated the improvement in the quality of the developed SPCE. The measured current peak depends on variables such as electrode materials, reaction time, potential, solvent, surface properties of the compound, electrode area, pH, and temperature. To achieve maximum sensitivity, the optimal immobilization condition should be investigated [26]. The reaction time for antibody-HRP conjugated with carboxylated MWCNT using EDC/NHC crosslinker was optimized. The signal-to-blank ratio ( $S/B = \Delta I_{100}/\Delta I_0$ ) indicates the signal enhancing effect of the electrochemical method [6,36]. Our S/B results showed that the ratio leveled off after 30 min of conjugation using both DPV and SWV methods (Fig. S1). The duration of the immune-complex formation highly influenced the detection performance of the immunosensor [3]. Fig. S2 shows that the 30-min duration of immune-complex formation yielded the highest S/B ratio with both DPV and SWV methods. Therefore, the 30-min duration for antibody-HRP loading and immune-complex formation was chosen for the SPCE modification.

#### 3.2.2. Blocking effects on the immunosensors

The blocking process is vital for immunosensor detection because it protects the immobilized antibodies, and it avoids nonspecific binding of impurities on electrodes. That affects detection specificity and the response current [4]. Efficient blocking

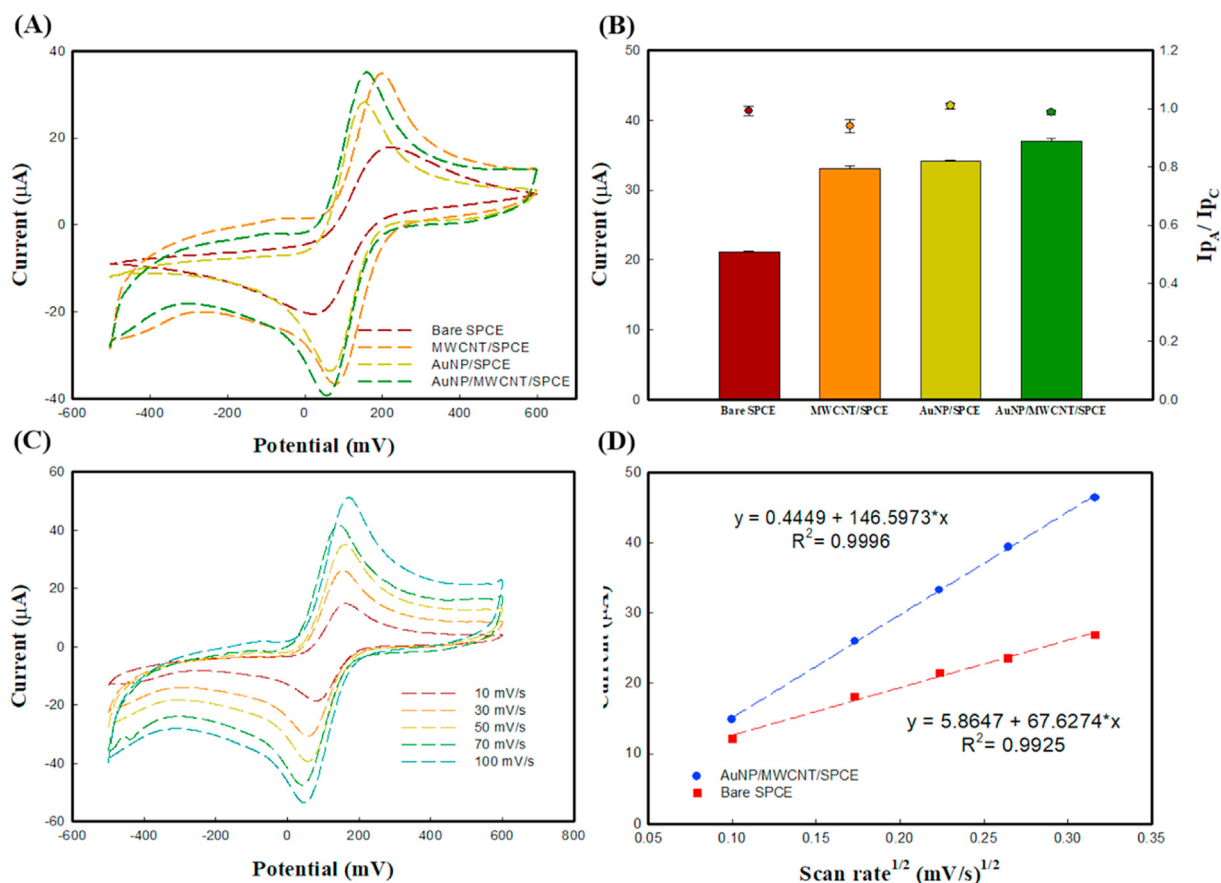


**Fig. 3.** (A) Cyclic voltammograms (CV) of bare SPCE, AuNP/SPCE, MWCNT/SPCE, AuNP/MWCNT/SPCE. (B) Maximal currents and  $I_{pA}/I_{pC}$  ratio of different SPCEs by CV using 3 mM ferricyanide in PBS. (C) CV of AuNP/MWCNT/SPCE measured in potential window of -500 to +600 mV vs. Ag pseudo-reference electrode at different scan rates (from inner to outer): 10, 30, 50, 70, 100  $mV s^{-1}$ . (D) Linear relationship of scan rate on the anodic peak current about bare SPCE and AuNP/MWCNT/SPCE.

reagents exhibited lower steric barriers and allowed the recognition of a specific recognition of an analyte at an extremely low concentration. Therefore, 11 blocking agents were coated on the biosensors and evaluated for their ability to prevent the non-specific binding from serum proteins. The chemicals tested included 5% PPS, DL-dithiothreitol, potassium thiocyanate, L-cysteine, 3-mercaptopropionic acid, 2-mercaptoethanol, polyethylene glycol, polyvinyl pyrrolidone, polyvinyl alcohol, bovine serum albumin, and 100% human serum. The current ratio of pure human serum and 100 pg/ml PTH-spiked serum indicated signal enhancement. The S/B from SWV was 501.3%, and it was 335.2% from DPV (Fig. 4) using PTH-spiked human serum. The human serum had the largest blocking effect (S/B ratio), which was validated by both methods.

### 3.3. Estimation the activity of antibody-HRP on SPCE

To prove that enzyme activity was related to target binding, the amperometric *i*-t response and Eq. (4) were applied to calculate the enzyme's *K*<sub>cat</sub> [37]. Fig. 5 shows the dose effects of H<sub>2</sub>O<sub>2</sub>/HQ (0 mM, 2 mM, 4 mM, and 8 mM) on amperometric response and *K*<sub>cat</sub> value. When the PTH concentration was increased from 0 to 300 pg/ml, HRP's *K*<sub>cat</sub> on SPCE decreased from 1083.980 M<sup>-1</sup>s<sup>-1</sup> to 787.181 M<sup>-1</sup>s<sup>-1</sup> (Table S2). This phenomenon suggested that the immuno-complex affected the redox reaction of the HRP. As the concentration of PTH increased, the thickness of immuno-complexes increased. Sequentially the catalytic activity decreased, and the peak current decreased linearly in 10 pg/ml–300 pg/ml PTH. The non-electroactive immunocomplex also acted as a blocking layer against electron- and mass-transfer to insulate the electron transfer of the H<sub>2</sub>O<sub>2</sub>/HQ. This can be ascribed to the formation of the antigen-antibody complex, which insulated the conductive support and hindered the transfer of electrons to the electrode [3]. Researchers have shown that higher concentrations of antigen decreased the current signal of the HRP-labeled antibody. This was because the antigen occupied the limited binding sites of antibody-HRP to form immuno-complex [3,38]. The specific interaction between antigen and antibody led to the formation of immuno-layers on the electrode. Antibody-HRP and PTH complex increased the steric hindrance, which decreased the electrode active sites and reduced the charge transfer rate. Therefore, there was a decrease in the peak current and redox reaction of H<sub>2</sub>O<sub>2</sub>/HQ.

### 3.4. Effects of capture antibody concentration using SWV/DPV methods

Fig. 6 shows the linear response curve of currents and PTH concentration in a dose-dependent manner. Two calibration curves were obtained by SWV and DPV methods in the serum PTH range (1–300 pg/ml) using three independent replicates. The linear regression equation was expressed as:  $I (\mu A) = 274.29 - 8.72 \ln [PTH]$ , and the limit of detection for DPV was 0.886 pg/ml (Fig. 6 (A, B)). The linear regression equation of PTH concentration for SWV was expressed as:  $I (\mu A) = 742.36 - 35.96 \ln [PTH]$ , and the limit of detection was 0.065 pg/ml. The performance of PTH immunosensors was compared using ELISA, SWV, and DPV methods (Table 1). Our immunosensors had better recovery and precision than the traditional ELISA kit. PTH recovery results are 81%–113% using DPV, 93%–106% using SWV, and 15%–291% using ELISA. These results showed that the developed immunosensors had good precision and accuracy as compared to the traditional ELISA method.

Table 2 summarizes the comparison of our immunosensors to the sensors reported in the literature [6,17,18,22]. These immunosensors adopted impedance, chronocoulogram, and CV methods to quantify PTH. Our proposed SPCE immunosensor could detect PTH in serum using both DPV and SWV methods with fast and precise performance. Since intact PTH has a half-life of several minutes and its normal level in serum is around 13 pg/ml–85 pg/ml [39], the detection specificity and sensitivity of this immunosensor could apply to the physiological condition, and it has good repeatability.

### 3.5. Interference assay and storage stability of the immunosensor

The 100 pg/ml of PTH-spiked serum was used as the control for the SWV and DPV methods. Some salts, amino acids, and organic acids have been used as interfering substances to evaluate their effect on PTH detection [19]. To evaluate the selectivity of the developed SPCE, six interfering compounds—insulin, lysozyme (LYZ), ascorbic acid (ASA), immunoglobulin (IgG), ovalbumin (OVA), and serum albumin (BSA)—were dissolved in human serum and evaluated. Fig. 7 shows that the signal change caused by these six high-concentration interfering substances was significantly smaller than the signal from the 100 pg/ml of PTH-spiked serum. The signal sensitivity of the PTH immunosensor against the interfering

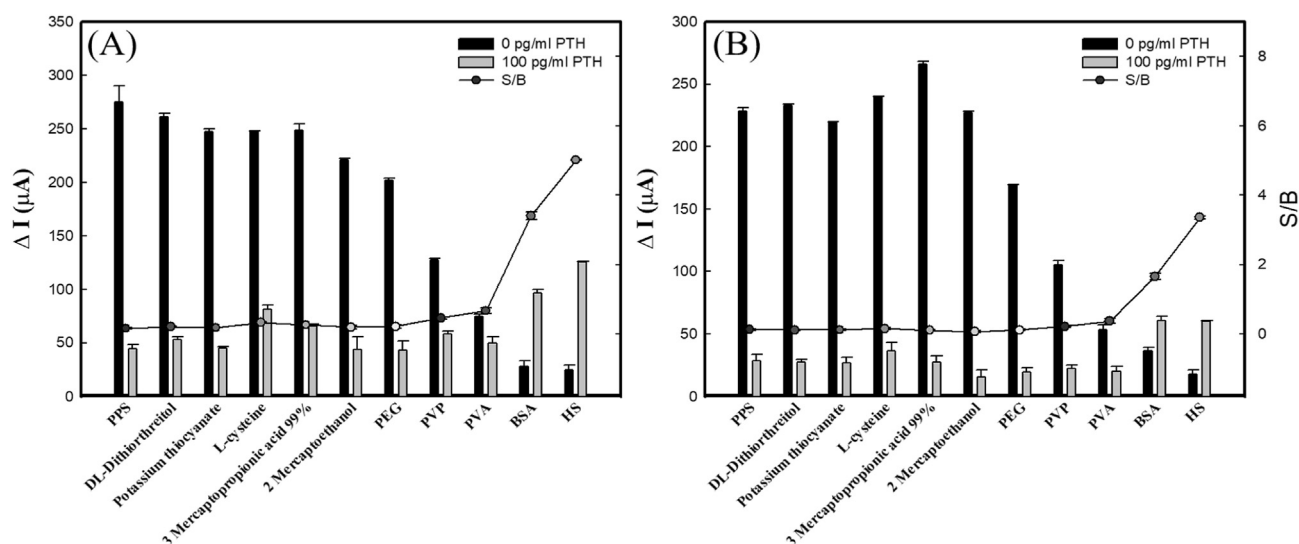
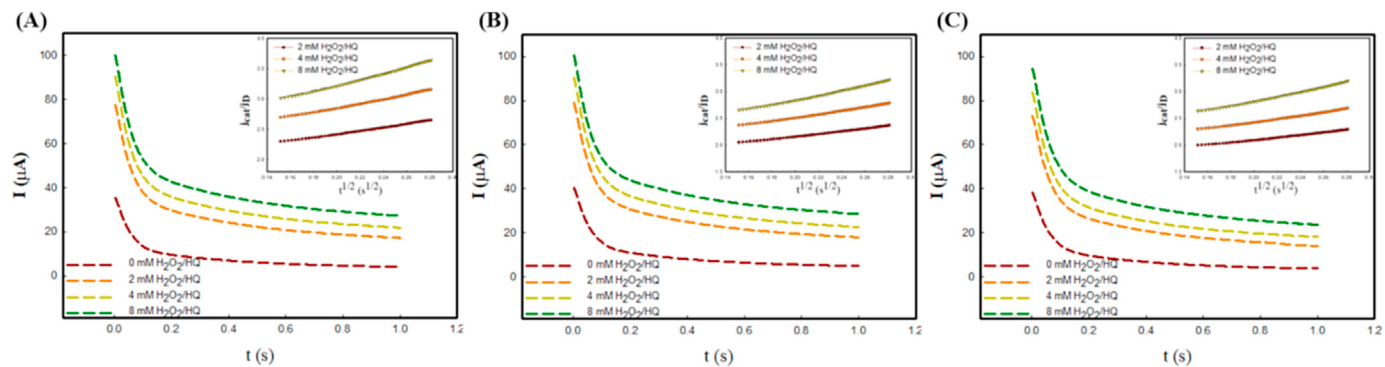
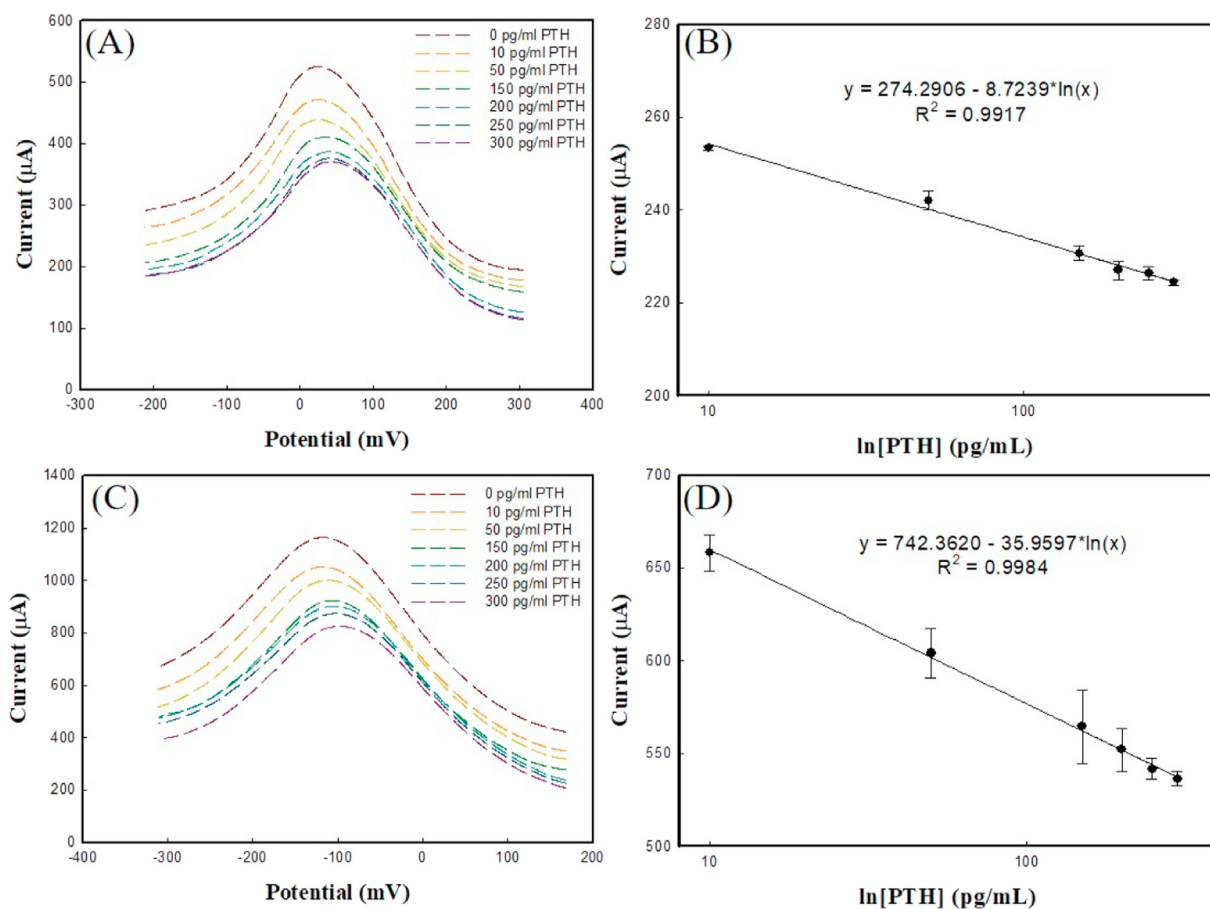


Fig. 4. Effects of blocking agents on signal of signal-to-blank ratio using the SWV (A) and DPV (B) methods (n = 3).





**Fig. 5.** Effects of PTH on antibody-HRP activity using (A) 0 pg/ml, (B) 30 pg/ml, (C) 300 pg/ml PTH at constant  $V$  ( $-420$  mV). In the inset, the linear response is shown by fixing the potential  $-420$  mV for 10 s.



**Fig. 6.** Standard curve of PTH dosage in human serum using the immunosensors of DPV (A, B) and SWV (C, D) ( $n = 3$ ). Immunosensor was treated with different concentrations of PTH for 30.0 min, and then use DDW to wash away the uncaptured PTH. The 5 mM  $H_2O_2$ /HQ mixture was used in the SWV and DPV methods.

**Table 1**  
Performance of PTH immunosensors using SWV and DPV versus ELISA.

PTH spiked serum (pg/ml)	DPV (pg/ml)	DPV recovery (%)	SWV (pg/ml)	SWV recovery (%)	ELISA (pg/ml)	ELISA recovery (%)
10	11.05	110.47	10.44	104.43	–15.69	–156.93
50	40.5	81.00	46.88	93.76	79.39	158.78
150	148.47	98.98	141.27	94.18	171.27	114.18
200	226.03	113.02	199.07	99.54	172.88	86.44
250	243.98	97.59	265.34	106.14	266.36	106.54
300	306.85	102.28	307.76	102.59	291.46	97.15

**Table 2**  
Literature survey of PTH immunosensors.

Materials used in electrode	Range (fg/ml)	LOD (fg/ml)	RSD (%)	Storage (day)	Principle	Reference
Ag, avidin, BSA-modified ITO electrode	$10^2$ – $10^5$	100	1.10	—	chronocoulogram	[22]
cyanopropyltrimethoxy-silane ITO-PET electrode	$5 \times 10^{-2}$ – $1.5 \times 10^2$	0.026	2.59	70	EIS, CV	[17]
polydopamine, organic particles glassy carbon electrode.	$5 \times 10^4$ – $8 \times 10^6$	$1.7 \times 10^4$	5.76	—	electrochemi-luminescence	[19]
Au–Pt hybrid disk electrode	$10^3$ – $10^7$	360	8.0	10	DPV	[6]
mercaptohexanol epichlorhydrina-ethanolamine gold electrode	$10^2$ – $6 \times 10^2$	0.1	8.00	—	EIS	[18]
AuNP/MWCNT/SPCE	$10^3$ – $3 \times 10^5$	65	2.97	28	SWV	This work
AuNP/MWCNT/SPCE	$10^3$ – $3 \times 10^5$	886	7.77	28	DPV	This work

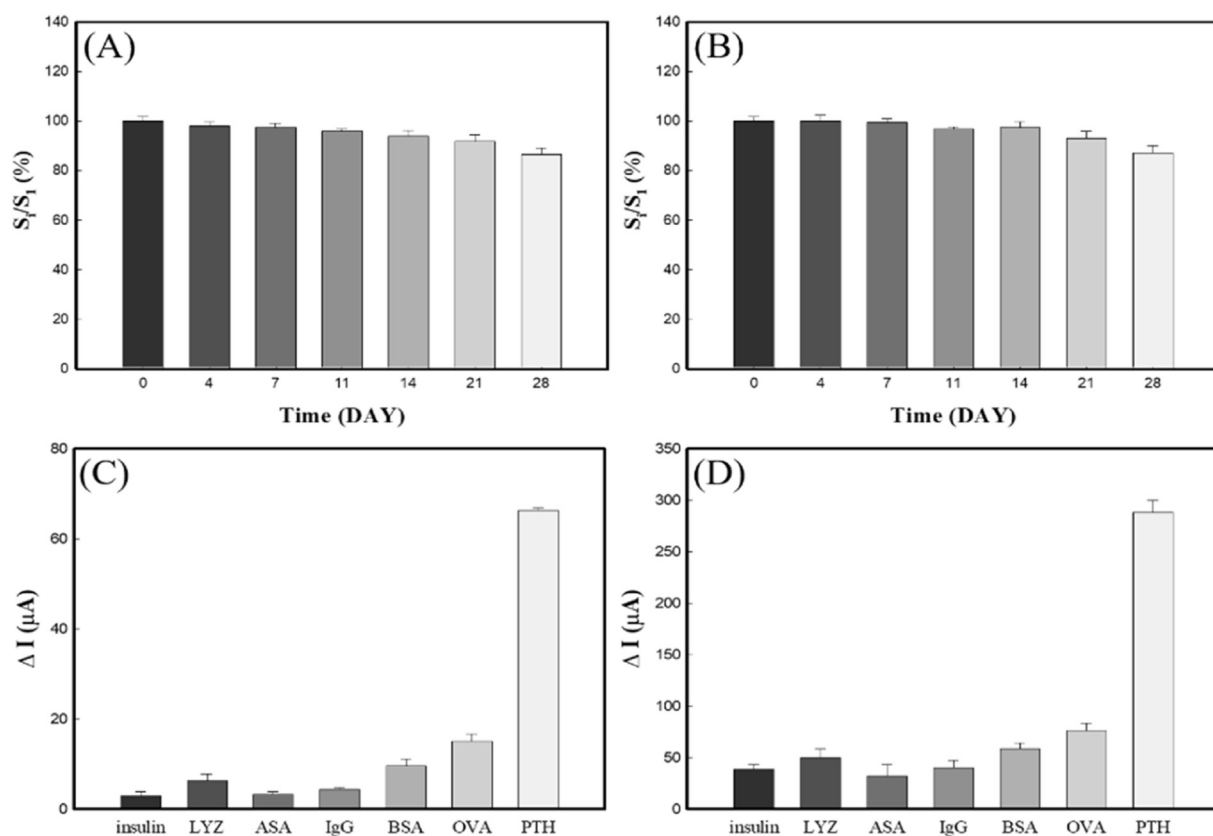


**Fig. 7.** Stability test of immunosensor using the SWV (A) and DPV (B) methods. Effects of interference molecules on immunosensor using the SWV (C) and DPV (D) methods ( $n = 3$ ).

compounds was 3.77-fold and 4.42-fold using the SWV and DPV methods. The results showed that the influence of interfering substances on the immunosensor was relatively small. The prepared immunosensor was stored at 4 °C for 28 days to evaluate its storage stability. PTH induction was evaluated based on the redox current of DPV and SWV. A signal of 100 pg/ml PTH using the freshly prepared immunosensor was set as a 100% control. After 28 days of storage, more than 85% of PTH sensing ability had been maintained as compared with freshly prepared SPCEs using the SWV and DPV methods (Fig. 7). The reproducibility and stability of the immunosensor were independently evaluated using 21 SPCEs over the 28-day storage. The relative standard deviations (RSD) of all measurements were within 3–8% for both voltammetric methods (Fig. 7 (A)(B) and Table 2). These results showed that this immunosensor had good stability and low interference under serum-spiked conditions as compared to those of the Au–Pt hybrid disk electrode [6]. Thus, a facile SPCE modification that meets the requirements for low cost, high sensitivity, bedside detection, and low-volume sample for PTH immunoassay has been successfully developed in this study.

#### 4. Conclusion

The nanocomposite of MWCNT and AuNP was used to fabricate the immune-SPCE and to provide the surface for the antibody-HRP conjugation. Two voltammetric methods, SWV and DPV, were compared, and their serum PTH assay was evaluated. We created a facile protocol for MWCNT and AuNP deposition on the surface of the working electrode. The surface was suitable for immobilizing the antibody-HRP and detecting PTH. The advantages of the nanocomposite include a large surface area and a connection network for fast electron transfer and antibody immobilization. We provided evidence of the rapid analysis of serum PTH, which can be used for clinical assays. The advantages of the developed PTH immunosensor include easy immobilization, low-cost and disposable electrode, label-free detection, and quick detection within a few minutes as compared to the expensive instruments used in the hospitals. The developed immunosensors showed good stability and reproducibility, and the detection limits of serum PTH were 0.065 pg/ml and 0.886 pg/ml using the SWV and DPV methods. Finally, the SWV method had a lower detection limit and higher

sensitivity as compared to the DPV method.

### CRedit authorship contribution statement

**Guan-Cheng Chen:** Funding acquisition, Formal analysis, Data curation, acquisition of data, analysis, interpretation of data. **Chi-Hsien Liu:** Conceptualization, Data curation, Writing - original draft, Writing - review & editing, Conception and design of study, interpretation of data, drafting the manuscript, revising the manuscript. **Wei-Chi Wu:** Conceptualization, Writing - original draft, Conception and design of study, drafting the manuscript.

### Declaration of competing interest

The authors declare that they have no known competing financial interests or personal relationships that could have appeared to influence the work reported in this paper.

### Acknowledgements

We express gratitude to Ministry of Science and Technology (MOST 108-2221-E-182-039), Chang Gung University (BMRP 758) and Chang Gung Memorial Hospital (2J0161, 2H0072, 2H0073) for funding and supporting this research. We appreciate the critical comments from Prof. Purnendu Parhi at Ravenshaw University, India.

### Appendix A. Supplementary data

Supplementary data to this article can be found online at <https://doi.org/10.1016/j.aca.2020.11.045>.

### References

- [1] C. Kokkinos, A. Economou, Emerging trends in biosensing using stripping voltammetric detection of metal-containing nanolabels – a review, *Anal. Chim. Acta* 961 (2017) 12–32.
- [2] X. Pei, B. Zhang, J. Tang, B. Liu, W. Lai, D. Tang, Sandwich-type immunosensors and immunoassays exploiting nanostructure labels: a review, *Anal. Chim. Acta* 758 (2013) 1–18.
- [3] J.T.J. Chen, F. Yan, H. Ju, A gold nanoparticles/sol-gel composite architecture for encapsulation of immunoconjugate for reagentless electrochemical immunoassay, *Biomaterials* 27 (2006) 2313–2321.
- [4] X.Y.W. Wen, C. Zhu, D. Du, Y. Lin, Recent advances in electrochemical immunosensors, *Anal. Chim. Acta* 89 (2017) 138–156.
- [5] T.Y.H. Jia, Y. Zuo, W. Wang, J. Xu, L. Lu, P. Li, Immunosensor for  $\alpha$ -fetoprotein based on a glassy carbon electrode modified with electrochemically deposited N-doped graphene, gold nanoparticles and chitosan, *Microchim. Acta* 184 (2017) 3747–3753.
- [6] A.G.A.K. Yagati, S.G. Chavan, C. Baek, M.-H. Lee, J. Min, Nanostructured Au-Pt hybrid disk electrodes for enhanced parathyroid hormone detection in human serum, *Bioelectrochemistry* 128 (2019) 165–174.
- [7] L. Wang, Y. Zhang, A. Wu, G. Wei, Designed graphene-peptide nanocomposites for biosensor applications: a review, *Anal. Chim. Acta* 985 (2017) 24–40.
- [8] T. Hong, W. Liu, M. Li, C. Chen, Recent advances in the fabrication and application of nanomaterial-based enzymatic microsystems in chemical and biological sciences, *Anal. Chim. Acta* 1067 (2019) 31–47.
- [9] L.O.K. Tan, S.K. Sethi, S. Saw, Comparison of the Elecsys PTH(1–84) assay with four contemporary second generation intact PTH assays and association with other biomarkers in chronic kidney disease patients, *Clin. Biochem.* 46 (2013) 781–786.
- [10] E.D.A.M. Ercan, E. Avci, Ç. Yücel, E.F. Oğuz, T. Turhan, M. Serdar, Determining biological variation of serum parathyroid hormone in healthy adults, *Biochem. Med.* 29 (2019), 030702.
- [11] M.S. Shawky, Quick parathyroid hormone assays: a comprehensive review of their utility in clinical practice, *Hormones* 15 (2016) 355–367.
- [12] S.E. Rodgers, J.L. Lew, The parathyroid hormone assay, *Endocr. Pract.* 17 (Suppl 1) (2011) 2–6.
- [13] W.U. Dittmer, P. de Kievit, M.W.J. Prins, J.L.M. Vissers, M.E.C. Mersch, M.F.W.C. Martens, Sensitive and rapid immunoassay for parathyroid hormone using magnetic particle labels and magnetic actuation, *J. Immunol. Methods* 338 (2008) 40–46.
- [14] R. MacNeill, R. Stromeyer, B. Urbanowicz, V. Acharya, M. Moussallie, LC-MS/MS quantification of parathyroid hormone fragment 1–34 in human plasma, *Bioanalysis* 5 (2013) 415–422.
- [15] L. Nyssen, M. Fillet, E. Cavalier, A.C. Servais, Highly sensitive and selective separation of intact parathyroid hormone and variants by sheathless CE-ESI-MS/MS, *Electrophoresis* 40 (2019) 1550–1557.
- [16] A.K. Yagati, A. Go, S.G. Chavan, C. Baek, M.H. Lee, J. Min, Nanostructured Au-Pt hybrid disk electrodes for enhanced parathyroid hormone detection in human serum, *Bioelectrochemistry* 128 (2019) 165–174.
- [17] I. Uludag, M. Sezginurk, An ultrasensitive electrochemical immunosensor platform based on disposable ITO electrode modified by 3-CPTMS for early detection of parathyroid hormone, *Turk. J. Chem.* 43 (2019) 1697–1710.
- [18] K.Y.H.M. Özcan, C. Çakar, T. Aydin, E. Asav, A. Sağiroğlu, M.K. Sezginurk, Ultrasensitive impedimetric biosensor fabricated by a new immobilisation technique for parathyroid hormone, *Appl. Biochem. Biotechnol.* 176 (2015) 1251–1262.
- [19] Y.L.S. Lia, Q. Ma, A novel polydopamine electrochemiluminescence organic nanoparticle-based biosensor for parathyroid hormone detection, *Talanta* 202 (2019) 540–545.
- [20] H.Y.K.H.-U. Kim, A. Kulkarni, C. Ahn, Y. Jin, Y. Kim, K.-N. Lee, M.-H. Lee, T. Kim, A sensitive electrochemical sensor for in vitro detection of parathyroid hormone based on a MoS<sub>2</sub>-graphene composite, *Sci. Rep.* 6 (2016) 34587.
- [21] M.K.S.H.M. Ozcan, Detection of parathyroid hormone using an electrochemical impedance biosensor based on PAMAM dendrimers, *Biotechnol. Prog.* 31 (2015) 815–822.
- [22] P.N.A. Bhatia, G. Kim, J. Kim, N.-S. Lee, Y.H. Yoon, H. Yang, Ultrasensitive detection of parathyroid hormone through fast silver deposition induced by enzymatic nitroso reduction and redox cycling, *ACS Sens.* 4 (2019) 1641–1647.
- [23] E.C. Rama, A. Costa-García, Screen-printed electrochemical immunosensors for the detection of cancer and cardiovascular biomarkers, *Electroanalysis* 28 (2016) 1700–1715.
- [24] V. Serafini, G. Martínez-García, J. Aznar-Poveda, J.A. Lopez-Pastor, A.J. Garcia-Sanchez, J. Garcia-Haro, S. Campuzano, P. Yáñez-Sedeño, J.M. Pingarrón, Determination of progesterone in saliva using an electrochemical immunosensor and a COTS-based portable potentiostat, *Anal. Chim. Acta* 1049 (2019) 65–73.
- [25] X.L.Y. Lu, C. Niyungeko, J. Zhou, J. Xu, G. Tian, A review of the identification and detection of heavy metal ions in the environment by voltammetry, *Talanta* 178 (2018) 324–338.
- [26] N. Abo El-Maali, Voltammetric analysis of drugs, *Bioelectrochemistry* 64 (2004) 99–107.
- [27] B.S.A. Chen, Electrochemical sensing and biosensing based on square wave voltammetry, *Anal. Methods* 5 (2013).
- [28] C.C.L.Y. Dai, Detection of 17 beta-estradiol in environmental samples and for health care using a single-use, cost-effective biosensor based on differential pulse voltammetry (DPV), *Biosensors (Basel)* (2017) 7.
- [29] Y.M.S. Ito, Porous carbon layers for counter electrodes in dye-sensitized solar cells: recent advances and a new screen-printing method, *Pure Appl. Chem.* 83 (2011) 2089–2106.
- [30] X. He, S.J. Chang, K. Settu, C.J. Chen, J.T. Liu, An anti-HCT-interference glucose sensor based on a fiber paper-based screen-printed carbon electrode, *Sensor. Actuatur. B Chem.* (2019) 297.
- [31] H. Hosseini, H. Ahmar, A. Dehghani, A. Bagheri, A.R. Fakhari, M.M. Amini, Au-SH-SiO<sub>2</sub> nanoparticles supported on metal-organic framework (Au-SH-SiO<sub>2</sub>@Cu-MOF) as a sensor for electrocatalytic oxidation and determination of hydrazine, *Electrochim. Acta* 88 (2013) 301–309.
- [32] Y. Wang, W. Wang, G. Li, Q. Liu, T. Wei, B. Li, C. Jiang, Y. Sun, Electrochemical detection of L-cysteine using a glassy carbon electrode modified with a two-dimensional composite prepared from platinum and Fe<sub>3</sub>O<sub>4</sub> nanoparticles on reduced graphene oxide, *Microchimica Acta* 183 (2016) 3221–3228.
- [33] J.Y. Wang, L.C. Chen, K.C. Ho, Synthesis of redox polymer nanobeads and nanocomposites for glucose biosensors, *ACS Appl. Mater. Interfaces* 5 (2013) 7852–7861.
- [34] Y. Wang, Y. Qu, G. Liu, X. Hou, Y. Huang, W. Wu, K. Wu, C. Li, Electrochemical immunoassay for the prostate specific antigen using a reduced graphene oxide functionalized with a high molecular-weight silk peptide, *Microchimica Acta* 182 (2015) 2061–2067.
- [35] S. Singh, S.K. Tuteja, D. Sillu, A. Deep, C.R. Suri, Gold nanoparticles-reduced graphene oxide based electrochemical immunosensor for the cardiac biomarker myoglobin, *Microchimica Acta* 183 (2016) 1729–1738.
- [36] J. Wang, J. Lu, S. Dong, N. Zhu, E. Gyimah, K. Wang, Y. Li, Z. Zhang, An ultrasensitive electrochemical biosensor for detection of microRNA-21 based on redox reaction of ascorbic acid/iodine and duplex-specific nuclease assisted target recycling, *Biosens. Bioelectron.* 130 (2019) 81–87.
- [37] D. Shi, Y. Sun, L. Lin, C. Shi, G. Wang, X. Zhang, Naked-eye sensitive detection of alkaline phosphatase (ALP) and pyrophosphate (PPi) based on a horseradish peroxidase catalytic colorimetric system with Cu(II), *Analyst* 141 (2016) 5549–5554.
- [38] F. Zhu, G. Zhao, W. Dou, Voltammetric sandwich immunoassay for *Cronobacter sakazakii* using a screen-printed carbon electrode modified with horseradish peroxidase, reduced graphene oxide, thionine and gold nanoparticles, *Mikrochim. Acta* 185 (2017) 45.
- [39] F.B.J.-C. Souberbielle, M.-L. Piketty, C. Cormier, S. Minisola, E. Cavalier, How the reference values for serum parathyroid hormone concentration are (or should be) established? *J. Endocrinol. Invest.* 40 (2017) 241–256.

## Research Article

# ***Helminthostachys zeylanica* Water Extract Ameliorates Airway Hyperresponsiveness and Eosinophil Infiltration by Reducing Oxidative Stress and Th2 Cytokine Production in a Mouse Asthma Model**

**Wen-Chung Huang,<sup>1,2</sup> Nai-Chun Ting,<sup>3</sup> Yu-Ling Huang,<sup>4</sup> Li-Chen Chen<sup>1,2,5</sup> ,  
Chwan-Fwu Lin<sup>1,6,7</sup> , and Chian-Jiun Liou<sup>2,8</sup> **

<sup>1</sup>Graduate Institute of Health Industry Technology, Research Center for Food and Cosmetic Safety, and Research Center for Chinese Herbal Medicine, College of Human Ecology, Chang Gung University of Science and Technology, Taoyuan City 33303, Taiwan

<sup>2</sup>Division of Allergy, Asthma, and Rheumatology, Department of Pediatrics, Chang Gung Memorial Hospital, Linkou, Guishan Dist., Taoyuan City 33303, Taiwan

<sup>3</sup>Graduate Institute of Clinical Medical Sciences, Chang Gung University, Taoyuan City 33303, Taiwan

<sup>4</sup>National Research Institute of Chinese Medicine, Ministry of Health and Welfare, Beitou, Taipei, Taiwan

<sup>5</sup>Department of Pediatrics, New Taipei Municipal Tu Cheng Hospital, Chang Gung Memorial Hospital and Chang Gung University, Taiwan

<sup>6</sup>Department of Cosmetic Science, Research Center for Food and Cosmetic Safety, and Research Center for Chinese Herbal Medicine, College of Human Ecology, Chang Gung University of Science and Technology, Taoyuan City 33303, Taiwan

<sup>7</sup>Department of Anesthesiology, Chang Gung Memorial Hospital, Linkou, Guishan Dist., Taoyuan City 33303, Taiwan

<sup>8</sup>Department of Nursing, Division of Basic Medical Sciences, Research Center for Chinese Herbal Medicine, Chang Gung University of Science and Technology, Taoyuan City 33303, Taiwan

Correspondence should be addressed to Li-Chen Chen; [lcchen@adm.cgmh.org.tw](mailto:lcchen@adm.cgmh.org.tw), Chwan-Fwu Lin; [cflin@mail.cgust.edu.tw](mailto:cflin@mail.cgust.edu.tw), and Chian-Jiun Liou; [ccliu@mail.cgust.edu.tw](mailto:ccliu@mail.cgust.edu.tw)

Received 21 May 2020; Revised 26 September 2020; Accepted 29 October 2020; Published 2 December 2020

Academic Editor: Cristina Contreras

Copyright © 2020 Wen-Chung Huang et al. This is an open access article distributed under the Creative Commons Attribution License, which permits unrestricted use, distribution, and reproduction in any medium, provided the original work is properly cited.

*Helminthostachys zeylanica* is a traditional folk herb used to improve inflammation and fever in Taiwan. Previous studies showed that *H. zeylanica* extract could ameliorate lipopolysaccharide-induced acute lung injury in mice. The aim of this study was to investigate whether *H. zeylanica* water (HZW) and ethyl acetate (HZE) extracts suppressed eosinophil infiltration and airway hyperresponsiveness (AHR) in asthmatic mice, and decreased the inflammatory response and oxidative stress in tracheal epithelial cells. Human tracheal epithelial cells (BEAS-2B cells) were pretreated with various doses of HZW or HZE (1 µg/ml–10 µg/ml), and cell inflammatory responses were induced with IL-4/TNF-α. In addition, female BALB/c mice sensitized with ovalbumin (OVA), to induce asthma, were orally administered with HZW or HZE. The result demonstrated that HZW significantly inhibited the levels of proinflammatory cytokines, chemokines, and reactive oxygen species in activated BEAS-2B cells. HZW also decreased ICAM-1 expression and blocked monocytic cells from adhering to inflammatory BEAS-2B cells *in vitro*. Surprisingly, HZW was more effective than HZE in suppressing the inflammatory response in BEAS-2B cells. Our results demonstrated that HZW significantly decreased AHR and eosinophil infiltration, and reduced goblet cell hyperplasia in the lungs of asthmatic mice. HZW also inhibited oxidative stress and reduced the levels of Th2 cytokines in bronchoalveolar lavage fluid. Our findings suggest that HZW attenuated the pathological changes and inflammatory response of asthma by suppressing Th2 cytokine production in OVA-sensitized asthmatic mice.



## 1. Introduction

Allergic asthma is a complex airway inflammatory disease, where antigens stimulate and induce airway hyperresponsiveness (AHR), activated leukocyte infiltration, and airway mucosal hyperplasia [1, 2]. During acute attacks of asthma, patients suddenly coughed, wheezed, and experienced chest tightness, shortness of breath, and dyspnea [3]. When an allergen is inhaled into airways, it stimulates the epithelial cells to release inflammatory cytokines and mediators for respiratory inflammation [3]. In addition, airway epithelial cells secrete chemokines to attract more inflammatory immune cells and infiltrate into lung tissues, causing a more severe inflammatory response [4]. Furthermore, inflamed epithelial cells are accompanied by oxidative damage to epithelial cells and lung tissue, as well as increased activation of immune cells to destruct lung function [5, 6]. In particular, infiltrate of pulmonary macrophages and neutrophils can induce oxygen-dependent cytotoxic effects to release more  $O_2^-$  against the invasion of allergens [7]. Moreover, the oxidizing substance released by those immune cells also causes pulmonary oxidative damage [8]. Therefore, reducing the inflammation and oxidative damage of airways would improve symptoms during the development of asthma in patients.

Recent studies found that the allergen-stimulated Th2 cell activity of the lungs could be an important mechanism in the development of chronic asthma [9]. Th2 cells could secrete IL-4, IL-5, and IL-13 to trigger asthma symptom, including increased eosinophil infiltration and AHR [4, 10]. Therefore, blocking the activity of Th2 cells may ameliorate asthma in patients.

Current clinical strategies include treatment with asthma medications that contain acute attack medication and prevention medication [11]. Smooth muscle vasodilators that reduce the airway contraction and allow patients to breathe can be effective in severe asthma. Moreover, patients may use oral corticosteroids for maintenance and prevention of asthma attacks [12]. The dosage of oral corticosteroids is slight with few serious side effects [13]. Steroids are immunosuppressants and inhibit the function of Th1 and Th2 cells [14]. Therefore, the general public is not treated with steroid drugs for asthma.

Traditional Chinese medicine, yoga, qigong, and homeopathy are very common alternative medicines [15]. Chinese medicine has widely been used for thousands of years, and there have been many herbal formulas, including Ding Chuan Tang and Xiao-Qing-Long-Tang, used to improve asthma symptoms in China and Taiwan [16–18]. These herbal formulas contained ephedra, which contains ephedrine that predominantly reduced smooth muscle contraction in asthmatic patients [19]. Yet, ephedrine is a refined amphetamine and may endanger the health of teenagers [20]. Hence, scholars and practitioners have studied and dispensed alternative herbal formulas to replace those traditional formulas. Many scholars found that other herbal formulas could attenuate AHR and eosinophil infiltration by suppressing the activity of Th2 cells in asthmatic mice, including MSSM-002 and Danggui Buxue Tang [21, 22].

*Helminthostachys zeylanica* (L.) Hook. (Ophioglossaceae) is a common anti-inflammatory folk herb in Taiwan and has been used to improve inflammatory diseases and as an antipyretic [23]. Ugonin K was isolated from *H. zeylanica* and had anti-inflammatory effects in lipopolysaccharide-(LPS-) stimulated macrophages [24]. *H. zeylanica* extracts could also decrease MMP-9 expression and the inflammatory response in bradykinin-induced brain astrocytes [25]. We also found that water extract of *H. zeylanica* could reduce LPS-induced acute lung injury [26]. However, it is not clear whether *H. zeylanica* could attenuate the inflammatory response of airways and improve asthma symptoms. In this study, we investigated whether the *H. zeylanica* ethyl acetate (HZE) extract and water (HZW) extract could reduce AHR and eosinophil infiltration in asthmatic mice, and decrease oxidative stress and inflammatory response in tracheal epithelial cells.

## 2. Materials and Methods

**2.1. *H. zeylanica* Extraction.** The roots of *H. zeylanica* were collected from Taipei, Taiwan, in July 2013. The plant was identified by comparison with the voucher specimen (NRICM-99-003) already deposited at the herbarium of National Research Institute of Chinese Medicine, Taiwan. The roots of *H. zeylanica* (1000 g) were heated with ethanol at 50°C for 4 h. After evaporation of the solvent, the ethanol extract was partitioned between water and ethyl acetate to give water extract (HZW: 23.8 g, yield 2.38%) and ethyl acetate extract (HZE: 14.2 g, yield 1.42%).

**2.2. HPLC Analysis of HZW.** HZW (7.1 mg) was dissolved in 2 ml methanol and responded by ultrasonic wave for 10 minutes at 25°C. After the filtration through a 0.45  $\mu$ m polyvinylidene fluoride membrane, the filtrate was injected into the Agilent 1100 series HPLC (10  $\mu$ l) system. The separation was performed on a COSMOSIL 5C<sub>18</sub>-AR-II column (5  $\mu$ m, 250  $\times$  4.6 mm, i.d.), which was eluted at a flow rate of 1.0 ml/min with a mobile phase gradient of A–B (A = H<sub>2</sub>O (0.05% formic acid), B = MeOH) varying as follows: 0–10 min: 90–80% A, 10–20% B; 10–40 min: 80–0% A, 20–100% B; and 40–50 min: 0–0% A, 100–100% B. The UV detection wavelength was set at 254 nm. The two standards are quercetin-3-O- $\beta$ -D-glucopyranosyl-4'-O- $\beta$ -D-glucopyranosyl-(1  $\rightarrow$  2)- $\beta$ -D-glucopyranoside (compound 1) and quercetin-4'-O- $\beta$ -D-glucopyranosyl-(1  $\rightarrow$  2)- $\beta$ -D-glucopyranoside (compound 2) [27].

**2.3. HZW and HZE Treatment of BEAS-2B Cells.** HZW was dissolved in PBS and HZE was dissolved in DMSO. The concentration of these stock solutions was 10 mg/ml. There was  $\leq$ 0.1% DMSO in the experimental culture medium. BEAS-2B cells (American Type Culture Collection, Manassas, VA, USA) were seeded in DMEM/F12 medium in cultured plates. The cells were pretreated with HZW or HZE (1–10  $\mu$ g/ml) for 1 h, and then treated with 10 ng/ml TNF- $\alpha$  and 10 ng/ml IL-4 for 24 h. The supernatants were collected, and cytokines or chemokines were detected using specific ELISA kits. Cell viability was measured using the MTT assay, and



the results were determined by the absorbance values at 570 nm using a microplate reader (Multiskan FC, Thermo, Waltham, MA, USA).

**2.4. Detection of Reactive Oxygen Species (ROS) Production.** BEAS-2B cells were stimulated with TNF- $\alpha$ /IL-4 and treated with HZW or HZE in 96-well plates for 24 h. Cells were then treated with 2',7'-dichlorofluorescein diacetate (DCFH-DA) (Catalog No. D6883; Sigma, St. Louis, MO, USA) for 30 min as described previously [28, 29]. Cells were then lysed for detection of ROS using a multimode microplate reader (BioTek Synergy HT, Bedfordshire, United Kingdom).

**2.5. Cell-Cell Adhesion Assay.** BEAS-2B cells were treated with various doses of HZW or HZE for 1 h and then stimulated with TNF- $\alpha$ /IL-4 for 24 h in 6-well plates as described previously [30, 31]. THP-1 cells (Bioresource Collection and Research Center, Taiwan) were treated with calcein-AM solution (Catalog No. C1359; Sigma) at 37°C for 30 min, and THP-1 cells were cocultured with BEAS-2B cells at 37°C for 30 min. Finally, THP-1 cells adhered to BEAS-2B cells were measured using fluorescence microscopy (Olympus, Tokyo, Japan).

**2.6. Experimental Animals.** The animals used in this study were 6- to 8-week-old female BALB/c mice, obtained from the National Laboratory Animal Center in Taiwan. Water and food were provided ad libitum, and mice were housed at constant temperature and humidity environment, and maintained on a 12 h light/dark cycle at the Animal Center of Chang Gung University, Taiwan. Animal experimental procedures were approved by the Laboratory Animal Care Committee of Chang Gung University of Science and Technology (IACUC approval number: 2013-001).

**2.7. Allergy Sensitization and Drug Treatment.** Asthma was induced in mice by 50  $\mu$ g ovalbumin (OVA) (Catalog No. A5503; Sigma) and 0.8 mg aluminum hydroxide (Thermo, Rockford, IL, USA) in 200  $\mu$ l normal saline via intraperitoneal injection on days 1-3 and 14, as described previously [32]. Mice were challenged and exposed with aerosolized 2% OVA using an ultrasonic nebulizer (DeVilbiss Pulmo-Aide 5650D, USA) for 20 min on days 14, 17, 20, 23, and 27. From day 14 to day 27, the mice were orally administered with saline (N and OVA groups), HZW, or HZE for 14 consecutive days. In every independent experiment, mice were divided into six groups (of 10 mice each): (1) normal control mice (N group) sensitized with normal saline; (2) OVA-sensitized control mice (OVA group) sensitized with OVA; (3-5) experimental group mice sensitized with OVA and orally administered with 1 mg/kg, 5 mg/kg, or 10 mg/kg HZW or HZE (named HZW1, HZW5, and HZW10 or HZE1, HZE5, and HZE10, respectively); and (6) prednisolone control (P group) OVA-sensitized mice orally administered with 5 mg/kg prednisolone.

**2.8. Measurement of AHR.** On day 28, the AHR of mice was measured to evaluate airway function via various inhaled doses of methacholine, as described previously [33]. All mice inhaled aerosolized methacholine (0-40 mg/ml) for 3 min,

respectively. A single-chamber, whole-body plethysmograph (Buxco Electronics, Troy, NY, USA) was used to record the values of enhanced pause (Penh), a measurement of AHR.

**2.9. Serum Collection and Splenocyte Cultures.** On day 29, mice were anesthetized with 4% isoflurane (Aesica, Queenborough, UK), and blood was collected from the orbital vascular plexus and centrifuged at 6000 rpm for 5 min at 4°C. The serum was collected to measure OVA-specific antibodies that were detected by ELISA as previously described [28]. Next, mice were sacrificed by CO<sub>2</sub> asphyxiation. Their splenocytes were isolated and cultured with 100  $\mu$ g/ml OVA in RPMI 1640 medium for 5 continuous days. The levels of cytokines in the supernatants were assayed as previously described [32].

**2.10. Bronchoalveolar Lavage Fluid (BALF) and Cell Collection.** Mice were anesthetized using 4% isoflurane, and BALF was collected as described previously [34]. Briefly, the mice were incubated with an indwelling needle into the trachea, and the lungs were washed three times using 1 ml normal saline. The supernatant was collected to detect the levels of cytokines and chemokines by ELISA. Additionally, Giemsa stain (Catalog No. GS500; Sigma) was used to stain cells for measuring cell counts and differentiated cell morphology.

**2.11. Histologic Analysis of Lung Tissue.** Lung tissues were embedded in paraffin and cut into 6  $\mu$ m thick sections. Hematoxylin and eosin (HE) staining was used to observe the eosinophil infiltration of the lungs. Eosinophil infiltration inflammatory index used fivepoint scoring system as described previously [35]. Briefly, the degree of cell infiltration was scored as follows: 0, no cell; 1, a few cells; 2, a ring of inflammatory cells of one cell layer; 3, a ring of inflammatory cells of two to four cell layers; and 4, a ring of inflammatory cells > four cell layers. Furthermore, periodic acid-Schiff (PAS) staining was used to evaluate goblet cell hyperplasia of the trachea as described previously [28]. The lung tissue slide was deparaffinized and stained with periodic acid solution for 5 min. Next, the slide was washed and added with Schiff's reagent for 15 min. Finally, hematoxylin solution was added, and the goblet cells were observed using a light microscope (Olympus, Tokyo, Japan).

**2.12. Glutathione (GSH) Assay.** A glutathione assay kit was used to determine the glutathione levels of the lungs, according to the manufacturer's instructions (Catalog No. CS0260; Sigma). 50 mg lung tissues was homogenized by homogenizer (FastPrep-24, MP Biomedicals, Santa Ana, CA, United States). The sample was centrifuged, and supernatant detected the level of total glutathione, including reduced GSH and glutathione disulfide using a multimode microplate reader (BioTek Synergy HT, Bedfordshire, United Kingdom).

**2.13. Malondialdehyde (MDA) Assay.** The lipid peroxidation assay kit (Catalog No. MAK085; Sigma) was used to evaluate the MDA level of the lungs, according to manufacturer's instructions. Lung tissues were homogenized by homogenizer (FastPrep-24, MP Biomedicals, Santa Ana, CA, United

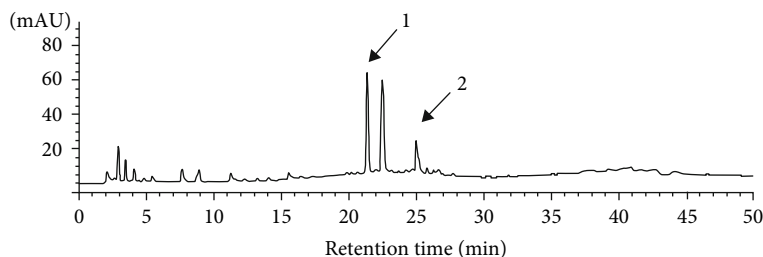


FIGURE 1: HPLC chromatograms of *H. zeylanica* water (HZW) extract. 1: quercetin-3-*O*- $\beta$ -D-glucopyranosyl-4'-*O*- $\beta$ -D-glucopyranosyl-(1  $\rightarrow$  2)- $\beta$ -D-glucopyranoside; 2: quercetin-4'-*O*- $\beta$ -D-glucopyranosyl-(1  $\rightarrow$  2)- $\beta$ -D-glucopyranoside.

States). The supernatant was treated with perchloric acid for protein precipitation. The tissue solution was centrifuged and collected supernatant to detect MDA expression by a multimode microplate reader (BioTek Synergy HT).

**2.14. Lung RNA Isolation and Real-Time PCR.** Lung tissues were homogenized and RNA extracted with TRIzol reagent (Catalog No. 15596026; Life Technologies, Carlsbad, CA, USA), as described previously [34, 36]. We used RNA to synthesize cDNA and a spectrofluorometric thermal cycler (iCycler; Bio-Rad) to investigate specific gene expression. The reaction cycling conditions were as follows: preincubated samples at 95°C for 10 min. Next, the PCR was performed as 40 cycles of 95°C for 15 seconds and 60°C for 1 minute.

**2.15. ELISA.** Cytokines, chemokines, and ICAM-1 were detected in the BALF and supernatants of cell cultures using specific ELISA kits, according to the manufacturer's instructions (R&D Systems, Minneapolis, MN, USA), as previously described [33]. Serum OVA-IgE and OVA-IgG1 were measured with specific ELISA kits (BD Biosciences). The OVA-IgG1 standard curve was used to calculate the units of IgG1, and the levels of OVA-IgE were determined by OD 450.

**2.16. Statistical Analysis.** Statistical analyses were performed with SPSS v19 (SPSS, Chicago, IL, USA). Animal experiment results were analyzed by one-way analysis of variance (ANOVA), followed by the Dunnett and post hoc test for multiple comparisons. Between two groups, an unpaired Student *t*-test was used in cell experiment. Statistical significance was set at  $P < 0.05$ , and the results were expressed as the mean  $\pm$  standard error of the mean (SEM) from three independent experiments.

### 3. Results

**3.1. HZW Inhibited the Levels of Cytokines and Chemokines in Inflammatory BEAS-2B Cells.** The HPLC fingerprint of *H. zeylanica* water (HZW) extract (Figure 1) showed compound 1 and compound 2 elute at 21.2 and 25.2 minutes, which was specific enough to be used for the identification of *H. zeylanica* [27]. The cytotoxicity of HZW and HZE in BEAS-2B cells was determined by MTT assay. Cell viability was not significantly affected by the doses of HZW or HZE  $\leq 10 \mu\text{g/ml}$  (Figures 2(a) and 2(b)). Therefore, in this current experiment, we used HZW and HZE doses from  $1 \mu\text{g/ml}$  to  $10 \mu\text{g/ml}$  *in vitro*. We used TNF- $\alpha$ /IL-4 to stimulate inflam-

mation in BEAS-2B cells to evaluate the anti-inflammatory effect of HZW and HZE. Our experimental results demonstrated that HZW could significantly reduce the levels of IL-6 and IL-8 at 5 and  $10 \mu\text{g/ml}$  (Figures 2(c) and 2(d)). We also found that HZW significantly reduced eotaxin (CCL11 and CCL24) production at 5 and  $10 \mu\text{g/ml}$  (Figures 2(e) and 2(f)). However, HZE was not as effective at reducing eotaxins and proinflammatory cytokines, although  $10 \mu\text{g/ml}$  HZE could significantly inhibit IL-6, IL-8, and CCL11 production. We also found that the  $10 \mu\text{g/ml}$  HZW group significantly decreased the levels of IL-6, IL-8, CCL11, and CCL24 compared with the  $10 \mu\text{g/ml}$  HZE group. Thus, HZW was better in reducing the inflammatory response than HZE.

**3.2. HZW Regulated ROS Production in BEAS-2B Cells.** BEAS-2B cells were treated with HZW or HZE and then stimulated with TNF- $\alpha$ /IL-4. Cells were lysed and detected with ROS using a multimode microplate reader. We found HZW decreased the ROS levels more than HZE in TNF- $\alpha$ /IL-4-activated BEAS-2B cells (Figure 3(a)).

**3.3. HZW Reduced Monocytic Cell Adhesion to BEAS-2B Cells.** HZW significantly suppressed the levels of intercellular adhesion molecule 1 (ICAM-1) compared with HZE in TNF- $\alpha$ /IL-4-activated BEAS-2B cells (Figure 3(b)). Additionally, HZW reduced the THP-1 cells that adhered to inflammatory BEAS-2B cells (Figures 3(c) and 3(d)), while HZE did not.

**3.4. HZW Improved AHR and Reduced the Inflammatory Cells in the BALF of OVA-Sensitized Mice.** AHR is one of the important features of asthma. It mainly evaluates the respiratory function when allergen or stimulus induces to increase sensitivity and reactivity of airways [37]. The AHR assay result showed that OVA-sensitized mice have Penh values that are increased in a dose-dependent manner compared with the normal mice. At  $40 \text{ mg/ml}$  methacholine, the HZW groups had significantly reduced the value of Penh compared with the OVA group (Figure 4(a)) (HZW1:  $6.22 \pm 0.56$ ,  $P = 0.08$ ; HZW5:  $5.01 \pm 0.30$ ,  $P < 0.01$ ; HZW10:  $4.18 \pm 0.38$ ,  $P < 0.01$  vs. OVA:  $7.68 \pm 0.39$ ). In HZE-treated OVA-sensitized mice, only HZE10 could suppress Penh values compared with the OVA group (Figure 4(c)) (HZE1:  $7.33 \pm 0.35$ ,  $P = 0.75$ ; HZE5:  $6.74 \pm 0.73$ ,  $P = 0.31$ ; HZE10:  $5.68 \pm 0.38$ ,  $P < 0.05$  vs. OVA:  $8.58 \pm 0.44$ ). Prednisolone-treated OVA-sensitized mice also significantly inhibited the Penh values compared to the OVA group mice. We also

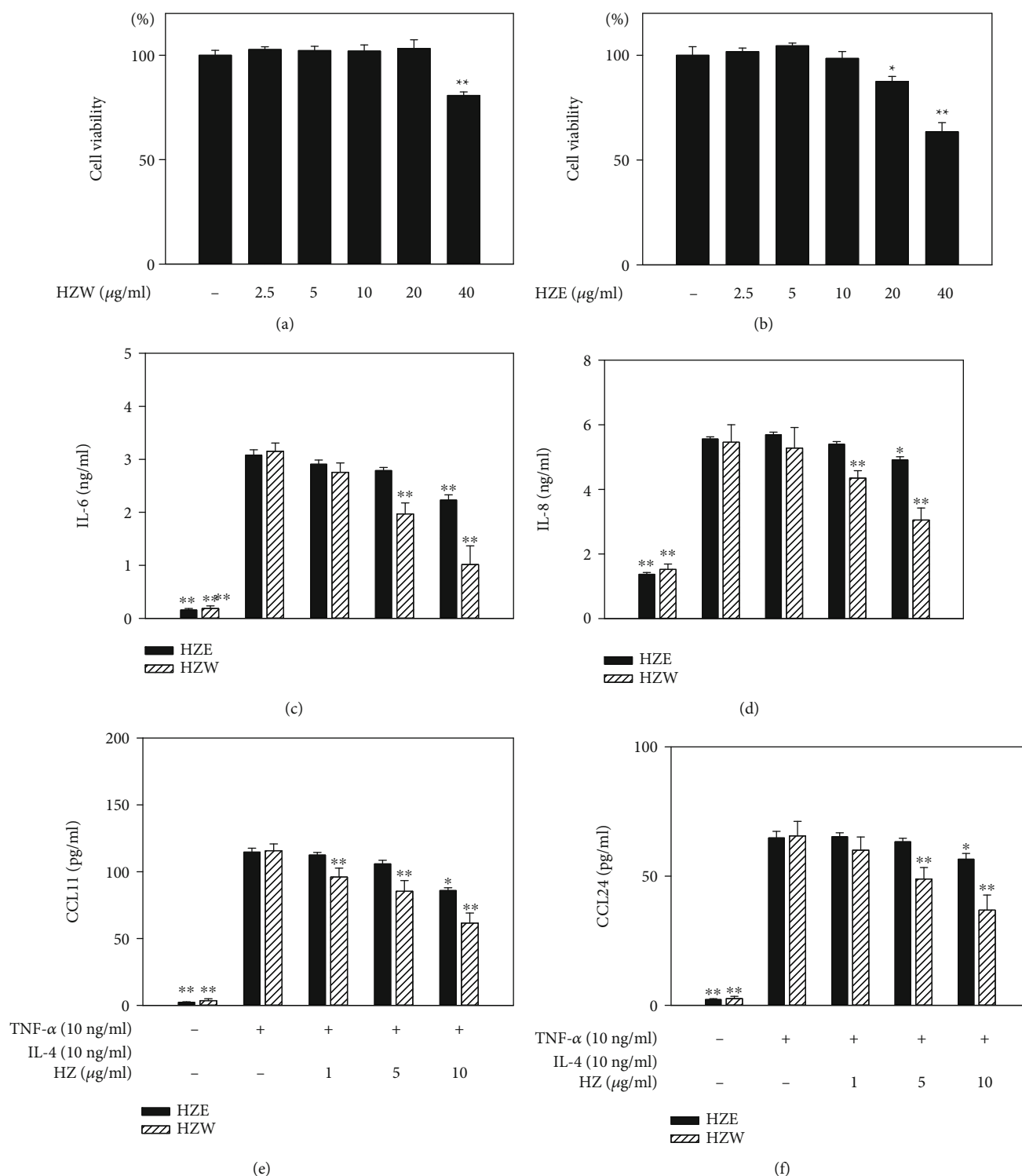


FIGURE 2: The effects of HZW and HZE on cytokine and chemokine productions in BEAS-2B cells. Cell viability of (a) HZW and (b) HZE in BEAS-2B cells. The levels of IL-6 (c), IL-8 (d), CCL11 (e), and CCL24 (f) were measured by ELISA. All data are presented as the mean  $\pm$  SEM. \* $P < 0.05$  and \*\* $P < 0.01$  compared with BEAS-2B cells stimulated with TNF- $\alpha$ /IL-4. HZ: *Helminthostachys zeylanica*. HZW was dissolved in PBS and HZE was dissolved in DMSO. Hence, vehicle HZE experiment contained 0.1% DMSO in medium and vehicle HZW experiment did not contain DMSO in medium.

investigated whether HZW and HZE could suppress inflammatory cells in the BALF of asthmatic mice. The result showed that HZW5 and HZW10 could significantly inhibit

eosinophils and total cells compared with the OVA group (Figure 4(b)). However, HZE did not significantly inhibit eosinophils and total cells compared with the OVA group

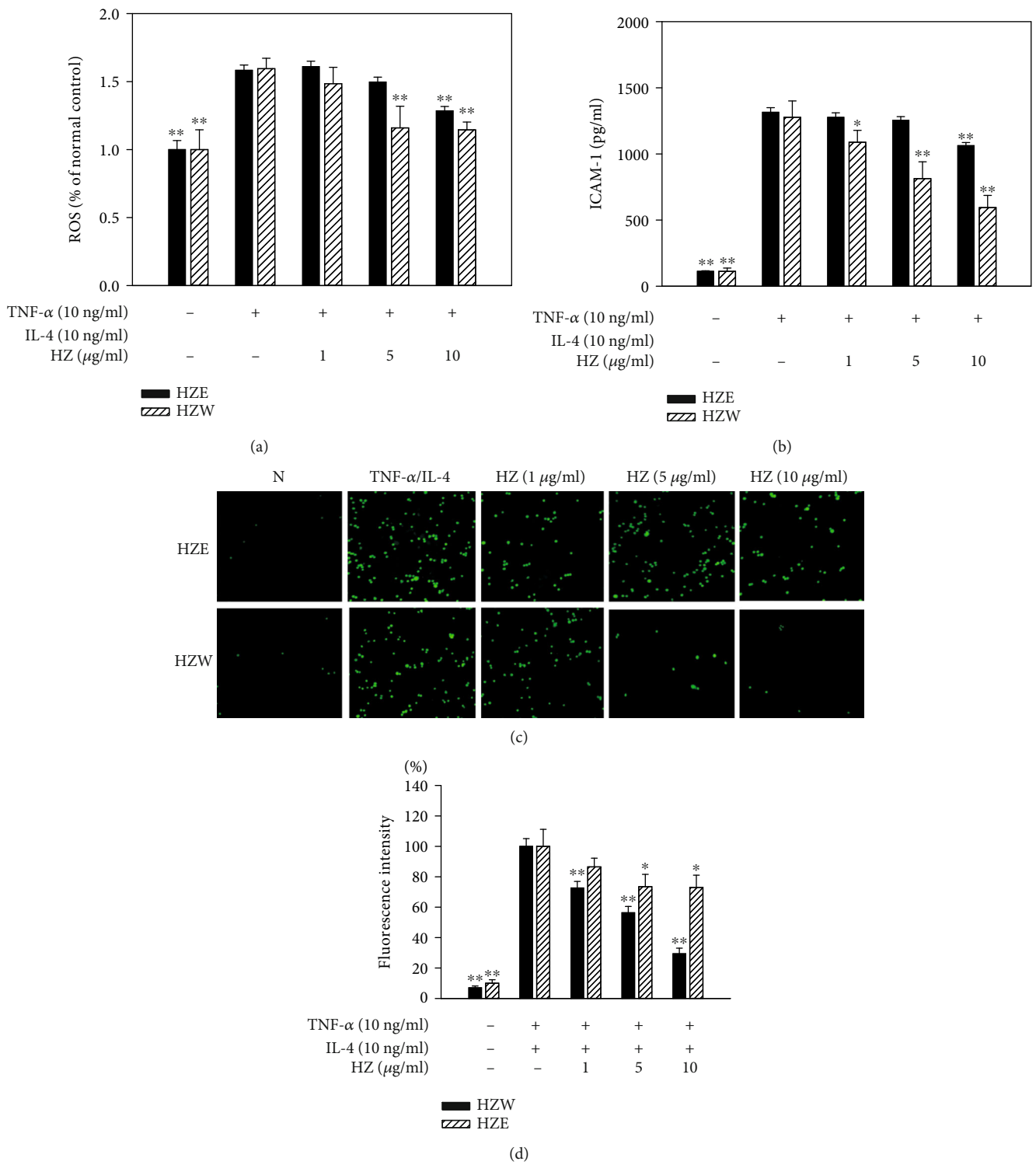


FIGURE 3: HZW and HZE inhibited ROS and THP-1 cell adhesion to the activated BEAS-2B cells. (a) Percentage of ROS detected in cells treated with HZW or HZE compared with TNF- $\alpha$ /IL-4-activated BEAS-2B. (b) The levels of ICAM-1, detected by ELISA, in BEAS-2B cells activated with TNF- $\alpha$ /IL-4. (c) Fluorescence microscopy images of THP-1 cells labeled with calcein-AM and mixed with normal (N) and TNF- $\alpha$ /IL-4-activated BEAS-2B cells, in the absence or presence of HZW or HZE. HZ: *Helminthostachys zeylanica*. (d) Fluorescence intensity of THP-1 cell adhesion to BEAS-2B cells. The data are presented as the mean  $\pm$  SEM. \* $P$  < 0.05 and \*\* $P$  < 0.01 compared with BEAS-2B cells stimulated with TNF- $\alpha$ /IL-4.

(Figure 4(d)). Prednisolone-treated OVA-sensitized mice also significantly inhibited eosinophils and total cells compared to the OVA-sensitized mice. Hence, we only analyzed how HZW ameliorates the effects of inflammation, oxidation, and the immune mechanism of asthma in the animal model.

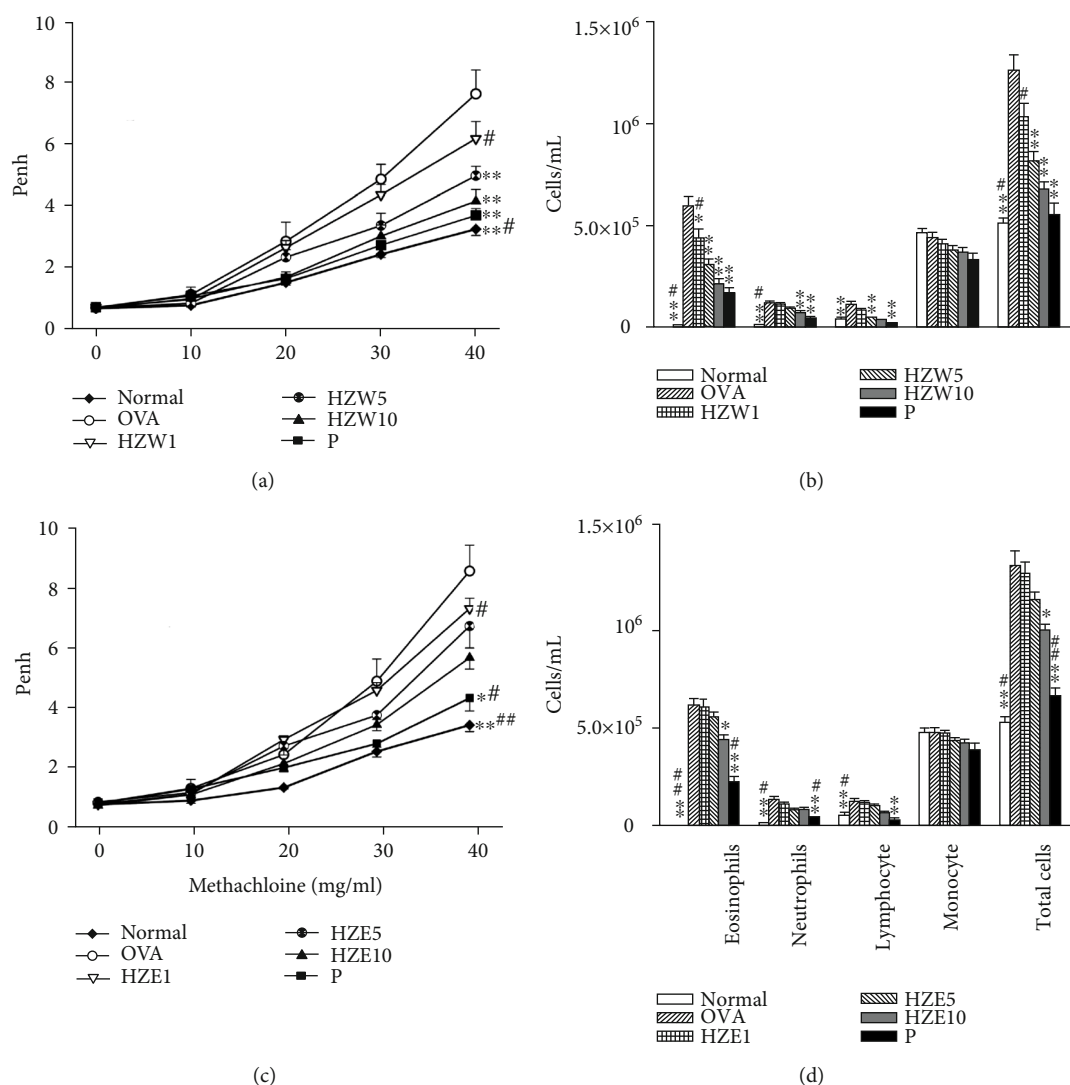


FIGURE 4: Effect of HZW or HZE on AHR and cell counts in the BALF of asthmatic mice. The AHR (Penh values) was measured after inhalation of increasing methacholine doses (10–40 mg/ml) in normal (N) and OVA-stimulated (OVA) mice, treated with or without HZW (a) or HZE (c) ( $n = 10$  mice/group, measured in three independent experiments). The numbers of inflammatory cells and total cells in the BALF from OVA-sensitive mice, treated with or without HZW (b) or HZE (d). All data are presented as the mean  $\pm$  SEM. \* $P < 0.05$  and \*\* $P < 0.01$  compared with the OVA control group. # $P < 0.05$  and ## $P < 0.01$  compared to the HZW10 or HZE10 group. Prednisolone (P) control orally administered with 5 mg/kg prednisolone as positive control.

**3.5. HZW Regulated the MDA and GSH Levels in the Lungs.** Asthma attacks would induce oxidative stress for causing lung cell damage [38]. We found that OVA-sensitized mice had significantly enhanced the MDA levels and reduced GSH production in lung tissue compared with normal mice (Figures 5(a) and 5(b)). HZW suppressed MDA and increased the GSH levels compared with OVA mice.

**3.6. HZW Attenuated Eosinophil Infiltration and Goblet Cell Hyperplasia in the Lungs.** In the lungs, infiltration of inflammatory cells is an important factor to cause pulmonary inflammation [39]. There were more eosinophils infiltrating between the blood vessels and bronchus of the lungs in OVA-sensitive mice than normal mice, and HZW could suppress eosinophil infiltration of the lungs in asthmatic mice (Figure 6). The PAS staining also showed HZW could

decrease goblet cell hyperplasia of airways compared with OVA-sensitive mice (Figure 7).

**3.7. HZW Regulated Cytokine and Chemokine Expression in BALF and Lung Tissue.** To analyze the levels of proinflammatory cytokine and Th2-associated cytokines in BALF, cytokines and chemokines were detected using ELISA. We found that HZW-treated mice had significantly suppressed the TNF- $\alpha$  levels compared with OVA-sensitized mice (Figure 8). HZW also significantly reduced IL-6, CCL11, IL-4, IL-5, and IL-13 compared with the OVA group, but did not decrease the levels of CCL24 in the BALF of asthmatic mice. The gene expression in lung tissues measured by real-time PCR demonstrated that HZW significantly reduced COX-2, CCL11 (not CCL24), ICAM-1, MUC5AC, IL-4, IL-5, and IL-13 gene expression compared with OVA-



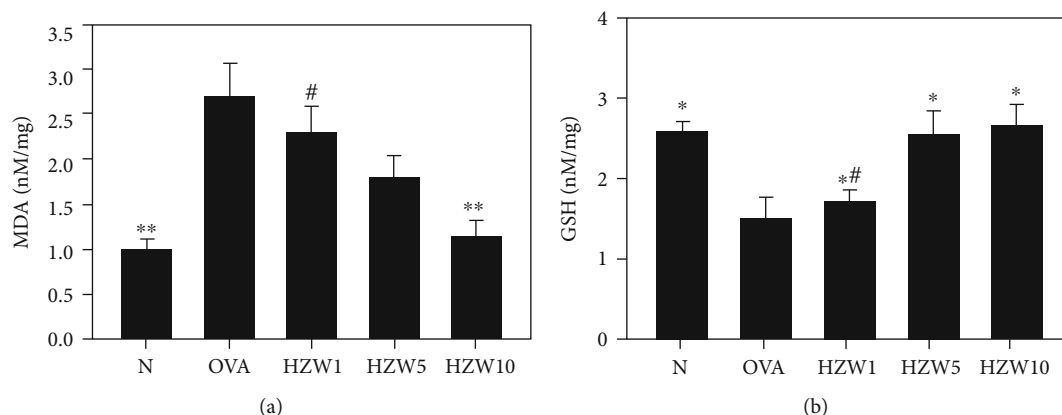


FIGURE 5: The effects of HZW on oxidative stress factors. The MDA level (a) and GSH activity (b) were measured in the lung tissues of mice. Data are presented as the mean  $\pm$  SEM. \* $P < 0.05$  and \*\* $P < 0.01$  compared with the OVA control group. # $P < 0.05$  compared to the HZW10 group.

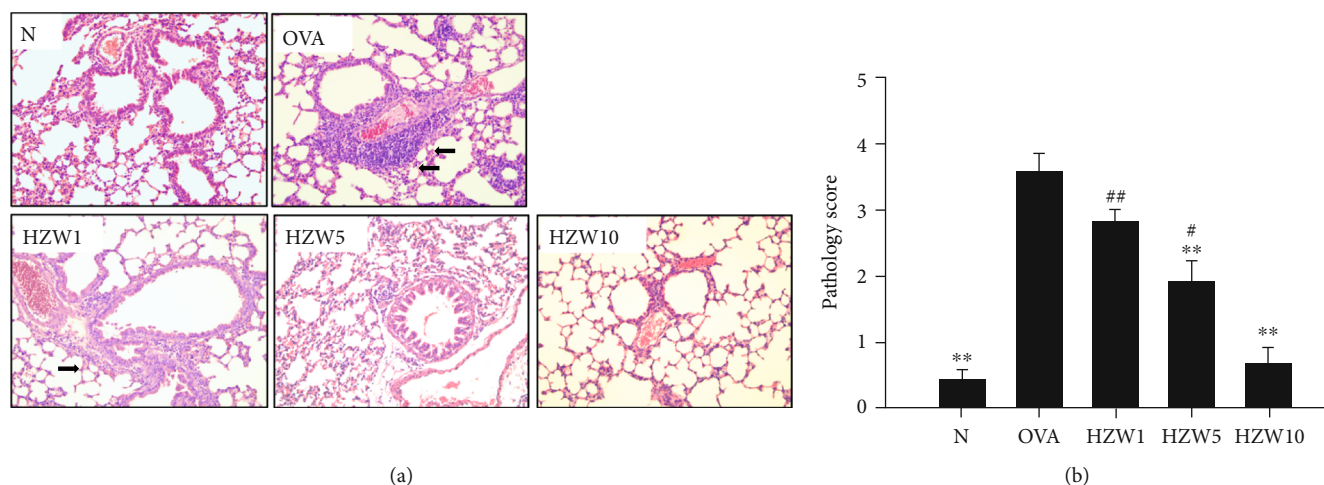


FIGURE 6: The effect of HZW on eosinophil infiltration of lung tissue in OVA-sensitized mice. (a) Hematoxylin and eosin staining of lung sections (6  $\mu$ m) observed eosinophil infiltration (200x magnification). Eosinophils were indicated with arrows. (b) The scoring of inflammation via pathological evaluation in lung sections. Data are presented as the mean  $\pm$  SEM. \* $P < 0.05$  and \*\* $P < 0.01$  compared with the OVA control group. # $P < 0.05$  and ## $P < 0.01$  compared to the HZW10 group.

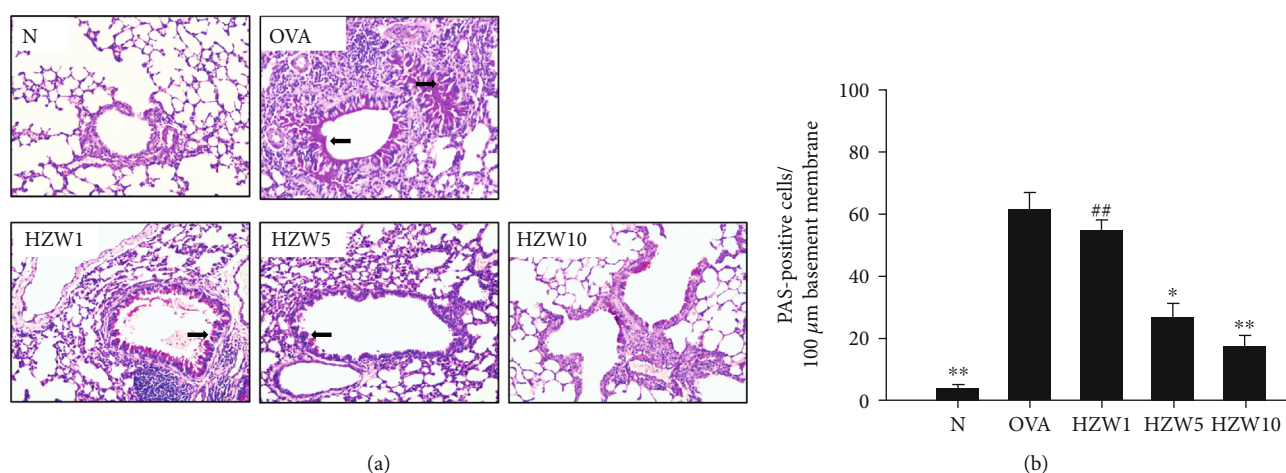


FIGURE 7: The effects of HZW on goblet cell hyperplasia in the lung tissue of OVA-sensitized mice. (a) Lung sections (6  $\mu$ m) were stained with PAS to observe goblet cell hyperplasia (200x magnification). Goblet cells were indicated with arrows. (b) Results expressed as the number of PAS-positive cells per 100  $\mu$ m of the basement membrane. Data are presented as the mean  $\pm$  SEM. \* $P < 0.05$  and \*\* $P < 0.01$  compared with the OVA control group. ## $P < 0.01$  compared to the HZW10 group.

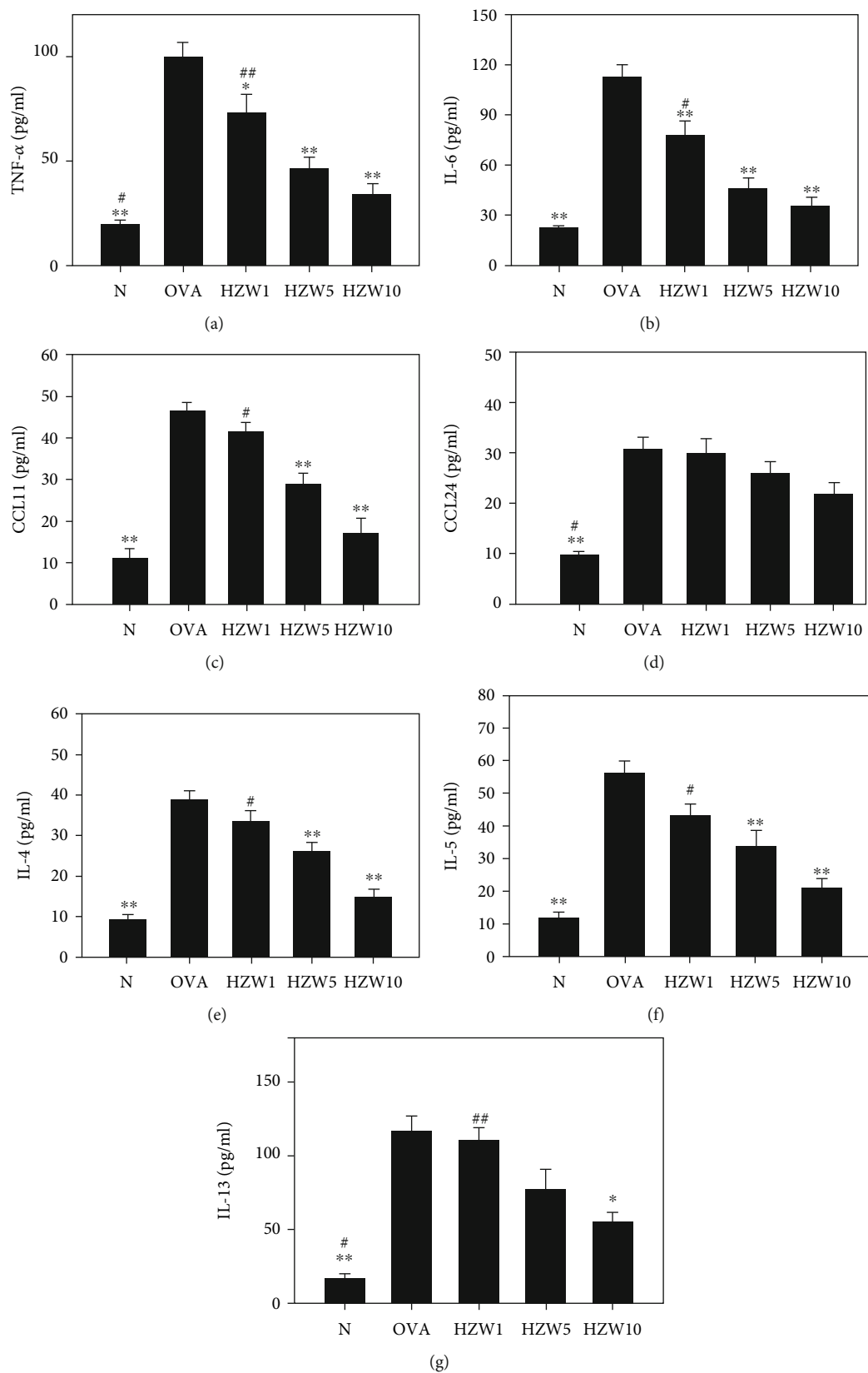


FIGURE 8: The effects of HZW on the levels of cytokines and chemokines in the BALF. The concentrations of TNF- $\alpha$  (a), IL-6 (b), CCL11 (c), CCL24 (d), IL-4 (e), IL-5 (f), and IL-13 (g) were measured by ELISA. All data are presented as the mean  $\pm$  SEM. \* $P$  < 0.05 and \*\* $P$  < 0.01 compared with the OVA control group. # $P$  < 0.05 and ## $P$  < 0.01 compared to the HZW10 group.

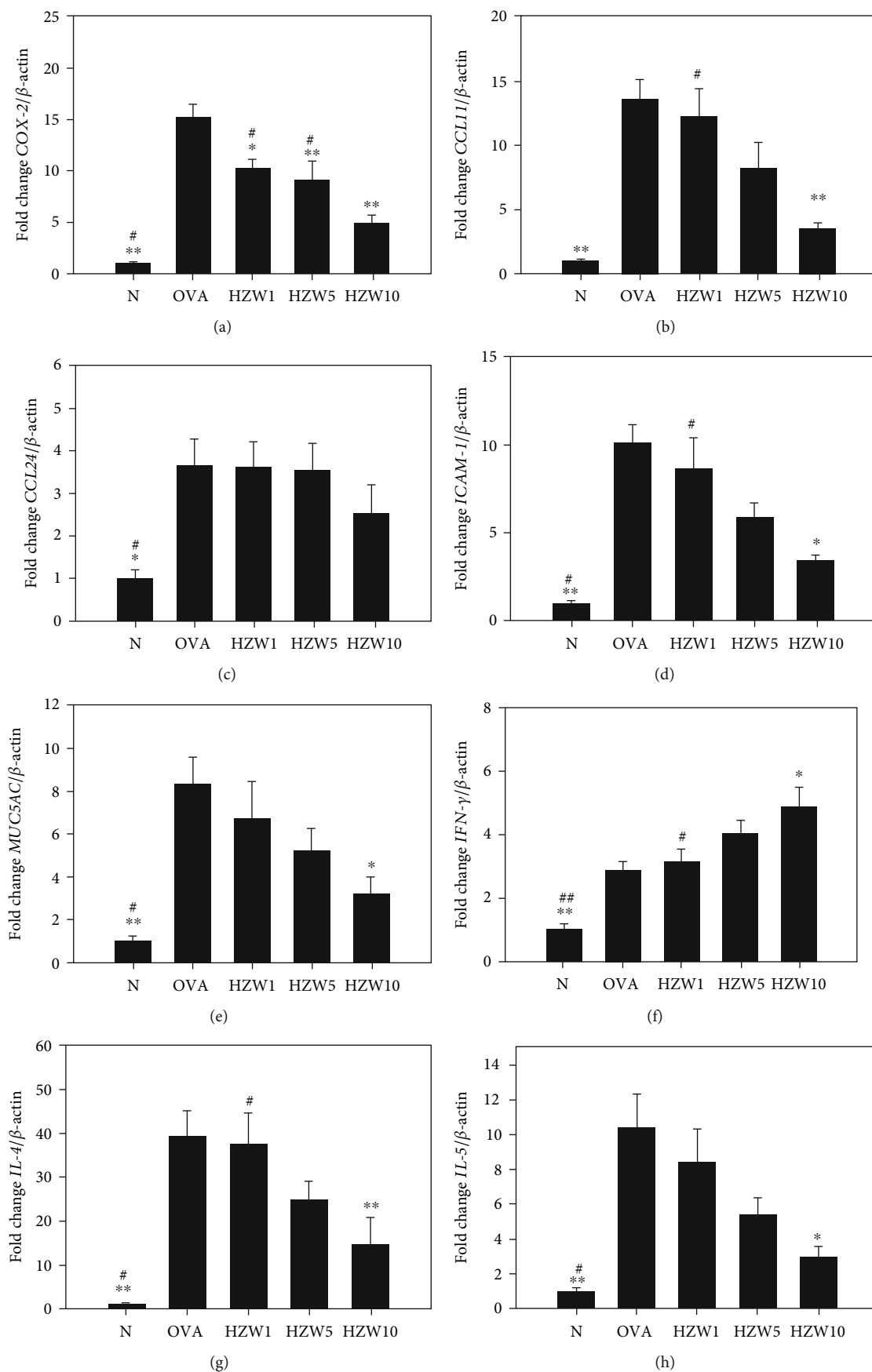


FIGURE 9: Continued.

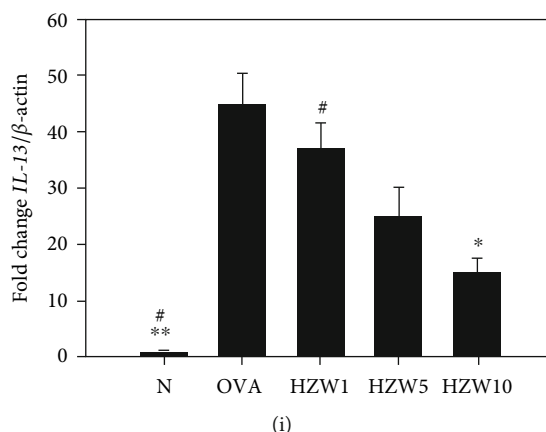


FIGURE 9: Effects of HZW on gene expression of cytokines, chemokines, and inflammatory mediators in the lungs. The gene expression levels of COX-2 (a), CCL11 (b), CCL24 (c), ICAM-1 (d), MUC5AC (e), IFN- $\gamma$  (f), IL-4 (g), IL-5 (h), and IL-13 (i) were determined by real-time PCR of RNA extracted from the lung tissues of normal (N) and OVA-stimulated (OVA) mice, treated with or without HZW. Fold changes in expression were measured relative to  $\beta$ -actin expression (internal control). Data are presented as the mean  $\pm$  SEM. \* $P < 0.05$  and \*\* $P < 0.01$  compared with the OVA control group. # $P < 0.05$  and ## $P < 0.01$  compared to the HZW10 group.

sensitized mice (Figure 9). However, HZW also increased IFN- $\gamma$  gene expression in asthmatic mice.

**3.8. HZW Regulated the Antibody and Cytokine Levels in Serum and Splenocytes.** To analyze the levels of OVA-specific antibodies in serum, HZW significantly attenuated the OVA-IgG1 and OVA-IgE levels compared with OVA-sensitized mice (Figures 10(a) and 10(b)). We also analyzed the levels of Th2-associated cytokines in splenocyte culture supernatants and found that mice treated with HZW10 had significantly reduced the levels of IL-4, IL-5, and IL-13 (Figures 10(c)–10(e)). Moreover, HZW increased the IFN- $\gamma$  levels compared with OVA-sensitized mice (Figure 10(f)).

#### 4. Discussion

Previous studies confirmed that *H. zeylanica* could improve liver damage in Wistar rats [40]. Previously, we found that HZW could also decrease inflammatory responses in lung tissues from LPS-treated mice [26]. In this current study, we found that HZW is more effective than HZE to reduce inflammatory response and decrease the ROS levels in TNF- $\alpha$ /IL-4-activated BEAS-2B cells. Also, HZW inhibited THP-1 cell adherence to inflammatory BEAS-2B cells more than HZE. We thought that HZW fraction should contain the main substance or compound that inhibited the inflammatory response of human tracheal epithelial cells. In the present study, we found that HZW significantly reduced oxidative stress and suppressed Th2-associated cytokines and chemokines in BALF. HZW could also inhibit the gene expression of inflammatory chemokines and cytokines in lung tissues. In addition, HZW significantly attenuated tracheal goblet cell hyperplasia, eosinophil infiltration of the lungs, and ameliorated AHR in asthmatic mice. Furthermore, HZW decreased the levels of Th2 cytokines in splenocyte culture medium and OVA-specific IgE in serum.

Recently, a study demonstrated that ugonin J and ugonin K were the main flavonoids of HZE [26]. A previous study

found that HZW analyzed with HPLC, and the UV detection wavelength was set at 254 nm. HZW could be isolated two bioactivity compounds, including quercetin-4- $O$ - $\beta$ -D-glucopyranosyl-(1  $\rightarrow$  2)- $\beta$ -D-glucopyranoside and quercetin-3- $O$ - $\beta$ -D-glucopyranosyl-4- $O$ - $\beta$ -D-glucopyranosyl-(1  $\rightarrow$  2)- $\beta$ -D-glucopyranoside [27]. These two pure compounds could suppress production of nitric oxide and proinflammatory cytokines in LPS-stimulated macrophage [27]. We thought that these two compounds should also have the potential to ameliorate respiratory inflammation and AHR and in asthmatic mice.

Asthma is a respiratory inflammatory disease. When patients inhale allergens, they stimulate an inflammatory response of airway epithelial cells [3]. Those epithelial cells then secrete inflammatory cytokines and chemokines for invasions of foreign substances [6]. Our experimental findings that HZW is effective at reducing the IL-6 levels in inflammatory tracheal epithelial cells suggest it may help prevent the development of lung inflammation in asthmatic patients. Asthmatic mice, treated with HZW, had suppressed the levels of IL-6 and TNF- $\alpha$  in BALF, and also reduced gene expression of inflammatory mediators (COX-2) in the lungs. Hence, HZW is a good natural plant extract with an anti-inflammatory effect in asthmatic mice.

During the asthma development process, immune cells and epithelial cells induce oxidative stress leading to lung tissue damage [41]. Researchers have found that patients could regulate oxidative stress, reduce allergic inflammation, and suppress asthma by taking an antioxidant supplement [42]. A previous study found that oral administration of high dose vitamin C could reduce inflammation and oxidative stress of the lungs and eosinophilic infiltration of BALF in OVA-sensitized mice [43]. Licochalcone A and quercetin also were found that could improve asthma by suppressing ROS and inflammation in OVA-induced asthmatic mice [44, 45]. Therefore, antioxidants have great potential to improve asthma symptoms. The antioxidant enzyme GSH can provide oxidation protection by reducing oxidative damage

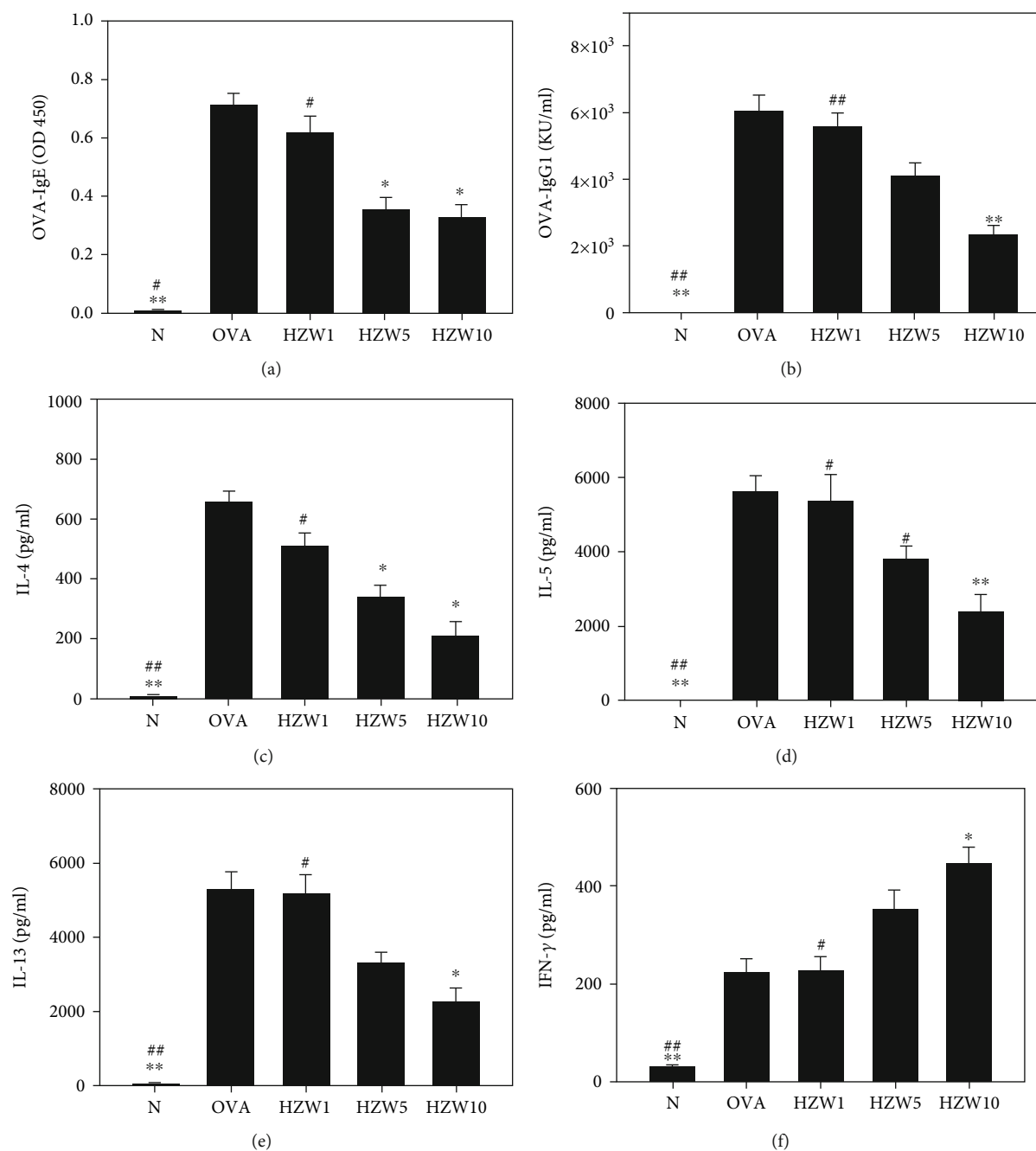


FIGURE 10: Effect of HZW on the levels of the OVA-specific antibodies and cytokines. HZW reduced the levels of OVA-IgE (a) and OVA-IgG1 (b) in serum as well as IL-4 (c), IL-5 (d), IL-13 (e), and IFN- $\gamma$  (f) produced by OVA-activated splenocytes. All data are presented as the mean  $\pm$  SEM. \* $P$  < 0.05 and \*\* $P$  < 0.01 compared with the OVA control group. # $P$  < 0.05 and ## $P$  < 0.01 compared to the HZW10 group.

and the chronic inflammatory response in the lungs of asthmatic mice [38]. Lipid peroxidation influences cellular function via oxidative damage and eventually leads to cell death [38]. Our results showed that HZW could effectively reduce ROS in tracheal epithelial cells and decrease the levels of MDA, a lipid peroxidation marker, in the lung tissue in asthmatic mice. Furthermore, HZW increased GSH expression to increase the protective effects against oxidative damage. Hence, HZW was effective at reducing lung damage by suppressing oxidative stress in asthmatic mice.

Excessive Th2 cytokines exacerbate the pathology response of asthma by increasing AHR, goblet cell hyperplasia, excessive mucus secretion, and inflammatory cell infiltration [4, 46]. Previous studies also found that IL-13 could aggravate AHR in asthmatic mice, causing shortness of breath and bronchoconstriction [1]. In clinical asthma cases, there are high IL-13 levels observed in BALF that induce AHR and difficulty of breathing [47]. Another study found that IL-13 knockout mice did not have significantly increased AHR compared with wild-type asthmatic mice [48]. We



found that HZW could significantly decrease IL-13 gene expression in the lungs and the IL-13 levels in BALF, and improve AHR in asthmatic mice. Furthermore, Th2 cells secrete excess IL-4 to induce B cell activation and secretion of more IgE to bind to the IgE $\epsilon$ R1 receptor of mast cells [3]. When patients inhale allergens, they form a complex with IgE and mast cells to induce mast cell activation and release histamine and leukotrienes, causing severe lung inflammation and allergic responses [6]. We found that HZW could significantly decrease the IL-4 levels and suppress OVA-specific IgE production in serum. These results confirm that HZW was effective at reducing the acute inflammatory response of airways and decreasing allergic response in asthmatic mice.

When combined with IL-13, IL-4 can promote goblet cell hyperplasia of the airway, and those goblet cells secrete excessive mucus leading to airway obstruction, breathing difficulties, and even death in asthmatic patients [18]. A previous study found that IL-4 or IL-13 knockout mice did not significantly increase goblet cell hyperplasia of the airway compared with wild-type asthmatic mice [9]. Here, we demonstrated that HZW reduced IL-4 and IL-13 production and decreased goblet cell hyperplasia in lung tissue, and also suppressed Muc5Ac gene expression in the lungs for improved mucus secretion.

Recently, a study demonstrated that active Th2 cells release more IL-5 to induce eosinophil proliferation and differentiation from the bone marrow [39]. In asthmatic patients, airway epithelial cells also secrete more eotaxins (CCL11, CCL24, and CCL26) to attract eosinophils that migrate into the lung tissue [6]. Eosinophils release more inflammatory substances, including eosinophil cationic protein and eosinophil peroxidase, to cause lung inflammation and oxidation damage in lung tissue [24]. HZW could significantly suppress CCL11 and IL-5 expression in the lungs and BALF, and also decrease the levels of CCL11 and CCL24 in inflammatory tracheal epithelial cells for reduced eosinophil differentiation and attraction to lung tissue. Hence, we thought that HZW mainly reduced CCL11 secretion of the lungs to decrease eosinophil infiltration in the lungs of asthmatic mice. In addition, HZW reduced ICAM-1 expression of tracheal epithelial cells that adhere to eosinophils and migrate into lung tissue to reduce the inflammation and allergic response in the lungs. In the current study, we confirmed that HZW inhibited the activity of Th2 cells, reducing lung inflammation and allergic reactions in asthmatic mice.

Steroids are clinical drugs for treating or preventing asthma [12]. However, steroids interfered with the function of immune cells and inhibited the expression of Th1 and Th2 cells [14]. Interferon- $\gamma$ , a Th1 cytokine, would suppress expression in asthmatic patient. In the present study, the gene expression of lung tissues demonstrated that HZW could increase IFN- $\gamma$  gene expression in asthmatic mice. Clinical trials found that herbal formulas, Ding Chuan Tang and ASHMI, reduced asthma symptoms and improved respiratory function by regulating the activity of Th1/Th2 cells [17, 49]. In this study, HZW inhibited allergic reactions and improved lung inflammation in asthmatic mice. Interestingly, HZW did not suppress the activity of Th2 and Th1 cells

as steroids. In steroid-resistant asthmatic patients, tracheal epithelial cells would release IL-8, thereby attracting more neutrophils into the lungs to cause serious inflammatory reactions. Our study found that the levels of IL-8 attenuated after BEAS-2B cells treated with HZW, indicating that HZW might reduce the inflammatory response in asthmatic patients.

In conclusion, our results demonstrated that HZW, but not HZE, significantly suppressed AHR, mucus hypersecretion, and eosinophil infiltration via blocked Th2 cytokine production in asthmatic mice. HZW also reduced oxidative stress and inflammation to prevent lung damage and maintain the function of the respiratory system. Thus, HZW may potentially ameliorate inflammation and antioxidative stress in asthma.

## Abbreviations

AHR:	Airway hyperresponsiveness
BALF:	Bronchoalveolar lavage fluid
DCFH-DA:	2',7'-Dichlorofluorescein diacetate
GSH:	Glutathione
HE:	Hematoxylin and eosin staining
HZW:	<i>Helminthostachys zeylanica</i> water
HZE:	<i>Helminthostachys zeylanica</i> ethyl acetate extracts
LPS:	Lipopolysaccharide
OVA:	Ovalbumin
MDA:	Malondialdehyde
PAS:	Periodic acid-Schiff
Penh:	Enhanced pause
ROS:	Reactive oxygen species.

## Data Availability

The data used to support the findings of this study are included with the article.

## Conflicts of Interest

The authors declare that there are no conflicts of interest.

## Authors' Contributions

WCH, NCT, CFL, and CJL are responsible for the experimental design and performance. WCH, NCT, YLH, and LCC are responsible for the data analysis and interpretation. LCC, CFL, and CJL are responsible for drafting the manuscript. Wen-Chung Huang and Nai-Chun Ting contributed equally to this work.

## Acknowledgments

This study was supported in part by grants from the Chang Gung Memorial Hospital (CMRPF1C0203, CMRPF1H0042, CMRPF1F0051-3, and CMRPF1J0031-3), the Chang Gung University of Science and Technology (EZRP3F0271 and ZRRPF3H0121), and the Ministry of Science and Technology in Taiwan (106-2320-B-255-007-MY3 and MOST-108-2320-B-255-001).


## References

- [1] S. Rayees, F. Malik, S. I. Bukhari, and G. Singh, "Linking GATA-3 and interleukin-13: implications in asthma," *Inflammation Research*, vol. 63, no. 4, pp. 255–265, 2014.
- [2] E. Leinaar, A. Alamian, and L. Wang, "A systematic review of the relationship between asthma, overweight, and the effects of physical activity in youth," *Annals of Epidemiology*, vol. 26, no. 7, pp. 504–510.e6, 2016.
- [3] A. Ray, M. Raundhal, T. B. Oriss, P. Ray, and S. E. Wenzel, "Current concepts of severe asthma," *The Journal of Clinical Investigation*, vol. 126, no. 7, pp. 2394–2403, 2016.
- [4] A. KleinJan, "Airway inflammation in asthma: key players beyond the Th2 pathway," *Current Opinion in Pulmonary Medicine*, vol. 22, no. 1, pp. 46–52, 2016.
- [5] P. S. Hiemstra, P. B. McCray Jr., and R. Bals, "The innate immune function of airway epithelial cells in inflammatory lung disease," *The European Respiratory Journal*, vol. 45, no. 4, pp. 1150–1162, 2015.
- [6] C. M. Lloyd and S. Saglani, "Epithelial cytokines and pulmonary allergic inflammation," *Current Opinion in Immunology*, vol. 34, pp. 52–58, 2015.
- [7] O. Ciepiela, M. Ostafin, and U. Demkow, "Neutrophils in asthma—a review," *Respiratory Physiology and Neurobiology*, vol. 209, pp. 13–16, 2015.
- [8] A. Auerbach and M. L. Hernandez, "The effect of environmental oxidative stress on airway inflammation," *Current Opinion in Allergy and Clinical Immunology*, vol. 12, no. 2, pp. 133–139, 2012.
- [9] J. W. Steinke and M. G. Lawrence, "T-cell biology in immunotherapy," *Annals of Allergy, Asthma, and Immunology*, vol. 112, no. 3, pp. 195–199, 2014.
- [10] R. Keyhanmanesh, R. Rahbarghazi, M. R. Aslani, M. Hassanpour, and M. Ahmadi, "Systemic delivery of mesenchymal stem cells condition media in repeated doses acts as magic bullets in restoring IFN- $\gamma$ /IL-4 balance in asthmatic rats," *Life Sciences*, vol. 212, pp. 30–36, 2018.
- [11] J. E. Fergusson, S. S. Patel, and R. F. Lockey, "Acute asthma, prognosis and treatment," *The Journal of Allergy and Clinical Immunology*, vol. 139, no. 2, pp. 438–447, 2017.
- [12] A. Arabkhazaeli, S. J. H. Vijverberg, C. K. van der Ent, J. A. M. Raaijmakers, and A. H. Maitland-van der Zee, "High incidence of oral corticosteroids prescriptions in children with asthma in early childhood," *The Journal of Asthma*, vol. 53, no. 10, pp. 1012–1017, 2016.
- [13] P. J. Barnes, "Glucocorticosteroids: current and future directions," *British Journal of Pharmacology*, vol. 163, no. 1, pp. 29–43, 2011.
- [14] J. M. Rodriguez, M. Monsalves-Alvarez, S. Henriquez, M. N. Llanos, and R. Troncoso, "Glucocorticoid resistance in chronic diseases," *Steroids*, vol. 115, pp. 182–192, 2016.
- [15] C. E. Ward and A. P. Baptist, "Characteristics of complementary and alternative medicine (CAM) use among older adults with asthma," *The Journal of Asthma*, vol. 53, no. 5, pp. 546–552, 2016.
- [16] F. Liu, N. X. Xuan, S. M. Ying, W. Li, Z. H. Chen, and H. H. Shen, "Herbal medicines for asthmatic inflammation: from basic researches to clinical applications," *Mediators of Inflammation*, vol. 2016, Article ID 6943135, 12 pages, 2016.
- [17] C. K. Chan, M. L. Kuo, J. J. Shen, L. C. See, H. H. Chang, and J. L. Huang, "Ding Chuan Tang, a Chinese herb decoction, could improve airway hyper-responsiveness in stabilized asthmatic children: a randomized, double-blind clinical trial," *Pediatric Allergy and Immunology*, vol. 17, no. 5, pp. 316–322, 2006.
- [18] S. D. Wang, L. J. Lin, C. L. Chen et al., "Xiao-Qing-Long-Tang attenuates allergic airway inflammation and remodeling in repetitive Dermatogoides pteronyssinus challenged chronic asthmatic mice model," *Journal of Ethnopharmacology*, vol. 142, no. 2, pp. 531–538, 2012.
- [19] H. M. Wang, S. K. Lin, C. H. Yeh, and J. N. Lai, "Prescription pattern of Chinese herbal products for adult-onset asthma in Taiwan: a population-based study," *Annals of Allergy, Asthma, and Immunology*, vol. 112, no. 5, pp. 465–470, 2014.
- [20] M. K. Lee, B. W. Cheng, C. T. Che, and D. P. Hsieh, "Cytotoxicity assessment of Ma-huang (Ephedra) under different conditions of preparation," *Toxicological Sciences*, vol. 56, no. 2, pp. 424–430, 2000.
- [21] X. M. Li, C. K. Huang, T. F. Zhang et al., "The Chinese herbal medicine formula MSSM-002 suppresses allergic airway hyperreactivity and modulates TH1/TH2 responses in a murine model of allergic asthma," *The Journal of Allergy and Clinical Immunology*, vol. 106, no. 4, pp. 660–668, 2000.
- [22] C. C. Lin, C. J. Liou, C. Y. Chiang, W. Y. Huang, and W. C. Huang, "Danggui Buxue Tang attenuates eosinophil infiltration and airway hyperresponsiveness in asthmatic mice," *Annals of Allergy, Asthma, and Immunology*, vol. 107, no. 6, pp. 501–509, 2011.
- [23] L. H. Su, Y. P. Li, H. M. Li et al., "Anti-inflammatory prenylated flavonoids from *Helminthostachys zeylanica*," *Chemical & Pharmaceutical Bulletin*, vol. 64, no. 5, pp. 497–501, 2016.
- [24] C. H. Lee, Y. L. Huang, J. F. Liao, and W. F. Chiou, "Ugonin K promotes osteoblastic differentiation and mineralization by activation of p38 MAPK- and ERK-mediated expression of Runx2 and osterix," *European Journal of Pharmacology*, vol. 668, no. 3, pp. 383–389, 2011.
- [25] H. L. Hsieh, S. H. Yang, T. H. Lee, J. Y. Fang, and C. F. Lin, "Evaluation of anti-inflammatory effects of *Helminthostachys zeylanica* extracts via inhibiting bradykinin-induced MMP-9 expression in brain astrocytes," *Molecular Neurobiology*, vol. 53, no. 9, pp. 5995–6005, 2016.
- [26] C. J. Liou, Y. L. Huang, W. C. Huang, K. W. Yeh, T. Y. Huang, and C. F. Lin, "Water extract of *Helminthostachys zeylanica* attenuates LPS-induced acute lung injury in mice by modulating NF- $\kappa$ B and MAPK pathways," *Journal of Ethnopharmacology*, vol. 199, pp. 30–38, 2017.
- [27] Y. L. Huang, C. C. Shen, Y. C. Shen, W. F. Chiou, and C. C. Chen, "Anti-inflammatory and antiosteoporosis flavonoids from the rhizomes of *Helminthostachys zeylanica*," *Journal of Natural Products*, vol. 80, no. 2, pp. 246–253, 2017.
- [28] W. C. Huang, L. W. Fang, and C. J. Liou, "Phloretin attenuates allergic airway inflammation and oxidative stress in asthmatic mice," *Frontiers in Immunology*, vol. 8, p. 134, 2017.
- [29] W. C. Huang, P. Y. Gu, L. W. Fang, Y. L. Huang, C. F. Lin, and C. J. Liou, "Sophoraflavanone G from *Sophora flavescens* induces apoptosis in triple-negative breast cancer cells," *Phyto-medicine*, vol. 61, p. 152852, 2019.
- [30] W. C. Huang, C. L. Lai, Y. T. Liang, H. C. Hung, H. C. Liu, and C. J. Liou, "Phloretin attenuates LPS-induced acute lung injury in mice via modulation of the NF- $\kappa$ B and MAPK pathways," *International Immunopharmacology*, vol. 40, pp. 98–105, 2016.

- [31] H. L. Peng, W. C. Huang, S. C. Cheng, and C. J. Liou, "Fisetin inhibits the generation of inflammatory mediators in interleukin-1 $\beta$ -induced human lung epithelial cells by suppressing the NF- $\kappa$ B and ERK1/2 pathways," *International Immunopharmacology*, vol. 60, pp. 202–210, 2018.
- [32] W. C. Huang, C. C. Chan, S. J. Wu et al., "Matrine attenuates allergic airway inflammation and eosinophil infiltration by suppressing eotaxin and Th2 cytokine production in asthmatic mice," *Journal of Ethnopharmacology*, vol. 151, no. 1, pp. 470–477, 2014.
- [33] C. J. Liou, C. Y. Cheng, K. W. Yeh, Y. H. Wu, and W. C. Huang, "Protective effects of casticin from *Vitex trifolia* alleviate eosinophilic airway inflammation and oxidative stress in a murine asthma model," *Frontiers in Pharmacology*, vol. 9, p. 635, 2018.
- [34] C. J. Liou, Y. R. Lai, Y. L. Chen, Y. H. Chang, Z. Y. Li, and W. C. Huang, "Matrine attenuates COX-2 and ICAM-1 expressions in human lung epithelial cells and prevents acute lung injury in LPS-induced mice," *Mediators of Inflammation*, vol. 2016, Article ID 3630485, 12 pages, 2016.
- [35] S. Myou, A. R. Leff, S. Myo et al., "Blockade of inflammation and airway hyperresponsiveness in immune-sensitized mice by dominant-negative phosphoinositide 3-kinase-TAT," *The Journal of Experimental Medicine*, vol. 198, no. 10, pp. 1573–1582, 2003.
- [36] S. Colicino, D. Munblit, C. Minelli, A. Custovic, and P. Cullinan, "Validation of childhood asthma predictive tools: a systematic review," *Clinical and Experimental Allergy*, vol. 49, no. 4, pp. 410–418, 2019.
- [37] C. B. Charron and S. Pakhale, "The role of airway hyperresponsiveness measured by methacholine challenge test in defining asthma severity in asthma-obesity syndrome," *Current Opinion in Allergy and Clinical Immunology*, vol. 16, no. 3, pp. 218–223, 2016.
- [38] S. H. Fatani, "Biomarkers of oxidative stress in acute and chronic bronchial asthma," *The Journal of Asthma*, vol. 51, no. 6, pp. 578–584, 2014.
- [39] S. Saglani and C. M. Lloyd, "Eosinophils in the pathogenesis of paediatric severe asthma," *Current Opinion in Allergy and Clinical Immunology*, vol. 14, no. 2, pp. 143–148, 2014.
- [40] S. R. Suja, P. G. Latha, P. Pushpangadan, and S. Rajasekharan, "Evaluation of hepatoprotective effects of *Helminthostachys zeylanica* (L.) Hook against carbon tetrachloride-induced liver damage in Wistar rats," *Journal of Ethnopharmacology*, vol. 92, no. 1, pp. 61–66, 2004.
- [41] Y. Ma, A. Ge, W. Zhu et al., "Morin attenuates ovalbumin-induced airway inflammation by modulating oxidative stress-responsive MAPK signaling," *Oxidative Medicine and Cellular Longevity*, vol. 2016, Article ID 5843672, 13 pages, 2016.
- [42] J. M. Gostner, K. Becker, F. Ueberall, and D. Fuchs, "The good and bad of antioxidant foods: an immunological perspective," *Food and Chemical Toxicology*, vol. 80, pp. 72–79, 2015.
- [43] P. Bansal, S. Saw, D. Govindaraj, and N. Arora, "Intranasal administration of a combination of choline chloride, vitamin C, and selenium attenuates the allergic effect in a mouse model of airway disease," *Free Radical Biology and Medicine*, vol. 73, pp. 358–365, 2014.
- [44] W. C. Huang, C. Y. Liu, S. C. Shen et al., "Protective effects of licochalcone A improve airway hyper-responsiveness and oxidative stress in a mouse model of asthma," *Cells*, vol. 8, no. 6, p. 617, 2019.
- [45] H. J. Park, C. M. Lee, I. D. Jung et al., "Quercetin regulates Th1/Th2 balance in a murine model of asthma," *International Immunopharmacology*, vol. 9, no. 3, pp. 261–267, 2009.
- [46] Z. W. Gu, Y. X. Wang, and Z. W. Cao, "Neutralization of interleukin-17 suppresses allergic rhinitis symptoms by down-regulating Th2 and Th17 responses and upregulating the Treg response," *Oncotarget*, vol. 8, no. 14, pp. 22361–22369, 2017.
- [47] K. Hirahara and T. Nakayama, "CD4+ T-cell subsets in inflammatory diseases: beyond the Th1/Th2 paradigm," *International Immunopharmacology*, vol. 28, no. 4, pp. 163–171, 2016.
- [48] S. L. Hall, T. Baker, S. Lajoie et al., "IL-17A enhances IL-13 activity by enhancing IL-13-induced signal transducer and activator of transcription 6 activation," *The Journal of Allergy and Clinical Immunology*, vol. 139, no. 2, pp. 462–471.e14, 2017.
- [49] K. Kelly-Pieper, S. P. Patil, P. Busse et al., "Safety and tolerability of an antiasthma herbal formula (ASHMI) in adult subjects with asthma: a randomized, double-blinded, placebo-controlled, dose-escalation phase I study," *The Journal of Alternative and Complementary Medicine*, vol. 15, no. 7, pp. 735–743, 2009.

Review

# Bioactive Agent Discovery from the Natural Compounds for the Treatment of Type 2 Diabetes Rat Model

Shih-Chun Yang <sup>1,†</sup>, Ching-Yun Hsu <sup>2,3,4,†</sup>, Wei-Ling Chou <sup>5</sup>, Jia-You Fang <sup>3,4,6,7</sup>  and Shih-Yi Chuang <sup>6,\*</sup>

<sup>1</sup> Department of Cosmetic Science, Providence University, Taichung 43301, Taiwan; yangsc@pu.edu.tw

<sup>2</sup> Department of Nutrition and Health Sciences, Chang Gung University of Science and Technology, Kweishan, Taoyuan 33303, Taiwan; cyhsu@mail.cgu.edu.tw

<sup>3</sup> Research Center for Food and Cosmetic Safety, Chang Gung University of Science and Technology, Kweishan, Taoyuan 33303, Taiwan; fajy@mail.cgu.edu.tw

<sup>4</sup> Research Center for Chinese Herbal Medicine, Chang Gung University of Science and Technology, Kweishan, Taoyuan 33303, Taiwan

<sup>5</sup> Department of Traditional Chinese Medicine, Chang Gung Memorial Hospital, Keelung 20401, Taiwan; chouweiling@gmail.com

<sup>6</sup> Pharmaceutics Laboratory, Graduate Institute of Natural Products, Chang Gung University, Kweishan, Taoyuan 33303, Taiwan

<sup>7</sup> Department of Anesthesiology, Chang Gung Memorial Hospital, Kweishan, Taoyuan 33303, Taiwan

\* Correspondence: d000014409@cgu.edu.tw; Tel.: +886-3-2118800; Fax: +886-3-2118236

† These authors contributed equally to this work.

Academic Editor: Béla Juhász

Received: 13 October 2020; Accepted: 27 November 2020; Published: 3 December 2020



**Abstract:** Diabetes mellitus is a well-known chronic metabolic disease that poses a long-term threat to human health and is characterized by a relative or absolute lack of insulin, resulting in hyperglycemia. Type 2 diabetes mellitus (T2DM) typically affects many metabolic pathways, resulting in  $\beta$ -cell dysfunction, insulin resistance, abnormal blood glucose levels, inflammatory processes, excessive oxidative reactions, and impaired lipid metabolism. It also leads to diabetes-related complications in many organ systems. Antidiabetic drugs have been approved for the treatment of hyperglycemia in T2DM; these are beneficial for glucose metabolism and promote weight loss, but have the risk of side effects, such as nausea or an upset stomach. A wide range of active components, derived from medicinal plants, such as alkaloids, flavonoids, polyphenol, quinones, and terpenoids may act as alternative sources of antidiabetic agents. They are usually attributed to improvements in pancreatic function by increasing insulin secretions or by reducing the intestinal absorption of glucose. Ease of availability, low cost, least undesirable side effects, and powerful pharmacological actions make plant-based preparations the key player of all available treatments. Based on the study of therapeutic reagents in the pathogenesis of humans, we use the appropriate animal models of T2DM to evaluate medicinal plant treatments. Many of the rat models have characteristics similar to those in humans and have the advantages of ease of genetic manipulation, a short breeding span, and access to physiological and invasive testing. In this review, we summarize the pathophysiological status of T2DM rat models and focus on several bioactive compounds from herbal medicine with different functional groups that exhibit therapeutic potential in the T2DM rat models, in turn, may guide future approach in treating diabetes with natural drugs.

**Keywords:** animal model; drug development; herbal medicine; insulin resistance; Type 2 diabetes mellitus



## 1. Introduction

Type 2 diabetes mellitus (T2DM) is a chronic, complex multisystem disease that causes multiple diabetes-related comorbidities, and requires a multifaceted and personalized approach to treatment. Although the complexity of T2DM is now more exhaustively understood, the scientific community believed that diabetes was a simple disease of the pancreas in the early 19th century. Over the past 30 years, people have acquired a deeper understanding and gained new insights about important contributors to T2DM, including the liver, muscle, kidney, fat cells, brain,  $\alpha$ -cells,  $\beta$ -cells, and intestines, as well as various hormones and even systemic inflammation, genetics, and the environment (Figure 1). From an enhanced scientific knowledge of the pathophysiologic progression of T2DM [1–6], new treatment options have become possible, thereby, increasing the potential for improving control over this complex disease. However, we need more suitable T2DM animal models for enhanced knowledge on both the pathophysiological progression and potential therapeutic drugs. Furthermore, those animal models must be relevant to the T2DM study, that the characteristics of the animal disease models should mimic the pathophysiology and the inherent history of the disease, or the model should develop T2DM complications with an etiology similar to clinical presentation and the pathophysiology of human disease. Insulin resistance (IR) classically refers to impaired sensitivity to insulin-mediated glucose disposal in muscles, body fat, and liver. Traditional Chinese herbal medicine has been found to play an important role in the T2DM treatment, by attenuating IR and regulating glucose tolerance, and other related mechanisms. In this review, we utilized the T2DM rat models, including genetically spontaneous and experimentally-induced diabetes models, characterized like the clinical manifestation of T2DM by hyperglycemia and IR, which is easily accessible and inexpensive. Furthermore, several bioactive compounds from herbal medicine with different functional groups, such as alkaloids, flavonoids, polyphenols, quinones, and terpenoids, exhibiting therapeutic potential in the T2DM rat models and in turn, may guide our approach in treating diabetes with natural drugs.

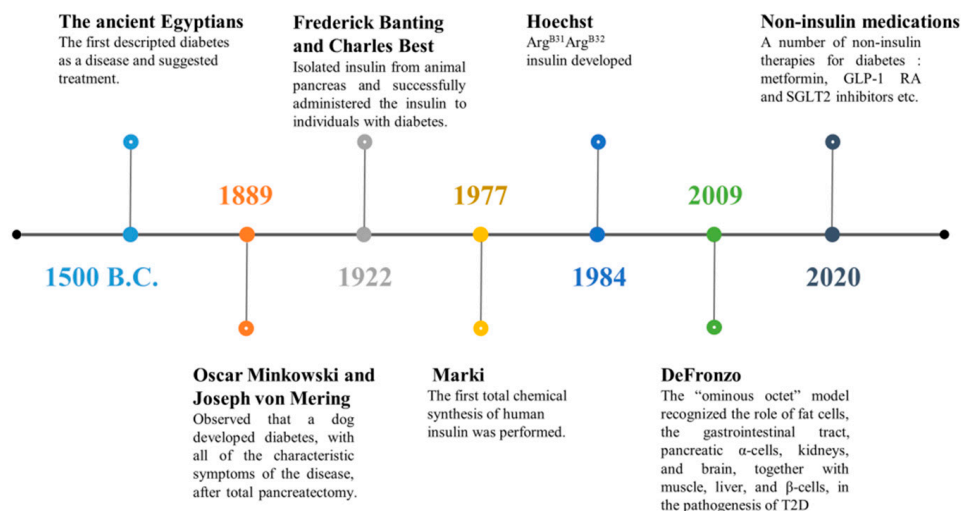


**Figure 1.** A timeline highlighting represents the development of insulin and T2DM as a therapeutic agent for the treatment of diabetes and the development of modified insulin products with more prolonged times of action.

## 2. Pathogenesis of T2DM

Diabetes is a common chronic metabolic disease characterized by hyperglycemia due to the deficiency of insulin secretion. Chronic hyperglycemia follows with a variety of complications, including retinopathy, nephropathy, neuropathy, and cardiovascular disorders [7]. The two most common types of diabetes are type 1 diabetes (T1DM) and T2DM. T1DM is generally thought to be caused by immune-related destruction of pancreatic  $\beta$ -cells producing insulin [8]. It is considered an autoimmune disease, and is most common in children and young people. T2DM is associated with



genetics, obesity, poor dietary habits, and generally poor nutrition. Unlike T1DM, T2DM is not a simple condition of insufficient insulin secretion. Obesity is one of the main predispositions towards the pathogenesis of T2DM. When nutrient intake is overloaded, the remaining calories from fat are stored as adipose tissue. Nonetheless, the capacity of fat cells to store calories is limited. Too much fat tissue leads to obesity and infiltration of inflammatory cells, resulting in chronic low-grade inflammation, increased lipolysis, and altered secretion of fat hormones (adipokines), including decreased blood adiponectin concentration, all contribute to IR in fat tissue [9–11]. This progression leads to disorders related to insufficient or abnormal insulin secretion, which affects the regulation of blood glucose metabolism [12]. Qing He's group has identified that a hypoxia response in adipose tissue has been reported during obesity. Hypoxia-inducible factor-1 (HIF-1) is activated during hypoxia, resulting in increased expression of c-Jun N-terminal kinase (JNK) and nuclear factor kappa-B kinase (NF- $\kappa$ B) to produce inflammation in adipose tissue [13]. A large number of inflammatory cytokines are released to further exacerbate IR and lipolysis. The aggravation of inflammation further impairs the regulation of peroxisome proliferator-activated receptor (PPAR) and accelerates fat cell death [14–16]. With the development of IR, hyperinsulinemia further causes free fatty acid (FFA) to be released from lipoprotein triglycerides hydrolysis [17]. Especially when the capacity of adipose tissue is insufficient, the remaining fat will accumulate in other body tissues, such as the liver, muscle, and even pancreas rather than fatty tissue, through a process called ectopic fat accumulation. For example, the accumulation of fat in striated muscle tissue reduces the glucose uptake of muscle. When fat accumulates in tissues other than adipose tissue, it will further aggravate IR. Therefore, increased FFA flux in IR and adipose tissue forms a vicious circle.

High levels of FFA are released from fat cells into the circulation and accumulate in other organs, thereby, further inducing lipid toxicity and accelerating systemic IR. For example, the accumulation of fat in striated muscle tissue reduces the glucose uptake of muscle. The accumulation of fat in the pancreas will also result in blocking insulin secretion and further cause a rise in blood glucose [17]. Therefore, considering the increased complexity of T2DM mechanism, its progression directly involves different organ systems. In Figure 2, DeFronzo described a systemic approach to the treatment of T2DM and provides eight key targets for therapeutic intervention, including fat cells, gastrointestinal tract, pancreatic  $\alpha$ -cells,  $\beta$ -cells, kidneys, and brain, together with skeletal muscle, and liver [6]. Reduced insulin sensitivity in the liver, muscle, and adipose tissue, and progressive dysfunction of pancreatic  $\beta$ -cells lead to impaired insulin secretion, and finally result in hyperglycemia. In patients with T2DM, IR leads to increased lipolysis and increased free fatty acid concentrations in fat cells, resulting in lipotoxicity [18]. Incretin hormone glucagon-like peptide-1 (GLP-1) are gut-derived hormones that can stimulate insulin secretion, and GLP-1 secretion in patients with T2DM is deficient resulting in promoting the process of T2DM [19]. Moreover, sodium-glucose cotransporter 2 (SGLT-2) expression in the kidneys increases excessively, inducing the kidney to continue reabsorbing glucose, rather than excrete it in the urine. This condition is considered to contribute to the maintenance of hyperglycemia in patients with T2DM [20]. Finally, IR also affects the brain and may cause damage of the hypothalamic regions of the brain, associated with appetite regulation. Hypothalamic IR in the brain can contribute to hyperglycemia in T2DM [21]. Overall, this polymorphism model of T2DM provides guidance for therapeutic interventions and also shows that the multisystem dysfunction of T2DM requires a combination of treatments for multiple diseases, rather than a single therapy to target one deficiency.

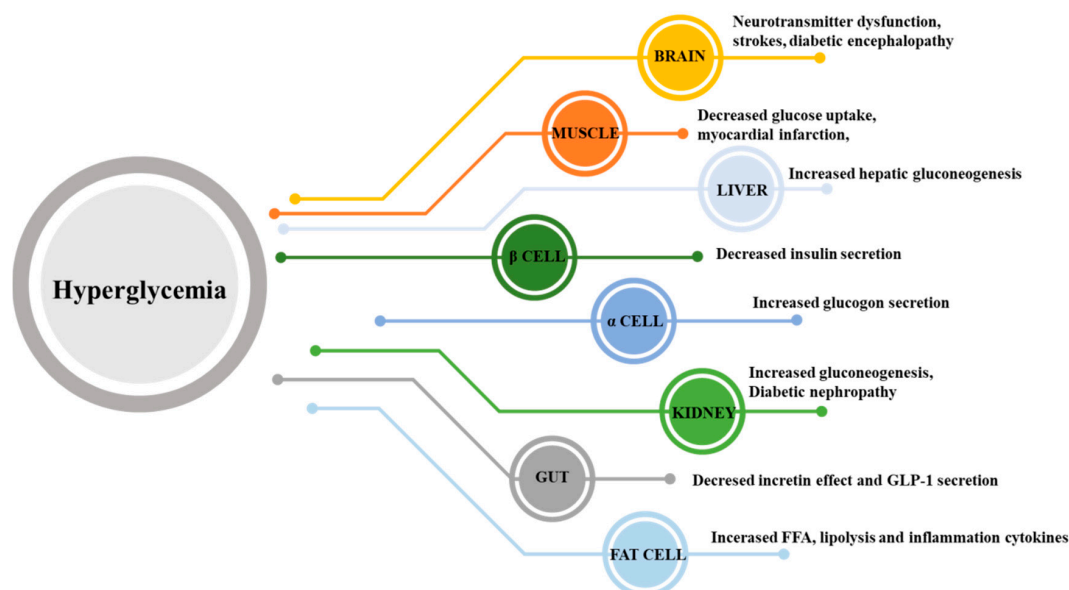


**Figure 2.** The ominous octet. Multiple defects of organ result from the development of glucose intolerance in T2D. The classical organ systems are targets for which available, including the pancreatic islet, liver, muscle and adipose tissue. The non-classical new organs interventions have been new targeted, have been more focus recently, including the intestine, kidney and brain.

### 3. The Current Drug Therapy for T2DM

Many antidiabetic drugs have been approved for the treatment of hyperglycemia due to T2DM [12]. Table 1 presents the various classes of available hypoglycemic drugs, based on the DeFronzo's description of T2DM pathogenesis and their target organs with pathophysiological defects. The classical and non-classical therapeutic target organ systems, include pancreatic islet, liver, muscle and adipose tissue, the intestine, kidney, and the brain. Metformin, as the first-line oral therapy remains the first drug of choice for all T2DM patients. The major mechanism of action, includes a decrease in hepatic gluconeogenesis and an increase in glucose uptake by skeletal muscle [12], reduction of IR via modification of glucose metabolic pathways, and promotion of weight loss. Glucagon-like peptide 1 (GLP-1) receptor agonists (e.g., liraglutide and exenatide) exhibit increased resistance to dipeptidyl peptidase 4 degradation [22,23], and has many clinical benefits, including inhibition of glucagon secretion by the  $\alpha$ -cells, stimulation of insulin secretion, and delayed gastric emptying thus promoting weight loss [24]. Moreover, there is a reduced risk of several side effects, including dyslipidemia, hypertension, and endothelial dysfunction [25]. Dipeptidyl peptidase 4 inhibitors (e.g., sitagliptin, vildagliptin, and saxagliptin), which can be taken orally could reduce endogenous GLP-1 degradation. They prolong the circulating half-life of endogenous incretins, thereby providing GLP-1 at physiological levels [22]. Thiazolidinediones (e.g., rosiglitazone and pioglitazone) are PPAR- $\gamma$  activators that cause an increase in adipokines levels, such as adiponectin, insulin sensitivity by acting on adipose, muscle, and liver tissue to increase glucose uptake and decrease hepatic glucose production [26,27]. Pioglitazone shows a potentially beneficial impact on cardiovascular disease, although it also carries a risk of bladder cancer [27]. The drug may cause side effects, such as fluid retention and edema, weight gain, and increased risk of heart failure. The sodiumglucose co-transporter 2 (SGLT-2) inhibitors are a novel group of compounds that antagonize the glucose transporter, which is responsible for about 90% of glucose reabsorption and is found primarily in the kidney. When this transporter is antagonized, excessive glucose in the renal tubules is not reabsorbed and is excreted in the urine [28], thus, resulting in hyperglycemia reduction. However, the primary side effect of SGLT-2 inhibition is an increase in urinary or genital infections.

**Table 1.** The pathophysiological defects of organs were targeted by various classes of available hypoglycemic drugs.

Organs	Class	Mechanism of Action	Side Effects
$\alpha$ -cell	GLP-1RA (incretin mimetic drugs: exenatide, liraglutide, albiglutide), DPP-4 inhibitors (saxagliptin, sitagliptin)	Stimulation of the GLP-1 receptor, inhibition of GLP-1 degradation	Nausea, gastrointestinal complaints
$\beta$ -cell	GLP-1RA (incretin mimetic drugs: exenatide, liraglutide, albiglutide), Thiazolidinediones (pioglitazone)	Stimulation of the GLP-1 receptor, reduction of IR and increase transcription of adipokines	Nausea, weight gain
Brain	GLP-1RA (incretin mimetic drugs: exenatide, liraglutide, albiglutide)	Stimulation of the GLP-1 receptor	Nausea,
Fat cell	Thiazolidinediones (pioglitazone)	Reduction of IR and increase transcription of adipokines	Weight gain
Gut	GLP-1RA (incretin mimetic drugs: exenatide, liraglutide, albiglutide)	Stimulation of the GLP-1 receptor	Nausea,
Liver	GLP-1RA (incretin mimetic drugs: exenatide, liraglutide, albiglutide), Thiazolidinediones (pioglitazone), Biguanide (metformin)	Stimulation of the GLP-1 receptor, reduction of IR and increase transcription of adipokines, enhancement the effect of insulin	Nausea, weight gain, lactic acidosis
Muscle	GLP-1RA (incretin mimetic drugs: exenatide, liraglutide, albiglutide), Thiazolidinediones (pioglitazone)	Stimulation of the GLP-1 receptor, reduction of IR and increase transcription of adipokines	Nausea, weight gain
Kidney	SGLT-2 inhibitors (canagliflozin, dapagliflozin, empagliflozin)	Inhibition of SGLT-2 in the kidney	Diabetic ketoacidosis

#### 4. Rat Models of T2D

Thoroughly characterized and clinically relevant animal models also play a vital role, and are promptly needed in understanding the pathogenesis of diabetes. These basic studies can combine the genetic and functional characteristics of diabetes to replace direct drug tests in humans. To further understand the T2DM disorder, many animal models have been developed to demonstrate the pathophysiology and complications of diabetes [29] and to achieve the purpose of managing T2DM with more effective and better therapeutics. Both genetically spontaneous and experimentally induced diabetes models were exist [30]. The symptom patterns induced in these animal models often include obesity, impaired glucose tolerance, IR, and the  $\beta$ -cell models that reflect the human condition in which obesity is closely related to T2DM development (Table 2).

**Table 2.** Summary of rat models of type 2 diabetes mellitus.

Type of Models	Abnormality	Ref.
Obese models (monogenic)		
Zucker fatty (ZF) rats	Obese	[31,32]
	Hyperinsulinemia, hyperlipidemia, and hypertension	
	IR and glucose intolerance	
	Susceptibility to infection	
	Decrease in T cell number	
	Increase in macrophage number	
	Augmentation of immunoglobulins and proinflammatory cytokines production	
Obese models (polygenic)		
OLETF rat	Obese	[32,33]
	Spontaneously hyperplasia	
	Cellular infiltration and degradation	
	Diabetic nephropathy	
Non-obese models		
Goto-Kakizaki (GK) rat	A decreased $\beta$ -cell mass	[32,33]
	Liver and skeletal muscle IR	
	Attenuation of phagocytic activity of macrophages	
	Augmentation of natural IgM production	
	Increased in the T cell ratios in the white blood and decreased B cells.	
Induced obesity		
HFD/STZ rat	Dysfunction in $\beta$ -cells	[34,35]
	IR and hypoinsulinemia	
	Hyperglycemia	
	Increased INSR/PI3K/AKT pathway and decreased levels of IL-6 and TNF- $\alpha$ .	
	Low level of circulating adiponectin	

#### 4.1. Zucker Fatty Rat and Zucker Diabetic Fatty Rat Models

Zucker fatty (ZF) rat strains, the monogenic models of obesity, are characterized by a deficiency in the leptin receptor that induces hyperphagia and the rats become obese at around 4 weeks of age [36]. These rats are hypertensive, hyperlipidemic, and hyperinsulinemic at around 4–8 weeks of age, and develop advanced IR, glucose intolerance and become completely diabetic. Immunological investigation of the ZF strain exhibits susceptibility to infection [37], T-lymphocytopenia [38], production of immunoglobulins and nitric oxide, and increased expression of tumor necrosis factor- $\alpha$  (TNF- $\alpha$ ) and interleukin-1 beta (IL-1 $\beta$ ) [39]. The Zucker diabetic fatty (ZDF) rat substrain with a diabetic phenotype is derived by inducing mutations in ZF strains, and they are less obese than the ZF rats. However, these rates exhibit more severe IR due to enhanced apoptosis levels in  $\beta$ -cells, representing a model of obesity-associated diabetes [37].

#### 4.2. Otsuka Long Evans Tokushima Fatty Rat

The Otsuka Long Evans Tokushima Fatty (OLETF) rat strain is selectively bred for the null expression of the cholecystokinin-1 receptor in the hypothalamus, resulting in spontaneous hyperphagia, involving obesity and late-onset hyperglycemia at an age of about 20–40 weeks [40,41]. Immunological investigations indicate cellular infiltration and degeneration in pancreatic islets [36]. The late-stage is characterized by hyperplasia, and the islets become fibrotic tissue. These rats also display diabetic

nephropathy [42]. This is an appropriate animal model to evaluate both disease progression and skeletal alterations observed in humans [43,44].

#### 4.3. Goto-Kakizaki Rat Models

The Goto-Kakizaki (GK) rat, a non-obese model of T2DM, is established by repeated breeding of glucose-intolerant Wistar rats [45]. GK rats have become hyperglycemic at an early age due to an insufficient insulin response resulting in aberrant blood glucose homeostasis [46]. Characteristics of this model, include hyperglycemia, peripheral IR, albuminuria, glomerulosclerosis, tubulointerstitial fibrosis, and development of neuropathy [47]. Retinopathy and neuropathy are also reported to develop late in the life of these animals [48,49]. The islets of GK rats exhibit several biochemical defects, including inflammation, fibrosis [50], decreased energy production, reduced adenylate cyclase activity [51], reduced insulin-stimulated insulin receptor substrate-1 tyrosine phosphorylation [52], and defective regulation of protein phosphatase-1, and -2A and mitogen-activated protein kinase activation in adipocytes [53]. Therefore, precise features of the islets in GK rats resemble those in T2DM patients.

#### 4.4. High-Fat Diet/Streptozotocin (HFD/STZ) Rat Model of Diabetes

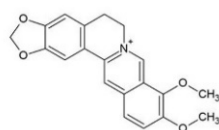
Streptozotocin (STZ), an antibiotic reagent, causes the production of reactive oxygen species in the  $\beta$ -cells of the pancreas, resulting in  $\beta$ -cell death, and is often used in animal models for the induction of T1DM [54]. In general, this model depends on the toxicity of STZ, which results from the transfer of the methyl-nitrosourea moiety from STZ to the DNA molecule, causing damage and subsequent DNA fragmentation [55]. STZ doses of 65–70 mg/kg are often used to induce T1DM in rats. However, Reed et al. [56] reported a new rat model of T2DM, known as the high-fat diet (HFD)/STZ rat. This model is referred to as a T2DM model, due to similar prediabetes and/or IR symptoms and hypoinsulinemia in patients [56]. Feeding Sprague-Dawley rats with a 40% kcal fat diet for 2 weeks, and subsequent intravenous injection with STZ further establishes the HFD/STZ rat model of T2DM relevant to the human condition [56–58]. The HFD/STZ rat models mimic the state of obesity, IR, and/or glucose intolerance in prediabetes conditions [58]. HFD/STZ rats have more pronounced dyslipidemia, glucose intolerance, hyperglycemia, and low levels of circulating adiponectin [59], similar to the metabolic profile of T2DM in humans. Recently, a high fat and sugar diet (HFSD) with the administration of STZ was suggested to establish a T2DM rat model, and it has been reported to be a better, and true mechanism of T2DM pathogenesis given the numerous alterations of protein expression in the INSR/PI3K/AKT pathway and levels of IL-6 and TNF- $\alpha$  [34,60]. No single animal model appears to encompass all of these characteristics, but many exhibit nearly similar characteristics of one or more aspects of T2DM in humans.

### 5. Anti-T2DM Drug Discovery Using T2DM Rat Models

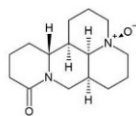
PubMed database published literature between April 2014 and April 2020 on T2DM rat models that had been treated with herbal medicine compounds were reviewed. For the search, the following combinations of terms were used as keywords: “herbal,” “drug,” “natural compound,” and “insulin resistance” or “T2DM rat models.” Herein, we have summarized the mechanisms of several representative bioactive components in T2DM rat models, including alkaloids, flavonoids, polyphenols, quinones, and terpenoids (Figure 3) used in the treatment of T2DM rat models, and which may help to provide valuable information on the application of pure herbal medicine compounds (Table 3).



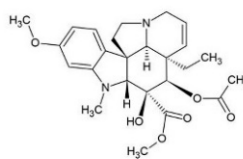
### Alkaloids



Berberine

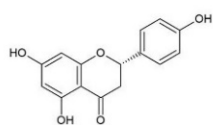


Oxymatrine

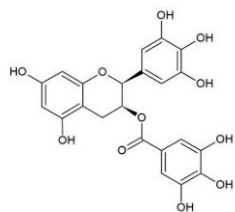


Vindoline

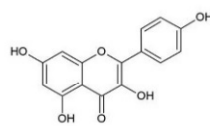
### Flavonoids



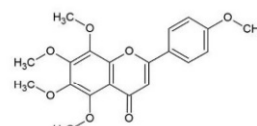
Naringenin



(-)-epigallocatechin-3-gallate (EGCG)

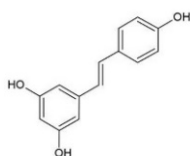


Kaempferol

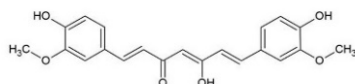


Tangeretin

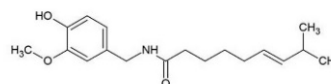
### Polyphenols



Resveratrol

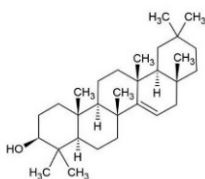


Curcumin

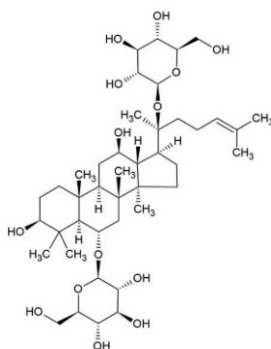


Capsaicin

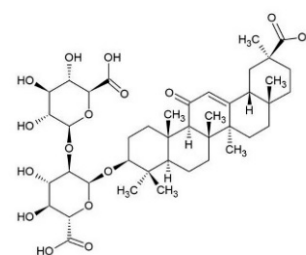
### Terpenoids



Taraxerol



Ginsenoside GR1



Glycyrrhizin

**Figure 3.** The chemical structures of anti-T2DM compounds introduced in this review.

**Table 3.** Natural bioactive compounds for the treatment of rat models of T2DM.

Structures	Treatment	Model	Improvement Effect	Ref.
<b>Alkaloids</b>				
Berberine	Oral	ZDF rats, HFD/STZ-induced rats	Increased insulin and decreased levels of HbA1c, TC, and TG Attenuated axonopathy	[61,62]
Oxymatrine	Oral	HFD/STZ-induced rats	Increased serum insulin and GLP-1, TC, TG, and GLUT-4 content	[63]
Vindoline	Oral	HFD/STZ-induced rats	Reduced fasting blood glucose, serum alanine transferase, aspartate aminotransferase, alkaline phosphatase, and levels of TNF- $\alpha$ and IL-6	[64]
<b>Flavonoids</b>				
Naringenin	Intragastric	HFD/STZ-induced rats	Decreased blood glucose and IR index, and improved antioxidation	[65]
(-)-epigallocatechin-3-gallate (EGCG)	Oral	Goto-Kakizaki rats	Improved mitochondrial function and autophagy in the heart of GK rats	[66]
Kaempferol	Intragastric	HFD/STZ-induced rats	Attenuated IR effect and inflammatory signal through inhibition of NF- $\kappa$ B and downstream cytokine production	[67]
Tangeretin	Oral	STZ-induced rats	Reduced plasma glucose, increased in the levels of insulin and hemoglobin and modulates the activities of hepatic enzymes	[68]
<b>Polyphenols</b>				
Resveratrol	Oral	STZ-nicotinamide-induced rats	Reduction in blood glucose and HbA1c levels Increased antioxidants activities of SOD, CAT, GSH, GPx, and PPAR- $\gamma$ and FALDH gene	[69]
Curcumin	Intraperitoneal	HFD/STZ-induced rats	Decreased fasting blood glucose, the pancreatic tissue destruction and apoptosis index, the expression of IL-1 $\beta$ , IL-6, TNF- $\alpha$ Block the phosphorylation of JNK and NF- $\kappa$ B protein to inhibit this signaling pathway	[70]
Capsaicin	Oral	HFD/STZ- induced rats	A TRPV1 agonist Decreased phosphorylation of tau protein Increased activity of PI3K/AKT and decrease activity of GSK-3 $\beta$	[71]
<b>Terpenoids</b>				
Taraxerol	Oral	HFD/STZ-induced rats	Inhibition of hypoglycemic, Insulin-sensitizing and inflammatory effects Activation of IRS1/PI3K/AKT/AMPK/GLUT4/GSK3 $\beta$ and inhibition of PKC/NF- $\kappa$ B	[72]
Ginsenoside	Intragastric	Goto-Kakizaki rats	Improvement of the blood glucose, body weight Inhibition of brain oxidative/nitrosative damage and IL-1 $\beta$ , IL-6, and TNF- $\alpha$ production	[73]
Glycyrrhizin	Intraperitoneal	ZDF rats	A HMGB1inhibitor. Reduced kidney inflammation Blocked TLR4 signaling pathways Blocked the pro-inflammatory cytokines Ameliorate dmacrophage and cell adhesion molecules, Against glomerular damage	[74]

### 5.1. Alkaloids

Alkaloids are a class of naturally-occurring compounds, derived from natural sources, such as plants, animals, bacteria, and fungi. They have a wide range of functions, including anti-spasmodic, anti-arrhythmic, anti-malarial, anticancer, antibacterial, and anti-hyperglycemic activity [75]. Various alkaloids, including berberine, oxymatrine, and vindoline are potentially effective against different diabetic models [76]. Berberine is the primary active component of *Rhizoma coptidis* and exhibits antidiabetic properties and hypoglycemic effects. Berberine has been shown to increase insulin and decrease HbA1c, cholesterol (TC), and total glucose (TG) blood levels in the ZDF rat model [61]. Berberine significantly attenuates axonopathy, and also restores PI3K/Akt/GSK3 $\beta$  signaling pathway in HFD/STZ rats. Oxymatrine has been demonstrated to increase serum insulin, liver and muscle glycogen and decrease fasting blood glucose, GLP-1, TC, TG, and muscle glucose transporter-4 levels in HFD/STZ rats [63]. Recently, vindoline, an indole alkaloid from the *Catharanthus roseus* plant, was reported to protect diabetic hepatic tissue from injury via antioxidant, anti-inflammatory, and anti-hypertriglyceridemia activities in a T2DM rat model [64]. Administration of vindoline in an HFD/STZ rat model significantly reduced fasting blood glucose, serum alanine transferase, aspartate aminotransferase, and alkaline phosphatase levels when compared to the diabetic controls [77]. Vindoline also stimulates the activity of superoxide dismutase and catalase and decreases the levels of TNF- $\alpha$  and IL-6. Histopathological findings show that vindoline improves the functions of both hepatic and pancreatic tissues in vivo.

### 5.2. Flavonoids

Flavonoids are bioactive compounds, found in flowers, nuts, fruits, and some vegetables; several investigators have focused on the use of flavonoids and related compounds for antidiabetic properties [77]. Some recent studies have suggested that flavonoid compounds including naringenin, (-)-epigallocatechin-3-gallate (EGCG), rutin, and kaempferol, among other flavonoids, may improve and stabilize the secretion of insulin from pancreatic  $\beta$ -cells. In diabetic animal models, flavonoids typically lead to reduced aldose reductase, regeneration of pancreatic  $\beta$ -cells, and increased insulin release. According to their biological properties, polyphenols may be useful nutraceuticals and supplementary treatments, and are involved in the regulation of carbohydrate and lipid metabolism, amelioration of hyperglycemia, dyslipidemia, and IR, and alleviate oxidative stress and inflammatory signaling pathways [78,79]. Naringin, a major flavanone glycoside obtained from grapefruit, was found to reduce blood glucose and IR index, glycosylated hemoglobin, inflammatory cytokines, and increase the levels of serum insulin, and glutathione in the antioxidant defense system in diabetic rat models [65,80]. Successful uptake of EGCG, a flavonoid-derived from green tea, was reported to improve mitochondrial function and autophagy in the hearts of GK rats with myocardial mitochondrial deficiency and oxidative stress [66]. Rutin is a flavonoid glycoside from flowers and fruits as a major source. In HFD/STZ rats, rutin treated by orally ameliorates the levels of TG and blood glucose, oxidative stress, TNF- $\alpha$  and IL-6 production, and cellular apoptosis pathways [81,82]. Another study found that kaempferol treatment may enhance insulin sensitivity and deterioration of IR in diabetic rats; the possible mechanisms may be the down-regulation of the IKK $\beta$ /NF- $\kappa$ B signal and subsequent inhibition of TNF- $\alpha$  and IL-6 production [67].

### 5.3. Polyphenols

Natural polyphenols in the plant kingdom are classified according to the number of phenol rings and structural elements that bind these rings, and include the common polyphenols such as resveratrol, curcumin, and capsaicin. Polyphenols have unique physical, chemical, and biological (metabolic and therapeutic) characteristics, based on the number of aromatic rings and functional groups in the phenol structure [83]. Polyphenols are also the most abundant antioxidants in the human diet. Increasing evidence indicates that various dietary polyphenols might prevent diabetes [78]. Resveratrol is a natural polyphenol widely found in grapes and blueberries [84]. The oral administration

of resveratrol in STZ/nicotinamide-induced rats decreased the fasting blood glucose and HbA1c levels and increased the antioxidant activity of superoxide dismutase, catalase, GSH, and glutathione peroxidase. Resveratrol has an important role in controlling hyperglycemia and plasma insulin levels and demonstrates increased expression of PPAR- $\gamma$  and FALDH in rat adipose tissue [69]. Curcumin is an acidic polyphenolic substance, with multiple physiological and pharmacological activities and remarkably low toxicity [85]. In accordance to some pharmacologic studies, curcumin exhibits neuroprotective effects, anti-hyperlipidemia, and hypolipidemic effects, and improves oxidative stress and inflammation [85–88]. Pharmacological evidence also indicates that curcumin significantly affects improvement in IR [89] and decrease in blood lipids, inflammatory cytokines [90], and plasma resistin levels [90] in diabetes animal models. In the T2DM rat models, curcumin plays an important role in decreasing fasting blood glucose, inhibiting inflammation, and reducing the apoptosis index in pancreatic islet  $\beta$ -cells in HFD/STZ rats. As part of the underlying mechanism, curcumin reduces TNF- $\alpha$ , IL-1 $\beta$ , IL-6, caspase-3, and Bax levels by blocking the phosphorylation of JNK and NF- $\kappa$ B protein signaling pathway [70]. Clinical characteristics of T2DM reveal a high-risk associated with Alzheimer's disease due to impaired insulin signaling pathways in brain tissue. Capsaicin is the major pungent compound obtained from hot chili peppers and is a highly selective agonist for the transient receptor potential vanilloid 1 (TRPV1), which was found to ameliorate IR [91]. TRPV1, a Ca<sup>2+</sup>-permeable nonselective cation channel, is expressed mainly in dorsal root ganglion cells and primary sensory afferents in the brains of humans and rats [92]. TRPV1 has a potential therapeutic value for obesity and diabetes [93]. Xu, et al. [71] demonstrated that dietary capsaicin reduced the risk of Alzheimer's disease in an HFD/STZ rat model. They found that rats receiving dietary capsaicin had a significant decrease in the levels of phosphorylation of AD-associated tau protein at special sites (serine 199, 202, and 396 in the hippocampus) compared with that in T2DM rats. The dietary capsaicin group increased PI3K/AKT and decreased GSK-3 $\beta$  activity, which was also observed in the hippocampus compared with that in T2DM control rats that did not receive capsaicin, indicating that capsaicin inhibited the phosphorylation of tau protein by increasing the PI3K/AKT and inhibiting GSK-3 $\beta$  activity. Dietary capsaicin may have potential use in the prevention of Alzheimer's disease in T2DM.

#### 5.4. Quinones

Quinones, a class of aromatic dicarbonyl compounds, are found predominantly in flowering plants, and fungi. In nature, quinone is biochemically involved in respiration and photosynthesis, and plays a vital role in electron transport, serving as electron carriers in redox reactions for energy transduction, and storage [94]. Anthraquinones are the largest class of naturally occurring quinones such as rhein, purpurin, and chrysophanol. Rhein is a lipophilic anthraquinone extensively found in medicinal herbs *Rheum palmatum* L. and has many pharmacological effects in protecting against liver and kidney damage, inflammation, excess oxidative reactions, and microbial infections. These pharmacological effects are used to treat hepatic disease [95], diabetes [96], atherosclerosis [97], and cancer [98]. However, many research reports demonstrate that sirtuin 1 (SIRT1) may play a vital role in the control of glucose homeostasis by regulating insulin secretion [99], down-regulating inflammation, improvement of IR [100], controlling fatty acid oxidation and mitochondrial biogenesis, and regulating hepatic glucose production [101]. Gerhart-Hines, et al. [101] indicated that the expression of SIRT1 was reduced in diabetic rats. However, the effect of rhein was to increase SIRT1 expression in HFD/STZ-induced diabetic rats, which improved IR and dyslipidemia. Furthermore, rhein dramatically decreased the levels of fasting plasma glucose, fasting insulin, homeostasis model assessment-insulin resistance index (HOMA-IR), TG, and TC, while renal tissues were significantly improved compared with those in diabetic rats that did not receive rhein. Chrysophanol is an anthraquinone isolated from *Rheum rhabarbarum* belonging to the *Polygonaceae* family. To date, it is known to exhibit several pharmacological effects, including anti-diabetes [102], anti-inflammatory [103], and anti-cancer activity [104]. Chrysophanol targets significantly decrease blood lipids, serum insulin levels in

diabetes, and reduces inflammatory cytokines, myocardial enzymes creatine kinase (CK) and lactate dehydrogenase (LDH), and increases SIRT1 protein expression. Chrysophanol also significantly ameliorates the cardiac pathological changes in diabetic animal models. Molecular dynamics studies suggest that chrysophanol inhibits activation of the *High Mobility Group Box 1* (HMGB1)/NF- $\kappa$ B pathway [105], increases GLUT 4 in muscle, induces phosphorylation of insulin receptor substrate-1, and docks well in the active site of DPP-IV, supporting its use as a significant DPP-IV inhibitor [104]. Chrysophanol is a generally used herb in traditional Chinese medicine for improving obesity. A study revealed the anti-obesity effects of chrysophanol by using HFD-induced rat models [106]. Chrysophanol dramatically decreased lipid accumulation in hepatocytes and decreased bodyweight, blood glucose, and blood levels of TG compared to those in HFD rats not receiving chrysophanol. In addition, the herbal compound reduced IL-6 and IL-1 $\beta$  levels and increased IL-10 expression to improve HFD-induced inflammation. The expression of lipolytic genes increased and those of lipogenic genes decreased in HFD rats treated with chrysophanol. Chrysophanol probably benefits from the activation of AMP-activated protein kinase (AMPK)/SIRT1, which leads to the down-regulation of sterol regulatory element-binding protein-1 [106].

### 5.5. Terpenoids

Persistent hyperglycemia causes the activation of protein kinase C (PKC) and the NF- $\kappa$ B signaling pathway associated with the production of IL-1 $\beta$ , IL-6, and TNF- $\alpha$ , revealing that inflammation plays a pivotal role in the development and progression of diabetic nephropathy (DN) [107,108]. Damage originating from the pathogenesis of DN, includes renal inflammation, accumulation of serum creatinine, urea, and uric acid, and release of urinary albumin [109]. Khanra et al. [72] showed that taraxerol, a pentacyclic triterpene from the leaf extract of the plant *Abroma augusta* L., exhibits protective effects against DN via the reduction in the secretion of proinflammatory cytokines, regulation of the serum lipid profile and blood glycemic status, and restoration of the renal physiologic function in T2DM rats. Taraxerol also stimulates the IRS1/PI3K/AKT/AMPK/GLUT4/GSK3 $\beta$  signaling pathways to mediate hyperglycemia and inhibits the PKC/NF- $\kappa$ B signaling pathway to improve inflammatory effects in T2DM rats [72]. Ginsenoside is the major bioactive compound in ginseng, which shows the therapeutic effects of ginsenoside in a diabetic GK rat model, wherein, ginsenoside ameliorated diabetic progression, including the levels of blood glucose, body weight, and Morris correlation index. The possible mechanism involved is inhibition of SOD, malondialdehyde (MDA), and inflammatory cytokines (IL-1 $\beta$ , and IL-6, and TNF- $\alpha$ ) [73]. Glycyrrhizin, a glycol-conjugated triterpene from *Glycyrrhiza glabra*, demonstrated anti-inflammatory properties and was shown to inhibit the cytokine activity of HMGB1. A recent study showed that the inhibition of HMGB1 by glycyrrhizin is an effective strategy for reducing kidney inflammation in a ZDF animal model [74]. The kidney cortex of ZDF rats showed an increase in toll-like receptor 4, phospho-p38 MAPK, and IL-1 $\beta$  expression, as well as an increase in macrophages compared to those in controls, and plays a major part in renal dysfunction. Furthermore, glycyrrhizin treatment blocked HMGB1-activated toll-like receptor 4 downstream signaling pathways, which may in turn block the transcriptional expression of the pro-inflammatory cytokines. Glycyrrhizin treatment also ameliorates the expression of macrophages and cell adhesion molecules, and provides protection against hyperglycemia-induced glomerular damage.

## 6. Conclusions

T2DM is a well-known common metabolic disease that is a risk to human health over the long term. Progression of T2DM from prediabetic state to overt diabetes and the development of complications occurs over many years. The assessment of interventions also takes years and requires large resources. The use of the appropriate animal model, based on diabetic syndromes, can provide substantial data on the pathophysiological mechanisms of T2DM in humans. While, no single animal model has been able to address all these characteristics, many animal models can provide very similar characteristics of one or more aspects of human T2DM. In this review article, we focused on the pathophysiological



status of T2DM rat models and several bioactive compounds from herbal medicine with different functional groups, which exhibit therapeutic potential for the T2DM rat models, at the same time, guiding our approach to the treatment of diabetes with natural drugs. Many risk factors and pathogenic processes in T2DM have been verified, including hyperglycemia, IR, lipid accumulation, excessive inflammation, oxidative stress, and adipokines, all of which are critically important in treating the disease. The diabetic rat models are considered to play an important role in presenting the pathogenesis of human T2DM and its complications, despite all the other limitations they offer. The diabetic rat models are essential for investigating and developing novel drugs for diabetes and its complications. The occurrence and prevalence of T2DM can be prevented by utilizing appropriate natural compounds derived from plant-based medicines. In this review, we suggested that these natural compounds can be used as drugs or dietary supplements to help prevent and treat T2DM. However, many questions still remain. Many natural compounds mentioned in our report have effects on hypoglycemia against T2DM, however, a notable side effect is that too much decrease in glycemia will cause patients to enter the hypoglycemic state.

**Author Contributions:** S.-Y.C. conceived the topic of the review article and wrote most of the draft. S.-C.Y. and C.-Y.H. took part in the writing and the discussion. W.-L.C. and J.-Y.F. wrote sections of the review and prepared the figures. All the authors made comments and suggestions for the writing of the review. All authors have read and agreed to the published version of the manuscript.

**Funding:** The authors are grateful for the financial support from Ministry of Science and Technology of Taiwan (MOST-109-2320-B-126-004-MY3) and Chang Gung Memorial Hospital (CMRPD1K0051-2 and CMRPD1F0331-3). The APC was funded by (MOST-109-2320-B-126-004-MY3).

**Conflicts of Interest:** The authors report no conflicts of interest in this work.

## References

1. Bliss, M. The discovery of insulin: The inside story. *Publ. Am. Inst. Hist. Pharm.* **1997**, *16*, 93–99.
2. Minkowski, O. Historical development of the theory of pancreatic diabetes by Oscar Minkowski, 1929: Introduction and translation by Rachmiel Levine. *Diabetes* **1989**, *38*, 1–6. [[CrossRef](#)]
3. Banting, F.G.; Best, C.H.; Collip, J.B.; Campbell, W.R.; Fletcher, A.A. Pancreatic Extracts in The Treatment of Diabetes Mellitus. *Diabetes* **1956**, *5*, 69–71. [[CrossRef](#)]
4. Märki, F.; Albrecht, W. Biological activity of synthetic human insulin. *Diabetologia* **1977**, *13*, 293–295. [[CrossRef](#)]
5. Monti, L.; Poma, R.; Caumo, A.; Stefani, I.; Picardi, A.; Sandoli, E.; Zoltobrocki, M.; Micossi, P.; Pozza, G. Intravenous infusion of diarginylinsulin, an insulin analogue: Effects on glucose turnover and lipid levels in insulin-treated type II diabetic patients. *Metabolism* **1992**, *41*, 540–544. [[CrossRef](#)]
6. DeFronzo, R.A. From the Triumvirate to the Ominous Octet: A New Paradigm for the Treatment of Type 2 Diabetes Mellitus. *Diabetes* **2009**, *58*, 773–795. [[CrossRef](#)]
7. Forbes, J.M.; Cooper, M.E. Mechanisms of Diabetic Complications. *Physiol. Rev.* **2013**, *93*, 137–188. [[CrossRef](#)]
8. Chillarón, J.J.; Le-Roux, J.A.F.; Benaiges, D.; Pedro-Botet, J. Type 1 diabetes, metabolic syndrome and cardiovascular risk. *Metabolism* **2014**, *63*, 181–187. [[CrossRef](#)]
9. McCarthy, M.I. Genomics, Type 2 Diabetes, and Obesity. *N. Engl. J. Med.* **2010**, *363*, 2339–2350. [[CrossRef](#)] [[PubMed](#)]
10. Kim, K.-A.; Shin, Y.-J.; Akram, M.; Kim, E.-S.; Choi, K.-W.; Suh, H.; Lee, C.-H.; Bae, O.-N. High Glucose Condition Induces Autophagy in Endothelial Progenitor Cells Contributing to Angiogenic Impairment. *Biol. Pharm. Bull.* **2014**, *37*, 1248–1252. [[CrossRef](#)] [[PubMed](#)]
11. Patel, P.; Abate, N. Body fat distribution and insulin resistance. *Nutrients* **2013**, *5*, 2019–2027. [[CrossRef](#)] [[PubMed](#)]
12. Kahn, S.E.; Cooper, M.E.; Del Prato, S. Pathophysiology and treatment of type 2 diabetes: Perspectives on the past, present, and future. *Lancet* **2014**, *383*, 1068–1083. [[CrossRef](#)]
13. He, Q.; Gao, Z.; Yin, J.; Zhang, J.; Yun, Z.; Ye, J. Regulation of HIF-1 $\alpha$  activity in adipose tissue by obesity-associated factors: Adipogenesis, insulin, and hypoxia. *Am. J. Physiol. Endocrinol. Metab.* **2011**, *300*, E877–E885. [[CrossRef](#)] [[PubMed](#)]

14. Feng, Y.-M.; Zhao, N.; Zhang, N.; Yu, C.-G.; Zhang, Q.; Thijs, L.; Staessen, J.A. Insulin Resistance in Relation to Lipids and Inflammation in Type-2 Diabetic Patients and Non-Diabetic People. *PLoS ONE* **2016**, *11*, e0153171. [[CrossRef](#)] [[PubMed](#)]
15. Nieto-Vazquez, I.; Fernández-Veledo, S.; Krämer, D.K.; Vila-Bedmar, R.; Garcia-Guerra, L.; Lorenzo, M. Insulin resistance associated to obesity: The link TNF-alpha. *Arch. Physiol. Biochem.* **2008**, *114*, 183–194. [[CrossRef](#)] [[PubMed](#)]
16. Li, Z.Y.; Song, J.; Zheng, S.L.; Fan, M.B.; Guan, Y.F.; Qu, Y.; Xu, J.; Wang, P.; Miao, C.Y. Adipocyte Metrnl Antagonizes Insulin Resistance through PPARgamma Signaling. *Diabetes* **2015**, *64*, 4011–4022. [[CrossRef](#)]
17. Sears, B.; Perry, M. The role of fatty acids in insulin resistance. *Lipids Health Dis.* **2015**, *14*, 1–9. [[CrossRef](#)]
18. Kashyap, S.; Belfort, R.; Gastaldelli, A.; Pratipanawatr, T.; Berria, R.; Pratipanawatr, W.; Bajaj, M.; Mandarino, L.; DeFronzo, R.; Cusi, K. A Sustained Increase in Plasma Free Fatty Acids Impairs Insulin Secretion in Nondiabetic Subjects Genetically Predisposed to Develop Type 2 Diabetes. *Diabetes* **2003**, *52*, 2461–2474. [[CrossRef](#)]
19. Nauck, M.A.; Vardarli, I.; Deacon, C.F.; Holst, J.J.; Meier, J.J. Secretion of glucagon-like peptide-1 (GLP-1) in type 2 diabetes: What is up, what is down? *Diabetologia* **2011**, *54*, 10–18. [[CrossRef](#)]
20. Wilding, J. The role of the kidneys in glucose homeostasis in type 2 diabetes: Clinical implications and therapeutic significance through sodium glucose co-transporter 2 inhibitors. *Metabolism* **2014**, *63*, 1228–1237. [[CrossRef](#)]
21. Obici, S.; Zhang, B.B.; Karkanias, G.; Rossetti, L. Hypothalamic insulin signaling is required for inhibition of glucose production. *Nat. Med.* **2002**, *8*, 1376–1382. [[CrossRef](#)] [[PubMed](#)]
22. Garber, A.J. Long-Acting Glucagon-Like Peptide 1 Receptor Agonists: A review of their efficacy and tolerability. *Diabetes Care* **2011**, *34*, S279–S284. [[CrossRef](#)] [[PubMed](#)]
23. Aroda, V.R.; Ratner, R. The safety and tolerability of GLP-1 receptor agonists in the treatment of type 2 diabetes: A review. *Diabetes Metab. Res. Rev.* **2011**, *27*, 528–542. [[CrossRef](#)] [[PubMed](#)]
24. Abu-Hamdah, R.; Rabiee, A.; Meneilly, G.S.; Shannon, R.P.; Andersen, D.K.; Elahi, D. Clinical review: The extrapancreatic effects of glucagon-like peptide-1 and related peptides. *J. Clin. Endocrinol. Metab.* **2009**, *94*, 1843–1852. [[CrossRef](#)]
25. Drucker, D.J.; Meier, J.J. The incretin system: Glucagon-like peptide-1 receptor agonists and dipeptidyl peptidase-4 inhibitors in type 2 diabetes. *Lancet* **2006**, *368*, 1696–1705. [[CrossRef](#)]
26. Mooradian, A.D.; Chehade, J.; Thurman, J.E. The Role of Thiazolidinediones in the Treatment of Patients with Type 2 Diabetes Mellitus. *Treat. Endocrinol.* **2002**, *1*, 13–20. [[CrossRef](#)]
27. Inzucchi, S.E.; Bergenstal, R.M.; Buse, J.B.; Diamant, M.; Ferrannini, E.; Nauck, M.; Peters, A.L.; Tsapas, A.; Wender, R.; Matthews, D.R.; et al. Management of hyperglycemia in type 2 diabetes: A patient-centered approach: Position statement of the American Diabetes Association (ADA) and the European Association for the Study of Diabetes (EASD). *Diabetes Care* **2012**, *35*, 1364–1379. [[CrossRef](#)]
28. White, J.R., Jr. A Brief History of the Development of Diabetes Medications. *Diabetes Spectr.* **2014**, *27*, 82–86. [[CrossRef](#)]
29. Calcutt, N.A.; Cooper, M.E.; Kern, T.S.; Schmidt, A.M. Therapies for hyperglycaemia-induced diabetic complications: From animal models to clinical trials. *Nat. Rev. Drug Discov.* **2009**, *8*, 417–430. [[CrossRef](#)]
30. Al-Awar, A.; Kupai, K.; Veszelka, M.; Szűcs, G.; Attieh, Z.; Murlasits, Z.; Török, S.; Pósa, A.; Varga, C. Experimental Diabetes Mellitus in Different Animal Models. *J. Diabetes Res.* **2016**, *2016*, 9051426. [[CrossRef](#)]
31. Srinivasan, K.; RamaRao, P. Animal models in type 2 diabetes research: An overview. *Indian J. Med. Res.* **2007**, *125*, 451–472. [[PubMed](#)]
32. Takeda, Y.; Shimomura, T.; Asao, H.; Wakabayashi, I. Relationship between Immunological Abnormalities in Rat Models of Diabetes Mellitus and the Amplification Circuits for Diabetes. *J. Diabetes Res.* **2017**, *2017*, 4275851. [[CrossRef](#)] [[PubMed](#)]
33. Cefalu, W.T. Animal Models of Type 2 Diabetes: Clinical Presentation and Pathophysiological Relevance to the Human Condition. *ILAR J.* **2006**, *47*, 186–198. [[CrossRef](#)] [[PubMed](#)]
34. Zhuo, J.; Zeng, Q.; Cai, D.; Zeng, X.; Chen, Y.; Gan, H.; Huang, X.; Yao, N.; Huang, D.; Zhang, C. Evaluation of type 2 diabetic mellitus animal models via interactions between insulin and mitogen-activated protein kinase signaling pathways induced by a high fat and sugar diet and streptozotocin. *Mol. Med. Rep.* **2018**, *17*, 5132–5142. [[CrossRef](#)] [[PubMed](#)]

35. Guo, X.-X.; Wang, Y.; Wang, K.; Ji, B.-P.; Zhou, F. Stability of a type 2 diabetes rat model induced by high-fat diet feeding with low-dose streptozotocin injection. *J. Zhejiang Univ. Sci. B* **2018**, *19*, 559–569. [[CrossRef](#)]
36. Phillips, M.S.; Liu, Q.; Hammond, H.A.; Dugan, V.; Hey, P.J.; Caskey, C.T.; Hess, J.F. Leptin receptor missense mutation in the fatty Zucker rat. *Nat. Genet.* **1996**, *13*, 18–19. [[CrossRef](#)]
37. Pick, A.; Clark, J.; Kubstrup, C.; Levisetti, M.; Pugh, W.; Bonner-Weir, S.; Polonsky, K.S. Role of apoptosis in failure of beta-cell mass compensation for insulin resistance and beta-cell defects in the male Zucker diabetic fatty rat. *Diabetes* **1998**, *47*, 358–364. [[CrossRef](#)]
38. Tanaka, S.I.; Isoda, F.; Yamakawa, T.; Ishihara, M.; Sekihara, H. T Lymphopenia in Genetically Obese Rats. *Clin. Immunol. Immunopathol.* **1998**, *86*, 219–225. [[CrossRef](#)]
39. Ruth, M.R.; Taylor, C.G.; Zahradka, P.; Field, C.J. Abnormal Immune Responses in fa/fa Zucker Rats and Effects of Feeding Conjugated Linoleic Acid. *Obesity (Silver Spring)* **2008**, *16*, 1770–1779. [[CrossRef](#)]
40. Kawano, K.; Hirashima, T.; Mori, S.; Saitoh, Y.; Kurosumi, M.; Natori, T. Spontaneous long-term hyperglycemic rat with diabetic complications. Otsuka Long-Evans Tokushima Fatty (OLETF) strain. *Diabetes* **1992**, *41*, 1422–1428. [[CrossRef](#)] [[PubMed](#)]
41. Kawano, K.; Hirashima, T.; Mori, S.; Natori, T. OLETF (Otsuka Long-Evans Tokushima Fatty) rat: A new NIDDM rat strain. *Diabetes Res. Clin. Pract.* **1994**, *24*, S317–S320. [[CrossRef](#)]
42. Lee, M.Y.; Shim, M.S.; Kim, B.H.; Hong, S.W.; Choi, R.; Lee, E.Y.; Nam, S.M.; Kim, G.W.; Shin, J.Y.; Shin, Y.G.; et al. Effects of Spironolactone and Losartan on Diabetic Nephropathy in a Type 2 Diabetic Rat Model. *Diabetes Metab. J.* **2011**, *35*, 130–137. [[CrossRef](#)] [[PubMed](#)]
43. Dirkes, R.K.; Ortinau, L.C.; Rector, R.S.; Olver, T.D.; Hinton, P.S. Insulin-Stimulated Bone Blood Flow and Bone Biomechanical Properties Are Compromised in Obese, Type 2 Diabetic OLETF Rats. *JBMR Plus* **2017**, *1*, 116–126. [[CrossRef](#)] [[PubMed](#)]
44. Ortinau, L.C.; Linden, M.A.; Rector, R.S.; Hinton, P.S. Exercise improves femoral whole-bone and tissue-level biomechanical properties in hyperphagic OLETF rats. *Appl. Physiol. Nutr. Metab.* **2017**, *42*, 884–892. [[CrossRef](#)] [[PubMed](#)]
45. Goto, Y.; Kakizaki, M.; Masaki, N.; Goto, Y.; Goto, Y. Production of Spontaneous Diabetic Rats by Repetition of Selective Breeding. *Tohoku J. Exp. Med.* **1976**, *119*, 85–90. [[CrossRef](#)]
46. Kawano, K.; Hirashima, T.; Mori, S.; Saitoh, Y.; Kurosumi, M.; Natori, T. An early insulin intervention accelerates pancreatic beta-cell dysfunction in young Goto-Kakizaki rats, a model of naturally occurring noninsulin-dependent diabetes. *Endocrinology* **1997**, *138*, 1106–1110.
47. Suzuki, S.; Toyota, T. GK rat. *Nihon Rinsho.* **1998**, *56* (Suppl. 3), 695–699.
48. Agardh, C.-D.; Agardh, E.; Hultberg, B.; Qian, Y.; Östenson, C.-G. The glutathione levels are reduced in Goto-Kakizaki rat retina, but are not influenced by aminoguanidine treatment. *Curr. Eye Res.* **1998**, *17*, 251–256. [[CrossRef](#)]
49. Murakawa, Y.; Zhang, W.; Pierson, C.R.; Brismar, T.; Ostenson, C.-G.; Efendic, S.; Sima, A.A.F. Impaired glucose tolerance and insulinopenia in the GK-rat causes peripheral neuropathy. *Diabetes Metab. Res. Rev.* **2002**, *18*, 473–483. [[CrossRef](#)]
50. Homo-Delarche, F.; Calderari, S.; Irminger, J.-C.; Gangnerau, M.-N.; Coulaud, J.; Rickenbach, K.; Dolz, M.; Halban, P.; Portha, B.; Serradas, P. Islet Inflammation and Fibrosis in a Spontaneous Model of Type 2 Diabetes, the GK Rat. *Diabetes* **2006**, *55*, 1625–1633. [[CrossRef](#)]
51. Salehi, A.; Henningsson, R.; Mosen, H.; Ostenson, C.G.; Efendic, S.; Lundquist, I. Dysfunction of the islet lysosomal system conveys impairment of glucose-induced insulin release in the diabetic GK rat. *Endocrinology* **1999**, *140*, 3045–3053. [[CrossRef](#)] [[PubMed](#)]
52. Dadke, S.S.; Li, H.C.; Kusari, A.B.; Begum, N.; Kusari, J. Elevated Expression and Activity of Protein-Tyrosine Phosphatase 1B in Skeletal Muscle of Insulin-Resistant Type II Diabetic Goto-Kakizaki Rats. *Biochem. Biophys. Res. Commun.* **2000**, *274*, 583–589. [[CrossRef](#)] [[PubMed](#)]
53. Kobayashi, T.; Nemoto, S.; Ishida, K.; Taguchi, K.; Matsumoto, T.; Kamata, K. Involvement of CaM kinase II in the impairment of endothelial function and eNOS activity in aortas of Type 2 diabetic rats. *Clin. Sci.* **2012**, *123*, 375–386. [[CrossRef](#)] [[PubMed](#)]
54. Furman, B.L. Streptozotocin-Induced Diabetic Models in Mice and Rats. *Curr. Protoc. Pharmacol.* **2015**, *70*, 1–20. [[CrossRef](#)] [[PubMed](#)]
55. Lenzen, S. The mechanisms of alloxan- and streptozotocin-induced diabetes. *Diabetologia* **2008**, *51*, 216–226. [[CrossRef](#)]

56. Reed, M.; Meszaros, K.; Entes, L.; Claypool, M.; Pinkett, J.; Gadbois, T.; Reaven, G. A new rat model of type 2 diabetes: The fat-fed, streptozotocin-treated rat. *Metabolism* **2000**, *49*, 1390–1394. [\[CrossRef\]](#)
57. Srinivasan, K.; Viswanad, B.; Asrat, L.; Kaul, C.; Poduri, R. Combination of high-fat diet-fed and low-dose streptozotocin-treated rat: A model for type 2 diabetes and pharmacological screening. *Pharmacol. Res.* **2005**, *52*, 313–320. [\[CrossRef\]](#)
58. Zhang, M.; Lv, X.-Y.; Li, J.; Xu, Z.-G.; Chen, L. The Characterization of High-Fat Diet and Multiple Low-Dose Streptozotocin Induced Type 2 Diabetes Rat Model. *Exp. Diabetes Res.* **2009**, *2008*, 704045. [\[CrossRef\]](#)
59. Guo, Z.; Zhang, R.; Li, J.; Xu, G. Effect of telmisartan on the expression of adiponectin receptors and nicotinamide adenine dinucleotide phosphate oxidase in the heart and aorta in type 2 diabetic rats. *Cardiovasc. Diabetol.* **2012**, *11*, 94. [\[CrossRef\]](#)
60. Hu, C.; Zhang, G.; Sun, D.; Han, H.; Hu, S. Duodenal-jejunal Bypass Improves Glucose Metabolism and Adipokine Expression Independently of Weight Loss in a Diabetic Rat Model. *Obes. Surg.* **2013**, *23*, 1436–1444. [\[CrossRef\]](#)
61. Dong, Y.; Chen, Y.-T.; Yang, Y.-X.; Zhou, X.-J.; Dai, S.-J.; Tong, J.-F.; Shou, D.; Li, C. Metabolomics Study of Type 2 Diabetes Mellitus and the AntiDiabetic Effect of Berberine in Zucker Diabetic Fatty Rats Using Uplc-ESI-Hdms. *Phytother. Res.* **2016**, *30*, 823–828. [\[CrossRef\]](#)
62. Wang, S.; He, B.; Hang, W.; Wu, N.; Xia, L.; Wang, X.; Zhang, Q.; Zhou, X.; Feng, Z.; Chen, Q.; et al. Berberine Alleviates Tau Hyperphosphorylation and Axonopathy-Associated with Diabetic Encephalopathy via Restoring PI3K/Akt/GSK3beta Pathway. *J. Alzheimers Dis.* **2018**, *65*, 1385–1400. [\[CrossRef\]](#)
63. Guo, C.; Zhang, C.-F.; Li, L.; Wang, Z.; Xiao, W.; Yang, Z. Hypoglycemic and hypolipidemic effects of oxymatrine in high-fat diet and streptozotocin-induced diabetic rats. *Phytomedicine* **2014**, *21*, 807–814. [\[CrossRef\]](#)
64. Goboza, M.; Aboua, Y.G.; Chegou, N.N.; Oguntibeju, O.O. Vindoline effectively ameliorated diabetes-induced hepatotoxicity by docking oxidative stress, inflammation and hypertriglyceridemia in type 2 diabetes-induced male Wistar rats. *Biomed. Pharmacother.* **2019**, *112*. [\[CrossRef\]](#)
65. Ren, B.; Qin, W.; Wu, F.; Wang, S.; Pan, C.; Wang, L.; Zeng, B.; Ma, S.; Liang, J. Apigenin and naringenin regulate glucose and lipid metabolism, and ameliorate vascular dysfunction in type 2 diabetic rats. *Eur. J. Pharmacol.* **2016**, *773*, 13–23. [\[CrossRef\]](#) [\[PubMed\]](#)
66. Liu, J.; Tang, Y.; Feng, Z.; Long, J. (–)-Epigallocatechin-3-gallate attenuated myocardial mitochondrial dysfunction and autophagy in diabetic Goto-Kakizaki rats. *Free Radic. Res.* **2014**, *48*, 898–906. [\[CrossRef\]](#)
67. Luo, C.; Yang, H.; Tang, C.; Yao, G.; Kong, L.; He, H.; Zhou, Y. Kaempferol alleviates insulin resistance via hepatic IKK/NF-kappaB signal in type 2 diabetic rats. *Int. Immunopharmacol.* **2015**, *28*, 744–750. [\[CrossRef\]](#) [\[PubMed\]](#)
68. Sundaram, R.; Shanthi, P.; Sachdanandam, P. Effect of tangeretin, a polymethoxylated flavone on glucose metabolism in streptozotocin-induced diabetic rats. *Phytomedicine* **2014**, *21*, 793–799. [\[CrossRef\]](#) [\[PubMed\]](#)
69. Sarkar, P.; Bhowmick, A.; Kalita, M.C.; Banu, S. Effects of Resveratrol and Mangiferin on PPARgamma and FALDH Gene Expressions in Adipose Tissue of Streptozotocin-Nicotinamide-Induced Diabetes in Rats. *J. Diet. Suppl.* **2019**, *16*, 659–675. [\[CrossRef\]](#) [\[PubMed\]](#)
70. Li, Q.; Deng, S.; Zhou, X.; Yu, X.; Chen, Z. Protection of Curcumin against Streptozotocin-Induced Pancreatic Cell Destruction in T2D Rats. *Planta Med.* **2020**, *86*, 113–120.
71. Xu, W.; Liu, J.; Ma, D.; Yuan, G.; Lu, Y.; Yang, Y. Capsaicin reduces Alzheimer-associated tau changes in the hippocampus of type 2 diabetes rats. *PLoS ONE* **2017**, *12*, e0172477. [\[CrossRef\]](#) [\[PubMed\]](#)
72. Khanra, R.; Bhattacharjee, N.; Dua, T.K.; Nandy, A.; Saha, A.; Kalita, J.; Manna, P.; Dewanjee, S. Taraxerol, a pentacyclic triterpenoid, from *Abroma augusta* leaf attenuates diabetic nephropathy in type 2 diabetic rats. *Biomed. Pharmacother.* **2017**, *94*, 726–741. [\[CrossRef\]](#) [\[PubMed\]](#)
73. Tian, Z.; Ren, N.; Wang, J.; Zhang, D.; Zhou, Y. Ginsenoside Ameliorates Cognitive Dysfunction in Type 2 Diabetic Goto-Kakizaki Rats. *Med. Sci. Monit.* **2018**, *24*, 3922–3928. [\[CrossRef\]](#) [\[PubMed\]](#)
74. Thakur, V.; Nargis, S.; Gonzalez, M.; Pradhan, S.; Terreros, D.; Chattopadhyay, M. Role of Glycyrrhizin in the Reduction of Inflammation in Diabetic Kidney Disease. *Nephron* **2017**, *137*, 137–147. [\[CrossRef\]](#)
75. Maiti, M.; Kumar, G.S. Polymorphic Nucleic Acid Binding of Bioactive Isoquinoline Alkaloids and Their Role in Cancer. *J. Nucleic Acids* **2009**, *2010*. [\[CrossRef\]](#)
76. Agrawal, R.; Sethiya, N.K.; Mishra, S.H. Antidiabetic activity of alkaloids of *Aerva lanata* roots on streptozotocin-nicotinamide induced type-II diabetes in rats. *Pharm. Biol.* **2013**, *51*, 635–642. [\[CrossRef\]](#)



77. Testa, R.; Bonfigli, A.R.; Genovese, S.; De Nigris, V.; Ceriello, A. The Possible Role of Flavonoids in the Prevention of Diabetic Complications. *Nutrients* **2016**, *8*, 310. [\[CrossRef\]](#)
78. Bahadoran, Z.; Mirmiran, P.; Azizi, F. Dietary polyphenols as potential nutraceuticals in management of diabetes: A review. *J. Diabetes Metab. Disord.* **2013**, *12*, 43. [\[CrossRef\]](#)
79. Jung, U.J.; Lee, M.K.; Jeong, K.S.; Choi, M.S. The hypoglycemic effects of hesperidin and naringin are partly mediated by hepatic glucose-regulating enzymes in C57BL/KsJ-db/db mice. *J. Nutr.* **2004**, *134*, 2499–2503. [\[CrossRef\]](#)
80. Mahmoud, A.M.; Ashour, M.B.; Abdel-Moneim, A.; Ahmed, O.M. Hesperidin and naringin attenuate hyperglycemia-mediated oxidative stress and proinflammatory cytokine production in high fat fed/streptozotocin-induced type 2 diabetic rats. *J. Diabetes Complicat.* **2012**, *26*, 483–490. [\[CrossRef\]](#)
81. Wang, Y.-B.; Ge, Z.-M.; Kang, W.-Q.; Lian, Z.-X.; Yao, J.; Zhou, C.-Y. Rutin alleviates diabetic cardiomyopathy in a rat model of type 2 diabetes. *Exp. Ther. Med.* **2015**, *9*, 451–455. [\[CrossRef\]](#) [\[PubMed\]](#)
82. Niture, N.T.; Ansari, A.A.; Naik, S.R. Anti-hyperglycemic activity of rutin in streptozotocin-induced diabetic rats: An effect mediated through cytokines, antioxidants and lipid biomarkers. *Indian J. Exp. Boil.* **2014**, *52*, 720–727.
83. Koch, W. Dietary Polyphenols-Important Non-Nutrients in the Prevention of Chronic Noncommunicable Diseases. A Systematic Review. *Nutrients* **2019**, *11*, 1039. [\[CrossRef\]](#) [\[PubMed\]](#)
84. Kasiotis, K.M.; Pratsinis, H.; Kletsas, D.; Haroutounian, S.A. Resveratrol and related stilbenes: Their anti-aging and anti-angiogenic properties. *Food Chem. Toxicol.* **2013**, *61*, 112–120. [\[CrossRef\]](#)
85. Mirzaei, H.; Shakeri, A.; Rashidi, B.; Jalili, A.; Banikazemi, Z.; Yaribeygi, H. Phytosomal curcumin: A review of pharmacokinetic, experimental and clinical studies. *Biomed. Pharmacother.* **2017**, *85*, 102–112. [\[CrossRef\]](#) [\[PubMed\]](#)
86. Daugherty, D.J.; Marquez, A.; Calcutt, N.A.; Schubert, D. A novel curcumin derivative for the treatment of diabetic neuropathy. *Neuropharmacology* **2018**, *129*, 26–35. [\[CrossRef\]](#) [\[PubMed\]](#)
87. Patel, S.S.; Udayabanu, M. Effect of natural products on diabetes associated neurological disorders. *Rev. Neurosci.* **2017**, *28*, 271–293. [\[CrossRef\]](#)
88. Faheem, N.M.; El-Askary, A. Neuroprotective role of curcumin on the hippocampus against the structural and serological alterations of streptozotocin-induced diabetes in Sprague Dawely rats. *Iran. J. Basic Med. Sci.* **2017**, *20*, 690–699.
89. Wu, Y.; Wang, F.; Reece, E.A.; Yang, P. Curcumin ameliorates high glucose-induced neural tube defects by suppressing cellular stress and apoptosis. *Am. J. Obstet. Gynecol.* **2015**, *212*, 802.e1–802.e8. [\[CrossRef\]](#)
90. Shehzad, A.; Ha, T.; Subhan, F.; Lee, Y.S. New mechanisms and the anti-inflammatory role of curcumin in obesity and obesity-related metabolic diseases. *Eur. J. Nutr.* **2011**, *50*, 151–161. [\[CrossRef\]](#)
91. Caterina, M.J.; Schumacher, M.A.; Tominaga, M.; Rosen, T.A.; Levine, J.D.; Julius, D. The capsaicin receptor: A heat-activated ion channel in the pain pathway. *Nat. Cell Biol.* **1997**, *389*, 816–824. [\[CrossRef\]](#) [\[PubMed\]](#)
92. Mezey, E.; Toth, Z.E.; Cortright, D.N.; Arzubi, M.K.; Krause, J.E.; Elde, R.; Guo, A.; Blumberg, P.M.; Szallasi, A. Distribution of mRNA for vanilloid receptor subtype 1 (VR1), and VR1-like immunoreactivity, in the central nervous system of the rat and human. *Proc. Natl. Acad. Sci. USA* **2000**, *97*, 3655–3660. [\[CrossRef\]](#)
93. Derbenev, A.V.; Zsombok, A. Potential therapeutic value of TRPV1 and TRPA1 in diabetes mellitus and obesity. *Semin. Immunopathol.* **2016**, *38*, 397–406. [\[CrossRef\]](#) [\[PubMed\]](#)
94. Gong, H.; He, Z.; Peng, A.; Zhang, X.; Cheng, B.; Sun, Y.; Zheng, L.; Huang, K. Effects of several quinones on insulin aggregation. *Sci. Rep.* **2014**, *4*, 5648. [\[CrossRef\]](#) [\[PubMed\]](#)
95. Guo, M.-Z.; Li, X.-S.; Shen, D.-M.; Guan, X.-Q.; Xu, H.-R.; Gao, J. Effect of Rhein on the development of hepatic fibrosis in rats. *Zhonghua Gan Zang Bing Za Zhi* **2003**, *11*, 26–29. [\[PubMed\]](#)
96. Du, H.; Shao, J.-Q.; Gu, P.; Wang, J.; Liu, Z. Effect of early intervention with rhein on islet function in db/db mice. *Nan Fang Yi Ke Da Xue Xue Bao* **2011**, *31*, 1526–1529.
97. Heo, S.-K.; Yun, H.-J.; Park, W.-H.; Park, S.-D. Rhein Inhibits TNF- $\alpha$ -Induced Human Aortic Smooth Muscle Cell Proliferation via Mitochondrial-Dependent Apoptosis. *J. Vasc. Res.* **2009**, *46*, 375–386. [\[CrossRef\]](#)
98. Shi, P.; Huang, Z.; Chen, G. Rhein Induces Apoptosis and Cell Cycle Arrest in Human Hepatocellular Carcinoma BEL-7402 Cells. *Am. J. Chin. Med.* **2008**, *36*, 805–813. [\[CrossRef\]](#)
99. Bordone, L.; Motta, M.C.; Picard, F.; Robinson, A.; Jhala, U.S.; Apfeld, J.; McDonagh, T.; Lemieux, M.; McBurney, M.; Szilvasi, A.; et al. Sirt1 regulates insulin secretion by repressing UCP2 in pancreatic beta cells. *PLoS Biol.* **2006**, *4*, e31. [\[CrossRef\]](#)



100. Picard, F.; Kurtev, M.; Chung, N.; Topark-Ngarm, A.; Senawong, T.; Machado De Oliveira, R.; Leid, M.; McBurney, M.W.; Guarente, L. Sirt1 promotes fat mobilization in white adipocytes by repressing PPAR- $\gamma$ . *Nature* **2004**, *429*, 771–776. [[CrossRef](#)]
101. Gerhart-Hines, Z.; Rodgers, J.T.; Bare, O.; Lerin, C.; Kim, S.-H.; Mostoslavsky, R.; Alt, F.W.; Wu, Z.; Puigserver, P. Metabolic control of muscle mitochondrial function and fatty acid oxidation through SIRT1/PGC-1 $\alpha$ . *EMBO J.* **2007**, *26*, 1913–1923. [[CrossRef](#)] [[PubMed](#)]
102. Lee, M.S.; Sohn, C.B. Anti-diabetic Properties of Chrysophanol and Its Glucoside from Rhubarb Rhizome. *Biol. Pharm. Bull.* **2008**, *31*, 2154–2157. [[CrossRef](#)] [[PubMed](#)]
103. Kim, S.J.; Kim, M.C.; Lee, B.J.; Park, D.H.; Hong, S.H.; Um, J.Y. Anti-Inflammatory activity of chrysophanol through the suppression of NF- $\kappa$ B/caspase-1 activation in vitro and in vivo. *Molecules* **2010**, *15*, 6436–6451. [[CrossRef](#)] [[PubMed](#)]
104. Prateeksha; Yusuf, M.A.; Singh, B.N.; Sudheer, S.; Kharwar, R.N.; Siddiqui, S.; Abdel-Azeem, A.M.; Fraceto, L.F.; Dashora, K.; Gupta, V.K. Chrysophanol: A Natural Anthraquinone with Multifaceted Biotherapeutic Potential. *Biomolecules* **2019**, *9*, 68. [[CrossRef](#)]
105. Xue, P.; Zhao, J.; Zheng, A.; Li, L.; Chen, H.; Tu, W.; Zhang, N.; Yu, Z.; Wang, Q.; Gu, M. Chrysophanol alleviates myocardial injury in diabetic db/db mice by regulating the SIRT1/HMGB1/NF- $\kappa$ B signaling pathway. *Exp. Ther. Med.* **2019**, *18*, 4406–4412.
106. Zhang, J.; Kang, H.; Wang, L.; Zhao, X. Chrysophanol ameliorates high-fat diet-induced obesity and inflammation in neonatal rats. *Die Pharm.* **2018**, *73*, 228–233.
107. Bhattacharjee, N.; Barma, S.; Konwar, N.; Dewanjee, S.; Manna, P. Mechanistic insight of diabetic nephropathy and its pharmacotherapeutic targets: An update. *Eur. J. Pharmacol.* **2016**, *791*, 8–24. [[CrossRef](#)]
108. Cooper, M.E. Interaction of metabolic and haemodynamic factors in mediating experimental diabetic nephropathy. *Diabetologia* **2001**, *44*, 1957–1972. [[CrossRef](#)]
109. Luis-Rodríguez, D.; Martínez-Castelao, A.; Gorris, J.L.; De-Álvarez, F.; Navarro-González, J.F. Pathophysiological role and therapeutic implications of inflammation in diabetic nephropathy. *World J. Diabetes* **2012**, *3*, 7–18. [[CrossRef](#)]

**Publisher’s Note:** MDPI stays neutral with regard to jurisdictional claims in published maps and institutional affiliations.



© 2020 by the authors. Licensee MDPI, Basel, Switzerland. This article is an open access article distributed under the terms and conditions of the Creative Commons Attribution (CC BY) license (<http://creativecommons.org/licenses/by/4.0/>).